NAVAL REACTORS PHYSICS HANDBOOK

VOLUME I

Selected Basic Techniques

DISCLAIMER

Portions of this document may be illegible in electronic image products. Images are produced from the best available original document.

NAVAL REACTORS HANDBOOKS

Liquid Metals Handbook.

First edition: Edited by R. N. Lyon, June 1950.

Second edition: Edited by R. N. Lyon, June 1952.

Third edition: (Sodium-NaK Supplement) Edited by C. B. Jackson. First printing June 1955; second printing (Revised), November 1955 (Available from Superintendent of Documents, Washington, D. C., 20402).

Metallurgy of Zirconium. Edited by B. Lustman and F. Kerze, Jr., July 1955 (Published by McGraw-Hill Book Company, New York).

The Metal Beryllium. Edited by D. W. White and J. E. Burke, July 1955 (Published by American Society for Metals, Cleveland).

Bibliography of Reactor Computer Codes, Report AECU-3078. Edited by R. S. Brodsky, December 1955 (Available from Superintendent of Documents, Washington, D. C., 20402—This compilation is being kept current by the Nuclear Codes Group Quarterly Newsletter—Inquiries should be sent c/o AEC Computing Facility, New York University).

Reactor Shielding Design Manual. Edited by T. Rockwell III, March 1956 (Published separately by Government Printing Office, McGraw-Hill Book Company, New York, and D. Van Nostrand Company, Princeton, New Jersey).

Corrosion and Wear Handbook for Water-Cooled Reactors. Edited by D. J. DePaul, March 1957 (Published separately by Government Printing Office and McGraw-Hill Book Company, New York).

Naval Reactors Physics Handbook. A. Radkowsky, Chairman of Editorial Board.

Volume I	Selected Basic Techniques. Edited by A. Radkowsky (Available from Superintendent of Documents, Washington, D. C., 20402).
Volume II	The Physics of Pressurized Water Reactors. Edited by S. Krasik, February 1959 (Classified Edition only, Volume I includes an updated discussion of those portions of Volume II which are of general interest).
Volume III	The Physics of Intermediate Spectrum Reactors. Edited by J. R. Stehn, September 1958 (Available from Superintendent of Documents, Washington, D. C., 20402).

The Shippingport Pressurized Water Reactor. Naval Reactors, Westinghouse Electric Corporation, and Duquesne Light Company, September 1958 (Published by Addison-Wesley Publishing Company).

The Metallurgy of Hafnium. Edited by D. E. Thomas and E. T. Hayes (Available from Superintendent of Documents, Washington, D.C. 20402).

Uranium Dioxide: Properties and Nuclear Applications. Edited by J. Belle, July 1961 (Available from Superintendent of Documents, Washington D. C., 20402).

Neutron Absorber Materials for Reactor Control. Edited by W. K. Anderson and J. S. Theilacker, January 1962 (Available from Superintendent of Documents, Washington, D.C., 20402).

NAVAL REACTORS PHYSICS HANDBOOK

VOLUME I

Selected Basic Techniques

Volume Editor

A. RADKOWSKY

1964

Naval Reactors, Division of Reactor Development
United States Atomic Energy Commission

EDITORIAL BOARD

This is the first volume of the Naval Reactors Physics Handbook, sponsored by the Naval Reactors office of the Atomic Energy Commission. This volume has been edited by an Editorial Board consisting of the following members:

A. Radkowsky, Chairman
Naval Reactors, A.E.C.

R. J. Breen
Bettis Atomic Power Laboratory*

R. Ehrlich
Knolls Atomic Power Laboratory

D. N. Schmoker
Naval Reactors, A.E.C.

D. S. Selengut
Knolls Atomic Power Laboratory

J. J. Taylor
Bettis Atomic Power Laboratory*

Others who have served on the Editorial Board for the Naval Reactors Physics Handbook:

J. R. Feldmeier
(Formerly, Bettis Atomic Power Laboratory*)

H. L. Garabedian
(Formerly, Bettis Atomic Power Laboratory*)

A. F. Henry
Bettis Atomic Power Laboratory*

H. Hurwitz, Jr.
(Formerly, Knolls Atomic Power Laboratory†)

S. Krasik
(Formerly, Bettis Atomic Power Laboratory*)

G. Mechlin
(Formerly, Bettis Atomic Power Laboratory*)

H. D. Nine
(Formerly, Naval Reactors, A.E.C.)

J. R. Stehn
(Formerly, Knolls Atomic Power Laboratory†)

P. E. Zweifel
(Formerly, Knolls Atomic Power Laboratory†)

*Operated by the Westinghouse Electric Corporation for the Atomic Energy Commission.
†Operated by the General Electric Company for the Atomic Energy Commission.

FOREWORD

The Naval Reactors Physics Handbook, seventh in a series of handbooks on basic reactor technology developed under the sponsorship of the Office of Naval Reactors of the Atomic Energy Commission, presents the analytical and experimental physics techniques which have been developed for the reactors designed in the Naval and Shippingport (PWR) Reactor Programs. Reactor physics has been strongly emphasized in these programs, and extensive experimental and computational facilities have been developed. Further, particular attention has been paid to obtaining from reactor operations as much physics information as possible. Prototype reactors have been carefully instrumented and an extensive series of physics tests have been carried out with the twofold objective of confirming and refining the physics calculations used in each particular reactor design and of obtaining increased general understanding of reactors.

Power reactors must meet many stringent requirements, such as size limitation, stability, and reliability. Above all, changes cannot be made in a finished core to compensate for design error. The fundamental importance of reactor physics in introducing new concepts and in establishing reactor parameters such as those relating to fuel loading, startup, control, power distribution, safety, and endurance is widely recognized. What is perhaps less well understood is the need for constant interplay of mechanical, metallurgical, and plant considerations with those of reactor physics to provide a well-balanced design. Close coordination of these elements has been stressed in the Naval Reactors and Shippingport Programs from their inception.

The physics methods described in these volumes are characterized by having been of direct utility in the design of actual power reactors. In addition, basic reactor theory developed in the Naval Reactors laboratories for the Naval Reactors and Shippingport Programs is covered. This includes many areas of reactor physics which have long presented particular difficulty, for example, the calculation of thermal neutron spectra, control rod effectiveness, self-shielding and transport effects, temperature coefficients of reactivity, and flux stability. Much of this work is applicable to many other types of reactors. It has been gratifying to note the widespread use of Naval Reactor computer codes throughout the reactor industry.

While I am pleased with the advances in physics which have been made in the course of the Naval Reactors and Shippingport Programs, I am not satisfied because I know that a great deal more must be done to improve our understanding of reactors and our ability to design them for longer life, more uniform power distribution, simpler control, greater safety, and more effective utilization of the fuel. I hope that by publishing our available data and techniques in these volumes we will provide impetus toward the solution of many of the basic reactor physics problems still outstanding.

My appreciation goes to the many who have given their time to the preparation, review, and editing of this book.

H. G. Rickover
Manager, Naval Reactors
Division of Reactor Development
U. S. Atomic Energy Commission

EDITOR'S PREFACE

The purpose of this work is to present the most pertinent parts of the body of physics knowledge which has been built up in the course of the Naval and Shippingport (PWR) Reactor Programs, with the aim of providing a background of understanding for those interested in nuclear core design. Much of the material has already been published either in scientific journals or in topical laboratory reports; scientists engaged in the Naval Reactors Program, as elsewhere, are encouraged to report their work in the normal manner. However, as is usual in rapidly expanding programs, much data have remained in the form of internal memoranda and other informal communications. It was felt to be desirable and timely to review and recapitulate the work which has been done on these programs and to make it available in convenient and readily applicable form. Wherever practicable, the chapters in these volumes have been prepared by authors who actively participated in the developments discussed.

Volume I of this handbook was planned to bring together topics in the basic theoretical and experimental material which are of especially wide interest, including those common to both thermal and intermediate neutron energy reactor types. The physics design of light water-moderated and -cooled reactors is covered in Volume II (classified), and that of intermediate neutron-energy power reactors in Volume III.

A brief explanation is necessary to explain the order in which these volumes have been issued. Originally, it was intended to publish the volumes in numerical order. However, the termination of Naval Reactors Programs on intermediate spectrum sodium-cooled reactors made it desirable to issue Volume III first while the team of scientists engaged in the intermediate spectrum work was still intact. Volume II was then issued shortly thereafter to make available an equivalent status of information on the design of light water power reactors. Advantage has been taken of the time lag in issuing Volume I to include an updated discussion of those portions of Volume II which are of general interest. The emphasis in Volume I is thus on light water reactor systems, and as many recent advances in reactor physics of the Naval and Shippingport Reactor Programs as possible have been included.

In connection with the responsibility for these volumes, it should be mentioned that all members of the Editorial Board have participated fully in this work by reading all chapters

and providing detailed comments. Reactor physics today is such a rapidly growing field that future editions of this handbook will undoubtedly be necessary. Criticism and suggestions by the readers will be welcomed and, if practicable, incorporated in later editions.

The writer wishes to express his appreciation to Vice Admiral H. G. Rickover for suggesting the preparation of this handbook and for giving encouragement at all times. Special thanks are also due to Theodore Rockwell, III, Technical Director, Naval Reactors, for many helpful suggestions. Finally, the writer is most grateful to all members of the Editorial Board and to all authors and chapter editors whose effort was essential to the preparation of these volumes.

A. Radkowsky
Chairman, Editorial Board
Naval Reactors Physics Handbook

TABLE OF CONTENTS

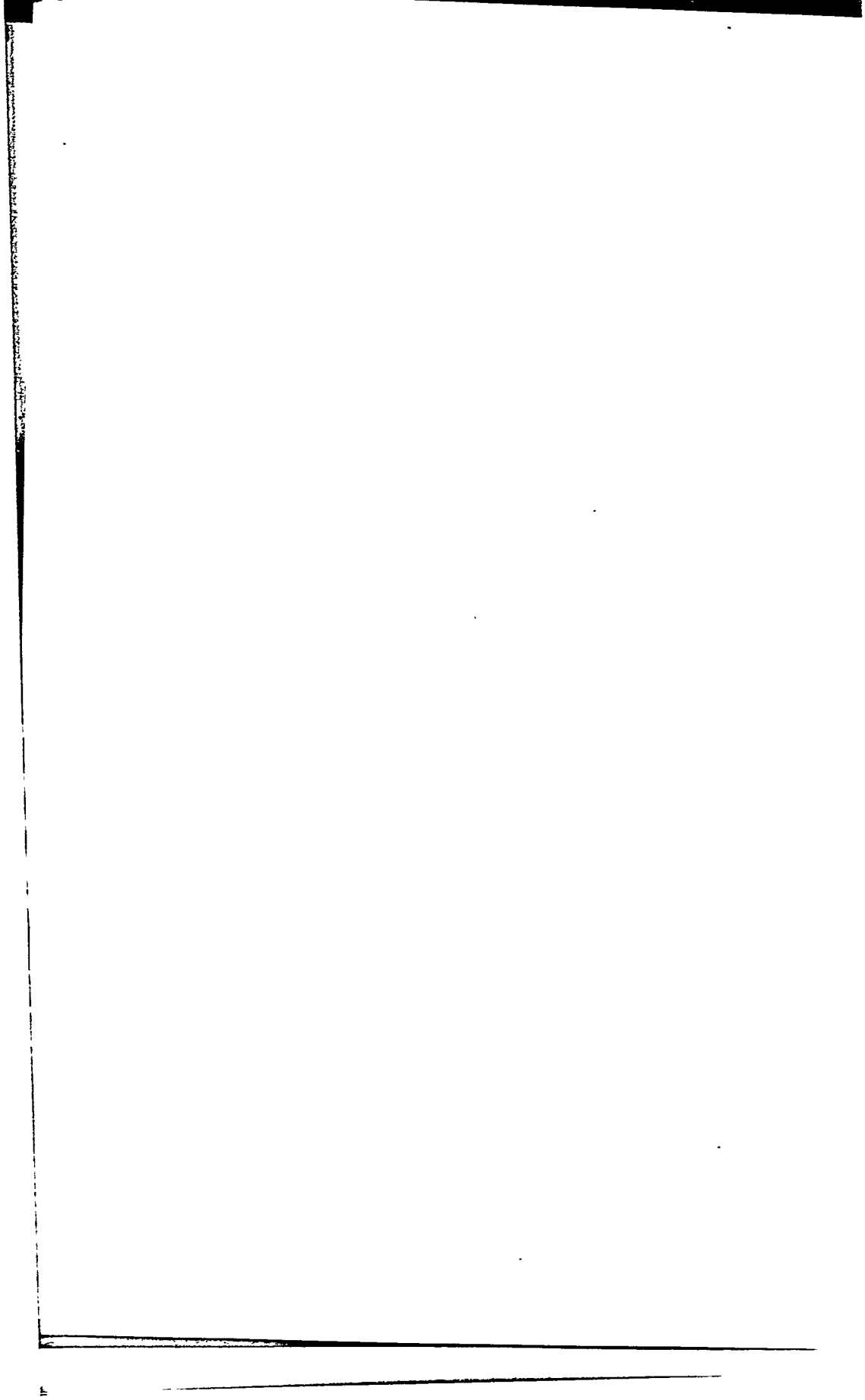

depletion effects, other than those due to transient fission product poisons, could be treated as perturbations. As a result, treatments based on age diffusion theory were adequate for the description of such cores. All calculations were performed on desk calculators.

At about this time several reactor design efforts of particular significance for the Naval Reactor program were begun. One of these, the power breeder program at the Knolls Atomic Power Laboratory (KAPL), consisted of reactor studies partly or primarily in the neutron intermediate energy spectrum. The KAPL program was subsequently reoriented towards the design of a naval reactor operating in the intermediate spectrum. Another design effort begun about this time was that of a small light-water power reactor, the prototype of the first Naval Reactor (STR). The work originated at the Oak Ridge National Laboratory and was transferred to the Argonne National Laboratory. Subsequent STR design work was carried out at the Bettis Atomic Power Laboratory. The development of light-water reactors for the Naval Reactors and Shippingport programs has continued at Bettis, KAPL, and the Naval Reactors Division of Combustion Engineering Corporation.

In each of these development programs of high performance cores the reactor properties have determined the direction and emphasis of the physics efforts.

For cores of the types studied at KAPL and elsewhere, in which fissions occurred principally at intermediate neutron energies, neutron multigroup analysis was developed. A basic treatment of multigroup diffusion theory is given in Chap. 2 of this volume, and Vol. III of this handbook gives a detailed account of the physics of intermediate energy spectrum reactors. While the Naval Reactors program at the present time utilizes light-water cooling and moderation, the fuel loading densities are often sufficiently high that a substantial fraction of the fissions occurs above thermal neutron energies. Hence, much of the physics work required for describing the intermediate energy spectrum is useful for light-water reactors. Advances in the following areas have been of particular benefit:

Statistical theory of resonances of fission products (Chap. 4).
Theory and direct measurement of Doppler broadening of resonances (Chap. 2 and Vol. III).
Interpretation of adjoints and calculation of reactivity coefficients (Chap. 5).
Self-shielding of resonances (Chaps. 2 and 4).
Critical assembly experimentation (Chap. 6).

1.2 REACTOR PHYSICS AND NUCLEAR DESIGN OF NAVAL REACTORS

In early cores of low fuel and poison loading, the high moderating power of light water produced a neutron spectrum quite closely thermal, and a two-group (or at most a four-group) treatment was considered appropriate. However, a major problem was presented as to the proper group parameters to be used; great effort has gone into the solution of this problem. Chapter 2 of this volume treats the calculation of parameters for fast neutrons, and Chap. 3 for thermal neutrons.

In the case of the fast group it was known that the continuous slowing-down model in use for heavy moderators would be inaccurate for hydrogen moderators. More suitable models for hydrogen slowing down were utilized. This work was supplemented by experimental determinations of the slowing-down distribution in light-water metal mixtures. A second difficulty was that, as a result of the high leakage in the cores being designed, the fast neutron spectrum was quite different from that in an infinite medium. In this case, since the fast neutron spectrum does not vary rapidly from point to point in the core, it is a good approximation for the purpose of computing parameters to assume a sinusoidal space dependence of the flux with a geometric buckling equal to that of the average material buckling in the region of interest. The multigroup treatment then becomes mathematically the same as the normal mode spectrum calculation for an infinite medium. The calculation yields the neutron spectrum appropriate to the region and, by averaging the energy-dependent cross sections over the spectrum, the fast group parameters can be obtained.

The importance of inelastic scattering by heavy elements in slowing down was recognized early, but accurate treatments were held back by lack of experimental data. In recent years a great many measurements have been made and, furthermore, an extensive program for calculating such cross sections has been developed. The calculation program is covered in Chap. 2 for elements of particular interest to the Naval Reactors program.

In the thermal energy region a formidable problem was presented by the rapid change in hydrogen binding and cross section with neutron energy. The Radkowsky prescription furnished a phenomenological method of obtaining the thermal transport mean free path from the measured variation of the hydrogen cross section with neutron energy. Since these core types had much greater thermal macroscopic absorption than the natural uranium graphite cores, it was necessary to take into account the deviation of the thermal spectrum from a

Maxwell distribution due to absorptions occurring before the neutrons could come into thermal equilibrium with the moderator. This was accomplished by application of the Wigner-Wilkins formalism and improved models.

Because of the small slowing-down length in light-water cores and the large amounts of reactivity associated with transient poisons (xenon and samarium) and temperature change, control requirements in these cores were relatively stringent and necessitated a close spacing of control rods. An associated problem was that the small thermal diffusion lengths resulted in large flux distortions due to heterogeneities, such as control rod water channels. Thus, to avoid excessive water-hole peaking it was necessary to utilize control rods consisting of thin plates in a relatively complex geometry, for example, cruciform. The overall result was a core which was quite complex from a physics standpoint. An accurate description of the flux peaks and the control rod worth requires an explicit representation of the control rods, structural members, water regions, fuel regions, and other features of the core affecting the neutron distribution. To provide such a description it has been necessary to carry on investigations in such areas as self-shielding and cell theory (Chap. 4) and blackness theory (Chap. 3), and to make full use of the best mathematical tools as they have become available, including successively desk calculators, small digital computers, manually adjusted electric network simulators, and large scale digital computers ultimately leading to large two- and three-dimensional diffusion theory computer programs (Chap. 7).

In addition to the development of methods for the static description of the cores, a great amount of work has been required to obtain suitable treatments of kinetics, safety, and stability problems (Chap. 5). The characteristics of light-water cores which are significant from a kinetics standpoint differ in many essential aspects from those of cores previously studied: for example, the light-water cores have much larger moderator and void negative temperature coefficients; much smaller metal reactivity coefficients; much smaller thermal neutron lifetimes; different potential accidents, such as the cold water accident; and different transient behavior occasioned by the need for rapid and flexible maneuvering.

In the Shippingport program, as an approach to economic power generation, the emphasis has been on use of fuels of high U^{238} content in order to minimize diffusion plant costs. This has led to the study of light-water uranium lattices which, owing to the relatively close spacing of the fuel elements, have unique characteristics: large interactions, particularly in U^{238} fission (fast effect) and in resonance absorption (Dancoff effect),

and a large contribution to slowing down by the uranium inelastic scattering. To understand and describe such lattices, a joint program was set up between the Bettis Atomic Power Laboratory and the Brookhaven National Laboratory in which sets of slightly enriched uranium fuel rods were studied, alternately, at Brookhaven in a subcritical or exponential assembly and at Bettis in a critical assembly. Some of the associated techniques are described in Chaps. 2 and 6 of this volume, and in Vol. II.[1] A new phase in the program began with the investigation of seed-blanket cores, which differed conceptually from the types of cores considered previously. The basic idea of the coupling of two quite dissimilar core regions, or of driving one core region by another, led to a deeper insight into the meaning and measurement of reactivity. It was necessary to treat such novel constructs as the extremely high neutron flux gradients existing between the seed and blanket regions, the seed-blanket power sharing, and the concept of a large core having essentially the kinetics properties of a small core (the seed). Furthermore, the depletion characteristics of these cores necessitated study of the properties of plutonium isotopes in light water and of fission products in very high burnup fuels in which most of the energy is derived from the fissioning of plutonium.

The advent of burnable poisons had a major effect on light-water reactor designs. In the first place, the much greater core endurances made possible by the use of burnable poisons resulted in depletions so large that the core parameters changed greatly throughout life. This made it necessary to examine the adequacy of the core from reactivity and thermal standpoints at many times during core life, so that in effect the reactor designer was faced with the problem of designing many cores. As a result of the initial neutron flux spatial variations, the cores, even if they were homogeneous to begin with, became heterogeneous both radially and axially after appreciable depletion. This made it imperative to develop codes to provide two- and even three-dimensional descriptions of the core, not only initially, but throughout life as well (Chaps. 4 and 7). The previously used rough approximation of stable fission product absorption as a constant number of thermal barns per fission was quite inadequate for accurate calculations of endurances with such high fuel depletions. It was found necessary to go to a detailed study of the data on individual fission products, taking into account successive transmutations and epithermal absorptions.

The great increase in fuel loading concomitant with the increase in endurances resulted in blacker cores, i.e., cores with much larger macroscopic thermal absorption cross

sections. This, in turn, necessitated a much more careful examination of neutron thermalization and the spatial variation of the neutron spectrum. The powerful variational technique was found to have many applications in the field. The extended use of burnable poisons led to their utilization outside the fuel, in lumped self-shielded form, both macroscopically (e.g., plates and rods) and microscopically (particles). This again introduced the need for extensive calculations and experiments to determine accurately the self-shielding of the poisons and, in some cases, of the fuel, both initially and as a function of fuel depletion. In many cases, conventional analytic methods have been inadequate and it has been necessary to utilize Monte Carlo techniques (Chaps. 3, 4, and 7).

The desire to obtain optimum reactor performance has also resulted in more complex designs. Local and gross zoning of fuel and burnable poisons has been studied to maintain power distributions of specified shapes and to minimize the number of mechanically moving control elements. In this connection, it is of interest to note that, as a core fuel loading increases, the emphasis of the problems changes. For example, in lightly loaded cores the reactivity associated with transient xenon and samarium is very large; secondly, it is often difficult to obtain a large, negative temperature coefficient of reactivity. On the other hand, in cores having a high fuel loading the xenon and samarium reactivity effect is small and the temperature coefficient large and negative, but major problems are presented in power peaking near geometric discontinuities and in shutting the core down with adequate margin. It is also noteworthy that the designer must aim at a balanced core design since changes in the core to improve one characteristic may adversely affect another. Thus, improvement of the power distribution often leads to a reduction in the effectiveness of a given set of control elements.

1.3 NUMERICAL ANALYSIS AND DIGITAL COMPUTER PROGRAMS

To provide detailed descriptions of these complex and advanced designs throughout core life, substantial effort has been placed on numerical analysis. Chapter 7 discusses some of the progress made in that effort, particularly in the treatment of the few-group two-dimensional nuclear diffusion equations, the transport equations, and Monte Carlo methods. Faster convergence rates in the numerical solutions have been obtained over the years by utilizing more sophisticated overrelaxation techniques. In addition, a more rigorous foundation for the basic numerical processes has been established.

This work in numerical analysis stimulated fundamental mathematical investigations in the nature of the spectrum of the multigroup diffusion operator and finite difference approximations to it. The results provided a mathematical basis for the concepts of criticality, multiplication factor, principal distribution, and importance function in nuclear reactor theory. The existence of expansions, similar to those in quantum mechanics, of the solution of the diffusion problems in terms of the characteristic functions associated with the diffusion operator was established.[3] This, again, provided a firm basis for handling many problems in reactor theory, e.g., involving perturbation theory and pulsed source techniques.

As a result of the extensive theoretical analysis advantages have been gained in computer utilization which can be exploited either for reduced design time or greater design capability. Some measure of the gain can be indicated by reviewing the effects of numerical analysis studies on successive programs of the PDQ (two-dimensional diffusion theory treatment) series of digital programs. QED-1 was the first two-dimensional few-group program for the IBM-704. Its successor, PDQ-1, gained in speed as well as convenience to the user by the insertion of automatically calculated overrelaxation factors in the iterative method. The time savings have varied with the experience and ability of the designer. However, since the convergence rate is very sensitive to the choice of overrelaxation factor, the improvement is substantial. PDQ-2 utilized Chebyshev polynomials to carry out the numerical method of solution and was estimated to decrease the overall time by a factor of 1.6. PDQ-3 utilized single line rather than point overrelaxation and increased the speed of a given problem by an average factor of 1.4 over PDQ-2 (some design problems actually showed improvements of a factor of 5). Finally, PDQ-4, produced for the Philco-2000, further decreased the average time by a factor of 1.4 by using double line overrelaxation (not including the increase in speed provided by the machine).

In addition to the improvements in iterative processes, improvements in the iteration strategy, i.e., the choice of the number of iterations performed in a single group before moving to the next group, provided an increase in the overall convergence rate. Such advances have, for example, been incorporated in KARE with the Peaceman-Rachford iteration procedure. Insertion of symmetry conditions of various kinds for half core, quarter core, and eighth core periodicity also introduced substantial factors of gain in speed for a specific problem. However, probably the most important result of the work in numerical analysis has been the development of an understanding of, and a sound theoretical foundation for, the

mathematical processes involved, providing insight into the approaches which should be taken for specific problems and the accuracy which can be expected (Chap. 7). Reference 4 is a review paper of this work and contains a rather complete bibliography for further reference.

The need for an accurate and detailed description of reactor behavior has had a marked effect on the development and verification of calculational tools used by the nuclear engineer in the design effort. The nuclear designer is faced with making a compromise between the accuracy and detail with which he desires to describe a reactor and the cost and limitations of computer machinery available to him. Since practical considerations dictate that extensive approximations be made in the techniques used to obtain design information, dependence on more basic calculations and comparisons with experiment for evaluating the accuracy and deficiencies of the design tools have been essential. For these reasons, the formulation and use of more exact calculations have been very important. The studies made in this area, in addition to yielding standards to which more approximate calculations may be compared, have supplied insight into the reactor physics phenomena of interest and guided the formulation of more approximate descriptions that retain the important features of the theory. The use of the more basic theory itself has also identified many areas of sensitivity and guided the reactor physicist in further studies.

While it is possible to develop definitive techniques in reactor theory, they are generally available only in a restricted sense. They may incorporate a detailed description of the energy behavior or the angular dependence but be limited in the spatial description available. For instance, the use of multigroup Monte Carlo has been extensive, but the tractable application of this technique has been limited to small cells in either the resonance region or the thermal neutron range.

1.4 SELECTION AND VERIFICATION OF CALCULATIONAL MODELS

While these basic techniques are accurate in their sphere of application, they are not general enough to obtain all the information about the reactor behavior that is desired. The essentials of these different techniques must be brought together in a self-contained nuclear design model that will describe the entire configuration. This usually requires drastic approximations in all of the variables. Practical examples of this are the use of few-group diffusion theory, performing spatial calculations at discrete points rather than continuously, representing

a group of fuel plates and water channels as a homogeneous region, and restricting the calculations to a few selected times during the core lifetime. Identifying this framework does not specify the calculational model but only outlines the ground rules within which the model will be formulated. The few-group cross sections, transport corrections, geometrical detail required, and spatial mesh necessary for the adequate description of flux shapes and depletion effects must be specified in such a manner that the essential features of the configuration are described accurately. This will often be supplemented by including self-shielding factors (for particles, plates, resonances, etc.) in the few-group parameters, using blackness theory to describe the effect of strong absorbers, or by adjusting the few-group parameters to get agreement with a more exact calculation. The basic theory is then used to evaluate the accuracy of the approximations and to identify the required improvements.

While many of the features of the model may be tested against standards, these comparisons must usually be made in a restricted sense, while other features are less susceptible to detailed comparison. Coupled with this is the lack of complete and accurate nuclear data with which to perform the calculations. The comparison and testing of the derived calculational model (using the best nuclear data available) with experimental measurements on critical reactor configurations are, thus, an essential step in further evaluating the limitations of the model. Especially important have been the clean critical assemblies which provide a simplified geometry especially designed to test particular aspects of the theory (Chap. 6). Originally, the experiments were carried out at room temperature. Since the parameters of light-water cores change appreciably from room to operating temperatures, pressurized critical facilities have been provided to permit studying the nuclear assemblies over a wide temperature range. In addition, the use of pulsed source techniques has permitted the study of the reactivities of subcritical assemblies. This has allowed the calculations to be checked at many points rather than merely at critical and has yielded reactor physics information from smaller amounts of material and smaller experimental effort.

The adequacy of the model for use in design problems is still dependent on the degree of detail and accuracy required by the design objectives. If these are extensive, the final stage of design must be paralleled with the testing of the model against a detailed mockup of the core. The amount of information required for design of the core does not allow the obtaining of all this information experimentally. Nor will it yield information on lifetime performance, but a careful analysis of the mockup

will supply a valuable normalization point and final verification of the ability of the design model to describe the core configuration. Finally, prototype cores have been heavily instrumented and extensive test programs conducted to verify the design calculations.

1.5 DEPENDENCE OF DESIGN DETAIL ON PERFORMANCE REQUIREMENTS

It may be fitting to close this chapter with a concrete example of the necessity for extending reactor physics calculations to greater detail as a result of increased core performance requirements. In early reactor designs only knowledge of the overall neutron flux and resultant power distributions was essential. As higher power densities were demanded, it was important to determine what has been called by analogy with quantum mechanics the fine structure, i.e., the power output of each individual fuel element. Finally, it has developed in the design of the second Shippingport core, as well as in other high performance cores, that it is necessary to go even beyond this point to what might be called the hyperfine structure, i.e., to the determination of the power distribution within a fuel element. In the second Shippingport core the design maximum power density in the seed is almost 500 watts/cc, more than twice that of the first Shippingport core. As shown in Fig. 1.1 each seed subassembly contains highly enriched oxide fuel wafers, 0.250 in. wide, embedded in zirconium plates. In order to reduce the power peaking, a zoning of each seed subassembly in 2 zones of fuel was adopted, based upon the calculated peak-to-average value of the hottest wafer in any zone to the average in the subassembly. This gave a calculated value for the peak-to-average of about 1.4 which was in reasonable agreement with experiment. However, examination of the power distribution indicated that there was a sharp gradient in the vicinity of the hottest wafer. A special experiment was devised to study this gradient, using four quarter-width wafers in place of the hottest wafer.

The induced gamma ray fission product activity of each quarter wafer was measured and an 18 percent rise in power found across the quarter-inch width of the wafer (Fig. 1.2). As a result of this unanticipated peaking, it was estimated that the thermal output of the core would be reduced by 10 percent. To rectify the situation a new zoning scheme was adopted (Fig. 1.3) with 3 fuel zones. Figures 1.4 and 1.5 compare the power peaks as a function of seed fuel depletion for the original and the new zoning schemes. This is an example in which refinement of reactor physics studies has led to a significant economic benefit in plant performance.

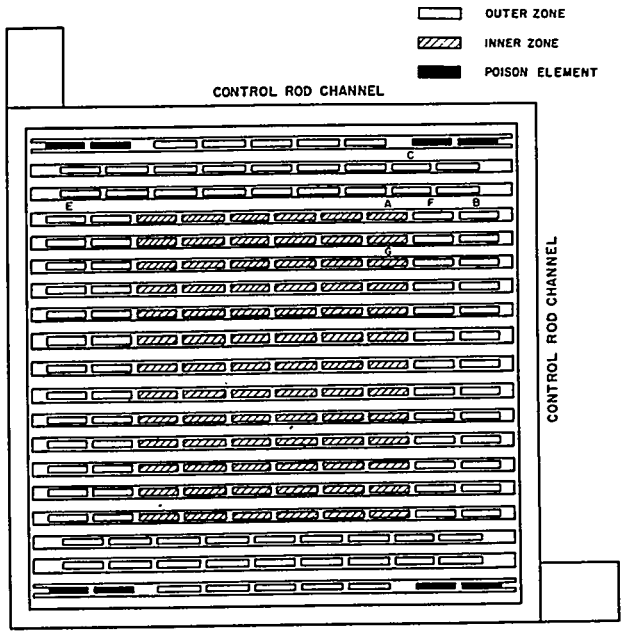

FIGURE 1.1. Shippingport Core 2 Seed 1 Original Seed Zoning.

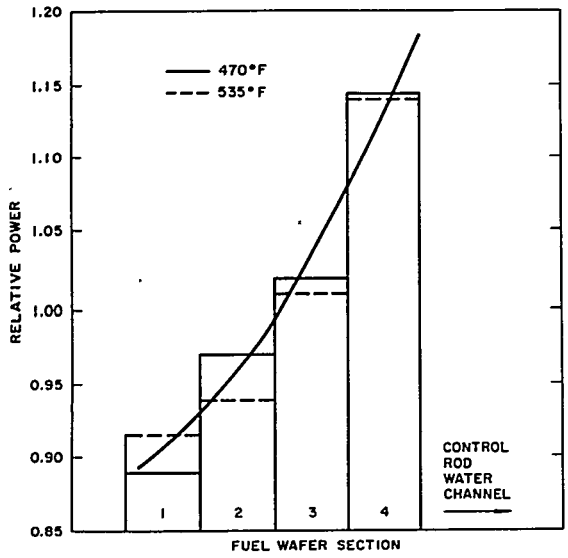

FIGURE 1.2. Shippingport Core 2 Seed 1 Distribution of Power within a Seed Fuel Wafer Located Adjacent to a Control Rod Water Channel.

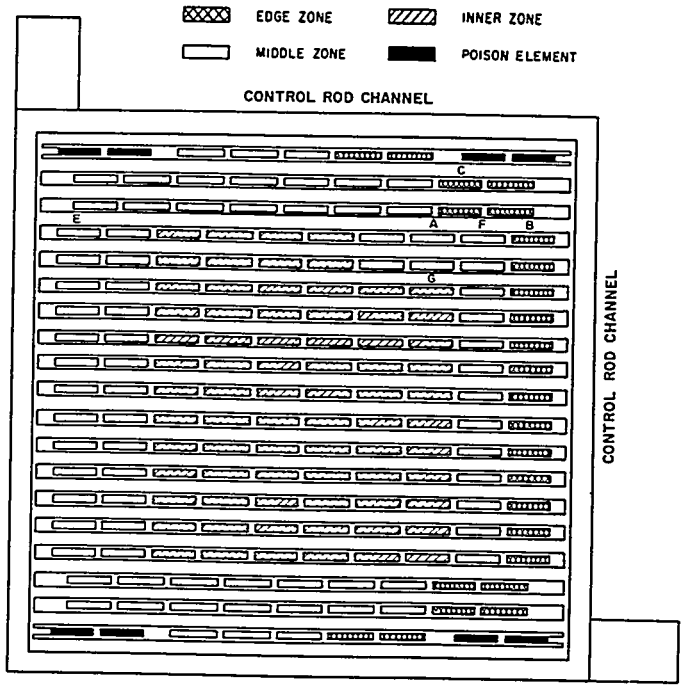

FIGURE 1.3. Shippingport Core 2 Seed 1, New Zoning of Seed to Optimize Power Distributions, Taking into Account Intrawafer Flux Gradients.

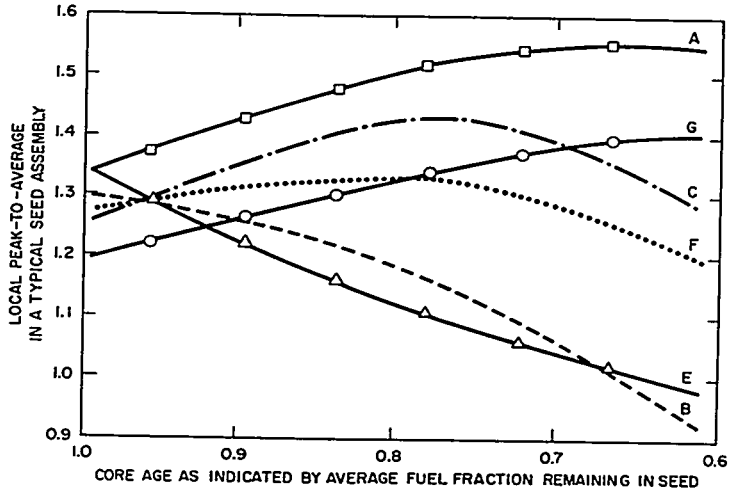

FIGURE 1.4. Shippingport Core 2 Seed 1, Peaking Factor Lifetime Variation as Calculated for Original Zoning (A, B, C, E, F, and G represent various points within the fuel assembly shown in Fig. 1.1).

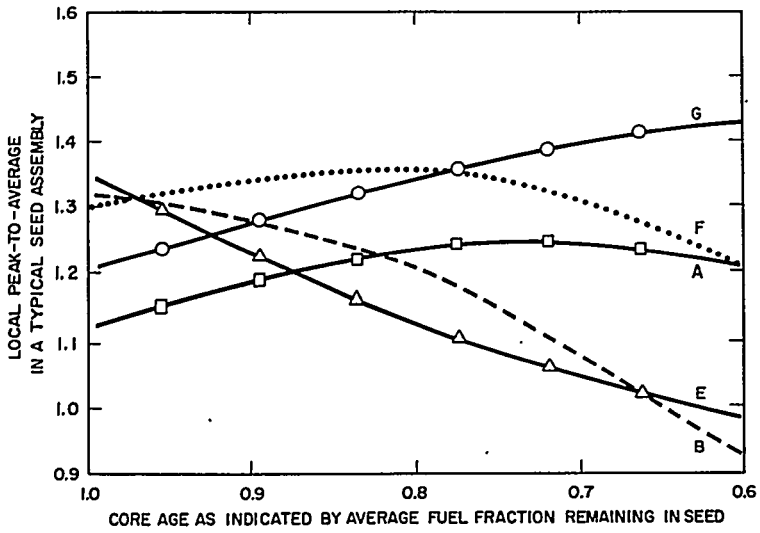

FIGURE 1.5. Shippingport Core 2 Seed 1, Peaking Factor Lifetime Variation as Calculated for New Zoning (A, B, E, F, and G represent various points within the fuel assembly shown in Fig. 1.3).

1.6 SUMMARY

The reactor physics work in the Naval Reactors and Shippingport programs has been guided by the objective of a detailed description of complex reactors designed for optimum performance. The need for accurate calculational and experimental techniques to meet design requirements has required the development of systematic procedures and appropriate tests of their adequacy. The following chapters describe a number of useful techniques and procedures that have evolved in the course of this program.

Finally, it should be pointed out that, as is inevitable in works of this kind, some very recent developments could not be included in this volume. As the work of the Naval Reactors and Shippingport programs continues to advance at a rapid pace into areas of great practical importance as well as of inherent physics interest, the editor must establish a cutoff point in time if a book is to be published.

REFERENCES

1. S. Krasik, Ed., "Naval Reactors Physics Handbook, Vol. II; The Physics of Pressurized Water Reactors," 1959.

2. J. R. Stehn, Ed., "Naval Reactors Physics Handbook, Vol. III; The Physics of Intermediate Spectrum Reactors," U.S. Govt. Printing Office, Washington, D.C., 20402, 1958.

3. G.J. Habetler and M.A. Martino, "The Multigroup Diffusion Equations of Reactor Physics," KAPL-1886, July 28, 1958.

4. R. S. Varga, "Numerical Methods for Solving Multi-Dimensional Multigroup Diffusion Equations" in "Nuclear Reactor Theory. Proceedings of Symposia in Applied Mathematics. Vol. XI," G. Birkhoff and E. P. Wigner, Eds., pp. 164-189, American Mathematical Society, Providence, 1961.

Chapter 2

THE NEUTRON SLOWING-DOWN PROBLEM

D. S. Selengut, Editor

2.1 INTRODUCTION

The basic problem of the reactor designer is identical with that of the engineer in any field: to achieve, within the restrictions of economics and the laws of nature, a configuration which meets some preassigned performance specifications. The problem is clearly one of synthesis, since it involves putting together a configuration or arrangement to satisfy some given goal. On the other hand, the way the designer must work in a new and complex field is essentially backwards. That is, he must try various combinations and configurations to see how they operate in the light of his performance requirements. His main tools are therefore the tools of analysis which tell him, given a particular design, how it will perform.

The design of nuclear reactors might seem at first glance somewhat different from most fields of engineering. Two of the obvious characteristics of the field are the large number of physicists employed in design work and the extreme reliance on large digital computers. One might argue, however, that these are largely the result of historical accident. Most of the procedures underlying standard design techniques were worked out by physicists in the early days of the Manhattan Project because the field was new, without any historical antecedents in the established fields of engineering, and because many of the needed techniques were commonplace in mathematical physics. The preoccupation with machine computation was partly due to the fact that the development of digital computers has closely paralleled in time the development of the field of nuclear energy. But it is equally a result of the complexity of the design problems to be solved, the high cost of experimentation, and the increasing demand for higher performance designs. There are parallel trends in other fields (aeronautical engineering is an obvious example) and it seems likely that reactor engineering provides one of the earliest examples of a trend that will continue in all the engineering disciplines.

From the standpoint of the designer, the required analytical tools can be characterized very simply: the analysis must furnish the neutron flux distribution in energy, position, angle, or any other pertinent variable once the designer has described the reactor, since as soon as the flux is given, the rate of any nuclear process, and hence the complete behavior of the system, is easily calculated in terms of cross-section data. This idealized requirement is a fairly natural one, given the background of the physicists who first developed the field of reactor theory. The behavior of neutrons in a scattering and multiplying medium is completely determined by the Boltzmann or transport equation, and the linear version at that, which must have seemed remarkably simple to anyone who had struggled with the nonlinear form of gas kinetic theory. In any case, provision of these analytical tools requires the same approaches and modes of thinking which have always been fundamental to physics research: formulation of the basic equations which define the field of interest, construction of models describing only part of the characteristics of the system to reduce its complexity, and analytical solutions of the simplified models to provide insight into the factors determining the qualitative behavior of the system.

Superimposed on this viewpoint of the physicist are the economic requirements which arise whenever a field of research is turned towards an applied goal. Designing a reactor requires not only insight into the physics but a detailed numerical description of it as well. Although a simplified model may indicate the direction in which a design should go, a tight design requires accurate and detailed numerical predictions to ensure that the performance will be as specified. The consequence of this is that numerical techniques and machine computations become essential in the design process and must be taken into account by the physicist developing methods of analysis. He must not only balance costs of computation against accuracy of the final result, but he must also be careful not to sacrifice understanding of the physics for generality in computation.

While the object of the reactor physicist is to solve the energy-dependent transport equation, it is convenient to divide this problem into two parts: the diffusion and slowing down of fission neutrons to the electron-volt energy range, and the thermalization process during which the neutron population comes into approximate thermal equilibrium with the scattering medium. Although the two problems are very similar from a formal standpoint, the separation is convenient because in practice different models and numerical techniques are more appropriate in one case than the other. In the slowing-down

problem the neutrons are primarily degraded in energy by elastic scattering. Inelastic scattering is often a secondary effect in highly enriched water-moderated reactors which can be added by relatively simple modifications to the analysis. The mean free path of epithermal neutrons is usually large enough so that irregularities in the structure are not clearly seen by the neutrons, and the flux distribution in space tends to be rather smooth, although considerable irregularities can develop in the energy distribution through the resonance region.

In the thermal region, on the other hand, the neutron energy may either increase or decrease during a collision, a situation which leads to somewhat more complicated numerical procedures than in the slowing-down problem. In addition, the shorter mean free path of thermal neutrons means that the detailed structure of the core becomes more significant, leading to large variations in the flux (and, hence, in the power distribution) which require a more detailed accounting of the neutron angular distribution to describe the transport effects in the neighborhood of heavy absorbers. The neutron thermalization problem is discussed in Chap. 3; the present chapter is concerned with neutron slowing down in the fast and epithermal energy range. Since the basic reactor physics is available in several textbooks, the material included here has been limited to areas of special interest in the design of high performance water-moderated reactors and to work which has been carried on within the Naval Reactors laboratories. The result is necessarily a series of somewhat loosely related topics, and an attempt has been made to keep each one as self-contained as possible.

With the exception of the first section, the contents of this chapter constitute a detailed elaboration of material already implicit in classical linearized kinetic theory. Before any calculations can be made, however, the basic physical parameters of the medium which describe the various neutron interaction probabilities must be at hand. A necessary preliminary to any design calculations is, therefore, the availability of the required neutron cross sections. It is with the calculation of these basic nuclear data from first principles that Sect. 2.2 is concerned. Unlike transport theory, the problem here lies outside of classical physics and requires quantum mechanics for its resolution. Nevertheless, the theoretical methods which are appropriate to the two fields do not differ nearly as much as might be expected. The reason is simply that the Boltzmann and the Schrödinger equations are both linear operator equations, and the same analytical and mathematical techniques apply to both: eigenfunction expansions,

perturbation theory, Green's function techniques, the variational method. Historically, in fact, much of the early work in reactor physics was a more or less direct transcription of well-known methods from quantum mechanics into the new context. One need only compare the eigenvalue problem of quantum mechanics with the determination of the criticality of a multiplying system, or the method partial waves to the spherical harmonic approach of transport theory, to see the close relationship of the two fields.

There are, nevertheless, characteristic differences. The complexity of quantum mechanical systems usually arises from the large number of particles (and, hence, the large number of coordinates) present, a situation which can frequently lead to simplification through a statistical or averaging approach. The corresponding complexity in reactor physics usually arises from the intricate geometrical configuration and the radically changing material properties dictated by practical considerations. A somewhat more fundamental difference, from the standpoint of the mathematician, is the fact that quantum mechanics is a self-adjoint theory, whereas reactor theory, at least in the general case, is not. To the physicist, the property of self-adjointness is simply another way of describing reciprocity between cause and effect. In quantum mechanics the invariance under time reversal (which goes back to classical mechanics) ensures that one can look upon a time-reversed solution as describing a possible evolution of the system which is on an equal footing with the given solution and requires only a change in the initial conditions to ensure its validity. In reactor physics this is no longer the case. The fact that a neutron will, in general, lose energy rather than gain it constitutes a fundamental asymmetry in the physical process, which prevents this kind of reversal of viewpoint without a corresponding reversal in the physical properties of the system, rather than just in the initial conditions. The net result is that the mathematical formalism of transport theory is somewhat wider than that required in quantum mechanics. The problems associated with nonself-adjoint operators, however, have long been studied by mathematicians and recognized as a natural extension of the self-adjoint case.

The material in Sect. 2.2 includes a description of the various nuclear models required to predict reaction rates and properties of the bound states of the nucleus and, in addition, a discussion of an extensive computer program which has been developed to calculate nuclear cross sections. This material is of considerable interest not only because of its intrinsic usefulness for the reactor designer, but also in the example which it provides of the interaction between pure and applied

research. The importance of nuclear data and the wide gaps in experimental information have been, respectively, recognized and deplored since the earliest days of reactor design. In the immediate postwar period the state of nuclear theory precluded any attempt to calculate cross sections; the only applications of nuclear theory were in attempts to predict trends in the material of interest by reference to data for neighboring elements.

The possibility of a more fundamental approach was recognized by some reactor physicists with the appearance of the work of Weisskopf and coworkers on the crystal ball or optical model. It is worth noting that the early papers given by nuclear physicists generally stressed that the work was pure research and that the designer should not exercise any hope that useful cross sections would emerge from this work in the forseeable future. In spite of this forbidding dictum, the need for nuclear data was sufficiently great so that at several installations individual attempts were made to program the best existing models for a digital computer, with the half-concealed viewpoint that perhaps even acknowledged incorrect data was better than none at all. The ability to test hypotheses numerically, and the rapid advance in the theory of nuclear reactions over the past 10 years, have led to the point where the theoretical prediction of cross sections is not only of direct practical application in reactor design, but has also been followed by parallel efforts within university research groups. The result is an interesting case study both of the rapid application of a field of basic physics, and of the mutual interaction between industrial and university research groups.

Having disposed of the question of nuclear data, we must return to the problem of solving the Boltzmann equation in the fast and epithermal energy range. The instinctive approach of the theoretical physicist, when faced with a problem of this nature, is to secure analytical insight by dealing with the simplest idealization which retains the properties he is interested in, and by using the standard tools of linear analysis to resolve whatever complexity remains into its component factors. Section 2.3 follows this tack by considering the slowing down of neutrons in a uniform medium under the influence of elastic scattering. The effect of boundaries and the space dependence of the neutron distribution is eliminated by assuming a sinusoidal variation of the flux with position. The complexity remaining is then due to the presence of various angle-dependent components of the vector flux which arise in the source of neutrons at a given energy due to scattering down from higher energies. Having isolated this feature in an otherwise simplified model, one can

use the fact, that a neutron scattered elastically by a heavy element will lose only a small fraction of its energy, to carry out a power series expansion in the energy loss. The result permits a consistent approximation to any desired order and makes it possible to study various approximation methods that have appeared in the literature on a consistent and systematic basis.

The preceding material, while providing a unifying viewpoint for several approximate treatments of slowing down, does not lend itself directly to any specific comparison with experiment. On the other hand, considerable experimental information is available on the spatial moments of the distribution of thermal neutrons resulting from an approximate point or plane source of high energy neutrons, and in particular on the age (or more precisely one-sixth of the second moment from a point source). While these experiments, in principle, constitute one of the simplest involving the space-energy distribution of fast neutrons, they also provide a very useful integral test both for cross-section data and for one's understanding of the slowing-down process. Because of the complexities of the actual experiment as opposed to the idealized one, and the corrections necessary to the data, the Monte Carlo method provides a very convenient way of analyzing such experiments with a minimum of uncertainty accruing from the theoretical machinery. Section 2.4 describes such an application of the Monte Carlo method and provides a specific example of some of the general techniques discussed in Chap. 7.

A fundamental problem which must be dealt with in low enrichment lattices is that of resonance capture. The motivation for the original work in this field was the design of natural uranium-graphite lattices. More recent applications, both within the Naval Reactors program on the PWR and elsewhere, have led to interest in very tight water-moderated lattices in which the close fuel rod spacing gives rise to strong mutual interactions, and to uranium oxide fuel elements, in which moderation within the fuel resonances becomes significant. The factors causing complexity in either case are the rapid energy variations of the neutron flux through the fuel resonances and the rapid space variation between fuel and moderator; the resulting problems have to be dealt with at the level of transport theory. Section 2.5 describes an approach which uses an understanding of the physics of the problem to factor it into several idealized subproblems that are simple enough to be treated on an analytical basis. In the course of the development, essential use is made of several results of one-velocity transport theory, calculations which might at first glance seem too restricted to have any practical application.

The two previous sections deal with the calculation of the age and the resonance escape probability, two fundamental but relatively isolated parts of the basic problem. As was remarked earlier, the requirement of the nuclear designer is an overall description of the neutron economy of his reactor in terms of the flux as a function of position and energy, and the multiplication constant of the system. It is with this overall problem that the next three sections of this chapter are concerned. The evolution of reactor design methods over the last 15 years has had some rather unexpected features, and much of this development has been influenced by work at the Naval Reactors laboratories. The basis of reactor physics was laid during the Manhattan Project in terms of macroscopic reactor theory, and most of the early design work was carried out in conjunction with exponential experiments and integral measurements of overall reactor parameters. Age-diffusion and two-group theory provided a natural vehicle for these calculations, since they were expressed in terms which could (with a little imagination) be identified with parameters measured directly in the laboratory.

With the achievement of chain reacting systems, the objective of the designer turned naturally from questions of feasibility to questions of high performance and to the exploration of the wide range of possibilities that emerged with the availability of highly enriched uranium. Not only were the possibilities which the designer had to consider far too many on which to carry out detailed experiments but, in addition, the need for optimization once the general configuration had been decided upon made it necessary to attach much greater weight than previously to calculations from first principles. Furthermore, the use of highly enriched fuel and the demands of compact, mobile military power plants meant that the earlier simplified models of large, completely thermal reactors were no longer adequate. These problems came to a head in the design of the first naval propulsion reactors and led directly to the development of multigroup methods.

From one standpoint, the multigroup method is nothing more than the application of classical finite difference methods to the reactor equations in the age-diffusion approximation. It is worth noting that the same class of engineering problems had existed for a long time in the area of time-dependent heat conduction, but no similar development had taken place. It would be incorrect to attribute this sudden reliance upon numerical methods to the possibility of machine computation, which was just then emerging, since the early multigroup calculations were carried out by hand. The development, rather, reflects the pressing requirements of a new class of nuclear

designs and the physics orientation of the individuals responsible for methods development with its implication that a simpler approach was inadequate.

The general multigroup techniques are discussed in Sect. 2.6, together with a detailed summary of an existing multigroup program which incorporates many of the refinements developed since the method first came into use. Besides improvements in differencing techniques, procedures have been developed to incorporate transport and self-shielding effects as well as more general slowing-down models which relax some of the limitations of age-diffusion theory. Nevertheless, considerable uncertainty invariably remains as to the accuracy of these transport theory approximations. To reduce this uncertainty, a further development has taken place during the past few years. This is the extension of the multigroup method to the transport equation itself, rather than the diffusion approximation, and is only made possible by the rapid development of digital computers. Since even with the fast computers presently available one is severely limited by the time required for a multigroup transport calculation, the numerical procedure which is appropriate for a problem of this kind is very strongly influenced by the physics of the problem. This interaction is discussed in some detail in Sect. 2.7 which describes a quite general, one-dimensional discrete ordinate code of this type. It illustrates the great complexity involved in refining the solution of a fairly realistic reactor problem much beyond the semi-intuitive description of diffusion theory. It also provides an interesting contrast both in physical transparency and numerical complexity with the Monte Carlo calculations described in Sect. 2.4.

To return to the development of reactor design methods, with the advent of large digital computers, the age-diffusion multigroup method became much more feasible than a hand computational procedure. One might have expected it to become the standard design tool, and for a limited period it was. The reason for this short duration was the evolution of reactor designs in response to increasing demands for higher performance. From relatively simple configurations that could be analyzed in terms of equivalent one-dimensional models, engineering requirements continually increased the complexity of the cores being studied to the point where two- and eventually even three-dimensional representations have become necessary.

At the same time, however, it was becoming apparent that in a water-moderated core the large energy loss when a neutron was scattered made the neutron energy spectrum much less sensitive to the details of the cross sections than

was the case in other materials. Since the computation time required was more or less proportional to the number of groups, a kind of reverse evolution began to take place which eventually led back to a few-group representation, using perhaps two or three groups to represent the fast and intermediate neutrons in much the same manner as had been done in the very early hand calculations. The difference now (besides the much more detailed representation of space effects) was that no direct experimental data were available to provide the group constants needed in the new calculations. The alternative was to calculate these group constants from first principles, approximating the space dependence of the flux by a sinusoidal variation, thereby reducing the problem to an equivalent infinite-medium calculation similar to that discussed in Sect. 2.3. From this point on, actual multigroup calculations (those in which no preliminary estimate of the flux spectrum is required in order to initiate the calculation) were relegated primarily to the role of procedures for checking the accuracy of the faster few-group methods. Few-group theory, described in detail in Sect. 2.8, has since become the standard method in design calculations.

One last development remains which has been the result of increased core complexity and the continuing requirement for longer core endurance. As a result of both of these tendencies, the core spectrum, and hence the required group constants, change radically as functions of position and time. To calculate these constants in detail for all the cases needed to give a satisfactory representation of the core during its life would make studies of the lifetime behavior of a core, in the number required to achieve a final design, very expensive. For a given design region, however, the parameters which affect the group constants are relatively few in number: the metal-water ratio, the amount of fuel present, and the buckling. This suggests the possibility of bypassing the computation of the exact spectrum by fitting the group-averaged cross sections over a relatively narrow range of interest for a particular class of designs, and calculating the desired few-group constants from simple algebraic formulas, instead of having to integrate the infinite medium slowing-down equations. A specific procedure for doing this, described in Sect. 2.9, has been instrumental in keeping the machine time used from advancing faster than it has in response to increasingly tight design requirements. A second scheme for fitting cross sections by means of a variational technique is also described. Although slower, this method has the advantage of greater accuracy over a wider range of parameters, and is representative of more recent approaches to problems in reactor physics.

In summary, the topics included in this chapter, while not intended to be a connected account of neutron moderation and diffusion, illustrate a number of points in the development of reactor theory. First is the reciprocal influence between the problems of reactor technology and nuclear theory which has led to the development of methods for calculating nuclear cross sections from first principles with a minimum of experimental information. Second is the complementarity which exists between the designer's need for precise numerical values at a specific design point and his need to understand the physics which underlies a system's general behavior if he is to make sense out of the myriad possibilities which he must deal with in arriving at the design point. Finally, there is the importance of those attitudes and methods of approach which are characteristic of the physicist in dealing with a complex problem by making simplified models which enable him to factor the complexity of the real world into workable subunits. The net result of this work during the past decade has been the development of a technology which, while it bears a superficial resemblance to earlier procedures, represents a substantial increase in both scope and accuracy, and provides an effective tool for the class of high performance reactors with which the designer is now concerned.

2.2 CALCULATION OF NUCLEAR CROSS SECTIONS

N. C. Francis, D. T. Goldman, and C. R. Lubitz

A. Introduction

As reactor design methods become more and more refined, the need for accurate nuclear reaction cross sections becomes increasingly important. In this section will be described certain methods in use today for the calculation of these quantities.

The most reliable nuclear cross sections are furnished by careful measurements of the desired quantities. However, calculated cross sections must be used when measurements are not available. Since in the present state of nuclear theory accurate predictions of nuclear cross sections are not always possible, calculated cross sections should be used only until good experimental values become available. Calculated nuclear cross sections are of value for the following reasons:

1. Cross sections which have been measured at a few isolated points can be theoretically extrapolated into unmeasured regions.
2. Calculated results may be used to check the validity and consistency of experimental data.

3. Calculated results can serve as a guide in selecting regions where experiments should be performed.

An attempt has been made to be logically complete in each of the topics treated. Thus, there is sufficient descriptive material with the principal equations to permit their derivation. As a further aid, references to more detailed treatments are given throughout. Topics that are either of particular interest in cross-section work or for which good discussions are not easily available elsewhere are treated in greater detail than others.

Section 2.2.B treats a collection of topics which are important in understanding later discussions. For the most part, these are topics of general validity, independent of any particular nuclear model. In a sense, this section is kinematical in that it provides a framework on which to hang the model-dependent details of later discussions.

Section 2.2.C discusses the optical model of nuclear reactions, wherein the average nuclear force field is represented by a potential well. The principal points explored are the physical interpretation of the model and the mathematical techniques for its solution.

The theory of compound nucleus formation and decay is treated in Sect. 2.2.D. The single and multilevel formulas are only touched on, since they are discussed in great detail in many other places. A generalization of the Hauser-Feshbach statistical theory to include spin-dependent penetrabilities is given.

Section 2.2.E covers the direct interaction model of nuclear reactions. Following a derivation of the integral equation satisfied by the wave function of the system, which is exact but insoluble in practice, approximations are introduced that render it soluble. These approximations are valid for processes in which only a few of the outer nucleons of the target participate. If instead the incident neutron interacts with the inner, tightly bound nucleons, a long-lived compound nuclear state will usually be formed, and this requires a different treatment.

For certain nuclei, light enough to undergo strong direct interactions but still possessed of large resonances, a theory which unifies the two models is required. This relatively little-used, but potentially important, unified model is described in Sect. 2.2.F.

Throughout the formal development of nuclear reaction theory, extensive use is made of the stationary state eigenfunctions of various nuclei: the target, the intermediate or compound nucleus, and the residual nucleus. In view of the great difficulties involved in actually finding these state functions, the most useful nuclear theories are those which

use only very general properties of these states (statistical models) or do not require them at all (optical model). However, since their more or less explicit representation is demanded by direct interaction theory, Sect. 2.2.G mentions some of the current models and gives references to various detailed discussions.

Finally, in Sect. 2.2.H the computer program ABACUS is discussed, a valuable tool for computing cross sections, and a few examples of actual reaction analyses are given. The examples illustrate some of the procedures which can be employed in analyzing nuclear cross sections. However, the following outline gives a more explicit description of the overall process in the construction of a set of cross sections for reactor calculations. In the absence of relevant data, various steps may be omitted or more crudely approximated.

1. Using ABACUS, one fits optical model parameters to elastic scattering angular distribution data and total cross-section measurements at isolated energies. These are then cross-checked with polarization data and average s-wave resonance data, or both. (The optical model predicts the average ratio of s-wave, p-wave, etc., reduced widths to level spacing.[1])
2. A smooth curve is then interpolated to the optical model parameters determined, so that they are available at all energies of interest (usually zero to 10 or 12 Mev). This permits a complete calculation of (energy-averaged) elastic scattering and the average value of cosine θ which occurs in the transport cross section. In addition, the total cross section and the nonelastic cross section can be compared with the usually extensive body of experimental data.
3. Inelastic cross sections are next computed by the Hauser-Feshbach theory to as high an incident energy as knowledge of the target's spin and parity assignments permits and checked with whatever experimental data exist. If discrepancies occur, the data are examined for evidence of direct interaction effects. These are computed and the theoretical values adjusted accordingly.
4. Since the complexity of the Hauser-Feshbach method rarely permits it to be carried at energies at which more than 20 states can be excited, it must be augmented at higher energy by some simpler method. It is common to employ formulas based on the evaporation model (Sect. 2.2.D.3), but these statistical theories always predict too few particles scattered with small energy loss due to their neglect of direct interaction effects. For this reason, they must be augmented by estimates based on actual measurements at high energy.

5. Another type of cross section which is required for reactor calculations is the absorption cross section. At low energies this is usually the (n, γ), or radiative capture cross section, plus the (n, f), or fission cross section, for those elements that are thermally fissile. At higher energies, other processes which lead to a loss of neutrons are (n, p) and (n, α). These cross sections, if required only in toto, can be estimated from experimental nonelastic cross sections or from the optical model absorption cross section. If they are required in detail, then statistical models (Hauser-Feshbach, evaporation) can provide the compound nucleus contribution, with direct interaction calculations supplying the remainder.
   The $(n, 2n)$ cross section may be appreciable in certain instances, but usually has to be handled on an individual basis, depending on the reactor calculation program for which it is intended. The fission cross section also must depend heavily on experiment, since the methods described here are not immediately applicable to its calculation.
6. In addition to the cross sections so far described, all of which have a smooth dependence on energy, most reactor calculations require information on scattering, capture, and fission resonances. These are the exclusive province of experiment, since there is at present no way to predict all of their characteristics theoretically.
   However, theory does provide information on the average properties, widths, and spacings (Sect. 2.2.D.2.a) of these resonances, which can be of use. In addition, multilevel theory (Sect. 2.2.D.2.b) permits more accurate calculations (with the aid of certain additional parameters) of cross sections from resonance parameters than does the simpler Breit-Wigner one-level theory.
   Finally, if the position of a broad resonance is known, it can be described by an appropriate optical model direct interaction calculation. The prediction of the giant neutron resonances by the optical model itself is well known.[1] Coupled with a single particle or collective model direct interaction calculation, it is also capable of describing considerably narrower (i.e., kilovolt width) resonances. This is useful for the extrapolation, interpolation, and checking purposes already mentioned.

B. General Considerations

1. *Form of the Wave Function*

In a quantum mechanical treatment of nuclear reactions, the wave function describing the system plays a central role.

While present mathematical techniques do not permit the exact calculation of such functions, an examination of their general form provides a basis for discussing various approximation schemes.

If a neutron is incident on a target nucleus of mass number A, the appropriate configuration space coordinates are the position vectors of the target nucleons $\vec{r}_1, \vec{r}_2, \ldots, \vec{r}_A$, and that of the incident neutron $\vec{r}_0$. (The arrows denote vectors, their absence implies the corresponding scalar magnitude, and a caret denotes a unit vector: thus, $\vec{r} = r\hat{r}$, $\vec{k} = k\hat{k}$, etc.)

A basic postulate of quantum mechanics is that the eigenfunctions of a system's Hamiltonian operator constitute a complete set in which to expand its actual wave function. If the eigenfunctions $\phi_\alpha(\vec{r}_1, \vec{r}_2, \ldots, \vec{r}_A)$ of the target nucleus Hamiltonian H_T are used in this manner the expansion coefficients will depend on the remaining coordinate, $\vec{r}_0$:

$$\Psi = \sum_\alpha \psi_\alpha(\vec{r}_0)\ \phi_\alpha(\vec{r}_1, \ldots, \vec{r}_A)\ . \qquad \text{Eq. (2.1)}$$

To avoid unessential complications, ignore for the moment the intrinsic spins of the particles. Also, write sums over quantum numbers as though they were discrete. Either the sum sign can be understood to contain integrals over the continuous eigenvalues, or else the system can be enclosed in a box to render its eigenvalues discrete (Ref. 2, p. 43, 49). The Schrödinger eigenvalue equation for the target nucleus wave functions is

$$(H_T - E_T^\alpha)\ \phi_\alpha(\vec{r}_1, \ldots, \vec{r}_A) = 0. \qquad \text{Eq. (2.2)}$$

The symbol α represents a set of quantum numbers which completely specify each eigenfunction, T refers to the target nucleus, and E_T^α is the total energy of the α^{th} target nucleus state.

Although the coefficients $\psi_\alpha(\vec{r}_0)$, the bombarding neutron wave functions, are not easily calculable, they do have known asymptotic forms. The ground state coefficient $\psi_0(\vec{r}_0)$ is asymptotically an incident plane wave plus an outgoing, scattered wave. The other coefficients are purely outgoing or decaying waves, since no neutrons are incident on the target in its excited states. Thus,

$$\psi_\alpha(\vec{r}_0) \underset{r_0 \to \infty}{\sim} e^{i\vec{k}_0 \cdot \vec{r}_0}\ \delta_{\alpha 0} + f_\alpha(\hat{r}_0)\frac{e^{ikr_0}}{r_0} \qquad \text{Eq. (2.3)}$$

where $\delta_{\alpha\beta}=1$ if $\alpha=\beta$ and is zero otherwise; f_α is the scattering amplitude for the α^{th} excited state ($\alpha=0$ refers to the ground state); $\vec{r}_0$ is the coordinate of the incident neutron, referred to the target nucleus' center of mass as origin; k_α is the wave number for scattering from the α^{th} state; and $\vec{k}_0$ is the incident wave vector.

For incident energies below the threshold for the excitation of the state ϕ_α, the corresponding wave number k_α becomes imaginary, causing the scattered wave to damp exponentially: $k_\alpha \to i\gamma_\alpha$.

The form of Eq. (2.3) restricts the validity of the present treatment to systems which are found in their ground states under normal conditions. This is true of nuclei, since thermal agitation excites an appreciable number of them to excited states only at enormously high temperatures. On the other hand, the atoms and molecules making up the scattering material are capable of vibrating against their weak intermolecular binding forces, and these modes are already well excited at ordinary temperatures. The problem of neutron scattering at energies below about 1 electron volt must cope with this situation, and this theory of chemically bound (as opposed to more strongly nuclearly bound) systems is treated in Chap. 3, Sect. 3.2.

From Eq. (2.3) one can obtain the differential cross section for elastic $(\alpha=0)$ or inelastic $(\alpha\neq 0)$ scattering to a particular state, defined as the outgoing flux per steradian divided by the incoming flux per cm^2 (Ref. 3, p. 137),

$$\sigma_\alpha(\hat{r}_0)=\frac{k_\alpha}{k_0}\,|f_\alpha(\hat{r}_0)|^2. \qquad \text{Eq. (2.4)}$$

Conservation of energy is expressed by the relation

$$\frac{\hbar^2 k_0^2}{2m}+E_T^0=\frac{\hbar^2 k_\alpha^2}{2m}+E_T^\alpha. \qquad \text{Eq. (2.5)}$$

The normalization of the wave function is also of interest, and although the Dirac delta function should be employed to normalize properly the continuous spectrum eigenfunctions, the notation is simpler, assuming a box-normalized discrete spectrum, and leads to the same conclusion. Let the nuclear eigenfunctions be orthonormal, and the total wave function be normalized to unity. Then,

$$(\phi_\alpha, \phi_\beta) = \delta_{\alpha\beta} \qquad \text{Eq. (2.6)}$$

and

$$(\Psi, \Psi) = 1 = \left(\sum_\alpha \phi_\alpha, \sum_\beta \psi_\beta \phi_\beta\right) = \sum_\alpha (\psi_\alpha, \psi_\alpha) \ . \qquad \text{Eq. (2.7)}$$

From Eq. (2.7) it is seen that the ground state wave function, $\psi_0(\vec{r}_0)$, is normalized to a value less than unity whenever the other ψ_α's $(\alpha \neq 0)$ fail to vanish; i.e.,

$$(\psi_0, \psi_0) = 1 - \sum_{\alpha \neq 0} (\psi_\alpha, \psi_\alpha) \leq 1. \qquad \text{Eq. (2.8)}$$

Physically, this has the meaning that some neutrons which begin in the plane wave part of ψ_0 end up as outgoing waves in other $(\alpha \neq 0)$ channels. From the standpoint of ψ_0, some particles (or more precisely, some probability of finding particles) have been lost or destroyed, although no actual loss has occurred. In the section dealing with the optical model (2.2.C), it will be shown that if a potential-scattering model is employed to generate approximate values of ψ_0, the potential must contain an imaginary component, in the sense of complex variable theory, to produce wave functions satisfying Eq. (2.8).

2. *Partial Wave Expressions: Elastic, Reaction, and Total Cross Sections*

Additional relations of interest and general validity emerge from a partial wave expansion of ψ_0. For simplicity, the equations appropriate to the relative motion of two spinless systems (0 + 0) will be written, but in Sect. 2.2.C it will be generalized to the important case that one member has spin 1/2. The angular dependence of the 0 + 0 system involves only the angle θ between the incident beam, $\hat{k}$, and emergent particle, $\hat{r}$, $(\cos\theta = \hat{k} \cdot \hat{r})$, and the wave function has the familiar form determined essentially by the asymptotic form of Eq. (2.3):*

$$\psi_0(\vec{r}) = \frac{1}{kr} \sum_{\ell=0}^{\infty} i^\ell (2\ell + 1) e^{i\delta_\ell} u_\ell(r) P_\ell(\cos\theta). \qquad \text{Eq. (2.9)}$$

*In the following paragraphs the subscript zero on $\vec{r}_0$ and $\vec{k}_0$ will be suppressed. The incident particle and its wave vector are meant throughout.

The phase shift δ_ℓ is defined in terms of the asymptotic form of the ℓ^{th} radial wave function.

$$u_\ell(r) \underset{r\to\infty}{\sim} \sin\left(kr - \frac{\ell\pi}{2} + \delta_\ell\right). \qquad \text{Eq. (2.10)}$$

Equation (2.10) is valid for interactions which have a limited or finite range, since it represents a general solution to the radial wave equation for a freely moving, noninteracting particle. The inclusion of the term $\ell\pi/2$ is conventional, and accords with the usual definition of the spherical Bessel function (Ref. 1, pp. 78-79). The phase shifts can be found by analyzing experimental data or from numerical solutions to the wave equation, as described in Ref. 2, pp. 106-107.

The most important exceptions to Eq. (2.10) are the Coulomb wave functions (Ref. 1, p. 118) which have the form:

$$\psi_0(\vec{r}) = \frac{1}{kr}\sum_{\ell=0}^{\infty} i^\ell (2\ell+1)\, e^{i(\sigma_\ell + \delta_\ell)}\, u_\ell^c(r)\, P_\ell(\cos\theta) \qquad \text{Eq. (2.11)}$$

$$u_\ell^c(r) \underset{r\to\infty}{\sim} \sin\left(kr - \frac{\ell\pi}{2} - \gamma \ln 2kr + \sigma_\ell + \delta_\ell\right) \qquad \text{Eq. (2.12)}$$

where σ_ℓ is the Coulomb phase shift,

$$\sigma_\ell = \operatorname{Arg}\Gamma(\ell + 1 + i\gamma) \qquad \text{Eq. (2.13)}$$

and γ is the Coulomb parameter, defined in terms of the atomic numbers of the colliding particles, z and z', the relative velocity, v, and the charge of the proton e,

$$\gamma = zz'e^2/\hbar v. \qquad \text{Eq. (2.14)}$$

The partial wave expansion of the scattering amplitude can be obtained from Eq. (2.9) by using the well known expression for a plane wave and the asymptotic form of the spherical Bessel function (Ref. 1, p. 78, p. 105)

$$e^{i\vec{k}\cdot\vec{r}} = \sum_\ell i^\ell (2\ell+1) j_\ell(kr) P_\ell(\hat{k}\cdot\hat{r}) \qquad \text{Eq. (2.15)}$$

$$j_\ell(kr) \underset{r\to\infty}{\sim} \frac{1}{kr}\sin\left(kr - \frac{\ell\pi}{2}\right). \qquad \text{Eq. (2.16)}$$

From Eqs. (2.3) and (2.10) one obtains

$$f_0(\hat{r}) = \frac{1}{2ik}\sum_{\ell}(2\ell+1)\,(\eta_\ell - 1)\,P_\ell(\hat{k}\cdot\hat{r}) \qquad \text{Eq. (2.17)}$$

where

$$\eta_\ell \equiv e^{2i\delta_\ell}. \qquad \text{Eq. (2.18)}$$

η_ℓ is often termed the reflection coefficient for the ℓ^{th} partial wave. It gets this name from the form of the asymptotic wave function,

$$\psi_0(\vec{r}) \underset{r\to\infty}{\sim} \frac{1}{2ikr}\sum_{\ell} i^\ell (2\ell+1)\left[\eta_\ell\, e^{i\left(kr-\frac{\ell\pi}{2}\right)} - e^{-i\left(kr-\frac{\ell\pi}{2}\right)}\right]P_\ell(\hat{k}\cdot\hat{r}) \qquad \text{Eq. (2.19)}$$

in which, relative to an incoming wave* of unit amplitude, the outgoing wave has amplitude η_ℓ. Reflection coefficient is perhaps not the best name, since for no scattering at all (plane wave) $|\eta_\ell| = 1$; this, in a sense, represents no reflection at all, but the difficulty is only semantic.

From Eq. (2.4) it is seen that the differential cross section for elastic scattering is the absolute square of $f_0(\hat{r})$ [Eq. (2.17)].

The total elastic cross section can be obtained by integrating the differential cross section or, alternatively, the flux of the scattered wave in Eq. (2.3) over a large sphere around the origin. The flux is (the asterisk denotes complex conjugation)

$$\vec{j}(\vec{r}) = \frac{\hbar}{m}\,Im\,(\psi_0^*\nabla\psi_0) \qquad \text{Eq. (2.20)}$$

of which only the radial component is needed. This yields (Ref. 4, pp. 320-323)

$$\sigma_e = \pi\lambda\!\!\!^{-2}\sum_{\ell}(2\ell+1)\,|1-\eta_\ell|^2 \equiv \sum_{\ell}\sigma_e^{(\ell)} \qquad \text{Eq. (2.21)}$$

*The full description of an outgoing or ingoing wave requires the introduction of its time dependence. The outgoing wave has a phase angle $(kr - Et/\hbar)$. The phase of this wave remains constant as both r and t increase and, thus, the wave appears to be proceeding outward.

where $\lambda\!\!\!^{-} = 1/k$ is the reduced wave length.

Similarly, the reaction cross section counts the number of particles in the whole wave function Eq. (2.9) which enter, but do not leave, the same large sphere. The ratio of this net inward flux to the incident flux is

$$\sigma_r = \pi \lambda\!\!\!^{-2} \sum_{\ell} (2\ell + 1)\, T_\ell \equiv \sum_{\ell} \sigma_r^{(\ell)} \qquad \text{Eq. (2.22)}$$

where

$$T_\ell = 1 - |\eta_\ell|^2 \qquad \text{Eq. (2.23)}$$

is the penetrability of the ℓ^{th} partial wave. The physical interpretation of this apparent loss of particles has been discussed earlier. Note that the term penetrability accords with the designation of reflection coefficient for η_ℓ .

The total cross section is defined as

$$\sigma_T = \sigma_e + \sigma_r \qquad \text{Eq. (2.24)}$$

and has the partial wave expansion

$$\sigma_T = 2\pi \lambda\!\!\!^{-2} \sum_{\ell} (2\ell + 1)\,(1 - Re\,\eta_\ell) \equiv \sum_{\ell} \sigma_T^{(\ell)}. \qquad \text{Eq. (2.25)}$$

It should be emphasized that the ground state wave function $\psi_0(\vec{r}_0)$ is the basis for Eqs. (2.21), (2.22), and (2.25). Thus, although it provides a detailed description of the elastic scattering, it provides only an overall description of the other possible reactions. Equation (2.22) tells us that some particles were not scattered elastically, but it provides no information on what did actually happen to them.

3. *The Optical Theorem*

Another relation which follows from the fact that $\psi_0(\vec{r}_0)$ determines both the elastic scattering amplitude and the total cross section is the so-called optical theorem,

$$\sigma_T = \frac{4\pi}{k}\, Im\, f_0(\theta = 0). \qquad \text{Eq. (2.26)}$$

It stems from the fact that particles which scatter elastically and with no deviation ($\theta = 0$ is straight ahead) are really unscattered. All others enter into either σ_r or σ_e ; i.e., into

σ_T . Using Eq. (2.20) and the definition preceding Eq. (2.22), which defines the reaction cross section as the net inward flux (per unit incident flux) through a large sphere surrounding the scatterer, one obtains

$$\sigma_r = -\frac{a^2}{k} \, Im \int_{r=a} \psi_0^* \, \frac{\partial \psi_0}{\partial r} \, d\hat{r}. \qquad \text{Eq. (2.27)}$$

The radius of the sphere is a, and $d\hat{r} \equiv \sin\theta d\theta d\phi$ is the element of solid angle. Instead of using the partial wave form for ψ_0, which leads to Eq. (2.22), Eq. (2.3) is used directly. Omitting two terms which are of higher order in $1/r$, Eq. (2.27) becomes

$$\sigma_r = -\frac{a^2}{k} \, Im \int_{r=a} \left\{ i\vec{k}\cdot\vec{r} + \frac{ik\,|f_0|^2}{r^2} + \frac{ik\,f_0}{r} \, e^{i(kr - \vec{k}\cdot\vec{r})} + \frac{if_0^*\,\vec{k}\cdot\vec{r}}{r^2} \, e^{-i(kr-\vec{k}\cdot\vec{r})} \right\} d\hat{r}. \qquad \text{Eq. (2.28)}$$

In this equation the first term integrates to zero, and the second to the negative of the elastic cross section, using Eq. (2.4) with a set equal to zero:

$$\sigma_e = \int |f_0|^2 \, d\hat{r}. \qquad \text{Eq. (2.29)}$$

Transferring this to the left-hand side, one gets, after a little manipulation,

$$\sigma_r + \sigma_e = \sigma_T = -\,a\,Re\, e^{ika} \int_{r=a} (1 + \hat{k}\cdot\hat{r}) f_0 e^{-i\vec{k}\cdot\vec{r}} d\hat{r}. \qquad \text{Eq. (2.30)}$$

It can be shown that in the limits as $a \to \infty$, the only contribution to the integral comes from the stationary phase point at $\hat{k}\cdot\hat{r} = 1$, i.e., zero degrees scattering angle. With the azimuthal angle ϕ and $\mu = \hat{k}\cdot\hat{r} = \cos\theta$ as variables, one can integrate by parts on μ, using the relation $e^{-ika\mu} = \frac{i}{ka}\frac{d}{d\mu} e^{-ika\mu}$

$$\sigma_T = -2\pi a\,Re\, e^{ika}\left(\frac{i}{ka}\right)\int_{-1}^{1} (1+\mu) f_0 \, \frac{d}{d\mu} \, e^{-ika\mu} d\mu. \qquad \text{Eq. (2.31)}$$

The resulting integral is $O(1/a)$ and therefore negligible, while the integrated part gives

$$\sigma_T = \frac{2\pi}{k} Im\, e^{ika} 2 f_0(0)\, e^{-ika} = \frac{4\pi}{k} Im\, f_0(0). \qquad \text{Eq. (2.32)}$$

Equation (2.32), as can be seen by inspecting the terms in Eq. (2.28), results from interference between the incident and scattered waves. When the target nucleus or the bombarding particle, or both, have nonzero internal angular momenta, there will be elastically scattered particles which are associated with wave functions different from (but degenerate with) the ground state wave function ϕ_0 in Eq. (2.1). These will be incoherent with the incident wave and will therefore not contribute to $f(0)$ in Eq. (2.32).

4. *Energy-Averaged Cross Sections*

The material presented in the preceding paragraphs is, for all practical purposes, mathematically exact. However, it is not very convenient in the resonance region of nuclear reactions. At low energies and in general in regions of low nuclear level density, nuclear reactions exhibit narrow resonances in the cross section versus energy plot, or excitation function. As the energy of the incident neutron increases, these resonances crowd together to form a smooth curve. (The transition region depends on the experimental resolution.)

Correspondingly, the exact reflection coefficients of Sect. 2.2.B.2 have a resonant behavior at low energy but become smooth at higher energies. As a first step in analyzing such resonance data, it is useful to have a set of smoothly varying reflection coefficients, $<\eta_\ell>$, which reproduce the average experimental data. These approximate coefficients define cross sections somewhat differently from Eqs. (2.21) and (2.22) because of the nonlinear dependence of the σ's on the η's.[1]

The energy-average over an interval I is defined by

$$<\eta_\ell(\epsilon)> = \frac{1}{I}\int_{\epsilon - I/2}^{\epsilon + I/2} \eta_\ell(\epsilon')\, d\epsilon' \qquad \text{Eq. (2.33)}$$

with similar expressions for the averaged $\langle\sigma_e\rangle$ and $\langle\sigma_r\rangle$. Then

$$\langle\sigma_e^{(\ell)}\rangle \equiv \pi\lambda\!\!\!^{-2}\,(2\ell+1)\,\langle|1-\eta_\ell|^2\rangle \qquad \text{Eq. (2.34)}$$

$$= \pi\lambda\!\!\!^{-2}\,(2\ell+1)\left\{|1-\langle\eta_\ell\rangle|^2 - |\langle\eta_\ell\rangle|^2 + \langle|\eta_\ell|^2\rangle\right\} \qquad \text{Eq. (2.35)}$$

$$= \sigma_{se}^{(\ell)} + \sigma_{ce}^{(\ell)}. \qquad \text{Eq. (2.36)}$$

The two new cross sections defined in Eq. (2.36) are the shape elastic cross section

$$\sigma_{se}^{(\ell)} = \pi\lambda\!\!\!^{-2}\,(2\ell+1)\,|1-\langle\eta_\ell\rangle|^2 \qquad \text{Eq. (2.37)}$$

which has the conventional definition, Eq. (2.21), in terms of the average reflection coefficients, and the compound elastic cross section

$$\sigma_{ce}^{(\ell)} = \pi\lambda\!\!\!^{-2}(2\ell+1)\left(\langle|\eta_\ell|^2\rangle - |\langle\eta_\ell\rangle|^2\right). \qquad \text{Eq. (2.38)}$$

The rapidly fluctuating resonance part of the cross section, $\sigma_e^{(\ell)} - \langle\sigma_e^{(\ell)}\rangle$, is discussed further in Sect. 2.2.D.

The average phase shifts determine only σ_{se} and not $\langle\sigma_e\rangle$, since $\langle|\eta_\ell|^2\rangle$ is not obtainable from $\langle\eta_\ell\rangle$. Similarly, the $\langle\eta_\ell\rangle$ do not determine $\langle\sigma_r\rangle$ since

$$\langle\sigma_r^{(\ell)}\rangle = \pi\lambda\!\!\!^{-2}\,(2\ell+1)\left(1-\langle|\eta_\ell|^2\rangle\right). \qquad \text{Eq. (2.39)}$$

However, the combination

$$\langle\sigma_r^{(\ell)}\rangle + \sigma_{ce}^{(\ell)} = \pi\lambda\!\!\!^{-2}(2\ell+1)\left(1 - |\langle\eta_\ell\rangle|^2\right) \qquad \text{Eq. (2.40)}$$

denoted by $\sigma_c^{(\ell)}$, is determined by the $\langle\eta_\ell\rangle$. The latter cross section is called the compound nucleus formation cross section and has the interpretation that following the formation of the compound nucleus, either a reaction may occur, $\langle\sigma_r\rangle$, or the particle may be elastically re-emitted, (σ_{ce}). Both of these events constitute a loss of particles from the standpoint of the fictitious wave function defined in terms of the $\langle\eta_\ell\rangle$:

$$\langle\psi_0(\vec{r})\rangle = \frac{1}{kr}\sum_{\ell=0}^{\infty} i^\ell(2\ell+1)\, e^{i\bar{\delta}_\ell}\, \langle u_\ell(r)\rangle P_\ell(\cos\theta) \qquad \text{Eq. (2.41)}$$

where $\bar{\delta}_\ell$ is defined by the equation*

$$\langle\eta_\ell\rangle = e^{2i\bar{\delta}_\ell} \qquad \text{Eq. (2.42)}$$

and

$$\langle u_\ell(r)\rangle \underset{r\to\infty}{\sim} \sin(kr - \ell\pi/2 + \bar{\delta}_\ell). \qquad \text{Eq. (2.43)}$$

If the quantities in Eq. (2.26) are energy-averaged according to Eq. (2.33) one gets

$$\langle\sigma_T\rangle = \frac{4\pi}{k}\, Im\, \langle f_0(0)\rangle, \qquad \text{Eq. (2.44)}$$

---

*A new symbol $\bar{\delta}_\ell$ is required by the fact that Eq. (2.33) would be violated by the relation

$$\langle\eta_\ell\rangle = e^{2i\langle\delta_\ell\rangle}. \qquad \text{Eq. (2.45)}$$

No use is made of the energy-averaged phase shift $\langle\delta_\ell\rangle$.

since k is a slowly varying function of energy. Identifying $\langle f_0(\theta)\rangle$ with the scattering amplitude determined by the asymptotic form of Eq. (2.41), one finds that $\langle\psi_0\rangle$, the energy average of the incident particle wave function, can be used to calculate the average scattering amplitude, $\langle f_0\rangle$, which, using Eq. (2.44), can be used to calculate the energy average of the total cross section. The shape elastic part of the total elastic scattering cross section can also be found by using $\langle f_0\rangle$. In Sect. 2.2.C a potential well model (called the optical or cloudy crystal ball model) will be used to calculate $\langle f_0\rangle$, the total cross section, and the shape elastic scattering cross section.

C. Optical Model

1. Introduction

For many years attempts have been made to analyze various nuclear reactions by replacing the actual nucleus with an average potential well. The sizes of nuclei determine the range of this potential well as roughly $1.5A^{1/3}f$. (A is used for the mass number, and the fermi, $f = 10^{-13}$ cm, is taken as the unit of length.) Similarly, the binding energy of nucleons and their approximately known kinetic energies within the nucleus fix the depth of the potential well at some tens of Mev.

These range and depth values in turn fix the widths of the potential scattering resonances at from a few hundred kev to about one Mev. There is no possibility of explaining the electron volt widths observed in many neutron reactions. For this purpose, as was pointed out by N. Bohr many years ago, one must employ the concept of a long-lived compound nucleus (see Sect. 2.2.D).

However, it was first observed by Bethe,[5] and later by Feshbach, Porter, and Weisskopf,[1] that if the narrow resonances in neutron scattering data are averaged out as in Sect. 2.2.B.4, the resulting gross structure problem can be analyzed on a potential well model. In this model, all nuclear coordinates are suppressed and only the coordinate of the incident neutron with respect to the center of mass of the target remains. Since this one-particle wave function is to be viewed as the ground state coefficient $\psi_0(\vec{r}_0)$ in Eq. (2.1), and the relation given by Eq. (2.8) must be satisfied, the potential may need to be complex.

To see this, note that a consequence of the Schrödinger equation

$$-\frac{\hbar^2}{2m}\nabla^2\psi_0 + V\psi_0 = E\psi_0 \qquad \text{Eq. (2.46)}$$

is the continuity equation (Ref. 2, p. 23)

$$\nabla \cdot \vec{j} = \frac{2}{\hbar} W \rho_0 \qquad \text{Eq. (2.47)}$$

where $W = Im\ V$, and $\rho_0 = \psi_0^* \psi_0$ is the probability density. It follows from Eq. (2.47) that a negative W will destroy probability, and that Eq. (2.8) can be satisfied as a consequence.

The classical analog of a complex potential is a region of complex dielectric constant, a device often used to represent a light-absorbing medium. The analogy is quite close, and the potential well model is often referred to as the optical model or the cloudy crystal ball model. The latter name reflects the fact that the absorption is not very strong, especially in comparison to the quite black nucleus which the compound nucleus picture was thought to imply.

2. *Solution of the Schrödinger Equation with a Spin-Orbit Potential*

Since the solution of Eq. (2.46) for the case of a central (i.e., dependent only on r) nonspin-dependent potential is well known, the slightly more general case will be given here for which V contains a spin-orbit coupling term:

$$V(r) = V_c(r) + V_s(r)\, \vec{L} \cdot \vec{S} \qquad \text{Eq. (2.48)}$$

where V_c, V_s are the central and spin-orbit potentials, respectively, $\vec{L}$ is the orbital angular momentum operator, and $\vec{S}$ is the spin angular momentum operator. (Both $\vec{L}$ and $\vec{S}$ are dimensionless, being measured in units of $\hbar$.)

Just as one would proceed in the nonspin case by expanding the wave function in spherical harmonics $Y_{\ell m}(\hat{r})$, (the Condon and Shortley definition is used, Ref. 6, p. 50 or Ref. 4, p. 783), so one expands here in spin harmonics, $Y_{\ell jm}(\hat{r}, \sigma)$. These are functions of both the angles θ and ϕ (abbreviated by $\hat{r}$) and the spin coordinate σ. They are constructed in such a manner that they diagonalize the operator $\vec{L} \cdot \vec{S}$. This is equivalent to diagonalizing the square of the total angular momentum, $\vec{J} = \vec{L} + \vec{S}$, since

$$\vec{J}^2 = \vec{L}^2 + \vec{S}^2 + 2\vec{L} \cdot \vec{S}. \qquad \text{Eq. (2.49)}$$

For this reason they are labeled with the eigenvalue j. They satisfy the equations:

$$\vec{J}^2\,\mathcal{Y}_{\ell jm} = j(j+1)\mathcal{Y}_{\ell jm}$$

$$\vec{L}^2\,\mathcal{Y}_{\ell jm} = \ell(\ell+1)\mathcal{Y}_{\ell jm}$$

$$\vec{S}^2\,\mathcal{Y}_{\ell jm} = \frac{1}{2}\left(\frac{1}{2}+1\right)\mathcal{Y}_{\ell jm} \qquad \text{Eq. (2.50)}$$

$$\vec{L}\cdot\vec{S}\,\mathcal{Y}_{\ell jm} = \frac{1}{2}\left\{j(j+1) - \ell(\ell+1) - \frac{1}{2}\left(\frac{1}{2}+1\right)\right\}\mathcal{Y}_{\ell jm}.$$

They are also diagonal in the z-component of $\vec{J}$

$$J_z\,\mathcal{Y}_{\ell jm} = m\,\mathcal{Y}_{\ell jm}$$

but not in L_z or S_z. The orbital quantum number, ℓ, must have integral values while the total angular momentum quantum number is half integral. The $\mathcal{Y}_{\ell jm}$ can be given an explicit representation in terms of spherical harmonics, certain numerical coefficients known as Clebsch-Gordan coefficients (Ref. 6, p. 73; Ref. 4, p. 789) denoted by $C^{j_1\ j_2\ j_3}_{m_1\ m_2\ m_3}$, and the eigenfunctions $\chi_{1/2,m_s}$ of the operators S^2 and S_z:

$$\mathcal{Y}_{\ell jm}(\hat{r},\sigma) = \sum_{m_\ell m_s} C^{\ell\ 1/2\ j}_{m_\ell\ m_s\ m}\, Y_{\ell m_\ell}(\hat{r})\,\chi_{1/2,m_s}(\sigma). \qquad \text{Eq. (2.51)}$$

The coordinate σ, like the eigenvalue m_s, can take on only two values, $\pm 1/2$. The $\chi_{1/2,m_s}$ are defined by (Ref. 4, p. 785; Ref. 2, p. 223)

$$\chi_{1/2,m_s}(\sigma) = \delta_{m_s,\sigma}. \qquad \text{Eq. (2.52)}$$

A general wave function $\psi(\vec{r},\sigma)$ has the interpretation that $|\psi(\vec{r},\sigma)|^2$ is the probability of finding the particle at the point $\vec{r}$ with its z-component of spin angular momentum equal to σ. In Eq. (2.51) the summation is over the range of the m's defined as follows:

$$-\ell \le m_\ell \le \ell$$

$$-1/2 \le m_s \le 1/2. \qquad \text{Eq. (2.53)}$$

When the expansion

$$\psi(\vec{r}, \sigma) = \sum_{j=1/2,\, 3/2, \ldots}^{\infty} \sum_{\ell=j-1/2}^{j+1/2} \sum_{m=-j}^{j} \frac{\kappa_{\ell jm}}{r} u_{\ell jm}(r) \mathcal{Y}_{\ell jm}(\hat{r}, \sigma) \quad \text{Eq. (2.54)}$$

is substituted into Eq. (2.46), it can be shown that the radial wave functions satisfy the equation

$$\frac{d^2 u_{\ell j}(x)}{dx^2} + \left[1 - \frac{\ell(\ell+1)}{x^2} - \frac{V_c(x)}{E} - \frac{\gamma_{\ell j} V_s(x)}{E}\right] u_{\ell j}(x) = 0. \quad \text{Eq. (2.55)}$$

The notation in Eq. (2.55) is as follows:

$$\begin{aligned} x &= kr \\ k &= \sqrt{\frac{2mE}{\hbar^2}} \\ \gamma_{\ell j} &= \frac{1}{2}\ell \text{ if } j = \ell + 1/2 \\ &= -\frac{1}{2}(\ell+1) \text{ if } j = \ell - 1/2 \end{aligned} \quad \text{Eq. (2.56)}$$

while $\kappa_{\ell jm}$ in Eq. (2.54) is a constant to be determined. Since the radial equation is independent of the eigenvalue m, a consequence of the central nature of V_c and V_s, it has been omitted as a label on $u_{\ell j}$ in Eq. (2.55).

The second order differential equation [Eq. (2.55)] can be solved by a variety of numerical techniques. It possesses two linearly independent solutions, one of which can be chosen to be regular at the origin. The particular combination of these solutions which represents the physical problem at hand is determined by the boundary conditions:

1. $\psi(\vec{r}, \sigma)$ must be finite at the origin.
2. Far from the origin, ψ must have the form of a plane wave plus a spherical outgoing wave.

The first of these conditions dictates the use of the regular solution to Eq. (2.55). The second condition is expressed by the equation:

$$\psi(\vec{r}, \sigma) \underset{r\to\infty}{\sim} e^{i\vec{k}\cdot\vec{r}} \chi_{1/2,\,\mu}(\sigma) + f_\mu(\hat{r}, \sigma) \frac{e^{ikr}}{r}. \quad \text{Eq. (2.57)}$$

This differs from its nonspin analog, Eq. (2.3), in that the incident wave now carries a spin function, so that it represents a particle with $S_z = \mu$. Also, the scattering amplitude depends on both the direction of emission $\hat{r}$ and the spin coordinate σ. The label μ on f denotes its dependence on the incident spin direction.

As in the nonspin case (Ref. 2, p. 103) use is made of Eq. (2.57) by taking the asymptotic form of the plane wave, splitting it into incoming and outgoing spherical waves, and demanding that the incoming part of Eq. (2.54) agree with it.

Starting from Eqs. (2.50) and (2.51), one can expand P_ℓ by means of the addition theorem for spherical harmonics:

$$P_\ell(\hat{k}\cdot\hat{r}) = \frac{4\pi}{2\ell+1}\sum_{m=-\ell}^{\ell} Y^*_{\ell m}(\hat{k})\, Y_{\ell m}(\hat{r}). \qquad \text{Eq. (2.58)}$$

Then the spin harmonics are introduced using the inverse of Eq. (2.51):

$$Y_{\ell m_\ell}(\hat{r})\chi_{1/2,\,m_s}(\sigma) = \sum_{j=\ell-1/2}^{\ell+1/2}\sum_{m=-j}^{j} C^{\ell\ 1/2\ j}_{m_\ell\ m_s\ m}\,\mathcal{Y}_{\ell jm}(\hat{r},\sigma). \qquad \text{Eq. (2.59)}$$

This gives

$$e^{i\vec{k}\cdot\vec{r}}\,\chi_{1/2,\,\mu}(\sigma) \underset{r\to\infty}{\sim} \frac{2\pi}{ikr}\sum_{\ell m_\ell jm} i^\ell\, C^{\ell\ 1/2\ j}_{m_\ell\ \mu\ m}$$

$$\cdot\, Y^*_{\ell m_\ell}(\hat{k})\,\mathcal{Y}_{\ell jm}(\hat{r},\sigma)\left[e^{i(kr-\ell\pi/2)} - e^{-i(kr-\ell\pi/2)}\right]. \qquad \text{Eq. (2.60)}$$

Just as in the nonspin case (only with the additional quantum number j), the regular solution to Eq. (2.55) has the asymptotic form (Ref. 2, p. 103)

$$u_{\ell j}(r) \underset{r\to\infty}{\sim} \sin\left(kr - \frac{\ell\pi}{2} + \delta_{\ell j}\right) \qquad \text{Eq. (2.61)}$$

where $\delta_{\ell j}$ is the spin-dependent phase shift, not to be confused with the symbol for the Kronecker delta. Splitting this into complex exponentials and comparing with Eq. (2.60), one gets the complete expression for $\psi(\vec{r},\sigma)$:

$$\psi(\vec{r},\sigma) = \frac{4\pi}{kr}\sum_{\ell m_\ell jm} i^\ell\, C^{\ell\ 1/2\ j}_{m_\ell\ \mu\ m}\, Y^*_{\ell m_\ell}(\hat{k})\,\mathcal{Y}_{\ell jm}(\hat{r},\sigma)\, e^{i\delta_{\ell j}}\, u_{\ell j}(r). \qquad \text{Eq. (2.62)}$$

One of the m-sums in Eq. (2.62) is fictitious, since the Clebsch-Gordan coefficient vanishes unless $m_\ell + \mu = m$. The other sum can be eliminated by taking the z-axis in the direction $\hat{k}$ and using the relation

$$Y_{\ell m}(\hat{z}) = \sqrt{\frac{2\ell+1}{4\pi}}\,\delta_{m0}.$$

By examining the outgoing part of Eq. (2.62) in the asymptotic region, one can find the scattering amplitude:

$$f_\mu(\hat{r},\sigma) = \frac{2\pi}{k}\sum_{\ell m_\ell j m} i^{\ell+1}\, C^{\ell\ 1/2\ j}_{m_\ell\ \mu\ m}\, Y^*_{\ell m_\ell}(\hat{k})\,\mathcal{Y}_{\ell_j m}(\hat{r},\sigma)\,(1-\eta_{\ell_j}). \qquad \text{Eq. (2.63)}$$

3. *Polarized and Unpolarized Cross Sections*

If one wants to know the probability of measuring a certain value for an observable D in a system whose wave function is ψ, one expands ψ in the eigenfunctions ϕ_d of D:

$$\psi = \sum_d \alpha_d \phi_d. \qquad \text{Eq. (2.64)}$$

The eigenvalues d are defined by

$$(D - d)\,\phi_d = 0. \qquad \text{Eq. (2.65)}$$

Then a fundamental postulate of quantum mechanics states that $|\alpha_d|^2$ is the probability of measuring d.

Expanding the spin harmonic in Eq. (2.63) according to Eq. (2.51) yields the expression

$$f_\mu(\hat{r},\sigma) = f^+_\mu(\hat{r})\,\chi_{1/2\ +1/2}(\sigma) + f^-_\mu(\hat{r})\,\chi_{1/2\ -1/2}(\sigma). \qquad \text{Eq. (2.66)}$$

The squares of the coefficients in this expansion give the probabilities of measuring a spin quantum number of $+1/2$ or $-1/2$. Hence,

$$\sigma^\pm_\mu(\hat{r}) = |f^\pm_\mu(\hat{r})|^2 \qquad \text{Eq. (2.67)}$$

is the cross section for finding a scattered particle traveling in the direction $\hat{r}$ with the spin component $\pm 1/2$, if the incident particle is in the spin state μ.

If the incident beam contains a mixture of particles with spin up and down ($\mu = \pm 1/2$), with weights $W_{\pm}$, then the cross section for finding particles with $m_s = \pm 1/2$ will be a weighted sum (assume $W_+ + W_- = 1$):

$$\sigma^{\pm}_{\text{weighted}}(\hat{r}) = W_+ \sigma^{\pm}_{1/2}(\hat{r}) + W_- \sigma^{\pm}_{-1/2}(\hat{r}). \qquad \text{Eq. (2.68)}$$

For an unpolarized incident beam, $W_+ = W_- = 0.5$. Likewise, if the particle detector has unequal efficiencies for measuring spin-up and spin-down particles, one has to take this into account in determining the experimental cross section. For equal efficiencies, $\epsilon_+ = \epsilon_- = 1$, one merely sums over the spin states of the outgoing particles. For an unpolarized incident beam and an unpolarized detector, the measured unpolarized cross section will be

$$\sigma(\hat{r}) = \frac{1}{2} \sum_{m_s \mu} \sigma_{\mu}^{2m_s}(\hat{r}). \qquad \text{Eq. (2.69)}$$

When all the required substitutions have been made in Eq. (2.69), the application of standard techniques in the theory of Clebsch-Gordan and associated coefficients reduces it to a relatively simple form. (Henceforth, the designation shape elastic will be used for this cross section in accordance with Sects. 2.2.B.4 and 2.2.C.1.)

In the notation of Lepore,[7] it can be written as

$$\sigma(\theta) = \frac{1}{4k^2} \left(|a|^2 + |b|^2 \right) \qquad \text{Eq. (2.70)}$$

where

$$a(\theta) = \sum_{\ell=0}^{\infty} \sum_{j=\ell-1/2}^{\ell+1/2} P_{\ell}(\cos\theta)(j + 1/2)(\eta_{\ell j} - 1) \qquad \text{Eq. (2.71)}$$

and

$$b(\theta) = \sum_{\ell=0}^{\infty} \sin\theta \frac{d P_{\ell}(\cos\theta)}{d(\cos\theta)} \left[\eta_{\ell, \ell+1/2} - \eta_{\ell, \ell-1/2} \right] . \qquad \text{Eq. (2.72)}$$

The angular integrated or total shape elastic cross section can be obtained from Eq. (2.70) by integrating over the whole solid angle of $\hat{r}$. Making use of the coupling rule for spherical harmonics (Ref. 8, p. 61), one obtains

$$\sigma_{se} = \frac{\pi\lambda^2}{2} \sum_{\ell=0}^{\infty} \sum_{j=\ell-1/2}^{\ell+1/2} (2j+1) \left|1 - \eta_{\ell j}\right|^2 \qquad \text{Eq. (2.73)}$$

which may be compared with Eq. (2.37).

In a similar manner, one can construct fluxes or currents of particles with spin up and spin down. The experimental reaction cross section will again involve an average over the initial spin states and a sum over the final. The end result for an unpolarized beam is

$$\sigma_r = \frac{\pi\lambda^2}{2} \sum_{j,\ell} (2j+1) \left(1 - \left|\eta_{\ell j}\right|^2\right), \qquad \text{Eq. (2.74)}$$

a generalization of Eq. (2.22). Finally, adding Eqs. (2.73) and (2.74),

$$\sigma_T = \pi\lambda^2 \sum_{j,\ell} (2j+1)\, Re\,(1 - \eta_{\ell j}). \qquad \text{Eq. (2.75)}$$

The polarization of the outgoing neutron is defined as the expectation value of its intrinsic spin operator. It is usually simplest to take the direction of polarization as the z-axis, in which case only $\langle S_z \rangle$ is nonzero. The numerical value of $\langle S_z \rangle$ in units of $\hbar/2$ is the experimentally quoted value of the polarization. In the problem at hand, only two directions enter the problem: the incident direction $\hat{k}$ and the outgoing direction $\hat{r}$. The spin, an axial vector, is therefore in the direction of the vector product $\hat{r} \times \hat{k}$. Its magnitude, using the $a(\theta)$ and $b(\theta)$ previously defined, is[7]

$$\vec{P}(\theta) = \frac{\lambda^2\, Im\,(ab^*)}{2\sigma_e(\theta)} \frac{\vec{k}\times\vec{r}}{|\vec{k}\times\vec{r}|}. \qquad \text{Eq. (2.76)}$$

As the denominator indicates, in the present context one must use the entire elastic cross section, shape plus compound, rather than merely $|a|^2 + |b|^2$. It is assumed that compound elastic particles are emitted unpolarized and so do not contribute to the numerator. Experimentally, of course, it is possible only to measure σ_e, the breakup into σ_{se} and σ_{ce} being a purely theoretical distinction.

4. *Specific Well Shapes*

Early optical model calculations usually employed a square well (and no spin-orbit potential):

$$V_c(r) = -V_{c0}(1 + i\xi) \qquad r < r_0$$
$$= 0 \qquad r \geq r_0 \,. \qquad \text{Eq. (2.77)}$$

Later, detailed comparisons with experimental data showed that the sharp edge of this well reflected too strongly and permitted too little penetration of the incident wave into the nucleus. As a result the predicted reaction cross sections were too low. A number of rounded edge potentials were then suggested, the most commonly used one being that of Woods and Saxon:[9]

$$V_c(r) = -V_{c0}\,\rho(r)\,,$$
$$\rho(r) = \left[1 + e^{\frac{r-R}{a}}\right]^{-1}\,, \qquad \text{Eq. (2.78)}$$

where R is the Saxon radius, and a is the diffuseness parameter. The thickness of the rounded edge is a function of the diffuseness parameter a, reducing to zero thickness (square well) for $a = 0$.

The imaginary part of the potential can be given the same shape as the real part, as in Eq. (2.77), by taking V_{c0} complex in Eq. (2.78), but the trend is toward a concentration of the imaginary part on the surface of the nucleus (so-called "surface absorption"). This was shown by Bjorklund, Fernbach, and Sherman[10,11] to reproduce the mass dependence of the various cross sections with a more realistic variation of parameters than the "volume absorption" potentials in which the imaginary potential is proportional to $\rho(r)$ [see Eq. (2.78)].

Theoretical analyses frequently suggest a mixture of volume plus surface absorption, such as

$$i\,W(r) = -i\,W_v\,\rho(r) - i\,W_s\,e^{-\left(\frac{r-R}{b}\right)^2}\,. \qquad \text{Eq. (2.79)}$$

The second term here has the Gaussian shape originally introduced in Refs. 10 and 11.

The shape of the spin-orbit potential, $V_s(r)$, is quite arbitrary, since any reasonable shape will fit the data with a suitable

choice of parameters. The popular choice is the Thomas form factor,* familiar from atomic physics (Ref. 12, p. 502):

$$V_s(r) = -2\,V_{s0}(\hbar/\mu_\pi c)^2 \frac{1}{r}\frac{d}{dr}\rho(r). \qquad \text{Eq. (2.80)}$$

Generally speaking, the sensitivity of the model to the experimental data is insufficient to fix a possible imaginary component for V_s and it is taken real. The strength V_{s0} in Eq. (2.80) is required to be an adjustable parameter because the Thomas term itself, a consequence of special relativity (Ref. 2, p. 276), is inadequate to explain observed polarizations (the principal experimental data which fix V_s). Just as in the shell model (Ref. 13, p. 59; Ref. 14, Chap. II; Refs. 15 and 16; Ref. 17, Chap. 6), a much stronger force is required to fit the data.

For charged particle reactions it is necessary to add to V_c a Coulomb potential. The particular form of this potential is more or less arbitrary, but due to the insensitivity of the Coulomb potential to the charge distribution producing it, any reasonable choice will give equivalent results. The conventional form is the potential of a uniformly charged sphere of radius r_s:

$$V_{\text{Coulomb}}(r) = \frac{Ze^2}{2r_s}\left[3-\left(\frac{\gamma}{r_s}\right)^2\right] \quad r \le r_s$$

$$= \frac{Ze^2}{r} \quad r \ge r_s. \qquad \text{Eq. (2.81)}$$

The sphere radius, r_s, is often set equal to the Saxon radius R or given a value determined by high-energy electron scattering.

5. *Determining the Potential Well Shape from Total, Elastic, and Inelastic Cross-Section Data and from Average Resonance Parameters*

In their classic paper on the optical model, Feshbach, Porter, and Weisskopf[1] determined the range and depth of the complex square well which fitted a large number of total and elastic cross section measurements. This technique is still the principal method used. In addition, they also made use of the relationship [compare Eqs. (2.33) and (2.23)]

$$T_\ell \approx 2\pi \frac{\langle \Gamma_{n\ell} \rangle}{D_\ell} \qquad \text{Eq. (2.82)}$$

*The occurrence of the pi-meson Compton wavelength and the factor 2 make this definition conform to that of Refs. 10 and 11.

where T_ℓ is the penetrability of an ℓ^{th} partial wave neutron. It is calculated in the optical model [Eq. (2.23)] and determines the reaction cross section. D_ℓ is the average level spacing in the compound nucleus between states involving incident ℓ-wave neutrons, and $\Gamma_{n\ell}$ is the neutron width which appears in the Breit-Wigner resonance formula (Sect. 2.2.D.2). The physical meaning of the relationship is discussed by Blatt and Weisskopf (Ref. 4, p. 388).

In terms of the optical model reflection coefficients $\eta_{\ell j}$, the penetrability is [compare Eqs. (2.23) and (2.40)]

$$T_\ell \equiv 1 - |\eta_\ell|^2 = \sum_{j=\ell-1/2}^{j=\ell+1/2} \frac{2j+1}{2(2\ell+1)} T_{\ell j} \qquad \text{Eq. (2.83)}$$

where

$$T_{\ell j} = 1 - |\eta_{\ell j}|^2 \qquad \text{Eq. (2.84)}$$

so that T_ℓ is a measure of how strongly an ℓ-wave neutron is absorbed to form a compound nucleus. The experimentally determined values of $<\Gamma_{n\ell}>/D_\ell$ for levels (resonances) of a particular angular momentum are usually given in the form of neutron strength function plots, $<\Gamma^0_{n\ell}>/D_\ell$, where $\Gamma^0_{n\ell}$ is the reduced width associated with $\Gamma_{n\ell}$. For s-waves, $\Gamma^0_{n0} = \Gamma_{n0}/\sqrt{E}$ while for p-waves, $\Gamma^0_{n1} = \Gamma_{n1}/x^2\sqrt{E}$ (for small $x = kR$). These reduced widths differ from Blatt and Weisskopf's (Ref. 4, p. 390) by a factor $\sqrt{8m R^2/\hbar^2}$ which is essentially a single particle reduced width amplitude (Ref. 4, p. 420; Ref. 17, Chap. V. G). For example, Ajzenberg-Selove and Lauritsen[18] give reduced widths in units of the Wigner-Teichmann single particle reduced width

$$\gamma^2_{WT(SP)} = \frac{3\hbar^2}{2mR}. \qquad \text{Eq. (2.85)}$$

This is an estimate based on a single particle wave function that is constant in value and normalized to unity inside a sphere of radius R. The Blatt and Weisskopf definition is related to that of Wigner and Teichmann by

$$\gamma_{BW} = \frac{1}{R}\gamma^2_{WT}. \qquad \text{Eq. (2.86)}$$

The square-root quantity, $\gamma_{WT}/\sqrt{R}$ or $\sqrt{\gamma_{BW}}$, is called a reduced width amplitude.

Using Eqs. (2.82) and (2.83) one finds the s-wave strength function,

$$\frac{1}{D_0}\langle\Gamma^0_{n0}\rangle = \frac{T_{0\,1/2}}{2\pi\sqrt{E}} \qquad \text{Eq. (2.87)}$$

and the p-wave strength function,

$$\frac{1}{D_1}\langle\Gamma^0_{n1}\rangle = \frac{T_{1\,1/2} + 2T_{1\,3/2}}{6\pi x^2\sqrt{E}}. \qquad \text{Eq. (2.88)}$$

The s-wave strength function has been measured for many nuclei by averaging the parameters observed for individual resonances.[19] For example, for Zr^{90}, $\langle\Gamma^0_{n0}\rangle/D_0 = 0.5 \times 10^{-4}$ and the thermal elastic scattering cross section has been measured as 6.3b. These two measurements are sufficient to determine the real and imaginary potential strengths.

Additional useful experimental information results if the s-state contribution is subtracted from the total compound nucleus cross section at low energies. Since only one additional partial wave contributes appreciably to the cross section, the p-wave strength function can be found.[20]

On the basis of the measurement of p-wave resonances and, hence, strength functions, it should be possible to fix the optical model parameters more precisely. However, at present there exists considerable experimental difficulty in determining consistent p-wave strength functions.[21,22]

Finally, as will be shown in Sect. 2.2.D, the Hauser-Feshbach theory of the compound nucleus makes use of these same penetrabilities, thus providing another method for finding the correct well parameters.

6. *Numerical Techniques for Solving the Radial Equation*

A) CONTINUUM STATES. As the work of Sect. 2.2.C.2 showed, the numbers of interest are the phase shifts $\delta_{\ell j}$ and the reflection coefficients $\eta_{\ell j} = e^{2i\delta_{\ell j}}$. Looking at Eq. (2.61) it is seen that in principle one can forward integrate out from the origin until $u_{\ell j}$ assumes the form of a sine wave and then can read off $\delta_{\ell j}$. In practice, it is simpler to carry this integration only out to some cutoff radius R_c where the potential is negligible and at that point to join on to a suitable combination of known free particle functions. The forward integration can be carried out on Eq. (2.55) using complex arithmetic, or Eq. (2.25)

can be split into a pair of coupled equations for the real and imaginary parts of $u_{\ell j}$. In either case, equivalent difference equations are employed, and $u_{\ell j}$ is assigned the value zero at $r = 0$ and some arbitrary value at the first mesh point, since the normalization and overall phase turn out to be immaterial. At the cutoff, one evaluates numerically the logarithmic derivative, $f_{\ell j}$, defined as follows:

$$f_{\ell j} \equiv X_c \left. \frac{du_{\ell j}/dx}{u_{\ell j}} \right|_{x = X_c = kR_c} \qquad \text{Eq. (2.89)}$$

The analytically specified wave function for $r > R_c$ must have this same value for its logarithmic derivative at $r = R_c$.

For the free particle wave functions one first defines the regular function

$$F_\ell(x) = x j_\ell(x) \underset{x \to \infty}{\sim} \sin\,(x - \ell\pi/2) \qquad \text{Eq. (2.90)}$$

and the irregular function

$$G_\ell(x) = -\,x n_\ell(x) \underset{x \to \infty}{\sim} \cos\,(x - \ell\pi/2). \qquad \text{Eq. (2.91)}$$

The functions $j_\ell(x)$ and $n_\ell(x)$ are the spherical Bessel functions (of order half-an-odd-integer) defined by Morse (Ref. 2, p. 78; Ref. 4, p. 331). Then one constructs the outgoing and ingoing wave combinations

$$u_\ell^+(x) = G_\ell(x) + i F_\ell(x) \underset{x \to \infty}{\sim} e^{i\,(x - \ell\pi/2)} \qquad \text{Eq. (2.92)}$$

$$u_\ell^-(x) = G_\ell(x) - i F_\ell(x) \underset{x \to \infty}{\sim} e^{-i(x - \ell\pi/2)}. \qquad \text{Eq. (2.93)}$$

Equations (2.19) and (2.62) indicate that the required combination of outside wave functions is

$$\eta_{\ell j}\, u_\ell^+ - u_\ell^- \underset{r \to \infty}{\sim} \eta_{\ell j}\, e^{i\left(kr - \frac{\ell\pi}{2}\right)} - e^{-i\left(kr - \frac{\ell\pi}{2}\right)} \qquad \text{Eq. (2.94)}$$

If one defines the standard logarithmic derivative

$$X_c \left. \frac{du_\ell^+/dx}{u_\ell^+} \right|_{x = X_c} \equiv \Delta_\ell + iS_\ell, \qquad \text{Eq. (2.95)}$$

then matching the logarithmic derivative of Eq. (2.94) to the numerically determined logarithmic derivative from Eq. (2.89) yields

$$\eta_{\ell j} = \frac{f_{\ell j} - \Delta_\ell + iS_\ell}{f_{\ell j} - \Delta_\ell - iS_\ell} \cdot \left. \frac{G_\ell - iF_\ell}{G_\ell + iF_\ell} \right|_{x = X_c} . \qquad \text{Eq. (2.96)}$$

The coefficient of the outgoing wave, $\eta_{\ell j}$, may then be used to calculate σ_r [Eq. (2.74)], σ_{se} [Eq. (2.73)], and σ_T [Eq. (2.75)].

B) BOUND STATES. The procedure here is the same as in continuum states, with four differences: (1) The energy in Eq. (2.55) is negative. This does not affect the numerical procedures. (2) The outside function is the decaying spherical Hankel function (Ref. 1, p. 79) of imaginary argument, $h_\ell^{(1)}(i\gamma r)$, instead of Eq. (2.94). (3) In general, the outside logarithmic derivative will not match the inside one. It will only do so if the particular energy under consideration actually admits a discrete bound state. (4) The potential must be real for determining bound states. To solve a bound state problem, it is necessary to vary the energy or some potential well parameter until the inside and outside logarithmic derivatives are equal.

C) CHARGED PARTICLE SCATTERING. It is appropriate here to describe the effect of the inclusion of a Coulomb term in the nuclear potential. For $r < R_c$ the radial equation can still be integrated numerically, and the solution and its derivative matched at the boundary $r = R_c$ to the solutions of a radial equation with only a Coulomb potential term. These Coulomb wave functions are well tabulated and their generating functions known.[23] Thus, it is possible to treat proton scattering in a manner similar to neutron scattering. Since the latter is of more importance in reactor problems, it is discussed in greater detail than Coulomb scattering.

D. The Compound Nucleus Model

1. Introduction

Around 1935, following the earliest observations of resonances in the scattering of neutrons, attempts were made to explain these on the basis of potential scattering models. Since it was recognized that the narrow widths implied additional particle-particle interactions, these were introduced as perturbations.[24] Breit and Wigner succeeded in this way in explaining the shapes of the resonances, but the widths they obtained were too large.

At the same time Bohr[25] emphasized the fact that the incident particle must interact strongly with all the target nucleons in order to produce states with the observed long lifetimes. This made perturbation theory inapplicable and led to various formulations of reaction theory in which a central role is played by the quasistationary states of the compound nucleus.[26-28] These theories are most useful in regions of isolated resonances, although, being formally exact, they can in principle describe nuclear reactions in any region. These theories are described in excellent review articles (Ref. 14, Chap. V; Refs. 15, 16, 29), which analyze the scattering of particles from a potential well according to the methods of compound nucleus theory, a very useful device for gaining insight into the theory's structure.

2. *Theory of Isolated Resonances*

The most useful and well known result of the above-mentioned theories is the rigorous derivation of formulas for nuclear cross sections in regions of nonoverlapping resonances. For some reactor applications these fluctuations are of great importance. When the structural material or fuel element cladding has sharp resonances in the epithermal range, the macroscopic cross sections can swing sufficiently to produce important neutron flux depression effects. Most control rod elements have epithermal resonances which must be calculated in detail if reliable evaluations of the control rod worth are desired. Even the high energy sharp resonances in O^{16} produce large swings in the neutron leakage flux. Although the location and shape of these resonances cannot be predicted at present, a combination of theory and experiment can supply useful information about them. The theory furnishes a formula for the cross section as a function of various parameters, and so the measurements can be directed to finding a few parameters instead of all the details of the cross section. Most resonances may be calculated using a single-level Breit-Wigner formula given below. However, the description of the U^{235} cross section in and near the thermal energy range is best calculated with the formula discussed below in multilevel theory. The calculation of the interference of the O^{16} scattering resonances is most accurately done using the unified model (Sect. 2.2.F).

A) BREIT-WIGNER SINGLE-LEVEL FORMULA. Since the primary application of Breit-Wigner theory in thermal reactor design is to s-wave neutrons, the results presented here are limited to that case. For derivations, the reader is referred to Refs. 30, 31, and Ref. 4, Chap. VIII.

The elastic scattering cross section is characterized near an isolated resonance by interference between the resonant amplitude and the smoothly varying potential scattering amplitude:

$$\sigma_e = \frac{4\pi}{k(E_0)} g \left| \frac{\Gamma_n(E_0)}{2(E - E_0 + i\Gamma/2)} + k(E_0)R \right|^2 + 4\pi (1 - g) R^2 \qquad \text{Eq. (2.97)}$$

where $g = \frac{2J+1}{2(2I+1)}$ is the statistical factor, J is the angular momentum of the compound nucleus, I is the angular momentum of the target, E is the incident neutron energy (ev), E_0 is the resonance energy, $\Gamma_n = \sqrt{E}\,\Gamma_n^0$ is the width for emission or absorption of neutrons by the compound nuclear state in question, and R is a radius of approximately nuclear dimensions, often called the hard sphere radius because of the form of the potential scattering amplitude (Ref. 4, p. 328).* Neglecting processes such as (n, p) and (n, α), which are usually negligible at low energies, the neutron total width is

$$\Gamma = \Gamma_n + \Gamma_\gamma + \Gamma_f \qquad \text{Eq. (2.98)}$$

where Γ_γ and Γ_f are the partial widths for capture and fission, respectively.

The (n,γ) or capture cross section is

$$\sigma_{n,\gamma} = \frac{\pi}{k(E_0)} \sqrt{\frac{E_0}{E}}\, g \frac{\Gamma_n(E_0)\Gamma_\gamma}{(E - E_0)^2 + (\Gamma/2)^2} \qquad \text{Eq. (2.99)}$$

and the fission cross section is obtained by replacing Γ_γ by Γ_f in Eq. (2.99).

When all the resonance parameters have been measured for a particular resonance, the use of Eqs. (2.97) and (2.99) is straightforward. For most resonances, however, one or several of the parameters must be estimated. If, for example, a value of Γ_γ is known for one resonance of the nucleus in question or a neighboring one, this value can be used for all of them. When I is known but J is not, one can use the formulas: $g = 1$ for $I = 0$; $g \cong 1/2$ for large I, say $I \gtrsim 9/2$. For intermediate values of I, J values can be assigned arbitrarily, except that

*Both k and Γ_n are energy-dependent quantities, proportional to $E^{1/2}$. In tabulations such as Ref. 30, k or λ, and Γ_n mean these quantities evaluated at $E = E_0$. The notation used here makes this explicit. The energy dependence of Γ is usually neglected.

since the density of resonance levels is proportional to $2J + 1$, the assigned J values should be consistent with this.

It is in general impossible to predict the location or neutron width of a particular resonance. In the absence of other information, however, these quantities can be assigned so as to produce average distributions in accordance with known rules. Thus, if $x = \Gamma_n^0 / \langle \Gamma_n^0 \rangle$, where $\langle \Gamma_n^0 \rangle$ is the average of the reduced width over a region containing many resonances, the probability of observing a particular value of x is given by the Porter-Thomas distribution[32]

$$P(x) = \frac{1}{2\sqrt{\pi}} \sqrt{\frac{2}{x}}\ e^{-x/2} \ . \qquad \text{Eq. (2.100)}$$

Similarly, the distribution of the spacings between levels of a particular value of angular momentum J is well approximated by the Wigner distribution[33,34]

$$Q(y) = \frac{\pi}{2} y\, e^{-\frac{\pi y^2}{4}} \qquad \text{Eq. (2.101)}$$

where $y = D/\langle D \rangle$. The values of $\langle D \rangle$ and $\langle \Gamma_n^0 \rangle$, which are averages of these quantities over many resonances, must be estimated from neighboring nuclei.

In general, the fission partial width Γ_f fluctuates more than Γ_γ but less than Γ_n^0. The distribution of $z = \Gamma_f / \langle \Gamma_f \rangle$ for U^{235} is approximately

$$R(z) = e^{-z} \ . \qquad \text{Eq. (2.102)}$$

This distribution of fission widths should be used only where the actual parameters are unmeasured.

B) MULTILEVEL THEORY: THE INTERFERENCE OF FISSION RESONANCES. The interference of neighboring resonances is neglected in the single-level Breit-Wigner theory. However, inspection of certain low-energy neutron cross sections, for example U^{235}, indicates that interference effects are important. In particular, the degree of asymmetry of the fission cross section requires the inclusion of such effects

for its quantitative description. Vogt[35] has developed multilevel resonance theory formulas for this application. These are:

$$\sigma_T = \frac{6.52 \times 10^5}{\sqrt{E}} \operatorname{Re} \left\{ (1 - e^{-2ikR}) \frac{2g}{\sqrt{E}} + i e^{-2ikR} \sum_{\lambda\lambda'} \left(\Gamma^0_{\lambda n}\right)^{1/2} \left(\Gamma^0_{\lambda' n}\right)^{1/2} A_{\gamma\gamma'} \right\} \qquad \text{Eq. (2.103)}$$

$$\sigma_{nn} = \frac{6.52 \times 10^5}{E} g \left| 1 - e^{-2ikR} \left\{ 1 + i \sum_{\lambda\lambda'} \left(\Gamma_{\lambda n}\right)^{1/2} \left(\Gamma_{\lambda' n}\right)^{1/2} A_{\lambda\lambda'} \right\} \right|^2 \qquad \text{Eq. (2.104)}$$

$$\sigma_{n\gamma} = \frac{6.52 \times 10^5}{2\sqrt{E}} \sum_{\lambda\lambda'\lambda''} \Gamma_{\lambda\gamma} \left(\Gamma^0_{\lambda' n}\right)^{1/2} \left(\Gamma^0_{\lambda'' n}\right)^{1/2} A_{\lambda\lambda'} A^*_{\lambda\lambda''} \qquad \text{Eq. (2.105)}$$

$$\sigma_{nf} = \frac{6.52 \times 10^5}{2\sqrt{E}} \sum_{\lambda\lambda'\mu\mu'} \left(\Gamma^0_{\lambda n}\right)^{1/2} \left(\Gamma^0_{\lambda' n}\right)^{1/2} \vec{g}_{\mu f} \cdot \vec{g}_{\mu' f} A_{\lambda\mu} A^*_{\lambda'\mu'} \qquad \text{Eq. (2.106)}$$

E, g, and R were defined in the previous paragraph; $\lambda = 1, 2, \ldots, n$ is an index numbering the resonance levels under consideration; $\Gamma_{\lambda\gamma}$ and $\Gamma_{\lambda n}$ are the γ-ray and neutron widths for the level λ, respectively; $\vec{g}_{\lambda f}$ are so-called fission channel vectors, i.e., sets of m constants, one per fission channel, to be assigned in such a way as to fit the observed cross sections. For each channel, λ, the vectors $\vec{g}_{\lambda f}$ satisfy the relation

$$\vec{g}_{\lambda f} \cdot \vec{g}_{\lambda f} = \Gamma_{\lambda f} \cdot \qquad \text{Eq. (2.107)}$$

The inverse of the matrix A is defined as follows:

$$(A^{-1})_{\lambda\lambda'} = (E_\lambda - E)\, \delta_{\lambda\lambda'} - \frac{i}{2} \vec{g}_{\lambda f} \cdot \vec{g}_{\lambda' f} \cdot \qquad \text{Eq. (2.108)}$$

Assuming two fission channels, with one negative and three positive energy resonances, Vogt was able to represent within 2 percent the fission, total, and (n, γ) cross sections for neutron energies up to 1.5 ev. From the reactor physics viewpoint, the use of the multilevel formula permits the generation of all U^{235} cross sections below 1.5 ev as a function of only 24 resonance parameters and a simple formula. This is helpful

for generating cross sections in digital computer programs and economical for cross section information storage. Also, since the multilevel method of analysis is being used increasingly by many experimentalists, it is likely that the experimental results will be more frequently available as multilevel instead of single level parameters. According to J. A. Harvey of Oak Ridge National Laboratory, U^{235} and U^{233} have already been analyzed in this way.[36,37]

3. *Statistical Theory of Compound Nucleus Reactions*

At energies higher than that for which the theory of the preceding paragraphs is relevant, the resonances become dense enough so that it is impossible to treat them individually. This suggests the use of theories which focus on the average properties of very many compound nuclear levels, so-called statistical theories.

One class of theories deals with the nucleus as a system in thermodynamic equilibrium. These are described, for example, in Ref. 14, Chap. VII, and Ref. 38, and are useful for estimating the energy spectra of particles emitted from the compound nucleus. The characteristic quantities of these theories are nuclear temperatures and level densities. Measurements on certain nuclei at isolated energies permit theoretical extrapolation to other regions of mass and energy.

Another class of theory, based more directly on ordinary reaction theory, has been developed by Wolfenstein[39] and Hauser and Feshbach.[40] They assume that the incident neutron and target nucleus combine to form a compound nucleus which subsequently decays. The decay of the compound nucleus of a particular total and z-component of angular momentum is assumed to be independent of its mode of formation.

The factors governing the probability of formation, and by arguments of detailed balancing also of the decay, of the compound nucleus are given in terms of penetrabilities [Eq. (2.83)]. A particularly simple version of this theory was described by Feshbach, et al., in their optical model paper.[1] A spinless neutron impinging on a zero-spin target nucleus with orbital angular momentum ℓ_i has a cross section for forming the compound nucleus see [Eq. (2.40)]

$$\sigma_c^{(\ell_i)} = \pi\lambda\!\!\!^{-2}\,(2\ell_i + 1)\,T_{\ell_i}(E). \qquad \text{Eq. (2.109)}$$

This is multiplied by the probability w_{ℓ_i} that the compound nucleus will decay by emitting the particle with the same angular momentum and energy.

The final factor is $|Y_{\ell_i 0}(\hat{r})|^2$, the angular distribution of a particle with angular momentum ℓ_i, z-component $m_i = 0$ (the incident plane wave has $m_i = 0$, and this is conserved in the reaction). The assumption of incoherent addition then allows the simple summation

$$\sigma_{ce}(\theta) = \sum_{\ell_i} \sigma_c^{(\ell_i)} w_{\ell_i} \left| Y_{\ell_i 0}(\hat{r}) \right|^2 \qquad \text{Eq. (2.110)}$$

a statistical estimate of the compound elastic cross section.

The aforementioned connection with the optical model is made by observing that, in terms of penetrabilities, the probability w_{ℓ_i} that the compound nucleus decays with the emission of a particle of energy E and orbital angular momentum ℓ_i is

$$w_{\ell_i} = \frac{T_{\ell_i}(E)}{\sum_{\ell_f, p} T_{\ell_f}(E_p)} . \qquad \text{Eq. (2.111)}$$

The denominator in Eq. (2.111) represents the sum of all decay modes, namely, all possible final angular momenta ℓ_f, and all possible states of excitation of the residual nucleus, E_p. The numerator is a particular one of these, the penetrability associated with elastic ℓ_i-wave emission.

When the target spin is included, it becomes possible for the particle to change its ℓ_i value, since only the total angular momentum is conserved. In addition, one needs to make use of the angular momentum coupling relations referred to earlier. Feshbach, et al.,[1] also gives a heuristic derivation of the formula for this case.

An additional generalization[41] permits the employment of the spin-orbit penetrabilities $T_{\ell j}$ [Eq. (2.84)], viz.,

$$\sigma(J_i, J_f; E, E'; \theta) = \frac{\pi}{k^2} \sum_{\substack{J_i j_i j_f \\ \ell_i \ell_f}} \frac{(-)^{J_i - J_f} T_{\ell_i j_i}(E)\, T_{\ell_f j_f}(E')}{2(2J_i + 1) \sum_p T_{\ell_p j_p}(E'_p)}$$

$$\cdot \sum_{L \text{ even}} P_L(\cos\theta)\, Z(\ell_f j_f \ell_f j_f; 1/2\, L)\, Z(\ell_i j_i \ell_i j_i; 1/2\, L) \qquad \text{Eq. (2.112)}$$

$$\cdot W(J j_f J j_f; J_f L)\, W(J j_i J j_i; J_i L)$$

where $W(a, b, c, d, e, f)$ and $Z(a, b, c, d, e, f)$ are Racah coefficients tabulated by Biedenharn, [42] and

E is the initial energy of the neutron;

E' is the final energy of the final state particle (neutron, proton);

J_i is the total angular momentum of the target nucleus;

J_f is the total angular momentum of the final nucleus;

$T_{\ell_i j}(E)$ is the nuclear penetrability; this quantity is calculated with the optical model described in Sect. 2.2.C;

J_i is the total angular momentum quantum number of the incident neutron, lying in the range

$$|J - J_i| \leq j_i \leq J + J_i$$

and may assume only half integral values;

ℓ_i is the orbital angular momentum of the incident neutron,

$$\ell_i = j_i \pm 1/2;$$

J is the total angular momentum of the compound nucleus; if J_i is integral (half-integral), then J is half-integral (integral); all J values must be included up to values for which the contribution to the sum is negligible.

j_f is the total angular momentum of the final state particle.

To perform compound nucleus calculations, the parity and spin of all energetically possible final states of the target nucleus must be known.

If the parity of J_i and J_f are $\begin{Bmatrix}\text{same}\\ \text{different}\end{Bmatrix}$, the possible values of ℓ_f are $\begin{Bmatrix}\text{even}\\ \text{odd}\end{Bmatrix}$ when ℓ_i is even and conversely when ℓ_i is odd.

$E'_{p|}$ is a possible final value of the energy of the particle. The summation over p includes all final particle energies permitted by energy conservation. To each E'_p there corresponds a state of the final nucleus, $E_p(J_f)$, such that $E'_p + E_p(J_f) = E + E(J_i)$, where $E(J_i)$ is the initial energy of the target nucleus (zero for a target in the ground state).

An important characteristic of the compound nucleus angular distribution given by Eq. (2.112) is that it is symmetrical about the 90-degree scattering angle. This is a consequence of the statistical assumption that only geometrical, and not

physical, considerations limit the number of participating compound states. Subject to this approximation, which should be a good one away from regions of unusually low density of compound states, the transport cross section σ_{tr} is independent of the compound elastic angular distribution:[43]

$$\sigma_{tr} = 2\pi \int_{-1}^{+1} \sigma_e(\theta)\,[1 - \cos\theta]\, d(\cos\theta) \qquad \text{Eq. (2.113)}$$

$$= \sigma_{se} + \sigma_{ce} - 2\pi \int_{-1}^{1} \sigma_{se}(\theta) \cos\theta\, d(\cos\theta)\,.$$

The angle-integrated cross section for the transition from the initial state $(J_i, E) \rightarrow (J_f, E')$ is obtained from Eq. (2.112),

$$\sigma(J_i J_f; E, E') = \frac{\pi}{k^2} \sum_{\substack{j_i \ell_i \\ j_f \ell_f}} \frac{T_{\ell_i j_i}(E)}{2(2I_i + 1)} \sum_J \frac{T_{\ell_f j_f}(E')(2J+1)}{\sum_p T_{\ell_p j_p}(E'_p)}\,. \qquad \text{Eq. (2.114)}$$

When the incident energy of the neutron is below that of the first excited state in the target, only compound elastic scattering is energetically possible, and Eq. (2.114) reduces to (since $E' = E'_p = E$, and $\sum_J (2J+1) = (2i_i+1)(2J+1)$, the multiplicity of initial states of the system)

$$\sigma(J_i J_i; EE) = \frac{\pi}{2k^2} \sum_{\ell_i j_i} (2i_i + 1)\, T_{\ell_i j_i}(E)\,. \qquad \text{Eq. (2.115)}$$

Equations (2.115) and (2.74) are identical, as they should be if it is recalled that $\lambda\!\!\!^{-} = 1/k$ and $T_{\ell j} = 1 - |\eta_{\ell j}|^2$.

The statistical compound nucleus theory is especially useful in calculating elastic and inelastic neutron scattering and (n,p) reaction cross sections for neutrons of energy less than 5 Mev. The compound nucleus theory formula presented here may be applied to the calculation of each of these cross sections, if the proton penetrabilities are obtained from a coulomb-modified potential.

E. The Direct Interaction Model

1. Introduction

The compound nucleus (Hauser-Feshbach) theory of nuclear reactions has been discussed as a method for predicting inelastic cross sections to be used in criticality calculations. For water-moderated reactors, the use of Hauser-Feshbach theory to predict metal inelastic neutron cross sections does not introduce errors of more than a few percent in the reactivity. However, certain predictions of this theory are definitely in error. For example, the angular distribution of the final state particles is predicted to be symmetric about 90 degrees. However, neutrons of energy above several Mev have angular distributions that strongly favor the forward direction, especially for collisions in which the target nucleus is weakly excited. These inelastically scattered neutrons are of importance in accurate shielding calculations.

In addition to the inability of the compound nucleus theory to predict the angular distribution of such neutrons, its prediction of the magnitude of this cross section is frequently incorrect. A probable example of this is the discrepancy between the calculated and experimental values for the excitation of the 2.18 Mev level of Zr^{90}.[41]

The cross section for (n,p) reactions in light nuclei shows discrepancies with compound nucleus theory even when the incident neutron energy is only a few Mev above the threshold for the reaction.[44] (These (n, p) cross sections are of importance in calculating the activation of reactor materials and in estimating changes in macroscopic physical characteristics due to transmutation of the elements.)

Numerous other examples could be listed in which the compound nucleus theory does not adequately predict reaction cross sections. Although the number of failures of the compound nucleus theory seems to be ever increasing, this model is quite useful in predicting most cross sections needed for reactor design.

The remaining cases, some of which have just been discussed, fall under the heading of direct interaction theory, so-called because the system is assumed to proceed directly from the initial to the final state without the intermediate step of compound nucleus formation. The primary reasons for studying direct interaction effects are: (1) Their study can help in determining when compound nucleus predictions should not be trusted. (2) Even though compound nucleus theory is usually adequate, a particular reactor material might be poorly suited for compound nucleus calculations.

For example, the most accurate cross sections of Li, Be, B, C, and O are calculated with the direct interaction or unified models. (3) In reactor design, a small cross section can have a big effect. For example, in most of the nonelastic collisions of a 10-Mev neutron, the neutron is either absorbed or it loses most of its energy. These neutrons are of little importance in deep neutron penetration calculations. However, the smaller number of neutrons that lose only a small amount of energy and whose scattering angle is small are the ones that leave the shield and must therefore be counted accurately. These neutrons are direct interaction neutrons. (4) Since direct interaction effects are always present to some degree, it is essential to use the direct interaction model if improved predictions of nuclear reaction cross sections are desired.

Although the direct interaction model is an extreme one, it is probably no more extreme than the compound nucleus model. In the compound nucleus model, the incident neutron is assumed to enter the nucleus and have a large number ($\sim 10^6$) of collisions. On the other hand, a direct interaction collision requires only one or at most a few collisions with the nucleons in the nucleus. Since the excitation of the target nucleus to a highly excited state is likely to require many collisions, the compound nucleus theory should be used to calculate the cross section for inelastic collisions with large neutron energy losses. The weak excitation of the target nucleus is expected to require only a few collisions, so that the direct interaction model should be successful here. The cross section for (n, p) collisions in the important threshold region is extremely small in compound nucleus theory, and the direct interaction contribution here is expected to be appreciable. A general rule to follow is that if the compound nucleus calculation of a cross section yields a small result, it is advisable to calculate that cross section in the direct interaction model. Another useful rule is related to the basic assumptions of compound nucleus theory. In deriving the compound nucleus theory formulas, it is assumed that the density of nuclear resonance states is so high that the levels overlap. Therefore, in calculating the cross sections for those light nuclei where this high level density approximation is not valid, the direct interaction model must be employed.

In a direct interaction process an incident particle collides with a nucleon in the nucleus and any combination of the colliding particles may be emitted. The calculations that describe this quantitatively are called distorted wave Born approximation calculations and are described in the next section. The Born approximation refers to the fact that only one collision is included in the calculation. However, the direct interaction

calculation is not to be interpreted as a conventional perturbation theory calculation in which the nuclear potential produces the transition. Instead, the interaction is assumed to be an effective one which includes the average effect of high order processes.

2. *Direct Interaction Formulation of Nuclear Reaction Theory*

In Sect. 2.2.B the wave function describing a nuclear reaction was discussed. The following paragraphs will sketch the manner in which such a wave function can be formally constructed. The procedure is to expand the wave function in the eigenfunctions of the residual nucleus for the reaction under investigation. For elastic and inelastic scattering of neutrons, the residual nucleus is the same as the target nucleus. For (n, p) reactions, it is the nucleus ${}_{z-1}h^{A}_{N+1}$, and so on. If the other reaction product is a composite particle (deuteron, alpha particle, etc.), the expansion must also contain its internal eigenfunctions. Finally, the expansion set involves wave functions describing the relative motion of the two pieces. It is from the asymptotic form of these relative motion wave functions that the cross section can be read off.

By first converting the Schrödinger equation to an integral equation, the above expansion can be used to exhibit explicitly the form of the various outgoing waves. Initially, the procedure appropriate to elastic and inelastic scattering will be dealt with.

If H denotes the Hamiltonian of the system, and E_{lab} its total energy in the laboratory coordinate system, the wave function Ψ satisfies the time-independent Schrödinger equation,

$$(E_{\text{lab}} - H)\Psi = 0. \qquad \text{Eq. (2.116)}$$

The Hamiltonian is the sum of the kinetic energies of each particle, denoted by T_i for the i^{th} particle, and the interaction energies between each pair of particles, V_{ij}:

$$H = \sum_{i=1}^{A+1} T_i + \sum_{i<j=1}^{A+1} V_{ij}. \qquad \text{Eq. (2.117)}$$

There are A nucleons in the target; the incident nucleon is the $A+1^{\text{st}}$.

If ∇_i^2 is the Laplacian operator for a particle with position $\vec{r}_i$ (and mass m_i), then there exists the identity:

$$\frac{\nabla_1^2}{m_1} + \frac{\nabla_2^2}{m_2} = \frac{\nabla^2}{\mu} + \frac{\nabla_c^2}{M}. \qquad \text{Eq. (2.118)}$$

In Eq. (2.118) ∇^2 is the Laplacian in the relative coordinate $\vec{r}_1 - \vec{r}_2$, μ is the reduced mass $m_1 m_2/(m_1 + m_2)$, ∇_c^2 is the Laplacian in the center-of-mass coordinate $\vec{R}_c = (m_1 \vec{r}_1 + m_2 \vec{r}_2)/(m_1 + m_2)$, and $M = m_1 + m_2$ is the total mass.

By successive application of Eq. (2.118), it is possible to split the kinetic energy into an internal contribution T_{int} which involves only the coordinates of the A nuclear particles, a relative term T_{rel} involving the distance of the incident nucleon from the target's center-of-mass, $\vec{r}_{\text{rel}}$, and a term T_{cm} involving the center-of-mass coordinate of the entire system, $\vec{R}$.

Analogously, the interaction terms can be grouped into those which involve only the target nucleons, and those which involve the incident neutron as one member of the pair:

$$\sum_{i<j=1}^{A+1} V_{ij} = \sum_{i<j=1}^{A} V_{ij} + \sum_{i=1}^{A} V_{i,\,A+1} \qquad \text{Eq. (2.119)}$$

$$\equiv V_{\text{int}} + V(A+1). \qquad \text{Eq. (2.120)}$$

In Eq. (2.120), V_{int} is the internal potential energy, and $V(A+1)$ is the true interaction between the neutron and target nucleus. Because it is extremely difficult to solve the Schrödinger equation with the interaction $V(A+1)$, this interaction is split into an average term and a residual, and the latter is treated approximately:

$$V(A+1) = V_{\text{rel}} + V_{\text{res}}. \qquad \text{Eq. (2.121)}$$

The operator V_{rel} is some operator which acts only on the relative coordinate between the neutron and the center of mass of the target nucleus and, hence, represents the average effect of all the nucleons. The residual is simply $V_{\text{res}} = V(A+1) - V_{\text{rel}}$. Equation (2.116) can now be written

$$[E_{\text{lab}} - H_{\text{int}} - H_{\text{rel}} - T_{\text{cm}}]\,\Psi = V_{\text{res}}\,\Psi \qquad \text{Eq. (2.122)}$$

where the target or internal Hamiltonian is $H_{int} = T_{int} + V_{int}$, the relative motion Hamiltonian is $H_{rel} = T_{rel} + V_{rel}$ and T_{cm} is the kinetic energy of the center of mass of the entire system.

The bracket on the left-hand side of Eq. (2.122) contains three independent energy terms, so that the eigenfunctions of the whole operator can be written as products of the eigenfunctions of each of its parts. In particular, the appropriate eigenfunction of the operator T_{cm} is simply a plane wave, expressing the fact that the center of mass of the entire system translates in a uniform manner. If $\vec{K}_c$ is a vector in the direction of this motion, with magnitude K_c given in terms of the center-of-mass kinetic energy E_{cm} by $\hbar^2 K_c^2/2M$, then the substitution

$$\Psi = e^{i\vec{K}_c \cdot \vec{R}} \psi \qquad \text{Eq. (2.123)}$$

results in the equation for ψ:

$$[E - (H_{int} + H_{rel})] \psi = V_{res} \psi. \qquad \text{Eq. (2.124)}$$

In Eq. (2.124), $E \equiv E_{lab} - E_{cm}$, and a translation has been made from the laboratory coordinates to a set with origin at the center of mass of the system. Thus, E is the energy in the center-of-mass system, ψ is the corresponding wave function, and $\vec{R} \equiv 0$.

Equation (2.124) will now be solved as though it were an inhomogeneous equation, with inhomogeneous term $V_{res}\psi$. Since this term is in fact homogeneous, the result of the solution will be an integral equation for ψ. The technique of solution by means of Green's functions is standard and involves the expansion of ψ in the eigenfunctions of $H_{int} + H_{rel}$. For further details on this procedure, see Ref. 2, pp. 160, 230. One defines the eigenfunctions and eigenvalues of the operator occurring in Eq. (2.124) by

$$[E_\omega - (H_{int} + H_{rel})] \phi_{E_\omega}(\tau) = 0. \qquad \text{Eq. (2.125)}$$

Then ψ satisfies the integral equation,

$$\psi = \psi_{inc} - \int G_E(\tau, \tau') V_{res}(\tau') \psi(\tau') d\tau' \qquad \text{Eq. (2.126)}$$

where $G_E(\tau,\tau')$ is the Green's function for the Hamiltonian in Eq. (2.125), and τ denotes the various spatial and spin coordinates. G_E is given (in spectral representation) by

$$G_E(\tau,\tau') = \sum_{E_\omega} \frac{\phi_{E_\omega}(\tau)\,\phi^*_{E_\omega}(\tau')}{E_\omega - E} \cdot \qquad \text{Eq. (2.127)}$$

The term ψ_{inc} is the incident wave, satisfying Eq. (2.125) and having the form of a product of the target ground state and a solution to the potential scattering problem involving V_{rel}. The latter was discussed in Sect. 2.2.C. The sum over E_ω in Eq. (2.127) includes any continuous eigenvalues.

One may write ϕ_{E_ω} as a product of the eigenfunctions of H_{int} and H_{rel},

$$\phi_{E_\omega}(\tau) = u_{E_\alpha}(\tau_{int})\, v_{E_\beta}(\tau_{rel}) \qquad \text{Eq. (2.128)}$$

where

$$(E_\alpha - H_{int})\, u_{E_\alpha}(\tau_{int}) = 0 \qquad \text{Eq. (2.129)}$$

$$(E_\beta - H_{rel})\, v_{E_\beta}(\tau_{rel}) = 0 \qquad \text{Eq. (2.130)}$$

and

$$E_\alpha + E_\beta = E_\omega. \qquad \text{Eq. (2.131)}$$

This permits writing $G_E(\tau,\tau')$ in terms of the Green's function for the operator H_{rel}:

$$G_E(\tau,\tau') = \sum_{E_\alpha E_\beta} \frac{u_{E_\alpha}(\tau_{int})\, v_{E_\beta}(\tau_{rel})\, u^*_{E_\alpha}(\tau'_{int})\, v^*_{E_\beta}(\tau'_{rel})}{E_\beta - (E - E_\alpha)} \qquad \text{Eq. (2.132)}$$

$$= \sum_{E_\alpha} u_{E_\alpha}(\tau_{int})\, u^*_{E_\alpha}(\tau'_{int})\, g_{E-E_\alpha}(\tau_{rel},\tau'_{rel}) \qquad \text{Eq. (2.133)}$$

where

$$g_E(\tau_{rel},\tau'_{rel}) = \sum_{E_\beta} \frac{v_{E_\beta}(\tau_{rel})\, v^*_{E_\beta}(\tau'_{rel})}{E_\beta - E}. \qquad \text{Eq. (2.134)}$$

If one now specializes V_{rel} to be a spherically symmetric potential with a spin-orbit term of the type discussed in Sect. 2.2.C, it is possible to derive (Ref. 3, p. 113) the following partial wave expansion, suppressing the subscript rel on r_{rel},

$$g_E(\tau_{rel}, \tau'_{rel}) = \frac{-2\mu}{\hbar^2 k_E r^2} \sum_{\ell jm} u_{\ell j}(r_<) h_{\ell j}(r_>) \mathcal{Y}_{\ell jm}(\hat{r}, \sigma) \mathcal{Y}^{\dagger}_{\ell jm}(\hat{r}', \sigma') \qquad \text{Eq. (2.135)}$$

where

$$r_< \begin{cases} = r & r < r' \\ = r' & r > r' \end{cases}$$

and

$$r_> \begin{cases} = r' & r < r' \\ = r & r > r' \end{cases} \qquad \text{and } k_E = \sqrt{\frac{2\mu E}{\hbar^2}}.$$

Both $u_{\ell j}(r)$ and $h_{\ell j}(r)$ are solutions of Eq. (2.130), differing only in their boundary conditions. The radial function $u_{\ell j}$ is regular at $r = 0$ while $h_{\ell j}$ is irregular, and

$$\lim_{r\to\infty} h_{\ell j}(r) = \exp\left[i(k_E r - \ell\pi/2 + \delta_{\ell j})\right]. \qquad \text{Eq. (2.136)}$$

After the various substitutions are made, one obtains, as $r \to \infty$

$$\psi \underset{r\to\infty}{\sim} \psi_{inc} + \frac{2\mu}{\hbar^2} \int d\tau' \sum_{E_a} \frac{e^{ik_{E-E_a} r}}{r} u_{E_a}(\tau_{int}) u^*_{E_a}(\tau'_{int}) \qquad \text{Eq. (2.137)}$$

$$\cdot \frac{1}{k_{E-E_a} r'} \sum_{\ell jm} (-i)^{\ell} e^{i\delta_{\ell j}} u_{\ell j}(r') \mathcal{Y}_{\ell jm}(\hat{r}, \sigma) \mathcal{Y}^{\dagger}_{\ell jm}(\hat{r}', \sigma') V_{res}(\tau') \psi(\tau').$$

If $Y_{\ell jm}(\hat{r}, \sigma)$ is expanded according to Eq. (2.51), then ψ takes the following form:

$$\psi \underset{r\to\infty}{\sim} \psi_{inc} + \frac{\mu}{2\pi\hbar^2} \sum_{E_a} \frac{e^{ik_{E-E_a} r}}{r} \sum_{\nu} \chi_{\nu}(\sigma) u_{E_a}(\tau_{int}) \left\langle u_{E_a}(\tau'_{int}) \psi_f, V_{res} \psi \right\rangle \qquad \text{Eq. (2.138)}$$

$$\psi_f = \frac{4\pi}{k_{E-E_a} r'} \sum_{\ell jmm_\ell} i^{\ell} C^{\ell \; \frac{1}{2} \; j}_{m_\ell \; \nu \; m} Y^{m_\ell *}_{\ell}(\hat{r}) e^{-i\delta^*_{\ell j}} u^*_{\ell j}(r') \mathcal{Y}_{\ell jm}(\hat{r}', \sigma') \qquad \text{Eq. (2.139)}$$

ψ_f is the solution to the scattering problem, Eq. (2.46), involving the complex conjugate of the potential well, $V = V_{rel}$, with an in-going wave boundary condition (Ref. 3, p. 113).

Equation (2.138) exhibits the wave function for the problem in terms of an expansion in the internal states of the target nucleus, $u_{E_\alpha}(r_{int})$ and the internal states (simply spin eigenfunctions $\chi_\nu(\sigma)$ in this instance) of the scattered neutron. The radial dependence of the relative motion of the pair is given by the e^{ikr}/r factor, while the angular dependence of the reaction products is contained in the $\hat{r}$-dependence of the matrix element, $\langle u_{E_\alpha}\psi_f, V\psi\rangle$. The angular brackets denote an integration over all primed variables.

The differential cross section for the process which leaves the nucleus in the state u_{E_α} and the neutron in the state $\chi_\nu(\sigma)$ is [Eq. (2.4)]

$$\left(\frac{d\sigma}{d\Omega}\right)_{E_o,\,\nu_o \to E_\alpha,\,\nu} = \frac{k_{E-E_\alpha}}{k_{E-E_o}} \left| \frac{\mu}{2\pi\hbar^2} \left\langle u_{E_\alpha}\psi_f, V_{res}\psi \right\rangle \right|^2 . \qquad \text{Eq. (2.140)}$$

A) EFFECT OF THE PAULI PRINCIPLE. Equation (2.138), although a formally exact solution to the Schrödinger equation, does not yet take into account the requirement of the exclusion principle, that the wave function be antisymmetric in the coordinates of all identical particles. This means that Eq. (2.138) must be antisymmetrized in the proton coordinates and neutron coordinates separately, or alternatively one may introduce an additional coordinate for each particle, the isotopic spin variable, and antisymmetrize with respect to all the nucleons.

This procedure of direct antisymmetrization, while straightforward, does not yield a particularly useful form of the wave function, since in the additional terms which occur different nucleons assume the role of scattered particle. This makes it difficult to read off the cross section for the scattering of one particular nucleon. (In an antisymmetric wave function, any one nucleon is equivalent to any other identical particle.) For this reason, it is more convenient to re-solve the problem, once per nucleon, allowing each nucleon in turn to be the scattered one whose wave function is given by Eq. (2.138). With all of the various asymptotic forms of ψ determined, it can be antisymmetrized to yield an asymptotic form in which only one particular particle is distant from the target (Ref. 2, p. 235).

The result of this procedure is the appearance of exchange amplitudes, which enter the cross section formula, Eq. (2.140),

coherently. These terms are usually small enough to neglect, so that the task of calculating them can be avoided.

B) INTRODUCTION OF THE TRANSITION OPERATOR. It is the function of nuclear models (Sect. 2.2.G) to provide approximations to the internal wave functions u_{E_a} in Eq. (2.138). Since the interaction V_{res} is supposed to be known, the usefulness of Eqs. (2.138) and (2.140) rests on finding suitable approximations for ψ. The best known of these is the first Born approximation

$$\psi \approx \psi_{inc} . \qquad \text{Eq. (2.141)}$$

This is the first term in an iterative solution to Eq. (2.138). Higher Born approximations can be generated by successive iterations, but the series rarely converges. The usefulness of the Born approximation does not rest on the dubious convergence properties of the Born series, but rather on the fact that for many reactions the residual term, $\psi - \psi_{inc}$, does not change the predictions based on Eq. (2.141) quantitatively when it is used in the matrix element.

For certain purposes, it is convenient to define an operator T which produces the same result when operating on ψ_{inc} as V_{res} does when operating on ψ:

$$T\psi_{inc} = V_{res}\psi. \qquad \text{Eq. (2.142)}$$

Just as V_{res} is a sum of A two-particle interactions,

$$V_{res} = \sum_{i=1}^{A} \left(V_{i,A+1} - \frac{1}{A} V_{rel} \right), \qquad \text{Eq. (2.143)}$$

so one writes

$$T = \sum_{i=1}^{A} t_{i,A+1} \qquad \text{Eq. (2.144)}$$

where t_{ij} is the t-matrix or effective interaction between two nucleons inside the nucleus. According to the ideas expressed in the introduction, all but one (or a few) of these terms may now be dropped, keeping only those corresponding to the nucleons which participate in the reaction. These are generally the outer, loosely bound ones.

Further simplification is achieved by transforming to momentum space and expanding the t-operator in powers of the relative momentum of the two particles. Keeping only the lowest term, and assuming it to be a constant, is equivalent to taking a zero range interaction potential approximation for t_{ij}, since the Fourier transform of a constant is the Dirac delta function. This yields finally a distorted wave Born approximation with contact interaction, with which it is not too difficult to calculate. In the following discussion a specific example is given.

3. *The (n,p) Direct Interaction Cross Section*

The direct interaction formula for neutron inelastic scattering or (n,p) reactions is now presented. To be definite, the formula for the (n,p) cross section is given, but this introduces no loss in generality since the same result applies to the (n,n') reaction, provided that the appropriate effective interaction is used and the coulomb terms are omitted.

To represent the nucleon wave function, a single particle model is used, and it is assumed that the incoming neutron interacts with a single proton bound in a nuclear well to the remaining nucleons. The transition matrix is given by

$$M(\theta) = \langle \psi_f, t_{np} \psi_i \rangle \qquad \text{Eq. (2.145)}$$

where ψ_i and ψ_f are the initial and final states of the system and t_{np} is a finite range effective internucleon potential. The initial and final states of the system are described by the following approximate wave functions: The initial state is considered to be a product of a distorted wave neutron scattering function [see Eq. (2.62)] and a proton bound to a core (designated by the subscript c) consisting of the remaining nucleons. It is

$$\psi_i = \frac{4\pi}{kr} \sum_{\substack{\tilde{\sigma}_p \ell m \tilde{m} \\ j \mu \tilde{\sigma} m_p \mu_i \mu_p}} i^{\ell} C^{\ell\ 1/2\ j}_{\tilde{m}\ \tilde{\sigma}\ \mu} C^{\ell\ 1/2\ j}_{m\ \sigma\ \mu} Y_{\ell m}(\hat{k}_n)$$

$$\cdot Y_{\ell \tilde{m}}(\hat{r}_n)^* \chi_{1/2 \tilde{\sigma}}(\sigma_n)\, e^{i\delta_{\ell j}}\, u_{\ell j}(r_n)\, C^{\ell_p\ 1/2\ j_p}_{m_p\ \tilde{\sigma}_p\ \mu_p} C^{j_p\ j_c\ j_i}_{\mu_p\ \mu_c\ M_i}$$

$$\cdot Y_{\ell_p m_p}(\hat{r}_p)\, R_{\ell_p j_p}(r_p) \chi_{1/2 \tilde{\sigma}_p}(\sigma_p)\, \phi_{j_c \mu_c}(\text{core}) \qquad \text{Eq. (2.146)}$$

where C is the Clebsch-Gordan coefficient, Y is the spherical harmonic, χ is the spin function, δ is the phase shift, R is the radial part of the bound state wave function, ϕ is the core wave function (refers to all nucleons but the proton), and u is the radial part of the (distorted) partial wave.

A similar expression holds for ψ_f with the roles of the neutron and proton reversed, since one assumes the neutron is captured into a single particle state. The transition matrix element can now be evaluated if one assumes that the core does not participate in the interaction and if recoil is neglected. The interaction between the neutron and proton is expanded in Legendre polynomials of the included angle,

$$t_{np} = \sum_q f_q(r_n, r_p)\, P_q(\hat{r}_n \cdot \hat{r}_p) \qquad \text{Eq. (2.147)}$$

where the f_q terms are expansion coefficients. The differential cross section is then given by

$$\sigma(\theta) = \frac{1}{(4\pi)^2}\left(\frac{2\mu}{\hbar^2}\right)^2 \frac{k_p}{k_n}\, \frac{1}{2(2J_i+1)} \sum_{\substack{\sigma_i\sigma_f \\ M_iM_f}} |M(\theta)|^2 \qquad \text{Eq. (2.148)}$$

where $k_n(k_p)$ is the wave number of the neutron (proton), and μ is the reduced mass of the system. In the following equation, the W's are Racah coefficients, and the $u^{\pm}_{\ell j}$ are the outgoing and incoming parts of the radial wave function defined by Eq. (2.92):

$$\sigma(\theta) = \left(\frac{2\mu}{\hbar^2}\right)^2 \frac{k_p}{k_n}\frac{1}{2} \sum_{\substack{\ell\ell' jj' \\ \tilde{\ell}\tilde{\ell}'\tilde{j}\tilde{j}' \\ q\tilde{q}\,Lf}} i^{\ell-\ell'-\tilde{\ell}+\tilde{\ell}'}(-)^{\ell+\tilde{\ell}+1-2j_n+2J_f+2j_c+j'-\tilde{j}'-f} \cdot (2\ell_n+1)(2\ell_p+1)(2\ell+1)(2\tilde{\ell}+1) \cdot (2j+1)(2\tilde{j}+1)(2j'+1)(2\tilde{j}'+1) \cdot (2j_p+1)(2j_n+1)(2J_f+1)(2f+1)$$

$$\sqrt{\frac{(2\ell'+1)(2\tilde{\ell}'+1)}{(2q+1)(2\tilde{q}+1)}}\, RI^{jj'j_pj_n}_{\ell\ell'\ell_p\ell_nq}\, RI^{\tilde{j}\tilde{j}'j_pj_n}_{\tilde{\ell}\tilde{\ell}'\ell_p\ell_n\tilde{q}}\, P_L(\hat{k}_n \cdot \hat{k}_p) \qquad \text{Eq. (2.149)}$$

$$\cdot C^{\ell\tilde{\ell}L}_{000}\, C^{\ell'\tilde{\ell}'L}_{000}\, C^{\ell_p q\ell'}_{000}\, C^{\ell_p\tilde{q}\tilde{\ell}'}_{000}\, C^{\ell\ell_n q}_{000}\, C^{\tilde{\ell}\ell_n\tilde{q}}_{000}$$

$$\cdot W(j'\ell'j_p\ell_p;\, 1/2\; q)\, W(\tilde{j}'\tilde{\ell}'j_p\ell_p;\, 1/2\; \tilde{q})\, W(j\ell j_n\ell_n;\, 1/2\; q)\, W(j\ell\tilde{j}\tilde{\ell};\, 1/2\; L)$$

$$\cdot W(\tilde{j}\tilde{\ell}j_n\ell_n;\, 1/2\; \tilde{q})\, W(j'\ell'\tilde{j}'\tilde{\ell}';\, 1/2\; L)\, W^2(J_f i_n J_i i_p;\, j_c f)\, W(\tilde{j}\tilde{q}fj_p;\, i_n\tilde{j}_n')$$

$$\cdot W(\tilde{j}\tilde{j}'jj';\, fL)\, W(j\, q\, f\, j_p;\, i_n j')$$

where

$$RI^{jj'j_pj_n}_{\ell\ell'\ell_p\ell_n\ q} = \int\int dr_n dr_p f_q(r_n, r_p)\, R_{\ell_n j_n}(r_n)\, R_{\ell_p j_p}(r_p)\, u_{\ell' j'}(r_p) u^*_{\ell j}(r_n) .$$

Eq. (2.150)

$u_{\ell j}(r)$ is a distorted-wave neutron scattering wave function with asymptotic form

$$u_{\ell j}(r) \underset{r\to\infty}{\sim} (2ik)^{-1} \left[\eta_{\ell j} u^+_\ell(r) - u^-_\ell(r)\right] .$$

(For a comparison between experiment and a similarly formulated theory, see Ref. 44. Additional material can be found in Ref. 17, Chap. V.B.)

4. Direct Interaction Model of (γ,n) Reaction

Although total (n, γ) reaction cross section predictions calculated with compound nucleus theory (Sect. 2.2.D.3) agree qualitatively with experiment, direct interaction model calculations of photonuclear reactions are needed to find the following quantities: (1) the cross section for neutron capture with the emission of a high energy γ-ray; (2) the photonuclear cross section in light nuclei between the resonances of the compound nucleus.

The calculation described here is an example of the latter. Simple model wave functions are used to describe both the initial and final states, similar to those of the preceding paragraph. The primary difference is that here the optical potential is real.

Following Francis, Goldman, and Guth, [45] the electric dipole operator is written as [46]

$$\vec{r}\cdot\vec{\epsilon} = \frac{4\pi}{3} r \sum_\lambda Y_{1\lambda}(\hat{r}) Y^*_{1\lambda}(\hat{\epsilon}). \qquad \text{Eq. (2.151)}$$

Here $\hat{\epsilon}$ is a unit vector in the direction of the photon-electric field, and the cross section in the distorted wave Born approximation is

$$\sigma_{\gamma n} = \frac{kp\mu e'^2}{2\pi h^2 c} |\langle f|\vec{r}\cdot\vec{\epsilon}|i\rangle|^2 \qquad \text{Eq. (2.152)}$$

where k is the energy of the incoming photon, p is the momentum of the outgoing neutron in the center-of-mass system, μ is the reduced mass of the system, and e' is the effective charge* $(e' = -eZ/(A+1))$.

The initial (bound) wave function is given by the single particle model as

$$\psi_i = \sum_{m_i \sigma_i} C^{\ell_i\, 1/2\, j_i}_{m_i\, \sigma_i\, \mu_i}\, Y_{\ell_i m_i}(\hat{r}) \frac{u_i(r)}{r} \chi_{1/2, \sigma_i}(\sigma) \qquad \text{Eq. (2.153)}$$

where $u_i(r)/r$ is a bound-state solution to the one-particle Schrödinger wave equation, and $\chi_{1/2,\sigma_i}$ is the spin wave function. The adjoint final wave function appearing in Eq. (2.152), a distorted wave, is

$$\psi_f^+ = 4\pi \sum_{\ell_f m_f m_f'} (-i)^{\ell_f} C^{\ell_f\, 1/2\, j_f}_{m_f'\, \sigma_f'\, \mu_f} C^{\ell_f\, 1/2\, j_f}_{m_f\, \sigma_f\, \mu_f} Y_{\ell_f m_f'}(\hat{r}) \cdot \chi^+_{1/2, \sigma_f} Y_{\ell_f m_f}(\hat{p})\, u_{\ell_f j_f}(r) \qquad \text{Eq. (2.154)}$$

where η and u have been defined in Sect. 2.2.C.6. The total (i.e., angle-integrated) and differential cross sections for the (γ, n) process are, respectively,

$$\sigma_T = \frac{2\pi k e'^2 \mu}{9 p \hbar^2 C} \sum_{\ell_f j_f} \frac{\left| RI^{j_f}_{\ell_f} \right|^2}{2j_i + 1} Z^2(\ell_f j_f \ell_i j_i; 1/2\, 1)$$

$$\sigma_d = \frac{k e'^2 \mu}{36 p \hbar^2 C} \sum_{\substack{\ell_f \ell_f' j_f j_f' \\ \epsilon L}} \frac{i^{\ell_f - \ell_f'} (-)^{j_i - 3/2} RI_{\ell_f j_f}\, RI^*_{\ell_f' j_f'}}{(2j_i+1)\,[(2j_f+1)(2j_f'+1)]^{1/2}} \qquad \text{Eq. (2.155)}$$

$$\cdot P_L(\hat{p} \cdot \hat{\epsilon})\, [Z(\ell_f j_f \ell_i j_i; 1/2\, 1)\, Z(\ell_f' j_f' \ell_i j_i; 1/2\, 1)$$

$$\cdot Z(\ell_f j_f \ell_f' j_f'; 1/2\, L) Z(1 j_f 1 j_f'; j_1\, L)]$$

*The effective charge of a neutron in electric dipole transitions results from the fact that the center of charge and mass are not equal. Let $\vec{r}$ be the position vector of the neutron with respect to the center of mass of the core of charge Z and mass number A. The dipole moment of the core with respect to the center of mass of the $(A+1)$ nuclear system is $-eZ\vec{r}/(A+1)$. Therefore, the $Z_{eff} = -Z/(A+1)$ and $e' = -\frac{Ze}{A+1}$.

where

$$RI_{\ell_j} = \int_o^\infty r u_i(r)\, u_{\ell_j}(r)\, dr \qquad \text{Eq. (2.156)}$$

$$= 2i\, e^{i\delta_{\ell_j}} \operatorname{Im} \left\{ e^{i\delta_{\ell_j}} \int_o^\infty r u_i u_\ell^+ \, dr \right\} \qquad \text{Eq. (2.157)}$$

$P_L(\hat{p}\cdot\hat{\varepsilon})$ is the L^{th} order Legendre polynomial of the angle between the neutron direction, $\hat{p}$, and the γ-ray polarization, $\hat{\varepsilon}$, and $Z(abcd;ef)$ is the coefficient introduced by Blatt and Biedenharn.[47] The polarization of the outgoing neutron is proportional to the trace of the expectation value of the Pauli spin matrix.[48] The formula for the polarization is

$$P = (\sigma_d)^{-1} \frac{k\mu e'^2}{\hbar^2 cp} \frac{\sqrt{5}}{48} \sum_{\ell_f \ell'_f j_f j'_f} i\,(-)^{j_f - j_i + \ell_f} RI_{\ell_f j_f} RI^*_{\ell'_f j'_f}$$

$$\cdot \left[(2\ell_f + 1)(2\ell'_f + 1)\right]^{1/2} C^{\ell_i \ell'_f 2}_{o\ o\ o} \sin 2\theta$$

$$\cdot X(\ell'_f \ell_f 2;\ j'_f\ j_f 2;\ 1/2\ 1/2\ 1)\, Z(1j_f \ell_i\ 1/2;\ j_i \ell_f)$$

$$\cdot Z(1j'_f \ell_i\ 1/2;\ j_i \ell'_f)\, Z(1j'_f\ 1j_f;\ j_i 2) \qquad \text{Eq. (2.158)}$$

where θ is the angle between photon and neutron directions, the z axis is taken to be in the $\vec{k}\cdot\vec{p}$ direction, and X is the 9-j coefficient (Ref. 8, p. 193).

F. Unified Treatment of Optical Model and Resonance Reactions

Neither the optical model nor the Breit-Wigner formulas may be used to describe completely the elastic scattering of Mev neutrons by C^{12}, O^{16}, or other light nuclei. For these nuclei the resonances are few in number and the cross-section energy variation is very large. Since the conventional complex potential well optical model is able to describe accurately only slowly varying cross sections, its use is inadequate for the description of the important details of the cross section. However, for energies between the compound nucleus resonances, the energy dependence of the differential cross

section can be predicted accurately with the optical model, provided that a real potential well is used.* The contribution to the cross section from the compound nucleus resonances is included by adding a resonance phase shift to the real optical model phase shift:

$$\delta_{\ell j} = (\delta_{\ell j})_{\text{o.m.}} - (\phi_{\ell j})_R \qquad \text{Eq. (2.159)}$$

where $(\delta_{\ell j})_{\text{o.m.}}$ is the optical model phase shift, $\delta_{\ell j}$ is the phase shift used in the elastic scattering cross section formulas, and $(\phi_{\ell j})_R$ is the resonant phase shift determined by the resonance parameters:

$$(\phi_{\ell j})_R = \tan^{-1} \frac{\Gamma_{\ell j}}{2(E-E_R)}. \qquad \text{Eq. (2.160)}$$

Here E_R is the resonance energy and $\Gamma_{\ell j}$ is the width of the resonance. Equation (2.160) differs from the Breit-Wigner single level theory in two important aspects: (1) The hard sphere is replaced by the corresponding optical model phase shift. (2) Although the resonance phase shift is of the Breit-Wigner form, the energy dependence of $\Gamma_{\ell j}$ and E_R is different. The resonance width is given by

$$\Gamma_{\ell j} = 2\pi \left| \int \psi_0(A) u_{\ell j}(r_0) \sum_{i=1}^{A} V(|\vec{r}_0 - \vec{r}_i|) \Psi_R(A+1)\, d\vec{r}_0 \ldots d\vec{r}_A \right|^2$$

Eq. (2.161)

where $u_{\ell j}(r_0)$ is the optical model scattering state, $\sum_i V(|\vec{r}_0 - \vec{r}_i|)$ is the interaction of the incident nucleon with all of the nucleons of the struck nucleus, $\psi_0(A)$ is the wave function of the target nucleus, and $\psi_R(A+1)$ is the quasistationary state of the $(A+1)$ nucleon system

$$(E_R - H)\psi(A+1) = 0, \qquad \text{Eq. (2.162)}$$

and a slightly different normalization is employed for $u_{\ell j}$:

$$\lim_{r\to\infty} u_{\ell j}(r) = \sqrt{\frac{2\mu p}{\pi}} \cdot \frac{\sin(pr + \delta_{\ell j} - \ell\pi/2)}{pr}. \qquad \text{Eq. (2.163)}$$

*It is assumed that the nonelastic cross section is negligible, so that the imaginary part of the potential which is introduced to remove particles from the incident beam is absent [see Eq. (2.47)].

For light nuclei where Eq. (2.161) for $\Gamma_{\ell j}$ is to be evaluated, the compound nucleus resonances are not very much sharper than the single particle optical model resonances. For example, in O^{16} the 1 Mev $\ell = 2$, $j = 3/2$ resonance has a width of 96.0 kev, while the 433 kev $\ell = 1$, $j = 3/2$ resonance has a width of 41 kev. Since the compound nucleus state is wide, the mode of excitation of this state is a simple one and the direct interaction evaluation of $\Gamma_{\ell j}$ should give reasonable results. In this evaluation of $\Gamma_{\ell j}$, the nuclear two-body interaction is replaced by the effective potential, and the target and compound state are calculated in the shell model. For example, a possible compound nucleus state is formed when an $(s, 1/2)$ and $(d, 5/2)$ neutron combine with the angular momentum 1/2, negative parity core, to give the total angular momentum 3/2, negative parity compound nucleus state. The ease with which the compound state can be formed suggests that this direct interaction interpretation is reasonable. This model can also be used to calculate directly the Γ_γ of the resonance, using standard techniques in the theory of multipole transitions (Ref. 49, Chap. 13).

G. Models of Nuclear Bound States

The study of bound state nuclear wave functions and their energy level sequences is a broad field, encompassing the whole of nuclear physics. One need only mention the shell model,[4,13-17,49] the collective model,[14-17,49] the alpha-particle model[4] and its modern counterpart, the cluster model,[50] the uniform,[4] liquid drop,[4] Fermi gas,[4] and other statistical models[38] to appreciate the difficulty of giving a brief discussion of this topic.

However, since in the direct interaction discussion (Sect. 2.2.E) independent particle or shell model wave functions were employed, these will be described briefly. This model is the nuclear analog of the atomic Hartree scheme. It considers each nucleon to be moving independently of the others in the average field produced by them. For illustration, assume that the smoothed-out potential arising from all the other nucleons is a harmonic oscillator potential. Figure 2.1 is a diagram of the energy levels of a three-dimensional oscillator with an appropriate spin-orbit term included.[13] The lowest energy level is $1s_{1/2}$, where the subscript denotes the total spin, $j = 1/2$; the orbital quantum number is given by the letter $s(\ell = 0)$; and the integer is the radial quantum number. The next group of energy levels are $1p$. Since the intrinsic spin is 1/2, the total spin can be $j = 1/2$ or $3/2$. Because of a splitting of the levels caused by spin-orbit coupling, the energy level with the

greater spin lies lower and is so depicted in Fig. 2.1. The total number of particles which can occupy a given level is $2j+1$. Above each level is written the maximum number of particles it can contain. There are certain definite gaps in the energy level scheme. For a particle to move from a state just below to one just above these gaps requires considerably more energy than to move to an adjacent level. Analogous to the atomic case, these large energy divisions separate closed shells of the nucleons. The total number of nucleons in a closed shell plus the number of nucleons in lower-lying closed shells is termed a magic number. The magic numbers are given to the right of Fig. 2.1 and represent the maximum number of particles contained in all the levels below the energy gap.

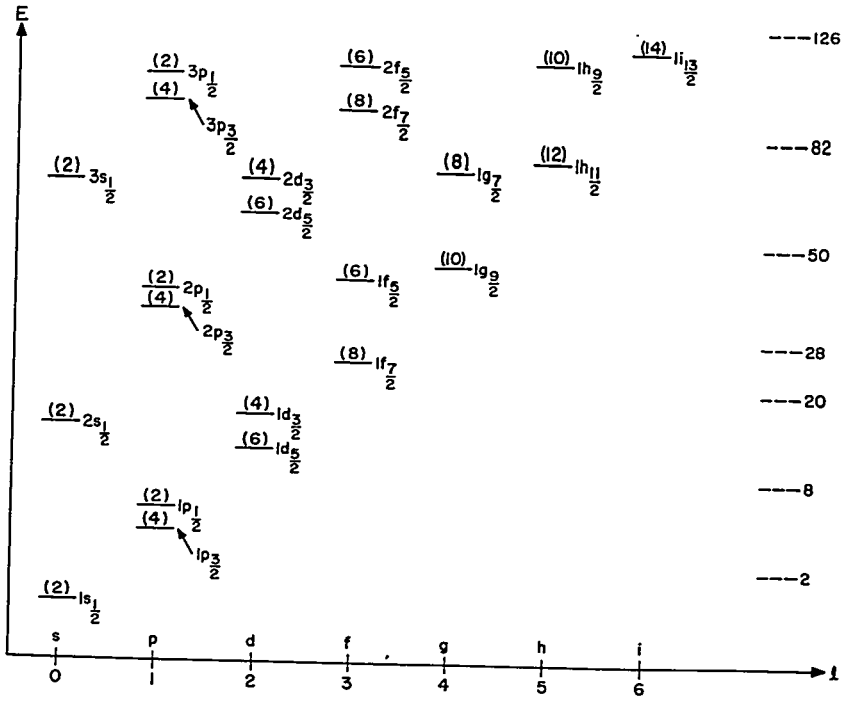

FIGURE 2.1. Energy Level Diagram for the Harmonic Oscillator Shell Model with Spin-Orbit Coupling. (Closed shells are marked at the right.)

Protons and neutrons are considered to retain their identity in the nucleus and to fill their own shells separately. Thus, nuclei possessing either a magic number of protons or neutrons should have such characteristics as large binding energy,

numerous isotopes or isobars, and small thermal capture cross sections comparable to the characteristics of the closed shell atoms, i.e., the inert gases. Some or all of the above features occur in the magic nuclei.[13, 51]

Many properties of nuclei are approximately determined by the particles outside the closed shells. It can be demonstrated that under the assumption of $j-j$ coupling with strong short range forces the ground states of nuclei with an even number of neutrons and an even number of protons have spin and parity $0+$, so that frequently the ground state properties of a nucleus with an odd nucleon are described by just the proton or neutron outside the even-even core.[52] Additional descriptive material can be found in the book by Mayer and Jensen.[13]

Many nuclear models have been utilized in the past to explain nuclear behavior. A concise description of them has been given by Moszkowski,[53] including a discussion of the properties of nonspherical nuclei. Briefly, these can be separated into nuclei which exhibit rotational spectra and those exhibiting vibrational spectra. For nuclei with atomic weight A given by $155 \geq A \geq 185$ and $A \approx 225$ and some with $A \approx 25$, the low lying energy levels resemble those of a symmetric top. This rotational spectrum is

$$E_k(I) = E_k^0 + \frac{\hbar^2}{2\mathcal{I}} I(I+1) \qquad \text{Eq. (2.164)}$$

where E_k^0 is a constant, $\mathcal{I}$ is the moment of inertia, I is the rotational quantum number, and k is the quantum number corresponding to the projection of I on the z-axis of a fixed reference frame. Nuclei with vibrational spectra have atomic weights in the region $60 \leq A \leq 150$ and $190 \leq A \leq 220$. The inclusion of rotational and vibrational states in a model of nuclear structure is necessary for detailed understanding of nuclear levels and transitions. Collective effects may also have an important effect in scattering.[54]

H. Cross-Section Calculations

1. *Description of Computer Program ABACUS*

A digital computer program, ABACUS-1,[55, 56] has been written for the calculation of nuclear cross sections of interest in reactor physics. The program can be used to calculate the total and shape elastic scattering cross sections in the cloudy crystal ball model (optical model) and the compound elastic and inelastic scattering cross sections in Hauser-Feshbach

theory. In addition, the program is able to find an optimum set of cloudy crystal ball parameters. The best set of parameters minimizes Q, which is defined to be a weighted sum of squares of differences between theory and experiment,

$$Q = \sum_{i=1}^{N} \omega_i (\sigma_i^{th} - \sigma_i^{exp})^2 \qquad \text{Eq. (2.165)}$$

where ω_i are the weights to be assigned to the i^{th} cross section. The weight ω_i should be large when the cross section is especially important for reactor design and when σ_i^{exp}, the experimentally measured i^{th} cross section, is measured precisely. The cross sections σ_i^{th} or σ_i^{exp} can be the total cross section, the elastic scattering angular distribution, or angle-integrated elastic, shape elastic, or compound elastic cross sections.

ABACUS will also perform radial wave function integrations needed for the calculation of direct interaction neutron capture and inelastic scattering cross sections.

2. *Elastic Scattering of Neutrons by Aluminum*

There are two reasons for starting the calculational discussion with elastic scattering: (1) The elastic scattering magnitude and angular distribution are needed for the calculation of the fast flux in the core, reflector, and shield. (2) The cloudy crystal ball parameters obtained from the theory-experiment match of the elastic scattering can be used to predict the inelastic scattering.

Although the calculational procedure that is described here is general and can be applied to most reactor materials, neutron elastic scattering in aluminum has been chosen as an illustration. At 14.1, 7.0, and 4.1 Mev the experimental neutron-Al^{27} elastic angular distributions and the total cross section are available. At these energies the best set of cloudy crystal ball parameters is found by minimizing Q, which in this example is the weighted sum of the squares of the differences between calculated and measured elastic and total neutron cross sections. The theoretical results at 7.0 and 14.1 Mev are calculated using only the cloudy crystal ball model, the compound nucleus contribution to the elastic scattering being neglected. At these high energies, many decay modes are available to the compound nucleus, and the ground state channel contributes very little.

The best sets of cloudy crystal ball parameters appear in Table 2.1. The elastic scattering angular distributions calculated using these parameters appear in Figs. 2.2 and 2.3 together with the experimental angular distributions. At both 7.0 and 14.1 Mev, the agreement between the shape of the experimental and theoretical curves is good, while the agreement is excellent when the cross sections are large. The most significant feature of the results is that the variation with energy of the cloudy crystal ball parameters is small. The spin orbit potential strength, V_{SO}, and both the strength, W, and the range, b, of the surface imaginary potential are constant to within 6 parts in 1000. The potential well radius changes by 1 percent and the real potential strength, V_0, changes by 5 percent while the diffuseness parameter of the Saxon potential changes by about 15 percent. The cloudy crystal ball model may, therefore, be described as a model in which cross sections are calculated with potential well parameters which vary slowly with energy. On the other hand, both the predicted and measured elastic scattering differential cross sections exhibit strong energy variations.

Since experimental results are available at 4.1 Mev, the cloudy crystal ball angular distributions and total cross sections have been calculated here. The cloudy crystal ball parameters used are the averages of the best parameters of 7.0 and 14.1 Mev. The comparison of the experimental and theoretical elastic scattering angular distributions is seen in Fig. 2.4. The third curve of Fig. 2.4 is the cloudy crystal ball shape elastic scattering angular distribution that minimizes Q, the weighted average of squares of the difference in the calculated and measured cross sections. The best calculated shape elastic cross sections lie below the experimental curve at large scattering angle. This disagreement is reduced significantly when the compound elastic contribution to the elastic cross section is included.

3. *Inelastic Scattering: Compound Nucleus (Hauser-Feshbach Theory) Predictions*

The energies selected for this calculation are 4.4 and 2.5 Mev, the respective energies of the Weddell[57] and Day[58] experiments. Weddell detects both the elastically and inelastically scattered neutrons with photographic emulsions. The scattered neutrons are observed at 82 degrees from the direction of the 4.4-Mev incident neutron beam. The theoretical cross section uses the values of the parity and angular momentum of the energy levels of the target nucleus shown in Fig. 2.5.

TABLE 2.1 — OPTICAL MODEL PARAMETERS FOR Al^{27}

Energy (Mev)	V_R (Mev)	V_I (Mev)	V_{SO} (Mev)	R(f)	a(f)	b(f)	σ_T (barns)	σ_{el} (barns)	Exp σ_T (barns)
4.1	45.68	5.44	5.00	3.72	0.655	0.980	2.37	1.33	2.40
7.0	46.83	5.48	5.01	3.75	0.733	0.993	1.98	0.98	2.00
14.1	44.30	5.51	5.01	3.70	0.620	0.998	1.63	0.86	1.70

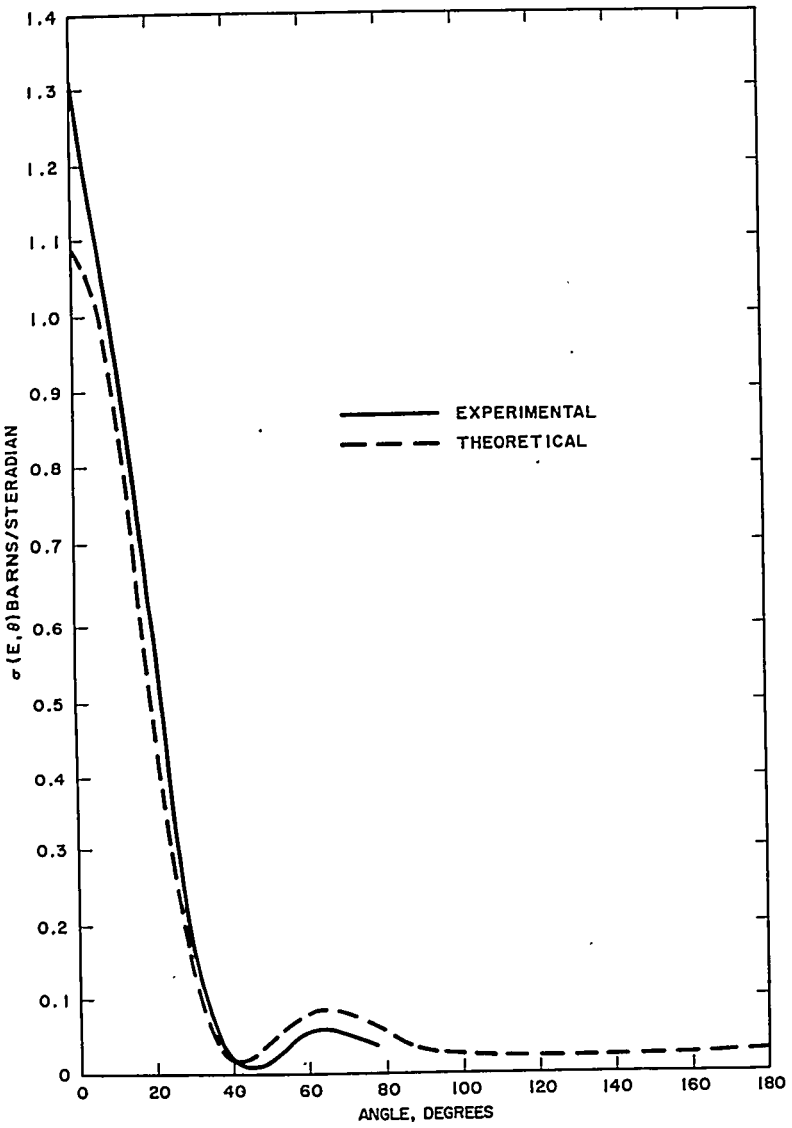

FIGURE 2.2. 14.1-Mev Neutron Al^{27} Elastic Scattering Angular Distribution Calculated from Parameters in Table 2.1.

The angular momentum and parity of the 2.208, 2.976 Mev levels are found from the analysis of the neutron inelastic cross sections. The parity of the 3.68, 3.95, and 4.05 Mev levels have been assumed to be positive, and the angular momentum of the 3.95 Mev state has been taken to be 0.5. The positive

parity assumption for the levels of the unknown parity is reasonable since all of the known parities at energies below 5 Mev are positive. The assignment of 0.5 for the angular momentum of the 3.95-Mev state may be in error, but the cross section for the excitation of this state by 4.4-Mev neutrons is only 0.007 barn and is, therefore, negligible.

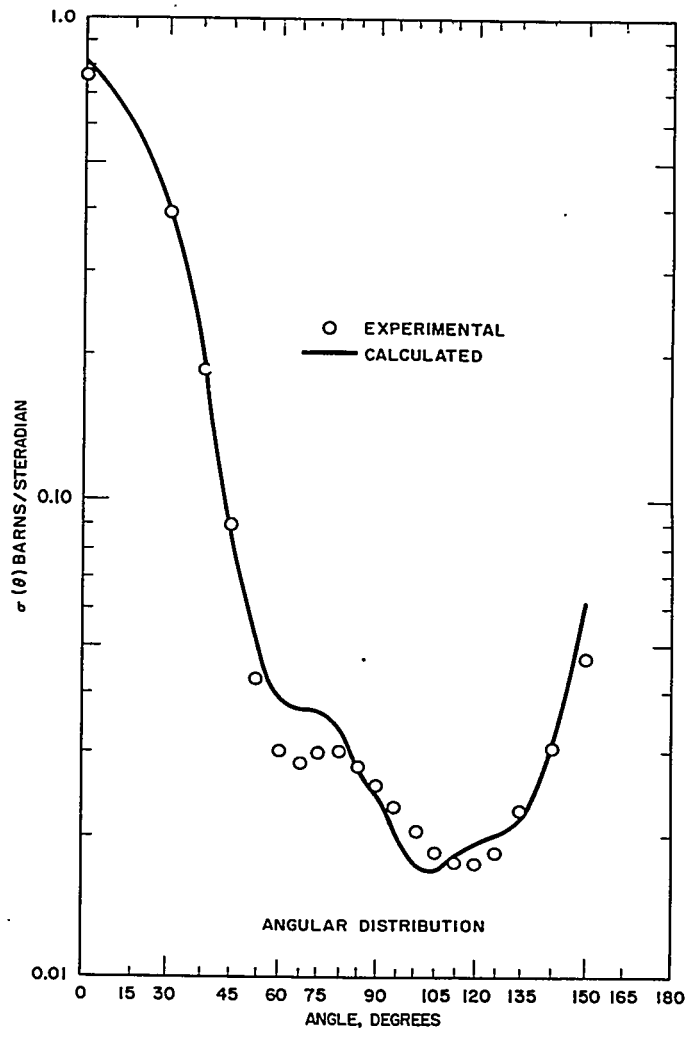

FIGURE 2.3. 7.0-Mev Neutron Al^{27} Elastic Scattering Angular Distribution Calculated from Parameters in Table 2.1.

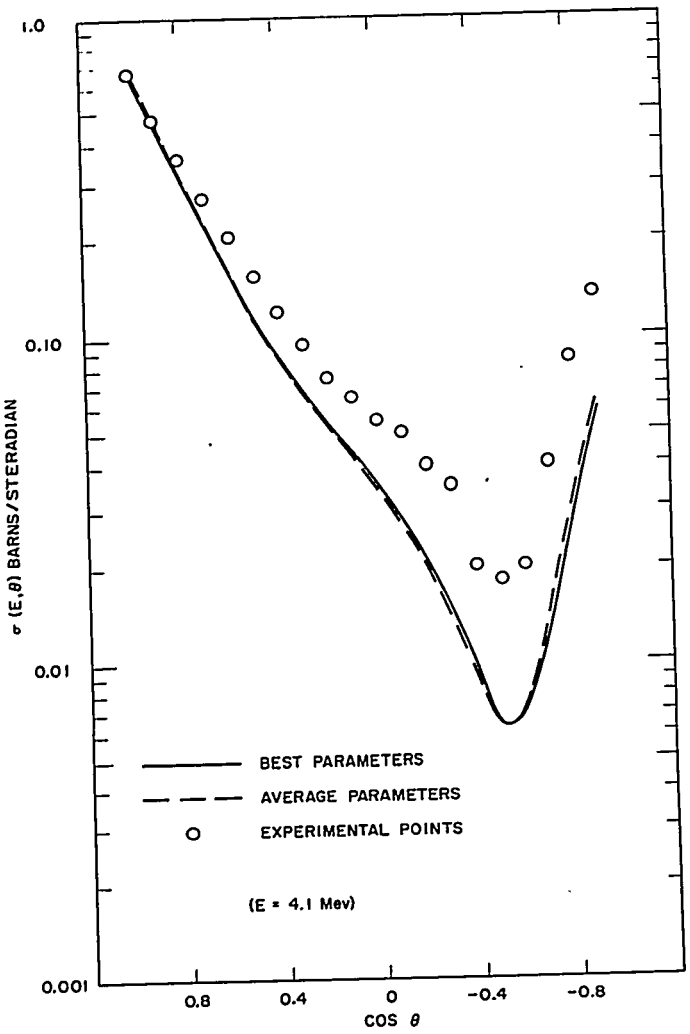

FIGURE 2.4. Comparison of Experimental and Theoretical Shape Elastic Scattering Angular Distributions, Al^{27}.

The cross section for the excitation of each individual level has not in every case been resolved by Weddell. Instead, he presents certain cross sections as sums of two levels. Table 2.2 gives the comparison between the calculated and measured cross sections. The calculated cross sections are obtained with cloudy crystal ball potential well parameters that give the best elastic scattering angular distribution. The inelastic cross section agreement between theory and experiment is always within the uncertainty of the measurement except for excitation of the 2.729-Mev level. The predicted cross section of

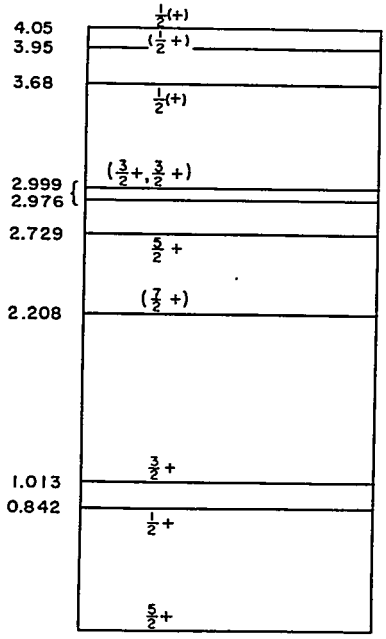

FIGURE 2.5. Al^{27} Energy Levels, Spins, and Parities.

10.0 mb/ster is more than a factor of 3 times the upper limit reported by Weddell for the 2.729-Mev level. This disagreement is unexplained, and an additional measurement would be desirable.*

The compound elastic scattering angular distribution has been calculated and added to the shape elastic prediction to give the total elastic scattering angular distributions at 4.1 Mev. The theoretical and experimental angular distributions so obtained are shown in Fig. 2.6. The inclusion of the compound nucleus part of the elastic scattering cross section is seen to improve appreciably the agreement with experiment. A quantitative indication of the improvement is obtained by noting that the value of Q has decreased from 6 to 1 with the inclusion of the compound elastic part of the elastic scattering angular distribution.

At 2.5 Mev, it is possible to illustrate further the use of Hauser-Feshbach theory. Here Day[58] measured the cross section for γ-ray emission following neutron inelastic scattering.

*Measurements by J.H. Towle and W.B. Gilboy[59] are in better agreement with theory if the spin of the 2.999 Mev level is assigned 9/2+.

TABLE 2.2 — EXPERIMENTAL AND THEORETICAL CROSS SECTIONS FOR THE SCATTERING OF 4.4-Mev NEUTRONS BY Al^{27}

Level	A	B
0	46 ± 10	49.0
0.844 + 1.016 (unresolved)	19 ± 7	13.8
2.208	15 ± 5	18.3
2.729	< 3	10.4
2.976 + 2.999 (unresolved)	10 ± 5	10.0

NOTE: A. Experimental differential cross section at 82 degrees in mb/ster.

B. Theoretical cross sections with 2.208(7/2+) and both members of the 3-Mev doublet (3/2+). These are total cross sections divided by 4h, except for the elastic scattering results.

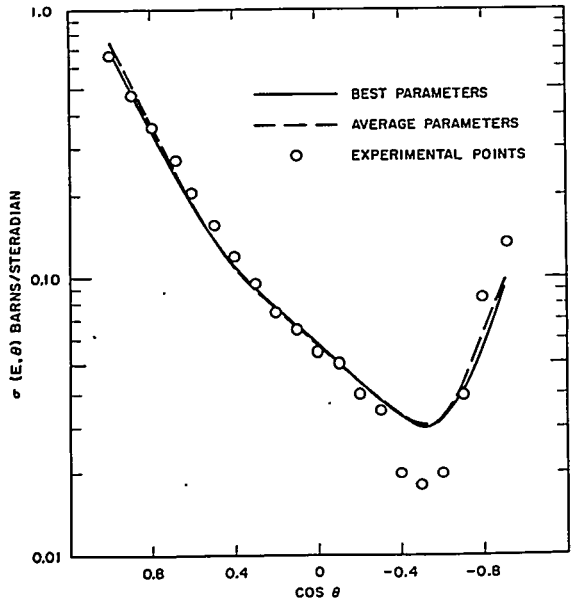

FIGURE 2.6. Total Elastic Scattering Angular Distributions at 4.1-Mev Neutrons by Al^{27}.

Although Day measured the cross section for γ-ray emission at only one angle, 95 degrees to the incident neutron direction, the angle-integrated cross section can be obtained by multiplying the differential value by 4π. No error would be introduced by this procedure if the γ-ray angular distribution were isotropic. Furthermore, if the inelastically scattered neutrons were emitted isotropically, the excited target nucleus could not remember the direction of the incident neutron and the γ-rays would be isotropic. The calculated angular distribution of neutrons inelastically scattered with the excitation of the first three levels are shown in Fig. 2.7. Since all the angular distributions are nearly isotropic, it is plausible that the γ-ray angular distribution is also nearly isotropic. Having the γ-ray cross sections for all of the transitions permits the calculation of the neutron inelastic cross sections. In Table 2.3, these experimental cross sections are compared with Hauser-Feshbach predictions obtained using the 4.1-Mev cloudy crystal ball parameters. The calculated and measured inelastically scattered neutron spectra have the same shape, but the magnitude of the total inelastic cross sections disagree. The remaining difference in the normalization of the spectra can be eliminated if the experimental cross section is normalized to be consistent with the inelastic cross section for the excitation of the 2.208-Mev level measured by Cranberg and Levin [60] using the time of flight technique. The normalized inelastic cross sections appear in column A of Table 2.3.

TABLE 2.3 — EXPERIMENTAL NEUTRON INELASTIC CROSS SECTIONS

Level	A	B
0.842	108 ± 12	95
1.013	238 ± 22	242
2.208	146 ± 13	155

NOTE: A. R.B. Day, renormalized to the data of Cranberg and Levin, $4\pi \frac{d\sigma}{d\omega}$ (90deg) mb.

B. Theoretical cross sections using 2.208(7/2+).

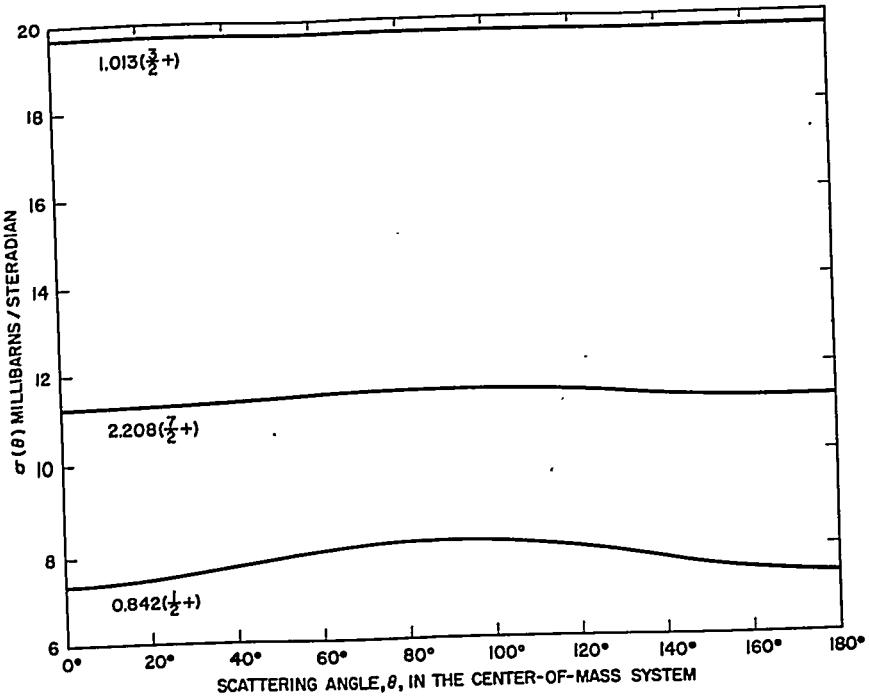

FIGURE 2.7. Inelastic Scattering Cross Sections for the First Three Excited States in Al^{27}. (Hauser-Feshbach calculations at $E_n = 2.5$ Mev in the center-of-mass system.)

4. *Direct Interaction Model Calculation of Neutron Radiative Capture in C^{12}*

The capture of thermal neutrons in C^{12} has been calculated with the direct interaction model whose formulas were given in Sect. 2.2.E.4. The connection with the (γ, n) cross section which was presented there is made via the principle of detailed balance.[4] Let $\sigma(\gamma, n)$ be the cross section for the photoemission of a neutron from the ground state of C^{13}. The inverse reaction is the cross section $\sigma(n, \gamma)$ for the capture of the neutron by C^{12} to form C^{13} in its ground state. The principle of detailed balance states the following:

$$\sigma(n, \gamma) = \sigma(\gamma, n)\frac{E^2}{p^2c^2}\frac{(2J_{13} + 1)}{(2J_{12} + 1)} \qquad \text{Eq. (2.166)}$$

where E is the energy of the photon, p the momentum of the neutron, c the velocity of light, and J_{13} and J_{12} are the total angular momenta of C^{13} and C^{12}, respectively.

To evaluate $\sigma(n, \gamma)$, a radial integration must be performed. This radial integral contains the following three factors: (1) the continuum neutron wave function of the initial state thermal neutron; (2) the position vector $\vec{r}$ of the neutron (the transition is dipole); (3) the single particle bound neutron state that represents C^{13}. Both the continuum and bound single particle states are calculated with ABACUS. The bound C^{13} state is assumed to have the following properties: (1) the binding energy of the struck neutron is 4.946 Mev, the energy required to remove a neutron from C^{13}; (2) the total and orbital angular momentum of single particle state is 1/2 and 1 to agree with the 1/2(-) experimental determination of the angular momentum and parity.

The potential well parameters that generate this single particle bound state are (Sect. 2.2.C.4):

$$V_{c0} = -47.08 \text{ Mev}$$
$$V_{SO} = -\ 9.45 \text{ Mev}$$
$$R = 2.86f$$
$$a = 0.6f$$

The strength of the potential V_{c0} is selected to give the experimental binding energy of C^{13}. The radius, R, and diffuseness, a, have conventional values.

The continuum state single particle model wave function is required to have the correct nuclear phase shift. The single particle model must, therefore, reproduce the C^{12} neutron elastic scattering angular distribution. With this constraint

$$V_{c0} = -59.3 \text{ and } V_{SO} = -\ 7.11 \text{ Mev.}$$

The calculated (n, γ) cross section can now be found to be 4.8 mb or about twice the experimental value. The factor of two error can be understood and partially eliminated if one modifies the C^{13} bound state. It has been assumed that the wave function for this state may be approximated by a single particle state, i.e., that the C^{12} core is in its ground state. In a more realistic model of the C^{13} nucleus, the wave function of C^{13} would be expanded as a sum of products of C^{12} core states (ground and excited) and single particle neutron states.

The ground state core term in this expansion is multiplied by a single particle state similar in shape to the one used in the calculation reported here. The normalization will differ, however. In the calculation used here it was assumed that the single particle state is normalized to unity. In the exact C^{13} wave function, the probability that the core is in its ground

state is equal to the integral of the square of the single particle wave function. Although it is difficult to calculate this probability from first principles, it can be easily estimated if it is assumed that both Be^9 and C^{13} have the same probability that their respective cores are in the ground state. The Be^9 (γ, n) experiment gives a value of 0.6 for this probability. Folding this value into the theoretical C^{12} (n, γ) cross section reduces the difference between theory and experiment to 16 percent.

2.3 SLOWING-DOWN THEORY IN A UNIFORM MEDIUM

H. J. Amster

A. Introduction

To obtain a practical solution of the transport equation one must usually resort to a finite differencing of the vector flux in one or more of its independent variables. While the transport equation can be differenced in all variables at the start, it has been found convenient for most practical problems to make initially analytic approximations for some terms in the transport equation and then to perform the required differencing. The accuracy of these analytic approximations will determine a bound on solution accuracy that can be obtained in the limit of zero differencing.

This section systematically presents most of the analytic approximations commonly used in slowing-down theory. These approximations are made in the computation of the source due to elastic neutron scattering. Methods will also be given for systematically improving these approximations through the addition of correction terms. Since methods of treating the elastic scattering source are applicable to the transport equation regardless of the spatial dependence and angular representation of the vector flux, the one-dimensional transport equation for a uniform medium with a Legendre polynomial expansion of the vector flux will be sufficient for illustration. These methods are frequently used in multigroup slowing-down calculations to obtain few-group diffusion theory coefficients. For these, one uses a uniform medium calculation with spatial dependence removed through the assumption of a cosine spatial dependence of the scalar flux.

B. Decomposition of the Transport Equation

The transport equation in one dimension is [61]

$$\mu \frac{\partial \psi(u, \mu)}{\partial z} + \Sigma_T(u)\, \psi(u, \mu) = S(u, \mu) \qquad \text{Eq. (2.167)}$$

where $\psi(u, \mu)\, du 2\pi d\mu$ is the vector flux with lethargies in du and directions whose cosines with the z axis are in $d\mu$ (u and μ are both measured in the laboratory system); $\Sigma_T(u)$ is the total cross section; and $S(u, \mu)du2\pi d\mu$ is the net source of neutrons entering the intervals du and $d\mu$. Only the case when the source and, therefore, the resulting flux is independent of the azimuthal angle ϕ is considered. The dependence of ψ, Σ_T, and S on the spatial coordinate z is to be understood but is omitted in the notation.

A common method is to solve Eq. (2.167) for the various Legendre components of the vector flux, $\psi_L(u)$, where

$$\psi(u, \mu) = \sum_{L=0}^{\infty} \frac{2L + 1}{4\pi} \psi_L(u)\, P_L(\mu). \qquad \text{Eq. (2.168)}$$

Since for many problems the dependence of the vector flux on direction is weak, the summation in Eq. (2.168) is approximated by a finite number of terms. When this summation is inserted into Eq. (2.167) and use is made of the orthogonality of the Legendre components, as many coupled equations for the $\psi_L(u)$ result as terms retained in Eq. (2.168), so that values for the $\psi_L(u)$ can be determined.[62]

The source term $S(u, \mu)$ contains both external contributions (e.g., a Po-Be source) of presumably known strength and contributions which depend on values of the vector flux for other lethargies and directions at the same space point. To account for the latter type of source contribution, the whole range of relevant lethargies is split into a finite number of intervals called groups. The source of neutrons due to elastic and inelastic scattering depends on the flux only at smaller lethargies, so that by working with successively higher lethargy groups one can always evaluate these contributions to the source. Since the source due to fissioning can depend on the flux at all lethargies, iterations are required to find the strength of this type source: that is, a source due to fissioning is guessed at and the flux solved for; then, a new fission source of neutrons can be calculated, and its value will produce a better estimate of the flux, etc.

C. The Source Due to Elastic Scattering

For the lethargies of interest to reactor calculations, a source neutron arising from fission or inelastic scattering involves a distribution that usually depends strongly on exit lethargy but weakly on exit direction. Thus, the source due to fission and inelastic scattering is often taken as a function of u but not of μ, and depends on the net number of neutrons at each lethargy but not on their angular distribution. In other words, the source has only a P_0 Legendre component and depends only on the P_0 component of the flux, $\psi_0(u)$.

In contrast, the angular as well as energy distribution of elastically scattered neutrons usually depends strongly on the exit values. Thus, there may be several nonvanishing Legendre components of this source, and one would expect each to depend on all the Legendre components of the vector flux at smaller lethargies. The main features of these dependencies were treated in full generality by Zweifel and Hurwitz,[63] whose notations are here retained. However, the use of the delta function for linking energy loss and scattering angle can be made more interpretable, as will be attempted here; less cumbersome steps and final equations will also result. (A closely related procedure is given in Ref. 64 which avoids the delta function entirely.)

Let $\sigma(u, U)dU$ be the cross section for a neutron with incident lethargy u to be elastically scattered and experience a lethargy increase between U and $U + dU$. By the conservation of energy and momentum, there is a one-to-one relationship between the lethargy increase U and the cosines of the scattering angle in the laboratory and center-of-mass systems, μ_o and μ_c, respectively (U is measured in the laboratory system). Therefore, $\sigma(u, U)$ can be obtained in terms of the more familiar quantity, $\sigma^c(u, \mu_c)$, the differential scattering cross section in the center-of-mass system:

$$\sigma(u, U)dU = -\sigma^c(u, \mu_c)2\pi d\mu_c \qquad \text{Eq. (2.169)}$$

where the minus sign is used because an increase of U corresponds to a decrease in μ_c.

In transport theory, it is convenient to work in terms of $\sigma(u; \mu_o, U)2\pi d\mu_o dU$, the cross section for a neutron with incident lethargy u to be elastically scattered by an angle whose cosine in the laboratory system is in $d\mu_o$ and which will experience a lethargy gain of value in dU. This cross section is defined as though there were a complete distribution into all values of

μ_o and U, as would be the case for inelastic scattering. However, for elastic scattering, the exit neutron has to be deflected by a definite angle, specified as $\cos^{-1} \mu_o(U)$, once its lethargy gain U is determined. Thus,

$$\sigma(u; \mu_o, U) = \sigma(u, U)\, \delta\left[\mu_o - \mu_o(U)\right]. \qquad \text{Eq. (2.170)}$$

That is, the probability that a neutron will scatter into $d\mu_o$ and dU equals the probability that it will scatter into dU times the probability that having gained lethargy U the neutron will be deflected by an angle whose cosine is $d\mu_o$. Since the latter factor has to be zero for values of μ_o not equal to $\mu_o(U)$, but its integral over μ_o must be unity, it equals the delta function shown.

It is now desired to expand the three-variable cross section in Legendre polynomials,

$$\sigma(u; \mu_o, U) = \sum_{L=0}^{\infty} \frac{2L+1}{4\pi} B_L(u, U)\, P_L(\mu_o). \qquad \text{Eq. (2.171)}$$

From Eq. (2.170),

$$B_L(u, U) = 2\pi \int_{-1}^{1} P_L(\mu_o)\, \sigma(u; \mu_o, U)\, d\mu_o = 2\pi\, \sigma(u, U)\, P_L\left[\mu_o(U)\right]. \qquad \text{Eq. (2.172)}$$

The neutron source due to elastic scattering will be a sum of contributions involving the macroscopic cross sections of each isotope in the medium. The source per unit atom density for a single isotope is

$$J(u, \mu) = \int_{u-q}^{u} du' \int_{o}^{2\pi} d\phi' \int_{-1}^{1} d\mu'\, \sigma\left[u'; \mu_o(\mu', \phi', \mu), u-u'\right] \psi(u', \mu') \qquad \text{Eq. (2.173)}$$

where q is the greatest lethargy gain that a neutron can experience in an elastic collision. Equation (2.173) equates the source with an integral of the contributions for each value of the coordinates of the vector flux.

The scattering angle, $\cos^{-1} \mu_o$, is the angle between the direction (μ', ϕ') of the incident neutrons contributing and the direction (μ, ϕ) of the exit neutrons forming the source; from the addition theorem (Ref. 65, p. 389), it has the remarkable property that

$$\int_0^{2\pi} d\phi'\, P_L\left[\mu_o(\mu', \phi', \mu)\right] = 2\pi P_L(\mu) P_L(\mu'). \qquad \text{Eq. (2.174)}$$

When Eq. (2.172) is inserted into Eq. (2.171), and the resulting expression along with Eq. (2.168) substituted into Eq. (2.173), the orthogonality of the Legendre polynomials and Eq. (2.174) yields

$$J(u, \mu) = \sum_{L=0}^{\infty} \frac{2L+1}{4\pi} J_L(u) P_L(\mu) \qquad \text{Eq. (2.175)}$$

where

$$J_L(u) = \int_{u-q}^{u} du' P_L\left[\mu_o(u-u')\right] \psi_L(u') \sigma(u', u-u'). \qquad \text{Eq. (2.176)}$$

Transforming the variable of integration to the lethargy gain

$$U = u - u' \qquad \text{Eq. (2.177)}$$

yields the shorter form

$$J_L(u) = \int_0^q dU P_L\left[\mu_o(U)\right] \psi_L(u-U) \sigma(u-U, U). \qquad \text{Eq. (2.178)}$$

Finally, a form that is convenient for treating heavy moderators[66] can be obtained by using Eq. (2.169) and transforming the variable of integration to μ_c, the cosine of the scattering angle in the center-of-mass system, which will produce a lethargy gain U,

$$J_L(u) = 2\pi \int_{-1}^{1} d\mu_c P_L\left[\mu_o(\mu_c)\right] \psi_L\left[u-U(\mu_c)\right] \sigma^c\left[u-U(\mu_c), \mu_c\right]. \qquad \text{Eq. (2.179)}$$

This form is completely in terms of familiar quantities and has the explicit dependences,[66]

$$\mu_o(\mu_c) = \frac{\mu_c + \gamma}{\sqrt{1 + 2\gamma\mu_c + \gamma^2}} \qquad \text{Eq. (2.180)}$$

and

$$U(\mu_c) = -\ln\left[1 - \frac{2\gamma}{(1+\gamma)^2}(1-\mu_c)\right] \qquad \text{Eq. (2.181)}$$

where γ is the ratio of the neutron mass to the moderator mass.

One extremely convenient property of J_L is that it depends only on the single Legendre component of the vector flux, ψ_L. Since this property is a direct consequence of the addition theorem and the orthogonality of the Legendre polynomials, it is hard to interpret physically. Only when $L = 0$ does Eq. (2.179) have a simple meaning. In this case, $J_0(u)du$ equals the rate at which all neutrons are scattered into du regardless of direction; $\psi_0[u-U(\mu_c)]du$ equals the flux of all neutrons that would go into du if scattered through an angle $\cos^{-1}\mu_c$; and $\sigma^c[u-U(\mu_c),\mu_c]$ equals the cross section for these neutrons to be so scattered.

D. Heavy Moderator Approximations[66]

Since the lethargy gain $U(\mu_c)$ approaches zero as the moderator mass becomes infinite, good approximations will result for heavy moderators when $\psi_L(u-U)\sigma^c(u-U,\mu_c)$ in Eq. (2.179) is expanded in powers of U to obtain

$$J_L(u) = \sum_{n=0}^{\infty} \frac{d^n}{du^n}\ \psi_L(u)\, G_L^n(u) \qquad \text{Eq. (2.182)}$$

where

$$G_L^n(u) = \frac{2\pi}{n!}\int_{-1}^{1} P_L\ [\mu_o(\mu_c)]\ [-U(\mu_c)]^n\ \sigma^c(u,\mu_c)\, d\mu_c. \qquad \text{Eq. (2.183)}$$

The quantities G_L^n form the usual input constants for most multigroup codes. Some examples for P_1 codes are, in the more common notation,

$$G_0^o = \sigma_s;\ G_0^1 = -\xi\sigma_s;\ G_1^0 = \bar{\mu}\sigma_s. \qquad \text{Eq. (2.184)}$$

Equation (2.183) provides a way of calculating G_L^n directly from the differential cross section, e.g., the SUMNUM code[67] calculates $\sigma^c(u,\mu_c)$ from an optical model, uses the explicit dependences in Eqs. (2.180) and (2.181), and performs a numerical integration to yield values for G_L^n directly as output.

Cross-section data are often supplied, however, in terms of $B_L(u)$, the expansion coefficients of σ^c,

$$\sigma^c(u, \mu_c) = \sum_{L=0}^{\infty} \frac{2L+1}{4\pi} B_L^c(u) P_L(\mu_c). \qquad \text{Eq. (2.185)}$$

Thus,

$$G_L^n(u) = \sum_{L'=0}^{\infty} T_{LL'}^n B_{L'}^c(u) \qquad \text{Eq. (2.186)}$$

where

$$T_{LL'}^n(\gamma) = \frac{2L'+1}{2n!} \int_{-1}^{1} P_L[\mu_o(\mu_c)] [-U(\mu_c)]^n P_{L'}(\mu_c) d\mu_c. \qquad \text{Eq. (2.187)}$$

E. Expansion Coefficients for Heavy Mass Approximation

An examination of Eqs. (2.181) and (2.187) shows two reasons why $T_{LL'}^n(\gamma)$ vanishes as γ goes to zero; not only does U itself vanish, but while doing so, U flattens in the range over which the Legendre polynomials are becoming orthogonal. If one pictures the product of the Legendre polynomials as approaching a Clebsch-Gordan summation of these functions with the least rapidly oscillating one having an order $L-L'$, he would intuitively expect that the relative importance of the two effects causing $T_{LL'}^n(\gamma)$ to vanish with small γ might somehow depend on the comparison of n with $L-L'$. Indeed, the following theorem has been proved[66]: As γ approaches zero, $T_{LL'}^n(\gamma)$ approaches zero at least as fast as the faster of γ^n and $\gamma^{L-L'}$.

An instance where $T_{LL'}^n$ vanishes faster than the minimum rate given by the theorem is

$$T_{0L'}^0 = \delta_{L'}^0. \qquad \text{Eq. (2.188)}$$

However, Eq. (2.188) is the only common obvious instance and, in the treatment to follow, deviations from the limits of the theorem, except as expressed in Eq. (2.188), will be considered accidental, i.e., if they occur at all, it will be unpredictably and rarely. No such accidents happen, for example, in the expansions in γ of all the explicit forms of $T_{LL'}^n$ presented in Ref. 63. If $T_{LL'}^n$ does accidentally vanish faster than the estimate, there generally will be no unexpected error introduced; the only effect is that terms that could have been neglected will be retained.

As is usual when expansions are applied, there is the difficult but important question of how small γ must be in order to use the estimates of the theorem in actual transport calculations. The coefficient of the vanishing power of γ in the theorem is usually too complicated to evaluate analytically, and even its qualitative dependence on the indices n, L, and L' is not apparent. For example, once it has been established that $|L-L'|>n$, the further influence of n on the size of $T^n_{LL'}$ is uncertain from the intuitive considerations expressed above, for while a large n makes U^n vanish rapidly, it also makes this weighting factor less flat.

F. Termination of Series

The summations of Eqs. (2.182) and (2.186) can be terminated consistently, i.e., all terms up to a given power of γ can be retained according to the theorem and Eq. (2.188). How consistent these terminations are, in the sense of how they affect the accuracy of the flux calculation, depends on $(d^n/du^n)B^c_{L'}\psi_L$ as well as $T^n_{LL'}$, and the former quantity itself depends on many more variables than just the masses involved. Thus, while it is assumed that the coefficients of $T^n_{LL'}$ are all of the same order of magnitude in the following consistency arguments, one might conceivably, in the presence of further information about particular mixtures and geometries, have reason to terminate the summations somewhat differently.

As an example consider the P_1 approximation with two terms retained in Eq. (2.182). It is convenient to neglect terms with higher derivatives than the first because when the multigroup codes approximate the derivatives with group differences, values of $\psi_L(u)$ for only the previous group are used, so that time and storage are saved. Unlike the treatment described in Sect. 2.7, however, a rigorous solution will not be approached as the group widths tend to zero.

First, with isotropic scattering in the center-of-mass system ($B^c_{L'}=0$ for $L'\neq 0$), Eqs. (2.182) and (2.186) are

$$J_0=\psi_0\left[T^0_{00}B^c_0\right]+\frac{d}{du}\psi_0\left[T^1_{00}B^c_0\right]\cdots \qquad \text{Eq. (2.189)}$$

$$J_1=\psi_1\left[T^0_{10}B^c_0\right]+\frac{d}{du}\psi_1\left[T^1_{10}B^c_0\right]\cdots \qquad \text{Eq. (2.190)}$$

Since the neglected terms in Eqs. (2.189) and (2.190) have n's greater than unity, the theorem shows that all are of higher order in γ than the first power. According to Eq. (2.188) and the theorem, the two terms in Eq. (2.189) are expected to be of order unity and γ, respectively. In Eq. (2.190) the first term is of order γ since $|L-L'|=1$. The second term in Eq. (2.190) is not one order higher than the first, as one might expect, but rather it vanishes as the power of γ given by $|L-L'|=n=1$ and, therefore, should be retained to make a consistent P_1 approximation.[68]

It is now appropriate to reconsider the two Eqs. (2.189) and (2.190), including the possibility of anisotropic scattering by altering them to the general form of Eqs. (2.182) and (2.186). Because of Eq. (2.188), the first term in Eq. (2.189) is unaltered, but the second term should have the part in brackets replaced by

$$G_0^1 = \sum_{L'=0}^{\infty} T_{0L'}^1 B_{L'}^c .$$

According to the theorem, terms in this series for $L' > 1$ are of higher order in γ than the first power, and their effect will be of the same order as terms already omitted by terminating Eqs. (2.189) and (2.190) at two terms. Another point is that determining all $T_{LL'}^n$ themselves only to order γ introduces no more error than has already been accepted by retaining only two terms in Eqs. (2.189) and (2.190).

Going on to Eq. (2.190) for anisotropic scattering, one finds that the G_1^0 coefficient of ψ_1 is dominated by the term $T_{11}^0 B_1^c$, which does not vanish for small γ. This result is not really surprising, since Eq. (2.179) and the definition of B_L^c show clearly that as γ (and, therefore, U) approaches zero,

$$\lim_{\gamma \to 0} J_L(u, \gamma) = \psi_L(u) B_L^c(u)$$

and, therefore, the value of $T_{LL'}^0$ for zero γ is exactly $\delta_L^{L'}$. Thus, where anisotropic scattering is present, the second term in Eq. (2.190) does actually vanish faster than the first by one order in γ but only because the anisotropy prevents the first term from vanishing at all.

Finally, an examination of G_1^1 shows that in the P_1 approximation, Legendre coefficients of order higher than B_2^c have an effect of the same order in γ as terms already omitted when the lethargy expansions are terminated with the first derivative terms.

G. Calculation of $T^n_{LL'}$

Recursion formulas provide a convenient method for determining numerical values of $T^n_{LL'}$ because these quantities are needed for all values of the indices less than or equal to those which give the last term in the above expansions. Values for all $T^n_{LL'}$, accurate to any desired degree, can be obtained from the following relations:[66]

$$T^0_{0L'} = \delta^0_{L'} \qquad \text{Eq. (2.191)}$$

$$T^0_{1L'} = \frac{L'}{2L'-1}(-\gamma)^{L'-1} - \frac{L'+2}{2L'+3}(-\gamma)^{L'+1} \qquad \text{Eq. (2.192)}$$

$$T^1_{0L'} = (-1)^{L'+1}(2L'+1) \times \sum_{p=L'+\delta^0_{L'}}^{\infty} \frac{(p!)^2 \alpha^p}{p(p-L')!(p+L'+1)!}$$

where

$$\alpha = 4\gamma(1+\gamma)^{-2} \qquad \text{Eq. (2.193)}$$

$$T^n_{L+1,L'} = (2L'+1)\left[\frac{2L+1}{L+1}\right] \sum_{p=0}^{\infty} T^0_{1p} \sum_{m=p-L'}^{p+L'}$$

$$(pL'00\ pL'm0)^2 \frac{T^n_{Lm}}{2m+1} - \frac{L}{L+1} T^n_{L+1,L'} \qquad \text{Eq. (2.194)}$$

$$T^{n+1}_{LL'} = \frac{2L'+1}{n+1} \sum_{p=0}^{\infty} T^1_{0p} \sum_{m=p-L'}^{p+L'}$$

$$(pL'00\ pL'm0)^2 \frac{T^n_{Lm}}{2m+1}. \qquad \text{Eq. (2.195)}$$

(The notation of Condon and Shortley[6] is used for the Clebsch-Gordan coefficients.)

Although some of the summations in Eqs. (2.191) to (2.195) look formidable, the task of evaluating the various $T^n_{LL'}$ from these equations will be greatly reduced for low order approximations if one makes estimates from the theorem and then terminates the series so as to accept errors in $T^n_{LL'}$ close to the same order in γ as the order in γ already ignored in the expansion for the slowing-down current.

It is also possible to get formulas directly for the Taylor series expansion coefficients of $T^n_{LL'}$ in special cases. For example,

$$T^0_{LL'} = \sum_{r=|L-L'|}^{\infty} b^r_{LL'} \gamma^r \qquad \text{Eq. (2.196)}$$

and

$$T^2_{0L'} = (-1)^{L'} (2L'+1) \times \sum_{p=L'+\delta^1_{L'}+2\delta^0_{L'}}^{\infty} \frac{(p!)^2 \alpha^p}{p(p-L')!\,(p+L'+1)!} \sum_{j=1}^{p-1} \frac{1}{j} \qquad \text{Eq. (2.197)}$$

where $b^r_{LL'}$ can be obtained from the relationship

$$b^{r+1}_{Lp} = \frac{(p+1)(p+2-r)}{(2p+3)(r+1)} b^r_{L,p+1} - \frac{p(p+r-1)}{(2p-1)(r+1)} b^r_{L,p-1} \qquad \text{Eq. (2.198)}$$

with $b^0_{Lp} = \delta^L_p$. Values of $T^0_{LL'}$ are of special interest because they can be used to obtain the Legendre components of the differential cross sections in the laboratory system from those in the center-of-mass system. Table 2.4 has been worked out from Eq. (2.198). The values are consistent with the theorem but show that for $n = 0$, $b^r_{LL'}$ vanishes frequently even when the theorem does not require it to do so.

Figures 2.8 through 2.11 give all values of $T^n_{LL'}$ needed for age and Greuling-Goertzel approximations in P_1 codes[69] as functions of the moderator mass number A. The actual quantities plotted were $A^p T^n_{LL'}$, where p equals the larger of n or $|L-L'|$. As expected from the theorem, the curves are smoother than would be those for $T^n_{LL'}$ alone. The figures contain plots for a single value of p and algebraic sign of $T^n_{LL'}$. The values of p included are 1 and 2 but not 0, since the only coefficients for $p = 0$ are

$$T^0_{00} = 1 \text{ and } T^0_{11} = 1 - \frac{3}{5}A^{-2}.$$

The trivial values $T^0_{01} = T^0_{02} = 0$ were also omitted from the $p = 1$ and 2 plots, respectively.

TABLE 2.4 — TABULATION OF $b^r_{LL'}$ FOR CALCULATING $T^0_{LL'} = \sum_{r=0}^{\infty} b^r_{LL'} \gamma^r$

	r	0	1	2	3	4	5	6
L	L'							
0	0	1	0	0	0	0	0	0
	1	0	0	0	0	0	0	0
	2	0	0	0	0	0	0	0
	3	0	0	0	0	0	0	0
	4	0	0	0	0	0	0	0
	5	0	0	0	0	0	0	
	6	0	0	0	0	0		
	7	0	0	0	0			
	8	0	0	0				
	9	0	0					
1	0	0	2/3	0	0	0	0	0
	1	1	0	-3/5	0	0	0	0
	2	0	-2/3	0	4/7	0	0	0
	3	0	0	3/5	0	-5/9	0	0

TABLE 2.4 — TABULATION OF $b^r_{LL'}$ FOR CALCULATING $T^0_{LL'} = \sum_{r=0}^{\infty} b^r_{LL'} \nu^r$ (Continued)

	r	0	1	2	3	4	5	6
L	L'							
1	4	0	0	0	-4/7	0	6/11	0
	5	0	0	0	0	5/9	0	
	6	0	0	0	0	0		
	7	0	0	0	0			
	8	0	0					
	9	0	0					
2	0	0	0	1/5	0	1/35	0	1/105
	1	0	6/5	0	-12/35	0	-2/35	0
	2	1	0	-11/7	0	3/7	0	17/231
	3	0	-6/5	0	196/105	0	-82/165	0
	4	0	0	48/35	0	-816/385	0	2784/5005
	5	0	0	0	-32/21	0	640/273	
	6	0	0	0	0	128/77		
	7	0	0	0	0			

TABLE 2.4 — TABULATION OF $b^r_{LL'}$ FOR CALCULATING $T^0_{LL'} = \sum_{r=0}^{\infty} b^r_{LL'} \gamma^r$ (Continued)

	r	0	1	2	3	4	5	6
L	L'							
2	8	0	0	0				
	9	0	0					
3	0	0	0	0	0	0	0	0
	1	0	0	24/35	0	0	0	0
	2	0	12/7	0	-4/3	0	0	0
	3	1	0	-46/15	0	65/33	0	0
	4	0	-12/7	0	48/11	0	-372/143	0
	5	0	0	50/21	0	-220/39	0	
	6	0	0	0	-100/33	0		
	7	0	0	0	0			
	8	0	0	0				
	9	0	0					
4	0	0	0	0	0	-1/63	0	-2/231
	1	0	0	0	4/21	0	4/77	0

TABLE 2.4 — TABULATION OF $b^r_{LL'}$ FOR CALCULATING $T^0_{LL'} = \sum_{r=0}^{\infty} b^r_{LL'} \gamma^r$ (Continued)

	r	0	1	2	3	4	5	6
L	L'							
4	2	0	0	10/7	0	-340/693	0	-2030/21021
	3	0	20/9	0	-112/33	0	124/143	0
	4	1	0	-390/77	0	5787/1001	0	-1692/1573
	5	0	-20/9	0	2300/273	0	-27416/5005	
	6	0	0	40/11	0	-848/693		
	7	0	0	0	-2240/429			
	8	0	0	0				
	9	0	0					
5	0	0	0	0	0	0	0	0
	1	0	0	0	0	0	0	0
	2	0	0	0	160/231	0	0	0
	3	0	0	80/33	0	-80/39	0	0
	4	0	30/11	0	-6900/1001	0	592/143	0

TABLE 2.4 — TABULATION OF $b^r_{LL'}$ FOR CALCULATING $T^0_{LL'} = \sum_{r=0}^{\infty} b^r_{LL'} \gamma^r$ (Continued)

	r	0	1	2	3	4	5	6
L	L'							
5	5	1	0	-295/39	0	521/39	0	
	6	0	-30/11	0	476/33	0		
	7	0	0	735/143	0			
	8	0	0	0				
	9	0	0					
6	0	0	0	0	0	0	0	1/429
	1	0	0	0	0	0	-2/143	0
	2	0	0	0	0	25/143	0	23/429
	3	0	0	0	700/429	0	-266/429	0
	4	0	0	525/143	0	-795/143	0	3414/2431
	5	0	42/13	0	-476/39	0	8156/663	
	6	1	0	-581/55	0	4970/187		
	7	0	-42/13	0	55272/2431			

TABLE 2.4 — TABULATION OF $b^r_{LL'}$ FOR CALCULATING $T^0_{LL'} = \sum_{r=0}^{\infty} b^r_{LL'} \gamma^r$ (Continued)

	r	0	1	2	3	4	5	6
L	L'							
6	8	0	0	448/65				
	9	0	0					
7	0	0	0	0	0	0	0	0
	1	0	0	0	0	0	0	0
	2	0	0	0	0	0	0	0
	3	0	0	0	0	896/1287	0	0
	4	0	0	0	448/143	0	-6720/2431	0
	5	0	0	336/65	0	-120736/9945	0	
	6	0	56/15	0	18424/935	0		
	7	1	0	-3108/221	0			
	8	0	-56/15	0				
	9	0	0					
8	0	0	0	0	0	0	0	0

TABLE 2.4 — TABULATION OF $b^r_{LL'}$ FOR CALCULATING $T^0_{LL'} = \sum_{r=0}^{\infty} b^r_{LL'} \gamma^r$ (Continued)

	r	0	1	2	3	4	5	6
L	L'							
8	1	0	0	0	0	0	0	0
	2	0	0	0	0	0	0	-28/2431
	3	0	0	0	0	0	392/2431	0
	4	0	0	0	0	4410/2431	0	-10248/12155
	5	0	0	0	1176/221	0	-52528/5525	
	6	0	0	588/85	0	-1568/55		
	7	0	72/17	0	-43008/1105			
	8	1	0	-1716/65				
	9	0	-72/17					
9	0	0	0	0	0	0	0	0
	1	0	0	0	0	0	0	0
	2	0	0	0	0	0	0	0
	3	0	0	0	0	0	0	0
	4	0	0	0	0	0	32256/46189	0

TABLE 2.4 — TABULATION OF $b^r_{LL'}$ FOR CALCULATING $T^0_{LL'} = \sum_{r=0}^{\infty} b^r_{LL'} \gamma^r$ (Continued)

	r	0	1	2	3	4	5	6
L	L'							
9	5	0	0	0	0	16128/4199	0	
	6	0	0	0	2688/323	0		
	7	0	0	288/323	0			
	8	0	90/19	0				
	9	1	0					

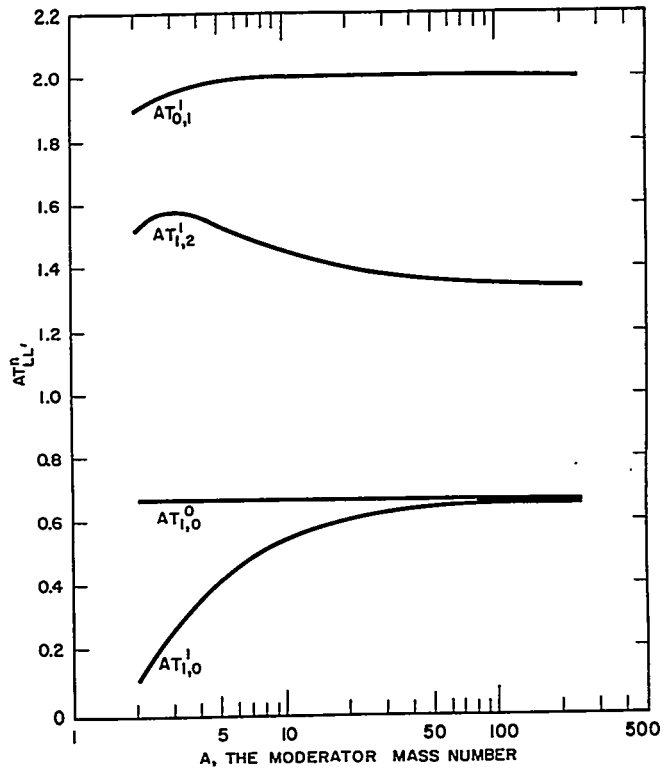

FIGURE 2.8. Positive $T^n_{LL'}$ That Vanish as Fast as the First Power of 1/A.

H. Explicit Forms and Recursion Relations for the Quantities $T^n_{LL'}$

E. M. Gelbard and D. R. Harris

1. Introduction

From the point of view of the foregoing section there appears to be little need for great accuracy in the computation of the quantities $T^n_{LL'}$. There are, however, other applications of the $T^n_{LL'}$ (for example, the transformation of measured cross sections between the center-of-mass and laboratory systems) where the desire for consistency and reproducibility of transformations made by different groups gives rise to the need for greater accuracy. It is of some interest to investigate additional methods for computing the $T^n_{LL'}$ which are more

suitable if great accuracy is desired for large blocks of quantities. Two such methods will be presented in this section. First, a general closed-form expression for the matrix elements, valid for all L, L', and n, will be derived; secondly, new recursion relations, not for the T's themselves but for closely related quantities, will be developed.

2. *General Closed Expression for* $T^n_{LL'}$

It is convenient to use U as the variable of integration, varying between 0 and U' when μ_c varies between 1 and -1:

$$U' = 2\ln\frac{1+\gamma}{1-\gamma}. \qquad \text{Eq. (2.199)}$$

The cosines μ_c and μ_0 can be expressed in terms of U:

$$\mu_c = 1 - \frac{(1+\gamma)^2}{2\gamma}(1-e^{-U}) = \frac{2e^{-U} - 1 - e^{-U'}}{1-e^{-U'}} \qquad \text{Eq. (2.200)}$$

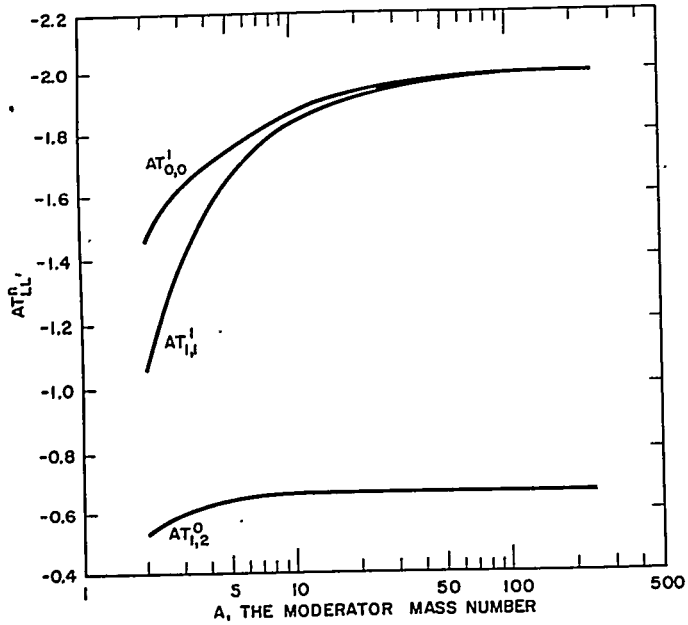

FIGURE 2.9. Negative $T^n_{LL'}$ That Vanish as Fast as the First Power of 1/A.

$$\mu_0 = \frac{1+\gamma}{2\gamma} e^{-U/2} - \frac{1-\gamma}{2\gamma} e^{U/2} = \frac{e^{U'/2}e^{-U/2} - e^{U/2}}{e^{U'/2}-1} . \qquad \text{Eq. (2.201)}$$

Then Eq. (2.187) becomes, as a function of U',

$$T^n_{LL'}(U') = \frac{(-1)^n}{n!} \frac{2L'+1}{2} \int_0^{U'} dU \left(-\frac{d\mu_c}{dU}\right) U^n P_L\left(\mu_0(\mu)\right) P_{L'}\left(\mu_c(U)\right)$$

Eq. (2.202)

or

$$T^n_{LL'}(U') = \frac{(-1)^n}{n!} \frac{2L'+1}{2} \frac{2}{1-e^{-U'}} \int_0^{U'} dU e^{-U} U^n P_L$$

$$\left(\frac{e^{U'/2}e^{-U/2} - e^{U/2}}{e^{U'/2}-1}\right) P_{L'}\left(\frac{2e^{-U} - 1 - e^{U'}}{1-e^{-U'}}\right) . \qquad \text{Eq. (2.203)}$$

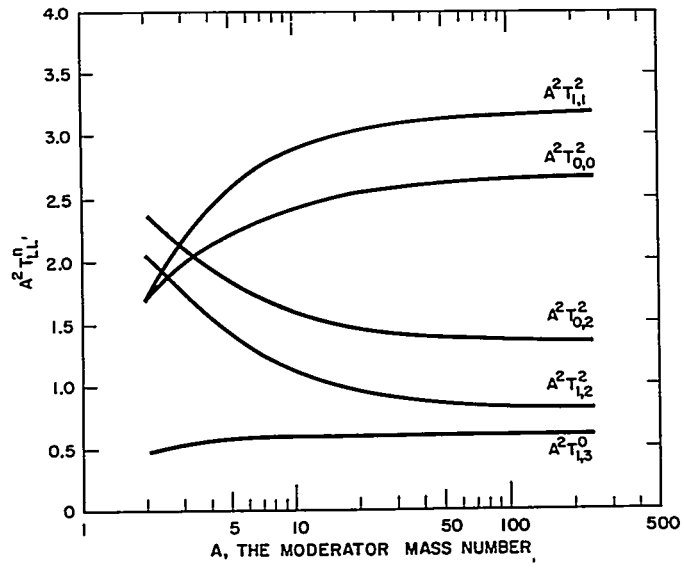

FIGURE 2.10. Positive $T^n_{LL'}$ That Vanish as Fast as the Second Power of 1/A.

Subsequent results, for conciseness, will be reduced to linear combinations of the elementary integrals $T_{00}^{n}(U')$. For $n = 0, 1, 2$ these are

$$T_{00}^{n}(U') = \begin{cases} 1 \quad \text{for } n = 0 & \text{Eq. (2.204a)} \\ \dfrac{1 - (1 + U')e^{-U'}}{1 - e^{-U'}} \quad \text{for } n = 1 & \text{Eq. (2.204b)} \\ 1 - \dfrac{(1 + U' + U'2/2)e^{-U'}}{1 - e^{-U'}} \quad \text{for } n = 2. & \text{Eq. (2.204c)} \end{cases}$$

Now $P_L(\mu)$ can be expressed as a finite series in powers of μ:

$$P_L(\mu) = \sum_{j=0}^{\frac{L}{2} \text{ or } \frac{L-1}{2}} q_{Lj}\,\mu^{L-2j} \qquad \text{Eq. (2.205)}$$

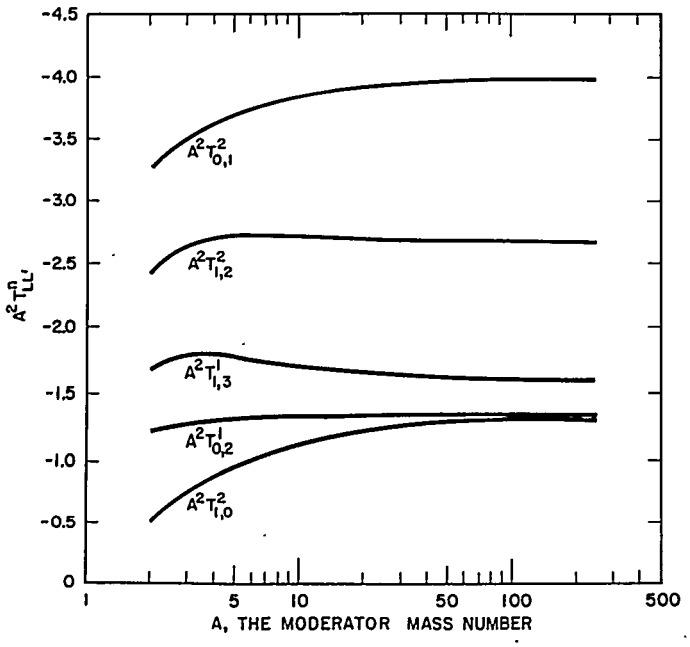

FIGURE 2.11. Negative $T^{n}_{LL'}$ That Vanish as Fast as the Second Power of 1/A.

where

$$q_{Lj} \equiv \frac{(-1)^j (2L-2j)!}{2^L (L-j)!\,(L-2j)!\,j!}. \qquad \text{Eq. (2.206)}$$

Expanding the Legendre polynomials, one has

$$T^n_{LL'}(U') = \frac{(-1)^n}{n!}\,\frac{2L'+1}{2}\,\frac{2}{1-e^{-U'}}\int_0^{U'} dU e^{-U} U^n \sum_{j=0}^{\frac{L}{2}\text{ or }\frac{L-1}{2}} q_{Lj} \left[\frac{e^{U'/2}e^{-U/2}-e^{U/2}}{e^{U'/2}-1}\right]^{L-2j} \sum_{j'=0}^{\frac{L'}{2}\text{ or }\frac{L'-1}{2}} q_{L'j'} \left[\frac{2e^{-U}-1-e^{-U'}}{1-e^{-U'}}\right]^{L'-2j'}. \qquad \text{Eq. (2.207)}$$

Finally, expanding the brackets by the binomial theorem, and rearranging,

$$T^n_{LL'}(U') = \sum_{j=0}^{\frac{L}{2}\text{ or }\frac{L-1}{2}} \sum_{k=0}^{L-2j} \sum_{j'=0}^{\frac{L'}{2}\text{ or }\frac{L'-1}{2}} \sum_{k'=0}^{L'-2j'} q_{Lj} \binom{L-2j}{k} q_{L'j'} \binom{L'-2j'}{k'} (2L'+1)(-1)^{k+k'} 2^{L'-2j'-k'} \times \frac{e^{U'/2\,[L-2j-k]}\left[1+e^{-U'k'}\right]}{\left[e^{U'/2}-1\right]^{L-2j}\left[1-e^{-U'}\right]^{L'-2j'}} \left\{\frac{(-1)^n}{n!}\,\frac{1}{2}\,\frac{2}{1-e^{-U'}}\int_0^{U'} dU U^n e^{-U\left[1+\frac{L}{2}-j-k+L'-2j'-k'\right]}\right\}. \qquad \text{Eq. (2.208)}$$

But the brace in Eq. (2.208) is just

$$\frac{T^n_{00}\left(U'\left[1+\frac{L-2j}{2}-k+L'-2j'-k'\right]\right)}{\left[1+\frac{L-2j}{2}-k+L'-2j'-k'\right]^{n+1}},$$

and introducing the explicit expressions for q_{Lj} and $q_{L'j'}$ one obtains the desired result:

$$T^n_{LL'}(U') = \sum_{j=0}^{\frac{L}{2}\text{ or }\frac{L-1}{2}} \sum_{k=0}^{L-2j} \sum_{j'=0}^{\frac{L'}{2}\text{ or }\frac{L'-1}{2}} \sum_{k'=0}^{L'-2j'} \frac{(2L-2j)!\,(-1)^{k+j}}{(L-j)!\,(1-2j-k)!\,j!\,k!}$$

$$\times \frac{(2L'-2j')!\,(2L'+1)\,(-1)^{k'+j'}}{(L'-j')!\,(L'-2j'-k')!\,j'!\,k'!\,2^{L+2j'+k'}}$$

$$\times \frac{e^{[L-2j-k]\,U'/2}\left[1+e^{-U'}\right]^{k'}}{\left[e^{U'/2}-1\right]^{L-2j}\left[1-e^{-U'}\right]^{L'-2j'}} \frac{T^n_{00}\left(U'\left[1+\frac{L-2j}{2}-k+L'-2j'-k'\right]\right)}{\left[1+\frac{L-2j}{2}-k+L'-2j'-k'\right]^{n+1}}$$

Eq. (2.209)

This general expression contains a finite number of terms, and is readily evaluated in terms of the T^n_{00}, which are themselves calculated from Eq. (2.204). For example,

$$T^n_{01}(U') = \frac{3\times 2^{-n}}{1-e^{-U'}}\,T^n_{00}(2U') - 3\,\frac{1+e^{-U'}}{1-e^{-U'}}\,T^n_{00}(U'). \quad \text{Eq. (2.210)}$$

3. *Computation of $T^n_{LL'}$ via Recursive Computation of $s^n_{mL'}$*

A) $n=0$. Use of the closed form expression for T is advisable when individual T's are to be computed. But if it is necessary to generate $T^n_{LL'}$ for all $L<N_1$, $L'<N_2$, and $n<N_3$, a different approach is probably more efficient. To develop this alternate method, return to the definition of T. It will be convenient to expand the polynomial $P_{L'}(\mu_0)$, so that

$$T^n_{LL'} = \frac{(-1)^n}{n!}\left(\frac{2L'+1}{2}\right)\sum_j q_{Lj}\int_{-1}^{1} d\mu_c\,\mu_0^{L-2j}P_L(\mu_c)\,U^n \equiv$$

$$\frac{(-1)^n}{n!}\left(\frac{2L'+1}{2}\right)\sum_j q_{Lj}\,t^n_{L-2j,\,L}. \quad \text{Eq. (2.211)}$$

Making use of the relation between μ_0 and U, one finds that

$$t^n_{\ell L} = \sum_{r=0}^{\ell} (-1)^{\ell-r} \left(\frac{M+1}{2}\right)^r \left(\frac{M-1}{2}\right)^{\ell-r} \binom{\ell}{r} \int_{-1}^{1} d\mu_c U^n e^{-\frac{mU}{2}} P_L(\mu_c) =$$

$$\sum_{r=0}^{\ell} (-1)^{\ell-r} \left(\frac{M+1}{2}\right)^r \left(\frac{M-1}{2}\right)^{\ell-r} \binom{\ell}{r} s^n_{mL}, \qquad \text{Eq. (2.212)}$$

where $M = 2r-\ell$. It should be noted that the number of terms contained in Eqs. (2.211) and (2.212) is small if L is small. For $L = 3$ Eq. (2.211) contains only two terms while Eq. (2.212) has four. Therefore, for $L \leq 3$, the computation of the s^n_{mL} is the principal part of the computation of T. It will be shown that the s^n_{mL} satisfy some very simple recursion relations. To this end, consider first the special case when $n = 0$. Now

$$s^0_{mL} = \int_{-1}^{1} e^{\frac{mU}{2}} P_L(\mu_c) d\mu_c = \int_{-1}^{1} \left(1 - \frac{\alpha}{2} + \frac{\alpha}{2}\mu_c\right)^{\frac{m}{2}} P_L(\mu_c) d\mu_c. \qquad \text{Eq. (2.213)}$$

Here $\alpha = 1 - \exp(-U')$. One may write

$$s^0_{mL'} = \left(\frac{\alpha}{2}\right)^{\frac{m}{2}} \int_{-1}^{1} \left(\frac{2-\alpha}{\alpha} + \mu_c\right)^{\frac{m}{2}} P_L(\mu_c) d\mu_c$$

$$= \left(\frac{\alpha}{2}\right)^{\frac{m}{2}} \left\{ \left(\frac{2-\alpha}{\alpha} + \mu_c\right)^{\frac{m}{2}+1} P_L(\mu_c) \int_{-1}^{1} - \int_{-1}^{1} \left(\frac{2-\alpha}{\alpha} + \mu_c\right)^{\frac{m}{2}+1} P'_L(\mu_c) d\mu_c \right\}$$

$$\left(\frac{m}{2}+1\right) = f_{mL'} - \frac{\left(\frac{\alpha}{2}\right)^{\frac{m}{2}}}{\left(\frac{m}{2}+1\right)} \left\{ \left(\frac{2-\alpha}{\alpha}\right) \int_{-1}^{1} \left(\frac{2-\alpha}{\alpha} + \mu_c\right)^{\frac{m}{2}} P'_{L'}(\mu_c) \right.$$

$$\left. + \int_{1}^{1} \left(\frac{2-\alpha}{\alpha} + \mu_c\right)^{\frac{m}{2}} \mu_c P'_{L'}(\mu_c) d\mu_c \right\}. \qquad \text{Eq. (2.214)}$$

It will be seen that

$$f_{mL'} = \frac{2}{\alpha}\left\{1-(-1)^{L'}(1-\alpha)^{\frac{m}{2}+1}\right\}\Big/\left(\frac{m}{2}+1\right). \qquad \text{Eq. (2.215)}$$

For later work it will be convenient to define

$$C_m = 1\Big/\left(\frac{m}{2}+1\right), \qquad \text{Eq. (2.216)}$$

and

$$g^0_{mL'} = \frac{2}{\alpha}\left\{1-(-1)^{L'}(1-\alpha)^{\frac{m}{2}+1}\right\}, \qquad \text{Eq. (2.217)}$$

so that

$$f_{mL'} = C_m g^0_{mL'}. \qquad \text{Eq. (2.218)}$$

Now

$$P'_L(x) = (2L-1)P_{L-1}(x) + (2L-5)P_{L-3}(x) + \ldots$$

$$xP'_L(x) = LP_L(x) + (2L-3)P_{L-2}(x) + (2L-7)P_{L-4}(x) + \ldots. \qquad \text{Eq. (2.219)}$$

In abbreviated notation,

$$P'_L(x) = \sum^{L-1}{}'(2\ell+1)P_\ell(x),\ xP'_L(x) = LP_L(x) + \sum^{L-2}(2\ell+1)P_\ell(x). \qquad \text{Eq. (2.220)}$$

In this notation one has [from Eq. (2.214)]

$$s^0_{mL'} = f_{m,L'} - C_m\left\{\left(\frac{2-\alpha}{\alpha}\right)\sum^{L'-1}{}'(2\ell+1)s^0_{m\ell} + L's^0_{mL'} + \sum^{L'-2}{}'(2\ell+1)s^0_{m\ell}\right\},$$

$$s^0_{m,L'-2} = f_{m,L'-2} - C_m\left\{\left(\frac{2-\alpha}{\alpha}\right)\sum^{L'-3}{}'(2\ell+1)s^0_{m\ell} - (L'-2)s^0_{m,L'-2} + \sum^{L'-4}(2\ell+1)s^0_{m\ell}\right\}.$$

Eq. (2.221)

Since $f_{mL'} = f_{m,L'-2}$,

$$s^0_{mL'}\left[1 + C_m L'\right] = -C_m\left(\frac{2-\alpha}{\alpha}\right)(2L'-1)s^0_{m,L'-1} + \left[1-C_m(L'-1)\right] s^0_{m,L'-2}$$

Eq. (2.222)

for $L' > 1$. Equation (2.222), supplemented by appropriate starting conditions, completely determines the $s^0_{m,\ell}$ (unless $m = -2$). Starting conditions, like the recursion relation itself, follow immediately from Eq. (2.221). One finds that

$$s^0_{m0} = f_{m0} = C_m g^0_{m0} \qquad \text{Eq. (2.223)}$$

and

$$s^0_{m1}\left[1 + C_m\right] = C_m\left[g^0_{m1} - \left(\frac{2-\alpha}{\alpha}\right)s^0_{m0}\right]. \qquad \text{Eq. (2.224)}$$

When $m = -2$, $C_m = \infty$. Note, however, that Eqs. (2.222) and (2.223) are valid for all $m \neq -2$ and that, in particular, they are valid for nonintegral m. Therefore, by a limiting argument

$$L's^0_{-2,L'} = -\left(\frac{2-\alpha}{\alpha}\right)(2L'-1)s^0_{-2,L'-1} - (L'-1)s^0_{-2,L'-2}, \qquad \text{Eq. (2.225)}$$

$$s^0_{-2,1} = \left[g^0_{-2,1} - \left(\frac{2-\alpha}{\alpha}\right)s^0_{-2,0}\right]. \qquad \text{Eq. (2.226)}$$

In addition one can show that

$$s^0_{-2,0} = -\frac{2}{\alpha}\ln(1-\alpha). \qquad \text{Eq. (2.227)}$$

B) $n \neq 0$. To generalize Eqs. (2.222) through (2.227) and derive recursion relations valid for all n, one can proceed with the aid of a simple device. Clearly,

$$-2\frac{\partial}{\partial x}s^n_{x,L'}\Bigg|_{x=m} = -2\frac{\partial}{\partial x}\int_{-1}^{1} U^n e^{-\frac{mU}{2}} P_L(\mu_c)d\mu_c\Bigg|_{x=m} = s^{n+1}_{m,L'}.$$

Eq. (2.228)

Differentiating Eqs. (2.222) through (2.224) with respect to the left-hand subscript, one finds that

$$s^n_{m0} = C_m \left[g^n_{m0} + n s^{n-1}_{m0} \right], \; m \neq -2 \qquad \text{Eq. (2.229)}$$

$$s^n_{m0} = C_m \left[g^n_{m1} - \left(\frac{2-\alpha}{\alpha} \right) s^n_{m0} + n s^{n-1}_{m0} \right], \; m \neq -2 \qquad \text{Eq. (2.230)}$$

and

$$s^n_{mL'} \left[1 + C_m L' \right] = -C_m \left(\frac{2-\alpha}{\alpha} \right) (2L'-1) s^n_{m,L'-1} + \left[1 - C_m (L'-1) \right] s^n_{m,L'-2}$$

$$+ n C_m \left[s^{n-1}_{mL'} - s^{n-1}_{m,L'-2} \right], \; L' > 1, \; m \neq -2 \, . \qquad \text{Eq. (2.231)}$$

Here

$$g^{n+1}_{mL'} = -2 \frac{\partial}{\partial x} g^n_{x,L'} \Big|_{x=m} \, . \qquad \text{Eq. (2.232)}$$

In particular

$$g^0_{mL'} = \frac{2}{\alpha} \left\{ 1 - (-1)^{L'} (1-\alpha)^{\frac{m}{2}+1} \right\} \qquad \text{Eq. (2.233)}$$

as before, while

$$g^n_{mL'} = \frac{2}{\alpha} (-1)^{L'} (1-\alpha)^{\frac{m}{2}+1} \ln^n (1-\alpha), \; n > 0 \, . \qquad \text{Eq. (2.234)}$$

One finds by direct integration that

$$s^n_{-2,0} = \frac{2}{\alpha(n+1)} \left[-\ln(1-\alpha) \right]^{n+1} \qquad \text{Eq. (2.235)}$$

and, by a limit argument,

$$s^n_{-2,1} = g^n_{-2,1} - \left(\frac{2-\alpha}{\alpha} \right) s^n_{-2,0} + n s^{n-1}_{-2,1}, \qquad \text{Eq. (2.236)}$$

$$s^n_{-2,L'} = -\left(\frac{2-\alpha}{\alpha} \right) (2L'-1) s^n_{-2,L'-1} - (L'-1) s^n_{-2,L'-2}$$

$$+ n \left[s^{n-1}_{-2,L'} - s^{n-1}_{-2,L'-2} \right] \, . \qquad \text{Eq. (2.237)}$$

Equations (2.229) through (2.237) include the preceding recursion relations for $n=0$. They completely determine the $s^n_{mL'}$ for all indices.

4. Other Recursion Relations

While it is true that Eqs. (2.229) through (2.237) determine the s matrix elements and, thereby, the T's, one may derive simpler recursion relations that are also quite useful. Returning to the definition of the s matrix, one sees that

$$s^n_{m,L'} = \int_{-1}^{1} U^n \left[1-\frac{\alpha}{2}+\frac{\alpha}{2}\mu_c\right]^{\frac{m}{2}} P_{L'}(\mu_c)d\mu_c$$

$$= \int_{-1}^{1} U^n \left[1-\frac{\alpha}{2}+\frac{\alpha}{2}\mu_c\right]^{\frac{m-2}{2}} \left[1-\frac{\alpha}{2}+\frac{\alpha}{2}\mu_c\right] P_{L'}(\mu_c)d\mu_c$$

$$= \int_{-1}^{1} \left(1-\frac{\alpha}{2}\right) U^n \left[1-\frac{\alpha}{2}+\frac{\alpha}{2}\mu_c\right]^{\frac{m-2}{2}} P_{L'}(\mu_c)d\mu_c$$

$$+\frac{\alpha}{2}\int_{-1}^{1} U^n \left[1-\frac{\alpha}{2}+\frac{\alpha}{2}\mu_c\right]^{\frac{m-2}{2}} \mu_c P_{L'}(\mu_c)d\mu_c . \qquad \text{Eq. (2.238)}$$

Since

$$xP_L(x)=\left(\frac{L+1}{2L+1}\right)P_{L+1}(x)+\frac{1}{(2L+1)}P_{L-1}(x), \qquad \text{Eq. (2.239)}$$

Eq. (2.238) implies that

$$s^n_{mL'} = \left(1-\frac{\alpha}{2}\right)s^n_{m-2,L'}+\frac{\alpha}{2}\left\{\left(\frac{L'+1}{2L'+1}\right)s^n_{m-2,L'+1}\right.$$

$$\left.+\left(\frac{L'}{2L'+1}\right)s^n_{m-2,L'-1}\right\} . \qquad \text{Eq. (2.240)}$$

One has, in Eq. (2.240), a relation involving recursion on m. It is not a convenient relation to use by itself because it involves only alternate m values. However, if the $s^n_{m,L'}$ are known for $m=M$ and $m=M+1$, Eq. (2.240) may be used to generate $s^n_{m,L'}$ for all $m>M+1$. One might invoke the earlier relations to get $s^n_{M,L'}$ and $s^n_{M+1,L'}$, then switch to Eq. (2.240) in dealing with higher M values. It seems desirable to use Eq. (2.240) whenever possible, since it is somewhat simpler than Eq. (2.231).

5. *Roundoff Problems*

In principle, the computation of T matrix elements from the closed-form expression in Sect. 2.3.H.3, or the recursion relation in Sect. 2.3.H.4, is completely straightforward. In practice, however, the methods developed in Sects. 2.3.H.3 and 2.3.H.4 must be handled with great care since, for small γ, roundoff problems become quite severe. When using the closed-form expression, roundoff errors may be controlled through recourse to double-precision arithmetic. But roundoff errors are so rapidly amplified in the recursive calculation that double-precision is inadequate. To solve Eqs. (2.226) through (2.234) accurately, it is necessary to invoke a rather roundabout procedure. These recursion relations are unstable when used to step ahead from L' to $L'+1$. They must be used, instead, to step backward in L'. To illustrate backward recursion, consider the $n=0$ case explicitly.

Suppose one wishes to compute $s^o_{mL'}$, $0 \le L' \le 10$. Pick $L'_{\max} \equiv M > 10$. In practice one may take $M=20$. Define $S^o_{m,M}=0$, $S^o_{m,M-1}=1$. Use Eq. (2.219) to generate $S^o_{m,L'}$ for all $M-2 \ge L' \le 0$. Then, it can be shown that

$$s^o_{mL'} = K^o_{mo}\, S^o_{mL'} \qquad \text{Eq. (2.241)}$$

$$K^o_{mo} = s^o_{mo}/S^o_{mo}\,. \qquad \text{Eq. (2.242)}$$

If all arithmetic is done in double precision, roundoff errors in $S^o_{mL'}$ and $s^o_{mL'}$ (and, subsequently, in $t^o_{QL'}$ and $T^o_{LL'}$) will be insignificant. A similar method is feasible in the case $n \neq 0$.

Thus, the use of the recursion relations requires double-precision arithmetic, coupled with a backward recursion technique. Nevertheless, experience has shown that the recursive method described above is very efficient in computations yielding large blocks of $T^n_{LL'}$s.

I. Slowing-Down Density[70] and the Generalized Greuling-Goertzel Approximation

H. J. Amster

Let $q(u,\mu)d\mu d\phi$ equal the rate at which neutrons with lethargies less than u are being slowed down to all lethargies greater than u and at the same time are being scattered into the solid angle $d\mu d\phi$. It is possible to obtain the Legendre components of $q(u,\mu)$ in terms of those of the vector flux in a manner entirely analogous to the treatment for the slowing-in density $J(u,\mu)$ described in Sect. 2.3.C. Instead of working with the kernel $\sigma^0(u',\mu_0,U)d\mu_0\,dU$, which is the cross section for a neutron with lethargy u' to have a lethargy gain in dU and a cosine of the laboratory system scattering angle in $d\mu_0$, one simply uses

$$\int_{u-u'}^{q} \sigma(u;\mu_0,U')\,dU'\,d\mu_0 \qquad \text{Eq. (2.243)}$$

which is the cross section for a neutron with lethargy u' to scatter to lethargies greater than u and have scattering angle cosines in $d\mu_0$.

By steps which are similar to those with which Eq. (2.176) was derived for $J_L(u)$, one can obtain

$$q_L(u) = \int_{u-q}^{u} \Psi_L(u') \int_{u-u'}^{q} B_L(u',U')\,dU'\,du' \qquad \text{Eq. (2.244)}$$

where

$$q(u,\mu) = \sum_{L=0}^{\infty} \frac{2L+1}{4\pi}\, q_L(u)\, P_L(\mu)\,. \qquad \text{Eq. (2.245)}$$

Thus,

$$\frac{dq_L(u)}{du} = -\int_{u-q}^{u} \Psi_L(u')\,B_L(u',u-u')\,du' + \Psi_L(u)\int_{0}^{q} B_L(u,U')\,dU'\,. \qquad \text{Eq. (2.246)}$$

The first term on the right side of Eq. (2.246) is just $-J_L(u)$ and, from Eqs. (2.169), (2.172), and (2.183), the integral in the second term is equal to $G_L^0(u)$. Therefore,

$$J_L(u) = \Psi_L(u)\, G_L^0(u) - \frac{dq_L(u)}{du}. \qquad \text{Eq. (2.247)}$$

By changing the variable of integration in Eq. (2.244) from u' to $U \equiv u - u'$ and by expanding in a power series, one obtains

$$q_L(u) = \int_0^q \int_U^q \Psi_L(u - U)\, B_L(u-U, U')\, dU'\, dU$$

$$= \sum_{n=0}^{\infty} \frac{d^n}{du^n} \left[\Psi_L(u) \int_0^q \frac{(-U)^n}{n!} \int_U^q B_L(u, U')\, dU'\, dU \right]. \qquad \text{Eq. (2.248)}$$

An integration by parts yields

$$\int_0^q \frac{(-U)^n}{n!} \int_U^q B_L(u, U')\, dU'\, dU = \frac{(-1)^n}{(n+1)!} \left[U^{n+1} \int_U^q B_L(u, U')\, dU' \right]_{U=0}^{q}$$

$$- \int_0^q \frac{(-U')^{n+1}}{(n+1)!} B_L(u, U')\, dU' = 0 - G_L^{n+1}(u) \qquad \text{Eq. (2.249)}$$

from which it follows that

$$q_L(u) \equiv - \sum_{n=0}^{\infty} \frac{d^n}{du^n} G_L^{n+1}(u)\, \Psi_L(u). \qquad \text{Eq. (2.250)}$$

Instead of numerically solving the transport equation for the Ψ_L's with the help of Eq. (2.182), one can solve simultaneously the additional coupled equations that can be formed for $q_L(u)$ and use Eq. (2.247) to obtain $J_L(u)$. The auxiliary equations come from Eq. (2.250) for $q_L(u)$; the expressions formed are

$$G_L^1 q_L - G_L^2 \frac{dq_L}{du} = \left[\left(G_L^1\right)^2 + G_L^1\left(\frac{d}{du} G_L^2\right) - G_L^2\left(\frac{d}{du} G_L^1\right)\right] N_L$$

$$- \sum_{n=2}^{\infty} \left[G_L^1 \frac{d^n}{du^n}\left(G_L^{n+1}\Psi_L\right) - G_L^2 \frac{d^n}{du^n}\left(G_L^n \Psi_L\right)\right] \qquad \text{Eq. (2.251)}$$

chosen so that no terms containing the first derivative of $G_L^n \Psi_L$ appear.

A corollary to the theorem of Sect. 2.3.E is that G_L^n must vanish at least as fast as γ^n. Therefore, the summation over n in Eq. (2.251) vanishes at least as fast as γ^4, while the coefficient of q_L vanishes at least as fast as γ; for this reason, the summation is neglected in the Greuling-Goertzel approximation. The one derivative of q_L is approximated as a finite difference in the multigroup codes, and values of q_L and, therefore, J_L would be expected to be accurate to order γ^2. This situation should be contrasted with Eq. (2.182), which requires two derivatives in order to obtain an equivalent accuracy.

Greuling and Goertzel originally treated only the case of isotropic scattering (their published paper[71] is much different from their original work[68]) and P_1 approximations. Thus, with $G_L^n(u) = T_{L0}^n B_0(u)$, they obtained the simple special case of Eq. (2.251),

$$T_{L0}^1 q_L - T_{L0}^2 \frac{dq_L}{du} = \left(T_{L0}^1\right)^2 B_0 \Psi_L \text{ for } L = 0 \text{ and } 1. \qquad \text{Eq. (2.252)}$$

Subsequent to Ref. 66, these authors published an article[71] treating the same subject from the point of view of a synthetic kernel, and anisotropic scattering was considered. In the notation used here, their equation taking the place of Eq. (2.251), for $L = 0$ was the more complicated form,

$$\lambda_0 \frac{dq_0}{du} + \left[1 + 2\frac{d\lambda_0}{du} - \lambda_0 \frac{\dfrac{d^2\lambda_0}{du^2}}{\left(1 + \dfrac{d\lambda_0}{du}\right)^2}\right] q_0$$

$$= - G_0' \left(1 + \frac{d\lambda_0}{du}\right) \Psi_0 , \qquad \text{Eq. (2.253)}$$

where

$$\lambda_0 \equiv - G_0^2/G_0' . \qquad \text{Eq. (2.254)}$$

With λ_0 and q_0 both of order γ, the last term in the coefficient of q_0 in Eq. (2.253) is of order γ^3, the size of the error already accepted in Eq. (2.253); thus, no loss of accuracy would be expected if this term were neglected completely. Furthermore, Eq. (2.251) shows that only terms of order γ^3 will be neglected if $-G_0^1 \frac{d\lambda_0}{du} \psi_0$ in the right side of Eq. (2.253) is taken as $-\frac{d\lambda_0}{du} q_0$. Thus, when neglecting terms no larger than the magnitude of an already existing error, Eq. (2.253) becomes identical with Eq. (2.251). While these two equations will not lead to identical results for medium weight nuclei, no advantage other than simplicity has been suggested for one over the other.

The final comment on Eq. (2.251) is that for $L > 1$, it is possible for the equation to lead to values of q_L in error by terms of smaller order than γ^3. For example, if the scattering is isotropic, the $L = 2$ equation will have a $G_2^1 = T_{20}^1 B_o \sim \gamma^2$ instead of γ, so that q_2 will be omitting terms of order γ^2 instead of γ^3.

J. Slowing Down by Hydrogen

Since the preceding approximations and consistency arguments were all based on ignoring terms of various order in powers of γ, the considerations all become useless when hydrogen, with γ equal to unity, is the moderator. However, hydrogen has two properties that make it easier to handle than heavy elements: (1) q, the maximum lethargy gain of a neutron colliding with hydrogen, is infinite, and (2) the scattering cross section $\sigma^c(u,\mu_c)$ in the center-of-mass system is independent of μ_c for all lethargies of interest to reactor calculations (isotropic scattering).

From Eqs. (2.169) and (2.181), one finds that for $\gamma = 1$,

$$\sigma(u, U) = 4\pi\sigma^c(u) e^{-U} , \qquad \text{Eq. (2.255)}$$

so that Eqs. (2.176) and (2.244) yield, respectively,

$$J_L(\mu) = \int_{-\infty}^{u} du' P_L\left[\mu_0(u - u')\right] \Psi_L(u') \sigma_S(u') e^{-(u-u')} \qquad \text{Eq. (2.256)}$$

and

$$q_L(u) = \int_{-\infty}^{u} du' \Psi_L(u') \sigma_S(u') \int_{u-u'}^{\infty} dU' e^{-U'} P_L\left[\mu_0(U')\right], \qquad \text{Eq. (2.257)}$$

where Eq. (2.172) was used in Eq. (2.257) and where

$$\sigma_S(u) \equiv B_0(u) = 4\pi\sigma^C(u) = G_0^0(u) \qquad \text{Eq. (2.258)}$$

is the total scattering cross section. Although G_L^0 has been introduced here, no use is being made of an erroneous expansion for $\gamma = 1$ since Eq. (2.247) is rigorous.

Since $P_0[\mu_0] = 1$, one finds that

$$J_0(u) = q_0(u), \qquad \text{Eq. (2.259)}$$

so that Eq. (2.247) yields an auxiliary equation for $q_0(u)$,

$$q_0(u) + \frac{dq_0(u)}{du} = \sigma_S(u)\Psi_0(u). \qquad \text{Eq. (2.260)}$$

An equation of this form is far more convenient to use than Eq. (2.257) because it is much simpler to store the value of $q_0(u)$ at the adjacent lower lethargy group than to store the values of $\Psi_0(u)$ for all lower lethargy groups.

Equations (2.180) and (2.181), with $\gamma = 1$, can be combined to form

$$\mu_0(U) = e^{-U/2}, \qquad \text{Eq. (2.261)}$$

so that, with $P_1[\mu_0] = \mu_0$, Eqs. (2.257) and (2.258) show that

$$J_1(u) = \frac{3}{2} q_1(u). \qquad \text{Eq. (2.262)}$$

Therefore, with $G_1^0 = T_{10}^0 \sigma_S = \frac{2}{3}\sigma_S$ according to Eq. (2.192), Eq. (2.247) yields

$$q_1(u) + \frac{2}{3}\frac{dq_1(u)}{du} = \frac{4}{9}\sigma_S(u)\Psi_1(u). \qquad \text{Eq. (2.263)}$$

Similar equations could have been made for $J_0(u)$ and $J_1(u)$, so that the use of Eq. (2.247) would not have been needed to obtain the J's. The q's are usually considered instead of the J's because of the form of Eqs. (2.260) and (2.263) being identical to that of the Greuling-Goertzel approximation [(Eq. (2.251) with the summation omitted)].

It is not true that J_L is a numerical constant times q_L for hydrogen when $L > 1$. Thus, no simple equations of the type above exist for $L > 1$. However, one could write $P_L(\mu_0)$ as an L^{th} degree polynomial in μ_0 and write one of the above type equations for each of the powers of μ_0.

Very often shortcuts are taken in calculating the J's in addition to those mentioned above. Despite the consistency arguments based on powers of γ. J_1 is often much smaller than J_0 because ψ_1 is smaller than ψ_0 and is, therefore, not treated as accurately. For example, the Selengut-Goertzel approximation applies Eq. (2.250), with only one term retained, to all isotopes when $L = 1$ and to all isotopes except hydrogen when $L = 0$; the exact Eq. (2.260) treats hydrogen when $L = 0$. The effect of using more terms in the described expansions than those required for the Greuling-Goertzel approximation for heavy isotopes has not been evaluated numerically. However, the sufficiency of any given approximation may be estimated by comparisons with a much more detailed calculation such as the Monte Carlo slowing-down calculation described in Sect. 2.4.

2.4 MONTE CARLO AGE CALCULATIONS IN A UNIFORM MEDIUM

H.J. Amster and R.C. Gast

A. Introduction

Monte Carlo provides a valuable means of obtaining a standard for slowing-down calculations. This standard is useful for providing a check of approximate slowing-down methods such as those discussed in Sect. 2.3. It also provides a desirable means of checking against experiment some integral effects of cross section and source description, e.g., age measurements in a uniform medium using a plane source of neutrons. The Monte Carlo scheme discussed in this section was primarily developed for this latter use, but it is also applicable for the former use through a comparison of Monte Carlo age with an approximate age. In addition to age, this scheme will provide at a specified energy the spatial distribution of the scalar flux

and also the spatial distribution of the activation of a resonance-detecting foil with a specified angular sensitivity. More specifically, this scheme will provide the scalar flux, or activation, per unit volume per unit energy at specified positions and energies for the problem of a plane source in an infinite homogeneous medium. Thus, in addition to comparing calculated age versus experimental age, comparisons involving much greater information may be made, i.e., the calculated versus experimental activation shapes.

B. Theory

The scheme just mentioned is made possible through a combination of Monte Carlo and analytic methods. The analog type of Monte Carlo (see Chap. 7, Sect. 7.3.C) assigns a definite position and exit energy to each collision; hence, a prohibitively large number of histories would have to be run to determine neutron density. Purely analytic schemes, such as the moments method, will give estimates of neutron density, but it is difficult to attain high accuracy in the spatial dependence of this density. A more thorough description of the theory in this section, along with illustrative examples and a formal proof, is presented in the description of the DAEDALUS code,[72] with which such calculations can be performed. Additional discussion of the theory of combined analytic Monte Carlo methods, as well as other methods for reducing the variance in Monte Carlo calculations, is discussed in Chap. 7, Sect. 7.3.

The combination of Monte Carlo and analytic methods for DAEDALUS is obtained by treating all spatial dependence of the vector flux analytically. The energy degradation of neutrons is treated completely by Monte Carlo except for the analytic treatment of the last collision. The analytic treatment of vector flux can be visualized through consideration of successive collisions. For the first flight, for a given neutron, there is an exponential probability along its path for the first collision. After the fair random choice of scattering angle and calculation of corresponding exit energy, there is a new collision probability function for the second collision along the second flight. This second flight originates from some point on the first flight with a probability given by the first collision probability. It follows that this second flight may be integrated along the first flight to obtain flux contributions to any spatial point as the result of two collisions. This process is generalized to any number of collisions. Thus, in a homogeneous medium the directions and energies of a particular neutron slowing down can be calculated by Monte Carlo without reference to the location

of each collision. With these angles and energies as parameters, it is possible to calculate the probability that the neutron had any particular collision between parallel planes at distances z and $z + dz$ from the point of origin.

The probability that a neutron departing at a distance z' in a given direction from a source plane in an infinite medium will be scattered at distances between z and $z + dz$ from the plane is

$$Q(z', z)dz = \frac{\Sigma^S}{|\mu|} \exp\left[(z' - z)\frac{\Sigma^T}{\mu}\right]dz \quad \text{(if the exponent is negative)}$$

$$= 0 \quad \text{(if the exponent is positive)}$$

Eq. (2.264)

where μ is the cosine of the angle between the direction of travel and the z axis, and Σ^S and Σ^T are the macroscopic scattering and total cross sections of the medium. The value of $Q(z', z)\,dz$ is zero for the above exponent positive, since a neutron flight from z' to the right cannot have its first scattering to the left of z' and vice versa.

Let $P_i(z)dz$ be the probability that a neutron, furnished by the source at $z = 0$, will have an $(i+1)^{st}$ scattering collision in the interval dz. Evidently,

$$P_0(z) = Q_0(0, z) \qquad \text{Eq. (2.265)}$$

where the subscript i on $Q_i(z', z)$ will from now on mean that in Eq. (2.264) $\mu = \mu_i$, $\Sigma^S = \Sigma_i^S$, and $\Sigma^T = \Sigma_i^T$, the values of these parameters that affect the neutron immediately after its collision i.

$P_i(z)$ for $i > 0$ can be obtained from the equation

$$P_i(z) = \int_{-\infty}^{\infty} P_{i-1}(z_i)\, Q_i(z_i, z)\, dz_i \qquad \text{Eq. (2.266)}$$

which states that the scattering rate for the $(i+1)^{st}$ collision is a sum of contributions from all possible positions of the previous collision i; the amount from the positions in dz_i is the scattering rate times the probability that the next collision of a neutron departing from z_i will be a scattering in dz.

By induction, the solution to Eq. (2.266) was first shown by Berger and Dogett[73] and later by Drawbaugh[74] to be

$$P_i(z) = \sum_{k=0}^{i} a_k\, e^{-b_k z} \prod_{j \neq k}^{i} a_j (b_j - b_k)^{-1} \qquad \text{Eq. (2.267)}$$

where $a_k = \Sigma_k^S/\mu_k$ and $b_k = \Sigma_k^T/\mu_k$, and where an exponential is understood to be identically zero if its argument is positive. The first b_i in the sequence of b's for a given neutron history, that can cause round off error in the term $\prod_{j\neq k}^{i} a_j(b_j - b_k)^{-1}$ truncates the collisions that are treated analytically. The remainder of the collisions are treated by analog Monte Carlo.

An alternate way of calculating $P_i(z)$ is first to calculate $P_t(z)$, where $0 \leq t \leq i$. Then, analog Monte Carlo is used to calculate (1) z_{ti}, the z coordinate of the $(i+1)$ collision minus that of the $(t+1)$ and (2) w_{ti}, the probability that a neutron which completed its $(t+1)$ collision will remain unabsorbed immediately after its $(i+1)$ collision. An average of the quantity

$$P_i(z) = w_{ti}P_t(z - z_{ti}) \qquad \text{Eq. (2.268)}$$

over many histories will then equal that from the definition of Eq. (2.267).

The number of collisions for which DAEDALUS calculates the spatial distribution analytically equals the smaller of (1) the number of collisions that could be calculated analytically in a given history without roundoff error exceeding a specified value and (2) an input number (usually around 4) chosen to minimize computing time for a given statistical accuracy. A definite, though broad, minimum usually does exist, since increasing the number of analytic calculations increases both the statistical accuracy and computing time per history. Furthermore, with most cross sections decreasing with increasing energy, calculating the spatial effects analytically is more beneficial for the first collisions than it is for the last.

Consideration is now given to the further steps needed to calculate the number of neutrons at locations in dz and with energies between the specified value E_R and $E_R - dE_R$. Although not essential to the formulation, a simplification almost always true in practice will be assumed: Only isotropic scattering in the center-of-mass system can occur for collisions which might slow a neutron to an energy below E_R (the other collisions have no restrictions on the differential cross-section description).

Let E_i be the energy of a neutron immediately after its i^{th} collision. Then, if the r^{th} collision is defined as the one that changes the energy of the neutron from above E_R to below, r can be identified as the value of i for which

$$E_{i-1} > E_R > E_i . \qquad \text{Eq. (2.269)}$$

When the neutron has energy E_{r-1}, the probability density for being scattered into a lower energy interval is constant for exit energies above αE_{r-1}($\alpha < 1$ and depends only on the mass of the scatterer) and zero for energies below. Thus, the ratio of the number of neutrons that scatter into dE_R in one collision to the number that scatter below E_R is

$$\frac{dE_R}{E_R - \alpha E_{r-1}}. \qquad \text{Eq. (2.270)}$$

Once Monte Carlo has established the fact, through Eq. (2.269), that a collision r will change the energy from E_{r-1} to some value below E_R, then the above ratio can be used to give a sample of the net flow of neutrons from E_{r-1} into dE_R. This step is possible because, in the absence of up-scattering, all neutrons that are scattered to energies below the interval dE_R will never be scattered into dE_R and, with dE_R infinitesimal, all neutrons scattered into dE_R once will never be scattered in again.

Now $P_{r-1}(z)dz$, with r defined by Eq. (2.269), gives the number of neutrons in dz that do scatter below E_R in a particular history. Thus, the rate of neutrons flowing from E_{r-1} to dE_R at positions in dz is

$$\frac{P_{r-1}(z)dzdE_R}{E_R - \alpha E_{r-1}}. \qquad \text{Eq. (2.271)}$$

To be conventional, one now speaks of neutrons in the lethargy interval $du_R = -dE_R/E_R$ at energy E_R, so that the slowing-in source becomes

$$-\frac{P_{r-1}(z)dzdu_R}{1 - \alpha\dfrac{E_{r-1}}{E_R}}. \qquad \text{Eq. (2.272)}$$

By the conservation of energy and momentum, it is possible to calculate μ^S_{R-1}, the cosine of the scattering angle required by a neutron whose energy is changed from E_{r-1} to E_R. From μ^S_{R-1}, μ_{r-1}, and an azimuthal angle of scattering determined by Monte Carlo, one can calculate μ_R, the cosine of the angle between the z axis and the direction of those neutrons which were slowed down into the interval du_R.

The flux of neutrons in any interval dz is an integral of the contributions from the slowing-in source at all positions.

The contribution from each position is the source of neutrons at that position times $1/\Sigma^S(E_R)$, the chance that a neutron from there will be scattered in dz:

$$\phi(u_R, z) = \frac{1}{1 - \alpha E_{r-1}/E_R} \int_{-\infty}^{\infty} P_{r-1}(z_R) \left[\frac{Q_R(z_R, z)}{\Sigma_R^S} \right] dz_R \qquad \text{Eq. (2.273)}$$

where the subscript R on Q means that in Eq. (2.264), $\mu = \mu_R$, $\Sigma^S = \Sigma_R^S$, $\Sigma^T = \Sigma_R^T$, cross sections evaluated at the energy E_R. A comparison of Eq. (2.264) with Eq. (2.267) shows that

$$\phi(u_R, z) = \frac{P_R(z)}{\Sigma_R^S (1 - \alpha E_{r-1}/E_R)} \qquad \text{Eq. (2.274)}$$

where $P_R(z)$ is exactly like $P_r(z)$ except that a_r and b_r should be replaced by $a_R = \Sigma_R^S/\mu_R$ and $b_R = \Sigma_R^T/\mu_R$.

Although ϕ is an estimate of the scalar flux, there is the direction $\cos^{-1}\mu_R$ associated with it. Thus, the activation of a foil placed parallel to the source plane is given by $F(\mu_R)\phi$, where $F(\mu_R)$ is the angular sensitivity given in Fig. 2.12. Since the same value of μ_R is associated with each value of z, $F(\mu_R)$ for all spatial positions has to be determined only once for each history.

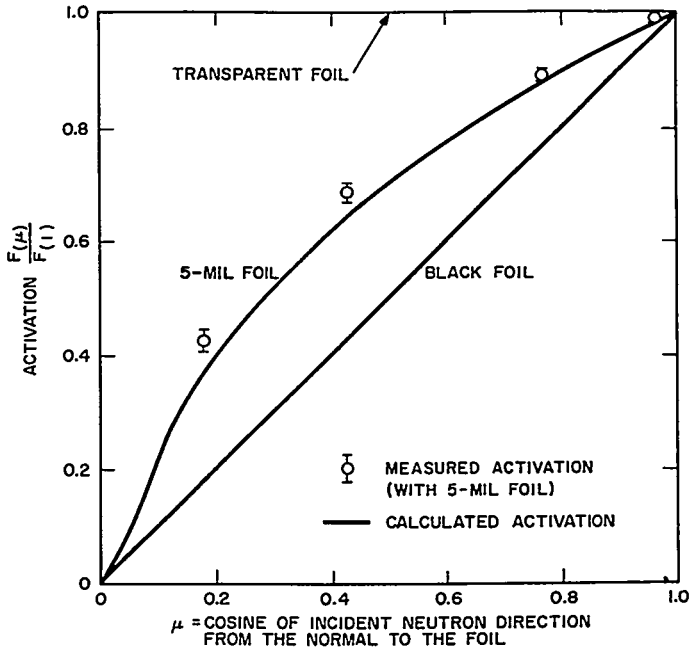

FIGURE 2.12. Foil Activation as a Function of Incident Neutron Direction.

Since E_{r-1} might take on any value between E_R and E_R/α, it is possible for ϕ in Eq. (2.274) to become infinite. That is, if a neutron happens to have an energy just slightly below E_R/α, its chance of slowing down below E_R may become so small that the ratio in Eq. (2.272) divided by $dv_R dz$ may blow up. Although the possibility of an actual machine overflow for an IBM-704 seems remote, it is statistically beneficial to avoid Eq. (2.274) when the difference between the two terms in the denominator is in danger of becoming small.

If a collision is recognized as risky in view of its energy and target species (when hydrogen is the scatterer, the above difficulties are not present because the α of hydrogen is zero), the history is split to avoid the possibility of a singularity. Thus, if a collision $j+1$ is with the nonhydrogenous moderator and the incident energy E_j is such that

$$E_R/\alpha > E_j \qquad \text{Eq. (2.275)}$$

the probability that the exit energy E_{j+1} will be in dE_R is

$$\frac{dE_R}{(1-\alpha)E_j}.$$

The flux from these particular neutrons, for instance $\varphi_1(\mu_R, z)$, can be calculated analytically in a fashion similar to the one leading to Eq. (2.274), and there results

$$\varphi_1(u_R, z) = \frac{P_R(z)}{\Sigma_R^S (1-\alpha)E_j/E_R}. \qquad \text{Eq. (2.276)}$$

Besides those neutrons scattering from E_j directly into dE_R, contributions to the flux in dE_R are possible for the fraction of neutrons whose values of E_{j+1} are above E_R; this fraction is

$$\gamma = \frac{E_j - E_R}{E_j(1-\alpha)}. \qquad \text{Eq. (2.277)}$$

Monte Carlo can be used to get this second contribution to the flux by continuing the standard Monte Carlo procedure ending with Eq. (2.274), except that (1) the weighting factor γ should multiply the answer, and (2) the energy E_{j+1} must be picked by Monte Carlo from a distribution between E_j and E_R

(since those below E_R have already been accounted for). Note that γ and the coefficient of $P_R(z)$ in Eq. (2.276) cannot become infinite. Although a similar procedure could be extended to eliminate the danger of collisions subsequent to the risky collision also becoming risky, the actual danger involved is considered negligible

From the spatial distributions derived above, it is now possible to calculate analytically contributions to the age and other spatial moments from individual histories. The DAEDALUS code, thus, averages these quantities directly, and requires no numerical integrations.

C. Neutron Distribution from a Plane Fission Source in Water

This section presents the results of a DAEDALUS calculation for a plane fission source in water in which an isotropic fission source with spectrum

$$S(E) = 0.484\, e^{-E} \sinh \sqrt{2E}$$

was treated. Elastic scattering and absorption were considered the only possible reactions. The cross sections were described as being constant in energy over each of 277 groups ranging from zero to 18.4 Mev. The group sizes varied greatly, since they were chosen only to describe the energy dependence of the cross sections, not flux. Considerably larger groups were subsequently found to give negligibly different results. The energy dependence of the source, its angular dependence, and that of the elastic scattering were tabulated in great detail to remove any doubt of representational accuracy. The hydrogen and oxygen cross sections came from Ref. 75.

The vector flux in DAEDALUS is evaluated at the energy of the lowest indium resonance. The detecting foil angular sensitivity is obtained by assuming that the vector flux per unit lethargy is constant over all energies where neutrons are absorbed by indium. Therefore, the final foil sensitivity is obtained by integrating over lethargy a monoenergetic sensitivity obtained as follows: Assuming the indium foils are beta counted, then the sensitivity of a foil to neutrons from a given direction and of a given energy is obtained by integrating, through the thickness of the foil, its activation at a given depth times the average escape probability of a beta particle produced there. This escape probability was obtained experimentally [76] and fitted with two exponentials.

Figure 2.12 shows $F(\mu)$, the relative number of beta counts that are observed when neutrons impinge upon a foil at an

angle $\cos^{-1}\mu$ with respect to the normal surface. The curved line shows the results of numerically integrating over the first three resonances in indium for a 5-mil 88.3 mg/cm^2 foil covered by 0.44 g/cm^2 of cadmium. It has since been learned that the higher energy resonances lead primarily to excited states that decay faster than those of the lowest energy resonance. While it would have been better to neglect them, their effect proved to be very small. The experimental points[76] were determined by exposing such foils to a collimated beam of neutrons emerging from a reactor. A transparent, i.e., extremely thin, foil not covered by cadmium would measure scalar flux and give the horizontal line shown, while a black foil, i.e., a foil for which every incident neutron would contribute the same to the beta counting rate, would produce the diagonal line.

The spatial distributions of the scalar flux, the activation of the foil of Fig. 2.12, and the activation of a black foil were normalized to unit area. Table 2.5 lists the scalar flux and its age, the activation distributions minus the flux, and the activation ages minus the scalar flux age; the errors quoted are probable (50 percent confidence) errors. For a unit source, i.e., one whose integral over space and lethargy is one, the scalar flux should be 0.674 times as large. Because much of the spatial calculation was performed analytically, neighboring points are correlated; e.g., if the estimate of flux is too high at one value of z, it is probably too high at adjacent values of z.

Table 2.5 shows that the foil activations are so close to the scalar flux that the analysis of a plane fission-source age experiment would not be very sensitive to the values of the curves in Fig. 2.12. This is a consequence of the source being a plane rather than a point, for the black foil activation age is 0.51 cm^2 smaller than the scalar flux age for a point source,[77] while it is 0.15 cm^2 larger for a plane source.

The scalar flux due to an isotropic point source can be obtained from scalar flux due to the same source distributed uniformly over an infinite plate:

$$\phi_{\text{point}}(r) = -\frac{1}{2\pi r}\frac{d}{dr}\phi_{\text{plane}}(r), \qquad \text{Eq. (2.278)}$$

where r is the distance to either source. Since the spatial dependence of the scalar flux contributed by one history is a sum of exponentials in Eq. (2.267), it would have been possible in principle to perform this required differentiation in Eq. (2.278) analytically, so that the calculation could have directly yielded point source scalar flux and probable error. Such use, however, was not anticipated in the DAEDALUS code.

TABLE 2.5 — CALCULATIONS FOR PLANE FISSION SOURCE IN WATER

Distance from Source (cm)	Scalar Flux	Foil Activation Minus Scalar Flux	Black Foil Activation Minus Scalar Flux
0	$(0.758 \pm 0.004) \times 10^{-1}$	$(-0.5 \pm 0.1) \times 10^{-3}$	$(-0.7 \pm 0.2) \times 10^{-3}$
0.25	$(0.761 \pm 0.004) \times 10^{-1}$	$(-0.6 \pm 0.2) \times 10^{-3}$	$(-0.9 \pm 0.3) \times 10^{-3}$
0.50	$(0.754 \pm 0.003) \times 10^{-1}$	$(-0.5 \pm 0.2) \times 10^{-3}$	$(-0.8 \pm 0.2) \times 10^{-3}$
1.00	$(0.732 \pm 0.003) \times 10^{-1}$	$(-0.4 \pm 0.1) \times 10^{-3}$	$(-0.6 \pm 0.2) \times 10^{-3}$
1.75	$(0.689 \pm 0.003) \times 10^{-1}$	$(-0.3 \pm 0.2) \times 10^{-3}$	$(-0.5 \pm 0.3) \times 10^{-3}$
3.00	$(0.598 \pm 0.002) \times 10^{-1}$	$(-0.2 \pm 0.1) \times 10^{-3}$	$(-0.4 \pm 0.1) \times 10^{-3}$
4.25	$(0.487 \pm 0.003) \times 10^{-1}$	$(0.9 \pm 1.2) \times 10^{-4}$	$(0.2 \pm 0.3) \times 10^{-4}$
6.00	$(0.340 \pm 0.001) \times 10^{-1}$	$(0.28 \pm 0.05)\ 10^{-3}$	$(0.41 \pm 0.08) \times 10^{-3}$
7.75	$(0.228 \pm 0.002) \times 10^{-1}$	$(1.0 \pm 0.7) \times 10^{-4}$	$(0.13 \pm 0.09) \times 10^{-3}$
10.00	$(0.135 \pm 0.001) \times 10^{-1}$	$(0.8 \pm 0.3) \times 10^{-4}$	$(0.11 \pm 0.04) \times 10^{-3}$
15.00	$(0.436 \pm 0.003) \times 10^{-2}$	$(0.9 \pm 1.2) \times 10^{-4}$	$(0.1 \pm 0.2) \times 10^{-4}$
20.00	$(0.161 \pm 0.002) \times 10^{-2}$	$(0.3 \pm 0.5) \times 10^{-5}$	$(-0.9 \pm 1.4) \times 10^{-6}$
30.00	$(0.267 \pm 0.003) \times 10^{-3}$	$(0.2 \pm 0.2) \times 10^{-5}$	$(0.3 \pm 0.3) \times 10^{-6}$
40.00	$(0.57 \pm 0.01) \times 10^{-4}$	$(1.3 \pm 0.4) \times 10^{-6}$	$(1.1 \pm 0.3) \times 10^{-6}$
50.00	$(0.14 \pm 0.01) \times 10^{-4}$	$(0.2 \pm 0.1) \times 10^{-6}$	$(-7.8 \pm 3.4) \times 10^{-8}$
Ages (cm^2):	25.2 ± 0.1	0.15 ± 0.05	0.15 ± 0.05

Graphical differentiation of a plot of the results in Table 2.5 yields the theoretical scalar flux from a point fission source in water as displayed with the corresponding experimental values of foil activation in Figs. 2.13 and 2.14. Figure 2.13 compares the calculated flux with smoothed curves through the experimental data of Lombard and Blanchard[78] and those of Hill, Roberts, and Fitch[79] whose values of 27.3 cm^2 and 30.9 cm^2, respectively, for the age bound almost all the other experimental determinations. The plots are normalized to the same area under the curves. The errors indicated on the calculated curve are estimated probable errors due to both the statistics of Monte Carlo and the graphical differentiation. To emphasize the difference between the calculated and experimental curves for $r < 30$, Fig. 2.14 shows some experimental points in a linear plot for which the results of each experiment are normalized to the same area. The wide spread of the

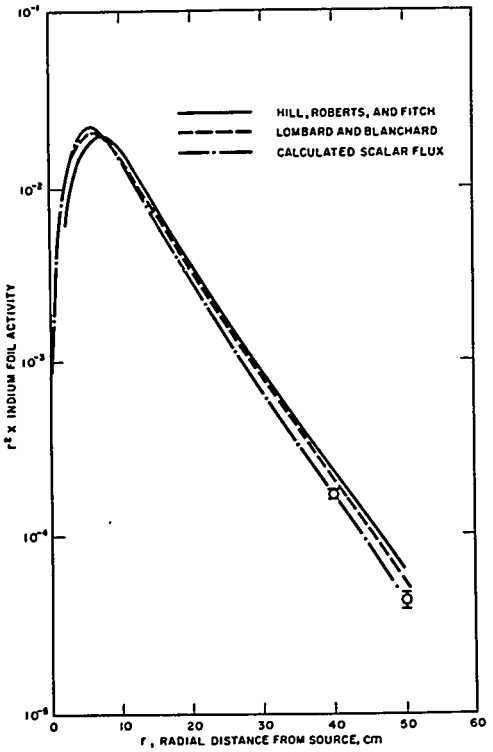

FIGURE 2.13. Two Extreme Experimental Determinations of Foil Activation from a Point Fission Source in Water Compared with a Calculated Curve for the Scalar Flux. (All curves are normalized to enclose the same area and turn out to have the same slope far from the source.)

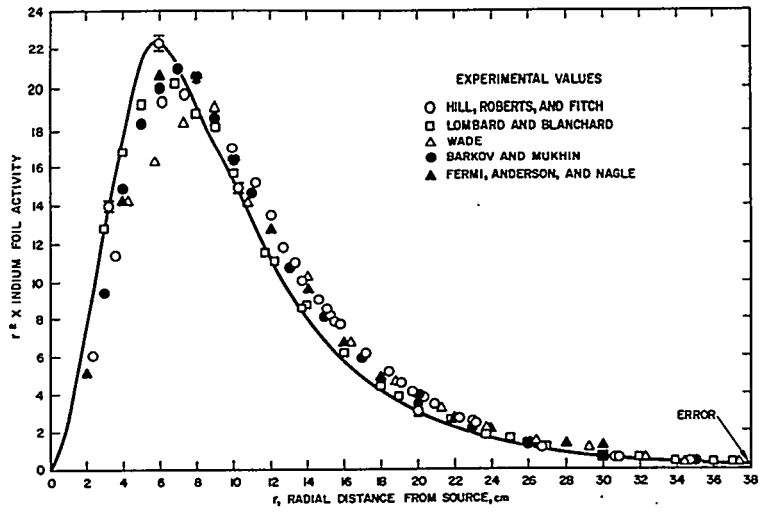

FIGURE 2.14. Experimental Determinations of Foil Activation from a Point Fission Source in Water Compared with a Calculated Curve for the Scalar Flux. (The values for each experiment and the calculation were normalized to enclose the same area. Near the source, the values from each experiment disagree with the calculated curve and values from other experiments; the reason is probably inaccurate corrections for the effect of the source.)

experimental points suggests that there were large systematic errors in correcting the data back to the values from an idealized point source. For the ages corresponding to the other data plotted, Wade[80] obtained 31 cm^2; Fermi, et al.,[81] assuming a smaller attenuation rate for large distances than all subsequent measurements, obtained 32.4 cm^2; and Barkov and Mukhin[82] obtained 29.4 cm^2. The activation curves for a point source, as given by the above experiments, with the exception of Fermi's, agree well with the calculated values beyond 30 cm. (If any of these activation curves for $r \geq 30$ were spliced onto the calculated curve for $r \leq 30$, the resulting age would be changed less than 1 percent.) Not plotted are data from Doerner, et al., [83] who used a geometry correction to give the age due to a plane, rather than a point, source. They obtained 27.86 cm^2 for the age and also gave a complete table of values from previous point source experiments, including 30.03 cm^2 from Hoover and Arnette, 26.7 cm^2 from Blosser and Truby, and 27.0 cm^2 from Pettus, which are not shown on the graphs.

The measured activation curve for a point fission source in water agrees better with calculated values of the scalar flux far from the source than near it. One would first suspect that

the cross sections used in the calculation are more accurate at high than low energy. However, the low energy cross sections are believed to be much more reliable than those at high energies, and a close examination of the point source experiments shows that many questionable corrections affected the flux near the source more strongly than the flux far away. Furthermore, the various experiments disagree with each other on the shape of the activation curve near the source. Hence, resolution of the discrepancy between theory and experiment represented by Figs. 2.13 and 2.14 seems to require further detailed investigation of experimental corrections and of cross sections, say below 2 Mev.

2.5 RESONANCE CAPTURE

S. Stein

A. Introduction

Neutrons slowing down in lattices that contain U^{238} are subject to capture in resonances. The resonances are characterized by extremely large cross sections confined to an energy range which is small compared to a group in a typical multigroup scheme. The resulting strong variations in the neutron flux, as a function both of energy and position, are incompatible with the usual simple techniques of group averaging and spatial homogenization. In general, slowing-down calculations in resonance capturing lattices rely on a previous determination of the correct resonance escape probability which is then imposed on the multigroup calculation by suitable self-shielding factors. Although such a calculation implicitly contains most of the complexities of the slowing-down problem, consideration of an idealized model permits considerable simplification without introducing significant errors in many of the practically encountered lattices. Approximate treatments of more complex lattices are discussed in Chap. 4.

The present model is defined by the following assumptions:

1. The lattice extends to infinity in all directions.
2. There is an energy E_U such that resonances occurring at energies above E_U may be replaced by a smooth cross section and such that neutron sources, inelastic scattering, and anisotropic scattering (in the center-of-mass system) are negligible below E_U.
3. If E_L denotes the energy at which the slowing-down calculation terminates and E_1 the energy of the peak of the lowest lying resonance, then

$$E_L \gg kT \qquad \text{Eq. (2.279)}$$

where T is the moderator temperature, and k is the Boltzmann constant; and

$$E_1 - E_L \gg \Gamma \qquad \text{Eq. (2.280)}$$

where Γ is the total width of the resonance at half maximum.

4. At E_U the flux per unit volume per unit lethargy is approximately independent of position and lethargy and is given by the asymptotic flux in a homogenized cell,

$$\phi = q(E_U)/ <\xi\Sigma_s> \qquad \text{Eq. (2.281)}$$

where $q(E_U)$ is the slowing-down density averaged over a cell at E_U, and $<\xi\Sigma_s>$ is the cell-averaged slowing-down power.

$$<\xi\Sigma_s> = \sum_{\text{Regions}} \frac{V_i}{V_{\text{cell}}} \cdot \sum_{\text{Isotopes}} \xi_j \Sigma^i_{sj} \qquad \text{Eq. (2.282)}$$

The first assumption makes it possible to restrict the problem spatially to a single cell of the lattice. The second and third restrict the range of energies and also the types of interactions which need be considered. The last provides necessary starting values since, in general, most of the captures will occur at energies in the lower part of the range, and results will not be sensitive to errors in this assumption.

The resonance escape probability can now be defined as the probability that a neutron slowing down past E_U will escape capture at energies above E_L. By virtue of neutron balance, this can be expressed in terms of slowing-down densities as

$$p = q(E_L)/q(E_U). \qquad \text{Eq. (2.283)}$$

Note that as defined $1-p$ includes smooth capture as well as the true resonance capture, which occurs between E_U and E_L. It has become customary to think in terms of a resonance energy range and to include all captures within this range in resonance capture. An approximate separation is possible, but the details of such a separation may vary with the problem.

B. The Resonance Cross Sections

Many of the arguments made in the rest of this discussion depend only on the localized (in energy) character of the resonances and not on their detailed shape. Where the line shape is

required, it is assumed that the Doppler-broadened form of the Breit-Wigner single-level formula applies. Many sources[84] discuss the theoretical origin of this shape. For purposes of reference and notation, some of the properties of the Doppler-broadened shape will be stated here.

The cross section for radiative capture for a single resonance is given by

$$\sigma_c = 4\pi\lambda\!\!\!^{-2}_o g \frac{\Gamma_n \Gamma_\gamma}{\Gamma^2} \left(\frac{E_o}{E}\right)^{1/2} \Psi(x, \theta) \qquad \text{Eq. (2.284)}$$

where

E_o is the energy of the resonance peak

E is the neutron energy

$4\pi\lambda\!\!\!^{-}_o$ is the wave length of a neutron of energy E_o

Γ_n is the scattering width at E_o

Γ_γ is the radiative width at E_o

Γ is the total width at E_o

g is the ratio of the statistical weights of the compound nucleus and the neutron plus target nucleus

x is defined by

$$x = \frac{2}{\Gamma}(E - E_o) \qquad \text{Eq. (2.285)}$$

θ is defined by

$$\theta = \frac{4E_o kT}{A\Gamma^2} \qquad \text{Eq. (2.286)}$$

where

k is the Boltzmann constant

T is the absorber temperature

A is the ratio of the mass of the absorber nucleus to that of the neutron.

The shape function, $\psi(x, \theta)$, is given by

$$\Psi(x, \theta) = (4\pi\theta)^{-1/2} \int_{-\infty}^{\infty} \frac{\exp\left[-(x-y)^2/4\theta\right]}{1 + y^2}\, dy. \qquad \text{Eq. (2.287)}$$

In practice, any energy dependence of the widths in Eq. (2.284) is usually negligible over the significant range of a single resonance, and the values at E_o are used in the expressions above. In the same range, the factor $(E_o/E)^{1/2}$ is not usually significantly different from unity and is frequently ignored (with one reservation to be discussed). These approximations will not result in significant errors if $E_o >> \max\left\{\frac{\Gamma}{\Gamma}\sqrt{\theta}\right.$, and the assumptions in Sect. 2.5.A assure this condition.

The scattering cross section for a single resonance is

$$\sigma_s = 4\pi\lambda\!\!\!^{-2}_o\, g \left(\frac{\Gamma_n}{\Gamma}\right)^2 \Psi(x, \theta) + \left(4\pi\lambda\!\!\!^{-2}_o\, g^2 \frac{\Gamma_n^2}{\Gamma^2}\, \sigma_p\right)^{1/2} \chi(x, \theta) \qquad \text{Eq. (2.288)}$$

where σ_p is the potential scattering cross section of the absorber and

$$\chi(x, \theta) = (\pi\theta)^{-1/2} \int_{-\infty}^{\infty} \frac{y \exp\left[-(x-y)^2/4\theta\right]}{1 + y^2}\, dy. \qquad \text{Eq. (2.289)}$$

A discussion of the physical origin and important properties of the Doppler functions ψ and χ is given by Dresner;[84] Roe[85] gives some additional properties useful in their numerical evaluation. Routines for numerical evaluation are included in many codes treating resonance capture.[86]

Of special interest for this discussion are the unbroadened or natural forms $(\theta = 0)$

$$\Psi(x, 0) = 1/(1 + x^2) \qquad \text{Eq. (2.290)}$$

$$\chi(x, 0) = 2x/(1 + x^2) \qquad \text{Eq. (2.291)}$$

as well as

$$\int_{-\infty}^{\infty} dx\, \Psi(x, \theta) = \pi. \qquad \text{Eq. (2.292)}$$

In the wings of the resonance ($x^2 \gg \theta$) both Ψ and χ approach the natural line shapes.

At any energy the capture cross section is a sum of contributions from each of the resonances, as is the scattering cross section. The scattering cross section, however, also contains a contribution from potential scattering, which is present as an energy-independent background (Ref. 43, p. 44). An additional contribution arises as a result of the aforementioned reservation. This is the so-called $1/v$ cross section. The cross section in Eq. (2.284) is not symmetric about E_o, exhibiting near zero energy an energy dependence which is

$$\sigma_c \approx \text{constant} \cdot E^{-1/2}. \qquad \text{Eq. (2.293)}$$

On the high-energy side of the resonance there is a monotonic and more rapid drop in the cross section. The combined tails of all resonances frequently result in a significant contribution to the capture cross section at energies above E_L. For U^{238}, and many other materials, a satisfactory approximation may be obtained by using the symmetric form of Eq. (2.284),

$$\sigma_c = 4\pi\lambda\!\!\!^{-2}_o \frac{\Gamma_n \Gamma_\gamma}{\Gamma^2} \Psi(x, \theta) \qquad \text{Eq. (2.294)}$$

together with an $E^{-1/2}$ cross section which reproduces the 2200 m/s capture cross section. This continuation of the thermal cross section will be referred to as the $1/v$ cross section.

The term smooth cross section will be used to designate any residual capture other than the cross section arising from individually treated resonances. When the symmetric form of Eq. (2.294) is used for the resolved resonances, it will also include the difference between the true cross section and the symmetric one, the difference consisting chiefly of the $1/v$ tail.

C. Analytical Models

Of the numerous papers that present an analytic approach to the calculation of resonance escape probability in lattices containing* U^{238}, only Refs. 84, 87, 88, and 89 are cited; of these, the first three include descriptions of the work of many others.

*Although the methods discussed may be applied to thorium lattices as well, the assumption of widely spaced resonances may not be made for such interesting materials as U^{235} and natural hafnium.

The works cited exploit the line character of resonance absorption: the resonances are assumed narrow enough that there is little probability that a neutron scattered by a moderator nucleus will emerge with an energy in the range of a resonance if its initial energy was within that range. Consequently, this probability is either neglected or treated as a small correction. This common assumption permits a general treatment which is helpful in identifying the difference between the various models and in determining the areas where further study is needed. The general treatment outlined here leads to the reduction of the problem to determining the solution of a standard one-energy transport equation. This is followed by a discussion of the one-energy problem and various approximate solutions.

Customarily, two major limiting cases for a single resonance are identified and each treated separately: the narrow resonance (NR) and the narrow resonance with infinite absorber mass (NRI). In dealing with materials such as UO_2, a third situation can arise, the narrow resonance with infinite absorber mass and internal moderator (NRM). In all three cases, the aforementioned assumption applies to moderator collisions, viz., after scattering of a resonance neutron by a moderator nucleus, removal from the resonance is overwhelmingly likely. The distinction is based on what happens in a scattering collision with an absorber nucleus. In the NR case, removal is probable; in the NRI case, the neutron energy changes negligibly, a limit obtained by letting the mass of the absorber nucleus become infinite. The third possibility (NRM) arises when a moderator is present in the absorbing material, but the absorber mass is effectively infinite. A general expression for the resonance escape probability, reducible to any of the three cases, can be obtained at the cost of introducing some artificial cross-section conventions.

It is assumed that the resonances are widely spaced, so that neutrons slowing down into the range of a resonance are supplied mainly from an asymptotic flux independent of lethargy and position. The origin for lethargy will be chosen at an energy well above the resonance in question but below the preceding one. In considering a single resonance, the energy dependence of cross sections of all materials other than the resonant absorber may be neglected.

Let Σ_r denote a macroscopic cross section for removal or scattering which on the average changes the neutron energy by many times the resonance width. Let Σ_s denote a cross section for scattering with negligible energy change, and Σ_c a capture cross section. Consider a two-region cell of arbitrary shape,

with Region I containing the absorber, and Region II containing a nonabsorbing moderator. The NR, NRI, and NRM situations give rise to the one-energy transport equation:

$$\Omega \cdot \nabla \Psi(\vec{r}, \vec{\Omega}, u) + (\Sigma_{ci} + \Sigma_{ri} + \Sigma_{si})_u \Psi = \frac{\Sigma_{si}(u)}{4\pi} \int d\vec{\Omega}' \Psi(\vec{r}, \vec{\Omega}', u) + \frac{S_i}{4\pi}, \quad i = 1, 2$$

Eq. (2.295)

where the index i specifies the region, $\Psi(\vec{r},\vec{\Omega},u)$ is the flux of neutrons at a point $\vec{r}$, direction $\vec{\Omega}$, lethargy u per cm^2-second-steradian-unit lethargy. The sources S_i are uniform in each region, and lethargy and angle independent, and are the rate at which neutrons slow down into a unit lethargy at u per cm^3-sec.

The NR case is obtained[87] by setting

$$S_1 = \Sigma_{r1}(0)\, \phi_o \equiv \Sigma_{r1}(0) \cdot \int d\Omega \Psi(\vec{r}, \Omega, 0) \qquad \text{Eq. (2.296)}$$

$$\Sigma_{s1}(u) = 0. \qquad \text{Eq. (2.297)}$$

The NRI case[87] is given by

$$S_1 = 0 \qquad \text{Eq. (2.298)}$$

$$\Sigma_{r1}(u) = 0 \qquad \text{Eq. (2.299)}$$

and the NRM[87] case by

$$\Sigma_{r1} = \text{energy-independent scattering cross section of internal moderator} \qquad \text{Eq. (2.300)}$$

$$\Sigma_{s1} = \text{absorber scattering cross section} \qquad \text{Eq. (2.301)}$$

$$S_1 = \Sigma_{r1}\, \phi_o. \qquad \text{Eq. (2.302)}$$

In all three cases,*

$$\Sigma_{s2} = 0 = \Sigma_{c2} \qquad \text{Eq. (2.303)}$$

$$S_2 = \Sigma_{r2} \phi_o. \qquad \text{Eq. (2.304)}$$

*Additional cases can be similarly obtained by a suitable interpretation of the parameters in Eq. (2.295). Such cases would include heavy diluents in the absorber or moderator region, or both, capture in the moderator region, etc.

The flux distribution through the resonance is determined in all three cases by the one-energy transport equation [Eq. (2.295)]. A further simplification can be obtained by relating the flux in the cell to that in another problem in which the source is entirely in Region I. This will result in an expression for the absorption rate in Region I in terms of $P(1,2)$, defined as the probability that a neutron born in a flat source distribution in Region I will have its first collision, other than scattering without energy change, in Region II. (The first collision may occur after crossing one or more cell boundaries.) This procedure will be carried out leading to the expression of the resonance escape probability in terms of $P(1,2)$, which will be referred to as the lattice escape probability.

Define a new variable, $\xi(\vec{r}, \vec{\Omega}, u)$ by means of

$$\left.\begin{aligned} \xi(\vec{r}, \vec{\Omega}, u) &= \frac{S_2}{4\pi\Sigma_{r2}} - \Psi(\vec{r}, \vec{\Omega}, u) \\ &= \frac{\phi_o}{4\pi} - \Psi(\vec{r}, \vec{\Omega}, u) \end{aligned}\right\} \qquad \text{Eq. (2.305)}$$

The new variable is the reduction in the flux below its off-resonance value due to the increased cross sections at resonance. It also satisfies a one-energy transport equation:

Region I:

$$\Omega \cdot \nabla \xi(\vec{r}, \vec{\Omega}, u) + (\Sigma_{c1} + \Sigma_{r1} + \Sigma_{s1})_u \xi = \frac{\Sigma_{s1}(u)}{4\pi} \int d\Omega' \, \xi(\vec{r}, \vec{\Omega}', u) + \frac{1}{4\pi}\left[\left(\Sigma_{c1} + \Sigma_{r1}\right)\phi_o - S_1\right] \qquad \text{Eq. (2.306)}$$

Region II:

$$\Omega \cdot \nabla \xi + \Sigma_{r2} \xi = 0. \qquad \text{Eq. (2.307)}$$

This is the desired form with source only in Region I. The lattice escape probability is the absorption rate in Region II in a flux distribution which satisfies the same pair of equations, except that the source would be $1/(4\pi V_1)$. Consequently, the absorption rate in Region II in the distribution $\xi(\vec{r}, u, \vec{\Omega})$ is given by $V_1 [(\Sigma_{c1} + \Sigma_{r1})\phi_o - S_1] P(1,2)$, in Region I by $V_1 [(\Sigma_{c1}+\Sigma_{r1})\phi_o - S_1] [1-P(1,2)]$. The latter includes neutrons which are removed to lower energies, as well as those which are truly absorbed.

$$\left[\Sigma_{c1} + \Sigma_{r1}\right]\int_{V_1} d\vec{r}\int d\vec{\Omega}\xi(\vec{r}, \Omega, u) = V_1\left[(\Sigma_{c1} + \Sigma_{r1})\phi_o - S_1\right]\left[1-P(1,2)\right].$$

Eq. (2.308)

Integration of Eq. (2.305) over solid angle and over Region I leads to the result [Eq. (2.308)],

$$\int_{V_1} d\vec{r}\int d\vec{\Omega}\Psi(\vec{r}, \vec{\Omega}, u) = V_1\left\{\phi_o\, P(1,2) + \frac{S_1}{\Sigma_{c1} + \Sigma_{r1}}\left[1-P(1,2)\right]\right\}.$$

Eq. (2.309)

The rate of captures in Region I is, per unit lethargy, $\Sigma_{c1}(u)$ times the integral in Eq. (2.309), so that, introducing the explicit sources,

$$\Sigma_{c1}(u)\int_{V_1} d\vec{r}\int d\vec{\Omega}\Psi(\vec{r}, \vec{\Omega}, u) = \Sigma_{c1}(u)\, V_1\phi_o\left\{\frac{\Sigma_{r1}(o)}{\Sigma_{c1}(u) + \Sigma_{r1}(u)} + P(1,2)\left[1-\frac{\Sigma_{r1}(o)}{\Sigma_{c1}(u) + \Sigma_{r1}(u)}\right]\right\}.$$

Eq. (2.310)

The left side of Eq. (2.310) is the absorption rate in a cell, per second, per unit lethargy. By the asymptotic assumption,

$$\phi_o = q/\langle\xi\Sigma_s\rangle \qquad \text{Eq. (2.311)}$$

where q is the slowing-down density above the resonance. The difference between the slowing-down densities above and below the resonance is the number absorbed per unit cell volume. Consequently, if a resonance escape probability is defined for the single resonance, in analogy to Eq. (2.283),

$$P_{res} = 1 - \frac{\int_{res} du\int_{V_1} d\vec{r}\int d\vec{\Omega}\Sigma_{c1}(u)\Psi(\vec{r}, \vec{\Omega}, u)}{(V_1 + V_2)\, q}. \qquad \text{Eq. (2.312)}$$

Substitution of Eqs. (2.310) and (2.311) into the last equation yields, with N_a the absorber number density,

$$p = 1 - \frac{V_1 N_a}{\langle \xi \Sigma_s \rangle (V_1 + V_2)} \int du\, \sigma_{c1}(u) \left\{ \frac{\Sigma_{r1}(o)}{\Sigma_{c1}(u) + \Sigma_{r1}(u)} + P(1,2) \left(1 - \frac{\Sigma_{r1}(o)}{\Sigma_{c1}(u) + \Sigma_{r1}(u)} \right) \right\}. \qquad \text{Eq. (2.313)}$$

The result expressed in Eq. (2.313) neglects the reduction in the source due to captures at higher energies within the resonance. For a close-packed lattice this may be an appreciable effect. In such a case, however, the reduction should be well approximated by assuming a source at lethargy u proportional to the probability of escaping capture at lethargies above u. An analysis similar to that given in Ref. 89 modifies Eq. (2.313) to

$$p^{-1} = \exp\left[\frac{N_a V_1}{\langle \xi \Sigma_s \rangle (V_1 + V_2)} \int du\, \sigma_{c1}(u) \left\{ \frac{\Sigma_{r1}(o)}{\Sigma_{c1}(u) + \Sigma_{r1}(u)} + P(1,2) \left(1 - \frac{\Sigma_{r1}(o)}{\Sigma_{c1}(u) + \Sigma_{r1}(u)} \right) \right\} \right]. \qquad \text{Eq. (2.314)}$$

The integrand is conventionally identified as the effective cross section, and the integral as the resonance integral (RI). Equation (2.314) is conveniently discussed in terms of the resonance integral,

$$RI = \int_{\text{res}} du\, \sigma_{c1}(u) \left\{ \frac{\Sigma_{r1}(o)}{\Sigma_{c1}(u) + \Sigma_{r1}(u)} + P(1,2) \left(1 - \frac{\Sigma_{r1}(o)}{\Sigma_{c1}(u) + \Sigma_{r1}(u)} \right) \right\}. \qquad \text{Eq. (2.315)}$$

Equation (2.315) appears in varying generality in the references previously cited, and most of the physics of the treatment of a single resonance is contained in the arguments leading to it.

The calculation of $P(1,2)$, while far from trivial, can be related to the considerable knowledge of the one-energy transport equation available in the literature. The first term in the integral is geometry-independent and is the volume term. In its original sense,[90] however, the term is a misnomer, since the wings of the resonance will provide a contribution to the uniform captures across the absorber element through the second, or surface, term.

D. The One-Energy Problem

The cell escape probability, $P(1, 2)$, might be described as a quasifamiliar concept chiefly because of its close connection with the escape probability given by Case, de Hoffmann, and Placzek,[91] to which it reduces in an important limit. Before discussing it in detail, the transport equation [Eqs. (2.306) and (2.307)] is restated in a briefer notation. In Region I

$$\vec{\Omega} \cdot \nabla \xi (\vec{r}, \vec{\Omega}) + \Sigma_1 \xi = \frac{c\Sigma_1}{4\pi} \int d\vec{\Omega}' \xi(\vec{r}, \vec{\Omega}') + \frac{1}{4\pi} . \qquad \text{Eq. (2.316)}$$

In Region II

$$\vec{\Omega} \cdot \nabla \xi + \Sigma_2 \xi = 0 . \qquad \text{Eq. (2.317)}$$

The usual continuity conditions apply at the interface, and periodic conditions apply at the cell's outer boundary. The lethargy dependence is irrelevant for present purposes and has been suppressed; the cell escape probability $P(1, 2)$ is related to the variable ξ through the following expression:

$$P(1, 2) = \frac{\Sigma_2}{V_1} \int_{V_2} d\vec{r} \int d\vec{\Omega} \xi(\vec{r}, \vec{\Omega}) . \qquad \text{Eq. (2.318)}$$

Where the symmetry of the cell is such that the flux is uniform over the interface, an alternative form of Eq. (2.318) is

$$P(1, 2) = \frac{S}{V_1} \int d\vec{\Omega}\, \vec{n} \cdot \vec{\Omega}\, \xi(\vec{s}, \vec{\Omega}) \qquad \text{Eq. (2.319)}$$

where $\vec{s}$ denotes a point on the interface, $\vec{n}$ is the unit vector normal to the absorber surface (directed out), and S is the area of the absorber surface.

If the moderator dimensions are large compared to a mean free path in the moderator, it is clear that reflected neutrons will be unimportant. The cell escape probability will tend to P_o, the escape probability of the isolated fuel lump, i.e., the probability of escaping before an absorbing collision, but not necessarily on first flight. Tabulations for slabs[92] and cylinders[93] have been published. If c, the ratio of the scattering to total cross section, vanishes also, as in the NR case, $P(1, 2)$ reduces to the well-known first flight escape probability of the isolated absorber, which has been obtained for slabs, cylinders, and spheres,[91] as well as hollow cylinders[94] and some other shapes.[91]

The dimensions of water-moderated lattices are such that reflections are important. In this case, much less is known concerning $P(1, 2)$. For vanishing c, an integral expression for slab geometry is available (Ref. 87, p. 25 ff.), and some Monte Carlo results for a hexagonal lattice of cylinders have been obtained.[95] Much of the literature has been devoted to an attempt to find simple but accurate estimates (Ref. 87, p. 25 ff.). Some results, and their application to resonance capture,[89] are discussed below.

The P_o-blackness expression for the effective resonance integral[89] can be obtained* by using an approximate P_1-blackness solution[92] to Eqs. (2.316) and (2.317) in Eq. (2.318), which yields for slabs

$$P(1, 2) = \frac{S}{4\Sigma_1 (1 - c) V_1} \cdot \frac{F_o}{1 + \gamma_1^1 F_o} \cdot \qquad \text{Eq. (2.320)}$$

where, if t_2 is the moderator half-thickness,

$$\gamma_1^1 = \frac{\sqrt{3}}{4} \coth \sqrt{3}\, \Sigma_2 t_2 - \frac{1}{2} \quad \frac{F_1}{F_o} \cdot \qquad \text{Eq. (2.321)}$$

The capture fractions[92] F_m are defined as the probability of absorption before escape from the absorber region if a flux proportional to $(\vec{n} \cdot \vec{\Omega})^m$ enters uniformly over its surface in the absence of internal sources. They are functions only of the

*See Chap. 3, Sect. 3.6.

cross sections and geometry of the absorber, closely related to the escape probability of the isolated absorber; for slabs[92] and cylinders[93] they are tabulated at least through $m = 1$. For isotropic incidence $(m = 0)$,

$$F_o = \frac{4\Sigma_1(1-c)V_1}{S} P_o . \qquad \text{Eq. (2.322)}$$

Again, in slab geometry, if $c = 0$ and t_1 is the absorber half-thickness,

$$F_m = 1 - (m+2) E_{m+3}(2\Sigma_1 t_1) \qquad \text{Eq. (2.323)}$$

where $E_m(x)$ denotes an exponential integral,[91]

$$E_m(x) = \int_1^\infty e^{-xu} u^{-m} du . \qquad \text{Eq. (2.324)}$$

Near the center of a resonance $(\Sigma_1 t_1 >> 1/2)$, F_1 and F_o are nearly equal, even for c as large as 0.5; in the wings of a resonance $(\Sigma_1 t_1 \sim 1/2)$, $\gamma_1 F_o \to 0$. Consequently, little error is introduced in Eq. (2.320) if the ratio F_1/F_o is set equal to unity in Eq. (2.321), yielding

$$\gamma_1 = \frac{\sqrt{3}}{4} \coth \sqrt{3}\Sigma_2 t_2 - \frac{1}{2} \qquad \text{Eq. (2.325)}$$

$$P(1,2) = \frac{S}{4\Sigma_1(1-c)V_1} \cdot \frac{F_o}{1+\gamma_1 F_o} . \qquad \text{Eq. (2.326)}$$

In this form γ_1 depends only on geometry and moderator properties.

In the same approximation, with the cylindrical geometry of Fig. 2.15, and treating the void in P_1 approximation also, a similar result holds. Equation (2.326) applies, with F_o the capture fraction for a cylinder,[93] and

$$\gamma_1(\text{cyl}) = \frac{\sqrt{3}}{4} \frac{K_o(\kappa r_1) I_1(\kappa r_2) + I_o(\kappa r_1) K_1(\kappa r_2)}{\kappa_1(\kappa\sigma_1) I_1(\kappa r_2) - I_1(\kappa r_1) K_1(\kappa r_2)} \qquad \text{Eq. (2.327)}$$

$$\kappa = \sqrt{3}\Sigma_2 . \qquad \text{Eq. (2.328)}$$

The functions $K_n(x)$ and $I_n(x)$ are modified Bessel functions.[96]

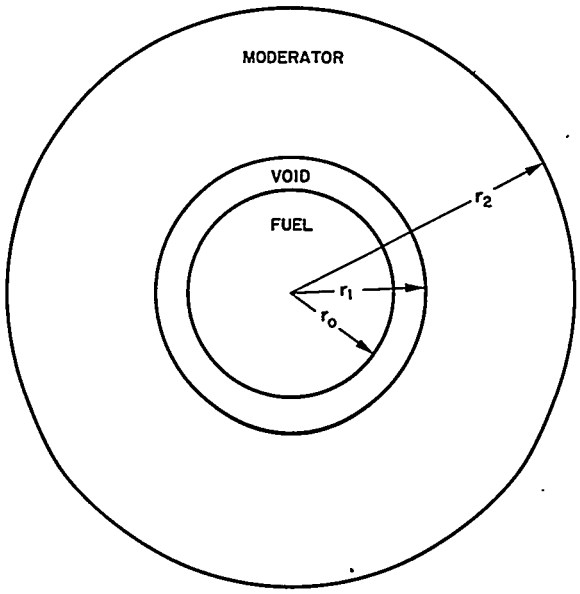

FIGURE 2.15. Cylindrical Cell Geometry.

Greater accuracy was later obtained for slabs with a double P_o-blackness* solution:[92]

$$P(1,2) = \frac{S}{4\Sigma_1(1-c)V_1} \cdot \frac{F_o}{1+\gamma_2 F_o} \qquad \text{Eq. (2.329)}$$

where

$$\gamma_2 = \frac{1}{2}\left[\coth 2\Sigma_2 t_2 - 1\right]. \qquad \text{Eq. (2.330)}$$

An equally simple but more precise expression was provided by means of the double-blackness[92] method:*

$$P(1,2) = \frac{S}{4\Sigma_1(1-c)V_1} \cdot \frac{F_o}{1+\gamma_3 F_o} \qquad \text{Eq. (2.331)}$$

where

$$\gamma_3 = \frac{2E_3(2\Sigma_2 t_2)}{1-2E_3(2\Sigma_2 t_2)}. \qquad \text{Eq. (2.332)}$$

*See Chap. 3, Sect. 3.6.

The last was obtained in a more general form by Nordheim (Ref. 87, p. 25 ff.). Figures 2.16, 2.17, and 2.18, from Ref. 92, compare the slab approximations for $c = 0$, an important case. The ordinate is the ratio of the approximate cell escape probability to an exact one obtained from numerical integration of the transport solution. The double-blackness approximation is adequate.

The approximations in Eqs. (2.326), (2.329), and (2.331) all yield resonance integrals of the form [returning to the notation of Eq. (2.315)]:

$$RI = \int_{res} du \; \frac{\sigma_{c1}(u)}{\sigma_{c1}(u) + \sigma_m(u)} \left\{ \sigma_m(u) + \frac{S}{4V_1 N_o} \frac{F_o(u)}{1 + \gamma F_o(u)} \left(1 - \frac{\sigma_m(o)}{\sigma_c(u) + \sigma_m(u)} \right) \right\}$$

Eq. (2.333)

where N_o is the number density of the absorber, and

$$\sigma_m(u) = \Sigma_{r1}(u)/N_o. \qquad \text{Eq. (2.334)}$$

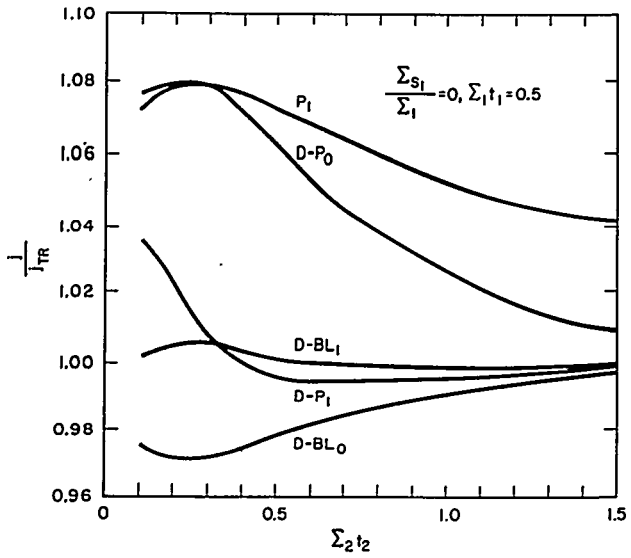

FIGURE 2.16. Ratio of Current Predicted by Various Blackness Approximations to Transport Result Where $\Sigma_{s_1}/\Sigma_1 = 0$, $\Sigma_1 t_1 = 0.5$.

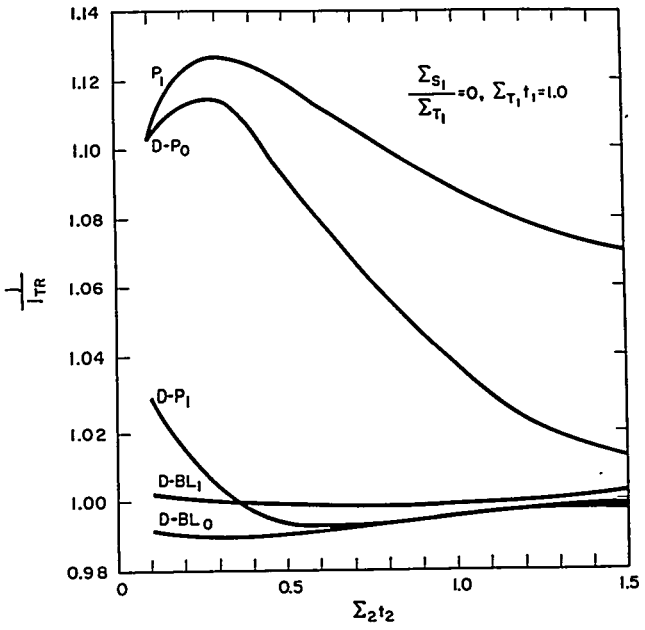

FIGURE 2.17. Ratio of Current Predicted by Various Blackness Approximations to Transport Theory Result Where $\Sigma_{s_1}/\Sigma_{t_1} = 0$, $\Sigma_{t_1} t_1 = 1.0$.

With the symmetric form of the cross section, Eq. (2.333) can, for resonance fulfilling the conditions of the model, be rewritten with negligible error:

$$RI = \frac{\Gamma}{E_o} \int_o^\infty dx \, \frac{\sigma_{c1}(x)}{\sigma_{c1}(x) + \sigma_m(x)} \left\{ \sigma_m(x) + \frac{S}{4V_1 N_o} \, \frac{F_o(x)}{1 + \gamma F_o(x)} \left(1 - \frac{\sigma_m(\infty)}{\sigma_c(x) + \sigma_m(x)} \right) \right\}. \qquad \text{Eq. (2.335)}$$

The first term in Eq. (2.335) is Wigner's volume term.[90] The second, under the assumptions that every absorber collision results in either capture or moderation, and that the absorber element is opague as long as $\sigma_{c1}(x)$ is appreciable, yields a linear dependence[90] on S/M. In fact, the dependence on absorber dimensions of F_o is important and is responsible for the slower variation with S/M which has been observed for isolated fuel elements.

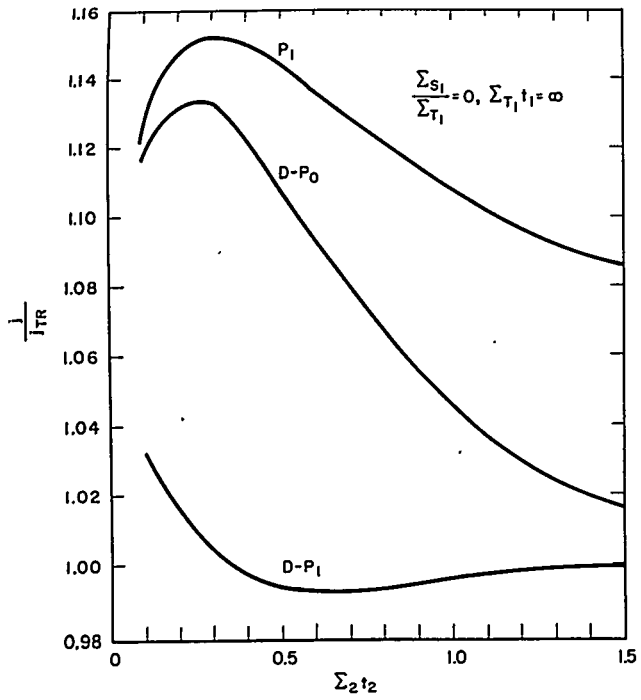

FIGURE 2.18. Ratio of Current Predicted by Various Blackness Approximations to Transport Theory Result Where $\Sigma_{s_1}/\Sigma_{t_1} = 0$, $\Sigma_{t_1} t_1 = \infty$.

E. The Practical Width

The discussions on analytical models and the one-energy problem have been concerned with analytic reduction of the calculation of resonance integrals in certain limiting situations. Which is pertinent to a particular resonance has not been specified. Qualitatively, the answer may be found in terms of the practical resonance width.

The concept of the practical width, Δ, was originally proposed by Wigner[90] and has recently been discussed in the more general framework of Eq. (2.315) by Nordheim[87] and others. In brief, it is the full width of the energy interval in which the resonance cross section is greater than the off-resonance cross section of the absorbing region. It represents qualitatively the interval in which the flux in a large absorbing region is reduced by the abnormally large cross section. For the large resonances of U^{238}, this is very much greater than either the natural or Doppler widths. If this interval is small (large) compared to the average energy loss in an absorber collision, removal after a scattering will be probable (improbable). (Multiple scatterings by moderator within a single resonance are

in nearly all practical cases improbable.) If Δ is small, the NR (or NRM) description should be better than the NRI approximation. When removal by absorber scattering is unlikely, the scattered neutron still may be captured by the resonance, and little error results from neglecting the change in energy, since it is of no interest at what energy, within a resonance, the neutron is captured. Consequently, these broad resonances are in 0^{th} order NRI cases. The small scattering probabilities (Γ_n/Γ) usually associated with these resonances also tend to reduce the errors from neglect of energy change.

The average energy change, δ, in a collision with an absorber nucleus is

$$\delta = \frac{2}{A} E_o \,, \qquad \text{Eq. (2.336)}$$

and the distinction between NR and NRI cases may be expressed in terms of large or small values for the ratio δ/Δ. In practice, Nordheim,[87] Dresner,[84] and others have treated all resonances as either the NR or NRI cases, depending upon whether δ/Δ is greater than or less than one. The resulting error has been found to be small after summing all resonances. This is in part due to the minor contributions of borderline resonances.

Nordheim[97] has compared numerical integrals based on Eq. (2.315) with Hellstrand's[98,99] isolated rod data. Although the flat source assumption was retained, and the comparison necessarily includes uncertainties in the description of the unresolved resonances, the agreement obtained for U^{238}, metal and oxide, was quite good, generally within 5 percent. The accuracy of the double-blackness approximation [Eq. (2.331)], which for isolated rods is equivalent to Eq. (2.315), suggests that lattices can be equally well handled by means of Eq. (2.331). A more stringent test in terms of Monte Carlo calculations would eliminate the large uncertainties from unresolved resonances, since the same resonances could be used in both calculations. Also lattices could be treated, supplementing the isolated rod data.

A discussion of equivalence relations and comparison with experimental data are given in Chap. 6, Sect. 6.5.B.

2.6 MULTIGROUP DIFFUSION THEORY

E. L. Wachspress

A. Introduction

The Boltzmann equation for neutron diffusion has been solved only for very simple cases. It is, therefore, necessary to make

simplifying assumptions in order to analyze the complex configurations of practical interest. These assemblies are usually large compared with the mean free path of a neutron, so that the Boltzmann equation may be approximated by a diffusion type differential equation.

Because nuclear properties of reactor materials often vary erratically with respect to energy, solution of the energy-dependent neutron diffusion equation is rarely attempted. Instead, one develops a set of coupled differential equations, each representative of a different energy interval. These sets are called the multigroup equations.

A basic feature of all multigroup calculations[65] is the subdivision of the continuous neutron energy spectrum into a finite number of groups and subsequent determination of an average neutron flux in each group as a function of position. The particular formulation for a small number of wide energy groups, sometimes distinguished from other group diffusion calculations by the term few-group, is treated in detail in Sect. 2.8.

Among the diverse areas which must be considered for multigroup calculations are:

1. Neutron cross sections (Sect. 2.2)
2. Choice of energy groups
3. Averaging of cross sections within each group (Sect. 2.8)
4. Coupling of groups through neutron slowing down and fissioning
5. Energy and spatial self-shielding effects (Sect. 2.5; Chap. 3, Sect. 3.6; Chap 4, Sect. 4.2)
6. Boundary conditions
7. Existence theorems regarding solutions and numerical methods for obtaining solutions (Chap. 7, Sect. 7.2).

A general description of the multigroup formulation follows. Detailed analysis of various aspects of multigroup calculations is provided in this chapter and in Chap. 3. The particular case of few-group calculations is described in Sect. 2.8.

B. The Group Diffusion Equations

It is convenient to use lethargy rather than energy as a variable in the group diffusion equations. The lethargy, u, is defined by

$$u = \ln \frac{10^7}{E}, \qquad \text{Eq. (2.337)}$$

where E is in ev.

The energy of fission neutrons is less than 10^7 ev, while the energy of thermal neutrons is of order of magnitude 0.02 ev. The lethargy varies, therefore, between zero and 20 for multigroup problems.

The diffusion equations may be written:[100]

$$\left.\begin{aligned} -\nabla\cdot D(r,u)\,\nabla\phi(r,u) + \Sigma_a(r,u)\,\phi(r,u) &= -\frac{\partial q(r,u)}{\partial u} + S(r,u) \\ -\nabla\cdot D(r,u_T)\,\nabla\phi(r,u_T) + \Sigma_a(r,u_T)\,\phi(r,u_T) &= q(r,u_T) + S(r,u_T) \end{aligned}\right\} \text{Eq. (2.338)}$$

where

r = space variable
u = lethargy
ϕ = neutron flux
Σ_{tr} = macroscopic transport cross section
D = diffusion coefficient (approximated by $\frac{1}{3\Sigma_{tr}}$ when the absorption is small)
u_T = thermal lethargy
Σ_a = macroscopic removal cross section (including inelastic scattering and absorption)
S = source due to fission neutrons and inelastically scattered neutrons
q = slowing-down density due to elastic scattering.

The multigroup equations are obtained by subdividing the continuous lethargy range into discrete intervals: $\Delta u_n = u_{2n} - u_{1n}$, and integrating the energy-dependent diffusion equation over each interval:

$$-\int_{u_{1n}}^{u_{2n}} \nabla\cdot D(r,u)\,\nabla\phi(r,u)\,du + \int_{u_{1n}}^{u_{2n}} \Sigma_a(r,u)\,\phi(r,u)\,du$$

Eq. (2.339)

$$= q(u_{1n}) - q(u_{2n}) + \int_{u_{1n}}^{u_{2n}} S(r,u)\,du.$$

In order to solve this set of coupled partial differential equations, it is necessary to have some relation between the flux and the slowing-down density. The simplest relation is that of age theory:

$$q = \xi\Sigma_s\phi \qquad \text{Eq. (2.340)}$$

where Σ_s is the macroscopic scattering cross section and ξ is the average logarithmic energy loss in the scattering region (Ref. 65, Chap. 6). This approximation can be obtained by writing the slowing-down density in terms of an integral over the neutron flux at higher energies and expanding the integrand in a power series in energy. The procedure is valid provided the product of the scattering cross section and the flux changes slowly over the energy interval through which a neutron can be scattered. Age theory is, therefore, an appropriate description for slowing down in heavy elements when the absorption is small compared to the scattering cross section. When these conditions are not satisfied (for example, when hydrogen is present, when the absorption is significant, or when inelastic scattering occurs), a more detailed treatment of the slowing-down density is required. Some specific procedures are discussed in Sect. 2.6.H.

The thermal neutrons may be treated in one or more groups, depending upon how detailed an analysis of the thermal spectrum is desired. This is considered in detail in Chap. 3.

The manner in which the integration over lethargy is performed for all groups is of fundamental importance, and several methods are used to account for flux variation within each lethargy group. Consider, for example, the absorption term. Usually, the slowing-down density varies more slowly with lethargy than the flux. By assuming a constant slowing-down density q_n in the group, one obtains:

$$\int_{u_{1n}}^{u_{2n}} \Sigma_a(r;u)\phi(r,u)\,du = \int_{u_{1n}}^{u_{2n}} \frac{\Sigma_a}{\xi\Sigma_s}(\xi\Sigma_s\phi)\,du = q_n \int_{u_{1n}}^{u_{2n}} \frac{\Sigma_a}{\xi\Sigma_s}\,du.$$

Eq. (2.341)

If one solves for slowing-down density rather than neutron flux, the absorption term is given by the right-hand side of Eq. (2.341). If, however, one wishes to solve for an average group flux then one uses the additional relationship

$$\phi_n = \left(\frac{1}{\xi\Sigma_s}\right)_n q_n = \left[\frac{1}{\Delta u_n}\int_{u_{1n}}^{u_{2n}} \frac{1}{\xi\Sigma_s}\,du\right] q_n.$$

Thus, the coefficient of the average group flux obtained from the absorption term in Eq. (2.339) is for this scheme:

$$\frac{\left(\int_{u_{1n}}^{u_{2n}} \frac{\Sigma_a}{\xi\Sigma_s}\,du\right)}{\left(\int_{u_{1n}}^{u_{2n}} \frac{du}{\xi\Sigma_s}\right)} \Delta u_n = \Sigma_{an}\,\Delta u_n \ .$$

For this calculation one needs the microscopic cross sections, $\sigma(u)$, as a function of lethargy for each material, i, and the density, N_i, of atoms of each type. Macroscopic cross sections can then be obtained by formulas of the form $\Sigma(u) = \sum_i \sigma_i(u) N_i$. Some procedures for determining nuclear cross sections for use in multigroup calculations are described in Sect. 2.2.

The source terms on the right side of Eq. (2.338) present various problems. The slowing-down densities at u_{1n} and u_{2n} must be related to group average slowing-down densities (or fluxes). One postulates an equation of the form

$$q_n = \omega_{1n}\, q(u_{1n}) + \omega_{2n}\, q(u_{2n}) \qquad \text{Eq. (2.342)}$$

where ω_{1n} and ω_{2n} are predetermined scalars, sometimes estimated by experience, sometimes taken to be 1/2, and sometimes computed by solving auxiliary slowing-down equations (see Sect. 2.6.H for a specific procedure). Since $q(0) = 0$, this enables computation of the slowing-down source in terms of group average fluxes:

$$\left.\begin{aligned} q(u_{1n}) &= \frac{1}{\omega_{2,n-1}}\left[q_{n-1} - \omega_{1,n-1}\, q(u_{1,n-1})\right] \\ q(u_{2n}) &= \frac{1}{\omega_{2n}}\left[q_n - \omega_{1n}\, q(u_{1n})\right] \\ q_n &= \frac{\phi_n}{\left(\frac{1}{\xi\Sigma_s}\right)_n} \end{aligned}\right\} \qquad \text{Eq. (2.343)}$$

Hydrogenous type moderators lead to further complications as a result of the large energy loss possible from a neutron collision with an atom of low mass. Slowing down due to hydrogen scattering may be considered separately through recursion formulas derived from an integral equation for hydrogenous moderation.

Recursion formulas for the slowing-down source are discussed in Sects. 2.3 and 2.7. The Greuling-Goertzel, Selengut-Goertzel, and consistent P-1 formulations have been widely used.

Inelastic scattering in the source term presents no particular conceptual difficulties. The inelastic scattering source from group m to n is:

$$S_{in}(m \to n) = \int_{u_{1n}}^{u_{2n}} du \int_{u_{1m}}^{u_{2m}} \Sigma_{in}(u' \to u)\, \phi(u')\, du'.$$

The inelastic scattering cross section for the group diffusion equations is defined as

$$\Sigma_{mn} = \Sigma_{in}(m \to n) = \frac{S_{in}(m \to n)}{\phi_m}.$$

so that the total inelastic source in group n is

$$\left(S_{in}\right)_n = \sum_{m<n} \Sigma_{mn} \phi_m. \qquad \text{Eq. (2.344)}$$

The fission source term is of the form

$$S_f(r, u) = \nu \left[\int_0^{u_c} \Sigma_f \phi\, du' + \int_{u_c}^{\infty} \Sigma_f \phi\, du' \right] \chi(u)$$

where

u_c = thermal cut-off lethargy

ν = number of neutrons emitted per fission

χ = fission spectrum normalized to $\int_0^{\infty} \chi(u')\, du' = 1$

Σ_f = macroscopic fission cross section.

This source, in terms of group average fluxes, is

$$S_{fn}(r) = \nu\chi_n \sum_m \Sigma_{fm}\phi_m \Delta u_m \qquad \text{Eq. (2.345)}$$

(Δu is taken as unity for the thermal group and ϕ_T is the integrated thermal flux.)

Combining all the terms in the group diffusion equation thus far discussed, one obtains a system of equations of the form

$$-\nabla \cdot D_n(r)\nabla\phi_n(r)\Delta u_n + \left(\Sigma_{an}(r)\Delta u_n + \frac{1}{\omega_{2n}(r)}\right)\phi_n(r)$$
$$= \left(1 + \frac{\omega_{1n}(r)}{\omega_{2n}(r)}\right) q(u_{1n}, r) + \sum_{m<n} \Sigma_{mn}(r)\phi_m(r) + \nu\chi_n \sum_m \Sigma_{fm}(r)\phi_m(r)\Delta u_m$$

Eq. (2.346)

where by Eq. (2.343)

$$q(u_{1,n=1}, r) = 0$$

$$q(u_{1,n>1}, r) = \frac{1}{\omega_{2,n-1}}\left[\frac{\phi_{n-1}(r)}{\left(\frac{1}{\xi(r)\Sigma_s(r)}\right)_{n-1}} - \omega_{1,n-1}(r)q(u_{1,n-1}, r)\right] .$$

These equations are linear and homogeneous in the group fluxes, and may be written in the form

$$M\phi = \nu F\phi \qquad \text{Eq. (2.347)}$$

where

- ϕ = a flux vector with components in each lethargy group
- M = a differential diffusion operator
- ν = a physical constant equal to the average number of neutrons released by fission
- νF = the neutron production matrix.

This system has nontrivial solution only when $1/\nu$ is an eigenvalue of the differential operator $M^{-1}F$. (It is shown in Chap. 7, Sect. 7.2, that M^{-1} exists while F may be singular. Hence, one considers $M^{-1}F$ rather than $F^{-1}M$.) It would be fortuitous to have this condition satisfied for any given configuration, since the physical constant $1/\nu$ is not in general an eigenvalue of $M^{-1}F$. Hence, one must examine the multigroup formulation in an attempt to find some parameter which will enable solution in general. This is best seen physically by observing that Eq. (2.347) is a static equation and that a steady-state nonzero flux exists only for an assembly that is just critical.

C. Time Dependence and Criticality

A nontrivial steady-state solution to Eq. (2.338) exists only when $1/\nu$ is an eigenvalue of $M^{-1}F$. This is a stable solution which may be realized physically only when $1/\nu$ is equal to the eigenvalue of largest modulus. It can be shown that the corresponding flux eigenfunction is nonnegative (see Chap. 7, Sect. 7.2). When this condition is satisfied, the system is critical; a chain reaction will be maintained with neither growth nor decay of the neutron flux level.

If one neglects delayed neutron effects and assumes all fission neutrons are released instantaneously, then space and time variation may be separated in the time-dependent group diffusion equation:

$$M\Phi = \nu F\Phi - \frac{\partial n}{\partial t}. \qquad \text{Eq. (2.348)}$$

Here, n is the neutron density and has component n_m in group m where $n_m = \frac{1}{v_m}\Phi_m$ with v_m the average velocity of the group.

One may multiply Eq. (2.348) by the diagonal matrix of group velocities, V, to obtain the eigenvalue equation

$$VM\Phi = \nu VF\Phi - \frac{\partial \Phi}{\partial t},$$

and if $\Phi = \phi(r, u)e^{\omega t}$,

$$\omega\phi(r, u) = V(\nu F - M)\phi(r, u) \qquad \text{Eq. (2.349)}$$

Thus, the exponent ω in the time dependence is an eigenvalue of the operator $V(\nu F - M)$. Of greatest physical importance is the eigenfunction belonging to the largest (algebraic) eigenvalue, $\omega = \omega_1$. This is the fundamental nonnegative mode, and ω_1 is a measure of its growth or decay. When $\omega_1 = 0$, the configuration is critical; when $\omega_1 < 0$, it is subcritical; and when $\omega_1 > 0$, it is supercritical.

In certain cases, one actually solves Eq. (2.349) rather than Eq. (2.347). This is, in general, a difficult task for reasons described in Sect. 2.6.D. The following alternative approach is customarily used to simplify computations: Denote the largest eigenvalue of $\nu M^{-1} F$ by k:

$$k \phi = \nu M^{-1} F \phi^{p-1}$$

It can be shown that k is also the ratio of neutron production to loss, each integrated over the entire reactor, for a pseudo steady-state configuration.* This eigenvalue k is, therefore, called the multiplication constant. With regard to criticality:

$k = 1$ for a critical assembly
$k > 1$ for a supercritical assembly
$k < 1$ for a subcritical assembly.

D. Computation Strategy

To solve the system of equations for k and the flux eigenvector, one assumes a fission source distribution, $S_f(r, u)$, and calculates the fluxes for each group successively, starting with the highest energy (lowest lethargy) group. The operator M in Eq. (2.347) is lower triangular in lethargy,† so that M^{-1} is computed by successive inversion of the monoenergetic group diffusion operators. This inversion corresponds to the solution of an elliptic type differential equation in each group. The group source consists of the assumed fission source for the group plus terms arising from the various slowing-down processes.

Numerical methods for inverting the monoenergetic group diffusion operator are described in Chap. 7, Sect. 7.2. Successive fission source estimates are generated by

$$(k \phi)^p = \nu M^{-1} F \phi^{p-1} \qquad \text{Eq. (2.350)}$$

---

*If the number of neutrons released on the average by fission were ν/k rather than ν, then the configuration would be critical. The symbol ν_c has been used instead of ν/k to denote the critical ν for a configuration.

† Referring to Eq. (2.346), one observes that with an assumed fission source term, the right-hand side of Eq. (2.346) for group n depends only upon fluxes of groups $m < n$. A lower triangular matrix has no elements above the main diagonal.

until some measure of the fission source error is less than a preassigned termination criterion. Convergence to the fundamental mode is assured in both the continuous spatial representation and the discrete representation commonly used for reactor studies. Convergence of Eq. (2.350) is often accelerated by extrapolation (linear combination of successive iterates). Differencing techniques are applied to replace the differential operator by a matrix (Chap. 7, Sect. 7.2).

To solve Eq. (2.349), one must in general invert all energy groups simultaneously, although it is sometimes possible to add an estimated $\frac{\omega}{v}$ to the group removal cross section, compute k by Eq. (2.350), and iterate on ω until $k = 1$. The difficulty associated with simultaneous group inversion, especially for two- and three-space-dimension computations, led to the use of Eq. (2.350) with criticality in terms of k rather than ω, as in Eq. (2.349).

E. Boundary Conditions: Continuity at Interfaces

The monoenergetic neutron diffusion equation is of elliptic type (Ref. 15, Vol. I, Chap. VI) and requires boundary conditions of the form

$$\alpha(r_B, u)\,\phi(r_B, u) + \beta(r_B, u)\,\frac{\partial}{\partial n}\,\phi(r_B, u) + \gamma(r_B, u) = 0 \qquad \text{Eq. (2.351)}$$

where

r_B is a point on the boundary
α, β, and γ are specified functions
$\frac{\partial}{\partial n}\phi$ is the derivative of the flux in the direction of the outward normal at the bounding surface.

A unique stable solution is assured when $\alpha \geq 0, \beta \geq 0$, and $\alpha + \beta > 0$. In the absence of an external source, γ is zero. The usual boundary conditions (with $\gamma = 0$) are flux zero ($\alpha = 1, \beta = 0$), current zero ($\alpha = 0, \beta = 1$), or an impedance (or radiation) type condition of specified $\frac{\alpha}{\beta} > 0$. The latter is obtained by enclosing a portion of the reactor by a boundary surface and characterizing the region outside by its albedo.

Diffusion theory implies continuity of flux and net current normal to any surface. The current continuity condition can be satisfied at a plane boundary between two dissimilar regions.

If, however, a material region is bounded by a surface with a corner point or cusp, the current continuity condition cannot be satisfied at that point. This is a mathematical consequence of the assumptions required to reduce the integral Boltzmann equation to the group diffusion differential equation.

Since most configurations of interest have interfaces where the diffusion theory continuity condition cannot be satisfied everywhere, an alternative condition is imposed. It has already been mentioned that one often reduces the diffusion differential equation to a system of linear equations by differencing techniques and solves for flux values at discrete points in space rather than for a continuous function in space. Each difference equation is obtained by integration of the diffusion equation over a small volume. The current continuity condition is replaced by an integral neutron conservation condition. The number of neutrons leaving an elemental volume equals the number entering all neighboring volumes from that volume. This less restrictive neutron conservation condition can be satisfied everywhere in a complex configuration. It also assures a positive definite space diffusion operator for each energy group, a characteristic which is used in proving the existence of a unique solution and in the analysis of numerical methods for solving the equations.

F. Adjoint Equations

In addition to the equation thus far considered, one is sometimes concerned with the adjoint equations. The adjoint flux, $\phi^+(r,u)$, for a critical reactor is the relative probability that a neutron of lethargy u at point r will eventually produce a fission. For this reason the adjoint flux is often called the importance function. Effects of small changes in a configuration may be conveniently analyzed by perturbation theory which utilizes both fluxes and adjoints.

An adjoint diffusion equation may be derived in a straightforward manner from the Boltzmann equation. Alternatively, one may obtain the differential equation adjoint to the age diffusion equation itself [Eq.(2.346)] or even the adjoint matrix to the system of linear equations from which numerical flux values are obtained. The particular adjoint equation selected depends upon the manner in which it is to be used.

For example, if one wishes to determine the effect on reactivity of a small cross-section change, the adjoint to the final difference equation matrix is adequate. This is, in fact, the most frequently used adjoint. Alternatively, one can work directly with the adjoint differential equation. For example, suppose one wishes to estimate the truncation error associated

with discrete lethargy groups rather than a continuous energy spectrum. Macroscopic cross sections can be derived by schemes which use adjoint rather than flux spectrum averaging. Let the matrix representation of the group diffusion equation be $k\varphi = \nu A\varphi$. Let the matrix representation of the adjoint group diffusion equation be $k'\varphi^+ = \nu A'\varphi^+$, where A' is approximately equal to the transpose, A^T, of A. The matrices A' and A^T are not identical because of the approximations in going from the energy continuum to the group diffusion equations. A comparison of the values obtained for k and k' gives some indication of the reactivity error associated with the energy group subdivision of the continuous spectrum. One may compute

$$k'\phi' = \nu(A')^T\phi'$$

and by comparison of ϕ' with ϕ gain some knowledge of the flux error arising from the discrete energy group formulation. As the lethargy widths go to zero, k' approaches k and ϕ' approaches ϕ. Flux-adjoint cross-section weighting may enable higher accuracy with given lethargy intervals.

Adjoint equations are solved in the same manner as flux equations. Slowing down is replaced by up-scattering in the adjoint system. The matrix M in the adjoint formulation of Eq. (2.347) is upper triangular in lethargy. The adjoint fluxes are computed in reverse order (from thermal lethargy to $u = 0$), so that the solution usually does not involve simultaneous group inversion.

G. Space and Energy Self–Shielding

Problems arise from the fact that cross sections are not slowly varying in either space or energy. Group diffusion theory cross sections are a function of the flux spectrum in a region. When several materials occur within a few neutron mean free paths, the spectra (and cross sections) are a function of the geometry as well as the atomic densities. Transport effects are sometimes of considerable importance, and means for incorporating transport effects in multigroup calculations are discussed in the following section. A variational procedure for estimating spectrum effects in heterogeneous systems is described in Chap. 3, Sect. 3.7.

If the absorption mean free path of a material is small compared with the thickness of that material, there is a geometric self-shielding or large surface absorption with internal flux depression. The effective cross section of such a material is less than the actual value because of this reduced

internal flux in the high cross-section energy region. Such self-shielding effects must be taken into account when homogenizing a region for computation. This is of particular concern in the treatment of resonance capture (Sect. 2.5) and control materials.

Various procedures for applying transport corrections within the diffusion theory framework are in use. These procedures are especially valuable for representing heterogeneities discretely instead of smearing several materials together into one homogeneous region. The blackness or thin region theory described in Chap. 3, Sect. 3.6 gives reasonable agreement with experiment.

H. Illustrative Example: P_1 Multigroup[101]

1. Basic Equations

Some of the concepts described here are more easily understood in terms of a specific multigroup program. A one-space dimension P_1 multigroup program which uses the Greuling-Goertzel approximation (Sect. 2.3.H) for the slowing down will now be considered as an illustrative case. The basic equations are:

$$\nabla \cdot \underline{j} + (\Sigma_a + \Sigma_{in})\,\phi + \sum_i \frac{\partial q_i}{\partial u} = S \qquad \text{Eq. (2.352a)}$$

$$\gamma_i \frac{\partial q_i}{\partial u} + q_i = (\xi \Sigma_s)_i \,\phi \qquad \text{Eq. (2.352b)}$$

$$\frac{1}{3} \nabla \phi + \Sigma_{tr} \underline{j} + \sum_i \frac{\partial \underline{p}_i}{\partial u} = 0 \qquad \text{Eq. (2.352c)}$$

$$\zeta_i \frac{\partial \underline{p}_i}{\partial u} + \underline{p}_i = (\eta \Sigma_s)_i \underline{j} \qquad \text{Eq. (2.352d)}$$

where

$\underline{j}$ and ϕ are the current and the scalar flux, respectively

i is an index denoting various isotopes

q_i is the isotropic slowing-down density due to the i^{th} isotope

$\underline{p}_i$ is the anisotropic slowing-down density due to the i^{th} isotope

S is the fission source, S_f, plus the inelastic scattering into lethargy group n

γ_i, ξ_i, ζ_i, and η_i are parameters whose value may be deduced from the slowing-down properties of each isotope
Σ_a, Σ_s, and Σ_{in} are the macroscopic absorption, scattering, and inelastic scattering cross sections, respectively.

Integration of Eq. (2.352a) over each nonthermal lethargy group [as in Eq. (2.339)] gives

$$\Delta u_n \left\{ \nabla \cdot \underline{j}_n + \left[(\Sigma_a^s + \Sigma_{in}) \phi \right]_n \right\} + \sum_i (q_{in} - q_{i,n-1}) = (S\Delta u)_n - (1 - p_{an}) \sum_i q_{i,n-1} \qquad \text{Eq. (2.353)}$$

where the absorption cross section has been split into a smooth absorption term, Σ_a^s, and a contribution due to resonances which appears as the last term on the right-hand side of Eq. (2.353). The group resonance escape probability, p_{an}, is discussed in Sect. 2.5.E.

Integration of Eq. (2.352c) gives the additional group n equation (characteristic of P_1 multigroup):

$$\Delta u_n \left[\frac{1}{3} \nabla \phi_n + (\Sigma_{tr} \underline{j})_n \right] + \sum_i (\underline{p}_{in} - \underline{p}_{i,n-1}) = 0. \qquad \text{Eq. (2.354)}$$

Equations (2.352b) and (2.352d), for the isotropic and anisotropic slowing down, are treated in an identical fashion, so that the derivation of the recursion formula corresponding to Eq. (2.343) for $\underline{p}_i$ will suffice. Multiply Eq. (2.352d) by

$$\frac{1}{\zeta_i} e^{u/\zeta_i}$$

and integrate to get

$$\underline{p}_{in} = e^{-u_n/\zeta_{in}} \int_{u_{n-1}}^{u_n} e^{u/\zeta_i} \left[\frac{(\eta \Sigma_s)_i}{\zeta_i} \right] \underline{j} \, du + e^{-\Delta_n \left(\frac{u}{\zeta_i} \right)} \underline{p}_{i,n-1}$$

where

$$\Delta_n\left(\frac{u}{\zeta_i}\right)=\left(\frac{u_n}{\zeta_{in}}-\frac{u_{n-1}}{\zeta_{i,n-1}}\right).$$

The integral may be evaluated by assuming

$$\int e^{u/\zeta}\,\frac{\eta\Sigma_s}{\zeta}\,\underline{j}\,du=(\eta\Sigma_s)_n\,\underline{j}_n\int e^{u/\zeta}\left(\frac{du}{\zeta}\right)$$

so that

$$\underline{p}_{in}=\left[1-e^{-\Delta_n\left(\frac{u}{\zeta_i}\right)}\right](\eta\Sigma_s)_{in}\,\underline{j}_n+e^{-\Delta_n\left(\frac{u}{\zeta_i}\right)}\,\underline{p}_{i,n-1}.$$

Eq. (2.355)

The corresponding equation for q_{in} is

$$q_{in}=(\xi\Sigma_s)_{in}\left[1-e^{-\Delta_n(u/\gamma_i)}\right]\phi_n+e^{-\Delta_n(u/\gamma_i)}\,q_{i,n-1}.$$

Eq. (2.356)

If one replaces e^{-x} by the approximation $\dfrac{1-\frac{x}{2}}{1+\frac{x}{2}}$, then Eqs. (2.355) and (2.356) reduce to the following:

$$q_{in}=\frac{(\xi\Sigma_s)_{in}}{\frac{1}{2}+\frac{\gamma_{in}}{\Delta u_n}}\,\phi_n-\left(\frac{\frac{1}{2}-\frac{\gamma_{in}}{\Delta u_n}}{\frac{1}{2}+\frac{\gamma_{in}}{\Delta u_n}}\right)q_{i,n-1}$$

Eq. (2.357)

$$\underline{p}_{in} = \frac{(\eta\Sigma_s)_{in}}{\frac{1}{2} + \frac{\zeta_{in}}{\Delta u_n}} \underline{j}_n - \left(\frac{\frac{1}{2} - \frac{\zeta_{in}}{\zeta u_n}}{\frac{1}{2} + \frac{\zeta_{in}}{\Delta u_n}} \right) \underline{p}_{i,\,n-1} \cdot \qquad \text{Eq. (2.358)}$$

These latter equations can also be derived from central difference approximations in Eqs. (2.352b) and (2.352d), and Eqs. (2.357) and (2.358) will be used for simplicity in the ensuing discussion. [Equations (2.355) and (2.356) are more precise over a wider range of parameters.]

Substituting Eqs. (2.357) and (2.358) into (2.353) and (2.354), one obtains

$$\nabla \cdot \underline{j}_n + \left[(\Sigma_{in} + \Sigma_a^s)_n + \sum_i \frac{(\xi\Sigma_s)_{in}}{\frac{\Delta u_n}{2} + \gamma_{in}} \right] \phi_n$$

$$= S_n + \sum_i q_{i,\,n-1} \left[\frac{1}{\frac{\Delta u_n}{2} + \gamma_{in}} - \frac{(1 - p_{an})}{\Delta u_n} \right] \qquad \text{Eq. (2.359)}$$

and

$$\frac{1}{3} \nabla \phi_n + \left[\Sigma_{tr,\,n} + \sum_i \frac{(\eta\Sigma_s)_{in}}{\frac{\Delta u_n}{2} + \zeta_{in}} \right] \underline{j}_n = \sum_i \underline{p}_{i,\,n-1} \Big/ \left[\frac{\Delta u_n}{2} + \zeta_{in} \right]. \qquad \text{Eq. (2.360)}$$

2. Transverse Buckling

To solve a problem with only one space variable, some assumption must be made with regard to the other two space variables. A flux distribution characteristic of the fundamental mode of a homogeneous reactor of similar dimensions is assumed along each of the two directions for which space variation is not computed. Cartesian coordinates will be considered here for simplicity, and it will be assumed that the z variation is to be computed. Then:

$$\left.\begin{aligned} \phi(x, y, z) &= \cos B_x x \cos B_y y \, \phi(z) \\ \underline{j}_z(x, y, z) &= \cos B_x x \cos B_y y \, j_z(z) \vec{Z} \\ \underline{j}_x(x, y, z) &= \sin B_x x \cos B_y y \, j_x(z) \vec{X} \\ \underline{j}_y(x, y, z) &= \cos B_x x \sin B_y y \, j_y(z) \vec{Y} \end{aligned}\right\} \qquad \text{Eq. (2.361)}$$

where $\vec{X}$, $\vec{Y}$, and $\vec{Z}$ are the unit vectors. Similar expressions are used for q and $\underline{p}$. To simplify notation, define the following quantities:

$$\sigma_n \equiv \frac{S_n(x,y,z) + \sum_i q_{i,n-1}(x,y,z)\left[\dfrac{1}{\dfrac{\Delta u_n}{2} + \gamma_{in}} - \dfrac{(1-p_{an})}{\Delta u_n}\right]_{x,y,z}}{\cos B_x x \cos B_y y}$$

$$\alpha_n \equiv (\Sigma_{in} + \Sigma_a^s)_n + \sum_i \frac{(\xi\Sigma_s)_{in}}{\dfrac{\Delta u_n}{2} + \gamma_{in}}$$

Eq. (2.362)

$$\beta_n \equiv 3\left[\Sigma_{tr,n} + \sum_i \frac{(\xi\Sigma_s)_{in}}{\dfrac{\Delta u_n}{2} + \zeta_{in}}\right]$$

$$t_{\rho n} = \frac{3\sum_i (P_\rho)_{i,n-1}}{\left[\dfrac{\Delta u_n}{2} + \zeta_{in}\right]}, \quad \rho = x, y, \text{ or } z.$$

Substituting Eqs. (2.361) and (2.362) into (2.359):

$$\frac{\partial J_z(z)_n}{\partial z} + B_x(J_x)_n + B_y(J_y)_n + [\alpha\phi(z)]_n = \sigma_n. \qquad \text{Eq. (2.363)}$$

The three components of Eq. (2.360) give with (2.361) and (2.362):

$$\frac{\partial\phi(z)_n}{\partial z} + [\beta J_z(z)]_n = t_{zn} \qquad \text{Eq. (2.364)}$$

$$-B_x\phi_n(z) + [\beta J_x(z)]_n = t_{xn} \qquad \text{Eq. (2.365)}$$

and

$$-B_y\phi_n(z) + [\beta J_y(z)]_n = t_{yn}. \qquad \text{Eq. (2.366)}$$

Solving Eqs. (2.365) and (2.366) for $J_x(z)$ and $J_y(z)$ and substituting into Eq. (2.363), one obtains with $(B_x^2 + B_y^2) = B^2$:

$$\frac{\partial [J_z(z)]_n}{\partial z} + \left(\alpha_n + \frac{B^2}{\beta_n}\right) [\phi(z)]_n = \sigma_n - \frac{B_x}{\beta_n} t_{xn} - \frac{B_y}{\beta_n} t_{yn}$$

Eq. (2.367)

which may be written in the form

$$\frac{\partial J_z(z)_n}{\partial z} + \Big(a(z)\,\phi(z)\Big)_n = S_n(z) \qquad \text{Eq. (2.368)}$$

where $a_n(z)$ and $S_n(z)$ are defined by Eq. (2.367).

3. Spatial Difference Equations

Let the subscript m denote the m^{th} mesh point, assume a uniform spacing of h cm, and integrate Eq. (2.368) from the midpoint of the mesh interval preceding point m to the midpoint of the integral following it. To first order in h:

$$\Big(J_{z,\,m+1/2} - J_{z,\,m-1/2}\Big) + \frac{h}{2}\Big(a_{m+} + a_{m-}\Big)\phi_m = \frac{h}{2}\Big(S_{m+} + S_{m-}\Big).$$

Eq. (2.369)

(The group subscript has been suppressed here.)

The $m+$ and $m-$ subscripts indicate parametric values to the right and left of point m, respectively. From Eq. (2.364) one obtains in the same manner:

$$\Big(\phi_{m+1} - \phi_m\Big) + h\beta_{m+} J_{z,\,m+1/2} = h t_{m+1/2} \qquad \text{Eq. (2.370a)}$$

and

$$\Big(\phi_m - \phi_{m-1}\Big) + h\beta_{m-} J_{z,\,m-1/2} = h t_{m-1/2}.$$

Eq. (2.370b)

Solving Eqs. (2.370a) and (2.370b) for the J_z's and substituting into Eq. (2.369), one obtains the basic three-point difference equation to be solved simultaneously in each group:

$$+\frac{1}{\beta_{m+}h}\left(\phi_m-\phi_{m+1}\right)+\frac{1}{\beta_{m-}h}\left(\phi_m-\phi_{m-1}\right)$$

$$+\frac{h}{2}\left(a_{m+}+a_{m-}\right)\phi_m=\frac{h}{2}\left(S_{m+}S_{m-}\right)-\left[\frac{t_{m+1/2}}{\beta_{m+}}-\frac{t_{m-1/2}}{\beta_{m-}}\right].$$

Eq. (2.371)

4. Boundary Conditions (Cartesian Coordinates)

Boundary conditions may be of the form

$$J_{\substack{n\\ \text{left}\\ \text{boundary}}}=-C_n\phi_{\substack{n\\ \text{left}\\ \text{boundary}}};\qquad J_{\substack{n\\ \text{right}\\ \text{boundary}}}=-C_n\phi_{\substack{n\\ \text{right}\\ \text{boundary}}}.$$ Eq. (2.372)

By integrating Eq. (2.368) from the boundary to the midpoint of the first interval, one obtains for the left boundary

$$J_{z_{m=0}}=J_{z_{m=1/2}}+\frac{h}{2}a_{o+}\phi_o-\frac{h}{2}S_{o+}=-C_L\phi_o.$$

Eq. (2.373)

Solving for $J_{z_{1/2}}$ and substituting the result into Eq. (2.370a) with $m = 0$, one obtains a two-point difference equation at the left boundary. The right boundary is handled in the same fashion.

The alternative boundary condition of $\phi_{\text{left boundary}}$ or $\phi_{\text{right boundary}}$ equal to zero may be treated by Eq. (2.371) with the zero value used in the equation at point $m = 1$ or the next to last point.

5. Method of Solution

In order to facilitate discussion of the procedure used to solve the equations, one may write explicitly the term S_n appearing in Eq. (2.368):

$$S_n = S_{f,n} + S_{in,n} + \sum_i q_{i,n-1}\left[\frac{1}{\frac{\Delta u_n}{2} + \gamma_{in}} - \frac{1-p_{an}}{\Delta u_n}\right] \qquad \text{Eq. (2.374)}$$

where

$$S_{f,n} = \frac{\chi_n}{\lambda}\sum_{n'}\left\{\left[\left(\nu\Sigma_f^s\right)\phi\Delta u\right]_{n'} + \sum_i \nu_{in'}\left(1-p_{f,n'}\right)q_{i,n'-1}\right\} = \chi_n f \qquad \text{Eq. (2.375)}$$

and

$$S_{in,n} = \sum_{n' \neq g} K_{n'n}(\Sigma_{in}\phi\Delta u_{n'}). \qquad \text{Eq. (2.376)}$$

In these equations

$\chi_n \Delta u_n$ is the fraction of the fission spectrum feeding into group n;

$p_{f,n'}$ is the fission resonance escape probability in group n;

$\Sigma_{in,n'}$ is the macroscopic inelastic scattering cross section in group n';

$K_{n'n}\Delta u_{n'}$ is the probability that a neutron inelastically scattered in group n' will be scattered into group n.

The approach described in Sect. 2.6.D is used. For the first lethargy group $S_n = S_{f,n}$ since the only contribution to the source term is due to fissions. Thus, with $t_{n=1} = 0$ the first group difference equations [Eq. (2.371)] are solved by a standard technique for inverting three-term linear systems.

The values for the J_z are determined at the midpoints of the intervals by means of Eqs. (2.370a) and (2.370b). Equations (2.365) and (2.366) are then used to evaluate transverse currents

at mesh points. Equations (2.357) and (2.358) are used to calculate the values of q and $\underline{p}$ in the first group.

It is then possible to compute S_2 at mesh points and t_2 at mesh interval midpoints. The second group fluxes are found next from Eq. (2.371), and so on through all the groups. An improved fission source is computed from the fluxes and q's, and the fission source iteration described in Chap. 7, Sect. 7.2 is used to generate successive iterates until some error criterion is satisfied.

6. Thermal Group

The thermal group is treated in a slightly different manner because of its inherently different characteristics. The basic equations are

$$\nabla \cdot J_T + (\Sigma_a \phi)_T = \sum_i q_{i,\,T-1} \qquad \text{Eq. (2.377)}$$

and

$$\frac{1}{3} \nabla \phi_T + (\Sigma_{tr} J)_T = \sum_i p_{i,\,T-1}. \qquad \text{Eq. (2.378)}$$

The parameters in Eq. (2.371) are redefined as follows:

$$a_T = \Sigma_{a,\,T} + D_T B^2 \text{ where } D_T = \frac{1}{3\,\Sigma_{tr,\,T}} \qquad \text{Eq. (2.379)}$$

$$S_T = \sum_i q_{i,\,T-1} - \frac{B_x}{\Sigma_{tr,\,T}} \sum_i p_{xi,\,T-1} - \frac{B_y}{\Sigma_{tr,\,T}} \sum_i p_{yi,\,T-1},$$

Eq. (2.380)

and

$$t_{\rho T} = 3 \sum_i (P_\rho)_{i,\,T-1}. \qquad \text{Eq. (2.381)}$$

Because of the difficulties associated with a one-velocity model of the thermal group, there are several procedures in use for determining $\Sigma_{a,\,T}$ and D_T. These thermal group con-

stants may be precomputed by whatever procedure is considered appropriate and inserted as input to the program. An extended discussion of this problem is given in Chap. 3.

2.7 MULTIGROUP TRANSPORT THEORY

R. C. Gast

A. Introduction

Multigroup transport theory refers to the means of obtaining solutions and properties of the transport equation which has been differenced, using many groups in its lethargy dependence. Due to the limited number of analytic solutions that may be obtained without also differencing the spatial and angular variables, multigroup transport theory refers, in practice, to the transport equation differenced in all variables. The differencing in space and angle is taken sufficiently accurate so that ordinarily most of the solution error, when compared with the rigorous transport solution, is due to the lethargy differencing. This balance of differencing of the transport equation variables is justified for problems without severe lethargy variation in cross sections or source, but with relatively severe angular variation in the vector flux. For other problems, another balance may be desirable; for example, the very fine lethargy and spatial differencing but coarse angular differencing sometimes used in resonance escape calculations.

There has been a continuing effort to obtain accurate solutions of the steady-state transport equation in the slowing-down region, in order to make experimental comparisons and to check the accuracy of more approximate and much more rapid design methods. One effort in this direction has been the RDR-5 and PREP codes.

B. Description and Discussion of the Method

Some of the details of theory and practice of a multigroup transport calculational procedure through computer codes will be given. RDR-5 is a code developed by C. W. Dawson,[102] E. H. Bareiss,[103] and D. Schiff[104] which will obtain for slab geometry the spatial dependence of a 10-ordinate vector flux of each lethargy point when all the required transfer coefficients are given. PREP is a code which will accept up to 20 Legendre components of the elastic differential cross section in either the laboratory or center-of-mass system and compute the required transfer coefficients; it supplies the input data for RDR-5.

The transport equation in slab geometry may be written in the following form:

$$\mu \frac{\partial \psi}{\partial x} + \Sigma^T(u, x)\,\psi(u, \mu, x) = \sum_i N_i(x) \int_{u-q_i}^{u} du' \int_{-1}^{1} d\mu'\,\psi(u', \mu' x)$$

$$\cdot \sum_{L=0}^{\infty} \frac{2L+1}{2} B_L^i(u', U)\, P_L(\mu)\, P_L(\mu');\ U = u - u' \qquad \text{Eq. (2.382)}$$

where $N_i(x)$ is the number density of the i^{th} isotope, q_i is the maximum lethargy gain for the i^{th} isotope, and $B_L^i(u', U)$ is the L^{th} Legendre component of the scattering kernel. The scattering kernel has been expanded in spherical harmonics, the addition theorem used, and the integration over the azimuthal angle carried out.

This equation, with lethargy, angle, and space dependence, can be reduced to a system of linear first-order differential equations in the space variable by differencing the lethargy and angle dependence. The results may be written as

$$\mu_\ell \frac{\partial \psi_{\ell n}}{\partial x} + \Sigma_n^T(x)\,\psi_{\ell n}(x) = \sum_i N_i(x) \sum_{n'=1}^{n} \sum_{\ell'=1}^{10} R_{\ell'} \psi_{\ell' n'}$$

$$\cdot \sum_{L=0}^{9} \frac{2L+1}{2} B_L^i(n', n)\, P_L(\mu_\ell)\, P_L(\mu_{\ell'})$$

Eq. (2.383)

where $R_{\ell'}$ is the weight used in the angular integration (ℓ refers to the angular ordinates and n to the lethargy point). The manner in which the transfer coefficients, $B_L^i(n', n)$, are specified will depend upon the assumptions used in making the lethargy integration. This will be discussed at length later as will be the assumptions used in the angular integration.

If one ignores the spatial differencing, Eq. (2.383) is used in RDR-5. RDR-5 solves these equations by computing the slowing-in source for a given lethargy point, then by doing spatial iterations until convergence. The forward ordinates are used when moving to the right and the backward ordinates when moving to the left, thereby achieving greater uncoupling of the

equations. No attempt is made to accelerate the convergence rate. C. W. Dawson has pointed out that problems with relatively narrow groups (Δu at approximately 0.25) require very few iterations per group (usually 3 to 8), so that there is less to be gained by improving convergence than for the few-group case.

The capacity of RDR-5 is sufficient to do 10 ordinate problems with 99 lethargy points, a maximum of 99 regions, 6 compositions, and approximately 300 spatial mesh points. The source may be input as a 10-ordinate vector source at the left boundary, center, and right boundary of each region, a three-point interpolation formula being used. Output includes scalar flux, slowing-in source, and vector flux given as values of the 10 ordinates.

C. Angular Differencing

Two forms of angular differencing will be discussed here. The first is obtained by a choice of angular abscissas, μ_ℓ, and weights, R_ℓ, yielding equivalence with a P_n spherical harmonics approximation, n being any odd value up to and including 9. The second results from a choice of abscissas and weights leading to equivalence with a double P_n spherical harmonics approximation, where n can be any value up to and including 4. It should be noted that many other forms of angular differencing can be specified by a choice of abscissas and weights in a discrete ordinate formulation and that this flexibility constitutes one of the principal advantages of the method.

1. Single P_ℓ Approximation

The angular differencing which will give equivalence with a P_ℓ spherical harmonics approximation has been discussed in the PREP report[105] and given in more detail in Ref. 106. In addition to the references cited in Ref. 106, which cover previous work on this form of differencing, there is an earlier derivation of the method given by R. D. Richtmyer[107] and a subsequent derivation given by G. Goertzel.[108] Only the final result is stated here; that equivalence with a $P_{\ell-1}$ approximation can be obtained using ℓ ordinates with a Legendre-Gauss quadrature if the scattering kernel and source have been expanded in spherical harmonics and truncated after the ℓ^{th} term (in Eq. (2.383) this truncation is equivalent to a P_9 approximation).

The μ_ℓ and R_ℓ in Eq. (2.383) are the Legendre-Gauss ordinates and weights, respectively, for a 10-ordinate quadrature. The Legendre-Gauss quadrature method using ℓ discrete

ordinates, and the spherical harmonics method keeping terms of order $\ell-1$ and less, are defined to be equivalent if their fluxes are identical in the directions of the discrete ordinates used in the Gauss quadrature for all space points and all values of energy. Thus, knowing the solution by one method, one may immediately write it for the other, since the form of a polynomial of degree $m-1$, as furnished by the spherical harmonics method, is uniquely determined by its values at m points.

Two characteristics of the method should be noted. The first is that no approximations are made concerning the scattering kernel or source; the only limitation is with regard to the sufficiency of the P_ℓ approximation to the flux. The second characteristic to be noted is the fact that negative vector fluxes can occur in both the P_ℓ and double P_ℓ discrete ordinate formulation. This behavior is analogous to the Gibbs' phenomenon (Ref. 15, p. 745) in the spherical harmonics approximation.

Comparisons of the scalar fluxes computed by a P_1, P_3, and an RDR-5 P_9 solution appear on Figs. 2.19 and 2.20. The fluxes for 1.20 Mev neutrons due to a plane fission source in a large medium of hydrogen are shown. Figure 2.19 is a semilog plot over a range of 90 cm. Figure 2.20 is a linear plot over a range of 20 cm; it emphasizes the differences close to the source. The P_1 solution was obtained by the P1MG code.[101] The P_3 solution was obtained by a reinterpretation of the SLOP-1 code.[109] Another comparison between an RDR-5 P_9 solution and a P_3 solution for the spatial shape of the scalar flux in an infinite medium, obtained from a moments method code and a moments inversion code,* gave similar qualitative results.

Comparisons between RDR-5 P_9 slowing-down solutions and P_∞ solutions with rigorous lethargy treatment are discussed in Sect. 2.7.D.

2. *Double P_ℓ Approximation*

A second form of differencing, providing equivalence with a double P_ℓ approximation, has been presented in Ref. 106. However, it seems appropriate to give more details concerning the form this approximation takes in the RDR-5 Eq. (2.383).

In the double spherical harmonics method, as first proposed by Yvon,[110] one expands $\psi(u, \mu, x)$ in terms of $P_\ell(2\mu-1)$ for $\mu > 0$ and in terms of $P_\ell(2\mu+1)$ for $\mu < 0$. The usefulness of this procedure arises from the fact that a discontinuous ψ, such

*These codes were developed by B. O'Reilly at Bettis Atomic Power Laboratory.

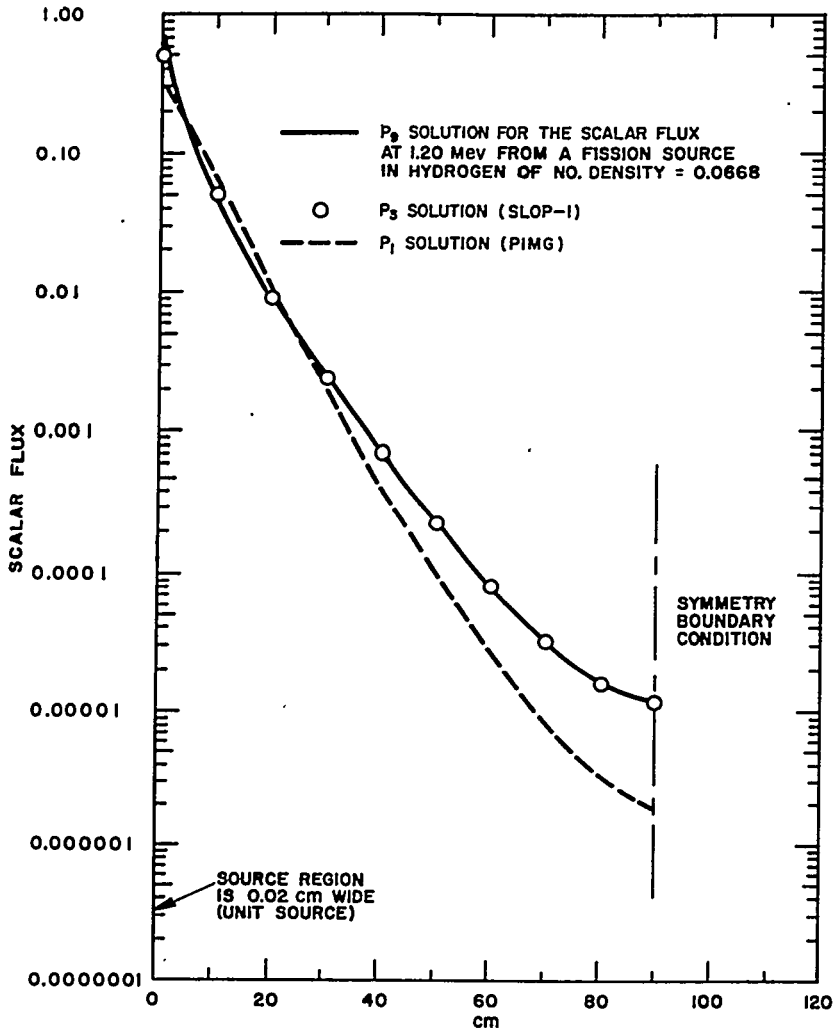

FIGURE 2.19. Comparison of RDR-5 with SLOP-1 and P1MG.

as would arise at a plane interface, can be better approximated by such expansions. The concept of equivalence, between the double P_ℓ equations and the angular differencing is analogous to that in the single P_ℓ approximation.

The double P_ℓ approximation does not have a unique form. Intuitive arguments given by Mertens,[111] and independently by Gelbard (Ref. 106, p. 14), suggest that in a double P_{N-1} approximation (which makes use of orthogonality over the half range of μ) the scattering kernel should be expanded in ordinary spherical harmonics and truncated after the $2N-1$ term. From the results given in Ref. 106, this double P_{N-1} approximation

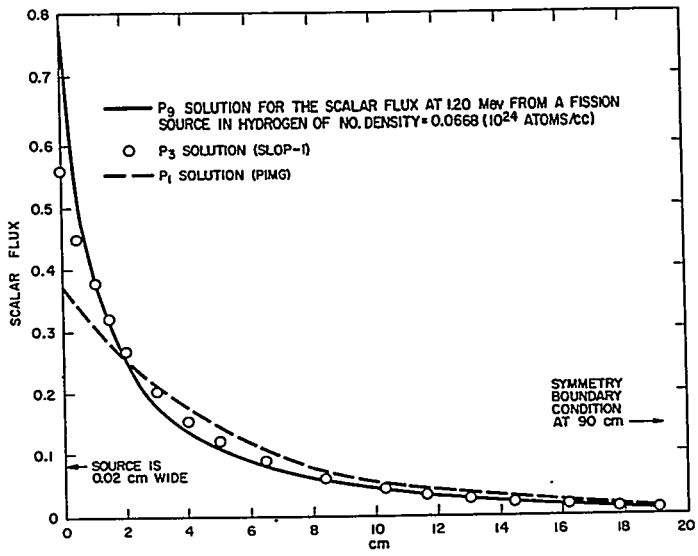

FIGURE 2.20. Comparison of RDR-5 with SLOP-1 and P1MG.

can be put in the form of Eq. (2.383) by writing the scattering kernel as

$$\Sigma(\mu, \mu', u, u') = \sum_{L=0}^{2N-1} \frac{2L+1}{2} B_L(u', U) I_L(\mu) I_L(\mu') \qquad \text{Eq. (2.384)}$$

where the $B_L(u', U)$ are still the Legendre components of the scattering kernel, but the Legendre polynomials have been replaced by the $I_L(\mu)$ functions to be defined below. (The source is represented in terms of these $I_L(\mu)$ functions in a similar manner.) Use of this kernel results in the following discrete ordinate form of the transport equation:

$$\bar{\mu}_\ell \frac{\partial \psi_{\ell n}}{\partial x} + \Sigma_n^T(x)\, \psi_{\ell_n}(x) = \sum_i N_i(x) \sum_{n'=1}^{n} \sum_{\ell'=1}^{2N} \bar{R}_{\ell', \psi_{\ell' n'}}$$

Eq. (2.385)

$$\sum_{L=0}^{2N-1} \frac{2L+1}{2} B_L^i(n', n) I_L(\bar{\mu}_\ell) I_L(\bar{\mu}_{\ell'})$$

where $\bar{\mu}_\ell$ for a double P_{N-1} approximation is related to the μ_ℓ for an ordinary Legendre-Gauss quadrature by

$$\mu_\ell = 2\bar{\mu}_\ell - 1, \quad 0 < \bar{\mu}_\ell < 1$$

$$= 2\bar{\mu}_\ell + 1, \quad -1 < \bar{\mu}_\ell < 0$$

and where the weights are related by $\bar{R}_\ell = \frac{R_\ell}{2}$.

The functions $I_L(\mu)$ are defined as

$$I_L(\mu) = P_L(\mu) \text{ for } L \leq N-1$$

$$I_L(\mu) = \sum_{q=0}^{N-1} P_q(2\mu - 1)\, a_q^L$$

for $0<\mu<1$, and $N \leq L \leq 2N-1$.

The values of $I_L(\mu)$ for negative values of μ may be obtained from $I_L(-\mu) = (-1)^L I_L(\mu)$. The constants, a_q^L, are defined as

$$a_q^L = (2q+1) \int_0^1 P_L(\mu)\, P_q(2\mu - 1)\, d\mu .$$

A recursion relationship for these constants is given by

$$a_q^{L+1} = \frac{2L+1}{2(L+1)} \left[\frac{q+1}{2q+3}\, a_{q+1}^L + \frac{q}{2q-1}\, a_{q-1}^L + a_q^L \right] - \frac{L}{L+1}\, a_q^{L-1}.$$

Starting values for this formula are obtained from

$$a_0^L = (-1)^{\frac{L-1}{2}} \frac{L!}{2^{L-1}(L)(L+1)\left[\left(\frac{L-1}{2}\right)!\right]^2} \qquad L \text{ odd}$$

$$a_0^L = 0 \qquad L \text{ even}$$

and $a_q^L = 0$ for $q > L$.

It is apparent from the definition of $I_L(\mu)$, that if, in a double P_{N-1} approximation, a kernel and source are used which are truncated after the $N-1$ term of their spherical harmonics expansion (so that $I_L(\mu) = P_L(\mu), L \leq N-1$), Eqs. (2.383) and (2.385) are identical except for weights and ordinates, and only trivial changes are required to make RDR-5 compute in a double P_n approximation. In the more general case, although the form of the transfer coefficients, $B_L^i(n', n)$, are the same in both approximations, a more significant change is required to recast a P_9 equivalent computer program into its double P_4 equivalent.

D. Lethargy Differencing

There are a number of possible approximations that can be used to obtain the transfer coefficients, $B_L^i(n, n')$, needed in the RDR-5 program. Since some of these have features superficially superior to the scheme adopted, it seems appropriate to review them before presenting a detailed discussion of the advantages and limitations of the approximations actually used by PREP.[105] Reference should be made to Sect. 2.3 for a general discussion of slowing down in a uniform medium.

1. Some Possible Lethargy Assumptions

The root of the difficulty in determining the transfer coefficients is associated with erratic dependence of the $B_L^i(u', U)$ on U. For each isotope, i, these quantities are defined by[63,105]

$$B_L^i(u', U)\,dU = -2\pi\sigma^i\left(u', \mu_s(U)\right) P_L\left(\mu_0(U)\right) d\mu_s(U) \qquad \text{Eq. (2.386)}$$

where

μ_0 is the scattering angle in the laboratory system

μ_s is the scattering angle in the laboratory or center-of-mass system

$\sigma^i(u', \mu_s)$ is the differential scattering cross section of isotope i, for the incident lethargy u' in whichever system μ_s is measured (see work of Zweifel and Hurwitz, Ref. 63); $U = u - u'$.

Thus, $B_L^i(u', U)$ as a function of U over the range 0 to q_i (the maximum lethargy gain for a collision with nucleus i) is the

product of the slowly varying function, $-2\pi\sigma^i(u', \mu_s(U)) \frac{d\mu_s(U)}{dU}$, and the rapidly varying Legendre polynomial, $P_L(\mu_s(U))$. Thus, difficulties in determining elements of the transfer matrices, $B_L^i(n', n)$, are to be expected if the group widths used are not considerably smaller than q_i.

The most straightforward method for converting Eq.(2.382) into a multigroup lethargy form is to choose a group structure and integrate over a given lethargy group u_{n-1} to u_n, replacing the integrals $\int_{u-q_i}^{u}$ on the right-hand side by sums over all the groups below the lethargy u_n. If some simplifying assumption is made (such as that $\psi(u, \mu, x)$ is constant or linear in lethargy within each group), the essential difficulty of this approach concerns evaluation of coefficients of the type

$$\int_{u_{n-1}}^{u_n} du \int_{u_{k-1}}^{u_k} du' B_L^i(u', u - u).$$

The erratic behavior of the $B_L^i(u', U)$ as a function of the lethargy gain, U, requires a detailed double integration for each group and each isotope. Since performing a single integration (as is done in PREP) is in itself a very formidable numerical problem, the double integral approach is thought to be impractical.

The other extreme from the double numerical integral approach is to evaluate Eq. (2.382) only at discrete lethargy points, making the approximation that the integrand in Eq. (2.382) is linear in u' between the discrete lethargy points.[112] However, unless the lethargy group widths, $u_{n-1} - u_n$, are much smaller than all the q_i, the erratic behavior of the $B_L^i(u', U)$ as a function of U introduces serious inaccuracies in this approach. For example, if the group widths are of the order of q_i, then the oscillation in $B_L^i(u', U)$ as a function of U makes it quite unlikely that a point value of the integrand will provide an accurate measure of the desired average value. There is also difficulty with an isotropic flux problem where only the isotropic component of the kernel is used. For example, in a heavy isotope slowing-down problem in which the mesh width is greater than q_i, it is found in numerical calculations that this form of differencing is not stable, and one does not obtain the correct asymptotic flux below the source lethargy range.

Another approach to the numerical solution of Eq. (2.382) involves expanding the differential cross section in the center-of-mass system times the flux in a Taylor series in u' about u. The age and Greuling-Goertzel approximations are the two most common examples of this approach (see Sect. 2.3). Its

great advantage arises from the fact that very simple equations are obtained for the slowing-down density, and differencing in lethargy is readily made by assuming this quantity to be linear across a group. However, results obtained using this method do not converge to the correct answer as the group width approaches zero. Thus, in practice, the rapid Placzek oscillations in the slowing-in source, which occur in the first few q_i lethargy intervals above (i.e., below, in energy) a source, are not predicted by this approach. Since the ability to describe this region accurately is desired, another method of dealing with the slowing-in source must be sought.

With the double integral approach impractical, and the discrete approach inadequate, a class of compromise methods arises; these involve use of a discrete value for one parameter in $B_L^i(u', U)$ and integration over the other variable. The physical significance of the $B_L^i(u', U)$ suggests that such an approach may be quite accurate, since the definition [Eq. (2.386)] shows that dependence on u' is through the differential scattering cross section and should, thus, be relatively smooth, while dependence on U is through a rapidly varying Legendre polynomial. Accordingly, assumption of a constant or linear behavior of $B_L^i(u', U)$ in u' over a group and integration over U suggest themselves as a fruitful approach.

Along with an assumed behavior of $B_L^i(u', U)$, some assumption regarding the flux behavior across a group must be made if a practical approximate solution to Eq. (2.382) is to be obtained. It is important, in this connection, to permit the flux to behave in a manner consistent with the assumed u' behavior of the $B_L^i(u', U)$. Thus, if the differential cross section (and hence u' behavior of $B_L^i(u', U)$ is assumed constant within a group, Eq. (2.382) shows the flux will in general be discontinuous across a group boundary. (Assumption of a discontinuous, groupwise constant source will produce the same results.) It would, therefore, be inconsistent to make this assumption and at the same time to approximate the flux as a series of connected segments, linear across each group. Such a procedure would prevent the flux from behaving as it, in physical fact, should if the actual physical cross sections were, as functions of u', a series of disconnected flat segments. Dealing with the collision density, $\Sigma^T(u, x)\,\psi(u, \mu, x)$, as a variable is not a satisfactory solution to this difficulty, since the transfer coefficients would then involve integration of quantities $B_L^i(u', U)/\Sigma^T(u', x)$ over u'; they would, thus, depend on the number densities of the isotopes rather than on the microscopic nuclear properties alone. Thus, a PREP-like problem would have to be run for each mixture of isotopes in each RDR-5 problem; compilation of permanent RDR-5 library would not be

possible. Moreover, even if the collision density were to be used as the independent variable, discontinuities would result in finite regions problems because of the leakage term, $\mu \frac{\partial \psi}{\partial x}$.

If the cross sections and source are input as connected linear segments, a rigorous solution of Eq. (2.382) will lead to a continuous flux. Thus, a flux shape approximated by a series of linearly connected segments appears called for; a shape approximated by a discontinuous series of flat segments cannot, except in the limit of zero width, provide a close correspondence to the rigorous solution. Unfortunately, it has been found in actual test cases that both the linearly connected and groupwise flat flux shape assumptions result in incorrect asymptotic flux values below the source range.

In summary, the situation with regard to the possible lethargy assumptions is:

1. A double integration to obtain the coefficients $B_L^i(u', u)$ is impractical.
2. A discrete approximation is inadequate.
3. Age or Greuling-Goertzel theory is adequate asymptotically (i.e., several q_i intervals from the source), but does not yield a rigorous solution in the limit of zero group width.
4. If the u' dependence of $B_L^i(u', U)$ is taken as constant across a group, a flux behavior which permits discontinuities at lethargy group interfaces must be assumed.
5. If the u' dependence of $B_L^i(u', U)$ is taken as linear across a group, assumption of either linear or flat flux behavior within a group leads to incorrect asymptotic flux values.

2. *The Lethargy Assumptions Used in PREP*

The preceding discussion suggests the desirability of a lethargy differencing which will give results at least as good as those obtained with the age or Greuling-Goertzel approximation for those isotopes with q_i less than the mesh width, and which will give results approaching an exact solution as the mesh width becomes less than q_i. A scheme having these properties may be obtained by assuming groupwise constant cross sections and sources, together with a flux behavior suggested by item (4) in the summary of possible lethargy assumptions. Specifically the PREP procedure now in use is to assume that cross sections and sources are groupwise constant and that the fluxes are linear across a group but have discontinuities at lethargy interfaces between groups with different cross sections or sources. The discontinuities in flux are achieved by introducing groups of zero lethargy width.

An alternative procedure has been proposed by Certaine[113] in connection with the moments equations. This proposal is to assume that, for each isotope, each Legendre component of the differential cross section multiplied by the flux is linear across the group and continuous at group interfaces. Since no specific assumption is made about the behavior of the individual components and the flux, there is ambiguity in interpreting the implied behavior of these quantities. The most useful interpretation pictures the cross sections as having their actual physical shape across the group, but to approximate this shape as linear across the group and continuous at interfaces. It is to be noted that assuming linearity and continuity for the cross-section flux products and the cross sections themselves implies that a different flux is associated with each component of the differential cross section for each isotope within the group (although at end points a single flux is consistent). Hence, a certain haziness of interpretation is inherent in the Certaine assumption. This arises from the fact that the cross-section flux products are in general not linear in lethargy across a group. Assuming that they are leads to a contradiction for all but groupwise constant cross sections.

It will appear in the discussion on the form of transfer coefficients that the PREP code is capable of producing transfer coefficients for either the zero group picture or Certaine's lethargy scheme. Which approximation is more suitable depends on the problem at hand. The zero group scheme is expected to give a more accurate mathematical approximation to the exact solution for the artificial problem it solves (i.e., one in which cross sections are groupwise constant). This expectation is based on the fact that for groupwise constant cross sections the flux shape within a group will generally, in physical fact, be close to linear but will have discontinuities at group interfaces. Thus, the assumed flux shape corresponds reasonably well with the correct flux shape. It follows that the zero group method may ordinarily be taken as a good mathematical standard against which to test more gross approximations. On the other hand, flat cross sections, discontinuous at group interfaces, are never found in nature. Unless the physical cross sections oscillate across a group (in which case a flat average value may be the best choice), it is probably better to represent them as connected linear segments. Certaine's method is here interpreted as having this behavior. However, for actual linearly continuous cross sections, the cross-section flux products may be rather curved across a group width. Assumption that they are linear may result in an approximate solution which differs significantly from the exact solution. Thus, Certaine's method may lead to a solution closer

to physical reality but farther from mathematical exactness. At present, numerical results have been obtained for only the zero group approximation. If the alternative method is sufficiently accurate, it is to be preferred, since the zero groups roughly double the computation time. Decision on this question must await further study.

3. Form of the Transfer Coefficients

The lethargy part of the slowing-in source in Eq. (2.382) computed at an exit lethargy point, u_n, may be written in the following form if the cross sections are assumed to be group-wise constant and the flux linear:

$$I = \int_{u-q_i}^{u} du'\, \psi(u', \mu', x)\, B_L^i(u', U)\Big|_{u=u_n}$$

$$= \sum_{n'=2}^{n} \int_{u_n-u_{n'}}^{u_n-u_{n'-1}} B_{Ln'}(U) \left[\psi_{n'-1} + \frac{\psi_{n'}-\psi_{n'-1}}{(u_{n'}-u_{n'-1})} (u_n - u_{n'-1} - U) \right] dU$$

Eq. (2.387)

where $I = 0$, if $u_n - u_{n'} < q$, and where $u_n - u_{n'-1}$ is set $= q$ if $u_n - u_{n'-1} \geq q$. In Eq. (2.387) $B_{Ln'}(U) \equiv B_L(u', U)\,|_{u'=u_{n'}}$ with the latter quantity defined by Eq. (2.386). The condition on limits arises from the fact that a q_i interval back from the exit lethargy, u_n, will not in general be at a mesh point. By rewriting the sums,

$$\sum_{n'=2}^{n} \left[f_{n'-1} \right] \psi_{n'-1}$$

involving $\psi_{n'-1}$ as

$$\sum_{n'=1}^{n} \left[f_{n'} \right] \psi_{n'}$$

one may transform the sum in Eq. (2.387) into one involving $\psi_{n'}$ alone. Comparison with Eq. (2.383) then yields the following expression for the transfer coefficients:

$$B_L^i(n';n) = (1+\delta_{n'}^n)\int_{u_n-u_{n'+1}}^{u_n-u_{n'}} \frac{B_{L,n'+1}(U)}{u_{n'+1}-u_{n'}}(u_{n'+1}-u_n+U)\,dU$$

$$+(1-\delta_{n'}^n)\int_{u_n-u_{n'}}^{u_n-u_{n'}-1} \frac{B_{L,n'}(U)}{u_{n'}-u_{n'-1}}(u_n-u_{n'-1}-U)\,dU \qquad \text{Eq. (2.388)}$$

where $\delta_{n'}^n$ is the Kronecker delta, and the same convention on limits applies as in Eq. (2.387).

Equation (2.388) is the form of the transfer coefficients derived in Ref. 105. If the assumption of linear flux and constant cross sections is replaced by that of linear cross-section flux products, the integrand in Eq. (2.387) becomes

$$\left[B_{Ln'-1}(U)\,\psi_{n'-1}+\frac{B_{Ln'}\psi_{n'}-B_{Ln'-1}\psi_{n'-1}}{u_{n'}-u_{n'-1}}(u_n-u_{n'-1}-U)\right].$$

It turns out that the corresponding transfer coefficient may be obtained by replacing $B_{L,n'+1}(U)$ by $B_{L,n'}(U)$ in Eq. (2.388). If this is done* one obtains the form of the transfer coefficients as given by Certaine. Thus, with zero groups permitted, one may input cross sections and source into PREP as groupwise constant, as linear and connected, or as a combination of these, i.e., linear but not connected.

From the form of $B_L^i(u',U)$, it is evident that the integrals in Eq. (2.388) could be performed analytically, as has been done by Certaine. However, in order to avoid programming and calculational difficulties, the PREP code performs the required integrations over lethargy numerically. A change of variable is made from U to $\mu_c(U)$, so that the range of integration is from -1 to 1 instead of 0 to q. The number of mesh points to be used over the interval -1 to 1 is an input number

*This change has been incorporated in PREP, but is not indicated in the first edition of Ref. 105.

(order of 200 usually used). An appropriate fraction of this number is then used by the code to calculate each transfer coefficient. All isotopes are treated alike, and as the lethargy mesh width goes to zero, a rigorous lethargy treatment is obtained. To permit the jump discontinuities in flux at group end points (induced by the discontinuous cross sections or source) requires the use of two lethargy points per group (i.e., the points at the top and bottom of the group). Thus, between each regular group, there appears a group of zero width. This allows the jump discontinuities to occur in a rigorous fashion. All lethargy points are put explicitly into PREP, and the calculations for the zero groups carried out as though they had a small finite width permitted to approach zero. Since the transfer coefficients defined by Eq. (2.388) involve only integrals from u_n to zero, $B_L^i(n', n-1) = B_L^i(n', n)$ if $n-1$ and n encompass a zero group ($u_{n-1} = u_n$). Accordingly, only one of these two identical sets is computed by PREP. Two complete sets of spatial iterations must be done for each group by RDR-5, the result being the two end-point values of the flux.

4. *Accuracy of the PREP Lethargy Treatment*

A brief discussion of the accuracy of the PREP lethargy treatment for the case of groupwise constant input will be followed by some numerical examples to illustrate specific features. With the PREP lethargy treatment, a spatially independent problem involving hydrogen and neglecting absorption is calculated rigorously. This is also the case with the differencing obtained by assuming a linear slowing-down density as in the MUFT[114] or P1MG[101] codes.

For the same problem with absorption, RDR-5-PREP gives second order accuracy in the lethargy increment Δu for the end point flux over a group of width Δu. RDR-5-PREP and MUFT both give first order accuracy in Δu for the mean flux across a group. It should be observed that with a lethargy treatment which assumes linear flux, it is desirable to have the end point flux as accurate as possible, since the slowing-down kernel will weigh the bottom of the group more heavily when computing the slowing-in source for the subsequent lethargy points.

For a spatially dependent problem involving hydrogen with small buckling, RDR-5 and MUFT both give first order accuracy in Δu for the mean flux. The end point flux in RDR-5 is also of first order accuracy. However, the magnitude of the error term is smaller in RDR-5 than in MUFT.

As already indicated if one considers a pure heavy isotope slowing-down problem in which the mesh width becomes greater

than the maximum lethargy gain per collision, the lethargy differencing in PREP is stable, and the solution given by RDR-5 goes over to an age-type solution. That is, while the calculation leads to considerable error in the neighborhood of a sharp source, it nevertheless gives the asymptotic flux quite accurately. This fact should not be too surprising when one recalls that in age theory the scattering collision density is assumed to be linear in lethargy over the interval q_i of possible incident lethargies, whereas in PREP it is assumed to be linear between mesh points, an assumption which will result in an exact solution of the Greuling-Goertzel equations for a spatially independent case with no absorption.

As the mesh width narrows, in the PREP differencing, for a problem with a sharp source (or sink), more and more details of the Placzek oscillations appear. This is reflected in an RDR-5-PREP solution of a spatially dependent, pure heavy isotope problem shown in Fig. 2.21. The scalar flux spectrum at 0 and 90 cm, where symmetry boundary conditions have been applied, are shown for a mass 16 isotope with isotropic scattering in center-of-mass system. An isotropic plane source of half width 0.01 cm was used. The source was uniformly distributed in lethargy over the first coarse group. The differences in solutions close to the source, induced by varying the lethargy mesh width, are due to smeared Placzek oscillations. After about 4 q intervals there is good agreement.

One might hope to decrease the number of groups needed by using a very thin group to define the region occupied by a sharp source or sink, while jumping to large groups immediately below in the region of violent Placzek oscillations. The hope would be to pass through this lethargy region and obtain the correct asymptotic flux. In general such a procedure is not possible, and this circumstance constitutes the greatest limitation of the differencing scheme used in PREP. To avoid difficulties one should use a lethargy mesh roughly the size of that used to represent the source or sink until at least 2 or 3 q intervals removed, since if the group structure is fairly uniform this difficulty cannot arise. Figure 2.22 shows what can happen if these restrictions are not adhered to. A severe limiting case involving a source group of zero width, followed by large groups (having width in q intervals as indicated on the curve), was examined. It is apparent that the errors are significant. Nevertheless, it is to be noted that the lethargy treatment is such that solutions do not diverge.

5. *Comparisons with Rigorous Solutions*

A calculation that is rigorous, within statistical error, is given by the DAEDALUS code (see Sect. 2.4) developed by H. J.

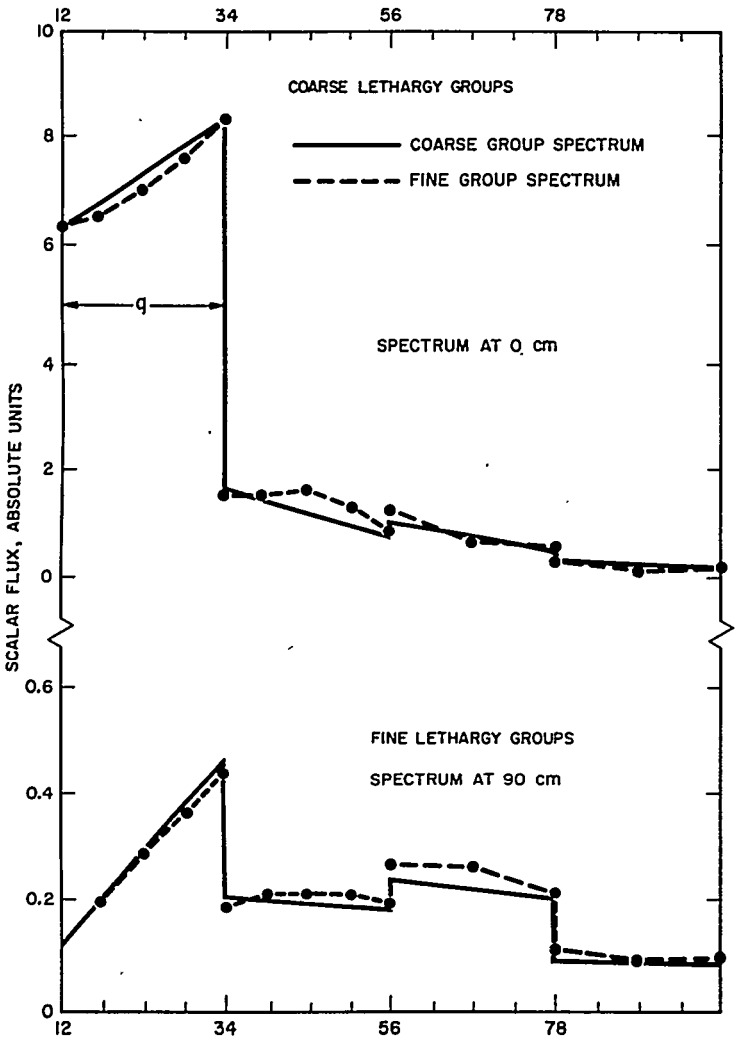

FIGURE 2.21. Comparison of Flux Spectra with a Coarse and Fine Lethargy Group Structure for a Plane Fission Source in Oxygen (No. Density = 0.0334).

Amster, et al.[72] A problem with a monoenergetic source in an infinite medium of hydrogen with constant cross sections was compared with RDR-5 over a range of 14 mean free paths. A similar calculation was done for a pure heavy isotope problem. In both cases the agreement was excellent, the only significant discrepancy being at the source, where a P_9 approximation evidently fails to give accurate flux peaks. Details of these comparisons are included in the DAEDALUS report.[72]

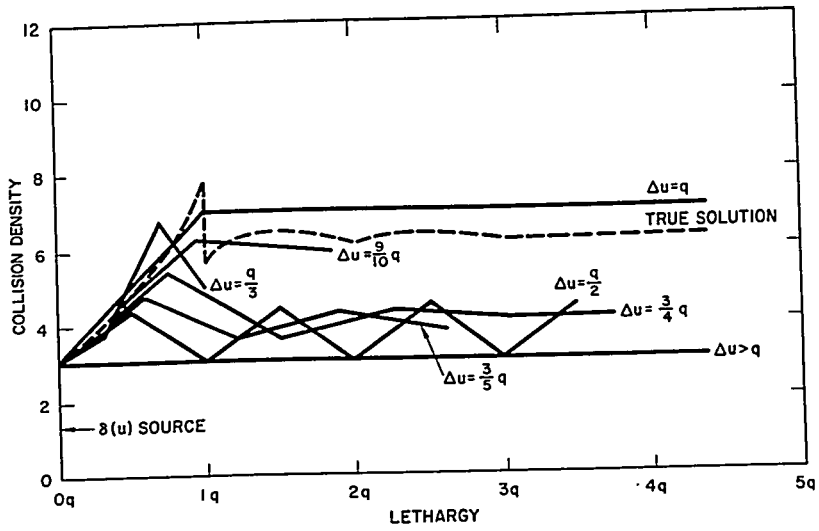

FIGURE 2.22. PREP Lethargy Treatment for an Infinite Medium of a Pure Heavy Isotope with a Monoenergetic Source at $u = 0$. (Lethargy mesh spacings are indicated on the curves.)

Another valid solution for a monoenergetic source in hydrogen with constant cross sections in an infinite medium is given above a lethargy of approximately $u = \ln \frac{E_0}{E} = 10$ (source taken as lethargy zero) by the work of G. C. Wick.[115]

This solution provides a comparison with RDR-5 over a greater range of distance than the DAEDALUS problem mentioned above. Results are given in Fig. 2.23. Also shown are some plots of the angular flux pattern at a few locations. The lengths of the rays in these patterns represent the relative number of neutrons moving in that direction (each pattern has an arbitrary normalization). The angular flux appears to be sufficiently well behaved that a P_9 approximation is almost certainly adequate. Moreover, a lethargy mesh sufficiently fine to give good results was used. Thus, one concludes that this problem is principally a test of the spatial differencing rather than the angular or lethargy ones, and the fact that the RDR-5 solution falls above Wick's solution at large distances must be ascribed to the spatial approximation. The mesh width used, expressed in mean free paths, is indicated at the bottom of the figure. It appears that, although a spatial differencing has been incorporated into RDR-5 which makes use of an exponential fit between mesh points,[102] one cannot use an extremely large spatial mesh. From the graph one can deduce that a spatial mesh not greater than 0.5 mean free paths should be used. In slab problems at locations where neutrons moving

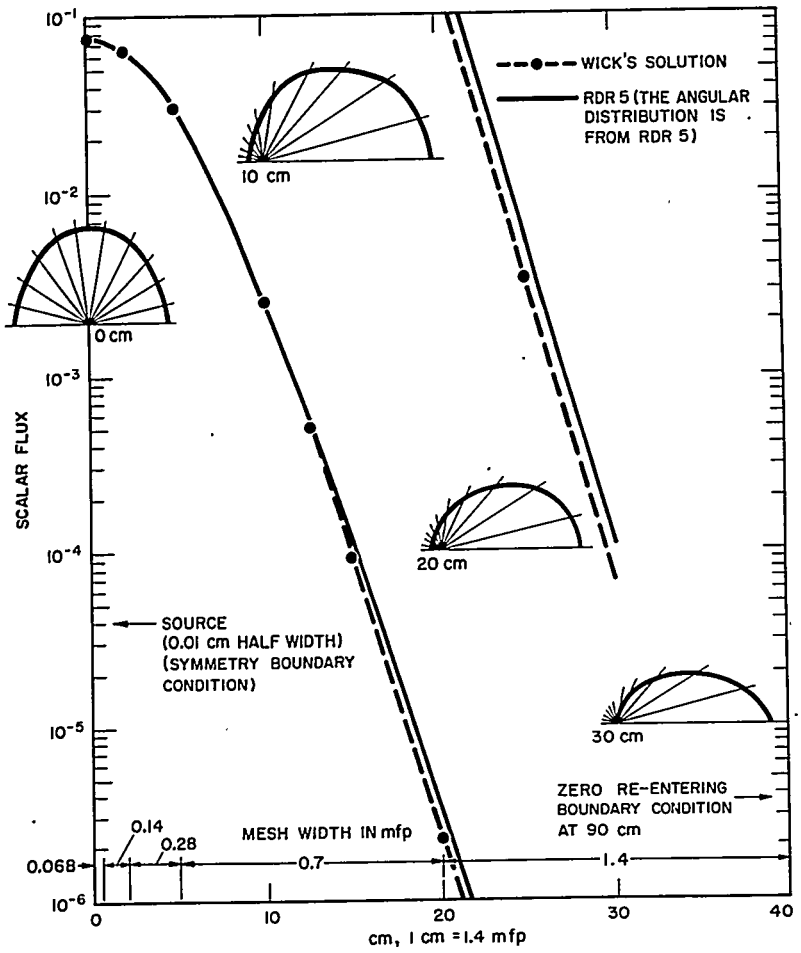

FIGURE 2.23. Plot of Scalar Flux and Vector Flux at 2 ev in Hydrogen (Constant Cross Section) Monoenergetic Source at 2 Mev.

parallel to an interface are of importance (for example, near a plane source), a much finer mesh should be used. In problems with variable cross sections, the relevant mean free paths are those which principally determine the spatial shape.

6. *Recursion Formulas for the Hydrogen Source*

In an RDR-5 slowing-down problem that covers a large lethargy range without inelastic scattering, the heavy isotope scattering matrix will be quite small compared to the scattering matrix for hydrogen. Since an appreciable part of the computing

time goes into calculating the slowing-in source due to hydrogen, it appears advantageous to treat this part of the slowing-in source by recursion formulas. The remaining matrix for the heavy isotopes will then consist principally of zeros, and multiplication by these zero elements could be eliminated. It should be noted, however, that if a relatively full inelastic scattering matrix is included in the slowing-down calculation, some of the advantage of the recursion treatment for hydrogen is lost.

The recursion formulas are obtained in the following way: If in Eq. (2.382) one expands the flux in Legendre polynomials, the hydrogen part of the slowing-in source may be written as

$$\eta_H(x, u_i, u_n) = N_H(x) \sum_{\ell=0}^{9} \frac{2\ell + 1}{2} P_\ell(\mu_i) \eta_\ell^n$$

where

$$\eta_\ell(u) = \int_0^u du' \psi_\ell(x, u') B_i^H(u', U)$$

where

$$B_\ell^H(u', U) = \sigma_s^H(u') e^{-U} P_\ell\left(e^{-\frac{U}{2}}\right)$$

$$= \sigma_s^H(u') \sum_{k=0}^{\ell} a_\ell^k e^{-\left(1 + \frac{k}{2}\right) U}$$

and where a_ℓ^k are constants.

One may write

$$\eta_\ell(u) = \sum_{k=0}^{\ell} a_\ell^k \eta_\ell^k(u)$$

where

$$\eta_\ell^k(u) = \int_0^u du' \psi_\ell(u') \sigma_s^H(u') e^{-\left(1 + \frac{k}{2}\right) U} .$$

If one now differentiates the expression for $\eta_\ell^h(u)$, one obtains

$$\frac{d\eta_\ell^h(u)}{du} = -\left(1 + \frac{k}{2}\right) \eta_\ell^h(u) + \Psi_\ell(u) \sigma_s^H(u) . \qquad \text{Eq. (2.389)}$$

This differential equation may be solved by inserting an assumed lethargy variation of $\psi_\ell(u)\sigma_s^H(u)$. As previously, one assumes for $u_{n-1} < u < u_n$

$$\psi_\ell(u)\,\sigma_s^H(u) = \psi_\ell^{n-1}\,\sigma_s^{Hn-1} + \frac{\psi_\ell^n\,\sigma_s^{Hn} - \psi_\ell^{n-1}\,\sigma_s^{Hn-1}}{u_n - u_{n-1}}\left(u - u_{n-1}\right).$$

Upon solving Eq. (2.389) and applying the boundary condition that $\eta_\ell^k(u_{n-1}) = \eta_\ell^{k,n-1}$, one obtains

$$\eta_\ell^{kn} = \eta_\ell^{k,n-1}\,A_n^k + \sigma_s^{Hn}\,\psi_\ell^n\,B_n^k + \sigma_s^{H,n-1}\,\psi_\ell^{n-1}\,C_n^k \qquad \text{Eq. (2.390)}$$

where

$$A_n^k = e^{-\left(1+\frac{k}{2}\right)\left(u_n - u_{n-1}\right)}$$

$$B_n^k = \left[\frac{\frac{k}{2}\left(u_n - u_{n-1}\right) - u_{n-1}}{\left(1+\frac{k}{2}\right)^2\left(u_n - u_{n-1}\right)}\right]\left[1 - e^{-\left(1+\frac{k}{2}\right)\left(u_n - u_{n-1}\right)}\right]$$

$$C_n^k = \left[\frac{u_n}{\left(1+\frac{k}{2}\right)^2\left(u_n - u_{n-1}\right)}\right]\left[1 - e^{-\left(1+\frac{k}{2}\right)\left(u_n - u_{n-1}\right)}\right]$$

The expression for η_ℓ^{kn} as given by Eq. (2.390) is in terms of the Legendre components of the flux. It may be written, however, in terms of the flux at the Gaussian ordinates by making use of

$$\bar{\psi}_k^n = \sum_{S=0}^{9} \frac{2S+1}{2} P_S(\mu_k)\psi_S^n \qquad \text{Eq. (2.391)}$$

(this is for the P_9 case[106]) where ψ_S^n is the Legendre component of the flux and $\bar{\psi}_k^n$ is the value of the flux at the k^{th} ordinate. Multiplying Eq. (2.391) by $P_\ell(\mu_k)$ and integrating rigorously with a Gaussian quadrature, one obtains

$$\psi_\ell^n = \sum_{S=1}^{10} R_S P_\ell(\mu_S)\,\bar{\psi}_S^n$$

where R_S are constants. Inserting this expression into Eq. (2.390), yields the form of hydrogen source recursion formulas.

Estimating computing time, using the recursion formulas rather than a scattering matrix, leads to the conclusion that the advantage of the former increases as the order of P approximation decreases or as the number of groups increases. Recursion formulas have not been incorporated in the present version of RDR-5.[102]

7. *Inelastic Matrix for RDR-5*

Since the inelastic scattering is symmetric about the incident direction, one may write the inelastic kernel for the i^{th} isotope (in the P_9 approximation for example) as

$$\sum_{k=0}^{9} \frac{2k+1}{4\pi} B_{ik}^{in}(u', u)\, P_k(\mu_0).$$

The inelastic part of the slowing-in source becomes

$$\sum_{i=1}^{I} \int_0^u du' \int_{-1}^{1} d\mu'\, N_i(x) \sum_{k=0}^{9} \frac{2k+1}{4\pi}\, B_{ik}^{in}(u', u)\, P_k(\mu)\, P_k(\mu')\, \psi(x, \mu', u').$$

The inelastic part of the lethargy integration for an exit lethargy, u_n, is given by

$$J_{in}^{ikn}(x, \mu') = \int_0^{u_n} \psi(x, \mu', u')\, B_{ik}^{in}(u', u_n)\, du'. \qquad \text{Eq. (2.392)}$$

If it is assumed that the $B_{ik}^{in}(u', u_n)$ are slowly varying functions of u' (as would be the case if, for example, the evaporation model is valid), it follows that $\psi(x, \mu', u')\, B_{ik}^{in}(u', u_n)$ may be reasonably represented by a sequence of straight lines. Upon making this assumption in Eq. (2.392), one obtains the form of $J_{in}^{ikn}(x, \mu')$ required by RDR-5:

$$J_{in}^{ikn}(x, \mu') \Big| \mu' = \mu_\ell = \sum_{n'=1}^{n} \psi_{n'\ell}\, B_{in}^{nn'ik}$$

where

$$B_{in}^{nn'\,ik} = B_{ik}^{in}(u_{n'}, u_n) \left[(1 - \delta_{n'}^{1}) \left(\frac{u'_n - u'_n - 1}{2} \right) + \left(1 - \delta_{n'}^{n}\right) \left(\frac{u_{n'+1} - u_{n'}}{2} \right) \right].$$

As in the case of the Legendre components of the differential cross section for elastic scattering, the $B_{ik}^{in}(u', u_n)$ should be considered as linear in u' between mesh points.

For normalization, it is required that

$$\int_{u'}^{\infty} B_{i0}^{in}(u_n', u)\, du = \sigma_n^{in}$$

where σ_n^{in} is the inelastic cross section (similar expressions are obtained for the higher P components).

E. Conclusions

As stated in the introduction, RDR-5 and PREP represent a means of solving the transport equation in the slowing-down lethargy range with a particular balance of differencing. In a slab reactor slowing-down problem, if one attempts to represent explicitly the structure of the reactor, which is composed of resonance absorbers, then one needs fine differencing in space, angle, and lethargy. The RDR-5 balance of differencing would be sufficient for the angular and spatial dependence of the vector flux but would be insufficient for the lethargy dependence in that more than 100 lethargy groups would be required. It is not practical to increase the number of lethargy groups in RDR-5 because of excessive machine running time. It is this limitation of RDR-5, when it was applied to a homogeneous medium, that provided the motivation for the homogeneous medium Monte Carlo standard, DAEDALUS (see Sect. 2.4). RDR-5 may be considered a standard only for those problems where 100 lethargy groups are sufficient.

2.8 FEW-GROUP APPROXIMATIONS

R. L. Hellens

A. Introduction

The design of water-moderated reactors is considerably facilitated by the particular scattering properties of hydrogen. Since a neutron may lose much of its initial energy in a hydrogen collision, the hydrogen in a reactor core will largely determine the fast neutron flux level and energy distribution.

Further, since the hydrogen cross section falls rapidly with increasing energy in the region of the fission spectrum, the cross section below this region being large and eventually quite constant, most leakage from a water-moderated core occurs before the neutrons are degraded to energies below 100 kev. Consequently, the often important capture and fission events which occur in the kilovolt energy range and below interact only weakly with the leakage process. Although qualitative remarks such as these are never precisely true, the common representation of the fast neutrons by a single or by a few energy groups is intuitively reasonable for hydrogen moderation, since the major fast effects tend to act in series. This discussion will describe a few-group scheme which approximates the competition between fission, capture, and leakage and which yields the same results as a multigroup calculation in the limit of a bare core.

It should be pointed out at the start that the only value of a few-group reactor description is the avoidance of the computational effort involved in a multigroup solution. The enormous amount of data to be processed in a multigroup, two-dimensional core lifetime study is almost beyond the capability of present-day computing equipment if much geometrical detail is required, and the time and expense to perform such calculations are not justified if simpler methods are adequate. For water-moderated cores, satisfactory results can often be obtained using only two, three, or four groups of neutrons.

The essential point of a few-group scheme is simple. The spatial distribution of all fast neutrons in a given medium is taken to be sinusoidal and the energy spectrum is calculated in the P_1 or B_1 approximation, to be discussed in the next section, or in the Selengut-Goertzel modification of either of these approximations. The equations are then integrated over broad energy bands and, from the known spectra for this sinusoidal spatial distribution, effective group constants constructed. These broad groups can be defined in a variety of ways, but the only useful forms are those with group constants which are not very sensitive to the wave number of the spatial mode chosen. The few-group eigenvalue problem is then solved using these constants for the fast groups.

In Sect. 2.8.B the equations for the energy spectrum are given, which are the basis for the MUFT code.[114] Several common forms of the few-group equations are discussed in Sects. 2.8.C and 2.8.D, and some indication of the dependence of the eigenvalue on reactor size and group number is given. In Sect. 2.8.E the numerical calculation of group constants is discussed, together with some estimates of the truncation error incurred by the usual numerical procedures.

B. Single Mode Model

The derivation of group equations as an approximation to the Boltzmann equation can be achieved by a spherical harmonics expansion of both the neutron distribution and the scattering functions (a P_n approximation). However, an alternate scheme employed by Selengut[116,117] for a treatment of bare homogeneous reactors will be followed here (a B_n approximation), since it provides an indication of the influence of the higher spherical harmonics on the neutron distribution when the scattering cross section is represented by a finite number of terms. A detailed treatment of the theory involved has been given by Hurwitz and Zweifel.[62]

The time-independent Boltzmann equation for a reactor without external source takes the following form when capture, fission, and a general scattering cross section $\Sigma_s(u', u, \mu_o)$ are included:

$$\vec{\Omega}\cdot\nabla\psi(\vec{r}, u, \vec{\Omega}) + \Sigma(u)\psi(\vec{r}, u, \vec{\Omega}) = \frac{1}{k}\frac{\chi(u)}{4\pi}\iint_0^\infty du'd\Omega'\nu\Sigma_f(u')\psi(\vec{r}, u', \Omega') + \iint_0^\infty du'd\Omega'\frac{\Sigma_s(u', u, \mu_o)}{2\pi}\psi(\vec{r}, u', \Omega') \qquad \text{Eq. (2.393)}$$

where $\psi(\vec{r}, u, \vec{\Omega})$ is the vector flux density for position $\vec{r}$, lethargy u, and direction $\vec{\Omega}$; $\mu_o = \vec{\Omega}\cdot\vec{\Omega}'$ is the cosine of the angle between the neutron directions before and after scattering; $\chi(u)$ represents the fission spectrum; ν the number of neutrons born in fission; $\Sigma(u)$, $\Sigma_f(u')$, $\Sigma_s(u', u, \mu_o)$ the total macroscopic cross section and the cross sections for fissioning and differential scattering. If the geometry is restricted to one dimension and the scattering function is expanded in Legendre polynomials, one obtains[118] for linear anisotropy in the scattering cross section and $k=1$

$$\mu\frac{\partial\psi(x, u, \mu)}{\partial x} + \Sigma(u)\psi(x, u, \mu) = \frac{\nu}{2}\chi(u)\int_{-1}^{+1}d\mu'\int_0^\infty du'\Sigma_f(u')\psi(x, u', \mu') + \frac{1}{2}\int_0^\infty du'\int_{-1}^{+1}d\mu'\Sigma_{so}(u', u)\psi(x, u', \mu') + \frac{3}{2}\mu\int_0^\infty du'\int_{-1}^{+1}d\mu'\mu'\Sigma_{s1}(u', u)\psi(x, u', \mu') \qquad \text{Eq. (2.394)}$$

where μ is the direction cosine with respect to the x axis and

$$\Sigma_s(u', u, \mu_o) = \sum_{\ell=0}^{\infty} \frac{2\ell+1}{2} \Sigma_{s\ell}(u', u) P_\ell(\mu_o)$$

so that

$$\Sigma_{so}(u', u) = \int_{-1}^{+1} d\mu_o \Sigma_s(u', u, \mu_o)$$

$$\Sigma_{s1}(u', u) = \int_{-1}^{+1} d\mu_o \mu_o \Sigma_s(u', u, \mu_o) . \qquad \text{Eq. (2.395)}$$

The solution of Eq. (2.394) in a multiregion system will yield an energy spectrum which is a function of the spatial coordinates. Since an equivalent few-group formulation with constant coefficients is sought, the spatial dependence of the spectrum would have to be averaged in an appropriate way before the energy averages are defined. The inclusion of such complications, however, more or less defeats the purpose of the few-group description since, in effect, the complete solution of the problem is required for the specification of the group constants.

To separate the spatial dependence, consider the equations which determine the spectra for some sinusoidal spatial variation, $\psi(x,u,\mu)=\psi(B,u,\mu)e^{-iBz}$. If the flux is now written in an expansion of Legendre coefficients

$$\psi_\ell(B, u) = \int_{-1}^{+1} d\mu \, \psi(B, u, \mu) P_\ell(\mu) \qquad \text{Eq. (2.396)}$$

one has

$$[\Sigma(u) - iB\mu] \, \psi(B, u, \mu) = \frac{\nu}{2} \chi(u) \int_0^{\infty} du' \Sigma_f(u') \psi_o(B, u')$$

$$+ \frac{1}{2} \int_0^{\infty} du' \Sigma_{so}(u', u) \, \psi_o(B, u') + \frac{3}{2} \mu \int_0^{\infty} du' \Sigma_{s1}(u', u) \psi_1(B, u'). \qquad \text{Eq. (2.397)}$$

The relation between the ℓ^{th} coefficient and the first two, which represent flux and current, is seen to be

$$\psi_\ell(B, u) = \left[\int_{-1}^{+1} d\mu \left\{ \frac{P_o(\mu) P_\ell(\mu)}{\Sigma(u) - iB\mu} \right\} \right] \left[\frac{\nu}{2} \chi(u) \int_0^\infty du' \Sigma_f(u') \psi_o(B, u') + \frac{1}{2} \int_0^\infty du' \Sigma_{so}(u', u) \psi_o(B, u') \right]$$

$$+ \left[\int_{-1}^{+1} d\mu \left\{ \frac{P_1(\mu) P_\ell(\mu)}{\Sigma(u) - iB\mu} \right\} \right] \left[\frac{3}{2} \int_0^\infty du' \Sigma_{s1}(u', u) \psi_1(B, u') \right] .$$

Eq. (2.398)

In this expression none of the Legendre coefficients of the neutron distribution is neglected, although their interrelations have been partially misrepresented by the neglecting of all components of the scattering function beyond the P_1 term.

If the scattering function is represented by its first N terms, N simultaneous integral equations [Eq. (2.398)] will result involving the first N Legendre coefficients only, which are then determined except for normalization. All further $\psi_\ell(B, u)$ are given directly in terms of these known coefficients. In the case considered here the following two coupled equations appear, involving only the flux and current:

$$\psi_o(u) = \frac{\nu\chi(u)\beta}{\Sigma(u)} \int_0^\infty du' \Sigma_f \psi_o(u') + \frac{\beta}{\Sigma(u)} \int_0^\infty du' \Sigma_{so}(u', u) \psi_o(u')$$

$$+ 3 \frac{(1-\beta)}{a\Sigma(u)} i \int_0^\infty du' \Sigma_{s1}(u', u) \psi_1(u') \qquad \text{Eq. (2.399)}$$

$$\psi_1(u) = \nu\chi(u) \left[\frac{1-\beta}{a\Sigma(u)} \right] i \int_0^\infty du' \Sigma_f \psi_o(u')$$

$$+ \frac{1-\beta}{\alpha\Sigma(u)}\, i \int_0^\infty du'\Sigma_{so}(u', u)\,\psi_o(u')$$

$$+ 3\left[\frac{1-\beta}{\Sigma(u)\,\alpha^2}\right] \int_0^\infty du'\,\Sigma_{s1}(u', u)\,\psi_1(u'). \qquad \text{Eq. (2.400)}$$

Here $\alpha(B) = B/\Sigma(u)$ and $\beta(B) = \tan^{-1}\alpha/\alpha$.

In place of the one-velocity diffusion theory relation between the current and gradient of the flux, which defines the diffusion constant, a similar but somewhat more complicated expression is found by eliminating terms between these two equations. Thus,

$$\gamma(u)\psi_1(u) = i\,\frac{B}{3\Sigma}\,\psi_o + \frac{1}{\Sigma(u)} \int_0^\infty du'\,\Sigma_{s1}(u', u)\,\psi_1(u') \qquad \text{Eq. (2.401)}$$

where γ is defined as

$$\gamma(B, u) = \frac{\beta\alpha^2}{3(1-\beta)}.$$

Fick's law is obtained when no neutron degradation accompanies the anisotropic scattering. Writing $\Sigma_{s1}(u',u) = \Sigma_{s1}(u')\,\delta(u'-u)$, one has

$$\psi_1(u) = \left[3\,[\gamma(u) - \Sigma_{s1}(u)]\right]^{-1} iB\,\psi_o.$$

For $\gamma = 1$ the usual diffusion constant is obtained, since $\Sigma_{s1} = \bar{\mu}_o\Sigma_{so}$, where $\bar{\mu}_o$ is the average cosine of the scattering angle and

$$D = \left[3\Sigma_{tr}\right]^{-1}.$$

For small values of α

$$\gamma(B, u) \sim 1 + \frac{4}{15}\left[\frac{B}{\Sigma(u)}\right]^2$$

so that for large reactors this transport theory correction vanishes. Selengut[117] points out that the effect of $\gamma(u)$ is to decrease the leakage for a given flux gradient particularly

from a small reactor. When degradation accompanies the anisotropic scattering, the effective diffusion constant is not simply a function of cross sections only but depends in addition on the form of the current spectrum.

The Eqs. (2.399) and (2.400) can be written in a form usually employed in the spherical harmonics scheme.[118] With some rearrangement it is found that

$$-i\beta\psi_1(B,u)+\Sigma\psi_o(B,u)=\nu\chi(u)\int_0^\infty du'\,\Sigma_f\psi_o(B,u')$$
$$+\int_0^\infty du'\,\Sigma_{so}(u',u)\,\psi_o(B,u') \qquad \text{Eq. (2.402)}$$
$$-\frac{iB}{3}\,\psi_o(B,u)+\gamma(B,u)\,\Sigma(u)\psi_1(B,u)=\int_0^\infty du'\,\Sigma_{s1}(u',u)\psi_1(B,u').$$

The approximation made here, usually designated as the B_1 approximation, has neglected the higher terms in the spherical harmonics expansion of the scattering function. However, if $\gamma(B,u)$ is set equal to one, the effect of the higher Legendre coefficients on the flux and current vanishes as well, and the P_1 approximation results. Although both approximations yield the second moment of the spatial distribution from a point source exactly, the B_1 approximation provides better estimates of the higher moments than the P_1 approximation. A discussion of the relative properties of these approximations can be found in the papers by Hurwitz and Zweifel,[62] and Wilkins, et al.[119]

C. Group Equations

From the well known results just reviewed, it is clear that energy-dependent diffusion equations describe the P_1 flux spectrum only so long as no appreciable degradation accompanies the anisotropic scattering. In heavy moderators the neglect of anisotropic degradation usually does not lead to sufficient error to affect reactor design, but in hydrogenous systems such simplification, which is the basis of the Selengut-Goertzel approximation, produces substantial changes in the spatial distribution of the fast flux because of the relatively strong anisotropic slowing-down effect of the hydrogen itself. Group diffusion equations can be obtained, however, for a few-group scheme by adopting a different approximation procedure which does not require suppression of the anisotropic degradation. The approximation is made in such a way that the few-group solution of the reactor eigenvalue problem is identical

with the correct P_1 solution for the limiting case of a bare reactor.

Consider again the B_1 Eqs. (2.399) and (2.400) and define a function

$$D(B, u) = \psi_1(B, u) \Big/ [iB\psi_o(B, u)] \cdot$$

As mentioned before, if the integral in the second equation is eliminated by the approximation

$$\Sigma_{s1}(u', u) = \Sigma_{s1}(u')\,\delta(u' - u)$$

so that

$$\int_0^\infty du'\,\Sigma_{s1}(u', u)\,\psi_1(u') = \Sigma'_{s1}(u)\,\psi_1(u)$$

then $D(u)$ is a function only of the cross sections and appears as a diffusion constant. Without this additional approximation $D(u)$ will be a function of the flux and current spectra for the given sinusoidal mode.

In general, since $D(u)$ can be found from the solution of Eq. (2.402), an equation relating the flux to the source can be written:

$$[D(u, B)\,B^2 + \Sigma(u)]\,\psi_o(u, B) = \frac{\nu\chi(u)}{k}\int_0^\infty du'\,\Sigma_f(u')\,\psi_o(u', B) + \int_0^\infty du'\,\Sigma_{so}(u', u)\,\psi_o(u', B). \qquad \text{Eq. (2.403)}$$

This is simply the critical equation for a reactor mode with wave number B; for a bare reactor with zero flux on the periphery there is a set of B values which satisfy the boundary conditions. Each value of B implies through Eq. (2.403) a value of k. The flux and current spectra, however, depend only on B.

The flux shape in the interior of a bare core can generally be characterized to a high degree of precision by a single wave number B, the square of which is called the buckling. The flux shape associated with B^2 extrapolates to zero at some point beyond the physical boundary of the core. Accordingly, if this extrapolation length is known, a value of B^2 can be specified for the core, and the corresponding eigenvalue k can be computed.

By integrating Eq. (2.403) over lethargy bands with $u_n \leq u \leq u_{n-1}$ group equations result for the bare reactor with buckling B^2. For convenience the following group constants are defined:

$$\Phi_n(B) = \int_{u_{n-1}}^{u_n} du\, \psi_o(u, B) \qquad J_n(B) = -i \int_{u_{n-1}}^{u_n} du\, \psi_1(u, B)$$

$$D_n(B) = J_n / B \Phi_n$$

$$\Sigma_{an}(B) = \int_{u_{n-1}}^{u_n} du\ \Sigma_a(u)\, \psi_o(u, B) / \Phi_n.$$

Eq. (2.404)

$$\nu\Sigma_{fn}(B) = \int_{u_{n-1}}^{u_n} du\, \nu\Sigma_f(u)\, \psi_o(u, B) / \Phi_n$$

$$\chi_n = \int_{u_{n-1}}^{u_n} du\, \chi(u)$$

$$\Sigma_{rnm}(B) = \int_{u_{m-1}}^{u_m} du \int_{u_{n-1}}^{u_n} du'\, \Sigma_{so}(u', u)\, \psi_o(u', B)\ \Phi_n .$$

For the n^{th} group equation,

$$\left[D_n B^2 + \Sigma_{an} + \sum_m \Sigma_{rnm} \right] \Phi_n = \frac{\chi_n}{k(B)} \sum_m \nu\Sigma_{fm} \Phi_m + \sum_m \Sigma_{rmn} \Phi_m \qquad \text{Eq. (2.405)}$$

where $k(B)$ represents the eigenvalue of the problem. Use has been made of the fact that

$$\int_{u_{n-1}}^{u_n} du'\, \Sigma_{so}(u')\, \psi_o(u', B) = \sum_m \int_{u_{m-1}}^{u_m} du \int_{u_{n-1}}^{u_n} du'\, \Sigma_{so}(u', u)\, \psi_o(u', B)$$

in the scattering term on the left-hand side of Eq. (2.405).

In dealing with water-moderated reactors it is convenient to distinguish between thermal and fast neutrons on the basis that the latter are not affected by the thermal motion of the moderator atoms. The thermal group will, therefore, be chosen wide enough that neutrons in the thermal group are not scattered up into any of the fast groups. If the reactor is also large enough for the P_1 approximation of the slowing-down process to be applicable, two, three, or four broad groups of neutrons appear to provide a description of the variation of the epithermal neutron spectrum in space adequate for most design purposes. If in fact the lethargy widths of the intermediate groups are chosen such that $\exp\,[u_{n-1}-u_n] >> 1$, cross coupling of the groups can be neglected even for hydrogen scattering, and considerable simplification of the computational problem inherent in Eq. (2.405) results:

$$\left[D_n B^2 + \Sigma_{an} + \Sigma_{rn}\right]\Phi_n = \frac{\chi_n}{k}\sum_m \nu\Sigma_{fm}\Phi_m + \Sigma_{r(n-1)}\Phi_{n-1}. \qquad \text{Eq. (2.406)}$$

Here one defines

$$\Sigma_{rn}(B) = \int_{u_n}^{u_{n+1}} du \int_{u_{n-1}}^{u_n} du'\,\Sigma_{so}(u', u)\,\psi_o(u', B)/\Phi_n(B)\ .$$

No general group width criterion can be given for inelastic scattering, but if the condition for hydrogen is met, the range of inelastic degradation will usually be small in lethargy (usually $\Delta u < 5$ for a lethargy scale $u = \ln \frac{10\ \text{Mev}}{E}$) compared to the combined width of the first two high-energy neutron groups.

If the solution of the eigenvalue problem for a bare core with buckling B^2 is desired, either the multigroup P_1 equation [Eq. (2.403)] or the few-group equation [Eq. (2.406)] could be employed and, if the group constants were calculated for the correct mode, would yield identical results. Further, if the group constants were entirely independent of B, the inverse problem of determining the critical size of a bare reactor could be solved without iteration, using the group constants computed for any buckling.

In practice, the group constants are not entirely independent of B, so that various group schemes will give differing eigenvalues. In Fig. 2.24 an example is given of a slightly enriched bare core of geometrical buckling $B^2 = 97 \times 10^{-4}\ \text{cm}^{-2}$, the eigenvalues being given for two-, three-, and four-group models as a

function of the buckling used in computing the group constants by MUFT. These eigenvalues are obtained by solving the critical determinant implied by Eq. (2.406) with the geometrical buckling B^2 (appearing in the terms $D_n B^2 \Phi_n$) taken as 97×10^4 cm^{-2}. If the required few-group constants (D_n, Σ_{an}, etc.) are obtained by using 97×10^{-4} cm^{-2} in the MUFT computation, the resulting eigenvalues will be independent of the number of energy groups employed, since solving Eq. (2.406) for any few-group scheme will be entirely equivalent to solving the multigroup P_1 Eq. (2.403). However, if the B^2 used in MUFT differs from the geometrical buckling, the eigenvalues from Eq. (2.406) will differ from the critical eigenvalue by amounts which depend on the number of few groups used. It will be noticed that the four-group eigenvalue exhibits about half the error shown by the two-group model; this type of behavior is

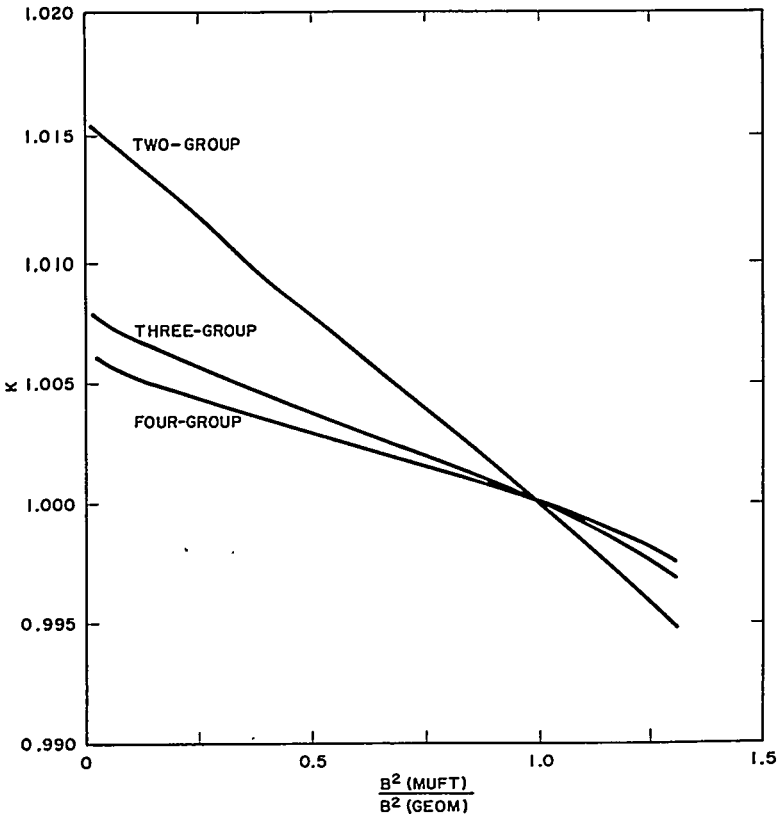

FIGURE 2.24. Effect on Few-Group Eigenvalues of Using Bucklings in MUFT Calculations Which Differ from Geometrical Buckling of a Bare Core.

generally observed with P_1 constants. The spread between two- and four-group eigenvalues is most pronounced for small reactors and, of course, decreases as the reactor increases in size, since the leakage becomes less important. Because of the way the group equation [Eq. (2.405)] is obtained, the differences between eigenvalues vanish for an infinite system.

In the computation of the eigenvalue of a multiregion reactor, the P_1 few-group result is no longer identical with that given by the P_1 multigroup calculation, and very little can be said about the precision of the few-group scheme in general. Figure 2.25 shows the sensitivity to choice of MUFT B^2 when a water reflector is added to the slab core of Fig. 2.24. Apparently, the same trends in eigenvalue accompany changes in the buckling used in computing the core group constants as are found for a bare core. The fact that k is relatively insensitive to B^2 (MUFT) justifies to some extent use of the few-group method.

There is also a small dependence of the eigenvalue on the buckling chosen in the computation of the reflector group constants. If this choice has an important effect in a particular case, the application of the few-group scheme becomes questionable, for it will be noticed that Eq. (2.402) used in computing the group constants does not apply in the reflector, since there is no fission source present there. In practice,

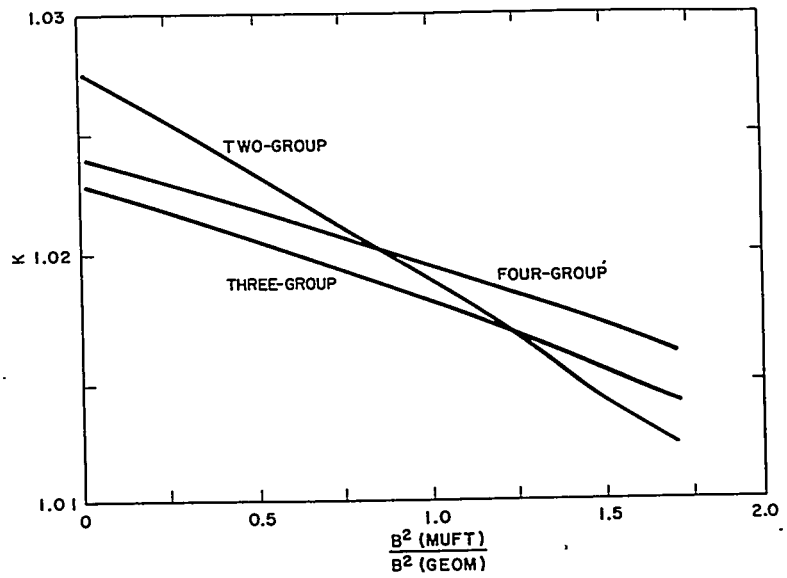

FIGURE 2.25. Dependence of Few-Group Eigenvalues on MUFT Buckling for a Reflected Slab.

reflector constants found using a fission source and a small buckling value have proved to be satisfactory.

D. Special Forms of the Group Equations

For the case of two neutron groups, several useful reductions of the eigenvalue equation [Eq. (2.406)] are often used which involve physically descriptive parameters such as the resonance escape, fast fission factor, and age. Although the definition of these parameters is not unique, they can be precisely stated for any given model in terms of reaction rates and slowing-down density. The range of applicability of the model depends on how invariant the presumed constants are to the buckling of the system. Several such reductions are described here.

1. Two-Group Critical Equation

Designating the fast group by subscript 1, the thermal neutron group by 2, one finds that Eq. (2.406) can be rewritten for a bare reactor as

$$k = \frac{(\eta f)_1 (1 - p_1)}{(1 + \tau B^2)} + \frac{(\eta f)_2 p_1}{(1 + L^2 B^2)(1 + \tau B^2)} \qquad \text{Eq. (2.407)}$$

where

$$(\eta f)_1 = \frac{\nu \Sigma_{f1}}{\Sigma_{a1}}$$

$$\tau = \frac{D_1}{\Sigma_{r1} + \Sigma_{a1}}$$

$$p_1 = \frac{\Sigma_{r1}}{\Sigma_{r1} + \Sigma_{a1}}$$

$$(\eta f)_2 = \frac{\nu \Sigma_{f2}}{\Sigma_{a2}}$$

$$L^2 = \frac{D_2}{\Sigma_{a2}}$$

This arrangement describes conveniently both thermal and intermediate reactor systems without treating the fast effects as a small correction applied to the thermal neutron terms. It will be noticed that with these definitions fast fissioning does not augment the neutron age. No internal fast cycling

occurs because the fissions in both groups are treated in a similar way. Changes in the overall neutron spectrum due to U^{235} loading enter primarily through p_1 in highly enriched systems; for slightly enriched systems $(\eta f)_1$ will also increase as p_1 decreases with increasing U^{235} loading.

2. *Four-Factor Critical Equations*

The four-factor two-group model is a further reduction of Eq. (2.406) which has been widely used in both reactor design and the analysis of critical experiments. In applying this model to U^{235} - U^{238} mixtures no explicit mention of the fast fission in U^{235} is made, so that a peculiar definition of the resonance escape p_1 is required. The fast fission and capture in U^{238} above the fission threshold at 0.8 Mev is represented by a factor ϵ, the latter being defined as the number of neutrons slowing down past the U^{238} fission threshold per neutron produced in other than U^{238} fission.

This method of treating the fast effect in U^{238} was convenient in early calculations of graphite systems in which little coupling between adjacent fuel elements occurred. The fast multiplication was treated as a separate internal chain reaction dependent primarily on the geometry of the single element, the problem being solved by a monoenergetic successive generation treatment. However, in water-moderated systems, the close packing which results in large buckling also produces strong fast neutron coupling between fuel elements, so that the single element effect is usually little more than a perturbation on the homogeneous result.

To reduce the two group form of Eq. (2.406) to the four-factor model, let the fast group be split into one band above (superscript 1, lethargy band 0 to u_1) and one below (superscript 2, lethargy band u_1 to u_c) the U^{238} threshold. Further, let the absorption in the lower band be separated into a part proportional to the U^{235} fission and a residual part, Σ_{a1}^{2R};

$$\Sigma_{a1}^{1}\Phi_1 = \int_0^{u_1} du\,\Sigma_a(u)\psi_o(u,B)$$

$$\Sigma_{a1}^{2}\Phi_1 = \int_{u_1}^{u_c} du\,\Sigma_a(u)\psi_o(u,B), \text{ etc.}$$

$$\Sigma_{a1}^{2R} = \Sigma_{a1}^{2} - \frac{\nu\Sigma_{f1}^{2}}{(\eta f)}.$$

Here $(\eta f) = (\,[\eta f]_2\,)$ is the neutron production per neutron absorbed in the thermal group. The group equation [Eq. (2.406)] then becomes

$$\left[D_1 B^2 + \Sigma_{r1} + \Sigma_{a1}^{1} + \Sigma_{a1}^{2R} + \frac{\nu\Sigma_{f1}^{2}}{(\eta f)}\right]\Phi_1 = \frac{1}{k}\left[\nu\Sigma_{f1}^{1}\Phi_1 + \nu\Sigma_{f1}^{2}\Phi_1 + \nu\Sigma_{f2}\Phi_2\right]$$

$$\left[D_2 B^2 + \Sigma_{a2}\right]\Phi_2 = \Sigma_{r1}\Phi_1 .$$

The net source term in the fast group equation can be written as

$$\frac{\eta f \epsilon}{k}\left[\frac{\nu\Sigma_{f1}^{2}\Phi_1 + \nu\Sigma_{f2}\Phi_2}{\nu\Sigma_{f2}\Phi_2}\right]\Sigma_{a2}\Phi_2$$

which becomes

$$\frac{\eta f \epsilon}{k}\left[\frac{\Sigma_{r1} + \dfrac{\nu\Sigma_{f1}^{2}}{(\eta f)}}{\Sigma_{r1}}\right]\Sigma_{a2}\Phi_a$$

if $D_2 B^2$ is neglected in comparison with Σ_{a2}. Removing from the total source the absorption in the top part of the first group preserves the definition of the fast fission factor described above:

$$\epsilon = 1 + \frac{\left(\nu\Sigma_{f1}^{1} - k\Sigma_{a1}^{1}\right)\Phi_1}{\nu\Sigma_{f2}\Phi_2 + \nu\Sigma_{f1}^{2}\Phi_1}. \qquad \text{Eq. (2.408)}$$

Since the coefficient of Σ_{a1}^{1} is taken to be $k = 1$, the variation of k with buckling (or reactor period in the time-dependent case) for the four-factor model will be different from that given by Eq. (2.406), even in a bare reactor, as in Eq. (2.407).

The familiar four-factor equations are now obtained by letting

$$\Sigma_1 = \Sigma_{r1} + \Sigma_{a1}^{2R} + \frac{\nu\Sigma_{f1}^{2}}{\eta f}$$

and renormalizing the fast to slow flux ratio,

$$\Phi_2' = \left[1 + \frac{\nu\Sigma_{f1}^2}{\eta f \Sigma_{r1}}\right]\Phi_2 .$$

One then has (neglecting D_2B^2)

$$\left[D_1B^2 + \Sigma_1\right]\Phi_1 = \frac{\eta f \epsilon}{k}\Sigma_{a2}\Phi_2'$$

$$\left[D_2B^2 + \Sigma_{a2}\right]\Phi_2' = p_R\Sigma_1\Phi_1 \qquad \text{Eq. (2.409)}$$

with the resonance escape being given as the probability of escaping capture by the cross sections which contribute to Σ_{a1}^{2R}:

$$p_R = \frac{\Sigma_1 - \Sigma_{a1}^{2R}}{\Sigma_1}$$

$$\tau = \frac{D_1}{\Sigma_1} \qquad \text{Eq. (2.410)}$$

The critical equation for the four-factor form of the two-group equations is then

$$k = \frac{\eta f \epsilon p_R}{(1 + \tau B^2)(1 + L^2B^2)} . \qquad \text{Eq. (2.411)}$$

Comparing the two critical equations [Eqs. (2.407) and (2.411)], it is clear that the ages and migration areas $(\tau + L^2)$ appearing in the two expressions differ in a way dependent on the amount of absorption occurring at energies above the U^{238} fission threshold. More important, however, is the difference between the resonance escape probabilities, for in Eq. (2.407) p_1 represents the probability of escaping fast absorption by any process (fission or capture) whereas in Eq. (2.411) p_R accounts only for those absorptive events which are neither included in ϵ nor proportional to the $\nu\Sigma_{f(u)}$ of U^{235}. The renormalization of either fast or thermal flux required in this scheme is an undesirable feature for multi-region reactor calculations.

Although the definition of p_R appears at first sight to be rather involved, it is particularly convenient for U^{235} - U^{238} systems of low enrichment. As the representative example

below shows, p_R corresponds rather closely to the resonance escape of a system containing U^{238} as the only absorber but with $1/v$ continuation of the thermal U^{238} capture cross section subtracted.

The following illustrative case is taken from a MUFT calculation of the fast constants for a TRX^{120} 1.0 percent enriched lattice of 0.600-in. diameter rods with a water-to-uranium volume ratio of unity. The resonance self-shielding factor (see Sect. 2.8.F) was $L = 0.635$ and the buckling $B^2 = 9.66 \times 10^{-4}$. For Eq. (2.407) the constants of importance are

$$\tau_1 = 31.2 \text{ cm} \qquad p_1 = 0.529$$

and the fast and thermal contributions to k are

$$k = 0.303 + 0.716 = 1.019.$$

For Eq. (2.411) the appropriate constants obtained using the definitions [Eqs. (2.408) and (2.410)] are

$$\epsilon = 1.110 \qquad p_R = 0.680 \qquad \tau = 33.6,$$

which result in $k = 1.018$. Now if the usual, simple calculation of the resonance escape is made, considering only the U^{238} and water in the mixture and using the MUFT cross sections one gets

$$p = \exp\,[-L(RI)] = 0.648.$$

In terms of effective resonance absorption cross section this difference in p amounts to about 1.3 *b*. The effective resonance absorption cross section of the $(1/v)$ continuation of the thermal U^{238} cross section is about 1.1 *b*.

3. *Alternate Form of Two-Group Equations*

There is one other form of the two-group equations which has the appearance of the four-factor form described in Ref. 116 but which does not require the flux renormalization that results from transferring the epithermal U^{235} fission to the thermal group. In this scheme all fast fission is included in the fast group as in Ref. 114, but the eigenvalue is taken to be directly related only to the thermal fission rate. This results in all of the fast fission being treated as an internal chain reaction (as is the U^{238} fission in Ref. 116) which augments the age by often substantial amounts. The resulting

age is then related to the second moment of the distribution of neutrons entering the thermal group from a point source of fission neutrons; the fast fissions which occur during slowing down tend to spread this distribution.

Except for this difference in the physical interpretation of the quantities which enter the group equations, the difference between this form of the two-group equations and that described in Ref. 114 is trivial. The equations themselves and definition of the constants are easily found from Eq. (2.406):

$$\left[D_1 B^2 + \Sigma_1\right] \Phi_1 = \frac{\nu\Sigma_{f2}}{k} \Phi_2 \qquad \text{Eq. (2.412)}$$

$$\left[D_2 B^2 + \Sigma_{a2}\right] \Phi_2 = (\epsilon p)\Sigma_1 \Phi_1 .$$

Here,

$$\Sigma_1 = \Sigma_{r1} + \Sigma_{a1} - \nu\Sigma_{f1} \qquad \text{Eq. (2.413)}$$

$$(\epsilon p) = \frac{\Sigma_{r1}}{\Sigma_{r1} + \Sigma_{a1} - \nu\Sigma_{f1}}$$

so that the augmented age becomes

$$\tau = \frac{D_1}{\Sigma_{r1} + \Sigma_{a1} - \nu\Sigma_{f1}} \qquad \text{Eq. (2.414)}$$

and the critical equation is similar in form to Eq. (2.411):

$$k = \frac{(\eta f)_2 (\epsilon p)}{(1 + \tau B^2)(1 + L^2 B^2)} . \qquad \text{Eq. (2.415)}$$

Although $k = 1$ occurs for the same reactor configuration for all three critical equations [Eqs. (2.407), (2.411), and (2.415)], the variations of k with configuration will be different. Thus, the correlation between computed changes in k and reactor periods cannot be made through the same inhour formula.

E. The Time–Dependent Problem

The time-dependent problem has been treated extensively in the literature by a variety of methods. Many of the techniques

developed, although quite general, are awkward to use properly in computing the expected results of critical experiments, in particular the relation between changes in the configuration of a reactor and the observed reactor period. On the other hand, the simple inhour formula is inadequate even in a bare core because of the difference in worth of the delayed and prompt neutrons and the variation in yield of delayed neutrons from various fissionable isotopes. In multiregion systems, such as seed and blanket cores, the exact solution of the problem is very involved in practice although straightforward in principle.

A few-group scheme is here described which distinguishes between prompt and delayed neutron leakage, fission and capture effects. Simple analytic results can be obtained for a bare core corresponding to the inhour formula if the delayed neutron yield is the same for all fissionable isotopes. If the latter is not true, the analytic result becomes unwieldy but can be simplified by the introduction of approximate isotopic fission ratios. In reflected or multiregion systems a numerical approximation procedure can be used with present spatial integration codes which is probably correct to terms of order B^2, but which is again exact for a bare core.

The linearity of Eq. (2.403) in the flux implies that the prompt and delayed neutron sources, and the flux arising from these sources, can be separated into two components which satisfy separate equations linked only through the fission integral. The introduction of time-dependent terms does not alter this situation; the averaging process can be carried through as before to yield few-group equations which have the following form in the case of two groups:

$$D_1 B^2 \Phi_1 + (\Sigma_{r1} + \Sigma_{a1})\,\Phi_1 = \frac{1}{k} \sum_j \left[\nu\Sigma_{f1}^j \Phi_1 + \nu\Sigma_{f2}^j \Phi_2 + \nu\Sigma_{f3}^j \Phi_3\right] \left(1 - \sum_i \beta_i^j\right) - \frac{1}{v_1} \frac{d\Phi_1}{dt}$$

$$D_2 B^2 \Phi_2 + (\Sigma_{r2} + \Sigma_{a2})\,\Phi_2 = \sum_i \lambda_i C_i - \frac{1}{v_2} \frac{d\Phi_2}{dt} \qquad \text{Eq. (2.416)}$$

$$D_3 B^2 \Phi_3 + \Sigma_{a3} \Phi_3 = \Sigma_{r1} \Phi_1 + \Sigma_{r2} \Phi_2 - \frac{1}{v_3} \frac{d\Phi_3}{dt}.$$

Here both indices (1) and (2) designate the fast neutron group (say, 0.625 ev $\leq E \geq$ 10 Mev) with constants appropriate to (1), the prompt neutron source, and (2), the delayed neutrons

presumed to be emitted with a single energy.[121] Since this analysis is concerned with the very slow changes encountered in critical experiments, the fast and thermal prompt neutron lifetime will be taken as zero for convenience $(1/v_1 = 1/v_2 = 1/v_3 = 0)$. The constants β_i^j represent the yield of delayed neutrons with decay constant λ_i from the fissionable isotope j. The concentration of delayed neutron emitters, C_i, is given by

$$\frac{dC_i}{dt} = \frac{1}{k} \sum_j \left(\nu\Sigma_{f1}^j \Phi_1 + \nu\Sigma_{f2}^j \Phi_2 + \nu\Sigma_{f3}^j \Phi_3 \right) \beta_i^j - \lambda_i C_i. \qquad \text{Eq. (2.417)}$$

The secular equation for the system is found by letting both flux Φ_ℓ and C_i vary as $e^{\omega t}$ and by substituting $\lambda_i C_i$ from Eq. (2.417) into Eq. (2.416):

$$\begin{aligned}
\frac{\Sigma_{r1}}{p_1}(1 + \tau_1 B^2)\,\Phi_1 &= \frac{1}{k} \sum_{j i \ell} \nu\Sigma_{f\ell}^j \Phi_\ell (1 - \beta_i^j) \\
\frac{\Sigma_{r2}}{p_2}(1 + \tau_2 B^2)\,\Phi_2 &= \frac{1}{k} \sum_{j \ell i} \frac{\lambda_i \beta_i^j}{\omega + \lambda_i} \nu\Sigma_{f\ell}^j \Phi_\ell \qquad \text{Eq. (2.418)} \\
\Sigma_{a3}(1 + L^2 B^2)\,\Phi_3 &= \Sigma_{r1}\Phi_1 + \Sigma_{r2}\Phi_2
\end{aligned}$$

where

$$\tau_2 \equiv \frac{D_2}{\Sigma_{a2} + \Sigma_{r2}}; \quad p_2 \equiv \frac{\Sigma_{r2}}{\Sigma_{a2} + \Sigma_{r2}}.$$

If the delayed neutron yields are the same for all isotopes, an expression for k is readily found by elimination of the fluxes. However, in the general case, the secular equation is quadratic in k, contains a series of prompt-delayed source cross product terms, and is so cumbersome as to be of little value as an analytic relation.

In practice, one isotope (designated by superscript o) usually provides most of the fission rate, so that the deviation of the β_i^j of the other isotopes from β_i^o can be treated as a small effect. Under these conditions, the terms α_i^p and α_i^d in the following expressions for the prompt and delayed neutron source

terms may be taken as constants without appreciably altering the relation between reactor configuration and period:

$$\text{Prompt source} = \sum_{j\ell i} (1-\beta_i^o)\,\nu\Sigma_{f\ell}^j \Phi_\ell\,(1-\alpha_i^p)$$

$$\text{Delayed source} = \sum_{j\ell i} \frac{\lambda_i \beta_i^o}{\omega+\lambda_i}\,\nu\Sigma_{f\ell}^j \Phi_\ell\,(1+\alpha_i^d)$$

$$\alpha_i^p = \frac{\beta_i^o}{1-\beta_i^o}\,\alpha_i^d$$

$$\alpha_i^d = \frac{\sum_{j\ell} (\beta_i^j - \beta_i^o)\,\nu\Sigma_{f\ell}^j \Phi_\ell}{\beta_i^o \sum_{j\ell} \nu\Sigma_{f\ell}^j \Phi_\ell}.$$

Substitution of these source expressions into Eq. (2.418) yields exactly

$$k = k^p \sum_i [1-\beta_i^o(1+\alpha_i^d)] + k^d \sum_i \frac{\beta_i^o \lambda_i}{\omega+\lambda_i}(1+\alpha_i^d) \qquad \text{Eq. (2.419)}$$

where

$$k^p = \frac{(\eta f)_1(1-p_1)}{(1+\tau_1 B^2)} + \frac{(\eta f)_3 p_1}{(1+\tau_1 B^2)(1+L^2B^2)}$$

$$k^d = \frac{(\eta f)_2(1-p_2)}{(1+\tau_2 B^2)} + \frac{(\eta f)_3 p_2}{(1+\tau_2 B^2)(1+L^2B^2)}$$

and the same designation of group constants as in Eq. (2.407).* Equation (2.419) is correct so long as the dependence of α_i^d on reactor configuration, period, etc., through the flux ratios is included. If the delayed and prompt group constants are the same in the stationary case, $k = k^p$; otherwise k will be a few tenths percent larger than k^p.

If the system is now altered by changing either group constants or geometrical size, k will remain fixed but k^p, k^d,

*Here k^p is the eigenvalue that would be obtained by solving a prompt neutron problem with no delayed neutrons; k^d, correspondingly, is the eigenvalue of a delayed neutron problem without prompt neutrons present.

α_i^d, and ω will all change. The resulting relation between k^p and ω will be in error if α_i^d is held constant but, if the fission ratios and β_i^k values are such that $\alpha_i^d << 1$, the error should be small. Let the initial and final states of the system be designated by (a) and (b), and let the average delayed neutron yield be $\bar{\beta}_i = \beta_i^o(1 + \alpha_i^d)$:

$$\frac{k_b^p - k_a^p}{k_a^p} \cong \frac{k_a^d}{k_a^p} \frac{\sum_i \bar{\beta}_i \left(\frac{\omega_b}{\omega_b + \lambda_i} - \frac{\omega_a}{\omega_a + \lambda_i} \right)}{\sum_i [1 - \bar{\beta}_i]} - \frac{k_b^d - k_a^d}{k_a^p} \frac{\sum_i \frac{\bar{\beta}_i \lambda_i}{\omega_b + \lambda_i}}{\sum_i [1 - \bar{\beta}_i]}$$

where the approximate equality is indicated since the change in α_i^d has been neglected. Since k^d is ordinarily within 25 percent of k^p, the second term on the right-hand side can be combined with the left-hand side to give

$$\frac{k_b^p - k_a^p}{k_a^p} \cong \frac{k_a^d}{k_a^p} \sum_i \bar{\beta}_i \left(\frac{\omega_b}{\omega_b + \lambda_i} - \frac{\omega_a}{\omega_a + \lambda_i} \right) \cdot \quad \text{Eq. (2.420)}$$

In this modified inhour formula, the effects of different fast fission, leakage, and capture for prompt and delayed neutrons are included in the ratio k_a^d/k_a^p; an approximate account of isotopic differences in delayed neutron yield is represented by $\bar{\beta}_i$. The quantity $\frac{k^d}{k^p} \bar{\beta}_i$ is often referred to as the effective delayed neutron yield.

In many applications of this few-group formalism to reactor design, the bare core formula Eq. (2.420) is not applicable because of spatial variations in the group constants and fissionable materials. Means of obtaining an approximate correction in such cases are discussed in Chap. 5, Sect. 5.2.D.

F. Computation of Few-Group Constants

In the preceding discussion of the few-group equations, consistent definitions of the group constants have been described in terms of the solutions of Eq. (2.402). Under certain particular conditions, such as the Selengut-Goertzel P_1 approximation with only hydrogen degradation, an analytic solution of Eq. (2.402) can be made which displays at least the form of the constants. In general, however, numerical solutions are necessary if proper account is to be taken of inelastic scattering, shielded resonance capture, fast fission, etc., in either P_1 or B_1 approximations. Several computer codes

(MUFT-2, -3, -4, and -5) [114,122-125] have been developed to provide flux and current spectra from a multigroup approximation of Eq. (2.402) and to construct from these solutions the various few-group constants. These codes are similar in general form but differ in the detail permitted in both the microscopic cross section library and the few-group output because of the different capabilities of the several computers. The main features of these codes concerned with the solution of Eq. (2.402) are summarized here; the few-group edits of the MUFT codes are essentially defined in Sect. 2.8.C.

1. *The MUFT Codes*

For numerical solution, the scattering integrals which appear in Eq. (2.402) are represented by three terms associated with hydrogen recoil scattering, heavy element recoil scattering, and inelastic scattering. Only the second term introduces further approximation through the use of age theory, but its effect in water-moderated systems is usually small. For hydrogen scattering it is convenient to define the P_0 and P_1 scattering-in integrals explicitly:

$$\eta_o(u) = \int_o^u du' \, \Sigma_H(u') \, e^{-(u-u')} \psi_o(u')$$

$$\eta_1(u) = \int_o^u du' \, \Sigma_H(u') \, e^{-\frac{3}{2}(u-u')} \psi_1(u') \, . \qquad \text{Eq. (2.421)}$$

The hydrogen scattering integrals can be eliminated by use of the differential equations,

$$\frac{\partial \eta_o}{\partial u} = -\eta_o(u) + \Sigma_H \psi_o(u)$$

$$\frac{\partial \eta_1}{\partial u} = -\frac{3}{2} \eta_1(u) + \Sigma_H \psi_1(u) \, . \qquad \text{Eq. (2.422)}$$

This procedure simplifies machine computations, since fluxes at all lethargies below u, which would be required to compute the integrals explicitly, need no longer be stored in the fast memory.

The heavy element scattering may be approximated by the age or Greuling-Goertzel theory Taylor expansions, [61,68] which for heavy isotope, k, lead to the equations

$$\int_o^u du' \Sigma_{so}^k(u', u)\, \psi_o(u') = \Sigma_{so}^k(u)\psi_o(u) - \frac{\partial q_o^k(u)}{\partial u}$$

$$\int_o^u du' \Sigma_{s1}^k(u', u)\, \psi_1(u') = \Sigma_{s1}^k(u)\psi_1(u) - \frac{\partial q_1^k(u)}{\partial u}$$

where the q_o and q_1 are defined by

$$(\lambda_o)_k \frac{\partial (q_o)^k}{\partial u} + (q_o)^k = \Sigma_{so}^k(u)(\xi_o)^k \psi_o$$

$$(\lambda_1)_k \frac{\partial (q_1)^k}{\partial u} + (q_1)^k = \Sigma_{so}^k(u)(\xi_1)^k \psi_1 .$$

$(\xi_o)^k$ being the average logarithmic decrement for collisions with isotope k and $\lambda_o, \lambda_1, \xi_1$ being the Greuling-Goertzel parameters defined in Refs. 66 and 126, $(\xi_1)^k$ the η_k of Ref. 126. The inelastic scattering cannot be described by any generally applicable scattering function and is, therefore, treated at any particular lethargy as a source $\omega(u)$ dependent on the known fluxes at lower lethargy.

With these explicit representations of the scattering integrals, Eq. (2.402) can be written in conjunction with Eq. (2.422) as four differential equations. Since the fission spectrum resulting from fast fission is taken to be the same as from thermal fission, the source normalization is of no consequence in computing group constants:

$$\left(\Sigma_a^{(u)} + \Sigma_{in}^{(u)}\right) \psi_o(B,u) - iB\psi_1(B,u) = \chi(u) - \frac{\partial \eta_o}{\partial u} - \sum_k \frac{\partial (q_o)^k}{\partial u} + \omega(u)$$

$$-\frac{iB}{3}\psi_o(B,u) + [\gamma(B,u)\Sigma(u) - \Sigma_{s1}(u)]\, \psi_1(B,u)$$

$$= -\left[\frac{2}{3}\frac{\partial \eta_1}{\partial u} + \sum_k \frac{\partial (q_1)^k}{\partial u}\right]\delta . \qquad \text{Eq. (2.423)}$$

The four different approximations mentioned previously can be obtained from the system of Eqs. (2.422) and (2.423) by forcing various terms to assume certain values throughout the calculation according to the scheme:

B_1 approximation	$\gamma=\gamma(B,u)$; $\delta = 1.0$
P_1 approximation	$\gamma=1.0$; $\delta = 1.0$
$SG\ B_1$ approximation	$\gamma=\gamma(B,u)$; $\delta = 0$
$SG\ P_1$ approximation	$\gamma=1$; $\delta = 0$

A discussion of the properties of these approximations and a comparison of typical results obtained from them is given elsewhere.[122] Both the B_1 and P_1 approximations give the correct second moment of the slowing-down distribution. The B_1 approximation gives, in addition, more accurate values of higher moments. The Selengut-Goertzel approximation gives high values of the second moment (~20 percent high for a fission spectrum in pure H_2O). With the present capacity of computing machines, the fact that Eq. (2.423) can be reduced to a single equation [eliminating $\psi_1(B,u)$] is no longer as significant as it was when the approximation was originally derived.

The multigroup equations are formed by integrating the terms in the differential equations [Eqs. (2.422) and (2.423)] over the n^{th} lethargy group $u_{n-1} \leq u \leq u_n$. If the individual group widths are made small, the approximation of the average of a product by the product of the average values can be used except for groups in which resonance absorption occurs. For the latter, it is necessary to consider the variation of flux and absorption cross section within the group in order to obtain an accurate absorption integral for the group.

In the MUFT codes the absorption integral is evaluated by integrating the analytic Selengut-Goertzel flux shape within the group over a Breit-Wigner single resonance shape, assuming that scattering out of the group occurs by hydrogen alone and neglecting the effect of leakage on the absorption rate. Thus, if there are j resonances in the n^{th} group, the absorption rate is written as the sum of hydrogen and heavy element slowing down across u_{n-1} multiplied by $(1-p_n)$, the resonance capture probability of the group:

$$\int_{u_{n-1}}^{u_n} du\, \Sigma_a^R(u)\psi_o(u) = (1-p_n)\left[\eta_o(u_{n-1}) + \sum_k q_o^k\left(u_{n-1}\right)\right]$$

with the resonance escape probability for the group given by

$$p_n = \prod_j \exp\left[-L_{jn}(RI)_{jn}\right]$$

where $(RI)_{jn}$ is the homogeneous resonance integral of the j^{th} resonance, and the self-shielding factor L_{jn} accommodates the changes in resonance integral produced by lumping and Doppler effects. These input factors can be determined by such treatments of heterogeneous and temperature effects as Richtmyer's Monte Carlo[127] codes or Stein's approximate method.[89]

2. *Numerical Errors in Calculated Group Constants*

E. M. Gelbard and D. R. Harris

It is shown here that two sources of error in MUFT-like group calculations are not as important as might be anticipated. Consider a uniform infinite medium in which neutrons are slowed only by collisions with hydrogen. The flux per unit lethargy ψ_o and the slowing-down density η satisfy the equations

$$\Sigma_a \psi_o = -\frac{\partial \eta}{\partial u} + \chi \qquad \text{Eq. (2.424)}$$

$$\frac{\partial \eta}{\partial u} + \eta = \Sigma_H \psi_o \qquad \text{Eq. (2.425)}$$

where Σ_H is the hydrogen scattering cross section, Σ_a is the absorption cross section, and $\chi_{(u)}$ is the neutron source per unit lethargy. These are Eqs. (2.422) and (2.423) for the present special case. Integrate Eqs. (2.424) and (2.425) over the lethargy group extending between $\hat{u}$ and $\check{u}$ with $\hat{u}-\check{u}=\Delta$. Then,

$$\frac{1}{\Delta}\int \Sigma_a \psi_o \, du = \frac{\hat{\eta}-\check{\eta}}{\Delta} + \frac{1}{\Delta}\int \chi_{(u)}\, du \qquad \text{Eq. (2.426)}$$

$$\frac{\hat{\eta}-\check{\eta}}{\Delta} + \frac{1}{\Delta}\int \eta \, du = \frac{1}{\Delta}\int \Sigma_H \psi_o \, du\,. \qquad \text{Eq. (2.427)}$$

Here $\hat{\eta}$ and $\check{\eta}$ represent the slowing-down densities at $\hat{u}$ and $\check{u}$, respectively. Subscripts representing group number are ignored.

In the MUFT codes the integral $\int \eta \, du/\Delta$ in Eq. (2.427) is replaced by $(\hat{\eta}+\check{\eta})/2$. The error in this approximation can be

estimated by truncating the Taylor series expansion of η about $\hat{u}$ at three terms, whence

$$\frac{1}{\Delta}\int \eta du - \frac{\hat{\eta}+\check{\eta}}{2} = -\frac{\Delta^2}{12}\left.\frac{\partial^2\eta}{\partial u^2}\right|_{\hat{u}}. \qquad \text{Eq. (2.428)}$$

The expansion is taken about $\hat{u}$ because at high energies, where the MUFT approximation is in question, the bulk of the integral comes from lethargies near $\hat{u}$. This error is evaluated numerically later.

Another approximation replaces each of the cross section times flux integrals by a product of lethargy-averaged cross section $\bar{\Sigma}$, and flux, ψ_o. The error here, e.g., is

$$\frac{1}{\Delta}\int \Sigma_H \psi_o \, du - \bar{\Sigma}_H \bar{\psi}_o = \text{cov}\, \Sigma_H \psi_o \qquad \text{Eq. (2.429)}$$

where $\text{cov}\, \Sigma_H \psi_o$ represents the covariance of Σ_H and ψ_o:

$$\text{cov}\, \Sigma_H \psi_o = \frac{1}{\Delta}\int (\Sigma_H \psi_o - \bar{\Sigma}_H \bar{\psi}_o)\, du. \qquad \text{Eq. (2.430)}$$

The covariance is positive if Σ_H generally is larger than $\bar{\Sigma}_H$ and when ψ_o is larger than $\bar{\psi}_o$. The covariance is zero if either Σ_H or ψ_o is constant and at low energies; where both Σ_H and ψ_o are nearly constant, the covariance must be very small.

To evaluate the errors numerically consider a particular physical situation which is typical of many water-moderated reactor problems, viz., one which is dominated by the fission spectrum and by hydrogen scattering. The errors are expected to be worst at large energies where the fission source per unit energy can be approximated by

$$\chi(E) \approx a e^{-E/\theta} \qquad \text{Eq. (2.431)}$$

where a and θ are constants. Ignoring Σ_a, Eq. (2.424) becomes

$$\frac{\partial \eta}{\partial E} = -\chi(E) = a e^{-E/\theta} \qquad \text{Eq. (2.432)}$$

which can be integrated directly to yield

$$\eta = a\theta e^{-E/\theta} = a\theta \exp\left(-\frac{E_o}{\theta} e^{-u}\right). \qquad \text{Eq. (2.433)}$$

The usual relation between energy and lethargy has been employed:

$$E = E_o e^{-u} \qquad \text{Eq. (2.434)}$$

where E_o is taken to be 10 Mev. The flux is determined from Eq. (2.425) as

$$\Psi_o(E) = \Sigma_H^{-1}\, a\left(1 + \frac{\theta}{E}\right) e^{-E/\theta} \text{ per unit energy} \qquad \text{Eq. (2.435)}$$

and

$$\Psi_o = \Sigma_H^{-1}\, a(E+\theta) e^{-E/\theta} = \Sigma_H^{-1}\, a\left(E_o e^{-u} + \theta\right) \exp\left(-\frac{E_o}{\theta} e^{-u}\right). \qquad \text{Eq. (2.436)}$$

These expressions will be used to evaluate the error terms in Eqs. (2.428) and (2.429).

In the present case where high energy absorption is ignored, MUFT computes correctly the slowing-down density because it can be shown from Eq. (2.426) that the slowing-down density is correctly determined as the total neutron source at higher energies. The group neutron flux $\bar{\Psi}_o$ is in error, however. According to Eq. (2.429),

$$\bar{\Sigma}_H \bar{\Psi}_o = \frac{1}{\Delta} \int \Sigma_H \Psi_o \, du - \operatorname{cov} \Sigma_H \Psi_o \qquad \text{Eq. (2.437)}$$

and eliminating the integral by use of Eq. (2.427),

$$\bar{\Sigma}_H \bar{\Psi}_o = \frac{\hat{\eta} - \check{\eta}}{\Delta} + \frac{1}{\Delta} \int \eta \, du - \operatorname{cov} \Sigma_H \Psi_o . \qquad \text{Eq. (2.438)}$$

Applying Eq. (2.428)

$$\bar{\Sigma}_H \bar{\Psi}_o = \frac{\hat{\eta} - \check{\eta}}{\Delta} + \frac{\hat{\eta} + \check{\eta}}{2} - \frac{\Delta^2}{12} \left.\frac{\partial^2 \eta}{\partial u^2}\right|_{\hat{u}} - \operatorname{cov} \Sigma_H \Psi_o . \qquad \text{Eq. (2.439)}$$

The third and fourth terms on the right-hand side of Eq. (2.431) represent the error in the MUFT calculation of $\bar{\Psi}_o$. The covariance is conveniently evaluated by using two-term Taylor series expansions for Σ_H and Ψ_o about the group midpoint:

$$\operatorname{cov} \Sigma_H \Psi_o \approx \frac{\Delta^2}{12} \left.\frac{\partial \Sigma_H}{\partial u}\right|_{\check{u}+\frac{\Delta}{2}} \left.\frac{\partial \Psi_o}{du}\right|_{\check{u}+\frac{\Delta}{2}} . \qquad \text{Eq. (2.440)}$$

The error terms can be evaluated by use of the analytic expressions for $\eta(u)$ and $\Psi_o(u)$ given in Eqs. (2.433) and (2.436), while Σ_H is well approximated in any MUFT group by

$$\Sigma_H = CE^{-\gamma} \qquad \text{Eq. (2.441)}$$

where γ is listed in Table 2.6. The error in group flux is

$$\bar{\Psi}_o - \frac{1}{\bar{\Sigma}_H}\left[\frac{\hat{\eta}-\check{\eta}}{\Delta} + \frac{\hat{\eta}+\check{\eta}}{2}\right] \approx -\frac{\Delta^2}{12}\frac{\hat{\eta}}{\bar{\Sigma}_H}\frac{\check{E}}{\theta}\left(\frac{\check{E}}{\theta}-1\right) - \frac{\Delta^2}{12}\gamma\left[\frac{E_m^2}{\theta^2} - \gamma\left(1+\frac{E_m}{\theta}\right)\right]\frac{\eta_m}{\bar{\Sigma}_H} \qquad \text{Eq. (2.442)}$$

TABLE 2.6 — EXPONENT IN $\Sigma_H = CE^{-\gamma}$

MUFT Group	γ	MUFT Group	γ	MUFT Group	γ
1	0.878	10	0.550	19	0.340
2	0.800	11	0.510	20	0.310
3	0.700	12	0.518	21	0.222
4	0.638	13	0.500	22	0.158
5	0.620	14	0.486	23	0.104
6	0.582	15	0.458	24	0.064
7	0.578	16	0.438	25	0.058
8	0.558	17	0.400	26	0.042
9	0.558	18	0.384	27	0.040

where Σ_m is the energy and η_m is the slowing-down density corresponding to the lethargy midpoint of the group. It can be shown $\bar{\Psi}_o$ is of order $\hat{\eta}\bar{\Sigma}_H^{-1}\left(1+\frac{\check{E}}{\theta}\right)$ so that the errors relative to $\bar{\Psi}_o$ are

$$\text{Relative error in } \bar{\Psi}_o \approx -\frac{\Delta^2}{12}\frac{E}{\theta}\frac{\frac{\check{E}}{\theta}-1}{\frac{\check{E}}{\theta}+1}$$

$$-\frac{\Delta^2}{12}\gamma\left[\frac{E_m^2}{\theta^2}-\gamma\left(1+\frac{E_m}{\theta}\right)\right]\Bigg/\left(1+\frac{\check{E}}{\theta}\right). \qquad \text{Eq. (2.443)}$$

In the upper MUFT groups

$$\Delta = 1/4$$
$$\theta \approx 4/3$$
$$\gamma \approx 2/3$$

so that each of the two error terms in Eq. (2.443) is negative and varies between -1/4 percent and -4 percent for the upper MUFT groups.

Thus, the true flux at high energies is less than the flux calculated by MUFT in the upper groups in consequence of these two effects alone. It can be inferred that these two effects tend to make MUFT ages and fast neutron reaction rates too large.

3. *Analytic Solution for Selengut-Goertzel Approximation*

If both inelastic and heavy element, energy degrading scattering are ignored in the Selengut-Goertzel approximation of Eqs. (2.422) and (2.423), an analytic expression can be found for the probability of a fission neutron reaching the thermal neutron group. When $\delta = 0$ a simple relation involving only cross sections exists at each lethargy between the current and the flux gradient,

$$\Psi_1(u) = iBD\Psi_o(u)$$

where in the P_1 approximation

$$D = \left[3\left(\Sigma(u) - \Sigma_{s1}(u)\right)\right]^{-1}.$$

Equation (2.402) then takes the form

$$\left(\Sigma_H + \Sigma_a + DB^2\right) \Psi_o(B,u) = \int_o^u du' \Sigma_H(u') e^{-(u'u')} \Psi_o(B,u') + \chi(u) \int_o^\infty du' \nu\Sigma_f(u') \Psi_o(B,u') \quad \text{Eq. (2.444)}$$

Since the fission integral will depend on B and, thus, affect the age to the thermal neutron group, the fission integral is split into fission neutrons produced in thermal fission $u_c \leq u' \leq \infty$ and produced by fast fission $o \leq u' \leq u_c$. For this purpose the fission ratio β is defined as

$$\beta(B) = \frac{\int_o^{u_c} du' \nu\Sigma(u') \Psi_o(B,u')}{\int_{u_o}^\infty du' \nu\Sigma_f(u') \Psi_o(B,u')}$$

and for convenience $R(u,B)$ is introduced as

$$R(u,B) = \frac{\Sigma_a + DB^2}{\Sigma_H + \Sigma_a + DB^2} .$$

Equation (2.444) can then be solved for the slowing-down density $\eta_o(u)$ per unit thermal fission neutron production $\left(\int_{u_c}^\infty du'\nu\Sigma_f(u')\Psi_o(B,u') = 1\right)$. To do this, Eq. (2.444) is first differentiated with respect to u and then used to remove the integral from the result, the substitution $(\Sigma_a + \Sigma_a + DB^2)\Psi_o(B,u) = \eta_o(u) + (1 + \beta(B))\chi(u)$ is made in the derivative, and an integration from lethargy o to u is performed $(\eta_o(0) = 0)$. The result is

$$\eta(u) = (1 + \beta(B)) \int_o^u du' \chi(u') \left[1 - R(u', B)\right] \exp\left[-\int_{u'}^u du'' R(u'', B)\right] . \quad \text{Eq. (2.445)}$$

By expanding this expression to first order in B^2, the approximate dependence of the slowing-down density on buckling can be seen:

$$\eta(u) \cong (1 + \beta(B)) \int_o^u du' \chi(u') p(u', u) \left[1 - B^2 \tau_A(u', u)\right] . \quad \text{Eq. (2.446)}$$

Here the resonance escape probability and age for slowing down from lethargy u' to u have been defined as

$$p(u', u) = \frac{\Sigma_H(u')}{\Sigma_H(u') + \Sigma_a(u')} \exp\left[-\int_{u'}^{u} du'' \cdot \frac{\Sigma_a(u'')}{\Sigma_H(u'') + \Sigma_a(u'')}\right] \quad \text{Eq. (2.447)}$$

$$\tau_A(u', u) = \frac{D(u')}{\Sigma_H(u') + \Sigma_a(u')} + \int_{u'}^{u} du'' \cdot \frac{D(u'')}{\Sigma_H(u'')\left(1 + \frac{\Sigma_a}{\Sigma_H}\right)^2} . \quad \text{Eq. (2.448)}$$

It will be noticed that in the Selengut-Goertzel approximation both the resonance escape probability and the age have first flight corrections associated with them, which do not appear in age diffusion theory. In hydrogenous systems, these terms are important, since the neutron can both travel appreciable distances and risk capture before any energy loss occurs.

The age given by Eq. (2.448) represents slowing down from fission into the thermal group without fast fission cycling and corresponds to the age which appears in Sect. 2.8.D.1. If group equations are used in which fast fission does not appear explicitly, the buckling dependence of the source factor $(1 + \beta(B))$ must be accounted for explicitly with the result, as in Sects. 2.8.D.2 and 2.8.D.3, that the age is augmented. In this event $\beta(B)$ may be expanded about $B^2 = 0$ as

$$\beta(B) = \beta_o - B^2\beta_2$$

so that Eq. (2.446) becomes

$$\eta(u) \cong (1 + \beta_o) \int_o^u du' \chi(u') p(u', u) \left[1 - B^2 \tau_c(u', u)\right] \quad \text{Eq. (2.449)}$$

with

$$\tau_c(u', u) = \frac{D(u')}{\Sigma_H(u') + \Sigma_a(u')} + \int_{u'}^{u} du'' \cdot \frac{D(u'')}{\Sigma_H(u'')\left(1 + \frac{\Sigma_a}{\Sigma_H}\right)^2} + \frac{\beta_2}{1 + \beta_o} . \quad \text{Eq. (2.450)}$$

In the four-factor form, Sect. 2.8.D.2, only the U^{238} fission is included in β so that the augmentation is usually small (<10 percent); in Sect. 2.8.D.3, however, all epithermal fission appears in β, and the resultant increase in age is significant.

2.9 FAST GROUP FITTED CONSTANTS IN FEW-GROUP THEORY

P. A. Ombrellaro

A. Introduction

In depletion calculations, the few-group space-dependent flux in the fast-energy range is calculated using fast few-group constants such as those described in Sect. 2.8.C. During reactor lifetime, it is necessary to account for changes in the fast group constants due to changes in the energy flux spectrum, which is directly correlated with the change in concentrations of the elements composing the medium.

Multigroup digital programs for calculating few-group constants, such as the MUFT[114] programs described in Sect. 2.8.F, can account for changes in the constants, but it is generally too expensive to incorporate such programs in the automatic group constants preparation component of depletion programs. Some of the depletion calculational models contain several hundred subregions of varying compositions, and for each subregion a set of group constants is needed for each diffusion calculation. Since for many subregions the group constants must be recomputed at each lifetime step, the calculation of few-group constants obtained using a multigroup program would require a considerable amount of computer time. Thus, in order to compute group constants more easily in depletion codes, it is necessary to rely on simple models or fitting procedures which give few-group constants with the same accuracy as those resulting from a multigroup calculation.

Two schemes for calculating fast few-group constants are described here. The first, called the fitted cross-section scheme,[128, 129] expresses the fast group constants in terms of effective microscopic cross sections. These cross sections are obtained by fitting the simple group constant formulas to the group constants obtained from a multigroup program such as MUFT.

The second scheme uses a variational method[130] to solve the energy-dependent diffusion equations based on the assumption that, for a given composition, the flux spectrum is adequately given as a linear combination of two flux base

spectra, and similarly the current spectrum is given as a linear combination of two current base spectra. Each set of base spectra for the flux and current is chosen to represent a soft and a hard spectrum. The coefficients for linearly combining the base spectra are provided by the theory and depend only on the concentrations of the elements composing the medium and the buckling B^2. Once the coefficients for combining the flux and current base spectra are obtained, the few-group constants are easily obtained.

In both schemes, the energy range from 10 Mev to 0.625 ev is represented in terms of lethargy, and few-group constants are obtained for a three-, two-, and one-group representation of the energy range. In addition to the descriptions of the fitted cross section and variational schemes, some computational results using these methods are presented.

B. Fitted Cross-Section Scheme*

1. General Formulation of the Three-and Two-Group Schemes

In the few-group schemes, the energy range from 10 Mev to 0.625 ev is expressed in terms of lethargy and is represented by three, two or one broad-lethargy groups. In the three-group scheme, the division between the first and second groups occurs at 0.821 Mev, corresponding to a lethargy of $u = 2.5$, while that between the second and third groups is at 5.53 kev, corresponding to a lethargy of $u = 7.5$. The lower energy limit of the third group is at 0.625 ev which corresponds to a lethargy of $u = 16.5884$. In the two-group scheme, the division between the first and second groups is at $u = 7.5$. Thus, the epithermal group, although represented by the third group of the three-group scheme and the second group of the two-group scheme, is the same for each scheme. Since the resonances of most elements appear in the epithermal group, it will be designated as the resonance group. In the one-group scheme, one group is chosen to represent the entire energy range from 10 Mev to 0.625 ev.

The fast-group constants employed in the few-group diffusion equations are those defined by Eq. (2.404). These are the diffusion constant D, the removal cross section Σ_r, the absorption cross section Σ_a, and the fission neutron production cross

*This type of fitted cross-section scheme for calculating fast few-group constants in depletion digital programs was first introduced by R.L.Hellens.

section $\nu\Sigma_f$. Additional parameters of interest for the criticality calculations are those given by Eq. (2.407), namely, the group age

$$\tau = \frac{D}{\Sigma_r + \Sigma_a} \qquad \text{Eq. (2.451)}$$

and the resonance escape p given by

$$p = \frac{\Sigma_r}{\Sigma_r + \Sigma_a}. \qquad \text{Eq. (2.452)}$$

In the three- and two-group schemes, a set of parameters $D_g, \Sigma_{rg}, \Sigma_{ag}, \nu\Sigma_{fg}, p_g$, and τ_g are defined for each few group g.

Using this notation, the age-to-thermal parameters for the three- and two-group schemes are defined as

$$\tau = \chi_1(\tau_1 + \tau_2 + \tau_3) + \chi_2(\tau_2 + \tau_3) \qquad \text{Eq. (2.453)}$$

in the three-group scheme, and

$$\tau = (\tau_1 + \tau_2)$$

in the two-group scheme, where χ_g is the fraction of fission neutrons emitted in group g.

In each of the few groups, the group constants $D_g, \Sigma_{rg}, \Sigma_{ag}$, and $\nu\Sigma_{fg}$ can be represented by simple equations written in terms of effective microscopic cross sections for each group g: [128, 129]

$$D_g = 3\left[\sum_i N^i \bar{\sigma}^i_{trg}\right]^{-1}$$

$$\Sigma_{rg} = \sum_i N^i \bar{\sigma}^i_{rg}$$

$$\Sigma_{ag} = \sum_i N^i \bar{\sigma}^i_{ag} \qquad \text{Eq. (2.454)}$$

$$\nu\Sigma_{fg} = \sum_i N^i (\nu\bar{\sigma}_f)^i_g$$

where N^i is the atom density for element i and the group index g is taken as $g = 1,2,3$ for the three-group scheme, and $g = 1,2$ for the two-group scheme. For each group g, the effective microscopic cross sections for element i are defined as

$$\bar{\sigma}_{trg} = \text{transport cross section}$$

$$\bar{\sigma}_{rg} = \text{removal cross section}$$

$$\bar{\sigma}_{ag} = \text{absorption cross section} \qquad \text{Eq. (2.455)}$$

$$(\nu\bar{\sigma}_f)_g = \text{fission production cross section.}$$

Because resonance absorbers are normally present in a medium, the removal and absorption macroscopic cross sections in the resonance group must be treated differently, since the removal cross section is affected by the variable energy self-shielding of the resonance absorption. Hence, the above equations do not apply. However, the removal and absorption cross sections in the resonance group can be obtained for media containing two resonance absorbers by the formula

$$(\Sigma_{r3} + \Sigma_{a3}) \frac{(a + p_3)}{(a + 1)} = (\Sigma'_{r3} + \Sigma_{a3}) \qquad \text{Eq. (2.456)}$$

Since the epithermal groups in both the three- and two-group schemes are chosen to be the same, Eq. (2.456) applies to both. In this equation, p_3 is the resonance escape probability, and the parameter a is a fitted constant which is determined empirically. The total macroscopic cross section on the right-hand side of Eq. (2.456) is defined as $(\Sigma'_{r3} + \Sigma'_{a3}) = \sum_i N^i(\bar{\sigma}'^i_{r3} + \bar{\sigma}'^i_{a3})$, where $\bar{\sigma}'^i_{r3}$ and $\bar{\sigma}'^i_{a3}$ are fitted smooth (nonresonance) microscopic removal and absorption cross sections for element i. Here smooth cross sections (indicated by primes) refer to cross sections which do not include resonance effects.

2. Resonance Group Removal and Absorption Cross Sections

To show the origin of Eq. (2.456), consider the three-group critical equation given by Eq. (2.406):

$$(D_1 B^2 + \Sigma_{r1} + \Sigma_{a1})\,\Phi_1 = \chi_1$$

$$(D_2 B^2 + \Sigma_{r2} + \Sigma_{a2})\Phi_2 = \chi_2 + \Sigma_{r1}\,\Phi_1 \qquad \text{Eq. (2.457)}$$

$$(D_3 B^2 + \Sigma_{r3} + \Sigma_{a3})\,\Phi_3 = \Sigma_{r2}\,\Phi_2$$

where the fission source is taken as unity, and χ_1, χ_2 represent the fraction of the integrated fission spectrum in groups one and two. For small values of B^2, the leakage term D_3B^2 is small and can be neglected. Thus, for the third group, where resonances occur, the group equation becomes

$$(\Sigma_{r3} + \Sigma_{a3})\Phi_3 = \Sigma_{r2}\,\Phi_2 \qquad \text{Eq. (2.458)}$$

which from Eq. (2.452) can be written as

$$\Sigma_{r3} = p_3\Sigma_{r2}\,\Phi_2/\Phi_3\,. \qquad \text{Eq. (2.459)}$$

From Eq. (2.452) it follows also that

$$\Sigma_{a3} = \frac{(1-p_3)}{p_3}\Sigma_{r3} \qquad \text{Eq. (2.460)}$$

It is clear from these equations that in order to calculate Σ_{r3} and Σ_{a3}, it is necessary to know p_3, Σ_{r2}, Φ_2, and Φ_3. However, a simple procedure for calculating Σ_{r3} and Σ_{a3} is the following.

The few-group parameters in any given group depend only on the source in the group and the removal rate out of the previous group. This can be seen from Eq. (2.457) where, for example, the second group constants and flux depend only on the source χ_2 of the group and the removal rate out of the first group given by $\Sigma_{r1}\Phi_1$. On this basis, consider the three-group constants for a given medium obtained from a MUFT calculation for the case in which resonance effects are present and, again, for the case in which the resonance effects are suppressed. One then finds that the group constants in groups one and two for the two cases are the same; however, the group constants in the third group, where resonances occur, are different. On the basis that D_3B^2 can be neglected, let Eq. (2.458) represent the third group equation for the case in which resonance effects are present, and

$$(\Sigma'_{r3} + \Sigma'_{a3})\Phi'_3 = \Sigma_{r2}\,\Phi_2 \qquad \text{Eq. (2.461)}$$

the equation for the case in which the resonance effects are suppressed. In both cases, the second group removal rate $\Sigma_{r2}\Phi_2$ is the same; therefore, one can set Eq. (2.458) equal to Eq. (2.461), and the resulting equation can be written as

$$\frac{\Sigma_{r3}}{p_3}\Phi_3 = (\Sigma'_{r3} + \Sigma'_{a3})\Phi'_3\,. \qquad \text{Eq. (2.462)}$$

Since Σ'_{r3} and Σ'_{a3} do not include the resonance effects, they can be defined, as in Eq. (2.454), in terms of the fitted effective microscopic cross sections $\bar{\sigma}^{i}_{r3}$ and $\bar{\sigma}^{a}_{a3}$.

It is convenient to eliminate the fluxes in Eq. (2.462) by setting

$$\Phi_3 = \frac{(\underline{a} + p_3)}{(\underline{a} + 1)} \Phi'_3 \qquad \text{Eq. (2.463)}$$

where $\underline{a}$ is a parameter and p_3 is the resonance escape. The reason is that for a given medium the difference between Φ_3 and Φ'_3 is due to the resonance effects which are reflected in the resonance escape p_3. One would then expect that the ratio of Φ_3/Φ'_3 would, in some way, vary with p_3. The assumption here is that Φ_3/Φ'_3 varies linearly with p_3, a quantity which is easily obtained from multigroup calculations when fitting the parameter $\underline{a}$. Furthermore, one can arrive at such a formula from Eq. (2.462). From Eqs. (2.459), (2.460), and (2.462), one can define the absorption rate $\Sigma_{a3}\Phi_3$ as that given by

$$\Sigma_{r3} \frac{(1 - p_3)}{p_3} \Phi_3 = (\Sigma'_{r3} + \Sigma'_{a3})(1 - p_3)\Phi'_3 . \qquad \text{Eq. (2.464)}$$

An approximately symmetric form of this equation is

$$\Phi_3 = \frac{\left[(\Sigma'_{r3} + \Sigma'_{a3}) - p_3(\Sigma'_{r3} + \Sigma'_{a3}) + \Sigma_{r3} - \Sigma_{r3}\right]}{\left[\frac{\Sigma_{r3}}{p_3} - \Sigma_{r3} + (\Sigma'_{r3} + \Sigma'_{a3}) - (\Sigma'_{r3} + \Sigma'_{a3})\right]} \Phi'_3 . \qquad \text{Eq. (2.465)}$$

By rearranging terms and factoring $\left[\frac{\Sigma_{r3}}{p_3} - (\Sigma'_{r3} + \Sigma'_{a3})\right]$ out of both the numerator and denominator, the resulting equation is that given by Eq. (2.463) with the parameter $\underline{a}$ defined as

$$\underline{a} = \frac{\left[(\Sigma'_{r3} + \Sigma'_{a3}) - \Sigma_{r3}\right]}{\left[\frac{\Sigma_{r3}}{p_3} - (\Sigma'_{r3} + \Sigma'_{a3})\right]} .$$

Thus, by substituting Φ_3 given by Eq. (2.463) into (2.462), one obtains

$$\frac{\Sigma_{r3}}{p_3}\frac{[\underline{a}+p_3]}{[\underline{a}+1]} = (\Sigma'_{r3}+\Sigma'_{a3}) \qquad \text{Eq. (2.466)}$$

which is an equation of the form given by Eq. (2.456).

If the third group parameters obtained from MUFT calculations are substituted into Eq. (2.466), one will find that the parameter $\underline{a}$ varies with both metal-to-water volume ratio and concentration of the resonance elements. Thus, an attempt to fit the parameter $\underline{a}$ so as to arrive at one value of $\underline{a}$ which would hold for any given composition would be difficult. One can, however, obtain a fitted value of $\underline{a}$ by limiting the number of resonance elements to one or two. Since the consideration of one resonance element is rather limiting, the two-resonance element case will be discussed here. Another aspect of the problem is self-shielding factors which accommodate changes in the resonance integrals produced by lumping and Doppler effects.[89] In MUFT, for example, one finds that the third group constants for a given medium show a variation with self-shielding and this variation is reflected in the parameter $\underline{a}$ and the resonance escape p_3. If the same self-shielding factor L is allowed for all resonance elements, one can in principle associate a fitted parameter $\underline{a}$ with each choice of L. However, the changes in the group constants produced by changes in concentration of the resonance elements are much greater than those produced by varying the self-shielding factor. Since the fitted value of $\underline{a}$ is really an average value of the parameters $\underline{a}$ resulting from changes in metal-to-water volume ratios, any sensitivity of the fitted $\underline{a}$ on self-shielding would be lost, and a self-shielding factor L equal to unity in the MUFT calculations is quite adequate. The subsequent treatment of resonances will be limited to media containing U^{238} and zirconium as resonance elements. Since p_3 is a product of resonance escape probabilities for each element in a medium, it is only natural to separate out of this quantity the resonance contributions, so that the remaining contributions can be calculated using fitted cross sections. The resonance contributions would then be obtained from other methods. In order to do this, the absorption cross section Σ_{a3} is defined as

$$\Sigma_{a3} = \Sigma_{aS3} + \Sigma_{aR3}\,. \qquad \text{Eq. (2.467)}$$

Here Σ_{aS3} is a smooth (nonresonance) macroscopic absorption cross section which is expressed as

$$\Sigma_{aS3} = \sum_i N^i \bar{\sigma}^i_{S3} \qquad \text{Eq. (2.468)}$$

where $\bar{\sigma}^i_{S3}$ is a smooth fitted effective microscopic cross section for the i^{th} element, and Σ_{aR3} is a resonance macroscopic absorption cross section given by

$$\Sigma_{aR3} = \Sigma^{28}_{aR3} + \Sigma^{Zr}_{aR3} . \qquad \text{Eq. (2.469)}$$

In the last equation, the superscripts 28 and Zr refer to U^{238} and zirconium, respectively. On the basis of this, the resonance escape p_3 is approximated as

$$p_3 = p^{28}_{R3} p^{28}_{S3} p^{Zr}_{R3} p^{Zr}_{S3} p_{o3} \qquad \text{Eq. (2.470)}$$

where for each resonance element, p_{S3} represents a nonresonance contribution and p_{R3} represents a resonance contribution to the escape probability p_3. The quantity p_{o3} represents the contribution to p_3 due to all elements other than U^{238} and zirconium. For the discussion that follows, the subscript 3 will be omitted because the treatment of resonances applies only to the third group. In Eq. (2.470), the components are chosen as

$$p^{28}_S = \frac{\Sigma_r}{\Sigma_1} ; \quad \Sigma_1 = \Sigma_r + \Sigma^{28}_{aS} \qquad \text{Eq. (2.471)}$$

$$p^{Zr}_S = \frac{\Sigma_1}{\Sigma_2} ; \quad \Sigma_2 = \Sigma_1 + \Sigma^{Zr}_{aS} \qquad \text{Eq. (2.472)}$$

$$p^{28}_R = \frac{\Sigma_2}{\Sigma_3} ; \quad \Sigma_3 = \Sigma_2 + \Sigma^{28}_{aR} \qquad \text{Eq. (2.473)}$$

$$p^{Zr}_R = \frac{\Sigma_3}{\Sigma_4} ; \quad \Sigma_4 = \Sigma_3 + \Sigma^{Zr}_{aR} \qquad \text{Eq. (2.474)}$$

$$p_o = \frac{\Sigma_4}{\Sigma_5} ; \quad \Sigma_5 = \Sigma_4 + \Sigma^o_a \qquad \text{Eq. (2.475)}$$

where Σ_a^o is given by Eq. (2.468) for all elements other than U^{238} and zirconium. The product $p_S^{28}\, p_S^{Zr}\, p_R^{28}\, p_R^{Zr}\, p_o$ then results in the definition of p given by Eq. (2.470). The motivation for this is that when these expressions are substituted into Eq. (2.466), the resulting equation will then involve only the smooth absorption cross sections, which can be calculated from the fitted microscopic cross sections, and the resonance escape probabilities p_R^{28} and p_R^{Zr}, which contain the absorption cross sections Σ_{aR}^{28} and Σ_{aR}^{Zr}. Using Eqs. (2.471) and (2.472), the expression for p given by Eq. (2.470) becomes

$$p = p_o p_R^{28} p_R^{Zr} \frac{\Sigma_r}{\Sigma_2}.$$

When this expression is substituted for p_3 in Eq. (2.466), one obtains, after rearrangement of terms, the expression

$$\frac{a\Sigma_2}{p_o} + p_R^{28} p_R^{Zr} \Sigma_r = p_R^{28} p_R^{Zr} (a+1)(\Sigma_r' + \Sigma_a'). \qquad \text{Eq. (2.476)}$$

It is desirable to eliminate p_o from this equation, since this also contains Σ_{aR}^{28} and Σ_{aR}^{Zr}. To do this, one calculates from the product $p_R^{28}\, p_R^{Zr}$ given by Eqs. (2.473) and (2.474):

$$\Sigma_4 = \frac{\Sigma_2}{p_R^{28} p_R^{Zr}}. \qquad \text{Eq. (2.477)}$$

Substituting this expression into the denominator of Eq. (2.475), one obtains, after rearrangement of terms,

$$\left[\Sigma_2 + p_R^{28} p_R^{Zr} \Sigma_a^o\right] = \frac{\Sigma_4 p_R^{28} p_R^{Zr}}{p_o}. \qquad \text{Eq. (2.478)}$$

The numerator of this expression is from Eq. (2.477) just Σ_2, so that Eq. (2.478) becomes

$$\left[\Sigma_2 + p_R^{28} p_R^{Zr} \Sigma_a^o\right] = \frac{\Sigma_2}{p_o}. \qquad \text{Eq. (2.479)}$$

Substituting Eq. (2.479) into Eq. (2.476) gives

$$a\left[\Sigma_2 + p_R^{28}\, p_R^{Zr}\, \Sigma_a^o\right] + p_R^{28}\, p_R^{Zr}\, \Sigma_r = p_R^{28}\, p_R^{Zr}\, (a+1)(\Sigma_r' + \Sigma_a') \,. \qquad \text{Eq. (2.480)}$$

From this equation and the definiton of $\Sigma_2 = \Sigma_r + \Sigma_{aS}^{28} + \Sigma_{aS}^{Zr}$, Σ_r can be determined as

$$\Sigma_r = \frac{(a+1)\, p_R^{28}\, p_R^{Zr}\, (\Sigma_r' + \Sigma_a') - a\left(\Sigma_{aS}^{28} + \Sigma_{aS}^{Zr} + p_R^{28}\, p_R^{Zr}\, \Sigma_a^o\right)}{\left[a + p_R^{28}\, p_R^{Zr}\right]} \,. \qquad \text{Eq. (2.481)}$$

Since fitted cross sections for Σ_{aR}^{28} and Σ_{aR}^{Zr} cannot be easily obtained, the quantities p_R^{28} and p_R^{Zr} can be determined from the method given in Sect. 2.9.B.4. Thus Σ_r in the third group is determined from macroscopic cross sections which can be calculated from fitted effective microscopic cross sections, the fitted constant a, and the resonance escape probabilities which can be determined from the method described in Sect. 2.9.B.4. Once Σ_r is determined, the macroscopic absorption cross section in the third group can also be obtained. From Eq. (2.477) and the definition $\Sigma_4 = \Sigma_r + \Sigma_{aS}^{28} + \Sigma_{aS}^{Zr} + \Sigma_{aR}^{28} + \Sigma_{aR}^{Zr}$, the total absorption for U^{238} and zirconium is

$$\Sigma_{aS}^{28} + \Sigma_{aS}^{Zr} + \Sigma_{aR}^{28} + \Sigma_{aR}^{28} = \left(\frac{\Sigma_2}{p_R^{28}\, p_R^{Zr}} - \Sigma_r\right) . \qquad \text{Eq. (2.482)}$$

If the macroscopic absorption cross section Σ_a^o is added to this equation, one obtains the macroscopic absorption cross section in the third group as

$$\Sigma_a = \Sigma_a^o + \frac{\left(\Sigma_r + \Sigma_{aS}^{28} + \Sigma_{aS}^{Zr} - p_R^{28}\, p_R^{Zr}\, \Sigma_r\right)}{p_R^{28}\, p_R^{Zr}} \,. \qquad \text{Eq. (2.483)}$$

3. *Calculational Procedures*

The pure element effective microscopic cross sections given in Eq. (2.454) and (2.455) are obtained by the following

procedure. For a binary mixture of water and a metal element* i, one can define the group constants, in group g as

$$\Sigma_{trg} = [3\,D_g]^{-1} = \frac{\Sigma^w_{trg}}{1+S} + \frac{S}{1+S}\,\Sigma_{tr,g}$$

$$\Sigma_{rg} = \frac{\Sigma^w_{rg}}{1+S} + \frac{S}{1+S}\,\Sigma^i_{rg}$$

$$\Sigma_{ag} = \frac{\Sigma^w_{ag}}{1+S} + \frac{S}{1+S}\,\Sigma^i_{ag} \qquad \text{Eq. (2.484)}$$

$$(\nu\Sigma_f)_g = \frac{S}{1+S}\,(\nu\Sigma_f)^i_g .$$

These formulas are then fitted to group constants resulting from multigroup calculations for binary mixtures of metal and water. In these equations, the metal-to-water volume ratio, S, is chosen as the variable, and Σ^w_g and Σ^i_g are the macroscopic cross sections for water and metal, respectively. The formulas for Σ_{rg}, Σ_{ag} and $(\nu\Sigma_{fg})$ are also used to determine the third group fission production cross section, the smooth removal and absorption cross sections, and the smooth absorption cross sections for U^{238} and zirconium. A least squares fitting is done of the coefficients Σ^w_g and Σ^i_g to the few-group constants resulting from multigroup calculations. In order to show the procedure, consider the fitting of the removal cross section. Let Σ^k_{rg}, $(k = 1 \ldots n)$, represent in group g a set of removal cross sections for a binary mixture of the element i and water corresponding to a set of metal-to-water volume ratios S_k, $(k = 1 \ldots n)$. From the n values of Σ^k_{rg} obtained from multigroup calculations one constructs, using Eq. (2.484), the mean square deviation ϵ^2 given by

$$\epsilon^2 = \frac{1}{n}\sum_{k=1}^{n}\left(\frac{\Sigma^w_{rg}}{1+S_k} + \frac{S_k}{1+S_k}\,\Sigma^i_{rg} - \Sigma^k_{rg}\right)^2 . \qquad \text{Eq. (2.485)}$$

The coefficients Σ^w_{rg} and Σ^i_{rg} are then determined by minimizing this expression with respect to each of these coefficients.

*Any element other than hydrogen and oxygen is here referred to as a metal element.

Thus, on differentiating Eq. (2.485) with respect to Σ_{rg}^{w} the resulting equation is

$$\Sigma_{rg}^{w} \sum_{k=1}^{n} \left(\frac{1}{1+S_k}\right)^2 + \Sigma_{rg}^{i} \sum_{k=1}^{n} \frac{S_k}{(1+S_k)^2} = \sum_{k=1}^{n} \left(\frac{\Sigma_{rg}^{k}}{1+S_k}\right). \quad \text{Eq. (2.486)}$$

Similarly, by differentiating Eq. (2.485) with respect to Σ_{rg}^{i}, one obtains

$$\Sigma_{rg}^{w} \sum_{k=1}^{n} \frac{S_k}{(1+S_k)^2} + \Sigma_{rg}^{i} \sum_{n=1}^{n} \left(\frac{S_k}{1+S_k}\right)^2 = \sum_{k=1}^{n} \Sigma_{rg}^{k} \frac{S_k}{(1+S_k)}. \quad \text{Eq. (2.487)}$$

From these two equations, the coefficients Σ_{rg}^{w} and Σ_{rg}^{i} are determined as

$$\Sigma_{rg}^{w} = \frac{\left[\left(\sum_{k=1}^{n} \frac{S_k}{(1+S_k)^2}\right)\left(\sum_{k=1}^{n} \Sigma_{rg}^{k} \frac{S_k}{(1+S_k)}\right) - \left(\sum_{k=1}^{n} \left(\frac{S_k}{1+S_k}\right)^2\right)\left(\sum_{k=1}^{n} \frac{\Sigma_{rg}^{k}}{1+S_k}\right)\right]}{\left[\left(\sum_{k=1}^{n} \frac{S_k}{(1+S_k)^2}\right)^2 - \left(\sum_{k=1}^{n} \left(\frac{S_k}{1+S_k}\right)^2\right)\left(\sum_{k=1}^{n} \left(\frac{1}{1+S_k}\right)^2\right)\right]} \quad \text{Eq. (2.488)}$$

$$\Sigma_{rg}^{i} = \frac{\left[\left(\sum_{k=1}^{n} \Sigma_{rg}^{k} \frac{S_k}{1+S_k}\right)\left(\sum_{k=1}^{n} \left(\frac{1}{1+S_k}\right)^2\right) - \left(\sum_{k=1}^{n} \frac{S_k}{(1+S_k)^2}\right)\left(\sum_{k=1}^{n} \frac{\Sigma_{rg}^{k}}{(1+S_k)}\right)\right]}{\left[\left(\sum_{k=1}^{n} \left(\frac{S_k}{1+S_k}\right)^2\right)\left(\sum_{k=1}^{n} \left(\frac{1}{1+S_k}\right)^2\right) - \left(\sum_{k=1}^{n} \frac{S_k}{(1+S_k)^2}\right)^2\right]} \quad \text{Eq. (2.489)}$$

The effective microscopic cross section $\bar{\sigma}_{rg}^{i}$ for the i^{th} element is then obtained by dividing Σ_{rg}^{i}, given by Eq. (2.489), by the pure element atom density N^i

$$\bar{\sigma}_{rg}^{i} = \frac{\Sigma_{rg}^{i}}{N^i}.$$

The fitted removal cross section for water Σ_{rg}^{w} is separated into its component hydrogen and oxygen cross sections. To

do this, it is necessary to obtain from multigroup calculations for pure hydrogen a set of removal cross sections corresponding to various atom densities of hydrogen. These atom densities are chosen as those corresponding to the various S_k values used in determining Σ_{rg}^{w}. For hydrogen, the formulas corresponding to Eq. (2.454) are

$$\begin{aligned} \Sigma_{trg} &= N^H \bar{\sigma}_{trg}^H \\ \Sigma_{rg} &= N^H \bar{\sigma}_{rg}^H \\ \Sigma_{ag} &= N^H \bar{\sigma}_{ag}^H \end{aligned} \qquad \text{Eq. (2.490)}$$

and those corresponding to Eq. (2.484) are

$$\begin{aligned} \Sigma_{trg} &= \frac{\Sigma_{trg}^H}{1+S} \\ \Sigma_{rg} &= \frac{\Sigma_{rg}^H}{1+S} \\ \Sigma_{ag} &= \frac{\Sigma_{ag}^H}{1+S}. \end{aligned} \qquad \text{Eq. (2.491)}$$

The microscopic fitted removal cross section for hydrogen is determined by making a least squares fit of Σ_{rg} given by Eq. (2.491) to the removal cross sections Σ_{rg}^k for hydrogen obtained from multigroup calculations. The fitting procedure gives

$$\Sigma_{rg}^H = \sum_{k=1}^{n} \frac{\Sigma_{rg}^k}{(1+S_k)} \Bigg/ \sum_{k=1}^{n} \left(\frac{1}{1+S_k}\right)^2. \qquad \text{Eq. (2.492)}$$

The microscopic removal cross section $\bar{\sigma}_{rg}^H$ is then obtained from $\bar{\sigma}_{rg}^H = \Sigma_{rg}^H / N^H$, where N^H is the normal atom density for hydrogen. Once $\bar{\sigma}_{rg}^H$ is determined, the microscopic removal cross section for oxygen $\bar{\sigma}_{rg}^O$ is calculated from

$$\bar{\sigma}_{rg}^O = \frac{\Sigma_{rg}^w}{N^O} - 2\bar{\sigma}_{rg}^H$$

where N^O is the normal atom density of oxygen. The microscopic cross sections $\bar{\sigma}_{trg}^i$, $\bar{\sigma}_{ag}^i$, and $(\nu\bar{\sigma}_f)_g^i$ are determined in the

same manner. In Table 2.7 are presented fitted microscopic cross sections for hydrogen, oxygen, zirconium, U^{235}, U^{238}, carbon, B^{10}, and iron obtained by the least squares method. The cross sections were calculated using the P_1 three- and two-group constants obtained from the MUFT–4 program described in Sect. 2.8.F for binary mixtures of metal and water with S varying (except for uranium and boron 10) from 0 to 2.5 and a buckling $B^2 = 0.0025\ \text{cm}^{-2}$. The buckling B^2 was chosen small to obtain essentially infinite medium cross sections.

The fitted parameter $\underline{a}$ is obtained by making a least squares fit of the formula given by Eq. (2.466) to the group constants obtained from multigroup calculations for mixtures of water, U^{238}, and zirconium. For these cases, the metal-to-water volume ratio is varied, but the relative concentrations of zirconium and U^{238} are held fixed. For a given metal-to-water volume ratio, let Σ_r^k and p_k represent the removal cross section and resonance escape for the case in which resonance effects are included, and let $(\Sigma'_{rk} + \Sigma'_{ak})$ represent the total cross section for the case in which resonance effects are suppressed. From Eq. (2.466), the mean square deviation for n choices of S is given by

$$\epsilon^2 = \frac{1}{n} \sum_{k=1}^{n} \left[\frac{\Sigma_r^k}{p_k} \frac{(\underline{a} + p_k)}{(\underline{a} + 1)} - \left(\Sigma'_{ak} + \Sigma'_{rk}\right) \right]^2 . \qquad \text{Eq. (2.493)}$$

Differentiating Eq. (2.493) with respect to $\underline{a}$ and solving for the parameter $\underline{a}$, one finds

$$\underline{a} = \frac{\displaystyle\sum_{k=1}^{n} \left[\left(\Sigma'_{rk} + \Sigma'_{ak}\right) \Sigma_r^k \frac{(1 - p_k)}{p_k} - \left(\Sigma_r^k\right)^2 \frac{(1 - p_k)}{p_k} \right]}{\displaystyle\sum_{k=1}^{n} \left[\frac{\left(\Sigma_r^k\right)^2}{p_k} \frac{(1 - p_k)}{p_k} - \left(\Sigma'_{rk} + \Sigma'_{ak}\right) \Sigma_r^k \frac{(1 - p_k)}{p_k} \right]} .$$

However, from Eq. (2.460), $\Sigma_a = \frac{(1-p)}{p} \Sigma_r$, and the equation for $\underline{a}$ reduces to

$$\underline{a} = \frac{\displaystyle\sum_{k=1}^{n} \left[\left(\Sigma'_{rk} + \Sigma'_{ak}\right) \Sigma_a^k - \Sigma_r^k \Sigma_a^k \right]}{\displaystyle\sum_{k=1}^{n} \left[\frac{\Sigma_r^k \Sigma_a^k}{p_k} - \left(\Sigma'_{rk} + \Sigma'_{ak}\right) \Sigma_a^k \right]} . \qquad \text{Eq. (2.494)}$$

TABLE 2.7 — THREE FAST GROUP FITTED MICROSCOPIC CROSS SECTIONS (barns)

Element	$\bar{\sigma}_{trg}$	$\bar{\sigma}_{rg}$	$\bar{\sigma}_{aSg}$	$(\bar{\nu}\bar{\sigma}_f)_g$	ν
Hydrogen					
Group 1	1.593	1.498	0.00004		
Group 2	2.562	2.175	0.00019		
Group 3	6.295	2.215	0.01400		
Oxygen					
Group 1	1.727	0.292	0.0314		
Group 2	4.128	0.052	0.0000		
Group 3	4.110	0.054	0.0003		
Zirconium					
Group 1	3.877	0.6470	0.0572		
Group 2	7.716	0.0006	0.0135		
Group 3	6.522	0.0000	0.0076		
Uranium-235					
Group 1	4.168	0.0627	1.1070	3.640	2.79
Group 2	7.270	0.0000	2.4070	4.692	2.48
Group 3	20.830	0.0000	35.950	60.980	2.46
Uranium-238					
Group 1	7.354	3.056	0.4980	1.210	2.71
Group 2	9.444	0.000	0.3120	0.000	0.00
Group 3	9.163	0.000	0.3250	0.000	0.00
Carbon					
Group 1	1.713	0.238	0.0001		
Group 2	3.867	0.118	0.0000		
Group 3	4.815	0.074	0.0000		

TABLE 2.7 — THREE FAST GROUP FITTED MICROSCOPIC CROSS SECTIONS (barns) (Continued)

Element	$\bar{\sigma}_{trg}$	$\bar{\sigma}_{rg}$	$\bar{\sigma}_{aSg}$	$(\bar{\nu}\bar{\sigma}_f)_g$	ν
Boron					
Group 1	2.59	0.352	0.4290		
Group 2	8.04	0.000	2.1410		
Group 3	152.00	0.000	152.00		
Iron					
Group 1	2.418	0.507	0.0012		
Group 2	1.448	3.680	0.0000		
Group 3	0.063	9.680	0.0000		
TWO GROUP CROSS SECTIONS (barns)					
Hydrogen					
Group 1	1.933	0.995	0.0001		
Group 2	6.295	2.215	0.0140		
Oxygen					
Group 1	2.524	0.183	0.0159		
Group 2	4.110	0.054	0.0003		
Zirconium					
Group 1	5.627	0.169	0.0322		
Group 2	6.522	0.000	0.0076		
Uranium-235					
Group 1	5.089	0.000	1.909	4.152	2.61
Group 2	20.830	0.000	35.950	60.980	2.46
Uranium-238					
Group 1	9.344	0.749	0.406	0.613	2.73
Group 2	9.163	0.000	0.325	0.000	0.00

TABLE 2.7 — THREE FAST GROUP FITTED MICROSCOPIC CROSS SECTIONS (barns) (Continued)

Element	$\bar{\sigma}_{trg}$	$\bar{\sigma}_{rg}$	$\bar{\sigma}_{aSg}$	$(\bar{\nu}\bar{\sigma}_f)_g$	ν
Carbon					
Group 1	2.450	0.106	0.0001		
Group 2	4.815	0.074	0.0000		
Boron					
Group 1	3.236	0.000	1.262		
Group 2	152.000	0.000	152.000		
Iron					
Group 1	3.203	0.120	0.0005		
Group 2	0.063	9.680	0.00000		

4. *Resonance Escape Probabilities for Uranium - 238 and Zirconium*

It will now be shown that the resonance escape probabilities p_R^{28} and p_R^{Zr} given by Eqs. (2.473) and (2.474) can be calculated from the homogeneous resonance integrals of U^{238} and zirconium.

The third group equation given by Eq. (2.458) is equivalent to

$$\int_{u_{n-1}}^{u_n} \Sigma_{aS}(u)\,\psi_o(u)du + \int_{u_{n-1}}^{u_n} \Sigma_{aR}(u)\,\psi_o(u)du + \eta_o(u_n) + \sum_i q_o^i(u_n) \qquad \text{Eq. (2.495)}$$

$$= \eta_o(u_{n-1}) + \sum_i q_o^i(u_{n-1})$$

with $u_n = 16.5884$ and $u_{n-1} = 7.5$. This equation results when Eq. (2.423), with the leakage, the inelastic scattering, the fission spectrum and δ set equal to zero, is integrated over the lethargy band of the third group. Here η_o and q_o^i are the hydrogen and heavy element isotropic slowing-down densities. For simplicity, assume that all absorptions other than U^{238} and zirconium can be neglected. In Sect. 2.8.E, it is shown that if the group contains resonances, the resonance absorption rate

is written as the sum of the hydrogen and heavy element slowing-down densities at the upper energy end of the group multiplied by $(1-p)$, the resonance capture probability of the group. Thus,

$$\int_{u_{n-1}}^{u_n} \Sigma_{aR}(u)\,\psi_o(u)\,du = (1-p)\left[\eta_o(u_{n-1}) + \sum_i q_o^i(u_{n-1})\right] \qquad \text{Eq. (2.496)}$$

where p is the resonance escape probability. From Eqs. (2.495) and (2.496), it follows that

$$p = \frac{\displaystyle\int_{u_{n-1}}^{u_n} \Sigma_{aS}(u)\,\psi_o(u)\,du + \eta_o(u_n) + \sum_i q_o^i(u_n)}{\eta_o(u_{n-1}) + \displaystyle\sum_i q_o^i(u_{n-1})}. \qquad \text{Eq. (2.497)}$$

Substituting Eq. (2.495) for the denominator of Eq. (2.497), and using the definitions

$$\Phi_3 = \int_{u_{n-1}}^{u_n} \psi_o(u)\,du$$

$$\Sigma_{aS}^{28} + \Sigma_{aS}^{Zr} = \int_{u_{n-1}}^{u_n} \Sigma_{aS}(u)\psi_o(u)\,du \Big/ \Phi_3$$

$$\Sigma_{aR}^{28} + \Sigma_{aR}^{Zr} = \int_{u_{n-1}}^{u_n} \Sigma_{aR}(u)\psi_o(u)\,du \Big/ \Phi_3$$

$$\Sigma_r = \frac{\left[\eta_o(u_n) + \displaystyle\sum_i q_o^i(u_n)\right]}{\Phi_3}$$

one obtains

$$p = \frac{\Sigma_{aS}^{28} + \Sigma_{aS}^{Zr} + \Sigma_r}{\Sigma_{aS}^{28} + \Sigma_{aS}^{Zr} + \Sigma_{aR}^{28} + \Sigma_{aR}^{Zr} + \Sigma_r} \qquad \text{Eq. (2.498)}$$

which is the expression for the product $p_R^{28} p_R^{Zr}$ obtained from the product of Eqs. (2.473) and (2.474). A similar procedure is used to establish the individual expressions for p_R^{28} and p_R^{Zr}.

Now consider the j^{th} resonance (i.e., a resonance of U^{238} or zirconium) to lie within a small lethargy interval $u_g - u_{g-1}$ within the third group. The homogeneous resonance integral $(RI)_{jg}$ is there evaluated by integrating the $1/E$ flux shape within the group over a Breit-Wigner single resonance shape, assuming that the scattering out of the group is due to hydrogen alone. Then by definition let

$$p^{jg} = e^{-(RI)_{jg}} = e^{-\int_{u_{g-1}}^{u_g} \frac{\Sigma_a}{\Sigma_a + \Sigma_{sH}} du} \qquad \text{Eq. (2.499)}$$

where Σ_{sH} is the scattering cross section for hydrogen and Σ_a contains contribution only from the j^{th} resonance in the g^{th} group. It is convenient to rewrite Eq. (2.499) approximately as

$$p^{jg} = e^{-\int_{-\infty}^{\infty} \frac{dE}{E\left[1 - \frac{R\sigma_{sH}}{\sigma_a}\right]}} \qquad \text{Eq. (2.500)}$$

with $R = N^H/N^a$ representing the number of hydrogen atoms per absorber (U^{238} or zirconium) atom. With $\sigma_a(E)$ represented by the single level Breit-Wigner formula, direct evaluation of the integral is possible. Thus,

$$\sigma_a = \frac{\sigma_o \Gamma_\gamma v_o}{\Gamma v} \Big/ \left[1 + (E - E_o)^2 \Big/ (\Gamma/2)^2\right] \qquad \text{Eq. (2.501)}$$

with

Γ_γ = gamma width of the level
$\Gamma = \Gamma_\gamma + \Gamma_n$ representing the total width
E_o = resonance energy
$\sigma_o = 4\pi \lambda\!\!\!^{-2}_o g \Gamma_n / \Gamma$.

Substituting Eq. (2.501) into Eq. (2.500), and integrating over the resonance keeping $1/Ev$ constant at $1/E_o v_o$, the resonance integral becomes

$$(RI)_{jg} = \int_{-\infty}^{\infty} \frac{\Sigma_a du}{\Sigma_a + \Sigma_{sH}} = \frac{\pi}{2} \frac{\sigma_o \Gamma_\gamma}{E_o R \sigma_{sH}} \Big/ \sqrt{1 + \frac{\sigma_o \Gamma_\gamma}{R\sigma_{sH}\Gamma}}. \qquad \text{Eq. (2.502)}$$

In general, the group g may contain several resonances; then the resonance escape p_g for the group is given by $p_g = \prod_j p^{jg}$ The total resonance escape over all multigroups g is given by

$$p_R = \prod_g p_g = e^{-\sum_j (RI)_j} . \qquad \text{Eq. (2.503)}$$

Now let k represent any one of the resonance levels of U^{238} and ℓ any one of the resonance levels of zirconium. From Eq. (2.503), it follows that

$$p_R = p_R^{28} p_R^{Zr} = e^{-\left[\sum_k (RI)_k^{28} + \sum_\ell (RI)_\ell^{Zr}\right]}$$

so that

$$p_R^{28} = e^{-\sum_k (RI)_k^{28}}$$

$$p_R^{Zr} = e^{-\sum_\ell (RI)_\ell^{Zr}} . \qquad \text{Eq. (2.504)}$$

For convenience, the resonance integral given by Eq. (2.502) is written

$$(RI)_j = \frac{\pi}{2} \frac{N_a}{N^H} \frac{m_j}{\sigma_{sH}} \Big/ \sqrt{1 + \frac{r^j N_a}{N^H \sigma_{sH}}} \qquad \text{Eq. (2.505)}$$

with $m^j = \sigma_c^j \Gamma_\gamma^j / E_o^j$ and $r^j = \sigma_o^j \Gamma_\gamma^j / \Gamma^j$. For simplicity in calculating the $(RI)_j$, the scattering cross section for hydrogen is taken as $\sigma_{sH} = 20$ barns, a constant over the third group. The value of σ_{sH} was obtained by averaging, with a $1/E$ spectrum, the multigroup hydrogen scattering cross sections taken from a MUFT-4 library over the lethargy range of the third group. In Table 2.8 are given values of the resonance parameters m^j and r^j for U^{238} and zirconium taken from a MUFT-4 library. The parameters are identified according to the 54-group structure of MUFT-4.

TABLE 2.8 — MUFT-4 RESONANCE PARAMETERS

Zirconium (Element Number 103)		
Group Number	m^{ℓ}	r^{ℓ}
26	0.00165	1.53
27	0.0044	3.12
28	0.0137	7.14
30	0.0696	22.80
31	0.348	71.0

URANIUM-238 (Element Number 120)		
Group Number	m^{k}	r^{k}
29	0.074418	172.2
29	0.059908	269.38
29	0.066207	282.89
29	0.045295	682.37
29	0.078844	577.98
29	0.062423	633.82
29	0.074706	413.16
29	0.08095	725.91
30	0.093348	829.63
30	0.12758	561.20
30	0.10171	1002.6
30	0.12635	847.1
30	0.11623	1038.9
30	0.1540	1054.2
30	0.15779	1250.3
30	0.061802	1147.0
31	0.1149	1470.0
31	0.13664	1604.5

TABLE 2.8 — MUFT-4 RESONANCE PARAMETERS (Continued)

URANIUM-238 (Element Number 120) (Continued)

Group Number	m^k	r^k
31	0.1330	1060.0
31	0.026261	379.32
31	0.30184	1616.0
31	0.026145	318.13
31	0.29617	2268.1
32	0.43157	2388.9
32	0.005599	95.599
32	0.5848	2645.5
32	1.086	2778.3
32	1.3893	1677.8
33	0.26886	2612.7
33	0.09649	533.11
34	1.702	5507.8
34	3.9884	475.36
35	0.02599	94.777
35	0.77661	2358.9
36	6.4250	9906.5
39	28.351	17683.0
41	39.616	24469
44	0.03552	14.728
45	82.665	20853

5. *One-Group Scheme**

The one fast-group constants are calculated using the three fast-group fitted constants. The group equations for three fast groups are given by Eq. (2.457). If these equations are added, the result is

$$B^2 \sum_{g=1}^{3} D_g \Phi_g + \Sigma_{r3} \Phi_3 + \sum_{g=1}^{3} \Sigma_{ag} \Phi_g = 1 \qquad \text{Eq. (2.506)}$$

since $\chi_1 + \chi_2 =$ unity. The one group constants are then defined as

$$D = \sum_{g=1}^{3} D_g \Phi_g \Big/ \sum_{g=1}^{3} \Phi_g$$

$$\Sigma_r = \Sigma_{r3} \Phi_3 \Big/ \sum_{g=1}^{3} \Phi_g \qquad \text{Eq. (2.507)}$$

$$\Sigma_a = \sum_{g=1}^{3} \Sigma_{ag} \Phi_g \Big/ \sum_{g=1}^{3} \Phi_g$$

$$\nu\Sigma_f = \sum_{g=1}^{3} (\nu\Sigma_f)_g \Phi_g \Big/ \sum_{g=1}^{3} \Phi_g$$

with the fluxes Φ_g determined from Eq. (2.457) as

$$\Phi_g = \frac{\chi_g - \Sigma_{r(g-1)}}{(B^2 D_g + \Sigma_{rg} + \Sigma_{ag})} \qquad \text{Eq. (2.508)}$$

*This one-group fitted cross-section scheme was first suggested by E. M. Gelbard.

where $\Sigma_{ro} = \chi_3 = 0$.

In order to calculate the one fast-group constants, one first calculates the three-group fitted constants by the method described in Sects. 2.9.B.1 and 2.9.B.2, and then uses these constants to calculate the fluxes given by Eq. (2.508). Once the fluxes are calculated, they are used to calculate the one-group constants by taking a flux-weighted average of the three-group fitted constants, as in Eq. (2.507). In Eq. (2.508), the χ's have the values

$$\chi_1 = 0.75165$$

$$\chi_2 = 0.24817$$

It has been shown in Sects. 2.9.B.1 and 2.9.B.2 that the two-group constants can be calculated directly from two-group fitted cross sections. An alternate method is provided by the reduction of the three group equations to two groups. Since the third group of the three-group scheme is the same as the second group of the two-group scheme, it is only necessary to consider the first two-group equations of Eq. (2.457). Adding the first and second group equations of Eq. (2.457), one obtains

$$B^2 \sum_{g=1}^{2} D_g \Phi_g + \Sigma_{r2} \Phi_2 + \sum_{g=1}^{2} \Sigma_{ag} \Phi_g = 1. \qquad \text{Eq. (2.509)}$$

The constants in the first group of the two-group scheme are provided by definitions similar to those of Eq. (2.507), with the exception that the summing extends from $g = 1$ to $g = 2$. For example,

$$D_1 = \sum_{g=1}^{2} D_g \Phi_g \Big/ \sum_{g=1}^{2} \Phi_g .$$

The fluxes are determined as in Eq. (2.508).

C. Computational Results

The fitted cross-section scheme was originally developed taking into account only one resonance element (U^{238}), and it was developed for the automatic group constant preparation

component of the one-dimensional burnup digital program CANDLE.[131] More recently, the scheme was extended to include two resonance elements (U^{238} and zirconium) for incorporation into the one- and two-dimensional burnup program KARE.[132] In this program, the fast-group fitted cross-section scheme is combined with the variational procedure for calculating thermal group constants described in Chap. 3, Sect. 3.7; the group constant preparation component of KARE is called FICS.

Before the fast fitted cross-section scheme was incorporated into KARE, B. Miller reported it as having been tested against a version of the MUFT-4 program. Group constants for a series of experimental cores were calculated using both the fitted cross-section scheme and MUFT-4. These were compared and then used with thermal group constants calculated by SOFOCATE,[133] a program for calculating thermal group constants, in the one-dimensional diffusion program WANDA[134] to make criticality calculations. For the test, a FORTRAN program called FIT was used to calculate the three-, two-, and one-group fast constants. This program uses the microscopic cross sections given in Table 2.7, and a value of the fitted constant $a = 0.16$.

One of the cores analyzed was Core 1 which had a metal-to-water volume ratio $S = 1.17$ and a loading $\ell = 58$ g/liter of U^{235}. In Table 2.9, the three-, two-, and one-group fitted constants for this core are compared with those obtained from MUFT-4 for a buckling $B^2 = 0.0025$ cm^{-2}. For this case, the agreement is quite good. For the cores considered, it was noted that some of the fitted constants differed from the MUFT-4 constants by as much as 6 percent; however, the WANDA calculations still resulted in reasonably good eigenvalues.

In Table 2.10, criticality results for three cores obtained from WANDA calculations based on MUFT-4-SOFOCATE constants and FIT-SOFOCATE constants are compared. The cores considered are the following:

Core 1: $S = 1.17$; $\ell = 58$ g/liter

Core 32: $S = 1.38$; $\ell = 155$ g/liter

Core 11: $S = 1.75$; $\ell = 78$ g/liter

From Table 2.10, it is noted that the four-, three-, and two-group WANDA eigenvalues obtained using fitted and SOFOCATE constants agree to within 1 percent with those obtained from using MUFT-4 and SOFOCATE constants.

TABLE 2.9 - FAST FITTED GROUP CONSTANTS COMPARED WITH MUFT 4 CONSTANTS

Core 1: $S = 1.17$, $\ell = 58$ g/liter U^{235}

Elements: Water, Zirconium, U^{235} and U^{238}; MUFT-4 $B^2 = 0.0025$ cm^{-2}

THREE-GROUP CONSTANTS

Group 1	D_g	Σ_{rg}	Σ_{ag}	$\nu\Sigma_{fg}$	τ_g	p_g	$\left(\frac{\nu\Sigma_f}{\Sigma_a}\right)_g$	τ
M	2.0399	0.065302	0.001892	0.000543	30.3585	0.971837	0.287	
F	2.0243	0.065205	0.001915	0.000552	30.1594	0.971469	0.288	
%	-0.76	-0.15	+1.2	+1.8	-0.66	-0.03	+0.35	
Group 2								
M	1.04736	0.068124	0.000677	0.000702	15.2231	0.990164	1.04	
F	1.05161	0.067762	0.000662	0.000699	15.3689	0.990324	1.06	
%	+0.41	-0.53	-2.2	-0.49	+0.96	+0.02	+2.0	
Group 3								
M	0.821397	0.066222	0.007664	0.009243	11.1171	0.896268	1.206	49.1545
F	0.829286	0.067962	0.007578	0.009080	10.9781	0.899682	1.198	49.0116
%	+0.96	+2.9	-1.1	-1.8	-1.25	+0.38	-0.66	-0.29

TABLE 2.9 — FAST FITTED GROUP CONSTANTS COMPARED WITH MUFT 4 CONSTANTS (Continued)

Core 1: S = 1.17, ℓ = 58 g/liter U^{235}

Elements: Water, Zirconium, U^{235} and U^{238}; MUFT 4 B^2 = 0.0025 cm^{-2}

TWO-GROUP CONSTANTS

Group 1	D_g	Σ_{rg}	Σ_{ag}	$\nu\Sigma_{fg}$	τ_g	p_g	$\left(\frac{\nu\Sigma_f}{\Sigma_a}\right)_g$	τ
M	1.48877	0.037827	0.001217	0.000631	38.1301	0.968822	0.5185	
F	1.47373	0.037245	0.001244	0.000624	38.2828	0.967675	0.5016	
%	-1.01	-1.54	+2.0	-1.1	+0.39	-0.12	-3.0	
Group 2								
M	0.821397	0.066222	0.007664	0.009243	11.1171	0.896268	1.206	49.2386
F	0.829286	0.067962	0.007578	0.00908	10.9781	0.899682	1.198	49.2609
%	+0.96	+2.9	-1.1	-1.8	-1.25	+0.38	-0.66	+0.05

ONE-GROUP CONSTANTS

Group 1	D_g	Σ_{rg}	Σ_{ag}	$\nu\Sigma_{fg}$	τ_g	p_g	$\left(\frac{\nu\Sigma_f}{\Sigma_a}\right)_g$	τ
M	1.26688	0.022018	0.003361	0.003495	49.9171	0.867573	1.04	49.9083
F	1.26954	0.02221	0.0033	0.003394	49.7586	0.870659	1.03	49.7586
%	+0.2	+0.89	-1.8	-2.8	-0.31	+0.36	-0.96	+0.29

M represents MUFT 4 group constants.
F represents fitted group constants.
% are relative to MUFT 4 values.

TABLE 2.10 — WANDA EIGENVALUE CALCULATIONS

FOUR GROUPS: THREE FAST GROUPS AND ONE THERMAL GROUP

MUFT-4 Buckling $B^2 = 0.0025\ cm^{-2}$

Core	S	ℓ (g/liter)	$B_T^2\ (cm^{-2})$	λ_{MS}	λ_{FS}	%
1	1.17	58	0.00258	1.0182	1.0194	0.12
32	1.38	155	0.00192	1.0165	1.0253	0.86
11	1.75	77	0.00224	1.0150	1.0212	0.60

THREE GROUPS: TWO FAST GROUPS AND ONE THERMAL GROUP

MUFT-4 Buckling $B^2 = 0.0025\ cm^{-2}$

Core	S	ℓ (g/liter)	$B_T^2\ (cm^{-2})$	λ_{MS}	λ_{FS}	%
1	1.17	58	0.00258	1.0266	1.0262	0.04
32	1.38	155	0.00192	1.0280	1.0362	0.79
11	1.75	77	0.00224	1.0242	1.0282	0.39

TWO GROUPS: ONE FAST GROUP AND ONE THERMAL GROUP

Core	S	ℓ (g/liter)	$B_T^2\ (cm^{-2})$	λ_{MS}	λ_{FS}	%
1	1.17	58	0.00258	1.0540	1.0542	0.013
32	1.38	155	0.00192	1.066	1.0730	0.65
11	1.75	77	0.00224	1.0556	1.0605	0.46

λ_{MS} represents eigenvalue using MUFT 4 and SOFOCATE constants.

λ_{FS} represents eigenvalue using FIT and SOFOCATE constants.

B_T^2 represents transverse (geometrical) buckling used in WANDA.

D. Variational Procedure for Calculating Fast Group Constants

As an effort to obtain better fitted cross sections based on more than two resonance elements, a variational procedure for calculating fast few group constants[130, 135] has been developed.* The basic assumption made in this model is that for a given medium (1) the flux spectrum can be adequately described as a linear combination of two base flux spectra and (2) the current spectrum can be adequately described as a linear combination of two base current spectra. The coefficients for combining the base flux spectra and the base current spectra are provided by the theory, and depend only on the concentrations of the elements composing the medium and the buckling B^2. Once the coefficients are calculated, the flux and current spectra for the medium are determined and three-, two-, and one-group constants can be easily obtained.

In Sect. 2.8.F, the P_1 equations, resulting from the Boltzmann equation when inelastic scattering and slowing down by hydrogen and heavy elements are considered, are given by Eq. (2.423) as

$$\left[\Sigma_a(u) + \Sigma_{in}(u)\right] \psi_o(u) + BJ(u) + \sum_i \frac{\partial q_o^i}{\partial u} = \chi(u) + w(u)$$

$$\left[\Sigma_T(u) - \Sigma_{s1}(u)\right] J(u) = \frac{B}{3}\psi_o(u) - \frac{\partial \rho}{\partial u} \qquad \text{Eq. (2.510)}$$

when one sets in Eq. (2.423) the quantities $J(u) = -i\psi_1(u)$, where $i = \sqrt{-1}$, $\frac{\partial \rho}{\partial u} = \frac{2}{3}\frac{\partial \eta_1}{\partial u}$, $\delta = 1$, and $\frac{\partial q_1^i}{\partial u} = 0$ for heavy elements, and writes

$$\sum_i \frac{\partial q_o^i}{\partial u} = \frac{\partial}{\partial u}\left[\eta_o + \sum_i q_o^i\right] .$$

Consistent with these modifications, the auxiliary equations which define the slowing-down densities are given by

$$(\lambda_o)_i \frac{\partial q_o^i}{\partial u} + q_o^i = \xi_o^i \Sigma^i_{so}(u)\psi_o(u)$$

$$(\lambda_1)_H \frac{\partial \rho}{\partial u} + \rho = \xi_1 \Sigma_{Sh}(u) J(u) \qquad \text{Eq. (2.511)}$$

*This work was done in cooperation with F. D. Federighi.

where $(\lambda_o)_H = 1, (\lambda_1)_H = 2/3, \xi_o^H = 1$, and $\xi_1 = (2/3)^2$. If one separates the absorption cross section into resonance and smooth (non-resonance) contributions and integrates the terms in Eq. (2.510) over a lethargy interval $\Delta u_n = u_n - u_{n-1}$, one obtains, in accordance with Sect. 2.8, the equations

$$\left[\Sigma_{an}^S + \Sigma_{in,n}\right]\phi_n \Delta u_n + BJ_n \Delta u_n + \sum_i \left(q_{on}^i - q_{on-1}^i\right) + (1 - p_n) \sum_i q_{on-1}^i = \chi_n \Delta u_n + w_n \Delta u_n$$

$$\left[\Sigma_{Tn} - \Sigma_{s1}\right] J_n \Delta u_n = \frac{B}{3}\phi_n \Delta u_n - (\rho_n - \rho_{n-1}) \qquad \text{Eq. (2.512)}$$

where Σ_a^S represents the macroscopic smooth absorption cross section. In these equations, the group width Δu_n is assumed small so that

$$\int_{u_{n-1}}^{u_n} \Sigma(u)\psi_o(u)\,du = \Sigma_n \phi_n \Delta u_n \quad .$$

Integrating the terms in Eq. (2.511) gives

$$q_{on}^i = \frac{\left[\left(\lambda_o\right)_i - \Delta u_{n/2}\right]}{\left[\left(\lambda_o\right)_i + \Delta u_{n/2}\right]} q_{on-1}^i + \frac{\left(\xi_o \Sigma_{so}\right)_n^i \phi_n \Delta u_n}{\left[\left(\lambda_o\right)_i + \Delta u_{n/2}\right]}$$

$$\rho_n = \frac{\left[\left(\lambda_1\right)_H - \Delta u_{n/2}\right]}{\left[\left(\lambda_1\right)_H + \Delta u_{n/2}\right]} \rho_{n-1} + \frac{\left(\xi_1 \Sigma_{sH}\right)_n J_n \Delta u_n}{\left[\left(\lambda_1\right)_H + \Delta u_{n/2}\right]} \qquad \text{Eq. (2.513)}$$

with $q_{oo}^i = \rho_o = 0$. The quantity $(\lambda_o)_i$ for heavy elements will now be taken as zero, so that the isotropic heavy element slowing down is treated by the age approximation. Thus, in Eq. (2.512) hydrogen is treated exactly, the isotropic heavy element slowing down is treated by the age approximation, and the anisotropic slowing down of heavy elements is neglected. The resonance escape probability p_n given in Eq. (2.512) is defined in the following way. Let k represent, in the interval Δu_n, the k^{th} resonance level of the i^{th} element. Then p_n is given by

$$p_n = \prod_i p_n^i$$

with

$$p_n^i = e^{-\sum_k L_{kn}^i (RI)_i^{nk}} \qquad \text{Eq. (2.514)}$$

where L_{kn} is a self-shielding factor for the k^{th} level of the i^{th} resonance element.

From Eq. (2.513) it is noted that the slowing-down density in the multigroup n involves the fluxes (the currents for hydrogen anisotropic slowing down) and the slowing-down cross sections of the previous multigroups. Thus, the isotropic slowing-down density for the i^{th} element can be written for the multigroup n as

$$q_{on}^{i} = \sum_{k=1}^{n} N^{i} a_{kn}^{i} (\xi_o)_k^i \phi_k \Delta u_k$$

where, for the i^{th} element, N^i is the atom density, $(\xi_o)_k^i = (\xi_o \sigma_{so})_k^i$ is the microscopic slowing-down cross section in multigroup k, and the parameter a_{kn}^i involves the products of the ratio $\left[(\lambda_o)_i - \frac{\Delta u_k}{2}\right] \cdot \left[(\lambda_o)_i + \frac{\Delta u_k}{2}\right]^{-1}$ for the various groups k.

The inelastic scattering rate $w^i(u_n)$ is similarly defined as

$$w_n^i = \sum_{k=1}^{n-1} N^i \frac{\sigma^i{}_{in,kn}}{\Delta u_n} \phi_k \Delta u_k$$

where $w_1^i = 0$, and $\sigma_{in.\,kn}^i$ is the microscopic cross section in group n resulting from neutrons inelastically scattered from group k to group n.

For j multigroups, each equation of Eq. (2.512) gives a matrix equation:

$$\sum_i N^i \begin{bmatrix} a_{11}^i & 0 \cdots\cdots 0 \\ \cdot & \cdot \\ \cdot & \cdot \\ a_{j1}^i \frac{\Delta u_1}{\Delta u_j} & a_{j2}^i \frac{\Delta u_2}{\Delta u_j} \cdots\cdots a_{jj}^i \end{bmatrix} \begin{bmatrix} \phi_1 \\ \cdot \\ \cdot \\ \phi_j \end{bmatrix}$$

$$+ \sum_i N^i \begin{bmatrix} P_1 & & 0 \\ & \ddots & \\ 0 & & P \end{bmatrix} \begin{bmatrix} 0 & \cdots & 0 \\ a_{11}\xi_{o1}^i \frac{\Delta u_1}{\Delta u_2} & 0 \cdots 0 & \\ \cdot & & \cdot \\ a_{1,j-1}\xi_{o1}^i \frac{\Delta u_1}{\Delta u_j} & \cdots & a_{j-1,j-1}\xi_{oj-1}^i \frac{\Delta u_{j-1}}{\Delta u_j} \; 0 \end{bmatrix} \begin{bmatrix} \phi_1 \\ \cdot \\ \cdot \\ \phi_j \end{bmatrix}$$

$$+ \begin{bmatrix} B & & 0 \\ & \ddots & \\ 0 & & B \end{bmatrix} \begin{bmatrix} J_1 \\ \cdot \\ \cdot \\ J_j \end{bmatrix} = \begin{bmatrix} \chi_1 \\ \cdot \\ \cdot \\ \chi_j \end{bmatrix} \qquad \text{Eq. (2.515)}$$

and

$$-\begin{bmatrix} B/3 & & \\ & \ddots & 0 \\ & & B/3 \end{bmatrix}\begin{bmatrix} \phi_1 \\ \vdots \\ \phi_j \end{bmatrix} + \sum_i N^i \begin{bmatrix} C^i_{11} & & 0 \\ & & \\ C^i_{j1}\frac{\Delta u_1}{\Delta u_j} & C^i_{j2}\frac{\Delta u_2}{\Delta u_j} \cdots & C^i_{jj} \end{bmatrix}\begin{bmatrix} J_1 \\ \vdots \\ J_j \end{bmatrix} = \begin{bmatrix} 0 \\ \vdots \\ 0 \end{bmatrix}$$

Eq. (2.516)

where N^i represents the atom density of element i. In these equations, the first matrix of Eq. (2.515) contains the absorption, inelastic scattering, and isotropic slowing-down cross sections, while the second matrix of Eq. (2.516) contains the transport cross sections for all elements and the hydrogen anisotropic slowing-down cross sections. Also for convenience of notation $P_n = (1-p_n)$. If one combines all the matrices involving the flux and all the matrices involving the current, Eqs. (2.515) and (2.516) can be written as a $2j \times 2j$ matrix

$$\begin{bmatrix} A_{11} & \cdots & A_{1j} & B_{11} & \cdots & B_{1j} \\ \vdots & & \vdots & \vdots & & \vdots \\ A_{j1} & \cdots & A_{jj} & B_{j1} & \cdots & B_{jj} \\ -D_{11} & \cdots & -D_{1j} & C_{11} & \cdots & C_{1j} \\ \vdots & & \vdots & \vdots & & \vdots \\ -D_{j1} & \cdots & -D_{jj} & C_{j1} & \cdots & C_{jj} \end{bmatrix}\begin{bmatrix} \phi_1 \\ \vdots \\ \phi_j \\ J_1 \\ \vdots \\ J_j \end{bmatrix} = \begin{bmatrix} \chi_1 \\ \vdots \\ \chi_j \\ 0 \\ \vdots \\ 0 \end{bmatrix}$$

Eq. (2.517)

which is denoted by $H\Psi = S$. Here, for convenience, each diagonal matrix and lower triangular matrix is written as a $j \times j$ matrix with the understanding that some of the elements are zero.

For the variational scheme, it is necessary to obtain the adjoint to Eq. (2.517). This is given by

$$\left[\phi_1^+\Delta u_1 \cdots \phi_j^+\Delta u_j J_1^+\Delta u_1 \cdots J_j^+\Delta u_j\right] \begin{bmatrix} A_{11} \cdots A_{1j} & B_{11} \cdots B_{1j} \\ \vdots & \vdots \\ A_{j1} \cdots A_{jj} & B_{j1} \cdots B_{jj} \\ -D_{11} \cdots -D_{1j} & C_{11} \cdots C_{1j} \\ \vdots & \vdots \\ -D_{j1} \cdots -D_{jj} & C_{j1} \cdots C_{jj} \end{bmatrix}$$

$$= \left[S_{11}^+\Delta u_1 \cdots S_{1j}^+\Delta u_j S_{21}^+\Delta u_1 \cdots S_{2j}^+\Delta u_j\right] \qquad \text{Eq. (2.518)}$$

where the term on the right represents the adjoint source. Thus, the adjoint equation is given by $\Psi^+ H = S^+$.

In the variational method described in Chap. 3, Sect. 3.7.D, one writes the stationary functional J as

$$J = \frac{\left(\Psi^+, \chi\right)\left(S^+, \Psi\right)}{\Psi^+, H\Psi} \qquad \text{Eq. (2.519)}$$

where $(K, \psi) = \int_o^u K(u')\Psi(u')du'$ defines the inner product. The functional J is stationary with respect to small variations of Ψ and ψ^+ about their exact values. For rigorous solutions of Ψ and Ψ^+, Eq. (2.519) reduces to

$$J(\Psi, \Psi^+) = (\Psi^+, \chi) = (S^+, \Psi) .$$

Here the weighted average desired is

$$J(\psi, \Psi^+) = (S^+, \Psi) \qquad \text{Eq. (2.520)}$$

so that the stationary value for the multigroup case is given by

$$J = \sum_{n=1}^{j} S_{1n}^+ \phi_n \Delta u_n + \sum_{n=1}^{j} S_{2n}^+ J_n \Delta u_n . \qquad \text{Eq. (2.521)}$$

In solving Eq. (2.518), it is necessary to specify the adjoint sources. These sources are determined by the weighted average given by Eq. (2.521) which one desires to be stationary. For example, if one desires that the stationary value represent the total absorption rate $J = \sum_{n=1}^{j} \Sigma_{an} \phi_n \Delta u_n$, the source terms in Eq. (2.521) are then chosen as $S_{1n}^{\dagger} = \Sigma_{an}$ and $S_{2n}^{\dagger} = 0$. For the problem under consideration, the quantity which is made stationary is the net loss of neutrons due to isotropic slowing down in the energy range from 10 Mev to 0.625 ev. For each multigroup n the net loss of neutrons due to isotropic slowing down is given, from Eq. (2.512), as $\sum_i q_{on}^i - \sum_i q_{on-1}^i$; therefore, the net loss of neutrons due to isotropic slowing down in the entire fast energy range, which is here chosen to be made stationary, is given by

$$J = \sum_{n=1}^{j} \left(\sum_i q_{on}^i - \sum_i q_{on-1}^i \right)$$

or

$$J = \sum_i q_{oj}^i . \qquad \text{Eq. (2.522)}$$

Since $q_{on}^i = \sum_{k=1}^{n} N^i a_{kn}^i (\xi_o)_k^i \phi_k \Delta u_k$, then in Eq. (2.522),

$$q_{oj}^i = \sum_{k=1}^{j} N^i a_{kj}^i (\xi_o)_k^i \phi_k \Delta u_k$$

and

$$J = \sum_{k=1}^{j} \sum_i N^i a_{kj}^i (\xi_o)_k^i \phi_k \Delta u_k . \qquad \text{Eq. (2.523)}$$

Comparing Eq. (2.523) with Eq. (2.521) gives

$$S_{1n}^{\dagger} = \sum_i N^i a_{nj}^i (\xi_o)_n^i$$

$$S_{2n}^{\dagger} = 0$$

so that the adjoint source term in multigroup n, $S_{1n}^{\dagger}$ in Eq. (2.518), is defined by the total macroscopic slowing-down cross section in the group because

$$J = \sum_{n=1}^{j} \sum_i N^i a_{nj}^i (\xi_o)_n^i \phi_n \Delta u_n . \qquad \text{Eq. (2.524)}$$

In the scheme, the basic assumption involved is that the flux and current spectra for a given medium can be each represented as a linear combination of two base spectra, namely, a soft and a hard spectrum. Thus, at a given lethargy u_n, the flux is given by

$$\phi_n = \alpha_1 \phi_{Sn} + \alpha_2 \phi_{hn}$$

and the current by

$$J_n = \beta_1 J_{Sn} + \beta_2 J_{hn} .$$

Here α_1 and α_2 are the coefficients for linearly combining the two base flux spectra ϕ_{Sn} and ϕ_{hn} and β_1, β_2 are the coefficients for combining the two base current spectra J_{Sn} and J_{hn}. The adjoint flux and current spectra are similarly defined. For example,

$$\phi_n^+ \Delta u_n = \alpha_1^+ \phi_{Sn}^+ \Delta u_n + \alpha_2^+ \phi_{hn}^+ \Delta u_n .$$

The soft and hard flux and current spectra are obtained from multigroup solution of $H\Psi = \chi$, and the soft and hard adjoint flux and current spectra from multigroup solution of $\Psi^+ H = S^+$.

Each base spectrum is separated into three modes, where each mode is characterized by the spectrum in a particular lethargy range. The lethargy ranges are chosen to be those which define the lethargy ranges of the first, second, and third groups of the three-group scheme. In each of these modes, one needs a different set of coefficients for combining the base spectra. Thus, in matrix notation, the state vector Ψ is given by

$$\Psi = \Phi\gamma$$

where

$$\Phi\gamma = \begin{bmatrix} \phi_S^1\phi_h^1 & & & & & & 0 \\ & \phi_S^2\phi_h^2 & & & & & \\ & & \phi_S^3\phi_h^3 & & & & \\ & & & J_S^1 J_h^1 & & & \\ & & & & J_S^2 J_h^2 & & \\ 0 & & & & & & J_S^3 J_h^3 \end{bmatrix} \begin{bmatrix} \alpha_{11} \\ \alpha_{12} \\ \cdot \\ \cdot \\ \cdot \\ \alpha_{32} \\ \beta_{11} \\ \beta_{12} \\ \cdot \\ \cdot \\ \cdot \\ \beta_{32} \end{bmatrix}$$

Eq. (2.525)

Here, for example, $\phi_S^1, \phi_S^2, \phi_S^3$ represent the modes of the soft base flux spectrum, where

$$\phi_S^1 = \begin{bmatrix} \phi_{S1} \\ \vdots \\ \phi_{Sk} \end{bmatrix} \quad \phi_S^2 = \begin{bmatrix} \phi_{Sk+1} \\ \vdots \\ \phi_{Sm} \end{bmatrix} \quad \phi_S^3 = \begin{bmatrix} \phi_{Sm+1} \\ \vdots \\ \phi_{Sj} \end{bmatrix}$$

with k = multigroup 10 corresponding to $u = 2.5$
m = multigroup 25 corresponding to $u = 7.5$
j = multigroup 54 corresponding to $u = 16.5884$.
Similarly, the adjoint state vector Ψ^+ is given by

$$\Psi^+ = \gamma^+ \Phi^+$$

with

$$\gamma^+\Phi^+ = \left[\alpha_{11}^+ \cdots \alpha_{32}^+ \beta_{11}^+ \cdots \beta_{32}^+\right] \begin{bmatrix} \phi_S^{1+\Delta} & & & & & \\ \phi_h^{1+\Delta} & & & & & \\ & \phi_S^{2+\Delta} & & & & \\ & \phi_h^{2+\Delta} & & & & \\ & & \ddots & & & \\ & & & & j_S^{3+\Delta} & \\ & & & & j_h^{3+\Delta} & \end{bmatrix} \qquad \text{Eq. (2.526)}$$

where, for example,

$$\phi_S^{1+\Delta} = \left[\phi_{S1}^+ \Delta u_1 \phi_{S2}^+ \Delta u_2 \cdots \phi_{Sk}^+ \Delta u_k\right].$$

Substituting $\Phi\gamma$ for Ψ and $\gamma^+\Phi^+$ for Ψ^+ in Eq. (2.519) and (2.520), and using the definitions

$$\begin{aligned} \mathcal{S}^+ &= S^+\Phi \\ \mathcal{S} &= \Phi^+ X \\ \mathcal{H} &= \Phi^+ H \Phi \end{aligned} \qquad \text{Eq. (2.527)}$$

one obtains

$$J = \frac{\left(\gamma^+, \mathcal{S}\right)\left(\mathcal{S}^+, \gamma\right)}{\left(\gamma^+, \mathcal{H}\gamma\right)} \qquad \text{Eq. (2.528)}$$

and

$$J = \left(\mathcal{S}_1^+ \gamma\right). \qquad \text{Eq. (2.529)}$$

For Eq. (2.528) to give Eq. (2.529),

$$\mathcal{H}\gamma = \mathcal{S}. \qquad \text{Eq. (2.530)}$$

Therefore, the equation which determines the coefficients γ is

$$\gamma = \mathcal{H}^{-1}\mathcal{S}. \qquad \text{Eq. (2.531)}$$

From Eqs. (2.515), (2.516), (2.517), (2.526), and (2.527), it follows that $\mathcal{H}$ is a 12×12 matrix consisting of base spectra weighted elements of the matrix $\mathcal{H}$. Thus the matrix $\mathcal{H}$ can be written as

$$\mathcal{H} = \sum_i N^i \begin{bmatrix} \tilde{\alpha}_{11}^i \cdots \tilde{\alpha}_{16}^i & & \\ \vdots & 0 & \\ \tilde{\alpha}_{61}^i \cdots \tilde{\alpha}_{66}^i & & \\ & \tilde{C}_{11}^i \cdots \tilde{C}_{16}^i & \\ & \vdots & \\ 0 & \tilde{C}_{61}^i \cdots \tilde{C}_{66}^i & \end{bmatrix} + \begin{bmatrix} R_{11} \cdots R_{16} & 0 \cdots 0 \\ \vdots & \vdots \\ R_{61} \cdots R_{66} & 0 \cdots 0 \\ 0 \cdots 0 & 0 \cdots 0 \\ \vdots & \vdots \\ 0 \cdots 0 & 0 \cdots 0 \end{bmatrix}$$

$$+ B \begin{bmatrix} 0 \cdots 0 & \beta_{11} \cdots \beta_{16} \\ \vdots & \vdots \\ 0 \cdots 0 & \beta_{61} \cdots \beta_{66} \\ -\delta_{11} \cdots -\delta_{16} & 0 \cdots 0 \\ \vdots & \vdots \\ -\delta_{61} \cdots -\delta_{66} & 0 \cdots 0 \end{bmatrix} \qquad \text{Eq. (2.532)}$$

with $B = \sqrt{B^2}$ where B^2 is the buckling. With reference to Eqs. (2.515) and (2.516), the submatrices $\tilde{\alpha}^i$ and $\tilde{C}^i$ for each element i and the submatrices β and δ are defined as follows. The elements $\tilde{\alpha}^i_{\ell m}$ are base flux and adjoint flux weighted elements of the matrix

$$\begin{bmatrix} \alpha^i_{11} & 0 & \cdots & 0 \\ \vdots & & & \vdots \\ \alpha^i_{j1}\dfrac{\Delta u_1}{\Delta u_j} & & \cdots & \alpha^i_{jj} \end{bmatrix}$$

and the elements $C^i_{\ell m}$ consist of base current and adjoint current weighted elements of the matrix

$$\begin{bmatrix} C^i_{11} & 0 & \cdots & 0 \\ \vdots & & & \\ C^i_{j1}\dfrac{\Delta u_1}{\Delta u_j} & & \cdots & C_{jj} \end{bmatrix}$$

The elements $\beta_{\ell m}$ are base current and adjoint flux weighted elements of the matrix

$$\begin{bmatrix} B & 0 \\ \vdots & \\ 0 & B \end{bmatrix}$$

with B factored out of the matrix, and $\delta_{\ell m}$ are flux and adjoint current weighted elements of the matrix

$$\begin{bmatrix} B/3 & 0 \\ \vdots & \\ 0 & B/3 \end{bmatrix}$$

also with B factored out of the matrix. Furthermore, the submatrix R is given by

$$\begin{bmatrix} R_{11} \cdots R_{16} \\ \vdots \quad \vdots \\ R_{61} \cdots R_{66} \end{bmatrix} = \sum_i N^i \begin{bmatrix} \phi^+_{S1} \cdots \phi^+_{Sk} & 0 \cdots 0 \\ \phi^+_{h1} \cdots \phi^+_{hk} & 0 \cdots 0 \\ 0 \cdots 0 & \phi^+_{Sk+1} \cdots \phi^+_{Sm} \; 0 \cdots 0 \\ 0 \cdots 0 & \phi^+_{hk+1} \cdots \phi^+_{hm} \; 0 \cdots 0 \\ 0 \cdots 0 & \phi^+_{Sm+1} \cdots \phi^+_{Sj} \\ 0 \cdots 0 & \phi^+_{hm+1} \cdots \phi^+_{hj} \end{bmatrix}$$

$$\times \begin{bmatrix} P_1 & & 0 \\ & \ddots & \\ 0 & & P_j \end{bmatrix} \begin{bmatrix} q^{i1}_{So} & q^{i1}_{ho} & q^{i2}_{So} & q^{i2}_{ho} & q^{i3}_{So} & q^{i3}_{ho} \\ \vdots & & & & & \\ q^{i1}_{Sj-1} & q^{i1}_{hj-1} & q^{i2}_{Sj-1} & q^{i2}_{hj-1} & q^{i3}_{Sj-1} & q^{i3}_{hj-1} \end{bmatrix} \quad \text{Eq. (2.533)}$$

where the slowing-down densities $q^i_S q^i_h$ involve the base flux spectra in their various modes. It should be recalled that $P_n = (1-p_n)$ where p_n is the resonance escape in multigroup n. Since resonances occur only in the third group of the three-group scheme, the resonances occur only in the third mode; thus, p_n for groups $n=1$ to $n=m$ is unity and, thus, Eq. (2.533) becomes a 2×6 matrix

$$\begin{bmatrix} R_{51} \cdots R_{56} \\ R_{61} \cdots R_{66} \end{bmatrix}$$

$$= \sum_i N^i \begin{bmatrix} \phi^+_{Sm+1} \cdots \phi^+_{Sj} \\ \phi^+_{hm+1} \cdots \phi^+_{hj} \end{bmatrix} \begin{bmatrix} (1-p_{m+1}) & & 0 \\ & \ddots & \\ 0 & & (1-p_j) \end{bmatrix} \begin{bmatrix} q^{i1}_{Sm} & q^{i1}_{hm} & \cdots & q^{i3}_{Sm} & q^{i3}_{hm} \\ \vdots & \vdots & & \vdots & \vdots \\ q^{i1}_{Sj-1} & q^{i1}_{hj-1} & \cdots & q^{i3}_{Sj-1} & q^{i3}_{hj-1} \end{bmatrix}$$

Eq. (2.534)

One permanently establishes a set of base spectra for each buckling. For each buckling, the base spectra are combined with the cross sections for each element i of the operator H to obtain a set of lethargy-independent 12×12 matrices given by the first term of Eq. (2.532). The third term of Eq. (2.532) is a matrix with constant elements. Similarly, using the base spectra, one establishes a 2×29 adjoint base flux matrix, and a 29×6 slowing-down matrix for each element i given by the first and third terms of Eq. (2.534). These matrices comprise part of the scheme's cross-section library. For the calculation of P_n, the library consists of cross sections and resonance parameters independent of material composition or base spectra. Thus, to calculate $\mathcal{H}$, it is only necessary to specify the material composition (atom density for each element i) and the quantity B. Similarly, one establishes for each set of base spectra a source matrix with constant elements. From Eqs. (2.515), (2.526), and (2.527) it is found that $\mathcal{S}$ is a 12×1 matrix containing base adjoint flux weighted elements of the fission spectrum matrix. The source matrix $\mathcal{S}$ is independent of material composition and consists of elements which are constants. This matrix also comprises part of the cross-section library.

Thus, once $\mathcal{H}$ is determined, the coefficients γ are easily calculated from $\gamma = \mathcal{H}^{-1}\mathcal{S}$ by a matrix multiplication of a 12×12 and 12×1 matrix. After the coefficients γ are calculated, the group constants are calculated from the scheme's group constant library established for each set of base spectra.

As indicated, the spectrum modes are chosen so that they correspond to the lethargy bands of the three-group scheme. Thus, by flux weighting lethargy-dependent microscopic cross section for an element i with the base spectra corresponding to the three modes, one obtains cross-section spectrum integrals which apply directly to groups $g = 1, 2, 3,$ of the three-group scheme. These cross-section integrals combined with the integrated base flux and current spectra constitute the scheme's group constant library from which not only the three-group constants are obtained, but also the two- and one-group constants. The parameters that constitute the group constant library are the following:

1. Φ_{Sg} and Φ_{hg}, which represent the integrated soft and hard base flux spectra in group g.

2. J_{Sg} and J_{hg}, which represent the integrated soft and hard base current spectra in group g.

3. $(\sigma_{aS}\phi)^i_{Sg}$ and $(\sigma_{aS}\phi)^i_{hg}$, which represent the soft and hard base flux spectrum weighted microscopic smooth absorption cross section for element i in group g.
4. $(\nu\sigma_{fs}\phi)^i_{Sg}$ and $(\nu\sigma_{fS}\phi)^i_{hg}$, which represent the soft and hard base flux spectrum weighted microscopic smooth fission production cross sections for element i in group g.
5. The matrix

$$\begin{bmatrix} q^{1i}_{Sk} & q^{1i}_{hk} & 0 & 0 & 0 & 0 \\ q^{1i}_{Sm} & q^{1i}_{hk} & q^{2i}_{Sm} & q^{2i}_{hm} & 0 & 0 \\ q^{1i}_{Sj} & q^{1i}_{hj} & q^{2i}_{Sj} & q^{2i}_{hj} & q^{3i}_{Sj} & q^{3i}_{hj} \end{bmatrix}$$

for each element i. The elements q^{gi}_{Sn} of the matrix are the microscopic slowing-down density for element i at the multigroup n consisting of microscopic slowing-down cross sections weighted with the soft base flux spectrum of group g. Similarly, the element q^{gi}_{hn} is the slowing-down density at multigroup n consisting of microscopic slowing-down cross sections weighted with the hard base flux spectrum of group g.

To give an example of how the group constants are calculated, consider the calculation of the one-group constants. Once the vector γ is determined, the coefficients $(\alpha_{11}, \alpha_{12}, \alpha_{21}, \alpha_{22}, \alpha_{31}, \alpha_{32}, \beta_{11}, \beta_{12}, \beta_{21}, \beta_{22}, \beta_{31}, \beta_{32})$ are determined. For convenience of notation, denote the coefficients which multiply the soft base spectra by α_{g1}, and β_{g1}, and those which multiply the hard base spectra by α_{g2} and β_{g2}. For the one-group case then, the diffusion constant is given by

$$D = \frac{\sum_{g=1}^{3} \left(\beta_{g1} J_{Sg} + \beta_{g2} J_{hg}\right)}{B\left[\sum_{g=1}^{3} \left(\alpha_{g1} \Phi_{Sg} + \alpha_{g2} \Phi_{hg}\right)\right]}$$

where $B = \sqrt{B^2}$ and B^2 is the buckling.

Given the material composition, the slowing-down density matrix is calculated from item 5 as

$$\begin{bmatrix} q_k \\ q_m \\ q_j \end{bmatrix} = \sum_i N^i \begin{bmatrix} q_{Sk}^{1i} & q_{hk}^{1i} & 0 & 0 & 0 & 0 \\ q_{Sm}^{1i} & q_{hm}^{1i} & q_{Sm}^{2i} & q_{hm}^{2i} & 0 & 0 \\ q_{Sj}^{1i} & q_{hj}^{1i} & q_{Sj}^{2i} & q_{hj}^{2i} & q_{Sj}^{3i} & q_{hj}^{3i} \end{bmatrix} \begin{bmatrix} \alpha_{11} \\ \alpha_{12} \\ \alpha_{21} \\ \alpha_{22} \\ \alpha_{31} \\ \alpha_{32} \end{bmatrix}$$

The removal cross section is given by

$$\Sigma_r = \frac{q_j}{\sum_{g=1}^{3} \left(\alpha_{g1} \Phi_{Sg} + \alpha_{g2} \Phi_{hg} \right)}.$$

From item 3, the macroscopic quantities $(\Sigma_{aS} \Phi)_{Sg}$ and $(\Sigma_{aS} \Phi)_{hg}$ are calculated as $(\Sigma_{aS} \Phi)_{Sg} = \sum_i N^i (\sigma_{aS} \Phi)_{Sg}^i$ and $(\Sigma_{aS} \Phi)_{hg} = \sum_i N^i (\sigma_{aS} \Phi)_{hg}^i$. The smooth (nonresonance) contribution to the absorption cross section is, therefore, given by

$$\Sigma_{aS} = \frac{\sum_{g=1}^{3} \left(\alpha_{g1} (\Sigma_{aS} \Phi)_{Sg} + \alpha_{g2} (\Sigma_{aS} \Phi)_{hg} \right)}{\sum_{g=1}^{3} (\alpha_{g1} \Phi_{Sg} + \alpha_{g2} \Phi_{hg})}.$$

For the resonance contribution to the absorption cross section, one makes use of parameters which were used to calculate $\mathcal{H}$.

From Eq. (2.534), the resonance capture rate in each multigroup of the resonance group is given by

$$\begin{vmatrix} (\Sigma_{aR}\phi)_{m+1} \\ \cdot \\ \cdot \\ \cdot \\ \cdot \\ \cdot \\ (\Sigma_{aR}\phi)_j \end{vmatrix} = \sum_i N^i \begin{bmatrix} 1-p_{m+1} & & & & \\ & \cdot & & 0 & \\ & & \cdot & & \\ & & & \cdot & \\ 0 & & \cdot & & \\ & & & \cdot & \\ & & & & 1-p_j \end{bmatrix}$$

$$\begin{bmatrix} q_{Sm}^{i1} & q_{hm}^{i1} & q_{Sm}^{i2} & q_{hm}^{i2} & q_{Sm}^{i3} & q_{hm}^{i3} \\ \cdot & \cdot & \cdot & \cdot & \cdot & \cdot \\ \cdot & \cdot & \cdot & \cdot & \cdot & \cdot \\ \cdot & \cdot & \cdot & \cdot & \cdot & \cdot \\ \cdot & \cdot & \cdot & \cdot & \cdot & \cdot \\ q_{Sj-1}^{i1} & q_{hj-1}^{i1} & q_{Sj-1}^{i2} & q_{hj-1}^{i2} & q_{Sj-1}^{i3} & q_{hj-1}^{i3} \end{bmatrix} \begin{bmatrix} \alpha_{11} \\ \alpha_{12} \\ \alpha_{21} \\ \alpha_{22} \\ \alpha_{31} \\ \alpha_{32} \end{bmatrix}$$

The resonance absorption cross section is given by

$$\Sigma_{aR} = \frac{\sum_{n=m+1}^{j} (\Sigma_{aR})_n}{\sum_{g=1}^{3} (\alpha_{g1}\Phi_{Sg} + \alpha_{g2}\Phi_{hg})}$$

and the total absorption cross section $\Sigma_a = \Sigma_{aS} + \Sigma_{aR}$.

The fission production cross section includes both resonance and nonresonance contributions. The smooth (nonresonance) contribution is calculated using item 4, where

$$(\nu\Sigma_{fS}\phi)_{Sg} = \sum_i N^i (\nu\sigma_{fS}\phi)^i_{Sg}$$

$$(\nu\Sigma_{fS}\phi)_{hg} = \sum_i N^i (\nu\sigma_{fS}\phi)^i_{hg}$$

and therefore

$$\nu\Sigma_{fS} = \frac{\sum_{g=1}^{3} \left[\alpha_{g1} (\nu\Sigma_{fS}\phi)_{Sg} + \alpha_{g2} (\nu\Sigma_{fS}\phi)_{hg}\right]}{\sum_{g=1}^{3} (\alpha_{g1}\Phi_{Sg} + \alpha_{g2}\Phi_{hg})}$$

The resonance contribution is calculated in the following way. From Eq. (2.514), one obtains the fission resonance escape for the element i as

$$p_{nf}^{i} = e^{-\sum_{k} \alpha_{nk}^{i} L_{kn}^{i} (RI)_{i}^{nk}}$$

where α_{nk}^{i} is the fission to absorption ratio for the k^{th} level of the i^{th} fissionable element in the multigroup n. From Eq. (2.534)

$$\begin{bmatrix} (\nu\Sigma_{fR}\phi)_{m+1}^{i} \\ \cdot \\ \cdot \\ \cdot \\ \cdot \\ \cdot \\ (\nu\Sigma_{fR}\phi)_{j}^{i} \end{bmatrix} = \sum_{i} N^{i} \begin{bmatrix} (1-p_{m+1,f}^{i}) & & & & \\ & \ddots & & & \\ & & \cdot & & \\ & & & \cdot & \\ & & & & \cdot \\ & & & & (1-p_{jf}^{i}) \end{bmatrix}$$

$$\begin{bmatrix} q_{Sm}^{i1} & q_{hm}^{i1} & \cdots & q_{hm}^{i3} \\ \cdot & \cdot & & \cdot \\ \cdot & \cdot & & \cdot \\ \cdot & \cdot & & \cdot \\ \cdot & \cdot & & \cdot \\ \cdot & \cdot & & \cdot \\ q_{Sj-1}^{i1} & q_{hj-1}^{i1} & \cdots & q_{nj-1}^{i3} \end{bmatrix} \begin{bmatrix} \alpha_{11} \\ \alpha_{12} \\ \alpha_{21} \\ \alpha_{22} \\ \alpha_{31} \\ \alpha_{32} \end{bmatrix}$$

where the sum over i extends over all elements comprising the medium. For the i^{th} fissionable element

$$\nu\Sigma_{fR}^{i} = \frac{\sum_{n=m+1}^{j} (\nu\Sigma_{fR}\phi)_n^j}{\sum_{g=1}^{3} (a_{g1}\Phi_{Sg} + a_{g2}\Phi_{hg})}$$

and the total resonance production cross section $\nu\Sigma_{fR} = \sum_i \nu\Sigma_{fR}^i$ where the sum extends over all fissionable elements that have resonances. It follows that the total fission production cross section is given by .

$$\nu\Sigma_f = \nu\Sigma_{fS} + \nu\Sigma_{fR} .$$

The other parameters, such as the group age τ_g and the overall age τ, are given by

$$\tau_1 = \tau = \frac{D}{\Sigma_r + \Sigma_a} .$$

For the calculation of the three-, two-, and one-group constants, the soft spectra have been chosen to be those for pure water, while the hard spectra have been chosen to be those for a medium having a metal-to-water volume ratio $S = 1.75$ and a loading of x gm/liter of U^{235}, where x is of the order of a few hundred. Base spectra have been obtained for three values of B^2, namely $B^2 = 0.0025$ cm^{-2}, $B^2 = 0.005$ cm^{-2}, and $B^2 = 0.01$ cm^{-2}, and for each buckling a library has been generated.

In calculating the hard base spectra, the resonance elements included are U^{235}, U^{238}, and zirconium. The library for the few-group constant calculations contain in addition to U^{235}, U^{238}, and zirconium nine other resonance elements. For experimental purposes, a FORTRAN program called MUSK has been developed for calculating group constants based on the variational method. For a medium containing ten elements, six of which are resonance elements, MUSK calculates all of the group constants for the three-, two-, and one-group schemes in 1.4 seconds on the TRANSAC. In Table 2.11, the group constants calculated by MUSK for a given medium having a buckling $B^2 = 0.005$ are compared with those obtained form a MUFT-5 calculation.[124] In general, the agreement between the MUSK and MUFT-5 constants is within 2 percent.

TABLE 2.11 — COMPARISON OF MUSK AND MUFT GROUP CONSTANTS

$S = 1.5 \quad \ell = 50$ g/liter $U^{235} \quad B^2 = 0.005$ cm^{-2}

Elements: water, zirconium, U^{235}, U^{238}

Base spectra of MUSK S = 0 and S = 1.75 with

$\ell = x$ g/liter of U^{235}

THREE-GROUP SCHEME

Group 1	D_g	Σ_{rg}	Σ_{ag}	$(\nu\Sigma_f)_g$	τ_g	τ
M	2.05006	6.00548-2	2.04795-3	4.04620-4	33.0108	
V	2.05388	5.99519-2	2.06669-3	4.04980-4	33.1171	
%	0.19	0.17	0.91	0.09	0.32	
Group 2						
M	1.03465	5.84388-2	8.16203-4	5.16872-4	17.4610	
V	1.03276	5.80825-2	8.21206-4	5.19563-4	17.5331	
%	0.18	0.61	0.61	0.52	0.41	

TABLE 2.11 — COMPARISON OF MUSK AND MUFT GROUP CONSTANTS (Continued)

$S = 1.5$ $\ell = 50$ g/liter U^{235} $B^2 = 0.005$ cm^{-2}

Elements: water, zirconium, U^{235}, U^{238}

Base spectra of MUSK S = 0 and S = 1.75 with

ℓ = x g/liter of U^{235}

THREE-GROUP SCHEME (Continued)

Group 3	D_g	Σ_{rg}	Σ_{ag}	$(\nu\Sigma_f)_g$	τ_g	τ
M	8.50827-1	5.64975-2	6.73496-3	7.71009-3	13.4555	55.7237
V	8.52585-1	5.59527-2	6.72191-3	7.61522-3	13.6034	56.0235
%	0.21	0.96	0.19	1.2	1.1	0.54

TWO-GROUP SCHEME

Group 1	D_g	Σ_{rg}	Σ_{ag}	$(\nu\Sigma_f)_g$	τ_g	τ
M	1.47558	3.30627-2	1.35107-3	4.68128-4	42.8776	
V	1.47518	3.29173-2	1.36083-3	4.69918-4	43.0356	
%	0.03	0.44	0.72	0.38	0.37	

TABLE 2.11 — COMPARISON OF MUSK AND MUFT GROUP CONSTANTS (Continued)

$S = 1.5 \quad \ell = 50$ g/liter $U^{235} \quad B^2 = 0.005$ cm^{-2}

Elements: water, zirconium, U^{235}, U^{238}

Base spectra of MUSK S = 0 and S = 1.75 with

$\ell = x$ g/liter of U^{235}

TWO-GROUP SCHEME (Continued)

Group 2	D_g	Σ_{rg}	Σ_{ag}	$(\nu\Sigma_f)_g$	τ_g	τ
M	8.50827-1	5.64975-2	6.73496-3	7.71009-3	13.4555	56.3233
V	8.52585-1	5.59527-2	6.72191-3	7.61522-3	13.6034	56.6291
%	0.21	0.96	0.19	1.2	1.1	0.54

ONE-GROUP SCHEME

Group 1	D_g	Σ_{rg}	Σ_{ag}	$(\nu\Sigma_f)_g$	τ_g	τ
M	1.27015	1.85775-2	3.12140-3	2.84944-3	58.535	58.5247
V	1.26992	1.84470-2	3.12832-3	2.82565-3	58.8597	58.8494
%	0.02	0.70	0.22	0.83	0.55	0.55

M = MUFT-5 data
V = MUSK data
exponent (-2) = 10^{-2}

REFERENCES

1. H. Feshbach, C.E. Porter, and V.F. Weisskopf, "Model for Nuclear Reactions with Neutrons," Phys. Rev. 96, 448-464 (1954).
2. L. I. Schiff, "Quantum Mechanics," McGraw-Hill Book Company, Inc., New York, 1949.
3. N. F. Mott and H. S. W. Massey, "The Theory of Atomic Collisions," 2nd Ed., The Clarendon Press, Oxford, 1949.
4. J. M. Blatt and V. F. Weisskopf, "Theoretical Nuclear Physics," John Wiley and Sons, Inc., New York, 1952.
5. H. A. Bethe, "A Continuum Theory of the Compound Nucleus," Phys. Rev. 57, 1125-1144 (1940).
6. E. U. Condon and G. H. Shortley, "The Theory of Atomic Spectra," University Press, Cambridge, England, 1953.
7. J. V. Lepore, "Polarization of Neutrons and Protons by Scattering," Phys. Rev. 79, 137-142 (1950).
8. M. E. Rose, "Elementary Theory of Angular Momentum," John Wiley and Sons, Inc., New York, 1957.
9. R. D. Woods and D. S. Saxon, "Diffuse Surface Optical Model for Nucleon-Nuclei Scattering," Phys. Rev. 95, 577-578 (1954).
10. F. E. Bjorklund, S. Fernbach, and N. Sherman, "Optical Model of Nucleus with Absorbing Surface," Phys. Rev. 101, 1832-1833 (1956).
11. F. E. Bjorklund and S. Fernbach, "Optical-Model Analyses of Scattering of 4.1-, 7-, and 14-Mev Neutrons by Complex Nuclei," Phys. Rev. 109, 1295-1298 (1958).
12. E. C. Kemble, "Fundamental Principles of Quantum Mechanics," McGraw-Hill Book Company, Inc., New York, 1937.
13. M. G. Mayer and J. H. D. Jensen, "Elementary Theory of Nuclear Shell Structure," John Wiley and Sons, Inc., New York, 1955.
14. P. M. Endt and M. Demeur, Eds., "Nuclear Reactions," Interscience Publishers, Inc., New York, 1959.
15. P. M. Morse and H. Feshbach, "Methods of Theoretical Physics," 2 Vols., McGraw-Hill Book Company, Inc., New York, 1953.
16. S. Flugge, Ed., "Handbuch der Physik," Vol. X, Springer-Verlag, Berlin, 1960.
17. F. Ajzenberg-Selove, Ed., "Nuclear Spectroscopy," Part B, Academic Press, Inc., New York, 1960.
18. F. Ajzenberg-Selove and T. Lauritsen, "Energy Levels of Light Nuclei. VI," Nucl, Phys. 11, 1-340 (1959).
19. D. J. Hughes, "Neutron Cross Sections," p. 112 et seq., Pergamon Press, Inc., New York, 1957.

20. A. Saplakoglu, L. M. Bollinger, and R. E. Coté, "Properties of s-Wave and p-Wave Neutron Resonances in Niobium," Phys. Rev. 109, 1258-1262 (1958).

21. L. W. Weston, K. K. Seth, E. G. Bilpuch, and H. W. Newson, "Neutron Capture Cross Sections in the Kev Region. Part II. Spin-Orbit Coupling and the Optical Model," Ann. Phys. 10, 477-489 (1960).

22. J. H. Gibbons, R. L. Macklin, P. D. Miller, and J. H. Neiler, "Average Radiative Capture Cross Sections for 7- to 170-Kev Neutrons," Phys. Rev. 122, 182-201 (1961).

23. A. Tubis, "Tables of Nonrelativistic Coulomb Wave Functions," LA-2150, August 1957.

24. G. Breit and E. P. Wigner, "Capture of Slow Neutrons," Phys. Rev. 49, 519-531 (1936).

25. N. Bohr, "Neutron Capture and Nuclear Constitution," Nature 137, 334-338 (1936).

26. H. A. Bethe and G. Placzek, "Resonance Effects in Nuclear Processes," Phys. Rev. 51, 450-484 (1937).

27. P. L. Kapur and R. E. Peierls, "Dispersion Formula for Nuclear Reactions," Proc. Roy. Soc. (London) A 166, 277-295 (1938).

28. E. P. Wigner and L. Eisenbud, "Higher Angular Momenta and Long Range Interaction in Resonance Reactions," Phys. Rev. 72, 29-41 (1947).

29. A. M. Lane and R. G. Thomas, "R-Matrix Theory of Nuclear Reactions," Rev. Mod. Phys. 30, 257-353 (1958).

30. D. J. Hughes and R. B. Schwartz, "Neutron Cross Sections," BNL-325 (2nd Ed.), U. S. Government Printing Office, Washington, D. C., July 1, 1958.

31. R. G. Moore, Jr., "Nuclear Reaction Cross-Section Theory," Rev. Mod. Phys. 32, 101-116 (1960).

32. C. E. Porter and R. G. Thomas, "Fluctuations of Nuclear Reaction Widths," Phys. Rev. 104, 483-491 (1956).

33. E. P. Wigner, "Results and Theory of Resonance Absorption" in "Conference on Neutron Physics by Time-of-Flight Held at Gatlinburg, Tennessee, November 1 and 2, 1956," R.C. Block, W. M. Good, J. A. Harvey, H. W. Schmitt, and G. T. Trammell, Eds., ORNL-2309, July 1, 1957.

34. "Symposium on Statistical Properties of Atomic and Nuclear Spectra," State University of New York, Stoneybrook, Long Island, New York, May 3, 1963.

35. E. Vogt, "Resonance Theory of Neutron Cross Sections of Fissionable Nuclei," Phys. Rev. 112, 203-214 (1958).

36. E. Vogt, "Low-Energy Neutron Cross Sections of Fissionable Nuclei," Phys. Rev. 118, 724-733 (1960).

37. N. J. Pattenden and J. A. Harvey, "Measurement of the Neutron Total Cross Section of U^{233} from 0.07 to 10,000 ev," Nucl. Sci. Eng. 17, 404-410 (1963).

38. T. Ericson, "The Statistical Model and Nuclear Level Densities," Advances in Phys. 9, 425-511 (1960).

39. L. Wolfenstein, "Conservation of Angular Momentum in the Statistical Theory of Nuclear Reactions," Phys. Rev. 82, 690-696 (1951).

40. W. Hauser and H. Feshbach, "The Inelastic Scattering of Neutrons," Phys. Rev. 87, 366-373 (1952).

41. D. T. Goldman and C. R. Lubitz, "Calculation of Inelastic Neutron Scattering: Zirconium-90, Zirconium-92, Niobium-93, and Aluminum-27," KAPL-2163, August 15, 1961.

42. L. C. Biedenharn, "Tables of the Racah Coefficients," ORNL-1098, March 21, 1952.

43. A. M. Weinberg and E. P. Wigner, "The Physical Theory of Neutron Chain Reactors," University of Chicago Press, Chicago, 1958.

44. R. D. Albert, S. D. Bloom, and N. K. Glendenning, "(p, n) Angular Distributions from Mirror Nucleus Targets: C^{13}, B^{11} and Be^{9}," Phys. Rev. 122, 862-869 (1961).

45. N. C. Francis, D. T. Goldman, and E. Guth, "Photoneutron Disintegration below the Giant Resonance: Beryllium-9 and Carbon-13," Phys. Rev. 120, 2175-2184 (1960).

46. R. G. Sachs, "Nuclear Theory," p. 238, Addison-Wesley Publishing Company, Inc., Reading, Mass., 1953.

47. J. M. Blatt and L. C. Biedenharn, "The Angular Dependence of Scattering and Reaction Cross Sections," Phys. Rev. 82, 123 (1951).

48. W. Czyz and J. Sawicki, "Polarization of Nucleons from Photonuclear Reactions," Nuovo Cimento 3, Series 10, 864-869 (1956).

49. K. Siegbahn, Ed., "Beta- and Gamma-Ray Spectroscopy," John Wiley and Sons, Inc., New York, 1955.

50. Y. C. Tang, F. E. Khanna, R. C. Herndon, and K. Wildermuth, "Be^{9} in the Cluster Model," Nucl. Phys. 35, 421-433 (1962).

51. D. T. Goldman and J. R. Stehn, "Chart of the Nuclides," 6th Ed., General Electric Company, Schenectady, New York, 1961.

52. M. G. Mayer, "On Closed Shells in Nuclei. II," Phys. Rev. 75, 1969-1970 (1949).

53. S. A. Moszkowski, "Models of Nuclear Structure" in "Handbuch der Physik," Vol. XXXIX, S. Flugge, Ed., pp. 411-550, Springer-Verlag, Berlin, 1957.

54. D. M. Chase, L. Wilets, and A. R. Edmonds, "Rotational-Optical Model for Scattering of Neutrons," Phys. Rev. 110, 1080-1092 (1958).

55. E. H. Auerbach, N. C. Francis, and D. T. Goldman, "ABACUS: A Digital Computer Program for Calculating Cross Sections from Complex Potential Models" in "Reactor Technology Report No. 15 - Physics," KAPL-2000-12, pp. I.21-I.22, December 1960.

56. D. T. Goldman, C. R. Lubitz, and A. W. Thomas, "An Improved Version of ABACUS for Calculating Cross Sections from Complex Potential Models" in "Reactor Technology Report No. 19 - Physics," KAPL-2000-16, pp. I.20-I.21, December 1961.

57. J. B. Weddell, "Scattering of 4.4-Mev Neutrons by Aluminum, Calcium, Chromium, and Bismuth," Phys. Rev. 104, 1069-1072 (1956).

58. R. B. Day, "Gamma Rays from Neutron Inelastic Scattering," Phys. Rev. 102, 767-787 (1956).

59. J. H. Towle and W. B. Gilboy, "Spin Assignments in Al^{27} from Neutron Scattering Studies," Nucl. Phys. 39, 300-317 (1962).

60. L. Cranberg and J. S. Levin, "Neutron Scattering at 2.45 Mev by a Time-of-Flight Method," Phys. Rev. 103, 343-352(1956).

61. R. E. Marshak, "Theory of the Slowing Down of Neutrons by Elastic Collision with Atomic Nuclei," Rev. Mod. Phys. 19, 185-238 (1947).

62. H. Hurwitz, Jr., and P. F. Zweifel, "Slowing Down of Neutrons by Hydrogenous Moderators," J. Appl. Phys. 26, 923-931 (1955).

63. P. F. Zweifel and H. Hurwitz, Jr., "Transformation of Scattering Cross Sections," J. Appl. Phys. 25, 1241-1245 (1954).

64. G. A. G. De Coulon, L. D. Gates, and W. R. Worley, "Spectral Shift Control Reactor Basic Physics Program-Theoretical Analysis. Part II. BPG Computer Program Report," BAW-1230 (Pt. II), January 1962.

65. S. Glasstone and M. C. Edlund, "The Elements of Nuclear Reactor Theory," D. Van Nostrand Company, Inc., Princeton, N. J., 1952.

66. H. Amster, "Heavy Moderator Approximations in Neutron Transport Theory," J. Appl. Phys. 29, 623-627 (1958).

67. H. J. Amster and L. M. Culpepper, "Surface Modified Nuclear Optical Model: Description of the SUMNUM Code for the NORC Computer," WAPD-TM-87, October 1957.

68. E. Greuling, F. Clark, and G. Goertzel, "A Multigroup Approximation to the Boltzmann Equation for Critical Reactors," NDA 10-96.

69. H. J. Amster and C. B. Noll, "Graphs of Coefficients for Determining Multigroup P-1 Constants from Differential Scattering Cross Sections," WAPD-TM-284, July 1961.

70. H. J. Amster, "Anisotropy in the Slowing Down of Neutrons" in "Bettis Technical Review, Reactor Physics and Mathematics," WAPD-BT-17, February 1960, pp. 65-68.

71. G. Goertzel and E. Greuling, "An Approximate Method for Treating Neutron Slowing Down," Nucl. Sci. Eng. 7, 69-72 (1960).

72. H. J. Amster, H. G. Kuehn, and J. Spanier, "EURIPUS-3 and DAEDALUS - Monte Carlo Density Codes for the IBM-704," WAPD-TM-205, February 1960.

73. M. J. Berger and J. Dogett, "Reflection and Transmission of Gamma Radiation by Barriers: Semianalytic Monte Carlo Calculation," J. Res. Natl. Bur. Std. 56, 89-98 (1956).

74. D. W. Drawbaugh, "On the Solution of Transport Problems by Conditional Monte Carlo," Nucl. Sci. Eng. 9, 185-197 (1961).

75. E. S. Troubetzkoy, "Volume C, Fast Neutron Cross Sections of Iron, Silicon, Aluminum, and Oxygen" in "Final Report Covering the Period December 17, 1958-September 30, 1959," NDA-2111-3 (Vols. A, B, and C), November 1, 1959.

76. H. J. Amster and R. C. Gast, "The Analysis of Foil Activation Experiments in Infinite Homogeneous Media," Nucl. Sci. Eng. 11, 167-178 (1961).

77. H. Goldstein, P. F. Zweifel, and D. G. Foster, Jr., "The Slowing Down of Neutrons in Hydrogenous Media-- Status of Theory and Experiment" in "Proceedings of the Second United Nations International Conference on the Peaceful Uses of Atomic Energy, Geneva, 1958," Vol. 16, pp. 379-405, United Nations, Geneva, 1958.

78. D. B. Lombard and C. H. Blanchard, "Fission-to-Indium Age in Water," Nucl. Sci. Eng. 7, 448-453 (1960).

79. J. E. Hill, L. D. Roberts, and T. E. Fitch, "Slowing Down Distribution of U^{235} Fission Neutrons from a Point Source in Light Water," J. Appl. Phys. 26, 1013-1017 (1955).

80. J. W. Wade, "Neutron Age in Mixtures of D_2O and H_2O," Nucl. Sci. Eng. 4, 12-24 (1958).

81. E. Fermi, H. L. Anderson, and D. Nagle, "Nuclear Physics Research Report for Month Ending March 25, 1944," CP-1531, p. 6.

82. L. M. Barkov and K. N. Mukhin, "The Slowing Down of Fission Neutrons in Water," J. Nucl. Energy 4, 91-93 (1957).

83. R. C. Doerner, R. J. Armani, W. E. Zagotta, and F. H. Martens, "Age of Fission Energy Neutrons to Indium Resonance in Water," Nucl. Sci. Eng. 9, 221-240 (1961).

84. L. Dresner, "Resonance Absorption in Nuclear Reactors," p. 33, Pergamon Press, Inc., New York, 1960.

85. G. M. Roe, "The Absorption of Neutrons in Doppler Broadened Resonances," KAPL-1241, October 15, 1954.

86. R. D. Richtmyer, R. Van Norton, and A. Wolfe, "The Monte Carlo Calculation of Resonance Capture in Reactor Lattices" in "Proceedings of the Second United Nations International Conference on the Peaceful Uses of Atomic Energy, Geneva, 1958," Vol. 16, pp. 180-186, United Nations, Geneva, 1958.

87. L. W. Nordheim, GA-638 (Rev.), 1959.

88. G. I. Marchuk, "Numerical Methods for Nuclear Reactor Calculations," Suppl. Nos. 3-4 of Atomnaya Energiya., Translation, Consultants Bureau, Inc., New York, 1959.

89. S. Stein, "Resonance Capture in Heterogeneous Systems," WAPD-139, November 1955.

90. E. P. Wigner, E. Creutz, H. Jupnik, and T. Snyder, "Resonance Absorption of Neutrons by Spheres," J. Appl. Phys. 26, 263 (1955).

91. K. M. Case, F. de Hoffmann, and G. Placzek, "Introduction to the Theory of Neutron Diffusion, Vol. I," U. S. Government Printing Office, Washington, D.C., 1953.

92. C. W. Maynard, "Blackness Theory and Coefficients for Slab Geometry," Nucl. Sci. Eng. 6, 174-186 (1959).

93. G. W. Stuart and R. W. Woodruff, "Method of Successive Generations," Nucl. Sci. Eng. 3, 339-373 (1958).

94. J. Dwork, P. L. Hofmann, H. Hurwitz, Jr., and E. F. Clancy, "Self-Shielding Factors for Infinitely Long, Hollow Cylinders," KAPL-1262, January 10, 1955.

95. W. Rothenstein, "Collision Probabilities and Resonance Integrals for Lattices," Nucl. Sci. Eng. 7, 162-171 (1960).

96. G. N. Watson, "A Treatise on the Theory of Bessel Functions," 2nd Ed., The Macmillan Company, New York, 1944.

97. L. W. Nordheim, "A New Calculation of Resonance Integrals," Nucl. Sci. Eng. 12, 457-463 (1962).

98. E. Hellstrand, "Measurements of the Effective Resonance Integral in Uranium Metal and Oxide in Different Geometries," J. Appl. Phys. 28, 1493-1502 (1957).

99. E. Hellstrand and G. Lundgren, "The Resonance Integral for Uranium Metal and Oxide," Nucl. Sci. Eng. 12, 435-436 (1962).

100. R. Ehrlich and H. Hurwitz, Jr., "Multigroup Methods for Neutron Diffusion Problems," Nucleonics 12 (2), 23-30 (1954).

101. H. Bohl, Jr., E. M. Gelbard, G. R. Culpepper, and P. F. Buerger, "P1MG — A One-Dimensional Multigroup P_1 Code for the IBM-704," WAPD-TM-135, July 1959.

102. C. Dawson, "Multigroup Transport Code RDR-5," David Taylor Model Basin Report 1450, December 1960.

103. E. H. Bareiss, "Flexible Transport Theory Routines for Nuclear Reactor Design," David Taylor Model Basin Report DTMB-1030, December 1956.

104. D. Schiff, "Derivation of the Equations for the One-Dimensional Slab and Cylindrical Multigroup Transport Codes," WAPD-146, March 1956.

105. H. J. Amster and L. M. Culpepper, "The PREP Code for Calculating Group and Angle Transfer Cross Sections of Elastic Scattering for the RDR-5 Transport Code on the NORC Computer," WAPD-TM-117, February 1958.

106. R. Gast, "On the Equivalence of the Spherical Harmonics Method and the Discrete Ordinate Method Using Gauss Quadrature for for the Boltzmann Equation," WAPD-TM-118, April 1958.

107. R. D. Richtmyer, "Difference Methods for Initial-Value Problems," p. 139, Interscience Publishers, Inc., New York, 1957.

108. G. Goertzel, "The Method of Discrete Ordinates," Nucl. Sci. Eng. 4, 581-587 (1958).

109. H. Bohl, E. Gelbard, P. Buerger, and G. Culpepper, "SLOP-1, A Thermal Multigroup Program for the IBM-704," WAPD-TM-188, October 1960.

110. J. Bengston, "Neutron Self-Shielding of a Plane Absorbing Foil," CF-56-3-170, March 1, 1956, pp. 7-12.

111. R. Mertens, "Contribution to the Theory of the Multiple Scattering of Particles," Simon Stevin, Suppl., 30, 11 pp. (1954).

112. H. B. Keller, "Approximate Solutions of Steady-State Neutron Transport Problems for Slabs," NYO-8671, July 1, 1958.

113. J. Certaine, "A Solution of the Neutron Transport Equation. Part II: NDA-Univac Moment Calculations," NYO-6268, May 31, 1955.

114. H. Bohl, Jr., E. M. Gelbard, and G. H. Ryan, "MUFT-4—Fast Neutron Spectrum Code for the IBM-704," WAPD-TM-72, July 1957.

115. G. C. Wick, "On the Space Distribution of Slow Neutrons," Phys. Rev. 75, 738-756 (1949).

116. D. S. Selengut, "Conditions for Criticality in Certain Types of Nuclear Reactors," AECD-3024, September 1950.

117. D. S. Selengut, "Critical Mass Calculations for Bare Hydrogen Moderated Reactors by Means of Transport Theory," APEX-121, September 1952.

118. A. M. Weinberg and L. C. Noderer, "Theory of Neutron Chain Reactions; Vol. I. Diffusion and Slowing Down of Neutrons Chapters I-IV," ORNL-51-5-98, May 15, 1951.

119. J. E. Wilkins, Jr., R. L. Hellens, and P. F. Zweifel, "Status of Experimental and Theoretical Information on Neutron Slowing-Down Distributions in Hydrogenous Media" in "Proceedings of the International Conference on the Peaceful Uses of Atomic Energy, Geneva, 1955," Vol. 5, pp. 63-76, United Nations, New York, 1956.

120. S. J. Lukasik, "Summary of TRX Analysis Calculations," WAPD-TM-75, July 1957.

121. L. Friedman, "Few Group Constants for Delayed Neutrons," WAPD-TM-6, June 1956.

122. R. L. Hellens, "Neutron Slowing Down in Group Diffusion Theory," WAPD-114, May 1956.

123. R. L. Hellens, R. W. Long, and B. H. Mount, "Multigroup Fourier Transform Calculation -- Description of MUFT-III Code," WAPD-TM-4, July 1956.

124. H. Bohl, Jr. and A. P. Hemphill, "MUFT-5 — A Fast Neutron Spectrum Program for the Philco-2000," WAPD-TM-218, February 1961.

125. C. D. Petrie, "SLAG, A Multigroup Age Calculation," KAPL-1789, June 1957.

126. A. F. Henry, "54 Group Library for P-1 Programs," WAPD-TM-224, April 1960.

127. R. D. Richtmyer, "Monte Carlo Study of Resonance Escape in Hexagonal Reactor Lattices," NYO-6479, May 1955.

128. P. A. Ombrellaro, "Effective Fast Group Cross Sections in Four Group Theory," WAPD-TM-63, May 1957.

129. P. A. Ombrellaro, "Effective Fast Group Cross Sections in Few Group Diffusion Theory," KAPL-M-PAO-1, March 7, 1961.

130. G. P. Calame, F. D. Federighi, and P. A. Ombrellaro, "A Two-Mode Variational Procedure for Calculating Thermal Diffusion Theory Parameters," Nucl. Sci. Eng. 10, 31-39 (1961).

131. O. J. Marlowe and P. A. Ombrellaro, "CANDLE — A One-Dimensional Few-Group Depletion Code for the IBM-704," WAPD-TM-53, May 1957.

132. J. A. Archibald, Jr., "The KARE System for Computing Life Studies Automatically," Trans. Am. Nucl. Soc. 3 (1), 64-65 (1960).

133. H. Amster and R. Suarez, "The Calculation of Thermal Constants Averaged Over a Wigner-Wilkins Flux Spectrum: Description of the SOFOCATE Code," WAPD-TM-39, January 1957.

134. O. J. Marlowe, C. P. Saalbach, L. M. Culpepper, and D. S. McCarty, "WANDA — A One-Dimensional Few Group Diffusion Equation Code for the IBM-704," WAPD-TM-28, November 1956.

135. P. A. Ombrellaro and F. D. Federighi, "A Variational Procedure for Calculating Fast Group Diffusion Theory Parameters," Trans. Am. Nucl. Soc. 5 (1), 63-64 (1962).

Chapter 3

THE NEUTRON THERMALIZATION PROBLEM

R. J. Breen, Editor

3.1 INTRODUCTION

The neutron energy spectrum in reactors is conveniently divided into two parts: fast and thermal. The fast neutrons include the fission spectrum, the energy range of most artificial neutron sources, and are primarily characterized by scattering collisions (either elastic or inelastic) which do not add energy to the neutron. The thermal neutrons have energies of the order of the kinetic energy of the moderator and are involved in scattering collisions where the neutron energy may be either increased or decreased. The point on the energy scale which separates the fast and thermal neutrons is usually chosen high enough so that the number of neutrons that have scattering collisions below that energy point and subsequently reappear above that energy will be negligible. While this energy cut point is dependent on the temperature of the moderator, a value of the order of 1 ev is usually adequate for all practical temperatures in a water-moderated reactor. Practical considerations help dictate what the specific choice will be. For example, if a particular isotope has a single resonance between 1 and 2 ev, it may be convenient to allow the thermal neutron range to include the resonance for ease in analyzing activation experiments. Most design calculations in the Naval Reactors program use 0.625 ev for the cut point, which is consistent with the cross-section libraries used in the MUFT slowing-down program.

A further distinction between fast and thermal neutrons arises from the molecular structure of the scattering nucleus. The energy of neutrons in the fast energy range is considerably greater than the molecular binding energies. Fast neutrons may be treated as having collisions with free atoms. In contrast, the thermal neutrons have energies of the order of the molecular binding energies, complicating the treatment of elastic scattering and requiring consideration of molecular inelastic scattering processes.

A third major difference between the two energy ranges of neutrons exists in their respective diffusion lengths. The shorter diffusion lengths found in the thermal range result in a larger sensitivity to the structural details. While the fast flux distribution is relatively flat over a subunit of a reactor, the thermal flux level may vary greatly from one component to another within that subunit. This results in the need to give considerable attention to geometrical representation in evaluating the contribution of the thermal neutrons to the multiplication factor and power distributions.

The subject matter of this chapter complements Chap. 2 in discussing problems involved in describing neutron energy dependence. Application of the tools and methods here described is given in Chap. 4, where reactor design techniques are discussed. Similarly, the material described in Chap. 5 on Kinetics and Stability assumes that a reasonable and tractable description of thermal neutrons is available.

Chapter 6, on the other hand, contains discussions of experiments which help to verify some of the techniques discussed here and to test the adequacy and sensitivity to some of the approximations that have been made. Of particular interest are the comparisons of measured and calculated power distributions described in Sect. 6.2 and the low energy spectral measurements described in Sect. 6.3.

The digital computer programs discussed or referenced in this chapter are described in Chap. 7, Sect. 7.4. Mathematical techniques necessary for the practical solution of some of the problems arising in Chap. 3 are also given there.

The material in Chap. 3 is arranged in three sets. The first set (Sect. 3.2, Inelastic Scattering of Thermal Energy Neutrons; Sect. 3.3, Sensitivity to the Neutron Scattering Kernel) is concerned with the evaluation and verification of nuclear properties of the moderators in the thermal group. Since the energy-dependent fission and absorption cross sections may be measured fairly accurately in the thermal energy range with existing experimental techniques, the fission and capture interaction rates may be treated in a straightforward manner. By contrast, more detailed information is required for treating scattering interactions. A complete description of the scattering process requires a knowledge of the scattering cross section as a function of the energy at which the collision is made and the energy to which the neutron is scattered and the angle through which the neutron is scattered. Experimental techniques today do not yield information for scattering processes as accurate nor as directly interpretable as for the fission and absorption cross sections. Because of the additional complexity involved, more emphasis must be placed on

developing a detailed analytical model for the scattering cross section and testing this model against experiments where integrated or average properties are measured.

While the problem of describing the scattering kernel is imposing, simple models have had considerable success in past years. This is partly due to the fact that any physical kernel is assumed to satisfy detailed balance, which ensures that for negligible absorption the neutrons will have a Maxwellian energy distribution at the temperature T of the moderator. It is to be anticipated that only for conditions where the spectrum deviates strongly from Maxwellian would spectra calculations possibly differ for different representations of the scattering kernel.

Section 3.2 describes the basic theory being used today to formulate the differential scattering cross section of chemically bound scatterers. When this theory is applied to a free gas of unit mass, the formulation that has been used extensively in recent years is obtained. This method for calculating the spectrum coupled with the Radkowsky prescription for defining the transport cross section of hydrogen in a water moderator has been the mainstay for nuclear design calculations in the Naval Reactors program. Other models of the kernel of a more complex nature continue to be studied. A measure of the importance of improving this description is given in Sect. 3.3, where the sensitivity of flux spectra and diffusion lengths to the choice of kernel are discussed.

The second and third sets of the discussions are similar to each other in that, assuming a knowledge of the nuclear properties, they both approach the problem of describing the thermal neutron flux, which is a function of energy, angle, and position. They differ markedly, though, in their secondary objectives. The second set (Sect. 3.4, Multigroup Theory; Sect. 3.5, Application of Monte Carlo Methods to Neutron Thermalization) emphasizes definitive calculations with considerable accuracy for a restricted class of problems, while the third set (Sect. 3.6, Blackness Theory for Slabs; Sect. 3.7, Approximations to Multigroup Methods; Sect. 3.8, A Two-Mode Variational Procedure for Calculating Thermal-Diffusion Theory Parameters) is concerned with more approximate techniques that may be included directly in an integrated design or analysis effort.

Two methods of performing accurate calculations are described in Sects. 3.4 and 3.5. The first technique reformulates the transport equation in a set of equations where the energy, angle, and space variables are treated at discrete points. The energy variable is handled in a direct fashion by breaking the energy range into a large number of energy intervals in which

simplifying assumptions about the cross sections and fluxes may be made. These energy groups are coupled to each other through the scattering term. Various approximations to the angular variable are considered. The second technique utilizes Monte Carlo methods for treating the space and angle variables but retains the discrete representation of the energy variable. While the first technique might be used in a limited sense in two spatial dimensions, its primary application has been in one-dimensional geometry. The Monte Carlo technique does not undergo a large increase in complexity when extended to two or three dimensions and has been the mainstay as a standard in geometries where more than one dimension is important. The digital computer programs that use these techniques are further distinguished by the fact that they are not usually coupled with the fast-group equations to form an eigenvalue (multiplication factor) calculation but require a specified source of neutrons slowing down into the thermal group.

The last three sections (3.6, 3.7, and 3.8) deal with methods for allowing the designer or analyst to approximate the more exact methods in the second set. The first of these three sections is concerned with the treatment of transport effects that exist when strong absorbers are present. While the theory and application of blackness theory are developed in a one-velocity framework in Sect. 3.6, the application of blackness theory to few-group calculations is described in Sect. 3.7 of this chapter and in Chap. 4, Sect. 4.2.D.

The application of blackness theory to strong absorbers has been very useful in determining effective cross sections to be used in the explicit description of the strong absorbers in diffusion theory calculations. Although the theory is developed in one dimension, the application has been effective in two-dimensional geometries where the strong absorbers have dimensions of the order of a few centimeters.

Besides the use of blackness theory for describing lumped absorbers, the double-blackness approach described in Sect. 3.6 yields a very useful tool for calculating the thermal utilization of a fuel plate-coolant channel lattice. The tables given in this section allow a fairly high order transport calculation for this geometry to be obtained in a simple manner if group-averaged cross sections are used.

When it is necessary to perform a more integrated reactor calculation, coupling the description of the thermal neutrons with a description of the fast neutrons to solve the eigenvalue problem, the models described in Sect. 3.7, Approximations to Multigroup Methods, are required. The different one-group models are described first with their deficiencies identified. These have been used to a great extent and represent the least

costly method of achieving the design task. Techniques have been evolved in some instances to correct these models to compensate for their inherent deficiencies. An example of this is the use of blackness theory to describe heavy absorbers, or where two-dimensional effects are important, adjusting the cross sections (D and Σ) for the absorber so that the relative absorption rates in diffusion theory agree with those in a corresponding Monte Carlo calculation.

The ability to perform an eigenvalue calculation while treating the energy spectra more accurately is available in the few-group methods described in Sect. 3.7. While these techniques are only now approaching the point where they can be used in extensive design calculations, they have already proved to be valuable in the analysis of experiments. Two different approaches to this problem are described in Sects. 3.7.C and 3.7.D. The first approach is to approximate the multigroup formulation with a smaller number of groups, each covering a sizable fraction of the thermal energy range. The formulation of these few-group cross sections and the comparison of the few-group and multigroup calculations for the P_1, double-P_1, and P_3 approximations to the transport equation are discussed.

The other method is to describe the energy dependence of the flux as the linear combination of two or more preselected spectra, each defined over the entire energy range. The coefficients of combination are obtained as a function of position yielding a spatial variation in the energy spectrum. Coupled equations are derived from a variational principle, and comparisons with multigroup calculations are given.

A similar approach is described in Sect. 3.8 for calculating infinite medium spectra. A technique is developed for setting up a library of cross sections averaged over the trial spectra so that cross sections averaged over a new spectrum can be obtained as a linear combination of those averaged over the trial spectra. This method could be used, for example, for the rapid generation of cross sections for depletion calculations when these calculations are sensitive to the spectrum variation with lifetime.

3.2 INELASTIC SCATTERING OF THERMAL ENERGY NEUTRONS

D. T. Goldman

A. Introduction

The calculation of neutron scattering is of importance in specifying the cross sections for the theory of neutron transport. Equation (3.1) is the usual general vector-flux equation

(the Boltzmann Equation, Ref. 1, Chap. IX) with the terms of interest to the present discussion underlined:

$$\frac{1}{v}\frac{\partial f(\vec{r},E,\vec{\Omega})}{\partial t} = -\vec{\Omega}\cdot\nabla f(\vec{r},E,\vec{\Omega}) - f(\vec{r},E,\vec{\Omega})\left[\underline{\Sigma_s(\vec{r},E)} + \Sigma_a(\vec{r},E)\right]$$

$$+\iint dE'd\vec{\Omega}' f(\vec{r},E',\vec{\Omega}')\,\underline{\Sigma_s(\vec{r},E'\to E,\vec{\Omega}'\to\vec{\Omega})} + \underline{S(\vec{r},E,\vec{\Omega})}\ . \qquad \text{Eq. (3.1)}$$

The first underlined term on the right-hand side of the equation is the energy and angle integrated differential cross section, viz.,

$$\Sigma_s(\vec{r},E) = \iint dE'd\vec{\Omega}'\,\Sigma_s(\vec{r},E\to E',\vec{\Omega}\to\vec{\Omega}')\ . \qquad \text{Eq. (3.2)}$$

There is no dependence on $\vec{\Omega}$, since the scattering cross section is assumed to be a function only of the angle of scattering, and a single integration over $\vec{\Omega}'$ removes the angular dependence. The $\Sigma_a(\vec{r},E)$ term denotes the removal cross section for all other processes, and methods for its calculation have been discussed in Chap. 2, Sect. 2.2. The next term of Eq. (3.1) contains $\Sigma_s(\vec{r},E'\to E,\vec{\Omega}'\to\vec{\Omega})$ explicitly, and this will be the quantity upon which most attention is focused. The final term, $S(\vec{r},E,\vec{\Omega})$ accounts for all possible sources of neutrons; it certainly contains all external sources. However, in practice, it is customary to begin the detailed solution of the Boltzmann equation with a specific upper energy limit. The neutrons which arise with a larger energy and are scattered down to the energy region of interest are, thus, to be included in the source term:

$$S(\vec{r},E,\vec{\Omega}) = \iint_{E_c}^{\infty} f(\vec{r},E',\vec{\Omega})\,\Sigma_s(\vec{r},E'\to E,\vec{\Omega}'\to\vec{\Omega})dE'd\vec{\Omega}' + \cdots\ . \qquad \text{Eq. (3.3.)}$$

General approximations to include these corrections to the source term will be discussed below.

The scattering of neutrons with energies below about one electron volt introduces new elements of complexity into reactor calculations. Because the energy of excitation of the chemical modes of the scatterer is, for this energy region, of the order of the incident neutron energy, the chemical properties of the scatterer will influence the scattering results. In this section, various analytical attempts made to solve the

scattering problem, culminating with the formal treatment of Zemach and Glauber, will be considered. Then, consideration will be given to the application of the theoretical treatment, using both analytical and numerical techniques, to the scattering of neutrons from commonly used reactor materials, such as water and polyethylene, and comparisons made with available experimental results. Finally, suggested extensions to both the theory and experimental data will be outlined.

Simple scattering models have been used extensively in the past, especially in combination with empirical or semiempirical results. In this section, techniques will be described which have been developed for placing the analysis of low energy neutron scattering on a firmer physical basis. In a subsequent section (Sect. 3.3) the results of using different models for scattering will be described in terms of differences in flux spectra, diffusion lengths, and in the analysis of pulsed neutron experiments.

There remains, in passing, the additional question of the use of neutron scattering information to determine the physical characteristics of the scatterer, analogous to the use of X-ray scattering for this purpose.[2] In fact, because of the convenient wave length energy relationship available with neutron beams, more detailed low energy (millivolt) information could be obtained. This problem has been examined both theoretically[3] and experimentally[4] and will not be treated at length here. Suffice it to say, it will be shown that the differential cross section is the four-dimensional Fourier transform of the space-time correlation function [see Eq. (3.14)], and a knowledge of this correlation function would then permit the calculation of the scattering cross section. Alternatively, an exact measurement of the differential cross section over an extended range of energies and scattering angles would enable one to calculate the correlation function which is related to the physical state of the scattering system. The exact relation will be presented later.

B. Theory of Scattering

What follows is a discussion of some of the original theoretical treatments for the scattering of neutrons by chemical systems which culminated in the general theory of Zemach and Glauber[5] (hereafter referred to as Z-G); the derivation of the formula for the differential cross section; the transform of the cross section, the correlation function, which will appear naturally as well as the classical interpretation; some general properties of the cross section; and some approximate methods for the calculation of the correlation function.

1. General

The treatment of the scattering of neutrons by bound nuclei has been considered by Fermi,[6] Placzek,[13] Wick,[8] and by Zemach and Glauber.[5] The last paper is the most directly relevant to reactor work and is the basis of the discussion here. Equation (2.8) of Zemach and Glauber's paper may be written for a density $\rho(E_i)$ of initial states in the form

$$\frac{d\sigma}{d\Omega} = \left(\frac{m}{2\pi\hbar^2}\right)^2 \frac{k}{k_o} \sum_{i,f} \int_{-\hbar k_o^2/2m}^{\infty} \delta\left(\frac{E_i - E_f}{\hbar} - \omega\right) \cdot d\epsilon\, \rho(E_i) \left| \int \psi_f^* \left\{ \int e^{-i\vec{K}\cdot\vec{r}} V(r)\, d\vec{r} \right\} \psi_i\, d\tau \right|^2 \qquad \text{Eq. (3.4)}$$

where m, $\vec{k}_o$, and $\vec{k} = \vec{K} + \vec{k}_o$ are the mass and initial and final wave vectors of the scattered particles; ψ_i, ψ_f, E_i, E_f are the initial and final wave functions of the corresponding energies of the scattering system; and the energy change

$$\epsilon = \hbar\omega = \frac{\hbar^2 k^2}{2m} - \frac{\hbar^2 k_o^2}{2m}.$$

The delta function ensures that only energy-conserving terms are included in the integration.

The potential appearing in Eq. (3.4) is the sum of the contributions due to individual scattering centers. For the two-body potential, the customary Fermi pseudopotential is utilized,[6] where the short-range neutron-nucleus potential is replaced by a delta function interaction with an appropriate strength to give the correct total cross section (Ref. 7, Chap. 5). Thus, the interaction potential may be written as

$$V(\vec{r}) = \sum_{\nu} V(\vec{r}, \vec{r}_\nu) = \frac{2\pi\hbar^2}{m} \sum_{\nu} a_\nu \delta(\vec{r} - \vec{r}_\nu) \qquad \text{Eq. (3.5)}$$

where a_ν is the scattering length of the scattering from a particle at the ν^{th} position.

Making the substitution for $V(\vec{r})$, the differential cross section in bra and ket notation is

$$\frac{d\sigma}{d\Omega} = \frac{k}{k_o} \sum_{i,f} \int_{-\hbar k_o^2/2m}^{\infty} \delta\left(\frac{E_i - E_f}{\hbar} - \omega\right) d\epsilon \rho(E_i) \left| \left(f \left| \sum_{\nu} a_\nu e^{-i\vec{K}\cdot\vec{r}_\nu} \right| i \right) \right|^2 .$$

Eq. (3.6)

Making use of the Fourier representation of the delta function, first introduced in this connection by Wick,[8] one can go over to a time-dependent, energy differential form of the cross section:

$$\frac{d^2\sigma}{d\Omega\, d\epsilon} = \frac{k}{2\pi k_o} \sum_{i,f} \rho(E_i) \int dt e^{-i\omega t} e^{i\frac{E_i - E_f}{\hbar}t} \left| \left(f \left| \sum_{\nu} a_\nu e^{-i\vec{K}\cdot\vec{r}_\nu} \right| i \right) \right|^2 .$$

Eq. (3.7)

This equation will be used extensively in subsequent discussions.

Except for a factor of the ratio of final to initial velocities of the neutron, the cross section is a function only of its momentum transfer and energy loss. Thus, one may write[9]

$$\frac{d^2\sigma}{d\Omega\, d\epsilon} = \frac{k}{k_o} \overline{S}(\vec{K}, \omega) \qquad \text{Eq. (3.8)}$$

where $\overline{S}(\vec{K}, \omega)$ is given by

$$\overline{S}(\vec{K}, \omega) = \frac{1}{2\pi} \sum_{i} \rho(E_i) \sum_{f} \int e^{i\left(\frac{E_i - E_f}{\hbar} - \omega\right)t} dt \left| \sum_{\nu} \left(f \left| a_\nu e^{-i\vec{K}\cdot\vec{r}_\nu} \right| i \right) \right|^2 .$$

Eq. (3.9)

From this point until the start of Sect. 3.2.B.2 (Zemach-Glauber Formalism), a presentation aimed at understanding the physical basis of the scattering system is given. This is of interest from the point of view of a model for the scatterer. The portion of the text which is concerned with direct application to the scattering of neutrons resumes at Sect. 3.2.B.2.

To clarify the meaning of the function $\bar{S}(\vec{K},\omega)$, examine its Fourier transform $\Gamma(\vec{r},t)$ defined as

$$\bar{S}(\vec{K},\omega) = \frac{N}{2\pi}\int e^{i(\vec{K}\cdot\vec{r}-\omega t)}\Gamma(\vec{r},t)\,d\vec{r}\,dt \qquad \text{Eq. (3.10)}$$

or

$$\Gamma(\vec{r},t) = \frac{1}{(2\pi)^3 N}\int e^{i(\omega t-\vec{K}\cdot\vec{r})}\bar{S}(\vec{K},\omega)\,d\vec{K}\,d\omega. \qquad \text{Eq. (3.11)}$$

The normalization $N/2\pi$ was introduced by Van Hove to make $\Gamma(\vec{r},t)$ independent of N and asymptotically equal to the number density of the scatterer as $N\to\infty$.

To understand the significance of the function Γ, substitute Eq. (3.9) into Eq. (3.11), reconstitute the delta function, and integrate over ω to get

$$\Gamma(\vec{r},t) = \frac{1}{(2\pi)^3 N}\sum_i \rho(E_i)\sum_f\sum_{\nu\nu'}\int d\vec{K}\,e^{-i\vec{K}\cdot\vec{r}} \cdot e^{i\frac{E_i-E_f}{\hbar}t}\left(i\left|a_\nu e^{i\vec{K}\cdot\vec{r}_\nu}\right|f\right)\left(f\left|a_{\nu'}\, e^{-i\vec{K}\cdot\vec{r}_{\nu'}}\right|i\right). \qquad \text{Eq. (3.12)}$$

Using the relation

$$e^{i\frac{Ht}{\hbar}}\Big|i\Big) = e^{i\frac{E_i t}{\hbar}}\Big|i\Big) \qquad \text{Eq. (3.13)}$$

(where H is the Hamiltonian governing the target motion), one can reduce Eq. (3.12) to

$$\Gamma(\vec{r},t) = \frac{1}{(2\pi)^3 N}\sum_i \rho(E_i)\sum_f\sum_{\nu\nu'}\int d\vec{K}\,e^{-i\vec{K}\cdot\vec{r}} \cdot\left(i\left|e^{iHt/\hbar}a_\nu e^{i\vec{K}\cdot\vec{r}_\nu}e^{-iHt/\hbar}\right|f\right)\left(f\left|a_{\nu'}e^{-i\vec{K}\cdot\vec{r}_{\nu'}}\right|i\right). \qquad \text{Eq. (3.14)}$$

Since there is now no dependence inside the summation on the final states of the scatterer, it is possible to sum over final states and make use of the orthonormality of the states of the system. This yields

$$\Gamma(\vec{r},t) = \frac{1}{(2\pi)^3 N} \sum_{\nu\nu'} d\vec{K}\, e^{-i\vec{K}\cdot\vec{r}} \left\langle a_\nu(t)\, e^{i\vec{K}\cdot\vec{r}_\nu(t)}\, a_{\nu'}\, e^{-i\vec{K}\cdot\vec{r}_{\nu'}} \right\rangle$$

Eq. (3.15)

where $\langle\ \rangle$ denotes the ensemble average of the expectation value of the quantity in the brackets, and $\vec{r}(t)$ is the Heisenberg operator

$$\vec{r}(t) = e^{iHt/\hbar}\,\vec{r}\,e^{-iHt/\hbar} \qquad \text{Eq. (3.16)}$$

satisfying the Heisenberg equation of motion

$$i\hbar\frac{d\vec{r}(t)}{dt} = \vec{r}(t)\,H - H\,\vec{r}(t).$$

The momentum transform appearing in Eq. (3.15) can be replaced by a space integral using the convolution formula for a Fourier transform of a product.[10] One obtains

$$\Gamma(\vec{r},t) = \frac{1}{N}\left\langle \sum_{\nu,\nu'=1}^{N} a_\nu(t)\,a_{\nu'} \int d\vec{r}'\ \delta(\vec{r}+\vec{r}_{\nu'}-\vec{r}')\,\delta(\vec{r}'-\vec{r}_\nu(t)) \right\rangle .$$

Eq. (3.17)

If a spin-independent Hamiltonian is assumed, there is no correlation between the spin and position coordinates, and one may write

$$\Gamma(\vec{r},t) = \frac{\langle a^2\rangle_{sp}}{N}\left\langle \sum_{\nu=1}^{N} \int d\vec{r}'\ \delta(\vec{r}+\vec{r}_{\nu'}-\vec{r}')\,\delta(\vec{r}'-\vec{r}_\nu(t)) \right\rangle$$

Eq. (3.18)

$$+\frac{\langle a^2\rangle_{sp}}{N}\left\langle \sum_{\nu\neq\nu'}^{N} \int d\vec{r}'\ \delta(\vec{r}+\vec{r}_{\nu'}-\vec{r}')\,\delta(\vec{r}'-\vec{r}_\nu(t)) \right\rangle$$

where $\langle a \rangle_{sp}$ denotes an average over the spin states of the particle and uncorrelated scattering lengths have been assumed. This can be written as

$$\Gamma(\vec{r}, t) = \langle a^2 \rangle_{sp} G_s(\vec{r}, t) + \langle a \rangle_{sp}^2 G_d(\vec{r}, t) \qquad \text{Eq. (3.19)}$$

where the subscripts s and d refer to the self and distinct parts which are equal to

$$G_s(\vec{r}, t) = \frac{1}{N} \left\langle \sum_{\nu=1}^{N} \int d\vec{r}' \, \delta(\vec{r} + \vec{r}_\nu(0) - \vec{r}') \, \delta(\vec{r}' - \vec{r}_\nu(t)) \right\rangle \qquad \text{Eq. (3.20)}$$

and

$$G_d(\vec{r}, t) = \frac{1}{N} \left\langle \sum_{\nu \neq \nu'}^{N} \int d\vec{r}' \, \delta(\vec{r} + \vec{r}_{\nu'}(0) - \vec{r}') \, \delta(\vec{r}' - \vec{r}_\nu(t)) \right\rangle . \qquad \text{Eq. (3.21)}$$

In order to assign physical significance to the function $G(\vec{r}, t)$ defined by

$$G(\vec{r}, t) = G_s(\vec{r}, t) + G_d(\vec{r}, t)$$

examine its value at time $t = 0$. All the operators commute, and one finds

$$G(\vec{r}, 0) = \frac{1}{N} \left\langle \sum_{\nu, \nu'=1}^{N} \delta(\vec{r} + \vec{r}_{\nu'} - \vec{r}_\nu) \right\rangle$$

$$= \delta(\vec{r}) + \frac{1}{N} \sum_{\nu \neq \nu'} \left\langle \delta(\vec{r} + \vec{r}_{\nu'} - \vec{r}_\nu) \right\rangle$$

$$= \delta(\vec{r}) + g(\vec{r})$$

or

$$G_s(\vec{r}, 0) = \delta(\vec{r})$$

$$G_d(\vec{r}, 0) = g(\vec{r}) .$$

Thus, the function $G(\vec{r},t)$, which will henceforth be called the correlation function, for $t=0$ states that the probability that a particle be found at position $\vec{r}$ is a delta function (the self part), while the probability that any other particle be found at position $\vec{r}$ (the distinct part) is given by the space correlation function or pair distribution function, $g(r)$. It is this function which is customarily measured in X-ray diffraction experiments.[11] For a wave length appropriate to molecular distances ($\approx$ one $\mathring{A}$) the energy of the electromagnetic radiation is too large to be affected by the chemical binding of the scatterer. Neutrons, on the other hand, have wave lengths and corresponding energies of just such a nature to be of use in determining the extended correlation function $G(\vec{r},t)$ which can be described as the probability that if a particle exists at the origin at time zero, there will be a particle at position $\vec{r}$ after time t. This can be separated into self and distinct parts.

In Eq. (3.17) the differential cross section may also be separated into a self and distinct part. One can write

$$\frac{d^2\sigma}{d\Omega d\epsilon} = \frac{d^2\sigma_s}{d\Omega d\epsilon} + \frac{d^2\sigma_d}{d\Omega d\epsilon} \qquad \text{Eq. (3.22)}$$

$$\frac{d^2\sigma_s}{d\Omega d\epsilon} = \langle a^2\rangle_{sp} \frac{N}{2\pi\hbar} \frac{k}{k_o} \int e^{i(\vec{K}\cdot\vec{r}-\omega t)} G_s(\vec{r},t)\, d\vec{r}\, dt \qquad \text{Eq. (3.23)}$$

and

$$\frac{d^2\sigma_d}{d\Omega d\epsilon} = \langle a\rangle^2_{sp} \frac{N}{2\pi\hbar} \frac{k}{k_o} \int e^{i(\vec{K}\cdot\vec{r}-\omega t)} G_d(\vec{r},t)\, d\vec{r}\, dt \qquad \text{Eq. (3.24)}$$

where the dependence on the scattering length is exhibited explicitly, and where the averaging is taken over states of the scattering system. For uncorrelated scattering lengths, $\langle a_i\rangle \langle a_j\rangle$ can be removed from the summation to become $\langle a\rangle^2$. If

$$\langle a\rangle^2_{sp} \frac{k}{k_o} \int e^{i(\vec{K}\cdot\vec{r}-\omega t)} G_s(\vec{r},t)\, d\vec{r}\, dt \qquad \text{Eq. (3.25)}$$

is added to Eq. (3.24) and subtracted from Eq. (3.23) the cross section is unaffected and can now be written as

$$\frac{d^2\sigma}{d\Omega d\epsilon} = \frac{d^2\sigma_{inc}}{d\Omega d\epsilon} + \frac{d^2\sigma_{coh}}{d\Omega d\epsilon}$$

where

$$\frac{d^2\sigma_{inc}}{d\Omega d\epsilon} = \frac{\langle a_{inc}\rangle_{sp}^2 N}{2\pi\hbar}\,\frac{k}{k_o}\int e^{i(\vec{K}\cdot\vec{r}-\omega t)}\,G_s(\vec{r},t)\,d\vec{r}\,dt \qquad \text{Eq. (3.26)}$$

$$\frac{d^2\sigma_{coh}}{d\Omega d\epsilon} = \frac{\langle a_{coh}\rangle_{sp}^2 N}{2\pi\hbar}\,\frac{k}{k_o}\int e^{i(\vec{K}\cdot\vec{r}-\omega t)}\,G(\vec{r},t)\,d\vec{r}\,dt \qquad \text{Eq. (3.27)}$$

and

$$\langle a_{inc}\rangle_{sp}^2 = \langle a^2\rangle_{sp} - \langle a\rangle_{sp}^2$$

$$\langle a_{coh}\rangle_{sp}^2 = \langle a\rangle_{sp}^2 \qquad \text{Eq. (3.28)}$$

The subscripts inc and coh refer to the incoherent and coherent parts of the scattering cross sections, respectively.

It can be shown that for the neutron-proton scattering system,

$$\langle a^2\rangle_{sp} = \langle a\rangle_{sp}^2 + \frac{3}{16}(a_t - a_s)^2$$

$$\langle a\rangle_{sp} = \frac{3}{4}a_t + \frac{1}{4}a_s$$

where a_t and a_s are the triplet and singlet scattering lengths, respectively (Ref. 7, Chap. 4). Since a_s is negative and much larger in magnitude than a_t, $\langle a\rangle^2/\langle a^2\rangle \ll 1$. Thus, for hydrogenous scattering materials, the incoherent approximation of setting $G(\vec{r},t) = G_s(\vec{r},t)$ has some validity, a fact pointed out by Nelkin.[12] For scattering states with intrinsic spins different from 1/2, more complicated analyses are, in general, necessary.

General properties of the scattering law can be derived and are useful either in calculating the differential cross section

or in demonstrating that a given cross section obeys these general rules. The first general principle of interest is the detailed balance condition which relates the cross section for momentum and energy gain to that of momentum and energy loss. It states that

$$S(\vec{K},\omega) = e^{-\frac{\hbar\omega}{T}} S(-\vec{K},-\omega). \qquad \text{Eq. (3.29)}$$

In Eq. (3.29) and henceforth the S functions will be used, which are the transforms of the G functions. They are equal to $\overline{S}$ with the dependence on the scattering amplitudes removed. Equation (3.29) is derivable from the expression for $\overline{S}(\vec{K},\omega)$, Eq. (3.9), by interchanging initial and final states and using the fact that $\rho(E_i) = e^{-E_i/T}$ will change to $\rho(E_f) = e^{-E_f/T}$. (In this case and all of the following, the defined temperature is in energy units, i.e., set k_B, the Boltzmann constant, equal to one.) This reduces to the familiar relationship between the cross sections for scattering up and scattering down in energy

$$\frac{d^2\sigma_{f\to i}}{d\Omega\, d\epsilon} = \frac{E_i}{E_f}\frac{d^2\sigma_{i\to f}}{d\Omega\, d\epsilon} e^{\frac{E_f - E_i}{T}}$$

The second general property is the sum rule first derived by Placzek[13]

$$\int d\omega(\hbar\omega) S(\vec{K},\omega) = \frac{\hbar^2 \vec{K}^2}{2M} \qquad \text{Eq. (3.30)}$$

where M is the mass of the scatterer. Note that Eq. (3.30) is independent of properties of the scattering system.

Additional overall properties of the scattering law can be derived. Schofield[14] has shown that a dispersion relation exists between the real and imaginary part of the correlation function

$$\text{Im } G(\vec{r},t) = -\tan\left(\frac{1}{2}\frac{\hbar}{T}\frac{\partial}{\partial t}\right) \text{Re } G(\vec{r},t). \qquad \text{Eq. (3.31)}$$

Furthermore, by replacing the real time coordinate t by a complex time suitably defined, Schofield was able to obtain a real space-time correlation function given by

$$F(\vec{r},t) = G(\vec{r}, t + i\hbar/T). \qquad \text{Eq. (3.32)}$$

The justifications of Eqs. (3.31) and (3.32) that follow directly from the detailed balance restriction on $S(\vec{K},\omega)$ and the definition of $G(\vec{r},t)$ have been given succinctly by Nelkin.[15] Egelstaff[16] has generalized the concept of complex time by introducing y time, where

$$y^{2n} = \left(t^2 + \frac{i\hbar}{T}\, t\right)^n \qquad \text{Eq. (3.33)}$$

and demonstrated that correlation functions of y time also satisfy fluctuation dissipation dispersion relations. Recently Becker has attempted to interpret these dispersion relations in terms of the theorems of irreversible thermodynamics.[17]

A method for the calculation of the correlation function $G(\vec{r},t)$ for liquids has been proposed by Vineyard.[18] He writes the correlation function as the sum of self and distinct parts

$$G(\vec{r},t) = G_s(\vec{r},t) + \int g(\vec{r}')\, H_o(\vec{r},\vec{r}';t)\, d\vec{r}' \qquad \text{Eq. (3.34)}$$

where $H_o(\vec{r},\vec{r}';t)$ is the probability that with the presence of a particle at the origin at time 0, another particle which was at $\vec{r}'$ at time 0 will migrate to position $\vec{r}$ at time t, all other quantities having been previously defined. If one now assumes that the migration probability of the second particle is independent of the distribution of all other particles of the system, $H(\vec{r},\vec{r}';t)$ reduces to

$$H_o(\vec{r},\vec{r}';t) \cong G_s(\vec{r}-\vec{r}';t) \qquad \text{Eq. (3.35)}$$

and

$$G(\vec{r},t) \cong G_s(\vec{r},t) + \int g(\vec{r}')\, G_s(\vec{r}-\vec{r}';t)\, d\vec{r}' \,. \qquad \text{Eq. (3.36)}$$

This is the convolution approximation, and forms the basis of the remainder of Vineyard's work. Although this has been derived classically, a completely analogous quantum mechanical form results. The four-dimensional Fourier transform of Eq. (3.36) yields the familar scattering laws [cf. Eqs. (3.8) and (3.10)]

$$\frac{d^2\sigma_{\text{inc}}}{d\Omega\, d\epsilon} = \langle a_{\text{inc}} \rangle^2_{sp}\, \frac{N}{2\pi\hbar}\, \frac{k}{k_o}\, S(\vec{K},\omega) \qquad \text{Eq. (3.37)}$$

and

$$\frac{d^2\sigma_{coh}}{d\Omega\, d\epsilon} = \langle a_{coh}\rangle_{sp}^2 \frac{N}{2\pi\hbar} \frac{k}{k_o} S(\vec{K},\omega)\left[1+\gamma(\vec{K})\right] \qquad \text{Eq. (3.38)}$$

where

$$\gamma(\vec{K}) = \int g(\vec{r})\, e^{i\vec{K}\cdot\vec{r}}\, d\vec{r}\,. \qquad \text{Eq. (3.39)}$$

Vineyard then shows that for two cases of interest, the perfect gas and diffusing atom models, one can write

$$G_s(\vec{r},t) = \frac{1}{\left(\pi w^2(t)\right)^{3/2}} e^{-r^2/w^2(t)} \qquad \text{Eq. (3.40)}$$

where $w(t)$ is a width function depending only on time. For a perfect Maxwellian gas,

$$w(t) = v_o\,|t| \qquad \text{Eq. (3.41)}$$

where $v_o = \sqrt{2T/M}$. For a diffusing atom undergoing random walk, the classical diffusion equation

$$D\nabla^2 G_s(\vec{r},t) = \frac{\partial G_s(\vec{r},t)}{\partial t} \qquad \text{Eq. (3.42)}$$

is satisfied. Integrating Eq. (3.42), one finds

$$G_s(\vec{r},t) = \frac{1}{4\pi D\,|t|^{3/2}} e^{-r^2/4D|t|} \qquad \text{Eq. (3.43)}$$

where D is the diffusion coefficient.

Since the diffusion model is inaccurate for short times (it assumes that collisions occur with infinite frequency), Vineyard proposed that a width given by Eq. (3.42) be used for $t \ll \tau_D$ and $w(t) = 2(D\,|t| + c)^{1/2}$ for $t \gg \tau_D$, where c and τ_D are constants to be determined. Singwi and Sjolander improved Vineyard's treatment of the diffusive motion of the atoms and numerically calculated the differential cross section.[19]

K. S. Singwi has indicated that more recent quantum mechanical calculations have shown qualitative agreement with experiment.[4]

2. Zemach-Glauber Formalism

Zemach and Glauber[5] have introduced an intermediate scattering function, $\chi(\vec{K}, t)$, as an aid in calculating the cross section. It will be seen in the following that the introduction of this function enables the calculation to proceed in a systematic way, at least for the illustrative examples given below which will be used as scattering models for the remainder of this work. $\chi(\vec{K}, t)$ is defined by

$$\overline{S}(\vec{K}, \omega) = \frac{1}{2\pi} \int_{-\infty}^{\infty} dt\, e^{-i\omega t} \chi(\vec{K}, t). \qquad \text{Eq. (3.44)}$$

With the use of this definition, Eq. (3.10), and Eq. (3.15), the expression for $\chi(\vec{K}, t)$ becomes

$$\chi(\vec{K}, t) = \sum_{\nu\nu'} \chi_{\nu\nu'}(\vec{K}, t)$$

$$= \sum_{\nu\nu'} \langle a_\nu a_{\nu'} \rangle_{sp} \sum_i \rho(E_i) \left(i \left| e^{i\vec{K}\cdot\vec{r}_\nu(t)} e^{-i\vec{K}\cdot\vec{r}_{\nu'}} \right| i \right).$$

Eq. (3.45)

It is also possible to write the expectation value appearing in Eq. (3.45) as

$$\left(i \left| e^{i\vec{K}\cdot\vec{r}_\nu(t)} e^{-i\vec{K}\cdot\vec{r}_{\nu'}} \right| i \right) = \left(i \left| e^{iHt/\hbar} e^{i\vec{K}\cdot\vec{r}_\nu} e^{-iHt/\hbar} e^{-i\vec{K}\cdot\vec{r}_{\nu'}} \right| i \right).$$

Eq. (3.46)

By virtue of the fact that the Hamiltonian appearing in Eq. (3.46) is a function of the momentum and coordinate of the scattering system, viz., $H = H(\vec{P}_\nu, \vec{r}_\nu)$, and since it can be demonstrated that the canonical commutation relation

$$\left[\vec{P}_\nu, e^{i\vec{K}\cdot\vec{r}_\nu} \right] = -\hbar \vec{K} e^{i\vec{K}\cdot\vec{r}_\nu}$$

Eq. (3.47)

holds, Z-G point out that the function $e^{i\vec{K}\cdot\vec{r}_\nu}$ acts as a translational operator on the momentum:

$$e^{i\vec{K}\cdot\vec{r}_\nu}\vec{p}_\nu e^{-i\vec{K}\cdot\vec{r}_{\nu'}} = e^{i\vec{K}\cdot(\vec{r}_\nu-\vec{r}_{\nu'})}(\vec{p}_\nu - \hbar\vec{K}). \quad \text{Eq. (3.48)}$$

The direct scattering term $(\nu=\nu')$ may now be simplified by introducing the momentum displaced Hamiltonian

$$H'_\nu = e^{i\vec{K}\cdot\vec{r}_\nu} H(\vec{p}_\nu,\vec{r}_\nu)\, e^{-i\vec{K}\cdot\vec{r}_\nu} = H(\vec{p}_\nu - \hbar\vec{K},\vec{r}_\nu) \quad \text{Eq. (3.49)}$$

so that Eq. (3.46) becomes

$$\left(i\left|e^{iHt/\hbar}\, e^{i\vec{K}\cdot\vec{r}_\nu}\, e^{-iHt/\hbar}\, e^{-i\vec{K}\cdot\vec{r}_{\nu'}}\right|i\right) = \left(i\left|e^{iHt/\hbar}\, e^{-iH'_\nu t/\hbar}\right|i\right). \quad \text{Eq. (3.50)}$$

As an illustration of the use of this formalism for the calculation of scattering cross sections, consider two models for the target particles, (1) free gas and (2) harmonic oscillator, both frequently used for flux calculations.

In the free gas model, which reduces to the familiar Wigner-Wilkins kernel for mass one,[20] the scattering atom is treated as a free particle with a Hamiltonian consisting of a kinetic energy term alone. Thus,

$$H = p^2/2M$$
$$H'_\nu = (\vec{p} - \hbar\vec{K})^2/2M \quad \text{Eq. (3.51)}$$

where M is the mass of the scatterer. Equation (3.50) reduces to

$$\left(i\left|e^{iHt/\hbar}\, e^{-iH't/\hbar}\right|i\right) = \left(i\left|e^{it(2\vec{p}\cdot\vec{K}-\hbar K^2)/2M}\right|i\right). \quad \text{Eq. (3.52)}$$

If wave functions ψ_i which are eigenfunctions of momentum (such as plane waves) are chosen for the scatterer, one can replace the expectation value appearing in Eq. (3.52) by just

the exponential where $\vec{p}$ is now an eigenvalue and not an operator. The sum over initial states appearing in Eq. (3.45) can now be done explicitly when it is recalled that for a gas in thermal equilibrium $\rho(E_i)$ is just the Boltzmann weighting factor. If the discrete summation is replaced by an integral, Eq. (3.45) becomes

$$\chi(\vec{K},t) = a^2 \int d\vec{p}\, e^{it(2\vec{p}\cdot\vec{K}-\hbar K^2)/2M} \frac{e^{-p^2/2MT}}{(2\pi MT)^{3/2}}$$

$$= a^2\, e^{-\frac{K^2}{2M}(it\hbar+t^2T)} \qquad \text{Eq. (3.53)}$$

The differential cross section can now be calculated by taking the inverse time Fourier transform of Eq. (3.53):

$$\frac{d^2\sigma}{d\Omega\, d\omega} = \frac{k}{k_o}\frac{a^2}{2\pi}\int e^{-it\left(\omega+\frac{\hbar K^2}{2M}\right)-\frac{t^2TK^2}{2M}}\, dt$$

$$= a^2\sqrt{\frac{M}{2\pi TK^2}}\,\frac{k}{k_o}\, e^{-\frac{M}{2TK^2}\left(\omega+\frac{\hbar K^2}{2M}\right)^2} \qquad \text{Eq. (3.54)}$$

Clendenin[21] has calculated the first four Legendre moments of the differential cross section given by Eq. (3.54). To do this, one replaces the integral of the cosine of the angle by the integral over K and then changes the variable of integration from K to

$$y = \omega/K + \hbar K/2M.$$

The results are quite involved; and here only $\frac{d\sigma}{d\epsilon}$ is presented, which is 4π times the zeroeth Legendre moment:

$$\frac{d\sigma}{d\epsilon} = 4\pi a^2\,\frac{M}{\hbar^2 k_o^2}\left\{\mathrm{Erf}\begin{pmatrix}u_2\\ v_2'\end{pmatrix} - \mathrm{Erf}\begin{pmatrix}u_1\\ v_1'\end{pmatrix}\right.$$

$$\left. + e^{\hbar^2\left(k_o^2-k^2\right)/2mT}\left[\mathrm{Erf}\begin{pmatrix}v_2\\ u_1'\end{pmatrix} - \mathrm{Erf}\begin{pmatrix}v_1\\ u_2'\end{pmatrix}\right]\right\} \qquad \text{Eq. (3.55)}$$

where the upper quantity is to be taken for $k \leq k_o$ and the lower for $k \geq k_o$. The other quantities appearing in Eq. (3.55) are defined as follows:

m = mass of incoming particle

M = mass of target particle

$$u\binom{1}{2} = \frac{\beta}{2}\left[\mp\left(\frac{1}{m}+\frac{1}{M}\right)\hbar k - \left(\frac{1}{m}-\frac{1}{M}\right)\hbar k_o\right]$$

$$u\binom{1}{2}' = \frac{\beta}{2}\left[\left(\frac{1}{m}-\frac{1}{M}\right)\hbar k \pm \left(\frac{1}{m}+\frac{1}{M}\right)\hbar k_o\right]$$

$$v\binom{1}{2} = \frac{\beta}{2}\left[\pm\left(\frac{1}{m}-\frac{1}{M}\right)\hbar k + \left(\frac{1}{m}+\frac{1}{M}\right)\hbar k_o\right]$$

$$v\binom{1}{2}' = \frac{\beta}{2}\left[\left(\frac{1}{m}+\frac{1}{M}\right)\hbar k \pm \left(\frac{1}{m}-\frac{1}{M}\right)\hbar k_o\right]$$

β = $M/2T$,

Erf = the error function defined by

$$\mathrm{Erf}(x) = \frac{2}{\sqrt{\pi}}\int_0^x e^{-t^2}\,dt\,.$$

The total cross section is the integral of Eq. (3.55) over all values of final energy, E. This result has been reported by von Dardel as[22]

$$\sigma(E_o) = \pi a^2\left[\frac{2}{\gamma\sqrt{\pi}}e^{-\gamma^2} + \left(1+\frac{1}{2\gamma^2}\right)\mathrm{Erf}\,\gamma\right] \qquad \text{Eq. (3.56)}$$

where

$$\gamma = \sqrt{\frac{M}{m}\frac{E_o}{T}} .$$

The customary high and low energy limits of the total cross section are apparent from Eq. (3.56). For $E_o \gg T$, $Erf\ \gamma \to 1$ and

$$\sigma(E_o) \xrightarrow[E_o \gg T]{} \pi a^2 .$$

In the other limit, $E_o << T$, Erf $\gamma \to \frac{2\gamma}{\sqrt{\pi}}$, and

$$\sigma(E_o) \xrightarrow[E_o \ll T]{} 4\pi a^2 \sqrt{\frac{mT}{\pi m E_o}} \sim \frac{1}{\sqrt{E_o}} \sim \frac{1}{v_o} ,$$

the familiar result that the total cross section exhibits a $1/v$ behavior for low incident energies.

The case of scattering by a perfect gas of protons is now examined. Here $M = m$ and Eq. (3.55) simplifies to

$$\frac{d\sigma}{d\epsilon} = 4\pi a^2 \frac{m}{\hbar^2 k_o^2} \text{ Erf } \left(\frac{\beta\hbar k}{m}\right) \quad \text{for } k \le k_o \qquad \text{Eq. (3.57)}$$

$$\frac{d\sigma}{d\epsilon} = 4\pi a^2 \frac{m}{\hbar^2 k_o^2} e^{-\frac{\hbar^2}{2mT}\left(k_o^2 - k^2\right)} \text{ Erf } \left(\frac{\beta\hbar k_o}{m}\right) \quad \text{for } k \ge k_o .$$

Eq. (3.58)

The slowing-down source can now be calculated for the example. Since the shape of the epithermal source is independent of the energy dependence of the epithermal flux, $\phi(E_o)$, the slowing-down source is equal to (Ref. 1, Chap. X)

$$S(E) = \int_{E_c}^{\infty} \frac{d\sigma(k \le k_o)}{d\epsilon} \phi(E_o)\, dE_o$$

$$= 2\pi a^2 \int_{E_c}^{\infty} \frac{1}{E_o} \operatorname{Erf} \sqrt{\frac{E}{T}}\, \phi(E_o)\, dE_o \qquad \text{Eq. (3.59)}$$

or

$$S(E) \propto N \operatorname{Erf} \sqrt{E/T}\,.$$

where N is chosen for proper normalization of the incoming flux (Ref. 1, Chap. XI) and is given by

$$N = 2\pi a^2 \int_{E_c}^{\infty} \frac{\phi(E_o)}{E_o}\, dE_o\,.$$

To calculate the cross section for the scattering from a vibrating system, it is more convenient to return to the time-dependent expression given by Eq. (3.45). Then Z—G write

$$\vec{r}_\nu(t) = \sum_\lambda \vec{C}_\nu^{(\lambda)} q_\lambda(t) \qquad \text{Eq. (3.60)}$$

where $q_\lambda(t)$ is the set of normal coordinates for the system ($\lambda = 1, \ldots, 2N-6$) and $\vec{C}_\nu^{(\lambda)}$ is the amplitude vector for each particle and each mode. Substituting Eq. (3.60) into Eq. (3.45), and making use of the fact that the Boltzmann distribution function may be expressed as the product of factors, one for each mode, one obtains

$$\langle \chi_{\nu\nu'} \rangle_T = \prod_\lambda \langle \chi_{\nu\nu'}^{(\lambda)} \rangle_T$$

$$= \prod_\lambda \left\langle e^{i\vec{K}\cdot\vec{C}_\nu^{(\lambda)} q_\lambda(t)}\, e^{-i\vec{K}\cdot\vec{C}_\nu^{(\lambda)} q_\lambda} \right\rangle_T \qquad \text{Eq. (3.61)}$$

The normal coordinate $q(t)$ can now be expressed as

$$q(t) = \frac{i}{\sqrt{2\omega}} \left(a\, e^{-i\omega t} - a^{\dagger}\, e^{i\omega t} \right) \qquad \text{Eq. (3.62)}$$

where ω is the frequency associated with that mode and a and $a^{\dagger}$ are the usual quantized operators satisfying the commutation relations[23]

$$[a, a^{\dagger}] = 1$$

$$[a, a] = [a^{\dagger}, a^{\dagger}] = 0 .$$

Then, making use of $\langle e^{Q} \rangle_T = e^{1/2 \langle Q^2 \rangle_T}$ which is valid for harmonic oscillator systems, Z—G are able to obtain

$$\langle \chi_{\nu\nu'} \rangle_T = \exp \left\{ -\frac{1}{2} \left[\left(\vec{K} \cdot \vec{C}_{\nu} \right)^2 + \left(\vec{K} \cdot \vec{C}_{\nu'} \right)^2 \right] \langle q^2(o) \rangle_T \right.$$

$$\left. + \left(\vec{K} \cdot \vec{C}_{\nu} \right) \left(\vec{K} \cdot \vec{C}_{\nu'} \right) \langle q(t)\, q(o) \rangle_T \right\} \qquad \text{Eq. (3.63)}$$

where the thermal averages can be shown to equal[23]

$$\langle q^2(t) \rangle_T = \langle q^2(o) \rangle_T = \frac{Z + 1}{2\omega (Z - 1)}$$

$$\langle q(t) q(o) \rangle_T = \frac{1}{2\omega} \left\{ \langle a\, a^{\dagger} \rangle_T\, e^{-i\omega t} + \langle a^{\dagger} a \rangle_T\, e^{i\omega t} \right\}$$

$$= \frac{1}{2\omega} \left\{ \left(\langle n \rangle_T + 1 \right) e^{-i\omega t} + \langle n \rangle_T\, e^{i\omega t} \right\}$$

where

$$\langle n \rangle_T = \frac{1}{Z - 1}$$

$$Z = e^{\omega / T}$$

so that

$$\langle q(t)\,q(o)\rangle_T = \frac{1}{2\omega(Z-1)}\left(Z\,e^{-i\omega t} + e^{i\omega t}\right). \qquad \text{Eq. (3.64)}$$

The substitution of Eq. (3.64) into Eq. (3.63) yields

$$\langle \chi_{\nu\nu'}\rangle_T = \exp\left\{-\frac{1}{2}\left[(\vec{K}\cdot\vec{C}_\nu)^2 + (\vec{K}\cdot\vec{C}_{\nu'})^2\right](Z+1)/2\omega(Z-1)\right\}$$

$$\cdot \exp\left\{(\vec{K}\cdot\vec{C}_\nu)(\vec{K}\cdot\vec{C}_{\nu'})(Z\,e^{-i\omega t} + e^{i\omega t})/2\omega(Z-1)\right\}.$$

Eq. (3.65)

One now can use the generating function for the modified Bessel function,[24]

$$e^{\frac{x}{2}(y + 1/y)} = \sum_{n=-\infty}^{\infty} y^n I_n(x)$$

identify

$$x = Z^{1/2}(\vec{K}\cdot\vec{C}_\nu)(\vec{K}\cdot\vec{C}_{\nu'})/\omega(Z-1)$$

$$y = Z^{-1/2} e^{i\omega t}$$

and obtain from Eq. (3.65)

$$\langle \chi_{\nu\nu'}\rangle_T = \exp\left\{-\left[(\vec{K}\cdot\vec{C}_\nu)^2 + (\vec{K}\cdot\vec{C}_{\nu'})^2\right]\frac{\coth \omega/2T}{4\omega}\right\}$$

$$\cdot \sum_{n=-\infty}^{\infty} e^{in\omega t}\, e^{-n\omega/2T}\, I_n\left(\frac{(\vec{K}\cdot\vec{C}_\nu)(\vec{K}\cdot\vec{C}_{\nu'})}{2\sinh \omega/2T}\right). \qquad \text{Eq. (3.66)}$$

The cross section may now be obtained from Eq. (3.66) by taking the inverse time transform. Note that this gives rise to a delta function $\delta(\epsilon - n\omega)$ which merely indicates mathematically that the energy transfer from a system of bound oscillators must be in units of the normal mode frequencies of oscillation.

These methods have been extended by various authors and by Zemach and Glauber themselves[25] to calculate the scattering cross section for realistic systems.

C. Applications

1. Water

Since water is one of the most common reactor materials, most of the theoretical and experimental investigations of neutron scattering have used water as a target. In a purely theoretical sense this is somewhat unfortunate because the complicated nature of the liquid system makes precise analysis difficult. From the viewpoint of practical application, however, this is the correct procedure.

Initial attempts to calculate the details of the neutron scattering cross section from the water molecule considered the influence of the hydrogen atoms on the scattering and neglected completely that of the oxygen atom. This procedure is valid in the high incident energy region where the total cross section for the scattering from hydrogen is much greater than that for the scattering from oxygen.[26] The hydrogen atoms were then considered as the constituents of a mass 1 gas, and for this approximation all the equations derived in the previous section are applicable [Eq. (3.45) et seq.]. The total cross section under this assumption is plotted in Fig. 3.1, where the experimental curve is also included. The mass 1 total cross section is seen to exhibit a behavior significantly different from the experimental results.

To reproduce the experimental thermal neutron scattering cross section from water, Radkowsky[27] suggested a model based upon the variation of the scattering length with incident neutron energy. The reasoning behind such a procedure follows.

For very large neutron wave lengths, corresponding to low neutron energies, the binding of the hydrogen atoms to the oxygen atom is much larger than the incident neutron energy. Alternatively, the incident neutron wave length is much larger than the molecular dimensions. For this system, the target protons are tightly bound to the oxygen atom and, instead of recoiling by themselves, the system of the water molecule recoils. Mathematically, this can be seen by observing that in

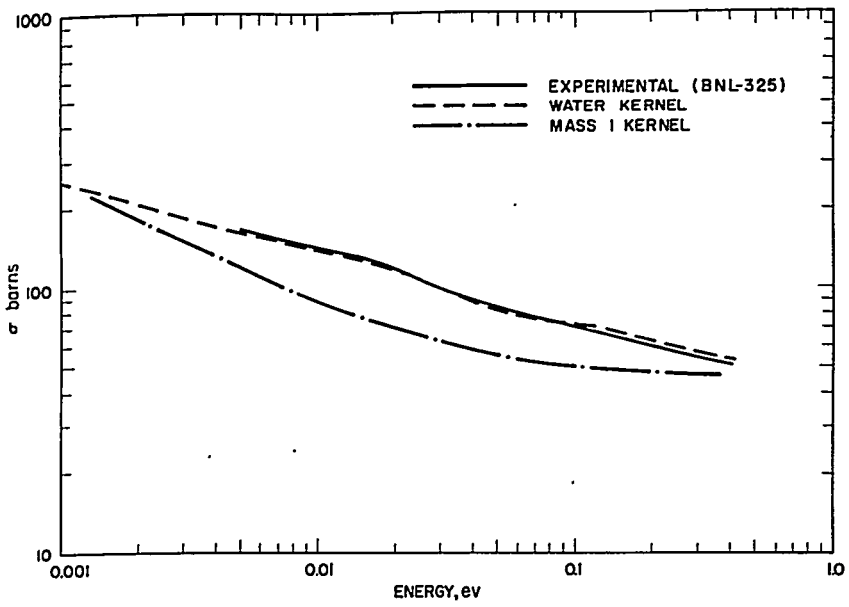

FIGURE 3.1. Total Cross Section for the Scattering of Thermal Energy Neutrons by Water.

the center-of-mass system the scattering is isotropic. The differential cross section in the center-of-mass system is, thus, given by

$$\sigma(\theta)\, d\cos\theta = C\, d\cos\theta \ .$$

The relationship between the differential cross section in the center-of-mass and laboratory systems has been given by Hurwitz and Zweifel.[28] The transport cross section, which occurs frequently in diffusion theory calculations (Ref. 1, Chap. XI) is defined as

$$\sigma_{tr}(E) = \sigma(E)\,(1 - \bar{\mu}) \qquad \text{Eq. (3.67)}$$

where $\bar{\mu}$, the first Legendre moment of the differential cross section, is

$$\bar{\mu} = \frac{2}{3A} \qquad \text{Eq. (3.68)}$$

and where A is the mass of the scatterer. Radkowsky proposed that the mass appearing in Eq. (3.68) be a function of incident energy. Implicit in this suggestion is the assumption that the

scattering in the center-of-mass system is isotropic, thus requiring that the entire contribution to the P_1 moment come from the term for which $E_o = E$, i.e., no energy transfer. $A(E)$ is determined from the experimental value of the total cross section. This value is then substituted into Eq. (3.68), where $\bar{\mu}$ is now a function of energy, and the transport cross section obtained from Eq. (3.67). The cross section thus obtained is plotted in Fig. 3.2. The results of reactor calculations using the Radkowsky scattering kernel are presented in Sect. 3.3, where it is seen that the agreement of the calculations with experiment is significantly better than using an uncorrected, constant mass kernel.

The present method for calculating the scattering of neutrons by moderators is to use a more realistic model of the scatterer in which its chemical binding properties are taken into account. An illustration of this technique is the early work of Nelkin who proposed a model for the scattering of neutrons by water.[29] As already noted, the neutron scattering is a function of the properties of the scattering system. The complicated phonon spectrum of water (Ref. 30, p. 487 ff.) is replaced by four distinct energy groups, given in Table 3.1, corresponding to an interaction Hamiltonian separable into four distinct components, one hindered rotational and three vibrational. These correspond, respectively, to the circular motion of the H-O-H molecule about its center of mass in the field of the other molecules and to the three degrees of freedom of the H-O bond

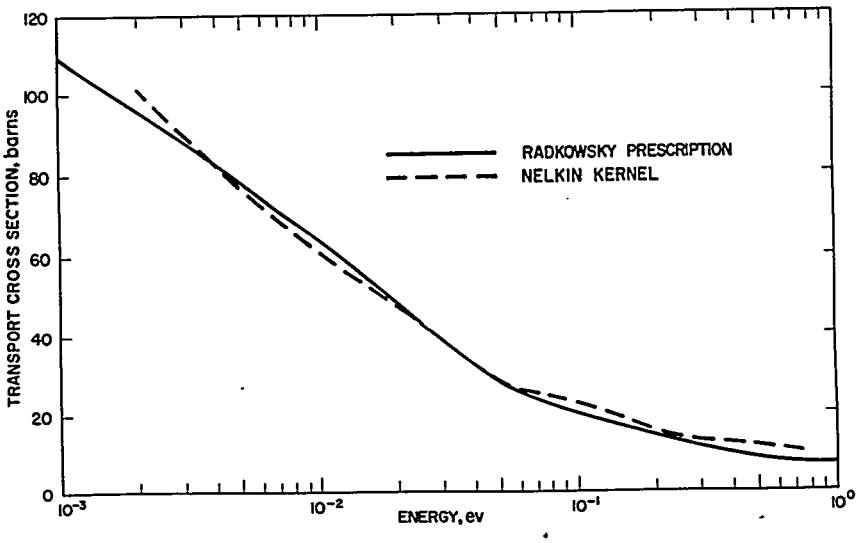

FIGURE 3.2. Calculated Transport Cross Section for the Scattering of Thermal Energy Neutrons by Water.

TABLE 3.1 – ENERGY LEVELS (ev) FOR WATER AND POLYETHYLENE

Nature of Level	H_2O	C_nH_{2n}
Hindered rotational (?)	0.06	0.089
Vibrational	0.205	0.187
Vibrational	0.474	0.354
Vibrational	0.488	0.533

in the molecule. To these motions must be added the free movement of the entire water molecule. Since an exact treatment of the 0.06 ev hindered rotational level[31] is quite lengthy,[32] this is replaced by Nelkin by a vibrational level. The original KERNEL program written at General Atomic[33] has been modified somewhat,[34] and a description follows.

Nelkin approximated the intermediate scattering function, χ, by a product of the χ's corresponding to the translation of the entire water molecule (assuming a gas of mass 18), the hindered rotational state and each of the vibrational states each separately temperature averaged. (Nelkin also assumed that the 0.474 and 0.488 ev states are two degenerate levels at 0.481 ev, but this nuance is of little importance in the general scheme and should introduce little error in the calculations.) Thus,

$$\chi \approx \chi_t \chi_r \chi_{v_1} \chi_{v_2} \qquad \text{Eq. (3.69)}$$

Since the equivalent Debye temperature for water is quite small, Nelkin justifies the treatment of the translational motion of the water molecule as free [see Eq.(3.53)]:

$$\chi_t \approx e^{-\frac{K^2}{2M}(it + Tt^2)} \qquad \text{Eq. (3.70)}$$

where M is the mass of the entire molecule.*

For the other modes of excitation, the scattering from an ensemble of oscillators has been calculated and can be written as [Eq. (3.65)]

$$\chi(\vec{K}, t) = \left\langle e^{\frac{K^2}{m} f(\omega, t)} \right\rangle \qquad \text{Eq. (3.71)}$$

where

$$f(\omega, t) = \frac{1}{2\omega} \left[(n+1) \left(e^{-i\omega t} - 1 \right) + n \left(e^{i\omega t} - 1 \right) \right]$$

$$n = \frac{1}{e^{\omega/T} - 1} \qquad \text{Eq. (3.72)}$$

and where the normalization has been adjusted so that in the limit of $t \to 0$ (large energy transfer), the free gas scattering results,

$$\chi(\vec{K}, t) \xrightarrow[t \to 0]{} e^{-\frac{1}{2} \frac{K^2}{m} (it + \bar{E} t^2)} \qquad \text{Eq. (3.73)}$$

since

$$f(\omega, t) \xrightarrow[t \to 0]{} -\frac{1}{2} (it + \bar{E} t^2) \qquad \text{Eq. (3.74)}$$

where

$$\bar{E}_i = \left[\frac{1}{e^{\omega_i / T} - 1} + \frac{1}{2} \right] \omega_i .$$

Note that for $E = T$, the familiar Sachs-Teller approximation for free rotation results.[35]

---

*For ease in notation K^2, the momentum, has been redefined in energy units, i.e., $\frac{K^2}{m}$ has dimensions of energy.

Alternatively, in the limit where the possible energy transfer is less than the oscillator frequency, Eq. (3.71) reduces to

$$\chi(\vec{K}, t) \xrightarrow[\frac{\omega}{T} \gg 1]{} e^{\frac{K^2}{2m\omega}(e^{-i\omega t} - 1)} \qquad \text{Eq. (3.75)}$$

The mass appearing in Eq. (3.71) must be determined separately. As mentioned previously, the rotational mass was chosen to be different in value from the vibrational mass. It was evaluated on the basis of the mass-tensor approximation[36] and found to be $m_r = 2.32$. The vibrational mass was determined so that in the high energy limit m in Eq. (3.73) was one. Thus,

$$1 = \frac{1}{M} + \frac{1}{m_r} + \frac{1}{m_v} \qquad \text{Eq. (3.76)}$$

or $m_v = 1.95$.

To simplify the calculational routine, the approximation was made of treating no more than one excitation exactly, using Eq. (3.72) and considering the other oscillations in either the high energy transfer [Eq. (3.73)] or zero energy transfer limit [Eq. (3.75)]. Thus, for water there are three natural regions corresponding to energy transfers of $\Delta E < 0.205$ ev, $0.205 \leq \Delta E < 0.481$ ev, and $0.481 \leq \Delta E \lesssim 0.8$ ev. Above an energy transfer of approximately 0.8 ev, the scattering is treated as that from a slowing-down source of single hydrogen atoms of effective temperature, $\bar{E}$,

$$\bar{E} = \frac{T}{M} + \frac{\bar{E}_r}{m_r} + \frac{\bar{E}_1}{3m_v} + \frac{2\bar{E}_2}{3m_v}. \qquad \text{Eq. (3.77)}$$

In Region I the hindered vibration is treated exactly, i.e., using

$$\chi_r = e^{\frac{K^2}{m_r} f(\omega_r, t)} \qquad \text{Eq. (3.78)}$$

and the translational motion is given by Eq. (3.70). The time transform is taken after expanding the distribution function f

as a series of modified Bessel functions according to the method of Zemach and Glauber [see Eq. (3.66)], and the resulting equation for the differential cross section is

$$\frac{d^2\sigma}{d\Omega\, d\epsilon} = \frac{\sigma_b}{4\pi}\sqrt{\frac{E}{E_o}}\sqrt{\frac{m}{2\pi\bar{E}K^2}}\, e^{-\frac{K^2}{2A}} \sum_{n=-\infty}^{\infty} e^{-\frac{n\omega}{2T}} I_n\left(\frac{K^2}{2B}\right) \cdot \exp\left[-\frac{m}{2\bar{E}K^2}\left(E - E_o - n\omega + K^2/2m\right)^2\right] \qquad \text{Eq. (3.79)}$$

where the undefined parameters are given in some detail by Nelkin.[29] In Region II the scattering from the lowest vibrational state is treated exactly and that from the translational and rotational states approximated by the high energy transfer limit. In Region III the degenerate double level at 0.481 ev is treated exactly and the other modes approximated in the high energy limit. It is, thus, easy to see that for these other two regions an equation identical to Eq. (3.79) is used with the parameters defined differently for each case, as given by Nelkin.[29] In this original work, Nelkin defined his regions corresponding to the incident neutron energy rather than the energy of transfer. The difference between the two schemes is illustrated in Fig. 3.3 where the primes refer to the present selection of parameters and the unprimed to the previous one. The broken lines refer to the present selection of the energy transfer regions. These would all have slopes of -45 degrees if the energy groups were equally spaced. The energies marked as ordinates and abscissas correspond to the phonon energies of the vibrating atoms. It is seen that there is a significant amount of overlap. Furthermore, the probability that a neutron with an energy much greater than the thermal energy of the moderator loses a large amount of energy is also large. Thus, in practice, the original scheme gave results not too different from the more realistic approach.

Equation (3.79) has been solved using the modified KERNEL program. This equation is applicable for the scattering of neutrons by systems possessing translational plus one vibrational degree of freedom. Use of this model will be made in calculating the cross section for the scattering of neutrons from another common reactor material, polyethylene. The machine program presently calculates the differential cross section for discrete sets of initial energies, E_i; final energies,

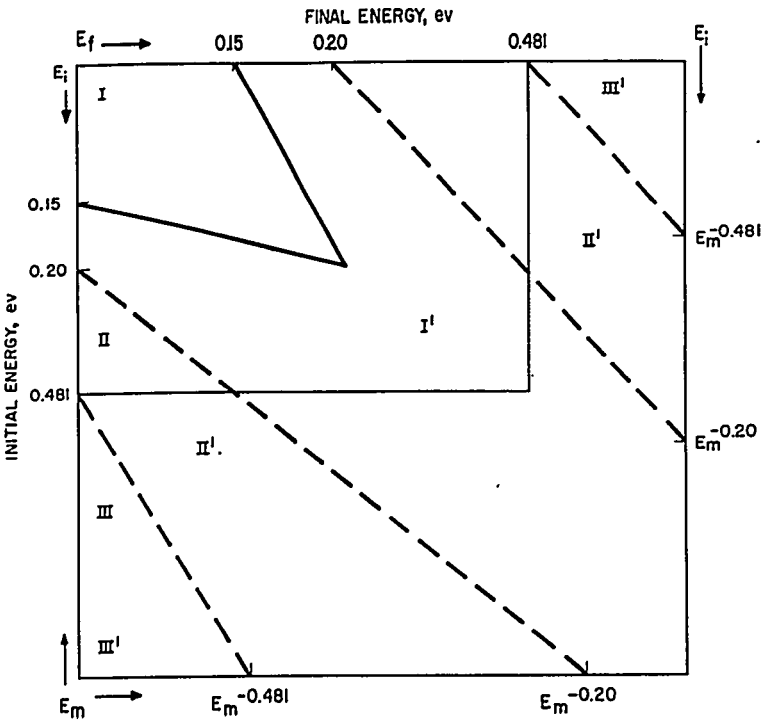

FIGURE 3.3. Schematic Diagram of the Scattering Kernel Matrix Indicating the Energy Regions for which the Choice of Parameters is Made.

E_l ; and cosines of the scattering angle, μ_k. In practice, only the values of $E_i \geq E_f$ are used in the calculation directly, and the detailed balance condition

$$\sigma(E_f \to E_i, \mu_k) = \sigma(E_i \to E_f, \mu_k) \frac{E_i}{E_f} e^{\frac{E_f - E_i}{T}} \qquad \text{Eq. (3.80)}$$

is used to calculate the energy gain portion of the scattering matrix. The various Legendre moments of the cross section defined by Eq. (3.80) are also computed for $\ell = 0,1,2,3$:

$$\sigma_\ell(E_i \to E_f) = \int d\mu \sigma(E_i \to E_f, \mu) P_\ell(\mu) \qquad \text{Eq. (3.81)}$$

where $P_\ell(\mu)$ is the ℓ^{th} order Legendre polynomial. Finally, the total and transport cross sections and sigma 2 and sigma 3 are calculated, defined respectively as follows

$$\begin{aligned}
\sigma(E_i) &= 2\pi \int dE_f \sigma_0(E_i \to E_f) \\
\sigma_{tr}(E_i) &= \sigma(E_i) - 2\pi \int dE_f \sigma_1(E_i \to E_f) \\
\sigma_2(E_i) &= \sigma(E_i) - 2\pi \int dE_f \sigma_2(E_i \to E_f) \\
\sigma_3(E_i) &= \sigma(E_i) - 2\pi \int dE_f \sigma_3(E_i \to E_f).
\end{aligned} \qquad \text{Eq. (3.82)}$$

Care must be taken in the numerical integration of the differential cross section to ensure that the integration scheme not introduce spurious results due to the replacing of an analytical continuous integration by a numerical finite size integration mesh. To see where this might arise, note that for energy transfers less than the lowest phonon excitation of the scattering system, the scattering is similar to that by a free gas. The differential cross section for the scattering of a neutron by a gas of mass M is given by Eq. (3.54). In the limit of zero energy transfer $\epsilon = 0$, and if attention is also focused on forward scattering, $K^2/2M \to 0$ and Eq. (3.54) becomes

$$\lim_{K^2/2M \to 0} \frac{1}{\sqrt{K^2/2M}} e^{-\frac{1}{4T}(K^2/2M)} = \lim_{K^2/2M \to 0} \frac{1}{\sqrt{K^2/2M}}.$$

This square-root singularity does not occur for $\epsilon \neq 0$ because for this case the differential cross section asymptotically approaches

$$\lim_{K^2/2M \to 0} \frac{1}{\sqrt{K^2/2M}} e^{-\epsilon^2 / 4TK^2/2M} = 0.$$

This statement emphasizes the fact that for scattering from a scatterer with a finite mass there cannot be energy change without a change in momentum.

To account numerically for the square-root singularity of the diagonal term, $(K^2/2M)^{-1/2}$ was subtracted from the calculated value of the differential cross section before the numerical integration over angle was undertaken. The analytical value of the integral of this quantity was then added to the result.

It is apparent that the presence of this integrable singularity must be handled properly when computing the total and energy exchange cross section. It is interesting to note, however, that this divergence has no effect on the calculation of infinite medium spectra. The possible source of error arises from the contribution of the term corresponding to forward scattering with no energy loss. This contribution cannot be separated from the unscattered flux and, hence, no error is introduced in the spectrum determination.

The total cross section as a function of energy was computed and the results compared with the experimental data. To calculate the scattering from water, the individual hydrogen cross sections were doubled and added to oxygen cross section (4 barns). The results are shown in Fig. 3.1. The agreement between experiment and theory for large incident energies was fixed by the requirement of Eq. (3.76), but the comparison over the whole energy range shown is quite good. The calculated transport cross sections using the Nelkin and Radkowsky methods are plotted in Fig. 3.2, and the similarity in the results indicates the applicability of the integration technique for the solution of certain integral problems.

A much more selective test of the quantitative accuracy of any scattering theory is to determine the accuracy with which the differential cross section is determined. The experimental determination of the differential cross section, however, is quite complicated and involves the use of large incident neutron fluxes with complicated electromechanical systems for energy and angle analysis of the scattered particles. A large experimental program is presently being undertaken by Egelstaff and his associates using the high flux reactor at Chalk River and a four-rotor neutron analyzer.[37] Egelstaff reports his results in terms of the dimensionless quantities α, β, and $S(\alpha, \beta)$,[38] defined as[16]

$$\alpha = \frac{E_i + E_f - 2\mu\sqrt{E_i E_f}}{T} \qquad \text{Eq. (3.83)}$$

the momentum transfer,

$$\beta = \frac{E_f - E_i}{T} \qquad \text{Eq. (3.84)}$$

the energy transfer (negative for an energy loss), and the symmetric scattering law

$$S(\alpha,\beta) = \frac{\pi\sigma(E_i \to E_f, \mu)}{\sigma_0} T\sqrt{\frac{E_i}{E_f}}\, e^{\beta/2}. \qquad \text{Eq. (3.85)}$$

$S(\alpha, \beta)$ has been so defined that it is invariant under the transformations $E_i \to E_f$ and $\beta \to -\beta$, separately and, thus, satisfies detailed balance explicitly. These quantities have been reconverted back into energy and angle variables for direct comparison with calculated numbers. An example of such a comparison, albeit the most satisfactory determined thus far, is shown in Fig. 3.4. There are admittedly large statistical errors associated with the experimental points and, since the curves have not been normalized to each other, this can be regarded as reasonably good agreement between experiment and theory.

Additional comparisons between theory and experiment using Egelstaff's representation directly were also undertaken. One such example is shown in Fig. 3.5.[39] The comparison looks reasonably close except for small α (small momentum change) when the theoretical curve goes to zero. This is inevitable in any theory which uses the free translation approximation since, for a gas kernel, $S/\alpha \to 0$ as $\alpha \to 0$. Thus, the need for including diffusive effects, which are apparent at small momentum and energy transfers, is seen.

The cross section for the scattering from water at 150°C was then calculated in order to compare some available data.[40] The total cross section for each incident neutron energy was about the same as that for the scattering from room temperature water. This can be understood because even at 150°C (corresponding to $E = 0.0364$ ev), the individual phonon energies are considerably larger than the thermal energy of agitation, and in the averaging process involved in the twofold integration the effect of the change is glossed over. For the differential cross section it is another matter. In Fig. 3.6 the

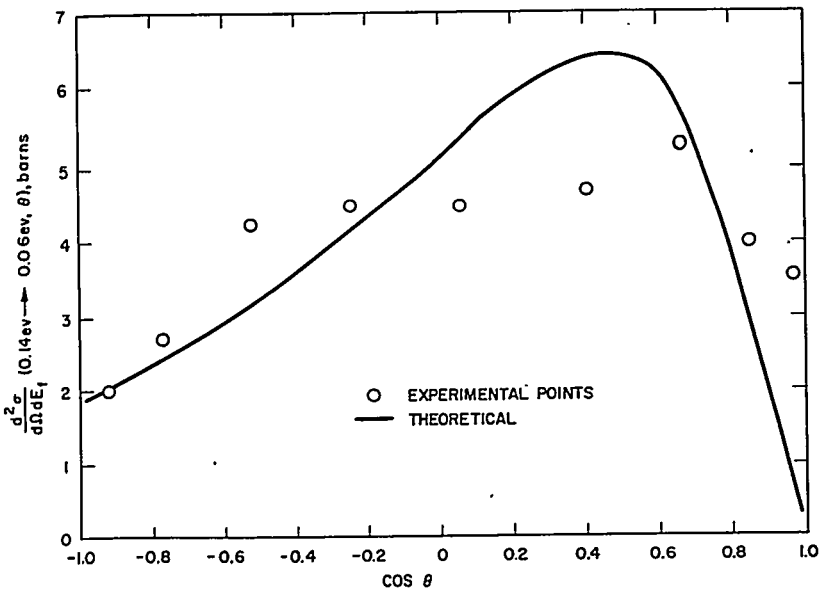

FIGURE 3.4. The Differential Cross Section of Water as a Function of the Cosine of the Scattering Angle for Initial Neutron Energy of 0.14 ev and Final Energy of 0.06 ev.

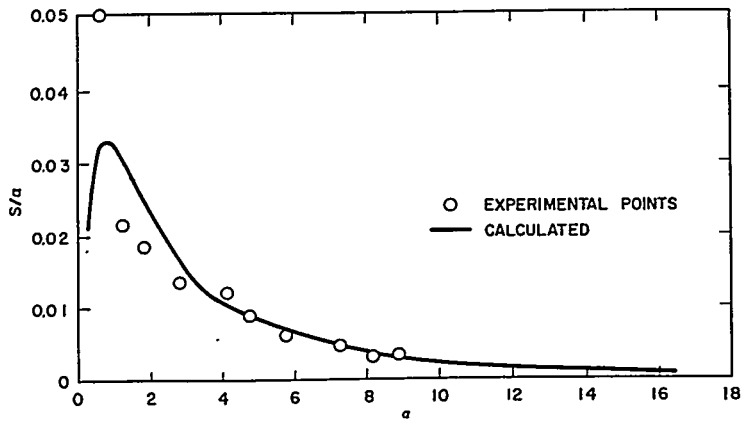

FIGURE 3.5. S/α as a Function of α for $\beta = 2.0$ (Room Temperature).

agreement between experiment and theory is once again divergent for small α. Since the relative energy transfer is smaller for this case than the previous one, the divergence

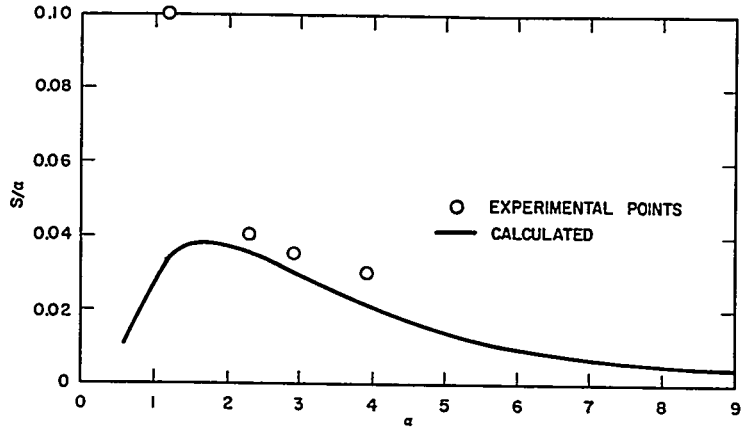

FIGURE 3.6. S/α as a Function of α for $\beta = 1.0$ (Temperature = 150°C).

between theory and experiment seems to occur at a somewhat larger value of α.

Egelstaff and Schofield have proposed that small energy transfer experiments be used to determine the diffusive nature of the scattering material.[40,41] An auxiliary function $p(\beta)$ is defined by

$$p(\beta) = \beta^2 \left[\frac{S_s(\alpha, \beta)}{\alpha} \right]_{\alpha \to 0} \qquad \text{Eq. (3.86)}$$

where $S_s(\alpha, \beta)$ is the self part of the scattering law. This function reproduces the physical nature of the scattering system. If one writes

$$S(\alpha, \beta) = \frac{1}{2\pi} \int_{-\infty}^{\infty} I(\alpha, t)\, e^{i\beta t}\, dt \qquad \text{Eq. (3.87)}$$

then, using $I_s(\alpha, t + i/2) = e^{-\alpha w(t)}$, it can be shown that

$$\ddot{w}(t) = 2 \int_{o}^{\infty} p(\beta) \cos \beta t \, d\beta \qquad \text{Eq. (3.88)}$$

where $w(t)$ is the width function. Integration of Eq. (3.88) twice with respect to time, making use of general properties of the scattering law, yields

$$w(t) = 2\int_o^\infty \frac{p(\beta)\ [\cosh \beta/2 - \cos \beta t]}{\beta^2}\ d\beta \ . \qquad \text{Eq. (3.89)}$$

and there is, thus, a procedure given for extending the calculation of the scattering law to regions where it has not been measured.

It is interesting to map the energy exchange regions in $\alpha-\beta$ space. This is done in Fig. 3.7 where the parameter regions are separated by vertical lines. The diffusion corrections could then be made explicitly in this new matrix scheme by requiring that the function $S(\alpha,\beta)$ given by the elements of this matrix satisfy Eq. (3.86) as determined by experiment.

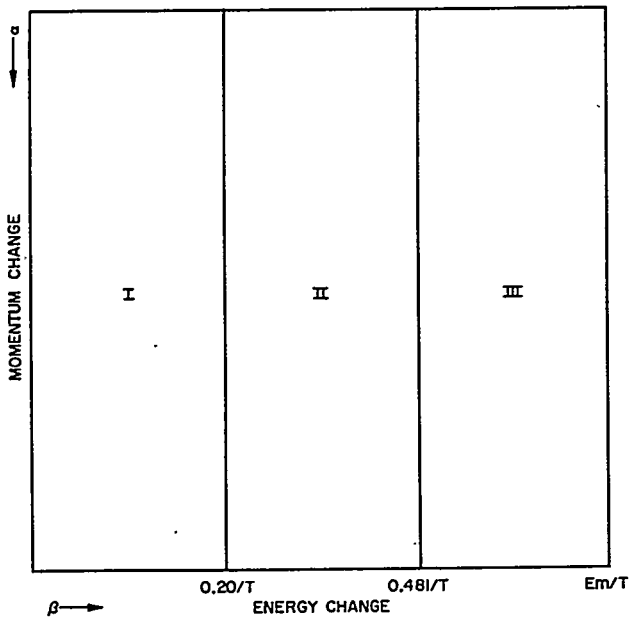

FIGURE 3.7. Schematic Representation of the Scattering Law S(α,β) Corresponding to the Energy Matrix of the Broken Lines of Fig. 3.3.

The methods described above are actually applicable for all neutron energies. However, for incident energies above a certain maximum, that is a certain energy above which the chemical effects are negligible, the hydrogen scattering from the atoms can be treated as that from a free gas. The average energy loss per collision is one-half the initial energy (Ref. 1, p. 281). On this basis it is possible to extend an approximate treatment of the scattering to somewhat lower energies as long as the assumption of large energy transfer is valid. It is then possible to use Placzek's or Wick's short collision time approximation[8,13] and expand the intermediate scattering function in powers of t. Thus, Corngold,[42] using Wick's expansion,[8] is able to calculate an integral representation for coefficients of the Taylor series of $g(\vec{K}, t)$ where

$$\chi(\vec{K}, t) = \exp\left(\frac{itK^2}{2M} g(\vec{K}, t)\right)$$

$$g(\vec{K}, t) = \sum_{n=o}^{\infty} \frac{(it)^n}{n!} g_n(\vec{K}). \qquad \text{Eq. (3.90)}$$

In a subsequent paper, Corngold indicated the method of calculating the energy loss moments, again in the short collision time approximation, and treated the case of scattering from a harmonic oscillator specifically.[43] He used Nelkin's model for liquid water and was able to replace the three normal mode frequencies by a single ω_{eff} in the calculation of expansion coefficients. Corngold then calculated the infinite medium neutron flux spectrum and found the shape in quite good agreement with the experimental results of Beyster, et al.;[44] certainly in much better agreement than he found using the free proton gas approximation for the scattering.

2. Polyethylene

In order to determine the range of application of the theory discussed above, the scattering of neutrons from polyethylene was examined. This substance is commonly used in reactor assemblies and, as such, this investigation has practical interest. In a later section (Sect. 3.3) it is shown that for reliable flux calculations it is necessary to have a realistic scattering model.

The chemical structure of the polyethylene is that of a long-chain organic molecule with the generic formula C_nH_{2n} (Ref. 30, p. 324). Thus, it seemed possible to treat the individual com-

ponent of the molecule, i.e., the H-C-H radical in a manner analogous to the representation of the water H-O-H molecule. To do this it was necessary to determine the frequency spectrum of the polyethylene molecule. The data of Nielsen and Woollett[45] were examined for solid polyethylene and the various energies of phonon excitation inferred from their results. On the basis of their data, there appears to be reasonably well-separated energy levels at energies of 0.089 ev, 0.187 ev, 0.354 ev, and 0.533 ev. These energies are given in Table 3.1 and are listed alongside their possible analogous water levels. The total cross section was then calculated assuming that each of the four levels corresponds to a normal mode of oscillation of the hydrogen atoms of the polyethylene molecule. This is an especially simple model and involves the selection of only one arbitrary parameter chosen so that at high neutron energies ($E_n \gtrsim 0.8$ ev) the total cross section is the same as that from a free proton gas. This takes the form of

$$1 = \frac{1}{M} + \frac{1}{m_v} \qquad \text{Eq. (3.91)}$$

where M is the total mass of the CH_2 group (14) and m_v is the effective vibrator mass. There are now four regions given by

Region I	$\Delta E < 0.187$ ev
Region II	$0.187 \leq \Delta E < 0.354$ ev
Region III	$0.354 \leq \Delta E < 0.533$ ev
Region IV	$0.533 \leq \Delta E \lesssim 0.8$ ev

In each region the translational motion is treated in the high energy limit and one of the vibrational modes is treated exactly, in complete analogy to the method used for water scattering. The differential cross section is again given by Eq. (3.79) with the parameters defined by Table 3.2.

The parameters listed in Table 3.2 have been used to calculate the neutron cross sections, utilizing the KERNEL program described previously. The total neutron cross section calculated by the program was compared with the experimental data of Bach, Bunch, Roesser, and Slovacek. These results agree quite well with earlier data of Rainwater, et al.,[46] and have much smaller statistical errors associated with them. The comparison is shown in Fig. 3.8 where the data of Bach, et al., and the theoretical cross section are plotted.

TABLE 3.2 — PARAMETERS ENTERING INTO EQ. (3.79) FOR THE SCATTERING OF NEUTRONS BY POLYETHYLENE AT ROOM TEMPERATURE

Parameter	Region I $\Delta E < 0.187$ ev	Region II $0.187 \text{ ev} \leq \Delta E < 0.354$ ev	Region III $0.354 \text{ ev} \leq \Delta E < 0.533$ ev	Region IV $0.533 \text{ ev} \leq \Delta E \lesssim 0.8$ ev
m	$m = M = 14$	$\frac{1}{m} = \frac{1}{M} + \frac{1}{4m_v}$ $m = 3.301$	$\frac{1}{m} = \frac{1}{M} + \frac{1}{2m_v}$ $m = 1.871$	$\frac{1}{m} = \frac{1}{M} + \frac{3}{4m_v}$ $m = 1.306$
$\bar{E}$	$\bar{E} = T$ $= 0.02550$ ev	$\bar{E} = m\left(\frac{T}{M} + \frac{\bar{E}_o}{4m_v}\right)$ $= 0.04216$ ev	$\bar{E} = m\left(\frac{T}{M} + \frac{\bar{E}_o + \bar{E}_1}{4m_v}\right)$ $= 0.06338$ ev	$\bar{E} = m\left[\frac{T}{M} + \frac{1}{4m_v}\left(\bar{E}_o + \bar{E}_1 + \bar{E}_2\right)\right]$ $= 0.09772$ ev
A	$A^{-1} = (4m_v)^{-1}\left[\omega_1^{-1} + \omega_2^{-1} + \omega_3^{-1} + \left(\omega_o \tanh\frac{\omega_o}{2T}\right)^{-1}\right]$ $A = 0.1951$ ev	$A^{-1} = (4m_v)^{-1}\left[\omega_2^{-1} + \omega_3^{-1} + \left(\omega_1 \tanh\frac{\omega_1}{2T}\right)^{-1}\right]$ $A = 0.4234$ ev	$A^{-1} = (4m_v)^{-1}\left[\omega_3^{-1} + \left(\omega_2 \tanh\frac{\omega_2}{2T}\right)^{-1}\right]$ $A = 0.9189$ ev	$A = 4m_v\omega_3 \tanh\frac{\omega_3}{2T}$ $= 2.303$ ev
B	$B = 4m_v\,\omega_o \sinh\frac{\omega_o}{2T}$ $= 1.068$ ev	$B = 4m_v\,\omega_1 \sinh\frac{\omega_1}{2T}$ $= 13.92$ ev	$B = 4m_v\,\omega_2 \sinh\frac{\omega_2}{2T}$ $= 789.6$ ev	$B = 4m_v\,\omega_3 \sinh\frac{\omega_3}{2T}$ $= 3.973 \times 10^4$ ev
ω	$\omega = \omega_o$ $= 0.089$ ev	$\omega = \omega_1$ $= 0.187$ ev	$\omega = \omega_2$ $= 0.354$ ev	$\omega = \omega_3$ $= 0.533$ ev

$M = 14$; $m_v = 1.08$; $\bar{E}_i = \left(\frac{1}{e^{\omega_i/T} - 1} + \frac{1}{2}\right)\omega_i$

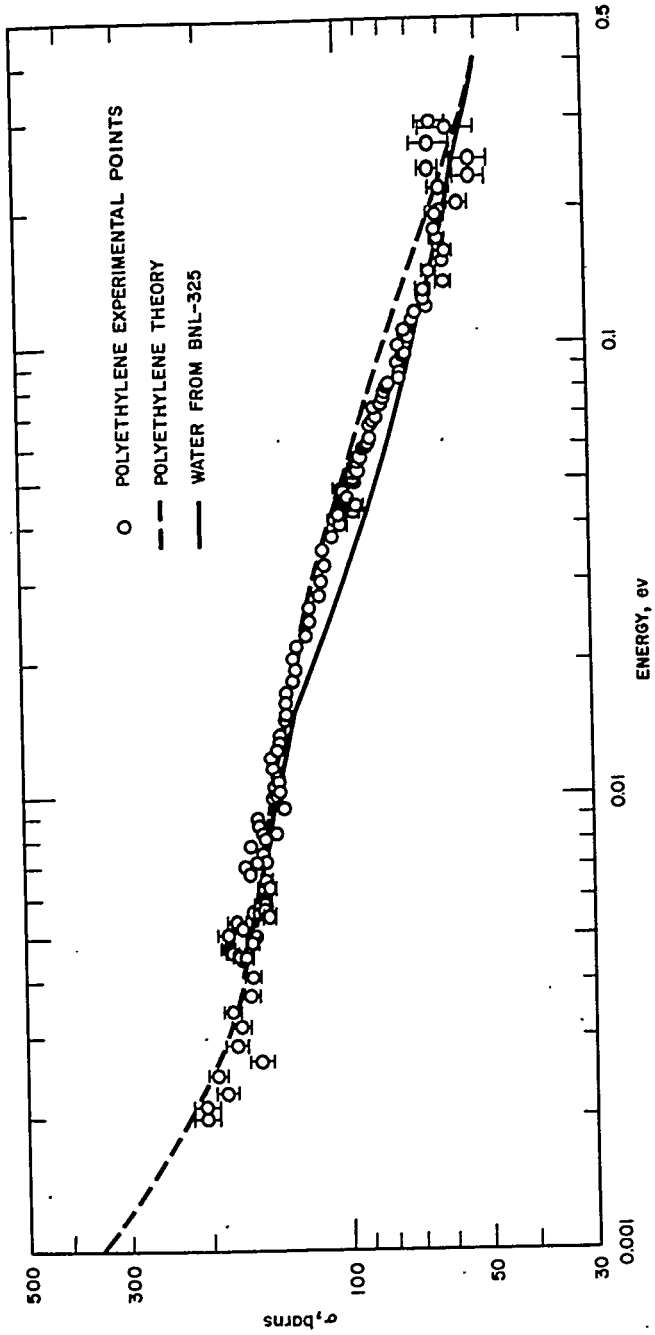

FIGURE 3.8. Total Cross Section for the Scattering of Thermal Energy Neutrons by Polyethylene.

It is apparent that calculated results are in quite good agreement with the experimentally measured total cross sections, a result not necessarily expected due to the naïveté of the model. The significance of these results is being investigated, but it would be of great benefit in this line to have available some differential cross section measurements, quantities which are just being measured. Scattering kernels based on this model have been used to calculate flux spectra. This is described more completely in Sect. 3.3. The agreement between theory and experiment is sufficiently good to make one confident of the reliability of such scattering models for use at least in infinite medium reactor physics calculations.[47]

3. *Other Materials*

The scattering of neutrons from a substance such as zirconium hydride is simple to analyze. The crystalline structure of ZrH is considered to consist of hydrogen atoms placed in the center of a regular tetrahedron of zirconium atoms, the zirconium atoms forming a face-centered cubic lattice. The acoustical and optical modes of vibration are well separated, and the amplitude of the optical is much greater. This mode can be described simply as the vibration of the hydrogen atom in the oscillator field produced by the zirconium atoms. Thus, Eq. (3.79) would be expected to be applicable for all energies with no additional approximations necessary, i.e., with the single vibrational mode with an energy equal to 0.13 ev treated exactly. These calculations have been performed and the results compared with experiment.[48] The agreement in the total cross section was very good. Some attempt was made to extend the method to other metallic hydrides.

The calculation and measurement of the scattering cross section of neutrons from carbon are also of obvious interest. The theoretical treatment must, of necessity, be much more complicated because of the complicated hexagonal crystalline structure of carbon. Parks, et al.,[49] has attempted to calculate the correlation function utilizing an appropriate representation of the carbon crystal, and the work is still in progress.

A significant amount of neutron scattering information has been obtained by the group associated with the Materials Test Reactor in Idaho[50,51,52] on a variety of organic moderators. Considerable theoretical interpretation has also been performed.[53]

D. Conclusions

General methods have been presented for calculating the scattering of neutrons of thermal energy by chemically bound

particles. For energies comparable to the chemical energy of the system ($\lesssim 1$ ev) it is necessary to treat the chemical motion of the scatterers quantitatively. This has been done in the pseudopotential approximation. The validity of this approximation is quite good but by no means complete. Indeed, in another problem which is also of interest in the field of reactor flux calculations, the high energy *(n, p)* cross section, a similar zero range potential is customarily used.[54] This nuclear physics problem can be regarded in many ways as similar to the scattering problem under discussion. In this problem, an incident neutron interacts with a proton bound this time not by a chemical potential but rather by a nuclear potential determined by the rest of the nucleons of the nucleus. The two situations are clearly not the same, among other reasons because the statistical mechanical representation of a nucleus is hardly exact. Furthermore, the incoming neutron plane wave is not unaffected by the nuclear potential, and the Born approximation which is itself only a perturbation-type expansion in the incoming neutron momentum[55] must be replaced by a distorted plane wave Born approximation.[56] Nevertheless an examination of the techniques used in the solution of the nuclear or solid state many body problem[57,58] might be useful in improving and extending the quantitative basis of the present thermal energy scattering problem.

Despite the limitations outlined, the present theoretical approach is quite reasonable and has been able to give reasonable predictions for appropriate quantities. Specifically, for the case of scattering from water, the incoherent approximation is applicable, and a molecular model of simple design can be used. That the model being used may be a little too crude has already been pointed out, and presently studies are being undertaken for the improvement of the model besides those indicated in the previous section. For example, the energy band around 0.06 ev in water and 0.09 ev in polyethylene might be treated as a two-dimensional hindered rotation and not as a three-dimensional oscillation as at present. In this connection, the scattering of neutrons from water vapor, a problem of interest in reactor calculations, could be considered. The hindered rotation should not be present but rather a true rotational energy band should occur. The cross section equation would then include the scattering from a rotator in the manner previously described.

An interesting problem is the possible temperature dependence of the chemical bonds. Some evidence of such variation has been noted in water. In paraffin, closely related to polyethylene, the measured diffusion length at liquid paraffin temperatures is somewhat higher than that calculated using

the polyethylene model,[59] which might also be indicative of the same temperature dependence phenomenon occurring.

One of the major fields of endeavor for reactor research is determining the validity of the application of the various calculational techniques in predicting reactor behavior. Another general problem which has been alluded to is a determination of the functional sensitivity of neutron flux calculations to gross and refined modifications of the scattering kernel. These problems are considered in Sect. 3.3.

There remains the overall picture of comparing the theoretical and experimental elastic and inelastic scattering cross sections themselves. There is need for experimental measurements of the differential cross section to fill the void which now exists, especially for incident neutron energies above about 0.2 ev. With the advent of high current linear accelerators and high flux reactors this seems quite promising. The available experimental data are more or less summarized by the proceedings of the Vienna Conference[60] and by the Brookhaven Thermalization Conference.[61] The results on water scattering are most complete, and even for that substance there remains a great deal to be done. Correspondingly, theoretical models must be developed to interpret and predict the experimental results.

3.3 SENSITIVITY TO THE NEUTRON SCATTERING KERNEL

A. Analysis of Thermal Neutron Spectra

F. D. Federighi

1. Introduction

In Sect. 3.2 physical models for thermal scattering kernels for water and polyethylene were discussed. Until recently, calculations of thermal neutron spectra in these materials have been performed with a mass 1, free atom scattering kernel. For that kernel it was assumed that the moderating material is composed of a free gas of protons. The chemical binding of these protons in molecules was neglected.

In the discussion of the Nelkin water kernel and the Goldman polyethylene kernel (Sect. 3.2), it was shown that one can use them to predict the total scattering cross sections quite well in contrast to the results from the free atom kernel. Although the use of a kernel which predicts the correct total scattering cross section is desirable, the significant justification for any kernel is its ability to predict quantities of direct interest in

reactor calculations. The use of these new kernels in calculations of infinite medium and spatially dependent thermal spectra as well as criticality are discussed in this section.

2. Infinite Medium Thermal Neutron Spectra

The free proton scattering kernel has long been used for calculations of infinite medium spectra in water and polyethylene systems. Calculations performed by Amster [62] with the free proton kernel have been compared with neutron spectra in water as measured by Poole.[63] These comparisons indicated that this model for the scattering law correctly predicted the thermal spectrum within the limits of experimental uncertainty. However, in recent years more precise experiments have become possible, and results (which will be given below) show that for more heavily absorbing media the free proton kernel is not adequate to calculate water and polyethylene spectra.

In order to show the sensitivity of infinite medium calculations to the various kernels, a series of calculations are described here. These calculations were done with the SWAK[64] code as follows. The infinite medium thermalization equation for energy E less than the energy of any source neutron is

$$[\Sigma_a(E) + \Sigma_s(E)]\ \phi(E) - \int_0^{E_c} \Sigma_s(E' \to E)\ \phi(E')dE' = S(E) \qquad \text{Eq. (3.92)}$$

where

Σ_a and Σ_s are the absorption and scattering cross sections;

$\Sigma_s(E' \to E)$ is the cross section for scattering from energy E' to the range dE about E;

$S(E) = \int_{E_c}^{\infty} \Sigma(E' \to E)\ \phi(E')\ dE'$ is the source of neutrons scattered from energies above E_c to energies below E_c;

$\phi(E)$ is the neutron flux, and E_c is a cutoff energy chosen so that the scattering from energies below E_c to energies above E_c can be neglected;

E_c also is below the energy of any source neutron.

If all quantities in Eq. (3.92) are evaluated at n values of $E(=E_i)$, and the integral replaced by a sum, the n equations

$$[\Sigma_a(E_i) + \Sigma_s(E_i)]\ \phi(E_i) - \sum_{j=1}^{n} \Sigma(E_j \to E_i)\ \phi(E_j)\ \Delta_j = S(E_i) \qquad \text{Eq. (3.93)}$$

are obtained. This represents a system of n linear equations in n unknowns (the $\phi(E_i)$) and can be solved by direct matrix inversion to obtain the flux spectrum $\phi(E_i)$.

Examples of flux spectra calculated with each of the three kernels (Nelkin, Mass 1, Goldman) are shown in Figs. 3.9 and 3.10. Figure 3.9 shows the infinite medium spectra for a region with only $1/v$ absorption and $\beta\gamma = 0.1$. $\beta\gamma = \Sigma_a(kT)/\xi\Sigma_s$ is the ratio of the macroscopic absorption cross section at kT to the asymptotic slowing-down power. Figure 3.10 shows these spectra for a region with $\beta\gamma = 0.8$. It is apparent from these graphs that the use of the different kernels yields quite different results and, therefore, experimental comparisons are needed. This is further evidenced by the large differences in averages over these spectra of a unit $1/v$ cross section given in Table 3.3.

A similar study of sensitivity of neutron spectra to scattering kernel has been performed by Clendenin[21] for different monatomic gases. It was found that the variation of the spectrum with ratio A of atomic mass to neutron mass is not

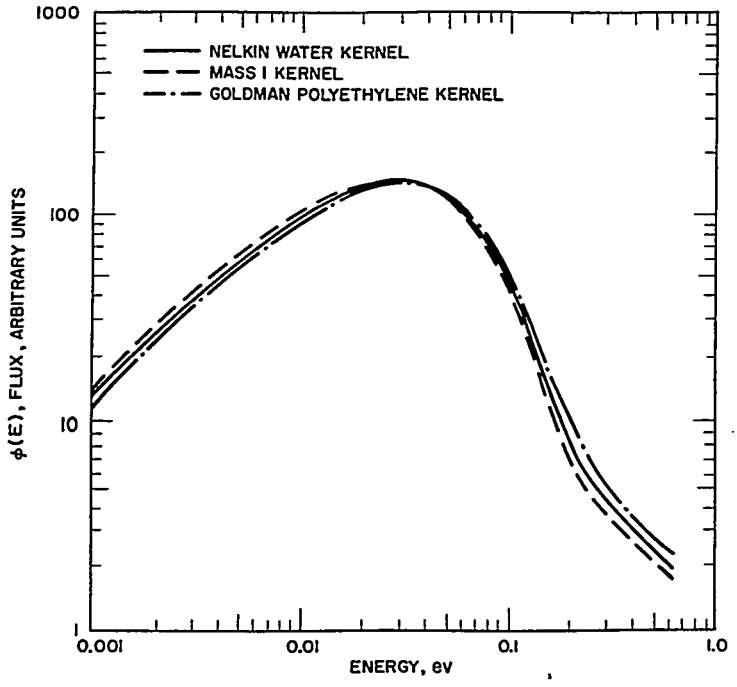

FIGURE 3.9. Infinite Medium Spectrum for Material with 1/v Absorption and $\beta\gamma = 0.1$.

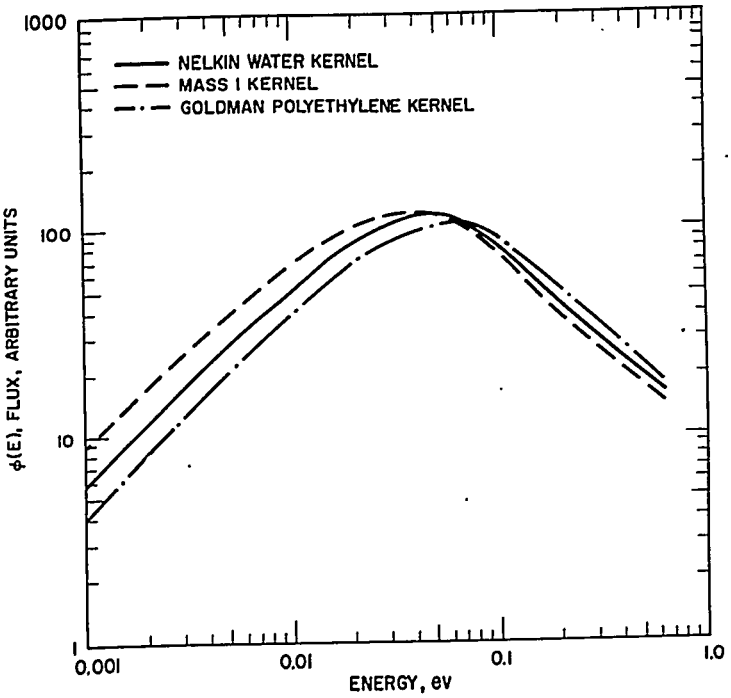

FIGURE 3.10. Infinite Medium Spectrum for Material with 1/v Absorption and $\beta\gamma = 0.8$.

very great for the range $1 \leq A \leq 20$. The difference in value of the absorption cross section Σ_a averaged over the spectra for $A = 1$ and $A = 20$ is about 4 percent for a composition in which $\beta\gamma = 0.16$. The essential characteristics which the monatomic gas models have in common are (1) agreement with the detailed balance relation,[20] and (2) the same value of $\xi\Sigma_s(E)$ for energies greater than E_c.

Beyster, et al.,[44] have measured infinite medium spectra in pure and poisoned water and polyethylene moderators. Figure 3.11 shows Beyster's experimental points as measured in various concentrations of boric acid. Also shown are the spectra as calculated on the basis of the free proton and bound water scattering models. All curves are normalized to the same $1/E$ high energy dependence. These curves show that the free proton kernel is not adequate to calculate spectra in water while the water kernel is much better able to predict these spectra. The agreement between calculations with the water kernel and Beyster's measurements of water poisoned with samarium is less satisfactory. Furthermore, calculations of Beyster's experiment in borated polyethylene (see Figs. 3.12 and 3.13)

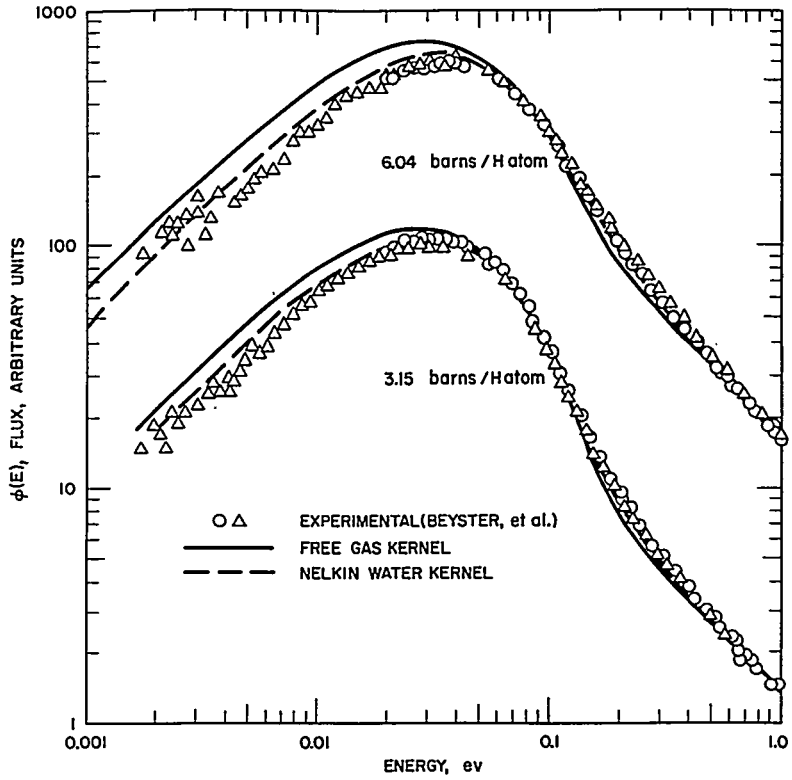

FIGURE 3.11. Calculated and Experimental Neutron Spectra in Boric Acid.

TABLE 3.3 — AVERAGES OF UNIT $\frac{1}{v}$ CROSS SECTION

$$\left[\frac{1}{v} = \frac{\int_0^{0.625} \sqrt{\frac{0.025\ eV}{E}}\ \phi(E)dE}{\int_0^{0.625} \phi(E)dE}\right]$$

Kernel	$\left\langle\frac{1}{v}\right\rangle$; $\beta\gamma = 0.1$	$\left\langle\frac{1}{v}\right\rangle$; $\beta\gamma = 0.8$
Mass 1	0.7826	0.5217
Water	0.7593	0.4901
Polyethylene	0.7292	0.4585

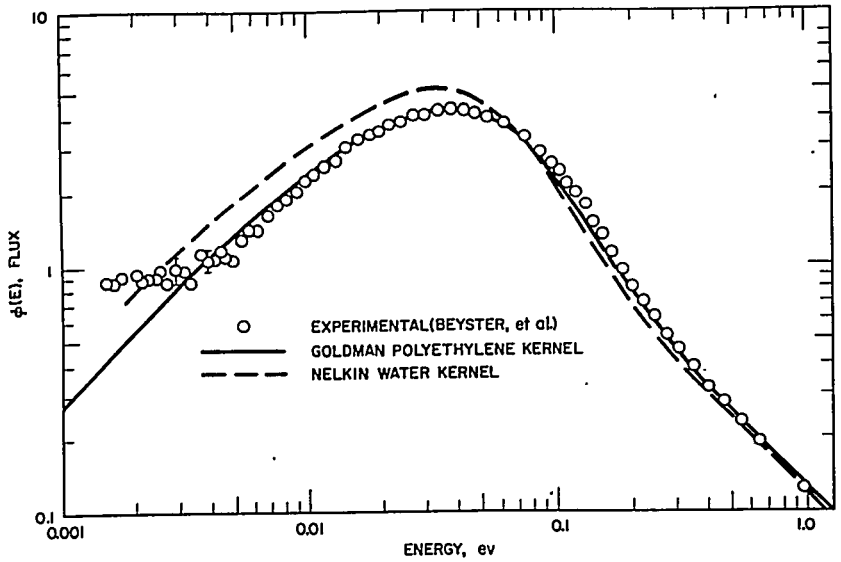

FIGURE 3.12. Calculated and Experimental Neutron Spectra in Borated Polyethylene (5.74 barns/H atom).

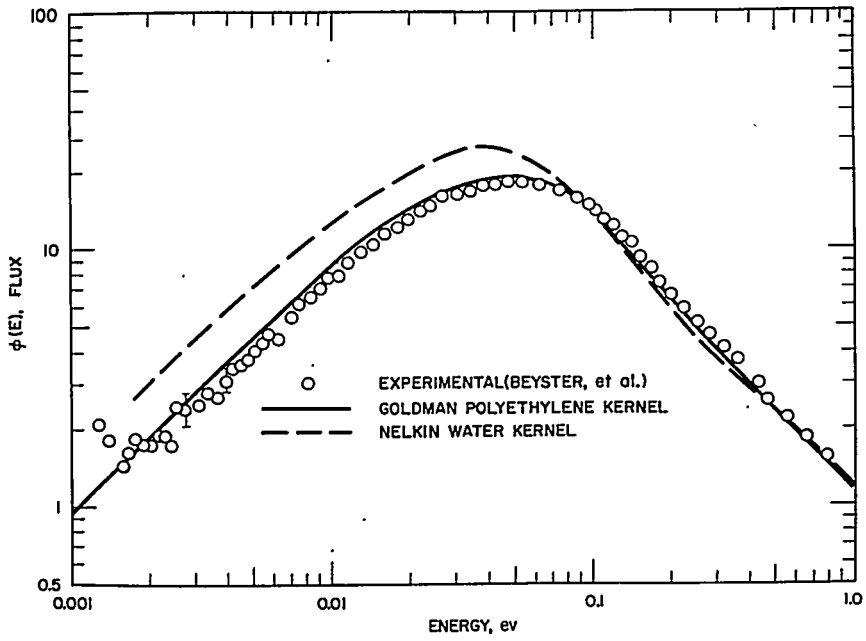

FIGURE 3.13. Calculated and Experimental Neutron Spectra in Borated Polyethylene (10.45 barns/H atom).

show that the water kernel should not be used to calculate polyethylene spectra but that the model created specifically for polyethylene must be used.

Thus, it is seen that infinite medium thermal spectra are quite sensitive to the form of the scattering kernel. Kernels are available for the prediction of these measured spectra with reasonable precision.

3. *Criticality and Spatially Dependent Spectra*

In Sect. 3.3.A.2 it was shown that the thermal spectrum itself is quite sensitive to the details of the scattering kernel. However, when quantities of more direct interest for reactor design are considered, this choice of scattering kernel becomes less important. Quantities such as thermal utilization and critical eigenvalues involve ratios of absorptions, and the spectrum differences tend to cancel. This will be evident from some examples.

The first example to be considered is a series of SWAKRAUM calculations by Storm and Greenhow. They performed criticality calculations on the one-dimensional lattice shown in Fig. 3.14. The three kernels used are listed in Table 3.4. The Radkowsky prescription (see Sect. 3.2) has been used to specify the P_1 component of the free atom kernel. In all these calculations the energy range above thermal was treated identically, so that all the differences are due directly to the scattering kernels used.

The position-dependent average macroscopic thermal absorption cross section in the fuel plates and the average microscopic thermal fission cross sections are shown in Figs. 3.15 and 3.16. From these curves the spectral differences due to kernel differences are apparent. The Nelkin water kernel produces a harder spectrum for which average cross sections are lower by 3 to 5 percent. The Goldman polyethylene kernel further reduces these cross sections by another 3 to 5 percent, reflecting the increased binding of the hydrogen atoms. However, the power shapes shown in Fig. 3.17 (normalized to the same total power) and the multiplication, k, (given in Table 3.5) as predicted by the different kernels show only minor differences. Similar results have been obtained by Parrish and Simms and by Edgar and Shannon in their analyses of a lattice consisting of boron plate in a fuel region. They obtained differences as large as 13 percent between average cross sections as calculated with the Radkowsky and Goldman kernels, but ratios of boron absorptions to total absorptions differ by at most 3-1/2 percent.

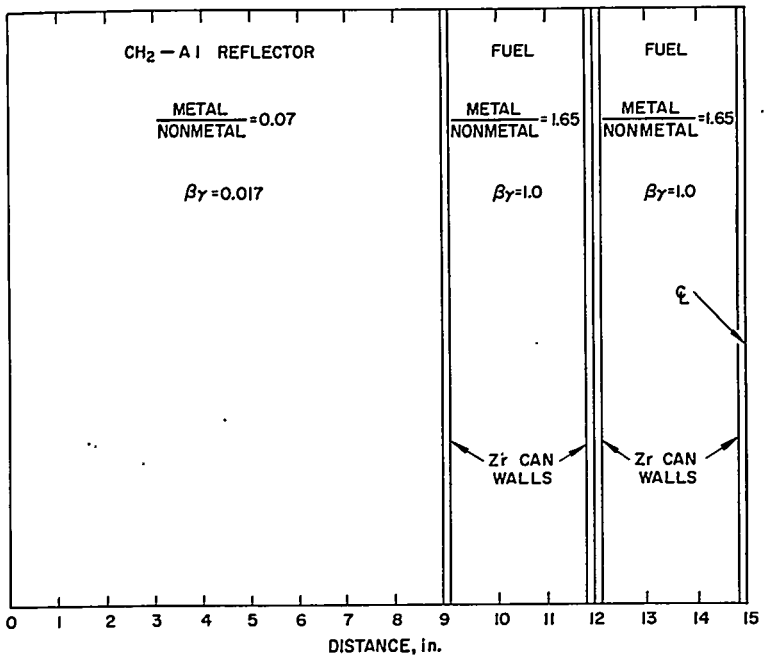

FIGURE 3.14. Geometry of Storm-Greenhow Lattice.

TABLE 3.4 — THE DIFFERENT SCATTERING KERNELS USED IN SENSITIVITY ANALYSES

Kernel Name	P_0 Kernel	P_1 Kernel
Radkowsky	Mass 1, free gas	Radkowsky prescription
Nelkin	P_0 water kernel	Diagonalized P_1 water kernel
Goldman	P_0 polyethylene kernel	Diagonalized P_1 polyethylene kernel

B. Analysis of Thermal Diffusion Length

G. P. Calame

A knowledge of the thermal diffusion length in a given medium, defined in the P_1 approximation by the relation

$$L = \sqrt{D/\Sigma_a} \qquad \text{Eq. (3.94)}$$

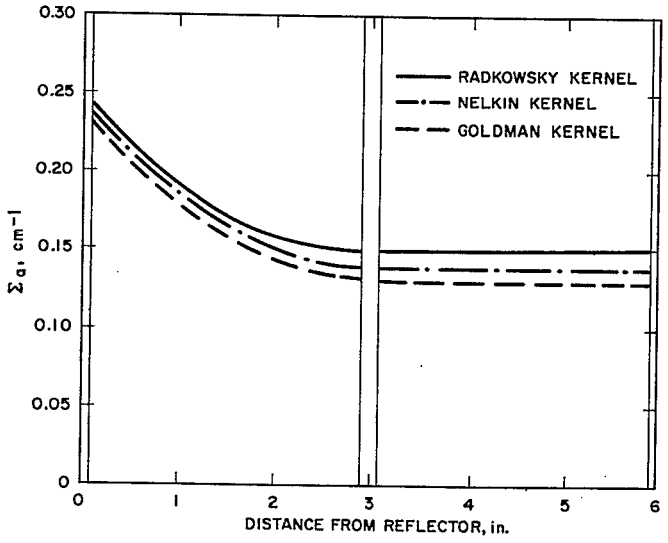

FIGURE 3.15. Macroscopic Thermal Absorption Cross Section in Storm-Greenhow Lattice.

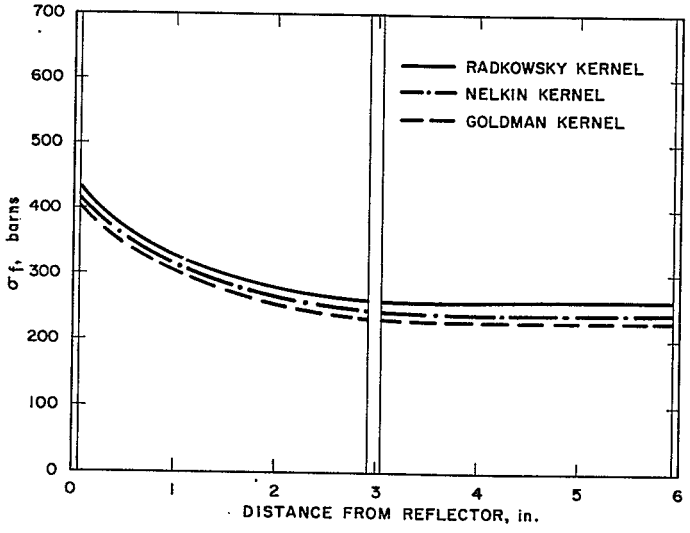

FIGURE 3.16. Microscopic Thermal Fission Cross Section in Storm-Greenhow Lattice.

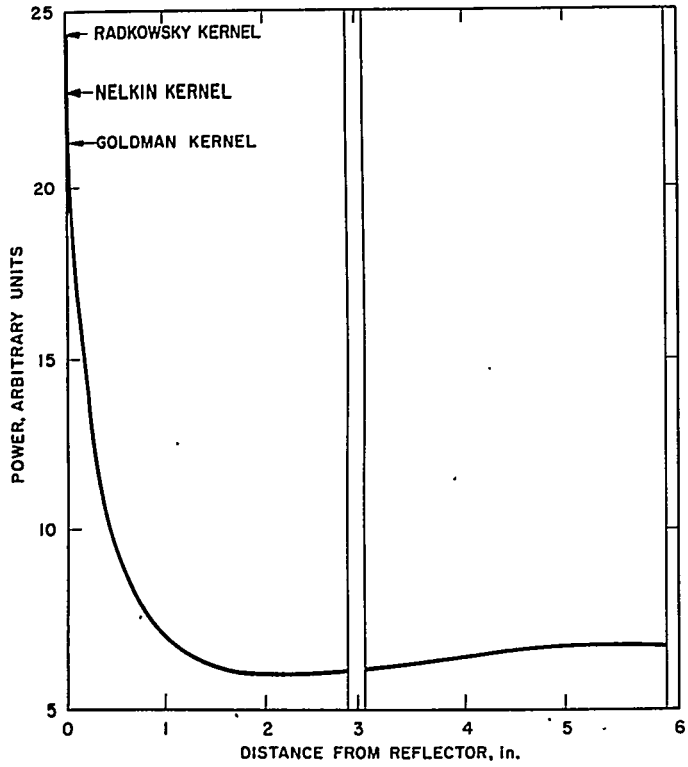

FIGURE 3.17. Power Distribution in Storm-Greenhow Lattice.

TABLE 3.5 — MULTIPLICATION OF STORM-GREENHOW LATTICE AS PREDICTED BY VARIOUS KERNELS

Kernel	k
Radkowsky, free gas	1.0311
Nelkin, water	1.0308
Goldman, polyethylene	1.0202

with D and Σ_a the energy-averaged diffusion coefficient and absorption cross section, respectively, is of fundamental importance in many reactor calculations. Those one-group models of the thermal energy region in which D and Σ_a represent quantities averaged over a Maxwellian spectrum, for example, tend to be considerably more successful in predicting flux transients

near water channels, and therefore power peakings, than do the models in which the averaging spectrum is some approximation to the infinite medium spectrum characteristic of the medium in question. The reason for this will be examined and the dependence of L on the quantities which enter into the defining equation indicated.

Consider a homogeneous medium in which the slowing-down source is independent of position, an assumption which may be relaxed, if necessary, by appealing to the formulation of Michael.[65] In such a medium, the thermal spectrum as a function of position and energy may be described in diffusion theory by the equation

$$-D(E)\nabla^2\ \phi(E,x) + \Sigma_t(E)\phi(E,x) - \int_o^{E_c} \Sigma_s(E' \to E)\ \phi(E',x)\,dE' = S(E)$$

Eq. (3.95)

in which the symbols have their conventional meanings and in which plane geometry has been assumed for simplicity. E_c is a cutoff energy, chosen so that the probability of a neutron's being scattered from an energy $E' < E_c$ to an energy $E > E_c$ is negligible.

Far from a material interface, the solution to Eq. (3.95) should become the infinite medium solution $\phi(E)$ which satisfies the equation

$$\Sigma_t(E)\ \phi(E) - \int_o^{E_c} \Sigma_s(E' \to E)\ \phi(E')\ dE' = S(E).$$

A comparison of the last equation with Eq. (3.95) shows that $\phi(E)$ is the particular solution of the former equation. Hence, $\phi(E,x)$ may be written

$$\phi(E,x) = \phi(E) + \gamma(E,x) \qquad \text{Eq. (3.96)}$$

and substitution of Eq. (3.96) into Eq. (3.95) then shows that the transient $\gamma(E,x)$ must satisfy the equation

$$-D(E)\nabla^2\gamma(E,x) = \Sigma_t(E)\gamma(E,x) - \int_o^{E_c} \Sigma_s(E' \to E)\ \gamma(E',x)\,dE'$$

Eq. (3.97)

The monoenergetic diffusion equation has solutions whose transients are of the form $\exp[\pm x/L]$, with L the diffusion length. Such solutions can be expected to approximate those of the energy-dependent equation above with good accuracy if the transients of the energy-dependent equation also are assumed to have the same spatial form. Solutions to Eq. (3.97) of the form

$$\gamma(E,x) = \gamma(E)C^{\pm x/L} \qquad \text{Eq. (3.98)}$$

may therefore be sought. The introduction of Eq. (3.98) into Eq. (3.97) then results in the equation

$$\frac{D(E)}{L^2}\gamma(E) = \Sigma_t(E)\gamma(E) - \int_o^{E_c} \Sigma_s(E' \to E)\gamma(E')\,dE'. \qquad \text{Eq. (3.99)}$$

Equation (3.99), which is identical with Hurwitz and Nelkin's[66] Equation 11, is an eigenvalue problem. Although the eigenvalue spectrum of the equation is not well understood, it appears that the spectrum contains at least a few discrete eigenvalues, and also a continuum, with the discrete eigenvalues L being greater in magnitude than those of the continuum.[67] A flux transient will in general consist of a sum over the eigenfunctions [Eq. (3.98)] of Eq. (3.99). Far from a material inhomogeneity, however, the eigenfunction with the largest L will dominate the transient which will there appear as an exponential characterized by the single relaxation length L_1. L_1, the largest eigenvalue of Eq. (3.99), is usually called the asymptotic diffusion length. The corresponding spectrum $\gamma_1(E)$ is the so-called diffusion hardened spectrum.[66]

The eigenvalues of Eq. (3.99) may be found numerically in a straightforward manner. The energy range from $E = 0$ to $E = 0.625$ ev is divided into a number of groups (32 groups were actually used) and the integral approximated by some numerical quadrature scheme, e.g., Simpson's rule. When this is done, Eq. (3.99) reduces to a matrix equation, the largest eigenvalue of which may be found by the standard technique of power iteration,[68] combined in cases where convergence is slow with convergence acceleration techniques such as the fractional iteration scheme of Wielandt.[69] The details of the calculation are described elsewhere.[70] Similarly, techniques such as matrix deflation[69,71,72] permit the higher eigenvalues to be found.

Table 3.6 lists the asymptotic diffusion lengths, L_1, for some of the lattices studied by Wright and Feiner[73,74,75] (these experiments are described in Chap. 6, Sect. 6.2.C of this

TABLE 3-6. — COMPARISON OF EXPERIMENTAL AND CALCULATED DIFFUSION LENGTHS NEAR HYDROGENOUS PERTURBATIONS

Lattice	$\beta\gamma$*	Gap Type†	Diffusion Lengths (cm)			
			Experimental	L_1	L_∞	L_M
C	0.18	A	2.35 ± 0.06	2.517	3.03	2.37
A	0.43	A	1.76 ± 0.06	1.749	2.23	1.56
		B	1.73 ± 0.17			
D	0.78	B	1.10 ± 0.03	1.095	1.42	0.93

*$\beta\gamma$ is the ratio of the macroscopic absorption cross section at E = 0.025 ev to the macroscopic slowing-down power $\xi\Sigma_s$ above thermal.

†The A-type perturbations (gaps) are composed of polyethylene and fuel; the B gaps have polyethylene alone. In lattice C lucite is used in place of polyethyene.

volume), and compares the L_1's with the experimental relaxation lengths observed by those authors. The frequently used diffusion lengths L_∞, computed by using the relation

$$L_\infty^2 = \left(\int_o^{E_c} D(E)\ \phi(E)dE \right) \Big/ \left(\int_o^{E_c} \Sigma_a(E)\ \phi(E)dE \right) \qquad \text{Eq. (3.100)}$$

are given for comparison, as are the Maxwellian averaged diffusion lengths computed by substituting the Maxwellian spectrum $M(E)$ for $\phi(E)$ in Eq. (3.100). The calculations were all performed with a mass 1, free proton P_o energy exchange kernel for $\Sigma_s(E' \rightarrow E)$, while the Radkowsky prescription[27] as applied to polyethylene[59] was used for the P_1 kernel, which enters into $D(E)$.

The asymptotic diffusion lengths are in good agreement with the experimental values and are in much better agreement than are the frequently used L_∞. It is interesting to note that

with the exception of lattice C, the asymptotic diffusion lengths are in better agreement with the experiments than are the Maxwellian averaged values, which tend to be too small. Nevertheless, the L_M are sufficiently close to the L_1 to explain why those one-group models which are adjusted to yield Maxwellian diffusion lengths yield better values for power peaking than do those models which use the L_∞ (see Sect. 3.7.B). The similarity of the L_1 to the L_M further suggests that the $\gamma_1(E)$'s are similar to a Maxwellian spectrum but with a somewhat higher average energy than that of a Maxwellian at the ambient temperature of the medium in question. That this is in fact the case is illustrated in Figs. 3.18 and 3.19, which exhibit the infinite medium spectrum, the Maxwellian spectrum, and γ_1 (the asymptotic diffusing spectrum) for lattices D and C, respectively.

For some configurations the proper diffusion length to use is the asymptotic one. The lattice C discrepancy, however, demonstrates that the asymptotic diffusion length is not

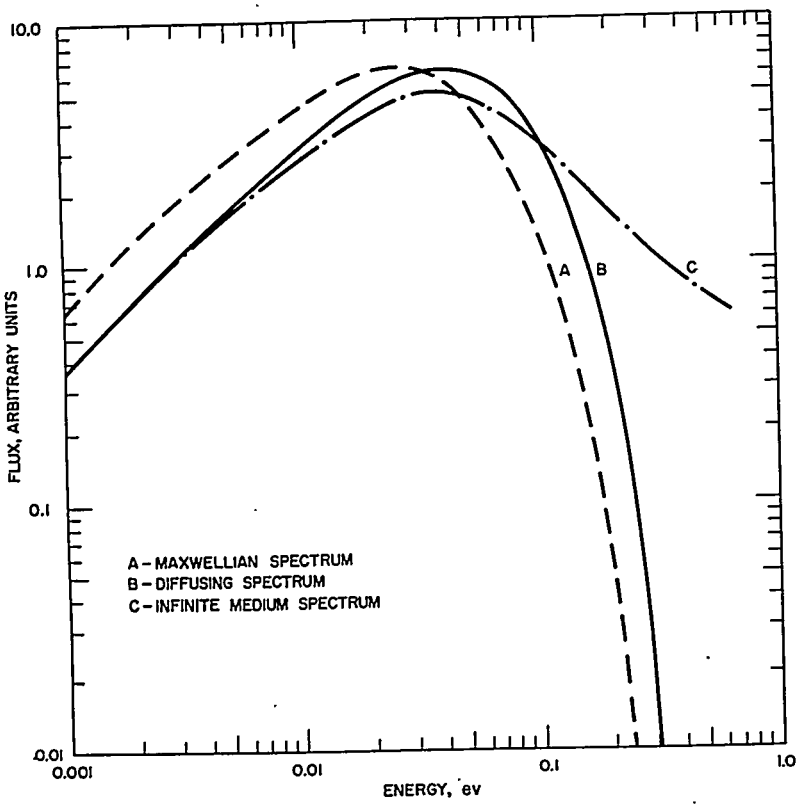

FIGURE 3.18. Characteristic Spectra for Lattice D ($\beta\gamma = 0.78$).

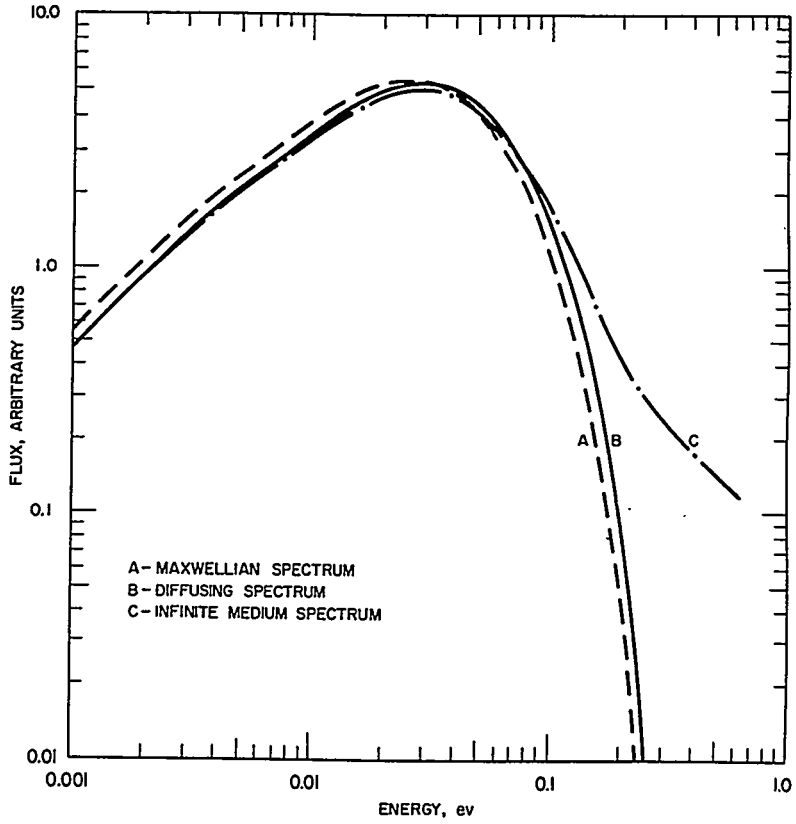

FIGURE 3.19. Characteristic Spectra for Lattice C ($\beta\gamma = 0.18$).

appropriate in all situations. That this should be so is clear when it is recalled that a flux transient will be a sum over the eigenfunctions of Eq. (3.99). Since the weight with which each eigenfunction enters into the sum will depend on the perturbation which gives rise to the transient in question, it will not, in general, be possible to define a single diffusion length that is valid for the description of all thermal flux transients within that medium. A direct experimental verification of the preceding statement has been furnished by the experiments of Wright and Feiner,[73,74] who find that the perturbations in flux shapes arising from inhomogeneities introduced into various media are characterized by relaxation lengths which depend on the nature of the inhomogeneity. Additional verification is furnished by the observation in Sect. 3.7.B that those one-group models of the thermal energy region that successfully predict power peaking near moderator channels fail to predict flux depression near lumped absorbers with satisfactory accuracy.

Theoretical verification of the statement is easily obtained by considering the lattice C configuration. The first three eigenvalues in lattice C are exhibited in Table 3.7. The eigenvalues, and the corresponding eigenfunctions, were used to analyze the lattice C experiment in the following manner.

TABLE 3.7 — HIGHER MODE DIFFUSION LENGTHS IN LATTICE C

L_1	L_2	L_3
2.517 cm	1.670 cm	1.629 cm

The lattices in the experiments are arranged so that the unperturbed flux is unbuckled in the direction of measurement of the transient.[73] The perturbed flux in the lattice is therefore taken as

$$\phi_\ell (E,x) = \phi_\ell (E) + \sum_{j=1}^{n} A_{\ell j} \gamma_{\ell j} (E) \exp \left[-x/L_{\ell j}\right]$$

Eq. (3.101)

where n is the number of modes that are to be retained in the calculation. The origin of the x coordinate is taken as the center of the perturbing slab. From symmetry conditions, the flux in the slab is then

$$\phi_s (E,x) = \phi_s (E) + \sum_{j=1}^{n} A_{sj} \gamma_{sj} (E) \cosh \left[x/L_{sj}\right] .$$

Eq. (3.102)

The infinite medium spectra ϕ_i, and the eigenfunctions and eigenvalues γ_{ij} and L_{ij}, are known from previous calculations. The A_{ij} are obtained by applying boundary conditions at the perturbation-lattice interface. Continuity of the first few energy moments of the current and flux are the conditions applied, conditions somewhat arbitrary. However, continuity of the zeroeth energy moment of the current (i.e., continuity of current) is necessary in order to ensure neutron conservation, and some numerical experimentation showed that, as long as continuity of total current was applied as a boundary condition, the values of the expansion coefficients A_{ij} were insensitive to the other conditions.

Computations of the lattice C experiment (lattice C perturbed by an A–type gap*) were performed by the above technique with the retention of one, two, and three terms in the sums. The one-term computation yields a transient characterized by the asymptotic diffusion length $L_1 = 2.517$ cm. A two-term expansion, in which the first two eigenfunctions in each region are retained, gives a different result: the lattice expansion coefficient of the second mode is fully 25 percent the magnitude of that of the first. The distortion of the transient produced by the sizable second mode contribution results in a transient which would be experimentally indistinguishable from an exponential with a relaxation length of 2.35 cm (Fig. 3.20), a value identical to the measured one (and also identical with L_M). A three-term expansion also predicts a relaxation length of 2.35 cm.

The Maxwellian relaxation length, then, would be the correct one to use in lattice C with the A–type perturbation. That it would not necessarily be the correct one to use near other perturbations in the lattice is illustrated by computing the transient near a more normal B–type perturbation in the lattice. The computations retaining one, two, and three modes all yielded higher mode expansion coefficients that were small (of the order of 1 percent) compared to that of the fundamental mode, with the result that the transient appeared as a single exponential with $L = 2.50$ cm, a value close to the asymptotic diffusion length in the lattice.

In general, then, the presence of the higher modes in flux transients means that the thermal neutron space-energy problem is not really separable and, consequently, a unique thermal diffusion length cannot be defined for use in all flux transient calculations within a given medium. Usually, perturbations such as water channels, which introduce into the neighboring media neutrons with a large Maxwellian component, will give rise to transients characterized by diffusion lengths that are approximately Maxwellian averaged ones simply because the leading term in the eigenfunction expansion of such a transient is the more or less Maxwellian diffusion hardened spectrum. A perturbation such as a lumped absorber, however, introduces (in a negative sense) into the neighboring media neutrons with a thermal component that is severely distorted from a Maxwellian, so that the leading term in the eigenfunction expansion of the resulting transient may no

*The A-type perturbation is a slab made of polyethylene and U^{235}. The U^{235} concentration in the slab is the same as that in the surrounding lattice. The B-type perturbation is a slab of pure polyethylene.

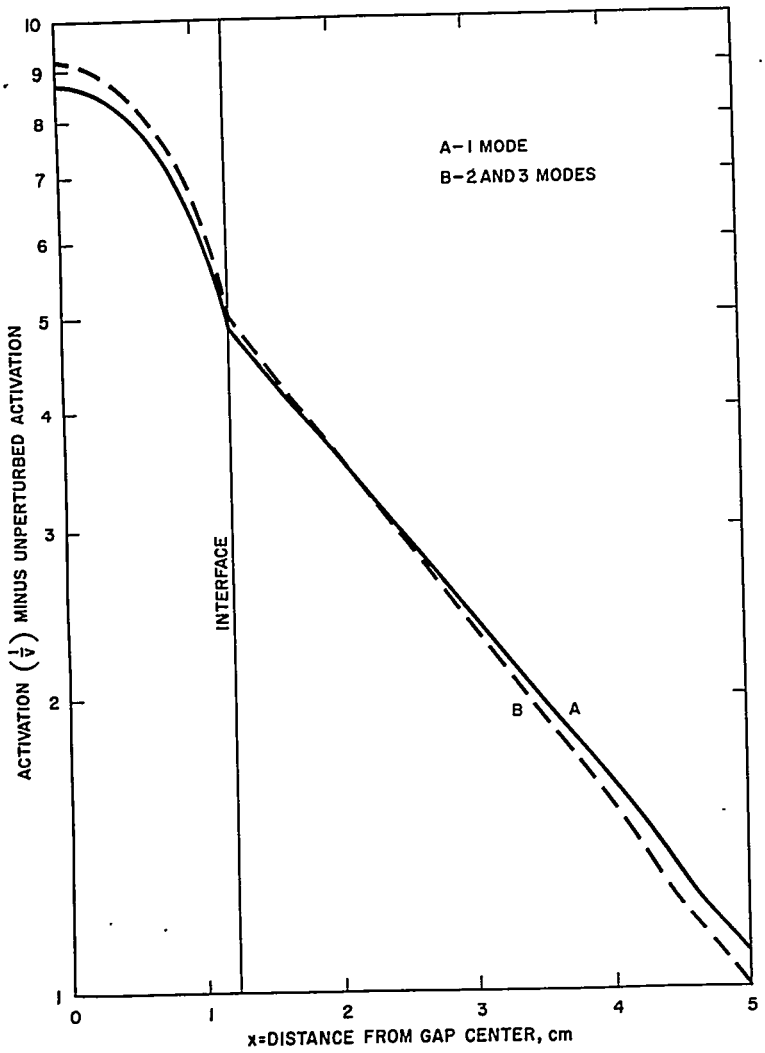

FIGURE 3.20. Activations of the 1/v Absorbing Foil Minus Unperturbed Activations Near an A-Type Perturbation in Lattice C; Curve A, One Eigenfunction Retained in the Expansion; Curve B, Two and Three Eigenfunctions Retained in the Expansion.

longer be the asymptotic eigenfunction. The diffusion length to use in such a case seems, at present, to be unpredictable.

The nonseparability of the space-energy problem influences the diffusion length to be used in any given situation. The P_0 and P_1 kernels used in the calculations might also be expected to influence the choice of L. This possibility has been studied

by computing L_1 for water using different combinations of commonly used kernels. Pure water was chosen because effects of the kernels on diffusion lengths should appear strongest in the pure moderator. The results of the calculations are presented in Table 3.8. The following points should be noted:

1. The choice of the P_0 energy exchange kernel has very little influence on L_1. The largest relative difference in L_1 due to the P_0 kernel is 0.6 percent.
2. The choice of the P_1 kernel has a somewhat greater influence on L_1. The largest relative difference due to the P_1 kernel for a given P_0 kernel is 1.8 percent.

The differences in the asymptotic diffusion lengths due to the kernels are, thus, small, a conclusion that has been reached independently by Gelbard, et al., [76] and the chief effect influencing the choice of L is the presence of higher eigenvalues in the transients.

Calculations of diffusion length may be based on the neutron pulse parameters or on direct eigenvalue calculations. Values of the pulse parameters have been obtained by Clendenin [77] over the temperature range from 20°C to 300°C. A P_{11} approximation was used in these calculations and applied to the Radkowsky and Nelkin models. Direct eigenvalue calculations have also been made for verification. [78]

Figure 3.21 compares the calculated values of diffusion length L with the measurements of Rockey and Skolnik [79] and Reier and deJuren. [80] Included also is the diffusion length at room temperature inferred from the measurements of Starr and Koppel. [81] While the agreement between both models and experiment is close for room temperature, the values for the two models diverge for the temperatures of reactor operation. The agreement between the experimental points is not sufficiently close to permit an unambiguous choice of model, although the data of Reier and deJuren agree well with the values of the Nelkin model.

TABLE 3.8 — COMPARISON OF DIFFUSION LENGTHS FOR WATER AT 68°F OBTAINED WITH VARIOUS SCATTERING KERNELS

P_0 Kernel	Mass 1 Free Gas			Nelkin Kernel		
P_1 Kernel	Radkowsky Prescription	Nelkin	Nelkin S-G*	Radkowsky Prescription	Nelkin	Nelkin S-G
L_1 (cm)	2.84†	2.79	2.79	2.86	2.81	2.81

*Selengut-Goertzel approximation.

† σ_a(kT) for H was taken as 0.325 mb.

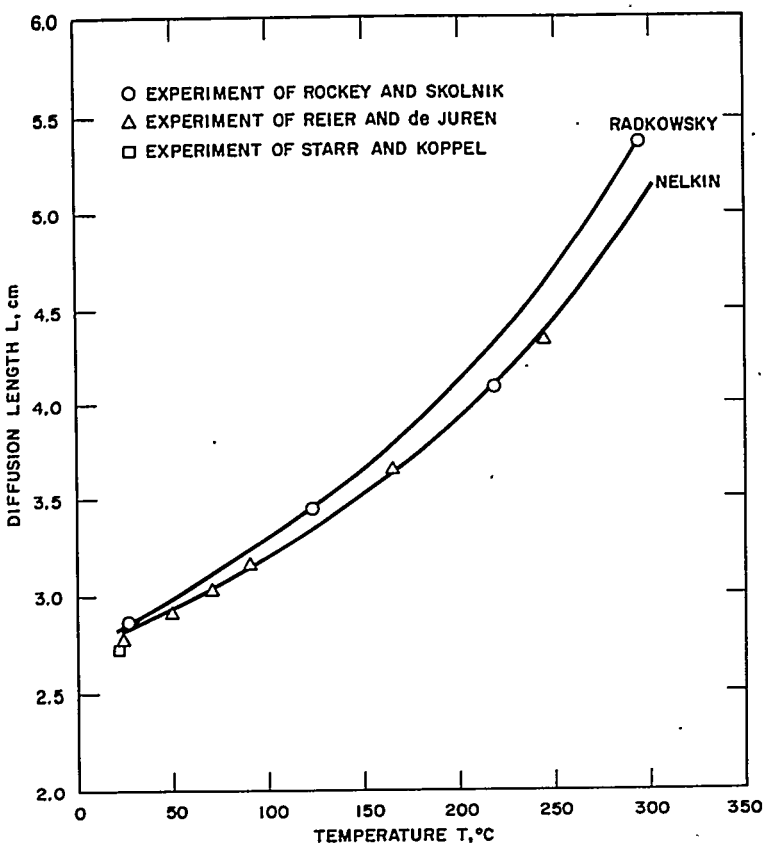

FIGURE 3.21. A Comparison of Calculated and Measured Diffusion Lengths for Water vs Temperature.

3.4 MULTIGROUP THEORY

E. M. Gelbard and N. Francis

A. Introduction

The thermal neutron flux, in any practically attainable situation, is a complicated function of the neutron's velocity and position. The parameters which define the state of the neutron are continuously variable. The neutron may occupy any position in the system, and it may move in any direction with any speed. In analog and Monte Carlo calculations, continuously variable neutron coordinates are perfectly admissible. But other computational procedures are applicable only if all

variables are discretized. In either case, the practical solution of these problems requires the extensive use of digital computer techniques.

Generally, it is convenient to introduce discrete variables in stages, treating spatial, energy, and angular coordinates separately. Correspondingly, it is convenient to classify computer programs according to the methods used to discretize the various coordinates. Thus, the term multigroup program will be used to designate any computer program which incorporates a certain prescribed treatment of the energy variable. More specifically, a computer program will be classed as a multigroup program if (1) the energy range under consideration is divided into a finite number of nonoverlapping intervals (or energy groups), and (2) the intervals are small enough that the cross sections within groups need not be averaged over precomputed spectra. These two conditions differentiate the multigroup from the conventional few-group method and the method of overlapping groups (see Sect. 3.7).

It should be pointed out that the terminology in the field of reactor computations is far from uniform. Quite commonly, for example, no distinction is drawn between few-group and multigroup codes. This distinction is made here because few-group and multigroup methods are based on different principles and serve different functions. In a few-group computation one must assume a flux spectrum within each energy group and each spatial region of the problem configuration. If the number of groups is small, details of the assumed spectra may strongly influence the computed flux shape. When estimates of the spectrum are properly chosen, the few-group method is both accurate and efficient. But in any case, the use of this method raises an important question: How is the reactor physicist to know whether a given few-group structure is adequate, whether some particular prescription for generating few-group constants is satisfactory? Before he can trust the few-group method he must be able to test its validity. For this purpose he needs a test code with many groups, i.e., a multigroup code.

In examining the difference between few-group and multigroup codes, one's attention is drawn to the energy mesh structure and to the treatment of energy spectrum effects. In the thermal energy range transport effects may be equally important. Therefore, a test code used in this range should be based on some refined treatment of the transport equation. Such reasoning has led to the development of multigroup transport codes.

The codes described below are to be regarded primarily as test codes. They are meant to serve as standards and, in their formulation, computing time has been sacrificed for ac-

curacy. Simpler computing tools (see Sect. 3.7) should be used whenever possible; but carefully selected multigroup calculations can play an important role in defining the limitations of simpler methods.

To classify codes as test codes or design codes helps one understand the operation of overall computing systems comprising many parts. Nevertheless, it should be stressed that these classes overlap. This section deals with codes which are primarily test codes, but there is no absolute distinction between nuclear design codes and test codes. Any code embodies compromises between running time and accuracy. The requirements of the problem and the limitations of available computers may lead to different compromises in different circumstances.

What follows is the derivation and solution of multigroup transport equations, with attention confined to the treatment of thermal neutron fluxes. Because the computation of flux and activation shapes in the thermal group is an important part of the nuclear design process, the calculational problems have been attacked by many people with different approaches and different techniques. Not all their work can be reported here. Much that is important has been passed over in order to concentrate on those methods which are most useful in the analysis of pressurized light water reactors.

Because the emphasis is on methods rather than particular codes, the discussion starts with multigroup methods in general terms. Section 3.4.B contains brief expositions of techniques often used to discretize the energy and angular variables. How such techniques are incorporated into practical computing tools is shown in Sect. 3.4.C. In Sect. 3.4.D the reader will find some comments on Monte Carlo methods. These form an important class in themselves, a class which is discussed more fully in Sect. 3.5.

B. Multienergy Transport Equation

1. Derivation of Basic Equations

In slab geometry the energy-dependent transport equation takes the form

$$\mu \frac{\partial}{\partial x} \psi(E, \mu, x) + \Sigma_t(E, x)\, \psi(E, \mu, x)$$

$$= s(E, \mu, x) + \int_0^\infty dE' \int d\hat{\Omega}'\, \Sigma_s(E' \to E, \hat{\Omega}' \to \hat{\Omega}, x)\, \psi(E', \mu, x). \qquad \text{Eq. (3.103)}$$

Here E' and E are, respectively, neutron energies before and after a scattering collision. Similarly, the vectors $\hat{\Omega}'$ and $\hat{\Omega}$ are related to initial and final neutron velocities,

$$\hat{\Omega} = \vec{v}/v, \quad \hat{\Omega}' = \vec{v}'/v'$$

while μ is the x component of $\hat{\Omega}$

$$\mu = \Omega_x.$$

All relevant information concerning the neutron's environment is contained in the quantities Σ_t, s, and Σ_s; Σ_t is the total cross section; s the density of neutron sources; Σ_s the scattering kernel.

Assume that s is given. To compute the neutron flux in a slab one must solve Eq. (3.103). This is a difficult task, in practice, for two reasons. First, we note that fluxes at all energies are coupled to each other through the scattering kernel. Secondly, the scattering kernel itself is, generally, a very complicated function of all its arguments and the form of the function may be quite uncertain. On the other hand, if both the initial and final energies of the neutron are large compared with kT and the chemical binding energy, these difficulties disappear. The kernel, $\Sigma_s(E' \to E, \hat{\Omega}' \to \hat{\Omega}, x)$, becomes relatively simple, and it may be assumed that $\Sigma_s = 0$ unless $E' \geq E$. Thus, the apparatus of slowing-down theory may be used to compute the flux.

For smaller E (i.e., $E \leq E_c$) one may write

$$\mu \frac{\partial \psi}{\partial x} + \Sigma_t \psi = s + \int_0^{E_c} dE' \int d\hat{\Omega}' \Sigma_s \psi + \int_{E_c}^{\infty} dE' \int d\hat{\Omega}' \Sigma_s \psi$$

Eq. (3.104)

where, for convenience, the arguments of all functions have been suppressed. Of course the value of E_c is somewhat arbitrary. In reactor design calculations in the Naval Reactors program it is customary to take $E_c = 0.625$ ev. Sometimes, in the analysis of experiments involving thermal neutrons, one uses E_c values as high as one electron volt.

It is now assumed that Eq. (3.103) has been solved for $E > E_c$. The last term in Eq. (3.104) is, then, a known function of E. It will be treated as part of the source:

$$S = s + \int_{E_c}^{\infty} dE' \int d\hat{\Omega}' \Sigma_s \psi \qquad \text{Eq. (3.105)}$$

$$\mu \frac{\partial \psi}{\partial x} + \Sigma_t \psi = S + \int_0^{E_c} dE' \int d\hat{\Omega}' \Sigma_s \psi . \qquad \text{Eq. (3.106)}$$

Often s represents a high energy source of some type. In such cases $s(E) = 0$ for $E < E_c$. Then,

$$S = \int_{E_c}^{\infty} dE' \int d\hat{\Omega}' \Sigma_s \psi \qquad \text{Eq. (3.107)}$$

i.e., slowing down is the only source of thermal neutrons. The work that follows will deal only with slowing-down sources, and the validity of Eq. (3.107) will therefore be assumed.

If the moderator consists of free protons, the energy spectrum of the source, S, is independent of the epithermal flux spectrum.[22] It follows that the energy spectrum of S is also independent of position. Generally, the spectrum of S will depend on the epithermal flux spectrum but it is postulated, nevertheless, that the source is separable in space and energy. The accuracy of the assumption of separability has not yet been thoroughly investigated.

Further, it is commonly assumed that S is isotropic. Again, this is not quite true. There is some evidence for the hypothesis that anisotropic slowing down is usually unimportant. But there are, no doubt, special cases in which anisotropic slowing down should not be ignored.

Unless the moderator is markedly anisotropic in structure the kernel, $\Sigma_s(E' \to E, \hat{\Omega}' \to \hat{\Omega}, x)$, cannot depend separately on $\hat{\Omega}'$ and $\hat{\Omega}$. It can be a function only of the dot product, $\hat{\Omega}' \cdot \hat{\Omega} = \cos \bar{\theta}$. Under very general conditions it is possible to expand the kernel into a series of the following form:

$$\Sigma_s(E' \to E, \hat{\Omega}' \to \hat{\Omega}, x) = \Sigma_s(E' \to E, \bar{\theta}, x) = \sum_{\ell=0}^{\infty} \left(\frac{2\ell + 1}{2} \right) \Sigma_{s_\ell} (E' \to E, x) P_\ell(\cos \bar{\theta})$$

Eq. (3.108)

where $P_\ell(\cos\bar{\theta})$ is a Legendre polynomial of the ℓ^{th} order. By the addition theorem for Legendre polynomials

$$P_\ell(\cos\bar{\theta}) = P_\ell(\mu)P_\ell(\mu') + 2\sum_{m=1}^{\ell}\frac{(\ell-m)!}{(\ell+m)!}P_\ell^m(\mu)P_\ell^m(\mu')\cos m(\phi-\phi') \cdot$$

Eq. (3.109)

In Eq. (3.106) the angular flux is independent of ϕ. Consequently, when Eqs. (3.108) and (3.109) are inserted into Eq. (3.106), all terms involving m's not equal to zero will vanish. If S is isotropic

$$\mu\frac{\partial}{\partial x}\psi(E,\mu,x) + \Sigma_t(E,x)\psi(E,\mu,x) = S(E,x)$$

$$+\sum_{\ell=0}^{\infty}\left(\frac{2\ell+1}{2}\right)P_\ell(\mu)\int_0^{E_c} d\mu' dE' P_\ell(\mu')\Sigma_{s_\ell}(E'\to E,x)\psi(E',\mu',x)$$

$$= S(E,x) + \sum_{\ell=0}^{\infty}\left(\frac{2\ell+1}{2}\right)P_\ell(\mu)\int_0^{E_c} dE'\,\Sigma_{s_\ell}(E'\to E,x)\,\psi_\ell(E',x).$$

Eq. (3.110)

As is usual,

$$\psi_\ell(E,x) = \int_{-1}^{1} d\mu P_\ell(\mu)\psi(E,\mu,x).$$

2. Discretization of Angular Variable

A) P_ℓ APPROXIMATION. The derivation of the conventional P_ℓ equations proceeds, in the multienergy case, precisely as in the one-energy case. It is assumed, in L^{th} order, that

$$\psi(E,\mu,x) = \sum_{\ell=0}^{L}\left(\frac{2\ell+1}{2}\right)\psi_\ell(E,x)P_\ell(\mu). \qquad \text{Eq. (3.111)}$$

Equation (3.110) is multiplied by $P_\ell(\mu)$ and integrated from $\mu = -1$ to $\mu = +1$. Taking note of the relation

$$(\ell+1)P_{\ell+1}(\mu) + \ell P_{\ell-1}(\mu) = (2\ell+1)\mu P_\ell(\mu) \qquad \text{Eq. (3.112)}$$

one finds that

$$(\ell + 1)\frac{\partial}{\partial x}\psi_{\ell+1}(E, x) + \ell\frac{\partial}{\partial x}\psi_{\ell-1}(E, x)$$

$$+ (2\ell + 1)\,\Sigma_t(E, x)\,\psi_\ell(E, x) = (2\ell + 1)\,\delta_\ell(E, x) \qquad \text{Eq. (3.113)}$$

if $\ell < L$, and

$$\ell\frac{\partial}{\partial x}\psi_{\ell-1}(E, x) + (2\ell + 1)\,\Sigma_T(E, x)\,\psi_\ell = \delta_\ell(E, x) \qquad \text{Eq. (3.114)}$$

for $\ell = L$. Here

$$\delta_\ell(E, x) = S(E, x)\,\delta_{\ell,0} + \int_0^{E_c} \Sigma_{s_\ell}(E' \to E, x)\,\psi_\ell(E', x)\,dE'. \qquad \text{Eq. (3.115)}$$

B) DOUBLE-P_ℓ APPROXIMATION (METHOD OF YVON). The method of Yvon is based on an expansion of the transport equation in the polynominals

$$\left[\pi_\ell(\mu)\right]_+ = P_\ell(2\mu - 1) \qquad \text{Eq. (3.116)}$$

when μ is greater than zero, and

$$\left[\pi_\ell(\mu)\right]_- = P_\ell(2\mu + 1) \qquad \text{Eq. (3.117)}$$

for μ's smaller than zero. It can be shown that

$$\int_0^1 d\mu \left[\pi_\ell(\mu)\right]_+ \left[\pi_m(\mu)\right]_+ = \int_{-1}^0 d\mu \left[\pi_\ell(\mu)\right]_- \left[\pi_m(\mu)\right]_- = \delta_{\ell m}/(2\ell + 1). \qquad \text{Eq. (3.118)}$$

Further

$$(\ell + 1)\left[\pi_{\ell+1}(\mu)\right]_+ + \ell\left[\pi_{\ell-1}(\mu)\right]_+ = (2\ell + 1)(2\mu - 1)\left[\pi_\ell(\mu)\right]_+ \qquad \text{Eq. (3.119)}$$

$$(\ell + 1)\left[\pi_{\ell+1}(\mu)\right]_- + \ell\left[\pi_{\ell-1}(\mu)\right]_- = (2\ell + 1)(2\mu + 1)\left[\pi_\ell(\mu)\right]_- \qquad \text{Eq. (3.120)}$$

Now assume that

$$\psi(E, x,\mu) = \sum_{\ell=0}^{L} (2\ell + 1)\, \Omega_\ell (E, x) \left[\pi_\ell(\mu)\right]_+ \qquad \text{Eq. (3.121)}$$

for $\mu > 0$, and

$$\psi(E, x, \mu) = \sum_{\ell=0}^{L} (2\ell + 1)\, \chi_\ell (E, x) \left[\pi_\ell(\mu)\right]_- \qquad \text{Eq. (3.122)}$$

for $\mu < 0$. Substitute Eqs. (3.119) through (3.122) into (3.110). Multiply Eq. (3.110) by $[\pi_\ell(\mu)]_+$ and integrate from $\mu = 0$ to $\mu = 1$. Then multiply Eq. (3.110) by $[\pi_\ell(\mu)]_-$, integrating from $\mu = -1$ to $\mu = 0$. These operations yield differential equations in the functions Ω and χ. It will be seen, however, that the resulting equations for any ℓ contain all the kernels, $\Sigma_{s\ell}(E' \to E)$. In practice, then, it is necessary to truncate the Legendre polynomial expansion of the differential scattering cross section. Thus, one is forced to introduce an approximation which is not necessary in the derivation of the P_ℓ equations. In the double-P_1 approximation it is customary to retain the terms Σ_{s0} through Σ_{s3} in the expansion of the kernel. To justify this practice it might be argued that since four independent functions are used to describe the flux, four should be used to describe the scattering process. In a sense, the angular flux and the differential scattering cross section will then be represented with the same degree of accuracy.

The general form of the double-P_ℓ equations is quite complicated when anisotropic scattering is present; this general form will not be exhibited here. All the essential features of the double-P_ℓ equations are implicit in the double-P_1 equations:

$$\Omega_0' + \Omega_1' + 2\Sigma_t \Omega_0 = \delta_0 + \frac{3}{2}\,\delta_1 - \frac{7}{8}\,\delta_3 \qquad \text{Eq. (3.123)}$$

$$\frac{1}{3}\,\Omega_0' + \Omega_1' + \frac{2}{3}\,\Omega_2' + 2\Sigma_t \Omega_1 = \frac{1}{2}\,\delta_1 + \frac{5}{4}\,\delta_2 + \frac{7}{8}\,\delta_3 \qquad \text{Eq. (3.124)}$$

$$\chi_1' + \chi_0' + 2\Sigma_t \chi_0 = \delta_0 - \frac{3}{2}\,\delta_1 + \frac{7}{8}\,\delta_3 \qquad \text{Eq. (3.125)}$$

$$\frac{1}{3}\,\chi_0' + \chi_1' + \frac{2}{3}\,\chi_2' + 2\Sigma_t \chi_1 = \frac{1}{2}\,\delta_1 - \frac{5}{4}\,\delta_2 + \frac{7}{8}\,\delta_3 . \qquad \text{Eq. (3.126)}$$

All scattering terms are contained in the S_ℓ:

$$S_0(E, x) = S(E, x) + \int_0^{E_c} \frac{1}{2} \left[\Omega_0(E', x) + \chi_0(E', x)\right] \Sigma_{s_0}(E' \to E, x)dE' \qquad \text{Eq. (3.127)}$$

$$S_1(E, x) = \int_0^{E_c} \frac{1}{2} \left[\Omega_0(E', x) - \chi_0(E', x) + \Omega_1(E', x) + \chi_1(E', x)\right] \Sigma_{s_1}(E' \to E, x)\, dE' \qquad \text{Eq. (3.128)}$$

$$S_2(E, x) = \int_0^{E_c} \frac{3}{4} \left[\Omega_1(E', x) - \chi_1(E', x)\right] \Sigma_{s_2}(E' \to E, x)\, dE' \qquad \text{Eq. (3.129)}$$

$$S_3(E, x) = \int_0^{E_c} \frac{1}{8} \left[\chi_0(E', x) - \Omega_0(E', x) + 3\Omega_1(E', x) + 3\chi_1(E', x)\right] \Sigma_{s_3}(E' \to E)dE' . \qquad \text{Eq. (3.130)}$$

C) COMPARISON OF P_ℓ AND DOUBLE-P_ℓ APPROXIMATIONS. The P_ℓ and double-P_ℓ approximations are, fundamentally, very closely related. It is natural to ask when one should be used in place of the other. Generally, it is better to approximate a continuous function by one high order polynomial of ℓ^{th} order (as in the P_ℓ method) than by two polynomials of order $(\ell - 1)/2$ (as in Yvon's method). Thus, for example, one finds that the P_3 diffusion length in one-energy problems is more accurate than the double-P_1 diffusion length. On the other hand, Yvon's method is to be preferred in cases where the flux is badly behaved near $\mu = 0$. It is important to note that the angular flux may actually be discontinuous at $\mu = 0$. This is true, for example, in the interior of a pure absorber. A different type of singularity occurs at the surface of a plane source where the flux becomes infinite at $\mu = 0$. If the width of the source (in mean free paths) is finite but small, the flux (though finite) may rise very steeply as μ approaches zero. Therefore, in problems containing thick pure absorbers or thin sources, Yvon's method is usually more accurate than the conventional spherical harmonics method. (For additional comments on the accuracy of Yvon's method, see Sect. 3.4.C.2.)

D) DISCRETE ORDINATE METHODS. Select a set of direction cosines (ordinates) μ_i, and weights w_i, so that

$$\int_{-1}^{1} g(\mu)\, d\mu = \sum_i w_i g(\mu_i) \qquad \text{Eq. (3.131)}$$

for some class of functions $g(\mu)$. Assume that

$$\mu_i \frac{\partial \psi_i(E, x)}{\partial x} + \Sigma_t(E, x)\psi_i(E, x) \approx S(E, x)$$

$$+ \sum_{\ell=0}^{\infty} \left(\frac{2\ell + 1}{2}\right) P_\ell(\mu_i) \int_0^{E_c} dE' \Sigma_{s\ell}(E' \to E) \psi_\ell(E', x) \qquad \text{Eq. (3.132)}$$

$$\psi_\ell(E, x) = \sum_i w_i P_\ell(\mu_i) \psi_i(E, x) \qquad \text{Eq. (3.133)}$$

and

$$\Sigma_{s_\ell}(E' \to E, x) = \sum_i w_i P_\ell(\mu_i) \Sigma_s(E' \to E, \bar{\theta}_i, x) \qquad \text{Eq. (3.134)}$$

where

$$\psi_i(E, x) = \psi(E, \mu_i, x). \qquad \text{Eq. (3.135)}$$

Equations (3.132) through (3.135) define a discrete ordinate approximation.

The actual values of μ_i and w_i may be adjusted from problem to problem or fixed by some general rule. Usually, the discrete ordinate method is used in conjunction with Gauss or double Gauss quadrature. Gauss quadrature leads to the following prescription.

In an L ordinate approximation the μ_i are the roots of $P_L(\mu)$,

$$P_L(\mu_i) = 0 \qquad \text{Eq. (3.136)}$$

and the weights are adjusted so that

$$\sum_{i=1}^{L} w_i \mu_i^n = \int_{-1}^{1} \mu^n d\mu, \; n = 0, 1, 2, \ldots (L-1). \qquad \text{Eq. (3.137)}$$

It can then be shown that

$$\sum_{i=1}^{L} w_i \mu_i^n = \int_{-1}^{1} \mu^n d\mu, \; n = 0, 1, 2, \ldots (2L-1). \qquad \text{Eq. (3.138)}$$

Equations (3.136) and (3.137) determine the Gauss quadrature weights and ordinates. No other weights and ordinates can satisfy Eq. (3.138). The ability of Gauss quadrature to integrate

a high order polynomial with a small number of ordinates constitutes its main advantage over other quadrature methods.

In double Gauss quadrature the μ_i are the roots of $\pi_L(\mu)$ rather than $P_L(\mu)$:

$$\left[\pi_L(\mu_i)\right]_+ = 0, \mu_i > 0$$

$$\left[\pi_L(\mu_i)\right]_- = 0, \mu_i < 0. \qquad \text{Eq. (3.139)}$$

The weights are determined from half-range integration formulas:

$$\sum_{i=1}^{L/2} w_i \mu_i^n = \int_0^1 \mu^n d\mu, \; n = 0,1,2,\ldots(L-1)$$

$$\sum_{i=L+1}^{2L} w_i \mu_i^n = \int_0^1 \mu^n d\mu, \; n = 0, 1, 2, \ldots (L-1) \qquad \text{Eq. (3.140)}$$

Equation (3.140) is then valid for $0 \leq n \leq 2L - 1$.

The Legendre polynomials play an important role in the Gauss and double Gauss quadrature procedures. In consequence, one may be led to suspect that these quadrature methods are related, somehow, to the P_ℓ and double-P_ℓ approximations. Actually the Gauss quadrature method (in slab geometry) is completely equivalent to the method of spherical harmonics.[82] In any system the directional flux, as computed by L ordinates Gauss quadrature is exactly the same as the flux in a P_{L-1} approximation. Similarly the double Gauss method is equivalent to Yvon's method.*

Thus, if Gauss or double Gauss quadrature is incorporated into the discrete ordinate equations, one has simply reformulated the P_ℓ or double-P_ℓ equations. But this discrete ordinate form is interesting for two reasons. First, it is often a convenient starting point for numerical computations (see Sect. 3.4.C.2); secondly, it displays in a new light the physical content of the P_ℓ and double-P_ℓ approximations.

E) THE S_n METHOD. Of the various methods which have been devised to treat the transport equation accurately the S_n method[83] is, perhaps, the most familiar. This method is attractive and powerful partly because of its versatility. S_n can be adapted to slab, cylindrical, and spherical geometries with little difficulty. When one is interested exclusively in slab

*This statement presupposes a slightly modified treatment of anisotropic scattering in the double Gauss method.

lattices, the versatility of S_n is not a decisively important consideration. But, when computations in cylindrical or spherical geometry are necessary, the S_n method can be very useful.

Although, in work on naval reactors, S_n is rarely used to analyze slabs, for the sake of simplicity its salient features in slab geometry will be described. Let $\mu = \hat{\Omega} \cdot \hat{\imath}$, where $\hat{\imath}$ is a unit vector in the positive x direction. Divide the range $-1 \leq \mu \leq 1$ into n equal subintervals. Suppose that the i^{th} subinterval is bounded by μ_{i+1} and $\mu_i (\mu_{i+1} > \mu_i)$. Now assume that the angular flux in each subinterval is linear in μ,

$$\psi(x, \mu) = \psi_i(x) + (\mu - \mu_i)\left[\psi_{i+1}(x) - \psi_i(x)\right]/\Delta\mu \qquad \text{Eq. (3.141)}$$

and integrate the transport equation, with respect to μ, over each subinterval. In this way one arrives at n coupled first-order equations in the functions $\psi_i(x)$. There are, however, $n+1$ functions $\psi_1(x), \psi_2(x), \ldots, \psi_{n+1}(x)$. One more equation is needed to determine these functions. In most S_n codes this supplementary equation is taken to be the transport equation itself in the direction $\mu = 1$. (This choice proves particularly convenient in nonslab geometries.)

In cylindrical and spherical geometries the transport equation contains derivatives with respect to the angular coordinates of $\hat{\Omega}$. If it is assumed that the flux is linear in these coordinates, simple expressions for the derivatives result. Thus, in cylindrical geometry, for example, and in high order, the S_n equations are much more tractable than the P_ℓ equations.

F) INTEGRAL METHODS. Preceding methods have been classified according to the prescriptions used to discretize the angular variable. It must be conceded that such a classification system has its limitations. Not all transport methods can be catalogued in this way. Integral methods, for example, do not necessarily involve any discretization of the angular variable.

In slab geometry the transport equation can be written in the form

$$\phi(x) = \int_a^b K(x, x')\left[\Sigma_s(x')\phi(x') + S(x')\right] dx', \; a \leq x \leq b \qquad \text{Eq. (3.142)}$$

where $\phi(x)$ is the scalar flux, $S(x)$ is the source and $K(x, x')$ is a kernel which depends on the exact nature of the problem. It has been postulated that the source and scattering are isotropic, and that x and x' both have the same finite range.

At $x = a$, one may have, for example, a plane of symmetry; and at $x = b$, a vacuum boundary.

Now divide the interval from a to b into n subintervals, and integrate Eq. (3.142) over each subinterval. Denote by $\bar{\phi}_i$ the average scalar flux in the i^{th} subinterval. Further, assume that the scalar flux and the source are constant in each subinterval. Then,

$$\bar{\phi}_i = \sum_{j=1}^{n} k_{ij} \left[\bar{\Sigma}_{sj} \bar{\phi}_j + \bar{S}_j \right]$$

$$k_{ij} = \int_{x_i}^{x_{i+1}} dx \int_{x_j}^{x_{j+1}} K(x, x')\, dx' / \Delta_i . \qquad \text{Eq. (3.143)}$$

Equation (3.143) may be solved, iteratively or noniteratively, in many ways.

It will be noted that Eq. (3.143) is exact in a purely absorbing medium if the source is really flat in each subinterval. In any case, the solution of Eq. (3.143) tends to the solution of the transport equations as the subinterval widths, Δ, tend to zero. Thus, the accuracy of the integral method, as described here, depends on spatial mesh widths and not on the fineness of an angular mesh.

The integral method is used in a digital computer program called TRANVAR.[84] While TRANVAR does not allow anisotropic scattering, it is possible to treat anisotropic scattering by the integral method at some cost in problem running time.

3. *Discretization of Energy Variable*

Two different methods for discretizing the energy variable are presented here. From the point of view of their relative accuracy, there appears little basis for choosing one method over the other. However, since both have been widely used in the Naval Reactors program, both will be discussed.

A) GROUP AVERAGING. This method will be applied, for illustrative purposes, to Eqs. (3.113) and (3.115). First the energy range $0 \leq E \leq E_c$ is divided into subintervals (or groups) of width Δ_i. Next, Eq. (3.113) is integrated over each subinterval. In this process it is assumed that, for any $f(E)$ and $g(E)$,

$$\int_{\alpha^i}^{\beta^i} dE f(E)\, g(E) = f^i g^i \Delta_i \qquad \text{Eq. (3.144)}$$

where

$$f^i = \int_{\alpha^i}^{\beta^i} dE f(E)/\Delta_i \,, \quad g^i = \int_{\alpha^i}^{\beta^i} dE g(E)/\Delta_i \,. \qquad \text{Eq. (3.145)}$$

The quantities α^i and β^i are the energy limits of the i^{th} group. One finds that

$$(\ell+1)\frac{\partial}{\partial x}\psi^i_{\ell+1}(x) + \ell\frac{\partial}{\partial x}\psi^i_{\ell-1}(x) + (2\ell+1)\bar{\Sigma}^i_t(x)\psi^i_\ell(x) = (2\ell+1)\delta^i_\ell(x) \qquad \text{Eq. (3.146)}$$

$$\delta^i_\ell(x) = S^i(x)\,\delta_{\ell 0} + \int_0^{E_c} \Sigma^i_{s_\ell}(E', x)\,\psi_\ell(E', x)\,dE' \,. \qquad \text{Eq. (3.147)}$$

Approximately

$$\delta^i_\ell(x) = S(x)^i\,\delta_{\ell 0} + \sum_j A^{ij}\psi^j_\ell \qquad \text{Eq. (3.148)}$$

where

$$A^{ij} = \int_{\alpha^j}^{\beta^j} dE' \int_{\alpha^i}^{\beta^i} dE\, \Sigma_s(E' \to E)/\Delta_j \,. \qquad \text{Eq. (3.149)}$$

Equations (3.146) and (3.148) jointly constitute a set of multigroup P_ℓ equations.

B) USE OF DISCRETE ENERGY POINTS. The independent variables in Eqs. (3.146) and (3.148) are group-averaged fluxes. It is also possible to work with the flux values at discrete energy mesh points. Introduce a set of energy points $E^1, E^2, E^3, \ldots, E^N = 0$. At these points

$$(\ell+1)\frac{\partial}{\partial x}\psi^i_{\ell+1}(x) + \ell\frac{\partial}{\partial x}\psi^i_{\ell-1}(x) + (2\ell+1)\Sigma^i_t(x)\,\psi^i_\ell(x) = (2\ell+1)\delta^i_\ell(x) \qquad \text{Eq. (3.150)}$$

where

$$\delta^i_\ell(x) = S^i(x)\,\delta_{\ell 0} + \int_0^{E_c} \Sigma_{s_\ell}(E' \to E^i, x)\,\psi_\ell(E', x)\,dE' \,. \qquad \text{Eq. (3.151)}$$

Now assume that the product $\Sigma_{s\ell}(E' \to E^i, x)\, \psi_\ell^i(x)$ is linear in the interval between any two energy mesh points. Then,

$$\int_0^{E_c} \Sigma_{s_\ell}(E' \to E^i, x)\, \psi_\ell(E', x)\, dE' = \frac{1}{2} \sum_{j=0}^{N-1} \Delta_j \left[\Sigma_{s_\ell}(E^{j+1} \to E^i, x)\, \psi_\ell^{j+1}(x) + \Sigma_{s_\ell}(E^j \to E^i, x)\, \psi_\ell^j(x) \right] = \sum_{j=0}^{N} B^{ij} \psi_\ell^j(x). \qquad \text{Eq. (3.152)}$$

It should be noted that, in using Eqs. (3.150) through (3.152), all terms containing ψ_ℓ^N are deleted, since the directional flux vanishes at $E = 0$.

C. Solution of the Multigroup Equations in One Dimension

The application of differencing techniques described above is exemplified in two multigroup thermal neutron codes which are discussed here. The description of these programs serves as an illustration of some of the practical problems involved in this area and of some of the steps that have been taken to solve these problems.

1. SLOP-1

A) GENERAL DESCRIPTION OF PROGRAM. SLOP-1[85] is a one-dimensional thermal multigroup program for the IBM-704. It is designed to compute the thermal flux level and energy spectrum, as a function of position, in a heterogeneous array of diffusing media. The several different versions of SLOP-1 which are now in operation may be separated into two distinct classes. Of most general interest are the SLOP-1 programs which compute the thermal flux due to a slowing-down source. In addition, however, modified SLOP-1 program tapes may be used to study pulsed neutron problems. The pulse version of SLOP-1 will not be discussed here specifically. Actually, the pulse and inhomogeneous versions differ very little.

Various approximations to the transport equation are programmed into SLOP-1: the flexibility of the program and the degree of precision incorporated in it are functions of geometry. Slab problems may be treated in the P_1, double-P_1, or P_3 approximations. In cylindrical and spherical geometries only the P_1 approximation is available. For the sake of brevity, concentration here is upon the SLOP-1 treatment of slabs.

The major limitations of SLOP-1 are: (1) isotropic slowing down into the thermal group, (2) regionwise constant slowing

down, (3) no transverse buckling, and (4) only one moderating material in any problem. A single set of transfer matrices is contained in every SLOP-1 library. These matrices are multiplied by the region-dependent number density of the moderator (which is always denoted as hydrogen) to form the A^{ij} defined by Eq. (3.149). Thus, in SLOP-1 the moderating material may vary in density from one region to another, but the microscopic scattering kernel must be the same in all regions. It follows, for example, that all regions must be at the same temperature. Restrictions on numbers of points, regions, and isotopes will be found in Ref. 85.

B) HEAVY ELEMENT TREATMENT. As indicated above, the moderating material in SLOP-1 is always taken to be hydrogen. In fact, the program was intended, primarily, for analysis of thermal neutron phenomena in water. For this reason, heavy element moderation was not considered important and was treated very crudely. It is not necessary that the moderating material should actually be hydrogen. With transfer matrices properly chosen, the program could be used to treat any mixture of which one moderating component is much lighter than all others. At present, however, all SLOP-1 libraries contain transfer matrices for hydrogen (bound or free), and only hydrogen moderation will be considered here.

Although the SLOP-1 treatment of heavy elements is the same in all geometries, it will be described here in the notation of slab geometry. In slab geometry, the transport equation takes the form:

$$\mu \frac{\partial}{\partial x} \psi(E, \mu, x) + \Sigma_t \psi(E, \mu, x)$$

$$= \frac{1}{2} s(E, x) + \sum_{\ell} \frac{2\ell+1}{2} P_\ell(\mu) \int_0^\infty \Sigma_{s_\ell}(E' \to E) \psi_\ell(E', x)\, dE'. \quad \text{Eq. (3.153)}$$

Here E is the neutron energy: the equation has already been averaged over the velocity distribution of scattering nucleons. Assume that, for the heavy elements, h, $K_\ell(E' \to E) \approx 0$ unless $E' = E$. Then,

$$\int_0^\infty \Sigma_{s_0 h}(E' \to E) \psi_0(E', x)\, dE' \approx \Sigma_{sh} \psi_0(E, x)$$

$$\int_0^\infty \Sigma_{s_1 h}(E' \to E)\, \psi_1(E', x)\, dE' \approx \bar{\mu}_h \Sigma_{sh} \psi_1(E, x). \quad \text{Eq. (3.154)}$$

The approximations implied by Eq. (3.154) are made in all versions of SLOP-1. Further, the higher moments of the heavy element scattering kernels are set equal to zero:

$$\int_0^\infty \Sigma_{s_\ell h}(E' \to E)\,\psi_\ell(E', x)\,dE' \approx 0 \text{ for } \ell > 1. \qquad \text{Eq. (3.155)}$$

It will be seen from Eq. (3.153) that the source is assumed to be isotropic. Assumptions relating to properties of the other physical parameters in Eq. (3.153) will be specified in subsequent discussions.

C) P_ℓ APPROXIMATION. In slab geometry with the indicated approximations for heavy elements, Eq. (3.153) leads directly to the P_1 equations [see Eq. (3.114)]:

$$\frac{\partial \psi_1(E, x)}{\partial x} + \left[\Sigma_{ah} + \Sigma_{aH} + \Sigma_{sH}\right] \psi_0(E, x) = s(E, x) + N_H \int_0^\infty \sigma_{s_0}(E' \to E)\,\psi_0(E', x)\,dE' \qquad \text{Eq. (3.156)}$$

$$\frac{1}{3}\frac{\partial \psi_0(E, x)}{\partial x} + \left[\Sigma_{ah} + \Sigma_{aH} + \Sigma_{sh}(1 - \bar{\mu}_h) + \Sigma_{sH}\right] \psi_1(E, x) = N_H \int_0^\infty \sigma_{s_1}(E' \to E)\,\psi_1(E', x)\,dE' \qquad \text{Eq. (3.157)}$$

where

ψ_0 and ψ_1 are the flux and current, respectively;
Σ_{ah} is the net absorption cross section of heavy elements;
Σ_{aH} is the absorption cross section of hydrogen;
Σ_{sH} is the scattering cross section of hydrogen;
s is an isotropic source distribution;
N_H is the number density of hydrogen;
σ_{s_0} and σ_{s_1} are the P_0 and P_1 components, respectively, of the hydrogen differential scattering cross section; and
$\bar{\mu}_h$ is the cosine of the scattering angle averaged over all collisions with heavy elements.

Before proceeding, it is convenient to truncate the range of integration in the energy transfer integrals at some energy E_c (see Sect. 3.4.B.1). To compensate, in part, for this truncation, isotropic slowing down into the range 0 to E_c may be included in the source $s(E, x)$. Since no anisotropic sources

are permitted in SLOP-1, anisotropic slowing down into the range 0 to E_c must be ignored. On all presently available library tapes, it is assumed that there is no source into the thermal energy range aside from slowing down.

Upon introduction of any desired numerical integration scheme, Eqs. (3.156) and (3.157) now take their final form:

$$\frac{\partial \psi_1^i(x)}{\partial x} + \left[\Sigma_{ah}^i + \Sigma_{aH}^i + \Sigma_{sH}^i - N_H a_0^{i,i}\right] \psi_0^i(x) = S^i(x) + N_H \sum_{i \neq j} a_0^{i,j} \psi_0^j(x) \qquad \text{Eq. (3.158)}$$

$$\frac{1}{3} \frac{\partial \psi_0^i(x)}{\partial x} + \left[\Sigma_{ah}^i + \Sigma_{sh}^i\left(1 - \bar{\mu}_h^i\right) + \Sigma_{sH}^i + \Sigma_{aH}^i - N_H a_1^{i,i}\right] \psi_1^i(x) = N_H \sum_{i \neq j} a_1^{i,j} \psi_1^j(x) . \qquad \text{Eq. (3.159)}$$

The $a_0^{i,j}$ and $a_1^{i,j}$ terms constitute hydrogen-scattering matrix elements. The relation between the matrix elements and the hydrogen-scattering kernels in Eqs. (3.156) and (3.157) depends on the nature of the numerical integration scheme.

D) ENERGY DIFFERENCING. The proper interpretation of the quantities ψ_1^i and ψ_0^i depends on the nature of the numerical integration scheme. For example, these quantities could represent group average fluxes and currents. However, the formulation of the SLOP-1 edit routines requires, instead, that they be values of the flux and current at energy mesh points (as described in Sect. 3.4.B.3.B), and that all cross sections, Σ^i, be evaluated at these same mesh points.

E) DOUBLE-P_1 APPROXIMATION. The SLOP-1 double-P_1 equations are given in Eqs. (3.123) through (3.129). They may be written as

$$\frac{\partial F_1^i}{\partial x} + \Sigma_0^i F_0^i = S^i + S_{0H}^i \qquad \text{Eq. (3.160)}$$

$$\frac{1}{3} \frac{\partial F_0^i}{\partial x} + \frac{2}{3} \frac{\partial f_2^i}{\partial x} + \Sigma_1^i F_1^i = S_{1H}^i \qquad \text{Eq. (3.161)}$$

$$\frac{2}{5}\frac{\partial F_1^i}{\partial x} + \frac{8}{15}\frac{\partial f_3^i}{\partial x} + \Sigma_2^i f_2^i = S_{2H}^i \qquad \text{Eq. (3.162)}$$

$$\frac{1}{3}\frac{\partial f_2^i}{\partial x} + \Sigma_3^i f_3^i = \frac{7}{8} S_{3H}^i \cdot \qquad \text{Eq. (3.163)}$$

For convenience, the following notation was introduced above:

$$F_0 = \Omega_0 + X_0$$

$$F_1 = \frac{1}{2}(\Omega_0 - X_0) + \frac{1}{2}(\Omega_1 + X_1)$$

$$f_2 = \frac{3}{4}(\Omega_1 - X_1)$$

$$f_3 = \frac{1}{8}(X_0 - \Omega_0) + \frac{3}{8}(\Omega_1 + X_1) \cdot$$

Further,

$$\Sigma_0^i = \Sigma_{ah}^i + \Sigma_{aH}^i + \Sigma_{sH}^i$$

$$\Sigma_t^i = \Sigma_0^i + \Sigma_{sh}^i$$

$$\Sigma_1^i = \Sigma_t^i - \bar{\mu}_h^i \Sigma_{sh}^i$$

$$\Sigma_2^i = \frac{16}{15}\Sigma_t^i$$

$$\Sigma_3^i = 2\Sigma_t^i$$

and

$$S_{\ell H}^i = N_H \sum_j a_\ell^{i,j} F_\ell^j \quad \text{for} \quad \ell = 0, 1;$$

$$= N_H \sum_j a_\ell^{i,j} f_\ell^j \quad \text{for} \quad \ell = 2, 3 \cdot$$

Following the substitutions $\phi_0^i = F_0^i + 2f_2^i$, $\phi_2^i = f_2^i$. Equations (3.160) through (3.163) become

$$\frac{\partial F_1^i}{\partial x} + \Sigma_0^i \phi_0^i = 2\Sigma_0^i \phi_2^i + S^i + \delta_{0H}^i \qquad \text{Eq. (3.164)}$$

$$\frac{\partial \phi_0^i}{\partial x} + 3\Sigma_1^i F_1^i = 3\delta_{1H}^i \qquad \text{Eq. (3.165)}$$

$$\frac{\partial f_3^i}{\partial x} + \left(\frac{7}{2}\Sigma_t^i - \frac{3}{2}\Sigma_{sh}^i\right)\phi_2^i = \frac{3}{4}\Sigma_0^i\phi_0^i - \frac{3}{4}S^i - \frac{3}{4}\delta_{0H}^i + \frac{15}{8}\delta_{2H}^i \qquad \text{Eq. (3.166)}$$

$$\frac{\partial \phi_2^i}{\partial x} + 6\Sigma_t^i f_3^i = \frac{21}{8}\delta_{3H}^i . \qquad \text{Eq. (3.167)}$$

To facilitate the iterative solution of Eqs. (3.164) through (3.167), diagonal terms in $\delta_{\ell H}^i$ will be transferred to the right-hand side wherever possible. Thus,

$$\frac{\partial F_1^i}{\partial x} + \left(\Sigma_0^i - N_H a_0^{i,i}\right)\phi_0^i = 2\left(\Sigma_0^i - N_H a_0^{i,i}\right)\phi_2^i + S^i + \delta_{0H}^{\prime i} \qquad \text{Eq. (3.168)}$$

$$\frac{\partial \phi_0^i}{\partial x} + 3\left(\Sigma_1^i - N_H a_1^{i,i}\right)F_1^i = 3\delta_{1H}^{\prime i} \qquad \text{Eq. (3.169)}$$

$$\frac{\partial f_3^i}{\partial x} + \left(\frac{7}{2}\Sigma_0^i + 2\Sigma_{sh}^i - \frac{15}{8}N_H a_2^{i,i} - \frac{3}{2}N_H a_0^{i,i}\right)\phi_2^i$$

$$= \frac{3}{4}\left(\Sigma_0^i - N_H a_0^{i,i}\right)\phi_0^i - \frac{3}{4}S^i + \frac{15}{8}\delta_{2H}^{\prime i} - \frac{3}{4}\delta_{0H}^{\prime i} \qquad \text{Eq. (3.170)}$$

$$\frac{\partial \phi_2^i}{\partial x} + \left(6\Sigma_0^i + 6\Sigma_{sh}^i - \frac{21}{8}N_H a_3^{i,i}\right)F_3^i = \frac{21}{8}\delta_{3H}^{\prime i} \qquad \text{Eq. (3.171)}$$

$$\delta_{\ell H}^{\prime i} = N_H \sum_{j \neq i} a_\ell^{i,j} F_\ell^j, \quad \ell = 0, 1;$$

$$= N_H \sum_{j \neq i} a_\ell^{i,j} f_\ell^j, \quad \ell = 2, 3 .$$

More simply

$$\frac{\partial F_1^i}{\partial x} + \alpha_0^i \phi_0^i = s_0^i \qquad \text{Eq. (3.172)}$$

$$\frac{\partial \phi_0^i}{\partial x} + \beta_0^i F_1^i = \iota_0^i \qquad \text{Eq. (3.173)}$$

$$\frac{\partial f_3^i}{\partial x} + \alpha_2^i \phi_2^i = s_2^i \qquad \text{Eq. (3.174)}$$

$$\frac{\partial \phi_2^i}{\partial x} + \beta_2^i f_3^i = \iota_2^i . \qquad \text{Eq. (3.175)}$$

Equations (3.172) through (3.175) are the basic SLOP-1 equations for slabs.

F) METHOD OF SOLUTION. Spatial difference equations are derived from Eqs. (3.172) through (3.175) by the following procedure. Equations (3.172) and (3.174) are integrated from the midpoint of one mesh interval to the midpoint of the next. Equations (3.173) and (3.175) are written, in central difference form, at interval midpoints. Finally, F_1^i and f_3^i are eliminated, leaving two coupled second-order difference equations in ϕ_0^i and ϕ_2^i. The resulting equations are given in detail in Ref. 85.

SLOP-1 solves the multigroup difference equations by a combination of iterative processes. Guessed starting values for ϕ_0^i and ϕ_2^i are supplied by the problem requestor. Given these starting values SLOP-1 constructs the source terms s_0^1, s_2^1, ι_0^1, and ι_2^1. The equations for ϕ_0^1 and ϕ_2^1 are then solved iteratively, and the guessed values for ϕ_0^1 and ϕ_0^2 are replaced in storage by the newly computed values. Next, the SLOP-1 program proceeds to construct sources for $i = 2$. In this process it uses the newly computed values for ϕ_0^1 and ϕ_2^1 and the guessed starting values for all other fluxes. As above, new values of ϕ_0^2 and ϕ_2^2 are computed iteratively, and guessed values of ϕ_0^2 and ϕ_2^2 are replaced in storage by the newly computed values, etc. Eventually all guessed ϕ_0's and ϕ_2's are replaced by computed first iterates of ϕ_0 and ϕ_2. At this point a new outer cycle begins. SLOP-1 computes a second iterate of the flux, using the first iterate as a guess, then a third iterate from the second iterate, and so on. The outer cycle terminates when the spatial shape of the net thermal flux has satisfied a specified convergence criterion.

2. *TET: Thermal Energy Transport Program*

The TET[86] program was written to study thermal neutron transport theory effects. It has the following capabilities:

(1) The source and energy exchange kernel can have anisotropic components up to and including the third order Legendre polynomials.
(2) The source may be supplied to one or several epithermal groups. The calculated epithermal flux in collisions with the moderator atoms feeds neutrons to the thermal energy range.
(3) As many as six different energy exchange kernels may be used for six mixture regions.
(4) The scattering terms in the Boltzmann equation may be integrated with respect to angle with any quadrature formula. At present, only Gauss quadrature formulas have been used for up to six angles in the 1/2 plane.

The TET program solves the following multigroup Boltzmann equation approximately:

$$\mu \frac{\partial \psi}{\partial x} + \Sigma_t \psi = \int_0^\infty dE' \int_{-1}^{1} d\mu \Sigma_s(E' \to E, \mu' \to \mu, x)\, \psi(E', \mu', x) + s(E, \mu, x). \qquad \text{Eq. (3.176)}$$

Let

$$\psi(E, \mu, x) = \sum_{i=0}^{N} \psi^i(\mu, x)\, Q^i(E)$$

$$Q^i(E) = \begin{cases} 1 & E_{i+1} \geq E \geq E_i \\ 0 & \text{otherwise} \end{cases} \qquad \text{Eq. (3.177)}$$

Then, substituting the $\psi(E, \mu, x)$ of Eq. (3.177) into Eq. (3.176), multiplying by $Q^i(E)$ and integrating gives

$$\mu \frac{\partial \psi^i}{\partial x} + \Sigma_t^i \psi^i = \sum_j \int_{-1}^{+1} \Sigma_s^{i,j}(\mu' \to \mu, x)\, \psi^j(\mu', x)\, d\mu' + S^i(\mu, x) \qquad \text{Eq. (3.178)}$$

where

$$\Delta E^i \psi^i(\mu, x) = \int_0^\infty Q^i(E)\psi(E, \mu, x)\, dE$$

$$\Delta E^i \Sigma_t^i \psi^i = \int_0^\infty Q^i(E)\Sigma_t(E)\, \psi(E, \mu, x)\, dE$$

$$\Delta E^i S^i(\mu, x) = \int_0^\infty Q^i(E) s(E, \mu, x) dE$$

and

$$\Delta E^i \Sigma_s^{i,j}(\mu' \to \mu, x) = \int_0^\infty \int_0^\infty Q^i(E) Q^j(E') \Sigma_s(E' \to E, \mu' \to \mu, x) dE dE'$$

In performing the above integrations it is assumed that the flux is constant over each energy mesh interval. The derivation presented here is a variant of the group averaging method (see Sect. 3.4.B.3.A).

Equation (3.178) is the multigroup approximation to the Boltzmann equation that the TET program solves. The multigroup equations are solved by iteration. For any group i, it is assumed that the vector flux is known at all of the other groups, $j \neq i$. Then, the desired one-velocity equation is

$$\mu \frac{\partial \psi^i}{\partial x} + \Sigma_t^i \psi^i = \int_{-1}^{+1} \Sigma_s^{i,i}(\mu' \to \mu, x)\, \psi^i(\mu', x)\, d\mu' + \delta^i(\mu, x) \qquad \text{Eq. (3.179)}$$

where

$$\delta^i(\mu, x) = S^i(\mu, x) + \int_{-1}^{+1} \sum_{j \neq i} \Sigma_s^{i,j}(\mu' \to \mu, x)\, \psi^j(\mu', x) d\mu'.$$

Equation (3.179) is solved with the following assumptions:

(1) Within each region the vector flux and source are linear in x.
(2) Only four Legendre components of the source and scattering law are present.
(3) Angular integrals which include the vector flux may be performed using the double Gauss quadrature formulas for six angles or less in the 1/2 plane.

The Boltzmann equation for group i, Eq. (3.179), is replaced by a set of N coupled first-order differential equations for the vector flux $\psi_\alpha(x)$ where

$$\psi_\alpha(x) = \psi(x, \mu_\alpha) \qquad \alpha = 1 \ldots N$$

and μ_α are the double Gauss angles. The coupled linear differential equations are next replaced by the equivalent integral equations. When it is assumed that the vector flux varies linearly in each region, the integral equation reduces to a set of algebraic equations of the constant and linear component of the vector flux in each region. These algebraic equations are solved by TET, using an iterative method.

In this qualitative discussion of thermal neutron transport theory effects, all results were for one-velocity problems. In each case, the cross section may be interpreted as cross sections averaged over an average thermal spectrum for the problem. Although the one-velocity conclusions about the importance of transport theory corrections are not expected to be always correct for the thermal multigroup problem, the qualitative predictions are valid. It should be remarked, however, that the one-velocity criteria for the validity of various transport theory approximations should be used with caution when the spectra show strong variations as a function of position. In this case, the comparison of the single and double-P_1 multigroup approximation results is needed.

Since the solution of the transport equation in general requires more time and effort than solving either the P_1 or double-P_1 equations, it is desirable to know when transport effects are important or, conversely, when P_1 or double-P_1 approximations suffice. A simple criterion for the validity of the diffusion theory solution requires a comparison of the ratio of the divergence of the diffusion theory current and capture rate, $\Sigma_a\phi$. When $\nabla\cdot(D\nabla\phi)/\Sigma_a\phi \ll 1$ and when the calculated flux is at least one diffusion length from a material interface or source plane, the diffusion theory prediction is reliable. On the other hand, when the leakage-absorption ratio is not small or when the region of interest is near to a material or source discontinuity, the diffusion theory prediction may be in error, and more accurate calculational predictions or experimental results should be used.

The double-P_1 approximation results can be discussed in a similar way. Let $\psi^+(\mu)$ and $\psi^-(\mu)$ be the double-P_1 approximation to the flux in the (+) and (-) hemispheres, respectively (see Sect. 3.4.B.2.B). Then, if

$$\psi^\pm(\mu) = a_\pm + b_\pm\mu$$

and if $\left|\frac{b\pm}{a\pm}\right| << 1$, the double-$P_1$ approximation results can be trusted. Here, in contrast to diffusion theory, the proximity of the boundary to the point in question is unimportant when the flux in each hemisphere is nearly isotropic.

Another approximate but simple way of estimating the accuracy of the double-P_1 approximation in the solution of thermal space-energy problems is to consider the one-velocity approximation and then compare double-P_1 calculations with more accurate ones. The cross sections must be considered as average thermal cross sections. In Figs. 3.22 through 3.24 the average scalar flux in slabs of optical thicknesses between 0.01 and 1 is calculated as a function of the number of angles in the 1/2 plane needed to describe the vector flux. The slab is in a vacuum and has a uniform isotropic source. The ratio c of scattering to total cross section is 0.5 and 0.75. The scattering is isotropic. The two-angle result is approximately equivalent to the double-P_1 approximation. A large number of angles are needed when the slab is thin. The physical reason is that the neutron distribution strongly favors large angles when the source region is thin.

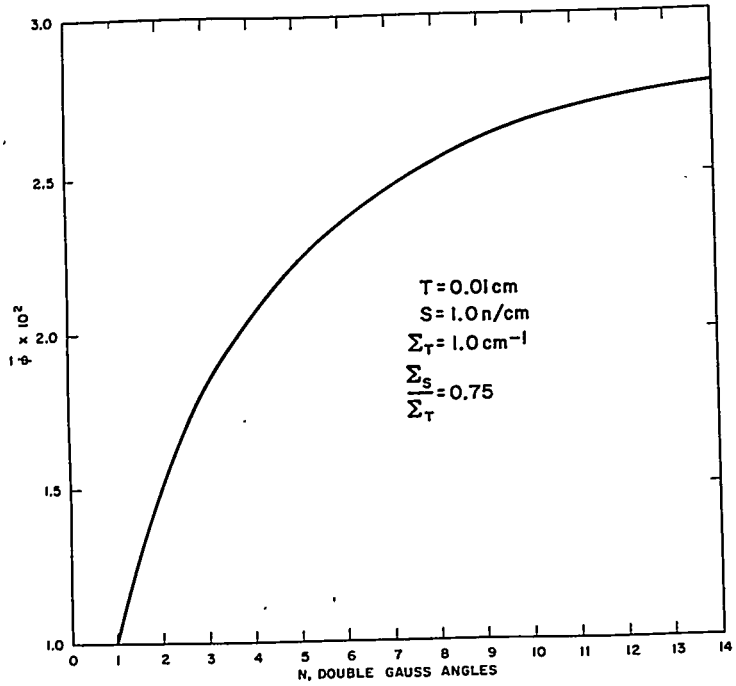

FIGURE 3.22. Average Flux vs Double Gauss Angles for a Slab with an Optical Thickness of 0.01 in a Vacuum.

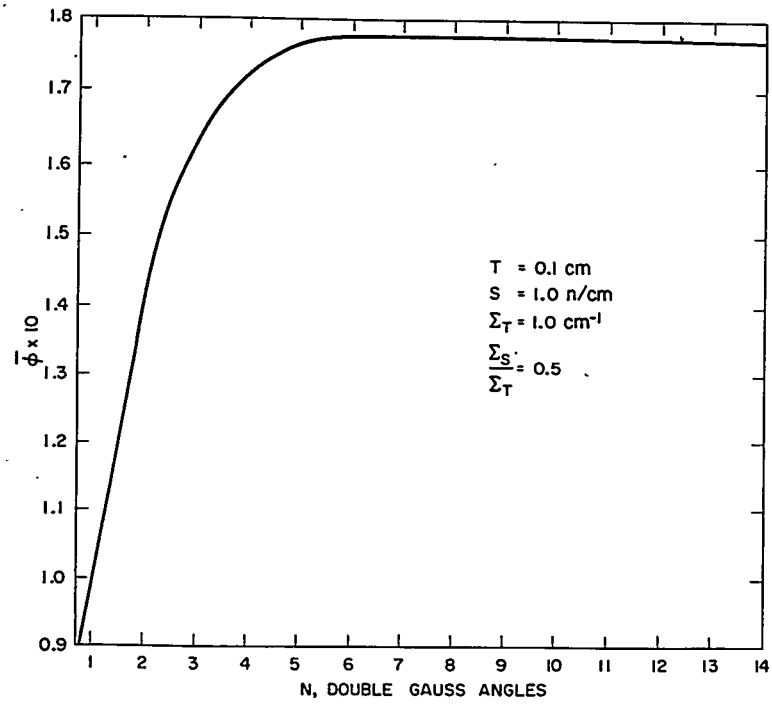

FIGURE 3.23. Average Flux vs Double Gauss Angles for a Slab with an Optical Thickness of 0.1 in a Vacuum.

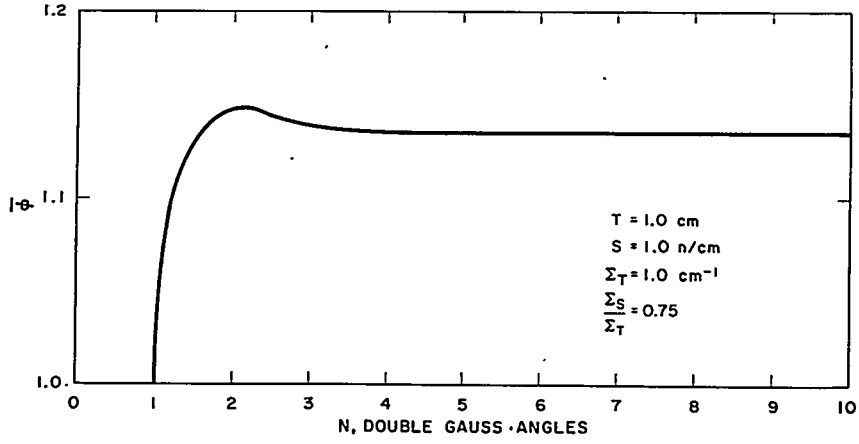

FIGURE 3.24. Average Flux vs Double Gauss Angles for a Slab with an Optical Thickness of 1.0 in a Vacuum.

Double-P_1 approximation results have also been found for moderator absorber periodic lattice problems. The scattering is assumed to be isotropic. The source is assumed to be isotropic and constant in the moderator region, and scattering is zero in the absorber. The moderator and absorber thickness range from 0.1 to 1 mean free path, while the following two values have been assumed for the scattering to absorption cross section ratio in the moderator: 0.5 and 0.9. The average flux in the moderator is exhibited in Figs. 3.25 through 3.28 as a function of the number of double Gauss quadrature angles used in the integration of the vector flux. Large errors are observed when only a few angles are included and when the moderator thickness is small.

The two types of problems, slab lattice and slab in vacuum, are introduced here as typical simple problems to demonstrate the sensitivity of the scalar flux to the refinement of this calculation. The general reactor design problem bears little resemblance to these examples. For this reason, it may be desirable to solve a one-velocity model of the multigroup problem to learn how many angles are needed to obtain the required precision.

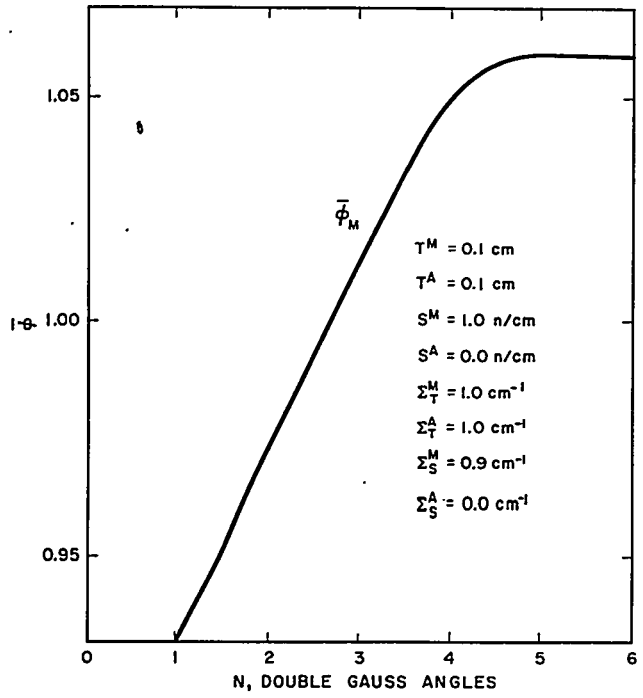

FIGURE 3.25. Average Flux in the Moderator vs Double Gauss Angles for a Two-Region Moderator-Absorber Slab Problem.

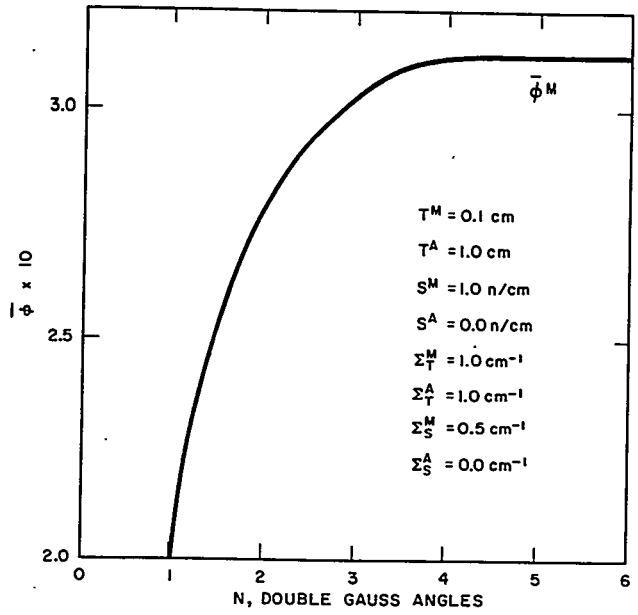

FIGURE 3.26. Average Flux in the Moderator vs Double Gauss Angles for a Two-Region Moderator-Absorber Slab Problem.

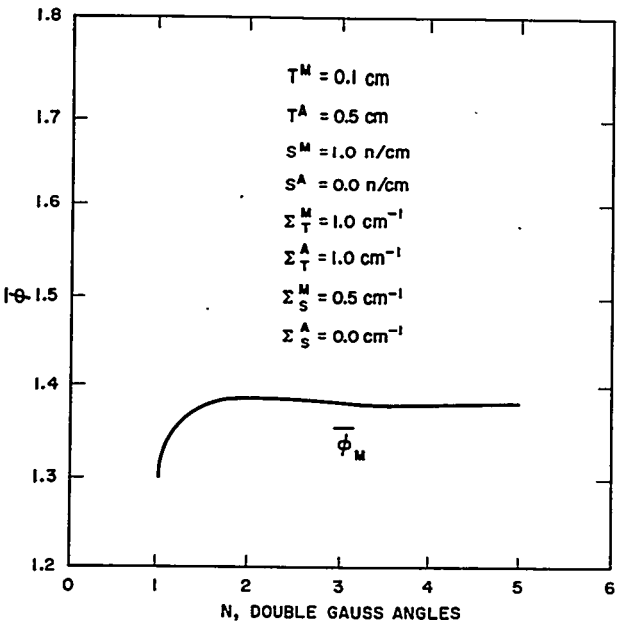

FIGURE 3.27. Average Flux in the Moderator vs Double Gauss Angles for a Two-Region Moderator-Absorber Slab Problem.

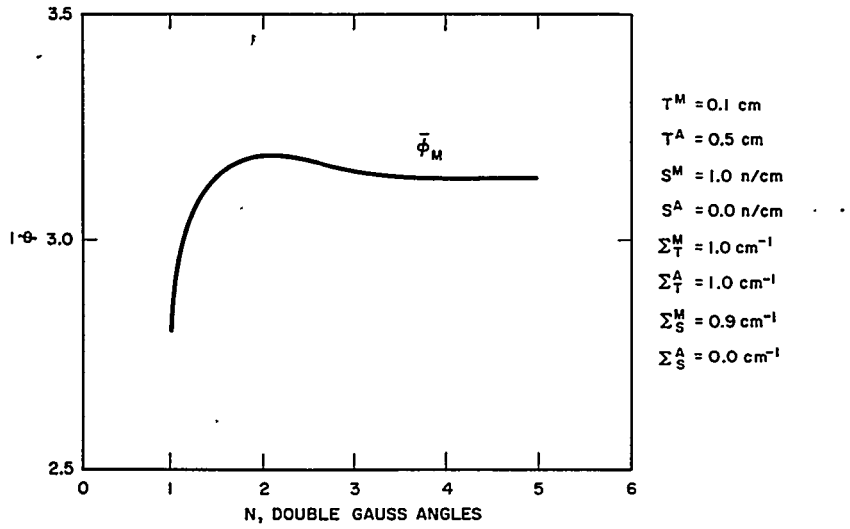

FIGURE 3.28. Average Flux in the Moderator vs Double Gauss Angles for a Two-Region Moderator-Absorber Slab Problem.

D. Multigroup Monte Carlo Techniques

The TET and SLOP-1 codes are meant to serve as standards, as tools of high precision used to check design procedures. Reliable standards are necessary in two dimensions also. However, accurate analytical calculations in two dimensions are very costly and, at this level of complexity, Monte Carlo methods come into prominence. While Monte Carlo techniques are discussed in detail in Sect. 3.5, it is appropriate to make a few comments here about the use of Monte Carlo in multigroup calculations.

Monte Carlo has been widely used in slowing-down calculations. The slowing-down process is straightforward and well understood, and there is no reason why it should not be simulated exactly in a Monte Carlo code. On the other hand, relatively little is known about the thermal scattering kernel of water, and little is lost through the introduction of a multigroup approximation to it.

The use of multigroup schemes in thermal Monte Carlo codes has three main advantages. First, the exit energy resulting from a collision can be selected from a discrete set of energies via a precomputed transfer matrix. By this means, one shortens the computing time per collision and the running time per history. Secondly, it is possible to write a simple multigroup code which will solve either a conventional Monte Carlo problem or its adjoint. In multigroup notation

the direct and adjoint calculation differ very little (see Sect. 3.7). The adjoint calculation cannot be incorporated so easily in a conventional Monte Carlo code. Finally, the transfer matrices can be changed without additional programming, an important feature at this time in view of present uncertainties regarding binding effects.

In principle, it is possible to represent any realistic scattering kernel through transfer matrices. Realistic transfer matrices would couple energy groups and scattering angles in a perfectly general way. However, complete and detailed information about the thermal scattering kernel is not yet available. Under these circumstances it seems unnecessary to use a general transfer matrix. Storage space and computing time can be saved by simplifying the kernel artificially, and the success of the Radkowsky kernel (see Sect. 3.2) indicates that such artificial kernels can, in fact, have great practical value.

The Radkowsky kernel itself, however, is not well suited to multigroup Monte Carlo computations. It is a Selengut-Goertzel kernel, i.e., the P_1 component of the scattering cross section is a delta function in energy. Consequently, the P_1 in-group scattering cross section will not vanish as the energy mesh width goes to zero. For small mesh widths, the in-group scattering pattern is completely nonphysical, having a very small P_0 component and a relatively large P_1 component. It follows that the differential cross section for back-scattering is negative, and a negative cross section leads to substantial difficulties in Monte Carlo. Thus, the Selengut-Goertzel approximation, while it is very useful in conjunction with analytic methods, is troublesome in a Monte Carlo code.

In fact, so long as one constructs the differential cross section from P_0 and P_1 components alone, the same basic problem persists. If $\bar{\mu} > 1/3$ in any group then, in that group, the cross section for back-scattering will be negative. Since $\bar{\mu}$ for hydrogen is approximately 2/3 at epithermal energies, no P_1 bound hydrogen kernel is suitable for Monte Carlo.

On the other hand, a simple and satisfactory kernel can be based on a multigroup version of the conventional transport approximation. Let $\bar{\mu}_H^i$ be the scattering angle, averaged over all hydrogen collisions in group m. In the spirit of the transport approximation, one might postulate that the fraction $(1 - \bar{\mu}_H^i)$ of all hydrogen collisions results in isotropic scattering, the fractions $\bar{\mu}_H^i$ in forward scattering. The exit group could be chosen from a probability derived from any desired P_0 transfer matrix. For the sake of simplicity, the choice of final energies and angles could be completely independent of each other. Such a kernel is incorporated in the MARC code (see Sect. 3.5.E).

3.5 APPLICATION OF MONTE CARLO METHODS TO NEUTRON THERMALIZATION

J. Spanier and G.J. Habetler

A. Introduction

The work presented here covers a period of approximately four years, during which time four separate Monte Carlo programs have been developed. Each of the programs attacks the problem of estimating thermal activation rates in cells in which local inhomogeneities are so severe that the usual diffusion-theory approximations are invalid. Because of the intended application of such techniques to the design of nuclear reactors, it was considered important to determine a specific technique that would be sufficiently accurate for design purposes, yet capable of solution to this degree of accuracy with a reasonable expenditure of computer time. Concerning these points, numerical experimentation is a necessary adjunct to theoretical studies.

In Monte Carlo programs, thousands of neutron life histories are simulated, using pseudorandom numbers, and certain functions of these histories are averaged in order to estimate unknown parameters. The efficiency of such estimating functions, as measured by the expected statistical error as a function of the number of histories processed, is calculated by the program as the mean square deviation, or variance, of the estimator. In practice, several estimators might be potential candidates for use in a program, all of which have the same theoretical mean value, but all of which have different associated uncertainties. In theory, one should select the estimator with the minimum uncertainty, for this will lead to the smallest size sample necessary to achieve a certain accuracy. On the other hand, the computing time per history depends on the type of estimator being used. For example, the simplest type of estimator involves classifying the neutron history into one of several final categories of interest. This is easy to program and relatively cheap per sample from the point of view of computing time. Other types of estimators involve the evaluation of an exponential at each collision point. Although such an estimator usually has smaller variance than a simpler type, the cost per history is increased considerably. Thus, a balance between these two factors is desirable so that, ideally, the program achieves a fixed level of uncertainty in a minimum of computing time.

In all programs herein described, the basic estimator, or random variable, is the average distance traveled by all the

particles in a given volume V of the phase space. This random variable yields an unbiased estimate of the integral of the flux over the volume V.* Thermal absorption rates in V are obtained by weighting the average distance traveled by the absorption cross section of V, and other reaction rates are obtained by weighting by the appropriate reaction cross sections, as desired.

The development given here will be chronological in order to illustrate best the systematic improvements made in efficiency and in range of application. The emphasis will be on theoretical methods of reducing the variance, although other techniques for reducing the computing time will also be mentioned. For a discussion of some of the theoretical concepts used here the reader is referred to Chap. 7, Sect. 7.3.

Each of the programs discussed is concerned with the estimation of thermal absorption rates and/or thermal fluxes. The first program, TUT-T5, was written for the IBM-704 and provides one-energy estimates of a regionwise distribution of absorption rates in a two-dimensional cell. The second program, TRAM, written originally for the IBM-704 and more recently translated to the Philco-2000, was designed to provide geometric and spectral information on the neutron population below 100 ev. TRAM uses 32 energy groups in this range and solves both two- and three-dimensional problems. TRAC, written for the Philco-2000, solves the same geometric problem as does TUT-T5, either in a one-energy mode, or in a mode which places a slowing-down region ahead of the one-energy thermal region. In the latter case, epithermal capture rates are also calculated. The last program, MARC, was written for the Philco-2000 and provides a multithermal group calculation of thermal activation rates and thermal fluxes in the same geometry as TUT-T5 and TRAC. The main features of MARC are its ability to solve both normal and adjoint transport problems and its flexible group structure.

B. One-Group Thermal Model: TUT-T5

The TUT-T5 program,[87] written for the IBM-704, provides a one-energy calculation of a regionwise distribution of activation rates in a two-dimensional rectangular quarter-cell. As used here, the term quarter-cell refers to the basic geometric unit of a regular rectangular array in the (x, y) plane.

Inasmuch as two of the other programs to be discussed, TRAC-1 and MARC-1, draw heavily from many of the concepts

*By this is meant that the theoretical mean value of this random variable taken over all possible histories is equal to the flux integral over V.

set down in TUT-T5, it seems appropriate to go into somewhat greater detail in describing TUT-T5 than in the other programs. For a complete description, including description of input, operating instructions, etc., the reader is referred to Ref. 87.

1. *The Physical Model*

This discussion begins with the physical model studied in TUT-T5. The model gives rise to the integro-differential transport equation

$$\nabla\cdot\vec{\omega}\,\psi(\vec{r},\vec{\omega}) + \Sigma_t(\vec{r})\,\psi(\vec{r},\vec{\omega}) = \int d\vec{\omega}'\psi(\vec{r},\vec{\omega}')\left[\frac{\Sigma_s^H(\vec{r})}{4\pi}\left(1+3\bar{\mu}(\vec{r})\vec{\omega}\cdot\vec{\omega}'\right)\right.$$

$$\left. + \frac{1}{4\pi}\left(\Sigma_s(\vec{r}) - \Sigma_s^H(\vec{r})\right)\right] + \frac{S(\vec{r})}{4\pi}$$

Eq. (3.180)

where

- $\vec{r}$ = a spatial vector in the (x, y) plane
- $\vec{\omega}$ = a unit direction vector
- $\psi(\vec{r},\vec{\omega})$ = the vector flux
- $\Sigma_t(\vec{r})$ = the total macroscopic cross section
- $\Sigma_s^H(\vec{r})$ = the macroscopic scattering cross section for hydrogen
- $\Sigma_s(\vec{r})$ = the total macroscopic scattering cross section
- $\bar{\mu}(\vec{r})$ = the average cosine of the scattering angle (laboratory system) for hydrogen scattering
- $\vec{\omega}\cdot\vec{\omega}'$ = the scalar product of the vectors $\vec{\omega}$, $\vec{\omega}'$
- $S(\vec{r})$ = the spatial source density, to be defined.

Before defining the source density it will be convenient to describe further the geometry of the model.

The geometric configuration consists of an infinite lattice of rectangular cells in the (x, y) plane. Each cell is assumed to be infinite in extent in the z-dimension, so that the model is two-dimensional spatially in the sense that the solution, $\psi(\vec{r},\vec{\omega})$, of Eq. (3.180) is independent of z. Each two-dimensional cell is, in turn, assumed to be symmetric about each of the two lines joining the midpoints of its opposite sides. These two lines divide the cell into four quarter-cells, the description of any one of which thus serves to specify the lattice network completely. The basic quarter-cell used by the program to construct the geometry is the one defined by the inequalities $0 \le x \le M_1$, $0 \le y \le M_2$ (Fig. 3.29). This basic quarter-cell may be subdivided

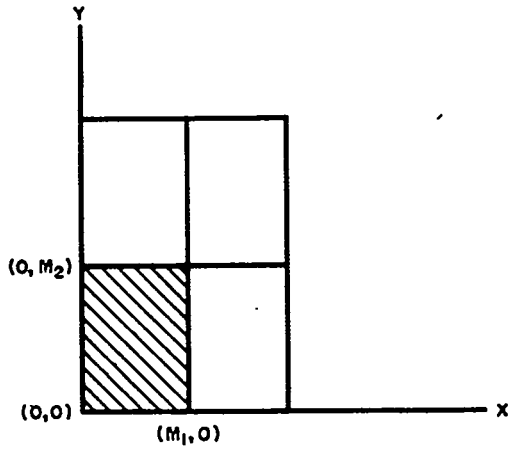

FIGURE 3.29. Basic Quarter-Cell Geometry.

into as many as 32 subrectangles in TUT-T5, each subrectangle being considered homogeneous. Each subrectangle defines a separate region of the geometry.

In addition to specifying a region number for each subrectangle of the quarter-cell, a composition number is also specified. A composition is defined as an arbitrary collection of regions and is used by the program to define the basic unit of output. That is, the output of the program consists of the activation rates for all compositions rather than for all regions.

Having described the geometric specifications, it is now possible to define the source density function $S(\vec{r})$ which occurs in Eq. (3.180). The source is isotropic and is assumed constant in each region, the level being arbitrary. Then,

$$S(\vec{r}) = S(x, y) = \frac{1}{\sum_{r=1}^{R} A_r S_r} \sum_{r=1}^{R} S_r \chi_r(x, y) \qquad \text{Eq. (3.181)}$$

can be written as the defining equation for S over the quarter-cell $0 \le x \le M_1$, $0 \le y \le M_2$. In Eq. (3.181),

A_r = the area of region r, $r = 1, \ldots, R$

S_r = an input constant specifying the source level in region r

χ_r = the characteristic function of region r, defined by

$$\chi_r(x, y) = \begin{cases} 1 \text{ if } (x, y) \text{ belongs to region } r \\ 0 \text{ otherwise} \end{cases}.$$

The function S is then extended over the entire (x, y) plane by symmetry and periodicity, as follows:

$$\left.\begin{aligned} S(x, y) = S(-x, y) = S(x, -y) = S(-x, -y),\ 0 \le x \le M_1,\ 0 \le y \le M_2 \\ S(x, y) = S(x \pm 2M_1, y) = S(x, y \pm 2M_2) \end{aligned}\right\} \text{Eq. (3.182)}$$

for all x, y.

The program considers two general types of events upon collision of a neutron with a nucleus: elastic scattering and absorption. The relative probabilities for each event are specified by the macroscopic cross sections for the process in question. Upon execution of a scattering collision, the distribution of new directions in the laboratory system is determined by the assumed distribution of scattering angles for the various elements. In TUT-T5, all elements, except hydrogen, are assumed to scatter isotropically in the laboratory system. As is evident from Eq. (3.180), the angular distribution arising from hydrogen scattering is assumed to be linear in the cosine of the scattering angle, which restricts $\bar{\mu}$, the average cosine, to lie in the range $0 \le \bar{\mu} \le 1/3$. Between collisions, the path lengths of particles measured in units of mean free path are distributed exponentially in the interval $0 \le t \le \infty$.

The problem solved by TUT-T5 is the estimation of each of the integrals

$$p_k = \int\int \chi_k(\vec{r})\, \Sigma_a(\vec{r})\, \psi(\vec{r}, \vec{\omega})\, d\vec{r}\, d\vec{\omega}, \qquad 1 \le k \le K, \qquad \text{Eq. (3.183)}$$

where the spatial integral is over the basic quarter-cell, the directional integral is over all directions, $\Sigma_a(\vec{r})$ is the macroscopic absorption cross section, $\chi_k(\vec{r})$ is the characteristic function for composition k (which limits the integration to composition k), and ψ is the solution of Eq. (3.180). The number p_k is called the activation rate for composition k. In view of the balance between captures and births expressed by

$$\int\int_{\text{cell}} \Sigma_a(\vec{r})\, \psi(\vec{r}, \vec{\omega})\, d\vec{r}\, d\vec{\omega} = \int\int_{\text{cell}} \frac{S(\vec{r})}{4\pi}\, d\vec{r}\, d\vec{\omega} = 1 \qquad \text{Eq. (3.184)}$$

p_k is a true probability, the capture probability for composition k.

2. The Track Length Estimator

The idea of constructing estimates from the neutron track lengths, which is used in TUT-T5, has been suggested before.[88]

Its use makes possible an accurate estimation of capture probabilities, even in rather small, poorly absorbing compositions.

A simpler type of estimate to use in such a program would be the ordinary binomial estimator which counts one in composition k for every neutron absorbed in composition k, and zero otherwise. For a sample of size N, this estimator would lead to the success ratio

$$\hat{p}_{N,k} = \frac{C_k}{N} \qquad \text{Eq. (3.185)}$$

where C_k is the number of neutrons absorbed in composition k out of the original sample of size N. The variance of this estimator, which measures the fluctuation of $\hat{p}_{N,k}$ from one sample of size N to another, is easily shown to be

$$V\left[\hat{p}_{N,k}\right] = \frac{p_k(1-p_k)}{N} \qquad \text{Eq. (3.186)}$$

where p_k is defined by Eq. (3.183). From this expression for the variance it is easy to see that the relative error in the estimate, $\sqrt{V/p_k}$, is very large when p_k is very small. Put another way, in attempting to estimate very small capture probabilities p_k with $\hat{p}_{N,k}$, a prohibitive number of samples would need to be processed in order to reduce the statistical uncertainty to reasonable limits. For this reason the track length estimator was used in TUT-T5.

For each random walk history C, random variables ρ_k are defined as follows:

$$\rho_k(C) = \sum_r{}' \Sigma_{a,r} d_r(C) \qquad \text{Eq. (3.187)}$$

where $\sum'$ denotes the sum over all regions r forming composition k; $\Sigma_{a,r}$ is the absorption cross section of region r; and $d_r(C)$ is the total distance traveled by C in all replicas of region r. It may be shown[89] that ρ_k is an unbiased estimate of the capture probability p_k; that is, that the theoretical average of the values of ρ_k taken over all possible histories C is exactly p_k. Furthermore, since each history C makes, in general, many contributions to the estimate of p_k (one for each track left in composition k), the variance of $\rho_k(C)$ has been shown in practice to be many times smaller than that of the binomial estimator $\hat{p}_{N,k}$ for small compositions k. This reduction in variance results in a corresponding reduction in the number of histories needed to achieve a given statistical error, hence a reduction in the total computing time per problem.

For each composition, each experiment is regarded as yielding one sample from an approximately normal population whose mean is the capture probability for that composition. That is, the average distance traveled by the neutrons of a single experiment is known to be approximately normally distributed about the flux integral over that composition. When the average distances are weighted by the appropriate absorption cross sections, this normality is preserved. A standard technique for obtaining confidence intervals for samples drawn from a normal population is through the use of Student's t-distribution. This is outlined below. The following definitions are made:

$w_r^{(E)}$ = sum of the distances (cm) traveled by all particles of experiment E in region r;

Σ_r = macroscopic absorption cross section (cm^{-1}) for region r;

$W_k^{(E)} = \sum_r' \frac{\Sigma_r w_r^{(E)}}{n}$, where the sum is over all regions r forming composition k;

$\overline{W}_k^{(E)} = 1/E \sum_{e=1} W_k^{(e)}$, the estimate after E experiments of the capture probability for composition k;

$\sigma_k^{(E)} = 1/E \sum_{e=1}^{E} \left[W_k^{(e)}\right]^2 - \left[\overline{W}_k^{(E)}\right]^2$, the sample variance associated with composition k after E experiments.

The theory which uses these quantities to predict statistical deviations in the numbers $\overline{W}_k^{(E)}$ will be found developed in detail in Ref. 90, Sect. 5. This theory yields the following asymptotic statements:

$$\text{Prob}\left\{\overline{W}_k^{(E)} - a\sqrt{\frac{\sigma_k^{(E)}}{E-1}} < p_k \leq \overline{W}_k^{(E)} + a\sqrt{\frac{\sigma_k^{(E)}}{E-1}}\right\} \sim \int_{-a}^{a} S_{E-1}(x)\,dx \qquad \text{Eq. (3.188)}$$

where a is an arbitrary constant, p_k is the unknown capture probability, and $S_{E-1}(x)$ is the Student's t-distribution with $E-1$ degrees of freedom. The function $S_{E-1}(x)$ is defined by

$$S_{E-1}(x) = \frac{1}{\sqrt{(E-1)\pi}} \frac{\Gamma\left(\frac{E}{2}\right)}{\Gamma\left(\frac{E-1}{2}\right)} \left(1 + \frac{x^2}{E-1}\right)^{-\frac{E}{2}} \qquad \text{Eq. (3.189)}$$

where

$$\Gamma(t) = \int_0^\infty x^{t-1} e^{-x}\, dx, \quad t > 0$$

is the gamma function. In words, Eq. (3.188) says that the probability that the number p_k lies in the interval of width $2a\sqrt{\sigma_k^{(E)}/(E-1)}$ about the number $\overline{w}_k^{(E)}$ is approximately the integral on the right. Values of the constant a may be chosen so that this integral takes on any desired value between zero and one. In practice, a 95 percent confidence interval should be used for making predictions about the data, although 50 percent confidence intervals are more frequently used in experimental work. Even if the 95 percent confidence interval is used, there is one chance in 20 of failing to include the true mean.

Most TUT-T5 problems run on the IBM-704 require about one to two hours to solve to a reasonable degree of accuracy. The amount of time needed to complete a problem and the approximate error as a function of the number of experiments processed fluctuate markedly from problem to problem. Experience gained in running many problems indicates that about 40 collisions are processed per second of computer time. Thus, if an estimate of the average number of collisions per particle is available, it should be possible to estimate roughly how much time is required per history. One estimate of the average number of collisions, based on a constant flux, is given by

$$\hat{C} = \frac{\sum_{r=1}^{R} \Sigma_{t,r} A_r}{\sum_{r=1}^{R} \Sigma_{a,r} A_r} \qquad \text{Eq. (3.190)}$$

where $\Sigma_{t,r}$, $\Sigma_{a,r}$ are the total and absorption cross section, respectively, of region r, and A_r is the area of region r. It is more difficult to predict the expected error as a function of the number of experiments. Usually, one hour of IBM-704 time is sufficient to reduce the 95 percent confidence limits to between 1 percent and 15 percent of the mean, independent of the size of the mean. This is made possible by the use of the track length estimator which seems to yield generally small errors in all compositions.

C. Three-Dimensional, Multigroup Program: TRAM

The IBM-704 program TRAM[91] was designed to provide detailed geometric and spectral information on the neutron

population below 100 ev in hydrogen-moderated assemblies.* TRAM solves the same problem as TUT-T5 but in the framework of 32 energy groups and in three dimensions.

1. *The Physical Model*

The geometric configuration consists of a finite number of regions. The composition of each region is assumed to be homogeneous. The interfaces between such regions and the bounding surfaces of such regions are assumed to be describable in either the linear form

$$Ax + By + Cz = K \qquad \text{Eq. (3.191)}$$

or the quadratic form

$$E(x-x_o)^2 + (y-y_o)^2 = K. \qquad \text{Eq. (3.192)}$$

As in TUT-T5, in addition to specifying regions, compositions (collections of regions) are defined for the purpose of output. That is, activation rates are calculated for compositions rather than regions. The original version of TRAM allowed up to 50 regions, 50 surfaces, and 20 compositions.

Source neutrons are generated uniformly within each region at a prespecified region-dependent rate. The source particles are determined stochastically by taking them to be the neutrons resulting from scattering 100 ev neutrons with hydrogen. These neutrons are followed from collision to collision until either they escape from the system or absorption occurs.

All elements except hydrogen scatter isotropically in the laboratory system without energy exchange. For hydrogen scattering, five different laws are used in various proportions in the 32 groups to provide a model which gives infinite medium spectra and diffusion lengths in agreement with measured values.

The transport equation on which TRAM is based is in the form

$$\nabla\cdot\vec{\omega}\,\psi(\vec{r},\vec{E}) + \Sigma_t(\vec{r}, E)\,\psi(\vec{r}, \vec{E}) = \int d\vec{E}'\,\psi(\vec{r}, \vec{E}')\,\Sigma_t(\vec{r}, E')\,C(\vec{E}', \vec{E}; \vec{r}) + S(\vec{r}, \vec{E}) \qquad \text{Eq. (3.193)}$$

*A version of TRAM is now also available on the Philco-2000.

where

$\vec{r}$ = a spatial vector in three-dimensional space
$\vec{E}$ = $E\vec{\omega}$ where E is the neutron energy
$\psi(\vec{r}, \vec{E})$ = the vector flux with energy E
$\Sigma_t(\vec{r}, E)$ = the total macroscopic cross section at energy E
$C(\vec{E}', \vec{E}; \vec{r})$ = the scattering kernel, to be defined
$S(\vec{r}, \vec{E})$ = the source density.

The source density has the form

$$S(\vec{r}, \vec{E}) = \frac{1}{\sum_{r=1}^{R} V_r S_r} \sum_{r=1}^{R} S_r \chi_r(\vec{r}) \frac{1}{4\pi} \frac{\chi_o(E)}{E_U} \qquad \text{Eq. (3.194)}$$

for $E_U > E \geq 0$. Here S_r is an input constant specifying the source level in region r, V_r is the volume of region r, $\chi_r(\vec{r})$ is the characteristic function of region r defined by

$$\chi_r(\vec{r}) = \begin{cases} 1 \text{ if } \vec{r} \text{ belongs to region } r \\ 0 \text{ otherwise} \end{cases}$$

and $\chi_o(E)$ is a similar characteristic function in energy

$$\chi_o(E) = \begin{cases} 1 \text{ if } E_U > E \geq 0 \\ 0 \text{ otherwise} \end{cases}$$

where, in TRAM, E_U is set at 100 ev.

For numerical computations, the microscopic total cross sections are assumed constant over each of the energy groups in TRAM. Hence, $\Sigma_t(\vec{r}, E)$ in Eq. (3.193) will be of the form

$$\Sigma_t(\vec{r}, E) = \sum_{i=1}^{32} \Sigma_{t,\,i}(\vec{r}) \chi_i(E) \qquad \text{Eq. (3.195)}$$

where $\chi_i(E)$ is defined by

$$\chi_i(E) = \begin{cases} 1 \text{ if } E_i \geq E > E_{i+1} \\ 0 \text{ otherwise.} \end{cases}$$

In this, it is assumed that the i^{th} group consists of those energies E for which

$$E_i \geq E > E_{i+1} .$$

The scattering kernel $C(\vec{E}', \vec{E}; \vec{r})$ has the form (see, e.g., Ref. 88, Appendix 2)

$$C(\vec{E}', \vec{E}; \vec{r}) = \frac{\Sigma_s(\vec{r}, E') - \Sigma_s^H(\vec{r}, E')}{\Sigma_t(\vec{r}, E')} \frac{1}{4\pi} \delta(E - E') + C_H(\vec{E}', \vec{E}; \vec{r}) \quad \text{Eq. (3.196)}$$

where $\Sigma_s(\vec{r}, E)$ is the total macroscopic scattering cross section, $\Sigma_s^H(\vec{r}, E)$ is the macroscopic scattering cross section for hydrogen, and $C_H(\vec{E}', \vec{E}; \vec{r})$ is the scattering kernel for hydrogen.

The TRAM scattering kernel for hydrogen is rather complicated in form and is best delineated by describing what happens physically.

The first nine energy groups in TRAM (down to 1/2 ev) are considered epithermal. In these groups, collisions with hydrogen are treated as isotropic in the center-of-mass system, with the target proton assumed to be at rest. The emergent neutron is not allowed to have an energy less than 0.96 kT; the total scattering cross section is adjusted for this condition.

Below 1/2 ev the thermal motion of the scattering proton is taken into account. For this purpose, TRAM allows the use of one of two Maxwellian distributions of proton velocities, one for 68°F (cold) and the other for 520°F (hot). The scattering is assumed isotropic in the center-of-mass system. This model is generally called the free scattering model.

In addition, the scattering model used in TRAM includes two types of hydrogen scattering without energy exchange: isotropic (in the laboratory system) and reverse scattering. Reverse scattering is defined as follows: Suppose the incident neutron has direction cosines (α, β, γ) and a random direction $(\alpha_o', \beta_o', \gamma_o')$ is chosen from the uniform distribution on the unit sphere; then, in reverse scattering, the emergent neutron has direction cosines $(\alpha', \beta', \gamma')$ in the laboratory system given by

$$\alpha' = \frac{\alpha_o' - \alpha}{D}; \quad \beta' = \frac{\beta_o' - \beta}{D}; \quad \gamma' = \frac{\gamma_o' - \gamma}{D}$$

$$D = \left[(\alpha_o' - \alpha)^2 + (\beta_o' - \beta)^2 + (\gamma_o' - \gamma)^2\right]^{1/2}. \quad \text{Eq. (3.197)}$$

Thus, reverse scattering is similar to isotropic center-of-mass system scattering for hydrogen (with the proton at rest) except that the incoming direction of the neutron is reversed. It is an artifice designed to help provide a simplified model of hydrogen scattering which is in agreement with the first two spherical moments of the scattering kernel of hydrogen to within the accuracy with which these are currently known.

It was found that a group-dependent combination of free scattering, isotropic scattering without energy exchange, and reverse scattering without energy exchange would give the desired total cross section, infinite medium spectrum, and $\bar{\mu}$ (the average cosine of the scattering angle) for energy groups 3 through 30 (down to 0.005 ev). In the remaining two groups, the kernel is approximated by a combination of isotropic scattering with energy exchange determined as in the free proton model and isotropic scattering without energy exchange.

2. Statistical Design

TRAM calculates two estimations of the capture probabilities. The first is the usual binomial estimator

$$P_k = \frac{C_k}{N} \qquad \text{Eq. (3.198)}$$

where C_k is the number of neutrons absorbed in composition k out of the original sample size N. The second is the track length estimator

$$\rho_k = \frac{\sum_{j=1}^{N} \sum_{i=1}^{32} \Sigma_{ai,k} d_{j,i,k}}{\sum_{k} \sum_{j=1}^{N} \sum_{i=1}^{32} \Sigma_{ai,k} d_{j,i,k}} \qquad \text{Eq. (3.199)}$$

where $d_{j,i,k}$ is the distance traveled by particle j, with energy in group i, through composition k, and $\Sigma_{ai,k}$ is the i^{th} group absorption cross section in composition k. This estimator is the natural extension of the one used in TUT for monoenergetic problems. As mentioned in Sect. 3.5.B, the track length estimator is more efficient than the binomial estimator for general reactor problems. For heavy absorber materials, however, the situation may be reversed. This is because the average path length per capture in such compositions is quite small. Therefore, a hybrid estimator was designed to provide maximum efficiency.

$$\tilde{\rho}_k = a_k P_k + (1 - a_k) \rho_k \qquad \text{Eq. (3.200)}$$

which has minimum variance for

$$a_k = \frac{V_{1,k} - V_{12,k}}{V_{1,k} + V_{2,k} - 2V_{12,k}} \qquad \text{Eq. (3.201)}$$

where $V_{1,k}$ is the true variance of the binomial estimator in composition k, $V_{2,k}$ is the variance of the track length estimator in composition k, and $V_{12,k}$ is the covariance of the two estimators.

With these definitions in mind, the automatic statistical edit of TRAM works as follows. TRAM carries out 25 experiments, each experiment involving N (of order of 300) particle histories. Each experiment yields one sample for the binomial estimator and the track length estimator. At the end of the 25 experiments, the sample mean of the binomial estimator

$$\bar{P}_k = \frac{1}{25}\sum_{i=1}^{25} P_{i,k} \qquad \text{Eq. (3.202)}$$

and the sample mean of the track length estimator

$$\bar{\rho}_k = \frac{1}{25}\sum_{j=1}^{25} \rho_{i,k}$$

are calculated. Their sample variances $V_{\bar{P}_k}, V_{\bar{\rho}_k}$, and sample covariance $V_{\bar{P}_k,\bar{\rho}_k}$ are also calculated. The hybrid estimator is then formed

$$\tilde{\bar{\rho}}_k = \tilde{a}_k \bar{\rho}_k + (1-\tilde{a}_k)\bar{P}_k \qquad \text{Eq. (3.203)}$$

where $\tilde{a}_k$ has the form of Eq. (3.201) but with the sample variances and covariance replacing the true ones

$$\tilde{a}_k = \frac{V_{\bar{\rho}_k} - V_{\bar{P}_k,\bar{\rho}_k}}{V_{\bar{\rho}_k} + V_{\bar{\rho}_k} - 2V_{\bar{P}_k,\bar{\rho}_k}} \qquad \text{Eq. (3.204)}$$

It can be shown[92] that the variance of $\tilde{\bar{\rho}}_k$ can be estimated by

$$V_{\tilde{\bar{\rho}}_k} = \frac{600\left[V_{\bar{P}_k} V_{\bar{\rho}_k} - V^2_{\bar{P}_k,\bar{\rho}_k}\right]}{23\left(V_{\bar{\rho}_k} + V_{\bar{\rho}_k} - 2V_{\bar{P}_k,\bar{\rho}_k}\right)} \left[\frac{1}{25} + \frac{(\bar{P}_k - \bar{\rho}_k)^2}{600\left(V_{\bar{P}_k} + V_{\bar{\rho}_k} - 2V_{\bar{P}_k,\bar{\rho}_k}\right)}\right].$$

Eq. (3.205)

The 95 percent confidence interval for the capture ratio in the k^{th} composition is then given by

$$\tilde{\bar{\rho}}_k - 2.07\sqrt{V_{\tilde{\bar{\rho}}_k}} \le C_k \le \tilde{\bar{\rho}}_k + 2.07\sqrt{V_{\tilde{\bar{\rho}}_k}} \qquad \text{Eq. (3.206)}$$

This result is based on the Student's t-distribution with 23 degrees of freedom.

3. *Generation of Random Numbers*

TRAM was designed to take advantage of the high-speed random-address large capacity memory of the IBM-704. As an example, consider the generation of pseudorandom numbers required in a Monte Carlo code, i.e., numbers on the unit interval which are approximately uniformly distributed and in some sense independent. These numbers are used, for example, in deciding between the various types of interactions at each particle collision, etc. A widely used method today for generating such numbers is the multiplicative congruence routine. TRAM achieved computational savings by replacing this method with the following method, which involved only one addition of numbers available in fast storage.

The 1000 numbers 000, 001, ..., 999 were permuted by a permutation generated from a set of 1000 numbers of the RAND random digit cards.[93] The resulting permuted sequence $\{n_j\}_{j=000}^{999}$, referred to as the basic sequence, appears to be an unsystematic scrambling of the given 1000 numbers. The k^{th} pseudorandom number to be used by TRAM, τ_k, is obtained from the basic sequence as follows. Let $k = 1000r + s, r, s \leq 999$. Then

$$\tau_k = \frac{n_r + n_s}{1000} + 0.0008 \pmod 1 . \qquad \text{Eq. (3.207)}$$

In this manner, 10^6 numbers can be generated without any subcycling. It can be seen from the formula that each block of 1000 numbers starting with $s = 0$ contains each of the values 0.0008, 0.0018, . . . , 0.9998 exactly once. This systematic sampling within each block of 1000 random numbers has the effect of reducing certain variances in the calculation. The addition of 0.0008 in Eq. (3.207) is to reduce the effect of certain round-off errors and zero-divide problems which were expected to occur if the sum of two τ's gives zero (mod 1). The set of $\{\tau_k\}$ has an average of 0.5003, which is not sensibly different from the desired average of 0.5000.

Besides these numbers, random variables with nonuniform distributions are also required. Of particular importance is the determination of intercollision distances measured in units of mean free paths. This variable has an exponential distribution and may be realized as the negative logarithm of a pseudo-random number. These numbers can be formed by evaluating a truncated power series for the logarithm of a random number.

The TRAM method, which is several times faster than such a technique, chooses from a discrete approximation to the exponential distribution by means of a random addressing procedure. A set of 1000 numbers, uniformly spaced with regard to the exponential distribution, is permuted, again by a set of RAND numbers, into a scrambled sequence

$$\ell_0, \ell_1, \ldots, \ell_{999}.$$

Whenever a random logarithm is required, the next random number τ is chosen and ℓ_τ is the realized value.

The random cosines (α, β, γ) are determined in a similar manner.

D. One-Group Thermal Model with Slowing Down: TRAC-1

The TRAC-1 program[94] for the Philco-2000 represents an attempt to incorporate the best variance reduction features of TUT-T5 and TRAM. TRAC-1 solves the same geometric problem as does TUT-T5, either in a one-energy mode or, on an input option, in a mode which places a slowing-down region ahead of the one-energy thermal region. In the latter case, epithermal capture probabilities, integrated over the epithermal energy spectrum, are provided for each composition as well as the usual thermal capture probabilities. In addition to the foregoing important difference, TRAC-1 incorporates the following features not present in TUT-T5:

1. The input format is considerably improved, especially the input needed to describe the geometry.
2. The improved combined random variable suggested by Martino[91] for TRAM (see Sect. 3.5.C) is incorporated, resulting in some reduction in variance, particularly in heavily absorbing regions.
3. Further reductions in running time have been achieved by cutting the amount of computation per history. Thus, floating point pseudorandom numbers and other variables which were formerly generated as needed are now generated and stored in advance on tape and in core. Some of these ideas were also first introduced in TRAM (see Sect. 3.5.C.3).
4. A technique based on the reciprocity theorem, due to C. W. Maynard,[95] makes it possible to calculate the scalar flux at a single point of the quarter-cell as well as to reduce substantially the variance in the capture probability of a single composition in one-energy mode problems.

5. As many as 75 different regions and 99 different compositions may be treated in TRAC-1. This compares with 32 regions and 25 compositions in TUT-T5 and 50 regions, 50 surfaces, and 20 compositions available in TRAM.

1. The Physical Model

When operating in the one-energy mode TRAC-1 behaves exactly like TUT-T5, except for the improvements cited above. Thus, the source density levels are specified for each region in the input, and these determine the fraction of starting neutrons in each region. Neutrons are followed from collision to collision, governed by the laws of the one-energy mode until absorption occurs in some region. The distance traveled in each region is recorded as well as the distribution of captures. One estimate of the capture probabilities (labeled fractional estimate) is based on the final distribution of captures. A second estimate (labeled track length estimate) is based on the sum of the track lengths in the various regions. Finally, a third estimate (labeled combined estimate) is obtained as a linear combination of the first two estimates, the coefficients being selected in such a way that the variance in each region is theoretically minimized. This is the same technique introduced by Martino for TRAM.

In the slowing-down mode the source is assumed uniform in energy between the limits E_L and $E_U (E_L < E_U)$ and spatially constant in each region, the levels being specified as in the one-energy mode. Epithermal neutrons slow down by collisions with hydrogen; these collisions are treated as isotropic in the center-of-mass system with an energy degradation which corresponds to the scattering angle. All nonhydrogen scattering is assumed isotropic in the laboratory system, and all epithermal absorption is assumed to be of the form c/v, where c is a constant and v the speed of the neutron. As soon as the energy of the neutron falls to or below the input value E_T, the neutron is regarded as thermalized, and the assumptions of the one-energy mode take over. If the neutron is absorbed epithermally, its epithermal contributions are recorded, and a new history is selected from the source distribution. The combined estimate of epithermal capture probabilities is constructed in a manner similar to that described above for the one-energy mode based on epithermal track lengths and the spatial distribution of neutrons absorbed at energies above E_T .

Using the same notation as was introduced in Sect. 3.5.C, the scattering kernel $C(\vec{E}', \vec{E}; \vec{r})$, which represents the probability density that a neutron entering a collision in the state

$(\vec{r}, \vec{E}')$ will leave with energy vector $\vec{E}$, may be represented as a sum

$$C = \sum_i p_i C_i$$

where p_i is the probability of a scattering event of type i and C_i is the corresponding kernel for that event. In the slowing-down region of TRAC-1, the elastic hydrogen and heavy element collisions give rise to an epithermal scattering kernel of the form

$$C_e(\vec{E}', \vec{E}; \vec{r}) = \frac{\Sigma_s(\vec{r}, E')}{\Sigma_t(\vec{r}, E')} \left\{ \frac{\Sigma_s^H(\vec{r}, E')}{\Sigma_s(\vec{r}, E')} \left[\frac{\sqrt{2E}}{E'} \right] \frac{1}{2\pi} \delta\left(\vec{\omega} \cdot \vec{\omega}' - \sqrt{\frac{E}{E'}} \right) + \frac{\Sigma_s(\vec{r}, E') - \Sigma_s^H(\vec{r}, E')}{\Sigma_s(\vec{r}, E')} \frac{1}{4\pi} \delta(E - E') \right\} \qquad \text{Eq. (3.208)}$$

where Σ_s is the total macroscopic scattering cross section, Σ_s^H is the macroscopic scattering cross section for hydrogen, and $\vec{\omega} \cdot \vec{\omega}'$ is the cosine of the scattering angle in the laboratory system.

In the thermal group, the scattering kernel takes the same form as for TUT-T5:

$$C_t(\vec{\omega}, \vec{\omega}; \vec{r}) = \frac{\Sigma_s(\vec{r})}{\Sigma_t(\vec{r})} \left\{ \frac{\Sigma_s^H(\vec{r})}{\Sigma_s(\vec{r})} \left[\frac{1 + 3\bar{\mu}(\vec{r}) \vec{\omega} \cdot \vec{\omega}'}{4\pi} \right] + \frac{1}{4\pi} \frac{\Sigma_s(\vec{r}) - \Sigma_s^H(\vec{r})}{\Sigma_s(\vec{r})} \right\} \qquad \text{Eq. (3.209)}$$

where $\bar{\mu}(\vec{r})$ is the average cosine of the scattering angle for hydrogen.

To complete the description of the components of the transport equation it remains to specify the epithermal and thermal source terms. In a slowing-down problem the source is isotropic and uniform in energy between the limits E_L and E_U. Since the thermal cutoff energy is input as E_T, if $E_L < E_T$ some of the neutrons are born thermally. Thus, the physical source density function for the epithermal range can be written

$$S_e(\vec{r}, \vec{E}) = \frac{1}{\sum_{r=1}^{R} A_r S_r} \sum_{r=1}^{R} S_r \chi_r(\vec{r}) \cdot \frac{1}{4\pi} \frac{\chi_0(E)}{E_U - E_L} \qquad \text{Eq. (3.210)}$$

for the range of energies $E_T < E \leq E_U$. In Eq. (3.210), the vector $\vec{r}$ ranges over the basic quarter-cell, A_r is the area of region r, S_r is an input constant specifying the source level in region r, $\chi_r(\vec{r})$ is the characteristic function of region r,

$$\chi_r(\vec{r}) = \begin{cases} 1 \text{ if } \vec{r} \text{ belongs to region } r \\ 0 \text{ otherwise} \end{cases}$$

and $\chi_0(E)$ is defined by

$$\chi_0(E) = \begin{cases} 1 \text{ if } E_M \leq E \leq E_U \\ 0 \text{ if } E < E_M \end{cases}$$

where E_M is the larger of E_T and E_L.

The source to the thermal group consists of those neutrons which have slowed into the thermal group via a collision at energies above E_T together with those neutrons (if any) which are born in the range $E_L \leq E \leq E_T$. Hence, the physical source density for the thermal group in TRAC-1 is

$$S_t(\vec{r},\vec{\omega}) = \int_0^{E_T}\int_{E_T}^{E_U}\int_{4\pi} d\vec{\omega}'\,dE'\,dE\,\psi_e(\vec{r},\vec{E}')\Sigma_s(\vec{r},E')C_e(\vec{E}',\vec{E};\vec{r}) + \frac{1}{\sum_{r=1}^{R} A_r S_r}\sum_{r=1}^{R} S_r\chi_r(\vec{r})\frac{1}{4\pi}\frac{E_T - E_L}{E_U - E_L} \qquad \text{Eq. (3.211)}$$

where the second term is zero if $E_L \geq E_T$ and where $\psi_e(\vec{r},\vec{E}')$ is the epithermal flux.

From the above considerations, the pair of coupled transport equations on which the slowing-down mode in TRAC-1 is based are

$$\nabla\cdot\vec{\omega}\psi_e(\vec{r},\vec{E}) + \Sigma_t(\vec{r},E)\psi_e(\vec{r},\vec{E}) = \int d\vec{E}'\,\psi_e(\vec{r},\vec{E}')\Sigma_t(\vec{r},E')C_e(\vec{E}',\vec{E};\vec{r}) + S_e(\vec{r},\vec{E}),\quad E_T \leq E < E_U \qquad \text{Eq. (3.212)}$$

and

$$\nabla\cdot\vec{\omega}\,\psi_t(\vec{r},\vec{\omega}) + \Sigma_t(\vec{r})\psi_t(\vec{r},\vec{\omega}) = \int d\vec{\omega}'\,\psi_t(\vec{r},\vec{\omega}')\Sigma_t(\vec{r})C_t(\vec{\omega}',\vec{\omega};\vec{r}) + S_t(\vec{r},\vec{\omega})$$

Eq. (3.213)

where ψ_e and ψ_t are the epithermal and thermal fluxes, respectively.

Then, the quantities estimated by TRAC-1 when operating in the slowing-down mode are

$$p_k^e = \int_{4\pi} \int_{E_T}^{E_U} \int_{C_k} d\vec{r}\,dE\,d\vec{\omega}\,\Sigma_a(\vec{r}, E)\psi_e(\vec{r}, \vec{E}) \qquad \text{Eq. (3.214)}$$

and

$$p_k^t = \int_{4\pi} \int_{C_k} d\vec{r}\,d\vec{\omega}\,\Sigma_a(\vec{r})\psi_t(\vec{r}, \vec{\omega}) \qquad \text{Eq. (3.215)}$$

the epithermal and thermal capture probabilities for composition k.

In the one-energy mode the transport equation is

$$\nabla \cdot \vec{\omega}\psi_1(\vec{r}, \vec{\omega}) + \Sigma_t(\vec{r})\psi_1(\vec{r}, \vec{\omega}) = \int d\vec{\omega}'\,\psi_1(\vec{r}, \vec{\omega}')\Sigma_t(\vec{r})\,C_t(\vec{\omega}', \vec{\omega}; \vec{r}) + \frac{1}{\sum_{r=1}^{R} A_r S_r} \sum_{r=1}^{R} S_r \chi_r(\vec{r}) \cdot \frac{1}{4\pi} \qquad \text{Eq. (3.216)}$$

and the one-energy capture probabilities estimated are

$$p_k' = \int_{4\pi} \int_{C_k} d\vec{r}\,d\vec{\omega}\,\Sigma_a(\vec{r})\psi_1(\vec{r}, \vec{\omega}). \qquad \text{Eq. (3.217)}$$

2. *The Adjoint Technique: The Flux at a Point*

An interesting technique, first used in TRAC calculations, drastically reduces the variance in a certain class of problems and makes possible the calculation of the flux at a point. The technique, which is due to C. W. Maynard,[95] is based on the reciprocity theorem. In a normal TRAC-1 problem, one is generally interested in knowing the capture probabilities throughout the quarter-cell. However, if one is interested in knowing only the capture probability in a single composition, prohibitively many histories may be required to achieve a tolerable statistical error, particularly if the composition is very small. Maynard's technique offers an alternative method of calculation which can result in considerable savings of computing time.

The results given in Ref. 95 are briefly summarized here as they apply to TRAC-1. It will be apparent in the development to follow that the flux calculation is, in a sense, a degenerate case of the calculation of the capture probability in a single region. All of the following discussion applies to one-energy mode problems only.

Suppose it is desired to calculate the capture probability in a single region r_0 of the quarter-cell and that no other information is required. (These results are easily extended to the estimation of the capture probability in a single composition. Attention is restricted to a single region for the sake of simplicity of notation.) Suppose further that a normal TRAC-1 run would result in poor statistics in the given region. Let S_r, Σ_r, A_r denote the source density, macroscopic absorption cross section, and area, respectively, of region r, $1 \leq r \leq R$. Let an auxiliary adjoint problem be defined by the same constants as the original problem but with a unit source density in region r_0 and zero source elsewhere. Let p_r denote the capture probability in region r and let I_r denote the flux integral over region r in the original problem. Then, by definition,

$$p_{r_0} = \frac{\Sigma_{r_0} I_{r_0}}{\sum_{r=1}^{R} S_r A_r} \qquad \text{Eq. (3.218)}$$

where R is the total number of regions of the geometry.

Using the reciprocity theorem, it may be shown that

$$I_{r_0} = \sum_{r=1}^{R} S_r I_r' \qquad \text{Eq. (3.219)}$$

where I_r' is the adjoint flux integral over region r in the auxiliary problem. Denoting by p_r' the capture probability in region r in the adjoint problem,

$$p_r' = \frac{\Sigma_r I_r'}{A_{r_0}} \qquad \text{Eq. (3.220)}$$

from which it follows that

$$p_{r_0} = \frac{\Sigma_{r_0} A_{r_0}}{\sum_{r=1}^{R} S_r A_r} \sum_{r=1}^{R} \frac{S_r p_r'}{\Sigma_r}. \qquad \text{Eq. (3.221)}$$

Equation (3.221) relates the capture probability in region r_0 of the original problem to the capture probabilities in all the regions of the adjoint problem. Thus, one may run the adjoint problem on TRAC-1, placing a unit source in region r_0, and estimate p_{r_0} through Eq. (3.221), obtaining estimates of the p_r' from the adjoint problem. The advantage in doing this is that each neutron in the adjoint problem contributes to the estimate of p_{r_0} through the p_r', so that each particle of the adjoint problem carries a higher statistical weight than in the original problem. This may result in a significant decrease in the statistical uncertainty for a given size sample, hence a corresponding decrease in the running time. Numerical examples of this are given in Ref. 95. One must recognize, however, that Eq. (3.221) applies only to the region r_0 and that it is not possible to infer other capture probabilities p_r without running other adjoint problems. Thus, one sacrifices the ability to compute in other regions for the sake of efficiency in the single region of interest.

Now suppose it is desired to estimate the scalar flux $\phi(x_0, y_0)$ at a single point of the quarter-cell. Let r_0 be the number of the region (not necessarily unique) containing (x_0, y_0). Then, by definition,

$$p_{r_0} = \frac{\Sigma_{r_0} \bar{\phi}_{r_0} A_{r_0}}{\sum_{r=1}^{R} S_r A_r} \qquad \text{Eq. (3.222)}$$

where $\bar{\phi}_{r_0} = l_{r_0} / A_{r_0}$ is the average flux in region r_0. If the region is sufficiently small, $\bar{\phi}_{r_0} = \phi(x_0, y_0)$. Substituting $\phi(x_0, y_0)$ in Eq. (3.222) and equating Eqs. (3.221) and (3.222) yields

$$\frac{\Sigma_{r_0} \phi(x_0, y_0) A_{r_0}}{\sum_{r=1}^{R} S_r A_r} = \frac{\Sigma_{r_0} A_{r_0}}{\sum_{r=1}^{R} S_r A_r} \sum_{r=1}^{R} \frac{S_r p_r'}{\Sigma_r} \qquad \text{Eq. (3.223)}$$

or

$$\phi(x_0, y_0) = \sum_{r=1}^{R} \frac{s_r p_r'}{\Sigma_r} . \qquad \text{Eq. (3.224)}$$

Although Eq. (3.224) is only approximately true for finite regions r_0, as region r_0 shrinks to the point (x_0, y_0) Eq. (3.224) becomes exact. It relates the scalar flux at (x_0, y_0) to the

capture probabilities in an adjoint problem with a point source at (x_0, y_0). For this reason a point source option is available in TRAC-1.

Inasmuch as Eqs. (3.221) and (3.224) are not presently programmed into TRAC-1, it is necessary to calculate them by hand using the numbers p_r' as provided by the appropriate adjoint problem. It is also necessary to calculate a confidence interval to use with estimates in question. This is done as follows:

Let C_r' be the confidence interval (either 50 percent or 95 percent) associated with the estimate p_r'. The confidence interval associated with the estimate of p_{r_0} obtained from Eq. (3.221) is rigorously

$$C_{r_0} = \frac{\Sigma_{r_0} A_{r_0}}{\sum_{r=1}^{R} S_r A_r} \left[\sum_{r=1}^{R} \left(\frac{S_r C_r'}{\Sigma_r} \right)^2 + \sum_{r \neq t} \frac{S_r S_t}{\Sigma_r \Sigma_t} \rho_{rt} C_r' C_t' \right]^{1/2} \qquad \text{Eq. (3.225)}$$

where ρ_{rt} is the correlation coefficient between the estimators p_r', p_t'. The program does not presently estimate the ρ_{rt}, but a pessimistic estimate is obtained by setting all $\rho_{rt} = 1$. Thus, a conservative estimate of C_{r_0} is given by the formula

$$C_{r_0} = \frac{\Sigma_{r_0} A_{r_0}}{\sum_{r=1}^{R} S_r A_r} \sum_{r=1}^{R} \frac{S_r C_r'}{\Sigma_r} . \qquad \text{Eq. (3.226)}$$

A similar analysis leads to the estimate

$$C_{00} = \sum_{r=1}^{R} \frac{S_r C_r'}{\Sigma_r} \qquad \text{Eq. (3.227)}$$

for the confidence interval to be associated with $\phi(x_0, y_0)$.

As in TUT-T5, the time per history of TRAC-1 fluctuates markedly from problem to problem, but a careful examination of the program shows that the bulk of the machine time is accounted for by three types of elementary events: hydrogen collisions, heavy element collisions, and boundary crossings. Timings of the three types of elementary events are as follows: TRAC-1 processes 154 hydrogen collisions per second, 373 heavy element collisions per second, and from 450 to 910 boundary crossings per second. The variability in the boundary

crossing time results from variability in the complexity of the geometry. Experience shows that TRAC-1 runs roughly 3.5 times as fast as TUT-T5, although for large problems with complicated geometries they may not be fairly compared, since TRAC-1 will treat many more regions than will TUT-T5. This gain in running time is primarily due to the fact that TUT-T5 is an IBM-704 program while TRAC-1 is a Philco-2000 program. In problems containing heavily absorbing regions, gains in running time will be greater because of the use of the minimum variance estimator in TRAC-1.

The statistical analysis for the minimum variance estimator used in TRAC-1 is based on a paper by Halperin.[92] It is similar to that used in TRAM and will not be further treated here.

E. Normal and Adjoint Multithermal Group Model: MARC-1

The last program to be discussed, MARC-1,[96] is a multithermal group calculation of thermal activation rates in the same geometry as TUT-T5 and TRAC-1. The main features of this program are its ability to calculate in either a normal or adjoint mode (based on normal or adjoint multigroup equations) and the ability to experiment with various hydrogen scattering kernels. The adjoint technique in MARC-1 is along the lines suggested by Maynard[95] for energy-dependent (nonself-adjoint) problems. The form of the kernel was specified by E. M. Gelbard, and the MARC-1 analysis was done jointly by E. M. Gelbard and J. Spanier.

Experience based on only a limited number of test problems indicates that MARC-1 is at least as fast as TRAC-1 (per collision). This is to be expected because the scattering routines in MARC-1 are simpler than in TRAC-1, on the average.

1. The Physical Model

The physical model implicit in MARC-1 may be described as follows: the basic rectangular quarter-cell (see geometry description for TUT-T5 and TRAC-1) may be subdivided into $R (\leq 60)$ rectangular subregions r, and the thermal energy range is divided into $G (\leq 36)$ energy groups i. Neutrons are introduced isotropically into this system with source spectrum $B^i (1 \leq i \leq G)$ and spatial density $S_r (1 \leq r \leq R)$. Scattering by hydrogen in group j may result either in transfer from group j to group i (with probability proportional to $\alpha^{i,j}$) or in a new direction in group j. The angular distribution of such a scattering has a component which is isotropic and a component which is either forward or backward. This is an extension

of the transport approximation for representing the angular distribution. Heavy element scattering may not change the energy group, and its angular distribution is also based on the transport approximation. Heavy element scattering is independent of the energy group while hydrogen scattering is not. Neutrons scatter from group to group and region to region and are ultimately absorbed in some group and region. As in the other programs, the neutron track lengths in each group and region are recorded as well as the final distribution of absorptions. These two types of estimates are combined as in TRAC-1 and TRAM to yield the linearly optimum minimum variance estimate of thermal activation rates.

The integro-differential transport equations for the multigroup model just described are

$$\vec{\omega}\cdot\nabla\psi^i(\vec{r},\vec{\omega})+\Sigma_t^i(\vec{r})\,\psi^i(\vec{r},\vec{\omega})=\sum_{j=1}^{G}\int d\vec{\omega}'\,\psi^j(\vec{r},\vec{\omega}')\cdot\left\{\frac{\alpha^{i,j}}{\sigma_{sH}^j}\Sigma_{sH}^j(\vec{r},\vec{\omega}\cdot\vec{\omega}')+\Sigma_{sh}^j(\vec{r},\vec{\omega}\cdot\vec{\omega}')\,\delta^{i,j}\right\}+\frac{S^i(\vec{r})}{4\pi};\ 1\le i\le G \qquad \text{Eq. (3.228)}$$

where

G = the number of energy groups

$\psi^i(\vec{r},\vec{\omega})$ = the vector flux in the i^{th} group

$\alpha^{i,j}$ = the transition matrix, representing transition from group j to group i

σ_{sH}^j = the microscopic scattering cross section for hydrogen in group j

$\Sigma_{sH}^j(\vec{r},\vec{\omega}\cdot\vec{\omega}')$ = $\Sigma_{sH}^j(\vec{r})f^j(\vec{\omega}\cdot\vec{\omega}')$ is the differential scattering cross section for hydrogen in group j, from $\vec{\omega}'$ to $\vec{\omega}$

$\Sigma_{sh}^j(\vec{r},\vec{\omega}\cdot\vec{\omega}')$ = $\Sigma_{sh}(\vec{r})g(\vec{\omega}\cdot\vec{\omega}')$ is the composite differential scattering cross section for heavy elements in group j, from $\vec{\omega}'$ to $\vec{\omega}$ (assumed independent of j)

$\delta^{i,j}$ = the Kronecker delta, $=1$ if $i=j$; $=0$ otherwise

$S^i(\vec{r})$ = the spatial source density in group i.

With respect to the above system of equations the following additional conditions are imposed:

1. $\displaystyle\sum_{i=1}^{G}\alpha^{i,j}=\sigma_{sH}^j$

2. $f^j(\vec{\omega}\cdot\vec{\omega}')$

$$=\frac{1}{4\pi}\left[1-|\bar{\mu}_H^j|+|\bar{\mu}_H^j|\,\delta(\vec{\omega}-\vec{\omega}')\,x_1(\bar{\mu}_H^j)+|\bar{\mu}_H^j|\,\delta(\vec{\omega}+\vec{\omega}')\,x_2(\bar{\mu}_H^j)\right]$$

where
δ denotes the Dirac delta function,

$$x_1(\bar{\mu}_H^j) = \begin{cases} 1 \text{ if } \bar{\mu}_H^j > 0 \\ 0 \text{ otherwise} \end{cases}$$

and

$$x_2(\bar{\mu}_H^j) = \begin{cases} 1 \text{ if } \bar{\mu}_H^j < 0 \\ 0 \text{ otherwise} \end{cases}$$

$\bar{\mu}_H^j$ being the average cosine of the scattering angle (laboratory system) for hydrogen;

3. $$g(\vec{\omega} \cdot \vec{\omega}') = \frac{1 - \bar{\mu}_h(\vec{r})}{4\pi}, \quad 0 \leq \bar{\mu}_h$$

where

$$\bar{\mu}_h(\vec{r}) = \frac{\sum_m \Sigma_{sm}(\vec{r})\bar{\mu}_m}{\Sigma_{sh}(\vec{r})}$$

and

$$\Sigma_{sh}(\vec{r}) = \sum_m N_m(\vec{r})\sigma_{sm}$$

$\Sigma_{sm}(\vec{r})$ being the macroscopic scattering cross section for heavy isotope m, $\bar{\mu}_m$ being the average cosine for isotope m, $N_m(\vec{r})$ being the number density for isotope m, and σ_{sm} being the microscopic scattering cross section for isotope m;

4. $$S^i(\vec{r}) = \frac{B^i}{\sum_{i=1}^{G} B^i} \frac{\sum_{r=1}^{R} S_r X_r(\vec{r})}{\sum_{r=1}^{R} S_r A_r}$$

where B^i are constants specifying the source spectrum, S_r are constants specifying the spatial source density in region r, $1 \leq r \leq R$, A_r is the area of region r, and

$$x_r(\vec{r}) = \begin{cases} 1 \text{ if } \vec{r} \text{ belongs to region } r \\ 0 \text{ otherwise} \end{cases}$$

5. Cell boundary conditions are applied at all four boundaries of the basic rectangular cell.

2. *The Normal and Adjoint Modes*

Let $x^i(\vec{r},\vec{\omega})$, $y^i(\vec{r},\vec{\omega})$, $1 \leq i \leq G$, be arbitrary functions, and let $\underline{X} = [x^i(\vec{r},\vec{\omega})]$, $\underline{Y} = [y^i(\vec{r},\vec{\omega})]$ represent vector functions with components x^i, y^i. Define an inner product on the space of such functions by

$$(\underline{X},\underline{Y}) \equiv \sum_{i=1}^{G} \iint d\vec{r}\, d\vec{\omega}\, x^i(\vec{r},\vec{\omega}) y^i(\vec{r},\vec{\omega}) \qquad \text{Eq. (3.229)}$$

the integrals being taken over all phase space. Then in operator notation the multigroup equations [Eq. (3.228)] may be written

$$M\underline{\psi} = \underline{S} \qquad \text{Eq. (3.230)}$$

where M is the (linear) multigroup operator, $\underline{\psi}$ the flux vector, and $\underline{S}$ the source vector. In the usual way, an adjoint operator $M^\dagger$ may be defined relative to the inner product [Eq. (3.229)] by

$$(M^\dagger \underline{X},\underline{Y}) = (\underline{X}, M\underline{Y}) \quad \text{for all} \quad \underline{X},\underline{Y}. \qquad \text{Eq. (3.231)}$$

The adjoint equations take the form

$$M^\dagger \underline{\psi}^\dagger = \underline{S}^\dagger \qquad \text{Eq. (3.232)}$$

or, in an expanded notation,

$$-\omega \cdot \nabla \psi^{\dagger i}(\vec{r},\vec{\omega}) + \Sigma_t^i(\vec{r})\,\psi^{\dagger i}(\vec{r},\vec{\omega}) = \sum_{j=1}^{G} \iint d\vec{\omega}'\, \psi^{\dagger j}(\vec{r},\vec{\omega}')$$

$$\cdot \left\{ \frac{a^{j,i}}{\sigma_{sH}^i}\, \Sigma_{sH}^i(\vec{r},\vec{\omega}\cdot\vec{\omega}') + \Sigma_{sh}^i(\vec{r},\vec{\omega}\cdot\vec{\omega}')\,\delta^{i,j} \right\} + S^{\dagger i}(\vec{r},\vec{\omega});\ 1 \leq i \leq G. \qquad \text{Eq. (3.233)}$$

Here $S^{\dagger i}(\vec{r},\vec{\omega})$ is an arbitrary source to the adjoint system.

One can see upon comparing the Eqs. (3.233) and (3.228) that the adjoint equations represent ordinary multigroup transport equations for neutrons traveling in the direction $-\vec{\omega}$. One can also see that the energy group transfer has been transposed so that up- and down-scattering have been interchanged in

passing from the normal to the adjoint equations. In addition, scattering from group j to group i in the adjoint system depends on the differential scattering cross section of hydrogen in group i.

From the definition of the adjoint operator $M^\dagger$ it follows that

$$(\underline{S}^\dagger, \underline{\psi}) = (\underline{\psi}^\dagger, \underline{S}) \quad . \qquad \text{Eq. (3.234)}$$

If $\underline{S}^\dagger$ is chosen to be the macroscopic absorption cross section in a given region r and zero outside this region, then the left-hand side of Eq. (3.234) becomes the thermal activation rate in region r. The equality [Eq. (3.234)] shows that such individual region activation rates may be estimated either by obtaining estimates of absorption weighted flux integrals or by estimates of source weighted adjoint flux integrals. In problems in which the activation in a single small region is desired, the estimate using fluxes might involve a very large variance due to the fact that relatively few histories make contributions to the flux estimator in the given region. Estimates involving adjoint flux integrals would, for such problems, be vastly more efficient because many more particles would contribute to the estimator. This idea is an extension to nonself-adjoint problems of that due to C. W. Maynard, which was discussed in Sect. 3.5.D.2.

Based on the above motivation, the MARC program was originally designed to operate in either a normal or adjoint mode in order to obtain both types of estimates of Eq. (3.234). The analog random walk process (see Chap. 7, Sect. 7.3), applied either to the normal or the adjoint equations, was originally specified. That is, the source $\underline{S}$ and operator M were used to generate random walk histories in the normal mode, while the source $\underline{S}^\dagger$ (which depends on the specific problem being solved) and operator $M^\dagger$ were used in the adjoint mode. The basic random variable used in MARC is the average of the distances traveled by the particles in a given energy group and region. This average provides an unbiased estimator of the integral of the flux (or adjoint flux) over the group and region, as has been previously mentioned. This average is then weighted by either the absorption cross section $\underline{S}^\dagger$ (in the normal mode) or by the source $\underline{S}$ (in the adjoint mode) to obtain estimates of $(\underline{S}^\dagger, \underline{\psi}) = (\underline{\psi}^\dagger, \underline{S})$.

3. *Variance Reduction in the Adjoint Mode*

A difficulty arises in attempting to represent properly the adjoint equations [Eq. (3.233)] in the Monte Carlo sampling model. To see how this comes about it is convenient to examine

the hydrogen scattering term in Eq. (3.233) more closely and to rewrite it as

$$\sum_{j=1}^{G}\int d\vec{\omega}'\left[\Sigma_{sH}^{j}(\vec{r})\psi^{\dagger j}(\vec{r},\vec{\omega}')\right]\left[\frac{\alpha^{j,i}}{\sum_{i=1}^{G}\alpha^{j,i}}\right]\left[f^{i}(\vec{\omega}\cdot\vec{\omega}')\right]\left[\frac{\sum_{i=1}^{G}\alpha^{j,i}}{\sigma_{sH}^{j}}\right]. \qquad \text{Eq. (3.235)}$$

In this way it may be seen that the first factor in the integral is the number of scattering events in group j, the second factor is the probability of scattering from group j to group i, and the third factor gives the probability density of changing direction from $\vec{\omega}'$ to $\vec{\omega}$. The factor left over, which is

$$W_j = \frac{\sum_{i=1}^{G}\alpha^{j,i}}{\sigma_{sH}^{j}}. \qquad \text{Eq. (3.236)}$$

may then be interpreted by the Monte Carlo program as a weighting factor which multiplies the weight of the neutron upon collision in group j. This is necessary in order to preserve a balance in the Monte Carlo representation of the adjoint equations [Eq. (3.233)]. This difficulty is not encountered in sampling the normal multigroup equations [Eq. (3.228)] because the corresponding weight factor is

$$\frac{\sum_{i=1}^{G}\alpha^{i,j}}{\sigma_{sH}^{j}} = 1$$

for all j by condition 1.

To investigate the efficiency of MARC, comparisons were made between MARC and the one-velocity program TRAC-1, since TRAC-1 deals with the same model as MARC except for the differences in the energy structure. It was discovered that, although the normal mode in MARC compared very favorably with TRAC-1, the adjoint mode in MARC was relatively less efficient in the sense of variance than in TRAC-1. It is likely that the use of weights necessary in the adjoint mode of MARC introduces an extra statistical variable which apparently increases the variance. This would be so if the weights used do not reflect accurately the importance of the event being weighted.

In attempting to reduce the variance in the adjoint mode in MARC several possibilities present themselves. If one thinks of the variance as being separated into two components, one arising from sampling in energy space and the other from sampling spatially, then it seems reasonable to attempt to reduce the energy component, since it is discrete. The scheme that evolved from the study actually eliminates the need for weights in the adjoint mode and is strongly motivated by the use of dual importance sampling in energy space (see Chap. 7, Sect. 7.3).

Inasmuch as heavy element scattering does not involve energy transfer, it is nonessential to the following discussion. Hence, terms involving heavy element scattering are omitted from the equations.

If the adjoint equations [Eq. (3.233)] are multiplied by constants k^i there results

$$-\vec{\omega}\cdot\nabla\eta^i(\vec{r},\vec{\omega})+\Sigma_t^i(\vec{r})\eta^i(\vec{r},\vec{\omega})=\sum_{j=1}^{G}\iint d\vec{\omega}'\,\frac{k^i}{k^j}\,\eta^j(\vec{r},\vec{\omega}')\cdot\left\{\frac{\alpha^{j,i}}{\sigma_{sH}^i}\,\Sigma_{sH}^i(\vec{r},\vec{\omega}\cdot\vec{\omega}')\right\}+k^i(S^\dagger)^i(\vec{r},\vec{\omega}) \qquad \text{Eq. (3.237)}$$

where

$$\eta^i(\vec{r},\vec{\omega})\equiv k^i\,\psi^{\dagger\,i}(\vec{r},\vec{\omega})\ . \qquad \text{Eq. (3.238)}$$

Since the extra variance in the adjoint mode is thought to arise because of the fluctuation in the weights, the first attempt at improvement is to determine the constants k^i so that the weights W_j become unity. The condition needed for unit weights in the transformed problem is

$$(\sigma_{sH}^i)_{\text{eff}}=\sum_{j=1}^{G}\frac{k^j}{k^i}\,\alpha^{i,j} \qquad \text{Eq. (3.239)}$$

where $(\sigma_{sH}^i)_{\text{eff}}$ is the effective hydrogen scattering cross section in the transformed problem. It is also required that

$$(\sigma_{aH}^i)_{\text{eff}}\equiv\sigma_{tH}^i-(\sigma_{sH}^i)_{\text{eff}}\geq 0 \qquad \text{Eq. (3.240)}$$

where $(\sigma^i_{aH})_{\text{eff}}$ is the effective hydrogen absorption cross section in the transformed problem. The necessary condition [Eq. (3.240)] may be written

$$\sum_{j=1}^{G} \frac{k^j}{k^i} a^{i,j} \leq \sigma^i_{tH} \qquad \text{Eq. (3.241)}$$

or

$$\sigma^i_{tH} k^i = \sum_{j=1}^{G} a^{i,j} k^j + T^i , \qquad T^i \geq 0 \qquad \text{Eq. (3.242)}$$

where T^i are arbitrary nonnegative constants. The equations [Eq. (3.242)] are the equations for the flux k^i in an infinite medium of hydrogen with a number density of unity and source spectrum T^i. Thus, if the k^i are chosen to be the infinite medium fluxes satisfying Eq. (3.242) and if the definitions [Eqs. (3.239) and (3.240)] are made, then the solution of the transformed adjoint equations [Eq. (3.237)] will involve only unit weights. The question now arises: What choice should be made for the source spectrum T^i? At this point dual importance sampling in the infinite medium problem is invoked to motivate the choice of the T^i.

The choice made is

$$T^i = B^i \qquad \text{Eq. (3.243)}$$

where B^i is the original source spectrum. This choice leads to a zero variance problem in case the original problem consists of an infinite medium of hydrogen and is designed to eliminate as much as possible of the variance which arises from sampling in energy space. In a typical problem, the variance might be reduced by as much as a factor of two or more as a result of this technique.

This method is interesting from a theoretical point of view, for it represents an unusual application of dual importance sampling. Ordinarily, dual importance sampling would make use of an approximate solution of the original transport equation in order to reduce the variance. In the present example use is made of the exact solution of an approximate transport equation (i.e., the infinite medium equation) to reduce the variance. In practice the success of such a method depends on the complicated details of the differences between the actual problem being solved and the infinite medium problem. For example, one might expect that if the spectrum were fairly constant from region to region in the problem whose solution is desired, then

the method would be quite successful. Conclusions based on test problems indicate that such a variation reduction technique is useful in enlarging the class of problems for which the adjoint mode of MARC would be preferred over the normal mode.

3.6 BLACKNESS THEORY FOR SLABS

C. W. Maynard

A. Introduction

The problem that will be considered is the approximation of the neutron flux distribution in a heterogeneous medium containing one or more regions having a large macroscopic absorption cross section. Problems of this type are constantly encountered in reactor design calculations (e.g., the treatment of control rods and lumped poisons). The straightforward use of diffusion theory in obtaining the solution to such a problem leads to serious errors. Direct approaches to overcoming the limitations of diffusion theory by use of high-order approximations to the neutron transport equation, such as the P_n, S_n, or Monte Carlo methods, are discussed in other sections of this volume. These direct methods are valuable for many situations but may not be available for the geometry occurring in a particular case; or, if available, the cost may be so great that they can only be used as comparison standards for more approximate schemes. Finally, even when direct methods are available and the need for accuracy could justify the expense, they usually contain other approximations (cell geometry, one-velocity, one-dimensional, etc.) and the results obtained with these methods must be forced on the low-order approximation procedures available for more extensive calculations. This situation led to attempts to develop simple procedures for modifying low-order approximations in such a fashion that the results agree with transport solutions to the accuracies required in design work.

Blackness theory attacks this practical problem of modifying low-order methods such as diffusion theory in regions where they would normally be inadequate. The approach is to break the problem into two steps which can be treated separately. The first stage extracts from the original problem an idealized problem in which the absorbing region is treated alone with transport theory. For example, the fraction of the incident neutrons absorbed by an absorbing body may be calculated for various assumed angular distributions of the incident flux. The second step incorporates into low-order procedures as much information from the solution of the idealized problem as allowed by the undetermined constants

of the low-order approximation. Examples of efforts along this line may be found in the work of Placzek,[97] Davison,[98] Marshak,[99] and others.

If an approach of this kind is to be practical, it must meet the following criteria. The idealized transport problem must either be easily solved or useful in a sufficient variety of cases to justify tabulation of key parts of the solution. Further, the manner of incorporating the results into low-order methods must not increase appreciably the labor of making the final more approximate calculations, and the accuracies achieved must meet the needs of design. Because of the indirectness of this approach, it is expected that the details of the final solution will be distorted; consequently, almost all emphasis on accuracy is centered on obtaining the relative absorption rate in the highly absorbing region which would be found from a transport solution of the complete problem. The indirectness of the approach also precludes any systematic error analysis. Thus, it is necessary to compare the results with solutions obtained by the direct transport methods mentioned earlier in a wide variety of cases in order to test the method. No mention is made here of spectrum averaging problems which arise in practice. This feature of blackness theory is discussed in Chap. 4, Sect. 4.2.

The idealized problem chosen in developing blackness theory is that of the absorbing region of the original problem isolated from any environment with an incident neutron distribution uniform over the surface. This distribution is chosen proportional to a small integral power of the direction cosine of the direction of incidence relative to a vector normal to the surface. (Other choices of basic incident distributions can be chosen, such as the Legendre polynomials of the direction cosine, as is done in Ref. 100.) To obtain some insight into the reasons for this choice, consider a one-dimensional two-region problem in which one region is highly absorbing and the other predominantly scattering. It is natural to attempt to solve this problem by using transport theory in only the highly absorbing region while retaining a simpler approach such as diffusion theory in the surrounding environment, since it is desirable to use the lowest order calculation in each region consistent with the required accuracy. If solutions of different orders are attempted in the two regions, the problem becomes one of matching the solutions at the boundary where different angular dependencies are implied on the two sides of the interface. Since the source is usually isotropic and occurs in the scattering medium, there is reason to expect the distribution incident on the absorber to be reasonably approximated by the lower order expression which is normally used in the scattering medium. On the other

hand, the distribution emerging from the absorber will have a very high-order variation with direction, but will be attenuated in magnitude relative to the incident distribution to the point where relatively crude conditions on it will suffice. These arguments lead to the prescription that the conditions at the interface may be taken as continuity of the angular distribution entering the absorber, with the assumption that it has the form implied by the approximation to be used in the scattering medium. The exit distribution can then be treated roughly by matching as many low-order moments as are needed to fix the constants in the scattering medium solution.

While the discussion has been carried out for wide regions, the same procedure will work for very thin regions as well. Certainly, if both scatterer and absorber are sufficiently small, the flux in both regions will be nearly isotropic. In this case, the flux entering and leaving the absorber will be a slowly varying function of direction, and then only a few low-order moments need be made continuous in order to obtain adequate matching conditions. As would be expected from the discussion, the proposed treatment of the matching conditions will lead to the greatest error in those cases where either or both regions are of intermediate optical thickness.

The term blackness theory has come to refer to a class of procedures for matching an approximate solution of the one-energy transport equation in one region to a very accurate solution in a second region. A detailed treatment of the one-dimensional problem will be given here. In Sect. 3.6.B the idealized transport problem for the primarily absorbing region is considered. Blackness coefficients for the absorbing region are defined as the transmitted and reflected contributions to the outgoing m^{th} moments due to an incident flux with an angular distribution of μ^n. These are related to the capture fractions given by Schiff and Stein[100] and are tabulated for the situations of greatest interest. In addition, a simple way suggested by Wachspress of approximating some of these coefficients is outlined.

This is followed (Sect. 3.6.C) by a set of matching conditions which couple the results of the idealized problem with the low-order approximation used in the regions adjoining the absorber. This allows the angular flux of the adjoining region to be specified at the absorber boundary in terms of the blackness coefficients. The general formulation for a three-region case is reduced to special cases of interest.

The application of blackness theory to both regions of a two-region cell is described in Sect. 3.6.D. This use of blackness theory (called double blackness) yields quite accurate results shown in Sect. 3.6.E, where a comparison of blackness theory

results with an accurate transport solution is given for two groups of problems.

In Sect. 3.6.F convenient forms of the boundary conditions are derived for the common case where diffusion theory is used outside of the absorber. Additional convenience is embodied in the definition of fictitious diffusion theory cross sections for the absorber region which reproduce the absorption rate as given by the boundary conditions. This form of the conditions has the additional advantage of allowing the constants to be further adjusted for any mesh corrections arising from the use of a finite-difference solution to the problem.

B. Blackness Coefficients

The coefficients needed in the matching conditions to be described are obtained by considering a slab of thickness τ bounded by a vacuum. The slab, which is assumed to scatter isotropically, has scattering cross section Σ_s and total cross section Σ. The angular flux incident on the left boundary is of the form μ^n (where μ is the cosine of the angle between the flux direction and the slab normal), and no neutrons enter the slab from the right. The solution to this problem must satisfy for $0 \leq x \leq \tau$:

$$\mu \frac{\partial \psi_n(x,\mu)}{\partial x} + \Sigma\psi_n(x,\mu) = \frac{\Sigma_s}{2}\int_{-1}^{1} d\mu' \psi_n(x,\mu')$$

subject to

$$\psi_n(0,\mu) = \mu^n, \mu > 0$$

and

$$\psi_n(\tau,\mu) = 0, \mu < 0 .$$

The coefficients of interest are

$$T_{mn}(\Sigma\tau, \Sigma_s/\Sigma) = \int_0^1 d\mu\ \mu^m \psi_n(\tau,\mu) \qquad \text{Eq. (3.244)}$$

and

$$R_{mn}(\Sigma\tau, \Sigma_s/\Sigma) = (-1)^m \int_{-1}^{0} d\mu\ \mu^m \psi_n(0,\mu) . \qquad \text{Eq. (3.245)}$$

The T_{mn} and R_{mn} are, respectively, the transmitted and reflected contributions to the outgoing m^{th} moments due to a μ^n incoming flux. They are defined to be always positive numbers and are functions of the optical thickness $\Sigma\tau$ and the scattering to total cross section ratio Σ_s/Σ.

In addition to the T_{mn} and R_{mn}, it is desirable to introduce the escape moments U_m defined by

$$U_m(\Sigma\tau, \Sigma_s/\Sigma) = \int_0^1 d\mu\, \mu^m \psi_e(\tau, \mu) \qquad \text{Eq. (3.246)}$$

for the slab isolated in a vacuum. The $\psi_e(\tau, \mu)$ is the angular flux at the right-hand boundary for the problem where no neutrons enter the slab through the boundaries, but a flat isotropic source of unit density exists in the slab. Thus, for $0 \le x \le \tau$

$$\mu \frac{\partial \psi_e(x, \mu)}{\partial x} + \Sigma \psi_e(x, \mu) = \frac{\Sigma_s}{2} \int_{-1}^{1} d\mu' \psi_e(x, \mu') + \frac{1}{2}$$

with

$$\psi_e(0, \mu) = 0, \quad \mu > 0$$

and

$$\psi_e(\tau, \mu) = 0, \quad \mu < 0 .$$

All escape moments U_m except U_0 are related to the R_{1n} and T_{1n} by the reciprocity theorem.

Considering a slab with entering angular flux $|\mu|^n$ at each boundary, the number of neutrons escaping the slab at each boundary is $R_{1n} + T_{1n}$. The number of neutrons entering at each boundary is $1/(n+2)$. Thus, the escape fraction is $(n+2)(R_{1n} + T_{1n})$, and the capture fraction becomes

$$F_n = 1 - (n+2)(R_{1n} + T_{1n}) .$$

The F_n are the quantities tabulated by Schiff and Stein[100] who also relate the escape fractions for an entering μ^n flux to the escape moments for an internal isotropic flat source. The relation obtained is [see Eq. (7) of Ref. 100]:

$$U_m = \frac{F_m - 1}{2\Sigma_a(m+1)}$$

or

$$U_m = \frac{1-(m+1)S_{1,\,m-1}}{2\Sigma_a(m+1)} \qquad \text{Eq. (3.247)}$$

where

$$S_{mn} = R_{mn} + T_{mn} \qquad \text{Eq. (3.248)}$$

and $\Sigma_a = \Sigma - \Sigma_s$ is the absorption cross section. Although the quantities S_{mn} are not independent of the R_{mn} and T_{mn}, they are of special importance and are, therefore, given their own symbol. S_{mn} represents the m^{th} outgoing half range moment for the entering angular flux μ^n in the case of a cell of half thickness $t = \tau/2$. U_1 represents the number of neutrons escaping from each boundary of the slab for a flat isotropic source inside the slab. Since a source of unit density is present, there are $2t$ neutrons produced in the slab. Thus, U_1 is related to the escape probability P through

$$P = U_1/t. \qquad \text{Eq. (3.249)}$$

The coefficients presented here are also similar to those presented by other authors. In particular, the R_{10}, T_{10}, and U_1 are identical to the $R/2$, $T/2$, and $\tau E/2$ of Wachspress.[101]

In general, the blackness coefficients must be computed numerically; however, in the case of a pure absorber they may be expressed analytically. In this case there is no reflection, and R_{mn} is zero. The angular flux is

$$\psi_n(x, \mu) = \mu^n e^{-\Sigma x/\mu}, \quad \mu > 0$$

$$= 0, \qquad \mu < 0.$$

Therefore,

$$T_{mn}(\Sigma\tau) = S_{mn}(\Sigma\tau) = \int_0^1 d\mu\, \mu^{m+n} e^{-\Sigma\tau/\mu} \qquad \text{Eq. (3.250)}$$

or

$$= E_{m+n+2}(\Sigma\tau)$$

where the $E_k(x)$ are the generalized exponential integral functions of order k.

Wachspress[101] has a simple way of approximating R_{10}, T_{10}, and U_1 when scattering is present and tables are not available.

The escape probability P is determined by the method of successive collisions, but the approximating assumption is made that those neutrons present after any collision are distributed uniformly and isotropically. The number of neutrons which escape without suffering any collisions are given by P_o, the escape probability from a purely absorbing slab of the same optical thickness as the original slab. There are $(\Sigma_s/\Sigma)(1-P_o)$ neutrons present after one collision. Since these are by assumption distributed in the same way as the source, $(\Sigma_s/\Sigma)(1-P_o)P$ will escape from the medium. The total escape is given by

$$P = P_o = \frac{\Sigma_s}{\Sigma}(1-P_o)P .$$

On solving for P and using the relation between P and U_1

$$U_1 = \frac{\tau}{2}\,\frac{P_o}{1-\frac{\Sigma_s}{\Sigma}(1-P_o)}$$

the expression for P_o is obtained from Eqs. (3.247) and (3.248) and from the expressions for the R_{10} and T_{10} of pure absorbers as

$$P_o(\Sigma\tau) = \frac{1-2E_3(\Sigma\tau)}{2\Sigma\tau} .$$

Similar arguments are made to find approximations for R_{10} and T_{10}. In this case an isotropic distribution is incident on one surface of the slab. If this incident distribution is of unit magnitude, the number of neutrons transmitted without collision is given by the transmission coefficient $T_{10}^{(o)}$ of a purely absorbing slab of optical thickness $\Sigma\tau$:

$$T_{10}^{(o)} = E_3(\Sigma\tau) = \frac{1-2\Sigma\tau P_o}{2} .$$

Those neutrons present after one collision, of which there are $\frac{\Sigma_s}{\Sigma}\left[\frac{1}{2}-E_3(\Sigma\tau)\right]$, are as before assumed to be uniformly and isotropically distributed. The number of these neutrons escaping through the face at which they originally entered the slab

is the same as the number reflected by the slab in this approximation. This number is just one half the escape probability times the neutrons that have had one collision

$$R_{10} = \frac{1}{2} P \frac{\Sigma_s}{\Sigma} \frac{1 - 2T_{10}^{(o)}}{2} = \frac{1}{2} \frac{\Sigma_s \tau (P_o)^2}{1 - \frac{\Sigma_s}{\Sigma}(1 - P_o)} .$$

Finally, the number escaping through the opposite face of the slab is equal to the number reflected (from symmetry) plus the number transmitted without collision

$$T_{10} = T_{10}^{(o)} + R = \frac{1}{2} \left[1 - 2\Sigma\tau P_o + \frac{\Sigma_s \tau (P_o)^2}{1 - \frac{\Sigma_s}{\Sigma}(1 - P_o)} \right] .$$

Since these expressions are only approximate and do not include all coefficients that may be needed, it is desirable to have numerical values for the blackness coefficients. The values of the R_{mn} and T_{mn} have been calculated for a wide range of $\Sigma\tau$ and Σ_s/Σ. A discrete ordinates code[102] using the double Gauss quadrature formula was employed. Twelve, 10, and 8 angles were used for optical thicknesses between 0.25 and 1.0, 1.25 and 2.0, and 2.5 and 20.0, respectively, for all except the pure scattering cases. The results have been checked for pure absorbers and for all scattering ratios where the optical thickness is 20.0. In this case the ratio of scalar flux to incident flux can be obtained analytically. The latter cases are essentially infinite in thickness. This ratio is, in terms of the coefficients, $1 + R_{10}$; but from the albedo problem[103] one obtains this as

$$\frac{\psi_{surface}}{\psi_{incident}} = \frac{2}{c} \left[1 - \sqrt{1-c} \right] .$$

Thus,

$$1 + R_{10} = \frac{2}{c} \left[1 - \sqrt{1-c} \right]$$

where $c = \Sigma_s / \Sigma$ is the scattering to total cross section ratio.

Comparison of the thick region results for $1 + R_{10}$ with the analytic results shows an error of less than 0.01 percent in all cases. The pure absorber coefficients were compared with tables of the E_k functions. For the smallest thickness ($\Sigma\tau = 0.25$) the error was 0.14 percent, while for all other thicknesses the errors were less than 0.05 percent. The pure scattering cases were obtained with 8 angles and fewer points and are probably only accurate to the order of 1 percent. The blackness coefficients are tabulated for m and n equal to zero and 1 in Tables 3.9 to 3.19. More extensive tables are given elsewhere.[104] U_0, which cannot be obtained from the R_{mn} and T_{mn}, is given in Table 3.20 and was obtained from calculations similar to those used for obtaining R and T.

C. Matching Conditions

The three-region case, in which the central region is to be treated only with coefficients which establish conditions on the solutions in the outer regions, is the most general type of problem to be treated here. The three regions are numbered I, II, and III from left to right, with Region II extending over $0 \leq x \leq \tau$ as shown in Fig. 3.30. Region II is restricted to isotropically scattering media and to a flat isotropic source of density Q^{II}. The angular fluxes at the two interfaces and in the three regions are designated by:

$$\psi_I(0, \mu), \qquad \psi_{II}(0, \mu), \qquad \psi_{II}(\tau, \mu), \qquad \psi_{III}(\tau, \mu) .$$

The idea is to require the angular flux incident on Region II from Regions I and III to be continuous into Region II, i.e.,

$$\psi_{II}(0, \mu) = \psi_I(0, \mu), \ \mu > 0$$

and

$$\psi_{II}(\tau, \mu) = \psi_{III}(\tau, \mu), \ \mu < 0 .$$

TABLE 3.9 - BLACKNESS COEFFICIENTS FOR SLABS*

$\Sigma_s/\Sigma = 0.0$

Σ_T	R_{00}	R_{01}	R_{10}	R_{11}	T_{00}	T_{01}	T_{10}	T_{11}
0.25	0000	0000	0000	0000	5185	3247	3247	2325
0.50	0000	0000	0000	0000	3265	2216	2216	1652
0.75	0000	0000	0000	0000	2170	1548	1548	1188
1.00	0000	0000	0000	0000	1485	1097	1097	- 1 8606
1.25	0000	0000	0000	0000	1034	- 1 7858	- 1 7858	- 1 6277
1.50	0000	0000	0000	0000	- 1 7311	- 1 5675	- 1 5675	- 1 4601
1.75	0000	0000	0000	0000	- 1 5219	- 1 4124	- 1 4124	- 1 3386
2.00	0000	0000	0000	0000	- 1 3755	- 1 3013	- 1 3013	- 1 2502
2.50	0000	0000	0000	0000	- 1 1980	- 1 1630	- 1 1630	- 1 1377
3.00	0000	0000	0000	0000	- 1 1065	- 2 8926	- 2 8926	- 2 7653
3.50	0000	0000	0000	0000	- 2 5801	- 2 4937	- 2 4937	- 2 4287
4.00	0000	0000	0000	0000	- 2 3193	- 2 2754	- 2 2754	- 2 2418
5.00	0000	0000	0000	0000	- 3 9926	- 3 8750	- 3 8750	- 3 7817
6.00	0000	0000	0000	0000	- 3 3168	- 3 2839	- 3 2839	- 3 2569
8.00	0000	0000	0000	0000	- 4 3405	- 4 3114	- 4 3114	- 4 2861
10.00	0000	0000	0000	0000	- 5 3810	- 5 3519	- 5 3519	- 5 3256
14.00	0000	0000	0000	0000	- 7 5042	- 7 4685	- 7 4685	- 7 4355
20.00	0000	0000	0000	0000	-10 7899	-10 7350	-10 7350	-10 6839

*All entries are of the form $-y\ xxxx = 0.xxxx \times 10^{-y}$.

TABLE 3.10 - BLACKNESS COEFFICIENTS FOR SLABS*

$\Sigma_s/\Sigma = 0.1$

$\Sigma\tau$	R_{00}	R_{01}	R_{10}	R_{11}	T_{00}	T_{01}	T_{10}	T_{11}
0.25	- 1 1880	- 1 1053	- 2 6544	- 2 3723	5347	3342	3309	2361
0.50	- 1 2323	- 1 1340	- 2 8887	- 2 5243	3432	2320	2290	1698
0.75	- 1 2492	- 1 1457	- 2 9901	- 2 5944	2316	1643	1618	1233
1.00	- 1 2565	- 1 1509	- 1 1037	- 2 6286	1606	1178	1159	- 1 9019
1.25	- 1 2600	- 1 1535	- 1 1061	- 2 6458	1131	- 1 8529	- 1 8383	- 1 6633
1.50	- 1 2616	- 1 1547	- 1 1072	- 2 6546	- 1 8080	- 1 6217	- 1 6107	- 1 4900
1.75	- 1 2624	- 1 1554	- 1 1078	- 2 6593	- 1 5822	- 1 4557	- 1 4474	- 1 3632
2.00	- 1 2629	- 1 1557	- 1 1081	- 2 6617	- 1 4225	- 1 3356	- 1 3293	- 1 2701
2.50	- 1 2632	- 1 1560	- 1 1084	- 2 6638	- 1 2263	- 1 1841	- 1 1805	- 1 1506
3.00	- 1 2633	- 1 1560	- 1 1085	- 2 6644	- 1 1234	- 1 1021	- 1 1001	- 2 8460
3.50	- 1 2633	- 1 1561	- 1 1085	- 2 6645	- 2 6807	- 2 5714	- 2 5596	- 2 4787
4.00	- 1 2633	- 1 1561	- 1 1085	- 2 6646	- 2 3790	- 2 3221	- 2 3153	- 2 2725
5.00	- 1 2633	- 1 1561	- 1 1085	- 2 6646	- 2 1202	- 2 1042	- 2 1020	- 3 8955
6.00	- 1 2633	- 1 1561	- 1 1085	- 2 6646	- 3 3901	- 3 3435	- 3 3359	- 3 2985
8.00	- 1 2633	- 1 1561	- 1 1085	- 2 6646	- 4 4311	- 4 3868	- 4 3781	- 4 3408
10.00	- 1 2633	- 1 1561	- 1 1085	- 2 6646	- 5 4939	- 5 4473	- 5 4371	- 5 3967
14.00	- 1 2633	- 1 1561	- 1 1085	- 2 6646	- 7 6824	- 7 6219	- 7 6076	- 7 5539
20.00	- 1 2633	- 1 1561	- 1 1085	- 2 6646	- 9 1140	- 9 1040	- 9 1016	- 10 9276

*All entries are of the form -y xxxx = 0.xxxx × 10^{-y}.

TABLE 3.11 - BLACKNESS COEFFICIENTS FOR SLABS*

$\Sigma_s/\Sigma = 0.2$

$\Sigma\tau$	R_{00}	R_{01}	R_{10}	R_{11}	T_{00}	T_{01}	T_{10}	T_{11}
0.25	- 1 3872	- 1 2169	- 1 1349	- 2 7679	5519	3444	3374	2399
0.50	- 1 4842	- 1 2796	- 1 1858	- 1 1097	3617	2436	2371	1748
0.75	- 1 5228	- 1 3062	- 1 2087	- 1 1254	2482	1751	1699	1285
1.00	- 1 5402	- 1 3187	- 1 2197	- 1 1333	1746	1273	1231	- 1 9495
1.25	- 1 5486	- 1 3248	- 1 2253	- 1 1374	1247	- 1 9321	- 1 9002	- 1 7052
1.50	- 1 5527	- 1 3280	- 1 2281	- 1 1396	- 1 9009	- 1 6868	- 1 6624	- 1 5256
1.75	- 1 5549	- 1 3296	- 1 2296	- 1 1407	- 1 6562	- 1 5085	- 1 4898	- 1 3930
2.00	- 1 5560	- 1 3305	- 1 2304	- 1 1414	- 1 4811	- 1 3779	- 1 3637	- 1 2946
2.50	- 1 5569	- 1 3311	- 1 2311	- 1 1419	- 1 2625	- 1 2109	- 1 2026	- 1 1666
3.00	- 1 5572	- 1 3314	- 1 2313	- 1 1421	- 1 1455	- 1 1188	- 1 1140	- 2 9493
3.50	- 1 5572	- 1 3314	- 1 2314	- 1 1421	- 2 8148	- 2 6740	- 2 6463	- 2 5439
4.00	- 1 5573	- 1 3314	- 1 2314	- 1 1421	- 2 4601	- 2 3849	- 2 3688	- 2 3132
5.00	- 1 5573	- 1 3315	- 1 2314	- 1 1421	- 2 1496	- 2 1275	- 2 1220	- 2 1051
6.00	- 1 5573	- 1 3315	- 1 2314	- 1 1421	- 3 4963	- 3 4287	- 3 4099	- 3 3570
8.00	- 1 5573	- 1 3315	- 1 2314	- 1 1421	- 4 5690	- 4 5000	- 4 4775	- 4 4214
10.00	- 1 5573	- 1 3315	- 1 2314	- 1 1421	- 5 6729	- 5 5964	- 5 5693	- 5 5056
14.00	- 1 5573	- 1 3315	- 1 2314	- 1 1421	- 7 9854	- 7 8785	- 7 8383	- 7 7477
20.00	- 1 5573	- 1 3315	- 1 2314	- 1 1421	- 9 1792	- 9 1600	- 9 1527	- 9 1363

*All entries are of the form -y xxxx = 0.xxxx $\times 10^{-y}$.

TABLE 3.12 - BLACKNESS COEFFICIENTS FOR SLABS*

$\Sigma_s/\Sigma = 0.3$

$\Sigma\tau$	R_{00}	R_{01}	R_{10}	R_{11}	T_{00}	T_{01}	T_{10}	T_{11}
0.25	- 1 5985	- 1 3355	- 1 2089	- 1 1189	5704	3552	3444	2439
0.50	- 1 7585	- 1 4387	- 1 2920	- 1 1726	3822	2564	2462	1804
0.75	- 1 8254	- 1 4845	- 1 3309	- 1 1992	2672	1875	1790	1343
1.00	- 1 8566	- 1 5068	- 1 3504	- 1 2131	1911	1383	1315	1005
1.25	- 1 8721	- 1 5181	- 1 3605	- 1 2205	1385	1027	- 1 9739	- 1 7549
1.50	- 1 8801	- 1 5241	- 1 3658	- 1 2245	1014	- 1 7661	- 1 7251	- 1 5688
1.75	- 1 8843	- 1 5272	- 1 3687	- 1 2267	- 1 7485	- 1 5738	- 1 5422	- 1 4296
2.00	- 1 8866	- 1 5290	- 1 3703	- 1 2279	- 1 5554	- 1 4312	- 1 4069	- 1 3252
2.50	- 1 8885	- 1 5304	- 1 3717	- 1 2289	- 1 3097	- 1 2455	- 1 2311	- 1 1873
3.00	- 1 8891	- 1 5309	- 1 3722	- 1 2293	- 1 1752	- 1 1409	- 1 1324	- 1 1085
3.50	- 1 8892	- 1 5310	- 1 3723	- 1 2294	- 2 9994	- 2 8136	- 2 7636	- 2 6316
4.00	- 1 8893	- 1 5311	- 1 3723	- 1 2294	- 2 5742	- 2 4722	- 2 4427	- 2 3691
5.00	- 1 8893	- 1 5311	- 1 3724	- 1 2294	- 2 1927	- 2 1611	- 2 1508	- 2 1273
6.00	- 1 8893	- 1 5311	- 1 3724	- 1 2295	- 3 6577	- 3 5563	- 3 5200	- 3 4432
8.00	- 1 8893	- 1 5311	- 1 3724	- 1 2295	- 4 7919	- 4 6800	- 4 6346	- 4 5470
10.00	- 1 8893	- 1 5311	- 1 3724	- 1 2295	- 5 9780	- 5 8462	- 5 7891	- 5 6840
14.00	- 1 8893	- 1 5311	- 1 3724	- 1 2295	- 6 1551	- 6 1349	- 6 1258	- 6 1094
20.00	- 1 8893	- 1 5311	- 1 3724	- 1 2295	- 9 3168	- 9 2760	- 9 2572	- 9 2240

*All entries are of the form -y xxxx = 0.xxxx × 10^{-y}.

TABLE 3.13 - BLACKNESS COEFFICIENTS FOR SLABS*

$\Sigma_s/\Sigma = 0.4$

$\Sigma\tau$	R_{00}	R_{01}	R_{10}	R_{11}	T_{00}	T_{01}	T_{10}	T_{11}
0.25	- 1 8232	- 1 4618	- 1 2877	- 1 1638	5901	3667	3518	2483
0.50	1059	- 1 6134	- 1 4089	- 1 2419	4051	2706	2562	1866
0.75	1162	- 1 6840	- 1 4683	- 1 2824	2891	2017	1895	1410
1.00	1213	- 1 7197	- 1 4992	- 1 3043	2106	1513	1415	1070
1.25	1239	- 1 7386	- 1 5158	- 1 3163	1553	1141	1063	- 1 8148
1.50	1253	- 1 7489	- 1 5249	- 1 3230	1156	- 1 8642	- 1 8026	- 1 6218
1.75	1260	- 1 7546	- 1 5300	- 1 3268	- 1 8658	- 1 6564	- 1 6082	- 1 4755
2.00	1265	- 1 7578	- 1 5329	- 1 3290	- 1 6517	- 1 4999	- 1 4623	- 1 3642
2.50	1268	- 1 7605	- 1 5355	- 1 3310	- 1 3732	- 1 2917	- 1 2690	- 1 2145
3.00	1270	- 1 7615	- 1 5364	- 1 3317	- 1 2163	- 1 1713	- 1 1576	- 1 1269
3.50	1270	- 1 7618	- 1 5367	- 1 3319	- 1 1263	- 1 1011	- 2 9285	- 2 7536
4.00	1270	- 1 7619	- 1 5368	- 1 3320	- 2 7416	- 2 5988	- 2 5493	- 2 4489
5.00	1270	- 1 7620	- 1 5368	- 1 3320	- 2 2592	- 2 2122	- 2 1942	- 2 1604
6.00	1270	- 1 7620	- 1 5368	- 1 3320	- 3 9176	- 3 7589	- 3 6936	- 3 5772
8.00	1270	- 1 7620	- 1 5368	- 1 3320	- 3 1180	- 4 9884	- 4 9017	- 4 7575
10.00	1270	- 1 7620	- 1 5368	- 1 3320	- 4 1548	- 4 1304	- 4 1189	- 4 1003
14.00	1270	- 1 7620	- 1 5368	- 1 3320	- 6 2745	- 6 2323	- 6 2116	- 6 1791
20.00	1270	- 1 7620	- 1 5368	- 1 3320	- 9 6595	- 9 5588	- 9 5088	- 9 4312

*All entries are of the form -y xxxx = 0.xxxx × 10^{-y}.

TABLE 3.14 - BLACKNESS COEFFICIENTS FOR SLABS*

$\Sigma_s/\Sigma = 0.5$

$\Sigma\tau$	R_{00}	R_{01}	R_{10}	R_{11}	T_{00}	T_{01}	T_{10}	T_{11}
0.25	1063	- 1 5966	- 1 3719	- 1 2119	6112	3791	3598	2529
0.50	1390	- 1 8063	- 1 5385	- 1 3188	4307	2865	2675	1935
0.75	1541	- 1 9091	- 1 6242	- 1 3770	3147	2181	2017	1488
1.00	1619	- 1 9638	- 1 6708	- 1 4097	2342	1669	1534	1148
1.25	1661	- 1 9939	- 1 6970	- 1 4285	1761	1283	1173	- 1 8882
1.50	1684	1011	- 1 7118	- 1 4394	1336	- 1 9882	- 1 9003	- 1 6884
1.75	1697	1021	- 1 7204	- 1 4458	1019	- 1 7632	- 1 6933	- 1 5343
2.00	1705	1027	- 1 7255	- 1 4496	- 1 7799	- 1 5906	- 1 5353	- 1 4153
2.50	1712	1032	- 1 7303	- 1 4532	- 1 4613	- 1 3553	- 1 3208	- 1 2515
3.00	1714	1034	- 1 7319	- 1 4545	- 1 2756	- 1 2147	- 1 1934	- 1 1528
3.50	1715	1034	- 1 7325	- 1 4549	- 1 1656	- 1 1302	- 1 1170	- 2 9311
4.00	1716	1035	- 1 7327	- 1 4551	- 2 9998	- 2 7917	- 2 7106	- 2 5684
5.00	1716	1035	- 1 7328	- 1 4552	- 2 3681	- 2 2948	- 2 2640	- 2 2129
6.00	1716	1035	- 1 7329	- 1 4552	- 2 1368	- 2 1105	- 3 9874	- 3 8013
8.00	1716	1035	- 1 7329	- 1 4552	- 3 1925	- 3 1569	- 3 1400	- 3 1144
10.00	1716	1035	- 1 7329	- 1 4552	- 4 2745	- 4 2248	- 4 2004	- 4 1643
14.00	1716	1035	- 1 7329	- 1 4552	- 6 5703	- 6 4686	- 6 4174	- 6 3431
20.00	1716	1035	- 1 7329	- 1 4552	- 8 1728	- 8 1421	- 8 1265	- 8 1041

*All entries are of the form -y xxxx = 0.xxxx $\times 10^{-y}$.

TABLE 3.15 - BLACKNESS COEFFICIENTS FOR SLABS*

$\Sigma_s/\Sigma = 0.6$

$\Sigma\tau$	R_{00}	R_{01}	R_{10}	R_{11}	T_{00}	T_{01}	T_{10}	T_{11}
0.25	1319	- 1 7408	- 1 4622	- 1 2633	6340	3924	3684	2579
0.50	1756	1021	- 1 6828	- 1 4046	4597	3045	2801	2013
0.75	1971	1166	- 1 8029	- 1 4857	3447	2375	2160	1579
1.00	2088	1247	- 1 8715	- 1 5336	2629	1859	1678	1243
1.25	2154	1295	- 1 9119	- 1 5624	2024	1460	1310	- 1 9799
1.50	2193	1323	- 1 9360	- 1 5799	1570	1149	1026	- 1 7739
1.75	2216	1340	- 1 9505	- 1 5906	1223	- 1 9053	- 1 8062	- 1 6120
2.00	2230	1350	- 1 9594	- 1 5972	- 1 9565	- 1 7145	- 1 6345	- 1 4843
2.50	2243	1360	- 1 9682	- 1 6037	- 1 5889	- 1 4464	- 1 3948	- 1 3039
3.00	2248	1364	- 1 9716	- 1 6063	- 1 3654	- 1 2797	- 1 2467	- 1 1911
3.50	2250	1365	- 1 9729	- 1 6073	- 1 2278	- 1 1757	- 1 1546	- 1 1204
4.00	2251	1366	- 1 9734	- 1 6077	- 1 1425	- 1 1105	- 2 9711	- 2 7594
5.00	2251	1366	- 1 9737	- 1 6079	- 2 5614	- 2 4394	- 2 3851	- 2 3030
6.00	2252	1366	- 1 9737	- 1 6079	- 2 2227	- 2 1753	- 2 1534	- 2 1212
8.00	2252	1366	- 1 9737	- 1 6079	- 3 3543	- 3 2808	- 3 2453	- 3 1947
10.00	2252	1366	- 1 9737	- 1 6079	- 4 5683	- 4 4518	- 4 3942	- 4 3137
14.00	2252	1366	- 1 9737	- 1 6079	- 5 1481	- 5 1180	- 5 1029	- 6 8199
20.00	2252	1366	- 1 9737	- 1 6079	- 8 6272	- 8 4998	- 8 4359	- 8 3474

*All entries are of the form -y xxxx = 0.xxxx $\times 10^{-y}$.

TABLE 3.16 - BLACKNESS COEFFICIENTS FOR SLABS*

$\Sigma_s/\Sigma = 0.7$

$\Sigma\tau$	R_{00}	R_{01}	R_{10}	R_{11}	T_{00}	T_{01}	T_{10}	T_{11}
0.25	1593	- 1 8955	- 1 5591	- 1 3187	6585	4068	3776	2632
0.50	2165	1260	- 1 8448	- 1 5011	4927	3249	2945	2101
0.75	2466	1463	1010	- 1 6122	3805	2605	2329	1687
1.00	2640	1583	1110	- 1 6816	2986	2094	1856	1359
1.25	2745	1657	1173	- 1 7257	2365	1688	1486	1097
1.50	2809	1703	1212	- 1 7539	1884	1363	1194	- 1 8872
1.75	2850	1733	1237	- 1 7721	1508	1101	- 1 9613	- 1 7181
2.00	2876	1752	1253	- 1 7839	1210	- 1 8909	- 1 7753	- 1 5817
2.50	2903	1772	1270	- 1 7965	- 1 7836	- 1 5842	- 1 5061	- 1 3822
3.00	2914	1780	1278	- 1 8019	- 1 5106	- 1 3837	- 1 3314	- 1 2515
3.50	2919	1784	1281	- 1 8042	- 1 3338	- 1 2523	- 1 2175	- 1 1656
4.00	2921	1785	1282	- 1 8052	- 1 2187	- 1 1661	- 1 1429	- 1 1092
5.00	2922	1786	1283	- 1 8058	- 2 9436	- 2 7209	- 2 6190	- 2 4747
6.00	2922	1786	1283	- 1 8060	- 2 4087	- 2 3134	- 2 2687	- 2 2066
8.00	2922	1787	1283	- 1 8060	- 3 7713	- 3 5940	- 3 5086	- 3 3921
10.00	2922	1787	1283	- 1 8060	- 3 1461	- 3 1127	- 4 9644	- 4 7442
14.00	2922	1787	1283	- 1 8060	- 5 5279	- 5 4076	- 5 3487	- 5 2692
20.00	2922	1787	1283	- 1 8060	- 7 3634	- 7 2807	- 7 2400	- 7 1854

*All entries are of the form -y xxxx = 0.xxxx $\times 10^{-y}$.

TABLE 3.17 - BLACKNESS COEFFICIENTS FOR SLABS*

$\Sigma_s/\Sigma = 0.8$

$\Sigma\tau$	R_{00}	R_{01}	R_{10}	R_{11}	T_{00}	T_{01}	T_{10}	T_{11}
0.25	1888	1062	- 1 6635	- 1 3783	6850	4223	3876	2690
0.50	2625	1531	1028	- 1 6105	5305	3483	3110	2202
0.75	3043	1810	1254	- 1 7615	4239	2882	2533	1816
1.00	3302	1988	1401	- 1 8623	3441	2392	2081	1505
1.25	3470	2106	1498	- 1 9306	2818	1991	1719	1252
1.50	3581	2185	1564	- 1 9774	2322	1659	1425	1043
1.75	3656	2238	1609	1010	1921	1385	1185	- 1 8702
2.00	3707	2275.	1640	1032	1594	1156	- 1 9863	- 1 7268
2.50	3765	2318	1676	1058	1103	- 1 8081	- 1 6860	- 1 5078
3.00	3793	2339	1693	1071	- 1 7669	- 1 5653	- 1 4785	- 1 3553
3.50	3807	2349	1701	1077	- 1 5346	- 1 3957	- 1 3343	- 1 2488
4.00	3813	2353	1706	1080	- 1 3733	- 1 2772	- 1 2338	- 1 1743
5.00	3818	2357	1709	1082	- 1 1825	- 1 1360	- 1 1146	- 2 8559
6.00	3819	2358	1709	1083	- 2 8941	- 2 6680	- 2 5619	- 2 4203
8.00	3820	2358	1709	1083	- 2 2152	- 2 1611	- 2 1354	- 2 1014
10.00	3820	2358	1709	1083	- 3 5184	- 3 3884	- 3 3263	- 3 2444
14.00	3820	2358	1709	1083	- 4 3018	- 4 2262	- 4 1900	- 4 1424
20.00	3820	2358	1709	1083	- 6 4242	- 6 3179	- 6 2670	- 6 2001

*All entries are of the form -y xxxx = 0.xxxx × 10^{-y}.

TABLE 3.18 - BLACKNESS COEFFICIENTS FOR SLABS*

$\Sigma_s/\Sigma = 0.9$

Σ_T	R_{00}	R_{01}	R_{10}	R_{11}	T_{00}	T_{01}	T_{10}	T_{11}
0.25	2205	1241	- 1 7763	- 1 4428	7138	4391	3984	2753
0.50	3147	1839	1238	- 1 7356	5742	3752	3299	2318
0.75	3728	2225	1546	- 1 9409	4772	3222	2783	1975
1.00	4119	2492	1764	1089	4034	2780	2374	1695
1.25	4395	2683	1920	1198	3446	2408	2040	1463
1.50	4595	2824	2036	1279	2965	2092	1762	1268
1.75	4742	2928	2121	1339	2563	1821	1527	1102
2.00	4851	3006	2186	1385	2224	1588	1328	- 1 9602
2.50	4996	3109	2271	1446	1685	1213	1009	- 1 7317
3.00	5078	3169	2320	1482	1285	- 1 9285	- 1 7708	- 1 5598
3.50	5127	3203	2349	1503	- 1 9829	- 1 7122	- 1 5903	- 1 4291
4.00	5155	3224	2366	1515	- 1 7534	- 1 5469	- 1 4528	- 1 3294
5.00	5181	3243	2382	1526	- 1 4441	- 1 3230	- 1 2671	- 1 1945
6.00	5190	3249	2387	1530	- 1 2622	- 1 1909	- 1 1578	- 1 1149
8.00	5194	3253	2390	1532	- 2 9157	- 2 6672	- 2 5511	- 2 4016
10.00	5195	3253	2390	1533	- 2 3199	- 2 2331	- 2 1925	- 2 1403
14.00	5195	3253	2390	1533	- 3 3909	- 3 2849	- 3 2353	- 3 1715
20.00	5195	3253	2390	1533	- 4 1670	- 4 1217	- 4 1005	- 5 7322

*All entries are of the form -y xxxx = 0.xxxx $\times 10^{-y}$.

TABLE 3.19 - BLACKNESS COEFFICIENTS FOR SLABS*

$\Sigma_s/\Sigma = 1.0$

$\Sigma\tau$	R_{00}	R_{01}	R_{10}	R_{11}	T_{00}	T_{01}	T_{10}	T_{11}
0.25	2568	1447	- 1 8989	- 1 5126	7433	4589	4101	2821
0.50	3744	2193	1479	- 1 8804	6256	4065	3521	2453
0.75	4555	2728	1904	1161	5445	3644	3096	2172
1.00	5162	3138	2233	1384	4838	3300	2767	1950
1.25	5638	3465	2497	1565	4362	3013	2503	1769
1.50	6024	3733	2714	1715	3976	2769	2287	1619
1.75	6345	3957	2895	1842	3655	2560	2105	1492
2.00	6616	4147	3050	1950	3384	2379	1950	1383
2.50	7052	4454	3299	2126	2949	2083	1701	1207
3.00	7387	4691	3492	2262	2613	1851	1508	1071
3.50	7653	4880	3645	2371	2347	1665	1355	- 1 9623
4.00	7870	5034	3770	2460	2130	1512	1230	- 1 8736

*All entries are of the form -y xxxx = 0.xxxx $\times 10^{-y}$.

TABLE 3.20 – U_0 NORMALIZED TO A UNIT SOURCE PER UNIT OF OPTICAL THICKNESS

Σ_s/Σ $\Sigma\tau$	0	0.1	0.2	0.3	0.4	0.5	0.6	0.7	0.8	0.9
0.25	0.2411	0.2481	0.2559	0.2642	0.2730	0.2825	0.2927	0.3036	0.3155	0.3282
0.50	0.3367	0.3520	0.3687	0.3871	0.4075	0.4303	0.4558	0.4847	0.5175	0.5553
0.75	0.3914	0.4131	0.4372	0.4645	0.4956	0.5313	0.5727	0.6215	0.6796	0.7502
1.00	0.4258	0.4521	0.4821	0.5166	0.5567	0.6040	0.6604	0.7290	0.8143	0.9232
1.25	0.4483	0.4783	0.5128	0.5531	0.6007	0.6578	0.7277	0.8152	0.9281	1.0793
1.50	0.4634	0.4962	0.5342	0.5790	0.6326	0.6980	0.7796	0.8844	1.0241	1.2200
1.75	0.4739	0.5086	0.5494	0.5977	0.6562	0.7285	0.8202	0.9406	1.1059	1.3476
2.00	0.4812	0.5175	0.5602	0.6113	0.6737	0.7516	0.8518	0.9858	1.1749	1.4625
2.50	0.4901	0.5283	0.5737	0.6286	0.6964	0.7825	0.8958	1.0521	1.2828	1.6598
3.00	0.4947	0.5341	0.5811	0.6383	0.7095	0.8010	0.9232	1.0959	1.3599	1.8187
3.50	0.4971	0.5371	0.5851	0.6436	0.7170	0.8119	0.9402	1.1246	1.4146	1.9452
4.00	0.4984	0.5388	0.5873	0.6467	0.7213	0.8185	0.9508	1.1435	1.4534	2.0462
5.00	0.4995	0.5403	0.5892	0.6494	0.7253	0.8247	0.9616	1.1639	1.4998	2.1875
6.00	0.4998	0.5407	0.5899	0.6503	0.7267	0.8271	0.9658	1.1728	1.5228	2.2740
8.00	0.5000	0.5409	0.5901	0.6507	0.7274	0.8282	0.9681	1.1783	1.5397	2.3570
10.00	0.5000	0.5409	0.5902	0.6508	0.7275	0.8284	0.9685	1.1794	1.5438	2.3865
14.00	0.5000	0.5409	0.5902	0.6508	0.7275	0.8284	0.9686	1.1796	1.5450	2.4006
20.00	0.5000	0.5409	0.5902	0.6508	0.7275	0.8284	0.9686	1.1796	1.5451	2.4024

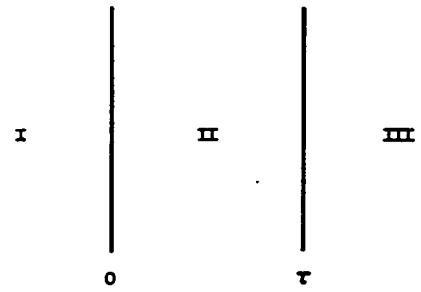

FIGURE 3.30. Three-Region Slab Configuration.

The moments of the distributions leaving Region II, i.e., of $\psi_{II}(0, \mu), \mu < 0$ and of $\psi_{II}(\tau, \mu), \mu > 0$, are to be determined from the incident distributions and the internal source by means of the transmission, reflection, and escape coefficients. As many moments will then be equated to the corresponding moments just outside Region II as are needed to determine the constants of the solutions in Regions I and III.

The angular flux at the interface in Region I is assumed to be of the form

$$\psi_I(0, \mu) = \sum_{n=0}^{N} A_n \mu^n, \mu > 0$$

and

$$\psi_I(0, \mu) = \sum_{n=0}^{N} C_n \mu^n, \mu < 0 .$$

In Region III, at $x = \tau$, the angular flux is assumed to be given by

$$\psi_{III}(\tau, \mu) = \sum_{n=0}^{N} B_n \mu^n, \mu < 0$$

and

$$\psi_{III}(\tau, \mu) = \sum_{n=0}^{N} D_n \mu^n, \mu > 0 .$$

From the assumption of continuity of the distribution entering Region II, it follows that

$$\psi_{II}(0, \mu) = \sum_{n=0}^{N} A_n \mu^n, \mu > 0$$

and

$$\psi_{II}(\tau, \mu) = \sum_{n=0}^{N} B_n \mu^n, \ \mu < 0 .$$

Defining the left and right half-range m^{th} moment of a function $f(x, \mu)$ by

$$L_f^m(x) = \int_{-1}^{0} d\mu \, \mu^m f(x, \mu)$$

and

$$R_f^m(x) = \int_{0}^{1} d\mu \, \mu^m f(x, \mu)$$

respectively, the matching conditions leaving Region II are continuity of the half-range moments of the angular flux across the interface. (Since the entering fluxes are already continuous, this is equivalent to making the ordinary full range moments continuous at the interfaces.)

Denote the m^{th} half-range moment of the flux leaving Region II at the $x = 0$ interface (i.e., to the left) by $L_{II}^m(0)$, and the left half-range moment at the interface in Region I by $L_I^m(0)$. Similarly, at the interface of Regions II and III the right-hand moments are denoted by $R_{II}^m(\tau)$ and $R_{III}^m(\tau)$, respectively. The boundary conditions on the flux leaving Region II can now be stated as

$$L_I^m(0) = L_{II}^m(0)$$

and

$$R_{II}^m(\tau) = R_{III}^m(\tau) .$$

$L_I^m(0)$ is given by

$$L_I^m(0) = \int_{-1}^{0} d\mu \, \mu^m \sum_{n=0}^{N} C_n \mu^n = \sum_{n=0}^{N} \frac{(-1)^{m+n} C_n}{m+n+1}$$

while $L_{II}^m(0)$ is*

$$L_{II}^m(0) = \sum_{n=0}^{N} \left[(-1)^m R_{mn} A_n + (-1)^{m+n} T_{mn} B_n \right] = (-1)^m Q^{II} U_m .$$

* $L_{II}^{m(0)}$ is obtained as the sum of the contributions reflected from Region I, $(-1)^m R_{mn} A_n$; that transmitted from Region III, $(-1)^{m+n} T_{mn} B_n$; and that due to the escape moment of the source in Region II, $(-1)^m Q^{II} U_m$, due regard having been given to signs.

Equating these yields

$$\sum_{n=0}^{N}\left[\frac{(-1)^n C_n}{m+n+1} - R_{mn}A_n - (-1)^n T_{mn}B_n\right] = Q^{II}U_m . \qquad \text{Eq. (3.251)}$$

Letting m range from 0 to N gives $N+1$ conditions on the $3N+3$ variables A_n, B_n, and C_n. At the other interface $R^m_{III}(\tau)$ is found to be

$$R^m_{III}(\tau) = \int_0^1 d\mu\, \mu^m \sum_{n=0}^{N} D_n \mu^n = \sum_{n=0}^{N} \frac{D_n}{m+n+1}$$

while $R^m_{II}(\tau)$ is

$$R^m_{II}(\tau) = \sum_{n=0}^{N}\left[(-1)^n R_{mn}B_n + T_{mn}A_n\right] + Q^{II}U_m .$$

Equating these expressions yields

$$\sum_{n=0}^{N}\left[\frac{D_n}{m+n+1} - (-1)^n R_{mn}B_n - T_{mn}A_n\right] = Q^{II}U_m \qquad \text{Eq. (3.252)}$$

a set of $N+1$ conditions for $m = 0$ to N on the coefficients A_n, B_n, and D_n. Taken with the previous $N+1$ conditions, there are in all $2N+2$ conditions on the $4N+4$ coefficients A_n, B_n, C_n, and D_n. This is the correct number of conditions at the boundaries of Region II, since the conditions are complete at the two boundaries treated, and an equal number of conditions can be fixed at the remaining boundaries of Regions I and III.

Various special cases can now be discussed. If, for example, the boundary vector fluxes in Regions I and III are actually expanded in a power series in μ for the full range of μ (i.e., -1 to 1), this requires

$$A_n = C_n$$

$$B_n = D_n .$$

This case is essentially the same as the P_n approximation; for a polynomial in μ over this range can equally well be expressed in terms of Legendre polynomials. The matching conditions for the P_n approximation are easily obtained from those given below

by simply substituting for the A_n and B_n their expressions in terms of Legendre coefficients.

The matching conditions now become

$$\sum_{n=0}^{N}\left[\left(\frac{(-1)^n}{m+n+1}-R_{mn}\right)A_n-(-1)^nT_{mn}B_n\right]=Q^{II}U_m \qquad \text{Eq. (3.253)}$$

and

$$\sum_{n=0}^{N}\left[\left(\frac{1}{m+n+1}-(-1)^nR_{mn}\right)B_n-T_{mn}A_n\right]=Q^{II}U_m. \qquad \text{Eq. (3.254)}$$

However, only $N+1$ of the $2N+2$ relations can be used in this case, since there are correspondingly only $2N+2$ coefficients involved. It turns out that one can match the even or the odd moments and obtain the transport boundary conditions in the limit where N tends to infinity. The odd moments are usually chosen in order to include the first moment which brings about neutron conservation. The reasoning involved in deciding that only even or odd moments can be matched is the same as that given by Stein[105] whose arguments may be taken over directly. It is worth noting that in matching the vector flux to the right (or left) and the half-range moments to the left (or right), one is of necessity matching ψ for $\mu>0$ (or $\mu<0$) and the full range moments.

Another special case of considerable interest is that of a slab cell. This case is obtained by taking the center line of Region II as an axis of symmetry and requiring in the present notation

$$B_n=(-1)^nA_n,$$

$$D_n=(-1)^nC_n.$$

Substitution in the matching conditions yields

$$\sum_{n=0}^{N}\left[\frac{(-1)^nC_n}{m+n+1}-S_{mn}A_n\right]=Q^{II}U_m \qquad \text{Eq. (3.255)}$$

at either boundary. This is a set of $N+1$ conditions on the $2N+2$ coefficients, A_n and C_n. In the special case of $N=0$, the first moment is usually matched, even though it goes with a power of μ not included in the angular flux. However, it is needed for neutron conservation. If full-range expansions are

used, the C_n are again equal to the A_n, and the conditions become

$$\sum_{n=0}^{N}\left[\frac{(-1)^n}{m+n+1}-S_{mn}\right]A_n=Q^{II}U_m \qquad \text{Eq. (3.256)}$$

where only the $(N+1)/2$ odd or even m may be used.

The matching conditions reduce in special cases to a number of well known boundary conditions. For example, the blackness boundary conditions for the P_1 approximation in a cell are the same as those given by Stein,[105] and for the noncellular case are the same as those of Goldsmith.[106] If double-P_n equations of the same order as the matching conditions were used to calculate the blackness coefficients, the conditions would be identical with those introduced by Bengston for Yvon's method.[107]

D. Double Blackness

In the preceding discussion, no mention was made of the approximation of the transport equation to be used in the outer regions. It was only necessary to require a full or half-range expansion of the solution at the boundary. This makes the conditions fit in rather naturally with the P_n and double-P_n approximations. However, the idealized problems from which the blackness coefficients were determined also have this property of being described in powers of μ at the boundary for directions into the medium, while for the exit distribution in these problems the information retained in the coefficients are also described in powers of μ. Consequently, after matching the results in one region to an expansion in powers of μ, the adjacent region can be treated in the same fashion without regard to the manner of treating the first region. The combined set of matching equations suffices to fix the constants that are not needed to meet the conditions at the remaining boundaries of these regions. Thus, in principle, it is possible to use the blackness matching conditions for both regions at an interface, and to use this procedure at each interface of the problem. There is a limitation to regions without sources or with only flat isotropic sources.

The restriction to flat isotropic sources is not necessary in principle, but the escape moments for sources of other shapes would lead to an inordinate amount of tabulation which is, thus, impractical. This method will be called the double blackness (DB1) approximation. The method is applied here to a two-region cell: Region I, $-t_1 \le x \le 0$; Region II, $0 \le x \le t_2$, as shown in Fig. 3.31.

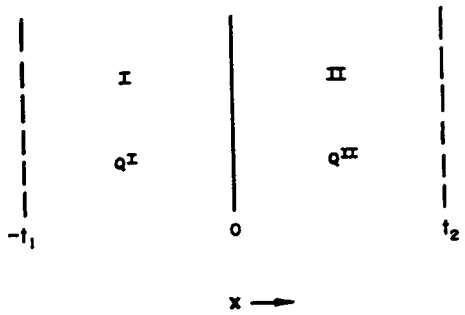

FIGURE 3.31. Two-Region Cell for DB1 Example.

As blackness coefficients for both regions are to be used, the region referred to is indicated by a superscript I or II. Flat isotropic sources of density Q^I and Q^{II} are assumed to be present in Regions I and II, respectively. The angular flux at the interface, as in the previous treatment of a cell, is assumed to have the form

$$\psi(0, \mu) = \sum_{n=0}^{N} A_n \mu^n, \qquad \mu > 0$$

$$= \sum_{n=0}^{N} C_n \mu^n, \qquad \mu < 0 .$$

The right-going half-range moments in Regions I and II are (treating Region I with blackness theory)

$$R_I^m = \sum_{n=0}^{N} (-1)^n S_{mn}^I C_n + Q^I U_m^I$$

and

$$R_{II}^m = \sum_{n=0}^{N} \frac{A_n}{m+n+1} .$$

The left-going half-range moments are (treating Region II with blackness theory)

$$L_I^m = \sum_{n=0}^{N} \frac{(-1)^{m+n} C_n}{m+n+1}$$

and

$$L_{II}^{m} = \sum_{n=0}^{N} (-1)^m S_{mn}^{II} A_n + (-1)^m Q^{II} U_m^{II}.$$

Equating the two left- and right-going moments gives

$$\sum_{n=0}^{N} \left[\frac{A_n}{m+n+1} - (-1)^n S_{mn}^{I} C_n \right] = Q^{I} U_m^{I} \qquad \text{Eq. (3.257)}$$

and

$$\sum_{n=0}^{N} \left[\frac{(-1)^n C_n}{m+n+1} - S_{mn}^{II} A_n \right] = Q^{II} U_m^{II}. \qquad \text{Eq. (3.258)}$$

This is a set of $2N+2$ equations in the $2N+2$ unknowns A_n, C_n. They can be solved and $\psi(0, \mu)$ constructed. Then j, for example, is given by

$$j = \sum_{n=0}^{N} \frac{A_n - (-1)^n C_n}{n+2} \qquad \text{Eq. (3.259)}$$

while ϕ becomes

$$\phi = \sum_{n=0}^{N} \frac{A_n + (-1)^n C_n}{n+1} \qquad \text{Eq. (3.260)}$$

where j is the current and ϕ is the scalar flux at the interface. As an example, the lowest order expansion would be to assume the flux isotropic in both directions, i.e., $N=0$. The equations for matching the first moments $(m=1)$ are

$$\frac{1}{2} C_0 - S_{10}^{II} A_0 = Q^{II} U_1^{II}$$

$$\frac{1}{2} A_0 - S_{10}^{I} C_0 = Q^{I} U_1^{I}.$$

Here

$$j = \frac{1}{2}(A_0 - C_0)$$

and

$$\Psi = A_0 + C_0$$

which, on solving the equations, leads to

$$j = \frac{Q^I U_1^I (1 - 2S_{10}^{II}) - Q^{II} U_1^{II} (1 - 2S_{10}^I)}{1 - 4S_{10}^I S_{10}^{II}}$$

and

$$\phi = \frac{2Q^I U_1^I (1 + 2S_{10}^{II}) + 2Q^{II} U_1^{II} (1 + 2S_{10}^{II})}{1 - 4S_{10}^I S_{10}^{II}}.$$

This is called the DBl_0 approximation, and it reduces to the ordinary double-P_0 result for the two-region problem if the S_{mn} and U_m are calculated in the double-P_0 approximation for each region. The next order approximation where $N = 1$ (the DBl_1 approximation) is not difficult to handle numerically, but the formulas for ϕ and j are cumbersome.

E. Applications and Results

There are three main types of problems for which the DBl approximations have been considered. These are the problems of resonance capture in a slab cell, absorption in control rods, and thermal utilization in a cell. Sample calculations have been carried out for the first and third of these problems. In the resonance capture problem, the moderator is assumed to remove the neutrons from the narrow group containing the resonance. This results in the moderator being treated formally as a pure absorber. The fuel scattering may remove neutrons from the group or scatter them isotropically, depending on whether the resonance is assumed to be thin or thick for fuel moderation. Flat isotropic sources due to slowing in from above the resonance can be introduced in both regions or in the moderator alone. In either case, knowledge of the current enables a calculation of the resonance absorption. Several series of problems of this type have been solved for the current. In the case of two pure absorbers with a source in the moderating region, a transport solution in integral form was evaluated numerically. The results are used for comparison and are shown in Fig. 3.32. The DBl_0 and DBl_1 approximations, i.e., using the lowest two orders of Eqs. (3.257) and (3.258), and the P_1, double-P_0, and double-P_1 approximations in Region

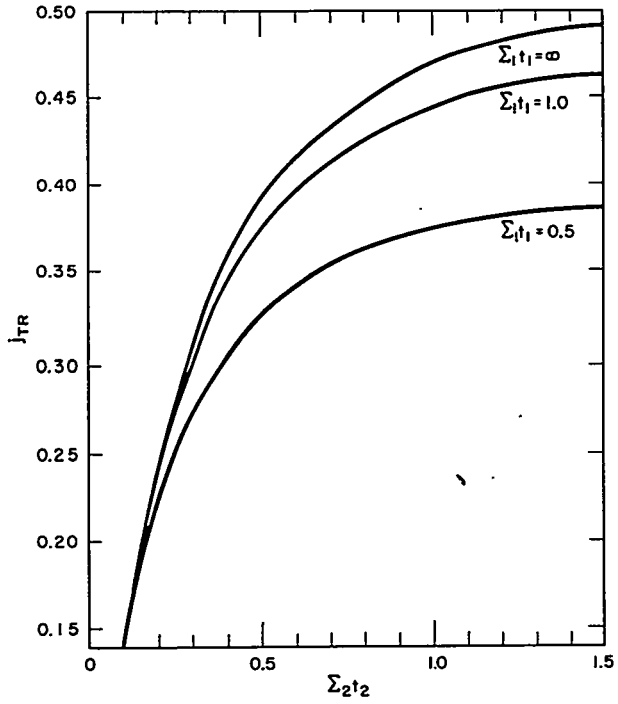

FIGURE 3.32. Interface Current in Purely Absorbing Slab Cell with Flat Source in One Region.

II, with blackness theory matching conditions for Region I from Eq. (3.255) for the double-P cases and Eq. (3.256) for the P_1 case, have been used to solve the same series of problems.

The approximate currents are divided by the corresponding transport solutions and plotted against the optical half thickness of Region II, holding Region I constant. The results are shown in Figs. 3.33, 3.34, and 3.35 for $\Sigma_1 t_1$ equal to 0.5, 1.0, and infinity, deviation from one representing the fractional error in the approximation. The DBl results are not shown on Fig. 3.35, since they are exact in that case. Figure 3.33 shows the poorest DBl_0 and DBl_1 results for this type of problem. These curves show a maximum error of only 0.5 percent for DBl_1 and 3 percent for DBl_0, which represents a considerable improvement over the other comparable approximations.

The situation encountered in calculating thermal utilization in a two-region slab cell is that of a strong absorber with scattering next to a weakly absorbing but strongly scattering moderator containing a flat isotropic source. The quantity needed to obtain the thermal utilization constant is the ratio

of the average flux in the fuel to the average flux in the moderator. This ratio can be obtained from a knowledge of the source strength in the moderator, the interface current, and the physical parameters of the cell. With a source in the moderator only, the average flux in the fuel is

$$\bar{\phi}_f = \frac{j}{\Sigma_{af} t_f}$$

while neutron balance in the moderator gives

$$\bar{\phi}_m = \frac{S_m t_m - j}{\Sigma_{am} t_m} .$$

The flux ratio is then

$$\frac{\bar{\phi}_f}{\bar{\phi}_m} = \frac{\Sigma_{am} t_m}{\Sigma_{af} t_f} \frac{j}{S_m t_m - j} .$$

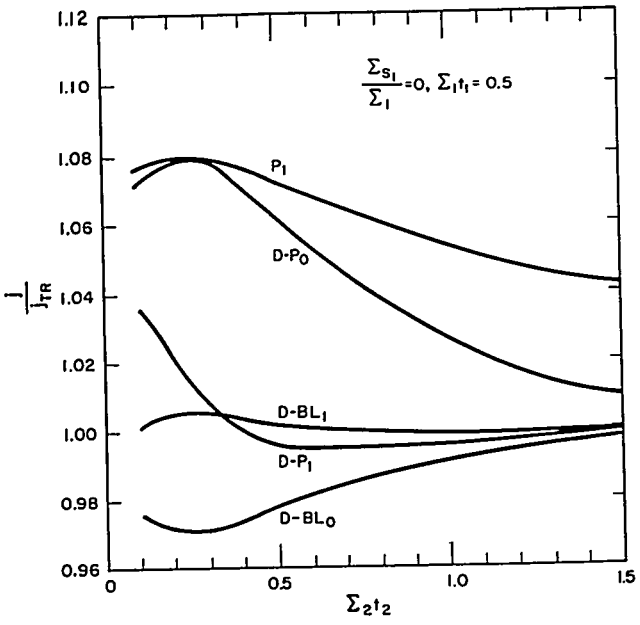

FIGURE 3.33. Ratio of Current Predicted by Various Blackness Approximations to Transport Theory Result.

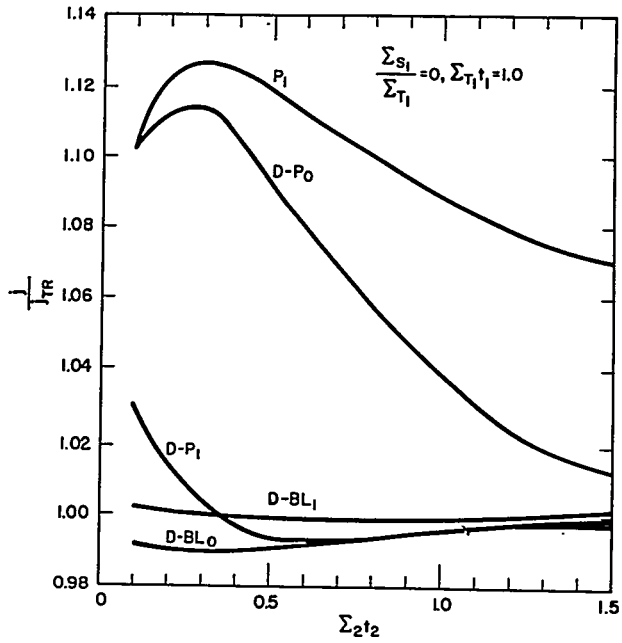

FIGURE 3.34. Ratio of Current Predicted by Various Blackness Approximations to Transport Theory Result.

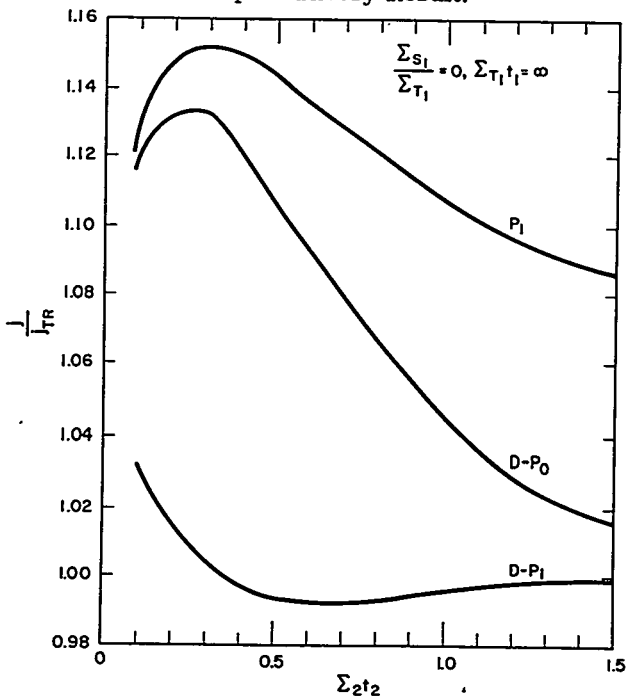

FIGURE 3.35. Ratio of Current Predicted by Various Blackness Approximations to Transport Theory Result.

This ratio has been calculated, using the DBl_0 and DBl_1 approximations of the current, for a group of problems covering a variety of cells for which the results are available from a number of other approximations.[108] A discrete ordinates solution of the problems is also available and has been used for comparison. All results are tabulated in Table 3.21. The DBl_0 results are seen to be comparable in most cases to the double-P_1 approximation, while the DBl_1 results are usually a significant improvement over other approximations. However, it should be noted again that the problems are for moderators having isotropic scattering and a flat source. This limits the ability to approximate the thermal utilization where anisotropic scattering and spatially varying sources are important.

A study of Figs. 3.33, 3.34, and 3.35 shows that all of the approximations have their maximum errors for a cell half thickness in the neighborhood of a quarter to a half of a mean free path. This is also in agreement with the results in Table 3.21. It appears that for a flat source in a region of this optical thickness, the interface flux varies in a very complicated manner as a function of angle which cannot adequately be represented by a low-order polynomial in μ. However, the advantage of blackness theory over other methods requiring the same interface angular distribution lies in the high-order calculation used away from the interfaces. In effect, blackness theory constrains the angular distribution only at the interfaces, not throughout the entire problem, and can, therefore, reduce the error considerably relative to the regular approximations.

F. Convenient Forms and Conclusions

The boundary or matching conditions given in Sect. 3.6.C are general and apply when arbitrary P_n and double-P_n approximations are to be used in regions adjacent to those for which blackness coefficients are employed. In practice, if a very high-order approximation is used, there is little need to employ blackness theory. If intermediate orders of approximation are contemplated, the general blackness conditions are necessary and result in worthwhile improvements in accuracy. However, the situation occurring most often employs the diffusion or P_1 approximation in all regions except those highly absorbing regions where blackness theory is to be used. In this case, the general blackness conditions can be given a form that is more convenient for applications. Due to the importance of these results in practice, they will be derived without reference to the general case given earlier.

TABLE 3.21 - COMPARISON OF THE $DB1_0$ AND $DB1_1$ APPROXIMATIONS WITH THE P_1, DOUBLE-P_0, P_3, AND DOUBLE-P_1 APPROXIMATIONS

Problem Parameters				$\bar{\phi}_f/\bar{\phi}_m$ (Percentage errors in parentheses)						
Problem Number	t_m (cm)	t_f (cm)	Σ_{af} (cm^{-1})	RDR 4	P_1	DP_0	P_3	DP_1	$DB1_0$	$DB1_1$
1	0.127	0.127	0.1	0.9685	0.9943 (2.7%)	0.9925 (2.5%)	0.9888 (2.1%)	0.9803 (1.2%)	0.9652 (-0.3%)	0.9698 (0.1%)
2	0.127	1.27	0.1	0.7824	0.8974 (14.7%)	0.8680 (10.9%)	0.8310 (6.2%)	0.7775 (-0.6%)	0.7721 (-1.3%)	0.7816 (-0.09%)
3	1.27	0.127	0.1	0.9209	0.9523 (3.4%)	0.9377 (1.8%)	0.9377 (1.8%)	0.9282 (0.8%)	0.9288 (0.9%)	0.9177 (-0.3%)
4	1.27	1.27	0.1	0.5904	0.6410 (8.6%)	0.5740 (-2.8%)	0.5977 (1.2%)	0.5873 (-0.5%)	0.5966 (1.1%)	0.5903 (-0.2%)
5	0.127	0.127	1.0	0.7881	0.9333 (18.4%)	0.9130 (15.8%)	0.8789 (11.5%)	0.8135 (3.2%)	0.7620 (-3.3%)	0.7914 (+0.4%)
6	0.127	1.27	1.0	0.2300	0.3281 (42.7%)	0.2786 (21.1%)	0.2549 (10.8%)	0.2233 (-2.9%)	0.2279 (-0.9%)	0.2272 (-1.2%)
7	1.27	0.127	1.0	0.5720	0.6591 (15.2%)	0.5933 (3.7%)	0.6009 (5.1%)	0.5745 (0.4%)	0.5905 (3.2%)	0.5692 (-0.5%)
8	1.27	1.27	1.0	0.1219	0.1333 (9.4%)	0.1054 (-13.5%)	0.1230 (0.9%)	0.1218 (-0.1%)	0.1219 (0%)	0.1219 (0%)

Since the P_1 approximation for one-dimensional problems implies an angular distribution of the form

$$\psi(x, \mu) = \frac{1}{2}\phi(x) + \frac{3}{2} j(x)\mu,$$

consider a source-free region with incident distributions on the left face and right face given, respectively, by

$$\psi_\ell(\mu) = \frac{1}{2}\phi_\ell + \frac{3}{2} j_\ell \mu$$

and

$$\psi_r(\mu) = \frac{1}{2}\phi_r + \frac{3}{2} j_r \mu .$$

The requirement of continuity of current at the left face is

$$j_\ell = \phi_\ell \left(\frac{1}{4} - \frac{1}{2} R_{10}\right) + j_\ell\left(\frac{1}{2} - \frac{3}{2} R_{11}\right) + \phi_r\left(-\frac{1}{2} T_{10}\right) + j_r\left(\frac{3}{2} T_{11}\right) .$$

The j_ℓ on the left-hand side is the current just to the left of the boundary, while the right-hand side is the current just inside the boundary and is obtained by considering the contributions to the current from the incident distribution, the reflected current, and the current transmitted from the distribution incident on the right face of the region. In similar manner, continuity of current across the right face requires

$$j_r = \phi_\ell\left(\frac{1}{2} T_{10}\right) + j_\ell\left(\frac{3}{2} T_{11}\right) + \phi_r\left(\frac{1}{2} R_{10} - \frac{1}{4}\right) + j_r\left(\frac{1}{2} - \frac{3}{2} R_{11}\right) .$$

On adding and subtracting these two equations, and rearranging, there results[106]

$$\frac{j_\ell - j_r}{\phi_\ell + \phi_r} = \frac{1}{2}\,\frac{1 - 2R_{10} - 2T_{10}}{1 + 3R_{11} + 3T_{11}} = \alpha$$

and

$$\frac{j_\ell + j_r}{\phi_\ell - \phi_r} = \frac{1}{2}\,\frac{1 - 2R_{10} + 2T_{10}}{1 + 3R_{11} - 3T_{11}} = \beta .$$

These two combinations of surface currents and fluxes are seen to depend on the functions of the transmission and reflection coefficients which have been labeled α and β. Thus, in a particular case, α and β can be calculated and these relations used as matching conditions. In the special case, where the absorbing region is symmetrically located (i.e., the center of the absorbing region is a symmetry or cell boundary), the additional requirements

$$j_r = -j_\ell$$

$$\phi_r = \phi_\ell$$

give an indeterminate form for β; but this relation is no longer needed. The remaining relation becomes

$$\frac{j_\ell}{\phi_\ell} = \alpha = \frac{1}{2}\,\frac{1-2(R_{10}+T_{10})}{1+3(R_{11}+T_{11})}$$

which is essentially the common logarithmic boundary condition.

There are two additional methods of introducing blackness theory into diffusion theory, and these are often more convenient than the boundary conditions just obtained. In both cases, the idea is to introduce effective constants into a diffusion-theory treatment of the absorbing region in such a way as to reproduce the blackness matching conditions. In one case, these effective (or fictitious) constants are found for the diffusion differential equation; in the other case, for the difference equation corresponding to the differential equation. In the case of the differential equation one has

$$\nabla^2 \phi(x) - k^2 \phi(x) = 0$$

with the solution

$$\phi(x) = Ae^{kx} + Be^{-kx}$$

where

$$k^2 = \frac{\Sigma_a}{D}$$

On choosing the origin of coordinates $x = 0$ at the left face of the region and denoting the thickness of the region by τ, the fluxes and currents at the left and right faces become

$$\phi_\ell = A + B$$

$$\phi_r = Ae^{k\tau} + Be^{-k\tau}$$

$$j_\ell = -kD(A - B)$$

$$j_r = -kD\left(Ae^{k\tau} - Be^{-k\tau}\right).$$

The combinations of these surface values

$$\frac{j_\ell - j_r}{\phi_\ell + \phi_r}$$

and

$$\frac{j_\ell + j_r}{\phi_\ell - \phi_r}$$

are equated to α and β from blackness theory, respectively.

The first function is

$$\frac{j_\ell - j_r}{\phi_\ell + \phi_r} = -kD\,\frac{A\left(1 - e^{k\tau}\right) - B\left(1 - e^{-k\tau}\right)}{A\left(1 + e^{k\tau}\right) + B\left(1 + e^{-k\tau}\right)} = \alpha$$

and the second

$$\frac{j_\ell + j_r}{\phi_\ell - \phi_r} = -kD\,\frac{A\left(1 + e^{k\tau}\right) - B\left(1 + e^{-k\tau}\right)}{A\left(1 - e^{k\tau}\right) + B\left(1 - e^{-k\tau}\right)} = \beta.$$

On multiplying these equations one finds

$$k^2D^2 = \alpha\beta,$$

the remaining factors equaling unity, as can be seen by carrying out the multiplications involved. On dividing the second relation into the first, and after some manipulation, there results

$$\left(\frac{e^{k\tau} - 1}{e^{k\tau} + 1}\right)^2 = \frac{\alpha}{\beta}.$$

These are solved for Σ_a and D in terms of α and β. Thus,

$$D\Sigma_a = \alpha\beta$$

and

$$k = \sqrt{\Sigma_a/D} = \frac{1}{\tau} \ln\left(\frac{1 + \sqrt{\alpha/\beta}}{1 - \sqrt{\alpha/\beta}}\right)$$

or

$$\Sigma_a = \frac{\sqrt{\alpha\beta}}{\tau} \ln\left(\frac{1 + \sqrt{\alpha/\beta}}{1 - \sqrt{\alpha/\beta}}\right)$$

and

$$D = \tau\sqrt{\alpha\beta}\left[\ln\frac{1 + \sqrt{\alpha/\beta}}{1 - \sqrt{\alpha/\beta}}\right]^{-1}.$$

As stated earlier, the use of these constants in the diffusion equation will give the same absorption and transmission by the region in question as would be obtained from the blackness matching conditions. However, if a finite difference solution is to be undertaken, a different set of effective constants may be employed with a built-in mesh correction, which allows a very coarse mesh to be used. In this case, the difference equation

$$-D\frac{\phi_{n+1} - 2\phi_n + \phi_{n-1}}{h^2} + \Sigma_a\phi_n = 0$$

takes the place of the diffusion equation and has the solution

$$\phi_n = Ae^{nkh} + Be^{-nkh}$$

where, as before, $k^2 = \Sigma_a/D$, h is the mesh spacing, and n is an integer, and one must require

$$\cosh kh - 1 = \frac{k^2h^2}{2}.$$

The surface fluxes are now

$$\phi_\ell = A + B$$

$$\phi_r = Ae^{Nkh} + Be^{-Nkh}$$

where $Nh = \tau$. The difference expression for the current is

$$j_n = -\frac{D}{2h}(\phi_{n+1} - \phi_{n-1}) .$$

Thus

$$j_\ell = -\frac{D}{h}\sinh kh(A - B)$$

and

$$j_r = -\frac{D}{h}\sinh kh(Ae^{k\tau} - Be^{-k\tau}) .$$

The ratios for α and β can be combined to give

$$\frac{\beta + \alpha}{\beta - \alpha} = \frac{j_\ell \phi_\ell + j_r \phi_r}{j_\ell \phi_r + j_r \phi_\ell}$$

which on substitution leads to

$$\frac{\beta + \alpha}{\beta - \alpha} = \cosh k\tau .$$

On solving this last result for k, one obtains

$$k = \frac{1}{\tau}\cosh^{-1}\left(\frac{\beta + \alpha}{\beta - \alpha}\right).$$

Similar steps lead to

$$\alpha + \beta = 2\frac{j_\ell \phi_\ell + j_r \phi_r}{\phi_\ell^2 - \phi_r^2} = \frac{2D}{h}\frac{\sinh kh}{\tanh k\tau}$$

which fixes D as

$$D = \frac{h(\alpha + \beta)}{2\sinh kh}\tanh k\tau$$

where k has been determined above, and τ, h, α, and β are given. Finally, from

$$\cosh kh - 1 = \frac{k^2 h^2}{2}$$

one obtains

$$\Sigma_a = \frac{2D}{h^2}(\cosh kh - 1) \cdot$$

At this point it is worthwhile to mention a variation on blackness theory based on the Milne problem, which considers a source at $x = -\infty$ with the neutrons migrating through a scattering medium to a vacuum at $x = 0$. This is another idealized representation of the real physical situation which has often been used to obtain a boundary condition for a perfectly absorbing region. The logarithmic boundary condition $\alpha = j/\phi$ for this case is 0.5 from blackness theory and 0.469 from the Milne problem, provided there is very little absorption in the source region. In the case where the Milne problem is taken as the actual problem, use of 0.469 for the boundary condition gives the exact current into the perfect absorber, and the blackness theory boundary condition yields a value for the current which is in error by about 6 percent. The problem analogous to the Milne problem, replacing the vacuum with an absorbing and scattering medium, cannot be solved rigorously. A procedure which has been used in some cases is to multiply the logarithmic boundary condition α obtained from blackness theory by the ratio of the no-absorption Milne problem α to the blackness-theory α for a perfect absorber (i.e., by 0.469/0.5). This is often called dirty blackness and, although it has little theoretical justification, the procedure works well in many cases.

Finally, it should be pointed out that results similar to those of the blackness theory results presented here have been given by Wachspress[101] under the name "Thin Region Theory." The matching conditions on diffusion solutions are the same as the double-P_0 conditions given here, but are applied to the P_1 approximation. This allows all transport coefficients to be stated in terms of the escape probability. The use of mesh-corrected fictitious constants was first introduced in this reference, and a procedure corresponding to the $DB1_0$ approximation is there described.

3.7 APPROXIMATIONS TO MULTIGROUP METHODS

G. P. Calame and M. Goldsmith

A. Introduction

Multigroup calculations of thermal neutron transport, which have been described in Sect. 3.4, consume considerable time

on computing machines. A large-scale two-dimensional multigroup calculation would be prohibitively long with any of the computers now available. In addition, in those problems which involve large regions where up-scattering is much more probable than the combined leakage and absorption, obtaining convergence is time consuming. Partially to circumvent some of the limitations of the multigroup method, especially those of long computing times the method requires, it is natural to attempt to simplify the problem by reducing considerably the number of energy groups with which the computations are performed, so that at most only a few groups are retained in the calculations. This class of approximations, the so-called few-group methods, are the subject of this section.

The most drastic reduction which can be made is that which retains only one group of neutrons. These one-group models described in Sect. 3.7.B consider all neutrons below a more or less arbitrarily selected energy, E_c, to be thermal neutrons, the spatial migration of which is assumed to be describable by a single, energy-independent equation. The constants appearing in the equation are cross sections averaged over the thermal energy range according to some recipe. The one-group models have the advantage of mathematical simplicity, so that computations in simple geometries may often be performed analytically, while calculations in complicated geometries are relatively simple to program for high-speed computers and require relatively little computing time. On the other hand, the one-group models may be too much of an oversimplification of a physically complicated problem, so that uniformly good results are not obtained by their use.

The mathematically simple one-group models described in Sect. 3.7.B frequently do not approximate adequately the multigroup models which, for purposes of the present section, will be taken as standards. The somewhat more complex few-group methods to be described have been developed more adequately to approximate the multigroup results. These few-group models are of two principal types. The more conventional method described in Sect. 3.7.C regards the thermal energy region as being divided into a few, nonoverlapping energy ranges (groups), and uses simple, usually infinite region, multigroup spectra to generate cross sections for the few energy group spatial calculation. The second method considers the neutrons to be distributed in a few populations, each of which covers the entire thermal energy range, and develops equations governing the migration of these few overlapping populations. This method is described in Sect. 3.7.D. Both methods may be applied very profitably to thermal neutron problems and

are in fact capable of giving excellent agreement with multigroup calculations in a small fraction of the computing time necessary for the multigroup calculations.

A cardinal consideration in all thermal energy calculations is the formulation of the scattering kernel. One approach to this problem, and that which is used in this and the following section, has been to try simple prescriptions which yield measured spectra and diffusion constants. Although the Radkowsky kernel, described in Sect. 3.2, has been chosen for use in this section, it will be clear that the methods discussed can be used with any kernel.

B. One-Group Methods

Most of the one-group models may be regarded as an attempt to solve the space-energy diffusion equation* in the j^{th} region of a multiregion problem

$$-\nabla\cdot D^j(E)\nabla\phi^j(\vec{r},E)+\left[\Sigma_a^j(E)+\Sigma_s^j(E)\right]\phi^j(\vec{r},E)$$

$$=\int_o^{E_c}\Sigma_s^j(E'\to E)\phi^j(\vec{r},E')dE'+S^j(\vec{r},E) \qquad \text{Eq. (3.261)}$$

by assuming that the spectrum everywhere in the j^{th} region is some known spectrum $\psi^j(E)$, so that $\phi^j(\vec{r},E)=\phi^j(\vec{r})\psi^j(E)$. If this assumption is made in Eq. (3.261), and the result integrated over energy, one obtains

$$-\nabla\int_0^{E_c}D^j(E)\psi^j(E)dE\,\nabla\phi^j(\vec{r})+\phi^j(\vec{r})\int_0^{E_c}\left[\Sigma_a^j(E)+\Sigma_s^j(E)\right]\psi^j(E)dE$$

$$=\phi^j(\vec{r})\int_0^{E_c}dE\int_0^{E_c}\Sigma_s^j(E'\to E)\psi^j(E')dE'+\int_0^{E_c}S^j(\vec{r},E)dE\,.$$

Eq. (3.262)

E_c may be regarded as a cutoff energy, chosen so that upscattering for an energy $E>E_c$ is negligible. In that case, the upper limit E_c of the E integration in the first term on the right of Eq. (3.262) may be replaced by infinity, and the order

*The diffusion equation is used here for purposes of exposition. The arguments that follow may be used in higher order transport approximations.

of integration changed so that the E integration is performed first. Since one has

$$\Sigma_s^j(E') = \int_0^\infty \Sigma_s^j(E' \to E)\,dE$$

it is evident that the last term on the left of Eq. (3.262) cancels the first term on the right. With the normalization

$$\int_0^{E_c} \psi^j(E)\,dE = 1$$

for the spectral shape function $\psi^j(E)$, Eq. (3.262) becomes the usual one-group diffusion equation for region j

$$-\nabla \cdot D^j \nabla \phi^j(\vec{r}) + \Sigma_a^j \phi^j(\vec{r}) = S^j(\vec{r}) \qquad \text{Eq. (3.263)}$$

where

$$D^j = \int_0^{E_c} D^j(E)\,\psi^j(E)\,dE$$

and

$$\Sigma_a^j = \int_0^{E_c} \Sigma_a^j(E)\,\psi^j(E)\,dE$$

are the spectrum-averaged diffusion constant and absorption cross section, respectively. A spectrum-averaged fission cross section may be defined similarly.

The various one-group models are obtained from the foregoing by specifying the spectral shape functions to be used. In the diffusion approximation, the resulting one-group equations are solved with the usual boundary conditions of flux and current continuity.

1. *Maxwellian Spectrum*

In the Maxwellian spectrum model $\psi^j(E)$ is the Maxwellian distribution $M(E)dE = (kT)^{-2} E \exp(-E/kT)dE$, with the average energy $3/2\,kT$ corresponding to the ambient temperature T of the region. The chief advantage of the model is simplicity. The spectrum and, therefore, the average microscopic cross sections that enter into Eq. (3.263) depend only on T and not on the region composition. In addition, the spatial flux transients that occur near interfaces with other media are characterized by diffusion lengths computed with all pertinent constants averaged over the Maxwellian spectrum. These Maxwellian diffusion lengths are approximately the correct ones to use in many transient calculations,[66,70,109,110] so that the model gives flux transients that often reasonably approximate the observed ones and, therefore, gives quantities, such as power peaking near water gaps, quite well.

The model, however, has a number of failings: (1) If the ambient temperatures of adjacent regions are different, the spectrum-averaged microsopic cross sections will be discontinuous at the interfaces between the regions and will result in a calculated discontinuity of foil activations at the boundaries. (2) Spatial flux transients near lumped absorbers are not predicted correctly. The discrepancies arise because lumped absorbers severely distort spectra in their vicinity, so that Maxwellian diffusion lengths are not the correct ones to use. (3) The model fails to predict reactor criticality very well.

The reason for this last difficulty is that at each point in fuel region j the model gives the ratio of fission rate to absorption rate, Σ_f^j/Σ_a^j, as the ratio of Maxwellian averages. In general, however, the spectrum in the medium will not be predominantly Maxwellian because the slower neutrons have shorter life expectancies in an absorbing region than do the faster neutrons. The more rapid disappearance of the slower neutrons causes an upward shift of the most probable neutron velocity, an effect commonly known as spectral hardening. If both the absorption and fission cross sections obeyed the $1/v$ law, the ratio of average cross sections Σ_f^j/Σ_a^j would be independent of the averaging spectrum $\psi^j(E)$. However, the cross sections are not all $1/v$. The fuel U^{235}, for example, has a resonance at 0.2 ev, and other materials that may be present in a reactor are likewise non-$1/v$ absorbers.[26] The ratio Σ_f^j/Σ_a^j, where the averages are taken over the spectrum actually present in the material, is therefore different from the Maxwellian-averaged ratio, leading to incorrect calculations of criticality.

2. Hardened Maxwellian Spectrum

In an effort to overcome the difficulty of (3) above, a simple scheme is sometimes used to account for the spectral hardening. The method is to treat the spectral shape function as a shifted Maxwellian with most probable energy corresponding to a calculated effective temperature, T_{eff}, which depends on the absorption present in the region. A number of prescriptions relating T_{eff} to T, the ambient temperature of the region (in absolute degrees), have been suggested.[111, 112] These are generally of the form

$$T_{\text{eff}} = T\left(1 + c\,\frac{\Sigma_a}{\xi\Sigma_s}\right)$$

where Σ_a is the (approximately) $1/v$ absorption cross section at energy kT, $\xi\Sigma_s$ is the slowing-down power at a thermal cutoff energy E_c of several kT, and c is an empirical constant. Knowledge of T_{eff} permits the computation of the average cross sections in Eq. (3.263).[112, 113] The model gives a reasonable description of infinite medium neutron spectra up to energies of the order of $4kT_{\text{eff}}$ (0.1 to 0.2 ev), but not at higher energies, at which the spectra begin to exhibit $1/E$ behavior. $E_c \approx 4kT_{\text{eff}}$ is, therefore, taken to be the upper limit of the thermal group.

Because the model allows for spectral hardening, it is reasonably good for criticality calculations in large cores, since the ratio Σ_f^j / Σ_a^j is given fairly well distant from interfaces. The scheme is not, however, without difficulties. First, the description of the thermal flux as a shifted Maxwellian is a poor one for values of $\Sigma_a/\xi\Sigma_s$ in excess of approximately 0.4 and in the presence of appreciable amounts of non-$1/v$ absorbers, so that the scheme is of use only in a limited range of reactor compositions. Second, the thermal diffusion lengths calculated by the model are not the approximately correct ones given by the unshifted Maxwellian averages, but are considerably longer. Thus, power peakings are not correctly computed. Finally, since the T_{eff} in adjacent regions are usually different, even if the ambient temperatures are the same, use of the model results in a calculated discontinuity of foil activations at boundaries between dissimilar media, since an abrupt change in T_{eff} implies an unrealistic discontinuity in the spectrum and, therefore, in the averaged microscopic cross sections at the boundary.

3. *Wigner-Wilkins and Related Constants*

The description of the hardening of neutron spectra in terms of Maxwellian distributions at effective temperatures is of limited use because of the difficulties mentioned above. The first of the difficulties may be overcome by the use of alternate, but somewhat more complex, descriptions of the hardening which have been developed, and which prove more useful in describing the thermal neutron spectra, especially in the range 0.1 to 1.0 ev. These alternate methods are all similar in that the spectrum expected to be present deep in the j^{th} region is computed numerically, using some model for the thermal neutron scattering law, and the computed spectrum is subsequently used to obtain the thermal average cross sections numerically.

In many water-moderated reactors absorption even in the core regions is often much less likely than scatterings, so that the neutron spectrum is expected to be relatively insensitive to the scattering law (because, in the limit as $\Sigma_a \to 0$, the detailed balance condition on the scattering law ensures that all the laws yield the same spectrum). Consequently, a number of models for the scattering law have been used. The simplest model of thermalization in aqueous media is that introduced by Wigner and Wilkins,[20] who represent the moderator as a gas of hydrogen atoms exhibiting a Maxwellian distribution of velocities. Under these conditions Wigner and Wilkins were able to derive a differential equation for the neutron spectrum. This equation forms the basis of the codes[114, 115] prepared by Amster and his coworkers. Alternative but more complicated models that have been used are a monatomic gas model of mass 2.75, proposed by Clendenin,[21] and extensions of the Nelkin model[29] described in Sect. 3.2.

The models described here can be applied to an almost unlimited range of core compositions, and yield good values for core criticality in asymptotic regions (i.e., in regions the bulk of which are far removed from interfaces). However, the other defects present in the hardened Maxwellian model also hold in the models under discussion, viz., the thermal diffusion lengths are too long so that power peakings are not correctly computed, and foil activations are calculated as being discontinuous across interfaces.

4. *Mixed Number Density Model*[116]

The chief advantage of the Wigner-Wilkins and related schemes (good values for the multiplication constant in

asymptotic regions) and some of the advantages of the Maxwellian scheme (Maxwellian-averaged diffusion lengths and, often, continuity of activation) may in some cases be realized in a single one-group model by using as a variable the neutron number density rather than the neutron flux. The use of the number density rather than the flux is motivated by the observation that the quantity of interest in both experimental analysis and nuclear design is the activation of an absorber. Thus, it is reasonable that activation continuity $(\sigma\phi)$ rather than flux continuity (ϕ) be used as a boundary condition. For a $1/v$ absorber, this may be obtained by using the number density as a variable, since

$$\int \sigma(E)\phi(E)dE \propto \int \frac{1}{v} v n(E)dE = \int n(E)dE = n \qquad \text{Eq. (3.264)}$$

where $n(E)$ is the energy-dependent neutron density. In terms of the number density, Eq. (3.263) is

$$-\nabla \cdot \overline{Dv} \nabla n + \overline{\Sigma_a v} n = S \qquad \text{Eq. (3.265)}$$

where the bars represent spectrum-averaged quantities, and the region indices j have been dropped for convenience.

Since it is desired to have the model yield correctly the reaction rate in asymptotic regions, $\overline{\Sigma_a v}\, n$ is equated to the asymptotic absorption rate, whence

$$\overline{\Sigma_a v} = \frac{\int \Sigma_a(E)\,\phi_{as}(E)dE}{n} = \frac{\int \Sigma_a(E)\,\phi_{as}(E)dE}{\int \frac{1}{v}\phi_{as}(E)dE} = \frac{\langle \Sigma_a \rangle_{as}}{\langle \frac{1}{v} \rangle_{as}}$$

where $\phi_{as}(E)$ is the asymptotic spectrum in the region. If, for example, a SOFOCATE[114] spectrum is assumed for $\phi_{as}(E)$, then

$$\overline{\Sigma_a v} = \frac{\langle \Sigma_a \rangle_{SOF}}{\langle \frac{1}{v} \rangle_{SOF}} . \qquad \text{Eq. (3.266)}$$

The fission cross section $\overline{\Sigma_f v}$ is, similarly,

$$\overline{\Sigma_f v} = \frac{\langle \Sigma_f \rangle_{SOF}}{\langle \frac{1}{v} \rangle_{SOF}} .$$

The diffusion constant is obtained by equating current terms in the flux and number density equations,

$$\overline{Dv} = \frac{\int D(E)\,\frac{\partial}{\partial x}\,\phi(x,E)\,dE}{\int \frac{\partial}{\partial x}\,n(x,E)\,dE} = \frac{\int D(E)\,\frac{\partial}{\partial x}\,\phi(x,E)\,dE}{\int \frac{1}{v}\frac{\partial}{\partial x}\phi(x,E)\,dE} .$$

That is, $\overline{Dv}$ is a coefficient defined in terms of averages over a gradient spectrum. Since gradient spectra near water channels tend to be Maxwellian in water-moderated, uranium-fueled reactors,[70, 109, 116] $\overline{Dv}$ in Eq. (3.265) is taken as

$$\overline{Dv} = \frac{\langle D\rangle_{\text{Max}}}{\left\langle \frac{1}{v}\right\rangle_{\text{Max}}} . \qquad \text{Eq. (3.267)}$$

In the above equations, $\langle\,\rangle$ denotes an average quantity, e.g.,

$$\langle \Sigma_a \rangle_{\text{Max}} = \int \Sigma_a(E) M(E)\,dE \Big/ \int M(E)\,dE .$$

Equation (3.265) is solved formally in the same way as in Eq. (3.263), subject to the boundary conditions of continuity of $\overline{Dv}\,\nabla n$ and n.

The thermal group representation given by Eqs. (3.265) to (3.267, has been successful in duplicating thermal activation shapes, as calculated by the thermal multigroup code SLOP-1,[85] largely because the ratio $\langle \Sigma_a \rangle_{\text{SOF}} / \langle 1/v \rangle_{\text{SOF}}$ is similar to $\langle \Sigma_a \rangle_{\text{Max}} / \langle 1/v \rangle_{\text{Max}}$ for most regions of interest in water-moderated uranium-fueled reactors. Hence, the diffusion length in the scheme

$$L^2 = \frac{\langle D\rangle_{\text{Max}}}{\left\langle \frac{1}{v}\right\rangle_{\text{Max}}} \cdot \frac{\left\langle \frac{1}{v}\right\rangle_{\text{SOF}}}{\langle \Sigma_a \rangle_{\text{SOF}}} \approx \frac{\langle D\rangle_{\text{Max}}}{\left\langle \frac{1}{v}\right\rangle_{\text{Max}}} \cdot \frac{\left\langle \frac{1}{v}\right\rangle_{\text{Max}}}{\langle \Sigma_a \rangle_{\text{Max}}} = \frac{\langle D\rangle_{\text{Max}}}{\langle \Sigma_a \rangle_{\text{Max}}}$$

is essentially the nearly correct Maxwellian diffusion length. In addition, the local thermal utilization

$$\overline{\Sigma_f v} \Big/ \overline{\Sigma_a v} = \frac{\langle \Sigma_f \rangle_{\text{SOF}}}{\left\langle \frac{1}{v}\right\rangle_{\text{SOF}}} \cdot \frac{\left\langle \frac{1}{v}\right\rangle_{\text{SOF}}}{\langle \Sigma_a \rangle_{\text{SOF}}} = \langle \Sigma_f \rangle_{\text{SOF}} \Big/ \langle \Sigma_a \rangle_{\text{SOF}}$$

is the asymptotic one, which leads to good values for the reactor multiplication constants.

The model has two shortcomings. The fact that the diffusion length is the Maxwellian one leads, as in the Maxwellian spectrum model, to an incorrect prediction of transients near lumped absorbers. Also, the fact that the scheme uses the nearly correct Maxwellian diffusion lengths in other transient calculations (e.g., power peaking near water gaps) depends on the ratio $\Sigma_a(E)/(1/v)$ being nearly independent of energy. In regions containing sizable amounts of non-$1/v$ absorber, the last ratio is not energy-independent. Nevertheless, the scheme is a highly useful one for the calculation of many of the reactor types considered in this volume.

C. Conventional Few-Group Approximations

R. M. Cantwell and M. Goldsmith

The discussion of one-group models given in Sect. 3.7.B was based on the selection of an assumed flux spectrum and averaging the cross sections over that spectrum [Eq. (3.262)]. In this discussion, numerical examples are given which illustrate some of the deficiencies of one-group models. A suitable approximation to the multigroup representation of thermal neutrons may be obtained by breaking up the integral of Eq. (3.262) into a few intervals between E=0 and E=E_C. This results in a corresponding set of equations coupled through the scattering terms where the cross sections in each of the few groups are averaged over a portion of the thermal neutron energy range.

While this procedure is straightforward in the diffusion approximation, the calculation of the few-group cross sections for the higher order transport approximations is more involved. This section defines the appropriate few-group cross sections to be used in the P_1, double-P_1, and P_3 approximation and the use of the multigroup program SLOP-1 to obtain them. This is followed by a comparison of few-group and multigroup calculations for both diffusing regions and thin absorbing plates, and completed with a discussion of the use of blackness theory (see Sect. 3.6) in few-group calculations.

1. The Few-Group Equations

The derivation of the few-group equations proceeds in the same manner as for the multigroup equations in Sect. 3.4 and will not be repeated here. Referring to Eqs. (3.160) to (3.163)

in Sect. 3.4, the double $-P_1$ equations, assuming flux but no higher F_n transfer, were shown to be

$$\frac{\partial F_1^i}{\partial x} + \Sigma_0^i F_0^i = S^i + \sum_j \alpha_0^{i,j} F_0^j$$

$$\frac{1}{3}\frac{\partial}{\partial x}(F_0^i + 2f_2^i) + \Sigma_1^i F_1^i = 0$$

$$\frac{2}{5}\frac{\partial F_1^i}{\partial x} + \frac{8}{15}\frac{\partial f_3^i}{\partial x} + \Sigma_2^i f_2^i = 0$$

$$\frac{1}{3}\frac{\partial f_2^i}{\partial x} + \Sigma_3^i f_3^i = 0 \qquad \text{Eq. (3.268)}$$

where the superscripts indicate the i^{th} group. S^i and $\sum_j \alpha_0^{i,j} F_0^j$ are sources in group i from energies, respectively, above and below the thermal cutoff energy, and

$$\Sigma_0^i = \Sigma_a^i + \Sigma_{sH}^i = \Sigma_t^i - \Sigma_{sh}^i$$

$$\Sigma_1^i = \Sigma_t^i - \bar{\mu}_h^i \Sigma_{sH}^i - \bar{\mu}_H^i \Sigma_{sh}^i$$

$$\Sigma_2^i = \frac{16}{15}\Sigma_t^i = \frac{8}{15}\Sigma_3^i$$

with the subscripts H and h indicating hydrogen and heavy elements, respectively. Introducing the substitutions $\psi_1 = F_0 + 2f_2$ and $\psi_2 = f_2$, Eqs. (3.268) may be written

$$-D_1^i \nabla^2 \psi_1^i + \Sigma_{t,1}^i \psi_1^i = 2\Sigma_{t,1}^i \psi_2^i + S^i + \sum_{j \neq i} \alpha_0^{i,j} F_0^j \qquad \text{Eq. (3.269a)}$$

$$-D_2^i \nabla^2 \psi_2^i + \Sigma_{t,2}^i \psi_2^i = \frac{3}{4}\left[\Sigma_{t,1}^i \psi_1^i - S^i - \sum_{j \neq i} \alpha_0^{i,j} F_0^j\right] \qquad \text{Eq. (3.269b)}$$

with

$$D_1 \equiv -\frac{F_1}{\nabla \psi_1}, \; D_2 \equiv -\frac{f_3}{\nabla \psi_2}, \; \Sigma_{t,1}^i = \Sigma_0^i - \alpha_0^{i,i}$$

and

$$\Sigma_{t,2}^i = \frac{3}{2}\Sigma_{t,1}^i + 2\Sigma_t^i \; .$$

The cross sections and diffusion constants appearing in Eqs. (3.269) may be edited from multigroup calculations of the F_0 and f_2 spectra in homogeneous quasi-infinite regions. One way of obtaining this few-group edit is from a SLOP-1 calculation at a single space point. Although the editing procedure has been described in detail in Ref. 85, it may be well to include a review of its salient features here. Consider the one-space point multigroup calculation illustrated in Fig. 3.36. Upon adoption of central differencing, $\nabla F_0(h/2)$ is approximated as $1/h\,F_0(h)$ and $\nabla^2 F_0(h)$ as $\frac{-2}{h^2}F_0(h)$. This latter relationship allows one to impose any desired buckling on the multigroup flux used to form the few-group constants.

The approximation to ∇F_0 forces the gradient spectrum to be proportional to the flux spectrum, so that integrating over the i^{th} few group one has in the P_1 approximation

$$D_1^i = \frac{-\int_i F_1\,dE}{\int_i \nabla F_0\,dE} = \frac{-\int_i D_1 \nabla F_0\,dE}{\int_i \nabla F_0\,dE} = \frac{-\int_i D_1 F_0\,dE}{\int_i F_0\,dE} \qquad \text{Eq. (3.270)}$$

where $D_1 = \frac{1}{3}\lambda$ transport. The appropriateness of D^i near interfaces, where the flux and gradient spectra may in fact be quite different, is open to serious question and will be considered later.

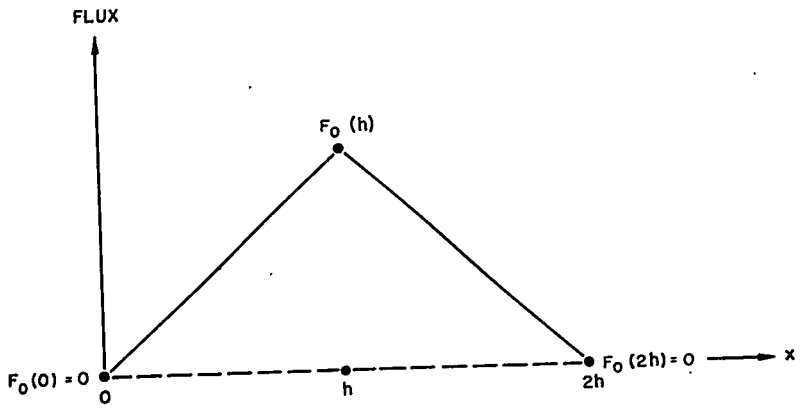

FIGURE 3.36. One-Point Multigroup Calculation.

The few-group isotropic transfer rates $\alpha_0^{i,j} F_0^j$ give the number of neutrons per cm^3 transferred per second from group j to group i so that, since $\alpha_0^{i,j}\ (i \neq j)$ has been assumed negligible for all elements but hydrogen,

$$\Sigma_{t,1}^i = \Sigma_a^i + \Sigma_{sH}^i - \alpha_0^{i,i} + D_1^i B_{tr}^2$$

where Σ_a^i is the absorption cross section, Σ_{sH}^i the hydrogen scattering cross section, and $D_1^i B_{tr}^2$ approximates any transverse leakage present. It is clear from Eq. (3.269a) that for P_1 calculations the few-group parameters, Σ_a^i, $\alpha_0^{i,i}$, and Σ_{sH}^i are to be obtained by flux weighting.

The parameter S_0^i represents that fraction of the epithermal neutrons which is scattered directly into the i^{th} group. Since moderation has been assumed to be by free protons only,

$$S_0^i(r) = S(r) \frac{\int_i erf\ \sqrt{E/kt}\, dE}{\int_0^{E_c} erf\ \sqrt{E/kT}\, dE} = \frac{S(r)\chi^i}{\sum_i \chi_i} \qquad \text{Eq. (3.271)}$$

where E_c is the highest energy of the thermal range. The χ_i included in the few-group edit are approximations by trapezoidal rule to these integrals. In comparing few-group and multigroup calculations, one should note that the SLOP-1 epithermal source is $S(r)\chi^i$, so that

$$S_0^i(\text{SLOP-1}) = S_0^i \left[\left(E_c - \frac{kT}{2} \right) erf \sqrt{E_c/kT} + \frac{kT}{\sqrt{\pi}} \sqrt{\frac{E_c}{kT}}\ e^{-E_c/kT} \right]$$

$$\approx S_0^i \left[E_c - \frac{kT}{2} \right] \text{ for } E_c >> kT$$

a condition adequately fulfilled for the calculations, since $E_c = 25\ kT$.

For double-P_1 calculations [Eqs. (3.269)] one needs in addition

$$D_2^i = \frac{-\int_i f_3 dE}{\int_i \Delta\psi_2 dE}$$

where f_3 is the double-P_1 approximation to F_3, and $\Sigma^i_{t,2} = 2\Sigma^i_t + 3/2\,\Sigma^i_{t,1}$ with

$$\Sigma^i_t = \frac{\int_i (\Sigma_s + \Sigma_a)\psi_2 dE}{\int_i \psi_2\, dE}.$$

One notes that $\Sigma_{t,2}$ contains a ψ_2 averaged component Σ^i_t and an F_0 averaged component $\Sigma_{t,1}$. This unusual mixture is caused by the presence of $\psi_1 = F_0 + 2\psi_2$ as an independent variable in Eq. (3.268) and does not indicate lack of rigor in editing these cross sections.

In the P_3 approximation Eq. (3.269b) becomes

$$-D^i_2 \nabla^2 F^i_2 + \Sigma_{t,2} F_2 = 2/3 \left[\Sigma^i_{t,1}\psi^i_1 - S^i_0 - \sum_{i \neq j} \alpha^{i,j}_0 F^j_0\right] \qquad \text{Eq. (3.272)}$$

with $\Sigma_{t,2} = 5/3\,\tilde{\Sigma}^i_t + 4/3\,\Sigma^i_{t,1}$ where $\tilde{\Sigma}^i_t$ and $\Sigma^i_{t,1}$ are averaged over the P_2 and P_0 moments of the flux, respectively. The methods just described are, thus, immediately applicable to P_3 calculations.

The few-group equations have been solved iteratively, which means that the group equations are solved separately in consecutive order using the latest values obtained for the fluxes in the other groups. When the last equation has been solved, one iteration has been done. The process is repeated, starting again with the first equation, until the group fluxes are seen to be relatively unchanged from one iteration to the next. A digital program for the Philco-2000 computer treats a system of diffusion equations linked by general flux coupling[117] (i.e., isotropic scattering may transfer neutrons between any two groups). Although such a program is capable of solving a great variety of reactor problems, discussion will be limited to purely thermal calculations.

The motivation for going from multigroup to few-group thermal calculations was to reduce digital computer time. However, even the few-group calculations are unreasonably time-consuming when the equations are solved iteratively unless some method can be found to accelerate convergence. The method adopted was overrelaxation.[118]

To test the effectiveness of overrelaxation in accelerating the convergence of few thermal group calculations, several simple problems were run in P_1 approximation with a variety of overrelaxation parameters. Three of the problems dealt with an infinite medium of pure water, contained three mesh

points, and met cell boundary conditions. Water was chosen because of the usual difficulty encountered, due to its small absorption cross section, in converging a thermal few-group or multigroup calculation containing large water regions. The fourth problem treated the cell of Fig. 3.37 and contained six mesh points in each region. Figure 3.38 gives as a function of the overrelaxation parameters the number of inner iterations required to converge the flux in each group to 5×10^{-4} percent. One observes from these curves that the number of iterations, at least in the simple problems considered, can be dramatically reduced by overrelaxation. The optimum overrelaxation parameter is not very critical. Both the optimum parameter and the minimum number of iterations seem to change little as a function of the number of groups. (Theoretically, the best infinite medium overrelaxation parameters [119] are 0.607 and 0.641 in two and three groups, respectively.) With the introduction of an absorbing medium, as in the core-water cell problem, the optimum parameter decreases slightly and becomes even less critical.

2. *Comparison of Few-Group and Multigroup Results*

The cell of Fig. 3.37 contains the essential features of one-dimensional core-reflector interface problems. This configuration was treated in one, two, three, four,* and 36 groups

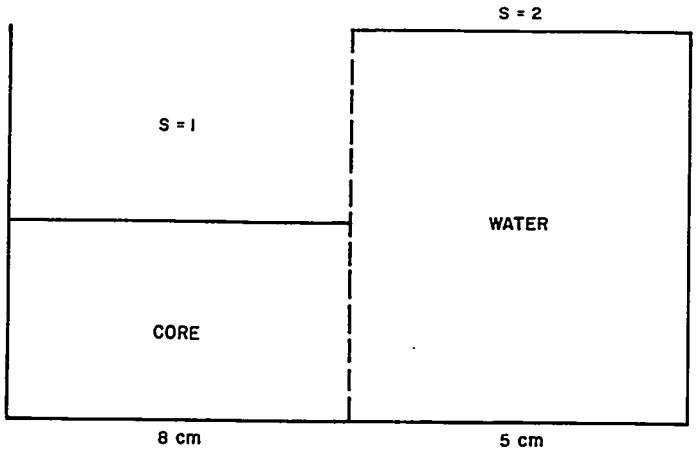

FIGURE 3.37. Cell Used in Few Thermal Group Studies.

*In the four-group scheme, group boundaries were placed at approximately kT, 4kT, 10kT, and 25kT. A three-group scheme combined the two higher groups, while the three higher groups were combined to form the two-group scheme.

using a mesh of 8 to 10 points per diffusion length. The variation of calculated power with the number of thermal groups used is shown in Fig. 3.39, while a quantitative presentation of the improvement in peak-to-average fission rates, as one passes from one to 36 thermal groups, is given in Table 3.22. One observes that a sufficiently accurate calculation of the power peaking may be carried out using only three thermal groups. The columns labeled "Max D" contain the results of calculations performed with Wigner-Wilkins averaged absorption and scattering constants but with Maxwellian averaged diffusion constants, i.e., those obtained by averaging λ transport over that portion of the Maxwellian spectrum included in the group.

From either the multigroup or few-group results it is possible to determine spatially dependent equivalent one-group constants which, when used in a one-group calculation, will yield a total flux and current at each point identical with that given by the

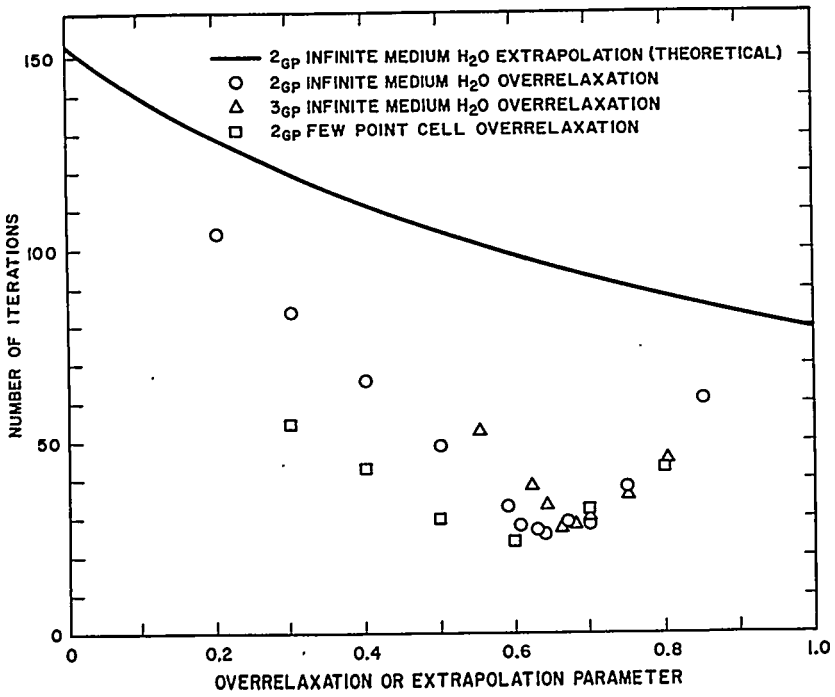

FIGURE 3.38. Convergence Behavior of Few-Group Calculation with General Flux Coupling.

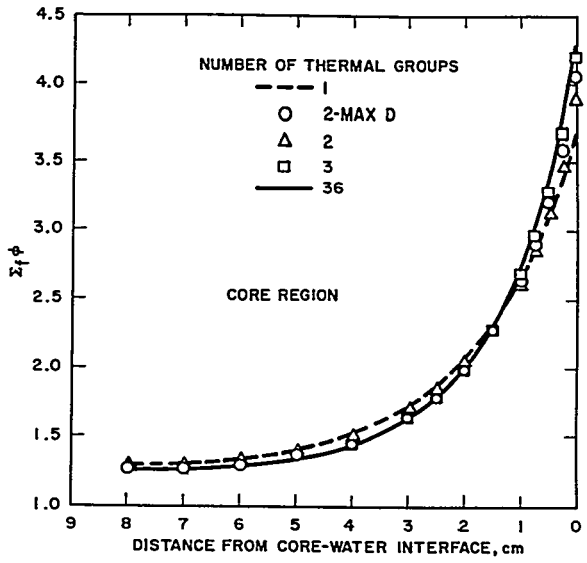

FIGURE 3.39. Power Distributions Computed by Various Multigroup Approximations.

group scheme from which they are generated. Spatially dependent one-group values of $\nu\Sigma_f$ and Σ_a associated with the power shapes of Fig. 3.39 show a uniform and rapid convergence to the multigroup result as the number of groups increases. However, convergence of the equivalent one-group diffusion constant is much slower, as is shown in Fig. 3.40. Infinite medium values of D averaged over hardened (SOFOCATE)[114] and Maxwellian spectra are shown together with pointwise D's edited from two-, three-, and 36-group results. Also shown is the pointwise D edited from a two-group scheme using appropriate portions of a Maxwellian spectrum rather than the hardened spectrum of Eq. (3.269). It appears that this two-group "Max D" is much closer to the 36-group result than is the two-group D based on a hardened spectrum. This result is obtained because, in the P_1 approximation, the pointwise equivalent one-group diffusion constant is given by

$$D = \frac{\int D(E)\nabla\phi(E)\,dE}{\int \nabla\phi(E)\,dE} .$$

TABLE 3.22 - COMPARISON OF PEAK-TO-AVERAGE POWER RATIOS

Number of Thermal Groups Employed	Peak-to-Average Power	Peak-to-Average Power (Max D)	λ*	λ* (Max D)
1	2.039	2.188	1.007	0.989
2	2.187	2.305	1.001	0.990
3	2.366	2.394	0.998	0.995
4	2.374	2.390	0.999	0.997
36	2.404	--	1.000	--

* λ is the $\iint \nu\Sigma_f \phi \, dx \, dE$ divided by the SLOP-1 (36-group) values of that parameter.

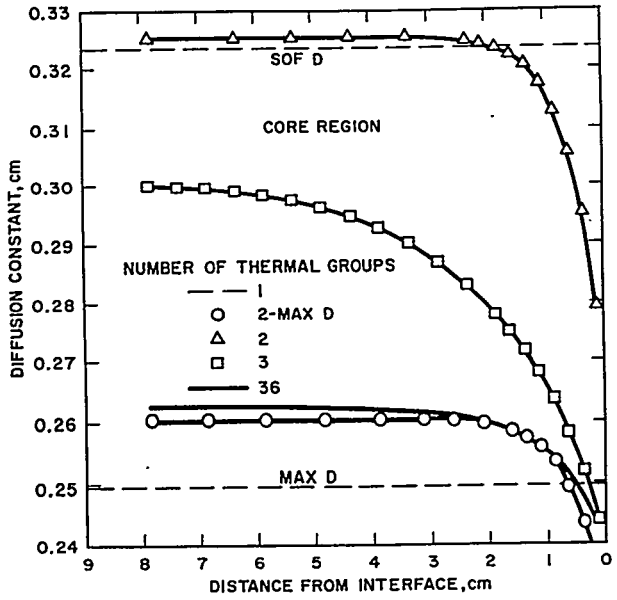

FIGURE 3.40. Equivalent One-Group Pointwise Values of the Thermal Diffusion Constant.

Since in each region of the present problem the source S is independent of position, the gradient spectrum is determined by neutrons flowing across the interface. One can show[70,109]

that far from the interface the gradient spectrum is very similar to a Maxwellian spectrum. Near the interface it would be difficult to predict a priori which method of obtaining D would be more appropriate. Table 3.22 indicates that in one- and two-groups improvement in power shape is counterbalanced by inaccuracy in the eigenvalue.

Few-group methods may be readily extended to apply to thin highly absorbing regions. Such regions present two distinct types of problems, depending upon whether one seeks the spatial dependence of reaction rates within the absorber or merely the integrated absorption rate. The latter case, which is common in control rod evaluation studies, permits replacement of the absorber by boundary conditions applied on its surface. A pointwise absorption rate calculation will be considered before returning to the boundary value problem.

A typical geometry, illustrated in Fig. 3.41, consists of a cell formed by a thin absorbing plate and adjacent core region. (The number densities of materials in the core region are: H: 0.03368, O: 0.01233 C: 0.00502, Zr: 0.02132, U^{235} :0.0001717, U^{238} :0.000012 $\times 10^{24}/cm^3$.) In the present problem the absorption cross section of the nonscattering plate varies as $1/v$ and produces an optical depth of 2 at 0.025 ev. The core material is identical with that of the preceding problem.

Few-group constants for the plate must be obtained, taking account of the absorber self-shielding, i.e., one must derive few-group Σ_a's by averaging over an approximation to the

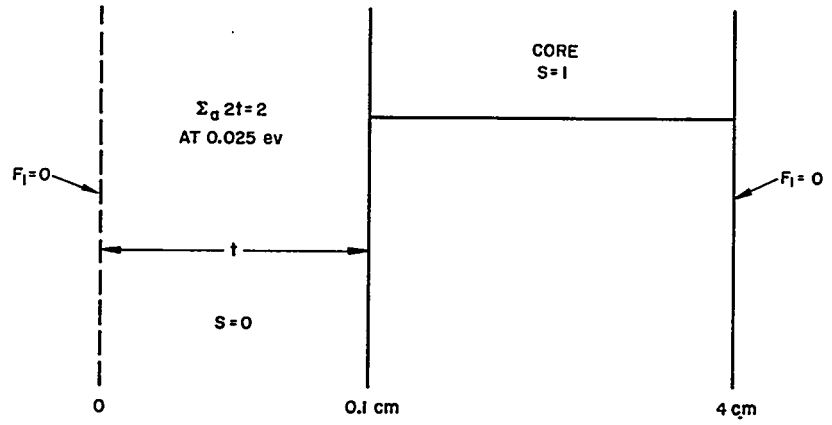

FIGURE 3.41. Core and Absorber Cell.

hardened flux in the absorber. As more and more thermal groups are used, the approximate flux need be less and less accurate.

To separate transport and spectral effects, consider first P_1 few-group and multigroup solutions to the problem of Fig. 3.41. At each energy

$$\bar{\phi}(E) = \frac{1}{2t}\int_{-t}^{t} \phi(x,E)\,dx = 1/2\left[\phi(t,E)+\phi(-t,E)\right]\frac{\tanh\left[\sqrt{\Sigma_a/D}\ t\right]}{\sqrt{D/\Sigma_a}}$$

$$= \frac{\phi(t,E)}{\sqrt{3\,\Sigma_a}}\tanh\sqrt{3\,\Sigma_a}\,t \qquad \text{Eq. (3.273)}$$

the last condition holding because one is applying cell boundary conditions, and the plate is a pure absorber of half width, t. If one approximates $\phi(t,E)$ as constant $\times\,\phi_{SOF}(E)$, where $\phi_{SOF}(E)$ is the infinite medium (SOFOCATE) core flux, there results

$$\Sigma_a^i = \frac{\int_i \phi_{SOF}(E)\tanh\left[\sqrt{3\,\Sigma_a(E)}\,t\right]dE}{\int_i \frac{\phi_{SOF}(E)\tanh\left[\sqrt{3\,\Sigma_a(E)}\,t\right]}{\Sigma_a(E)}dE} \qquad \text{Eq. (3.274)}$$

for the absorption cross section in the i^{th} group. This definition of the few-group absorption cross section was used to solve the absorber-core cell problem in one and four groups. Figure 3.42 and Table 3.23 show the excellent agreement between the four- and 36-group calculations. A very sensitive test of the few thermal group approximation is the computation of the equivalent one-group absorption cross section of a $1/v$ detector. As indicated in Fig. 3.43, the four- and 36-group parameters agree within 3 percent everywhere.

Since P_1 calculations are unrealistic in thin highly absorbing regions, a double-P_1 calculation was performed with absorption cross sections calculated from Eq. (3.274). As indicated in Table 3.23, the four- and 36-group absorption rates agree to within 0.4 percent.

3. P_3 and Double-P_1 Blackness Conditions

In many problems it is sufficient to determine the integrated absorption in a region rather than the position-dependent reaction rate, an accurate computation of which may require a large number of mesh points. (The number of mesh points in a thin absorber increases rapidly with the approximation used; a typical double-P_1 thermal calculation will require perhaps three times as fine a mesh as the corresponding P_1 calculation.) Accordingly, methods of replacing slab regions by surface boundary conditions have been developed.

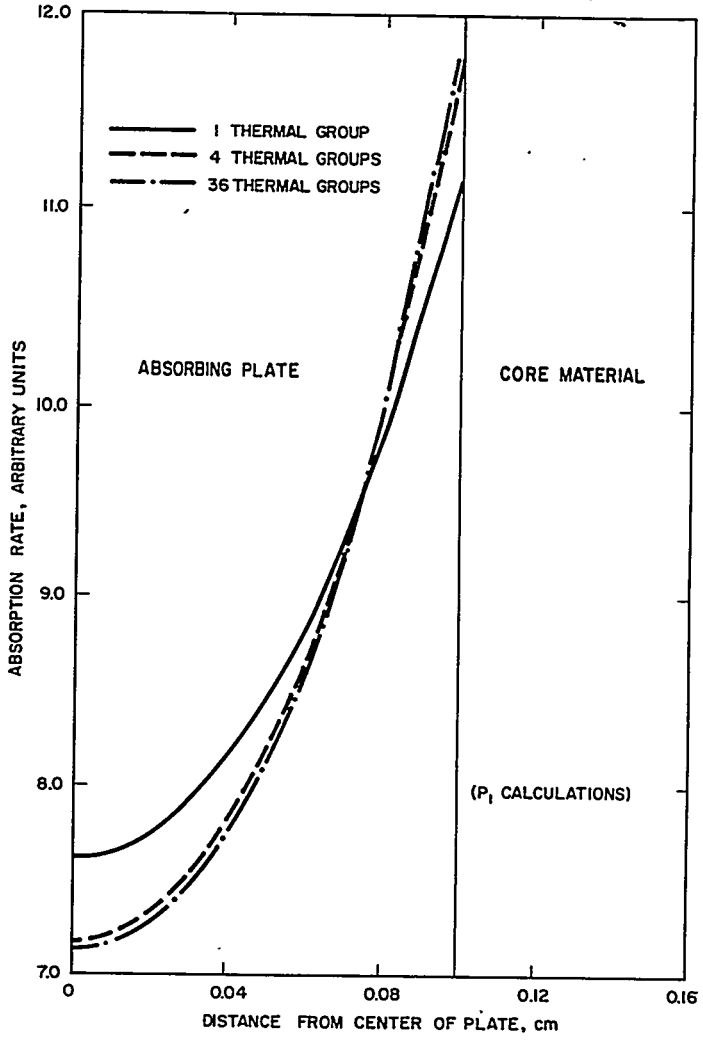

FIGURE 3.42. Comparison of One-Group, Four-Group, and 36-Group Calculations.

TABLE 3.23 - INTEGRATED ABSORPTION IN THIN PLATE

No. of Thermal Groups	P_1 Calculations $\int \Sigma_a \phi \, dx$	DP_1 Calculations $\int \Sigma_a \phi \, dx$
1	0.877	0.784
4	0.861	0.770
36	0.863	0.767

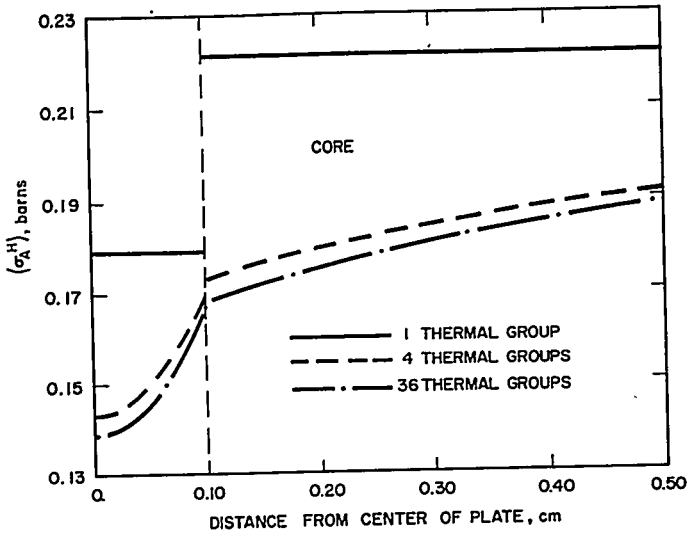

FIGURE 3.43. Microscopic Absorption Cross Section of $1/v$ Detector within and near Absorbing Plate (P_1 Calculations).

If one neglects transfer from one energy to another within a homogeneous slab, then at the + and - interfaces with the surrounding media

$$\begin{bmatrix} F_1^+ \\ F_1^- \\ F_3^+ \\ F_3^- \end{bmatrix} = -\begin{bmatrix} D_1 \nabla \psi_1^+ \\ D_1 \nabla \psi_1^- \\ D_2 \nabla \psi_2^+ \\ D_2 \nabla \psi_2^- \end{bmatrix} = \begin{bmatrix} w & y & x & z \\ -y & -w & -z & -x \\ p & r & q & t \\ -r & -p & -t & -q \end{bmatrix} \begin{bmatrix} \psi_1^+ \\ \psi_1^- \\ \psi_2^+ \\ \psi_2^- \end{bmatrix} \qquad \text{Eq. (3.275)}$$

and since fixing of the odd moments of the flux over the surface of a region uniquely determines the flux within, the entire role played by an absorber is specified by the constants $w, x, \ldots, t$. After deriving the values of these constants for appropriate monoenergetic problems, solution of the few-group problem will be considered.

To obtain monoenergetic values of $w, x,$ etc. when double-P_1 or P_3 approximations are employed in regions adjacent to the absorber, one matches [105,106] zeroeth and first moments of the flux just inside and outside the absorbing plate. The first set of boundary conditions, derived by a straightforward extension of the methods of Ref. 106, is that appropriate to a nonscattering plate when transport theory is used to calculate the flux within the absorber and a double-P_1 approximation in the surrounding media. Within the absorber, the vector flux $F(x, \mu)$ is determined by the transport equation

$$\mu \frac{\partial F(x, \mu)}{\partial x} + \Sigma_a F(x, \mu) = 0 \qquad \text{Eq. (3.276)}$$

so that

$$F(x, \mu) = F(0, \mu)\, e^{-\frac{\Sigma_a}{\mu} x} \qquad \text{Eq. (3.277)}$$

where μ is the cosine of the angle between the neutron's direction of flight and the x axis. Outside the absorber the double-P_1 approximation will be employed with Ω and χ (Fig. 3.44) representing the flux for $\mu > 0$ and $\mu < 0$, respectively. With these conventions, $\Omega = \Omega_0 + 3(2\mu - 1)\Omega_1$ and $\chi = \chi_0 + 3(2\mu + 1)\chi_1$ where

$$\Omega_N = \int_0^1 \Omega P_N(2\mu - 1)\, d\mu \quad \text{and} \quad \chi_N = \int_{-1}^0 \chi P_N(2\mu + 1) d\mu$$

The coefficients, $w, x, \ldots, t$ of Eq. (3.275) connect the full-range moments $F_n^{\pm}$ and may be found by first deriving the coupling between half-range moments and subsequently expressing the full-range moments in terms of these. Thus, at the + surface of the absorber (Fig. 3.43) the outward moving scalar flux just to the right of the interface is Ω_0^+, and equating this to the corresponding half range moment just inside the absorber yields

$$\Omega_0^+ = \int_0^1 \left[(\Omega_0^- - 3\Omega_1^-) + 6\mu\Omega_1^-\right] e^{-\frac{\Sigma_a T}{\mu}} d\mu \qquad \text{Eq. (3.278)}$$

$$= (\Omega_0^- - 3\Omega_1^-) E_2(\Sigma_a T) + 6\Omega_1^- E_3(\Sigma_a T)$$

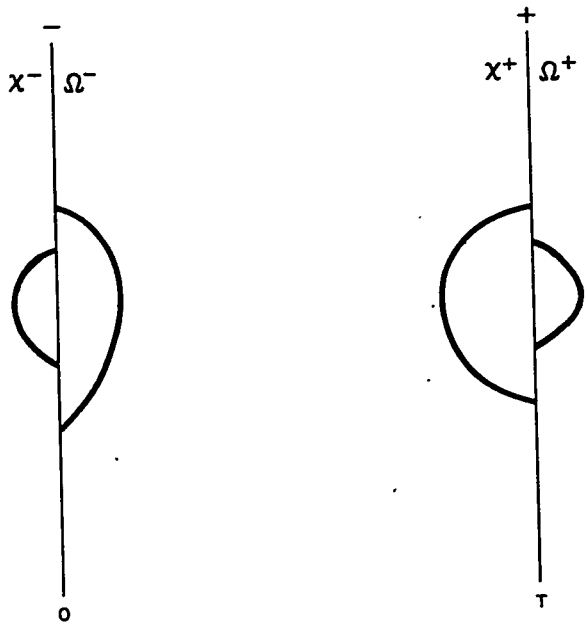

FIGURE 3.44. Absorbing Plate in Asymmetric Environment.

where T is the thickness of the plate. After similar matchings of half range contributions to scalar flux and current, one obtains

$$\begin{pmatrix} \Omega_0^+ \\ \Omega_1^+ \\ \chi_0^+ \\ \chi_1^+ \end{pmatrix} = \begin{pmatrix} A & B & 0 & 0 \\ \frac{B}{3} & D & 0 & 0 \\ 0 & 0 & \frac{D}{\Delta} & \frac{B}{\Delta} \\ 0 & 0 & \frac{B}{3\Delta} & \frac{A}{\Delta} \end{pmatrix} \begin{pmatrix} \Omega_0^- \\ \Omega_1^- \\ \chi_0^- \\ \chi_1^- \end{pmatrix} \qquad \text{Eq. (3.279)}$$

where the various parameters are defined as

$$\alpha = \left[D - \frac{B}{2}\right]\Delta^{-1}, \beta = \left[\frac{3}{2}A - B\right]\Delta^{-1}, \gamma = A + \frac{B}{2}$$

$$\delta = -\left(B + \frac{3}{2}D\right), \epsilon = -\frac{B}{4\Delta}, \zeta = \frac{3A}{4\Delta}$$

$$\eta = \frac{B}{4}, \theta = -\frac{3}{4}D, \text{ and } \Delta = AD - \frac{B^2}{3}, \text{ with } A = E_2, B = 6\left[E_3 - \frac{E_2}{2}\right]$$

$$D = -B + 12\left[E_4 - \frac{E_3}{2}\right], \text{ and } E_n(2\Sigma_a t) = \int_0^1 \mu^{n-2} \exp\left[-\frac{2\Sigma_a t}{\mu}\right] d\mu .$$

The transformation matrix of Eq. (3.279) and its inverse enable one to express any of the half-range moments on one side of the absorber in terms of those on the opposite side. The correlation of full and half-range moments follows from

$$F_n = \int_{-1}^{1} F(x,\mu)P_n(\mu)d\mu = \int_0^1 \Omega P_n(\mu)\,d\mu + \int_{-1}^{0} xP_n(\mu)d\mu \qquad \text{Eq. (3.280)}$$

and one obtains directly

$$F_1 = \frac{1}{2}(1, 1, -1, 1) \qquad \text{Eq. (3.281a)}$$

$$F_3 = \frac{1}{8}(-1, 3, 1, 3) \qquad \text{Eq. (3.281b)}$$

$$\psi_1 = (1, \frac{3}{2}, 1, -\frac{3}{2}) \qquad \text{Eq. (3.281c)}$$

$$\psi_2 = \frac{3}{4}(0, 1, 0, -1) \qquad \text{Eq. (3.281d)}$$

where ψ_1 and ψ_2 are defined as in Eq. (3.276) and the abbreviation, (a, b, c, d) has been employed for $a\Omega_0 + b\Omega_1 + cx_0 + dx_1$. Equations (3.281), (3.279), and perseverance lead to

$$\begin{bmatrix} w \\ x \\ y \\ z \end{bmatrix} = \frac{\left[\Gamma\right]^{-1}}{2} \begin{bmatrix} 1 \\ 1 \\ -1 \\ 1 \end{bmatrix} \qquad \text{Eq. (3.282)}$$

$$\begin{bmatrix} p \\ q \\ r \\ t \end{bmatrix} = \frac{\left[\Gamma\right]^{-1}}{8} \begin{bmatrix} -1 \\ 3 \\ 1 \\ 3 \end{bmatrix} \qquad \text{Eq. (3.283)}$$

$$\left[\Gamma\right] = \begin{bmatrix} 1 & 0 & \alpha & \epsilon \\ \frac{3}{2} & \frac{3}{4} & \beta & \zeta \\ 1 & 0 & \gamma & \eta \\ -\frac{3}{2} & -\frac{3}{4} & \delta & \theta \end{bmatrix}.$$

When the plate scatters as well as absorbs neutrons, analytic solutions of the transport equation are no longer available. However, one can readily find double $-P_1$ and P_3 approximations to the absorber flux and derive values of w, x, etc. which replace double $-P_1$ or P_3 calculations in the absorbing region.

The double $-P_1$ solution within the absorbing plate is given by

$$\psi_1 = A_1 \sinh K_1 x + A_2 \cosh K_1 x + A_3 \sinh K_3 x + A_4 \cosh K_3 x \qquad \text{Eq. (3.284a)}$$

$$\psi_2 = a(A_1 \sinh K_1 x + A_2 \cosh K_1 x + b(A_3 \sinh K_3 x + A_4 \cosh K_3 x) \qquad \text{Eq. (3.284b)}$$

where

$$K_1 = \sqrt{\frac{1}{2}\left(\delta + \sqrt{\delta^2 - 4\epsilon}\right)}$$

$$K_3 = \sqrt{\frac{1}{2}\left(\delta - \sqrt{\delta^2 - 4\epsilon}\right)}$$

T is the thickness of the plate

$$\delta = \alpha + \gamma,\ \epsilon = \alpha(\gamma + 2\beta),\ \beta = -\frac{3}{4}\frac{\Sigma_a}{D_2},\ \gamma = \frac{\Sigma_2}{D_2},$$

$$\alpha = \frac{\Sigma_a}{D_1},\ \Sigma_2 = \frac{7}{2}\Sigma_a + 2\Sigma_s,\ D_2 = \frac{1}{6(\Sigma_a + \Sigma_s)},$$

and

$$D_1 = \frac{1}{3(\Sigma_s - \Sigma_{s1} + \Sigma_a)},\ a = \frac{1}{2}\left(1 - \frac{K_1^2}{\alpha}\right),$$

and

$$b = \frac{1}{2}\left(1 - \frac{K_3^2}{\alpha}\right).$$

The P_3 expression differs from the double $-P_1$ expression only in that

$$D_2' = \frac{3}{7}\frac{1}{(\Sigma_a + \Sigma_s)},\ \Sigma_2' = 3\Sigma_a + \frac{5}{3}\Sigma_s, \text{ and } \beta' = \frac{-2}{3}\frac{\Sigma_a}{D_2}.$$

If for convenience one sets $x = 0$ and $x = T$ at the $-$ and $+$ sides of the plate respectively, he finds

$$\begin{bmatrix} \psi_1^+ \\ \psi_1^- \\ \psi_2^+ \\ \psi_2^- \end{bmatrix} = \begin{bmatrix} \sinh K_1 T & \cosh K_1 T & \sinh K_3 T & \cosh K_3 T \\ 0 & 1 & 0 & 1 \\ a \sinh K_1 T & a \cosh K_1 T & b \sinh K_3 T & b \cosh K_3 T \\ 0 & a & 0 & b \end{bmatrix} \begin{bmatrix} A_1 \\ A_2 \\ A_3 \\ A_4 \end{bmatrix}$$

Eq. (3. 285a)

and

$$\begin{bmatrix} D_1\nabla\psi_1^+ \\ D_2\nabla\psi_1^- \\ D_2\nabla\psi_2^+ \\ D_2\nabla\psi_2^- \end{bmatrix} = \begin{bmatrix} D_1K_1\cosh K_1T & D_1K_1\sinh K_1T & D_1K_3\cosh K_3T & D_1K_3\sinh K_3T \\ D_1K_1 & 0 & D_1K_3 & 0 \\ D_2aK_1\cosh K_1T & D_2aK_1\sinh K_1T & D_2bK_3\cosh K_3T & D_2bK_3\sinh K_3T \\ D_2aK_1 & 0 & D_2bK_3 & 0 \end{bmatrix} \begin{bmatrix} A_1 \\ A_2 \\ A_3 \\ A_4 \end{bmatrix}$$

Eq. (3.285b)

If double $-P_1$ is used outside the absorber as well, the constants become

$$\begin{bmatrix} w \\ x \\ y \\ z \end{bmatrix} = -\begin{bmatrix} \Lambda \end{bmatrix}^{-1} \begin{bmatrix} 0 \\ D_1K_1 \\ 0 \\ D_1K_3 \end{bmatrix} \qquad \text{Eq. (3.286)}$$

and

$$\begin{bmatrix} p \\ q \\ r \\ t \end{bmatrix} = -\begin{bmatrix} \Lambda \end{bmatrix}^{-1} \begin{bmatrix} 0 \\ a\,D_2K_1 \\ 0 \\ b\,D_2K_3 \end{bmatrix} \qquad \text{Eq. (3.287)}$$

where

$$\Lambda = \begin{bmatrix} \cosh K_1T & a\cosh K_1T & 1 & a \\ \sinh K_1T & a\sinh K_1T & 0 & 0 \\ \cosh K_3T & b\cosh K_3T & 1 & b \\ \sinh K_3T & b\sinh K_3T & 0 & 0 \end{bmatrix}.$$

Figure 3.45 illustrates the application of blackness boundary conditions to a typical thermal cell containing a $1/v$ absorbing sheet of unit optical depth at 0.025 ev and two water regions. As expected, the double-P_1 solution which meets transport theory blackness boundary conditions lies between the ordinary double-P_1 and double-P_3 solutions but very close to the double-P_1. Evidently, in this type of problem one has little to gain in accuracy by replacing double-P_1 with transport theory within the absorber when double-P_1 is used in adjacent regions. In the limit of a black plate, both these sets of blackness coefficients fulfill the requirements of no emergent flux or current.

A rigorous derivation of the few-group quantities $w^i, x^i, \ldots, t^i$ is beset with difficulties. For example:

$$x^i = \frac{\int_i x(E)\psi_2^+(E)\,dE}{\int_i \psi_2^+(E)\,dE}$$

where $\psi_2^+(E)$ is the P_2 component of the flux computed at the absorber surface. This surface value may be completely different from the asymptotic value of ψ_2. It was, therefore, decided to employ the approximation $x^i(\Sigma_a, \Sigma_s, \Sigma_{sl}) \approx x(\Sigma_a^i, \Sigma_s^i, \Sigma_{sl}^i)$, where the Σ_a^i are derived using the first equality in Eq. (3.273) and the corresponding form of Eq. (3.274). When applied to the cell of Fig. 3.41 this approximation and Eqs. (3.286) and (3.287) yield double-P_1 results identical to those given in Table 3.23.

Finally, to illustrate the application of few-group blackness boundary conditions when the absorbing plate is in an asymmetric environment, the cell formed by adding a water region to the left side of the core-absorber cell (Fig. 3.41) has been considered. The results of these calculations, given in Table 3.24, are as satisfactory as those obtained for symmetrically placed absorbers.

4. *Conclusion*

Conventional few-group calculations may be profitably applied to thermal neutron problems. In those calculations which involve thin highly absorbing plates, it has been found possible to reduce the error in absorption rate by an order of magnitude by using only four thermal groups. In problems involving large water reflectors, satisfactory few-group results may be obtained in a tenth the computing time necessary for the corresponding multigroup calculations.

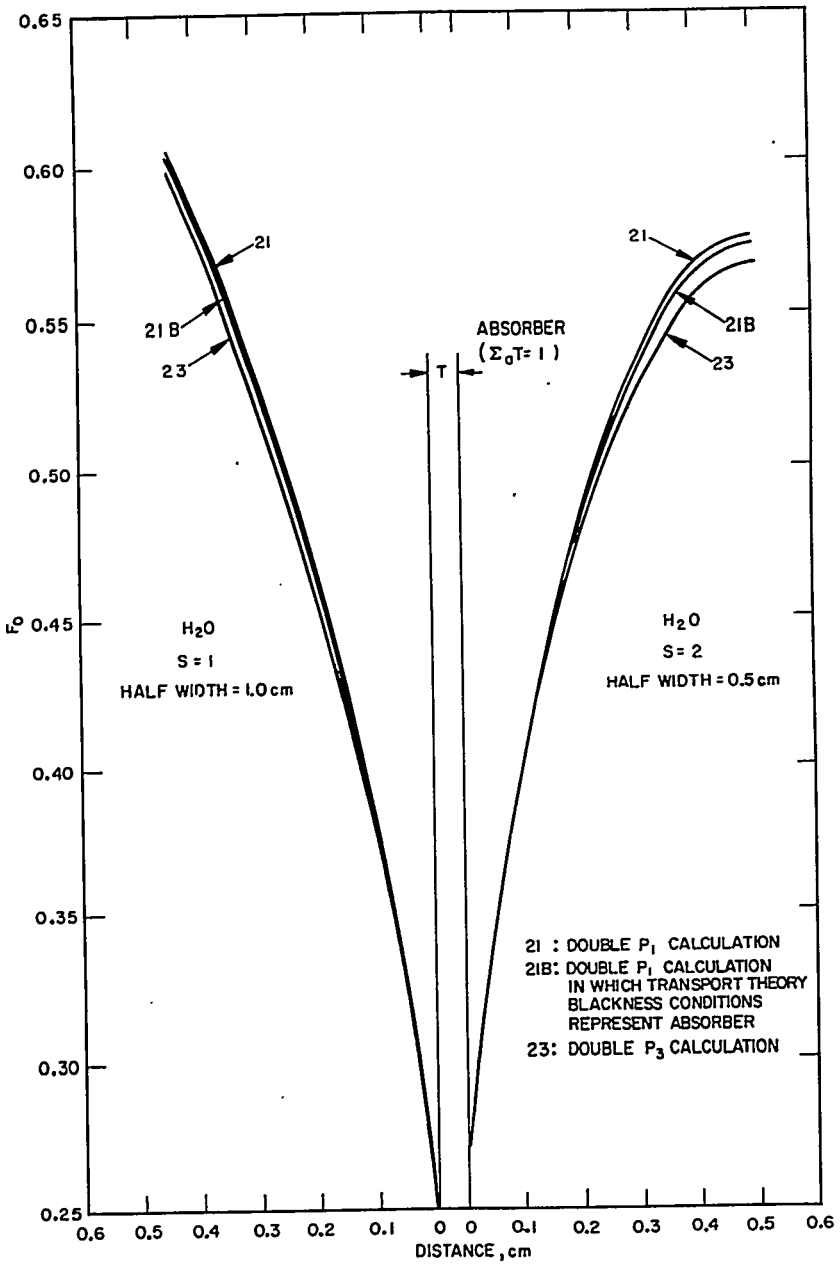

FIGURE 3.45. Comparison of Different Approximations to Flux Shapes near an Absorbing Plate.

TABLE 3.24 — COMPARISON OF INTEGRATED ABSORPTION RATES

Material	Water	Absorbing Plate (optical depth=2)	Core*	Core*
Width	0.6 cm	0.2 cm	1 cm	3 cm
Constant Source Strength	3	0	1	1
$\int \Sigma_a \phi dx$ (1-group calculation)	0.0140	1.403	0.294	1.402
$\int \Sigma_a \phi dx$ (4-group calculation)	0.0109	1.368	0.289	1.445
$\int \Sigma_a \phi dx$ (36-group calculation)	0.0103	1.364	0.288	1.451

*The number densities of materials in the core region are: H:0.024693 x 10^{24}/cm^3, O:0.012346, Zr:0.024781, Al:0.00324, U^{235}:0.0001964 and U^{238}:0.00001207. The core diffusion length is 2.145 cm.

D. Variational Approach to Thermal-Group Calculations

G. P. Calame and F. D. Federighi

1. Theory

A difficulty that arises in approximating the multigroup thermal neutron equations by a simpler few-group description is that the reduced few-group equations involve quantities (the few-group cross sections) averaged with respect to energy weight functions which are usually chosen according to some arbitrary recipe. This difficulty can be partially circumvented by using the variational method, a convenient mathematical tool which allows the reduction of complicated theories to simpler ones in a systematic manner.[120] The method also allows one to employ information available about the solution of the problem in obtaining the equations of a simplified theory. The Kantorovich variational method,[121,122] in particular, has been used to obtain approximate, but accurate, few-group solutions to the thermal space-energy problem.

The equation determining the thermal flux $\phi(r,E)$ as a function of position and energy is given in the P_1 approximation* by

$$-\nabla\cdot D^j(E)\nabla\phi^j(\vec{r},E)+\Sigma_t^j(E)\phi^j(\vec{r},E)$$

$$-\int_0^{E_c}\Sigma_s^j(E'\to E)\,\phi^j(\vec{r},E')\,dE'=S^j(\vec{r},E) \qquad \text{Eq. (3.288)}$$

where the superscript j refers to the j^{th} region, and

$D^j(E)$ = diffusion coefficient

$\Sigma_t^j(E)=\Sigma_a^j(E)+\Sigma_s^j(E)$ = total macroscopic cross section

$\Sigma_s^j(E'\to E)$ = macroscopic cross section for the transfer of a neutron of initial energy E' to final energy E by a scattering collision, the energy exchange kernel

$S^j(\vec{r},E)$ = slowing-down source to energy E from energies above E_c.

E_c is a cutoff energy, chosen so that $\Sigma_s^j(E'\to E)$ for $E>E_c$ and $E'<E_c$ is negligible, i.e., it is an energy above which negligible up-scattering occurs.

One possible form of an approximate solution to Eq. (3.288) may be constructed by considering some simple problems. Consider first a system in plane geometry consisting of two semi-infinite media with a common interface at $z=0$, so that z is the spatial variable. Let the medium to the left of the interface $(z\le 0)$ be medium one, and let the medium to the right of the interface be medium two. Let the slowing-down source in each medium be independent of position within the medium, so that $S^j(\vec{r},E)=S^j(E)$. Then, far to the left of the interface, deep in medium one, the neutron spectrum will be $\phi_1(E)$, the infinite medium spectrum characteristic of that material, i.e., the solution to the equation

$$\Sigma_t^j(E)\phi_j(E)-\int_0^{E_c}\Sigma_s^j(E'\to E)\phi_j(E')\,dE'=S^j(E) \qquad \text{Eq. (3.289)}$$

*The P_1 approximation is used for simplicity of exposition only. The techniques to be discussed may be, and in fact have been, used with higher order transport approximations.

with $j=1$. Similarly, far to the right of the interface, the spectrum will be $\phi_2(E)$. Near the interface, the spectrum is expected to be some intermediate one, and one should be well approximated by some linear combination of ϕ_1 and ϕ_2. In such a problem, an approximate solution of the form

$$\phi(z,E)=\chi_1(z)\phi_1(E)+\chi_2(z)\phi_2(E) \qquad \text{Eq. (3.290)}$$

might profitably be sought, where the $\chi_i(z)$ are the position-dependent coefficients of combination.

Consider now a problem with N different media. Following very roughly the reasoning of the previous paragraph, an approximate solution of the form

$$\phi(\vec{r},E)=\sum_{j=1}^{N}\chi_j(\vec{r})\,\phi_j(E) \qquad \text{Eq. (3.291)}$$

might be sought, where $\chi_j(\vec{r})$ would be expected to be large in the vicinity of region j and small elsewhere. The difficulty with developing the general approximation [Eq. (3.291)] in a practical reactor is that such a reactor typically consists of many regions of different compositions, so that the approximation would be an unwieldy one.

The infinite medium spectra $\phi_j(E)$ often bear a strong resemblance to each other. A frequently occurring situation is one in which the thermal absorption cross section in many of the regions does not depart appreciably from the $1/v$ law. It is possible to represent the infinite medium spectrum in the n^{th} such region as a linear combination of an infinite medium spectrum characteristic of a medium with little absorption (the absorption present being $1/v$) and an infinite medium spectrum characteristic of a medium with a large amount of $1/v$ absorption. That such a combination of two spectra yields a good approximation to an intermediate spectrum is illustrated in Fig. 3.46, where the infinite medium spectrum characteristic of water ($\beta\gamma=0.0159$) has been linearly combined with a spectrum characteristic of an infinite medium with a $\beta\gamma$ of 0.8 to yield an approximation to the spectrum of a medium with a $\beta\gamma$ of 0.4. The spectra were calculated using a mass one, free proton gas, energy exchange kernel. $\beta\gamma$ is here the ratio of the macroscopic $1/v$ absorption cross section at kT to the macroscopic slowing-down power at one ev.

The assumption will be made that the spectrum everywhere in a reactor may be approximated by the expression in Eq. (3.291), but with N representing not the number of media, but

rather the small* number of spectra that one expects will be sufficient to give an adequate representation of the spatially dependent spectrum in the reactor. Once the spectra one wishes to combine are chosen, it remains to develop equations for the coefficients of combination χ_i. This may be accomplished through the use of the variational method.

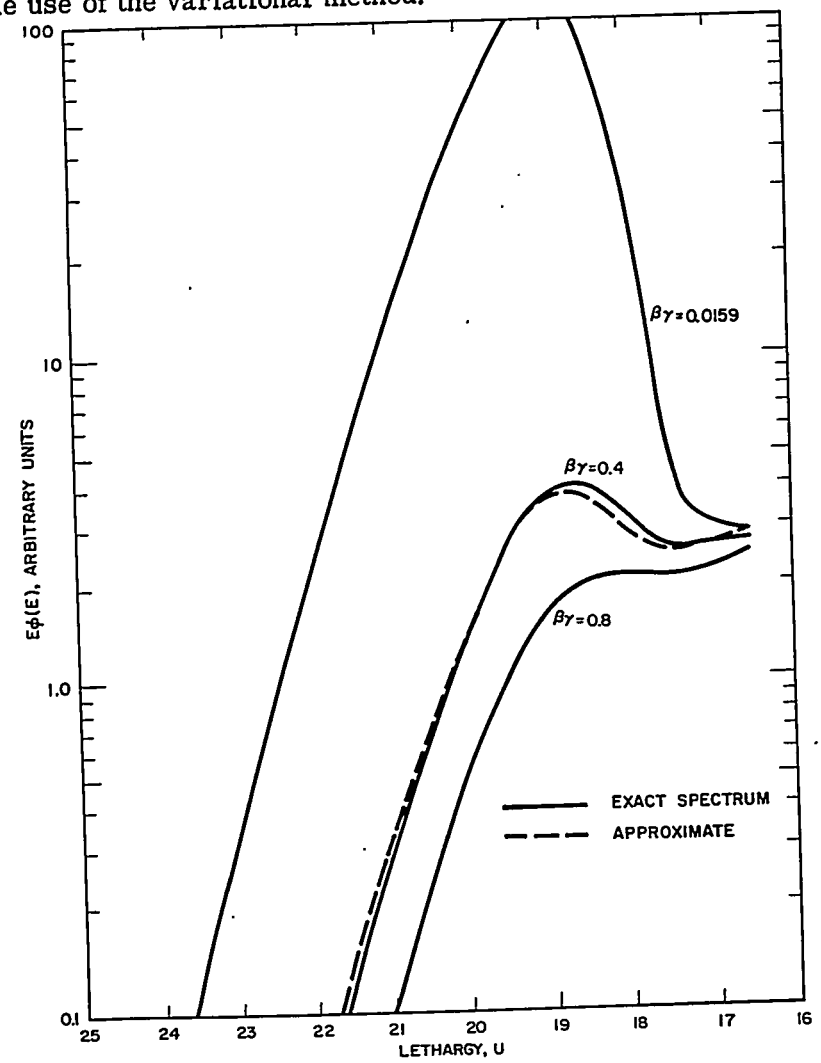

FIGURE 3.46. A Linear Combination of Two Infinite Medium Spectra to Yield an Approximation to an Intermediate Infinite Medium Spectrum.

*In practice, two spectra with coefficients of combination determined by the formalism that follows have been found sufficient for most cases, agreeing with multigroup calculations of the spectra to better than 3 percent in the worst cases. Four spectra have consistently yielded results which agree with multigroup calculation to within 1 percent.

Equation (3.288) is an inhomogenous equation of the form

$$H\phi = S(+ \text{ boundary conditions}) \qquad \text{Eq. (3.292)}$$

where, in region j, the operator H^j is defined by

$$H^j\phi = -\nabla \cdot D^j(E)\nabla\phi^j(\vec{r},E) + \Sigma_t^j(E)\phi^j(\vec{r},E) - \int_0^{E_c} \Sigma_s^j(E'\rightarrow E)\phi^j(\vec{r},E')dE' . \qquad \text{Eq. (3.293)}$$

If a particular weighted average of ϕ, say $(S^\dagger, \phi)$, is desired,* the Schwinger variational expression[123]

$$J(\tilde{\phi}^\dagger, \tilde{\phi}) = \frac{(S^\dagger, \tilde{\phi})\,(\tilde{\phi}^\dagger, S)}{(\tilde{\phi}^\dagger, H\tilde{\phi})} \qquad \text{Eq. (3.294)}$$

may be written. The functional J has the property that among all functions satisfying the boundary conditions of the problem (the so-called trial functions), the ones which make J stationary are the solutions to Eq. (3.292) and the adjoint equation†

$$H^\dagger\phi^\dagger = S^\dagger (+ \text{ adjoint boundary conditions}). \qquad \text{Eq. (3.295)}$$

Further, the value of at this stationary point is $(S^\dagger, \phi)$.[121] Approximate solutions to Eq. (3.288) which make J stationary for a given set of trial functions $\tilde{\phi}$ and $\tilde{\phi}^\dagger$ may then be obtained by substituting into J trial functions $\tilde{\phi}$ and $\tilde{\phi}^\dagger$ which contain variable parameters (and which satisfy the boundary conditions), performing the indicated integrations, and subsequently requiring the resulting functional to be stationary with respect to variations of the chosen parameters.

It is frequently desirable to use trial functions which do not satisfy the boundary conditions of the problem. It then becomes necessary to obtain a variational expression which permits relaxation of the boundary restrictions on the trial functions.

---

*Inner product notation will be used. The notation $(S^\dagger, \phi)$ means the integral of the product of the functions $S^\dagger$ and ϕ over all the variables of the system.

†The adjoint operator $H^\dagger$ is defined in the j^{th} region by

$$H^{j\dagger}\phi^\dagger = -\nabla \cdot D^j(E)\nabla\phi^\dagger(\vec{r},E) + \Sigma_t^j(E)\phi^\dagger(\vec{r},E) - \int_0^{E_c} \Sigma_s^j(E\rightarrow E')\phi^\dagger(\vec{r},E')dE' .$$

The boundary conditions at interfaces are that $\phi(\vec{r},E)$ and the normal component of $D(\vec{r},E)\nabla\phi(\vec{r},E)$ be continuous. The adjoint boundary conditions are that $\phi^\dagger(\vec{r},E)$ and the normal component of $D(\vec{r},E)\nabla\phi^\dagger(\vec{r},E)$ be continuous.

If the operator H as defined by Eq. (3.293) is written symbolically as

$$H^j \phi^j = - \nabla \cdot D^j \nabla \phi^j + K^j \phi^j \qquad \text{Eq. (3.296)}$$

the denominator of Eq. (3.294) may be written symbolically as

$$(\tilde{\phi}^\dagger, H\tilde{\phi}) = (-\tilde{\phi}^\dagger, \nabla \cdot D \nabla \tilde{\phi}) + (\tilde{\phi}^\dagger, K\tilde{\phi}). \qquad \text{Eq. (3.297)}$$

It may now be shown[124] that if Eq. (3.297) is replaced by

$$(\tilde{\phi}^\dagger, H'\tilde{\phi}) = (\nabla \tilde{\phi}^\dagger, D \nabla \tilde{\phi}) + (\tilde{\phi}^\dagger, K\tilde{\phi}) \qquad \text{Eq. (3.298)}$$

it is no longer required that the trial functions satisfy the continuity of current conditions at the interface. The trial functions, however, must still satisfy the flux continuity conditions.

The statement that the solutions to Eqs. (3.292) and (3.296) make J stationary is proved by considering the functional

$$J(\tilde{\phi}^\dagger, \tilde{\phi}) = \frac{(S^\dagger, \tilde{\phi})(\tilde{\phi}^\dagger, S)}{(\nabla \tilde{\phi}^\dagger, D \nabla \tilde{\phi}) + (\tilde{\phi}^\dagger, K\tilde{\phi})} . \qquad \text{Eq. (3.299)}$$

The statement that J as given by Eq. (3.299) is stationary means that there exist functions ϕ, $\phi^\dagger$, such that if trial functions

$$\tilde{\phi} = \phi + \delta\phi$$
$$\tilde{\phi}^\dagger = \phi^\dagger + \delta\phi^\dagger \qquad \text{Eq. (3.300)}$$

which differ from ϕ and $\phi^\dagger$ by the amounts $\delta\phi$ and $\delta\phi^\dagger$ are inserted into Eq. (3.299), then the change in the functional J is of second order in the quantities $\delta\phi$, $\delta\phi^\dagger$, i.e.,

$$\delta J = J(\phi^\dagger + \delta\phi^\dagger, \phi + \delta\phi) - J(\phi^\dagger + \phi) = 0 \qquad \text{Eq. (3.301)}$$

for all values of $\delta\phi^\dagger$ and $\delta\phi$ consistent with the boundary conditions of continuity of $\tilde{\phi}$ and $\tilde{\phi}^\dagger$. Using Eq. (3.299), this expression becomes

$$\delta J = \frac{(S^\dagger, \phi+\delta\phi)\,(\phi^\dagger+\delta\phi^\dagger, S)}{\left(\nabla\left[\phi^\dagger+\delta\phi^\dagger\right], D\,\nabla\left[\phi+\delta\phi\right]\right)+\left(\phi^\dagger+\delta\phi^\dagger, K\left[\phi+\delta\phi\right]\right)}$$

$$-\frac{(S^\dagger,\phi)\,(\phi^\dagger,S)}{(\nabla\phi^\dagger, D\nabla\phi)+(\phi^\dagger, K\phi)}.$$

Combining fractions, the numerator of δJ becomes (if second-order terms are neglected)

$$\left[(\phi^\dagger,S)\,(S^\dagger,\phi)+(\delta\phi^\dagger,S)\,(S^\dagger,\phi)+(\phi^\dagger,S)\,(S^\dagger,\delta\phi)\right]$$

$$\cdot\left[(\nabla\phi^\dagger, D\nabla\phi)+(\phi^\dagger,K\phi)\right]$$

$$-(\phi^\dagger,S)(S^\dagger,\phi)\left[(\nabla\phi^\dagger,D\nabla\phi)+(\phi^\dagger,K\phi)+(\nabla\delta\phi^\dagger,D\nabla\phi)+(\nabla\phi^\dagger,D\nabla\delta\phi)\right.$$

$$\left.+(\delta\phi^\dagger,K\phi)+(\phi^\dagger,K\delta\phi)\right].$$

The terms of zero order in this expression cancel. Dividing the resulting expression by

$$(\nabla\phi^\dagger, D\nabla\phi)+(\phi^\dagger,K\phi)$$

and using the definition $J_o = J(\phi^\dagger,\phi)$, this becomes

$$(\delta\phi^\dagger,S)(S^\dagger,\phi)+(\phi^\dagger,S)(S^\dagger,\delta\phi)-J_o\left[(\nabla\delta\phi^\dagger,D\nabla\phi)+(\nabla\phi^\dagger,D\nabla\delta\phi)\right.$$

$$\left.+(\delta\phi^\dagger,K\phi)+(\phi^\dagger,K\delta\phi)\right]. \qquad \text{Eq. (3.302)}$$

To discuss the behavior of this expression as the trial functions (i.e., the δ's) are varied, it is necessary to put it in a form in which there are no operators under the integral sign operating on any of the δ's. Thus, terms like

$$(\nabla\,\delta\phi^\dagger, D\,\nabla\phi) = \int_E\int_{\vec{r}}(\nabla\,\delta\phi^\dagger\;D\,\nabla\phi)\,dE\,d\vec{r}$$

must be integrated by parts by use of the divergence theorem to give

$$\int_E \oint_S \delta\phi^\dagger D \nabla \phi \cdot d\vec{S}\, dE - \int_E \int_{\vec{r}} \delta\phi^\dagger \nabla \cdot D \nabla \phi dE d\vec{r}$$

where the surface integral over each inner surface (boundary) must be performed twice: once with the surface element vector $d\vec{S}$ pointing in one direction, once with the vector pointing in the opposite direction. Rewriting the surface integral so that the integral over each inner surface is performed once only, one obtains, recalling the restrictions on the trial functions that $\tilde{\phi}$ and $\tilde{\phi}^\dagger$ must be continuous,

$$\int_E \int_S \delta\phi^\dagger \left[D(-) \nabla \phi(-) - D(+) \nabla \phi(+) \right] d S\, dE - \int_E \int_{\vec{r}} \delta\phi^\dagger \nabla \cdot D \nabla \phi dE d\vec{r}$$

where $(-)$ and $(+)$ refer to the spatial coordinate on opposite sides of the inner surfaces. (The trial functions are all assumed to satisfy the appropriate conditions on the outer surfaces.)

Similarly, the terms in $(\phi^\dagger, K\phi)$ like

$$\int_E \int_{\vec{r}} \phi^\dagger(E) \int_{E'} \Sigma_s(E' \to E) \delta\phi(E') dE' dE d\vec{r}$$

become by changing the order of integration and relabeling the dummy variables E' and E

$$\int_E \int_{\vec{r}} \delta\phi(E) \int_{E'} \Sigma_s(E \to E') \phi^\dagger(E') dE' dE d\vec{r} .$$

These substitutions enable Eq. (3.302) to be written

$$\left(\delta\phi^\dagger, \left[S(S^\dagger, \phi) + J_o \nabla \cdot D \nabla \phi - J_o K \phi\right]\right) + \left(\left[(\phi^\dagger, S) S^\dagger + J_o \nabla \cdot D \nabla \phi^\dagger - J_o K^\dagger \phi^\dagger\right] \delta\phi\right)$$

$$- J_o \int_E \int_S \left[\delta\phi^\dagger(S) \left(D(-) \nabla \phi(-) - D(+) \nabla \phi(+)\right) + \delta\phi(S) \left(D(-) \nabla \phi^\dagger(-) - D(+) \nabla \phi^\dagger(+)\right)\right] dE d S .$$

Eq. (3.303)

This representation shows that if δJ is to be zero for all independent arbitrary variations of the $\delta\phi$ terms, the coefficients of each of the terms in Eq. (3.303) must be zero. It should be noted that since $\phi^\dagger$ and ϕ can be varied in the interior without being varied on the surface, the coefficients of $\delta\phi$, $\delta\phi(S)$, etc., must each be zero separately.

The requirement that the coefficients of $\delta\phi^\dagger$ vanish yields the system of equations

$$J_o H\phi = (S^\dagger, \phi)S \qquad \text{Eq. (3.304)}$$

as the equation that the function ϕ which makes J stationary must satisfy. This is an eigenvalue problem of the form

$$A\phi = \lambda B\phi$$

where B is an integral operator with a separable kernel. To obtain the solution to Eq. (3.304), it will be written

$$H\phi = \alpha S \qquad \text{Eq. (3.305)}$$

where

$$\alpha = \frac{(S^\dagger, \phi)}{J_o} = \frac{(S^\dagger, \alpha\phi_o)}{J_o}$$

where ϕ_o is the solution to $H\phi_o = S$, or, finally,

$$J_o = (S^\dagger, \phi_o)$$

which demonstrates that the stationary value of J is $(S^\dagger, \phi_o)$. ϕ_o is called the normalized eigenfunction and is the one for which the variational expression was written. J is homogeneous in ϕ, so that any multiple of ϕ_o will make J stationary. However, all give an eigenvalue $J_o = (S^\dagger, \phi_o)$. The normalized eigenfunction can be picked out by equating the eigenvalue with $(S^\dagger, k\phi)$ and solving for k (here, ϕ is any eigenfunction).

The requirement that the coefficient of $\delta\phi^\dagger$ in the surface term vanish yields the continuity of current boundary condition. The above discussion also holds for $\delta\phi$ and $\delta\phi(S)$, yielding the adjoint equations [Eq. (3.295)].

Thus, if all sets of trial functions $\tilde{\phi}$ and $\tilde{\phi}^\dagger$ satisfy flux and adjoint continuity conditions at interfaces (and also the appropriate conditions at the outer boundaries of the reactor), the expression

$$J = \frac{(S^\dagger, \tilde{\phi})(\tilde{\phi}^\dagger, S)}{(\tilde{\phi}^\dagger, H'\tilde{\phi})} \qquad \text{Eq. (3.306)}$$

will be stationary for the set ϕ, $\phi^\dagger$ which satisfies Eqs. (3.292) and (3.295), and also the current continuity boundary conditions. Since the functional J is stationary about the solutions to these equations, it is possible to employ the Kantorovich variational method [121,122] to obtain approximate solutions to them. This method, which is a generalization of the more usual Rayleigh-Ritz approach, assumes that the functional dependence of one or more of the variables is known. The integrations over these variables are performed and the resulting expressions made stationary with respect to variations of the unknown functions of the remaining variables, with the result that equations for the functional dependence of the latter variables are obtained.

It has been indicated that $\phi(\vec{r}, E)$ should be well represented at any point in space by some linear combination of a few infinite medium spectra. A similar statement is true for the adjoint function. Therefore, trial functions of the form

$$\tilde{\phi}^j(\vec{r}, E) = \sum_{i=1}^{N} \chi_i^j(\vec{r})\phi_i(E) \qquad \text{Eq. (3.307a)}$$

$$\tilde{\phi}^{j\dagger}(\vec{r}, E) = \sum_{i=1}^{N} \chi_i^{j\dagger}(\vec{r})\,\phi_i^\dagger(E) \qquad \text{Eq. (3.307b)}$$

will be used in medium j. Here the χ_i are undetermined functions of $\vec{r}$, $\phi_i(E)$ is the infinite medium spectrum in medium i, and similarly for the $\chi_i^\dagger$ and $\phi_i^\dagger$. To have the trial functions represented by Eqs. (3.307) satisfy continuity of flux and adjoint across a boundary, and so be eligible trial functions for use in Eq. (3.306), the restriction that $\chi_i(\vec{r})$ and $\chi_i^\dagger(\vec{r})$ be continuous across boundaries is imposed. Inserting the trial functions of

Eqs. (3.307) into Eq. (3.306) and performing the energy integrations yields

$$J = \frac{\left(\sum_{j=1}^{M}\int_{V_j}\sum_{i=1}^{N} S_i^{j\dagger}(\vec{r}')\chi_i^j(\vec{r}')\,dV_j\right)\left(\sum_{j=1}^{M}\int_{V_j}\sum_{i=1}^{N} \chi_i^{j\dagger}(\vec{r})\,S_i^j(\vec{r})\,dV_j\right)}{\sum_{j=1}^{M}\int_{V_j}\sum_{i,k=1}^{N}\left(\nabla\chi_k^{j\dagger}(\vec{r}')\cdot D_{ki}^j\nabla\chi_i^j(\vec{r}') + \chi_k^{j\dagger}(\vec{r}')K_{ki}^j\chi_i^j(\vec{r}')\right)dV_j}$$

Eq. (3.308)

where

$$S_i^{j\dagger}(\vec{r}') = \int_0^{E_c} S^{j\dagger}(\vec{r},E)\,\phi_i(E)\,dE \qquad \text{Eq. (3.309a)}$$

$$S_i^{j\dagger}(\vec{r}) \int_0^{E_c} S^j(\vec{r},E)\,\phi_i^\dagger(E)\,dE \qquad \text{Eq. (3.309b)}$$

$$D_{ik}^j = \int_0^{E_c} \phi_i^\dagger(E)D^j(E)\phi_k(E)\,dE \qquad \text{Eq. (3.309c)}$$

and

$$K_{ik}^j = \int_0^{E_c} \phi_i^\dagger(E)\left[\Sigma_t^j(E)\phi_k(E) - \int_0^{E_c}\Sigma_s^j(E'\to E)\phi_k(E')dE'\right]dE\,.$$

Eq. (3.309d)

In Eq. (3.308), the order of operations is to perform the sums under the integrals, integrate the result over each region, and sum over all the M regions of the problem.

The expression in Eq. (3.308) is now made stationary with respect to variations of the $\chi^{j\dagger}$'s. This is accomplished formally in the same way as is the proof that Eq. (3.299) is stationary for variations of $\tilde{\phi}$ and $\tilde{\phi}^\dagger$ about ϕ and $\phi^\dagger$. $\chi^{j\dagger}$ in Eq. (3.308) is replaced by $\chi^{j\dagger}+\delta\chi^{j\dagger}$, χ^j is replaced by $\chi^j+\delta\chi^j$, and δJ, given by

$$\delta J = J(\chi^{j\dagger}+\delta\chi^{j\dagger},\,\chi^j+\delta\chi^j) - J(\chi^{j\dagger},\,\chi^j)$$

is evaluated, correct through first-order terms. The requirement that δJ be zero for arbitrary $\delta\chi^{j\dagger}$ then yields the consequence that the coefficient of $\delta\chi^{j\dagger}$ must be zero. The result is that the equations

$$\sum_{i=1}^{N} \left[-\nabla \cdot D^{j}_{ki} \nabla \chi^{j}_{i}(\vec{r}) + K^{j}_{ki} \chi^{j}_{i}(\vec{r}) \right] = S^{j}_{k}(\vec{r}) \qquad \text{Eq. (3.310)}$$

are obtained in the j^{th} region, together with the boundary condition that the normal component of

$$\sum_{i=1}^{N} D_{ki} \nabla \chi_{i}(\vec{r}) \qquad \text{Eq. (3.311)}$$

must be continuous across interfaces. Similar equations for the $\chi^{\dagger}$'s are obtained by making J stationary with respect to variations of the χ's. The point to the procedure is that it is expected that the stationary point of the functional Eq. (3.308) is near the stationary point of the functional Eq. (3.299), so that the functions which make Eq. (3.308) stationary will be good approximations to the functions which make Eq. (3.299) stationary. The latter functions are, as has been demonstrated, the governing equations of the system.

The system of Eqs. (3.310), together with flux continuity and the boundary conditions of Eqs. (3.311), has the structure of few-group diffusion equations and, therefore, represents a few-group approximation to the thermal space-energy problem. It must be emphasized that the groups represented by Eqs. (3.310) are not groups in the usual sense, such as are used in Sect. 3.7.C. They can best be described as overlapping neutron populations, the description of which is formally similar to the usual few-group equations. The major difference between the overlapping population equations and a more conventional few-group equation is that the differential spatial operator acts on all the $\chi_i(r)$ in each equation, rather than on only a single unknown in each equation.

Equations (3.310) may be solved analytically in simple cases, but it is generally better to solve it numerically. This may be accomplished in a number of ways. One method that has been used successfully is to write them as the matrix equation

$$-\nabla \cdot \underline{D}^{j} \nabla \underline{\chi}^{j} + \underline{K}^{j} \underline{\chi}^{j} = \underline{S}^{j} \qquad \text{Eq. (3.312)}$$

where $\underline{\chi}^j$ and $\underline{S}^j$ are N by 1 matrices at each point, and $\underline{D}^j$ and $\underline{K}^j$ are N by N matrices. Equation (3.312) is now converted to a difference equation, and a relation between the $\underline{\chi}^j$ at successive points is derived. Consider, for example, a problem in plane geometry in which $\underline{D}$ and $\underline{K}$ are constant in each region. $\underline{\chi}''$ is replaced by the central difference formula

$$\underline{\chi}_i'' = \frac{\underline{\chi}_{i+1} - 2\underline{\chi}_i + \underline{\chi}_{i-1}}{h^2} \qquad \text{Eq. (3.313)}$$

where the index j has been suppressed. $\underline{\chi}_i$ is the value of the $\underline{\chi}$ vector at the point z_i, and h is the mesh spacing, $h = z_i - z_{i-1}$. The substitution of Eq. (3.313) into Eq. (3.312) yields

$$\underline{\chi}_{i+1}'' = (2\underline{I} + h^2\underline{D}^{-1}\underline{K})\underline{\chi}_i - \underline{\chi}_{i-1} - h^2\underline{D}^{-1}\underline{S}_i \cdot \qquad \text{Eq. (3.314)}$$

$\underline{I}$ is the identity matrix. The assumption is now made that a relation between successive $\underline{\chi}_i$ of the form

$$\underline{\chi}_i = \underline{\alpha}_{+1}^{-1}\left(\underline{\chi}_{i+1} + \underline{\beta}_i\right) \qquad \text{Eq. (3.315)}$$

exists. The substitution of Eq. (3.315) into Eq. (3.314) shows that the successive $\underline{\chi}$ may indeed be related by Eq. (3.15), provided that the $\underline{\alpha}_i$ and $\underline{\beta}_i$ satisfy the recursion relations

$$\underline{\alpha}_{i+1} = 2\underline{I} + h^2\underline{D}^{-1}\underline{K} - \underline{\alpha}_i^{-1}$$

and

$$\underline{\beta}_i = \underline{\alpha}_i^{-1}\underline{\beta}_{i-1} + h^2\underline{D}^{-1}\underline{S}_i$$

respectively. The form of the last two equations is precisely that of the usual one-dimensional difference equations,[123] and the formalism of a one-group, one-dimensional computer program such as WANDA[125] may be taken over directly, with the exception that all operations in WANDA are replaced by the proper matrix operations, so that Eqs. (3.310) are integrated simultaneously. A program, SWAKRAUM,[126] has been written to accomplish the numerical integration of Eqs. (3.310) in just this way.

The coefficients in Eqs. (3.310) will, for a given choice of trial spectra $\phi_i(E)$, depend on the choice of $S^\dagger$ because the choice of $S^\dagger$ dictates the choice of the adjoint trial spectra. The solution $\phi(\vec{r}, E)$ that is obtained by solving Eqs. (3.310) will be a solution that makes J stationary in such a way as to

provide an estimate for $(S^\dagger, \phi)$. Different approximate solutions $\phi(\vec{r}, E)$ will be obtained for different choices of $S^\dagger$. It has been found that this causes little difficulty in practice, since the various approximate solutions are quite close to each other. The dependence of the solution on the choice of $S^\dagger$ may be removed, however, by converting Eq. (3.288) into an equation with a symmetric kernel by means of the substitution

$$\psi(\vec{r}, E) = \frac{\phi(\vec{r}, E)}{\sqrt{M(E)}}$$

where

$$M(E) = \frac{E}{(kT)^2} e^{-E/kT}$$

is the Maxwellian spectrum. The resulting equation is

$$-\nabla \cdot D^j(E)\nabla\psi^j(\vec{r}, E) + \Sigma_t^j(E)\psi^j(\vec{r}, E) - \int_0^{E_c} G^j(E' \to E)\psi^j(\vec{r}, E')dE' = \frac{S^j(\vec{r}, E)}{\sqrt{M(E)}}$$

Eq. (3.316)

where

$$G^j(E' \to E) = \frac{1}{\sqrt{M(E)}} \Sigma_s^j(E' \to E) \sqrt{M(E')}$$

is symmetric by detailed balance. The adjoint flux and source then become identical to the flux and source in Eq. (3.316), and it is unnecessary to find separate adjoint trial functions. This formulation has been used by Buslik[127] with the trial function

$$\psi(\vec{r}, E) = \sqrt{M(E)}\chi_1(\vec{r}) + \frac{\phi_2(E)}{\sqrt{M(E)}}\chi_2(\vec{r})$$

where $\phi_2(E)$ is the Wigner-Wilkins flux characterizing the medium with the hardest spectrum. (It can be demonstrated that when the symmetric formulation [Eq. (3.316)] is used, one of the trial spectra must be a Maxwellian in order to guarantee neutron conservation.) The difficulty is that the variational principle of Eq. (3.294) becomes one for $(S/M, \phi)$, a quantity of uncertain physical significance. Nevertheless, Shufler[128] reports excellent agreement with multigroup results, confirming the insensitivity of the result to the adjoint source. An additional feature of this approach is that the coupling of the two equations is much stronger in one direction

than in the other, resulting in rapid convergence when solved iteratively.

2. *Comparison with Multigroup Calculations*

SWAKRAUM[126] has been used to compute flux transients near inhomogeneities in reactor lattices, and the results compared to the SLOP-1[85] calculations. Some comparisons are shown in Figs. 3.47 to 3.53.

Figure 3.47 compares the fluxes in SLOP-1 and SWAKRAUM calculations of a flux transient near a gap-core interface*, one of the experiments of Wright and Feiner.[129] The two calculations agree very well, except in the center of the gap where the SWAKRAUM flux is 2 percent lower than the SLOP-1 flux. Two trial spectra were used in the SWAKRAUM calculations, viz., the infinite medium spectra for the gap and the core. That the overlapping group method yields a good approximation to the spatially dependent spectrum is shown in Fig. 3.48, in which the SWAKRAUM and SLOP-1 spectra at the gap-core interface are compared. Since the fluxes and the spectra agree, it is to be expected that the calculations of the activation of detecting foils will also agree. That this is the case is shown in Fig. 3.49, in which the activations of a manganese foil in the lattice near the gap are plotted versus position for the two calculations. The experimental points are also shown. It should be noted that the plot is a semilogarithmic one of foil activation at x minus foil activation at infinity, so that the differences observed between the calculations would not be noticeable on a linear plot of activations versus position.

Figure 3.50 shows a comparison calculation of a 3.4 weight percent boron-aluminum slab, 0.52 cm thick, inserted between a heavily loaded fuel region and a less heavily loaded fuel region in a core. The calculations were performed using a P_1 calculation, and using P_1 blackness theory in the slab. The agreement is good. Two spectra were used in the SWAKRAUM calculation. Figure 3.51, which compares the SLOP-1 and SWAKRAUM spectra in the middle of the slab, shows that two overlapping spectra lead to a good representation of the spatially dependent spectrum in this rather extreme case also.

*The gap, of half thickness 0.888 in., was composed of polyethylene, and loaded with 0.3545×10^{-3} moles/cc of U^{235}. The core composition was 0.02947 moles/cc of hydrogen, 0.01473 moles/cc of carbon, 0.09266 moles/cc of iron, 0.00652 moles/cc of aluminum, and 0.3727×10^{-3} moles/cc of U^{235}. Thus, the gap was characterized by a spectral hardness index of $\beta\gamma = 0.1$, while the core was characterized by a $\beta\gamma = 0.78$.

The use of two overlapping spectra has been found to be generally adequate, giving foil activation results that are within 3 percent of the SLOP-1 and/or experimental results in all cases investigated. Better agreement requires the use of four spectra, especially when a region contains a thermal resonance absorber. Figure 3.52 shows the SLOP-1 and SWAKRAUM spectra at the interface of a 1.776-cm full-width water gap and a core which was assumed to be normal density water spiked with 0.4×10^{-3} moles/cc of plutonium. The SWAKRAUM calculation was performed with two spectra; the infinite medium water and the water-plutonium spectra. The agreement is poor in the resonance region. Repetition of the SWAKRAUM calculation using four spectra, however, gives good agreement with SLOP-1 (Fig. 3.53). It should be mentioned

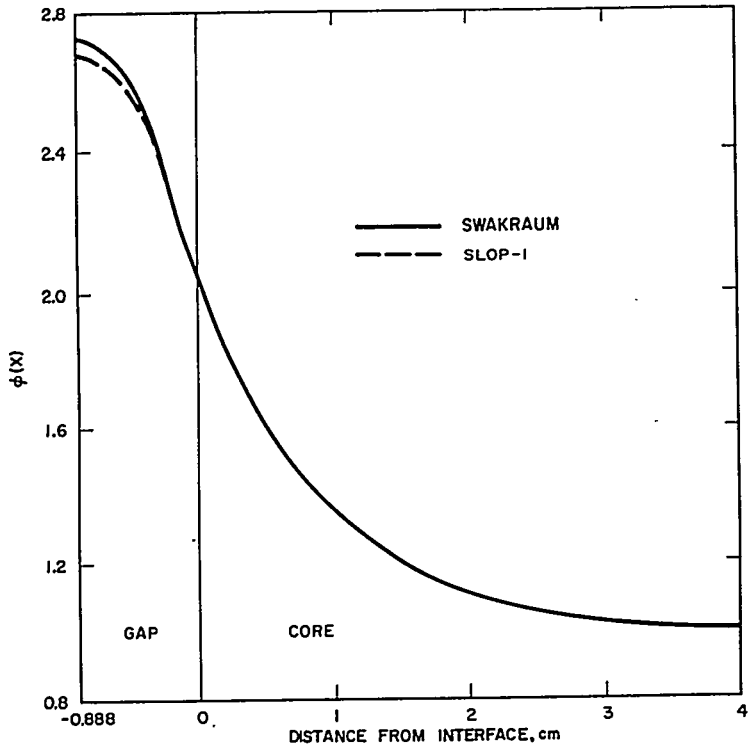

FIGURE 3.47. Comparison of SLOP-1 and SWAKRAUM Calculations of the Flux Transient near a Polyethylene Slab Inserted in a Core with a $\beta\gamma = 0.78$. (The P_1 approximation was used.)

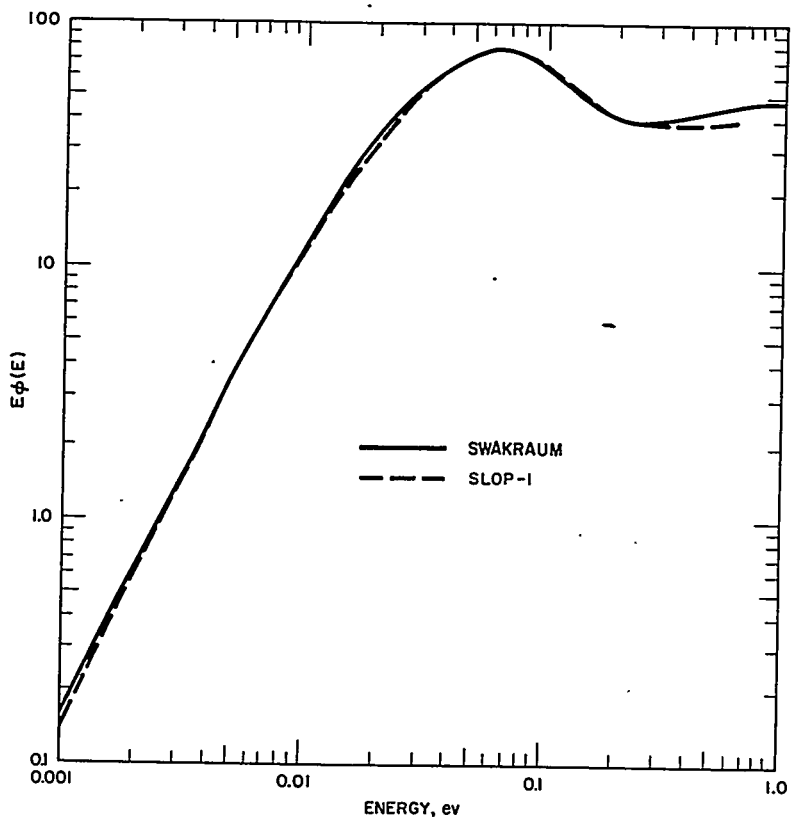

FIGURE 3.48. Comparison of SLOP-1 and SWAKRAUM Calculations of the Energy Spectrum at the Interface between a Polyethylene Slab and a Core with a $\beta\gamma = 0.78$.

that although the two-spectrum calculation yielded a comparatively poor representation of the detailed spectrum in and near the water gap, the computed flux transient agreed very well with the SLOP-1 calculation.

3.8 A TWO-MODE VARIATIONAL PROCEDURE FOR CALCULATING THERMAL-DIFFUSION THEORY PARAMETERS

P. A. Ombrellaro

A. Introduction

In depletion calculations, it is often necessary to account for changes not only in the fast group constants, but also for

changes in the thermal group constants caused by changes in the energy flux spectrum. Multigroup digital programs, such as the SOFOCATE[114] program, compute the thermal group constants averaged over a Wigner-Wilkins flux spectrum (see Sect. 3.7.B.3). However, it is rather expensive to incorporate such programs into the automatic group constant preparation component of depletion programs.

Thus, simpler approximate methods of obtaining the variation in thermal constants with depletion must be used. One approach is that of using fitted polynomials or tabulated data which give the behavior of the constants over the range of composition involved in depletion. This approach has been discussed in Chap. 2 with respect to fast constants and is conceptually the same for thermal constants. Another approach for the purpose of calculating thermal group constants rapidly is a two-mode variational procedure for approximating thermal diffusion theory parameters developed by Calame, Federighi, and Ombrellaro[130] for incorporation into the automatic group

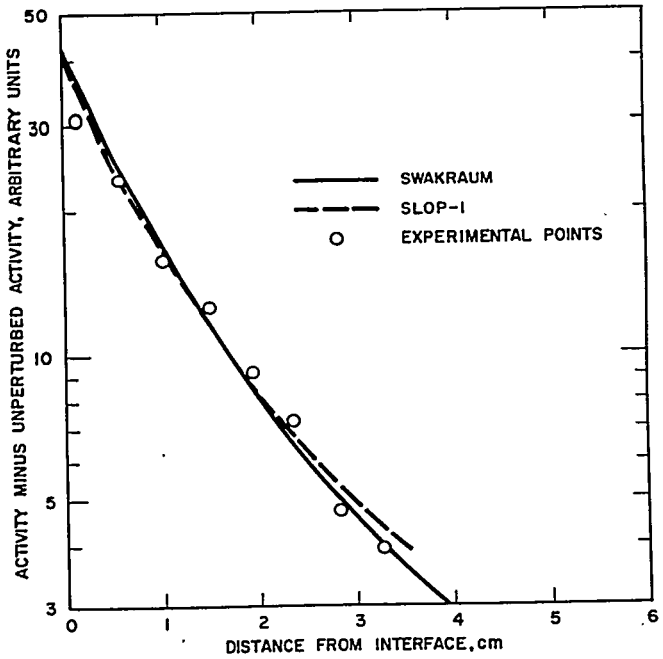

FIGURE 3.49. Activity of a 1/v Absorbing Foil Placed near a Polyethylene Slab in a Core with a $\beta\gamma = 0.78$, Minus the Activity of the Foil Deep in the Core as Calculated by SLOP-1 and SWAKRAUM in the Single P_1 Approximation.

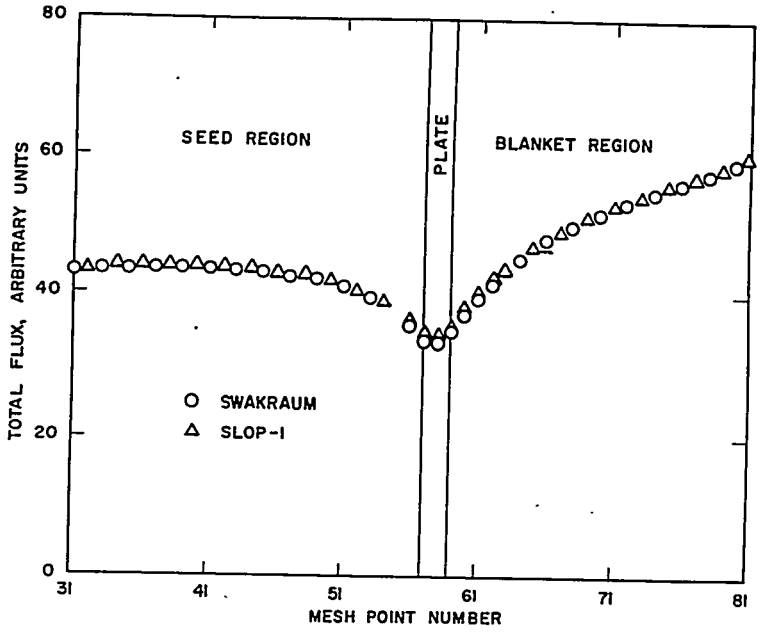

FIGURE 3.50. SLOP-1 and SWAKRAUM Calculations of the Flux near a Poison Plate Located between Seed and Blanket Regions in a Core.

constant preparation component of the KARE[131] program. The scheme, which is derived from the theory of the SWAKRAUM[124] program, described in Sect. 3.7, provides approximate Wigner-Wilkins[20] flux-spectrum-averaged thermal diffusion theory parameters.

As described in Sect. 3.7, the variational procedure is based on the assumption that a Wigner-Wilkins flux spectrum for a region can be well represented as a linear combination of two Wigner-Wilkins base spectra, namely, one characterized by a low $\beta\gamma$ and the other by a high $\beta\gamma$*. The coefficients for combining the two base spectra are provided by the theory and depend upon the concentrations of the component elements and the temperature of the medium. Once the approximate energy-dependent spectrum is calculated, the diffusion theory parameters are easily obtained from a flux weighted average of energy-dependent microscopic cross sections and diffusion

*$\beta\gamma$ is the ratio of the macroscopic absorption cross section at energy kT to the slowing-down power $\xi\Sigma_s$ at energies just above thermal. These energies are referred to as asymptotic energies in this section.

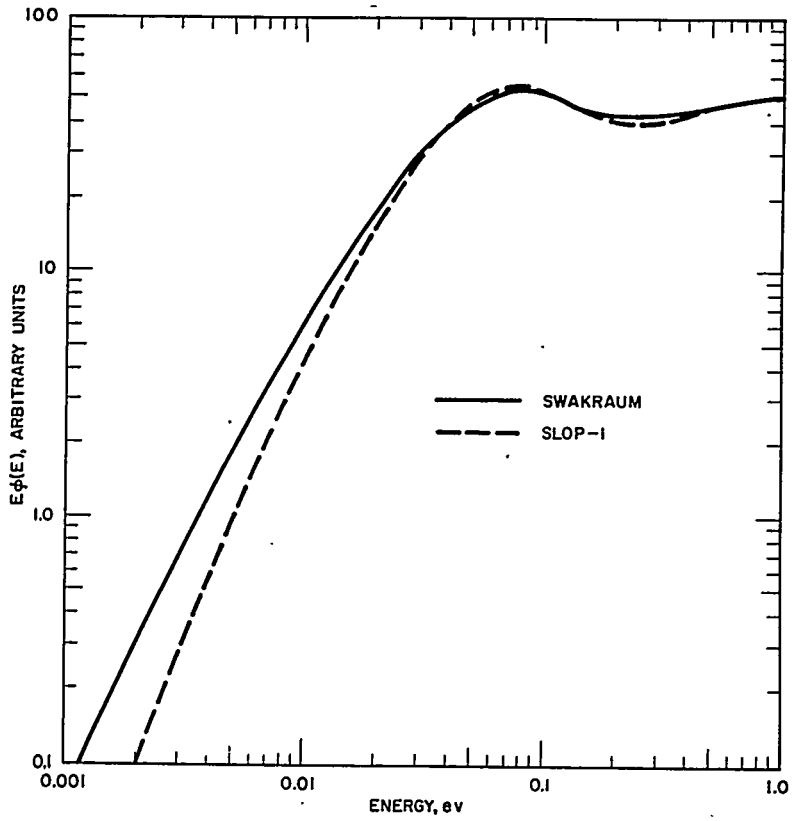

FIGURE 3.51. Comparison of SLOP-1 and SWAKRAUM Calculations of the Spectrum at the Center of the Poison Plate of Figure 3.50.

constants. Thus, the variational procedure gives a rather simple model for calculating thermal diffusion theory parameters. For experimental purposes, the variational procedure was programmed in FORTRAN language for the IBM-704, and the resulting program is called SPG. To test the validity of the variational procedure, the group constants calculated by SPG were compared with those obtained by the SOFOCATE program. It was found that the SPG results agree within 1 percent with those obtained from the SOFOCATE program. Moreover, because of the simplicity of the variational scheme, which amounts to finding the proper combination of the two base spectra, SPG calculates diffusion theory parameters much faster than SOFOCATE.

This section contains a description of the variational procedure for calculating thermal diffusion parameters and some comparisons of the results obtained from the SPG and SOFOCATE programs.

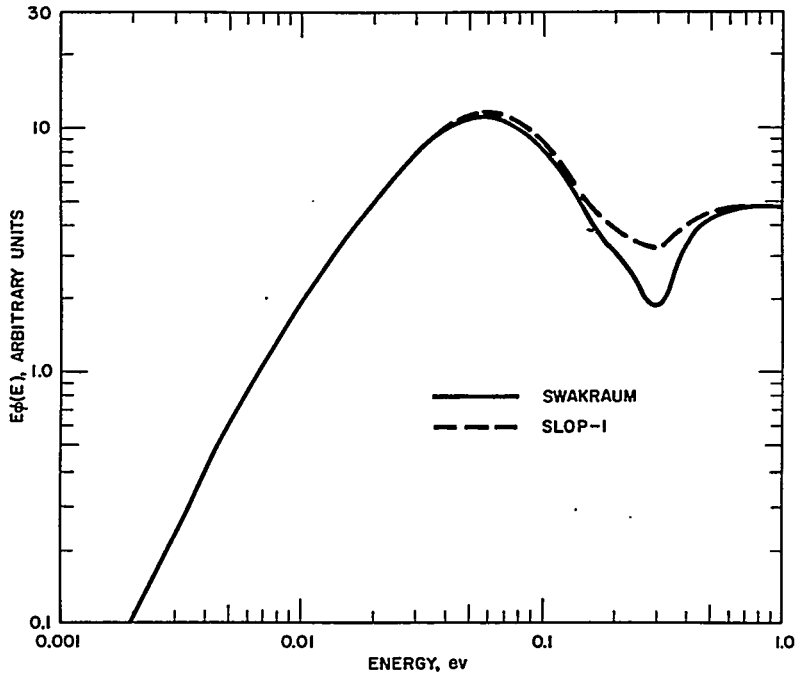

FIGURE 3.52. Comparison of SLOP-1 and Two Spectrum SWAKRAUM Calculations of the Spectrum at the Interface between a Water and a Water-Plutonium Region.

B. General Formulation

In the formulation of the theory, the energy range below 0.625 ev is represented in terms of lethargy. The infinite medium transport equation at lethargy u is then given by

$$\left[\frac{\Sigma_a(u)}{\Sigma_{SH}}+\frac{\Sigma^H_{s(u)}}{\Sigma_{SH}}\right]\phi(u)=\int_{u_c}^{\infty}\frac{\Sigma^H_s(u'\to u)}{\Sigma_{SH}}\phi(u')du'+\frac{S(u)}{\Sigma_{SH}}. \qquad \text{Eq. (3.317)}$$

This equation results from Eq. (3.261) where it is assumed that for elements other than hydrogen

$$\Sigma_s(u)\phi(u)-\int_{u_c}^{\infty}\Sigma_s(u'\to u)\phi(u')du'\approx 0,$$

and the cross sections are normalized with respect to the asymptotic energy value of the macroscopic scattering cross section for hydrogen, Σ_{SH}. To obtain a numerical solution of Eq. (3.317), the thermal energy range is divided into N equal

lethargy groups, and the integral equation is replaced by a matrix equation. Thus, Eq. (3.317) gives

$$\begin{bmatrix} \frac{\Sigma_a(u_1)}{\Sigma_{SH}} & & & \\ & \ddots & & 0 \\ & & \ddots & \\ 0 & & & \frac{\Sigma_a(u_N)}{\Sigma_{SH}} \end{bmatrix} \begin{bmatrix} \phi(u_1) \\ \vdots \\ \phi(u_N) \end{bmatrix}$$

$$+ \begin{bmatrix} \frac{\Sigma_s^H(u_1) - \Sigma_s^H(u_1 \to u_1)\Delta u}{\Sigma_{SH}} & \frac{-\Sigma_s^H(u_2 \to u_1)\Delta u}{\Sigma_{SH}} & \cdots & \frac{-\Sigma_s^H(u_N \to u_1)\Delta u}{\Sigma_{SH}} \\ \frac{-\Sigma_s^H(u_1 \to u_2)\Delta u}{\Sigma_{SH}} & \frac{\Sigma_s^H(u_2) - \Sigma_s^H(u_2 \to u_2)\Delta u}{\Sigma_{SH}} & \cdots & \frac{-\Sigma_s^H(u_N \to u_2)\Delta u}{\Sigma_{SH}} \\ \vdots & \vdots & & \vdots \\ \frac{-\Sigma_s^H(u_1 \to u_N)\Delta u}{\Sigma_{SH}} & \frac{-\Sigma_s^H(u_2 \to u_N)\Delta u}{\Sigma_{SH}} & \cdots & \frac{\Sigma_s^H(u_N) - \Sigma_s^H(u_N \to u_N)\Delta u}{\Sigma_{SH}} \end{bmatrix}$$

$$\begin{bmatrix} \phi(u_1) \\ \phi(u_2) \\ \vdots \\ \phi(u_N) \end{bmatrix} = \begin{bmatrix} \frac{S(u_1)}{\Sigma_{SH}} \\ \vdots \\ \frac{S(u_N)}{\Sigma_{SH}} \end{bmatrix}$$

Eq. (3.318)

where the hydrogen kernel matrix, denoted by the second term on the left-hand side of Eq. (3.318), includes the diagonal

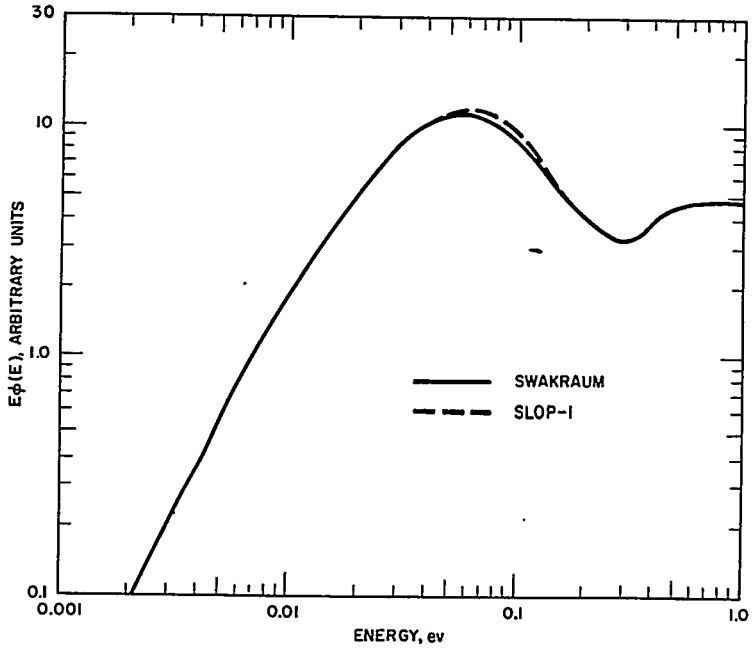

FIGURE 3.53. Comparison of SLOP-1 and Four Spectrum SWAKRAUM Calculations of the Spectrum at the Interface between a Water and a Water-Plutonium Region.

matrix of $\Sigma_s^H(u)$. Equation (3.318), therefore, represents a matrix equation of the form

$$H\phi = s \qquad \text{Eq. (3.319)}$$

which has the solution

$$\phi = H^{-1}s\,. \qquad \text{Eq. (3.320)}$$

An approximate, but quite accurate, solution of Eq. (3.320) can be obtained by using the variational method described in Sect. 3.7. To obtain the required variational expression for Eq. (3.320), it is necessary also to consider the solution to the auxiliary problem

$$\phi^\dagger H = s^\dagger \qquad \text{Eq. (3.321)}$$

where $\phi^\dagger$ and $s^\dagger$ are the adjoint flux and source. The desired variational expression is that given by Eq. (3.294), namely,

$$J(\phi, \phi^\dagger) = \frac{(\phi^\dagger, s)(s^\dagger, \phi)}{(\phi^\dagger, H\phi)} \qquad \text{Eq. (3.322)}$$

which becomes for the desired weighted average $(s^\dagger \phi)$,

$$J(\phi, \phi^\dagger) = (s^\dagger, \phi). \qquad \text{Eq. (3.323)}$$

The basic approximation which is made in the scheme is that for a given medium the lethargy-dependent spectrum ϕ given by the solution of Eq. (3.320) can be represented by a linear combination of a soft flux spectrum characterized by a low $\beta\gamma$ and a hard flux spectrum characterized by a high $\beta\gamma$. The base spectra ϕ_s and ϕ_h are solutions of Eq. (3.320) for a medium having a low $\beta\gamma$ (pure water) and a medium having a high $\beta\gamma$, respectively. Thus, for any given medium the flux at lethargy u_n is given by

$$\phi(u_n) = \alpha_1 \phi_s(u_n) + \alpha_2 \phi_h(u_n)$$

where α_1 and α_2 are the coefficients for combining the two base spectra. In matrix notation, the expression for the flux is given by $\phi = \Phi\alpha$ where

$$\Phi\alpha = \begin{bmatrix} \phi_s(u_1) & \phi_h(u_1) \\ \cdot & \cdot \\ \cdot & \cdot \\ \cdot & \cdot \\ \phi_s(u_N) & \phi_h(u_N) \end{bmatrix} \begin{bmatrix} \alpha_1 \\ \alpha_2 \end{bmatrix}. \qquad \text{Eq. (3.324)}$$

In a similar manner, the adjoint flux $\phi^\dagger$ for the given medium, determined from the solution of Eq. (3.321), is assumed to be a linear combination of the soft and hard adjoint base spectra $\phi_s^\dagger$ and $\phi_h^\dagger$, also determined from solving Eq. (3.321). When $s^\dagger = \Sigma_a$ in Eq. (3.321), Eq. (3.322) gives, as shown by Eq. (3.323), a variational expression for the total absorption rate in any medium. For this choice of adjoint source, it is found that the adjoint flux $\phi^\dagger$ for a given medium can be approximated by the function $\phi^\dagger = a + bE$, where a and b are constants.

In accordance with this, the soft and hard adjoint spectra are approximated by $\phi_s^\dagger = 1$ and $\phi_h^\dagger = E$, so that $\phi^\dagger = \alpha^\dagger \Phi^\dagger$ with

$$\alpha^\dagger \Phi^\dagger = \left(\alpha_1^\dagger \alpha_2^\dagger\right) \begin{vmatrix} 1 & \cdots & 1 \\ E_1 & \cdots & E_N \end{vmatrix} . \qquad \text{Eq. (3.325)}$$

Substituting $\Phi\,\alpha$ and $\alpha^\dagger \Phi^\dagger$ for ϕ and $\phi^\dagger$ in Eqs. (3.322) and (3.323), and using the definitions

$$\begin{aligned} \mathcal{S}^\dagger &= s^\dagger \Phi \\ \mathcal{S} &= \Phi^\dagger s \\ \mathcal{H} &= \Phi^\dagger H \Phi \end{aligned} \qquad \text{Eq. (3.326)}$$

Eqs. (3.322) and (3.323) become

$$I(\alpha, \alpha^\dagger) = \frac{(\alpha^\dagger, \mathcal{S})(\mathcal{S}^\dagger, \alpha)}{(\alpha^\dagger, \mathcal{H}\alpha)} \qquad \text{Eq. (3.327)}$$

and

$$I(\alpha, \alpha^\dagger) = (\mathcal{S}^\dagger, \alpha) \qquad \text{Eq. (3.328)}$$

Since, for the exact solutions ϕ and $\phi^\dagger$ Eq. (3.322) reduces to Eq. (3.323), it is required that Eq. (3.327) reduce to Eq. (3.328); this occurs when

$$\mathcal{H}\alpha = \mathcal{S} . \qquad \text{Eq. (3.329)}$$

Thus, from Eq. (3.329) it is seen that the coefficients α are calculated from

$$\alpha = \mathcal{H}^{-1}\mathcal{S} . \qquad \text{Eq. (3.330)}$$

Once the coefficients α_1 and α_2 are calculated from Eq. (3.330), the approximate Wigner-Wilkins spectrum is determined.

Figure 3.54 shows a comparison of the exact spectrum calculated using Eq. (3.320) for a medium characterized by a

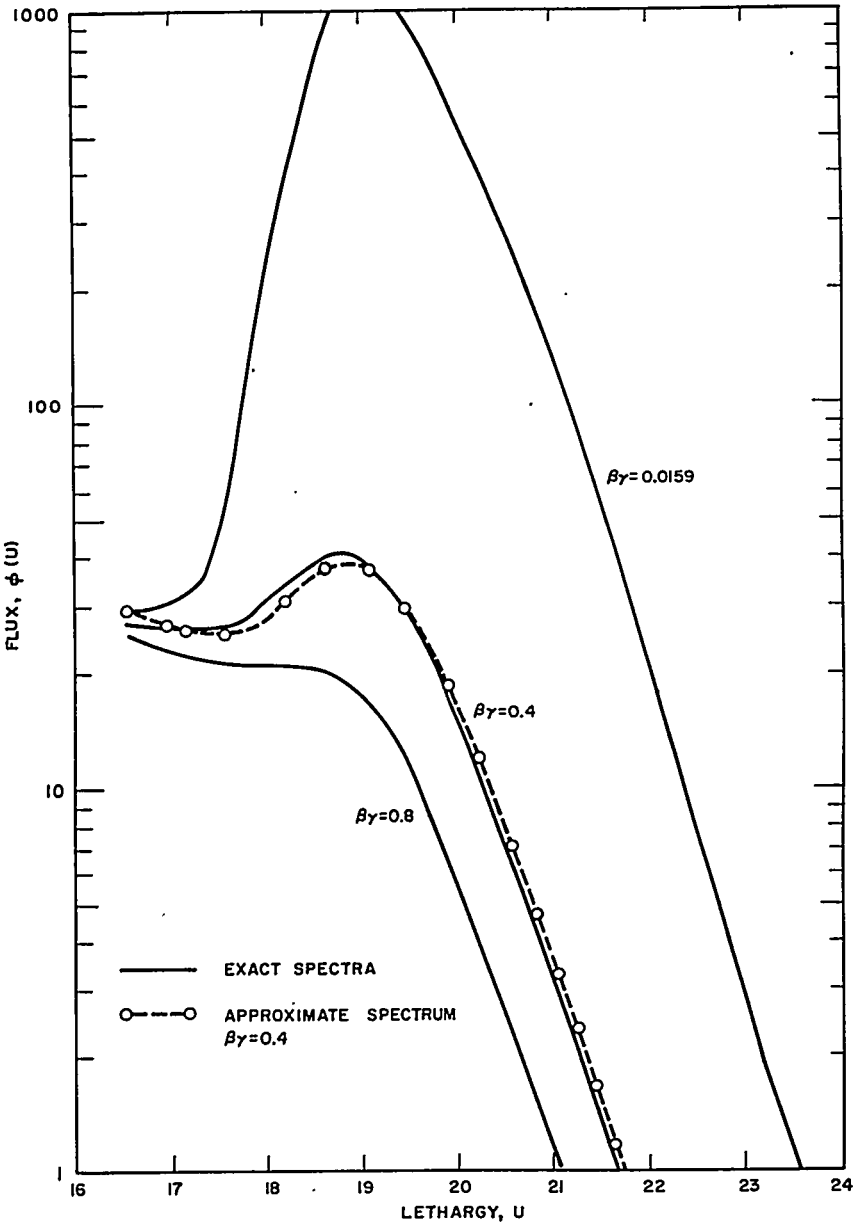

FIGURE 3.54. Comparison of the Approximate Spectrum for $\beta\gamma = 0.4$ Calculated with SPG Using Trial Spectra with $\beta\gamma = 0.0159$ and $\beta\gamma = 0.8$ with a SOFOCATE Calculation at 68° F.

$\beta\gamma = 0.4$, and the approximate spectrum obtained by combining base spectra characterized by $\beta\gamma$'s of 0.159 and 0.8 in accordance with Eqs. (3.324) through (3.330). As in the case of the actual spectrum, the base spectra were calculated using Eq. (3.320). Figure 3.54 shows that the agreement between the exact and the approximate spectrum is excellent, thereby verifying the adequacy of the approximation.

C. Procedure for Calculating Thermal Constants

In the operator H of Eq. (3.318), it is convenient to separate out of the total absorption cross section the non-$1/v$ components and the $1/v$ components. Thereby the matrix H, when written in terms of microscopic absorption cross sections, becomes

$$H = \sum_{i \neq \frac{1}{v}} \frac{N^i}{N^H} \begin{bmatrix} \frac{\sigma_a^i(u_1)}{\sigma_{SH}} & & & 0 \\ & \ddots & & \\ & & \ddots & \\ 0 & & & \frac{\sigma_a^i(u_N)}{\sigma_{SH}} \end{bmatrix}$$

$$+ \Gamma \begin{bmatrix} \left(\frac{0.0253}{E_o}\right)^{1/2} e^{u_{1/2}} & & & \\ & \ddots & & 0 \\ & & \ddots & \\ 0 & & & \left(\frac{0.0253}{E_o}\right)^{1/2} e^{u_N/2} \end{bmatrix}$$

$$+ \begin{bmatrix} K_{11} & K_{21} & \cdots & K_{N1} \\ K_{12} & K_{22} & \cdots & K_{N2} \\ \vdots & & & \\ K_{1N} & K_{2N} & \cdots & K_{NN} \end{bmatrix}$$

Eq. (3.331)

where

N^i/N^H = ratio of the atom density of the non-$1/v$ element i to that of hydrogen

$\sigma_a^i(u)$ = the microscopic absorption cross section for element i

σ_{SH} = asymptotic energy value of the microscopic cross section for hydrogen given as 20.7 barns

$\Gamma = \sum_i N^i \sigma_o^i / \Sigma_{SH}$, where for the $1/v$ element i, N^i is the atom density and σ_o^i is the absorption cross section at 0.0253 ev

$\left(\frac{0.0253}{E_o}\right)^{1/2} e^{u/2}$ = $1/v$ absorption cross section at lethargy u having unit cross section at 0.0253 ev ($E = E_o$ corresponds to $u = 0$)

K_{mn} = element in row n and column m of the hydrogen kernel matrix.

One permanently establishes a set of base spectra, a kernel matrix, and a source matrix for each given temperature. Then, for each temperature, the base spectra are combined with the cross section and kernel matrices of the operator H to obtain a set of lethargy-independent 2 x 2 matrices. This is done in the following manner. From Eqs. (3.331), (3.324), and (3.325), it follows that

$$\mathcal{H} = \Phi^\dagger H \Phi$$

$$= \sum_{i \neq 1/v} \frac{N^i}{N^H} \begin{bmatrix} \sum_{n=1}^{N} \frac{\sigma_a^i(u_n)\phi_s(u_n)}{\sigma_{SH}} & \sum_{n=1}^{N} \frac{\sigma_a^i(u_n)\phi_h(u_n)}{\sigma_{SH}} \\ \sum_{n=1}^{N} \frac{E_n \sigma_a^i(u_n)\phi_s(u_n)}{\sigma_{SH}} & \sum_{n=1}^{N} \frac{E_n \sigma_a^i(u_n)\phi_h(u_n)}{\sigma_{SH}} \end{bmatrix}$$

$$+ \Gamma \begin{bmatrix} \left(\frac{0.0253}{E_o}\right)^{1/2} \sum_{n=1}^{N} e^{u_n/2}\phi_s(u_n) & \left(\frac{0.0253}{E_o}\right)^{1/2} \sum_{n=1}^{N} e^{u_n/2}\phi_h(u_n) \\ \left(\frac{0.0253}{E_o}\right)^{1/2} \sum_{n=1}^{N} E_n e^{u_n/2}\phi_s(u_n) & \left(\frac{0.0253}{E_o}\right)^{1/2} \sum_{n=1}^{N} E_n e^{u_n/2}\phi_h(u_n) \end{bmatrix}$$

$$+\begin{bmatrix} \sum_{m=1}^{N}\sum_{n=1}^{N} K_{mn}\,\phi_s(u_n) & \sum_{m=1}^{N}\sum_{n=1}^{N} K_{mn}\,\phi_h(u_n) \\ \sum_{m=1}^{N}\sum_{n=1}^{N} E_m\,K_{mn}\,\phi_s(u_n) & \sum_{m=1}^{N}\sum_{n=1}^{N} E_m\,K_{mn}\,\phi_h(u_n) \end{bmatrix}. \qquad \text{Eq. (3.332)}$$

Each matrix in the preceding equation consists entirely of elements that are independent of material composition. These matrices comprise, at each temperature, the scheme's cross section library. It is seen from Eq. (3.332) that to compute the α matrix for a given medium, it is only necessary to specify the material's composition by the parameters N^i/N^H and Γ and thus compute $\mathcal{K}$, a 2×2 matrix consisting of a sum of a set of 2×2 library matrices which include the base spectra. From Eqs. (3.318), (3.325), and (3.326) is obtained the source matrix $\mathcal{S}$ for each temperature. Since $S(u)$ in Eq. (3.318) is due to hydrogen alone, it is given by $S(u)=N^H S'(u)$, where $S'(u)$ is the hydrogen slowing-down source independent of N^H. Thus, the source matrix $\mathcal{S}$ for each temperature is given by

$$\mathcal{S} = \begin{bmatrix} \sum_{n=1}^{N} \dfrac{S'(u_n)}{\sigma_{SH}} \\ \sum_{n=1}^{N} \dfrac{E_n S'(u_n)}{\sigma_{SH}} \end{bmatrix}. \qquad \text{Eq. (3.333)}$$

The temperature-dependent matrices $\mathcal{S}$ are also part of the library and are independent of material composition. Once $\mathcal{K}$ and $\mathcal{S}$ are calculated from Eqs. (3.332) and (3.333), the coefficients α_1 and α_2 are calculated from Eq. (3.330) as

$$\begin{bmatrix} \alpha_1 \\ \alpha_2 \end{bmatrix} = \frac{1}{(a_{11}a_{22} - a_{21}a_{12})} \begin{bmatrix} a_{22} & -a_{12} \\ -a_{21} & a_{11} \end{bmatrix} \begin{bmatrix} \sum_{n=1}^{N} \dfrac{S'(u_n)}{\sigma_{SH}} \\ \sum_{n=1}^{N} \dfrac{E_n S'(u_n)}{\sigma_{SH}} \end{bmatrix} \qquad \text{Eq. (3.334)}$$

where

$$\begin{bmatrix} a_{11} & a_{12} \\ a_{21} & a_{22} \end{bmatrix}$$

is the 2×2 matrix $\mathcal{H}$. Once the coefficients α_1 and α_2 are calculated, the average microscopic absorption and fission production cross sections for various elements can be easily obtained from a matrix multiplication of a matrix β consisting of base spectra weighted absorption and fission production cross sections and the matrix α. Thus, the matrix multiplication $\beta\alpha$ gives

$$\beta\alpha =$$

$$\begin{bmatrix} \alpha_1 \left(\frac{0.0253}{E_o}\right)^{1/2} \sum_{n=1}^{N} e^{u_n/2} \phi_s(u_n) + \alpha_2 \left(\frac{0.0253}{E_o}\right)^{1/2} \sum_{n=1}^{N} e^{u_n/2} \phi_h(u_n) \\ \vdots \qquad\qquad\qquad\qquad \vdots \\ \alpha_1 \sum_{n=1}^{N} \sigma_a^i(u_n)\phi_s(u_n) + \alpha_2 \sum_{n=1}^{N} \sigma_a^i(u_n)\phi_h(u_n) \\ \alpha_1 \sum_{n=1}^{N} \nu^1 \sigma_f^1(u_n)\phi_s(u_n) + \alpha_2 \sum_{n=1}^{N} \nu^1 \sigma_f^1(u_n)\phi_h(u_n) \\ \vdots \qquad\qquad\qquad\qquad \vdots \\ \alpha_1 \sum_{n=1}^{N} \nu^i \sigma_f^i(u_n)\phi_s(u_n) + \alpha_2 \sum_{n=1}^{N} \nu^i \sigma_f^i(u_n)\phi_h(u_n) \\ \alpha_1 \sum_{n=1}^{N} \phi_s(u_n) + \alpha_2 \sum_{n=1}^{N} \phi_h(u_n) \end{bmatrix}$$

Eq. (3.335)

where the last row of this matrix gives the integrated flux. The average microscopic cross sections for a given element are calculated by

$$\langle \sigma_a \rangle^i = \frac{\alpha_1 \sum_{n=1}^{N} \sigma_a^i(u_n)\, \phi_s(u_n) + \alpha_2 \sum_{n=1}^{N} \sigma_a^i(u_n)\, \phi_h(u_n)}{\alpha_1 \sum_{n=1}^{N} \phi_s(u_n) + \alpha_2 \sum_{n=1}^{N} \phi_h(u_n)} \qquad \text{Eq. (3.336)}$$

and

$$\langle \nu\sigma_f \rangle^i = \frac{\alpha_1 \sum_{n=1}^{N} \nu^i \sigma_f^i(u_n)\, \phi_s(u_n) + \alpha_2 \sum_{n=1}^{N} \nu^i \sigma_f^i(u_n)\, \phi_h(u_n)}{\alpha_1 \sum_{n=1}^{N} \phi_s(u_n) + \alpha_2 \sum_{n=1}^{N} \phi_h(u_n)} \qquad \text{Eq. (3.337)}$$

where the symbol σ_a^i represents also the unit $1/v$ cross section. To obtain the $1/v$ cross section for element i, one simply multiplies the average unit $1/v$ cross section given by Eq. (3.336) by σ_o^i, the absorption cross section for element i at 0.0253 ev. The diffusion theory parameters Σ_a and $\nu\Sigma_f$ are calculated as

$$\Sigma_a = \sum_i N^i \langle \sigma_a \rangle^i \qquad \nu\Sigma_f = \sum_i N^i \langle \nu\sigma_f \rangle^i \ .$$

Here Σ_a includes the $1/v$ cross sections given by $\langle \sigma_a \rangle_1 \sum_i N^i \sigma_o^i$ where $\langle \sigma_a \rangle_1$ is the average unit $1/v$ cross section. To calculate the average diffusion constant, it is necessary first to calculate a lethargy-dependent microscopic transport cross section given by

$$\begin{bmatrix} \Sigma_{tr}(u_1) \\ \cdot \\ \cdot \\ \cdot \\ \cdot \\ \Sigma_{tr}(u_N) \end{bmatrix} =$$

$$\begin{bmatrix} \Gamma \Sigma_{SH} \left(\frac{0.0253}{E_o}\right)^{1/2} e^{u_1/2} + \sum_i N^i \sigma_a^i(u_1) + N^H(1-\mu(u_1))\sigma_s^H(u_1) + \sum_i N^i(1-\bar{\mu}^i)\sigma_s^i \\ \cdot \\ \cdot \\ \cdot \\ \cdot \\ \Gamma \Sigma_{SH}\left(\frac{0.0253}{E_o}\right)^{1/2} e^{u_N/2} + \sum_i N^i \sigma_a^i(u_N) + N^H(1-\mu(u_N))\sigma_s^H(u_N) + \sum_i N^i(1-\bar{\mu}^i)\sigma_s^i \end{bmatrix}$$

Eq. (3.338)

where $(1-\mu(u_n))\,\sigma_s^H(u_n)$ and $(1-\bar{\mu}^i)\,\sigma_s^i$ describe the anisotropic character of the scattering cross section for hydrogen and element i, respectively; the quantity $(1-\bar{\mu}^i)\,\sigma_s^i$ for element i is a constant for all lethargies u_n. The lethargy-dependent diffusion constant is calculated as

$$\begin{bmatrix} D(u_1) \\ \cdot \\ \cdot \\ \cdot \\ D(u_N) \end{bmatrix} = \begin{bmatrix} 1/3\,[\Sigma_{tr}(u_1)]^{-1} \\ \cdot \\ \cdot \\ \cdot \\ \frac{1}{3}[\Sigma_{tr}(u_N)]^{-1} \end{bmatrix} \qquad \text{Eq. (3.339)}$$

from which the average diffusion constant is given by

$$\langle D \rangle = \frac{\alpha_1 \sum_{n=1}^{N} D(u_n)\,\phi_s(u_n) + \alpha_2 \sum_{n=1}^{N} D(u_n)\,\phi_h(u_n)}{\alpha_1 \sum_{n=1}^{N} \phi_s(u_n) + \alpha_2 \sum_{n=1}^{N} \phi_h(u_n)} \cdot \qquad \text{Eq. (3.340)}$$

D. Results

In calculating the base spectra using the equation $H\Phi = s$, the medium characterized by a low and a high $\beta\gamma$ can be considered to be made up of various proportions of $1/v$ and non-$1/v$ elements. It has been found, however, that by choosing base spectra for various temperatures on the basis of a medium consisting of only $1/v$ elements, one can obtain satisfactory cross sections and approximate spectra for cores consisting of U^{235}, U^{238}, and $1/v$ elements. Non-$1/v$ elements such as xenon may also be treated in this scheme as long as their concentration is sufficiently dilute that their presence has little effect on the spectrum.

Some results of diffusion theory parameters and average microscopic cross sections for two core compositions and pure water are represented in Tables 3.25, 3.26, and 3.27 for the temperatures 68°F, 300°F, and 500°F. For each temperature, the base spectra were established on the basis of a medium consisting of $1/v$ elements characterized by a $\beta\gamma = 0.016$ and a $\beta\gamma = 0.5$. At each given temperature, the approximate spectra for the composition given in the tables were then computed by taking linear combinations of the base spectra established for a given temperature using the coefficients α_1 and α_2 determined from the actual core compositions.

TABLE 3.25 — COMPARISON OF SPG AVERAGED MICROSCOPIC AND MACROSCOPIC CROSS SECTIONS WITH SOFOCATE AVERAGES FOR PROBLEM 1*

Diffusion Theory Parameters

	68°F		300°F		500°F	
	SOFOCATE	SPG	SOFOCATE	SPG	SOFOCATE	SPG
Σ_a (cm^{-1})	0.05823	0.05779	0.04900	0.04865	0.04376	0.04345
$\nu\Sigma_f$ (cm^{-1})	0.09101	0.09027	0.07615	0.07555	0.06771	0.06717
D (cm)	0.23000	0.23108	0.25670	0.25690	0.27750	0.27710

Microscopic Absorption Cross Sections (σ_a, barns)

	68°F		300°F		500°F	
Element	SOFOCATE	SPG	SOFOCATE	SPG	SOFOCATE	SPG
Unit 1/v	0.8060	0.7996	0.6921	0.6869	0.6252	0.6208
Hydrogen	0.2676	0.2655	0.2298	0.2281	0.2076	0.2061
Oxygen	0.1612×10^{-3}	0.1599×10^{-3}	0.1384×10^{-3}	0.1374×10^{-3}	0.1250×10^{-3}	0.1242×10^{-3}
Zirconium	0.1451	0.1439	0.1246	0.1236	0.1125	0.1117
Carbon	0.2579×10^{-2}	0.2559×10^{-2}	0.2215×10^{-2}	0.2198×10^{-2}	0.2001×10^{-2}	0.1987×10^{-2}
Aluminum	0.1854	0.1839	0.1592	0.1580	0.1438	0.1428
Uranium 235	0.5411×10^{3}	0.5371×10^{3}	0.4523×10^{3}	0.4490×10^{3}	0.4023×10^{3}	0.3995×10^{3}
Uranium 238	0.2200×10^{1}	0.2183×10^{1}	0.1889×10^{1}	0.1875×10^{1}	0.1707×10^{1}	0.1695×10^{1}

TABLE 3.25 — COMPARISON OF SPG AVERAGED MICROSCOPIC AND MACROSCOPIC CROSS SECTIONS WITH SOFOCATE AVERAGES FOR PROBLEM 1* (Continued)

Microscopic Absorption Cross Section (σ_a, barns)

	68°F		300°F		500°F	
	SOFOCATE	SPG	SOFOCATE	SPG	SOFOCATE	SPG
Xenon	0.2564×10^{7}	0.2505×10^{7}	0.2329×10^{7}	0.2289×10^{7}	0.2101×10^{7}	0.2070×10^{7}
Uranium 233	0.4725×10^{3}	0.4683×10^{3}	0.4045×10^{3}	0.4021×10^{3}	0.3658×10^{3}	0.3642×10^{3}
Hydrogen transport	0.3230×10^{2}	0.3191×10^{2}	0.2774×10^{2}	0.2744×10^{2}	0.2503×10^{2}	0.2479×10^{2}

Microscopic Fission Production Cross Sections ($\nu\sigma_f$, barns)

	68°F		300°F		500°F	
Element	SOFOCATE	SPG	SOFOCATE	SPG	SOFOCATE	SPG
Uranium 235	0.1127×10^{4}	0.1118×10^{4}	0.9428×10^{3}	0.9353×10^{3}	0.8383×10^{3}	0.8316×10^{3}
Uranium 233	0.1097×10^{4}	0.1090×10^{4}	0.9440×10^{3}	0.9376×10^{3}	0.8560×10^{3}	0.8499×10^{3}

*Hydrogen N = 0.04766
Oxygen N = 0.02347
Zirconium N = 0.01146
Carbon N = 0.00911
Aluminum N = 0.000477
Uranium 235 N = 0.00008077
Uranium 238 N = 0.00000585
All atom densities expressed in units of 10^{24} atoms/cm^3.

TABLE 3.26 — COMPARISON OF SPG AVERAGED MICROSCOPIC AND MACROSCOPIC CROSS SECTIONS WITH SOFOCATE AVERAGES FOR PROBLEM 2*

Diffusion Theory Parameters

	68°F		300°F		500°F	
	SOFOCATE	SPG	SOFOCATE	SPG	SOFOCATE	SPG
Σ_a (cm^{-1})	0.07642	0.07551	0.06600	0.06519	0.05977	0.05903
$\nu\Sigma_f$ (cm^{-1})	0.13640	0.13460	0.11750	0.11588	0.10620	0.10465
D (cm)	0.34040	0.34330	0.36540	0.36720	0.38610	0.38690

Microscopic Absorption Cross Sections (σ_a, barns)

	68°F		300°F		500°F	
Element	SOFOCATE	SPG	SOFOCATE	SPG	SOFOCATE	SPG
Unit 1/v	0.7345	0.7258	0.6474	0.6397	0.5932	0.5863
Hydrogen	0.2438	0.2409	0.2149	0.2123	0.1969	0.1946
Oxygen	0.1469×10^{-3}	0.1451×10^{-3}	0.1295×10^{-3}	0.1279×10^{-3}	0.1186×10^{-3}	0.1172×10^{-3}
Zirconium	0.1322	0.1306	0.1165	0.1151	0.1068	0.1055
Carbon	0.2350×10^{-2}	0.2322×10^{-2}	0.2072×10^{-2}	0.2047×10^{-2}	0.1898×10^{-2}	0.1876×10^{-2}
Aluminum	0.1689	0.1669	0.1489	0.1471	0.1364	0.1348
Uranium 235	0.4882×10^{3}	0.4824×10^{3}	0.4202×10^{3}	0.4150×10^{3}	0.3797×10^{3}	0.3750×10^{3}
Uranium 238	0.2005×10^{1}	0.1981×10^{1}	0.1767×10^{1}	0.1746×10^{1}	0.1619×10^{1}	0.1600×10^{1}

TABLE 3.26 — COMPARISON OF SPG AVERAGED MICROSCOPIC AND MACROSCOPIC CROSS SECTIONS WITH SOFOCATE AVERAGES FOR PROBLEM 2* (Continued)

Microscopic Absorption Cross Sections (σ_a, barns)

	68°F		300°F		500°F	
Element	SOFOCATE	SPG	SOFOCATE	SPG	SOFOCATE	SPG
Xenon 135	0.2306×10^{7}	0.2227×10^{7}	0.2128×10^{7}	0.2071×10^{7}	0.1940×10^{7}	0.1895×10^{7}
Uranium 233	0.4316×10^{3}	0.4271×10^{3}	0.3796×10^{3}	0.3763×10^{3}	0.3482×10^{3}	0.3456×10^{3}
Hydrogen transport	0.2938×10^{2}	0.2892×10^{2}	0.2590×10^{2}	0.2551×10^{2}	0.2370×10^{2}	0.2338×10^{2}

Microscopic Fission Production Cross Sections ($\nu\sigma_f$, barns)

	68°F		300°F		500°F	
Element	SOFOCATE	SPG	SOFOCATE	SPG	SOFOCATE	SPG
Uranium 235	0.1016×10^{4}	0.1003×10^{4}	0.8756×10^{3}	0.8635×10^{3}	0.7909×10^{3}	0.7798×10^{3}
Uranium 238	0.1004×10^{4}	0.9927×10^{3}	0.8865×10^{3}	0.8763×10^{3}	0.8152×10^{3}	0.8055×10^{3}

*Hydrogen N = 0.03136
Oxygen N = 0.01568
Zirconium N = 0.02067
Aluminum M = 0.002982
Uranium 235 N = 0.0001342
Uranium 238 N = 0.00000825
All atom densities expressed in units of 10^{24} atoms/cm^3.

TABLE 3.27 — COMPARISON OF SPG AVERAGED MICROSCOPIC AND MACROSCOPIC CROSS SECTIONS WITH SOFOCATE AVERAGES FOR PROBLEM 3*

Diffusion Theory Parameters

	68°F		300°F		500°F	
	SOFOCATE	SPG	SOFOCATE	SPG	SOFOCATE	SPG
Σ_a (cm^{-1})	0.01923	0.01908	0.01613	0.01605	0.01441	0.01434
$\nu\Sigma_f$(cm^{-1})	0.00000	0.00000	0.00000	0.00000	0.00000	0.00000
D (cm)	0.15950	0.1597	0.18680	0.18630	0.2071	0.2060

Microscopic Absorption Cross Sections (σ_a, barns)

	68°F		300°F		500°F	
Element	SOFOCATE	SPG	SOFOCATE	SPG	SOFOCATE	SPG
Unit 1/v	0.8676	0.8609	0.7281	0.7240	0.6501	0.6471
Hydrogen	0.2880	0.2858	0.2417	0.2404	0.2158	0.2148
Oxygen	0.1735×10^{-3}	0.1722×10^{-3}	0.1456×10^{-3}	0.1448×10^{-3}	0.1300×10^{-3}	0.1294×10^{-3}
Zirconium	0.1562	0.1550	0.1311	0.1303	0.1170	0.1165
Carbon	0.2776×10^{-2}	0.2755×10^{-2}	0.2330×10^{-2}	0.2317×10^{-2}	0.2080×10^{-2}	0.2071×10^{-2}
Aluminum	0.1995	0.1980	0.1674	0.1665	0.1495	0.1488
Uranium 235	0.5868×10^{3}	0.5824×10^{3}	0.4782×10^{3}	0.4758×10^{3}	0.4198×10^{3}	0.4181×10^{3}
Uranium 238	0.2368×10^{1}	0.2350×10^{1}	0.1987×10^{1}	0.1977×10^{1}	0.1775×10^{1}	0.1767×10^{1}

TABLE 3.27 — COMPARISON OF SPG AVERAGED MICROSCOPIC AND MACROSCOPIC CROSS SECTIONS WITH SOFOCATE AVERAGES FOR PROBLEM 2* (Continued)

Microscopic Fission Production Cross Sections (σ_a, barns)

	68°F		300°F		500°F	
Element	SOFOCATE	SPG	SOFOCATE	SPG	SOFOCATE	SPG
Xenon 135	0.2780×10^{7}	0.2736×10^{7}	0.2489×10^{7}	0.2460×10^{7}	0.2224×10^{7}	0.2204×10^{7}
Uranium 233	0.5078×10^{3}	0.5026×10^{3}	0.4247×10^{3}	0.4223×10^{3}	0.3795×10^{3}	0.3783×10^{3}
Hydrogen transport	0.3481×10^{2}	0.3438×10^{2}	0.2923×10^{2}	0.2895×10^{2}	0.2607×10^{2}	0.2587×10^{2}

Microscopic Fission Production Cross Sections ($\nu\sigma_f$, barns)

	68°F		300°F		500°F	
Element	SOFOCATE	SPG	SOFOCATE	SPG	SOFOCATE	SPG
Uranium 235	0.1222×10^{4}	0.1213×10^{4}	0.9971×10^{3}	0.9918×10^{3}	0.8751×10^{3}	0.8711×10^{3}
Uranium 233	0.1178×10^{4}	0.1170×10^{4}	0.9901×10^{3}	0.9857×10^{3}	0.8875×10^{3}	0.8837×10^{3}

*Hydrogen N = 0.06673
Oxygen N = 0.03336
All atom densities expressed in units of 10^{24} atoms/cm^3.

The difussion theory parameters and average microscopic cross sections presented in the tables have been obtained using microscopic cross sections and diffusion theory constants averaged with the approximate spectra. The results are also compared with the cross section and diffusion theory parameters obtained from the SOFOCATE program. The comparison shows that the SPG results agree with those of SOFOCATE within 1 percent. It should be noted, however, that although the agreement between the SPG and SOFOCATE parameters is within 1 percent, the ratio of $\nu\Sigma_f/\Sigma_a$ agrees to within 0.1 percent. Figures 3.55, 3.56, and 3.57 show, for the three compositions, a comparison of the approximate spectrum for each temperature calculated with SPG and the actual spectrum obtained from the SOFOCATE program.

An approximate estimate of the running time for SPG is 0.25 second per region for a region consisting of the unit $1/v$ element and 3 non-$1/v$ elements. As the number of non-$1/v$ elements is decreased, the running time is shortened. This variational cross section scheme, thus, provides a simple method for calculating thermal parameters and accounts for the changes in the parameters resulting from changes in the thermal spectrum.

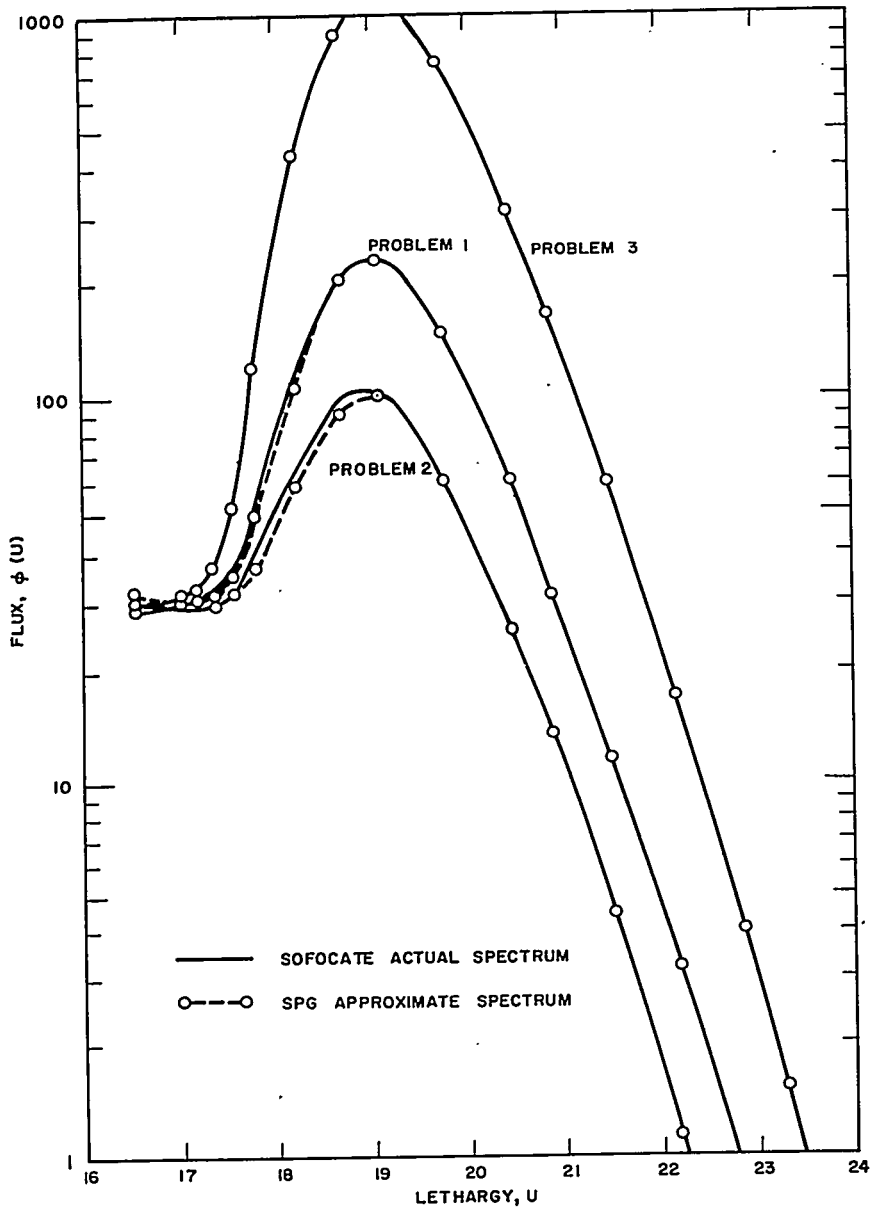

FIGURE 3.55. Comparisons of Approximate and SOFOCATE Spectra at 68° F.

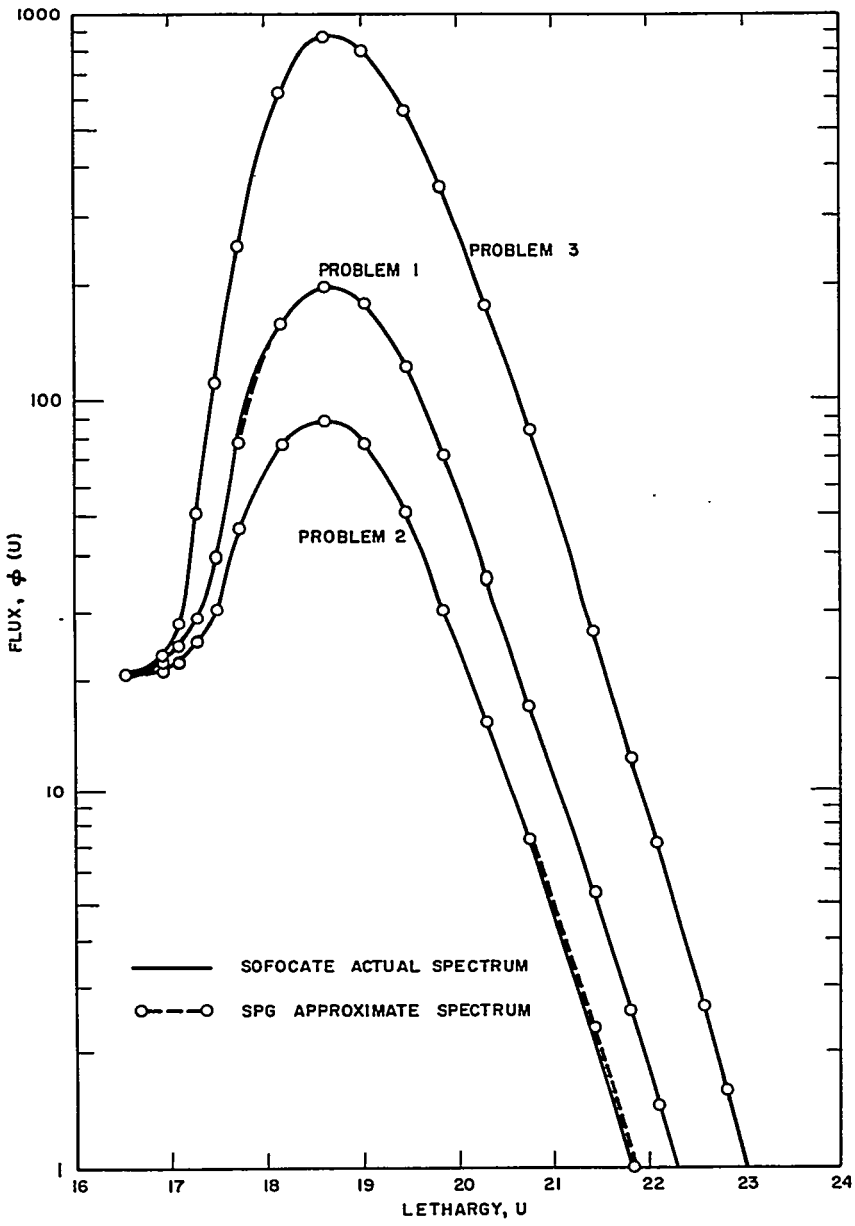

FIGURE 3.56. Comparisons of Approximate and SOFOCATE Spectra at 300° F.

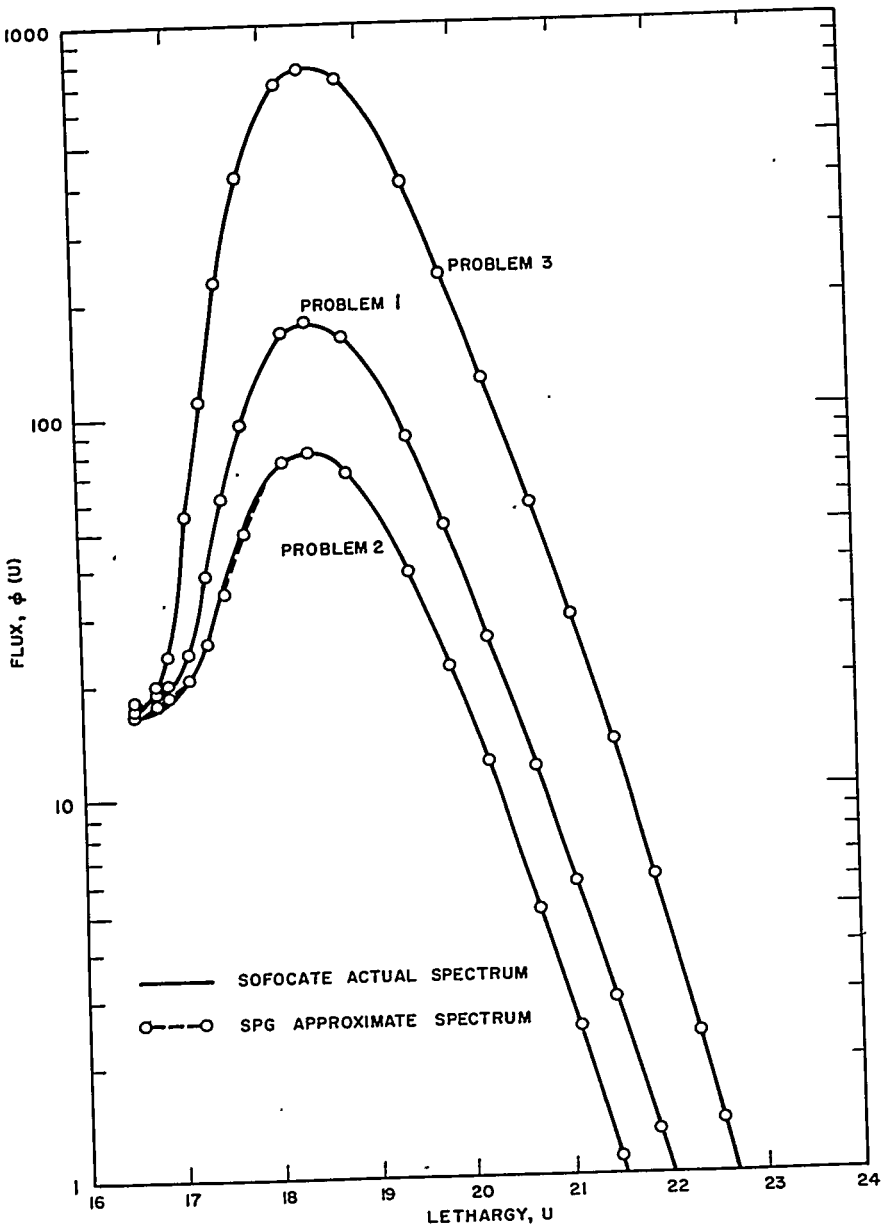

FIGURE 3.57. Comparisons of Approximate and SOFOCATE Spectra at 500° F.

REFERENCES

1. A. M. Weinberg and E. P. Wigner, "The Physical Theory of Neutron Chain Reactors," University of Chicago Press, Chicago, 1958.

2. C. Kittel, "Introduction to Solid State Physics," 2nd Ed., pp. 44-62, John Wiley and Sons, Inc., New York, 1956.

3. L. S. Kothari and K. S. Singwi, "Interaction of Thermal Neutrons with Solids" in "Solid State Physics; Advances in Research and Applications," Vol. 8, F. Seitz and D. Turnbull, Eds., pp. 109-190, Academic Press, Inc., New York, 1959.

4. B. N. Brockhouse, "Crystal and Liquid Dynamics from Neutron Energy Distribution" in "Proceedings of the Neutron Physics Symposium, Rensselaer Polytechnic Institute, May 1961, "M. L. Yeater, Ed., pp. 129-144, Academic Press, Inc., New York, 1962.

5. A. C. Zemach and R. J. Glauber, "Dynamics of Neutron Scattering by Molecules," Phys. Rev. 101, 118-129 (1956).

6. E. Fermi, "Motion of Neutrons in Hydrogenous Substances," Ric. Sci. 7, II, 13-52 (1936).

7. R. Sachs, "Nuclear Theory," Addison-Wesley Publishing Company, Inc., Cambridge, 1953.

8. G. C. Wick, "The Scattering of Neutrons by Systems Containing Light Nuclei," Phys. Rev. 94, 1228-1242 (1954).

9. L. Van Hove, "Correlations in Space and Time and Born Approximation Scattering in Systems of Interacting Particles," Phys. Rev. 95, 249-262 (1954).

10. H. Margenau and G. Murphy, "The Mathematics of Physics and Chemistry," 2nd Ed., p. 263, D. Van Nostrand Company, Inc., Princeton, N.J., 1956.

11. D. Harker, "The Diffraction of Short Wave-Length Radiation by Matter" in "Methods of Experimental Physics," Vol. 6, Part A, K. Lark-Horovitz and V. A. Johnson, Eds., p. 187, Academic Press, Inc., New York, 1959.

12. M. S. Nelkin, "The Egelstaff-Schofield Approach to Thermal Neutron Scattering Law Data," GAMD-1969, 1961.

13. G. Placzek, "The Scattering of Neutrons by Systems of Heavy Nuclei," Phys. Rev. 86, 377-388 (1952).

14. P. Schofield, "Space-Time Correlation Function Formalism for Slow Neutron Scattering," Phys. Rev. Letters 4, 239-240 (1960).

15. M. Nelkin, "Slow Neutron Inelastic Scattering and Neutron Thermalization," GA-1689, 1960.

16. P. A. Egelstaff, "The Theory of the Thermal Neutron Scattering Law" in "Inelastic Scattering of Neutrons in Solids and Liquids. Proceedings of the Symposium Held in Vienna, 11-14 October, 1960," pp. 25-38, International Atomic Energy Agency, Vienna, 1961.

17. R. L. Becker, "Fluctuation-Dissipation Relations for Neutron Diffraction," Bull. Am. Phys. Soc. [II] 6, 262 (1961).

18. G. H. Vineyard, "Scattering of Slow Neutrons by a Liquid," Phys. Rev. 110, 999-1010 (1958).

19. K. S. Singwi and A. Sjölander, "Diffusive Motions in Water and Cold Neutron Scattering," Phys. Rev. 119, 863-871 (1960).

20. E. P. Wigner and J. E. Wilkins, Jr., "Effect of the Temperature of the Moderator on the Velocity Distribution of Neutrons with Numerical Calculations for H as a Moderator," AECD-2275, 1944.

21. W. W. Clendenin, "The Monatomic Gas Model for Thermal Neutron Distributions in a Physical Moderator," J. Nucl. Energy, Part A: Reactor Science 13, 25-34 (1960).

22. G. F. von Dardel, "The Interaction of Neutrons with Matter Studied with a Pulsed Neutron Source," Trans. Roy. Inst. Technol., Stockholm, No. 75 (1954); Acta Polytech. No. 143, Phys. and Appl. Math. Ser. 2, No. 10, 3-104 (1954).

23. L. I. Schiff, "Quantum Mechanics," pp. 342-372, McGraw-Hill Book Company, Inc., New York, 1949.

24. G. N. Watson, "A Treatise on the Theory of Bessel Functions," 2nd Ed., The Macmillan Company, New York, 1944.

25. A. C. Zemach and R. J. Glauber, "Neutron Diffraction by Gases," Phys. Rev. 101, 129-136 (1956).

26. D. J. Hughes and R. B. Schwartz, "Neutron Cross Sections," BNL-325 (2nd Ed.), U.S. Government Printing Office, Washington, D. C., July 1, 1958.

27. A. Radkowsky, "Temperature Dependence of Thermal Transport Mean Free Path" in "Physics Division Report for April, May and June 1950," ANL-4476, 1950, pp. 89-101.

28. P. F. Zweifel and H. Hurwitz, Jr., "Transformation of Scattering Cross Sections," J. Appl. Phys. 25, 1241-1245 (1954).

29. M. Nelkin, "Scattering of Slow Neutrons by Water," Phys. Rev. 119, 741-746 (1960).

30. G. Herzberg, Spectra and Molecular Structure, Vol. II: Infrared and Raman Spectra of Polyatomic Molecules," 2nd Ed., D. Van Nostrand Company, Inc., New York, 1945.

31. D. J. Hughes, H. Palevsky, W. Kley, and E. Tunkelo, "Atomic Motions in Water by Scattering of Cold Neutrons," Phys. Rev. 119, 872-881 (1960).

32. S. Yip and R. K. Osborn, " 'Hindered Rotations' in Liquids and Slow Neutron Scattering" in "Proceedings of the Brookhaven Conference on Neutron Thermalization, April 30 to May 2, 1962. Vol. I," BNL-719, Vol. I, pp. 289-310.

33. D. H. Perkel, "A Family of Thermalization Codes," GAMD-754 (Rev.); AECU-4296, 1959.

34. F. D. Federighi and D. T. Goldman, "KERNEL and PAM: Programs for Use in the Calculation of the Thermal Scattering Matrix for Chemically Bound Systems," KAPL-2225, September 17, 1962.

35. R. G. Sachs and E. Teller, "Scattering of Slow Neutrons by Molecular Gases," Phys. Rev. 60, 18-27 (1941).

36. T. J. Krieger and M. S. Nelkin, "Slow-Neutron Scattering by Molecules," Phys. Rev. 106, 290-295 (1957).

37. P. A. Egelstaff, S. J. Cocking, and T. K. Alexander, "Four-Rotor Thermal-Neutron Analyser" in "Inelastic Scattering of Neutrons in Solids and Liquids. Proceedings of the Symposium Held in Vienna, 11-14 October, 1960," pp. 165-177, International Atomic Energy Agency, Vienna, 1961.

38. P. Egelstaff, "Compilation of Early Scattering Law Data," AERE-R-3931, 1962.

39. P. A. Egelstaff, S. J. Cocking, R. Royston, and I. Thorson, "The Thermal Neutron Scattering Law for Light and Heavy Water" in "Inelastic Scattering of Neutrons in Solids and Liquids. Proceedings of the Symposium Held in Vienna, 11-14 October, 1960," pp. 309-330, International Atomic Energy Agency, Vienna, 1961.

40. P. A. Egelstaff, "The Scattering of Thermal Neutrons by Moderators," Nucl. Sci. Eng. 12, 250-259 (1962).

41. P. A. Egelstaff and P. Schofield, "On the Evaluation of the Thermal Neutron Scattering Law," Nucl. Sci. Eng. 12, 260-270 (1962).

42. N. Corngold, "Thermalization of Neutrons in Infinite Homogeneous Systems," Ann. Phys. 6, 368-398 (1959).

43. N. Corngold, "Chemical Binding Effects in the Thermalization of Neutrons," Ann. Phys. 11, 338-358 (1960).

44. J. R. Beyster, J. L. Wood, W. M. Lopez, and R. B. Walton, "Measurements of Neutron Spectra in Water, Polyethylene, and Zirconium Hydride," Nucl. Sci. Eng. 9, 168-184 (1961).

45. J. R. Nielsen and A. H. Woollett, "Vibrational Spectra of Polyethylenes and Related Substances," J. Chem. Phys. 26, 1391-1400 (1957).

46. L. J. Rainwater, W. W. Havens, Jr., J. R. Dunning, and C. S. Wu, "Slow Neutron Velocity Spectrometer Studies of H, D, F, Mg, S, Si, and Quartz," Phys. Rev. 73, 733-741 (1948).

47. D. T. Goldman and F. D. Federighi, "Calculation of Thermal Neutron Flux Spectra in an Infinite Polyethylene Moderated Medium with Varying Amounts of Absorption" in "Proceedings of the Brookhaven Conference on Neutron Thermalization, April 30 to May 2, 1962. Vol. I," BNL-719, Vol. I, pp. 100-116.

48. A. W. McReynolds, M. S. Nelkin, M. N. Rosenbluth, and W. L. Whittemore, "Neutron Thermalization by Chemically-bound Hydrogen and Carbon" in "Proceedings of the Second United Nations International Conference on the Peaceful Uses of Atomic Energy, Geneva," Vol. 16, pp. 297-313, United Nations, Geneva, 1958.

49. D. E. Parks, D. H. Perkel, and N. F. Wikner, "Thermal-Neutron Spectra in Polycrystalline Graphite," Trans. Am. Nucl. Soc. 2 (1), 244 (1959).

50. P. D. Randolph, R. M. Brugger, K. A. Strong, and R. E. Schmunk, "Inelastic Scattering of Slow Neutrons from Methane," Phys. Rev. 124, 460-469 (1961).

51. K. A. Strong, G. D. Marshall, R. M. Brugger, and P. D. Randolph, "Scattering of Slow Neutrons from Propane Gas," Phys. Rev. 125, 933-937 (1962).

52. R. M. Brugger, "Scattering of Slow Neutrons by Solid and Liquid Terphenyls," Phys. Rev. 126, 29-39 (1962).

53. H. L. McMurry, "Calculation of Differential Scattering Cross Sections for Slow Neutrons" in "Proceedings of the Brookhaven Conference on Neutron Thermalization, April 30 to May 2, 1962. Vol. I," BNL-719, Vol. I, p. 144-171.

54. D. T. Goldman and C. R. Lubitz, "Calculation of (n,p) Cross Sections" in "Reactor Technology Report No. 15—Physics," KAPL-2000-12, December 1960, pp. I.15-I.17.

55. N. C. Francis, D. T. Goldman, and C. R. Lubitz, "Effective Interaction in Direct Reactions," Bull. Am. Phys. Soc. [II] 6, 296 (1961).

56. N. C. Francis, D. T. Goldman, and E. Guth, "Photoneutron Disintegration Below the Giant Resonance: Beryllium-9 and Carbon-13," Phys. Rev. 120, 2175-2184 (1960).

57. K. A. Brueckner and D. T. Goldman, "Single Particle Energies in the Theory of Nuclear Matter," Phys. Rev. 117, 207-213 (1960).

58. M. Gell-Mann and K. A. Brueckner, "Correlation Energy of an Electron Gas at High Density," Phys. Rev. 106, 364-368 (1957).

59. L. J. Esch, "Temperature Dependence of the Neutron Transport Cross Section in Paraffin and Polyethylene," KAPL-2204, February 1, 1962.

60. "Inelastic Scattering of Neutrons in Solids and Liquids. Proceedings of the Symposium Held in Vienna, 11-14 October, 1960," International Atomic Energy Agency, Vienna, 1961.

61. "Proceedings of the Brookhaven Conference on Neutron Thermalization, April 30 to May 2, 1962. Vols. I-IV," BNL-719, Vols. I-IV.

62. H. J. Amster, "The Wigner-Wilkins Calculated Thermal Neutron Spectra Compared with Measurements in a Water Moderator," Nucl. Sci. Eng. 2, 394-404 (1957).

63. M. J. Poole, "Measurement of Neutron Spectra in Moderators and Reactor Lattices-1," J. Nucl. Energy 5, 325-341 (1957).

64. F. D. Federighi and T. J. Reno, Jr., "SWAK, A Thermal Cross Section Program," KAPL-M-RPC-6, March 15, 1963.

65. P. Michael, "Thermal Neutron Flux Distributions in Space and Energy," Nucl. Sci. Eng. 8, 426-431 (1960).

66. H. Hurwitz, Jr., and M. S. Nelkin, "The Thermal Neutron Spectrum in a Diffusing Medium," Nucl. Sci. Eng. 3, 1-10 (1958).

67. N. Corngold, P. Michael, and W. Wollman, "The Time Decay Constants in Neutron Thermalization" in "Proceedings of the Brookhaven Conference on Neutron Thermalization, April 30 to May 2, 1962. Vol. IV," BNL-719, Vol. IV, pp. 1103-1130.

68. F. B. Hildebrand, "Methods of Applied Mathematics," p. 68 ff., Prentice-Hall, Inc., New York, 1952.

69. P. A. White, "The Computation of Eigenvalues and Eigenvectors of a Matrix," J. Soc. Ind. Appl. Math. 6, 393-437 (1958).

70. G. P. Calame, "The Direct Calculation of Diffusion Lengths and Diffusion Hardened Spectra," Nucl. Sci. Eng. 13, 32-39 (1962).

71. S. H. Crandall, "Engineering Analysis," p. 105, McGraw-Hill Book Company, Inc., New York, 1956.

72. V. N. Faddeeva, "Computational Methods of Linear Algebra," p. 225, Dover Publishing Company, New York, 1959.

73. W. B. Wright, F. Feiner, and A. D. Musto, "PPA Flux Transient Study. Part I. Experimental Data," KAPL-M-WBW-6, April 1959.

74. W. B. Wright and F. Feiner, "PPA Flux Transient Study. Part II. Diffusion Lengths and Gap Peaking," KAPL-M-WBW-7, May 1959.

75. W. B. Wright and F. Feiner, "Note on Position-Dependent Spectra," Nucl. Sci. Eng. 6, 81-82 (1959).

76. E. M. Gelbard, J. A. Davis, and E. Schmidt, "A Comparison of the Properties of the Nelkin and Radkowsky Thermal Neutron Scattering Kernels for Water" in "Proceedings of the Brookhaven Conference on Neutron Thermalization, April 30 to May 2, 1962. Vol. IV," BNL-719, Vol. IV, pp. 1175-1185.

77. W. W. Clendenin, "Temperature Dependence of Neutron Pulse Parameters in H_2O," Nucl. Sci. Eng. 18, 351-362 (1964).

78. W. W. Clendenin, "Relation of the Neutron Diffusion Length to Neutron Pulse Parameters in H_2O," Nucl. Sci. Eng. 19 (1964).

79. K. S. Rockey and W. Skolnik, "Measurements on the Diffusion Length of Thermal Neutrons in Water from 25 to 296°C," Nucl. Sci. Eng. 8, 62-65 (1960).

80. M. Reier and J. A. de Juren, "Diffusion Length of Thermal Neutrons in Water from 23°C to 244°C," J. Nucl. Energy, Parts A/B 14, 18-24 (1961).

81. E. Starr and J. Koppel, "Determination of Diffusion Hardening in Water," Nucl. Sci. Eng. 14, 224-229 (1962).

82. R. C. Gast, "On the Equivalence of the Spherical Harmonics Method and the Discrete Ordinate Method Using Gauss Quadrature for the Boltzmann Equation," WAPD-TM-118, April 1958.

83. B. G. Carlson, "Solution of the Transport Equation by S_n Approximations," LA-1891, February 1955.

84. F. D. Judge, "Variational Method in the Calculation of Reactor Neutron Flux Density," KAPL-2151, February 21, 1961.

85. H. Bohl, E. Gelbard, P. Buerger, and G. Culpepper, "SLOP-1, A Thermal Multigroup Program for the IBM-704," WAPD-TM-188, October 1960.

86. C. W. Dawson, "Thermal Energy Transport Code, TET," David Taylor Model Basin Report 1613, April 1962.

87. J. Spanier, H. Kuehn, and W. Guilinger, "TUT-T5 — A Two-Dimensional Monte Carlo Calculation of Capture Probabilities for the IBM-704," WAPD-TM-125, November 1959.

88. G. Goertzel and M. H. Kalos, "Monte Carlo Methods in Transport Problems" in "Physics and Mathematics," Vol. 2 of Progress in Nuclear Energy, Series I, D. J. Hughes, J. E. Sanders, and J. Horowitz, Eds., pp. 315-369, Pergamon Press, Inc., New York, 1958.

89. J. Spanier, "The Physics and Mathematical Analysis for the TUT-T5 Monte Carlo Code," WAPD-TM-186, January 1960.

90. J. Spanier, "Monte Carlo Methods and Their Application to Neutron Transport Problems," WAPD-195, July 1959.

91. M. A. Martino and W. W. Stone, "TRAM, A Monte Carlo Thermal Neutron Code for the IBM-704," KAPL-2039, June 19, 1959.

92. M. Halperin, "Almost Linearly Optimum Combination of Unbiased Estimates," J. Am. Statist. Assoc. 56, 36-43 (1961); KAPL-2068, January 1960.

93. Rand Corporation, "A Million Random Digits with 100,000 Normal Deviates," Free Press, Glencoe, Ill., 1955.

94. H. J. Berwind and J. Spanier, "TRAC-1. A Monte Carlo Philco-2000 Program for the Calculation of Neutron Capture Probabilities," WAPD-TM-229, March 1961.

95. C. W. Maynard, "An Application of the Reciprocity Theorem to the Acceleration of Monte Carlo Calculations," Nucl. Sci. Eng. 10, 97-101 (1961).

96. E. M. Gelbard, H. B. Ondis, and J. Spanier, "MARC — A Multigroup Monte Carlo Program for the Calculation of Capture Probabilities," WAPD-TM-273, May 1962.

97. K. M. Case, F. de Hoffman, and G. Placzek, "Introduction to the Theory of Neutron Diffusion, Vol. I," U. S. Government Printing Office, Washington, D. C., 1953.

98. B. Davison, "Influence of a Black Sphere and of a Black Cylinder upon the Neutron Density in an Infinite Non-Capturing Medium," Proc. Phys. Soc. (London) 64A, 881-902 (1951).

99. R. E. Marshak, "The Variational Method for Asymptotic Neutron Densities," Phys. Rev. 71, 688-693 (1947).

100. D. Schiff and S. Stein, "Escape Probability and Capture Fraction for Gray Slabs," WAPD-149, June 1956.

101. E. L. Wachspress, "Thin Regions in Diffusion Theory Calculations," Nucl. Sci. Eng. 3, 186-200 (1958).

102. L. A. Hageman, "HERD 1, 2, and 3 — IBM-704 Codes Used to Solve the One-Dimensional, One-Velocity Transport Equation with Isotropic Scattering," WAPD-TM-162, January 1959.

103. B. Davison and J. B. Sykes, "Neutron Transport Theory," The Clarendon Press, Oxford, 1957.

104. C. W. Maynard, "Blackness Theory and Coefficients for Slab Geometry," WAPD-TM-168, May 1959.

105. S. Stein, "Resonance Capture in Heterogeneous Systems," WAPD-139, November 1955.

106. M. Goldsmith, R. T. Jones, T. M. Ryan, S. Kaplan, and A. D. Voorhis, "Theoretical Analysis of Highly Enriched Light Water Moderated Critical Assemblies" in "Proceedings of the Second United Nations International Conference on the Peaceful Uses of Atomic Energy, Geneva, 1958," Vol. 12, pp. 435-445, United Nations, Geneva, 1958.

107. J. Bengston, "Neutron Self-Shielding of a Plane Absorbing Foil," CF-56-3-170, March 1956.

108. E. Gelbard, J. Davis, and J. Pearson, "Iterative Solutions to the P_1 and Double-P_1 Equations," Nucl. Sci. Eng. 5, 36-44 (1959).

109. E. M. Gelbard and J. J. Pearson, "Space and Energy Separability of the Thermal Flux in a Diffusing Medium," Nucl. Sci. Eng. 6, 453-455 (1959).

110. F. Feiner, S. Weinstein, and W. B. Wright, "Flux Transients Near Medium Discontinuities" in "Proceedings of the Brookhaven Conference on Neutron Thermalization, April 30 to May 2, 1962. Vol. III," BNL-719, Vol. III, pp. 900-931.

111. E. R. Cohen, "A Survey of Neutron Thermalization Theory" in "Proceedings of the International Conference on the Peaceful Uses of Atomic Energy, Geneva, 1955," Vol. 5, pp. 405-531, United Nations, New York, 1956.

112. R. W. Deutsch, "Computing Three-Group Constants in Neutron Diffusion," Nucleonics 15(1), 47-51 (1957).

113. J. A. Archibald, Jr., "CUREBO: A Generalized Two-Space-Dimensional Coding with Cross-Section and Depletion Calculations for the IBM-704," KAPL-1885, April 30, 1959.

114. H. Amster and R. Suarez, "The Calculation of Thermal Constants Averaged Over a Wigner-Wilkins Flux Spectrum: Description of the SOFOCATE Code," WAPD-TM-39, January 1957.

115. H. J. Amster and J. B. Callaghan, "KATE-1 — A Program for Calculating Wigner-Wilkins and Maxwellian Averaged Thermal Constants on the Philco-2000," WAPD-TM-232, October 1960.

116. R. J. Breen, "A One Group Model for Thermal Activation Calculations," Nucl. Sci. Eng. 9, 91-93 (1961).

117. R. M. Cantwell, "M0176 — A FORTRAN Program to Solve Several P-Approximations to the Few Group Neutron Transport Equation in Slab Geometry," WAPD-TM-320, April 1962.

118. G. G. Bilodeau, "Extrapolation Techniques for Real Symmetric Matrices," WAPD-TM-52, March 1957.

119. G. G. Bilodeau, W. R. Cadwell, J. P. Dorsey, J. G. Fairey, and R. S. Varga, "PDQ — An IBM-704 Code to Solve the Two-Dimensional Few-Group Neutron-Diffusion Equations," WAPD-TM-70, August 1957.

120. D. S. Selengut, "Variational Analysis of Multidimensional Systems" in "Nuclear Physics Research Quarterly Report for October, November, December 1958," HW-59126, 1959, pp. 89-124.

121. L. V. Kantorovich and V. I. Krylov, "Approximate Methods of Higher Analysis," pp. 240-357, Interscience Publishers, Inc., New York, 1958.

122. A. N. Lowan, "On the Kantorovich Treatment of Boundary Value Problems for Partial Differential Equations," UCRL-5249, 1958.

123. N. C. Francis, J. C. Stewart, L. S. Bohl, T. J. Krieger, "Variational Solutions of the Transport Equation" in "Proceedings of the Second United Nations International Conference on the Peaceful Uses of Atomic Energy, Geneva, 1958," Vol. 16, pp. 517-529, United Nations, Geneva, 1958.

124. G. P. Calame and F. D. Federighi, "A Variational Procedure for Determining Spatially Dependent Thermal Spectra," Nucl. Sci. Eng. 10, 190-201 (1961).

125. O. J. Marlowe, C. P. Saalbach, L. M. Culpepper, and D. S. McCarty, "WANDA — A One-Dimensional Few-Group Diffusion Equation Code for the IBM-704," WAPD-TM-28, November 1956.

126. F. D. Federighi and G. P. Calame, "Reactor Code Abstract No. 8," Nucl. Sci. Eng. 9, 416 (1961).

127. A. J. Buslik, "The Description of the Thermal Neutron Spatially Dependent Spectrum by Means of Variational Principles" in "Bettis Technical Review, Reactor Technology," WAPD-BT-25, May 1962, pp. 1-24.

128. S. L. Shufler, "A Comparison of a Self-Adjoint Variational Method to 36-Group Thermal Spectrum Calculations of Heterogeneous Arrays," Trans. Am. Nucl. Soc. 5 (1), 37-39 (1962).

129. W. B. Wright and F. Feiner, "Spectrum Effects to the Surface of Water Gaps and Black Slabs," Trans. Am. Nucl. Soc. 2 (1), 246 (1959).

130. G. P. Calame, F. D. Federighi, and P. A. Ombrellaro, "A Two Mode Variational Procedure for Calculating Thermal Diffusion Theory Parameters," Nucl. Sci. Eng. 10, 31-39 (1961).

131. J. A. Archibald, Jr., "The KARE System for Computing Life Studies Automatically," Trans. Am. Nucl. Soc. 3 (1), 64-65 (1960).

Chapter 4

REACTOR DESIGN TECHNIQUES

R. S. Wick, Editor

4.1 INTRODUCTION

In this chapter the application of the theoretical concepts heretofore discussed on slowing-down theory and thermal spectra to determine the nuclear characteristics of reactors is described. The heterogeneous and three-dimensional nature of actual reactors must be taken into account by properly extending the appropriate theory to the particular case, which is usually far from the idealized case. After the various calculational techniques are discussed, the chapter concludes with a description of how the depletion characteristics of burnable poisons may be advantageously used by the nuclear designer to achieve desirable reactor characteristics, thus unifying the application of the calculational techniques. The general steps in a typical reactor analysis are shown in Fig. 4.1. These steps encompass progressively less microscopic detail of the reactor, and the topics in this chapter follow the same pattern.

Section 4.2, Treatment of Self-Shielding in Isolated Plates, presents a description of the determination of macroscopic cross sections, taking into account the fact that neutron absorbing material may be in the form of plates, rods, or discrete particles embedded in structural elements. The discussion includes an approximate technique for treating discrete particles, in which a calculation model is assumed and compared to experiment, and a more sophisticated treatment of this problem, in which a theoretical and experimental basis for selecting a calculational model is developed. The section concludes with a description of how the macroscopic cross sections are determined, taking into account the fact that the bulk of the principal neutron absorbing material is in the form of fuel plates or rods, control rod blades, and burnable poison elements which are surrounded by a moderator. These explicit elements often cause major perturbations in the neutron flux.

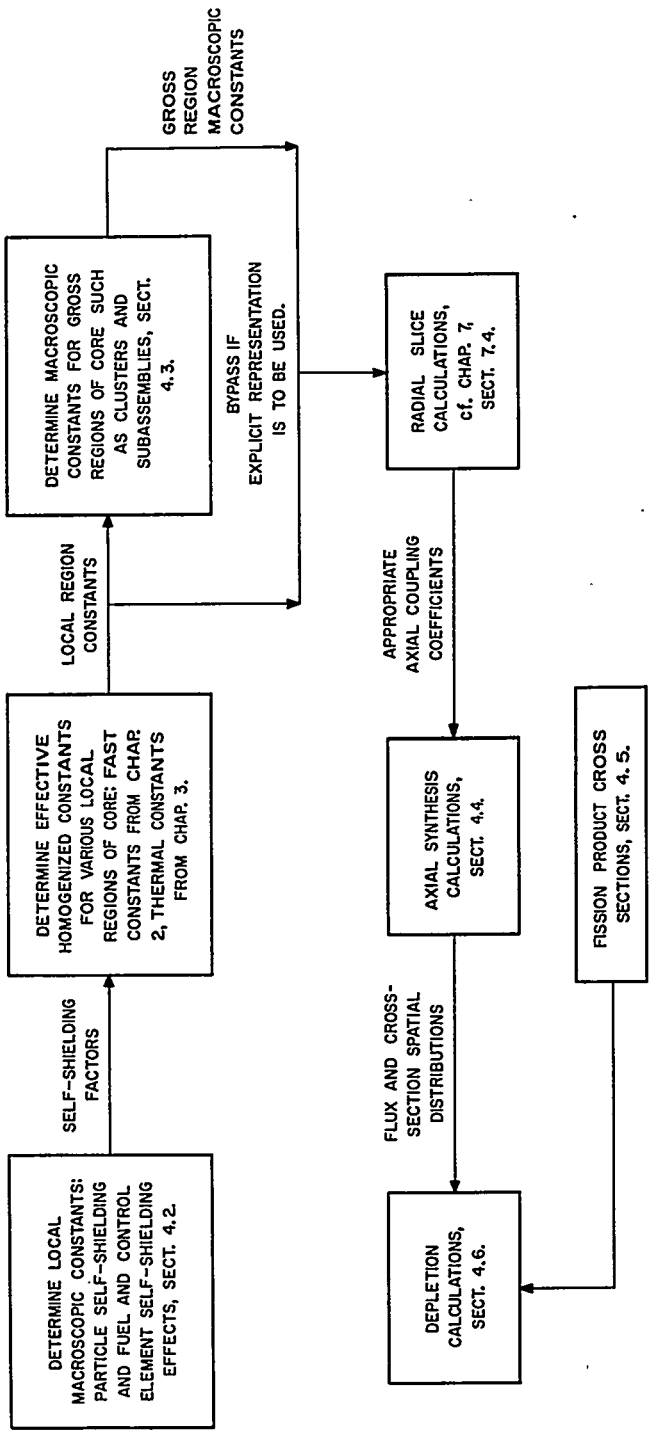

FIGURE 4.1. Schematic of Steps in Reactor Analysis.

In many calculations, larger regions of a core than those discussed in Sect. 4.2 can also be described by macroscopic cross sections representative of the region containing discrete neutron absorbing elements. Section 4.3, Homogenization Techniques, treats the problem of determining the macroscopic cross sections of the larger regions. These larger regions, isolated as a basic unit for study, usually include a group of fuel elements and associated poison plates, control rods, structural supporting material, and moderator. (In many cases the fuel elements and associated coolant are first treated as a group, as in Sects. 4.2.B and 4.2.C, before the larger unit is considered.) Many of the same approximations described in the section on self-shielding techniques, such as cell theory boundary conditions, are also used to determine the macroscopic cross sections of the larger regions. However, since the validity of the underlying assumptions of cell theory is more questionable for regions containing isolated absorbers, considerable discussion is devoted to the inaccuracies inherent in the use of cell theory to obtain effective cross sections for such regions.

The next topic, Synthesis Methods (Sect. 4.4), describes how, given an arbitrary spatial distribution of diffusion theory parameters, the kinetic (see Chap. 5) and static characteristics of the core can be calculated from sets of calculations encompassing less than the complete core. For example, it is often possible (because of computer limitations) or desirable (for economic reasons) to perform only two-dimensional radial calculations through a core and then axially to combine a number of these calculations to describe the entire core, a procedure termed synthesis. The availability of three-dimensional computer codes permits the checking of the accuracy of synthesis techniques for test cases (see Chap. 7). In most practical cases, the best approximation to a description of the axial coupling of these planes is sought. Where the fuel and poison have been partially depleted, or where control rods have been moved in or out of various axial regions of the core, or both, a core with a continuous variation in the composition of each axial plane results. Thus, as is brought out in detail in the next section, synthesis calculations over reactor life usually are not isolated from the concurrent depletion calculations. However, to emphasize the synthesis technique, it is assumed for the purpose of discussion that the macroscopic cross sections in each plane are known at the particular time of interest and that a three-dimensional steady-state power distribution is desired. The section discusses single channel synthesis and advanced techniques. The single channel synthesis method, the simplest approach to coupling together axially the radial slices

of the core, uses only a single set of axial coupling factors. Discussion of advanced techniques for coupling together axially the radial slices, such as the multichannel approach and variational techniques, deals with improved descriptions of more complicated configurations, especially for those cases where radial and axial separability of the flux is not a good approximation.

The next step in the reactor analysis sequence is to determine the depletion characteristics of the core. Before this can be done, information on the cross sections of the fission fragments must be available, because their poisoning effect is an important factor in the design of cores with high fuel depletions and long lifetimes. In Sect. 4.5, a method of combining experimental information on individual fission products into a total fission product treatment is described.

Section 4.6, Depletion Methods, answers the question: Given a spatial distribution of fuel and poison inventory (fixed and movable), the corresponding spatial distribution of cross sections, and the average temperature and power level of the core, what will the spatial distribution of fuel and poison inventory and the corresponding spatial distribution of cross sections be at a later time?

It is assumed that some method of calculating the spatial distribution of flux, given the spatial distribution of cross sections corresponding to the fuel and poison inventory, is available; but such a calculation is not in itself considered to be part of the depletion calculation in this section, since it has been discussed in Sect. 4.4. The depletion calculation for a core is usually broken down into a number of time intervals, depending on the rapidity of the changes in core characteristics.

Thus, the calculation of the depletion process defined here has been divided into: (1) the calculation of the change in the spatial distribution of the fuel and poison inventory with time and (2) the calculation or, more properly, the recalculation of the spatial distribution of macroscopic cross sections at the end of the time interval. These will be emphasized separately by first discussing the time dependence of the effective microscopic cross sections, considering separately those cross sections which vary relatively rapidly with time, because of either neutron spectrum changes or inventory changes, and those which vary relatively slowly. The limitations of computer capacities, the accuracy of various theoretical approaches, and the economics of computer utilization dictate the use of many approximate methods in depletion calculations. The approximate methods used to incorporate the changing cross sections and fluxes during a time interval into the calculation of the inventory change during the same time interval are, thus, described for

the case where the changes in cross section with time are relatively rapid. Next, the determination of the time dependence, i.e., the actual depletion equations, of the number densities is treated, taking into account the time variation of the cross sections. Finally, two integrated depletion systems, which actually include the spatial synthesis described in Sect. 4.4 and the depletion described in this section, are described.

Section 4.7, Burnable Poisons, describes, from a conceptual point of view rather than from a detailed calculational point of view, the special features of cores which employ burnable poisons as a means of obtaining desirable reactor characteristics. Thus, this section complements the preceding analysis techniques by illustrating how these techniques may be used in the development of a specific type of core design.

4.2 TREATMENT OF SELF-SHIELDING IN ISOLATED PLATES

A. Introduction

Neutron absorbing materials (fuel, burnable poisons, nonburnable poisons, and parasitic poisons) are present in pressurized water reactors in the form of plates or cylinders cooled by water and supported by associated structure. These plates (or rods) may be placed in the core in a manner such that they are relatively isolated from similar plates of the same type (for example, cruciform or cylindrical control rods), or they may be placed in uniform arrays (such as fuel plates or rods positioned on a more or less uniform array within a cluster or module which makes up the basic fueled assembly of the core). Further, neutron absorbing material in the form of discrete particles may be embedded in different elements of the cluster. (For a description of the mechanical arrangement of fuel plates, fuel rods, and cruciform control rods in the Pressurized Water Reactor (PWR) core which, for the purpose of discussion in this volume, may be considered as typical of pressurized water reactors, see Chap. 4 of Ref. 1.) A basic problem in the analysis of such geometric arrangements of neutron absorbing material is the appropriate determination of spatially and energy-averaged macroscopic cross sections which, when multiplied by the appropriately averaged neutron flux, yield the neutron absorption rates of these components. (These macroscopic cross sections are hereafter referred to as the effective macroscopic cross sections.) Thus, the true absorption must first be determined for these cases of nonuniform flux and material distribution.

Since, in general, the spatial and energy dependence of the flux obtained from an exact solution of the neutron transport equations is not separable, and since the solution depends on the boundary conditions, approximations must be made regarding the degree to which neutron absorption and the effective macroscopic cross sections can be geometrically localized. In addition, assumptions regarding separability of space and energy must often be made to permit a mathematically tractable solution.

A reasonable basis for determining the degree of detail with which a particular localized portion of a reactor can and should be examined is the degree to which the spatial and energy dependence of the neutron flux is separable. As the area described in the calculation is increased, a coarser description of the spatial and energy interdependence can often be assumed. Generally, more refined calculations for simple one-dimensional geometries can be performed and the effect of assuming separability estimated for the more complicated geometries on the basis of this comparison.

The effect of portions of a physical particle, plate, or rod shielding the other portions from the incident flux is defined as spatial self-shielding. There is an additional energy self-shielding phenomenon caused by the suppression of the neutron flux level at the energy under consideration because of the strong neutron absorption at a somewhat higher energy which acts as a source of neutrons for the energy in question (see Chap. 2). The discussion of self-shielding starts with the smallest units of neutron absorbing material, the particle, and then progresses to the larger units, such as rods and plates, arrays of plates, control rods, etc. Section 4.2.B presents a relatively simple method of treating particle self-shielding along with a comparison to experiment.

Since experimental results are limited as to the range of the neutron optical diameters of the particles, the volume fraction of highly absorbing particles in the plates or rods, and the number of types of absorbing particles, a more generalized treatment is given in Sect. 4.2.C. (In general, however, because of materials limitations it is expected that the formulation of Sect. 4.2.B will be adequate for most applications.) The discussion in Sect. 4.2.C is a much more elaborate and generalized treatment of particle self-shielding, stressing the theoretical aspects. In addition, it also discusses how the geometric factors which describe the particle distribution in space may be estimated experimentally, as contrasted to the technique in Sect. 4.2.B which assumes a particle distribution. This very generalized treatment is shown in the limiting condition of zero volume fraction to reduce to the result of Hurwitz and Zweifel[2]

and also, in the case of a single particle type, to the result of Doub described in Sect. 4.2.B. At present the theoretical approach of Sect. 4.2.C with its potential flexibility due to a larger number of parameters must be considered exploratory in nature. Section 4.2.D discusses the explicit representation of self-shielded plates in diffusion theory.

B. Particle Self-Shielding in Plates Loaded with Spherical Poison Particles

W. B. Doub

1. *Introduction*

The self-shielding properties of an unordered system of small poison spheres bound together in a neutral plate-type matrix are investigated in this discussion.

The problem has been solved by Case, et al.,[3] for the case of one poison sphere placed in a uniform neutron flux. The results of Ref. 3 have been extended exactly by Hurwitz and Zweifel[2] to the general case, with the restriction that the volume fraction of poison particles in the plate be small. For this case, Hurwitz and Zweifel found that the transmission of the plate is duplicated by another plate of the same size having a factor f_0 times as much poison material distributed homogeneously in it. The factor f_0 (particle self-shielding factor) is identical to the disadvantage factor P_0 (escape probability) which Case, et al., computed for the case of a single sphere in a uniform flux. An attempt to extend these results to the case of arbitrary volume fraction has been made by Burrus[4, 5] using heuristic arguments. He assumed the plate to be composed of slices, each of thickness equal to the average chord length of the spherical poison particles (= 4/3 radius). The average transmission of a single slice was computed on the basis of the fractional voids in the slice (= $1 - V$, where V = poison volume fraction) and also by the expression of Case, et al., for average transmission through a poison sphere. Then, the total transmission was taken to be the product of all the slice transmissions. As will be seen shortly, his formulation, though giving fair agreement with experiment, apparently neglects the ordering of the poison spheres due to the geometrical shape of the spheres themselves. The term ordering is used to denote any process which tends to make the neutron path lengths in the poison material in the plate less variable (i.e., it tends to make the plate poison apparently more homogeneous).

In this discussion, an alternative approximate method has been used to compute the case of arbitrary poison volume fraction. It gives good agreement with experiment.

In Sect. 4.2.B.2, a theoretical expression is derived for the particle self-shielding factor, f, for a set of uniform poison spheres of radius r randomly distributed in a matrix composed of nonabsorbing spheres of radius r. The above expression is extended to include the case when the matrix is also absorbing. In Sect. 4.2.B.3, an experiment is described and analyzed in which the particle self-shielding factor for a mixture of boron carbide spheres and aluminum spheres is determined, using measured transmissions of monoenergetic neutrons. In Sect. 4.2.B.4, the experimentally determined particle self-shielding factor referred to above is compared with the theoretical particle self-shielding factors of Burrus,[4,5] Hurwitz and Zweifel,[2] and this discussion.

2. *Theory*

The model is as follows: The purely absorbing poison particles of radius r are assumed to be embedded randomly in a plate of thickness a_1 and having a homogeneous binding material with absorption but no scattering. The average transmission per neutron through the plate for neutrons incident at an angle $\theta = \arccos \mu$ is (Fig. 4.2)

$$T(\Sigma_1, \Sigma_2) = \int_0^l p(C) \exp\left[-\Sigma_1 C - (l-C)\Sigma_2\right] dC \qquad \text{Eq. (4.1)}$$

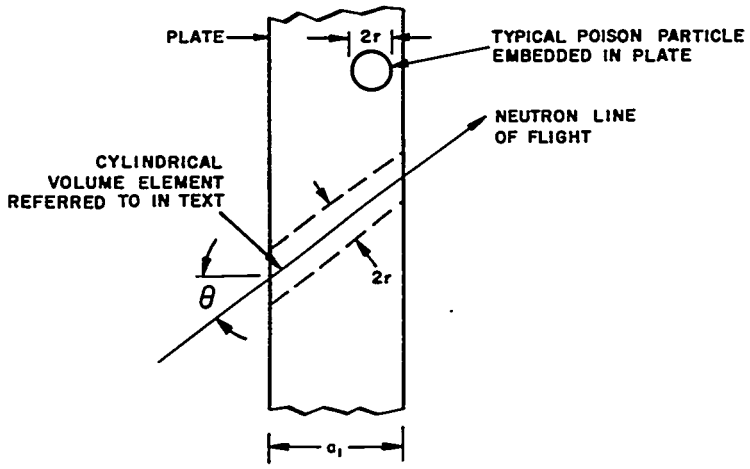

FIGURE 4.2. Schematic Showing Plate Geometry and Typical Neutron Line of Flight with its Associated Volume Element. (Any sphere whose center lies in the volume element will be intersected by the neutron line of flight [not to scale].)

where

C = total neutron path length contained in poison particles

Σ_1 = macroscopic absorption cross section of a poison particle

Σ_2 = macroscopic absorption cross section of the binder

$l = a_1/\mu$ = length of the neutron path in the plate

$p(C)dC$ = fraction of neutron paths (at fixed angle of incidence) which pass through a length C to $C + dC$ of poison particles.

Equation (4.1) reduces to

$$T(\Sigma_1, \Sigma_2) = e^{-l\Sigma_2} T(\Sigma_1 - \Sigma_2, 0). \qquad \text{Eq. (4.2)}$$

Thus, the problem is reduced to finding the transmission of the same set of poison particles, but with macroscopic absorption $\Sigma = \Sigma_1 - \Sigma_2$ and with a binder having no absorption. The transmission in this case is

$$T \equiv T(\Sigma, 0) = \int_0^l p(C)e^{-\Sigma C}dC. \qquad \text{Eq. (4.3)}$$

If it is now assumed that when a neutron path intersects a poison particle the neutron is transmitted through the particle with a probability $\bar{t}$ (the average neutron transmission per neutron-particle collision), Eq. (4.3) takes the form

$$T = \sum_{x=0}^{M} p(x)(\bar{t})^x \qquad \text{Eq. (4.4)}$$

where

x = number of poison particles whose centers lie in a volume element formed by the intersection of the plate and a cylinder of radius r whose axis coincides with the neutron path (Fig. 4.2)

$p(x)$ = probability that the above type volume element contains the centers of x poison particles (keeping the angle of incidence fixed)

M = maximum number of poison particles possible in the volume element under consideration (Fig. 4.2).

To determine $p(x)$, the following model is postulated which allows the poison particle positions to be influenced by crowding (i.e., two particles may not occupy the same position).* The division of the plate into cells is postulated. Each cell may contain either a poison particle or a portion of the matrix material. The total number of cells in the small volume element referred to above (Fig. 4.2) is set equal to M. The above model implies that the binding matrix consists of spheres of the same radius as the poison spheres. In this case, the appropriate distribution, $p(x)$, is hypergeometric[6] or, what is essentially equivalent, Bernoulli's binomial distribution.[5,6] However, the initial Eqs. (4.1) and (4.2) depend on the postulate of a homogeneous binding matrix. Thus, to obtain a workable solution to the problem, two mutually exclusive assumptions have been used, i.e., that the binding matrix is homogeneous and that it is particulated. However, if the spheres of a particulated binding matrix are nonself-shielded with respect to both absorption and scattering, they may be homogenized to allow the application of Eqs. (4.1) and (4.2). This is a very good approximation for the experimental sample discussed in Sect. 4.2.B.3. It is not certain whether one can reconcile the above two contradictory assumptions for the case of a homogeneous binding matrix; for, though Eqs. (4.1) and (4.2) apply, one no longer has the assumption of a particulated binding matrix and can no longer apply the same rules of probability to obtain a hypergeometric or binomial distribution for $p(x)$. In the limit of very high volume fraction of poison spheres, the distribution $p(x)$ is uninfluenced by whether the binder is particulated or not, since almost every cell is occupied by a poison sphere. Also, as will be seen, the hypergeometric or binomial distribution leads to an exact expression for the particle self-shielding in the limit of zero volume fraction. Thus, for very high and very low volume fractions, the above model is insensitive to whether the binding matrix is particulated or homogeneous. However, for volume fractions away from these limits (near 0.5, for instance), $p(x)$ will depend upon the particulation of the binding matrix.

The binomial distribution is chosen because it is easier to work with:

$$p(x) = \binom{M}{x} V_1^x (1 - V_1)^{M-x} \qquad \text{Eq. (4.5)}$$

where

$$\binom{a}{b} = \frac{a!}{b!(a-b)!}$$

*This derivation is somewhat similar to that presented by Burrus.[5]

V_1 = number fraction = fraction of cells in the sample occupied by poison spheres. Since the number of cells in the sample has been set equal to the maximum number of poison spheres which could be packed into the sample volume, one has the following relation:

$$V = gV_1 \qquad \text{Eq. (4.6)}$$

where

V = fraction of the geometrical sample volume occupied by the poison spheres.

g = fraction of the geometrical sample volume which is occupied by the set of poison spheres plus matrix spheres.

The theoretical value of g for perfectly packed spheres is 0.740.[7] However, for loosely packed spheres this value may drop as low as 0.5 to 0.6. Since the sample used in the present experiment was firmly packed, the maximum theoretical value 0.740 was used.

Now, substituting Eq. (4.5) into Eq. (4.4)

$$\begin{aligned} T &= \sum_{x=0}^{M} \binom{M}{x} V_1^x (1 - V_1)^{M-x} (\bar{t})^x \\ &= \sum_{x=0}^{M} \binom{M}{x} (V_1 \bar{t})^x (1 - V_1)^{M-x} \\ &= (V_1 \bar{t} + 1 - V_1)^M \end{aligned} \qquad \text{Eq. (4.7)}$$

where the binomial theorem has been used. There is also the obvious relationship

$$M\left(\frac{4}{3}\pi r^3\right) = g(\pi r^2 l)$$

or

$$M = \frac{3}{4} g(l/r) \; . \qquad \text{Eq. (4.8)}$$

The particle self-shielding factor f will now be defined:

$$T = \exp(-l V \Sigma f). \qquad \text{Eq. (4.9)}$$

Since $lV\Sigma$ represents the optical path of the homogenized poison, f may be interpreted as the fraction of the original poison material which, when homogenized, will give the same transmission as the original sample.

Combining Eq. (4.6), (4.7), (4.8), and (4.9), one has for the particle self-shielding factor

$$f = \frac{1}{\frac{2}{3}\gamma(V/g)} \ln\left[\frac{1}{1-(V/g)(1-\bar{t})}\right] \qquad \text{Eq. (4.10)}$$

where $\gamma = 2r\Sigma$. From now on take $g = 0.740$, so that

$$V = 0.740\, V_1 \ . \qquad \text{Eq. (4.11)}$$

A reasonable assumption for $\bar{t}$ is that it is the same as the transmission of a uniform current incident on a poison particle:[3]*

$$\bar{t} = \frac{2}{\gamma^2}\left[1-(1+\gamma)e^{-\gamma}\right]. \qquad \text{Eq. (4.12)}$$

The particle self-shielding function f in Eq. (4.10) is plotted in Fig. 4.3 as a function of the optical diameter γ and the number fraction V_1.

3. *Experimental Results*

Transmission measurements were performed on a sample containing 37 volume percent natural boron carbide spheres † of 87 μ mass-average radius. The measurements were performed at Brookhaven National Laboratory using a high resolution neutron crystal spectrometer. The transmission of this sample was measured at five neutron energies ranging from 0.03 to 1.23 ev. The measurements at 0.03 ev corresponded to an optical diameter $(2r\Sigma)$ in the boron carbide particles of approximately 0.5 to 0.6. Using the experimentally determined transmissions, the particle self-shielding factor was computed from an expression equivalent to Eq. (4.9).

A) SAMPLE DESCRIPTION. The various physical parameters of interest in the sample are presented in Table 4.1.

*Reference 3 derives Eq. (4.12) for a sphere placed in a uniform isotropic flux, but the same expression holds for a uniform current.

† Obtained from the American Lava Corporation.

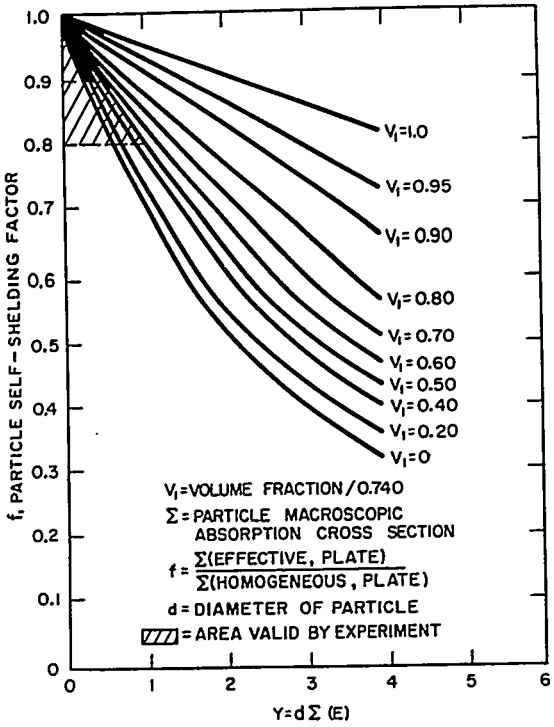

FIGURE 4.3. Particle Self-Shielding Factor vs Optical Diameter of Particle and Volume Fraction of Poison.

The sample contains a mixture of natural boron carbide spheres and aluminum spheres. The aluminum is used to dilute the boron carbide to the proper volume percent. This mixture is contained in an aluminum form of well-defined geometry, so that the thickness of the target mixture is uniform. An alternative method of holding the sample together by compacting the mixture under high pressure was not preferred for fear of cracking the boron carbide spheres, thus risking vitiation of measurements.

The density of the boron carbide particles was measured by comparing their density to that of a known fluid. The density of the fluid mixture (acetone and acetylene tetrabromide $[CH\,Br_2]_2$) was varied until the particles were balanced, i.e., half the particles floated and half did not. A volume displacement type measurement was not feasible because of the limited quantity of particles available.

The size distribution of the boron carbide spheres was measured by analyzing a photomicrograph of a portion of the sample (Fig. 4.4). An average mass-weighted diameter was computed from the measured distribution (Fig. 4.5).

TABLE 4.1 — PHYSICAL PARAMETERS OF THE SAMPLE

Thickness of boron carbide in mixture, g/cm^2	0.1377
Thickness of aluminum in mixture, g/cm^2	0.09124
a_1, thickness of mixture, cm	0.1529
a_3, thickness of aluminum in beam but external to mixture, cm	0.3259
Density of aluminum, g/cm^3	2.70
Density of boron carbide, g/cm^3	2.41
V_{Al}, volume fraction of aluminum in mixture	0.2210
V_{BC}, volume fraction of boron carbide in mixture	0.3737
d_A, average mass-weighted particle diameter of boron carbide, 10^{-4} cm	86.9
Particle diameter range of aluminum spheres, 10^{-4} cm	53-74
Boron in boron carbide particles, weight percent	72.4
Carbon in boron carbide particles, weight percent	24.0
Boron-to-carbon atom ratio in boron carbide particles	3.35

The boron-to-carbon atom ratio in the particles was determined from chemical analyses of a portion of the sample. It will be noted that this ratio and the density of the particles are not the book values. Presumably, this is caused by an excess of carbon present during the manufacture of the particles.

B) EXPERIMENTAL ARRANGEMENT AND PROCEDURE. A description of the crystal spectrometer used for the transmission measurements is given in Ref. 8. A schematic of the experimental arrangement is shown in Fig. 4.6. After adjusting the Bragg angle Φ to give the desired neutron energy, the following measurements were made on the sample:

1. Sample out of beam
   (a) C_0, on-Bragg counts and M_0, monitor counts
   (b) B_0, off-Bragg counts and M_{B_0}, monitor counts
2. Sample in beam
   (a) C, on-Bragg counts and M, monitor counts
   (b) B, off-Bragg counts and M_B, monitor counts

The off-Bragg counts were obtained by rotating the crystal off the Bragg angle by an amount slightly larger than the resolution

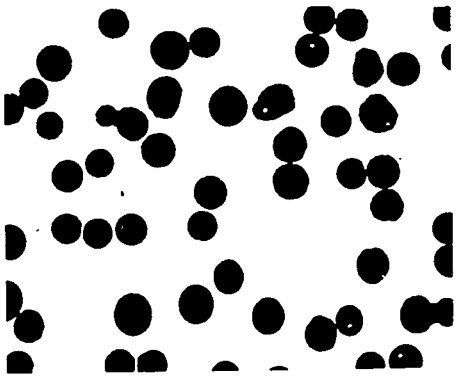

FIGURE 4.4. Photomicrograph of a Portion of the Boron Carbide Spheres Used in the Transmission Sample: 100 X.

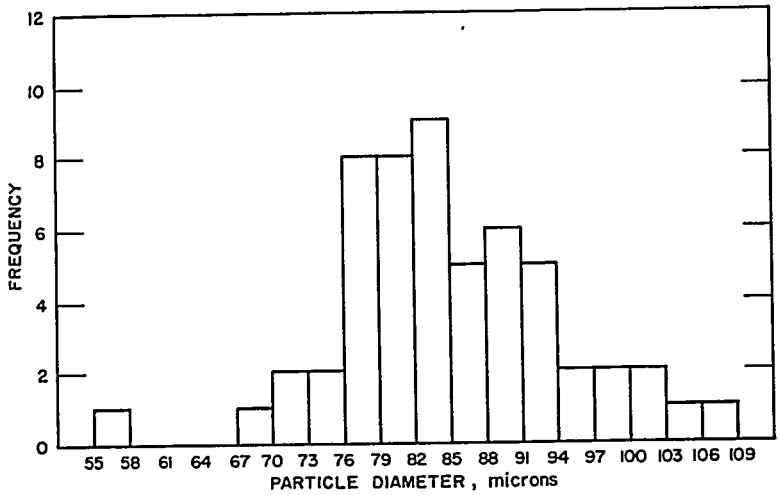

FIGURE 4.5. Histogram Showing Size Distribution of the Boron Carbide Spheres in the Sample.

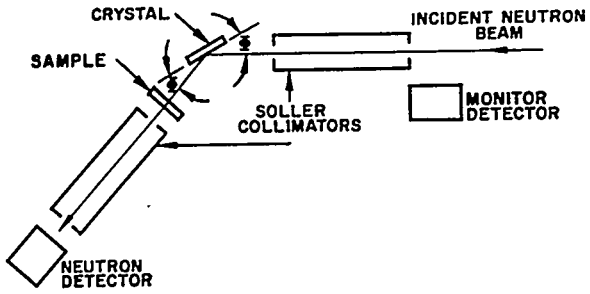

FIGURE 4.6. Schematic Showing Experimental Arrangement for the Transmission Measurements.

of the instrument. This measured the background associated with the on-Bragg counts. The experimental transmission is

$$T = \frac{\frac{C}{M} - \frac{B}{M_B}}{\frac{C_0}{M_0} - \frac{B_0}{M_{B_0}}}. \qquad \text{Eq. (4.13)}$$

Table 4.2 presents the experimental results.

C) ANALYSIS OF EXPERIMENT. The interpretation of the transmission data in terms of a particle self-shielding factor equivalent to Eq. (4.9) is complicated by:

1. Scattering as well as absorption is present.
2. The neutron beam traverses a portion of the aluminum sample holder as well as the mixture of boron carbide and aluminum particles.
3. The boron carbide particles are distributed in size.

In transmission measurements a scattering produces the same result as an absorption, i.e., removal from the incident beam. Thus, all results will hold if the absorption cross sections used previously are replaced with total cross sections. The effect of the pure aluminum structure in the path of the beam is subtracted out by computing its transmission from the known aluminum macroscopic cross section. Finally, the particle size distribution is accounted for by reducing the real sample to one which can be analyzed. The steps in this process are shown in Fig. 4.7, where the upper part (A) schematically shows the real arrangement and the middle part (B) shows that the aluminum particles have been homogenized over the region of the mixture but outside the boron carbide particles. The macroscopic cross section of the homogenized aluminum is Σ_H and is related to the pure aluminum cross section by

$$\Sigma_H = \frac{V_{Al}\,\Sigma_{Al}}{1 - V_{BC}} \qquad \text{Eq. (4.14)}$$

where

V_{Al} = volume fraction of aluminum in the mixture
V_{BC} = volume fraction of boron carbide in the mixture
Σ_{Al} = pure aluminum macroscopic cross section.

In Fig. 4.7 (C), the boron carbide particles with diameters d_1, $d_2, \ldots,$ and partial volume fractions $V_1, V_2, \ldots,$ have been grouped in separate sections of the sample. The thickness, b_i, of each section has been adjusted so that the volume fraction

of each section is equal to the gross boron carbide volume fraction, i.e., $b_i = a_1(V_i/V_{BC})$. The model shown can now be analyzed. The total transmission is the product of the transmissions of each section shown in Fig. 4.7 (C). The transmission of the section containing boron carbide particles of diameter d_i is given by Eq. (4.2), i.e.,

$$T_i(\Sigma_{BC}, \Sigma_H) = (\exp - b_i \Sigma_H)\, T_i(\Sigma_{BC} - \Sigma_H, 0) \qquad \text{Eq. (4.15)}$$

TABLE 4.2 — EXPERIMENTAL TRANSMISSIONS

Neutron Energy (ev)	Transmission, T_e
1.2263	0.509
0.364	0.307
0.1389	0.1634
0.0701	0.0843
0.03014	0.02817

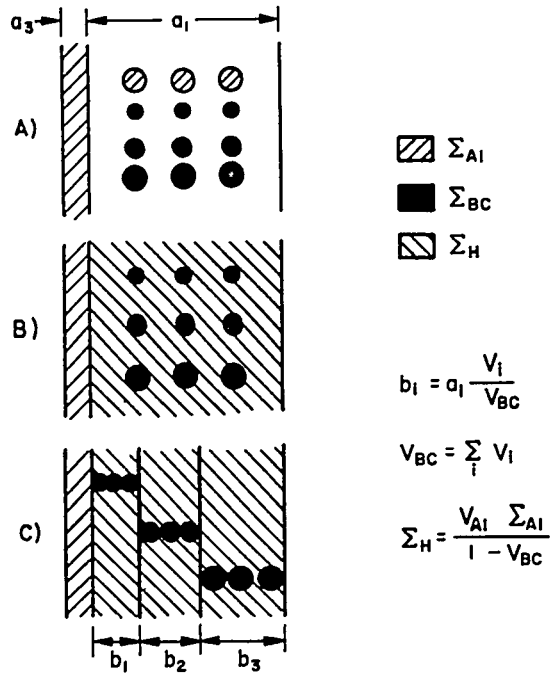

FIGURE 4.7. Schematic Showing Progressive Approximations Made in the Model of the Sample.

where Σ_{BC} = macroscopic cross section of the boron carbide spheres. Using Eq. (4.9),

$$T_i(\Sigma_{BC}-\Sigma_H, 0) = \exp\left[-b_i(\Sigma_{BC}-\Sigma_H)\, V_{BC} f_i\right]. \quad \text{Eq. (4.16)}$$

Since the total transmission through the sample is the product of the individual element transmissions,

$$T = \exp\left\{-a_3\Sigma_{Al} - a_1\Sigma_H - a_1 V_{BC}(\Sigma_{BC}-\Sigma_H)\bar{f}\right\} \quad \text{Eq. (4.17)}$$

where

$$\bar{f} = \sum_i f_i \frac{V_i}{V_{BC}} \quad \text{Eq. (4.18a)}$$

$$f_i = f(\gamma_i, V_{BC}) \quad \text{Eq. (4.18b)}$$

from Eq. (4.10), and

$$\gamma_i = d_i(\Sigma_{BC}-\Sigma_H). \quad \text{Eq. (4.18c)}$$

By inverting Eq. (4.17) and using the experimental transmissions $T = T_e$ given in Table 4.2, one may solve for $\bar{f} = \bar{f}_e$, the experimental particle self-shielding factor. Then, according to the model, this experimental value should be compared to a volume fraction-weighted (or mass-weighted) theoretical $\bar{f} = \bar{f}_{th}$, as given by Eqs. (4.10) and (4.18).

D) SUMMARY OF COMPUTATIONS. A summary of the method used to obtain the results shown in Fig. 4.8 is given below.

The experimental $\bar{f}$, i.e., $\bar{f}_e$, is given by inverting Eq. (4.17):

$$\bar{f}_e = \frac{\ln\left(\frac{1}{T_e}\right) - a_3\Sigma_{Al} - a_1\Sigma_H}{a_1 V_{BC}\Sigma_{BC} - a_1 V_{BC}\Sigma_H}. \quad \text{Eq. (4.19)}$$

The value of the term $a_1 V_{BC}\Sigma_{BC}$ in Eq. (4.19) is inferred at the highest energy (1.23 ev) from the experimental transmission (Table 4.2) and a theoretical f given by Eq. (4.18), i.e., the values of the experimental and theoretical particle self-shielding factors are normalized at the highest energy. The value of the term $a_1 V_{BC}\Sigma_{BC}$ at all lower energies is computed using the $1/v$ law for the boron cross section. This method for determining, in effect, the total amount of boron is accurate, even though it depends upon the use of an f whose validity is being tested, because f is close to one at high energy (1.23 ev) and will be insensitive to errors in theory. It is believed that this method

is superior to chemical analysis, for even if the chemical analysis is accurate (actually about 3 percent) the final value of $a_1 V_{BC} \Sigma_{BC}$ will depend upon the value assumed for the isotopic abundance of B^{10} (an uncertain number). The value of $a_1 V_{BC} \Sigma_{BC}$ at the highest energy E_1 (= 1.23 ev) is given by inverting Eq. (4.17):

$$a_1 V_{BC} \Sigma_{BC}(E_1) = \frac{1}{f(E_1)} \left\{ \ln \frac{1}{T_e(E_1)} - a_3 \Sigma_{Al}(E_1) - a_1 \Sigma_H(E_1) \left[1 - V_{BC} f(E_1)\right] \right\}. \quad \text{Eq. (4.20)}$$

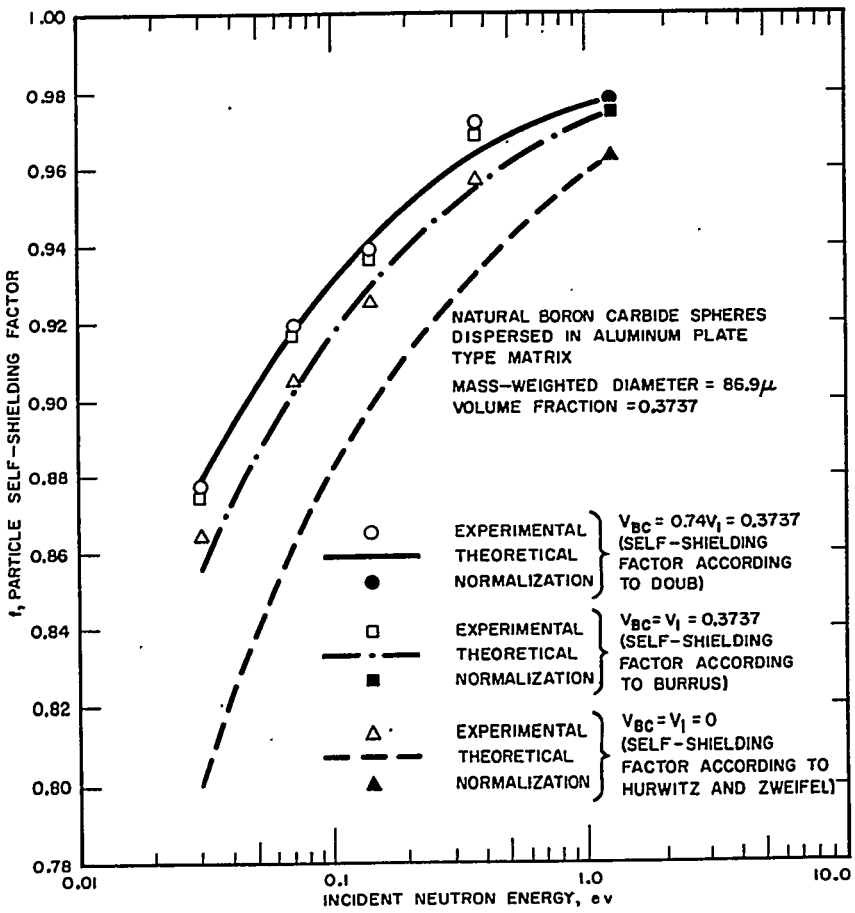

FIGURE 4.8. Comparison of Experimental and Theoretical Self-Shielding Factors as Given by Eq. (4.10), Burrus,[4,5] and Hurwitz and Zweifel,[3] Respectively. (All experimental points at the same energy are inferred from the same data. The separation of points in the figures is caused by the different self-shielding factors used in the normalization at the highest energy.)

The value of $f(E_1)$ is given by Eqs. (4.10) and (4.18). The value of $T_e(E_1)$ is given in Table 4.2. The value of $a_1 V_{BC} \Sigma_{BC}$ at any other energy is given by

$$a_1 V_{BC} \Sigma_{BC}(E) = a_1 V_{BC} \Sigma_{BC}(E_1) \left[\frac{R(E)}{R(E_1)}\right] \qquad \text{Eq. (4.21a)}$$

where

$$R(E) = \frac{1}{\sqrt{E}} \left\{ 1 + \frac{(\sigma_s)_B + \frac{1}{n}(\sigma_s + \sigma_a)_C}{\left(\sigma_a(E)\right)_B} \right\} \qquad \text{Eq. (4.21b)}$$

n = boron-to-carbon atom ratio in the boron carbide particles

$(\sigma_s + \sigma_a)_C = 4.8$ barns

$(\sigma_s)_B = 4$ barns

$\left(\sigma_a(2200\ m/sec)\right)_B = 755$ barns

Equation (4.21) expresses the $1/v$ absorption law and also contains scattering terms.

The theoretical value of f is given by Eqs. (4.10), (4.12), and (4.18) and is to be compared with the experimental value in Eq. (4.19). The computations indicated in these equations are tedious; an approximation has been made. One makes the approximation that f is linear in γ over the range covered in the experiment ($0 \leq \gamma \leq 0.65$; Fig. 4.3), i.e.,

$$f(\gamma) = f(\gamma_A) + \left(\frac{\partial f}{\partial \gamma}\right)_{\gamma=\gamma_A} (\gamma - \gamma_A)$$

where

γ_A = mass-averaged value of γ
$= d_A(\Sigma_{BC} - \Sigma_H)$

d_A = mass-averaged diameter of the boron carbide spheres.

Then, it follows that

$$\bar{f}_{th} = f(d_A\,[\Sigma_{BC} - \Sigma_H]\ ,\ V_{BC}) \qquad \text{Eq. (4.22)}$$

that is, the theoretical $\bar{f}$ is computed as if all the poison spheres had a uniform diameter d_A. The value of Σ_{BC} in Eq. (4.22) is given by Eq. (4.21), i.e.,

$$\Sigma_{BC}(E) = \frac{a_1 V_{BC} \Sigma_{BC}(E)}{a_1 V_{BC}}. \qquad \text{Eq. (4.23)}$$

The volume fraction V_{BC} in the denominator of Eq. (4.23) is determined from the measured mass and density of the boron carbide and the known volume of the sample container.

4. Discussion of Results

The experimental and theoretical values of $\bar{f}$ expressed in Eqs. (4.19) and (4.22), respectively, are compared in Fig. 4.8. The experimental and theoretical points have been forced together at the highest energy, as explained in Sect. 4.2.B.3. As can be seen, the agreement is good, thus validating the expression in Eq. (4.10) for the particle self-shielding. The particle self-shielding expression in Eq. (4.10) reduces in the limit of zero volume fraction to that given by Hurwitz and Zweifel. Since the Hurwitz-Zweifel calculations were exact in the same limit, the expression in Eq. (4.10) is exact for zero volume fraction. Also, experiment has verified the expression in Eq. (4.10) at 0.37 volume fraction. Thus, the expression in Eq. (4.10) is accurate at least in the zero to 40 volume percent range (and at least for optical particle diameters up to 0.7). The shaded area in Fig. 4.3 is a reasonable extrapolation of the range of V_1 and γ for which Eq. (4.10) is likely to be valid. In general, because of materials limitations it can be expected that most applications will be in this range.

For purposes of comparison and to ensure that the experimental method employed here is a fairly sensitive check, two alternative expressions for f have also been compared with experiment. The first expression is that given by Hurwitz and Zweifel,[2] and the second is that given by Burrus.[4,5] The comparisons were made in the same manner as for the particle self-shielding factor of this discussion. These are shown also in Fig. 4.8, where all experimental points at the same energy represent the same experimental data. The separation of the points is induced by different theoretical f's used in the normalizations at the highest energy. It is seen that the Hurwitz-Zweifel expression gives quite poor agreement and underestimates the particle self-shielding factor. The Burrus expression gives much better agreement with experiment but still not as good as Eq. (4.10). It also underestimates the particle self-shielding factor.

The particle self-shielding expression in Eq. (4.10) reduces to that of Hurwitz and Zweifel if one sets $V = 0$. The same expression reduces to the Burrus' expression if one sets $g = 1$. These observations are consistent with the following interpretation.

The Hurwitz-Zweifel expression is derived on the basis of complete freedom of placement of the poison particles in the sample (true for low volume fractions) and does not allow for the mutual exclusion of one particle by another from a given position in the sample. The Burrus expression, on the other hand, does take into account the mutual exclusion of one particle by another, but does so only on the basis of aligned particles which are cubic in shape. If the particles are spherical in shape, the resulting extra effectiveness of mutual exclusion is reflected by choosing $g = 0.74$ (or less for loosely packed samples). This, in effect, increases the volume excluded from the last poison particle placed in the sample from v to $v/0.74$. In any case, too great a freedom of position of the poison particles implies too great a variation in poison particle number density from point to point which, in turn, implies that the plate optical thickness has too much variation. Hence, the particle self-shielding factor is too small. As can be seen from Fig. 4.8, both the magnitudes and directions of the discrepancies of the Hurwitz-Zweifel and Burrus self-shielding expressions from experiment are consistent with the above interpretation. It is evident that the particle self-shielding factor must depend upon the volume fraction of poison particles in the sample, since near zero volume percent the factor is given by the Hurwitz-Zweifel expression, and near 100 volume percent it is 1.0.

It is of interest to note that, in the expression in Eq. (4.10) for the particle self-shielding factor, no parameters appear which depend upon the geometry, i.e., one may take the particle self-shielding function

$$\frac{\Sigma(\text{effective, object})}{\Sigma(\text{homogeneous, object})}$$

to be independent of the object geometry for most normal geometries and, hence, equal to Eq. (4.10).

C. Generalized Treatment of Particle Self-Shielding

C. H. Randall

1. Introduction

In this section a more general technique than the preceding one is described for predicting the nuclear characteristics of heterogeneous mixtures of materials. It should be pointed out that the calculational models of Doub (Sect. 4.2.B) and Hurwitz and Zweifel[2] are based on assumed material characteristics

which could be dependent on the manufacturing process. The model of Doub (binomial distribution) assumes essentially a random distribution of particles of approximately the same size and shape. Since it is not inconceivable that particular applications could lead to manufacturing processes where some of these simplifying assumptions may not be valid, it is worth indicating how one would develop a calculational model from more general principles. The particular example discussed in detail should not be construed as the ultimate and most general model, since each individual material will have its own characteristics. It should be noted that, as the volume fraction of particles increases, the shape deviates from a sphere, the range of particle sizes present increases, neutron optical diameters increase, and the need for a more generalized treatment becomes necessary. A specific characteristic of this type of material for which the model of Doub (Sect. 4.2.B) may be inaccurate is evidence of considerable large scale inhomogeneity in the material.

A particular model is developed in the following pages in detail for a particular case of particles embedded in a matrix material. Figure 4.9 is a sketch of a mixture containing two particle phases in contrast to the preceding analysis. A phase is defined as a spatially uniform medium exhibiting distinctive macroscopic nuclear properties. Specifying these spatially independent properties defines a phase. The method of approach is to determine when and how such complex mixtures can be represented by homogeneous materials. A homogeneous material is a single phase medium. The process of representing a mixture of materials by a homogeneous medium is generally referred to as homogenization. The defining properties of a homogeneous representation will be referred to as effective homogeneous properties or simply as effective properties.

The nature of the materials should be understood from the start. The fabrication processes always leave uncertainties concerning the microgeometry of any particular heterogeneous element. Microgeometry will refer to the detailed distribution of phases in a particular element. In Fig. 4.9 it refers to the exact shape, size, orientation, and location of the particles. Although it is unlikely that two elements produced by a given fabrication process will possess the same microgeometry, it is almost certain that they will share a common microstructure. Microstructure will be reserved to describe those average structural properties common to a collection (ensemble) of elements, e.g., phase volume fractions, mean particle diameter, etc. Since the microgeometry of a heterogeneous material cannot be controlled or measured in detail, the heterogeneous elements and their behavior can only be described statistically.

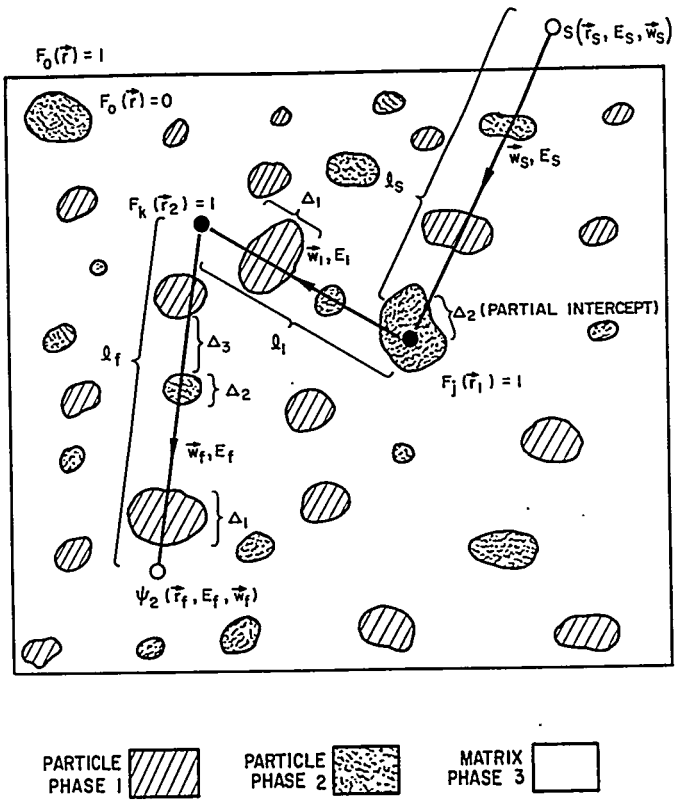

FIGURE 4.9. Neutron Track through a Heterogeneous Element.

To facilitate such a description, the behavior of a well specified fabrication process is considered rather than the behavior of poorly defined elements. It is imagined that the fabrication process is permitted to produce an infinitely large characteristic collection of heterogeneous elements. This collection will be referred to as the process ensemble. A quantity will be called a random variable if its value depends on which element of the process ensemble is referred to. The average value of a random variable taken over every element of this collection will be called its ensemble mean, and will be denoted by $\langle - \rangle$ around the quantity averaged. Occasionally a quantity will only be averaged over a specific part of the ensemble. Such averages will be referred to as conditional ensemble means and will be denoted by $\langle -/- \rangle$. The restricting condition will be written to the right of the slash.

The effect of random materials on the characteristics of a reactor system is to introduce some degree of uncertainty in them, that is, to make them random variables. Consider the

reactor problem sketched in Fig. 4.10, and suppose that the indicated heterogeneous elements are arbitrarily chosen from some process ensemble. Let X and Y be two system characteristics of interest, such as reactivity and the neutron absorption rate in one of the elements. These are random variables since they will, in general, depend on which elements of the process ensemble are inserted into the system. It is, therefore, impossible to predict exactly X and Y, and it is only feasible to describe their behavior statistically. All the information that can be obtained with respect to X and Y is contained in their joint probability density $p(x, y)$; $p(x, y)dx\,dy$ is the probability that X will lie between x and $x + dx$, and that Y will lie between y and $y + dy$. If $g(X, Y)$ is a function of X and Y then $\langle g(X, Y)\rangle = \int_{-\infty}^{+\infty} dx \int_{-\infty}^{+\infty} dy\, g(x, y)\, p(x, y)$. The marginal probability density of Y is $p(y) = \int_{-\infty}^{+\infty} dx\, p(x, y)$. The conditional probability density of X, given $Y = y$, is $p(x/y) = p(x, y)/p(y)$. The conditional mean of $g(X, Y)$, given that $Y = y$, is $\langle g(X, Y)/y\rangle = \int_{-\infty}^{+\infty} dx\, g(x, y)p(x/y)$.

If X is a significant characteristic (e.g., reactivity) it is usually important that its predicted value X_c have a given order of precision. The prediction error $(X - X_c)$ however, is itself a random variable, since X is one, and in general it cannot be arbitrarily restricted. One can nevertheless require that the probability of its exceeding some permissible margin of error,

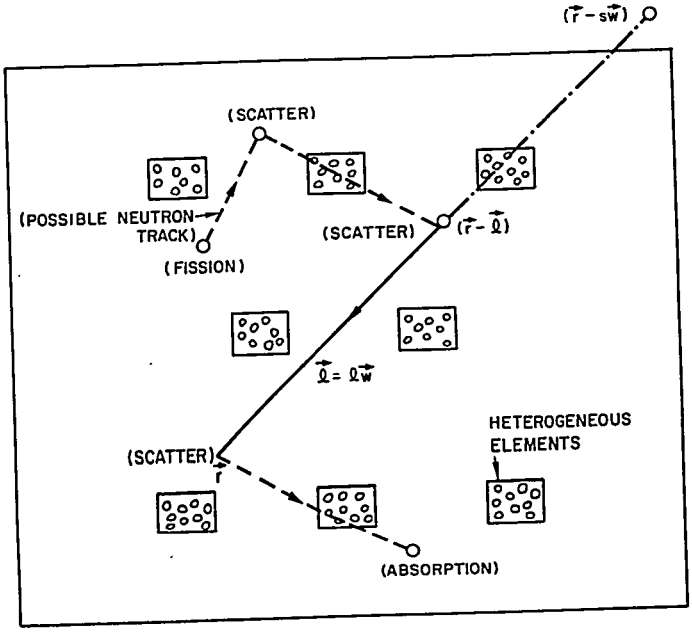

FIGURE 4.10. Neutron Track through a Reactor Containing Heterogeneous Elements.

say ϵ_X, be less than some small number P_X. The mean value $\langle X \rangle$ is the best predictor for X in the sense that it minimizes the variance of the prediction error. Also note that the mean error is then zero; that is, $\langle X \rangle$ is also an unbiased predictor. Thus, if a prediction for X is required, when possible $\langle X \rangle$ will be chosen.

If $X_c = \langle X \rangle$ and ϵ_X is the permissible error margin, the probability of the prediction error exceeding ϵ_X is less than $(\sigma_X / \epsilon_X)^2$ for the $\sigma_X >> \epsilon_X$. The variance of X is defined by $\sigma_X^2 = \langle X^2 \rangle - \langle X \rangle^2$ and is a measure of the probability of deviations of X from its mean value. It can be shown that the probability of deviations greater than $k\sigma_X$ is less than or equal to $1/k^2$, i.e., $P\{|X - \langle X \rangle| > k\sigma_X\} \leq 1/k^2$. If $(\sigma_X / \epsilon_X)^2 < P_X$, the criteria for prediction accuracy will be satisfied. This particular prediction error is an intrinsic part of the problem (process ensemble), and no improvement in accuracy is possible. If it is too large, the material fabrication process causing it is not appropriate for the particular application. Thus, in what follows, it will always be assumed that the variances of the significant characteristics are small enough to satisfy the prediction criteria.

To guarantee the predictability generally required of a reactor system, it is necessary to impose severe and often costly restrictions on reactor materials. It is essential that such restrictions do, in fact, guarantee the desired predictability with respect to all significant characteristics; but it is also important that such restrictions are no more severe than is actually necessary. Thus, any method of predicting characteristics should at least also indicate when the variances of a fabrication process are acceptable. The actual evaluation of these variances would relate the physical processes of interest to the necessary material quality control.

In addition to the inherent prediction error described above there will be approximation errors associated with any proposed homogenization procedure, since in general X_c will not equal $\langle X \rangle$. In a nonrandom system no homogeneous material can duplicate all the nuclear characteristics of a heterogeneous one. With respect to homogenization, the term preserve will be used in the following sense. Let the heterogeneous elements of a problem be homogenized, and let the resulting homogenized problem be solved. By computed will be meant from the exact transport solution of the homogenized problem. If this point of view were not adopted, the procedure developed would of necessity depend on the particular approximation to transport theory that was used to solve the homogenized problem. Now if the computed prediction X_c of a random variable X is essentially equal to the mean value $\langle X \rangle$, then the particular homogenization will be said to preserve X. If δ_X is

the permissible computational error, also dictated by the required precision, X_c will be said to be essentially equal to $\langle X \rangle$ if $|X_c - \langle X \rangle| < \delta_X$. In this event, note that the total prediction error $|X - X_c| > (\epsilon_X + \delta_X)$ with a probability less than $(\sigma_X / \epsilon_X)^2$.

Thus, given a reactor problem (including a statistical description of all heterogeneous elements) a formalism is sought that will (1) provide a homogeneous representation that will preserve certain significant system characteristics; (2) indicate the acceptability of the variances for this specified class of characteristics.

If the emitted neutron vector fluxes on the surfaces of all the heterogeneous elements of a reactor problem could be preserved, then so could any characteristics dependent on them. This is a sufficient condition but, in general, it is not necessary. If a particular problem and set of characteristics were specified, it could be determined for the particular case if the characteristics were preserved. These could include all the possible nuclear characteristics of a system with the possible exception of the detailed flux distributions within the elements themselves and their consequences. Given these fluxes a case, such as Fig. 4.10 represents, reduces to a deterministic boundary value problem independent of the homogenized heterogeneous elements. The interior fluxes will usually have relatively large variances associated with them and would be impossible to predict with precision. When they do not have large variances, it will turn out that they, too, will be preserved. Thus, homogenization to preserve the emitted vector fluxes appears to be the most general and still feasible goal. This is basically the same philosophy adopted in blackness theory and thin region theory. A material region is replaced by the boundary conditions it creates. Note that less is required for most approximate solutions to the neutron transport equation. For diffusion theory it is sufficient to preserve the scalar flux to current ratio on these surfaces.

Thus, with some loss of generality, the problem has been reduced to considering the means and variances of the emitted vector fluxes. The remainder of this section will be concerned with these quantities. Note that the arguments used were not meant to be rigorous and are only order of magnitude type observations. However, if a particular problem and set of random variables were specified, a sharper analysis of predictability and homogenization would be possible. At this point, however, it is more desirable to develop the general method of analysis with some sacrifice in precision.

First, a mean vector flux is defined, taking into account that there are random discrete (heterogeneous) materials present. It is shown that, if the discrete absorbers can be represented

as a homogeneous mixture, the flux can be represented as a continuous distribution in a manner which is consistent with the homogenization scheme. Next, effective transport cross sections are defined and the conditions to which these definitions apply are discussed. To evaluate these effective cross sections the nature of the spatial distribution of the discrete neutron absorbing particles must be defined. The methods of describing the statistical nature of the spatial distribution of the particles and the calculation of the mean neutron transmission through a plate containing these distributed particles are discussed next. Since, if more than one phase (material) of discrete particle is present, an accounting of the relative captures in each must be made for the purpose of reactivity and depletion calculations, the phase collision fractions are treated. The results of the above discussion are then used to formulate the microscopic self-shielding factor, and methods of determining from physical data the parameters which describe the particle distribution are discussed.

2. *The Mean Vector Flux*

Let $\psi(\vec{r}, \vec{w}, E)$ be the flux density for neutrons traveling in the direction $\vec{w}$, with energy E, at the field point $\vec{r}$. A homogeneous representation is sought to preserve the emitted ψ on the surface of the homogenized elements. The existence of such a representation is by no means certain. Sufficient conditions will be found for such a homogenization, and its effective properties will be defined. It will turn out that these conditions will also assure the predictability of the emitted ψ in the sense of their having a negligibly small variance.* Thus, the requirements set forth in the introduction for a homogeneous representation will be satisfied.

The integral transport equation for ψ may be written (Ref. 9, pp. 22-27)

$$\psi = H_o S + H_o H_1 \psi \qquad \text{Eq. (4.24)}$$

*If necessary conditions had been considered, a wide class of problems could have been included in the formalism developed; however, this would have required a much more elaborate analysis than that adopted here.

where H_0 and H_1 are the linear integral operators defined by

$$H_o\underline{\psi} = \int_o^\infty d\ell\, \iota(\vec{r} - \ell\vec{w}, \vec{r}; E)\, \underline{\psi(\vec{r} - \ell\vec{w}, E, \vec{w})}$$

$$= \int_o^\infty d\ell\, e^{-\int_o^\ell ds\, \Sigma(\vec{r} - s\vec{w}, E)}\, \underline{\psi(\vec{r} - \ell\vec{w}, E, \vec{w})}$$

$$H_1\underline{\psi} = \int_o^\infty dE' \int_{4\pi} d\vec{w}'\, C(\vec{w}'\, E' \to \vec{w}\, E; \vec{r})\, \underline{\psi(\vec{r}, E'\, \vec{w}')}. \qquad \text{Eq. (4.25)}$$

(The line "_____" indicates the function operated on, thus:

$$H_1 \text{———} = \int_o^\infty dE' \int_{4\pi} d\vec{w}'\, C(\vec{w}'\, E' \to \vec{w}E; \vec{r}) \text{———}.)$$

The transfer cross section

$$C = \Sigma_s(\vec{w}'\, E' \to \vec{w}\, E; \vec{r}) + \frac{\nu f(E)}{4\pi}\Sigma_f(\vec{r}, E'). \qquad \text{Eq. (4.26)}$$

The macroscopic properties have their conventional significance: $\Sigma(\vec{r}, E)$ is the total cross section, $\Sigma_f(\vec{r}, E)$ the fission cross section, $\nu f(E)$ the emission spectrum per fission, and $\Sigma_s(\vec{w}'\, E' \to \vec{w}\, E, \vec{r})$ the differential scattering cross section at $\vec{r}$. The symbol $\iota(\vec{r} - \ell\vec{w}, \vec{r}; E)$ denotes the transmission probability between $\vec{r} - \ell\vec{w}$ and $\vec{r}$ for neutrons having energy E. It will often be convenient to write ι_{12} for $\iota(\vec{r}_1, \vec{r}_2, E_1)$. $S(\vec{r}, \vec{w}, E)$ is any external neutron source.

The integro-differential form of the transport equation, the Boltzmann equation, is

$$H_o^{-1}\psi = [\vec{w} \cdot \nabla + \Sigma(\vec{r}, E)]\ \psi = S + H_1\psi.$$

The differential operator H_o^{-1} is the inverse of the integral operator H_o,* i.e., $H_oH_o^{-1} = I$. I is the identity operator, i.e., $I\psi(\vec{r}, E, \vec{w}) = \psi(\vec{r}, E, \vec{w})$.

*This relationship and the equivalence of the two forms of the transport equation are discussed in Ref. 9, pp. 24-26.

In reactor problems containing heterogeneous elements, the macroscopic cross sections are random variables. Their spatial dependence is related to the microgeometries of the elements, and these are random processes. As a consequence H_o, H_o^{-1}, and H_1 are linear stochastic operators (random operators). Because these operators relate ψ to the source, ψ is a random variable even if the source is not.

To exhibit these relationships explicitly the following notation is adopted:

$$F_j(\vec{r}) = \begin{cases} 1 & \vec{r} \text{ in phase } j \\ 0 & \vec{r} \text{ not in phase } j \end{cases} \qquad j = 1, 2, 3, \ldots, n \qquad \text{Eq. (4.27)}$$

where n is the total number of distinct phases present in the heterogeneous elements. These will be referred to as the phase characteristic functions. For example, in Fig. 4.9 the phase 1 characteristic function, $F_1(\vec{r})$, is equal to unity in the diagonal regions and vanishes everywhere else.

Also define

$$F_o(\vec{r}) = \begin{cases} 1 & \vec{r} \text{ not in a heterogeneous element} \\ 0 & \vec{r} \text{ in a heterogeneous element} \end{cases} \qquad \text{Eq. (4.28)}$$

In Fig. 4.10, $F_o(\vec{r})$ vanishes within the heterogeneous elements and is equal to unity everywhere else. The $F_j(\vec{r})$ locate the boundaries between phases and completely describe the microgeometries of the heterogeneous elements. The microgeometries are random processes; therefore, so are these functions. $F_o(\vec{r})$, on the other hand, is a well defined function that describes the interface between these elements and the rest of the system, which is also assumed to be well defined (nonrandom).

The ensemble averages

$$V_j(\vec{r}) = \langle F_j(\vec{r}) \rangle \qquad j = 1, 2, \ldots, n \qquad \text{Eq. (4.29)}$$

are defined to be the local phase volume fractions. They can be interpreted as the frequency with which the various phases appear at $\vec{r}$ in the process ensemble. In general, they are spatially dependent. Note that since $F_o(\vec{r})$ is not a random process it is invariant over the ensemble, and $V_o(\vec{r}) = \langle F_o(\vec{r}) \rangle = F_o(\vec{r})$. In any given heterogeneous element only one

phase can occupy each spatial point $\vec{r}$. As a consequence, at each $\vec{r}$ only one of the $F_j(\vec{r})$ can differ from zero and

$$F_j(\vec{r})F_k(\vec{r}) = \delta_{jk}\, F_j(\vec{r})j,\ k = 0, 1, 2, \ldots, n \qquad \text{Eq. (4.30)}$$

i.e., the product vanishes if $j \neq k$ and may equal unity if $j = k$. Furthermore,

$$\sum_{j=0}^{n} F_j(\vec{r}) = \sum_{j=0}^{n} V_j(\vec{r}) = 1\,. \qquad \text{Eq. (4.31)}$$

With the above notation it is a relatively simple matter to relate the material microstructures to the macroscopic cross sections and, hence, to the operators. Write

$$\Sigma(\vec{r}, E) = \sum_{j=0}^{n} F_j(\vec{r})\Sigma^j(\vec{r}, E)\,. \qquad \text{Eq. (4.32)}$$

For $j = 1, 2, \ldots n$, $\Sigma^j(\vec{r}, E) = \Sigma^j(E)$ is presumed to be a well defined (nonrandom) spatially independent phase j cross section and $\Sigma^o(\vec{r}, E)$ a well defined but, in general, spatially varying cross section in the rest of the system. This description implies that the only source of randomness present in the cross sections is in the poorly defined phase boundaries. In a clean reactor this is essentially true. As a reactor burns out, spatial inhomogeneities do develop in all the cross sections and, to some extent, they depend on the particular heterogeneous elements initially inserted in the core, i.e., the Σ^j become random variables. It will, therefore, be presumed that a clean core is under consideration.

In the notation introduced above

$$H_o^{-1}\_\_\_\_ = \vec{w}\cdot\nabla\_\_\_\_ + \sum_{j=0}^{n} \Sigma^j(\vec{r}, E)F_j(\vec{r})\_\_\_\_$$

$$H_o = \int_o^{\infty} d\ell \left\{ \exp - \sum_{j=0}^{n} \int_o^{\ell} ds\, F_j(\vec{r} - s\vec{w})\Sigma^j(\vec{r} - s\vec{w}, E) \right\} \_\_\_\_$$

$$H_1\_\_\_\_ = \sum_{j=0}^{n} F_j(\vec{r}) \int_o^{\infty} dE' \int_{4\pi} d\vec{w}'\, C^j(\vec{w}'\ E' \rightarrow \vec{w}\, E, \vec{r})\_\_\_\_\_$$

$$\equiv \sum_{j=0}^{n} F_j(\vec{r})\, H_1\_\_\_\_ \qquad \text{Eq. (4.33)}$$

and the operators, and consequently ψ, are explicitly related to the $F_j(\vec{r})$ and the microgeometries.

Averaging over the integro-differential equation,*

$$\vec{w} \cdot \nabla \langle \psi \rangle + \sum_{j=0}^{n} \Sigma^j \langle F^j \psi \rangle = \langle S \rangle + \int_o^\infty \int_{4\pi} dE' \, d\vec{w}' \sum_{j=0}^{n} C^j \langle F_j \psi \rangle$$

Eq. (4.34)

and

$$\vec{w} \cdot \nabla \langle \psi \rangle + \Sigma_{\text{eff}} \langle \psi \rangle = \langle S \rangle + \int_o^\infty \int_{4\pi} dE' \, d\vec{w}' \, C_{\text{eff}} \langle \psi \rangle. \quad \text{Eq. (4.35)}$$

Thus, an equation in $\langle \psi \rangle$ is obtained. The effective cross sections are defined by

$$\Sigma_{\text{eff}}(\vec{r}, E) = \sum_{j=0}^{n} \Sigma^j(\vec{r}, E) \left\langle F_j(\vec{r}) \psi(\vec{r}, E, \vec{w}) \right\rangle \Big/ \left\langle \psi(\vec{r}, E, \vec{w}) \right\rangle$$

$$C_{\text{eff}}(\vec{w}' E' \to \vec{w} E, \vec{r}) = \sum_{j=0}^{n} C^j(\vec{w}' E' \to \vec{w} E, \vec{r}) \left\langle F_j(\vec{r}) \psi(\vec{r}, E, \vec{w}) \right\rangle \Big/ \left\langle \psi(\vec{r}, E, \vec{w}) \right\rangle . \quad \text{Eq. (4.36)}$$

If these cross sections are spatially independent in the heterogeneous elements, they will define a homogenization.

Since F_j can only be zero or unity, $\langle F_j(\vec{r}) \psi(\vec{r}, E, \vec{w}) \rangle / \langle F_j(\vec{r}) \rangle$ is equal to $\langle \psi(\vec{r}, E, \vec{w}) / F_j(\vec{r}) = 1 \rangle$, the conditional mean flux at $\vec{r}$, given that $\vec{r}$ is in phase j. Therefore,

$$\frac{\left\langle F_j(\vec{r}) \psi(\vec{r}, E, \vec{w}) \right\rangle}{\left\langle \psi(\vec{r}, E, \vec{w}) \right\rangle} = \frac{\left\langle \psi(\vec{r}, E, \vec{w}) / F_j(\vec{r}) = 1 \right\rangle}{\left\langle \psi(\vec{r}, E, \vec{w}) \right\rangle} \left\langle F_j(\vec{r}) \right\rangle = V_j(\vec{r}) f_j(\vec{r}, E, \vec{w}).$$

Eq. (4.37)

*It will always be assumed that the averaging (essentially an integration) process commutes with all other integration and gradient operations. This is generally true for well behaved functions. See for example, Ref. 10, pp. 139-143.

V_j is the local volume fraction, and f_j can be regarded as the local flux depression or self-shielding factor for the j^{th} phase. With this interpretation the significance of the effective cross-section definitions is clear. The cross sections are simply the volume fraction flux depression weighted averages of the phase cross sections. They define a homogeneous representation of the heterogeneous elements if they are independent of $\vec{r}$.

If $\psi(\vec{r}, E, \vec{w})$ and $F_j(\vec{r})$ are uncorrelated, i.e., $\langle \psi F_j \rangle = \langle \psi \rangle \langle F_j \rangle$, it is implied that ψ is insensitive to the phase occupying $\vec{r}$. In this event $f_j = 1$. For the nonrandom materials in the reactor this is always true, since $\langle \psi F_o \rangle = \langle \psi \rangle F_o = \langle \psi \rangle V_o$ and, therefore, $f_o \equiv 1$. In general, ψ and F_j are correlated. For example, if j is the index of a heavy absorber it would be expected that ψ would be lower in phase j than on the average in all phases. As a consequence, f_j would be expected to be less than unity.

Since $\langle \psi \rangle$ is a solution of Eq. (4.35), such a homogenization would preserve the necessary $\langle \psi \rangle$. In practice, however, the f_j cannot be evaluated. Not only do they depend on the required solution $\langle \psi \rangle$ but also on $\langle F_j \psi \rangle$. To circumvent this difficulty, the integral Eq. (4.24) is utilized to obtain a more tractable homogenization.

Equation (4.24) is iterated, or the operators are formally manipulated, to obtain

$$\psi = H_o S + H_o H_1 [H_o S + H_o H_1 \psi] = H_o S + (H_o H_1) H_o S + (H_o H_1)^2 \psi$$

$$\psi = \sum_{\nu=0}^{\infty} (H_o H_1)^{\nu} H_o S = \sum_{\nu=0}^{\infty} \psi_{\nu}. \qquad \text{Eq. (4.38)}$$

This is the Neumann expansion of the integral equation and can be shown to converge for all subcritical systems. This is no real restriction. An operating reactor can be assumed to be slightly subcritical with a very long half-life, and the series will still converge. The ν^{th} term is the contribution to ψ from those neutrons that have suffered ν collisions since leaving the source and also includes those neutrons resulting from fissions. The $\psi_o = H_o S$ term is the uncollided flux. If Eq. (4.38) is averaged, the following expression for $\langle \psi \rangle$ is obtained

$$\langle \psi \rangle = \sum_{\nu=0}^{\infty} \langle (H_o H_1)^{\nu} H_o \rangle \langle S \rangle = \sum_{\nu=0}^{\infty} \langle \psi_{\nu} \rangle .$$

Eq. (4.39)

It has been assumed that the S, if it is random, is not correlated with the operators. Two random variables, X and Y, are said to be uncorrelated if $\langle XY \rangle = \langle X \rangle \langle Y \rangle$. They are said to be independent if $p(x/y) = p(x)$ or $p(y/x) = p(y)$. If they are independent they will also be uncorrelated.

It is instructive to consider in detail the individual terms of this expansion. In particular, consider $\langle \psi_2 \rangle$. Noting Eq. (4.33)

$$\langle \psi_2 \rangle = \left\langle (H_o H_1)^2 H_o \right\rangle \langle S \rangle = \left\langle \left(H_o \sum_{j=0}^{n} F_{jj} H_1\right)^2 H_o \right\rangle \langle S \rangle$$

$$= \sum_{j=0}^{n} \sum_{k=0}^{n} \left\langle H_o F_{jj} H_1 H_o F_{kk} H_1 H_o \right\rangle \langle S \rangle . \qquad \text{Eq. (4.40)}$$

Employing the notation of Fig. 4.9, where the subscript s refers to the source point, f to the field point, and 1 and 2 to the first and second collision points, Eq. (4.40) becomes

$$\left\langle \psi_2(\vec{r}_f, E_f, \vec{w}_f) \right\rangle = \sum_{j=0}^{n} \sum_{k=0}^{n} \int_o^\infty d\ell_f \int_o^\infty dE_1 \int_{4\pi} d\vec{w}_1 \int_o^\infty d\ell_1 \int_o^\infty dE_s$$

$$\int_{4\pi}^{\infty} d\vec{w}_s \int_o^\infty d\ell_s \left\langle S(\vec{r}_s, E_s, \vec{w}_s) \right\rangle$$

$$\left\langle t_{2f} F_k(\vec{r}_2) C^k(\vec{w}_1 E_1 \rightarrow \vec{w}_f E_f, \vec{r}_2) t_{12} F_j(\vec{r}_1) \right.$$

$$\left. C^j(\vec{w}_s E_s \rightarrow \vec{w}_1 E_1, \vec{r}_1) t_{s1} \right\rangle$$

$$= \sum_{j=0}^{n} \sum_{k=0}^{n} \int_o^\infty d\ell_f \cdots \int_o^\infty d\ell_s$$

$$C^j C^k \left\langle t_{2f} F_k(\vec{r}_2) t_{12} F_j(\vec{r}_1) t_{s1} \right\rangle$$

$$\left\langle S(\vec{r}_s, E_s, \vec{w}_s) \right\rangle .$$

Eq. (4.41)

Recall that $t_{12} = t(\vec{r}_1 \to \vec{r}_2, E_1)$ is the transmission probability between $\vec{r}$ and $\vec{r}_2$ for neutrons at energy E_1. Also note that

$$\vec{r}_f = \vec{r}_s + \ell_s \vec{w}_s + \ell_1 \vec{w}_1 + \ell_f \vec{w}_f.$$

The product $C^j C^k \langle t_{2_f} \cdots t_{s1} \rangle$ is the probability density for a three-segment (two-collision) path, with phase j occupying $\vec{r}_1$ and phase k occupying $\vec{r}_2$, such as the one depicted by Fig. 4.9. Thus, $\langle \psi_2 \rangle$ is the sum of the contributions from all such paths (i.e., with two collisons) contributing to $\langle \psi(\vec{r}_f, E_f, w_f) \rangle$. In a similar manner, $C^{\lambda_1} C^{\lambda_2} \cdots C^{\lambda_\nu} \langle t_{\nu f} F_{\lambda_\nu}(\vec{r}_\nu) \cdots F_{\lambda_1}(\vec{r}_1) t_{s1} \rangle$ is the probability for a $\nu+1$ segment (ν collision) path. The collection of all these probabilities provides an elementary description of the interaction of the heterogeneous materials and the neutron transport process. Homogenization is, in effect, an attempt to simplify appreciably this description.

To obtain a homogenization it will be necessary to reduce terms like $\langle t_{\nu f} \cdots t_{s1} \rangle$ to a product of elementary factors. To illustrate the ideas related to this factorization, consider again the neutron track pictured in Fig. 4.9. Because of the zero-one character of the F_j

$$\left\langle t_{2f} F_k(\vec{r}_2)\, t_{12}\, F_j(\vec{r}_1)\, t_{s1} \right\rangle = \left\langle F_j(\vec{r}_1)\, F_k(\vec{r}_2) \right\rangle \left\langle t_{2f} t_{12} t_{s1} / F_j(\vec{r}_1) = 1,\, F_k(\vec{r}_2) = 1 \right\rangle . \qquad \text{Eq. (4.42)}$$

If it can be assumed that the end points $\vec{r}_1$ and $\vec{r}_2$ are relatively far apart compared to the local microstructure correlation scale, then it follows that

$$\left\langle F_j(\vec{r}_1)\, F_k(\vec{r}_2) \right\rangle \cong \left\langle F_j(\vec{r}_1) \right\rangle \left\langle F_k(\vec{r}_2) \right\rangle \qquad \text{Eq. (4.43)}$$

$$\left\langle t_{2f} t_{12} t_{s1} / F_j(\vec{r}_1) = 1,\, F_k(\vec{r}_2) = 1 \right\rangle \cong \left\langle t_{2f} / F_k(\vec{r}_2) = 1 \right\rangle \left\langle t_{s1} / F_j(\vec{r}_1) = 1 \right\rangle \left\langle t_{12} / F_j(\vec{r}_1) = 1,\, F_k(\vec{r}_2) = 1 \right\rangle \qquad \text{Eq. (4.44)}$$

and

$$\left\langle t_{12} / F_j(\vec{r}_1) = 1,\, F_k(\vec{r}_2) = 1 \right\rangle \cong \frac{\left\langle t_{12} / F_j(\vec{r}_1) = 1 \right\rangle \left\langle t_{12} / F_k(\vec{r}_2) = 1 \right\rangle}{\left\langle t_{12} \right\rangle} \qquad \text{Eq. (4.45)}$$

The microstructure covariances are defined to be the $\text{cov}\left[F_j(\vec{r}_1)\,F_k(\vec{r}_2)\right] = \left\{\langle F_j(\vec{r}_1)F_k(\vec{r}_2)\rangle - \langle F_j(\vec{r}_1)\rangle\langle F_j(\vec{r}_2)\rangle\right\}$ and are typically of the form $f(\vec{r}_1, \vec{r}_2)\exp - |\vec{r}_1 - \vec{r}_2|/\Lambda$. As $|\vec{r}_1 - \vec{r}_2|$ increases they vanish exponentially. In the structure shown in Fig. 4.9 Λ (a measure of the correlation scale) would be expected to be on the order of a mean particle diameter.

Equation (4.43) states that the two end points are uncorrelated and implies that the presence of phase j at $\vec{r}_1$ in no way affects the probability of finding phase k at $\vec{r}_2$. It follows formally because $|\vec{r}_1 - \vec{r}_2| \gg \Lambda$, and the covariance will be negligibly small. Noting Fig. 4.9, this is almost intuitively obvious. If $|\vec{r}_1 - \vec{r}_2|$ is significantly larger than the particles, and no large scale effect such as clumping is present, then it would be expected that the probability of finding phase k at $\vec{r}_2$ is simply $V_k(\vec{r}_2) = \langle F_k(\vec{r}_2)\rangle$, independent of what phase occupies $\vec{r}_1$.

In essence, Eqs. (4.44) and (4.45) are of the same nature as Eq. (4.43). Equation (4.44) states that the path segment transmissions are uncorrelated and, furthermore, are only sensitive to the phases at their own end points. Equation (4.45) implies further that the transmissions from the end points to the middle of the segment, $\vec{r}_1$ to $\vec{r}_2$, are also uncorrelated.* Using Eqs. (4.43), (4.44), and (4.45), and noting that $\langle tF\rangle = \langle t/F = 1\rangle\langle F\rangle$,

$$\left\langle t_{2f} F_k(\vec{r}_2)\, t_{12} F_j(\vec{r}_1)\, t_{s1}\right\rangle$$

$$= \left\langle t_{2f}\right\rangle \left\{ \frac{\left\langle t_{2f} F_k(\vec{r}_2)\right\rangle}{\left\langle t_{2f}\right\rangle \left\langle F_k(\vec{r}_2)\right\rangle} \left\langle F_k(\vec{r}_2)\right\rangle \frac{\left\langle t_{12} F_k(\vec{r}_2)\right\rangle}{\left\langle F_k(\vec{r}_2)\right\rangle \left\langle t_{12}\right\rangle} \right\} \left\langle t_{12}\right\rangle$$

$$\left\{ \frac{\left\langle t_{12} F_j(\vec{r}_1)\right\rangle}{\left\langle t_{12}\right\rangle \left\langle F_j(\vec{r}_1)\right\rangle} \left\langle F_j(\vec{r}_1)\right\rangle \frac{\left\langle t_{s1} F_j(\vec{r}_1)\right\rangle}{\left\langle F_j(\vec{r}_1)\right\rangle \left\langle t_{s1}\right\rangle} \right\} \left\langle t_{s1}\right\rangle$$

Eq. (4.46)

*All of these arguments can be treated quantitatively if attention is restricted to some simple class of microstructures, and the more formal machinery of the theory of linear stochastic operators is utilized.

and a factorization is obtained. The terms of the form

$$f_j(\vec{r}_1, E_1, \vec{w}_1 \ell_1) = \frac{\langle t_{12} F_j(\vec{r}_1)\rangle}{\langle t_{12}\rangle \langle F_j(\vec{r}_1)\rangle} \qquad \text{Eq. (4.47)}$$

will become the phase j self-shielding factors in the effective cross sections finally obtained. A similar factorization can be applied to all the paths contributing to $\psi(\vec{r}_f E_f, \vec{w}_f)$ if for all significantly probable paths the distances between collisions (fission or scatter) are appreciably larger than the correlation scales. This will be assumed true.

For the case illustrated in Fig. 4.9, this condition is equivalent to assuming that the probability of two successive collisions in the same particle is negligibly small. In the absence of fissionable materials this will be so if the particles are small compared to the scattering mean free paths, which are on the order of centimeters. If fuel particles are present, the fission process must also be considered. When a neutron causes fission in a fuel particle, neutrons are emitted at relatively high energies. They will, as a consequence, have mean free paths on the order of the scatter mean free paths, and the probability of a second collision in the particle for this situation will also be very small. If, however, a neutron is scattered to a resonance or a thermal energy in the first collision in a fuel particle, there will be a good chance that it will also cause a fission before it can leave the particle. Hence, the above assumption must also imply that the probability for such scattering events is small. In almost all fuel materials the probability of a large energy loss in a single collision is negligible. As a consequence, the probability of scattering into the thermal range in a single collision is small. On the other hand, for those neutrons that possess an energy just above a resonance, there will be a good possibility of scattering into the resonance and then fissioning in the same particle. If this effect is neglected, the resulting errors will not, as a rule, be significant. In most cases, the majority of neutrons absorbed in a resonance will have been scattered into the resonance by other than the fuel phase.

For notational convenience define the operators

$$K_o \underline{\psi} = \int_o^\infty d\ell \left\langle t(\vec{r} - \ell\vec{w} \to \vec{r}, E) \right\rangle \underline{\psi(\vec{r} - \ell\vec{w}, E, \vec{w})}$$

$$K_1 \underline{\psi} = \sum_{j=0}^{n} {}_jK_1 \underline{\psi}$$

$$= \sum_{j=0}^{n} \int_o^\infty dE' \int_{4\pi} d\vec{w}' C^j(\vec{w}' E' \to \vec{w} E, \vec{r})$$

$$\left\{ \frac{\left\langle t(\vec{r} - \ell'\vec{w}' \to \vec{r}, E') F_j(\vec{r}) \right\rangle}{\left\langle t(\vec{r} - \ell'\vec{w}' \to \vec{r}, E') \right\rangle \left\langle F_j(\vec{r}) \right\rangle} \left\langle F_j(\vec{r}) \right\rangle \right.$$

$$\left. \frac{\left\langle t(\vec{r} \to \vec{r} + \ell\vec{w}, E) F_j(\vec{r}) \right\rangle}{\left\langle F_j(\vec{r}) \right\rangle \left\langle t(\vec{r} \to \vec{r} + \ell\vec{w}, E) \right\rangle} \right\} \underline{\psi(\vec{r}, E'\vec{w}')}$$

$$= \sum_{j=0}^{n} \int_o^\infty dE' \int_{4\pi} d\vec{w}' f_j(\vec{r}, E', -\ell'\vec{w}') V_j(\vec{r}) C^j(\vec{w}' E' \to \vec{w} E, \vec{r})$$

$$f_j(\vec{r}, E, +\ell\vec{w}) \underline{\psi(\vec{r}, E'\vec{w}')}.$$

Eq. (4.48)

Note that the f_j appear to depend not only on $\vec{r}$ and E (or $\vec{r}$ and E') but also on $\vec{\ell} = \ell\vec{w}$ (or $-\vec{\ell}' = -\ell'\vec{w}'$), the vector to the next (last) collision. This is generally not the case. The condition that ℓ be significantly larger than the correlation scales suppresses the dependency, except possibly at the interfaces of the heterogeneous elements. This point will be reconsidered in the next section.

Having assumed that all the paths contributing to $\psi(\vec{r}_f, E_f \vec{w}_f)$ can be factored after the manner of Eq. (4.46), Eq. (4.41) can be written as

$$\left\langle \psi_2(\vec{r}_f, E_f \vec{w}_f) \right\rangle = \sum_{j=0}^{n} \sum_{k=0}^{n} K_{o\,j} K_1 K_{o\,k} K_1 K_o \left\langle S \right\rangle = (K_o K_1)^2 K_o \left\langle S \right\rangle.$$

Eq. (4.49)

Adding all the ψ_ν, Eq. (4.39) becomes

$$\left\langle \psi(\vec{r}_f, E_f, \vec{w}_f) \right\rangle = \sum_{\nu=0}^{\infty} (K_o K_1)^\nu K_o \left\langle S \right\rangle . \qquad \text{Eq. (4.50)}$$

This is simply the Neumann expansion of the integral equation

$$\left\langle \psi \right\rangle = K_o \left\langle S \right\rangle + K_o K_1 \left\langle \psi \right\rangle \qquad \text{Eq. (4.51)}$$

an equation in $\langle \psi \rangle$ of the same form as Eq. (4.24).

It will now be demonstrated that the conditions used to obtain Eq. (4.51) are also sufficient to cause the variance of ψ to vanish. Squaring and averaging Eq. (4.38),

$$\left\langle \psi^2 \right\rangle = \sum_{\eta=0}^{\infty} \sum_{\nu=0}^{\infty} \left\langle \left[(H_o H_1)^\eta H_o S \right] \left[(H_o H_1)^\nu H_o S \right] \right\rangle . \qquad \text{Eq. (4.52)}$$

Using the factorization assumption again,

$$\left\langle \psi^2 \right\rangle = \sum_{\eta=0}^{\infty} \sum_{\nu=0}^{\infty} \left[(K_o K_1)^\eta K_o S \right] \left[(K_o K_1)^\nu K_o S \right] = \left\langle \psi \right\rangle^2 . \qquad \text{Eq. (4.53)}$$

Therefore, the variance of ψ,

$$\sigma_\psi^2 = \left\langle \psi^2 \right\rangle - \left\langle \psi \right\rangle^2 = 0 . \qquad \text{Eq. (4.54)}$$

Thus, it has been shown that the conditions necessary to effect a homogenization are also sufficient to assure the predictability of ψ.

3. *Effective Transport Cross Sections*

Effective transport cross sections are obtained by comparing the averaged operators K_o and K_1 with the unaveraged operators H_o and H_1. Redefine

$$K_1 \_\_\_\_ = \int_0^\infty dE' \int_{4\pi} d\vec{w}' \; C_{\text{eff}}(\vec{w}' E' \rightarrow \vec{w} E, \vec{r}) \_\_\_\_\_ . \qquad \text{Eq. (4.55)}$$

On comparison with K_1, defined by Eq. (4.48), the effective transfer cross section

$$C_{\text{eff}}(\vec{w}E' \to \vec{w}E, \vec{r}) = \sum_{j=0}^{n} f_j(\vec{r}, E', -\ell'\vec{w}')V_j(\vec{r})C^j(\vec{w}'E' \to \vec{w}E', \vec{r})\, f_j(\vec{r}, E, +\vec{w}\ell). \qquad \text{Eq. (4.56)}$$

Similarly, redefine

$$K_o\_\_\_\_ = \int_0^{\infty} d\ell\, e^{-\int_0^{\ell} ds\, \Sigma_{\text{eff}}(\vec{r} - s\vec{w}, E)} \_\_\_\_ . \qquad \text{Eq. (4.57)}$$

This will reduce to the definition of K_o when

$$\Sigma_{\text{eff}}(\vec{r}, E) = \sum_{j=0}^{n} f_j(\vec{r}, E, -\ell\vec{w})V_j(\vec{r})\Sigma^j(\vec{r}, E). \qquad \text{Eq. (4.58)}$$

Definition by Eq. (4.58) follows when it is noted that

$$\frac{d}{d\ell}\left\langle t(\vec{r} \to \vec{r} - \ell\vec{w}, E)\right\rangle = \frac{d}{d\ell}\left\langle \exp - \int_0^{\ell} ds \sum_{j=0}^{n} F_j(\vec{r} - s\vec{w})\Sigma^j(\vec{r} - sw, E)\right\rangle$$

$$= -\sum_{j=0}^{n} \Sigma^j(\vec{r} - \ell\vec{w}, E)\left\langle F_j(\vec{r} - \ell\vec{w})\, t(\vec{r} \to \vec{r} - \ell\vec{w}, E)\right\rangle$$

$$= -\left\langle t(\vec{r} \to \vec{r} - \ell\vec{w}, E)\right\rangle \Sigma_{\text{eff}}(\vec{r} - \ell\vec{w}, E) \qquad \text{Eq. (4.59)}$$

and, therefore,

$$\Sigma_{\text{eff}}(\vec{r} - \ell\vec{w}, E) = -\frac{d}{d\ell}\left\langle t(\vec{r} \to \vec{r} - \ell\vec{w}, E)\right\rangle \Big/ \left\langle t(\vec{r} \to \vec{r} - \ell\vec{w}, E)\right\rangle$$

$$= \frac{-d}{d\ell} \ln \left\langle t(\vec{r} \to \vec{r} - \ell\vec{w}, E)\right\rangle . \qquad \text{Eq. (4.60)}$$

When Eq. (4.60) is inserted into Eq. (4.57), the latter reduces to the K_o defined by Eq. (4.48).

The new local or microscopic self-shielding factors have been defined by

$$f_j(\vec{r}, E', -\ell'\vec{w}') = \frac{\left\langle F_j(\vec{r})\, t(\vec{r} \to \vec{r} - \ell'\vec{w}', E') \right\rangle}{\left\langle t(\vec{r} \to \vec{r} - \ell'\vec{w}', E') \right\rangle V_j(\vec{r})}$$

$$= \frac{\left\langle t(\vec{r} \to \vec{r} - \ell'\vec{w}', E') \Big/ F_j(\vec{r}) = 1 \right\rangle}{\left\langle t(\vec{r} \to \vec{r} - \ell'\vec{w}', E') \right\rangle}$$

$$= \frac{\left\langle F_j(\vec{r})\, t(\vec{r} - \ell'\vec{w}' \to \vec{r}, E') \right\rangle}{\left\langle t(\vec{r} - \ell'\vec{w}' \to \vec{r}, E') \right\rangle} \qquad \text{Eq. (4.61)}$$

and

$$f_j(\vec{r}, E, +\ell\vec{w}) = \frac{\left\langle F_j(\vec{r})\, t(\vec{r} \to \vec{r} + \ell\vec{w}, E) \right\rangle}{\left\langle t(\vec{r} \to \vec{r} + \ell\vec{w}, E) \right\rangle V_j(\vec{r})} \qquad \text{Eq. (4.62)}$$

Noting Fig. 4.11, Eq. (4.61) is the self-shielding factor for neutrons coming from the last collision and Eq. (4.62) is the self-shielding factor for neutrons going to the next collision.

These are mean transmission ratios, not flux ratios; and unlike the factors previously defined by Eq. (4.37), they can be evaluated without knowledge of $\langle\psi\rangle$. To do so, however, requires a statistical description of the heterogeneous materials.

If these effective cross sections are evaluated outside of the heterogeneous elements, $F_o(\vec{r}) = 1$ and $F_j(\vec{r}) = 0$ for $j = 1, 2, \ldots n$. As a consequence, $f_j(\vec{r})\, V_j(r) = \delta_{oj}$, that is, vanishes unless $j = 0$; and

$$\Sigma_{\text{eff}}(\vec{r}, E) = \Sigma^o(\vec{r}, E)$$

$$C_{\text{eff}}(\vec{w}'E' \to \vec{w}E, \vec{r}) = C^o(\vec{w}'E' \to \vec{w}E, \vec{r}). \qquad \text{Eq. (4.63)}$$

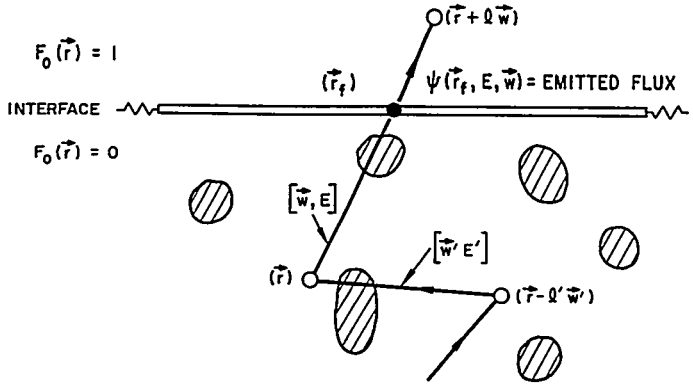

FIGURE 4.11. Interface Neutron Track.

Thus, the effective cross sections are identical to the actual cross sections outside of the random materials.

If $\vec{r}$ is in a heterogeneous element then $F_o(\vec{r}) = V_o(\vec{r}) = 0$, and only the spatially independent phase cross sections contribute to the effective cross sections. Although these effective cross sections provide a well defined (nonrandom) description of the heterogeneous materials, they may not define a homogenization. In general, $V_j(\vec{r})$ and $f_j(\vec{r})$ are spatially sensitive functions. If they are independent of $\vec{r}$, at least with respect to evaluating the emitted fluxes, the effective cross sections will be independent of $\vec{r}$ and will specify a homogenization.

The cause of the interface problem alluded to in the previous section is as follows. Consider the neutron track shown crossing the interface in Fig. 4.11. If one wishes to evaluate $f_j(\vec{r}, E, \ell\vec{w})$, and in the process notes that $t(\vec{r} \to \vec{r} + \ell\vec{w}, E) = t(\vec{r} \to \vec{r}_f, E)\, t(\vec{r}_f \to \vec{r} + \ell\vec{w}, E)$ and that $t(\vec{r}_f \to \vec{r}+\ell\vec{w}, E)$ is not a random variable, then

$$f_j(\vec{r}, E, \ell\vec{w}) = \frac{\left\langle t(\vec{r} \to \vec{r} + \ell\vec{w}, E)\, F_j(\vec{r}) \right\rangle}{\left\langle t(\vec{r} \to \vec{r} + \ell\vec{w}, E) \right\rangle}$$

$$= \frac{t(\vec{r}_f \to \vec{r} + \ell\vec{w}, E) \left\langle t(\vec{r} \to \vec{r}_f, E)\, F_j(\vec{r}) \right\rangle}{t(\vec{r}_f \to \vec{r} + \ell\vec{w}, E) \left\langle t(\vec{r} \to \vec{r}_f, E) \right\rangle}$$

$$= f_j(\vec{r}, E, \vec{r}_f - \vec{r}). \qquad \text{Eq. (4.64)}$$

The assumption that ℓ is large compared to the correlation scales in no way guarantees that $|\vec{r}_f - \vec{r}|$ will be. If $\vec{r}$ is close to the surface, $t(\vec{r} \to \vec{r}_f, E) \simeq 1$ and, therefore, $f_j \simeq 1$. As $|\vec{r} - \vec{r}_f|$ increases to several correlation lengths, f_j approaches an asymptotic value. For the case illustrated, this result simply states that the first layers of particles are not totally shielded. If the gross dimensions of the heterogeneous elements are large compared to the correlation scales this surface effect will be negligible, except in evaluating collision densities close to an interface. If they are not, the f_j will be spatially and orientation-dependent. In practice, some weighted average might be employed as a further approximation.

Equation (4.64) states that the f_j can be evaluated by computing the required transmissions only through the heterogeneous elements themselves. This considerably simplifies the problem of evaluating effective cross sections, since they only depend on the materials themselves and not on the surrounding environment.

The arguments leading to definitions in Eqs. (4.56) and (4.58) are in fact a justification for transmission (rather than flux) defined effective cross sections. Many writers have used the definition $\langle t(\vec{r} \to \vec{r} + \ell\vec{w}, E)\rangle = \exp -\ell\Sigma_{\text{eff}}$ to obtain the total effective cross section. As can be seen from Eq. (4.60) this is basically the same as Eq. (4.58); e.g., see the definition in Sect. 4.3.B. What is not often appreciated is the necessary change in the form of C_{eff}. On comparing definitions in Eqs. (4.36) and (4.56), it is seen that the transmission defined C_{eff} shields both the incident and emitted neutron in a collision, while the flux defined C_{eff} shields only the incident neutron. This difference is often of little consequence, but there are many cases where it could be significant.

Consider an infinite mixture of fuel particles in a non-absorbing matrix. Using the index U for the fuel and M for the matrix,

$$\Sigma_{\text{eff}}(E) = f_M(E)V_M\Sigma^M(E) + f_U(E)V_U\Sigma^U(E)$$

$$C_{\text{eff}}(\vec{w}'E' \to \vec{w}E) = f_U(E)\frac{f(E)}{4\pi}f_U(E')V_U\Sigma_f^U(E')$$

$$+ f_M(E)\Sigma_s^M(\vec{w}'E' \to \vec{w}E)V_M f_M(E') + f_U(E)\Sigma_s^U(\vec{w}'E' \to \vec{w}E)V_U f_U(E') \ .$$

Eq. (4.65)

The effect of this modification on the emitted fission spectrum is always negligible, since $f_U(E) \simeq 1$ at fission source energies. It is also worth noting that $\Sigma^U_{f_{\text{eff}}} / \Sigma^U_{\text{eff}} = \Sigma^U_f / \Sigma^U$; that is, the shielding does not alter the fission to absorption ratio in the fuel phase. If E is in a resonance or the thermal group, $f_U(E)$ will usually be significantly less than unity. In that event, the fuel phase contribution to slowing down will be suppressed. This situation occurs because neutrons slowing down in the fuel phase have a poorer chance to escape absorption than those slowing down in the matrix. If the slowing-down properties of the fuel and matrix differ appreciably, this could be a significant correction, particularly in resonance escape calculations.

It will be useful at this point to summarize the principal results obtained. The effective cross sections defined by Eqs. (4.56) and (4.58) define a homogenization: (1) if the mean free paths for scattering (on the order of centimeters) are significantly larger than the local correlation scales (in the illustrated examples on the order of particle diameters); (2) if, when fuel phases are present, the probability of the fuel phases scattering neutrons into a fuel resonance or the thermal group is relatively small (i.e., such scattering is principally accomplished by other materials); (3) if the heterogeneous elements are large compared to their correlation scales (e.g., an element is large compared to the particles it contains); (4) if the microstructure processes $\langle F_j(\vec{r}) \rangle$ are essentially stationary (statistically homogeneous). Conditions 1 and 2 are also sufficient for $\sigma^2_\psi \simeq 0$ for, at least, the emitted surface fluxes. As a result, these fluxes and their consequences can, in principle, be predicted accurately with the effective cross sections defined above. Subject to the above assumptions, all these results are independent of the class of materials considered.

Effective homogeneous cross sections can be specified to preserve a single nuclear characteristic (e.g., reactivity) even when conditions 1 to 4 are not satisfied. In general, they will differ from those specified by Eqs. (4.56) and (4.58) and will depend on the particular problem and the characteristic to be preserved. They could probably be estimated with a modification of existing variational techniques (e.g., Ref. 11). However, an analysis of the associated prediction errors would require a considerably more detailed statistical analysis than attempted here.

4. *Microstructure Model*

A description of a material's microstructure is required for the evaluation of its effective cross sections. Such a description, however, need only be sufficiently detailed to permit the evaluation of $\langle F_j(\vec{r}_1) \rangle$, $\langle \iota(\vec{r}_1 \to \vec{r}_2, E) \rangle$, and $\langle F_j(\vec{r}_1)\, \iota(\vec{r}_1 \to \vec{r}_2, E) \rangle$ for arbitrary $\vec{r}_1$ and $\vec{r}_2$ (see Fig. 4.9).

If the material satisfies the four conditions discussed above, much less is required. Condition 4 demands that the process be essentially stationary and, thus, that $\langle F_j(\vec{r}_1) \rangle = V_j$ be constant and the transmission averages be functions of $(\vec{r}_1 - \vec{r}_2)$ only. Condition 1 implies further that evaluation is only necessary for $|\vec{r}_1 - \vec{r}_2|$ significantly larger than the correlation scales (which because of the stationarity will also be independent of $\vec{r}$). For this condition, the f_j are asymptotic and also independent of $|\vec{r}_1 - \vec{r}_2|$. Condition 3 permits surface effects in the f_j to be neglected. The f_j may still depend on $\vec{w}_1$, the orientation of $(\vec{r}_1 - \vec{r}_2)$, unless the material is, in addition, isotropic. For the admissible materials, therefore, it is sufficient for a description to specify the V and permit the evaluation of $\langle F_j(\vec{r}_1)\, \iota(\vec{r}_1 \to \vec{r}_2, E) \rangle$ and $\langle \iota(\vec{r}_1 \to \vec{r}_2, E) \rangle$ for large $|\vec{r}_1 - \vec{r}_2|$.

A microstructure can be described by specifying a statistical process (model) to generate the process ensemble described in the introduction. For the most general microstructures, this is a formidable task and poses many unresolved problems. Nevertheless, it is generally possible to define mathematical models that produce reasonable results.* Such a model should be flexible enough to provide parameters to reflect the principal features of the random structure to be described. However, the amount of data required to estimate such parameters increases very rapidly with their number.

Rather than attempt to describe what a statistical model is, an example will be developed and its consequences evaluated. A statistical process will be specified to describe three phase mixtures, such as illustrated by Fig. 4.9. This particular choice has nothing to recommend it over other possible examples, except that it is a generalization of models that have agreed with observations and that it is not described in any of the available references. Before turning to the model itself, some of the more obvious features of the structure are discussed.

---

*See, for example, Refs. 12, 13, 14, 15, and Sect. 4.2.B.

The most prominent characteristics of a structure are the $V_j(\vec{r})$, the local volume fractions, which display any geometric bias in the phase loadings. Wall effects, the tendency of particular phases to be attracted or repelled by material boundaries, are typical of such bias. If the $V_j(\vec{r})$ are independent of $\vec{r}$ the process is said to be stationary and the material uniform to the first order. In this event, V_j is also the average j^{th} phase volume fraction and a measure of the total phase j loading.

Particle properties obviously exercise considerable influence over the material behavior. As might be inferred from Fig. 4.9, the distributions of individual particle intercepts (chords) are the most significant of these properties in transport phenomena. The requisite statistical description is related to $p_j(\Delta_j/\vec{r}_1, \vec{r}_2)$, the conditional probability density of noninterrupted j^{th} phase runs (e.g., particle intercepts) on a path, given its endpoints $\vec{r}_1$ and $\vec{r}_2$. The mean Δ_j, $\mu_j(\vec{r}_1, \vec{r}_2)$ and variance $\sigma^2_{\Delta_j}(\vec{r}_1, \vec{r}_2)$ of this distribution, in general, depend on $\vec{r}_1$, $\vec{w}_1$, and $\ell_1 = |\vec{r}_1 - \vec{r}_2|$. If a process is stationary and isotropic, the $\vec{r}_1$ and $\vec{w}_1$ sensitivity vanish; but not the ℓ_1 dependence.

This ℓ_1 dependence is the effect of partial intercepts at the endpoints of the paths (see Fig. 4.9). As ℓ_1 becomes small only partial intercepts contribute to the distribution. In the limit, as ℓ_1 goes to $d\ell_1$, $d\ell_1$ becomes the only probable intercept. In the other limit, as ℓ_1 becomes large compared to particle dimensions, the contributions of partial intercepts become negligible and the distribution loses its ℓ_1 sensitivity. This is the only case of interest, since ℓ_1 has been assumed to be large. If the material is stationary and isotropic,

$$p_j(\Delta_j/\ell_{1\max}) \equiv p_j(\Delta_j) \qquad \text{Eq. (4.66)}$$

is identical to the chord distribution obtained by randomly passing lines through all possible particles of the j^{th} phase. (For a detailed discussion of this relationship, see Ref. 15, Appendix I.)

This chord distribution has been obtained, and its mean and variance computed for a number of particle geometries, given that all particles are the same size (see Ref. 3, pp. 21-40). These results are summarized in Table 4.3. If the particles are geometrically similar, but are distributed in size over some characteristic dimension D (e.g., sphere diameter) with a mean value $\bar{D}$ and a relatively small variance σ_D^2, then (Ref. 15, Appendix I)

$$\mu \cong \mu(\bar{D})\,(1 + 2\,\sigma_D^2/\bar{D}^2)$$

$$X = (1+\sigma^2_\Delta/\mu^2) \cong \left[1 + \sigma^2_\Delta(\bar{D})/\mu^2(\bar{D})\right]\left(1 + \sigma_D^2/\bar{D}^2\right). \qquad \text{Eq. (4.67)}$$

TABLE 4.3 — CHORD DISTRIBUTION FOR PARTICLE GEOMETRIES

Particle	μ	$(1 + \sigma_\Delta^2/\mu^2)$
General	$\frac{4(\text{phase volume})}{(\text{phase surface})}$	--
Spheres, diam = D	(2/3) D	9/8
Hemisphere, diam = D	(4/9) D	1.2656
Infinite cylinder, diam = D (circular)	D	4/3
Infinite cylinder, side = S (square)	S	1.4870
Infinite cylinder, side = S (equilateral triangle)	$S/\sqrt{3}$	1.6840
Infinite cylinder, side = S (regular hexagon)	$S/\sqrt{3}$	1.3970
Tetrahedron, side = S	0.27216 S	1.5830
Oblate spheroid 2a = major axis, 2b = minor axis	(8/3)(b/B)	0.5625 (B/E) $\tanh^{-1}$ E
$E = \left[1 - \left(\frac{b}{a}\right)^2\right]^{1/2}$		
$B = \left[1 + \frac{(1 - E^2)}{E} \tanh^{-1} E\right]$		

The quantities $\mu(\bar{D})$ and $\sigma_\Delta^2(\bar{D})$ are the intercept mean and variance for particles for which $D = \bar{D}$. Thus, the μ_j are measures of particle size, and the $X_j = (1 + \sigma_\Delta^2/\mu^2)_j$ are measures of shape and size distribution. It can also be shown the μ_j is four times the volume-to-surface ratio of the j^{th} phase if the particles are distributed without a preferred orientation (Ref. 15, Appendix I).

An $\vec{r}$ or $\vec{w}$ sensitivity, or both, can result from any number of causes. The preferential orientation of nonsymmetric particles causes $\vec{w}$ dependence. If, to take an explicit case, the long axis of j^{th} phase particles tends to orient itself parallel to some direction $\vec{w}_o$, μ_j would be expected to exhibit an angular dependence and have a maximum at $\vec{w}_o$. An $\vec{r}$ sensitivity would result, for example, from any tendency for small particles to be attracted to, or repelled by, material boundaries.

Similar comments apply when j is that of the matrix (continuous) phase. In that case, $p_j(\Delta_j)$ is the distribution of free paths between particles, and μ_j is the mean free path between particles. The variance $\sigma^2_{\Delta_j}$, or X_j, is a measure of so-called particle packing. If particles tend to agglomerate they will leave gaps of matrix material, and $\sigma^2_{\Delta_j}$ will be relatively large. In the following model, however, packing will be measured by another, but related, parameter α.

In addition to the above noted features there often appear inhomogeneities on a scale much larger than particle dimensions. They are usually present to some degree even in stationary processes and are a peculiarity of each manufacturing technique. Depending on their magnitude and scale, compared to neutron mean free paths, they may only weakly affect the f_j. It will be assumed that this is the case and, furthermore, that the process is stationary and isotropic, at least to the extent that all the relevant averages are independent of $\vec{r}$ and $\vec{w}$. Although these assumptions are not essential, they are reasonable in many cases and considerably reduce the mechanics of evaluating the f_j.* The transmissions are independent of $\vec{r}$ and $\vec{w}$ and need only be computed as a function of ℓ and E. As a consequence, the f_j are not explicitly functions of $\vec{r}$ and $\vec{w}$, although they may still be functions of ℓ.

The model, which is by no means unique, is defined to describe a stationary isotropic two-particle phase material. The phases are indexed such that 3 is the matrix phase and $\mu_1 \geq \mu_2$. It is presumed that the ensemble is constructed such that the particle intercepts are distributed on ℓ, as follows. Let ℓ be partitioned into N_1 cells of length $S_1 = \ell/N_1$. Let each of these cells be independently assigned an intercept Δ_1, randomly chosen from the collection $p_1(\Delta_1)$, with probability P_1, or no intercept with probability $(1 - P_1)$. The remaining empty cells are now partitioned into N_2 cells of length S_2. In a similar manner, let these cells be assigned phase 2 intercepts, from the distribution $p_2(\Delta_2)$, with probability P_2.

*The effect of large scale inhomogeneities, and anisotropies, on neutron transmission is considered in Ref. 15.

It is further assumed that the Δ_j are placed in the S_j cells such that all admissible locations are equally probable. More precisely, let λ_j be the distance of Δ_j from the leading edge (neutron incidence side) of the cell. Let every $0 < \lambda_j \leq (S_j - \mu_j)$ be equally likely, that is, let

$$p_j(\lambda_j)\, d\lambda_j = \frac{d\lambda_j}{(S_j - \mu_j)}; \qquad 0 \leq \lambda \leq (S_j - \mu_j) \qquad \text{Eq. (4.68)}$$

0 otherwise.

(See Fig. 4.12.) Note that this assumption permits some physically unreal overlap of the Δ_j, since a Δ_j may exceed μ_j, permitting it to overlap into an adjacent cell and possibly onto another segment. This effect, however, is very small as a rule. Thus, a model is sufficiently defined to obtain the required means.

The joint distribution of the linear intercepts L_j, which are required to compute $\langle \iota \rangle$, is obtained as follows.* Let K_j be the number of j^{th} phase particle intercepts occurring on ℓ. The joint probability of K_1 and K_2 may be written

$$P\left\{K_1, K_2\right\} = P\left\{K_1\right\}\ P\ \left\{K_2/K_1\right\} \qquad \text{Eq. (4.69)}$$

where $P\{K_2/K_1\}$ is the conditional probability of K_2 given K_1. These are binomial distributions. $P_1\{K_1\}$ is the probability that K_1 out of $N_1 = (\ell/S_1)$ cells contain phase 1 intercepts. Since each of these cells are independently assigned an intercept with probability P_1,

$$P\left\{K_1\right\} = \binom{N_1}{K_1} P_1^{K_1} (1 - P_1)^{N_1 - K_1}. \qquad \text{Eq. (4.70)}$$

---

*The j^{th} phase linear intercept $L_j(\vec{r}_1 - \vec{r}_2)$ is defined to be the length of that part of $\vec{\ell} = (\vec{r}_1 - \vec{r}_2)$ that passes through the j^{th} phase. Noting Fig. 4.9,

$$L_j(\vec{r}_1 - \vec{r}_2) = \int_o^{\ell} ds\, F_j(\vec{r}_2 - s\vec{w}) = \sum_i \Delta_j^i$$

where the Δ_j^i are the individual j^{th} phase particle (or matrix segment intercepts). Notice also that

$$\iota(\vec{r}_1 - \vec{r}_2, E_1) = \exp\left[-\sum_{j=1}^{n} \Sigma^j(E_1) \int_o^{\ell} ds\, F_j(\vec{r}_2 - s\vec{w}_1)\right]$$

$$= \exp\left[-\sum_{j=1}^{n} \Sigma^j(E_1)\, L_j\right]$$

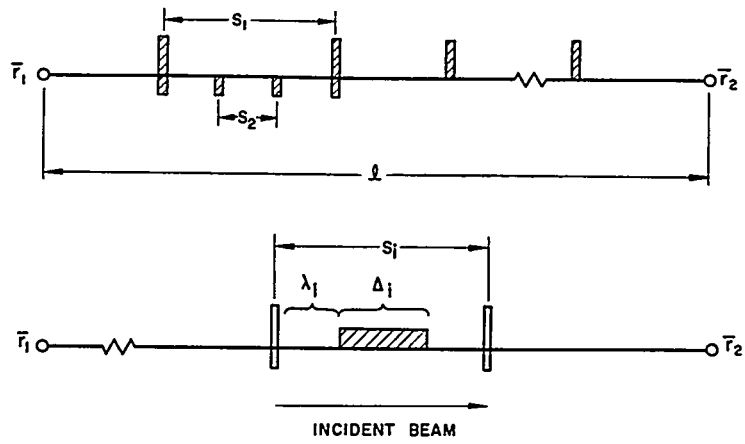

FIGURE 4.12. Cell Decomposition of a Neutron Path.

Similarly, $P\{K_2/K_1\}$ is the probability that K_2 out of $N_2 = (N_1 - K_1)S_1/S_2$ cells contains phase 2 intercepts. Since these are also assigned independently with probability P_2,

$$P\left\{K_2/K_1\right\} = \binom{N_2}{K_2} P_2^{K_2} \left(1 - P_2\right)^{N_2 - K_2} . \qquad \text{Eq. (4.71)}$$

Because L_j has been presumed to be simply the sum of K_j independent variables, that is, the Δ_j, its conditional distribution, given K_j, is

$$p(L_j/K_j) = p_j^{*K_j}(L_j) = \int d\,\Delta^1 \ldots \int d\,\Delta^{K-1}\, p_j(L_j - \Delta^1 \ldots - \Delta^{K-1})$$

$$p_j(\Delta^1) \ldots p_j(\Delta^{K-1}) \qquad \text{Eq. (4.72)}$$

which is called the k^{th} order convolution of $p_j(\Delta_j)$. Thus, since the joint probability density of L_1, L_2, K_1, and K_2,

$$p(L_1, L_2, K_1, K_2) = P\left\{K_1, K_2\right\}\, p(L_1/K_1)\, p(L_2/K_2) \qquad \text{Eq. (4.73)}$$

$$p(L_1, L_2) = \sum_{K_1=0}^{N_1} \sum_{K_2=0}^{N_2} p(L_1, L_2, K_1, K_2)$$

$$= \sum_{K_1=0}^{N_1} \binom{N_1}{K_1} P_1^{K_1} (1 - P_1)^{N_1 - K_1} {}^{*K_1}p_1(L_1)$$

$$\times \sum_{K_2=0}^{N_2} \binom{N_2}{K_2} P_2^{K_2} (1 - P_2)^{N_2 - K_2} {}^{*K_2}p_2(L_2). \qquad \text{Eq. (4.74)}$$

Note that L_1 is independent of L_2, but L_2 is not independent of L_1, that is, $p(L_1) = \int_o^\ell d L_1\, p(L_1, L_2)$ is not a function of L_2, but $p(L_2) = \int_o^\ell d L_2\, p(L_1, L_2)$ is a function of L_1. This is a consequence of the phase 1 particles being placed in the cells first and the phase 2 cells being placed in the remaining cells. The available N_2 cells depend on K_1, the number of phase 1 particles occupying cells.

Further, note that L_1 and L_2 determine L_3, since $L_1 + L_2 + L_3 = \ell$ and, finally,

$$p(L_1, L_2, L_3) = p(L_1, L_2)\ \delta[L_1 + L_2 + L_3 - \ell] \qquad \text{Eq. (4.75)}$$

where δ is the Dirac delta.

Averaging over Eq. (4.74), the mean phase intercepts are

$$\langle L_1 \rangle = \mu_1 P_1 N_1$$

$$\langle L_2 \rangle = \mu_2 P_2 (1 - P_1) N_1 S_1/S_2. \qquad \text{Eq. (4.76)}$$

Observing that $\langle L_j \rangle = \ell V_j$, that is, the mean j^{th} phase linear intercept is the length of the line times the j^{th} phase volume fraction,*

$$V_1 = P_1 \alpha_1$$

$$V_2 = P_2 \alpha_2 (1 - V_1/\alpha_1) \qquad \text{Eq. (4.77)}$$

where $\alpha_j = (\mu_j/S_j)$. Thus, the volume fractions and P_j are related.

*This is only true for a stationary isotropic process; otherwise, V_j would be an average of $V_j(\bar{r})$ on the line and, in general, a function of $(\bar{r}_1 - \bar{r}_2)$.

The α_j are defined to be effective linear packing factors* and are a measure of tendency of particles to agglomerate, that is, to pack; the greater α_j the greater this tendency. In some cases, $\mu_j/\Delta_{j\,max}$ is a good estimate for α_j. In a model for a two-phase system in which all Δ configurations are assumed equally probable [13,16] instead of distributed in cells, it can be shown that an $\alpha \cong [(2-V)X]^{-1}$ is implicit. Observations of two-phase systems, however, indicate that α will typically fall between 0.6 and 0.8 and that 0.65 is a reasonable estimate in most cases. Note also that the α_j and $p_j(\lambda_j)$ determine the distribution $p_3(\Delta_3)$ in this model. This is the distribution of free paths (in the matrix) between particles. The joint distribution density of the L_j's, Eq. (4.75), is sufficient to compute $\langle t(\vec{r}_1 \rightarrow \vec{r}_2 E)\rangle$, which will be done in the next section. With the additional information provided by the $p_j(\lambda_j)$, the $\langle F_j(\vec{r}_1)\, t(\vec{r}_1 \rightarrow \vec{r}_2, E)\rangle$ can be computed. This will be done in Sect. 4.2.C.6.

Note also that $\left\{ \langle F_j(\vec{r}_1) F_k(\vec{r}_2)\rangle - \langle F_j(\vec{r}_1)\rangle \langle F_k(\vec{r}_2)\rangle \right\} = 0$ if $|\vec{r}_1 - \vec{r}_2| > S_1$. As a consequence, the correlation scales for this model are all less than $S_1 = \mu_1/\alpha_1$. If this quantity is small compared to scattering mean free paths (centimeters) and the gross dimensions of the heterogeneous elements, then conditions 1 and 3 of the previous section are satisfied. Since stationarity has been assumed, condition 4 is also satisfied.

5. *Mean Transmission*

The mean transmission $\langle t(\vec{r}_1 \rightarrow \vec{r}_2, E)\rangle$ is obtained by averaging over Eq. (4.75). Thus,

$$t(\vec{r}_1 \rightarrow \vec{r}_2, E) = \left\langle \exp - \left[\sum_{j=1}^{3} \Sigma^j(E) L_j \right] \right\rangle$$

$$= e^{-\ell \Sigma^3(E)} \left\langle \exp - [L_1 \delta\Sigma^1(E) + L_2\, \delta\Sigma^2(E)] \right\rangle$$

$$= \left\{ (1-P_1)\,[1 - P_2\,(1-E_2')]^r + P_1 E_1' \right\}^{N_1} e^{-\ell\Sigma^3}$$

Eq. (4.78)

*These factors are discussed in considerable detail in Ref. 12 and Ref. 15, Appendix I.

where $\delta\Sigma^j = \Sigma^j - \Sigma^3$, $r = (S_1/S_2) = (\alpha_2\,\mu_1/\alpha_1\,\mu_2)$, $N_1 = (\ell\alpha_1/\mu_1)$, and P_1 and P_2 are defined by Eq. (4.77).

The average particle transmission $E\,(E)$, and P_o are defined by

$$E_j(E) = \int d\Delta_j p_j(\Delta_j)\, e^{-\Sigma^j(E)\Delta_j} = \left[1 - \mu_j\,\Sigma^j(E)\,P_{o_j}\right]. \qquad \text{Eq. (4.79)}$$

$E_j'(E)$ is just the same integral with Σ^j replaced by $\delta\Sigma^j$. If all the j^{th} phase particles are similar, that is, have the same shape, and are only distributed over some characteristic dimension D, then

$$E_j = \int dD\, p_j(D) \int d\Delta\; p_j(\Delta/D) = \int d\Delta\, p_j(D) E_j(D)\,. \qquad \text{Eq. (4.80)}$$

The quantity E_j is, therefore, the mean transmission for a single particle of size D averaged over the size distribution $P_j(D)$. Note that $P_{o_j}(D)$, that is P_{o_j} evaluated for a single particle size, is the uniform source escape probability for the particle, the so-called Placzek self-shielding factor. The collision probability $P_c = 1 - P_o$ is tabulated for several geometries in Ref. 3, pp. 24-42.

For relatively simple geometries and size distributions $P_j(D)$, the integration in Eq. (4.80) may be carried out. The resulting expressions, however, are seldom convenient. Furthermore, due to fabrication tolerances, particles are usually distributed in both shape and size and the details of these distributions poorly defined. Fortunately, the E_j are relatively insensitive to the higher moments of the $p_j(D)$ distributions and depend primarily on the μ_j and $\sigma^2_{\Delta_j}$. The following simple approximation for E_j has been found to give good agreement with tabulated values for single particles and would be expected to give even better agreement over most observed size and shape distributions:

$$E_j(E) \approx \left[1 + \mu_j\Sigma(\sigma_{\Delta_j}/\mu_j)^2\right]^{-\left[\mu_j/\sigma_{\Delta_j}\right]^2} \qquad \text{Eq. (4.81)}$$

The approximation is derived in Ref. 15, Appendix II.

The expression for $<\iota>$, given by Eq. (4.78), can be interpreted with the following argument. Since the N_1 cells of ℓ are

assumed independent, the mean transmission through all of them is the product of the mean transmissions through each of them, i.e., $\langle t(\vec{r}_1 \rightarrow \vec{r}_2, E) \rangle = t_1^{N_1}$. Here t_1 is the mean transmission across the width S_1 of a single cell. Thus, from Eq. (4.78),

$$t_1 = \left\{ (1 - P_1) \left[1 - P_2 (1 - E_2') \right]^r + P E_1' \right\} e^{-\Sigma^3 S_1} . \qquad \text{Eq. (4.82)}$$

If a particular S_1 cell has a Δ_1 intercept, its transmission is

$$\left\langle e^{-\delta\Sigma^1 \Delta_1} e^{-\Sigma^3 S_1} \right\rangle = e^{-\Sigma^3 S_1} E_1' \qquad \text{Eq. (4.83)}$$

which occurs with probability P_1. Multiplying Eq. (4.83) by P_1, the right-hand term of t_1 is obtained. If there is no Δ_1 intercept, an event which occurs with probability $(1 - P_1)$, then S_1 is partitioned into r subcells of length S_2. As these are also independent, the conditional mean transmission through the S_1 cell, given there is no Δ_1 intercept, must be t_2^r, where t_2 is the conditional mean transmission through an S_2 cell, given no Δ_1 intercept. Comparing with Eq. (4.78) again

$$t_2 = \left[1 - P_2 (1 - E_2') \right] e^{-\Sigma^3 S_2} . \qquad \text{Eq. (4.84)}$$

Equation (4.84) follows because an S_2 cell contains a Δ_2 intercept (and, thus, has a mean transmission $E_2' e^{-\Sigma^3 S_2}$) with probability P_2, and contains no Δ_2 intercept (and, thus, has a mean transmission $e^{-\Sigma^3 S_2}$) with probability $(1 - P_2)$. The sum of the products of these transmissions and their probabilities results in Eq. (4.84).

6. *Phase Collision Fractions*

In the general case, if there were several phases made up of distinct neutron absorbing materials, it would be necessary in depletion calculations to account for the different depletion rates of each of the neutron absorbing materials. Thus, it would be necessary to calculate the relative absorption in each phase rather than the total absorption due to all phases collectively.

In this particular model, it is convenient to compute the $\langle F_j(\vec{r}_1)\, t(\vec{r}_1 \to \vec{r}_2)\rangle$ indirectly from Phase Collision Fractions C_j. These are defined by

$$C_j(\vec{r}_1 \to \vec{r}_2, E) = \left\langle \int_o^{\ell} ds\, \Sigma^j(E)\, F_j(\vec{r}_1 + s\vec{w})\, t(\vec{r}_1 \to \vec{r}_1 + s\vec{w}, E) \right\rangle$$

$$= C_j(\vec{r}_1 \to \vec{r}_1 + \ell\vec{w}, E) = \Sigma^j(E) \int_o^{\ell} ds \left\langle F_j(\vec{r}_1 + s\vec{w})\, t(\vec{r}_1 \to \vec{r}_1 + s\vec{w}, E) \right\rangle$$

and also

$$= C_j(\vec{r}_2 \to \vec{r}_1, E) = \Sigma^j(E) \int_o^{\ell'} ds \left\langle F_j(\vec{r}_2 - s\vec{w})\, t(\vec{r}_2 \to \vec{r}_2 - s\vec{w}) \right\rangle$$

$$= C_j(\vec{r}_2 \to \vec{r}_2 - \ell'\vec{w}, E) \qquad \text{Eq. (4.85)}$$

and are the probabilities that a neutron traveling at energy E will suffer a collision in the j^{th} phase traveling between $\vec{r}_1$ and $\vec{r}_2$ (in either direction). Thus, they are the fraction of a beam of neutrons that will suffer j phase collisions between $\vec{r}_1$ and $\vec{r}_2$. Taking the derivatives of C_j with respect to $\vec{r}_2$ in the $+\vec{w}$ direction and with respect to $\vec{r}_1$ in the $-\vec{w}$ direction

$$+ \vec{w} \cdot \nabla_{\vec{r}_2} C_j = \frac{\partial C_j}{\partial \ell} = \Sigma^j(E) \left\langle F_j(\vec{r}_1 + \ell\vec{w})\, t(\vec{r}_1 \to \vec{r}_1 + \ell\vec{w}, E) \right\rangle$$

$$= \Sigma^j(E) \left\langle F_j(\vec{r}_2)\, t(\vec{r}_1 \to \vec{r}_2, E) \right\rangle \qquad \text{Eq. (4.86)}$$

and

$$- \vec{w} \cdot \nabla_{\vec{r}_1} C_j = \frac{\partial C_j}{\partial \ell'} = \Sigma^j(E) \left\langle F_j(\vec{r}_1)\, t(\vec{r}_1 \to \vec{r}_2, E) \right\rangle .$$

Since the material has been assumed stationary and isotropic, these derivatives are equal. Thus, given C_j, either equation may be used to evaluate the $\langle F_j t \rangle$. The C_j are computed as follows.

An S_2 cell is said not to contain a Δ_1 intercept only if the S_1 interval of which it is a subinterval contains no Δ_1 intercept. With this understanding, consider a single S_2 cell which contains no Δ_1 intercept, an event with probability $(1 - P_1)$. It then contains no Δ_2 intercept with probability $(1 - P_2)$, or does with

probability P_2. In the latter case, the only one in which there are phase 2 collisions, the average fraction of neutrons incident on the S_2 cell which collides in phase 2 is

$$\left\langle e^{-\lambda_2 \Sigma^3} \left[1 - e^{-\Sigma^2 \Delta_2}\right] \right\rangle$$

$$= \frac{\left[1 - E_2\right]}{\left[S_2 - \mu_2\right]} \int_0^{(S_2 - \mu_2)} d\lambda_2 \, e^{-\lambda_2 \Sigma^3} \qquad \text{Eq. (4.87)}$$

$$= \frac{\left[1 - E_2\right]\left[1 - e^{-\Sigma^3 \mu_2 (1/\alpha_2 - 1)}\right]}{(\Sigma^3 \mu_2)(1/\alpha_2 - 1)}$$

This result follows from averaging over the random variables λ_2 and Δ_2 (note Eq. (4.68) and Fig. 4.12). Since the probability of an S_2 cell containing a Δ_2 intercept (hence, no Δ_1) is $(1 - P_1)P_2$, the average phase 2 collision fraction across an S_2 cell is equal to

$$C_2(S_2) = \frac{(1 - P_1) P_2 \left[1 - E_2\right]\left[1 - e^{-\Sigma^3 \mu_2 (1/\alpha_2 - 1)}\right]}{(\Sigma^3 \mu_2)(1/\alpha_2 - 1)} \qquad \text{Eq. (4.88)}$$

In an S_1 cell containing no Δ_1 intercept (probability $[1 - P_1]$), there are r mutually independent S_2 cells each with a mean transmission t_2. The t_2 given by Eq. (4.84) applies, since it is given there is no Δ_1 intercept. The mean transmission of k such independent cells is t_2^k and, thus, the mean collision fraction (in all phases) is $(1 - t_2^k)$. Note that $[1 - t_2^k]$ is this conditional mean given no Δ_1 intercept and is not the unconditional mean. The phase 2 mean collision fraction of a sequence of r S_2 cells, given no Δ_1 intercept, is obtained by noting that on the average t_2^{k-1} (from an initially unit beam) is incident on the k^{th} cell. Of this fraction $C_2(S_2)/(1 - P_1)$ suffers phase 2 collision in that cell. The $(1 - P_1)$ is divided out of $C_2(S_2)$, since it is given that there is no Δ_1 intercept. Summing over the independent cells,

$$\sum_{k=1}^{r} \frac{C_2(S_2)}{\left[1 - P_1\right]} t_2^{k-1} = \frac{C_2(S_2)}{\left[1 - P_1\right]} \frac{\left[1 - t_2^r\right]}{\left[1 - t_2\right]} \qquad \text{Eq. (4.89)}$$

the total phase 2 collision fraction is obtained. Observing that no phase 2 collisions can occur if the S_1 cell, containing the rS_2 cells, contains a Δ_1 intercept, the above result is multiplied by the probability for no Δ_1, that is $(1 - P_1)$, to give the unconditional average phase 2 collision fraction in any S_1 cell

$$C_2(S_1) = \frac{\left[1 - t_2^I\right]}{\left[1 - t_2\right]} C_2(S_2). \qquad \text{Eq. (4.90)}$$

This states that the ratio of phase 2 to total collisions is the same for one S_2 cell or a sequence of them. This is a consequence of assuming that the S_2 cells are independent of one another.

Since the N_1 cells of length S_1 that make up ℓ are also mutually independent, it is more generally true that

$$C_j(\vec{r}_1 \rightarrow \vec{r}_2, E) = \sum_{k=1}^{N_1} C_j(S_1)\, t_1^{k-1} = \frac{\left[1 - t_1^{N_1}\right]}{\left[1 - t_1\right]} C_j(S_1)$$

$$= \frac{\left[1 - \left\langle t(\vec{r}_1 \rightarrow \vec{r}_2, E)\right\rangle\right]}{\left[1 - t_1\right]} C_j(S_1) \qquad \text{Eq. (4.91)}$$

where t_1 is the mean transmission across a single S_1 cell and is given by Eq. (4.82). This expression states that the ratio of j^{th} phase to total collisions across the N_1 independent S_1 cells of ℓ is identical to the ratio across a single S_1 cell.

As for Eq. (4.88), the phase 1 collision fraction in an S_1 cell is found to be

$$C_1(S_1) = \frac{P_1 \left[1 - E_1\right] \left[1 - e^{-\Sigma^3 \mu_1 (1/\alpha_1 - 1)}\right]}{(\Sigma^3 \mu_1)(1/\alpha_1 - 1)} \qquad \text{Eq. (4.92)}$$

Note that $C_2(S_2)$ depends on both P_1 and P_2, while $C_1(S_1)$ depends only on P_1. This occurs because the Δ_1 intercepts are placed first independently of the Δ_2 intercepts, and then the Δ_2 intercepts depend on how many Δ_1 intercepts occupy cells.

Inserting Eqs. (4.88), (4.90), and (4.92) in Eq. (4.91),

$$C_1(\vec{r}_1\rightarrow\vec{r}_2,E)=\frac{\left[1-\langle t\rangle\right]}{\left[1-t_1\right]}C_1(S_1)=\frac{\left[1-\langle t\rangle\right]}{\left[1-t_1\right]}\frac{P_1(1-E_1)\left[1-e^{-\Sigma^3\mu_1(1/\alpha_1-1)}\right]}{(\Sigma^3\mu_1)(1/\alpha_1-1)}$$

$$C_2(\vec{r}_1\rightarrow\vec{r}_2,E)=\frac{\left[1-\langle t\rangle\right]}{\left[1-t_1\right]}\;C_2(S_1)=\frac{\left[1-\langle t\rangle\right]}{\left[1-t_1\right]}\;\frac{\left[1-t_2^r\right]}{\left[1-t_2\right]}C_2(S_2)$$

$$=\frac{\left[1-\langle t\rangle\right]}{\left[1-t_1\right]}\;\frac{\left[1-t_2^r\right]}{\left[1-t_2\right]}\;\frac{(1-P_1)P_2\left[1-E_2\right]\left[1-e^{-\Sigma^3\mu_2(1/\alpha_2-1)}\right]}{(\Sigma^3\mu_2)(1/\alpha_2-1)}$$

Eq. (4.93)

and

$$C_3(\vec{r}_1\rightarrow\vec{r}_2,E)=\left[1-\left\langle t(\vec{r}_1\rightarrow\vec{r}_2,E)\right\rangle-C_1(\vec{r}_1\rightarrow\vec{r}_2,E)-C_2(\vec{r}_1\rightarrow\vec{r}_2,E)\right].$$

The $\langle F_j\,t\rangle$ are obtained by utilizing Eq. (4.86) and noting that the only place ℓ appears in the expressions for the C_j is in the $[1-\langle t\rangle]$ term, i.e., $\langle t\rangle = t_1^{N_1}$ and $N_1 = \ell/S_1 = \ell\alpha_1/\mu_1$. Thus,

$$\left\langle F_j(\vec{r}_1)\,t(\vec{r}_1\rightarrow\vec{r}_2,E)\right\rangle=\frac{1}{\Sigma^j(E)}\frac{\partial C_j}{\partial\ell}=\frac{-C_j}{\Sigma^j(E)}\frac{\dfrac{\partial}{\partial\ell}\left\langle t(\vec{r}_1\rightarrow\vec{r}_2,E)\right\rangle}{\left[1-\left\langle t(\vec{r}_1\rightarrow\vec{r}_2,E)\right\rangle\right]}.$$

Eq. (4.94)

These results can be generalized to an arbitrary number of particle phases.

7. Microscopic Self-Shielding Factor

If Eq. (4.94) is substituted into the defining Eq. (4.61), the microscopic self-shielding factors for this model are obtained,

$$f_j(\vec{r},E,\ell\vec{w})=\frac{-C_j}{V_j\Sigma^j\left[1-\langle t\rangle\right]\langle t\rangle}\frac{\partial\langle t\rangle}{\partial\ell}=-\frac{C_j}{\left[1-\langle t\rangle\right]V_j\Sigma^j}\frac{\partial\ln\langle t\rangle}{\partial\ell}.$$

Eq. (4.95)

Since $\langle \iota \rangle = \iota_1^{N_1}$ and $N_1 = \ell \alpha_1 / \mu_1$, it follows that

$$f_j(\vec{r}, E, \ell \vec{w}) = \frac{-\alpha_1 C_j}{V_j \mu_1 \Sigma^j \left[1 - \langle \iota \rangle\right]} \ln \iota_1 \cdot \qquad \text{Eq. (4.96)}$$

To be more explicit note Eqs. (4.77) and (4.79) and that $r = (\mu_1 \alpha_2 / \mu_2 \alpha_1)$, and then obtain

$$f_1(E) = \frac{\left[-\ln \iota_1\right]}{\left[1 - \iota_1\right]} \frac{\left[1 - e^{-\Sigma^3 \mu_1 (1/\alpha_1 - 1)}\right]}{(\Sigma^3 \mu_1)(1/\alpha_1 - 1)} P_{o_1}$$

$$f_2(E) = \frac{\left[-\ln \iota_1\right]}{\left[1 - \iota_1\right]} \frac{\left[1 - \iota_2^r\right]}{\left[1 - \iota_2\right]} \frac{\left[1 - e^{-\Sigma^3 \mu_2 (1/\alpha_2 - 1)}\right]}{(\Sigma^3 \mu_2)(1/\alpha_2 - 1)} \left[\frac{P_{o_2}}{r}\right]$$

and

$$f_3(E) = (1/V_3 \Sigma^3) \left[\alpha_1 (-\ln \iota_1) / \mu_1 - V_1 \Sigma^1 f_{mi_1} - V_2 \Sigma^2 f_{mi_2}\right]$$

Eq. (4.97)

where ι_1 is defined by Eq. (4.82) and ι_2 by Eq. (4.84). These factors are independent of $\vec{r}$, ℓ, and $\vec{w}$.

The ℓ sensitivity has been intentionally suppressed. In effect, the model assumes that ℓ, compared to the largest particles, is long enough to make the contributions of partial intercepts negligible. This is equivalent to assuming that ℓ is large compared to the correlation scale. On paths where this is not the case, particles appear smaller because of the partial intercepts at the end points. In the limit, as ℓ becomes vanishingly small, the particles appear infinitesimal, the material homogeneous, and the f_j go to unity. The manner in which the f_j go from unity to their asymptotic values depends on the shape and size distributions of the particles and the way in which they are packed locally.

This question was investigated in detail for a two-phase system in which every admissible (nonoverlapping) Δ configuration on $\vec{\ell}$ was assumed to be equally probable.[13,14,16] The

self-shielding curves in Ref. 13 show that f rapidly decreases from unity, at $\ell/\mu = 0$, to essentially its asymptotic value at an ℓ/μ between 5 to 20, depending on $\mu\Sigma$ and V. This behavior is interpreted as reflecting the lack of self-shielding in the first layers of particles seen by neutrons traversing $\vec{\ell}$. On the basis of these curves it is assumed that the asymptotic values given by Eq. (4.97) are reasonably accurate for an ℓ/μ greater than approximately 10. This is in effect a more precise statement of what is meant by requiring ℓ to be large with respect to the correlation scales.

The parameter $r = (S_1/S_2) = (\mu_1\alpha_2/\mu_2\alpha_1)$ was implicitly assumed to be an integer in the derivations (see Fig. 4.12). In general, this is not the case and, somewhat arbitrarily, r is interpreted as some average value. The applicability of this assumption also rests on the assumption that ℓ is relatively large compared to μ_1.

Further approximation can considerably simplify the f_j specified by Eq. (4.97). If it is assumed for the matrix material that $\Sigma^3 = 0$ and, hence, $E_j' = E_j$, Eq. (4.97) reduces to

$$\left.\begin{aligned} f_1 &= \frac{\left[-\ln t_1\right]}{\left[1-t_1\right]} P_{o_1} \\ f_2 &= \frac{\left[-\ln t_1\right]}{\left[1-t_1\right]} \frac{\left\{1-\left[1-P_2\mu_2\Sigma^2 P_{o_2}\right]^r\right\}}{(rP_2\mu_2\Sigma^2)} \\ f_3 &= 0 \end{aligned}\right\} \quad \text{Eq. (4.98)}$$

and

$$t_1 = \left\{(1-P_1)\left[1-P_2\mu_2\Sigma^2 P_{o_2}\right]^r + P_1 E_1\right\}.$$

If, in addition, there is only a single particle phase, that is, if $V_2 = 0$,

$$f_1 = \left[\frac{-\alpha_1}{V_1\mu_1\Sigma^1}\right] \ln\left\{1-\mu_1\Sigma^1 V_1 P_{o_1}/\alpha_1\right\}. \qquad \text{Eq. (4.99)}$$

This is the result obtained in Ref. 12.* When the particle phase consists of spheres of fixed radius a, with a packing factor $\alpha = 0.74$ (the physical packing factor for spheres) Eq. (4.99) applies† with

$$P_{o_1} = \frac{3}{8(a\Sigma)^3}\left[2(a\Sigma)^2 - 1 + (1 + 2a\Sigma)e^{-2a\Sigma}\right] . \quad \text{Eq. (4.100)}$$

If either $r \sim 1$ or $(V_2\mu_2\Sigma_2 P_{o2}/\alpha_2) \sim 0$, that is, if both mean particles are approximately the same size, or if the phase 2 volume fraction, cross section, or particle size is small, then in Eq. (4.98) f_1 and f_3 are unchanged but f_2 reduces to

$$f_2 = \frac{\left[-\ln t_1\right]}{\left[1 - t_1\right]} P_{o_2} . \quad \text{Eq. (4.101)}$$

If $\Sigma_1 V_1$ and $\Sigma_2 V_2$ are approximately zero then $t_1 \sim 1$ and $[-\ln t_1]$ $(1 - t_1) \sim 1$ and, thus, Eq. (4.98) reduces to

$$f_1 \cong P_{o_1} \qquad f_2 \cong P_{o_2} \qquad f_3 = 0 .$$

This is essentially the result reported by Hurwitz and Zweifel in Ref. 2.

8. *Parameter Estimation*

To evaluate the f_j for this model it is necessary to know at least the $V_j, \mu_j, \sigma^2_{\Delta_j}$, and α_j for the particle phases. It is usually possible to estimate these quantities from knowledge of the manufacturing process and to compute from them effective cross sections accurate enough for design calculations.‡ However, to realize greater accuracy, and to relate the f_j to material quality control, it is essential that techniques be established to monitor these parameters.**

---

*This result is in substantial agreement with a series of reactivity coefficient experiments by C. H. Randall and J. Duffy.

† This result is discussed in Sect. 4.2.B (see Eq. (4.10) ff.).

‡ This can be accomplished by using Table 4.3 and Eq. (4.67). As already noted, $\alpha \simeq 0.65$ is usually a good estimate.

** The question of necessary accuracy may be answered by computing the range of the f_j's for ranges of the parameters.

Although these quantities are defining parameters of the random process (process ensemble) characterizing the material of interest and are as significant as other material properties, they cannot be observed directly. Having specified a random process, however, it is possible to compute the probabilities of consequences of such a model as a function of these parameters. In particular, it is possible to compute the probability densities of conveniently observed random variables.

The parameters are estimated by comparing with observed distributions the parameter-dependent probability distributions computed from the model. There are a number of well established techniques for accomplishing this. For example, in the method of moments for K disposable parameters (i.e., quantities to be evaluated), the first K observed moments are equated to the first K expected moments (consequences of the model). The K equations in K unknowns are then solved for the parameters. Another, but more elaborate, procedure is to choose those values of the K parameters that produce a least squares (or minimum chi square) fit between the observed and expected histograms (frequency distributions).* These comparisons may also be employed to evaluate the adequacy of the model, that is, its goodness of fit. This step in effect checks the validity of the assumptions implicit in the model (e.g., stationarity, correlation scales, etc.). The essential feature of the technique is that observed microstructural features, reflected by parameters, are linked directly to events of interest, such as neutron transmission, by a single mathematical model for the material.

Although it is not essential, it is convenient when possible to use the same distributions to estimate material parameters as may be required for the analysis of the physical phenomena of interest. Thus, the linear phase intercepts L_j are obvious candidates for observation in this case, since their joint probability density is used to compute $\langle t \rangle$. The asymptotic (large ℓ) joint probability density of the L_j is given by Eqs. (4.74) and (4.75) for the model described above. To obtain sufficient sensitivity, it is frequently necessary to make observations at an ℓ too small for the asymptotic distribution to apply. It is then necessary to derive an $\ell = |\vec{r}_1 - \vec{r}_2|$ dependent distribution from the model.

To obtain accurate estimates of the parameters, a great deal of data must be collected and processed. The amount required for a given precision increases almost factorially

*For a complete description of these techniques see Ref. 17. An application of these techniques to this problem is discussed in Ref. 13.

with the number of parameters to be evaluated. Thus, it is necessary to have equipment to accomplish this rapidly and conveniently. Several such systems are available or are under development. Most experience to date has been with a modification of a microdensitometer. In essence, high contrast photomicrograph transparencies of metallographic sections (preferentially etched to obtain maximum contrast of a particular phase) are scanned by a very narrow slit of light of length ℓ. The fraction of the beam transmitted and sensed by a photocell is effectively proportional to the fraction of the line intercepting the contrasted phase, that is, essentially an L_j. The amplified signal from the photocell is digitized and punched on cards, ready for analysis in a computer. This particular system can automatically collect and record over 10,000 L_j per hour.

If in addition to being stationary and isotropic it can be further assumed that the material is ergodic (in the sense that the L_j probability density for random $\vec{r}$ and $\vec{w}$ in a single heterogeneous element is identical to the distribution over the entire process ensemble), then the L_j collected by the densitometer from a single element can be utilized to estimate the desired parameters. It must also be assumed that the scanned areas are large in comparison to the correlation scale of the largest order of inhomogeneities present. A computer program MEAN[13] has been written to estimate V, μ, and σ_Δ^2 from these data for two-phase systems and to evaluate the goodness of fit with a chi square test.* The material model incorporated in this program implicitly assumes that $1/\alpha = [2-V]X$.

It has been found that the MEAN program consistently overestimates μ by several percent and occasionally by considerably more. The former effect is due essentially to the fixed α of the model. Typically, the model underestimates particle packing, evaluating α at approximately 0.5 rather than the usually noted 0.6 to 0.8, and attempts to make up for this deficiency by increasing μ. The large overestimates of μ are generally due to large scale inhomogeneities that in many instances are obvious to the eye. In most cases, nevertheless, the fitted distributions generally agreed reasonably well with the observed.[14]

Thus, even though observed μ (interpreted as measures of effective particle size) deviated from physical values, the f's computed with the fitted distributions were fairly accurate and later agreed quite well with the model described above. In the latter, more flexible model, the observed and physically

*For a complete description of these techniques, see Ref. 17. An application of these techniques to this problem is discussed in Ref. 13.

expected μ are in agreement in the absence of large scale inhomogeneities. If large scale effects are to be considered, a more complex model will have to be defined incorporating some measure of their scale and magnitude.*

Measures of large scale inhomogeneities have been obtained using an X-ray photometer. This device can nondestructively measure in two-phase materials the volume of each phase intercepted by a concentrated X-ray beam. As with the densitometer, the signal can be digitized and punched on cards. Since the size of the beam is necessarily considerably larger than most particle dimensions, particle effects are suppressed. The variations that are observed in the transmitted beam are due to large scale effects and can be utilized to evaluate characterizing parameters as above.

A device currently being developed is expected to collect and record on computer tape on the order of 40,000 pieces of information in less than 5 seconds directly from metallographic sections. In essence, an electrostatic scanner is utilized to record on tape the field of view of a standard microscope. An appropriately programmed computer can then estimate the $V_j, \mu_j, \sigma_\Delta^2$, and α_j from these data. In addition it could estimate the $p_j(\Delta_j)$ distributions themselves as a function of $\vec{w}$ and test for spatial bias (lack of stationarity) or any other significant deviations from a given model. With such a device it is even possible to investigate quantitatively the assumed $p_j(\Delta_j)$ distributions and many other details of the fine structure of materials.

These devices and variables are only examples of the many possibilities for destructive and nondestructive parameter estimation. They provide the means for measuring and controlling the properties of reactor materials.

9. *Conclusions*

A relatively rigorous and general theoretical treatment has been developed whereby the behavior of a reactor system containing heterogeneous materials can be predicted by representing the heterogeneities by effective macroscopic cross sections (cf Eq. (4.58)) if (1) the spatial scale of the nuclear phenomena is large compared to the size of the material inhomogeneities (the scattering mean free paths are large compared to the material correlation scales); (2) the gross dimensions of the heterogeneous elements are large compared to the size of the material inhomogeneities (e.g., particle dimensions); (3) the fuel materials are relatively poor slowing-down media; and (4) the material is statistically homogeneous.

*This has been done in Ref. 15.

It should be noted that these conditions are met in most reactors. Further, this result is consistent with the various flux-weighting techniques described elsewhere in this chapter.

The microscopic (i.e., particle) self-shielding factors required to calculate the macroscopic cross sections of structural elements containing such particles can be determined from Eq. (4.61). (An example for a mixture of two particle types has been discussed in detail.)

A technique for describing the various parameters which influence the particle self-shielding in terms of measurable material properties can be used, thus avoiding the necessity of assuming the nature of the spatial distribution of particles.

D. Representation of Plate Self-Shielding in Diffusion Theory

W. H. Hannum

1. Introduction

Standard reactor design calculations employ a few energy group, few-dimensional, diffusion theory formalism. In this formalism, various interacting regions may be specifically described. The type of region here considered is one of strong local absorption which causes steep local gradients and highly directional fluxes. Examples are control rods and self-shielded burnable poisons in plate geometry. Diffusion theory (P_1) is inadequate for the description of such absorbers. Therefore, various means of adjusting the diffusion theory coefficients have been devised, so that diffusion theory yields the same results as higher order transport theory.

The problem considered in this section is to define an adequate diffusion theory representation for heterogeneous systems containing strongly absorbing plates.* Throughout this section, the term correct is taken to imply that the representation devised predicts the same relative capture rates among regions, and among absorbing nuclei, as a high order transport calculation would predict. The spatial distribution of captures within a strongly absorbing region calculated with adjusted diffusion theory constants, in general, will not be correct. However, if the correct relative capture rates among materials and regions are predicted, reactivity and relative depletion rates will be correctly predicted. In cases in which the spatial distribution may be significant, such as for power peaking within a fueled region, it is necessary to make allowance for the errors which may be introduced by the use of the

*The term plate is used throughout this section. The same general concepts apply to other geometries.

diffusion theory representation. While the comparisons discussed are only between relative capture rates, it is feasible to use the same procedures (and frequently the same calculations) to evaluate the errors in spatial distribution. This aspect of the problem is discussed further in Sect. 4.3.

The specific procedures employed for any given problem depend in large measure on (1) the specific region to be represented, and its nuclear properties; (2) the calculational tools available; and (3) the accuracy needed. Thus, considerable judgment and evaluation are necessary in deciding on the appropriate procedure to use for any given problem. The intent of this section is to describe various procedures which are available and to illustrate the type of situation which can be treated by each. The procedures are evaluated for specific cases to illustrate the degree of accuracy which may be expected and to illustrate ways of establishing the adequacy of the procedure for other cases.

It is assumed that the appropriate nuclear properties of the materials, such as cross sections as a function of energy, materials compositions, etc., are known. The cross sections are taken as having been corrected for particle self-shielding effects, as described in the previous section.

The most satisfactory procedure is to obtain an exact solution to a simplified problem involving only the absorber in a typical environment and to use this analytic solution, or an approximation to it, to determine a design representation. For one-energy, one-dimensional problems, an equivalent diffusion theory representation may be defined in terms of blackness theory (see Chap. 3, Sect. 3.6) which is dependent only on the properties of the plate in question and which can be compared to higher order transport solutions. More complex situations, which involve an energy spectrum or more than one dimension, can also, in some cases, be treated with various analytical approximations based on blackness theory and compared to more exact calculations, such as Monte Carlo. Thus, the approximations involved in extending blackness theory must depend on the specific type of problem considered.

In Sect. 4.2.D.2, the direct use of one-dimensional blackness theory is illustrated for the representation of an isolated hafnium control rod and of an isolated boron control element. This representation is that which would be used in diffusion theory calculations in which the control elements were explicitly described.

There are other types of problems which frequently occur in reactor design for which blackness theory, or a simple extension of blackness theory, cannot reasonably be expected to define an adequate representation. These situations include

problems which are essentially multidimensional (blackness theory, as currently formulated, is one-dimensional) or in which the spatial dependence of the neutron spectrum cannot be simply described. Elaborate or detailed calculations are necessary even with a simplified environment. For this situation, it is also frequently preferable to select the design representation by a procedure referred to as empirical blackness theory. This procedure involves the use of a diffusion theory representation which, except for a single parameter such as the effective absorption cross section, is arbitrarily selected. The final parameter is then selected as that which, in certain available cases, causes the diffusion theory calculation to yield the correct prediction of relative capture rate. This procedure for defining an explicit representation of an isolated control element is discussed in Sect. 4.2.D.3.

2. *Explicit Blackness Representation*

A) GENERAL THEORY. Much of the discussion of explicit representation of plate self-shielding in diffusion theory may be framed in terms of blackness theory.[18] The problem considered here is that of an infinite plate or a series of infinite plates in some given environment. It is assumed that diffusion theory is adequate to describe regions external to the plate or plates in question. The basis of blackness theory is in treating a plate as a boundary to an external diffusing medium or as an effective diffusing medium having diffusion and absorption constants adjusted so that the correct absorption of neutrons belonging to the P_0 and P_1 components of the flux is accounted for.

For an infinite source-free slab of thickness 2a, in which the ratio of scattering to absorption is negligibly small, two relationships between current j, and flux ϕ, may be defined. Expressing these relationships in terms of convenient parameters $\alpha(u)$ and $\beta(u)$,

$$\left.\begin{aligned} \alpha(u) &\equiv \frac{j^+ + j^-}{\phi^+ + \phi^-} = \frac{1 - 2E_3(z)}{2\left[1 + 3E_4(z)\right]} \\ \beta(u) &\equiv \frac{j^+ - j^-}{\phi^+ - \phi^-} = \frac{1 + 2E_3(z)}{2\left[1 - 3E_4(z)\right]}; \quad z \equiv 2a\Sigma_a(u) \end{aligned}\right\} \quad \text{Eq. (4.102)}$$

where*

$$E_{n+2}(z) \equiv \int_0^1 \mu^n \exp\left[-\frac{z}{\mu}\right] d\mu$$

and j^+, ϕ^+ and j^-, ϕ^- are the current and scalar fluxes at the right- and left-hand surface of the plate, respectively.

If the ratio of scattering to absorption in the absorbing slab is significant, these equations are not necessarily appropriate. Generally, the materials of the plate are sufficiently heavy (in the range where absorption is large), so that the energy change on internal scattering may be neglected. Under these circumstances, a one-velocity transport theory code, such as RDR-4,[19] HERD,[20] FLIP,[21] TET,[22] etc., can be used to obtain values of $\alpha(u)$ and $\beta(u)$.

If a reactor calculation employs a group diffusion code, slab boundary conditions in each group can be specified by relating the group currents $\int_{u_o}^{u_g} j^{\pm}(u)\,du$ at each surface of the slab to group fluxes $\int_{u_o}^{u_g} \phi^{\pm}(u)du$ for each group. The relationship is conveniently expressed by the parameters $<\alpha>$ and $<\beta>$, defined as

$$<\alpha> \equiv \frac{<j^+ + j^->}{<\phi^+ + \phi^->} = \frac{\int_{u_o}^{u_g} \alpha(u)\,[\phi^+(u) + \phi^-(u)]\,du}{\int_{u_o}^{u_g} [\phi^+(u) + \phi^-(u)]\,du}$$

Eq. (4.103)

and

$$<\beta> \equiv \frac{<j^+ - j^->}{<\phi^+ - \phi^->} = \frac{\int_{u_o}^{u_g} \beta(u)\,[\phi^+(u) - \phi^-(u)]\,du}{\int_{u_o}^{u_g} [\phi^+(u) - \phi^-(u)]\,du}\,.$$

Eq. (4.104)

*The notation used is that of Ref. 3.

In diffusion theory, these same ratios of flux and current are obtained if the absorber has

$$\left.\begin{aligned} \Sigma_a &= \frac{\sqrt{\langle\alpha\rangle\langle\beta\rangle}}{2t} \ln\left[\frac{1+\sqrt{\frac{\langle\alpha\rangle}{\langle\beta\rangle}}}{1-\sqrt{\frac{\langle\alpha\rangle}{\langle\beta\rangle}}}\right] \\ D\Sigma_a &= \langle\alpha\rangle\langle\beta\rangle \end{aligned}\right\} \quad \text{Eq. (4.105)}$$

In most digital computing programs, a finite difference approximation is used to represent spatial derivatives. The spatial mesh size associated with such a representation must be small in comparison with a diffusion length if the approximation is to represent accurately the continuous solution. For heavily absorbing plates treated as equivalent diffusing media, this requirement can result in a sizable number of mesh points interior to the plate and a consequent increase in computing time. There is, however, an advantage to retaining the equivalent diffusion medium approach, provided the required number of internal mesh points can be reduced. This advantage can be realized by incorporating the mesh size in equivalent diffusion medium into the values of the effective constants for that medium.[23] It can be shown, with no source inside the absorber and equal mesh spacing h, that a finite difference theory calculation with

$$\left.\begin{aligned} k &= \frac{1}{2a}\cosh^{-1}\left(\frac{\langle\beta\rangle+\langle\alpha\rangle}{\langle\beta\rangle-\langle\alpha\rangle}\right) \\ D &= \frac{(\langle\alpha\rangle+\langle\beta\rangle)h}{2\sinh kh}\tanh 2ka \\ \Sigma_a &= \frac{2D}{h^2}(\cosh kh-1) \end{aligned}\right\} \quad \text{Eq. (4.106)}$$

and

will yield boundary currents and fluxes identical with the desired continuous solution, Eq. (4.105)

For sufficiently large values of $a\Sigma_a(E)$, $\langle\beta\rangle$, and $\langle\alpha\rangle \to 0.5$. For this condition, $D\to 0$, and $\Sigma_a \to 2\langle\alpha\rangle/h$. Since the machine computation procedure generally breaks down for $D\to 0$, the black

slab is treated by choosing a value of k arbitrarily, such that $2ka >> 1$, and by using the finite D and Σ_a which result. A value of $2ka \sim 10$ has been found adequately large to yield results practically indistinguishable from the limiting case.

In applying this method, the mesh spacing h is frequently taken to equal the half-thickness a, at least one interior point being required if Simpson's rule is used to perform numerical integrals over the region. It is interesting to note that

$$\int_{-a}^{a} \Sigma_a \phi(x)\, dx$$

as given by Simpson's rule does not equal the net current except as $h \to 0$; whereas, if the trapezoidal rule is used, the two quantities are equal for all h. This circumstance is of concern if the depletion of material in the slab by neutron absorption is to be considered in depletion calculations.

In symmetric cases, the values of $<\alpha_i>$ alone serve to specify the absorber. Accordingly, any pair of values of D_i and Σ_{a_i} yielding the desired $<\alpha_i>$ may be used to describe the effective diffusion theory properties of the slab. In asymmetric configurations this freedom is, strictly speaking, not available. Both $<\alpha_i>$ and $<\beta_i>$ are needed for each group, and the corresponding D_i and Σ_{a_i} are uniquely determined. However, because determinations of $<\beta_i>$ involving spectral averages are at least as difficult as the analogous determination of $<\alpha_i>$, and because any averaging introduces a certain amount of theoretical error into the results, the temptation is strong to use some approximation for $<\beta_i>$ which obviates the need for detailed calculations. The approximation

$$<\alpha><\beta> \simeq \frac{1}{4} \qquad \text{Eq. (4.107)}$$

is approximately valid for $[\Sigma_a(u)/\Sigma_s] \geq 5.0$ (see Ref. 18). Many control materials fall within this category, so that this approximation is adequate. For other situations $<\beta>$ must be directly evaluated.

The examples used in this section describe absorbers embedded in homogeneous regions of core material. In practical situations, there may be substantial heterogeneities in the surrounding environment. For example, the PWR designs have 1/4 in. of water and 1/4 in. of zirconium between the surface of the control rod and the beginning of the fueled region. Caution must be taken to ensure that the comparative

calculations are not invalidated by misrepresentation of the surrounding medium. This question is discussed in Sect. 4.3.B.

B) EXAMPLE 1: HAFNIUM CONTROL ROD, RESONANCE ABSORPTION. The first problem to be discussed is that of obtaining an epithermal representation for an isolated one-dimensional slab of a resonance absorbing material. This problem may, in principle, be treated directly with blackness theory. Two practical problems arise in the calculation of group average blackness coefficients. These involve the availability and treatment of detailed nuclear data and the method of energy averaging the blackness coefficients.

For the case of hafnium, it is reasonable to do the energy averaging, assuming that the resonances are narrow and widely spaced. If the ratio of absorption to scattering in the external medium is small, and the absorber material is a resonance absorber with widely spread resonances, narrow in comparison with the average energy loss for collision in the external medium, the method of Stein (see Chap. 2, Sect. 2.5) is applicable. According to this approximation, the source of neutrons for the energy range including any particular resonance is spatially flat in the environment. The diffusion equation for the external medium at any lethargy u can be written

$$D(u)\,\frac{\partial^2 \phi(u,x)}{\partial x^2} - \Sigma(u)\,\phi(u,x) + S(u) = 0. \qquad \text{Eq. (4.108)}$$

For boundary conditions,

$$\frac{D}{\phi}\frac{\partial \phi}{\partial x}\bigg|_{+\text{ interface}} = \frac{j^+}{\phi^+}\,;\quad \frac{D}{\phi}\frac{\partial \phi}{\partial x}\bigg|_{-\text{ interface}} = \frac{j^-}{\phi^-}$$

and $\frac{\partial \phi}{\partial x} = 0$ at the external cell boundaries, the fluxes at the slab surfaces are

$$\left.\begin{aligned} \phi^+ &= \frac{S^+}{\Sigma}\,\frac{1}{1+\dfrac{j^+}{\phi^+}\sqrt{\dfrac{1}{D\Sigma}}\ \operatorname{ctnh}\ \sqrt{\dfrac{\Sigma}{D}}\,H} \\ \phi^- &= \frac{S^-}{\Sigma}\,\frac{1}{1+\dfrac{j^-}{\phi^-}\sqrt{\dfrac{1}{D\Sigma}}\ \operatorname{ctnh}\ \sqrt{\dfrac{\Sigma}{D}}\,H} \end{aligned}\right\} \qquad \text{Eq. (4.109)}$$

where H is the thickness of the media on each side of the slab, the properties of these two media being assumed identical except possibly for the source magnitudes. It follows that

$$\left.\begin{aligned}\left(\phi^{+}+\phi^{-}\right) &= \frac{S^{+}+S^{-}}{\Sigma}\ \frac{1}{1+c\,\alpha}\\ \text{and}\qquad\qquad\qquad\qquad\\ \left(\phi^{+}-\phi^{-}\right) &= \frac{S^{+}-S^{-}}{\Sigma}\ \frac{1}{1+c\,\beta}\end{aligned}\right\} \qquad \text{Eq. (4.110)}$$

where

$$c \equiv \sqrt{\frac{1}{D\Sigma}}\ \text{ctnh}\ \sqrt{\frac{\Sigma}{D}}\,H = \sqrt{3}\ \sqrt{\frac{\Sigma_{tr}}{\Sigma}}\ \text{ctnh}\ \left(\sqrt{3\Sigma_{tr}\Sigma}H\right) \simeq \sqrt{3}.$$

Under the assumption of narrow, widely spaced resonances, $\frac{S^{+}}{\Sigma}$ and $\frac{S^{-}}{\Sigma}$ are almost constant over the lethargy range corresponding to a given energy group. Final results are,

$$\langle\alpha\rangle = \frac{\displaystyle\int_{u_o}^{u_g} \frac{\alpha(u)\,du}{1+c\alpha(u)}}{\displaystyle\int_{u_o}^{u_g} \frac{du}{1+c\alpha(u)}}$$

Eq. (4.111)

and

$$\langle\beta\rangle = \frac{\displaystyle\int_{u_o}^{u_g} \frac{\beta(u)\,du}{1+c\,\beta(u)}}{\displaystyle\int_{u_o}^{u_g} \frac{du}{1+c\beta(u)}}$$

Since in practical cases $c \simeq \sqrt{3}$, the quantities $\langle\alpha\rangle$ and $\langle\beta\rangle$, under conditions such that the narrow resonance approximation is valid, depend only on the properties of the control slab.

The expressions in Eq. (4.111) are expected to be adequate for computing $\langle\alpha\rangle$ and $\langle\beta\rangle$ for the individual groups of a multigroup scheme. However, in a few-group theory involving

closely spaced resonances or nonresonance absorbers, or under conditions such that absorption in the external medium is significant, Eq. (4.111) does not apply. Under these circumstances improved approximations obtained analytically [24, 25] or an empirical representation can be used.

It is convenient for numerical evaluation to rewrite Eq. (4.111) as [18]

$$\langle \alpha \rangle = \frac{1}{\frac{\ln (E_{max}/E_{min})}{I} - \sqrt{3}} \qquad \text{Eq. (4.112)}$$

where

$$I = \int_{E_{min}}^{E_{max}} \frac{\alpha(E)\, dE}{[1 + \sqrt{3}\ \alpha(E)]\, E}.$$

Thus, the computation reduces to that of finding I.

The contribution of this integral from an isolated resonance is given by Stein's method[26] as

$$\int_{res} \frac{\alpha(E)\, dE}{[1 + \sqrt{3}\, \alpha(E)]\, E} = (\sigma_a)_{eff} N^{Hf} a$$

$$\simeq 0.9 \frac{\Gamma}{E_o} \sigma_a^{1/2}(E_o) \sqrt{2N^{Hf}a} \left[\frac{1}{2 + \sqrt{3}} + \frac{1}{2} \frac{\tan^{-1} \left(\frac{\sqrt{3}}{2} \right)^{1/2}}{\left(\frac{\sqrt{3}}{2} \right)^{1/2}} \right].$$

Eq. (4.113)

where Γ is the total width of the resonance, $\sigma_a(E_o)$ is the microscopic absorption cross section at the peak of the resonance (which occurs at energy E_o), and N^{Hf} is the number density of hafnium (or other absorber) atoms in the slab of thickness 2a.

The desired integral for hafnium cannot be obtained merely by summing Eq. (4.113) over all the known resonances. The low-lying resonances of hafnium overlap; consequently, use of Eq. (4.113) in that region seems inappropriate. In addition, there is, over the whole range of integration, a $1/v$ absorption not accounted for in Eq. (4.113). Accordingly, the integral I can be computed by dividing the energy span (taken here to be

0.625 to 5.53×10^3 ev) into three ranges. In the first range (0.625→10.0 ev), a numerical integration is performed with the values of $\alpha(E)$ obtained from Eq. (4.102). Table 4.4 gives the results, using the microscopic absorption cross section of hafnium directly from the curve appearing in BNL-325.[27]* In the range, 10→100 ev, Eq. (4.113) and the resonance parameters from Ref. 27 have been used; in addition, a $1/v$ contribution based on σ_a^{Hf} $(2200\ m/sec) = 105\ b$ is included, the interference with the resonance term being neglected. From 100 ev to 5.53×10^3 ev, a $1/v$ contribution is assumed.

The procedure just outlined is somewhat arbitrary but does not seem out of place when imperfect knowledge of the microscopic cross-section data is encountered. For slabs in the thickness range considered, however, there is a tendency toward saturation in the resonances, since $\alpha[\Sigma_a(u)t]$ cannot exceed 0.5. Thus, decreasing slab thickness by a factor of four decreases the contribution to I in the 0.625→10 ev range by a factor of only ~1.6. This circumstance suggests that sizable errors in the microscopic cross sections will not seriously affect the results. For other problems in which this saturation is not as prominent, it may be necessary to use more elaborate numerical techniques.

Since common design practice is to use two to four energy groups, the validity of the theory in this degree of approximation must be tested. The most unambiguous test of an approx-

TABLE 4.4 — EPITHERMAL ABSORPTION CROSS SECTIONS FOR HAFNIUM SLABS

Slab Thickness (in.)	0.220	0.110	0.055
Contribution to I (0.625 → 10 ev)	0.677	0.599	0.432
Contribution to I (resonance, 10→100 ev)	0.143	0.101	0.071
Contribution to I (1/v, 100→5.53×10^3 ev)	0.117	0.058	0.029
$\int_{0.625}^{5.53 \times 10^3} \frac{\alpha(E)\,dE}{[1+\sqrt{3}\ \alpha(E)]\,E}$	0.937	0.758	0.532
$\langle \alpha \rangle$	0.1256	0.0975	0.0651

*The specific numerical data and the data sources used are included for illustration only. More recent and preferable cross section representations are available.

imation is to compare the results of its use with those obtained by performing a more elaborate or detailed calculation for the same example. This method of validation has two limitations: (1) it does not predict the extent of the range over which an approximation, tested for particular cases, will be valid; and (2) it requires an assumption that errors associated with isolated effects will not augment one another when a composite approximation is made. The first difficulty can usually be circumvented by a spot check of the problem at hand. The second would require the use of more elaborate calculations, which frequently must wait for more elaborate computing machines and codes. The magnitude of the error which may be associated with use of these approximate values of $<\alpha>$ may be illustrated by a problem solved by both four-group and 55-group schemes. The multigroup calculation was performed using the P1MG code[28] with individual values of $<\alpha>$ for each of the 54 fast groups and for the single thermal group. The corresponding few-group problem was solved using a MUFT-WANDA scheme,[29] wherein fast few-group constants are obtained from a 54-group infinite medium (constant buckling) P_1 code (MUFT[30]). These constants are then used, together with one-group thermal constants, in a four-group spatial code (WANDA[31]). The thermal constants and the 54-group libraries are the same for both the few-group and the multigroup problems. The problem considered is a full core problem of a central slab of hafnium worth about 20 percent Δk in a zirconium-water-fuel medium, which is in turn reflected by an effectively infinite water reflector. The results of critical searches performed with both group structures are given in Table 4.5. The excellent agreement is apparently the result of a compensation of errors within the few-group scheme.

This compensation is illustrated by the data of Table 4.6, in which pertinent few-group results are compared with

TABLE 4.5 — COMPARISONS OF MULTIGROUP AND FEW-GROUP CALCULATIONS

	Values of k_{eff}
55 Energy Groups	1.00705
4 Energy Groups	1.00702
Fractional Difference	0.00003

TABLE 4.6 — COMPARISON OF FEW-GROUP $< \alpha >$'s AND CURRENTS FOR MULTIGROUP AND FEW-GROUP CALCULATIONS*

Energy Group	Few-Group Calculation		Multigroup Calculation	
	$< \alpha >$ Input	Current	$< \alpha >$	Current
1 (10 Mev → 0.821 Mev)	0	—	0	--
2 (821 kev → 5.53 kev)	1.023×10^{-2}	6.42×10^{-3}	1.023×10^{-2}	6.32×10^{-3}
3 (5.53 kev → 0.625 ev)	1.077×10^{-1}	4.27×10^{-2}	0.876×10^{-1}	4.05×10^{-2}
4 (0.65 ev → 0)	3.01×10^{-1}	3.78×10^{-2}	3.01×10^{-1}	3.57×10^{-2}

*The $< \alpha >$ values for Group 3 are consistent with one another but not with those appearing in Table 4.4. Also the $< \alpha >$ for Group 4 is not correct for this thickness of hafnium. Neither of these discrepancies affects the validity of the present comparison.

corresponding quantities arising from a few-group edit of the multigroup calculations. Specifically, the few-group values of $\langle \alpha \rangle$ are compared with the values

$$\langle \alpha \rangle = \sum_{N_1}^{N_2} \alpha_i \phi_i \Delta u_i \Big/ \sum_{N_1}^{N_2} \phi_i \Delta u_i \qquad \text{Eq. (4.114)}$$

obtained from the multigroup results (ϕ_i is the flux at the slab-fuel interface). The corresponding currents into the slabs for each group (normalized in all cases to a total source of unity) are also tabulated.

Evidently, there is a compensation of errors within the few-group calculation. As a result, the flux and the current-to-flux ratio in Group 3 are more in error than the current. (In error means different from the few-group edit of the multigroup calculation.) To illustrate this point further, values from the few-group edit of the multigroup calculation were used as input to a few-group problem. The resulting eigenvalue (to be compared with those in Table 4.5) is $k_{\text{eff}} = 1.0152$, which is more in error than the result obtained using the approximate value of $\langle \alpha \rangle$.

The conclusion is that the use of few-group $\langle \alpha \rangle$ values obtained from a few-group edit of a multigroup calculation does not improve the agreement between the few-group and multigroup eigenvalues. E.M. Gelbard has shown that agreement can be obtained if, along with the $\langle \alpha \rangle$ values, the pointwise few-group constants external to the absorber that result from the edit are also used. A further conclusion is that $\langle \alpha \rangle$ values computed with Eq. (4.112) lead to few-group eigenvalues which are in good agreement with the multigroup results. This last conclusion is a limited one, since it has been illustrated in only a few cases. Because reasons for the agreement are not apparent, computations of $\langle \alpha \rangle$ which assume a $1/E$ flux far from the control slab should be used with caution. If such computations yield results which lead to error in comparison with multigroup calculations, it would be preferable to search for and use that epithermal group $\langle \alpha \rangle$ value which gives the same current into the slab as the P1MG calculation.

C) EXAMPLE 2: BORON CONTROL ELEMENTS, NONRESONANCE ABSORPTION. Much of the development of the preceding section can be carried over directly to the determination of effective constants for a one-dimensional control element whose cross section is a smooth function of energy. The blackness formulation (up to the point of energy averaging) is directly applicable, and the cross sections are frequently more easily described when they vary smoothly with energy.

Thus, the areas requiring further development are the energy averaging and the evaluation of the adequacy of the procedures.

For a control slab in which the absorption cross section is a smooth function of energy, there is little reason to expect the averaging procedures previously defined (based on a thin resonance assumption) to be appropriate. Further, no analogous approximation is available which, without significant adjustments, will cause the group-averaged effective cross sections to be dependent on the absorber only. Since there is concern for the adequacy of even the more elaborate procedures, it is advisable to evaluate the procedures developed for a specific case of interest.

As before, it is assumed that P_1 is adequate to describe the regions external to the boron slab. It is also reasonable to assume that the previously defined energy average blackness coefficients [Eq. (4.111)] are adequate for computing $<\alpha>$ and $<\beta>$ for single energies or for individual groups of a multigroup representation. In terms of these assumptions, a P_1 multigroup solution, as is available using the P1MG code[28] for epithermal energies or SLOP-1 code[32] for thermal energies, may be used to evaluate potential one-dimensional design representations in the epithermal and thermal energy range.

For design calculations, it remains necessary to obtain group-averaged blackness coefficients. The energy averaging previously considered [Eq. (4.111)] is based on assumptions that the source of neutrons to any given energy range is spatially flat and that the spectrum far from the absorber varies with energy as $1/E$. For this problem, neither of these assumptions is necessarily valid. The spectrum, if significantly non $-1/E$, may be retained by keeping the $\phi(u)$ term which appears in Eqs. (4.103) and (4.104). To the extent that it is reasonable to ignore the source depression, the quantities $<\alpha>$ and $<\beta>$ may then be defined as

$$<\alpha> = \frac{\int_{u_o}^{u_g} \frac{\alpha(u)\,\phi(u)\,du}{1 + c\alpha(u)}}{\int_{u_o}^{u_g} \frac{\phi(u)\,du}{1 + c\alpha(u)}}$$

Eq. (4.115)

$$<\beta> = \frac{\int_{u_o}^{u_g} \frac{\beta(u)\,\phi(u)\,du}{1 + c\beta(u)}}{\int_{u_o}^{u_g} \frac{\phi(u)\,du}{1 + c\beta(u)}}$$

where $\phi(u)$ is taken as the flux spectrum far from the absorbing slab. Physically, however, the source to each lethargy is depressed near the slab for important (high) lethargies. The factor c which appears in Eq. (4.115) accounts for the spatial depression in the flux at lethargy u due to absorption at lethargy u, but does not account for the depression in the source. Thus, these averages may be expected to be in error, but by less than would be obtained by a direct average of α and β over $\phi(u)$.

In cases where the surface flux depression is small, a numerically simple approximation is to take $c = 0$. Thus,

$$\langle \alpha \rangle = \frac{\int_{u_o}^{u_g} \alpha(u)\,\phi(u)\,du}{\int_{u_o}^{u_g} \phi(u)\,du}$$

$$\langle \beta \rangle = \frac{\int_{u_o}^{u_g} \beta(u)\,\phi(u)\,du}{\int_{u_o}^{u_g} \phi(u)\,du} \qquad \text{Eq. (4.116)}$$

Neglecting the source depression problem for the moment, the problem of obtaining energy-averaged blackness coefficients is one of defining an appropriate spectrum, $\phi(u)$. The simplest form is to assume that the spectrum $\phi(u)$ is constant in lethargy, as was done for the hafnium example above. For the epithermal energy range, this may be adequate in some instances. A further simple, but approximate, allowance for changes in the incident spectrum is to consider $\phi(u)$ to be a Dirac delta function at the average energy, i.e., consider blackness coefficients $\alpha(\langle u \rangle)$ and $\beta(\langle u \rangle)$ While the theoretical justification of such a procedure is not clear, this does constitute a well defined procedure yielding absorption probabilities which will decrease for harder spectra and increase for softer spectra. A somewhat more explicit energy averaging can be obtained in terms of Eq. (4.115), considering $\phi(u)$ to be the spectrum characteristic of the materials of the surrounding medium. The definition of the surrounding medium may, in a practical

case, be less than obvious, except for an isolated plate in a large, effectively homogeneous medium. The case of a single plate in a large homogeneous medium may, however, be used to evaluate the adequacy of such procedures.

In the following illustrations,* three practicable but intuitively different schemes utilizing an infinite region spectrum based on the surrounding medium are compared with multigroup results for a simple geometry. The geometry considered is a two-region cell consisting of half of a boron slab adjacent to a homogeneous fuel-bearing region. The absorber (boron) is assumed purely absorbing with an absorption cross section which varies as $1/v$. Three values of optical thickness, $a\Sigma_a$ (0.0253 ev) = 0.5, 1.0, and 2.0, have been used. The description of the absorber utilized in the multigroup calculation is provided by P_1 blackness theory for a purely absorbing medium. This means that the condition $j/\phi = a$ is applied at the slab surface in each multigroup. In the few-group representation, the absorber is described by the same thermal boundary condition, $<a>$, as in the multigroup calculation. In the fast groups, the absorbing slab is described by P_1 blackness boundary conditions for each few group averaged over several types of spectra. The first few-group method utilizes the few-group data obtained by homogenizing the fuel-bearing region and the boron slab to determine the fast spectrum. This homogenized spectrum is used in averaging the P_1 blackness boundary conditions to define the boundary condition for each few group [Eq. (4.116)]. The second method utilizes the spectrum from a fuel-bearing region infinite medium spectrum calculation. The few-group spectrum-averaged boundary conditions describing the boron slab are the averages over this spectrum [Eq. (4.116)], not accounting for the flux depression at the surface of the absorber. The third method differs from the second method in that the determination of the spectrum-averaged boundary conditions accounts for the flux depression at the surface of the absorber [Eq. (4.115)]. The results of using these various approximations are summarized in Table 4.7.

Some comments on these results are appropriate. Particularly, the removal cross section to thermal energies should be considered, since approximately 75 percent of the source neutrons are thermalized. Comparing first the design cases based on the homogenized spectra to those using the separate fuel-bearing region spectra, the removal cross sections in the

*In this illustration, the epithermal representation is evaluated. The formulation, however, applies to any energy range.

TABLE 4.7 — COMPARISON OF VARIOUS EPITHERMAL BORON REPRESENTATIONS

Representation $a\Sigma_a$(0.0253 ev)	Calculated k_∞'s. 0.5	1.0	2.0
Multigroup	1.700	1.621	1.540
Four-Group			
α averaged over boron fuel homogenized spectrum [Eq. (4.116)]	1.695	1.612	1.523
α averaged over fuel spectrum [Eq. (4.116)]	1.688	1.612	1.526
α averaged over fuel spectrum [Eq. (4.115)]	1.692	1.614	1.531

fuel-bearing region are lower for the homogenized spectra due to the lower values of

$$\frac{\Sigma_s(u)}{\Sigma_a(u) + \Sigma_s(u)}.$$

The fuel-bearing region absorption cross sections are also less in these spectra, since the presence of boron hardens the spectrum. In few-group calculations, the fast group flux levels given by these constants will be somewhat higher than in the separate spectrum cases, and more boron absorption will occur for a given slab description. This effect is partially compensated, since the $<\alpha>$'s, of the homogenized spectra are less than those of the separate spectra. This results from the lower fluxes at the higher boron cross-section values in the homogenized case. The higher fraction of epithermal absorption in the fuel-bearing regions of these homogenized spectrum cases, even with their lower absorption cross sections, results from the removal cross sections being more strongly decreased than the absorption cross sections. Scheme 3 utilized the asymptotic removal and absorption cross sections for the entire fuel-bearing region and, hence, has a third group surface flux lower than that of the multigroup calculation. With an

$\langle\alpha\rangle$ averaged over the asymptotic multigroup fluxes, the net effect is good agreement.

At thermal energies, the choice of a valid energy-averaging formulation is not clear. The compensation inferred for the preceding illustration will not necessarily occur when the thermal energy range is treated as a single group. For some situations a specific averaging form [e.g., Eq. (4.115) or (4.116)] is adequate, but no reliable generalizations of this type have been identified.

3. *Empirical Blackness Theory*

The preceding discussion has considered problems in which the poison element can be adequately described in one dimension. The general situation with regard to defining a theoretical two-dimensional framework analogous to blackness theory has been discussed in Chap. 3. While several approximate schemes are available, there is no analytic formulation available with which to define quantities analogous to α and β, depending only on the characteristics of the control material, for other than one-dimensional geometries. In many situations, when the width of the absorber is large relative to the diffusion length in the surrounding region, values of α and β computed for infinite slabs may be expected to be appropriate. Thus, for these cases the procedures discussed previously may be used. When this approximation is not appropriate, an alternative procedure is required. The procedure to be described is formulated to avoid the restriction to one dimension and is based on the assumption that the effective constants for a strong absorber are expected to be primarily dependent on the cross sections of the absorber, its dimensions, and the diffusion theory mesh spacing to be used to describe the region and not the environment external to the lumped absorber.

Empirical blackness coefficients are defined directly in terms of effective diffusion theory constants (D and Σ_a). Further, an arbitrary relationship between D and Σ_a is defined. In the example to follow, the relationship which is used is

$$D^{\text{eff}} = \frac{1}{3\sum_a^{\text{eff}}}$$

where eff denotes effective diffusion theory constants to be determined for the lumped absorber. At this point, except for Σ_a^{eff}, all features of the design representation are defined independently of the physical properties of the absorber. The property of the desired Σ_a^{eff} is, when Σ_a^{eff} is used with the

remainder of the design representation, that the proper absorption rate in the absorber (relative to that in some normalizing region) will be calculated, the proper absorption rates being determined from more exact transport calculations.

Since in many design studies the exact location of the lumped absorber relative to the fueled and structural regions is a variable, it is desirable to have a technique of determining the effective absorption constant Σ_a^{eff} which does not require a separate determination of Σ_a^{eff} for every specific location and variation in environment studied. This desire is motivated by questions of economics of time and calculational expenses, since for each specific location a series of calculations could be performed to determine Σ_a^{eff}. To determine Σ_a^{eff} which will adequately approximate the absorption in the lumped absorber, a model cell geometry is chosen for empirically determining Σ_a^{eff} by comparing a high order transport theory calculation to diffusion theory design type calculations in which Σ_a is varied until the relative absorption rates in the design type calculation equals that of the high order transport calculation. This process is repeated for a range of actual lumped absorber cross sections, and the relationship between Σ_a^{eff} and the actual lumped absorber cross section is obtained. The model cell is thus defined as one which (1) includes the absorber in question, (2) includes an environment for the absorber typical of the physical environment, (3) can be accurately calculated (e.g., Monte Carlo or high order transport theory), (4) can be adequately described by the diffusion theory design model, using the Σ_a^{eff} obtained by the comparison with transport calculations described above.

The usefulness of the above procedure is dependent upon the sensitivity of Σ_a^{eff} to the actual physical location and environment of the lumped absorber. In the preceding discussion on blackness theory, it was observed that for some situations (narrow isolated resonances) an effective diffusion theory representation could be defined with reference only to the absorber itself. It may, therefore, be expected that the effective constants will sometimes not be strongly dependent on the model cell flux spectrum. Thus, the effective constants (correlation) should be correct if the environment (spectrum) is effectively that of the actual problem. For specific applications, it is advisable to evaluate the appropriateness of the model cell by determining that the predicted relative capture rate is not sensitive to the specific model cell used or to changes in the environment of the absorber, such as occurs during depletion.

This type of evaluation can be illustrated by a comparison of diffusion theory and Monte Carlo calculations having the

same absorber dimensions and mesh treatment as in the model cell, but with different environments. The effective diffusion theory constants have been obtained using a model cell in which the absorber is embedded in the center of a very large homogeneous fuel region. The actual geometry, a heterogeneous geometry, in which the absorber is located at the corner of a fuel region surrounded by an explicit water channel and some structure, has been calculated using diffusion theory and Σ_a^{eff} obtained from the model cell and with a more exact method. The TRAC code[33] has been used to obtain the one-energy Monte Carlo results for this example, and the PDQ code[34] for diffusion theory results. The results of these calculations are given in Fig. 4.13. The predictions of the boron capture fraction are low by the order of 7 percent with Σ_a^{eff} obtained from the model cell. This agreement, although not as good as in other situations, is still consistently better than that obtained using one-dimensional blackness theory which is also shown in Fig. 4.13. However, the best procedure would be to determine the effective constants from the more detailed Monte Carlo calculation for the exact location and environment once preliminary design studies have been completed.

The specific procedures needed to obtain this type of relationship between Σ_a^{eff} and the actual cross section of the lumped absorber can, for some applications, be simplified by the following considerations. In a model geometry, in which the environment is described as a homogeneous fuel region,

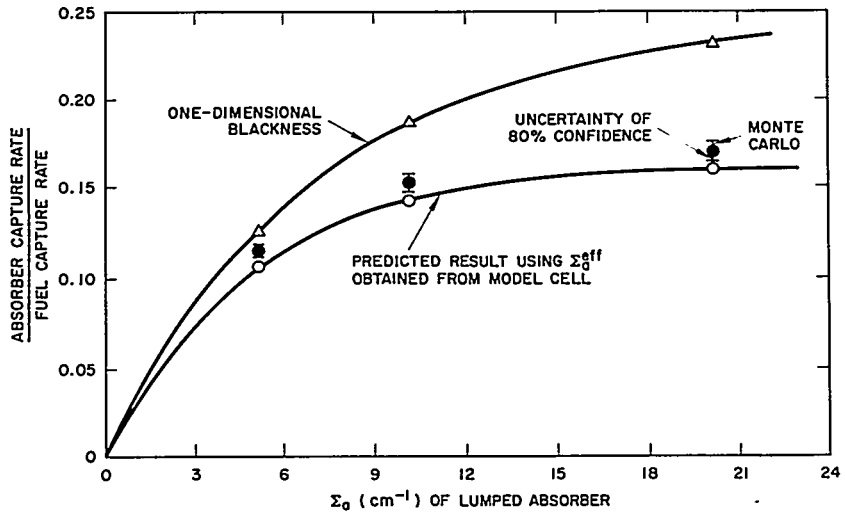

FIGURE 4.13. Relative Absorption Rates of a Two-Dimensional Absorber in a Heterogeneous Cell.

the capture rate in the absorber, relative to that in the fuel, can be written

$$\text{C.R.} = \frac{V_p \bar{\phi}_p \Sigma_a^p}{V_F \bar{\phi}_F \Sigma_a^F} = \frac{V_p}{V_F} g \Sigma_a^p \qquad \text{Eq. (4.117)}$$

where

V_p = volume of absorber
V_F = volume of fuel region
Σ_a^F = absorption cross section of fuel
Σ_a^p = absorption cross section of absorber

and

$g = \dfrac{\bar{\phi}_p}{\bar{\phi}_F}$, self-shielding factor of the absorber.

The terms in the expression for the capture rate, except for g, are physical properties of the problem. An indication as to the form of an approximate expression which will describe g is available from the solutions for two cases which have been explicitly solved. These cases involve absorbers in the form of a right circular cylinder and a semi-infinite slab in an infinite isotropic scattering medium. Examination of g^* vs ξ, where

$\xi = \dfrac{V}{S} \Sigma_a$
V = volume of the absorber
S = surface area of the absorber, and
Σ_a = absorption cross section of the absorber

shows that for a given ξ the value of g differs by no more than ~7.5 percent between these two geometries. The form of g for either of these geometries can be described by the empirical relation

$$g = \frac{1}{1 + \gamma\xi + \delta\xi^2} \qquad \text{Eq. (4.118)}$$

where γ and δ are constants. These observations suggest that the significant parameter in determining g may be ξ. For finite rectangular geometries, the variation in capture rate with

*For these problems (isolated absorbers in an infinite medium) g reduces to the ratio of flux in the absorber to the flux far from the absorber. Since there are several equivalent ways of defining the self-shielding factor, Sects. 4.6.C.3.B and 4.7.D, the reader is cautioned to be familiar with the appropriate definition for the case in question.

changes in the ratio of width to thickness of the absorber may be expected to be bounded by this ~ 7.5 percent difference between a semi-infinite slab geometry and a right circular cylinder. If this is correct, then the g of a rectangular absorber also can be written as

$$g_t = \frac{1}{1 + \gamma_t \xi + \delta_t \xi^2}$$

where the subscript t is used to denote transport (or Monte Carlo) solutions. The constants γ_t and δ_t can be evaluated by performing several transport (or Monte Carlo) calculations with varying ξ. The parameter ξ can be varied by changing either Σ_a or the volume-to-surface ratio of the absorber. Figure 4.14 shows the relationship obtained from various Monte Carlo calculations. In these problems, ξ was varied by changing both Σ_a^p and the volume-to-surface ratio of the poison. A least squares fit of the data shown in Fig. 4.14 gives values $\gamma_t = 3.593$ and $\delta_t = 0.426$. Thus, for this case, the expression used to describe g_t becomes

$$g_t = \frac{1}{1 + 3.593 \frac{V}{S} \Sigma_a^p + 0.426 \left(\frac{V}{S} \Sigma_a^p\right)^2} \qquad \text{Eq. (4.119)}$$

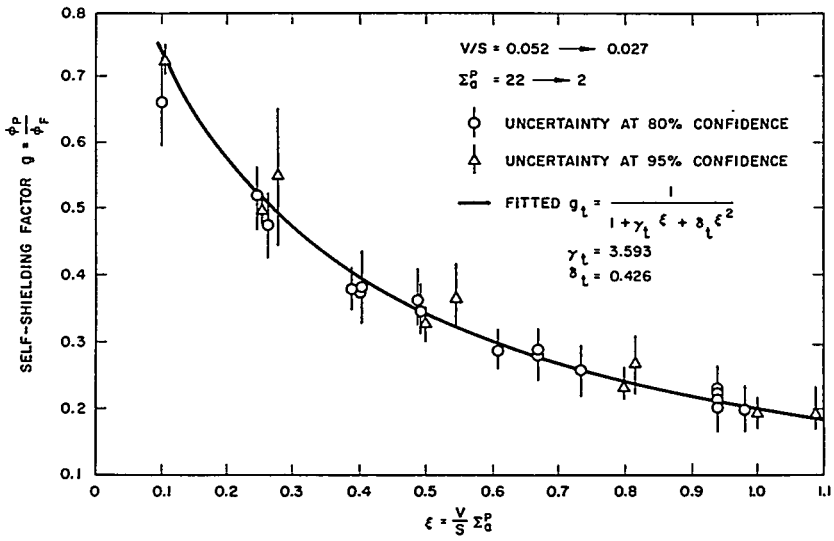

FIGURE 4.14. Monte Carlo g vs ξ for Various Absorbers.

The curve of g_t calculated from the above expression is also shown in Fig. 4.14.

Experience has shown that the g calculated by diffusion theory for Σ_a's in the range of interest for calculating effective poison constants can be described by

$$g_d = \frac{\overline{\phi}_{\text{poison}}}{\overline{\phi}_{\text{fuel}}} = \frac{1}{1 + \gamma_d \Sigma_a} \qquad \text{Eq. (4.120)}$$

The subscript d denotes diffusion theory, and the fluxes are the spatial average fluxes calculated in the diffusion theory problems.

The effective poison cross section is defined as that cross section which, in a diffusion theory calculation, yields the capture rate predicted by a Monte Carlo calculation in which the poison region is described by energy-averaged constants. Thus,

$$\left.\frac{V_p}{V_F \Sigma_a^F} g \Sigma_a^p\right|_{\text{Monte Carlo}} = \left.\frac{V_p}{V_F \Sigma_a^F} g \Sigma_a^{\text{eff}}\right|_{\text{diffusion theory}}$$

Eq. (4.121)

or

$$g_t \Sigma_a^p = g_d \Sigma_a^{\text{eff}} .$$

Substituting the analytic forms for g for each case in the above, the expression for the correlation becomes

$$\Sigma_a^{\text{eff}} = \frac{\Sigma_a^p}{1 + \left(\gamma_t \frac{V}{S} - \gamma_d\right) \Sigma_a^p + \delta_t \left(\frac{V}{S}\right)^2 \Sigma_a^{p\,2}}$$

Eq. (4.122)

This analytic expression can be used in several ways. The values of γ_t and δ_t depend only on the model cell selected (size and composition of environment) and, thus, may be evaluated for the model cell before any specific parameters of the absorber are known. The value of γ_d depends on the model cell and on the design model being used (e.g., mesh spacing in the absorber). Thus, the correlation can be adapted to changes in the design model by a single design calculation to determine γ_d.

Empirical blackness theory can be used for any problem in which a characteristic model cell can be defined. Two such applications, for which normal blackness theory cannot be used and for which empirical blackness theory must be used, can be mentioned. The first is the thermal neutron group representation of a small two-dimensional boron element, such as is present in the design of the second Shippingport core. The thermal multigroup Monte Carlo code MARC[35] can be used to define an adequate high order calculation of the absorption rate in the boron in a model cell.

A second application is the thermal representation of a one-dimensional control element whose cross section is a smooth function of energy. As has been observed previously (Table 4.7), no single one of the simply defined formulations for energy averaging of blackness coefficients is necessarily more valid than the others when the absorption cross section is a smooth function of energy. At thermal energies the SLOP-1 code,[32] for example, using a blackness theory description of the absorber, is adequate to define the correct solution.

4. Summary

In this section, the problem of representing material and structural heterogeneities in design calculations has been considered. The heterogeneities encountered in normal reactor designs are of two general types: (1) an isolated absorbing element and (2) a large lattice of absorbers in a primarily moderating medium.

In a design calculation, it is normal to describe large lattices as equivalent homogeneous media, while isolated absorbers are frequently represented explicitly. These problems have been discussed in such a manner as to suggest specific design procedures. In outline, particulate materials are first considered and calculational models outlined with which a particulate material can be described as an equivalent homogeneous material (Sects. 4.2.B and 4.2.C) which has the same interaction properties. The structural heterogeneities are then considered, utilizing the effective homogeneous materials, to obtain a means of accounting for structural heterogeneities in a finite-difference diffusion-theory design calculation, as described in Sect. 4.3. Depending on the problem and the design representation desired, one of the following procedures is used to represent a plate explicitly.

A) BLACKNESS REPRESENTATIONS.

1. Determine the absorption half-thickness $a\Sigma_a(u)$ as a function of energy from the thickness $(2a)$ of the region in

question and from the appropriate absorption cross section ($\Sigma_a(u)$) corrected for particle effects.

2. Determine the current-to-flux ratio $\alpha(u)$ at the absorber surface as a function of energy from Eq. (4.102). In performing this operation for resonance elements, use Stein's formulation [Eq. (4.127)] if the absorber contains isolated resonances. For overlapping resonances, an effective smooth cross section (or experimental) curve is used.
3. For a multigroup scheme, determine the average current-to-flux ratio for thermal groups by taking the arithmetic mean of the values of $\alpha(u)$ at the end points of the group. For each group in a few-group scheme, find $\langle\alpha\rangle$ from Eq. (4.115) over regions where the absorption is smooth or resonances overlap. Use the integral of Stein's formula [Eq. (4.127)] over regions for isolated resonances. For some applications, it may be convenient and adequate to assume $\phi(u) =$ const [Eq. (4.110)] or $c = 0$ [Eq. (4.116)].
4. For heavy absorbers, determine $\langle\beta\rangle$ values for the various groups from the approximation $\langle\alpha\rangle\langle\beta\rangle = 1/4$. If an equivalent D and Σ_a are desired to represent the control material, use Eq. (4.105) or (4.106). For gray absorbers, determine $\langle\beta\rangle$ analogously to $\langle\alpha\rangle$.
5. For absorbers with long slab blades, the blackness parameters may be determined as if the rods were infinite slabs.
6. In detailed calculations, the effect of heterogeneities in the structure immediately surrounding the absorber should be evaluated to determine the effect of the desired representation on the calculated absorption rates.

B) EMPIRICAL BLACKNESS THEORY.

1. Determine the capture rate in the absorber relative to that in some appropriate local environment by an adequate calculational tool. For this calculation, only the absorber and a characteristic environment are described. Monte Carlo calculations are appropriate for energy groups in which an accurate representation is required (for example, the TRAC,[33] MARC,[35] or TRAM[36] codes may be used for thermal single or multigroup calculations). For non-thermal groups, the TRAC or REP[37] codes may be used. For one-dimensional problems, use thermal multigroup calculations (for example, SLOP-1[32]).
2. Diffusion theory calculations for the same restricted problem are done for a series of absorber constants. For these calculations, the environment of the absorber is described as it was in Step 1.

3. The absorber representation which in the diffusion theory calculations predicts the appropriate relative capture rate, as defined in Step 1, is selected. This may be done either by trial and error, or with the aid of analytic expressions, such as Eq. (4.122).
4. It is advisable to test the constants selected in calculations which include changes in the surrounding fuel density expected to be encountered because of depletion to establish a range of adequacy of this representation.

It should be emphasized that the procedures discussed are all based on series of approximations. While these procedures have enjoyed considerable success in several situations, there is no real assurance that they will be adequate for all cases. An attempt has been made in the previous discussions to indicate ways in which the validity of the procedures has been or can be established for specific types of situations.

4.3 HOMOGENIZATION TECHNIQUES

R. S. Wick

A. Introduction

In the previous section methods of representing discrete neutron absorbers in various forms were developed. The goal of those methods was to permit an accurate representation in diffusion theory formulation of isolated or discrete absorbers (particles, plates, or rods) in explicit detail in neutron flux spatial calculations.

In this section methods of representing these isolated or discrete absorbers by a set of equivalent diffusion theory constants which apply to equivalent homogeneous regions that include the lumped absorber and surrounding material are discussed. An example would be the representation of a highly absorbing fuel plate and the adjacent water channel as single composition with its own set of equivalent diffusion theory constants. The plan of this section is first (Sect. 4.3.B) to outline the rudiments of cell theory as a method of determining homogenized constants with emphasis on the thermal energy range. Next, the methods of determining a homogeneous representation for the epithermal energy range is discussed (Sect. 4.3.C).

As implied, the first two portions of this section and in Sect. 4.2 of this chapter as well as in Chaps. 2 and 3, the common assumption is that it is possible to investigate in detail the local characteristics of a region of a reactor by the use of cell boundary conditions in the mathematical

formulation of the problem. These boundary conditions are those of zero neutron leakage into or from the region of interest. Note that in Sect. 4.2 the validity of this mathematical isolation of the region of interest was tacitly assumed, since both the diffusion theory formulation and the higher order transport theory calculations to which they were compared employed zero-current boundary conditions.

The next two portions (Sects. 4.3.D and 4.3.E) include discussions of the validity of the cell theory assumption as applied to arrays of absorbing plates and of full core calculations involving homogenization of much larger regions, including control rods and self-shielded burnable poison.

The term cell theory has often been applied to the process of isolating a local region from the remainder of the reactor for more detailed calculations. The basic assumption, the isolation of the region of interest from the remainder of the reactor, implies the use of cell theory boundary conditions wherein the gradients of the fluxes at the boundary of the region of interest are set equal to zero. It is possible to extend cell theory to take into account the nature of the material surrounding the particular region of interest. For example, in obtaining constants for a region of a core which is surrounded by other regions containing control rods, it is possible to examine the detailed solution by considering not only the region of interest but also, in the same calculation, parts of the surrounding regions containing the control rods and applying the zero-current boundary condition to this larger region. This technique is referred to as the composite cell model. On the other hand, the effect of adjacent regions on the region of interest may be represented by replacing the zero-current cell boundary conditions by estimated finite flux gradients proportional to the leakage into or out of the region of interest. The section concludes with a few remarks on modified or nonzero-current boundary conditions.

B. Methods of Obtaining Homogenized Constants from Cell Theory

The first step in obtaining homogenized constants for a portion of the reactor (referred to as the cell) is geometrically to define the cell boundaries. This process can best be illustrated by considering a specific application, such as shown in the simplified schematic in Fig. 4.15. The cell is defined as material within the pitch lines. In this case, the analysis would be broken down into various parts, as shown in Fig. 4.16. The unit subcell is first treated in detail and a set of equivalent diffusion theory P_1 constants obtained to represent the fuel-

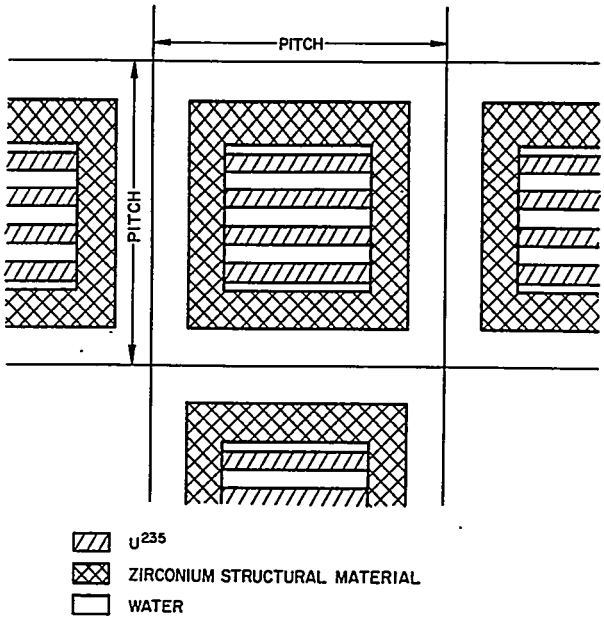

FIGURE 4.15. Array of Uniform Lattice Elements.

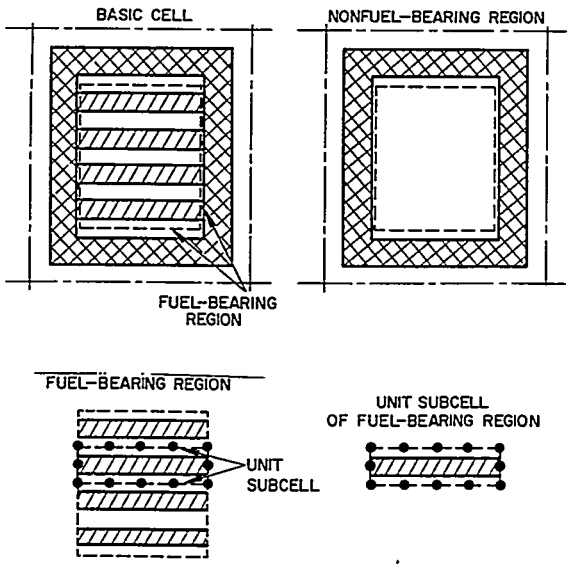

FIGURE 4.16. The Lattice Cell and Its Subregions.

bearing region. Another set of constants is used to represent the nonfuel-bearing region and, finally, a two-dimensional cell calculation, showing a fuel and a nonfuel-bearing region, is performed using diffusion theory. The results of this last calculation are used to obtain by appropriate flux volume-weighting schemes a set of equivalent homogenized diffusion theory constants to be used in subsequent core criticality and depletion studies. If the fuel plates are black enough to require transport theory to represent adequately the local self-shielding, a problem arises in representing the unit subcell by an equivalent set of P_1 diffusion theory constants. Most flux volume-weighting schemes applied to the unit subcell conserve the balance between the relative number of neutrons absorbed by the fuel and the moderator; hence, this relative balance within the volume of a particular subcell would be maintained in the subsequent diffusion theory calculations (neglecting two-dimensional effects within the unit subcell). However, there is considerable question as to the selection of an equivalent diffusion constant, D, for the unit subcell which would adequately represent the neutron leakage throughout the entire fuel-bearing region and to and from the nonfuel-bearing region. At this time, no rigorous mathematical treatment is available for obtaining this diffusion constant, D, although various schemes are used with varying degrees of success.

Since the selection of the various regions within the cell is not a simple problem, it is worth examining a more realistic case than that shown in Fig. 4.15. Consider the detailed structure of the experimental subassembly shown in Fig. 4.17. In general terms, fuel-bearing regions are identified as two identical homogenized regions separated by a thin metal-water region; a pure water region is shown in the central rod channel; and the remainder of the area around the perimeter of the fuel region is represented by other metal-water regions. Since the overall metal-to-water volume ratio (M/W) of the unrodded subassembly is 1.335, there is a large variation in local M/W ratio. In one homogenization scheme, most of the subassembly perimeter was represented by a single nonfuel region (Fig. 4.17). A revised homogenization scheme (Fig. 4.18) which represented local variations of M/W on the perimeter of the fuel region more accurately was also examined. (These two homogenization schemes will be called the initial and new homogenization schemes.)

Examination of Fig. 4.17 shows that homogeneous nonfuel region 6 includes high concentrations of structural metal at the subassembly corners. In effect, this choice of homogeneous representation moves part of the high metal concentration at the corners into adjacent subassembly edge areas where the

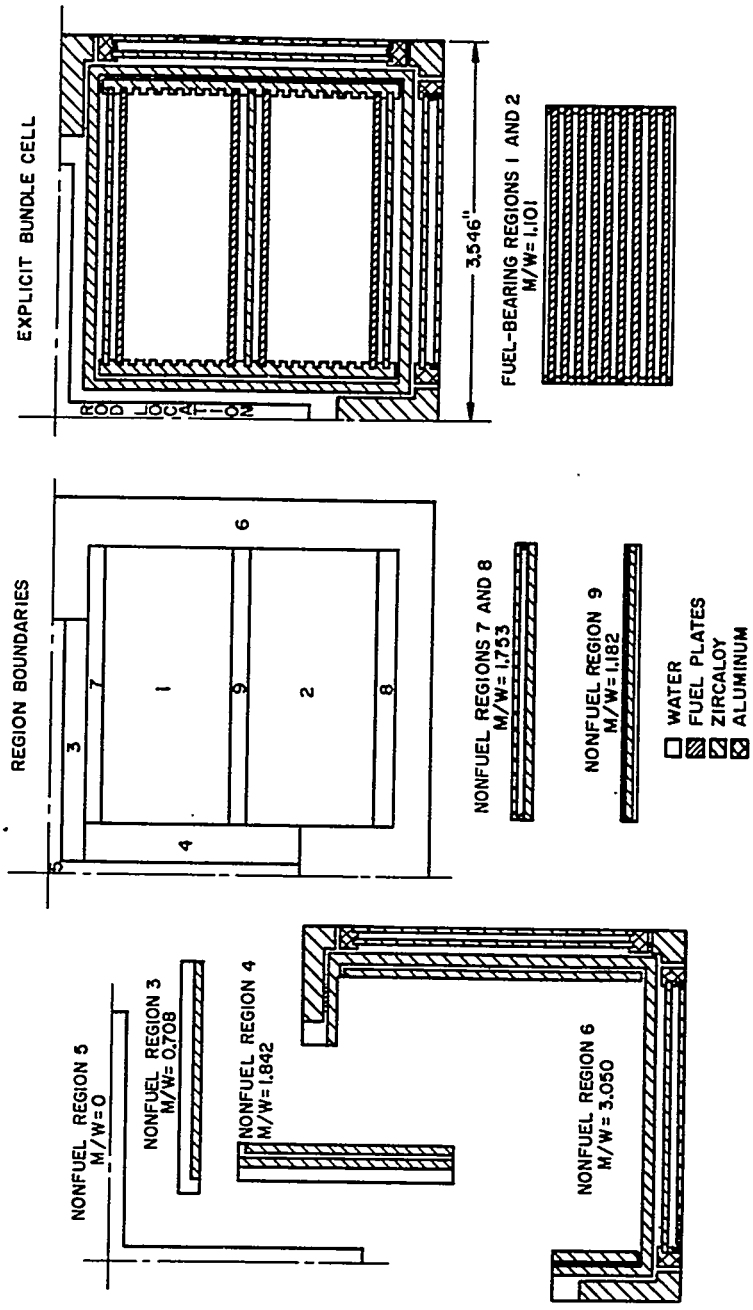

FIGURE 4.17. Typical Cell: Exploded View of Explicit Composition in Regions of Homogenization, Initial Scheme.

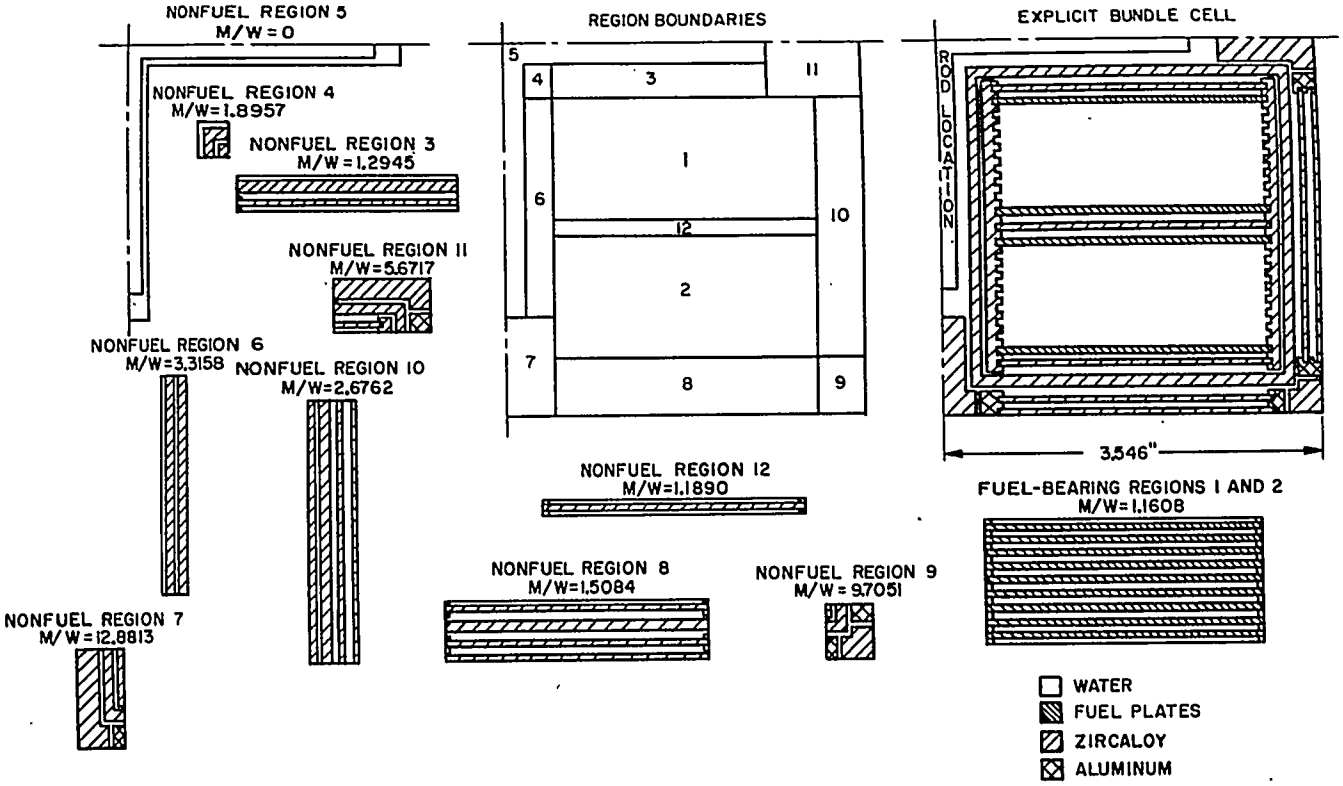

FIGURE 4.18. Typical Cell: Exploded View of Explicit Composition in Regions of Homogenization, New Scheme.

actual metal concentration is much lower. Since the apparent distribution of water concentration in the perimeter of the fuel region is also affected by this scheme, the actual spatial distribution of slowing-down source density to the thermal energy group is misrepresented to some extent. In the two subassembly edge areas between high metal concentration corner areas, the alternating metal and water strips are homogenized in a direction perpendicular to the bundle edge and also, in effect, by moving additional metal in from the corners parallel to the bundle edges. The thermal source misrepresentation is, therefore, two-dimensional in character.

In the new homogenization scheme (Fig. 4.18), the high metal concentrations at subassembly corners and the lesser metal concentrations of the bundle edge areas are represented as separate homogeneous regions. Consequently, the edge area homogenization is essentially one-dimensional in character, and the apparent thermal source density distribution is closer to the actual distribution. This improved thermal source representation is quite important, particularly if isolated lumped absorbers are present, since calculated core eigenvalues exhibit an appreciable dependence on the homogeneous representation of nonfuel regions. Flux and power shapes in the fuel region are also affected by nonfuel region homogenization. Although the difference in eigenvalue was negligible and the difference in the ratio of the maximum to average power in this subassembly as calculated with these two schemes for homogenization is only 1.5 percent, the fact that the selection of the homogenization scheme can lead to different results indicates the importance of care in selecting the homogenization scheme. The general rule for selecting a homogenization scheme is to be as explicit as possible in showing the location of the moderator with respect to the fuel regions, control rods, and isolated lumped absorbers.

A step concurrent with the first step is to define the neutron spectra for the region in question in order that the appropriately energy-averaged diffusion theory or transport theory constant may be determined for the subcell calculations. Since the spectrum changes locally within the region of interest as well as in an overall sense in going from one region to another, plausible assumptions regarding the average spectrum must be made. Because the fast spectrum does not vary to a great extent from region to region, it is customary to calculate an average fast flux spectrum for the average composition of the region. However, care must be taken to represent in appropriate detail the local removal from the epithermal group to the thermal group of neutrons by assigning macroscopic removal constants within the cell to regions where the

moderator is actually located, as has been noted. This point will be amplified further.

Next, assume that the group diffusion equations have been solved for a cell or region of the core wherein the current or flux gradient at the geometrical boundary has been set equal to zero. (It is tacitly assumed that an adequate scheme of defining the diffusion constants for the different regions within the cell has been defined by the previous discussion.) The problem solved may have been a homogeneous eigenvalue type, or it may have been a one-iteration problem of the inhomogeneous type with specified regionwise sources. (See Chap. 7 for a description of diffusion theory codes used for this type of calculation.) Historically, cell type calculations have been of the latter type in which the fast energy group is decoupled from the thermal group. For example, if a cell theory calculation in the thermal group is performed, assuming regionwise neutron slowing into the thermal energy range from higher energies proportional to the hydrogen present in each region, this is tantamount to the assumption that the spatial variation of the fission neutrons has disappeared during the slowing-down process. In this case, the equations solved are

$$\nabla D(\vec{r})\,\nabla\phi(\vec{r}) - \Sigma_a(\vec{r})\,\phi(\vec{r}) + S(\vec{r}) = 0 \qquad \text{Eq. (4.123)}$$

where

$D(\vec{r})$ = spatially dependent diffusion constant
$\Sigma_a(\vec{r})$ = spatially dependent absorption cross section
$\phi(\vec{r})$ = spatially dependent thermal flux
$S(\vec{r})$ = spatially dependent source of thermal neutrons
$\vec{r}$ = position vector.

The boundary conditions at the interface between different compositions are

$$D(\vec{r}-\vec{\epsilon})\,\nabla_n\phi(\vec{r}-\vec{\epsilon}) = D(\vec{r}+\vec{\epsilon})\,\nabla_n\phi(\vec{r}+\vec{\epsilon});\ (\lim\ \vec{\epsilon}\to 0)$$

Eq. (4.124)

and

$$\phi(\vec{r}-\vec{\epsilon}) = \phi(\vec{r}+\vec{\epsilon});\ (\lim\ \vec{\epsilon}\to 0) \qquad \text{Eq. (4.125)}$$

where $\vec{\epsilon}$ is a differential position vector and ∇_n represents the gradient normal to the interface.

Assume that the problem consists of n discrete regions over which the values of $\Sigma_a, \nu\Sigma_f$, and D are regionwise constant. If $\phi_i(\vec{r})$ represents the flux in the i^{th} region, then the

total number of absorptions which take place per unit time relative to the number of neutrons thermalized is

$$\frac{\sum_{i=1}^{n} \Sigma_{a,i} \int \phi_i(\vec{r})\, d\vec{r}}{\int_R S(\vec{r})\, d\vec{r}}. \qquad \text{Eq. (4.126)}$$

For convenience, normalize by setting

$$\int_R S(\vec{r})\, dr = 1. \qquad \text{Eq. (4.127)}$$

Note that the previous ratio [Eq. (4.126)] must be unity because the cell is defined as having zero-current boundary conditions. The number of fission neutrons produced per unit time relative to the number of neutrons thermalized [Eq. (4.126)] is

$$\sum_{i=1}^{n} \nu\Sigma_{f,i} \int \phi_i(\vec{r})\, d\vec{r} \qquad \text{Eq. (4.128)}$$

which for some values of i representing compositions not containing fissionable isotopes, $\Sigma_{f,i}$ will be zero. The number of fission neutrons produced per number of thermalized neutrons absorbed is

$$\frac{\sum_{i=1}^{n} \nu\Sigma_{f,i} \int \phi_i(\vec{r})\, d\vec{r}}{\sum_{i=1}^{n} \Sigma_{a,i} \int \phi_i(\vec{r})\, d\vec{r}} \qquad \text{Eq. (4.129)}$$

The purpose of cell theory is to provide average constants $\overline{\nu\Sigma_f}$ and $\overline{\Sigma_a}$ such that this ratio is preserved. That is, the quantities $\overline{\nu\Sigma_f}$ and $\overline{\Sigma_a}$ are the equivalent homogeneous constants which preserve the neutron balance within the confines of the cell where $\bar{\phi}$ is an average flux in the cell. Thus,

$$\frac{\overline{\nu\Sigma}_f \bar{\phi} \int_R d\vec{r}}{\overline{\Sigma}_a \bar{\phi} \int_R d\vec{r}} = \frac{\sum_{i=1}^{n} \nu\Sigma_{f,i} \int \phi_i(\vec{r})\, d\vec{r}}{\sum_{i=1}^{n} \Sigma_{a,i} \int \phi_i(\vec{r})\, d\vec{r}}. \qquad \text{Eq. (4.130)}$$

By algebraic rearrangement,

$$\frac{\overline{\nu\Sigma_f}}{\overline{\Sigma}_a} = \frac{\sum_{i=1}^{n} \overline{\nu\Sigma}_{f,i} \int \phi_i(\bar{r})\, d\bar{r} \Big/ \bar{\phi} \int_R d\bar{r}}{\sum_{i=1}^{n} \Sigma_{a,i} \int \phi_i(\bar{r})\, d\bar{r} \Big/ \bar{\phi} \int_R d\bar{r}}. \qquad \text{Eq. (4.131)}$$

It is readily apparent that it is immaterial how one defines $\bar{\phi}$, the equivalent spatially averaged flux, since it appears in both the numerator and denominator and, consequently, cannot affect the ratio $\overline{\Sigma}_f / \overline{\Sigma}_a$. One may define the average flux as

$$\bar{\phi} \equiv \frac{\sum_{i=1}^{n} \int \phi_i(r)\, d\bar{r}}{\sum_{i=1}^{n} \int_i d\bar{r}}. \qquad \text{Eq. (4.132)}$$

Substituting, one obtains

$$\frac{\overline{\nu\Sigma_f}}{\overline{\Sigma}_a} = \frac{\sum_{i=1}^{n} \overline{\nu\Sigma}_{f,i} \int \phi_i(\bar{r})\, d\bar{r} \Big/ \sum_{i=1}^{n} \int \phi_i(\bar{r})\, d\bar{r}}{\sum_{i=1}^{n} \Sigma_{a,i} \int \phi_i(\bar{r})\, d\bar{r} \Big/ \sum_{i=1}^{n} \int \phi_i(\bar{r})\, d\bar{r}}.$$

Eq. (4.133)

Setting the numerators and denominators of both fractions equal to each other,

$$\overline{\nu\Sigma_f} \equiv \frac{\sum_{i=1}^{n} \Sigma_{f,i} \int \phi_i(\bar{r})\, d\bar{r}}{\sum_{i=1}^{n} \int \phi_i(\bar{r})\, d\bar{r}} \qquad \text{Eq. (4.134)}$$

and

$$\overline{\Sigma}_a = \frac{\sum_{i=1}^{n} \Sigma_{a,i} \int \phi_i(\bar{r})\, d\bar{r}}{\sum_{i=1}^{n} \int \phi_i(\bar{r})\, d\bar{r}} . \qquad \text{Eq. (4.135)}$$

The quantities $\overline{\nu\Sigma}_f$ and $\overline{\Sigma}_a$ defined as above are called the flux volume-weighted equivalent homogeneous cell constants. Several things should be pointed out regarding the arbitrary definition of the average flux, $\bar{\phi}$. For example, redefine the average flux as that in the average in the j^{th} region:

$$\bar{\phi}' \equiv \frac{\int \phi_j(\bar{r})\, d\bar{r}}{\int_j d\bar{r}} . \qquad \text{Eq. (4.136)}$$

Then,

$$\frac{\overline{\nu\Sigma}_f}{\overline{\Sigma}_a} = \frac{\sum_{i=1}^{n} \Sigma_{f,i} \int \phi_i(\bar{r})\, d\bar{r} \Big/ \bar{\phi}' \int_R d\bar{r}}{\sum_{i=1}^{n} \overline{\Sigma}_{a,i} \int \phi_i(\bar{r})\, d\bar{r} \Big/ \bar{\phi}' \int_R d\bar{r}} \qquad \text{Eq. (4.137)}$$

and

$$\overline{\nu\Sigma'_f} \equiv \frac{\sum_{i=1}^{n} \Sigma_{f,i} \int \phi_i(\bar{r})\, d\bar{r}}{\int \phi_j(\bar{r})\, d\bar{r} \dfrac{\int_R d\bar{r}}{\int_j d\bar{r}}} \qquad \text{Eq. (4.138)}$$

$$\bar{\Sigma}'_a \equiv \frac{\sum_{i=1}^{n} \Sigma_{a,i} \int \phi_i(\bar{r})\, d\bar{r}}{\int \phi_j(\bar{r})\, d\bar{r} \dfrac{\int_R d\bar{r}}{\int_j d\bar{r}}} \qquad \text{Eq. (4.139)}$$

Even though $\bar{\Sigma}'_f$ and $\bar{\Sigma}'_a$ differ from Σ_f and $\bar{\Sigma}_a$, respectively, the ratio of fission neutrons produced to those absorbed is constant. However, the method of averaging does affect the flux volume-averaged diffusion length; hence, the method of averaging cannot be considered arbitrary. Note that the flux volume-weighting procedure is identical for multigroup cell theory calculations and is the same for each group as that described above.

To obtain a complete neutron balance throughout the core, i.e., an accounting of all possible neutron interactions, it is necessary to determine the appropriately averaged transport or diffusion constants for the various regions of the core as well as for the various subregions of the cell. The definition of an equivalent homogeneous diffusion constant via cell theory is not as straightforward conceptually as defining equivalent homogeneous absorption and fission cross sections, since by their very definition neutron balance between absorption in different types of material is conserved. As will be shown in the succeeding sections the description of the leakage from one region to another by employing constants obtained by the cell theory approximation is not straightforward and is, perhaps, that part of cell theory which leads to its weakness in many cases.

One of the basic problems of defining the equivalent homogeneous diffusion constant lies in the assumption that diffusion coefficients are scalar quantities. Examination of the simplified subassembly of Fig. 4.15 would lead to the expectation that, if the mean free paths of neutrons were significantly different in the different materials, there would be a different leakage perpendicular to the cross-sectional plane of the subassembly than in either the direction parallel or perpendicular to the fuel plates in the cross-sectional plane of the subassembly.

As was noted, the first step in the calculation of the subassembly or cluster via cell theory approximations is to replace the unit subcells consisting of a fuel plate and associated water

channel by an equivalent homogenized material. Flux volume-weighted absorption and fission cross sections can be obtained by using the flux-weighting procedure outlined above. Following the procedure to be outlined in subsequent sections, one could perform calculational tests to verify at least in one-dimension (i.e., a perpendicular section through the fuel plates) whether any particular edge effects occur where the unit subcells terminate and the subassembly structural material starts. It is, however, currently impossible on a practical scale to extend this type of theoretical comparison of models to a two-dimensional detailed explicit transport theory type calculation showing all the plates and structure. The importance of such effects can be assessed by making different assumptions and comparing the results of one-dimensional calculations.

The first decision to be made is that of determining how the equivalent diffusion constant for the fuel-water channel subcells will be defined. The second decision to be made is that of determining how the more gross regionwise local diffusion constants will be weighted to yield equivalent homogeneous region diffusion constants for the entire subassembly of Figs. 4.15 or 4.17. Once the local region constants have been determined if an axial synthesis of radial or horizontal sections of the core is to be performed (see Sect. 4.4) from explicit radial calculations (where the fuel plates and coolant channels have already been homogenized, but where fueled regions, nonfueled regions, control rods, lumped absorbers, etc., are explicitly represented), a similar decision has to be made regarding the determination of an equivalent diffusion constant for axial or transverse calculations.

There is extensive literature on the phenomenon of preferential or anisotropic diffusion of neutrons through a fuel plate-water channel infinite lattice.[38-46] The problem for more complicated configurations, such as those shown in Figs. 4.16 and 4.17, has not been attacked theoretically because of mathematical difficulties. A digest of the references just cited indicates that there is, based on one-energy type calculations, an anisotropic diffusion of neutrons in regions of alternating fuel plates and water channels. This effect is expressed by the difference in the diffusion length, L, for the direction perpendicular, $L_{\perp}$, and parallel, $L_{||}$, to the fuel plates. For a plane $(y-z)$ source at the origin of the x axis, the flux in a homogeneous region is

$$\phi = A e^{-x/L} \quad , \qquad \text{Eq. (4.140)}$$

where A is a normalization constant, and L is diffusion length. In the P_1 or diffusion theory approximation,

$$L^2 = \frac{D}{\Sigma_a} \qquad \text{Eq. (4.141)}$$

where D is the diffusion coefficient, and Σ_a is the macroscopic absorption constant. For the array of Fig. 4.19, Shevelev finds approximately

$$L_{\perp}^2 \simeq \frac{1}{3(\Sigma_a)_{ave}(\Sigma_{tr})_{ave}} \qquad \text{Eq. (4.142)}$$

where

$$(\Sigma_a)_{ave} = \frac{\delta_1 \Sigma_{a1} + \delta_2 \Sigma_{a2}}{\delta_1 + \delta_2} \qquad \text{Eq. (4.143)}$$

and

$$(\Sigma_{tr})_{ave} = \frac{\delta_1 \Sigma_{tr1} + \delta_2 \Sigma_{tr2}}{\delta_1 + \delta_2} \qquad \text{Eq. (4.144)}$$

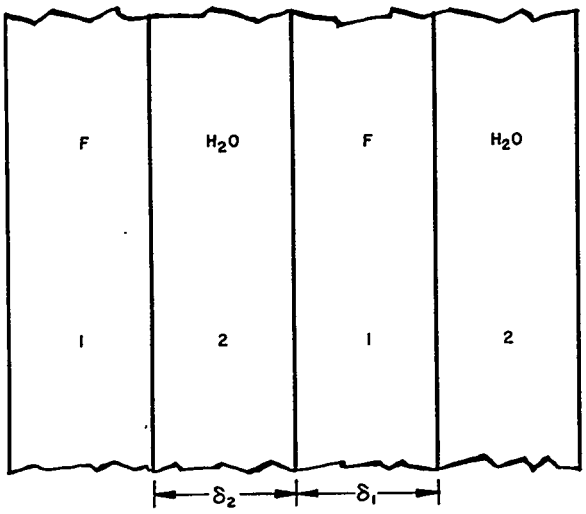

FIGURE 4.19. Nomenclature for Anisotropic Diffusion.

If one defines

$$D = \frac{1}{3\Sigma_{tr}} \qquad \text{Eq. (4.145)}$$

which is approximately true for little absorption, $(\Sigma_{tr})_{ave}$ becomes

$$(\Sigma_{tr})_{ave} = \frac{1}{3}\,\frac{\delta_1 \frac{1}{D_1} + \delta_2 \frac{1}{D_2}}{\delta_1 + \delta_2} \qquad \text{Eq. (4.146)}$$

or, since this implies

$$\left(\frac{1}{D}\right)_{ave} = 3(\Sigma_{tr})_{ave} \qquad \text{Eq. (4.147)}$$

$$L_{\perp}^2 = \frac{1}{\Sigma_a \left(\frac{1}{D}\right)_{ave}} \cdot \qquad \text{Eq. (4.148)}$$

Therefore, a good approximation to $L_{\perp}^2$ is obtained by volume weighting Σ_a and $1/D$ of the plate and water channel. Since the fluxes in the fuel and water channel are not greatly different, it would appear that a reasonable value of the diffusion coefficient would be the flux volume-weighted reciprocal value. That is,

$$D_1 = \frac{\phi_1 \delta_1 \frac{1}{D_1} + \phi_2 \delta_2 \frac{1}{D_2}}{\phi_1 \delta_1 + \phi_2 \delta_2} \qquad \text{Eq. (4.149)}$$

and

$$\Sigma_a = \frac{\phi_1 \delta_1 \Sigma_{a1} + \phi_2 \delta_2 \Sigma_{a2}}{\phi_1 \delta_1 + \phi_2 \delta_2} \qquad \text{Eq. (4.150)}$$

should give a reasonable estimate of $L_{\perp}^2$.
Shevelev indicates that for diffusion parallel to the plates,

$$L_{||}^2 \approx \frac{(D)_{ave}}{(\Sigma_a)_{ave}} \qquad \text{Eq. (4.151)}$$

where

$$D_{ave} = \frac{\delta_1 D_1 + \delta_2 D_2}{\delta_1 + \delta_2} \qquad \text{Eq. (4.152)}$$

or that the diffusion constant rather than the reciprocal diffusion constant should be volume-weighted.

Although the literature quoted indicates that in extreme cases the ratio of $L_{||}^2$ to $L_{\perp}^2$ may go as high as 2, the assumptions made in these analyses do not warrant serious considerations of these differences because of the small plate and channel dimensions in most pressurized water reactors. Reference 46 does contain experimental verification of the above phenomena. Since, in practice, diffusion theory is not used to obtain plate self-shielding factors (see Sect. 4.2) but higher order transport calculations perpendicular to the plates, the usual practice is to construct, for future diffusion theory calculations, the equivalent diffusion coefficient from flux volume-weighted transport cross sections. That is

$$D_{equivalent} = \frac{1}{3(\bar{\Sigma}_a + \bar{\Sigma}_{S0} - \bar{\Sigma}_{S1})}, \qquad \text{Eq. (4.153)}$$

where the $\bar{}$ indicates a flux volume weighting, as defined in Eq. (4.135).

Obtaining equivalent diffusion coefficients for a cell, such as described by Fig. 4.16 or 4.17 after the fuel region has been replaced by equivalent homogenized fuel-water channel subcells, presents similar conceptual difficulties to those discussed above. The following general rules may be used as a guide. If the equivalent homogeneous cell theory constants representing an entire cluster or subassembly, as described in Sect. 4.3.E, are to represent a radial or horizontal traverse of a core where the axial (or perpendicular to the plane of calculation) leakage is not significant relative to the radial leakage, flux volume weighting of $1/D$ may be used to obtain equivalent diffusion coefficients. Note that in the high energy groups, flux volume weighting $1/D$ or flux volume weighting D usually gives nearly similar results, since the fast fluxes are relatively flat. The choice between flux volume weighting $1/D$ or D often is not too significant in the thermal group, since the radial leakage term $D_{th}B_m^2$ (where B_m^2 is the material buckling) is usually insignificant relative to the fast leakage $D_f B_m^2$.

If radial explicit calculations, assuming the fuel plate-water channel arrays have been replaced by an equivalent homogeneous region, are to be patched or synthesized by axial calculations in the perpendicular direction (see Sect. 4.4), a flux volume weighting of D is usually obtained for this calculation.

When isolated lumped absorbers are present which produce large perturbations in the flux, there is no straightforward approach to obtaining the equivalent diffusion constant. The approximations used should be compared to more exact calculational models; or, if possible, a more explicit calculational model showing the isolated lumped absorbers explicitly should be used. These problems are discussed in greater detail in Sect. 4.3.E. In general, it is advisable to use more explicit representation of lumped absorbers rather than attempt to develop an equivalent homogeneous representation of them.

C. Arrays of Epithermal Self-Shielded Absorbers

W. H. Hannum

1. Introduction

The methods of determining homogeneous cross sections for arrays of plates with appreciable epithermal self-shielding differ from those just discussed, since resonance cross section varies so rapidly with energy that a simple averaging of the resonance cross section over the energy range of interest does not adequately describe resonance capture phenomena. An equivalent homogeneous representation can, however, be developed which describes a large regular array of absorbing plates. In this case, an equivalent homogeneous region is defined as one which maintains the proper slowing-down-to-capture ratio (or resonance escape probability) and the proper relative capture rates among the materials composing the actual heterogeneous array.

Lattices of resonance absorbers also require different techniques because of the strong interaction between spatial and energy-dependent effects. Although much work has been done on slightly enriched arrays, the specific illustrations of techniques to be used are based on studies in which the fuel material is natural uranium. Other reactor configurations are likely to represent less extreme resonance lattices, but many of the techniques to be described should be equally valid. For example, it may be desired to consider the resonance structure of U^{235} in a highly enriched lattice. The analytic procedures used for handling this situation are similar to those for natural uranium.

The general procedures described in Chaps. 2 and 3 are also available and appropriate for treatment of regular lattices. In fact, the calculational tools are, in general, specifically designed for calculations which employ zero-current or cell theory boundary conditions. The additional development required is in terms of an adequate design representation and of verifying the adequacy of the representations used (cf. Sect. 4.3.D).

The available design depletion codes include a special formulation with which to describe U^{238} (see Chap. 7 and also Sect. 4.6.D of this chapter). The basis of this scheme and the manner in which it is included in depletion calculations is discussed in detail elsewhere (see Sect. 4.6.D and Chap. 2, Sect. 2.9). From an operational point of view, it is sufficient to observe that the epithermal energy group diffusion theory parameters in the current diffusion theory depletion codes are expressed in terms of a quantity p_{R3}^{28}. This quantity, p_{R3}^{28}, is the probability of a neutron not being captured in the resonances of U^{238} per neutron captured in U^{238} or slowed down out of the resonance region. It may be observed that this is a special quantity defined for the depletion code formalism and bears no direct relationship to the resonance escape probability as it is commonly defined.

It is convenient to consider one further simplification of this problem. It is assumed that (with adjustments to be considered later) the smooth and effective cross sections involved in the definition of p_{R3}^{28} are to be energy-averaged over an energy spectrum characteristic of homogeneous materials distributions. If this is done using a formulation such as is present in the MUFT code,[30] the desired resonance capture probability is supplied in terms of L factors. The L factor is defined as the true heterogeneous resonance capture probability, as calculated by some method yet to be specified, divided by the capture probability in a homogeneous mixture of the materials as calculated by the MUFT code. Using this information, the cross sections appearing in the definition of p_{R3}^{28} are determined as appropriately energy-weighted averages. The problem of determining an appropriate diffusion theory representation of a large lattice of resonance absorbers is, thus, equivalent to that of obtaining appropriate heterogeneous resonance integrals, or L factors, discussed in Chap. 2, Sect. 2.5. This discussion will be restricted to the illustrations of the applicability of various procedures.

There are four general classes of techniques for the calculation of heterogeneous resonance integral. The first, the method of escape probabilities, is described in Ref. 47. The second involves the use of analytic approximations utilizing blackness theory (Sect. 4.2.D.2). The third involves a Monte Carlo calculation for the geometry in question. The fourth is the effective surface-to-mass formulation. The approximate techniques for one-dimensional lattices are considered first.*

*In the following examples there is frequently no distinction indicated between one- and two-dimensional situations in that analogous procedures are available for both one and two dimensions. Most of the calculational tools used are designed to handle regular lattices of fuel rods as well as plates, so that the same comments generally apply to rod lattices as to plate lattices.

2. *Blackness Theory Approximation*

For an infinite array of plates or rods in water, which can be represented by a cell consisting of a single plate or rod with its associated water and the boundary condition of zero neutron leakage, the theoretical formulation for the resonance escape probability used is that of S. Stein (see Chap. 2 and Ref. 26). This theoretical formulation is based on the following assumptions: (1) Moderation is due to the hydrogen in the water only; (2) the scattering cross section of the moderator is energy-independent over the entire resonance region; (3) absorption may be considered to occur in the fuel resonances only, i.e., the effect of a smooth absorption cross section may be treated separately; (4) the resonances of the absorber are assumed narrow and widely spaced, so that each resonance can be treated separately; (5) the source of neutrons slowing down in the water into each resonance energy range is spatially flat.

For this situation, the heterogeneous resonance integral written in terms of energy is given by

$$\text{RI (heterogeneous)} = \int_{E'}^{E''} \frac{1}{\ell \Sigma_s} \left(\frac{\alpha\,[x(E)]}{1 + c\,\alpha\,[x(E)]} \right) \frac{dE}{E} \qquad \text{Eq. (4.154)}$$

where E' and E'' are arbitrary cutoff energies below and above the level of the resonance, α is the blackness coefficient relating the current to the flux at the surface of the absorbing medium, ℓ is the half width of the water channel, and Σ_s is the macroscopic scattering cross section of hydrogen in the water channel. The energy dependence is expressed in terms of the resonance half width

$$x = \frac{2}{\Gamma}(E - E_o). \qquad \text{Eq. (4.155)}$$

E_o is the resonance energy and Γ is the total level width. It is assumed that each resonance is symmetric about E_o. The $1/E$ flux term, taken as $1/E_o$, may be removed from the integrand by assuming that the resonance is thin enough that the change in energy is negligible while integrating across the resonance. Further, the integrand is negligible beyond E' and E'' (for widely spaced resonances), so that the limits of

integration may be extended to 0 and ∞. The resonance integral then becomes

$$\text{RI (heterogeneous)} = \frac{2}{E_o} \int_o^\infty \frac{1}{\ell \Sigma_s} \left(\frac{a(x)}{1 + c\,a(x)} \right) dx \,.$$

Eq. (4.156)

The parameter c depends only on the cell geometry. For the uniform array of plates and water channels of half thickness ℓ,

$$c = \sqrt{3} \coth \left(\sqrt{3}\, \Sigma_s \ell \right) \,.$$

For cylindrical geometries,

$$c = \sqrt{3} \frac{K_o(kr_1)\, I_1(kr_2) + I_o(kr_1)\, K_1(kr_2)}{K_1(kr_1)\, I_1(kr_2) - I_1(kr_1)\, K_1(kr_2)} \qquad \text{Eq. (4.157)}$$

where

$k = \sqrt{3}\, \Sigma_s$

r_1 = fuel radius

r_2 = cell radius

The terms I_n, K_n are the Bessel function of complex arguments as defined by Watson.[48]

An approximate energy integration is available (Chap. 2, Sect. 2.5) for the case of no Doppler broadening by considering the absorbing region either as a black boundary or nearly transparent. This approximate integration leads to the expression

$$\text{RI (heterogeneous)} = A \frac{\Gamma}{E_o} \sqrt{\sigma_o} \sqrt{\frac{1}{2a N^{28}_{\text{fuel plate}}}} \left\{ \frac{1}{2 + c} + \frac{1}{2} \frac{\tan^{-1} \left(\frac{c}{2} \right)^{1/2}}{\left(\frac{c}{2} \right)^{1/2}} \right\}$$

Eq. (4.158)

where

N^{28} = number density of uranium in the plate

A = empirical constant = 0.9

σ_o = absorption cross section at the resonance energy

a = half-thickness of the plate.

This expression may be summed over all resonances to obtain a total resonance integral over known resonances [see Eq. (4.156)].

In this expression, it will be noted that the dependence on resonance parameters is confined to the factor

$$\frac{\Gamma}{E_o}\sqrt{\sigma_o}$$

which makes this procedure convenient for survey work when the effect of Doppler broadening may be ignored or estimated from other more explicit calculations.

These expressions can be readily adjusted for clad rods,[26] treating the clad as void, by replacing c in Eq. (4.158) by $\frac{r_o}{r_1}c$ where

r_0 = fuel radius

r_1 = radius of clad rod

This treatment of the resonance self-shielding has been extended by Wick[49] to the case of arrays uniformly interrupted by moderator regions which simulate actual mechanical structures. The solution of the one-energy problem showing the nonuniform array can be used to define effective absorber constants as a function of energy for each plate of an array, accounting for the interaction among plates in a nonuniform array. An energy averaging analogous to that of Stein [Eq. (4.156)] then yields relative capture rates or resonance escape probabilities for each individual plate. The application of this technique is discussed further in Sect. 4.3.D and in Ref. 49.

3. *Monte Carlo Methods*

A more detailed calculational tool is available for the calculation of a heterogeneous resonance escape probability in terms of Monte Carlo slowing-down formulations, such as is used in the REP codes (see Chap. 7 and Ref. 37). In this formulation, scattering (including resonance scattering), moderation, and absorption (both resonance and smooth) may be included in any of the several one- and two-dimensional geometric configurations. The inclusion of these other factors, particularly smooth capture, requires that some caution be used with the definition intended by the term resonance escape probability.

There are two ways in which such Monte Carlo calculations may be used in the calculation of p_{R3}^{28}. The first procedure which may be considered is to describe the physical problem in as

much detail as possible and to use the results of this calculation to establish p_{R3}^{28}. This type of representation must necessarily describe not only the resonance and moderating properties but also the smooth capture of all materials. Leakage perturbations would normally be ignored.

A second use of Monte Carlo resonance escape calculations is to supply information from which the L factor, or factors, can be determined for use in a homogeneous slowing-down code, such as MUFT. An L factor is defined as the true heterogeneous resonance integral divided by a homogeneous resonance integral. This factor then multiplies (for each resonance) the homogeneous resonance integral calculated by the slowing-down code. Even if a Monte Carlo calculation cannot conveniently be used to calculate the true heterogeneous resonance integral, it may still be feasible to use such a calculation to obtain an L factor by making one of several assumptions. It may be assumed that the ratio of heterogeneous to homogeneous resonance integral (L considered as a resonance self-shielding factor) is independent of such factors as smooth absorption.

A second condition would be that neutrons encounter the resonances before encountering any smooth cross section. In this case, the resonance integrals are

$$p_{res} = 1 - RI \simeq \exp(-RI)$$

where p_{res} is the probability of not being captured in a resonance. This, if resonance capture occurs first, is

$$p_{res} = 1 - \frac{\text{neutrons captured in resonances}}{\text{neutrons captured or slowed down past resonances}}$$

$$= 1 - \frac{\text{neutrons captured in resonances}}{\text{neutrons entering resonance range}} \quad \text{Eq. (4.159)}$$

For this case, these resonance integrals again may be calculated without reference to smooth capture.

A third situation in which L is independent of smooth absorption is when neutrons encounter the resonances after encountering all of the smooth cross section. In this case, some caution must be used in defining p_{res}. The probability of not being captured in resonances should be considered per neutron not captured in the smooth absorption. This again considers the probability of capture per neutron available for resonance capture. In this and the preceding cases, the p_{res} is not the p of the standard REP codes unless the smooth cross sections are set to zero. The proper p_{res} is, however, again invariant to smooth capture.

Thus, under one or another of these conditions, a heterogeneous resonance integral may be calculated with the smooth absorption cross section taken to be zero. This quantity is then assumed to be invariant to smooth absorption. With only resonance absorption considered, the total number of neutrons slowing down past the resonance energy range per neutron entering the resonance energy range may be written

$$p(MC) = 1 - \frac{\text{neutrons captured in resonances}}{\text{neutrons entering resonance range}} .$$

The significance of omitting the interfering smooth capture is discussed below.

To define an L factor, it is also necessary to obtain a homogeneous resonance integral which must contain approximations consistent with those used for the calculation of the heterogeneous resonance integral. One such condition is that this homogeneous resonance integral be appropriate to the case of no smooth absorption. Other conditions will depend on the homogeneous slowing-down model being used.

The preceding discussion of the procedures for calculating the resonance integrals involved in the L factor is not specifically limited to any given energy range. Thus, the discussion is equally applicable to the determination of the L factor for a single resonance or for the entire resonance energy range. For a single resonance, the interfering smooth capture may be ignored, with the smooth capture cross section being considered a combination of preceding and succeeding smooth cross sections. As described earlier, this case can be handled without consideration of the smooth capture. Thus, interfering smooth capture does not significantly affect the single resonance L factor. The smooth capture between resonances can, however, affect a single average L factor. Denoting the number of resonance captures as N, and identifying Monte Carlo numbers by the superscript R, and MUFT numbers by M, the single L factor for a pair of resonances with no smooth capture is

$$L_{2\,(\text{no smooth})} = \frac{N_1^R + N_2^R}{N_1^M + N_2^M} . \qquad \text{Eq. (4.160)}$$

Introducing p_s, the probability of not being captured by the smooth cross section between the resonances, the L factor with smooth capture becomes

$$L_2(\text{with smooth}) = \frac{N_1^R + p_s N_2^R}{N_1^M + p_s N_2^M}. \qquad \text{Eq. (4.161)}$$

$L_2(\text{no smooth})$ and $L_2(\text{with smooth})$ are equal (for $p_s \neq 0$, $N_i \neq 0$) if and only if the separate L factors are equal:

$$\frac{N_1^R}{N_1^M} = \frac{N_2^R}{N_2^M}.$$

For more than two resonances, there will tend to be some cancellation of differences between including and omitting the terms. If all individual resonances have the same L factor, then the total L factor is unaffected by the smooth capture. If the L factors differ, it will be coincidental if the single L is the same with and without interference. Thus, if a single L factor is used, some caution is necessary to ensure that it is an appropriate average.

4. *Effective Surface-to-Mass Formulation*

A procedure for interpolating among cases in terms of an effective surface-to-mass ratio, as suggested by Wigner and formulated by Nordheim,[50] may be used for many one- and two-dimensional geometries. It has been observed by Nordheim that the resonance integral for a fixed absorber composition and $(S/M)_{\text{eff}}$* is nearly independent of lattice spacing, moderator, and absorber shape. Such a parameterization of the problem has the advantage of permitting a relatively small number of experiments (or calculations) to determine the resonance integral in a wide variety of situations. The considerations and approximations leading to this prediction are discussed in Chap. 2, Sect. 2.5. The problem considered is an infinite mass absorbing nucleus, and under this assumption it is shown that the neglect of scattering in the absorbing region is a reasonable approximation for these resonances. Several empirical tests of the validity of this model have been made and show reasonable agreement with Monte Carlo results for various cases of practical interest.

*The eff here implies the inclusion of a Dancoff correction. The particular form of the Dancoff correction used is based on Wigner's rational approximation (see Chap. 2, Sect. 2.5).

In this formulation, the resonance integral may be expressed as a function of absorber composition

$$(S/M)_{\text{eff}} = \frac{(S/M)_{\text{Absorber}}}{1 + \dfrac{S_{\text{mod}}}{4\, V_{\text{mod}}\, \Sigma_s}} \,. \qquad \text{Eq. (4.162)}$$

$(S/M)_{\text{Absorber}}$ is the surface-to-mass ratio of the absorber, S_{mod} is the inner surface of the moderator, V_{mod} the moderator volume, and Σ_s the scattering cross section of the moderator. While the comparisons have been favorable, several operational limitations may be indicated. The range of validity of an expression, such as is given in Eq. (4.162) must be considered to be limited to the range in which it is determined. For very tightly coupled lattices, the range of applicability can be quite limited. Second, the form used here explicitly excludes consideration of temperature variations. Third, the formulation assumes a nonre-entrant fuel shape completely surrounded by moderator. A clad platelet geometry (e.g., PWR-2 blanket) is not characterized by fuel completely surrounded by moderator. Thus, direct calculations of specific cases of interest are required by Monte Carlo techniques.

5. Summary

1. A heterogeneous resonance integral is calculated. This may be done, for example, using the REP[37] code. This calculation should describe: (a) physical geometry and materials compositions, (b) Doppler-broadened resonance shapes, (c) a specific set of resonance parameters, (d) smooth cross sections set to zero, (e) $RI\,(\text{heterogeneous}) = -\ln\,[p(\text{rep})]$ where

$$p(\text{rep}) = 1 - \frac{\text{number of neutrons slowing down out of resonance energy range}}{\text{number of neutrons entering resonance energy range}} \,.$$

2. A homogeneous resonance integral is calculated, using the same resonance parameters as above. For example, this may be done using the MUFT[30] equations.

3. Using MUFT, an L factor is defined as

$$L = \frac{\text{RI(heterogeneous)}}{\text{RI(MUFT)}} \,.$$

4. A MUFT calculation is done using (a) homogeneous materials composition, (b) L as defined by Step 3. These energy-averaged constants are used as effective diffusion theory constants, or special functions such as p_{R3}^{28} are obtained from MUFT.

D. The Validity of Cell Theory for Arrays of Absorbing Plates

The validity of treating arrays of absorbing plates by cell theory will now be discussed. Two types of arrays are those which consist of (1) weakly absorbing plates and (2) strongly absorbing plates. These types are to be distinguished from arrays which contain isolated strongly absorbing plates, already discussed under the topic of self-shielding. The definition of weakly absorbing is that the self-shielding of this plate, while significant, is small (between approximately 0.9 to 1.0 plate disadvantage factor) when compared to control rod blades or self-shielded lumped burnable poisons. Strongly absorbing plates are encountered when considering plates containing nuclei of high resonance cross sections such as U^{238} or uniformly dispersed homogeneous poisons in fuel.

First, the validity of assigning each plate in an array its own half water channels for the purpose of defining a subcell and obtaining equivalent constants can be tested in a one-energy case. This can be done by assuming different subcell definitions and then checking whether a synthesis of these subcells agrees with a check calculation showing each plate explicitly. In the example, several possible sets of rational cells (the various shaded areas in Fig. 4.20) containing different groups of absorbing plates are treated separately to obtain thermal group constants, and the resulting calculated thermal utilization is compared to that calculated showing each plate in detail. The effect of water, control rod extension, and control rod at one end of the array is also considered. The same order transport theory was used in the detailed calculation as in the calculation of the plate-channel homogeneous constants by cell theory. The results indicated on Fig. 4.20 show the validity of the assignment of local region homogenized constants obtained with cell theory. The use of these local region constants in a two-dimensional calculation is illustrated in Fig. 4.21.

Second, the problem of calculating the power density in a specific plate by means of a cell theory is considered. When equivalent homogeneous constants are used to represent the fuel plates of Fig. 4.15, a continuous power will be calculated across the entire fuel-bearing region (Fig. 4.16), while in physical reality the power density will be discrete (in each plate). Since diffusion theory does not adequately describe the

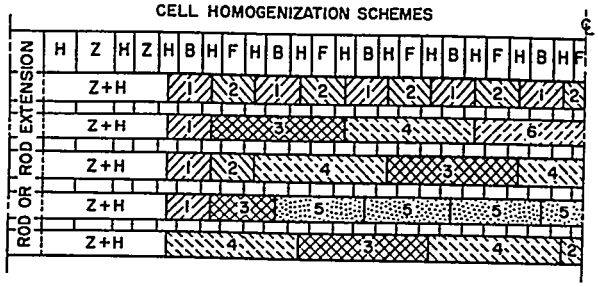

TABLE OF ηf

1-GROUP NO ROD	1-GROUP ROD	2-GROUP ROD
1.258	0.9582	1.018
1.261	0.9626	1.016
1.254	0.9587	1.012
1.257	0.9590	1.012
1.254	0.9607	1.015
1.257	0.9581	1.011

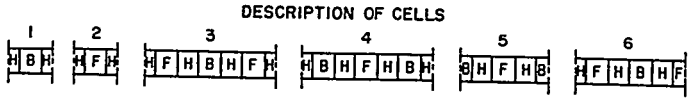

H=H_2O CHANNEL (Σ_a = 0.019139)
Z=ZIRCALOY-2 PLATE (Σ_a = 0.006862)
B=BORON ZIRCALOY-2 PLATE (Σ_a = 0.146728)
F=U^{235} ZIRCALOY-2 PLATE (Σ_a = 0.383864)

FIGURE 4.20. Study of Rational Subcell Arrangements.

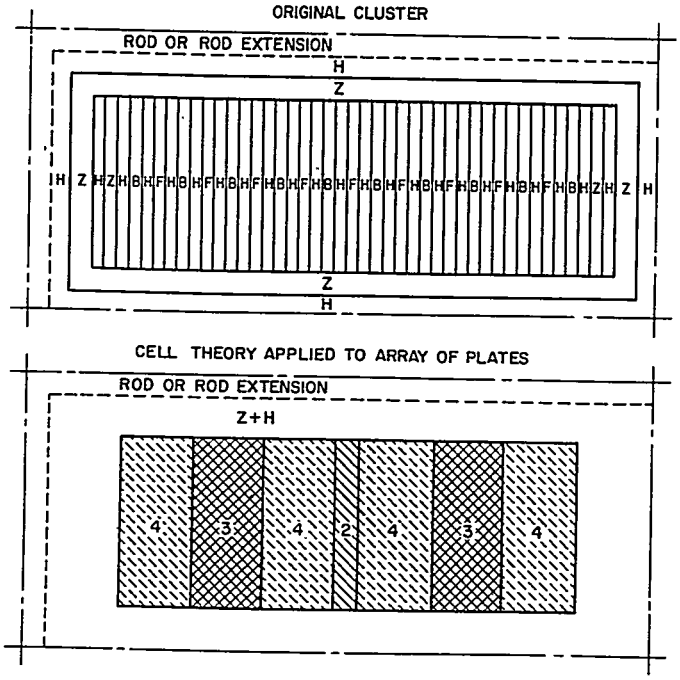

H = H_2O CHANNEL (Σ_a = 0.019139)
Z = ZIRCALOY-2 PLATE (Σ_a = 0.006862)
B = BORON ZIRCALOY-2 PLATE (Σ_a = 0.146728)
F = U^{235} ZIRCALOY-2 PLATE (Σ_a = 0.383864)

FIGURE 4.21. Use of Subcells in Subassembly Calculations.

strong gradients in the thermal flux which usually occurs in the region of local peak powers, the peak power calculated with cell theory homogenized constants relative to the average power can be underestimated by several percent, depending on the particular case. The importance of such a nonconservative estimate depends on the margins or allowances in the thermal design of the core. A method of determining the magnitude of this effect is to construct equivalent one-dimensional transport theory calculations explicitly showing the individual fuel plates and large water regions, and comparing these results to those of diffusion theory calculations employing the homogenized fuel region constants obtained from cell theory. A suitable empirical correction factor can then be determined from these calculations. Using homogenized fuel-bearing regions consisting of an integral number of plate-channel cells, it is important that the local variations in metal-to-water ratio be described in detail to represent adequately the local power distributions.

In determining the thermal group transport constants to be used in transport theory cell calculation of a fuel plate and its adjacent water channels, the assumption of the separability of space and energy within the thermal energy range is often made. A thermal spectrum is assumed or calculated, based on a homogeneous mixture of all the elements in the cell (see Chap. 3), and energy-weighted group constants subsequently determined for use in the spatial transport calculation. The emphasis is usually on refining the subsequent spatial calculation by using higher order transport theory. The validity of this assumption should be investigated for fuel plate-water channel array under consideration by performing calculations using a thermal multigroup transport code such as SLOP-1 (see Chaps. 3 and 7) and comparing the thermal utilization to that obtained, assuming separability of space and energy. An example of such a comparison for the geometry shown in Fig. 4.22 is given in Table 4.8. As would be expected, the nonseparability of space and energy becomes more pronounced as the channel spacing increases. It should be pointed out that Case II does represent an extreme set of channel dimensions relative to the plate size. The fuel loading density in the plates and the metal-to-water ratio are the most significant parameters, with nonseparability effects becoming more significant as (1) the loading increases, (2) the metal-to-water ratio decreases, and (3) the flux dip in the fuel plate proper increases. The effect of these parameters should be investigated for the particular design to determine whether the associated importance of the uncertainty in calculated ηf is consistent with the design reactivity margins or allowances and whether a more detailed calculational approach is warranted.

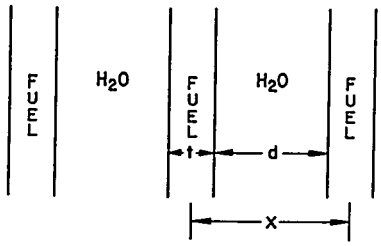

CASE	t-cm	N^{25} (atoms /barn-cm)	x-cm	d-cm	N^{H_2O} (atoms /barn-cm)
I	0.1782	0.0006401 3	0.340252	0.162052	0.066573
II	0.1782	0.0006401 3	1.36176	1.18356	0.036570

FIGURE 4.22. Geometry for Separability of Space and Energy Study.

TABLE 4.8 — COMPARISON OF GEOMETRY FOR SEPARABILITY OF SPACE AND ENERGY

Case	ηf	
	Separability Assumed	Nonseparable Solution
I	1.950	1.948
II	1.626	1.615

The problem of describing the resonance self-shielding factor for arrays of natural uranium plates (near to large water channels in a cluster) has been described in Ref. 49. The separability of space and energy assumption in the region containing the plates immediately adjacent to the large water channel at the edges of a cluster is suspect in the epithermal energy range if the plates are very strongly absorbing (i.e., contain resonances). Hence, cell theory constants would not be expected to describe the local resonance absorption in the plates directly adjacent to the large water channel that separate clusters containing arrays of these plates. (This effect, described in Ref. 49, has been verified experimentally and reported in Ref. 51.) Figure 4.23 presents the results of the calculations of Ref. 49. The more detailed calculational method for resonance capture indicates that considerably more resonance absorption takes

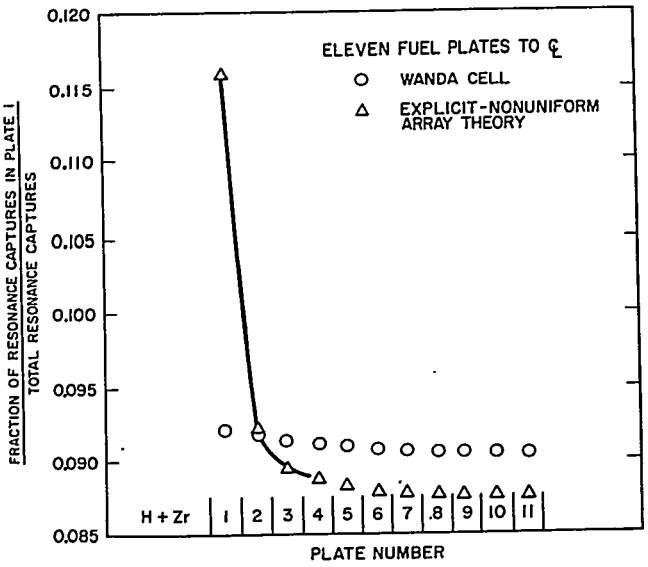

FIGURE 4.23. Comparison of Local Absorptions: Cell Theory vs Explicit.

place in the first plate nearest the end wide water channel (non-fuel-bearing region), as compared to a center plate distant from the end water channel, than an epithermal group homogenized two-region (fuel and nonfuel) calculation based on local fuel plate-water channel subcells would predict. The conventional cell theory approach which utilizes individual fuel plate-water channel subcells predicts an increase of 6 percent in resonance absorption of the end fuel plate relative to the center fuel plate. However, the more exact explicit case predicts an increase in absorption of the end fuel plate over a center plate of 24 percent. Such a preferential absorption in the end fuel plate indicates a preferential buildup of plutonium locally, which could lead to increased local thermal power peaks after considerable depletion has taken place. (A still different but somewhat similar type of phenomenon would be expected if a group of fuel plates containing a strong resonance absorber were placed next to a group of fuel plates not containing resonance absorbers, which would result in a spatially dependent epithermal removal cross section.)

The above discussion does point out the areas which should be investigated before attempting to use cell theory approximations in the epithermal energy range. The availability of Monte Carlo codes of greater flexibility permits the designer to investigate more rigorously the validity of these approximate calculational procedures.

E. The Validity of Cell Theory for Full Core Calculations

Attention is now turned to the problem of describing an entire reactor by homogenized constants obtained with cell theory. The reactor considered as an example consisted of an array of three clusters (7 in. by 7 in.) by three clusters (nine clusters), each containing a control rod channel and isolated lumped self-shielded absorbers located in the center of each of the four fuel subassemblies which constitute a cluster. Analysis of this core with (1) no control rods or isolated lumped absorbers, (2) control rods and no isolated lumped absorbers, (3) no control rods and isolated lumped absorbers, and (4) both isolated lumped absorbers and control rods inserted offers another opportunity to examine the effect of lumped absorbers on the validity of cell theory. The reactors analyzed are shown in Fig. 4.24. Calculations employing both cell theory and full core explicit representation were performed. The cells used for the four configurations are shown in Fig. 4.25. Zero-current boundary conditions were used in all cases, and local three-group diffusion theory constants identical to those used in the full core explicit calculations were assumed in the cell calculation. The equivalent homogenized cell theory constants were obtained with the flux volume weighting procedure described above. The equivalent cell theory constants were then used to describe the entire cross section of the core. The reflector constants used were identical to those in the explicit calculation. Thus, the full core calculation employing cell theory showed two regions: (1) the core itself represented by cell theory constants, and (2) the reflector.

The first quantity examined is the eigenvalue, λ (or k_{excess}), of these cores calculated explicitly and with cell theory constants. The fraction of the neutrons thermalized which are absorbed in lumped absorbers, either control rods or self-shielded lumped absorbers, f_{het}, is used as a convenient means of numerically identifying the degree of inhomogeneity. A plot of the difference in calculated eigenvalues by means of cell theory and explicit representation as a function of f_{het} is shown on Fig. 4.24. The case corresponding to no lumped absorbers (A) has a value of f_{het} equal to zero, and the error in eigenvalue resulting from the cell theory approximation is negligible.

It was found for this particular series of cases that there is some correlation between the degree of heterogeneity as defined by f_{het} and the error in using cell theory. Examination of the explicit and cell theory type calculations indicates that the thermal neutron captures in the various regions and material compositions of the core are not very well described by cell theory for those subassemblies adjacent to the reflector. This

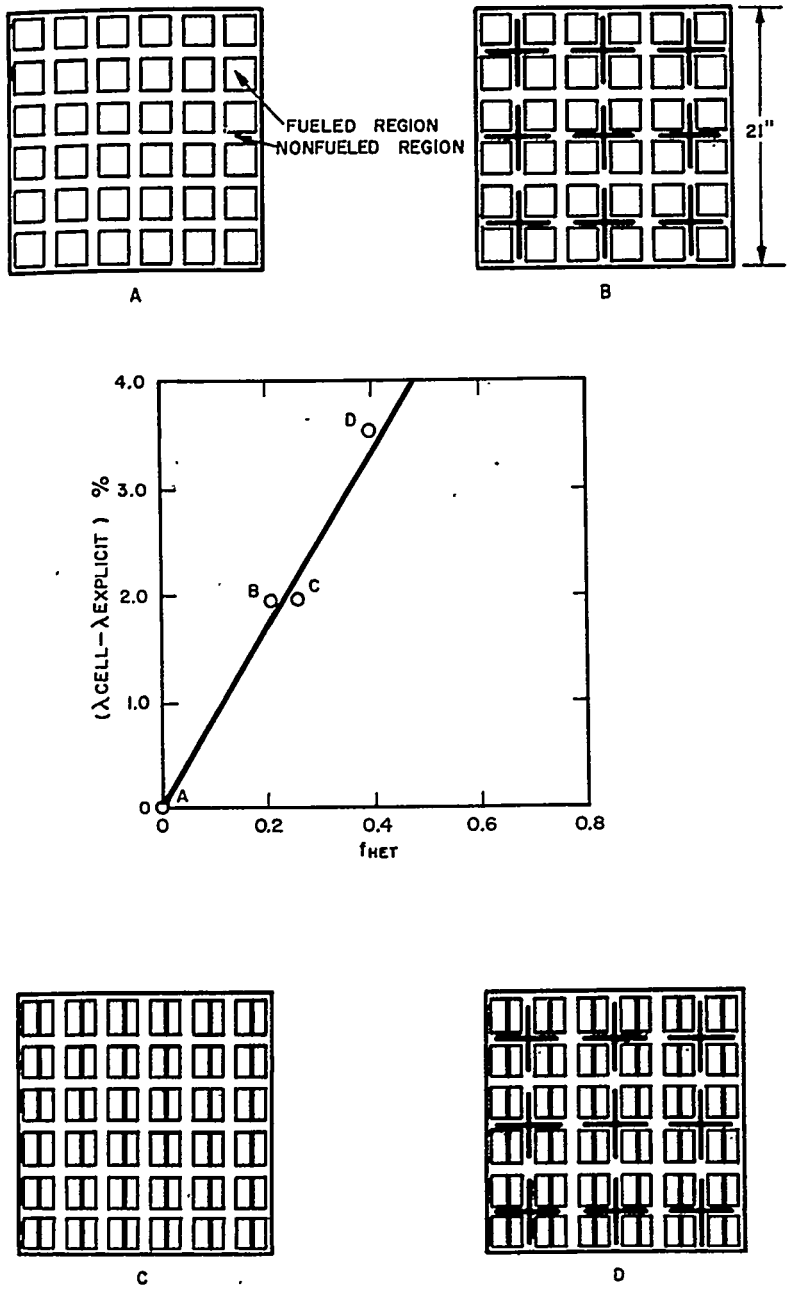

FIGURE 4.24. Comparison of Cell Theory to Explicit Representation.

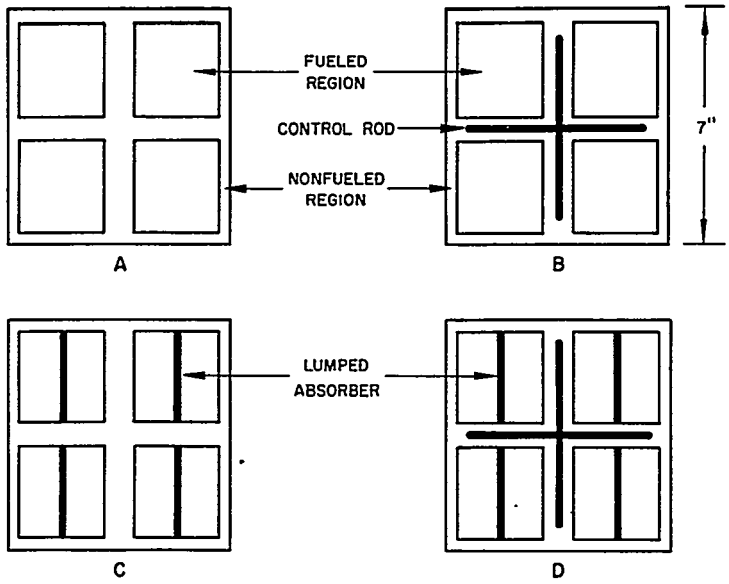

FIGURE 4.25. Cells Used to Describe Reactor.

is where cell theory would be expected to be least accurate, since the zero-current cell boundary conditions do not represent reality.

Two methods can be employed to obtain a better estimate of local behavior in regions of a core when the zero-current boundary condition is not an adequate representation. In the first, referred to as the composite cell model, a zero-current boundary condition is employed in a pseudo-cell calculation encompassing a considerably larger area than the region of immediate interest. Thus, the effect of the surrounding material on the nuclear behavior can be approximated, and flux-weighted constants obtained by the methods described above. In the second method, the different energy group leakages into a region can be determined approximately by performing a full core calculation employing homogeneous diffusion theory constants obtained from cell theory calculations of the type referred to above. With the currents thus approximated along the boundaries of the region of interest as boundary conditions, a more detailed calculation may be performed in the region. An alternate approach to this second method of taking into account the leakages into and out of the region is to determine the leakages along the boundary from a full-core explicit calculation rather than a full-core calculation employing homogeneous cell theory derived constants. The reasons for this approach would be to determine the leakages more accurately and also to permit a

less expensive depletion calculation to be done on the local region of interest. Very often, the power distribution and lifetime reactivity characteristics of the entire reactor can be inferred from the characteristics of a judiciously selected composite cell type calculation. In many cases, it has been found that the leakages into a particular region for which a depletion calculation is being performed do not change appreciably over core life.

F. Cell Calculations with Nonzero-Current Boundary Conditions

G. O. Mueller

Cell calculations are best performed on an inner subassembly or portion of a core in which net currents at each boundary are actually essentially zero. In many cores, such conditions are rarely met, and appropriate current conditions must be imposed upon the boundaries of the cell in order to calculate properly the portion of the core being investigated. The value of the boundary current can be determined from the results of a core calculation for which conventional boundary conditions are easily identified. By examining the values of the flux gradients along the mesh lines corresponding to the cell boundaries, the value of the current at the cell boundary can be calculated through the use of the albedo as a boundary condition.

The boundary current is evaluated from the expression

$$Z_g = -\frac{D_g \nabla \phi_g}{\phi_g} \qquad \text{Eq. (4.163)}$$

where

Z_g = boundary current for neutron energy group g
D_g = diffusion coefficient for group g in cell region adjacent to boundary
ϕ_g = group-dependent flux at boundary
$\nabla\phi_g$ = group-dependent flux gradient at boundary.

Group-dependent values of the boundary current can then be applied in lieu of the normal zero-current conditions at the cell boundaries. Constant average values of Z_g are usually applied along various lengths of the boundaries where the flux gradients are reasonably uniform. The use of several average values of Z_g along the boundary instead of point values saves considerable time and effort in input preparation without any noticeable sacrifice in accuracy.

The usual procedure in performing cell studies with non-zero-current boundaries is to set up a cell calculation model containing the same mesh and region definition as that in the portion of the core model being represented by the cell. Boundary currents are then determined from results of the core calculations and applied to boundaries of the cell. The results of the cell calculation are compared with results of the corresponding region in the core. If the cell reactivity or power distribution differs from that in the corresponding core region, the boundary conditions can be adjusted from their precalculated values until the cell results agree with core values. The degree of adjustment is usually not severe and can be accomplished by simple trial and error procedures. Having established the appropriate boundary currents, the cell model can be altered by increasing the mesh and structural detail, if power distribution corrections are to be made, or increasing the fuel region detail if better depletion patterns are desired.

Figure 4.26 represents a cell model of a portion of a core module. The module chosen lies adjacent to a reflector in a section of the core subject to large azimuthal current variations. The boundary conditions along the sides AD, AB, and BC are determined by evaluating Z_g at several representative mesh points along these boundaries, using results of a core diffusion theory calculation. DC is the outer boundary of the reflector; thus, a zero flux boundary condition exists along this line.

The power distribution resulting from the core calculation and two cell calculations at 12 representative points in the cell is shown in Fig. 4.26. The directions of the neutron currents at several locations along the boundaries are also shown. The cell calculations were performed with the same mesh and region definition as in the full-core model.

It can be readily seen that for this type of investigation the use of zero-current boundary conditions at boundaries AD, AB, and BC would not have given the correct power distribution within the cell. The use of precalculated Z_g values at the boundaries resulted in power distributions similar to those found in the overall core calculation.

Once the appropriate boundary conditions have been established, the mesh and region detail of the cell can be increased to investigate these effects at the beginning-of-life and during the lifetime of the core.

In performing cell depletion calculations as parameter studies of core behavior during life, it is often necessary to maintain the boundary currents at their beginning-of-life values, since information as to the variation of Z_g at any point during life will not be available until complete core calculations

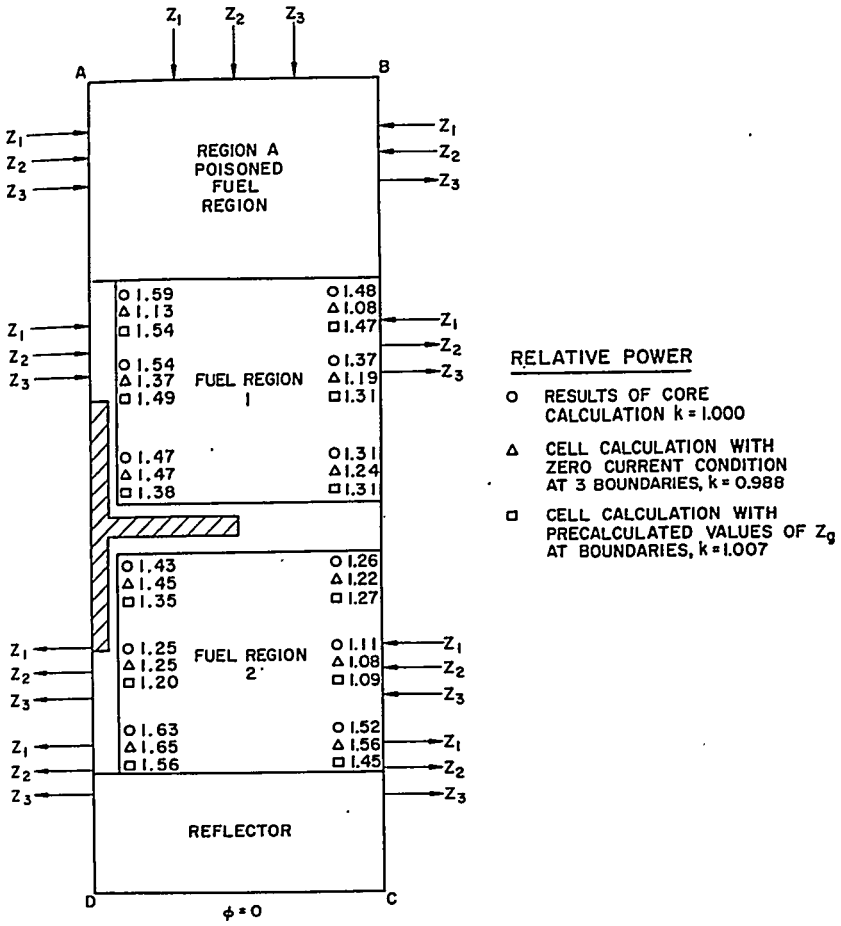

FIGURE 4.26. Cell Model Containing Nonzero Neutron Current Boundary Conditions.

have been performed. Recent studies have shown this approximation to be of little consequence in predicting core performance from cell depletion studies.

G. Summary

Since the preceding discussion points out that considerable error may occur in some cases in using cell theory to obtain equivalent homogeneous constants, several important factors must be kept in mind. (1) The errors in using cell theory boundary conditions may be acceptable in design calculations

if the designer is aware of them and makes appropriate corrections and allowances. The extent of the errors should be determined by utilizing test cases which show as much explicit detail as possible and by comparing the cell theory calculations with them in a manner similar to that described. (2) The cell theory method of obtaining homogenized constants is an approximation based on the assumption of the separability of space and energy and also the assumption that behavior of a particular region of the core is independent of events in the remainder of the core. Again, detailed calculational checks should be performed to assess the validity of these assumptions.

It is interesting to note that the principal differences between the cell theory approximation for obtaining equivalent homogeneous constants and the explicit representation lie in the inadequacies of the cell theory method to describe the leakage of neutrons to and from the region of interest. In general, it must be recommended that as much explicit detail as possible be represented in reactor calculations in those cases where severe heterogeneities are present.

4.4 SYNTHESIS METHODS

A. Introduction

The problem of developing three-dimensional flux and power distributions in a reactor from one- and two-dimensional calculations will now be discussed. The combination of calculations of different portions of a reactor (usually radial traverses which can be represented in considerable detail) into an overall reactor description has been termed synthesis. The methods developed to perform this synthesis of radial or two-dimensional plane calculations into a three-dimensional result have been continually evolving into more accurate and sophisticated techniques. Many early core designs were based on the single channel approach to synthesis, while more recent designs are based on the more sophisticated multichannel and variational techniques described below.

The single channel approach can be simply described as one in which a single axial calculation is used to relate the radial calculations to each other. The basic assumption is that the radial flux distributions are separable from the axial flux distribution. Relating a single axial calculation to the radial calculation is done by determining appropriately averaged radial or transverse leakages and flux volume-weighted cross sections from the radial calculations in each distinct plane representing a core cross-section configuration, such as no

control rods inserted or all control rods in a bank. The transverse leakages and cross sections are then employed in an axial calculation which serves to represent the axial leakage from one plane to another. Although the radial planes may be represented in a number of ways in the axial calculation, they are all basically the same since a single axial calculation is used to relate the radial planes to each other, thus implying separability of the radial and axial flux shapes. Section 4.4.B discusses this approach to the synthesis of three-dimensional flux and power shapes.

This approach (single channel) to describing nonseparable (flux and space) cases is improved by an extension of it to one which uses several simultaneous axial calculations to couple the radial planes together. In this method, the transverse leakages at several radial locations (channels) in each plane, representing a different configuration, are related to each other by means of coupling coefficients, and axial calculations are performed simultaneously to yield the axial flux distribution at the various radial locations (channels); thus, the basic assumption of separability of the single channel method is relaxed. The principal variations in the multichannel approach (Sect. 4.4.C) involve the selection of the method of describing the coupling in the radial planes of the various channels for which axial calculations are performed.

A third approach (Sect. 4.4.D), based on variational principles, may also be used to yield a three-dimensional result for nonseparable cases which the more elementary single channel synthesis approach cannot treat adequately. This approach relaxes the assumption of separability still further. In essence, it is assumed that the radial flux distributions are not independent of the axial flux distributions and that they vary continuously with the axial position. A set of trial radial distributions, representative of the possible extreme radial distributions, are combined by means of a variational principle applied to the flux distributions over the entire core to give the optimum combination of these trial radial flux distributions as a function of axial position, thus yielding a continuous distribution of flux in all three dimensions. The success of this method is dependent to some extent upon the selection of the trial radial flux distributions, since the variational principle only optimizes the mixing of the trial radial flux distributions selected.

B. Single Channel Synthesis

J. H. Leonard

A method involving a single axial function is known as single channel synthesis. Although many variations on the

basic method exist,[52,53] some of which are noted subsequently, this discussion, which follows the work of J. E. Meyer,[54] will indicate the fundamental approach as applied to the case of a pressurized water, heterogeneous reactor in which the control rods move parallel to the Z axis. In planes normal to the Z axis (radial planes), the (x,y) coordinates are used. The results would also apply if (r,θ) coordinates were used in the radial planes.

The quantities sought are the three-dimensional power distribution and the corresponding core eigenvalue. Although it is possible to synthesize the three-dimensional power distribution directly from two-dimensional (radial) power distributions, the approach here is to synthesize the three-dimensional neutron flux distribution in each energy group and, thence, to generate the power distribution. In each energy group, the flux $\phi(x,y,z)$ is approximated by the product of a single axial function $Z(z)$ and several radial shapes $\theta(x,y)$. Thus,

$$\phi(x,y,z) = Z(z) \cdot \theta(x,y)_i \qquad \text{Eq. (4.164)}$$

where subscript i indicates that the reactor is divided into several axial regions indexed by i, each of which has a characteristic radial flux shape in each energy group. The division into axial regions is based on control rod configuration, on amount of fuel depletion, and on the manner of fuel depletion in the various radial planes.

It is convenient, though not necessary, to choose the normalization such that the axial function Z is the average flux over the fueled cross-sectional area,

$$Z(z) = \frac{1}{A} \int_A \phi(x,y,z)\, dA \qquad \text{Eq. (4.165)}$$

where A denotes the portion of the radial plane which contains fuel and is assumed to be invariant with changes in z.

With this normalization, $\theta(x,y)$ in each group has an average value of 1,

$$\frac{1}{A} \int \theta\, dA = 1. \qquad \text{Eq. (4.166)}$$

Therefore, the function $\theta(x,y)$ gives the details of variations about the average flux in the radial plane. Note that any arbitrary three-dimensional flux could be written as $\phi(x,y,z) = Z(z)\theta(x,y,z)$ with $Z(z)$, the average flux, defined by Eq. (4.165) and $\theta(x,y,z)$ the variation about this average. The function $\theta(x,y,z)$, which varies but is continuous in the axial direction in an actual reactor, is replaced in the single channel synthesis by a group of functions $[\theta(x,y)]_i$ which is considered constant over a discrete number of axial regions but is, in general, discontinuous at interfaces between regions. The flux along any axial traverse through the core is, therefore, discontinuous; the average flux Z is a continuous function.

1. *Reduced Three-Dimensional Diffusion Equations*

Although the following development is carried out with two-energy groups, the extension to more than two groups can be made without further restriction. Consider the following two-group diffusion equations:

$$\nabla \cdot D_1 \nabla \phi_1 - (\Sigma_{R1} + \Sigma_{a1})\,\phi_1 + \frac{(\nu\Sigma_{f1})\,\phi_1 + (\nu\Sigma_{f2})\,\phi_2}{\lambda} = 0 \qquad \text{Eq. (4.167)}$$

$$\nabla \cdot D_2 \nabla \phi_2 - \Sigma_{a2}\phi_2 + \Sigma_{R1}\phi_1 = 0 \qquad \text{Eq. (4.168)}$$

where ϕ_1 and ϕ_2 refer to the fast and slow (thermal) flux, respectively, and where fluxes and properties are all considered functions of the three coordinates (x,y,z). The value of λ is equivalent to k_{eff}.

Upon substitution of Eq. (4.164) in these two equations, the leading term in each has the form

$$Z\nabla_r D \nabla_r \theta + \nabla_z D \nabla_z (Z\theta) \qquad \text{Eq. (4.169)}$$

where

∇_r denotes the operator $\left(\frac{\partial}{\partial x}\vec{i} + \frac{\partial}{\partial y}\vec{j}\right)$

∇_z denotes the operator $\left(\frac{\partial}{\partial z}\vec{k}\right)$

$\vec{i}, \vec{j}$, and $\vec{k}$ are unit vectors parallel to the x, y, and z axes, respectively.

This term, as written, takes into account that θ is a function of x, y, and z. However, it is assumed that the variation of both

θ and D with z is negligible. In many problems, this assumption is quite good within several large axial regions, but it is poor near the interfaces between these regions. Equation (4.169) becomes, with this assumption,

$$Z\nabla_r D\nabla_r\theta + \theta DZ'' \qquad \text{Eq. (4.170)}$$

where $Z''=d^2Z/dz^2$.

Substituting Eq. (4.170) into Eqs. (4.167) and (4.168) yields the reduced three-dimensional diffusion equations

$$Z_1\nabla_r D_1\nabla_r\theta_1 + \theta_1 D_1 Z_1'' - (\Sigma_{R1} + \Sigma_{a1})(\theta_1 Z_1) + \frac{(\nu\Sigma_{f1})\theta_1 Z_1 + (\nu\Sigma_{f2})\theta_2 Z_2}{\lambda} = 0$$

Eq. (4.171)

$$Z_2\nabla_r D_2\nabla_r\theta_2 + \theta_2 D_2 Z_2'' - (\Sigma_{a2})(\theta_2 Z_2) + (\Sigma_{R1})(\theta_1 Z_1) = 0 \ .$$

Eq. (4.172)

One such reduced three-dimensional equation is assumed to apply for each axial region. The equations are now solved for the function $\theta(x,y)$ in each such region.

2. Radial Solution

For each axial region of the reactor for which a radial solution, $\theta(x,y)_i$, is to be found, the axial leakage term is assumed proportional to the flux level, that is, it is equal to the product of the flux and an axial buckling term, so that

$$Z_1'' = -B_{Z1}{}^2 Z_1 \text{ and } Z_2'' = -B_{Z2}{}^2 Z_2 \ . \qquad \text{Eq. (4.173)}$$

This relationship is equivalent to the regionwise flux separability assumption of Eq. (4.164). Likewise, define F_r as the average fast-to-slow flux ratio (Z_1/Z_2) in the region. Note that B_{z1}^2, B_{z2}^2, and F_r will, in general, be functions of z. Substitution of these quantities in Eqs. (4.171) and (4.172) yields the radial diffusion equations

$$\nabla_r D_1\nabla_r(F_r\theta_1) - (\Sigma_{R1} + \Sigma_{a1} + D_1 B_{z1}^2)(F_r\theta_1)(F_r\theta_1) + \frac{(\nu\Sigma_{f1})(F_r\theta_1) + (\nu\Sigma_{f2})\theta_2}{\lambda_r} = 0$$

Eq. (4.174)

$$\nabla_r D_2 \nabla_r \theta_2 - (\Sigma_{a2} + D_2 B_{z2}^2)\theta_2 + \Sigma_{R1}(F_r \theta_1) = 0$$

Eq. (4.175)

where the eigenvalue for the radial problem is λ_r. All properties are assumed to be known functions of (x, y), so that if values are supplied for B_{z1}^2 and B_{z2}^2, Eqs. (4.174) and (4.175) can be solved by a two-dimensional diffusion code for the functions

$$f_1(x, y) = C_r \left[F_r \theta_1 (x, y) \right] \; ; \quad f_2(x, y) = C_r \left[\theta_2 (x, y) \right]$$

Eq. (4.176)

and for the eigenvalue λ_r. The normalization constant, C_r, of the diffusion code solution can be removed by the following equations:

$$\theta_1(x, y) = \frac{f_1(x, y)}{\frac{1}{A} \int_A f_1 \, dA} \; ; \; \theta_2(x, y) = \frac{f_2(x, y)}{\frac{1}{A} \int_A f_2 \, dA} \; .$$

Eq. (4.177)

which result in the proper normalization for θ_1 and θ_2 [Eq. (4.166)]. The value of F_r is calculated by

$$F_r = \frac{\int_A f_1 \, dA}{\int_A f_2 \, dA} \; .$$

Eq. (4.178)

Therefore, by supplying a value for B_{z1}^2 and B_{z2}^2, the quantities λ_r and F_r and the functions $\theta_1(x, y)$ and $\theta_2(x, y)$ are obtained using a suitable two-dimensional diffusion theory code. Knowledge of the actual values of B_{z1}^2 and B_{z2}^2 at any position of z requires that the functions $Z_1(z)$ and $Z_2(z)$ be available. Since they are not known at this stage, some approximation must be employed. An effective assumption involves setting B_{z1}^2 equal to B_{z2}^2 $(B_{z1}^2 = B_{z2}^2 = B_z^2)$ and adjusting B_z^2 so that λ_r is within 5 percent of the eigenvalue of the reactor being studied. (For example, $0.95 < \lambda_r < 1.05$ for the study of a critical reactor.) It is assumed that when this procedure is followed, the resulting functions $\theta_1(x, y)$ and $\theta_2(x, y)$ are good approximations of those which would be obtained if the proper values of B_{z1}^2 and B_{z2}^2 were used.

3. *Axial Solution*

By repeating the radial solution for each axial region into which the reactor is divided, the functions $\theta_1(x, y)$ and $\theta_2(x, y)$ are found. In addition, values of B_{z1}^2, B_{z2}^2 and the output values of F_r and λ_r are known for each axial region. These are used in a one-dimensional diffusion code to obtain the axial functions Z_1 and Z_2

The necessary one-dimensional equations can be obtained by integrating the reduced three-dimensional Eqs. (4.171) and (4.172) over some appropriate radial cross section of the core, A, and then dividing by the area A. Various cross sections are employed for this purpose. In some cases, it is appropriate to define A as the cross section of the fuel region of the core; in others, the entire core cross section is used; and in cases where one region of the reactor is of prime importance, the cross section of the important region may be appropriate. An example of the latter case is the seed-blanket reactor type, where the seed cross section is usually employed. Based on this integration, the one-dimensional axial solutions obtained for Z_1 and Z_2 are interpreted as average axial flux shapes for whichever region was used in the integration to determine flux-weighted material properties.

The following flux-weighted average properties are defined and substituted in the integrated equations:

$$\bar{D}_1 = \frac{1}{A}\int_A D_1\theta_1 dA \qquad \bar{D}_2 = \frac{1}{A}\int_A D_1\theta_2 dA$$

$$\overline{\nu\Sigma_{f1}} = \frac{1}{A}\int_A \nu\Sigma_{f1}\theta_1 dA \qquad \overline{\nu\Sigma_{r2}} = \frac{1}{A}\int_A \nu\Sigma_{f2}\theta_2 dA$$

$$\bar{\Sigma}_{a1} = \frac{1}{A}\int_A \Sigma_{a1}\theta_1 dA \qquad \bar{\Sigma}_{a2} = \frac{1}{A}\int_A \Sigma_{a2}\theta_2 dA$$

$$\bar{\Sigma}_{R1} = \frac{1}{A}\int_A \Sigma_{R1}\theta_1 dA \quad .$$

Eq. (4.179)

In addition, radial bucklings B_{r1}^2 and B_{r2}^2 are defined by

$$B_{r1}^2 = -\frac{\int_A \nabla_r D_1 \nabla_r \theta_1 dA}{A\bar{D}_1} \qquad B_{r2}^2 = -\frac{\int_A \nabla_r D_2 \nabla_r \theta_2 dA}{A\bar{D}_2}$$

Eq. (4.180)

With these substitutions after integration, Eqs. (4.171) and (4.172) become

$$\bar{D}_1 Z_1'' - \left(\bar{\Sigma}_{R1} + \bar{\Sigma}_{a1} + \bar{D}_1 B_{r1}^2\right) Z_1 + \frac{\left(\overline{\nu\Sigma_{f1}}\right) Z_1 + \left(\overline{\nu\Sigma_{f2}}\right) Z_2}{\lambda_z} = 0 \quad \text{Eq. (4.181)}$$

$$\bar{D}_2 Z_2'' - \left(\bar{\Sigma}_{a2} + \bar{D}_2 B_{r2}^2\right) Z_2 + \bar{\Sigma}_{R1} Z_1 = 0 \quad \text{Eq. (4.182)}$$

where λ_z denotes the eigenvalue of the axial problem. This procedure is applied to each axial region of the core, so that equations of the form of Eqs. (4.181) and (4.182) apply to each region with differences only in the constants (D, Σ_R, B_r^2, etc.). These equations can be solved by a one-dimensional diffusion code for the functions,

$$g_1(z) = C_z Z_1(z); \quad g_2(z) = C_z Z_2(z) \quad \text{Eq. (4.183)}$$

and for the eigenvalue λ_z. C_z is a power normalization for the axial problem, and the solution can be renormalized to give any desired average level to Z_1 or Z_2, or to the core average power. Note that all the average properties and the bucklings B_{r1}^2 and B_{r2}^2 will, in general, be different for each axial region. The axial position of the interface between the region containing the controlling rods and the adjacent region can be adjusted to determine critical rod positions and rod worths. The solution of the axial problem has resulted in functions $Z_1(z)$ and $Z_2(z)$ which, when combined with the correct group of radial functions $\theta_1(x,y)$ and $\theta_2(x,y)$, allow an approximate three-dimensional flux distribution to be determined [Eq. (4.164)]. It should be emphasized that the shapes $Z_1(z)$ and $Z_2(z)$ are average shapes and that, in general, there will be no (x,y) point through which an axial traverse can be made to obtain the same shapes.

Note that the most convenient means for evaluating B_{r1}^2 and B_{r2}^2 is by neutron balance, using the average properties λ_r, B_{z1}^2, B_{z2}^2, and F_r from the corresponding radial solutions. The equations needed for such evaluation are obtained by integrating Eqs. (4.174) and (4.175) over the area A and substituting the results in Eq. (4.180):

$$B_{r1}^2 = -\left(\bar{\Sigma}_{R1}/\bar{D}_1 + \bar{\Sigma}_{a1}/\bar{D}_1 + B_{z1}^2\right) + \frac{\left(\overline{\nu\Sigma_{f1}}/\bar{D}_1\right) + \left(\overline{\nu\Sigma_{f2}}/F_r\bar{D}_1\right)}{\lambda_r} \quad \text{Eq. (4.184)}$$

$$B_{r2}^2 = -\left(\bar{\Sigma}_{a2}/\bar{D}_2 + B_{z2}^2\right) + \left(\bar{\Sigma}_{R1}F_r/\bar{D}_2\right). \qquad \text{Eq. (4.185)}$$

4. Physical Interpretation of Average Properties

The flux-weighted averages of Eq. (4.179) can be interpreted directly in terms of neutron balance. $\bar{\Sigma}_{a1}Z_1A$, for example, is the number of fast neutrons absorbed per unit axial length in the portion of the radial plane defined by A; $\overline{\nu\Sigma_{f2}}Z_2A$ is the number of neutrons produced by thermal fission, etc. Likewise, $\bar{D}_2B_{r2}^2Z_2A$ is the number of slow (thermal) neutrons leaking out of or into the portion of the radial plane defined by A. Since the net leakage of thermal neutrons may, in many cases, be directed into the region A, B_{r2}^2 is quite often negative; B_{r1}^2 is, on the other hand, generally positive.

5. Synthesized Power Distributions

The local power density in watts/cm^3 is given by

$$K_1(\nu\Sigma_{f1})\phi_1 + K_2(\nu\Sigma_{f2})\phi_2 \qquad \text{Eq. (4.186)}$$

where K_1 and K_2 are the energy releases accompanying the production of each fission neutron during fast and slow fission, respectively. Units of K_1 and K_2 are (watt-sec/fission neutron). Utilizing the synthesized flux distributions obtained above, this local power density becomes

$$K_1(\nu\Sigma_{f1})Z_1\theta_1(x,y) + K_2(\nu\Sigma_{f2})Z_2\theta_2(x,y). \qquad \text{Eq. (4.187)}$$

The average power density in the region A is

$$\frac{1}{LA}\int_0^L \int_A (K_1\nu\Sigma_{f1}Z_1\theta_1 + K_2\nu\Sigma_{f2}Z_2\theta_2)\,dA\,dz$$

where L is the core axial length.
This becomes, after integrating over the radial plane,

$$\frac{1}{L}\int_0^L \left[K_1(\overline{\nu\Sigma_{f1}})Z_1 + K_2(\overline{\nu\Sigma_{f2}})Z_2\right] dz.$$

The local power density compared to the average power density in region A is denoted here by $P(x, y, z)$:

$$P(x,y,z) = \frac{[K_1(\nu\Sigma_{f1})Z_1\theta_1 + K_2(\nu\Sigma_{f2})Z_2\theta_2]}{\frac{1}{L}\int_0^L \left[K_1(\overline{\nu\Sigma_{f1}})Z_1 + K_2(\overline{\nu\Sigma_{f2}})Z_2\right] dz\,dA} \quad \text{Eq. (4.188)}$$

It can also be written as

$$P(x,y,z) = P_z(z)P_r(x,y,z) \quad \text{Eq. (4.189)}$$

where

$$P_z(z) = \frac{K_1(\overline{\nu\Sigma_{f1}})Z_1 + K_2(\overline{\nu\Sigma_{f2}})Z_2}{\frac{1}{L}\int_0^L \left[K_1(\overline{\nu\Sigma_{f1}})Z_1 + K_2(\overline{\nu\Sigma_{f2}})Z_2\right] dz} \quad \text{Eq. (4.190)}$$

and

$$P_r(x,y,z) = \frac{K_1(\nu\Sigma_{f1})Z_1\theta_1 + K_2(\nu\Sigma_{f2})Z_2\theta_2}{K_1(\overline{\nu\Sigma_{f1}})Z_1 + K_2(\overline{\nu\Sigma_{f2}})Z_2} \quad \text{Eq. (4.191)}$$

$P_z(z)$ can be evaluated from the axial solution above. However, since $P_r(x, y, z)$ contains the ratio (Z_2/Z_1), which is a function of z, it cannot be evaluated from the radial solution alone.

To obtain a radial power function P_r without knowledge of the axial solution, it can be assumed that $Z_1/Z_2 \cong F_r$, where F_r is obtained from the radial problem. Then, in the axial region i, the radial power distribution is given by

$$\left[P_r(x,y)\right]_i \cong \frac{K_1(\nu\Sigma_{f1})F_r\left[\theta_1\right]_i + K_2(\nu\Sigma_{f2})\left[\theta_2\right]_i}{K_1(\overline{\nu\Sigma_{f1}})F_r + K_2(\overline{\nu\Sigma_{f2}})} \quad \text{Eq. (4.192)}$$

This assumption enables a radial depletion study to be made without reference to an axial study. Otherwise, for each rod configuration, a range of fast-to-slow ratios would have to be

considered. Each ratio would result in a somewhat different radial depletion due to differences in the radial shapes of fast fission and slow fission power (i.e., differences between the functions θ_1 and θ_2). As an extension of this approach, the three-dimensional power distribution may be constructed directly from the axial and radial power distributions rather than from synthesized flux shapes. The results obtained from synthesizing power distributions are identical with those obtained from synthesized flux shapes only when the radial and axial flux components satisfy the assumption of separability. Since this assumption is never exactly met, the two methods for calculating power distributions will lead to somewhat different results in practice.

6. *Treatment of the Reflectors*

As previously indicated, the boundaries of the axial regions are usually selected to correspond with pronounced changes in axial composition. Thus, the reactor is generally divided into regions of different control rod configuration plus the top and bottom reflector regions. In the core regions, the flux-weighted constants used in the axial solution are obtained from radial solutions using Eqs. (4.179), (4.184), and (4.185). When constants for the reflectors are sought, a difficulty develops which emphasizes the importance of the assumptions made in the derivation.

By analogy with the treatment of the core regions, the reflector constants would be obtained by flux weighting of a calculation of a radial cross section through the reflector with an appropriate axial buckling value. From this calculation, flux-weighted constants and radial buckling values for use in the axial calculation would be obtained. However, it is apparent that the radial area, A, to be employed in the integrations is defined only for regions of the core proper, so that Eqs. (4.179), (4.184), and (4.185) cannot be unambiguously obtained. Further, buckling values obtained from the radial reflector calculation would generally be inappropriate. A value approximating that of the J_0 Bessel function would be obtained for the relatively homogeneous composition of the reflector beneath the core, whereas the heterogeneities of the core immediately above this reflector would generally lead to different values. Since it is intuitively apparent that the radial flux shapes in the non-multiplying reflectors will tend to follow those of the adjacent core section, the synthesis method may lead to unrealistic discontinuities in the buckling values at the top and bottom edge of the core. This is a consequence of the assumption of section-wise separability of axial and radial flux shapes which is violated in these vicinities.

The eigenvalue, flux shapes, and control rod worths obtained in the axial calculations are sensitive to the reflector properties employed, particularly to the lower reflector bucklings when the rods are controlling low in the core. Thus, it is necessary to employ some empirical means for determining reflector parameters which will lead to satisfactory values of the core characteristics. For this purpose a true three-dimensional calculation, or some other type of calculation not requiring the assumption of flux separability, can be employed. From such a calculation reflector radial bucklings can be determined for use in synthesis calculations, or synthesis calculations can be performed for this geometry and reflector bucklings established empirically which give the best match to the axial flux shapes, eigenvalue, or rod worth in the reference calculations. Since such a procedure can, at most, lead to proper values only for one of these three quantities, the treatment of the reflectors remains one of the most crucial aspects of the synthesis procedure.

7. *Extension of the Method*

In obtaining the radial solution for a given axial region, quantities B_{z1}^2 and B_{z2}^2 must be supplied. The very useful approach mentioned above involves letting $B_{z1}^2 = B_{z2}^2 = B_z^2$ and adjusting the buckling B_z^2 until the eigenvalue of the radial problem, λ_r, is within 5 percent of the eigenvalue of the reactor under study. However, once flux-weighted average properties have been determined and the axial problem has been run, the assumption of group-independent axial bucklings can be refined in the following manner by using the axial solution.

Consider the axial diffusion Eqs. (4.181) and (4.182), and integrate them with respect to z over the i^{th} axial region, which is considered to lie between the points z_{i-1} and z_i. Denoting integration with respect to z between z_{i-1} and z_i by $\int_i$, and assuming that better approximations of $B_{z1}^{2|}$ and $B_{z2}^{2|}$ in region i are given by

$$-\int_i Z_1'' \, dz \Big/ \int_i Z_1 \, dz \quad \text{and} \quad -\int_i Z_2'' \, dz \Big/ \int_i Z_2 \, dz$$

respectively, then for each axial region i the following equations are obtained:

$$B_{z1}^2 = -\left[\left(\bar{\Sigma}_{R1}\Big/\bar{D}_i\right) + \left(\bar{\Sigma}_{a1}\Big/\bar{D}_2\right) + B_{r1}^2\right] + \frac{\left(\overline{\nu\Sigma_{f1}}\Big/D_1\right) + \left(\overline{\nu\Sigma_{f2}}\Big/F_z D_1\right)}{\lambda_z}$$

Eq. (4.193)

$$B_{z2}^2 = -\left[\bar{\Sigma}_{a2}/\bar{D}_2 + B_{r2}^2\right] + \left(\bar{\Sigma}_{R1}\ F_z/\bar{D}_2\right) \qquad \text{Eq. (4.194)}$$

where

$$F_z = \frac{\int_i Z_1\, dz}{\int_i Z_2\, dz} \qquad \text{Eq. (4.195)}$$

and λ_z is the eigenvalue in the axial problem.

The values of B_{z1}^2 and B_{z2}^2 can be used as input in another radial problem for each axial region. This iteration between radial and axial problems converges quite rapidly and tends to eliminate errors due to differences in average fast-to-slow ratios and differences in eigenvalues in the radial and axial problems. A further refinement can be made by adding more axial regions. However, this procedure does not eliminate errors due to the axial variation in the functions θ_1 and θ_2, which have been neglected in this derivation. Such variations are quite important in the neighborhood of control rod tips, e.g., in explicit control rod problems and in the vicinity of the radial corners of the core near the bottom and top reflector, and are in many cases more important than the eigenvalue and fast-to-slow flux ratio effects.

8. Sample Problems

In the following problem, the flux-weighting synthesis technique is applied to a reactor which is infinite in the y direction (to suppress all y variations). The flux shapes are synthesized from two one-dimensional problems in the x direction and from a single one-dimensional problem in the z direction. The synthesized shapes and the resulting eigenvalue are compared to those from an exact two-dimensional (x, z) solution of the same problem.

The sample problem chosen for this test is shown in Fig. 4.27. It is a slab reactor 108 cm high and 92.6 cm thick, and is denoted as MURAL 1. A highly absorbing sheet is fully inserted in the center of the reactor. Two similar controlling sheets (located symmetrically) are partially inserted. The remainder of the controlling sheet channels and two additional channels in the outer portion of the core contain water. The core is surrounded on all sides by a 12-cm water reflector, and both fluxes go to zero on the periphery of the reflector.

MATERIAL PROPERTIES

MATERIAL	Σ_{R1}	Σ_{a1}	$\nu\Sigma_{f1}$	D_1	Σ_{a2}	$\nu\Sigma_{f2}$	D_2
FUEL	0.0160	-0.0008*	0*	1.70	0.0550	0.0832	0.420
CONTROL SHEET	0	0.10	0	0.50	1.50	0	0.10
WATER	0.0410	0	0	1.60	0.0120	0	0.230

*-FAST FISSIONING WAS APPROXIMATED BY A NEGATIVE FAST ABSORPTION

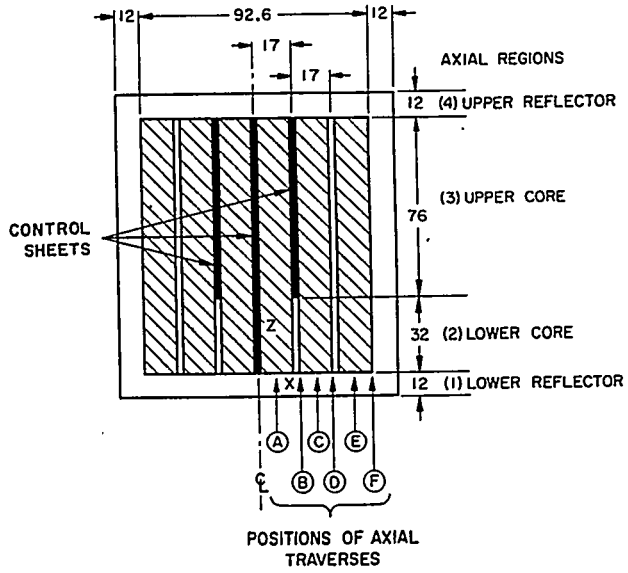

FIGURE 4.27. MURAL 1 Geometry Used for Demonstration of Single Channel Synthesis. (All dimensions in cm. All control sheet and water channels are 1.6 cm thick. MURAL 1 is infinite in the y direction.)

In MURAL 1, material properties are constant throughout the fueled cross section. In this case, the flux-weighted constants to be applied in the axial problem are taken to equal the fuel constants in the lower and upper core (Regions 2 and 3) and to equal the water constants in the lower and upper reflectors (Regions 1 and 4).

The following quantities are obtained as the result of a radial solution in each axial region:

Region	B_z^2	λ_r	F_r	B_{r1}^2	B_{r2}^2
Lower core (2)	0.00267	1.000	2.986	0.00477	-0.01986
Upper core (3)	0.00017	1.000	3.146	0.00645	-0.01127

In the radial solutions, B_{z1}^2 and B_{z2}^2 are considered equal to each other and to B_z^2; B_z^2 is adjusted to give an eigenvalue near 1. The radial flux shapes, θ_1 and θ_2, from these two solutions are shown in Figs. 4.28 and 4.29.

The radial bucklings B_{r1}^2 and B_{r2}^2 found above can be used as input for Regions 2 and 3 of an axial solution. The correct bucklings to be applied in the reflector Regions 1 and 4 are not

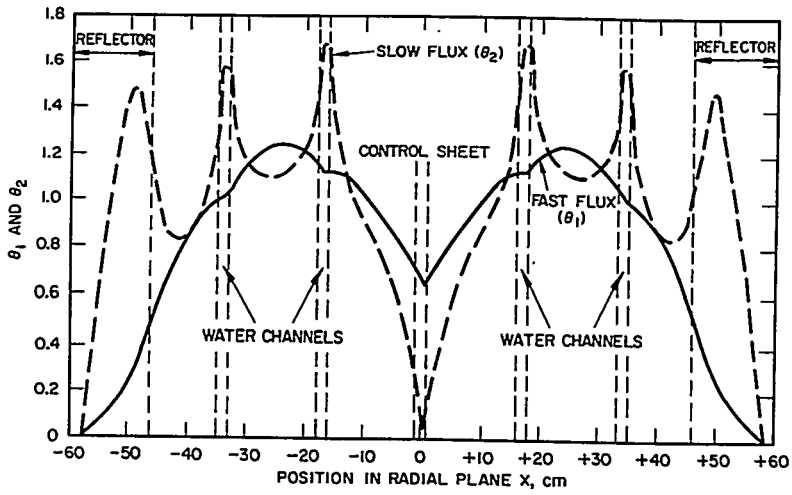

FIGURE 4.28. Radial Flux Shapes, Lower Core.

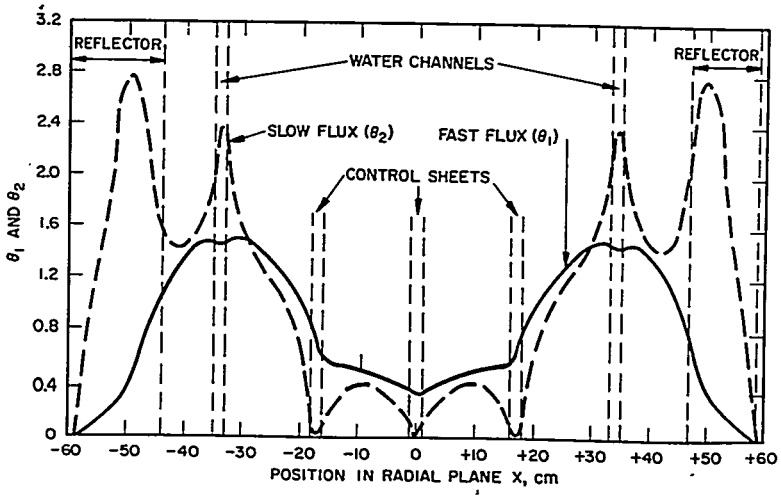

FIGURE 4.29. Radial Flux Shapes, Upper Core.

clearly defined, however. The reflector bucklings represent the net leakage of neutrons radially out of an area of the water of identical geometry to that of the radial fueled area of the core. It is probable that this net leakage is positive in both groups and that the correct radial bucklings are bounded by the bare-core buckling $(\pi/[92.6+24])^2 = 0.00073$, and by the fast radial buckling in the adjacent fueled region (0.00477 for the lower reflector, Region 1, and 0.00645 for the upper reflector, Region 4). When the former assumption is used, an eigenvalue $\lambda_z = 1.043$ is obtained; the latter gives $\lambda_z = 1.038$. The axial flux shapes, Z_1 and Z_2, are shown in Fig. 4.30. (The normalization gives an average value of 1 to the core slow flux.)

A two-dimensional (x, z) solution of MURAL 1 gives an eigenvalue $\lambda = 1.023$ compared to the values from the flux-weighted synthesis of 1.043 and 1.038. The slow flux for various axial traverses through the core, as calculated by the synthesis technique, is compared to the exact two-dimensional solution in Figs. 4.31 through 4.36. Both synthesized and exact fluxes are normalized to give a core average slow flux of 1. If power due to epithermal fissions is neglected, these curves are identical to the power shapes along traverses through a core with an average power density of 1. Note that the synthesis technique predicts the power distribution quite accurately between control sheet and water boundaries, but is less accurate as these discontinuities are approached.

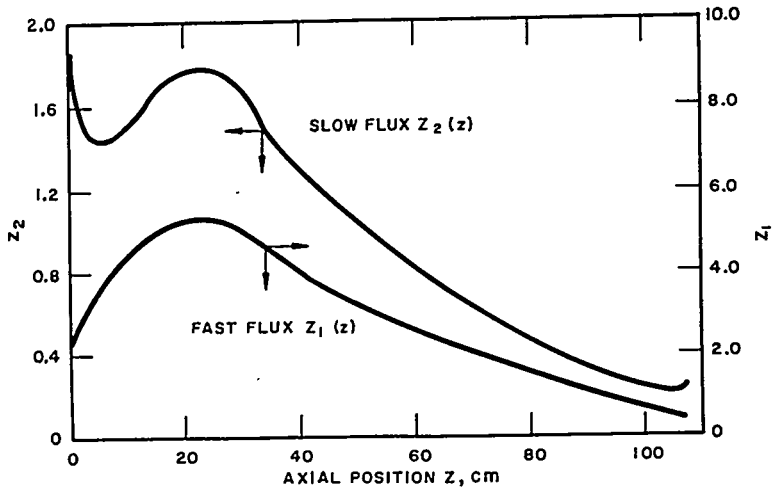

FIGURE 4.30. Average Axial Synthesized Flux Shapes.

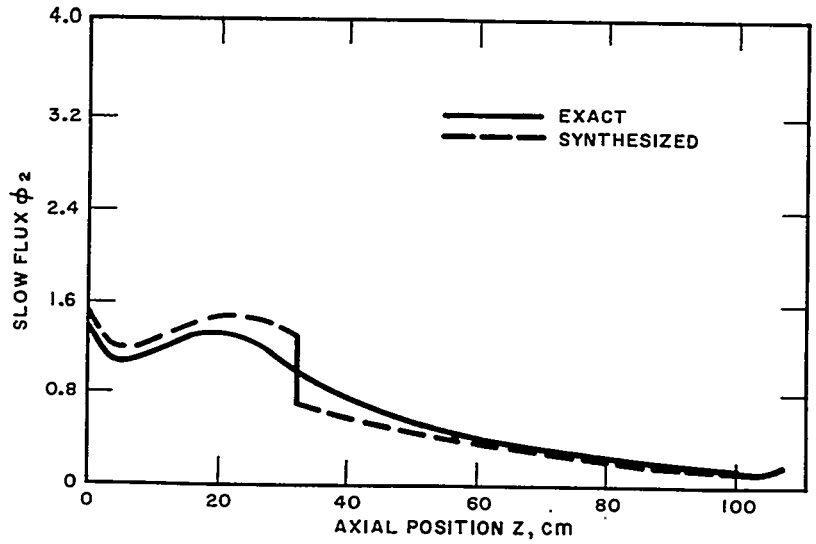

FIGURE 4.31. Axial Traverse A, Slow Flux.

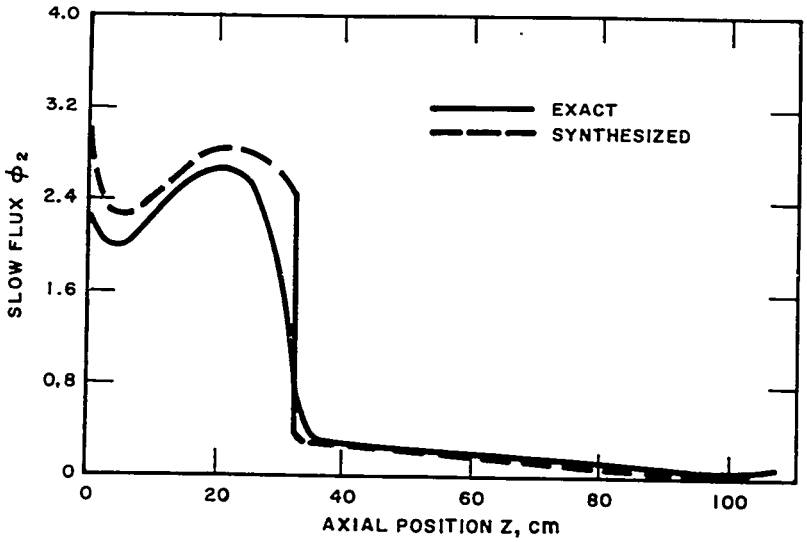

FIGURE 4.32. Axial Traverse B, Slow Flux.

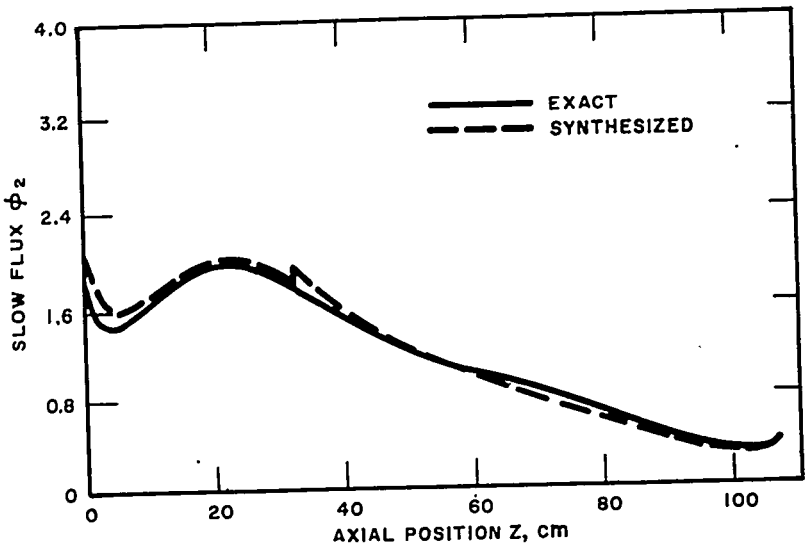

FIGURE 4.33. Axial Traverse C, Slow Flux.

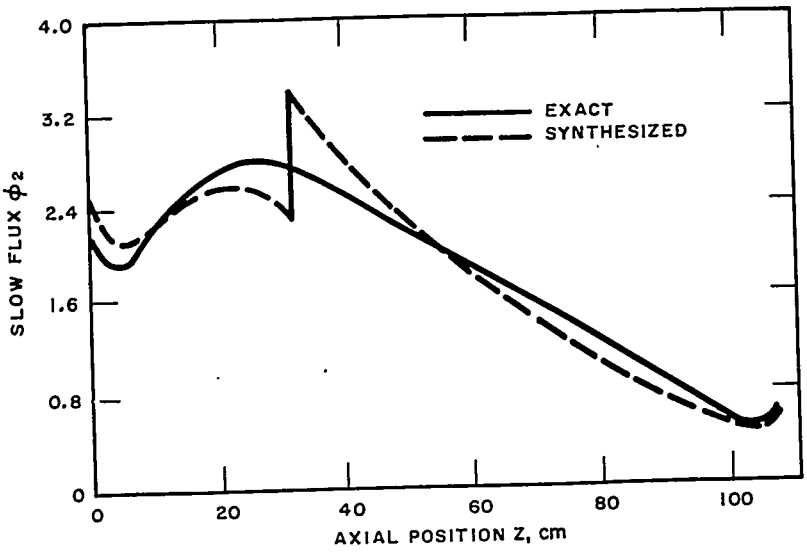

FIGURE 4.34. Axial Traverse D, Slow Flux.

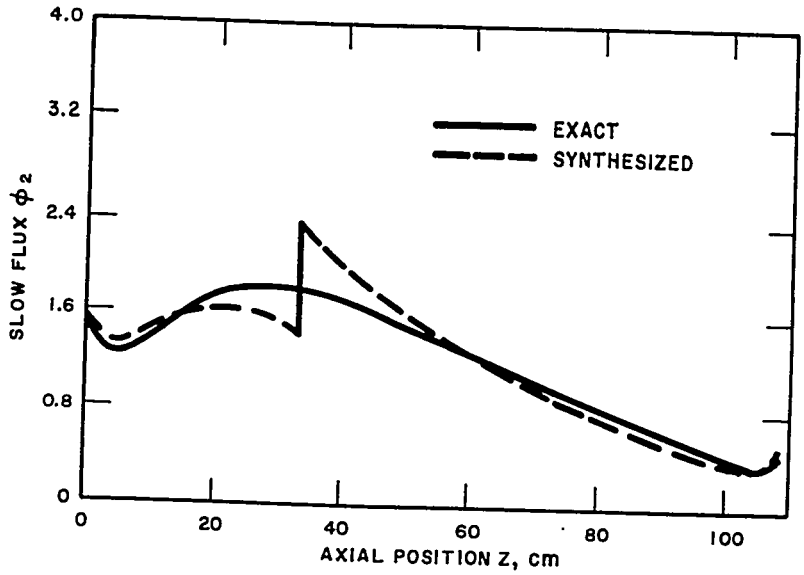

FIGURE 4.35. Axial Traverse E, Slow Flux.

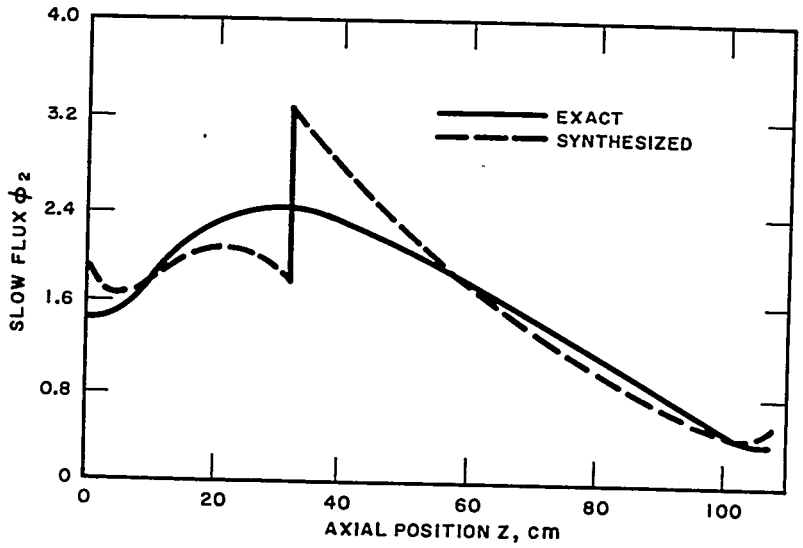

FIGURE 4.36. Axial Traverse F, Slow Flux.

In attempting to eliminate the eigenvalue discrepancy, the approach described in Sect. 4.4.B.7 has been applied to MURAL 1. As summarized above, the first pair of radial problems used $B_{z1}^2 = B_{z2}^2 = B_z^2$ (0.00267 for the lower core and 0.00017 for the upper core) and yielded $\lambda_r = 1.000$:

Region	F_r	λ_r	B_{r1}^2	B_{r2}^2
Lower core (2)	2.986	1.000	0.00477	-0.01986
Upper core (3)	3.146	1.000	0.00645	-0.01127

Use of the properties obtained in the radial problems resulted in an eigenvalue of 1.038 or 1.043, depending upon the radial reflector buckling used. (Note that in the following axial problems, the reflector bucklings in both groups will be taken equal to the fast radial buckling from the adjacent fuel region.) In computing group-dependent axial bucklings from Eqs. (4.193) and (4.194), the following results are obtained:

Region	F_z	λ_z	B_{z1}^2	B_{z2}^2
Lower core (2)	2.786	1.043	0.00313	-0.00496
Upper core (3)	3.094	1.043	-0.00022	-0.00180

The use of these group-dependent axial bucklings in a pair of radial problems, using Eqs. (4.184) and (4.185), yields the following:

Region	F_r	λ_r	B_{r1}^2	B_{r2}^2
Lower core (2)	2.804	1.032	+0.00484	-0.01917
Upper core (3)	3.101	1.044	+0.00640	-0.01104

The axial problem using these results as input gives:

Region	F_r	λ_z	B_{z1}^2	B_{z2}^2
Lower core (2)	2.822	1.032	+0.00302	-0.00426
Upper core (3)	3.108	1.032	-0.00008	-0.00153

Continuing the process for another pair of radial problems and another axial problem, the following results are obtained:

Region	F_r	λ_r	B_{r1}^2	B_{r2}^2
Lower core (2)	2.821	1.034	+0.00482	-0.01922
Upper core (3)	3.106	1.032	+0.00642	-0.01112

Region	F_z	λ_z	B_{z1}^2	B_{z2}^2
Lower core (2)	2.821	1.033	+0.00304	-0.00426
Upper core (3)	3.105	1.033	-0.00010	-0.00154

Therefore, in two iterations using the procedure in Sect. 4.4.B.7, the resulting eigenvalue of the flux-weighted synthesis method has been altered from 1.038 to 1.032 to 1.033. This is to be compared to the exact eigenvalue of 1.023. The refinement tends to reduce the errors due to differences in eigenvalue and fast-to-slow flux ratios in the radial and axial problems.

The remaining 1 percent discrepancy in eigenvalue is undoubtedly due chiefly to the rapid changes in radial shapes θ_1 and θ_2 in the exact solution near the interface between Regions 2 and 3. These changes are neglected in the synthesis method and are quite significant in MURAL 1. The analysis of a series of more uniform cores denoted by MURAL 2 through MURAL 5 has shown a much better agreement in both flux and eigenvalues for cores with less severe discontinuities. In all of these additional cases, the exterior core and reflector dimensions are identical to MURAL 1. Fuel, control sheet, and water properties are also the same. However, in all cases, the outer pair of water channels and the central control sheet are replaced by fuel material. In MURAL 2, the remaining two channels (at x = + 17 cm and x = -17 cm) are also filled with fuel material making a water-reflected homogeneous core. In MURAL 3, these remaining two channels are filled entirely with water; in MURAL 4 entirely with control-sheet material; and in MURAL 5 a control sheet is partially inserted in each channel, and the remainder of the channel is filled with water. The following eigenvalue comparison was obtained:

	Exact λ	Synthesis λ_z
MURAL 2 (homogeneous)	1.363	1.364
MURAL 3 (water)	1.347	1.349
MURAL 4 (sheet)	1.043	1.045
MURAL 5 (water and sheet)	1.141	1.155

In all of these cases, a group-independent B_z^2 was used in the radial problems and was adjusted to give a value of λ_r equal to that of the exact solution. It is interesting to note in MURAL 2 that an axial solution based on radial problems for which λ_r was 1 gave an axial value of $\lambda_z = 1.354$. Therefore, in MURAL 2, when λ_r was changed from 1.000 to 1.363, λ_z changed only from 1.354 to 1.364. This indicates first, that the eigenvalue of the axial problem is dependent on that of radial problem and, second, that for MURAL 2 the error introduced by an incorrect radial eigenvalue is not excessive. In MURAL 5, use of the refined approach in Sect. 4.4.B.7 yielded an eigenvalue $\lambda_z = 1.150$ as compared to the exact value $\lambda = 1.141$, an error comparable to that of MURAL 1.

9. *Assumptions and Limitations of the Single Channel Method*

The fundamental assumption employed in single channel synthesis is that of regionwise separability of the flux distribution into axial and radial components [Eq. (4.164)]. The consequences of this basic assumption lead to limitations of the method. Flux separability requires that sets of radial calculations be performed utilizing traverse (axial) buckling values which are regionwise constant to represent the axial leakage. Similarly, axial calculations are performed using regionwise constant radial buckling values. Since the reactivity of a core is dependent upon neutron leakages (as represented by bucklings), the calculated eigenvalue obtained by single channel synthesis is sensitive to the choice of these buckling values, as indicated in Sects. 4.4.B.6 and 4.4.B.7.

Further, the regionwise separability assumption implies that sets of radial flux shapes exist which are invariant within each of the several core axial sections. Thus, the axial distribution at any radial location is subject to discontinuities at the interface between regions of different radial flux shape. This property of single channel synthesis is undesirable because of the resultant discontinuous power shapes which are not physically significant.

The foregoing sample problem illustrates the inherent limitations of the conventional synthesis model. Not only do flux and power shapes for an axial traverse exhibit appreciable discontinuities which influence the calculated critical eigenvalue and thermal analyses, but considerable difficulties arise in connection with the treatment of the reflectors. Further, these problems tend to be more serious for cores with more pronounced heterogeneities. For a particular core, these difficulties can be minimized by selection of that approach which best represents the true solution for some simplified reactor of related geometry. Treatment of the reflectors, selection of the

radial area used for flux weighting, and synthesis of fluxes or powers directly are variations of the general method which can be employed to improve the results for a particular case. However, no general statements can be made regarding which of these variations is best, since all of these approaches utilize the same fundamental assumptions concerning flux separability which are violated to varying extents in different reactors. Specific examples of variations of the approach described here are given in Refs. 52 through 57.

10. Advanced Techniques

In view of the above limitations for the single channel approach to synthesis, numerous other methods have been explored to improve the representation of a heterogeneous core. One approach involves an axial model of several coupled channels where interchannel neutron leakage is expressed as a linear combination of channel average fluxes. The radial leakage representation is based on the detailed radial solutions. This multichannel flux synthesis method (Sect. 4.4.C) is based on the assumption of piecewise separability radially as well as axially, whereas single channel synthesis assumes complete radial separability in each axial zone. The second approach involves the combination of radial shapes to produce continuous axial shapes through the use of axially continuous weighting functions instead of the sectionwise weighting constants used in the conventional approach. Both of these advanced techniques enable more accurate representation of nonseparable cores than does the single channel method.

C. Multichannel Synthesis

E. L. Wachspress

1. Introduction

Multichannel flux synthesis differs from the single channel technique in that several flux distributions parallel to the z axis are computed simultaneously. Leakage between channels is represented as a linear combination of channel fluxes. The coefficients of combination are determined from detailed flux calculations perpendicular to the z axis (which will be referred to as x–y planes hereafter). Each channel represents a portion of the x–y planes, so that the flux determined by multiplication is discontinuous at channel and zone interfaces. This is illustrated in Fig. 4.37.

Single channel synthesis is based on the assumption of separability in that a single axial flux shape is computed for the region.

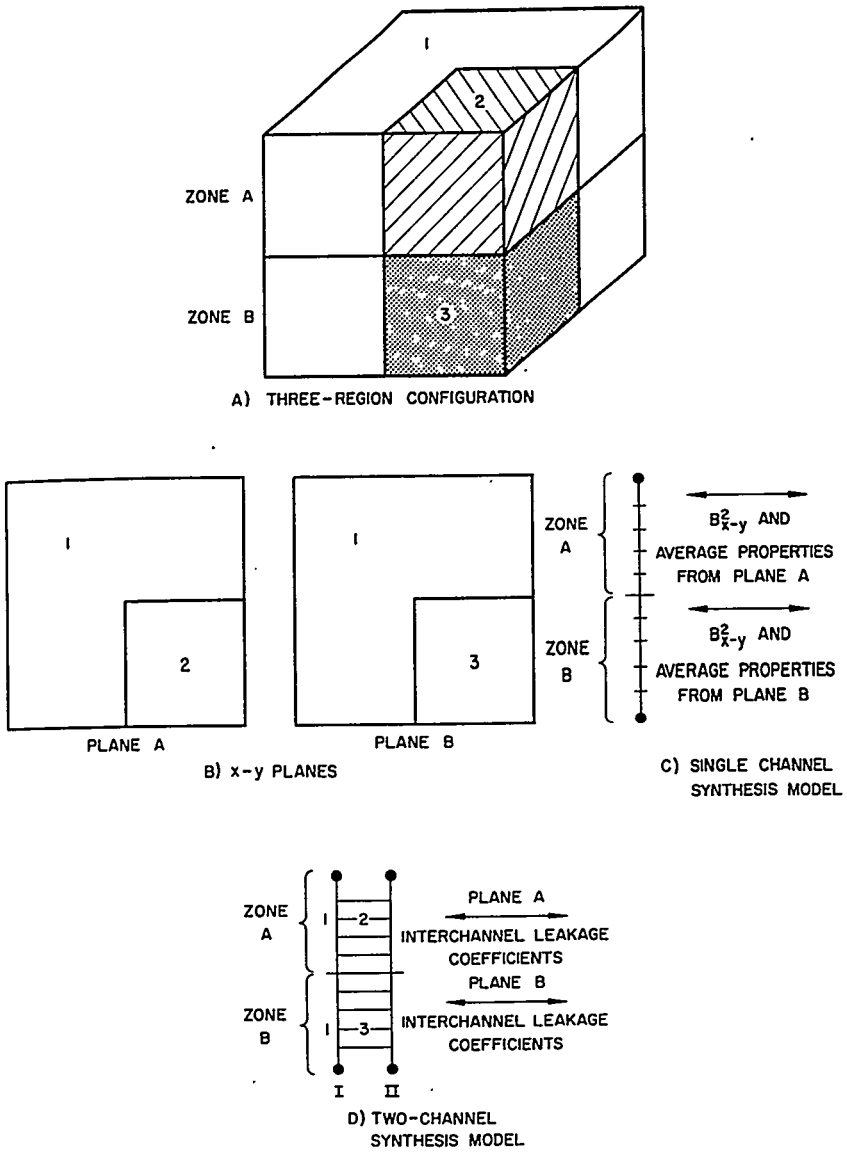

FIGURE 4.37. Single and Multichannel Models.

The basic assumption in multichannel synthesis is that local flux variation in several regions is separable with respect to the relative flux levels in these regions (or channels). The number of channels and x–y zones required depends upon desired accuracy and the degree of separability of the configuration. A conventional three-dimensional computation is the limiting case

where each point in the x–y plane is a channel and each x–y plane is a zone.

The KLAG program[58] provides for automatic multichannel synthesis of two-dimensional calculations and is based on the theory described below.

2. *Representation of Radial Leakage*

A) INTERCHANNEL COUPLING. The multichannel three-space-dimension model for the axial computation differs from conventional mockups in that radial leakage is not based on standard differencing techniques. A method for computing channel transfer coefficients in terms of radial leakage will now be described.

Consider channels c and c' with a common boundary, B (Fig. 4.38). The neutrons flowing across B from C to C' are given by the expression

$$j_{CC'} = \int_{x' \text{ on } B} dx' \int_{x \text{ in } C} G(x \to x')\phi(x)dx \qquad \text{Eq. (4.196)}$$

where ϕ is the neutron flux and $G(x \to x')$ is a leakage kernel. If ϕ_C is the average flux in channel C, the above equation can be written

$$j_{CC'} = \left[\int_{x'} dx' \int_{x} G(x \to x')S(x)dx\right]\phi_C \qquad \text{Eq. (4.197)}$$

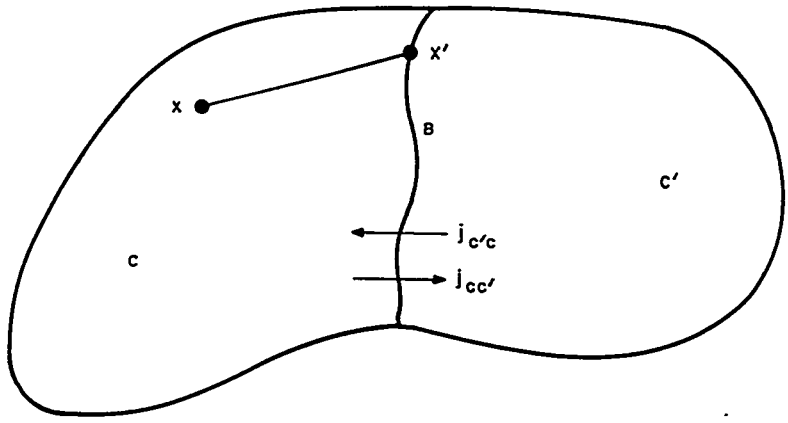

FIGURE 4.38. Interchannel Leakage.

where $S(x)$ is a normalized flux shape within channel C. The bracketed integral is the transfer coefficient, $P_{CC'}$, and the net leakage across the boundary is

$$L_{CC'} = i_{CC'} - i_{C'C} = P_{CC'}\phi_C - P_{C'C}\phi_{C'}. \qquad \text{Eq. (4.198)}$$

Since G and S are positive, these transfer coefficients are positive also.

The fluxes resulting from a two-space-dimension group diffusion calculation satisfy the diffusion equation within limits imposed by truncation error associated with finite grid spacing.

For any point on the boundary between C and C', diffusion theory gives the relationships[59]

$$i_{CC'}(x') = \frac{\phi(x')}{4} - \frac{D}{2}\nabla\phi\Big]_{x'}, \quad i_{C'C}(x') = \frac{\phi(x')}{4} + \frac{D\nabla\phi}{2}\Big]_{x'}$$

Eq. (4.199)

where $-D\nabla\phi]_{x'}$ is the net neutron leakage from C to C' at the point x' on the boundary. From two-space-dimension flux results, one readily obtains for each zone

$$P_{CC'} = \frac{i_{CC'}}{\phi_C} = \frac{\int i_{CC'}(x')\,dx' \cdot \int_C dx}{\int_C \phi(x)\,dx}$$

B) COUPLING BETWEEN CHANNELS AND EXTERIOR REGIONS. When the channels do not encompass the entire x–y plane, neutron leakage into the exterior regions must also be taken into account (Fig. 4.39). Suppose an exterior region (such as a water reflector) returns thermal neutrons to the channels. Negative bucklings would be required in the usual formulation where $P_{Ce} = L_{Ce}/\phi_C$ and L_{Ce} is negative. This thermal return is more closely related to the slowing-down source in the exterior region than to the channel thermal fluxes. It appears

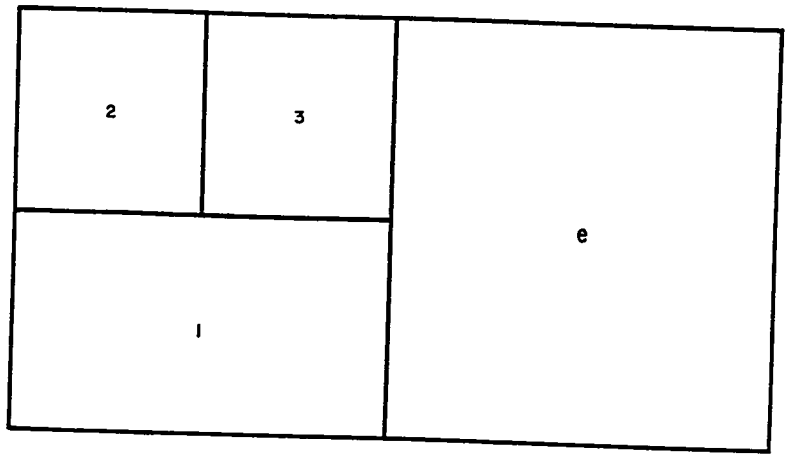

FIGURE 4.39. x–y Plane with Channels 1, 2, and 3 for Axial Model Plus Exterior Region, e.

more appropriate to express this leakage in terms of fast-group channel fluxes from which the exterior region slowing-down source is derived. This requires a leakage representation that is not diagonal in energy, and one approach will now be described.

In each group, the neutron diffusion equation is integrated over each exterior region, using Eq. (4.198) as though exterior regions were channels. These integrations are performed with x–y plane fluxes where exterior regions are included in the calculation model. The resulting equations may be written in matrix notation as

$$E\bar{\phi}_e = C\bar{\phi}_C$$

where

E = a square matrix of order equal to the number of exterior regions, e, times energy groups, g

C = a rectangular matrix with as many rows as E, but with a number of columns equal to the product of energy groups times channels

$\bar{\phi}_C, \bar{\phi}_e$ = vectors with components equal to the average group fluxes in the channels and exterior regions, respectively.

The inversion of E is not a difficult task with a computer, since the rank of E rarely exceeds 20. In fact, E is triangular when

there are no exterior fissionable regions. One may represent each component of ϕ_e as a linear combination of channel fluxes:

$$\bar{\phi}_e = E^{-1} C \bar{\phi}_C . \qquad \text{Eq. (4.200)}$$

Substituting Eq. (4.200) into (4.198) gives the final equation for representation of leakage between channels and exterior regions:

$$L_{C,e} = P_{Ce}\phi_C - P_{eC} \left[E^{-1} \; C\bar{\phi}_C \right]_e . \qquad \text{Eq. (4.201)}$$

The bracketed quantity is the linear combination of channel fluxes in Eq. (4.200) in terms of which the appropriate ϕ_e is represented. (In Eq. (4.201) the energy group index has been suppressed.)

Negative bucklings in the conventional leakage representation can destroy the nonnegativity properties required for the mathematical analysis (see Chap. 7, Sect. 7.2) of the three-space-dimension calculation. These properties are retained, however, by use of Eq. (4.201) for leakages between channels and exterior regions.

After a three-dimensional problem has been solved for channel fluxes, exterior fluxes can be obtained from Eq. (4.200) if needed. Thus, axial flux distributions are available for both channels and exterior regions. This method may reduce the number of channels required for a preassigned accuracy. Numerical results have not yet been obtained for this formulation, since current computer programs allow only for buckling representation of leakages between channels and exterior regions.

A simple numerical example may clarify this interchannel leakage representation. Consider a homogeneous slab of width a with a zero-current condition on the left boundary and zero flux on the right (Fig. 4.40). Assume a two-group calculation is to be performed with Channels 1 and 2 of Fig. 4.40 both

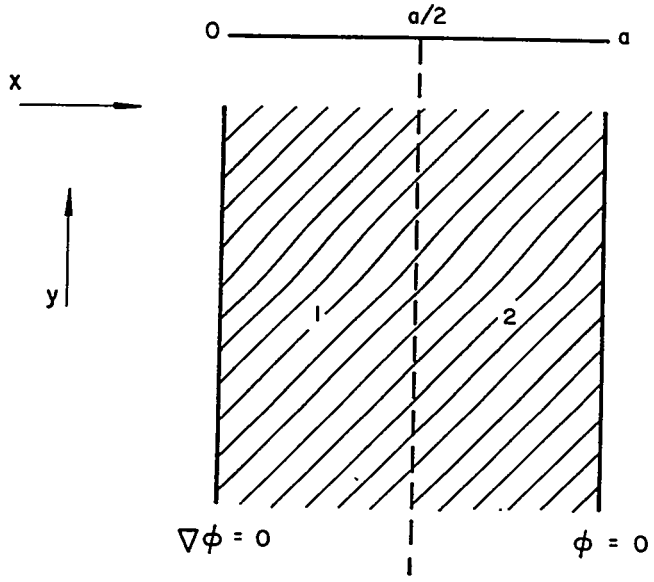

FIGURE 4.40. Homogeneous Slab. (Corresponds to an x–y plane in a synthesis calculation.)

interior. The slab fluxes, corresponding to the result of a detailed x–y plane calculation, are

$$\phi_1 = \cos \frac{\pi x}{2a} ,$$

and

$$\phi_2 = \frac{\Sigma_{1\to 2}}{D \frac{\pi^2}{4a^2} + \Sigma_2} \cos \frac{\pi x}{2a} .$$

and the eigenvalue is

$$k = \frac{\nu\Sigma_{1\to 2}\Sigma_f}{\left(D \frac{\pi^2}{4a^2} + \Sigma_1\right)\left(D \frac{\pi^2}{4a^2} + \Sigma_2\right)} .$$

In this equation, D is the diffusion coefficient for both Groups 1 and 2, Σ_1 and Σ_2 the total group removal cross sections, $\Sigma_{1\to 2}$ the slowing-down cross section from Group 1 to 2, Σ_f the fission cross section (second group only), and k the critical eigenvalue.

For Group 1, the leakage transfer coefficients are determined as follows:

$$\phi_{a/2} = \cos\frac{\pi}{4} = \frac{1}{\sqrt{2}}$$

$$-D\nabla\phi\Big]_{a/2} = \frac{D\pi}{2a}\sin\frac{\pi}{4} = \frac{D\pi}{2\sqrt{2}a}$$

$$j_{12} = \frac{\phi_{a/2}}{4} - \frac{D\nabla\phi}{2}\Big]_{a/2} = \frac{1}{4\sqrt{2}} + \frac{D\pi}{4\sqrt{2}a} = \frac{1}{4\sqrt{2}}\left(1+\frac{D\pi}{a}\right)$$

$$\bar{\phi}_1 = \frac{1}{a/2}\int_0^{a/2}\cos\frac{\pi x}{2a}\,dx = \frac{4}{\pi}\sin\frac{\pi}{4} = \frac{4}{\pi\sqrt{2}}$$

$$p_{12} = \frac{j_{12}}{\bar{\phi}_1} = \frac{\frac{1}{4\sqrt{2}}\left(1+\frac{D\pi}{a}\right)}{\frac{4}{\pi\sqrt{2}}} = \frac{\pi}{16}\left(1+\frac{D\pi}{a}\right)$$

$$\bar{\phi}_2 = \frac{1}{a/2}\int_{a/2}^{a}\cos\frac{\pi x}{2a}\,dx = \frac{4}{\pi}\left[\sin\frac{\pi}{2} - \sin\frac{\pi}{4}\right] = \frac{4}{\pi}\left(1-\frac{1}{\sqrt{2}}\right)$$

$$= \frac{4\left(\sqrt{2}-1\right)}{\sqrt{2}\pi}$$

$$p_{21} = \frac{j_{21}}{\bar{\phi}_2} = \frac{\frac{1}{4\sqrt{2}}\left(1-\frac{D\pi}{a}\right)}{\frac{4\left(\sqrt{2}-1\right)}{\sqrt{2}\pi}} = \frac{\pi\left(1-\frac{D\pi}{a}\right)}{16\left(\sqrt{2}-1\right)}$$

The leakage between Channels 1 and 2 is, thus, represented by

$$L_{12} = p_{12}\bar{\phi}_1 - p_{21}\bar{\phi}_2 = \frac{\pi}{16}\left(1 + \frac{D\pi}{a}\right)\bar{\phi}_1 - \frac{\pi\left(1 - \frac{D\pi}{a}\right)}{16\left(\sqrt{2}-1\right)}\bar{\phi}_2$$

and the first group diffusion equation integrated over Channel 1 is

$$\left(p_{12} + \Sigma_1\frac{a}{2}\right)\bar{\phi}_{\substack{\text{gp } 1\\ \text{ch } 1}} - p_{21}\,\bar{\phi}_{\substack{\text{gp } 1\\ \text{ch } 2}} = \frac{\nu\Sigma_f}{k}\,\frac{a}{2}\,\bar{\phi}_{\substack{\text{gp } 2\\ \text{ch } 1}}.$$

The leakage out of Channel 2 at $x = a$ is

$$-D\nabla\phi\Big]_{x=a} = \frac{D\pi}{2a}$$

so that the leakage coefficient from Channel 2 to exterior is

$$p_{2e} = \frac{L_{2e}}{\bar{\phi}_2} = \frac{\frac{D\pi}{2a}}{\frac{4\sqrt{2}-1}{\sqrt{2}\pi}}$$

or

$$p_{2e} = \frac{D\pi^2}{4a\left(2-\sqrt{2}\right)}.$$

The leakage from Channel 2 to exterior is, thus,

$$L_{2e} = \frac{D\pi^2}{4a\left(2-\sqrt{2}\right)}\bar{\phi}_{\text{ch }2}.$$

The first group diffusion equation integrated over Channel 2 is

$$-p_{12}\,\bar{\phi}^{\text{gp }1}_{\text{ch }1}+\left(p_{2e}+p_{21}+\Sigma_1\frac{a}{2}\right)\bar{\phi}^{\text{gp }1}_{\text{ch }2}=\frac{\nu\Sigma_f}{k}\,\frac{a}{2}\,\bar{\phi}^{\text{gp }2}_{\text{ch }2}\,.$$

The second group equations are determined in similar fashion. The leakage transfer coefficients are the same as for the first group because the flux shape [$S(x)$ in Eq. (4.197)] and diffusion coefficients are identical. The two-group two-channel integrated diffusion equations are:

$$\begin{bmatrix}
\left(p_{12}+\Sigma_1\frac{a}{2}\right) & -p_{21} & -\frac{\nu\Sigma_f}{k}\frac{a}{2} & 0 \\
-p_{12} & \left(p_{2e}+p_{21}+\Sigma_1\frac{a}{2}\right) & 0 & -\frac{\nu\Sigma_f}{k}\frac{a}{2} \\
-\Sigma_{1\to2}\frac{a}{2} & 0 & \left(p_{12}+\Sigma_2\frac{a}{2}\right) & -p_{21} \\
0 & -\Sigma_{1\to2}\frac{a}{2} & -p_{12} & \left(p_{2e}+p_{21}+\frac{\Sigma_2 a}{2}\right)
\end{bmatrix}
\begin{bmatrix}
\phi^{\text{gp }1}_{\text{ch }1} \\ \phi^{\text{gp }1}_{\text{ch }2} \\ \phi^{\text{gp }2}_{\text{ch }1} \\ \phi^{\text{gp }2}_{\text{ch }2}
\end{bmatrix}=0\,.$$

Now suppose that Channel 1 is replaced by an exterior region so that Channel 2 is the only one in the axial model. The simple buckling formulation for leakage between a channel and an exterior region gives:

$$L_{2e}=-\frac{D\pi}{2\sqrt{2}a}+\frac{D\pi}{2a}=\frac{D\pi}{2a}\left(-\frac{1}{\sqrt{2}}+1\right)=\frac{D\pi\left(\sqrt{2}-1\right)}{2\sqrt{2}a}$$

$$\bar{\phi}_2=\frac{4\left(\sqrt{2}-1\right)}{\sqrt{2}\,\pi}$$

so that

$$P_{2e} = + \frac{D\pi\left(\sqrt{2}-1\right)}{2\sqrt{2}\,a} \Bigg/ \frac{4\left(\sqrt{2}-1\right)}{\sqrt{2}\,\pi} = \frac{D\pi^2}{8a} .$$

The integrated equations for this single channel model are:

$$\begin{bmatrix} \left(\Sigma_1 \frac{a}{2} + \frac{D\pi^2}{8a}\right) & -\frac{\nu\Sigma_f}{k}\frac{a}{2} \\ -\left(\Sigma_{1\to 2}\frac{a}{2}\right)\left(\frac{\Sigma_2 a}{2} + \frac{D\pi^2}{8a}\right) & \end{bmatrix} \begin{bmatrix} \phi^{\text{gp } 1}_{\text{ch } 2} \\ \phi^{\text{gp } 2}_{\text{ch } 2} \end{bmatrix} = 0.$$

Multiplying these equations by $2/a$ gives the usual two-group matrix equations:

$$\begin{bmatrix} \left(\Sigma_1 + \frac{D\pi^2}{4a^2}\right) & -\frac{\nu\Sigma_f}{k} \\ -\Sigma_{1\to 2} & \left(\Sigma_2 + \frac{D\pi^2}{4a^2}\right) \end{bmatrix} \begin{bmatrix} \phi^{\text{gp } 1}_{\text{ch } 2} \\ \phi^{\text{gp } 2}_{\text{ch } 2} \end{bmatrix} = 0.$$

Now suppose that the leakage from Channel 2 to exterior is expressed as in Eqs. (4.200) and (4.201). The matrices E and C are

$$E = \begin{bmatrix} P_{12} + \Sigma_1 \frac{a}{2} & -\frac{\nu\Sigma_f \frac{a}{2}}{k} \\ -\Sigma_{1\to 2} & P_{12} + \Sigma_2 \frac{a}{2} \end{bmatrix}, \quad C = \begin{bmatrix} P_{21} & 0 \\ 0 & P_{21} \end{bmatrix}$$

For Eq. (4.200):

$$E^{-1}C = \frac{p_{21}\begin{bmatrix} \left(p_{12}+\Sigma_2\frac{a}{2}\right) & \frac{\nu\Sigma_f\frac{a}{2}}{k} \\ \Sigma_{1\to2}\frac{a}{2} & \left(p_{12}+\Sigma_1\frac{a}{2}\right) \end{bmatrix}}{\left[\left(p_{12}+\Sigma_1\frac{a}{2}\right)\left(p_{12}+\Sigma_2\frac{a}{2}\right)-\frac{\nu\Sigma_{1\to2}\Sigma_f a}{2k}\right] \equiv \mathfrak{D}}.$$

From Eq. (4.201), the leakage from Channel 2 to exterior is

$$L_{2e}^{\text{gp 1}} = (p_{2e}+p_{21})\phi_{\text{ch 2}}^{\text{gp 1}} - \frac{p_{21}p_{21}}{\mathfrak{D}}\left[\left(p_{12}+\Sigma_2\frac{a}{2}\right)\phi_{\text{ch 2}}^{\text{gp 1}} + \frac{\nu\Sigma_f a}{2k}\phi_{\text{ch 2}}^{\text{gp 2}}\right]$$

$$L_{2e}^{\text{gp 2}} = (p_{2e}+p_{21})\phi_{\text{ch 2}}^{\text{gp 2}} - \frac{p_{12}p_{21}}{\mathfrak{D}}\left[\Sigma_{1\to2}\frac{a}{2}\phi_{\text{ch 2}}^{\text{gp 1}} + p_{12} + \frac{\Sigma_1 a}{2}\phi_{\text{ch 2}}^{\text{gp 2}}\right]$$

The integrated equation for the single channel model with this leakage formulation is

$$\begin{bmatrix} \left[\Sigma_1\frac{a}{2}+(p_{2e}+p_{21}) - \frac{p_{12}p_{21}\left(p_{12}+\Sigma_2\frac{a}{2}\right)}{\mathfrak{D}}\right] & -\frac{\nu\Sigma_f a}{2k}\left(1+\frac{p_{12}p_{21}}{\mathfrak{D}}\right) \\ -\Sigma_{1\to2}\frac{a}{2}\left(1+\frac{p_{12}p_{21}}{\mathfrak{D}}\right) & \left[\Sigma_2\frac{a}{2}+(p_{2e}+p_{21}) - \frac{p_{12}p_{21}}{\mathfrak{D}}\left(p_{12}+\frac{\Sigma_1 a}{2}\right)\right] \end{bmatrix} \begin{bmatrix} \phi_{\text{gp 2}}^{\text{gp 1}} \\ \phi_{\text{gp 2}}^{\text{gp 2}} \end{bmatrix}$$

3. *Representation of Axial Leakage, Zone Coupling*

In single channel and multichannel synthesis computations, axial flux shapes are calculated for each channel. The two-dimensional zone fluxes may then be recalculated, with axial leakage based on the channel flux distributions.

This axial leakage may appear in the two-dimensional computations in the form of group and channel-dependent bucklings for each zone. Axial leakage may also be expressed in terms of the gross currents, as described in the discussion of radial leakage representation. Thus, axial leakage from zone z to z' in Channel C and Group g could be represented by

$$\underset{(c,g)}{L_{zz'}} = \underset{(c,g)}{P_{zz'}}\,\phi_{z,c,g} - \underset{(c,g)}{P_{z'z}}\,\phi_{z',c,g}$$

Eq. (4.202)

where

$$\underset{(c,g)}{P_{zz'}} = \frac{j_{zz',c,g}}{\phi_{z,c,g}} \cdot$$

Eq. (4.203)

It is the radial leakage representation in terms of channel transfer coefficients, $P_{cc'}$, which distinguishes multichannel synthesis from single channel synthesis. Axial leakage may be represented either by zone transfer coefficients or bucklings in single or multichannel computations. The initial two-dimensional calculations always have a buckling representation of axial leakage. During the iteration to consistency between the one-dimensional and two-dimensional leakages, either axial leakage formulation may be applied.

Coupling of the two-dimensional calculations through axial leakage transfer coefficients implies a need for simultaneous solution of the various zones. As this is not expedient, during the calculation of zone z the last estimate for adjacent zone fluxes may be used. This converts the zone calculations from eigenvalue to source problems. In matrix notation the fluxes satisfy

$$(A_{z,z-1}+A_{z,z+1}+M_z)\phi_z - A_{z-1,z}\phi_{z-1} - A_{z+1,z}\phi_{z+1} = \frac{\nu}{k}F_z\phi_z$$

where

A = the zone transfer coefficient matrix
M_z = the neutron diffusion operator for zone z (excluding axial leakage)

and

F_z = the fission operator for zone z.

Since ϕ_{z-1} and ϕ_{z+1} are values assumed from previous results for adjacent zones, the above equation may be written

$$M'_z \phi_z = \frac{\nu}{k} F_z \phi_z + S_z \qquad \text{Eq. (4.204)}$$

where

$$M'_z = (M_z + A_{z,z-1} + A_{z,z+1})$$

and

$$S_z = A_{z-1,z}\phi_{z-1} + A_{z+1,z}\phi_{z+1} \geq 0.$$

The vector S_z is known, and the value of k is that of the previous axial computation from which the A matrix was derived. The unknown flux in Eq. (4.204) is determined by conventional iteration techniques (see Chap. 7, Sect. 7.2):

$$\phi_z^{(p+1)} = M_z'^{-1} \left[\frac{\nu F_z}{k} \phi_z^{(p)} + S_z \right]. \qquad \text{Eq. (4.205)}$$

The simple numerical example used to illustrate the radial leakage formulation may also be used to indicate how Eq. (4.204) is obtained. Suppose detailed fluxes are required for planes parallel to the y axis in Fig. 4.40 and that Regions 1 and 2 are for $y_1 \leq y \leq y_2$. Then, the equation in Region 1 for $y_1 \leq y \leq y_2$, with the conventional buckling formulation for perpendicular leakage, is

$$\left.\begin{aligned} -D\frac{\partial^2}{\partial y^2}\phi_1(y) + \left(\Sigma_1 + \frac{D\pi^2}{4a^2}\right)\phi_1(y) &= \frac{\nu\Sigma_f}{k}\phi_2(y) \\ -D\frac{\partial^2}{\partial y^2}\phi_2(y) + \left(\Sigma_2 + \frac{D\pi^2}{4a^2}\right)\phi_2(y) &= \Sigma_{1\to 2}\phi_1(y) \end{aligned}\right\}.$$

The conventional multigroup iteration scheme gives

$$(k\phi)^{(p+1)} = \nu M^{-1} F \phi^{(p)},$$

where

$$M = \begin{bmatrix} \left(-D\frac{\partial^2}{\partial y^2} + \Sigma_1 + \frac{D\pi^2}{4a^2}\right) & 0 \\ -\Sigma_{1\to 2} & \left(-D\frac{\partial^2}{\partial y^2} + \Sigma_2 + \frac{D\pi^2}{4a^2}\right) \end{bmatrix} \text{ and } F = \begin{bmatrix} 0 & \Sigma_f \\ 0 & 0 \end{bmatrix}.$$

For Eq. (4.204), the leakage from Region 1 to 2 per unit length in the x direction is

$$\frac{2}{a}\left[P_{12}\phi_1 - P_{21}\phi_2\right]$$

so that

$$\frac{2}{a} P_{12} = A_{z,\,z+1}$$

and

$$\frac{2}{a} P_{2,\,1} = A_{z+1,\,z}.$$

Moreover,

$$M_z(y) = M_1(y) = \begin{bmatrix} \left(-D\frac{\partial^2}{\partial y^2} + \Sigma_1\right) & 0 \\ -\Sigma_{1\to 2} & \left(-D\frac{\partial^2}{\partial y^2} + \Sigma_2\right) \end{bmatrix}.$$

Thus,

$$M_z'(y) = M_1'(y) = \begin{bmatrix} \left(-D\frac{\partial^2}{\partial y^2} + \Sigma_1 + \frac{2}{a}p_{1,2}\right) & 0 \\ -\Sigma_{1\to 2} & \left(-D\frac{\partial^2}{\partial y^2} + \Sigma_2 + \frac{2}{a}p_{1,2}\right) \end{bmatrix}$$

The source term is

$$S_z = A_{z+1,z}\,\phi_{z+1} = A_{2,1}\,\phi_2 = \frac{2}{a}p_{21}\,\phi_2 .$$

For the two groups,

$$S_1 = \frac{2}{a}p_{21}\begin{bmatrix} \phi\ {}^{\text{gp 1}}_{\text{ch 2}} \\ \phi\ {}^{\text{gp 2}}_{\text{ch 2}} \end{bmatrix} \text{ Zone 2}$$

where the fluxes are obtained from latest results for Region 2.

Equation (4.204) for Region 1 may be written as

$$\begin{bmatrix} \left(-D\frac{\partial^2}{\partial y^2} + \Sigma_1 + \frac{2}{a}p_{1,2}\right) & 0 \\ -\Sigma_{1\to 2} & \left(-D\frac{\partial^2}{\partial y^2} + \Sigma_2 + \frac{2}{a}p_{12}\right) \end{bmatrix} \begin{bmatrix} \phi\ {}^{\text{gp 1}}_{\text{ch 1}}(y) \\ \phi\ {}^{\text{gp 2}}_{\text{ch 1}}(y) \end{bmatrix}$$

$$= \frac{\nu}{k}\begin{bmatrix} 0 & \Sigma_f \\ 0 & 0 \end{bmatrix}\begin{bmatrix} \phi\ {}^{\text{gp 1}}_{\text{ch 1}}(y) \\ \phi\ {}^{\text{gp2}}_{\text{ch1}}(y) \end{bmatrix} + \frac{2}{a}p_{21}\begin{bmatrix} \phi\ {}^{\text{gp 1}}_{\text{ch 2}} \\ \phi\ {}^{\text{gp 2}}_{\text{ch 2}} \end{bmatrix} \text{ Zone 2 .}$$

Note that the effective buckling in M'_z is

$$\frac{2}{a}P_{12} = \frac{2\pi}{16a}\left(1+\frac{D\pi}{a}\right) = \frac{D\pi^2}{4a^2} + \frac{\pi}{8a}\left(1-\frac{D\pi}{a}\right) .$$

When the last term on the right-hand side is positive, M'_z is less reactive than M_z, the latter having a buckling of $\frac{D\pi^2}{4a^2}$. This is true for $\frac{D\pi}{a} < 1$. Equation (4.199) relating the gross currents (j^+ and j^-) to the scalar flux and net leakage is valid only for regions with small buckling or, in this case, $\frac{D\pi}{2a} << 1$. Thus, the statement that $\nu\,[M'_z]^{-1}F$ is less critical than $\nu(M_z)^{-1}F$ applies only when the slab width is large compared to a neutron mean free path. This is usually true for synthesis calculations. Note that the condition $\frac{D\pi}{a} < 1$ corresponds to j_{21} and, hence, P_{21} greater than zero, which is true physically even when Eq. (4.199) is not valid for relating j to the scalar flux and gradient.

Since the matrix M'_z includes axial flow of neutrons out of zone z but not flow into z, it must be true that $\nu M'^{-1}_z F_z$ is less reactive than $\nu M_z^{-1} F_z$. Therefore, the iteration scheme in Eq. (4.205) is convergent, and conventional flux and source extrapolation procedures may be used in conjunction with it.

When axial leakage is represented by bucklings, negative bucklings occur in the less reactive zones. This can lead to divergence of the conventional iteration schemes and requires special consideration.

Another desirable characteristic of the zone transfer coefficient method is that the interdependence of flux shapes in the various zones is more realistically taken into account. The greater the importance of leakage into a zone, the greater will be the effect of adjacent zone flux shapes on the zone fluxes.

The treatment of zones which contain no fuel regions causes some concern in the buckling formulation, since there can be no two-dimensional calculation of a zone without fuel.* Radial leakages for axial calculations are related to values computed from adjacent zone two-dimensional calculations.

With the zone transfer coefficient scheme, such zones are special cases only in that no iteration is required in Eq. (4.205) when F_z is the null matrix.

*A multigroup calculation requires a fission source or a fixed source; otherwise the flux is zero (see Sect. 4.4.B.6).

4. *The Axial Computation*

The number of channels in the axial model depends upon the complexity of the configuration and the required accuracy. It is expedient to solve simultaneously for fluxes in all channels during the axial flux calculation. Axial mesh increments are identical for all channels. The number of planes at which fluxes are computed (number of points along the channels) depends upon the desired accuracy. Radial leakage for all planes within an axial zone is represented by channel transfer coefficients determined from the two-dimensional calculation of that zone. There are usually several axial points within each zone.

The three-dimensional axial problem is solved by an extension of the method used for solving one-dimensional problems. Determining neutron fluxes involves numerical inversion of the difference equation coefficient matrix. For one-space-dimension problems, this matrix is tridiagonal and may be inverted easily by Gaussian elimination.[60] For the multichannel problem, the coefficient matrix may be considered in terms of submatrices of rank equal to the number of channels. The coefficient matrix is tridiagonal in these submatrices rather than in the scalar elements of the one-dimensional problem (see Fig. 4.41). The multichannel axial problem is solved by Gaussian elimination, with matrix algebra replacing the scalar algebra of the one-dimensional scheme.

When the number of channels is sufficiently small, it is also feasible to solve for fluxes in all energy groups simultaneously in terms of an assumed fission distribution.* This converts the standard iteration procedure

$$(k\phi)^{(p)} = \nu M^{-1} F \phi^{(p-1)}$$

to

$$\left[\left(\frac{1}{k} - \frac{1}{k_e}\phi\right]^{(p)} = \nu\left(M - \frac{\nu}{k_e} F\right)^{-1} F\phi^{(p-1)} \cdot \right.$$

Eq. (4.206)

*This approach is also advantageous for all one-dimensional and single channel synthesis computations, provided that there are few energy groups.

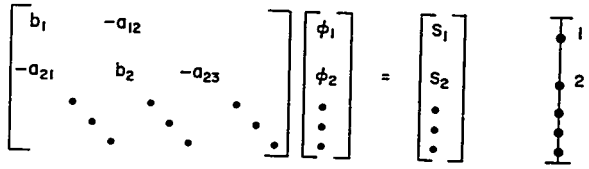

A) ONE-SPACE-DIMENSION

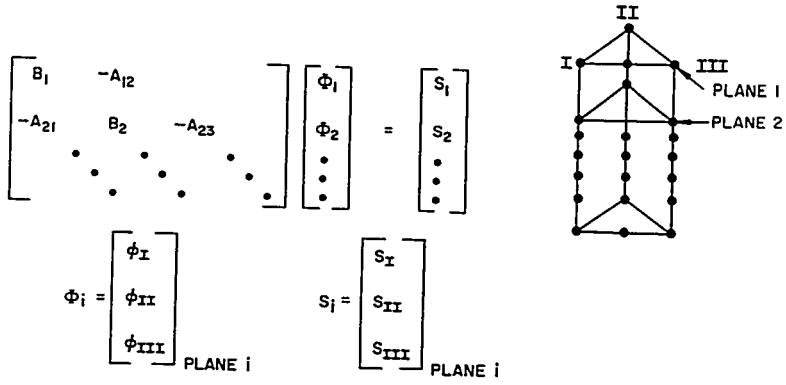

B_i INCLUDES ALL COEFFICIENTS RELATING FLUXES WITHIN PLANE i TO ONE ANOTHER.

$A_{i,j}$ INCLUDES ALL COEFFICIENTS OF FLUXES IN PLANE j WHICH APPEAR IN THE DIFFERENCE EQUATIONS OF PLANE i.

B) THREE-CHANNEL AXIAL PROBLEM

FIGURE 4.41. Axial Problem Matrix Representation.

where k_e is an assumed reactivity. The latter procedure is rapidly convergent when k_e is close to k. This technique is described in Chap. 7, Sect. 7.2. The vector Φ_i in Fig. 4.41 becomes

$$\Phi_i = \begin{bmatrix} \Phi_{\mathrm{I}} \\ \Phi_{\mathrm{II}} \\ \Phi_{\mathrm{III}} \end{bmatrix}_{\text{plane } i}$$

where

$$\Phi_I = \begin{bmatrix} \phi_{\mathrm{I}}^{g=1} \\ \phi^{g=2} \\ \cdot \\ \cdot \\ \cdot \end{bmatrix}, \text{ etc.}$$

and g is an energy group index. The coefficient submatrices are of rank equal to the number of channels times energy groups.

Once more, a sample problem may clarify this discussion. Let the homogeneous slab of Fig. 4.40 be represented by a square with sides of length a and zero-current boundary conditions at $y = 0$ and $y = a$ (see Fig. 4.42A). Let the reactor consist of two zones, the lower containing Regions 1 and 2 and the upper Regions 3 and 4, as in Fig. 4.42B. Suppose the three-dimensional multichannel model consists of two channels, one representative of Regions 1 and 3 (e.g., Channel 1) in Fig. 4.42B and the other of Regions 2 and 4 (e.g., Channel 2). Let the increments along the z axis be h.

One uses the coupling coefficients derived previously for this case for x–y leakage and the standard central difference representation for axial leakage:

$$\left.\frac{\partial \phi}{\partial z}\right|_{h(n+1/2)} = \frac{\phi[h(n+1)] - \phi(hn)}{h}$$

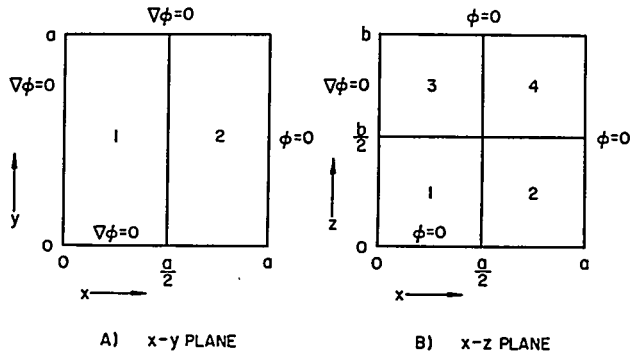

FIGURE 4.42. x–y and x–z Planes for Synthesis Calculation.

where n is the point index along the z axis, so that $n = 0, 1, 2, \ldots, b/h$.

Since for this example materials 1 and 2 are alike and 3 and 4 are alike, this is a truly separable problem. The flux distribution could actually be obtained by solving the one-dimensional problem in the z direction with a buckling (from the x–y leakage) of $B^2_{x-y} = \frac{\pi^2}{4a^2}$. The two-channel representation will be used, nevertheless, to illustrate the multichannel mockup. The multichannel difference equation grid is shown in Fig. 4.43.

The matrix equation satisfied at $z = nh$ will now be derived. There are four flux values which are written as the vector:

$$\Phi_{nh} = \begin{bmatrix} \Phi^1_{\mathrm{I}} \\ \Phi^2_{\mathrm{I}} \\ \Phi^1_{\mathrm{II}} \\ \Phi^2_{\mathrm{II}} \end{bmatrix}$$

where superscripts are the energy group indexes.

The equation for the flux in Channel 1 and Group 1 is obtained by integrating the neutron group diffusion equation over the Channel 1 part of the x–y plane and between $z = (n - \frac{1}{2})h$ and $(n + \frac{1}{2})h$, as follows:

(The symbol + or - after a parameter indicates how properties are averaged at zone interfaces, such as occurs at $z = \frac{N}{2} h$ in this case.)

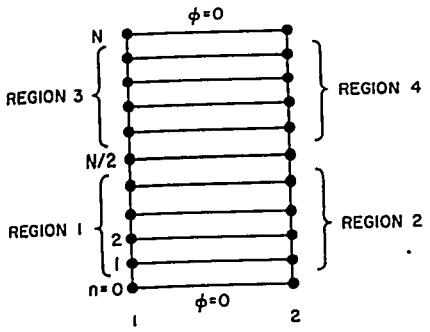

FIGURE 4.43. Multichannel Difference Equation Grid.

$$0 = \int_{z=(n-\frac{1}{2})h}^{z=(n+\frac{1}{2})h} \int_{\substack{x-y \\ \text{in I}}} \left[-\nabla \cdot D_I^1 \nabla \phi(x,y,z) + \Sigma_I^1 \phi(x,y,z) - \frac{\nu \Sigma_{f_I}^2}{k} \phi^2(x,y,z) \right] dx\, dy\, dz$$

$$= \int_{z=(n-\frac{1}{2})h}^{z=(n+\frac{1}{2})h} \left[-\frac{a^2}{2} \frac{\partial}{\partial z} D_I^1(z) \frac{\partial}{\partial z} \phi_I^1(z) + a \left(p_{12} \phi_I^1(z) - p_{21} \phi_{II}^1(z) \right) + \frac{a^2}{2} \Sigma_I^1(z) \phi_I^1(z) - \frac{a^2}{2} \frac{\nu \Sigma_{f_I}^2}{k} \phi_I^2(z) \right] dz$$

$$= \frac{a^2}{2} \left[(D_I^1)_- \times \frac{\phi_I^1(nh) - \phi_I^1(n-1)h)}{h} + (D_I^1)_+ \times \frac{\phi_I^2(nh) - \phi_I^2(n+1)h)}{h} \right]$$

$$+ \frac{ah}{4} \left[(p_{12})_+ + (p_{12})_- \right] \phi_I^1(nh) - \frac{ah}{4} \left[(p_{21})_+ + (p_{21})_- \right] \phi_{II}^1(nh)$$

$$+ \frac{a^2 h}{4} \left[(\Sigma_I^1)_+ + (\Sigma_I^1)_- \right] \phi_I^1(nh) - \frac{a^2 h \nu}{4k} \left[\left(\Sigma_{f_I}^2 \right)_+ + \left(\Sigma_{f_I}^2 \right)_- \right] \phi_I^2(nh).$$

If the first row of the 4×4 matrix B_n (see Fig. 4.41) at $z = nh$ is $\beta_1, \beta_2, \beta_3, \beta_4$, then

$$\beta_1 = \frac{a^2}{2h}\left[(D_I^1)_- + (D_I^1) \right] + \frac{ah}{4}\left[(p_{12})_+ + (p_{12})_-\right] + \frac{a^2 h}{4}\left[(\Sigma_I^1)_+ + (\Sigma_I^1)_- \right]$$

$$\beta_2 = -\frac{a^2 h\nu}{4k}\left[\left(\Sigma^2_{f_{I_+}}\right) + \left(\Sigma^2_{f_I}\right)_-\right]$$

$$\beta_3 = -\frac{ah}{4}\left[(p_{21})_+ + (p_{21})_-\right]$$

$$\beta_4 = 0 .$$

If the first row of $A_{n,n-1}$ in Fig. 4.41 is $[(\alpha_1)_-, (\alpha_2)_-, (\alpha_3)_-, (\alpha_4)_-]$ then

$$(\alpha_1)_- = \frac{a^2 (D_I^1)_-}{2h} , \quad (\alpha_2)_- = (\alpha_3)_- = (\alpha_4)_- = 0$$

and for $A_{n,n+1}$ with elements $\left[(\alpha_1)_+, (\alpha_2)_+ , (\alpha_3)_+, (\alpha_4)_+\right]$,

$$(\alpha_1)_+ = \frac{a^2}{2h}(D_I^1)_+ , \quad (\alpha_2)_+ = (\alpha_3)_+ = (\alpha_4)_+ = 0 .$$

When Wielandt's method is used [Eq. (4.206)], one uses an estimated eigenvalue, k_e in the B_n submatrices. By the analysis given in Chap. 7, Sect. 7.2, the matrix $\left[M - \frac{\nu F}{k_e}\right]^{-1}$ is non-negative if and only if $k_e > k$, where k is the true eigenvalue. Examination of the inverse enables one to establish bounds on k without the need for computing fluxes when this method is used. This is a convenient feature for reactor life studies where one is often interested only in k for some of the auxiliary calculations as, for example, shutdown safety and xenon override configurations.

Simultaneous group inversion has other far reaching consequences. In following a reactor transient, the neutron flux may be determined as a function of changing reactor properties and a delayed neutron source which is a function of past

history. For many dynamic studies, the flux calculation is a source rather than an eigenvalue problem:

$$\left[M(t) - \frac{\nu}{k}(1-\beta)F(t)\ \phi(t)\right] = S(t) \qquad \text{Eq. (4.207)}$$

where β is the delayed neutron fraction, and S is the delayed neutron source. Since the source is known from past history, the fluxes may be found directly by inverting the matrix $\left[M - \frac{\nu}{k}(1-\beta)F\right]$. No iteration is required when fluxes in all groups can be considered simultaneously.

The computer time required to solve the three-dimensional axial problem is of order magnitude equal to the time required to solve several one-dimensional problems. A major portion of the computer time for a synthesis study is in the two-dimensional computations.

Once a set of channel transfer coefficients has been determined from two-dimensional fluxes, the three-dimensional multichannel model may be used for parameter studies and dynamic analysis (see Chap. 5).

5. *Computation Strategy*

Radial and axial calculations must be coordinated through an overall computation strategy. This strategy is of most concern when leakage approximations are iterated to consistency and is common to single and multichannel synthesis. A group-independent buckling assumed for each zone may be adjusted during the initial zone-flux calculation to yield a desired reactivity.

An alternative approach which may reduce the two-dimensional computation time will now be described. The initial calculation is with the axial model. Geometric leakage transfer coefficients, based on an assumed flat flux, are used:

$$P_{cc'} = \frac{j^{+}_{cc'}}{\phi_c} = \frac{a\left(\frac{\phi_s}{4} + \frac{L}{2}\right)}{\phi_c} \approx \frac{a}{4}$$

where the surface flux, ϕ_s equals the channel average flux, ϕ_c, and the leakage, L, is zero. The parameter, a, in the above equation is the length of the boundary common to channels c and c'. This scheme will be referred to as perimeter coupling.

The axial flux shapes computed with this perimeter coupling may be used to obtain group and channel-dependent bucklings for two-dimensional zone computations. An examination of these fluxes should also aid in the selection of zones, and one

can visualize a computer program which selects zones automatically. In general, however, the reactivity and the radial flux shapes of this perimeter-coupled axial computation will be far from correct.

The initial two-dimensional zone computations are performed with group and channel-dependent bucklings when this strategy is used. (The axial-leakage transfer coefficient scheme may be applied on subsequent iterations.) For many applications, radial leakage transfer coefficients computed from the first two-dimensional flux results are adequate.

Having determined these flux-dependent transfer coefficients, one now repeats the axial calculation. Control elements may be adjusted to yield a desired reactivity with the multichannel axial model.

6. *Anticipated Applicability*

The range of applicability of this multichannel synthesis method is expected to be quite broad. A more significant consideration than range of applicability is the number of channels and zones needed for reactor design studies. This can be answered only by numerical experimentation. Preliminary results are given below. Each reactor must be analyzed separately, although some general guides may be obtained from past experience.

The success of single channel synthesis in reactivity calculations indicates that few channels are needed for reasonable reactivity estimates. With regard to power shapes, however, one channel is frequently inadequate. Thermal and hydraulic calculations often include only a few reactor channels, and it is hoped that these same channels may be used for nuclear and thermal computations.

7. *Numerical Results*

A) DESCRIPTION OF SAMPLE PROBLEM 1. Numerical synthesis studies were performed on a reactor, the configuration for which is shown in Fig. 4.44. The cross sections of the upper part of the inner fuel region include a distributed poison simulation of a bank of control rods. A detailed three-dimensional solution of the diffusion equation for this reactor (obtained by the program UFO[61]) was used as a standard for the comparison of results of various synthesis computations.

Several synthesis mockups which differed in their degree of detail were applied to the reactor to evaluate the accuracy that could be attained with each. The KLAG program[58] was used for both the single and multichannel synthesis calculations.

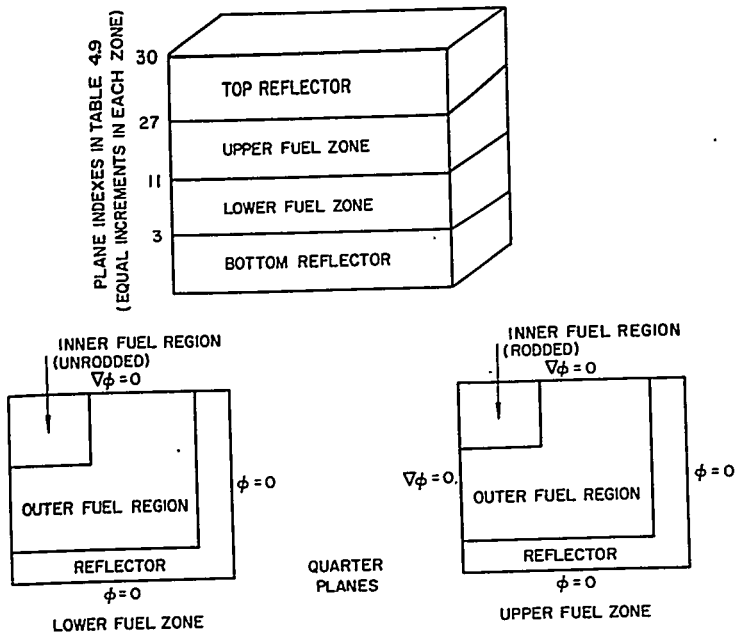

FIGURE 4.44. Configuration of Sample Problem 1.

The single channel model was the simplest and the crudest. Two-dimensional calculations were performed for the core configurations above and below the rod tips. The resulting radial flux shapes were used to flux-weight cross sections and, thus, create one radially homogeneous channel. Radial bucklings were calculated from the leakages from the core to the side reflector. A one-channel problem was run using the bucklings, and it produced fluxes and powers averaged radially over the core at each point of the vertical mesh.

In the next study, the inner and outer fuel regions were treated as separate channels, 1 and 2, respectively. As each channel contained only one material, it was not necessary to flux-weight the cross sections. The two-dimensional radial flux shapes were needed, nonetheless, to calculate interchannel and external leakages for the computation of transfer coefficients. The results of the two-channel study included fluxes and powers averaged over each of the two channels at the level of each vertical mesh point.

In the final study, a third channel was introduced for the side reflector region. Transfer coefficients were calculated between Channels 1 and 2 and between Channels 2 and 3. External leakage coefficients were calculated for Channel 3. The three-channel results yielded side reflector fluxes in addition to the fluxes and power obtained by the two-channel study.

Reactivities and powers obtained by each synthesis mockup are compared in Table 4.9. It can be seen that there is some improvement with the increase in channels, but that the single channel results may be adequate.

Axial bucklings for use in the original two-dimensional calculations were obtained in two ways:

1. A group and region-independent buckling which produced criticality was found by iteration for each two-dimensional configuration.

2. An axial calculation was performed with perimeter coupling, and group and channel-dependent bucklings were determined from the resulting flux shapes.

Two-dimensional calculations were performed with bucklings that were obtained by each method, and the results of each were used to calculate transfer coefficients for an axial calculation. Powers obtained from the axial calculations are compared in Table 4.10.

When the perimeter coupling method was used, the criticality obtained from the two-dimensional calculation for each zone agreed to within 1 percent with that calculated by UFO for the whole reactor. A comparison of axial bucklings in the lower zone calculated from different KLAG iterations is given in Table 4.11.

TABLE 4.9 — PLANE AVERAGED POWER DENSITIES

Plane	UFO	Single Channel Synthesis	Two-Channel Synthesis	Three-Channel Synthesis
3	2.20	2.27	2.33	2.20
7	2.56	2.52	2.55	2.60
11	1.62	1.65	1.60	1.60
15	0.564	0.574	0.568	0.549
18	0.270	0.267	0.270	0.260
22	0.098	0.096	0.099	0.093
27	0.028	0.032	0.034	0.025
30	2.20	2.27	2.33	2.20
k =	0.9829	0.9718	0.9780	0.9805

TABLE 4.10 — POWER DENSITIES BASED ON DIFFERENT AXIAL BUCKLINGS

Plane	UFO	Method 1	Method 2
3	2.20	2.20	2.17
7	2.56	2.60	2.58
11	1.62	1.60	1.61
15	0.564	0.549	0.560
18	0.270	0.260	0.268
22	0.098	0.093	0.098
27	0.028	0.025	0.027
k =	0.9829	0.9805	0.9848

TABLE 4.11 — AXIAL BUCKLINGS IN LOWER ZONE

	Perimeter Coupling	First Iteration	
	1	2	3
Group 1	0.00295	0.00252	0.00171
Group 2	0.00233	0.00169	0.00168
Group 3	-0.00357	-0.00198	-0.00133
	Perimeter Coupling	Second Iteration	
Group 1	0.00326	0.00215	0.000766
Group 2	0.00263	0.00113	0.000300
Group 3	-0.00376	-0.00322	-0.000919
Bucklings from Axial Calculation Based on Initial Two-Dimensional Calculations with Group and Channel-Independent Bucklings			
Group 1	0.00334	0.00206	0.000457
Group 2	0.00272	0.000769	0.00163
Group 3	-0.00394	-0.00317	-0.000833

B) SAMPLE PROBLEM 2. The method was tested further by applying it to a two-dimensional problem which had a sharper flux variation (see Fig. 4.45). The problem was mocked up with three channels and three zones. Since the problem was two-dimensional, the zone calculations were one-dimensional. This problem was selected to illustrate the greater refinement of multichannel synthesis over single channel synthesis for a highly nonseparable configuration.

As in the previous case, the first vertical calculation was performed with perimeter coupling. The results were used to calculate axial bucklings for each of the three zones. In turn, the results of the zone calculations were used to provide new transfer coefficients.

The same configuration was mocked up with one vertical channel. In Fig. 4.46, the synthesized results of both methods are compared with the results of a two-dimensional calculation. An axial traverse through the thermal flux peak was selected for this purpose.

C) SAMPLE PROBLEM 3. This test problem, described in Sect. 4.4.D, was solved first with three vertical channels and again with five vertical channels. The same strategy was used for both computations:

1. A perimeter-coupled γ computation was run to give axial leakage parameters.
2. A three-channel x computation (with axial leakage determined from Step 1) was run.
3. Results from Step 2 were used as input to a γ computation.

The channels are indicated in Fig. 4.47.

Step 1 differed from the usual computation and was used to indicate how two perpendicular KLAG calculations could be iterated to consistency to approximate plane calculations. Thus, instead of three separate one-dimensional radial calculations, one three-channel computation was performed. In three-dimensional synthesis calculations, this would require simultaneous solution of planes and would not be practical.

The results shown in Figs. 4.48 and 4.49 are self-explanatory. They may be compared with the results presented in Sect. 4.4.D. The KARE* program was used to obtain the exact solution. The values for reactivity, k, obtained by the three methods were:

$$k_{\text{KARE}} = 1.0133 \pm 0.0004$$

$$k_{\substack{5 \text{ channels} \\ \text{KLAG}}} = 1.0128$$

$$k_{\substack{3 \text{ channels} \\ \text{KLAG}}} = 1.010$$

*The KARE program is described in Sect. 4.6.E.1 and also in Chap. 7.

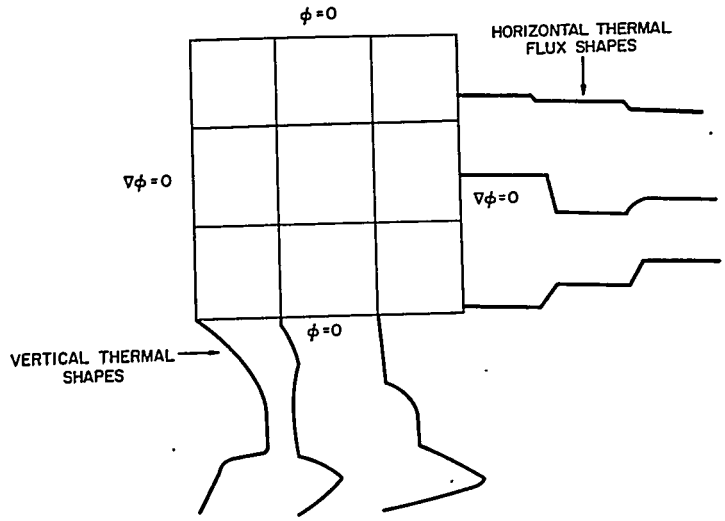

FIGURE 4.45. Sample Problem 2 with Flux Shapes.

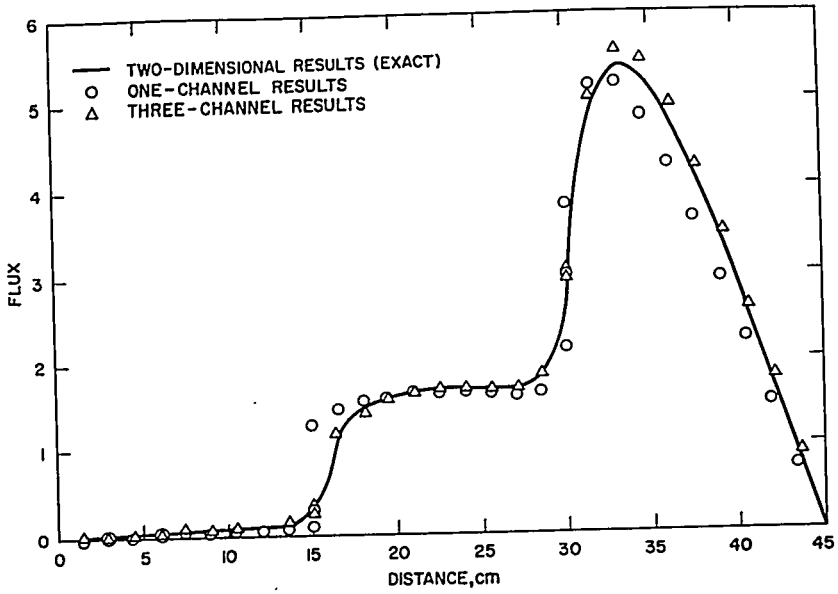

FIGURE 4.46. Vertical Thermal Flux Traverse.

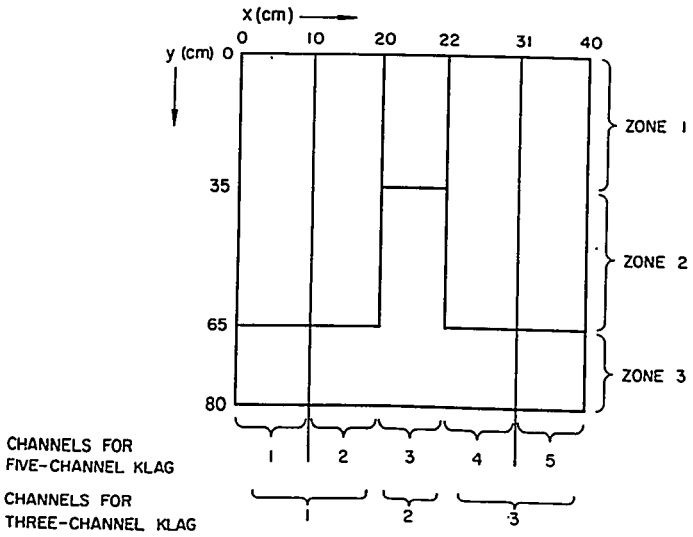

FIGURE 4.47. KLAG Models for Sample Problem 3.

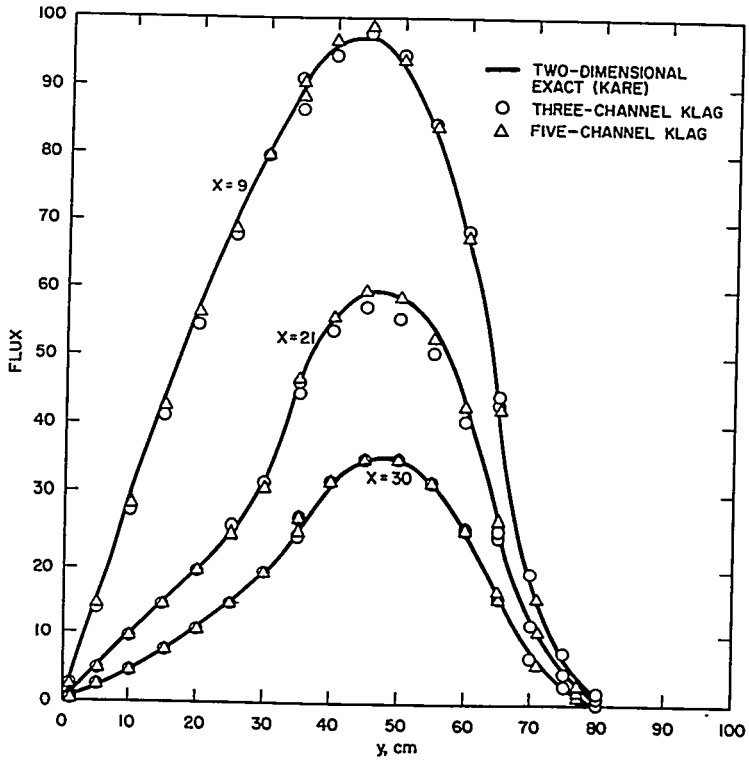

FIGURE 4.48. Group 1 Fluxes.

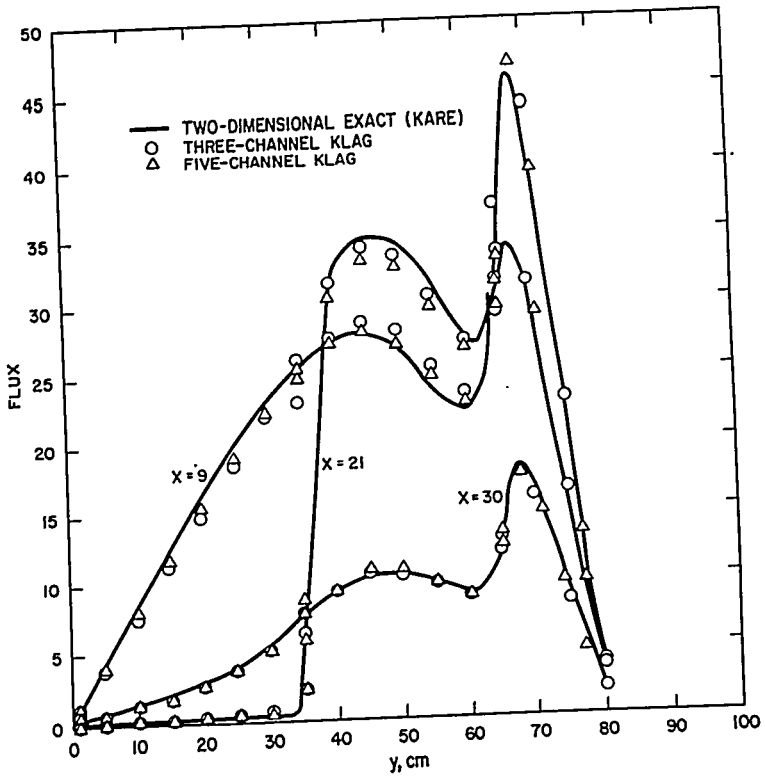

FIGURE 4.49. Group 2 Fluxes.

The KARE and PDQ results are not in exact agreement because different mesh spacing was used. Also, KARE and PDQ normalization is not identical. Accuracy of synthesis is independent of these effects in that the synthesized fluxes are compared in each case with a two-dimensional computation rather than an analytic solution.

D) SUMMARY OF SAMPLE PROBLEM RESULTS. If, in the first problem, the power shape obtained from the one-channel mockup is adequate for design purposes, the improvement that resulted from increasing the number of channels would not be appreciable. In the second problem, the advantages of three channels over one are more apparent.

The study demonstrated for these examples the practicality and speed of multichannel synthesis as well as the additional detail that it provides. It also indicated the advantage of using the perimeter coupling method to calculate the initial

axial bucklings. This suggests the possibility of running multichannel calculations with perimeter coupling prior to two-dimensional studies even when the vertical shape is, otherwise, of no particular interest.

The third problem illustrates how two multichannel problems may be synthesized to give an approximation to two-dimensional flux shapes. Excellent agreement with the exact solution was obtained. Results may be compared with those obtained by the variational method in Sect. 4.4.D.5.

D. Variational Synthesis

S. Kaplan

1. *Introduction of the Variational Methods and Review of Channel Methods*

The essential distinction between the channel methods of synthesis and the variational methods lies in the form used for the approximate flux. To illustrate this concisely consider a cylindrical reactor (Fig. 4.50) which is divided into two axial zones by a control rod bank.

In the rods-out zone, far from the rod interface, the flux distribution in energy group j assumes an asymptotic shape, $H_1^j(x, y)$, in the horizontal plane. Similarly, there is an asymptotic shape, $H_2^j(x, y)$, in the rods-in zone. The single channel synthesis assumes that the flux within each axial zone is separable into radial and axial components. In symbols, the form of approximation used by the single channel model is

$$\psi^j(x, y, z) = Z^j(z) \begin{cases} H_2^j(x, y), & z_R < z < L \\ H_1^j(x, y), & 0 < z < z_R \end{cases} \qquad \text{Eq. (4.208)}$$

If $H_1(x,y)$ and $H_2(x,y)$ are different functions the form of Eq. (4.208) is discontinuous at the plane $z = z_R$, the major shortcoming of the single channel method. In the multichannel method, the flux is not required to be separable over the complete horizontal plane but only over individual channels into which that plane is divided. For example, if there are three channels

$$\psi^j(x, y, z) = \begin{Bmatrix} Z_1(z), & x, y \text{ in channel 1} \\ Z_2(z), & x, y \text{ in channel 2} \\ Z_3(z), & x, y \text{ in channel 3} \end{Bmatrix} \times \begin{Bmatrix} H_2^j(x, y), & z_R < z < L \\ H_1^j(x, y), & 0 < z < z_R \end{Bmatrix}. \qquad \text{Eq. (4.209)}$$

This method reduces the flux discontinuities in the vertical direction at the cost of introducing them in the horizontal directions. However, if a sufficient number of channels is used, the discontinuities are quite small.

In the variational synthesis the form of solution is

$$\psi^j(x,y,z) = Z_1^j(z)H_1^j(x,y) + Z_2^j(z)H_2^j(x,y) \ . \qquad \text{Eq. (4.210)}$$

The idea is that at any axial level the true x, y shape can be well approximated by some mixture of the asymptotic shapes. The proportion of the mixture is given by the values of the coefficients $Z_k^j(z)$ at that level. If the $Z_k^j(z)$ are continuous functions, then the approximation of Eq. (4.210) will have no discontinuities.

For a reactor which has more than two axial zones, the approximate form of Eq. (4.210) is generalized to

$$\psi^j(x,y,z) = \sum_{k=1}^{K_j} Z_k^j(z)H_k^j(x,y) \ . \qquad \text{Eq. (4.211)}$$

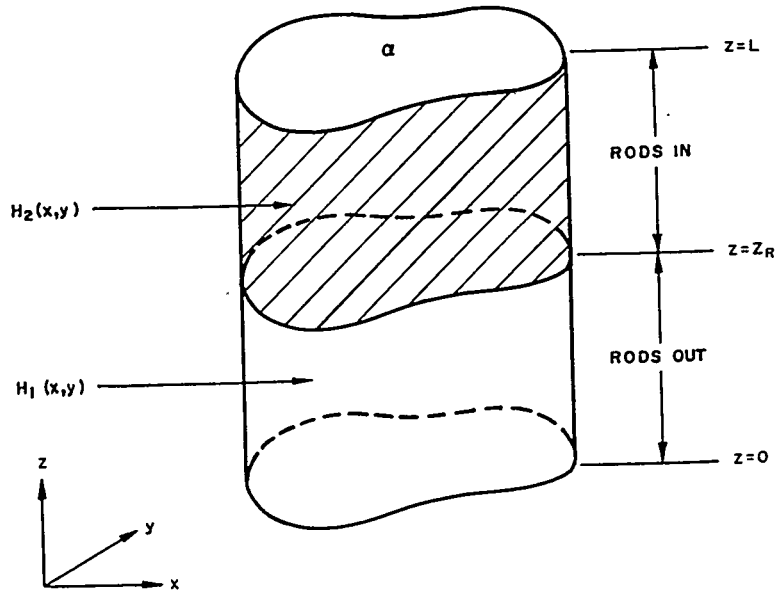

FIGURE 4.50. Cylindrical Reactor with Two Axial Zones.

Here the H_k^j (called the trial functions) are functions satisfying the boundary conditions in the x, y plane, and they are chosen intuitively such that an expression of the form of Eq. (4.211) could be expected to be a good approximation to the true solution. The set of trial functions should contain the asymptotic shapes of each axial zone but can also include other functions. The key problem in using the form of Eq. (4.210) or (4.211) is to find the mixing functions, $Z_k^j(z)$. Ideally, these should be determined so that the resulting synthesized solution is the best approximation to the true solution possible with the chosen H_k^j. The questions of what should be meant by best and how to achieve it are unsettled; however, one can think of several methods to find the $Z_k^j(z)$ which intuition suggests ought to be satisfactory. Four such schemes will be described: the variational, Galerkin, region balance, and multiple spot methods.

Although the motivation for synthesis methods is primarily to solve three-dimensional problems, the methods may be tested cheaply by synthesizing two-dimensional solutions from one-dimensional shapes and comparing with direct solutions of the two-dimensional problem. A test problem of this type is presented in Sect. 4.4.D.5. The equations appropriate to the four methods are developed in Sects. 4.4.D.3 and 4.4.D.4 following a definition of notation in Sect. 4.4.D.2.

2. Notation

For purposes of illustration consider a right cylindrical reactor occupying volume R, with surface S, and cross sectional area α. Over R a solution is sought to the J few-group diffusion equations, which in matrix notation are

$$-\nabla \cdot D \nabla \Phi + A \Phi = \frac{1}{\lambda} M \Phi \qquad \text{Eq. (4.212)}$$

where

$$\Phi = \text{col}(\phi^1, \phi^2, \ldots \phi^J)$$

$$D = \text{diag}(D^1, D^2, \ldots D^J)$$

$$A = (\Sigma^{ij})$$

$$M = (\chi^i \nu \Sigma_f^j) \ .$$

Here ϕ^j, D^j, χ^j, Σ_f^j, and Σ^{ij} are, respectively, the neutron flux, the diffusion constant, fraction of fission neutrons, fission cross section, and total cross section appropriate to energy group j; $-\Sigma^{ij}$ is the transfer cross section from group j to group

i. Equation (4.212) is to be solved subject to the conditions of continuous flux and current across interior surfaces and subject to the exterior boundary condition

$$\Phi = 0 \text{ on } S \ . \qquad \text{Eq. (4.213)}$$

Now, suppose solutions in the x, y plane are available representing the asymptotic shapes in each axial zone. Consider one of these solutions, say the k^{th} one. It consists of J functions of x and y, one for each energy group. Arrange these J functions into a diagonal matrix

$$H_k(x,y) = \text{diag}\left(H_k^1(x,y) \ldots H_k^j(x,y)\right). \qquad \text{Eq. (4.214)}$$

It is desired to synthesize an approximate flux matrix ψ which is a linear combination of K horizontal solutions H_k

$$\Psi(x,y,z) = \sum_{k=1}^{K} H_k(x,y) Z_k(z) \qquad \text{Eq. (4.215)}$$

where

$$Z_k(z) = \text{col}\left(Z_k^1(z), \ldots Z_k^J(z)\right) \ . \qquad \text{Eq. (4.216)}$$

The problem will be to determine the vectors $Z_k(z)$.

In principle, the $H_k^j(x,y)$ may be any convenient functions. However, physical intuition implies that for a good approximation the set of trial functions should include functions representing the asymptotic x, y shape in each axial zone. For improved accuracy additional x, y functions may be included. Also, the number of trial functions in each energy group need not be the same. This situation is included in Eq. (4.215) by regarding certain of the H_k matrices as having some zero diagonal elements.

In addition, in the variational method a synthesized adjoint flux will be used,

$$\Psi^*(x,y,z) = \sum_{k=1}^{K} H_k^*(x,y) Z_k^*(z) \qquad \text{Eq. (4.217)}$$

to approximate the true adjoint solution Φ^* satisfying

$$-\nabla \cdot D \nabla \Phi^* + A^T \Phi^* = \frac{1}{\lambda} M^T \Phi^* \qquad \text{Eq. (4.218)}$$

where A^T and M^T are the transposes of A and M, and Φ^* also obeys the boundary condition of Eq. (4.213). Again, intuition implies that the set of $H_k^{j*}(x,y)$ should include asymptotic adjoint shapes for each axial zone.

Synthesis of the adjoint flux is also of interest in connection with applications such as calculating three-dimensional void reactivity coefficients (see Chap. 5, Sect. 5.2, for a further discussion of the use of adjoint fluxes in reactor kinetics problems.)

3. *Variational Method*

The first method to be discussed for finding the Z_k is an elaboration of an illustrative example by Selengut[11] in which he outlines a general process for using variational methods in connection with nonself-adjoint problems. This variational method, as it is used here, differs from the usual variational methods in two respects. First, the functional in question is a bilinear functional of two arguments rather than quadratic. Thus, one has a stationary principle rather than an extremum principle. Secondly, the form of trial solution contains unknown functions rather than unknown scalars. The use of trial functions of this type is known variously as the Kantorovich method,[62,63] the Jennings method,[64] and the semidirect method.[65]

To formulate the present application consider the collection, $\mathfrak{U}$, of all continuous real valued functions defined over R which have piecewise continuous first and second partial derivatives and which vanish on S. Let U denote the space of $J \times 1$ column matrices, the elements of which belong to $\mathfrak{U}$. For any two members Ξ and Γ of U, one defines the following inner product symbols:

$$\langle \Xi, \Gamma \rangle \equiv \int_R \Xi^T \Gamma \, dR \qquad \text{Eq. (4.219)}$$

$$\langle \nabla\Xi, \nabla\Gamma \rangle \equiv \int_R \nabla\Xi^T \cdot \nabla\Gamma \, dR \qquad \text{Eq. (4.220)}$$

where the superscript T denotes a transpose and the dot in Eq. (4.220) indicates the usual vector dot product. Using this notation, consider the functional

$$F[\Xi, \Gamma] = \frac{\langle \nabla\Xi, D\nabla\Gamma \rangle + \langle \Xi, A\Gamma \rangle}{\langle \Xi, M\Gamma \rangle}. \qquad \text{Eq. (4.221)}$$

By the usual variational arguments, it follows that this functional is stationary with respect to independent variations of Ξ and Γ if and only if

$$\left\langle \nabla \delta\Xi, D\nabla\Gamma \right\rangle + \left\langle \delta\Xi, \left(A - F\left[\Xi, \Gamma\right] M\right) \Gamma \right\rangle = 0 \qquad \text{Eq. (4.222)}$$

and

$$\left\langle \nabla \delta\Gamma, D\nabla\Xi \right\rangle + \left\langle \delta\Gamma, \left(A^T - F\left[\Xi, \Gamma\right] M^T\right) \Xi \right\rangle = 0 \qquad \text{Eq. (4.223)}$$

for all admissible $\delta\Xi$ and $\delta\Gamma$. To obtain conditions on Ξ and Γ, it is necessary to manipulate the terms involving gradients. Consider the reactor as divided into subregions, R_i, over each of which D, $\nabla\Xi$, and $\nabla\Gamma$ are continuous. Applying the divergence theorem over each subregion, one obtains

$$\left\langle \nabla \delta\Xi, D\nabla\Gamma \right\rangle = \sum_i \int_{R_i} \nabla \delta\Xi^T \cdot D\nabla\Gamma \, dR$$

$$= \sum_i \int_{S_i} \delta\Xi^T D\nabla\Gamma \cdot \vec{N}_i dS - \int_R \delta\Xi^T \nabla \cdot D\nabla\Gamma \, dR$$

Eq. (4.224)

where S_i is the surface of R_i, and $\vec{N}_i$ is a unit normal to S_i. When the summation over i is performed, each element of an interior surface will be counted twice, once with the normal pointing one way and once with the normal the other way. Moreover, $\delta\Xi$ vanishes over the outer surface. Thus, Eq. (4.224) may be written

$$\left\langle \nabla \delta\Xi, D\nabla\Gamma \right\rangle = - \left\langle \delta\Xi, \nabla \cdot D\nabla\Gamma \right\rangle + \int_{\substack{\text{interior} \\ \text{surfaces}}} \delta\Xi^T \left\{ (D\nabla\Gamma)_{+\epsilon} - (D\nabla\Gamma)_{-\epsilon} \right\} \cdot \vec{N} \, dS$$

Eq. (4.225)

where each element of interior surface is counted only once, and the subscripts. $+\epsilon$ and $-\epsilon$ indicate limits as the surface is

approached from two sides. Putting Eq. (4.225) into Eq. (4.222) shows that F is stationary only if

$$\left\langle \delta\Xi, \left\{ -\nabla \cdot D\nabla + A - F\,[\Xi,\Gamma]\,M \right\} \Gamma \right\rangle + \int_{\substack{\text{interior} \\ \text{surfaces}}} \delta\Xi^T \left\{ (D\nabla\Gamma)_{+\epsilon} - (D\nabla\Gamma)_{-\epsilon} \right\} \cdot \vec{N}\, ds = 0 . \qquad \text{Eq. (4.226)}$$

Since $\delta\Xi$ is arbitrary, F is stationary only if

$$\left\{ -\nabla \cdot D\nabla + A - F\,[\Xi,\Gamma]\,M \right\} \Gamma = 0 \text{ in } R \qquad \text{Eq. (4.227)}$$

and $D\nabla\Gamma \cdot \vec{N}$ is continuous on interior surfaces; in other words, only if $\Gamma = \Phi$. A similar process starting with Eq. (4.223) shows that F is stationary only if $\Xi = \Phi^*$. Therefore, the functional F has the desired property.

The next step conceptually is to restrict the admissible class for F to functions in U which are of the form of Eqs. (4.215) and (4.217), thus obtaining a reduced functional which is then made stationary. However, one may bypass the step of explicitly displaying the reduced functional because Eqs. (4.222) and (4.223) are valid for all $\delta\Xi, \delta\Gamma, \Xi, \Gamma$, and Γ in U and, therefore, valid in particular for $\Gamma, \delta\Gamma, \Xi$, and $\delta\Xi$ in the restricted admissible class. One may, therefore, directly obtain the stationary conditions of the reduced functional by inserting Eqs. (4.215) and (4.217) into Eqs. (4.222) and (4.223) with Ξ replaced by Ψ^* and Γ replaced by Ψ. The result from Eq. (4.222) is

$$\sum_{i=1}^{K} \sum_{k=1}^{K} \left\{ \left\langle \nabla \left(H_i^* \delta Z_i^* \right), D\nabla \left(H_k Z_k \right) \right\rangle + \left\langle H_i^* \delta Z_i^*, \left\{ A - F\,[\Psi^*, \Psi]\,M \right\} H_k Z_k \right\rangle \right\} = 0 . \qquad \text{Eq. (4.228)}$$

The next step is to perform the integration over x and y. To do this it is best to consider each term separately:

$$\left\langle H_i^* \delta Z_i^*, A\, H_k Z_k \right\rangle = \int_0^L \left(\delta Z_i^* \right)^T \left[\int_a H_i^* A\, H_k \, dx\, dy \right] Z_k \, dz . \qquad \text{Eq. (4.229)}$$

The definition

$$A_{ik}(z) = \int_a H_i^* A\, H_k dxdy \qquad \text{Eq. (4.230)}$$

leads to

$$\left\langle H_i^* \delta Z_i^*,\, A\, H_k Z_k \right\rangle = \int_0^L \left(\delta Z_i^*\right)^T A_{ik} Z_k dz\,. \qquad \text{Eq. (4.231)}$$

Similarly, defining

$$M_{ik}(z) = \int_a H_i^* M H_k dxdy \qquad \text{Eq. (4.232)}$$

yields

$$\left\langle H_i^* \delta Z_i^*,\, M H_k Z_k \right\rangle = \int_0^L \left(\delta Z_i^*\right)^T M_{ik} Z_k dz\,. \qquad \text{Eq. (4.233)}$$

To handle the gradient terms, since $\nabla H_i^* \cdot \nabla Z_k$ and $\nabla \delta Z_i^* \cdot \nabla H_k$ are zero, note that

$$\left(\nabla H_i^* \delta Z_i^*\right)^T \cdot D \nabla (H_k Z_k) = \left[\left(\nabla H_i^*\right) \delta Z_i^* + H_i^* \nabla \delta Z_i^*\right]^T \cdot D \left[(\nabla H_k) Z_k + H_k \nabla Z_k\right]$$

$$= \left(\delta Z_i^*\right)^T \left(\nabla H_i^* \cdot D \nabla H_k\right) Z_k + \left(\nabla \delta Z_i^*\right)^T \cdot \left(H_i^* D H_k\right) \nabla Z_k\,. \qquad \text{Eq. (4.234)}$$

Therefore,

$$\left\langle \nabla \left(H_i^* \delta Z_i^*\right), \nabla (H_k Z_k) \right\rangle = \int_0^L \left(\delta Z_i^*\right)^T (DB_r^2)_{ik} Z_k dz + \int_0^L \left(\nabla \delta Z_i^*\right)^T \cdot D_{ik} \nabla Z_k dz \qquad \text{Eq. (4.235)}$$

where

$$\left(DB_r^2\right)_{ik}(z) = \int_a \nabla H_i^* \cdot D \nabla H_k dxdy \qquad \text{Eq. (4.236)}$$

and

$$D_{ik}(z) = \int_a H_i^* D H_k dxdy\,. \qquad \text{Eq. (4.237)}$$

With $L_n, n = 1, \ldots N$ denoting the values of the z variable at which $D_{ik}(z)$ or ∇Z_k are discontinuous, and with $L_o = 0, L_{N+1} = L$, it follows that

$$\int_0^L \left(\nabla \delta Z_i^*\right)^T \cdot D_{ik} \nabla Z_k dz = \sum_{n=0}^{N} \int_{L_n}^{L_{n+1}} \left(\nabla \delta Z_i^*\right)^T \cdot D_{ik} \nabla Z_k dz$$

Eq. (4.238)

$$= \left\{ \sum_{n=0}^{N} \int_{L_n}^{L_{n+1}} \nabla \cdot \left[\left(\delta Z_i^*\right)^T D_{ik} \nabla Z_k \right] dz \right\} - \int_0^L \left(\delta Z_i^*\right)^T \nabla \cdot D_{ik} \nabla Z_k dz$$

Eq. (4.239)

$$= \sum_{n=1}^{N} \left[\delta Z_i^*(L_n)\right]^T \left[D_{ik} \frac{d}{dz} Z_k \right]_{L_n+\epsilon}^{L_n-\epsilon} - \int_0^L \left(\delta Z_i^*\right)^T \nabla \cdot D_{ik} \nabla Z_k dz .$$

Eq. (4.240)

Therefore, one has the identity

$$\left\langle \nabla \left(H_i^* \delta Z_i^*\right) \cdot D \nabla H_k^* Z_k \right\rangle = \int_0^L \left(\delta Z_i^*\right)^T \left[-\nabla \cdot D_{ik} \nabla + (DB^2)_{ik} \right] Z_k dz + \sum_{n=1}^{N} \left[\delta Z_i^*(L_n)\right]^T \left[D_{ik} \frac{d}{dz} Z_k \right]_{L_n+\epsilon}^{L_n-\epsilon} .$$

Eq. (4.241)

Substituting Eqs. (4.229), (4.231), and (4.241) in Eq. (4.228) one obtains

$$\sum_{i=1}^{K} \sum_{k=1}^{K} \left\{ \int_0^L \left(\delta Z_i^*\right)^T \left[-\nabla \cdot D_{ik} \nabla + A_{ik} + (DB^2)_{ik} - F \left[\Psi^*, \Psi\right] M_{ik} \right] Z_k dz + \sum_{n=1}^{N} \left[\delta Z_i^*(L_n)\right]^T \left[D_{ik} \frac{d}{dz} Z_k \right]_{L_n+\epsilon}^{L_n-\epsilon} \right\} = 0 .$$

Eq. (4.242)

Equation (4.242) is to hold for all δZ_i^*; therefore, the reduced functional is stationary only if the Z_k form an eigensolution of the system

$$\sum_{k=1}^{K} \left\{ -\nabla \cdot D_{ik}(z)\nabla Z_k(z) + \left[A_{ik}(z) + \left(DB_r^2\right)_{ik}(z) \right] Z_k(z) \right\} = \frac{1}{\lambda} \sum_{k=1}^{K} M_{ik}(z) Z_k(z)$$

Eq. (4.243)

with the interface conditions

$$Z_k \text{ and } \sum_{k=1}^{K} D_{ik} \frac{d}{dz} Z_k \qquad \text{Eq. (4.244)}$$

continuous, the first interface condition following from the restriction of trial functions to those belonging to the class U, and the second following from Eq. (4.242).

The set of Eqs. (4.243) and (4.244) define the Z_k functions to be used in synthesizing the flux according to the variational method. To synthesize the adjoint flux, a similar system defining the Z_k^* functions can be derived as a consequence of Eq. (4.223):

$$\sum_{k=1}^{K} \left\{ -\nabla \cdot D_{ik}^*(z)\nabla Z_k^* + \left[A_{ik}^* + (DB_r^2)_{ik}^* \right] Z_k^* \right\} = \frac{1}{\lambda} \sum_{k=1}^{K} M_{ik}^* Z_k^*$$

Eq. (4.245)

where

$$D_{ik}^* = D_{ki},\ A_{ik}^* = A_{ki}^T,\ M_{ik}^* = M_{ki}^T \text{ and } (DB_r^2)_{ik} = (DB_r^2)_{ki} .$$

The interface conditions [Eq. (4.244)] are physically the continuity of flux and continuity of weighted integrals of current across horizontal sections.

4. *Methods of Galerkin, Region Balance, and Multiple Spot*

The Eqs. (4.233) and (4.234) defining the mixing functions by the variational method are the same equations one would have obtained if one had simply substituted the assumed form of Eq. (4.215) into the three-dimensional Eq. (4.212) and then multiplied both sides successively by the weighting functions H_i^* and integrated over α. From this point of view the question arises: Might one not have chosen some different set of weighting functions, $W_1 \ldots W_K$, and again obtain equations defining the Z_k functions? Formally, this can be done. It is clear that if the true solution is of the form of Eq. (4.215) then it makes no difference what weighting functions are used; all will yield the exact solution. When the true solution is not of the form of Eq. (4.215) there appears to be no comprehensive theory available which indicates the optimum choice of weighting functions. In any given problem the choice has to be based upon empirical evidence regarding accuracy and also upon consideration of convenience.

Several particular choices of weighting functions other than the adjoints are especially interesting. For example, the W_i may be chosen equal to the H_i, in which case one again obtains Eqs. (4.233) and (4.234), except that now in the definition of the x, y averaged quantities H_i replaces H_i^*; i.e., for example,

$$A_{ik} = \int_\alpha H_i A H_k \, dx dy$$

and so on. This choice of weight functions corresponds to an application of the method of Galerkin.[66,67] It has the practical advantage over the variational method that it is not necessary to calculate the adjoint x,y functions.

A second interesting choice is to divide the cross section, α, of the reactor in the x,y plane into K nonoverlapping subareas, α_i (which together need not necessarily make up all of α). The weighting functions, $W_i(x,y)$ are then defined as

$$W_i(x,y) = \begin{cases} 1; x,y \text{ in } \alpha_i \\ 0; x,y \text{ not in } \alpha_i \end{cases} \qquad \text{Eq. (4.246)}$$

where I is the $J \times J$ identity matrix. With these as weight functions, the coefficients in Eqs. (4.233) and (4.234) become

$$A_{ik}(z) = \int_{\alpha_i} AH_k \, dx\,dy$$

$$M_{ik}(z) = \int_{\alpha_i} MH_k \, dx\,dy$$

$$D_{ik}(z) = \int_{\alpha_i} DH_k \, dx\,dy$$

$$(DB^2)_{ik}(z) = -\oint_{\substack{\text{contour} \\ \text{of } \alpha_i}} \nabla \cdot D \nabla H_k \, dS \qquad \text{Eq. (4.247)}$$

The synthesized solution obtained with this choice of weighting function has the physical interpretation that at each elevation, z, and in each energy group, the total source into each region, α_i, equals the total removals plus leakage from that region. Thus, the neutron balance is satisfied in each region, and the method using these weighting functions is designated as the method of region balance. This method is simpler to use than either the Galerkin or the variational methods, since no integrals of products of fluxes or of fluxes and adjoints are required.

Finally, by analogy with a version of the conventional synthesis known as the spot method (see Refs. 55 and 56 and Sect. 4.4.B for examples) one may choose the weighting functions as delta functions:

$$W_i(x, y) = I\delta(x - x_i, y - y_i) \, .$$

Since there must be K such distinct functions, this method may suitably be called multiple spot. In this case, the coefficients in Eqs. (4.243) and (4.244) are

$$(DB^2)_{ik}(z) = -\nabla \cdot D(x_i, y_i, z) \nabla H_k(x_i, y_i)$$

$$A_{ik}(z) = A(x_i, y_i, z) H_k(x_i, y_i) \, .$$

and similarly for M_{ik} and D_{ik}. Here no integrals at all are required. The multiple spot method has the interpretation that the approximate solution satisfies neutron balance at each of the singularity points (x_i, y_i) at all z (see Ref. 66 for further discussion of the mathematical theory of the spot methods).

5. *Numerical Example*

An experimental computer program has been prepared to solve a finite difference approximation to the system of Eqs. (4.243) and (4.244) on the Philco S-2000 for two-energy groups and three trial functions $(I = 2, K = 3)$. The problem utilizes the Wielandt iteration method and, hence, requires a guessed eigenvalue as part of the input. This program has been used to synthesize fluxes for a range of test problems which, from their geometry, appear suitable to the use of three trial functions. A description is given of the results of one test problem typical of this range (see Fig. 4.51 and Table 4.12).

The trial functions used were one-dimensional (WANDA[31]) solutions in the x direction which were intended to represent the asymptotic x shapes in the rod-in zone, rod-out zone, and

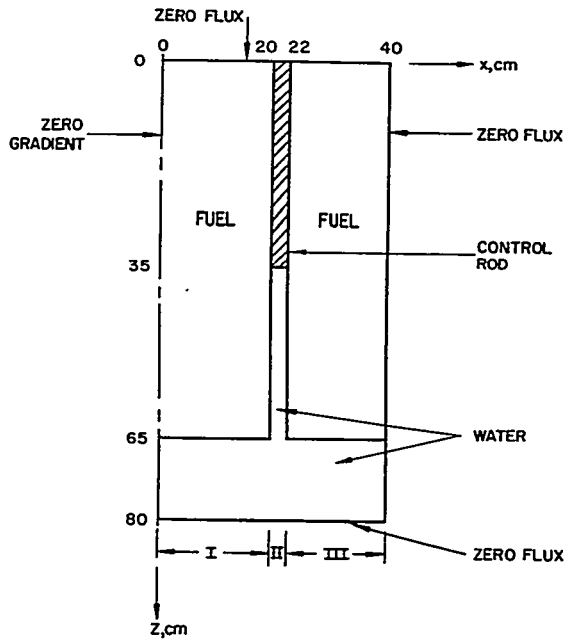

FIGURE 4.51. Test Problem Geometry.

TABLE 4.12 — TWO-GROUP CONSTANTS FOR TEST PROBLEM

	Fuel	Water	Control Rod
D^1	1.7	1.7	0.5
Σ_a^1	0	0	0.1
Σ_R^1	0.016	0.041	0
$\nu\Sigma_f^1$	0	0	0
D^2	0.42	0.23	0.1
Σ_a^2	0.055	0.012	1.5
$\nu\Sigma_f^2$	0.0832	0	0

reflector. These x direction shapes were obtained with transverse (z direction) bucklings of such a size that the eigenvalues of the x direction problems were approximately the same as that of the final synthesized two-dimensional shape.

In the variational method, the weighting functions used were the solutions of the x direction problems adjoint to those which yielded the trial functions. For the region balance method, the regions of integration are indicated by I, II, and III on Fig. 4.51. For the multiple spot method, neutron balance was required along the lines x = 9 cm, 21 cm, and 30 cm.

The results of synthesis by these four methods are presented in Figs. 4.52 to 4.55 where they are compared with a PDQ two-dimensional solution[34] and with a synthesis by the conventional method (single channel). The eigenvalues obtained by the various methods are listed in Table 4.13.

Figure 4.56 displays the shapes of the three mixing functions, $Z_i^2(z)$, for the thermal group as found by the variational method. These functions undergo rather violent contortions to make the transition across the control rod interface; however, the net synthesized results, as seen in Figs. 4.52 to 4.54, is quite smooth and satisfactory.

Note that in this application of the multiple spot method, one of the neutron balance lines has been chosen to lie within the control rod channel. This is important, for if it were not done the z direction Eq. (4.243) would have no information about the axial position of the rod. Loss of rod position information can also occur in another situation, a type of semisingularity. Such a situation could arise, for example, in the partial integration method if over Regions 1 and 3 one of the trial functions were a linear combination of the other two.

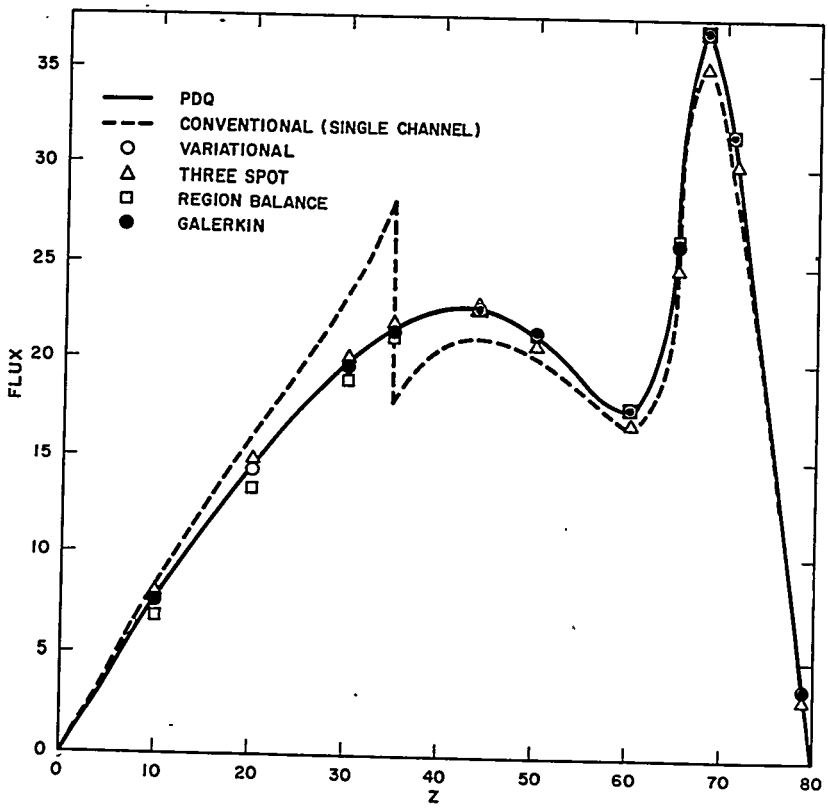

FIGURE 4.52. Flux Synthesis Thermal Group Traverse $X = 0$ cm.

Ordinary singularity must also be avoided; that is, the set of trial functions and the set of weight functions (for any given energy group) must each be a linearly independent set. If one of the sets were almost linearly dependent, this might conceivably lead to numerical difficulty in solving the finite difference analog of Eq. (4.243). In such a case, one could avoid the difficulty by orthogonalizing the trial functions; however, experience thus far indicates this may not be necessary.

6. *Conclusion*

In this section, the variational procedure outlined by Selengut[11] was applied to develop a flux synthesis method. It was pointed out that the equations resulting from the variational derivation may be regarded also as resulting from a special case of a more basic approximation procedure which appears repeatedly in many forms and with many names throughout applied mathematics. The basic procedure referred to is that

of assuming a solution of a certain form containing parameters, substituting this form into the governing equations, multiplying by weighting functions, and integrating to obtain equations specifying the parameters. The variational method is a special case in that it specifies a definite rule for choosing the weighting functions, namely, that they best approximate the true solution to the adjoint governing equations.

Three additional synthesis methods were discussed which corresponded to other choices of weighting functions. Advantages of the separate methods and numerical results using them were compared in a test problem. From the results of this test problem and from other test problems, it is evident that flux synthesis methods of the type proposed have the ability to yield much better approximations than the conventional synthesis at only slightly increased cost. Furthermore, the accuracy of the methods may be improved by using more trial functions. Thus, these synthesis methods may be considered to provide a bridge between conventional synthesis and direct solution using a three-dimensional mesh.

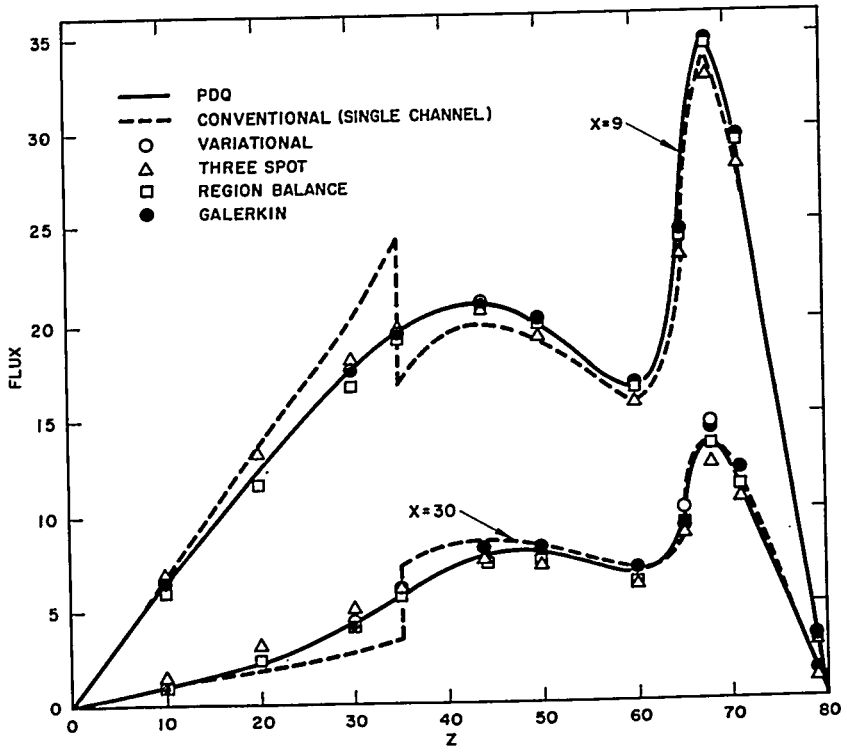

FIGURE 4.53. Flux Synthesis Thermal Group Traverses $X = 9$ and 30 cm.

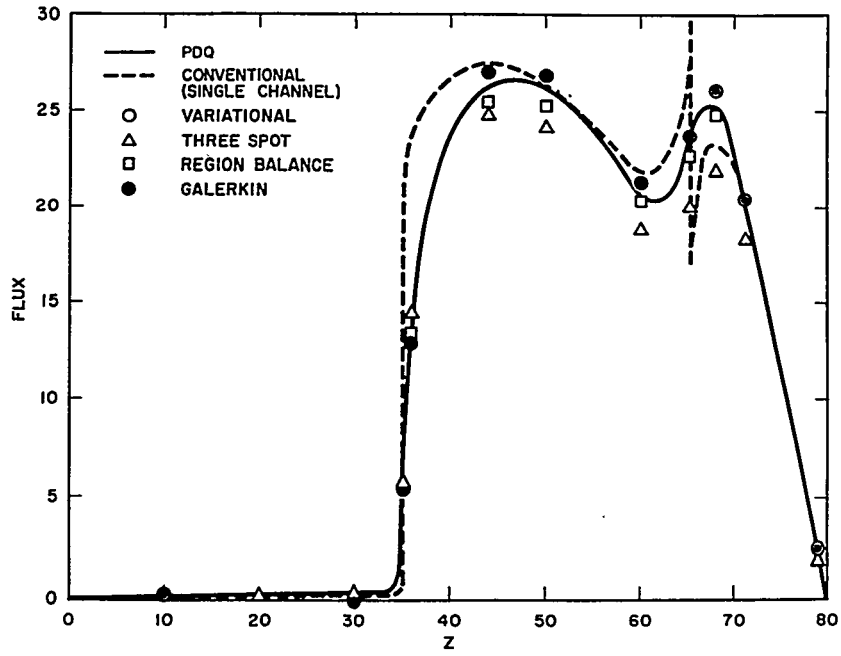

FIGURE 4.54. Flux Synthesis Thermal Group Traverse $X = 21$ cm.

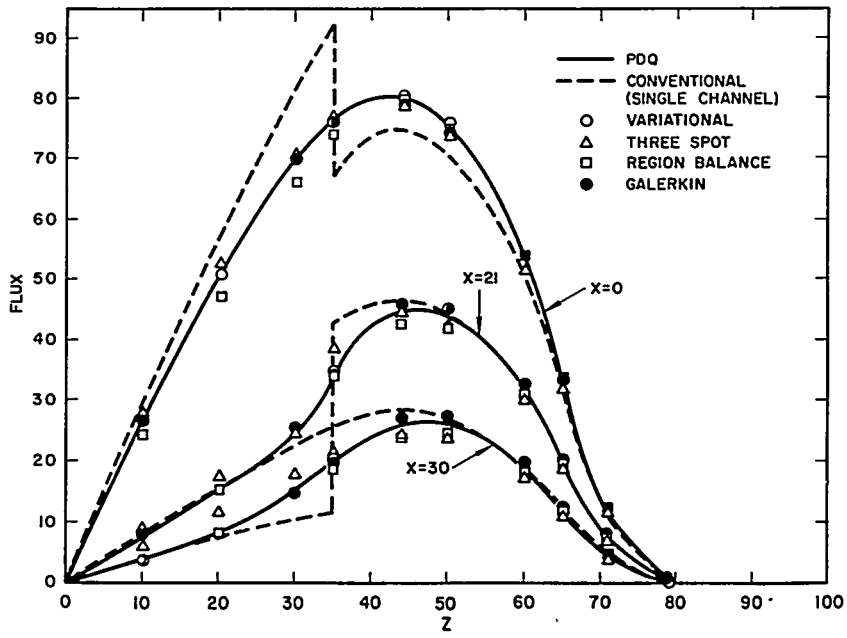

FIGURE 4.55. Flux Synthesis Fast Group Traverses $X = 0, 21, 30$ cm.

TABLE 4.13 — EIGENVALUE, λ, OF TEST PROBLEM

Method	Eigenvalue
PDQ	1.0171
Variational	1.0152
Galerkin	1.0156
Region balance	1.0153
Three spot	1.0282
Conventional (single channel)	1.0311

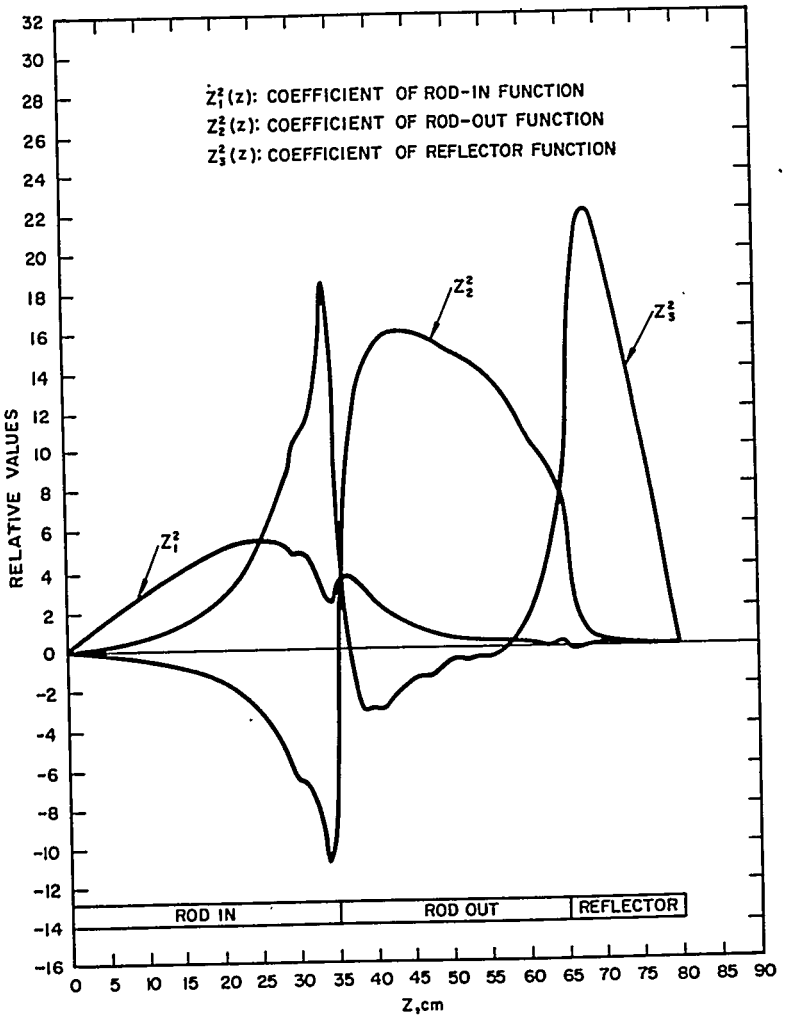

FIGURE 4.56. Mixing Functions, Variational Method, Slow Group.

4.5 GROSS FISSION PRODUCT POISONING

E. C. Hansen

A. Introduction

To predict correctly long term reactivity transients and lifetimes of highly enriched pressurized water reactors, an accurate knowledge of the gross fission product poisoning during, and at end of, core life is required. The gross poisoning at a given time in core life is a function of many variables, such as neutron spectra, self-shielding, and core power operating history. Therefore, of necessity, assumptions are introduced which allow a calculation of the gross poisoning to be made for design purposes. As part of the analysis of gross fission product poisoning, the effect of these assumptions upon the calculational results, i.e., any error introduced in the results or any limitation on the validity of the results, must be assessed.

In Sect. 4.5.B a detailed description is presented of the analysis required to calculate the gross fission product poisoning, excluding Xe^{135} and optionally, Sm^{149}, for an arbitrary neutron flux energy spectrum and flux spectrum history as a function of the fractional fuel depletion. In Sect. 4.5.B.5 the required experimental data, the basis of the calculational results, are presented. These data include the mass chain yields and 2200 m/sec absorption cross sections and conventional resonance integrals of the individual fission products.

In Sect. 4.5.C representative numerical results of the analysis described in Sect. 4.5.B are presented. These results are based on the experimental data presented in Sect. 4.5.B.5. The numerical results are in a form convenient for integration with an arbitrary few-group multiregion life study.

In Sect. 4.5.D the assumptions upon which the analysis is based are summarized. The effect of each assumption upon the calculational results, i.e., any error introduced in the results or any limitation on the validity of the results, is discussed.

It should be noted that even though the representative numerical results are primarily for highly enriched U^{235} systems, the techniques discussed are generally applicable to natural or slightly enriched systems where formation of fission products by fast fission in U^{238} and fission in Pu^{239} and Pu^{241} must be accounted for. The latter systems are included in the treatment by England.[68]

B. Analysis

The following discussion describes a method of calculating the gross fission product poisoning for an arbitrary neutron

flux spectrum and flux spectrum history as a function of fuel depletion.

1. *Basic Physical Assumptions*

This analysis is based on four physical assumptions. The distinction is made between those assumptions of a physical nature, which allow a mathematical statement of the problem to be made, and those assumptions of a mathematical nature, which allow a solution to be obtained from the mathematical statement of the problem. The assumptions of a mathematical nature are discussed in subsequent sections.

The four basic physical assumptions are:

1. The stable fission products are formed directly in fission. In this analysis, any fission product or isotope produced by an (n, γ) reaction in a fission product is considered stable if its half-life is greater than one year.
2. The radioactive fission product, formed by the (n, γ) reaction in a stable fission product formed directly in fission, decays instantaneously to the next stable fission product.
3. The fuel and individual fission products are infinitely dilute, i.e., there is no energy or spatial self-shielding.
4. A third order depletion scheme is considered.

Thus,

$$\xrightarrow{(n,f)} N_1 \xrightarrow{(n,\gamma)} N_2 \xrightarrow{(n,\gamma)} N_3 \xrightarrow{(n,\gamma)}$$

where N_1 is the stable fission product formed directly in fission and is considered a first order product; N_2 is the (n,γ) capture product of N_1 and is considered the second order product; and N_3 is the (n,γ) capture product of N_2 and is considered the third order product. In the analysis, all stable fission products were considered, when appropriate, as first, second, and third order products.

2. *Depletion Equations*

The system of coupled ordinary linear differential equations describing the time-dependent concentrations of N_1, N_2, and N_3 of the third order depletion scheme is:

$$\frac{dN_1}{dt} = \gamma_1 N_u \int_0^\infty dE\phi(E,t)\sigma_u^f(E) - N_1 \int_0^\infty dE\phi(E,t)\sigma_1(E)$$

Eq. (4.248)

$$\frac{dN_2}{dt} = N_1 \int_0^\infty dE\phi(E,t)\sigma_1(E) - N_2 \int_0^\infty dE\phi(E,t)\sigma_2(E) \qquad \text{Eq. (4.249)}$$

$$\frac{dN_3}{dt} = N_2 \int_0^\infty dE\phi(E,t)\sigma_2(E) - N_3 \int_0^\infty dE\phi(E,t)\sigma_3(E) \qquad \text{Eq. (4.250)}$$

In addition, the time-dependent fuel concentration N_u, is described by

$$\frac{dn_u}{dt} = -N_u \int_0^\infty dE\phi(E,t)\sigma_u^a(E) \; . \qquad \text{Eq. (4.251)}$$

For clarity, the arguments indicating the time dependence of the concentrations of N_1, N_2, N_3, and N_u have been suppressed. Also,

N_i = number density of i^{th} nuclide
γ_i = fission yield of i^{th} nuclide
$\sigma_i(E)$ = energy-dependent absorption cross section of the i^{th} nuclide
$\sigma_u^a(E)$ = energy-dependent absorption cross section of the fuel
$\sigma_u^f(E)$ = energy-dependent fission cross section of the fuel
$\phi(E,t)$ = time-dependent neutron flux energy spectrum

Equations (4.248), (4.249), (4.250), and (4.251) may be rewritten in terms of single cross sections, $\bar{\sigma}_i$, which includes epithermal effects and the total thermal flux, ϕ_3. Thus,

$$\frac{dN_1}{dt} = \gamma_1 N_u \bar{\sigma}_u^f \phi_3 - N_1 \bar{\sigma}_1 \phi_3 \qquad \text{Eq. (4.252)}$$

$$\frac{dN_2}{dt} = N_1 \bar{\sigma}_1 \phi_3 - N_2 \bar{\sigma}_2 \phi_3 \qquad \text{Eq. (4.253)}$$

$$\frac{dN_3}{dt} = N_2 \bar{\sigma}_2 \phi_3 - N_3 \bar{\sigma}_3 \phi_3 \qquad \text{Eq. (4.254)}$$

$$\frac{dN_u}{dt} = -N_u \bar{\sigma}_u^a \phi_3 \; . \qquad \text{Eq. (4.255)}$$

Again, for clarity, the arguments indicating the time dependence of the concentrations N_1, N_2, N_3, and N_u, the effective cross sections, $\bar{\sigma}_i$, and the total thermal flux, ϕ_3, have been suppressed.

In addition,

$$\phi_3(t) = \int_0^{E_c} dE\phi(E,t) \qquad \text{Eq. (4.256)}$$

$$\bar{\sigma}_i(t) = \int_0^{\infty} dE\phi(E,t)\sigma_i(E) \Big/ \int_0^{E_c} dE\phi(E,t) \qquad \text{Eq. (4.257)}$$

where E_c = thermal cutoff energy between the thermal group and the epithermal group.

Since only stable fission products are considered, the solutions to Eqs. (4.252), (4.253), (4.254), and (4.255) are not dependent upon the detailed time history of the total thermal flux, but rather on the integrated thermal flux time only. Thus, it is possible to use the fractional fuel depletion, β, as a convenient independent variable.

The fractional fuel depletion, β, is defined as

$$\beta \equiv \left\{N_u^o - N_u(t)\right\} / N_u^o \qquad \text{Eq. (4.258)}$$

where N_u^o = initial fuel number density.

Using Eqs. (4.255) and (4.258), the differential equations describing the time dependence of the concentrations of N_1, N_2, and N_3 may be written with the fractional fuel depletion as the independent variable. Thus,

$$\frac{d(N_1/N_u^o)}{d\beta} = \gamma_1 \frac{\bar{\sigma}_u^f}{\bar{\sigma}_u^a} - \frac{(N_1/N_u^o)}{(1-\beta)} \frac{\bar{\sigma}_1}{\bar{\sigma}_u^a} \qquad \text{Eq. (4.259)}$$

$$\frac{d(N_2/N_u^o)}{d\beta} = \frac{(N_1/N_u^o)}{(1-\beta)} \frac{\bar{\sigma}_1}{\bar{\sigma}_u^a} - \frac{(N_2/N_u^o)}{(1-\beta)} \frac{\bar{\sigma}_2}{\bar{\sigma}_u^a} \qquad \text{Eq. (4.260)}$$

$$\frac{d(N_3/N_u^o)}{d\beta} = \frac{(N_2/N_u^o)}{(1-\beta)} \frac{\bar{\sigma}_2}{\bar{\sigma}_u^a} - \frac{(N_3/N_u^o)}{(1-\beta)} \frac{\bar{\sigma}_3}{\bar{\sigma}_u^a} \qquad \text{Eq. (4.261)}$$

where, in general, the effective cross section ratio, $\bar{\sigma}_i/\bar{\sigma}^a_u$, is a function of the fractional fuel depletion.

It should be noted that in Eqs. (4.259), (4.260), and (4.261) the effective absorption cross sections appear only as ratios. Thus, solutions to Eqs. (4.259), (4.260), and (4.261) for (N_1/N^o_u), (N_2/N^o_u), and (N_3/N^o_u) are functions of ratios, not absolute magnitudes, of effective absorption cross sections.

From solutions of Eqs. (4.259), (4.260), and (4.261) for (N_1/N^o_u), (N_2/N^o_u), and (N_3/N^o_u) for arbitrary neutron flux spectra and flux spectrum histories, the gross fission product poisoning as a function of the fractional fuel depletion may be constructed. The gross fission product poisoning is formulated in terms of a fission product 2200 m/sec absorption cross section, σ^{fp}_o, and a fission product resonance integral, RI^{fp}, in the units of barns per original fuel atom per unit volume, defined as

$$\sigma^{fp}_o(\beta) = \sum_i \frac{N_i(\beta)}{N^o_u}\,\sigma^i_o \qquad \text{Eq. (4.262)}$$

$$RI^{fp}(\beta) = \sum_i \frac{N_i(\beta)}{N^o_u}\,RI^i . \qquad \text{Eq. (4.263)}$$

The summations are over all the stable fission products considered, and

$N_i(\beta)/N^o_u$ = the number density of the i^{th} stable fission product per unit original fuel number density

σ^i_o = 2200 m/sec absorption cross section of the i^{th} stable fission product

RI^i = conventional infinite dilution resonance integral of the i^{th} stable fission product

β = fractional fuel depletion.

Equations (4.262) and (4.263) represent a convenient formulation of the gross fission product poisoning for integration with an arbitrary few-group, multiregion life study.

In many applications the gross fission product poisoning is required in the units of barns per fission per unit volume. Thus, it is convenient to have a conversion factor available which will convert the results in barns per original fuel atom per unit volume to barns per fission per unit volume.

The required conversion factor is

$$C_f(\beta) = \overline{1+\alpha}/\beta \qquad \text{Eq. (4.264)}$$

where

$\overline{1+\alpha}$ = average fuel absorption to fission ratio
β = fractional fuel depletion.

Multiplying the results in barns per original fuel atom by this conversion factor yields fission product poisons in barns per fission units. For most cases in pressurized water reactors, a value of $\overline{1+\alpha}$ of 1.23 is typical. It should be pointed out that the value of $\overline{1+\alpha}$ is a variable depending on the case at hand.

The subsequent discussion will be in terms of the definitions presented in Eqs. (4.262) and (4.263), with the gross fission product poisoning expressed in the units of barns per original fuel atom per unit volume. With the conversion factor presented in Eq. (4.264), the conversion to the units of barns per fission per unit volume is elementary.

3. *Microscopic Cross Section Treatment*

To integrate numerically Eqs. (4.259), (4.260), and (4.261) for the required number densities, the effective cross section ratios, $\bar{\sigma}_i/\bar{\sigma}_u^a$, are required. To perform the integrations indicated in Eqs. (4.256) and (4.257) to obtain the effective cross sections, a description of the neutron flux energy spectrum is required.

The prescription used to obtain the effective thermal and resonance cross sections is based on a description of the neutron flux energy spectrum used by R. W. Deutsch.[69] The prescription is based on a neutron flux spectrum which is made up of a thermal component; a hardened Maxwellian characterized by an effective temperature, T_{eff}, up to a thermal cutoff, $E_c = 4kT_{\text{eff}}$; and an epithermal component, a $1/E$ tail above E_c.

In terms of the above description of the neutron flux energy spectrum, Eq. (4.257) is conveniently rewritten as

$$\bar{\sigma}_i(\beta) = \bar{\sigma}_{3i}(\beta) + \frac{\phi_2}{\phi_3}(\beta)\,\bar{\sigma}_{2i}(\beta) \qquad \text{Eq. (4.265)}$$

where the subscripts refer to Groups 2 and 3 of a conventional three-group description, and

$$\bar{\sigma}_{3i} = 0.93\left(\frac{T_o}{T_{\text{eff}}}\right)^{1/2}\sigma_o^i \qquad \text{Eq. (4.266)}$$

for a $1/v$ cross section in the thermal group

$$\bar{\sigma}_{2i} = RI^i/\Delta u \qquad \text{Eq. (4.267)}$$

$$\Delta u = 20.68 - \ln(T_{\text{eff}}) \qquad \text{Eq. (4.268)}$$

where T_{eff} is in degrees Rankine, and Eq. (4.267) implies that the upper cutoff of Group 2 is 1.83×10^5 ev:

$$\frac{\phi_2}{\phi_3} = \text{ratio of Group 2 to Group 3 neutron flux.}$$

For the uranium fuel cross section which is non-$1/v$ in the thermal region, a three-parameter fit to the averaged uranium absorption cross section as a function of T_{eff} has been obtained,

$$\bar{\sigma}^a_{3u} = \frac{1}{\sqrt{T_{\text{eff}}}} \left\{ 1569.08 - 2.83859\ T_{\text{eff}} + 9.68839\ (T_{\text{eff}})^2 \right\} . \qquad \text{Eq. (4.269)}$$

Using Eq. (4.268) the remainder of the fuel cross sections are constructed:

$$\bar{\sigma}^f_{3u} = \bar{\sigma}^a_{3u}/1.184 \qquad \text{Eq. (4.270)}$$

$$\bar{\sigma}^a_{2u} = \bar{\sigma}^a_{3u}/0.93\Delta u \qquad \text{Eq. (4.271)}$$

$$\bar{\sigma}^f_{2u} = \bar{\sigma}^a_{2u}/1.35 . \qquad \text{Eq. (4.272)}$$

The depletion dependence of the effective cross section ratio is reflected in the depletion dependence of the effective temperature and the Group 2 to Group 3 flux ratio. This is a convenient choice, since both these quantities are part of the edit from a KARE life study, and permits an examination of the effect of the neutron flux spectrum history on the calculated gross fission product poisoning using flux spectrum histories which have been calculated in design life studies.

To examine the effect upon the calculational results of the prescription used to obtain the effective thermal and resonance cross sections, an alternate prescription by E. C. Hansen was used to obtain the required effective cross sections.

As in the Deutsch prescription, the neutron flux energy spectrum is assumed to have two components: a thermal

Maxwellian and a resonance $1/E$ tail. The Hansen prescription is summarized in the following equations.

In terms of

$$\bar{\sigma}_2(\beta) = \bar{\sigma}_{3i}(\beta) + \frac{\phi_2}{\phi_3}(\beta)\,\bar{\sigma}_{2i}(\beta) \qquad \text{Eq. (4.265)}$$

The following definitions are obtained:

$$\bar{\sigma}_{3i}(\beta) = S_{th}(\beta)\,\sigma_o^i \qquad \text{Eq. (4.273)}$$

where

$$S_{th}(\beta) = \left\{ \frac{\sqrt{\frac{\pi T_o}{4T}} + \sqrt{\pi}\beta\gamma\left[\left(\frac{E_o}{E_1}\right)^{1/2} - \left(\frac{E_o}{E_c}\right)^{1/2}\right]}{(1+0.92\beta\gamma)^{1/2} + \frac{\sqrt{\pi}}{2}\beta\gamma \ln\frac{E_c}{E_1}} \right\} \qquad \text{Eq. (4.274)}$$

In addition,

$$\bar{\sigma}_{2i}(\beta) = \frac{1}{\ln\frac{E_c'}{E_c}} \left\{ 2\sigma_o^i \left[\left(\frac{E_o}{E_c}\right)^{1/2} - \left(\frac{E_o}{E_{cd}}\right)^{1/2}\right] + RI^i \right\} \qquad \text{Eq. (4.275)}$$

and

$$\frac{\phi_2}{\phi_3}(\beta) = \frac{\left[\frac{\sqrt{\pi}}{2}\beta\gamma/(1+0.92\beta\gamma)^{1/2}\right]\ln\frac{E_c'}{E_c}}{1 + \frac{\left(\sqrt{\pi}/2\right)\beta\gamma}{(1+0.92\beta\gamma)^{1/2}}\ln\frac{E_c}{E_1}} \qquad \text{Eq. (4.276)}$$

where

T = moderator temperature, °K
T_o = room temperature, 293°K
E_o = kT_o = 0.0253 ev
E_1 = $5kT\ (1+0.92\beta\gamma)^{1/2}$, ev
E_c = thermal cutoff energy, ev
E_c' = resonance cutoff energy, ev
E_{cd} = cadmium cutoff energy, ev
$\beta\gamma$ = $\Sigma_a(kT)/\xi\Sigma_s$, spectral index.

The validity of Eqs. (4.273), (4.274), (4.275), and (4.276) is discussed in detail by E. C. Hansen.[70]

4. *Solution of the Equations*

The above system of equations was coded for a digital computer with the numerical solution of the coupled differential Eqs. (4.260), (4.261), and (4.262) obtained using an extension of the Runge-Kutta method.[71] Appropriate convergence checks were employed. The name of the program is FISHY. The program allows the flux spectrum history to be specified arbitrarily by permitting as input an arbitrary depletion-dependent effective temperature and Group 2 to Group 3 flux ratio. The output consists of the number densities, normalized to the original fuel number density, of each stable fission product considered, its contribution to both σ_o^{fp} and RI^{fp}, and σ_o^{fp} and RI^{fp}, all as a function of fuel depletion.

To examine the effect upon the calculational results of the prescription used to obtain the effective thermal and resonance cross sections, the alternate prescription, suggested by E. C. Hansen,[70] was coded to obtain the effective cross sections. The differences in the calculational results are not significant when the Deutsch prescription[69] is used in place of the Hansen prescription.[70]

With the presented analysis, the gross fission product poisoning, expressed as a 2200 m/sec fission product absorption cross section, σ_o^{fp}, and a fission product resonance integral, RI^{fp}, may be calculated for an arbitrary neutron flux energy spectrum and flux spectrum history as a function of the fuel depletion.

The results may be conveniently integrated with any few-group structure, since they are presented as a 2200 m/sec absorption cross section, assumed $1/v$ in the thermal region, and a conventional resonance integral. Thus, regardless of the averaging procedures employed or the few-group structure chosen, the gross fission product poisoning may be integrated with the depletion calculation as if it were a conventional isotope with an experimentally measured 2200 m/sec absorption cross section and conventional resonance integral, albeit depletion-dependent.

5. *Experimental Data*

The experimental data required to calculate the gross fission product poisoning for U^{235} systems are the mass chain yields and 2200 m/sec absorption cross sections and conventional resonance integrals of the individual fission products. The mass chain yields are presented in Table 4.14. Unless otherwise noted, the individual yields were obtained from S. Katcoff.[72] The 2200 m/sec absorption cross sections and conventional resonance integrals of the individual stable fission products

TABLE 4.14 — FISSION PRODUCT YIELDS AND CROSS SECTIONS

Mass Number	Yield (%)	Mass Number	Yield (%)
77	0.0083	106	0.38
78	0.021	107	0.19
79	0.056	108	0.07*
80	0.08	109	0.03
81	0.14	110	0.024
82	0.28*	111	0.019
83	0.544	112	0.01
84	1.00	113	0.01
85	1.30	114	0.01†
86	2.02	115	0.011
87	2.49	116	0.01†
88	3.57	117	0.011
89	4.79	118	0.01†
90	5.77	119	0.01†
91	5.84	120	0.01†
92	6.03	121	0.015
93	6.45	122	0.013†
94	6.40	123	0.0013
95	6.27	124	0.02
96	6.33	125	0.021
97	6.09	126	0.05
98	5.78	127	0.13
99	6.06	128	0.37
100	6.30	129	0.9
101	5.0	130	2.0
102	4.1	131	2.93
103	3.0	132	4.38
104	1.8	133	6.59
105	0.9	134	8.06

TABLE 4.14 — FISSION PRODUCT YIELDS AND CROSS SECTIONS (Continued)

Mass Number	Yield (%)	Mass Number	Yield (%)
135	6.41	147	2.38
136	6.46	148	1.7
137	6.15	149	1.13
138	5.74	150	0.67
139	6.55	151	0.45
140	6.44	152	0.285
141	6.40	153	0.15
142	5.95	154	0.077
143	5.98	155	0.033
144	5.67	156	0.014
145	3.95	157	0.0078
146	3.07		

*J.D. Garrison and B.W. Roos.[74]
† C.R. Greenhow and E.C. Hansen.[75]

are presented in Table 4.15. Unless otherwise noted, the 2200 m/sec absorption cross sections were obtained from Ref. 73. Also, unless otherwise noted, the conventional resonance integrals were obtained from J.D. Garrison and B.W. Roos.[74]

The stable fission products considered in the calculations, and the identity and components of the three member chains used in the calculations, are presented in Table 4.16.

It should be noted that the contribution to the gross fission product poisoning by the U^{236}, produced in the (n, γ) reaction of U^{235}, is conveniently included in the calculational results. The contribution by the U^{236} capture products, Np^{237} and Pu^{238}, is also included. The fission yield of U^{236}, which is just the appropriately defined average capture to fission ratio, $\bar{\alpha}$, is strongly spectrum-dependent and, thus, depletion-dependent. The calculations account for this depletion dependence of the U^{236} fission yield.

TABLE 4.15 — FISSION PRODUCT 2200 m/sec ABSORPTION CROSS SECTIONS AND CONVENTIONAL RESONANCE INTEGRALS

Nuclide	σ_o (barns)	Resonance Integral (barns)
Selenium 82	2.1	1.4
Krypton 83	222	201
Krypton 84	0.16*	5.5
Krypton 85	7.0*	29.0
Krypton 86	0.06	0.04
Rubidium 85	0.91	0.67
Rubidium 87	0.12	0.21
Strontium 86	1.65	0.664‡
Strontium 87	3.3†	96†
Strontium 88	0.005	0.06
Strontium 90	1.0	1.8
Yttrium 89	1.31	0.78
Zirconium 90	0.1	0.04†
Zirconium 91	1.58	9.0
Zirconium 92	0.25	0.55
Zirconium 93	1.5†	28.0
Zirconium 94	0.076	0.2
Zirconium 96	0.053	0.07
Molybdenum 95	13.9	109
Molybdenum 96	1.2	0.48†
Molybdenum 97	2.2	16
Molybdenum 98	0.51	10.7
Molybdenum 100	0.3*	6.2
Technetium 99	22.0	201†
Ruthenium 100	1.5*	7.0
Ruthenium 101	5.0*	77
Ruthenium 102	1.44	11
Ruthenium 104	0.7	8.0
Ruthenium 106	9.0†	17.6†

TABLE 4.15 — FISSION PRODUCT 2200 m/sec ABSORPTION CROSS SECTIONS AND CONVENTIONAL RESONANCE INTEGRALS (Continued)

Nuclide	σ_o (barns)	Resonance Integral (barns)
Rhodium 103	156	1030
Palladium 104	6.0*	19.0
Palladium 105	11.0*	76
Palladium 106	6.0*	12
Palladium 107	10.0*	40
Palladium 108	10.4	169
Silver 109	91.0*	1420
Cadmium 110	0.2‡	30‡
Cadmium 111	87†	52
Cadmium 112	0.03	13
Cadmium 113	19,800*	652
Cadmium 114	1.24	15
Indium 115	191*	3300
Tin 116	0.1†	0.05†
Tin 117	3.5†	1.4†
Tin 124	0.2	12‡
Antimony 125	1.56†	0.62†
Tellurium 126	0.8	12.0
Tellurium 128	0.3	2.0
Tellurium 130	0.5	2.6
Iodine 127	6.2*	154
Iodine 129	27.0*	39
Xenon 128	2.5‡	1.01†
Xenon 129	45	240
Xenon 130	2.5‡	1.01†
Xenon 131	120	806
Xenon 132	0.2	1.8
Xenon 134	0.2	0.6
Xenon 136	0.15	0.1

TABLE 4.15 — FISSION PRODUCT 2200 m/sec ABSORPTION CROSS SECTIONS AND CONVENTIONAL RESONANCE INTEGRALS (Continued)

Nuclide	σo (barns)	Resonance Integral (barns)
Cesium 133	29.0	420
Cesium 134	137‡	55.1†
Cesium 135	8.7*	62
Cesium 137	0.11	0.3
Barium 136	0.4	0.161†
Barium 137	5.1	2.04
Barium 138	0.7	0.5
Lanthanum 139	8.9*	11.0
Cerium 140	0.66	0.5
Cerium 142	0.94*	1.3
Praseodymium 141	11.6	23.5
Neodymium 142	18.0	7.24†
Neodymium 143	324	130
Neodymium 144	5.0	12.0
Neodymium 145	60	245
Neodymium 146	10	25
Neodymium 148	3.4	48
Neodymium 150	1.5*	14
Promethium 147	180*	2510
Samarium 148	3.0	1.21†
Samarium 149	40,800*	3400
Samarium 150	85*	460
Samarium 151	12,400	2500
Samarium 152	216*	2500
Samarium 154	5.5	25
Europium 153	450	1380
Europium 154	1500‡	600†
Europium 155	14,000	5550†

TABLE 4.15 — FISSION PRODUCT 2200 m/sec ABSORPTION CROSS SECTIONS AND CONVENTIONAL RESONANCE INTEGRALS (Continued)

Nuclide	σ_o (barns)	Resonance Integral (barns)
Gadolinium 156	4.0*	44
Gadolinium 157	264,000	740
Uranium 236	7.0	400†
Neptunium 237	170	870†
Plutonium 238	403	160†

*J. D. Garrison and B. W. Roos.[74]
† C. R. Greenhow and E. C. Hansen.[75]
‡ W. H. Walker.[76]

TABLE 4.16 — THREE-MEMBER STABLE FISSION PRODUCT CHAINS*

Chain Number	Members
1	Uranium 236, Neptunium 237, Plutonium 238
2	Selenium 82, Krypton 83, Krypton 84
3	Krypton 83, Krypton 84, Krypton 85
4	Krypton 84, Krypton 85, Krypton 86
5	Krypton 85, Krypton 86, Rubidium 87
6	Rubidium 85, Strontium 86, Strontium 87
7	Krypton 86, Rubidium 87, Strontium 88
8	Rubidium 87, Strontium 88, Yttrium 89
9	Strontium 88, Yttrium 89, Zirconium 90
10	Yttrium 89, Zirconium 90, Zirconium 91
11	Strontium 90, Zirconium 91, Zirconium 92
12	Zirconium 91, Zirconium 92, Zirconium 93
13	Zirconium 92, Zirconium 93, Zirconium 94
14	Zirconium 93, Zirconium 94, Molybdenum 95

TABLE 4.16 — THREE-MEMBER STABLE FISSION PRODUCT CHAINS* (Continued)

Chain Number	Members
15	Zirconium 94, Molybdenum 95, Molybdenum 96
16	Molybdenum 95, Molybdenum 96, Molybdenum 97
17	Zirconium 96, Molybdenum 97, Molybdenum 98
18	Molybdenum 97, Molybdenum 98, Technetium 99
19	Molybdenum 98, Technetium 99, Ruthenium 100
20	Technetium 99, Ruthenium 100, Ruthenium 101
21	Molybdenum 100, Ruthenium 101, Ruthenium 102
22	Ruthenium 101, Ruthenium 102, Rhodium 103
23	Ruthenium 102, Rhodium 103, Palladium 104
24	Rhodium 103, Palladium 104, Palladium 105
25	Ruthenium 104, Palladium 105, Palladium 106
26	Palladium 105, Palladium 106, Palladium 107
27	Ruthenium 106, Palladium 107, Palladium 108
28	Palladium 107, Palladium 108, Silver 109
29	Palladium 108, Silver 109, Cadmium 110
30	Silver 109, Cadmium 110, Cadmium 111
31	Palladium 110, Cadmium 111, Cadmium 112
32	Cadmium 113, Cadmium 114, Indium 115
33	Indium 115, Tin 116, Tin 117
34	Tin 124, Antimony 125, Tellurium 126
35	Antimony 125, Tellurium 126, Iodine 127
36	Tellurium 126, Iodine 127, Xenon 128
37	Iodine 127, Xenon 128, Xenon 129
38	Tellurium 128, Iodine 129, Xenon 130
39	Iodine 129, Xenon 130, Xenon 131
40	Tellurium 130, Xenon 131, Xenon 132
41	Xenon 131, Xenon 132, Cesium 133
42	Xenon 132, Cesium 133, Cesium 134
43	Cesium 133, Cesium 134, Cesium 135
44	Xenon 134, Cesium 135, Barium 136
45	Cesium 135, Barium 136, Barium 137
46	Xenon 136, Cesium 137, Barium 138

TABLE 4.16 — THREE-MEMBER STABLE FISSION PRODUCT CHAINS* (Continued)

Chain Number	Members
47	Cesium 137, Barium 138, Lanthanum 139
48	Barium 138, Lanthanum 139, Cerium 140
49	Lanthanum 139, Cerium 140, Praseodymium 141
50	Cerium 140, Praseodymium 141, Neodymium 142
51	Praseodymium 141, Neodymium 142, Neodymium 143
52	Cerium 142, Neodymium 143, Neodymium 144
53	Neodymium 143, Neodymium 144, Neodymium 145
54	Neodymium 144, Neodymium 145, Neodymium 146
55	Neodymium 145, Neodymium 146, Promethium 147
56	Neodymium 146, Promethium 147, Samarium 148
57	Promethium 147, Samarium 148, Samarium 149
58	Neodymium 148, Samarium 149, Samarium 150
59	Samarium 149, Samarium 150, Samarium 151
60	Neodymium 150, Samarium 151, Samarium 152
61	Samarium 151, Samarium 152, Europium 153
62	Samarium 152, Europium 153, Europium 154
63	Europium 153, Europium 154, Europium 155
64	Samarium 154, Europium 155, Gadolinium 156
65	Europium 155, Gadolinium 156, Gadolinium 157

*The contribution to the gross fission product poisoning by any stable fission product not included is negligibly small.[77]

C. Representative Numerical Results

The gross fission product poisoning, including the contribution from U^{236}, Np^{237}, and Pu^{238}, was calculated for various neutron flux energy spectra and depletion-dependent flux spectrum histories using the computer program FISHY. The calculated gross poisoning is expressed as a fission product 2200 m/sec absorption cross section, σ_o^{fp}, and a fission product resonance integral, RI^{fp}, in the units, barns per original fuel atom per unit volume. The neutron flux energy spectra considered ranged from a very thermal spectrum at room temperature to a very hard spectrum at a typical pressurized water reactor

operating temperature. The flux spectrum histories included cases in which both T_{eff} and ϕ_2/ϕ_3 were constant, cases in which either or both T_{eff} and ϕ_2/ϕ_3 varied with depletion as $e^{-\beta}$, and finally cases in which depletion-dependent values for T_{eff} and ϕ_2/ϕ_3 were obtained for various core regions from calculated design life studies.

Typical results are presented in Figs. 4.57 and 4.58 for a number of assumed neutron flux spectra and flux histories. For all the cases examined, the maximum differences found were less than 5 percent. For comparison, the 1960 results of E.C. Hansen and C.R. Greenhow[78] are also presented. The differences between the presented results and the 1960 Hansen-Greenhow results are due to new values of cross sections obtained from more recent experimental measurements.

To examine the effect upon the calculational results of the prescription used to obtain the required effective cross section ratios, the gross fission product poisoning was calculated using both the Deutsch prescription[69] and the Hansen prescription.[70] The results were not significantly different.

Table 4.17 presents the representative values for the fission product 2200 m/sec absorption cross sections and resonance integrals for the gross fission product poisoning in typical core regions, with an arbitrary neutron flux energy spectrum and flux spectrum history at a specified history and at a specified fuel depletion. Values which include the contribution to the gross fission product poisoning by the Sm^{149} chain are also presented.

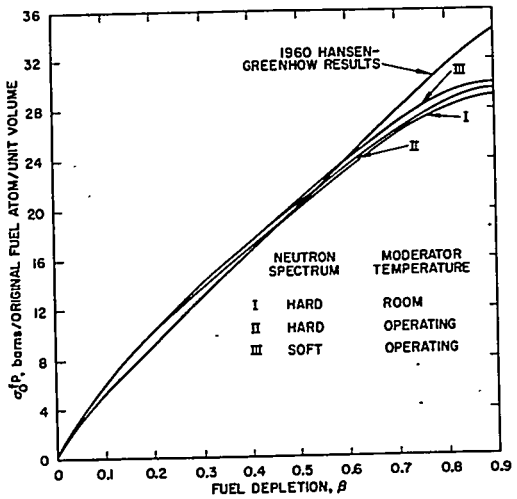

FIGURE 4.57. Fission Product 2200 m/sec Absorption Cross Section vs Fuel Depletion, Sm^{149} Chain Excluded but including U^{236}, Np^{237}, and Pu^{238}.

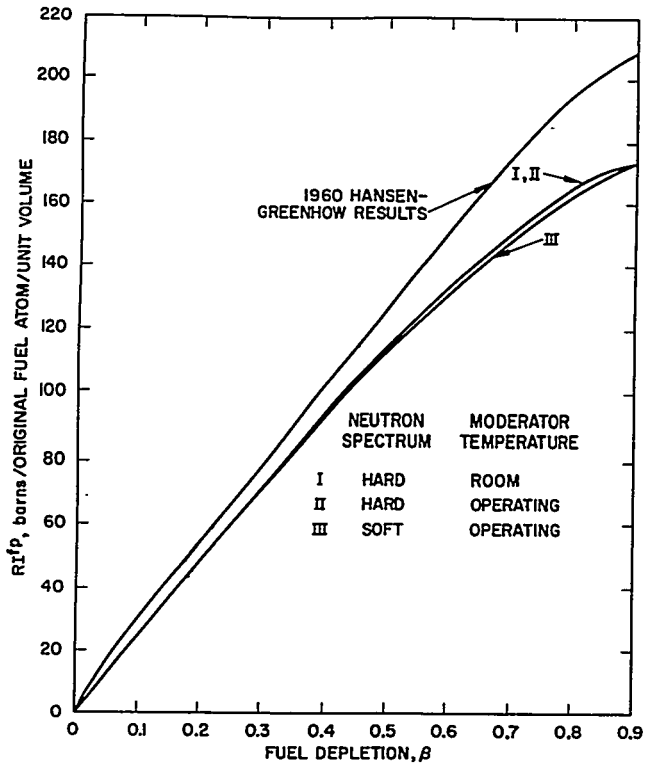

FIGURE 4.58. Fission Product Resonance Integral vs Fuel Depletion, Sm^{149} Chain Excluded but including U^{236}, Np^{237}, and Pu^{238}.

It should be noted that the fission product resonance integral, RI^{fp}, has a lower cutoff energy at 0.4 ev. If the presented results are used with a few-group analysis where the cutoff energy between the thermal and resonance group is other than 0.4 ev, the RI^{fp} may be corrected by adding the contribution by the $1/v$ cross section in the energy interval between the cutoff energy and 0.4 ev. In general, this correction is small.

The presented gross fission product poisoning expressed as a fission product 2200 m/sec absorption cross section, σ_o^{fp}, and a fission product resonance integral, RI^{fp}, has been incorporated in two alternate, but essentially equivalent, ways in the few-group depletion programs used for design life studies. In the KARE system the gross fission product parameters, σ_o^{fp} and RI^{fp}, including and excluding the Sm^{149} contribution, are incorporated in tabular form. Thus, when the gross fission product poisoning parameters are required to generate the representation of the gross poisoning in a given region at a specified fuel depletion, the parameters σ_o^{fp} and RI^{fp} are

TABLE 4.17 — GROSS FISSION PRODUCT ABSORPTION CROSS SECTIONS, BARNS, PER ORIGINAL FUEL ATOM PER UNIT VOLUME*

β	σ_o^{fp}†	σ_o^{fp}‡	RI^{fp}	RI^{fp}‡
0.0	0.0	0.0	0.0	0.0
0.1	6.24	0.846	2.72	2.55
0.03	10.5	2.35	8.04	7.63
0.05	12.2	3.64	13.2	12.7
0.07	13.3	4.78	18.3	17.7
0.10	14.5	6.28	25.8	25.1
0.20	17.7	10.3	50.4	49.3
0.30	20.4	13.7	74.1	72.6
0.40	22.9	17.0	96.8	94.9
0.50	25.4	20.2	118.2	116.0
0.60	27.6	23.1	138.0	136.0
0.70	29.5	25.8	156.0	153.0
0.80	30.9	27.9	170.9	167.0
0.90	31.2	29.0	177.0	174.0
0.95	31.3	29.2	180.0	176.0
1.00	31.2	29.0	177.0	174.0

*These results may be converted to the units, barns per fission per unit volume, by using the conversion factor defined by Eq. (4.264). A value of $\overline{1+\alpha}$ of 1.23 would be appropriate. U^{236}, Np^{237}, and Pu^{238} poisons are included.

† Including Sm^{149} chain.

‡ Excluding Sm^{149} chain.

obtained by using a table lookup subroutine, and then adjusting them for the neutron flux spectrum of the given region to yield the appropriate gross poisoning few-group constants. In the TURBO [79] program, the gross fission product poisoning is represented by two pseudo fission products which deplete automatically within the program. The yields, 2200 m/sec absorption cross sections, and conventional resonance integrals of these two pseudo fission products are specified such that the total poisoning by these two as a function of fuel depletion reproduces the presented values for the gross fission product poisoning. Either of the two methods is appropriate.

D. Discussion of Results

Because an exact analysis of the gross fission product poisoning is complex, the preceding analysis was based on assumptions which readily permitted the analysis to be made. The effect of these assumptions upon the calculational results, i.e., any error introduced in the results, or any limitation on the validity of the results, must be assessed.

In addition to the uncertainties arising from the assumptions made in the analysis, there are uncertainties in the results caused by errors in the experimental data, yields, 2200 m/sec absorption cross sections, and conventional resonance integrals, upon which the calculated results are based. A measure of these uncertainties is required.

A conventional linear propagation of error analysis was performed to obtain the standard deviations associated with the gross fission product poisoning parameters, σ_o^{fp} and RI^{fp}, in terms of the standard deviations of the experimental data, yields, 2200 m/sec absorption cross sections, and conventional resonance integrals of the individual stable fission products. The details of this analysis are presented by E. C. Hansen.[77] It was found that the uncertainty introduced in the calculated gross fission product poisoning is small. When the gross thermal poisoning is expressed as a 2200 m/sec absorption cross section, σ_o^{fp}, its standard deviation is 3 percent. When the gross resonance poisoning is expressed as a conventional resonance integral, RI^{fp}, its standard deviation is 7 percent. Both of these results are essentially independent of fuel depletion and neutron flux energy spectrum. It should be noted that the standard deviations are a measure of the precision of the results and not the accuracy.

The three major assumptions that formed the basis of the analysis are:

1. The stable fission products are formed directly in fission.

2. The radioactive fission product, formed by the (n, γ) reaction in a stable fission product formed directly in fission, decays instantaneously to the next stable fission product.
3. The fuel and individual fission products are infinitely dilute, i.e., there is no energy or spatial shelf-shielding.

An examination was made to determine the error introduced in the calculated results by the assumption that the stable fission products are formed directly in fission. The details of the examination are presented by E.C. Hansen.[77] It was found that the results overpredict the gross thermal poisoning by ~10 percent and the gross resonance poisoning by ~15 percent. Since these values are strongly dependent on the actual operating history of the core, the power level, and the rather scanty information on the absorption cross sections of the radioactive precursors, the results are approximate.

The error introduced by the second major assumption is dependent upon the half-life and absorption cross section of the radioactive fission product formed in the (n, γ) reaction in the stable fission product. If the half-life is relatively short and the absorption cross section relatively small, an insignificant error is introduced. This is usually the case. A notable exception is the radioactive Pm^{148} formed by the (n, γ) reaction in Pm^{147}. Recent measurements of the Pm^{148} absorption cross sections by R.P. Schumann [80] indicate that the absorption rate in high neutron fluxes can compete with the radioactive decay to form significant amounts of Pm^{149} which immediately decay to the thermal poison, Sm^{149}. T.R. England[68] has examined this in detail, and his results indicate that the poisoning by Sm^{149} formed by the neutron capture in Pm^{148} is comparable to the poisoning by the Sm^{149} formed directly in fission at fuel depletions greater than about 0.3 to 0.5. An examination of the results in Table 4.17 indicate that the Sm^{149} contribution is approximately 15 percent of the total thermal poisoning at $\beta = 0.6$. Thus, neglecting the source of Sm^{149} from the (n, γ) reaction in Pm^{148} can introduce an error of 15 percent in the total thermal poisoning. In addition, Pm^{148} and the higher order poisons from Sm^{149} will introduce as much as 5 percent more poison. Since these values are strongly dependent upon the power level and operating history of the core, these results are approximate.

The third major assumption introduces no error in the presented results if the fuel and individual fission products are infinitely dilute. For a heterogeneous system, the preliminary results of an examination of the effect of resonance self-shielding on the gross resonance poisoning indicate that, for a typical fuel region of a pressurized water reactor, the resonance poisoning is reduced ~5 percent at a fuel depletion

of 0.5. The details of the examination are presented by E.C. Hansen and F.D. Judge.[81] Again, since the effect is strongly dependent upon geometry and loading, the results are approximate.

The error introduced in the presented results by the prescription used to obtain the required effective cross sections was examined by calculating the gross fission product poisoning, using both the Deutsch prescription and the Hansen prescription to obtain the effective cross-sections. As stated in Sect. 4.5.C, no significant differences were found.

This relative insensitivity of the calculated gross fission product poisoning to variations in the prescriptions used to obtain the effective absorption cross sections and, in addition, the relative insensitivity of the results to the neutron flux energy spectrum and flux spectrum histories are due directly to the relative insensitivity of the effective absorption cross section ratios, $\bar{\sigma}_i/\bar{\sigma}_u^a$, to variations in these quantities.

From the definitions of the fission product 2200 m/sec absorption cross sections, σ_o^{fp}, and fission product resonance integrals, RI^{fp}, it is seen that these quantities are functions only of the individual number density ratios, $N_i(\beta)/N_u^o$. These, in turn, are functions only of the effective cross section ratios, $\bar{\sigma}_i/\bar{\sigma}_u^a$. Thus, the effect upon the calculated results of any variations in the effective absorption cross sections, $\bar{\sigma}_i$, is a tendency to cancel. It is this property, the dependence of the results on effective cross section ratios only, which allows such a complex physical system to be represented by such a concise description.

In the prescription used to obtain the effective absorption cross sections, $\bar{\sigma}_i$, it was assumed that the energy dependence of the cross sections is $1/v$ in the thermal energy region. An examination by E.A. Nephew[82] indicates that the cross sections of the important thermal poisons, excepting Sm^{149}, are essentially $1/v$ in the thermal energy range for the effective temperatures of interest. What small deviations exist have a tendency to cancel, since some of the cross sections have an energy dependence which is less than $1/v$ and others greater than $1/v$.

Finally, it should be noted that the contribution by the Sm^{149} presented in Table 4.17 is an average contribution to the gross poisoning. It accounts approximately for the strongly non-$1/v$ behavior of the Sm^{149} absorption cross section in the thermal energy region by being an average value of the Sm^{149} contribution in all spectra of interest.

The preceding discussion was not intended as an exhaustive examination of the uncertainties inherent in an analysis of the gross fission product poisoning. Rather, its purpose was to

indicate the present status of the calculations of the gross poisoning and to serve as a guide for future effort.

The gross fission product poisoning parameters, σ_0^{fp} and RI^{fp}, as presented in Sect. 4.5.C, are a convenient and relatively accurate way of representing the gross poisoning, as a function of fuel depletion, in a core region with an arbitrary neutron flux energy spectrum and flux spectrum history.

4.6 DEPLETION METHODS

W. A. Northrop and F. R. Urbanus

A. Introduction

The changes that take place in the composition of a reactor core during operation can have a major influence on its nuclear characteristics. The importance of these changes increases with the percentage fuel depletion which the reactor experiences. Since all modern power reactors must necessarily deplete a sizable percentage of their fuel, depletion effects for such reactors require careful analysis. This section presents the theories governing depletion effects and describes existing methods of applying these theories to reactor design.

In the development of most power reactors, the undepleted condition of the core is investigated rather thoroughly by critical experiments. Lifetime behavior, however, is not amenable to accurate examination by critical experiments and must, therefore, be predicted by analysis. Determination of lifetime behavior is often the most extensive and most important part of the core design program. After the initial development of a given type of core is completed, analysis of the depletion of the operating core permits verification of the design methods and subsequent application of improved depletion methods to replacement, or closely related, cores.

The examination of depletion effects is a complex task requiring use of many approximations and giving rise to a large number of alternative approaches. Common to all of these approaches, however, is a depletion cycle. This cycle, shown in Fig. 4.59, consists of calculations of macroscopic cross sections, spatial flux and power distributions, flux and power edits, depleted number densities, and depleted macroscopic cross sections for the next cycle. Each of these steps can be performed in many ways and in various degrees of detail. What follows is a presentation of the basic elements of depletion calculations and examples of methods now in use. First, however, it is instructive to expand somewhat on the various steps in the depletion cycle shown in Fig. 4.59.

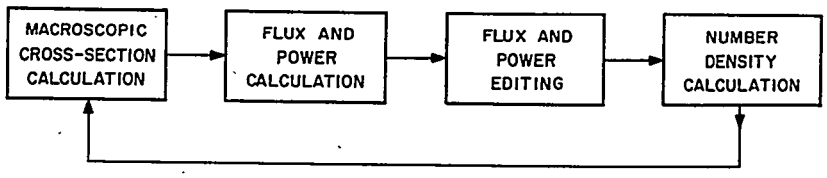

FIGURE 4.59. Block Diagram of Depletion Calculations.

The macroscopic cross-section calculation is straightforward, requiring only number densities and microscopic cross sections. Initial number densities are fixed by the design under study, and the microscopic cross sections may be supplied by any of several cross-section schemes, such as those discussed in Chap. 3, Sect. 3.7 and Chap. 2, Sect. 2.9.

The flux and power calculation is most directly performed in three-space dimensions with all significant structural details included in the calculation. Since this approach is not feasible on present computers, a great many approximate methods have been developed. These range from the grossly simplified one-dimensional analyses to the relatively accurate synthesis methods, to crude three-dimensional calculations. Prominent among the approximate methods is cell theory (Sect. 4.3) which may be used for direct investigation of composition perturbation effects or may merely provide input for larger calculations. Since these spatial calculations require use of a computer, decisions are always required regarding the spatial point mesh, the number of energy groups, the geometric detail displayed, and other factors. These decisions are governed by program limitations, computer time consumption, and cost. More detailed discussions of the available options in the spatial calculations are contained in Sects. 4.3 and 4.4.

Upon completion of the spatial flux and power calculation, it is necessary to obtain flux and power edits for subsequent use in the depletion or number density calculation. Once again, several options are available. If the depletion calculation is to be carried out for each point in the mesh, then the necessary edits are obvious. However, it is not always feasible to use point depletion, and edits by groups of points or regions are required. These edits would be used in region depletion. A still coarser editing might be required if cell theory were an integral part of the overall depletion cycle. In this case, a large calculation consisting of several cells would be edited cell by cell to provide a link between the cell calculation and the larger calculation. These remarks are expanded upon in Sects. 4.3 and 4.6.C.5.

The crucial step in the depletion cycle is the calculation of time-dependent number densities. The differential equations describing number density changes are quite straightforward, but their solution in complex situations requires several approximations. These compromises with rigor are necessitated not only by the desire to minimize computing costs but also by the implicit nature of the problem, i.e., the number density variations with time depend on flux variations which, in turn, are related in a very complicated way to number densities. To facilitate solution of the depletion equations, two alternate methods are used. These are called the constant power and constant flux methods.

The constant power method depends on the assumption that the power density at a point or in a region is constant for some interval of time. The constant flux method merely substitutes constant flux for constant power. The validity of these methods depends on the choice of time interval. In the limit of very short intervals, both methods are precise. Since the depletion calculations must be repeated for each time interval, the nuclear designer must balance accuracy against computing cost in choosing the time interval. With either the constant power or constant flux methods, additional assumptions are usually required. These deal with time variations of average microscopic cross sections, due to changes in the neutron energy spectrum, and self-shielding factors. These matters are discussed in the following sections.

Because the depletion of natural uranium as used in the PWR presents somewhat different depletion problems, this topic is treated separately in Sect. 4.6.D. Since a number of the aspects of depletion of natural and enriched uranium are common, those aspects which are different are emphasized there. The section closes with a description of two integrated depletion systems currently in use.

B. Effective Microscopic Cross Sections

The term effective microscopic cross sections refers to the cross sections used in the spatial flux calculations in lieu of the physical cross sections. These effective cross sections may differ from the physical cross sections for many reasons. First, the effective cross sections are always spectrum-averaged values over a given energy group structure and in that sense are not physical. Secondly, they may be spatially flux-weighted average cross sections such as would be obtained through homogenization of fine structure. Thirdly, they may be fictitious cross sections, such as those generated by blackness theory to account for transport effects in and near strong

absorbers. Since none of these cross sections are physical in the strict sense, they may be depletion-dependent. Depletion dependence arises through changes in spectra, in spatial flux distribution, and in the magnitude of blackness corrections.

The effective microscopic cross sections can be classified according to those which vary slowly with depletion and those which vary rapidly. The slowly varying cross sections may be held constant throughout an entire depletion study or, at least, throughout one time interval. For the rapidly varying cross sections, it is often necessary to account for their variation during a time interval or to employ very short time intervals.

1. Slowly Varying Cross Sections

The effective cross sections which vary slowly with depletion fall into two classes: those which vary because of spectrum variations and those which vary because of self-shielding factor variations. The first class is restricted to cross sections which are not strongly spectrum-dependent or to situations wherein the spectrum is not strongly depletion-dependent. One of these requirements is usually met in the above-thermal energy range. For example, many cross sections are not strongly energy-dependent in the above-thermal range, and their average values are insensitive to the spectrum. Scattering and transport cross sections frequently fall in this category.

In cases where cross sections are quite energy-dependent, their average values may still be in the slowly varying class because the choice of group structure minimizes spectrum dependence, i.e., if a large number of groups is chosen, the spectrum dependence of the average cross sections in each group diminishes. Above-thermal absorption and removal cross sections tend to be quite spectrum-dependent and may require use of several energy groups. The spectrum dependence of thermal group cross sections can be substantial and may require classifying these cross sections as rapidly varying. However, the consequences of rapid variation are often not significant, and it is usually possible to use techniques applied to slowly varying cross sections.

Variation of self-shielding factors during depletion may cause either rapid or slow changes in effective microscopic cross sections. Slow changes occur with lightly self-shielded materials, since in this case a large number density change has little effect on self-shielding. Effective cross sections for fuel and homogeneous poison are generally considered slowly varying.

Slowly varying cross sections may be treated in many ways during a depletion analysis. Some cross sections may

vary slowly enough that they can be held constant throughout the analysis. The remainder are generally recalculated at the beginning of each time interval for use in the succeeding interval. In a few cases, it is convenient to allow for variation within the time interval.

2. *Rapidly Varying Cross Sections*

Rapid variation of effective microscopic cross sections can arise from (1) strong depletion dependence of self-shielding factors for lumped absorbers, (2) strong depletion dependence of blackness coefficients for explicitly represented lumped absorbers, (3) spectral and number density dependence of average cross sections for resonance absorbers. Where any of these three situations exists in a depletion analysis, it is necessary to account for cross-section variation during each time interval or to employ very short time intervals. The latter alternative is often precluded by cost considerations. To exercise the first alternative, it is necessary to establish relationships between effective microscopic cross sections and the variables appearing in the depletion equations. With such relationships established, there are several methods of obtaining solutions to the depletion equations. These methods will be discussed briefly here and expanded in conjunction with discussions of Sect. 4.6.C.

When lumped absorbers are homogenized and assigned appropriate self-shielding factors, it is generally found that the self-shielding factor can be expressed as a simple polynomial in the number density of the absorber (see Sect. 4.2). In this form, the self-shielding factor can be incorporated in the depletion equations, as discussed in Sect. 4.6.C.3. Alternatively, the self-shielding factors can be held constant during subintervals of the major time interval and recalculated at the end of each subinterval. In this way, the self-shielding factors are varied in a stepwise manner during the basic depletion time interval, as described in Sect. 4.6.C.4.

When lumped absorbers are represented explicitly in a calculational model, fictitious cross sections must be utilized to obtain their proper absorption rates. These fictitious cross sections may vary rapidly with depletion due to the rapid change in absorber number density and the diminishing magnitude of the transport corrections. In most cases, the variation is sufficiently rapid that small time intervals must be used if the fictitious cross sections are to be held constant during the interval. Techniques for treating the variation within the interval are discussed in Sects. 4.6.C.3 and 4.6.C.4. The objective of these techniques is to permit large time

intervals between spatial calculations, thereby decreasing computing time.

Resonance absorbers may have highly depletion-dependent cross sections as a result of energy self-shielding effects. The importance of these effects depends on the magnitude of the resonance and the change in number density which takes place with depletion. Techniques for treating time-dependent resonance absorption are discussed in Sect. 4.6.C.4.

C. Number Density Calculations

1. Introduction

The purpose of this section is to state or derive the equations governing the compositional changes which occur in a reactor during its operation. The equations will apply to a unit of volume which is either homogeneous or has been homogenized by appropriate definition of self-shielding factors. Furthermore, it will be assumed that the unit of volume in question remains homogeneous and of spatially uniform composition as depletion takes place. The latter assumption becomes exact as the size of the volume unit is made arbitrarily small. The choice of volume unit size will be discussed in Sect. 4.6.C.5.

The depletion of the isotopes present in a reactor is described by a set of coupled differential equations. The general equations are described in Sect. 4.6.C.2. The solution of these equations is achieved by integrating them with respect to time over small time intervals, with certain assumptions being made concerning the time dependence of the cross sections and the fluxes during the time intervals. There are two fairly distinct approximations, the constant power and constant flux methods, which have been widely used.

The constant power approximation assumes that the power in each fuel-containing region is constant during the time interval. This is equivalent to assuming that the quantity of fuel depleted in each region is proportional to the power, which is why this is sometimes called the fuel-based method. The depletion of each isotope other than the fuel is calculated by using the depletion rates relative to the fuel depletion rate. These relative depletion rates are normally assumed to be constant during an interval, except for self-shielded poisons. The main advantages of this method are that the number of full power hours is readily obtained from the fraction of fuel depleted, and the time intervals can be quite long without introducing significant error. The disadvantages are that the equations do not apply for coupled fuel chains and are very complicated for coupled poison depletion chains. This method is described in Sect. 4.6.C.3.

The constant flux approximation involves determining the absolute values of the fluxes to achieve a given power level and assuming that these are constant over the time interval. In this case, the time interval in seconds is specified, and the power is not constant during the time interval because of the decreasing number density of the fuel. The effective full power hours at the end of a number of time intervals can be determined by finding the total fuel inventory remaining. In this method the variation of cross sections during the interval can be accounted for, and the buildup of short-lived fission products can be calculated explicitly. The depletion of coupled chains is straightforward even if more than one fissionable isotope is present. The variation of power during a time interval can be minimized by carrying out the depletion calculation in a number of small steps, renormalizing the flux level but not the flux shape at each small step as described in Sect. 4.6.C.4.

It should be observed that the basic depletion equations described below can also be thought of as governing the completely uniform depletion of a reactor. In other words, the unit of volume to which the equations are applied can be the whole reactor core instead of a small portion of the core. Frequently, such uniform depletion can give valuable insight into the behavior of a proposed reactor and reduce the need for performing detailed depletion studies.

2. The Equations

The general equation describing depletion of a single isotope fuel is

$$\frac{dN_F(\vec{r},t)}{dt} = -N_F(\vec{r},t) \int_0^\infty \phi(\vec{r},E,t)\sigma_F(E)dE \qquad \text{Eq. (4.277)}$$

where

$N_F(\vec{r},t)$ = the time-dependent fuel number density at point $\vec{r}$
$\phi(\vec{r},E,t)$ = the time and energy-dependent flux at $\vec{r}$
$\sigma_F(E)$ = the energy-dependent microscopic fuel absorption cross section.

If the flux spectrum is assumed to be invariant over some time interval, i.e.,

$$\phi(\vec{r},E,t) = \phi(\vec{r},t)\,\psi(E)$$

where $\psi(E)$ is a normalized flux spectrum, and if the energy variable is treated by a few-group technique, the depletion equation becomes

$$\frac{dN_F(\vec{r},t)}{dt} = -N_F(\vec{r},t) \sum_i^G \phi_i(\vec{r},t)\sigma_i \qquad \text{Eq. (4.278)}$$

where

$$\phi_i = \phi(\vec{r},t) \int_{i\text{ th group}} \psi(E)dE$$

$$\sigma_i = \frac{\int_{i\text{ th group}} \psi(E)\sigma_i(E)dE}{\int_{i\text{ th group}} \psi(E)dE}$$

G = number of energy groups

$\psi(E)$ = normalized flux spectrum $\int_o^\infty \psi(E)dE = 1.$

The solution of this few-group depletion equation is facilitated by assumptions regarding flux or power variation with time. Assumptions are required because of the implicit relationship between fluxes and number densities, i.e., there is no direct way of expressing fluxes in terms of the number densities. The two common assumptions made in solving the depletion equation are the constant flux and constant power assumptions. In both cases, the solution becomes very simple. In the constant flux case, the equation is rearranged as follows:

$$\frac{dN_F(\vec{r},t)}{N_F(\vec{r},t)} = -\sum_i^G \phi_i(\vec{r},t)\,\sigma_i\,dt. \qquad \text{Eq. (4.279)}$$

The right-hand side of Eq. (4.279) is assumed constant for an interval Δt and leads to the solution

$$\frac{N_F(\vec{r},t+\Delta t)}{N_F(\vec{r},t)} = \exp\left[-\left(\sum_i^G \phi_i\sigma_i\right)\Delta t\right]$$

which in infinite series form is

$$\frac{N_F(\vec{r}, t+\Delta t)}{N_F(\vec{r}, t)} = 1 - \left[\sum_i^G \phi_i(\vec{r}, t)\sigma_i\right]\Delta t + \frac{1}{2}\left[\sum_i^G \phi_i(\vec{r}, t)\sigma_i\right]^2 \Delta t^2 + \cdots \quad \text{Eq. (4.280)}$$

In the constant power case, the right-hand side of Eq. (4.278) is assumed constant and equal to

$$-N_F(\vec{r}, t)\sum_i^G \phi_i(\vec{r}, t)\sigma_i \text{ or } -N_F(\vec{r}, t+\Delta t)\sum_i^G \phi_i(\vec{r}, t+\Delta t)\sigma_i .$$

The solution is

$$\frac{N_F(\vec{r}, t+\Delta t)}{N_F(\vec{r}, t)} = 1 - \sum_i^G \phi_i(\vec{r}, t)\sigma_i \Delta t \quad \text{Eq. (4.281)}$$

which for small time intervals is close to Eq. (4.280). Thus, the two methods of computing fuel depletion approach each other as the time intervals decrease.

Burnable poison depletion is governed by exactly the same type of equation that governs fuel depletion. If the poison is a multi-isotope, the equations become coupled but are still basically simple. Solutions of the fuel and poison depletion equations will be discussed in more detail in the subsequent sections.

3. *The Constant Power Assumption, Fuel-Based Method*

R.C. Dahlberg and F.D. Judge

A) INTRODUCTION. The term constant power is strictly applicable only to the assumptions made in computing fuel depletion for each core region. It has, however, been used to describe the entire depletion technique, which is an outgrowth of the constant power assumption. This nomenclature will continue to be used here, although a more correct name would be fuel-based method. The latter arises because the independent variable in the depletion equations is taken to be the fraction of fuel remaining.

In this section, general equations will be developed for the constant power depletion scheme. For illustrative purposes, a three-group energy structure with absorption in the lower two groups will be discussed. Consideration will be given to self-shielding of both fuel and poison.

Three specific cases, wherein lumped materials are treated by homogenization with appropriate definition of self-shielding factors, will be discussed: (1) the depletion of burnable poison with group-dependent self-shielding factors; (2) the depletion of homogeneous poison, i.e., poison mixed with fuel; (3) the depletion of a combination of discrete and homogeneous poison with group-independent self-shielding factors.

The constant power assumption is used for determining the fuel depletion at each point or in each core subregion. The general fuel-poison relations are next used to determine the corresponding poison depletion in each subregion or at each point. The method is then extended to the depletion of explicitly represented lumped burnable poison. For this case, equations are developed to correct the errors introduced by the constant power assumption. These modifications allow the use of relatively large time steps in this type of depletion analysis.

B) HOMOGENEOUS REPRESENTATIONS.

1) Development of General Equations. The following notation will be used in this section:

- f Self-shielding factor
- $\bar{f}$ Energy-averaged self-shielding factor
- K Self-shielding parameter (constant)
- γ Self-shielding parameter (constant)
- $C(E)$ Self-shielding parameter, a function of the neutron energy
- t Time
- $P(t)$ Fraction of poison remaining at time t
- $P_d(t)$ Fraction of discrete poison remaining at time t
- $P_h(t)$ Fraction of homogeneous poison remaining at time t
- $U(t)$ Fraction of uranium (fuel) remaining at time t
- ϕ_i Total neutron flux in energy group i
- σ_i Average microscopic absorption cross section in energy group i.

The following subscripts will be used in this section:

- 1 Epithermal energy group
- 2 Thermal energy group
- u Uranium (fuel)
- p Poison
- p_h Homogeneous poison
- p_d Discrete poison

2) Poison Self-Shielding Representation. In developing the equations that relate poison residues to fuel residues, the following conditions are assumed:

1. Fuel and burnable poison are consumed but not produced during reactor operation.
2. There is only one species of fuel and one species of poison. The fuel fractions at any time are known. For actual core lifetime studies, the average power density at each point or in each region remains constant during the depletion step (constant power assumption).
3. The reactor power level is constant for a given interval of time. This assumption does not limit the usefulness of the schemes, since reactor operation can be expressed in terms of equivalent full power hours of operation. (If a radioactive burnable poison were involved, the core power history would have to be known or assumed.)

It should be noted that the self-shielding factor is defined here as the ratio of the average flux in the absorber to the average flux in the moderator. (For the various ways of defining self-shielding, see Sects. 4.2.D.3 and 4.7.D.)

The self-shielding factor of a discrete poison lump or plate is assumed to be of the following form, the utility of which will be apparent later:

$$f_{pd}(E,t) = \frac{K_{pd}}{1 + C_{pd}(E)P_d(t)} . \qquad \text{Eq. (4.282)}$$

With both poison and fuel in a plate,

$$f_{ph}(E,t) = f_u(E,t) = \frac{K_u}{1 + C_u(E)U(t) + C_{ph}(E)P_h(t)} \qquad \text{Eq. (4.283)}$$

and for a plate containing no poison,

$$f_u(E,t) = \frac{K_u}{1 + C_u(E)U(t)} . \qquad \text{Eq. (4.284)}$$

Initially, $U(0) = P(0) = 1.0$. C_u and C_p are functions of the energy and, in general, proportional to the optical thickness of the fuel and poison plates, respectively. They must be determined by auxiliary calculations of the flux distribution using a model which depicts all of the geometric detail of the region in question and a theory which adequately treats transport effects if present.

When the self-shielding factor is averaged over a specified energy interval, one can express the factors in the following form for discrete poison,

$$\overline{f_{pd}(t)} = \frac{K_p}{1 + \gamma_{pd} P_d(t)} \qquad \text{Eq. (4.285)}$$

with both poison and fuel in the plate,

$$\overline{f_{pf}(t)} = \overline{f_u(t)} = \frac{K_u}{1 + \gamma_u U(t) + \gamma_{ph} P_h(t)} \qquad \text{Eq. (4.286)}$$

with no poison in a fuel plate,

$$\overline{f_u(t)} = \frac{K_u}{1 + \gamma_u U(t)} . \qquad \text{Eq. (4.287)}$$

If the energy interval is taken to be the complete range, it is often possible to obtain good estimates of $\bar{f}$ from experiment. Thus, it is possible to define γ's and K's which fit the experimental data for the undepleted condition. Further experiments or calculations, or both, are required to determine if a valid two-parameter fit can be found to cover the entire depletion. However, assuming such fits exist, it is possible to use them in conjunction with the constant power assumption to derive a set of depletion equations for several cases.

*3) Discrete Poison Depletion, Two-Group.** The general equation [Eq. (4.278)] applies to either fuel or a one-isotope poison. If both sides of this equation are divided by the initial number density of fuel, it takes on the form (for absorption in two groups only)

$$\frac{dU}{dt} = - \bar{f}_{u_1} U\phi_1 \sigma_{u_1} - \bar{f}_{u_2} U\phi_2 \sigma_{u_2} . \qquad \text{Eq. (4.288)}$$

*The subscript d in P_d is omitted in the discussion, since the reference is clearly to discrete poison.

In this equation the fuel flux in group i is $\bar{f}_{u_i}\phi_i$ and $U = N_F(t)/N_F(o)$. An exactly analogous equation applies to the poison

$$\frac{dP}{dt} = -\bar{f}_{p_1} P\phi_1 \sigma_{p_1} - f_{p_2} P\phi_2 \sigma_{p_2}. \qquad \text{Eq. (4.289)}$$

It is convenient at this point to introduce two quantities, w and A, which are defined as follows:

$$w = \phi_1/\phi_2 \qquad \text{Eq. (4.290)}$$

$$A = \sigma_1/\sigma_2. \qquad \text{Eq. (4.291)}$$

The product wA is the ratio of epithermal to thermal absorptions; $1 + wA$ is then the ratio of total absorption to thermal absorptions. With the use of these quantities, Eqs. (4.288) and (4.289) become

$$\frac{dP}{dt} = -\phi_2 P\sigma_{p_2}\left(wA_p\bar{f}_{p_1} + \bar{f}_{p_2}\right) \qquad \text{Eq. (4.292)}$$

$$\frac{dU}{dt} = -\phi_2 U\sigma_{u_2}\left(wA_u\bar{f}_{u_1} + \bar{f}_{u_2}\right). \qquad \text{Eq. (4.293)}$$

By dividing Eq. (4.292) by Eq. (4.293) and using the self-shielding factors as defined in Eq. (4.285), the following expression is readily obtainable:

$$\frac{dU}{U\left[wA_u\dfrac{K_{u_1}}{1+\gamma_{u_1}U} + \dfrac{K_{u_2}}{1+\gamma_{u_2}U}\right]} = \frac{\sigma_{u_2}}{\sigma_{p_2}}\frac{dP}{P\left[wA_p\dfrac{K_{p_1}}{1+\gamma_{p_1}P} + \dfrac{K_{p_2}}{1+\gamma_{p_2}P}\right]}. \qquad \text{Eq. (4.294)}$$

If it is assumed that the products wA_p and wA_u are constant, the integration of Eq. (4.294) between times t and t', corresponding to U and U', and P and P', is straightforward, yielding

$$\left[\ln\frac{U'\left(wA_u\gamma_{u_2}K_{u_1}+\gamma_{u_1}K_{u_2}\right)+\left(wA_uK_{u_1}+K_{u_2}\right)}{U\left(wA_u\gamma_{u_2}K_{u_1}+\gamma_{u_1}K_{u_2}\right)+\left(wA_uK_{u_1}+K_{u_2}\right)}\right]\times\left[\frac{\gamma_{u_1}+\gamma_{u_2}}{wA_u\gamma_{u_2}K_{u_1}+\gamma_{u_1}K_{u_2}}\right.$$

$$\left.-\frac{1}{wA_uK_{u_1}+K_{u_2}}-\frac{\left(wA_uK_{u_1}+K_{u_2}\right)\gamma_{u_1}\gamma_{u_2}}{\left(wA_u\gamma_{u_2}K_{u_1}+\gamma_{u_1}K_{u_2}\right)^2}\right]+\frac{\gamma_{u_1}\gamma_{u_2}(U'-U)}{\left(wA_u\gamma_{u_2}K_{u_1}+\gamma_{u_1}K_{u_2}\right)}$$

$$+\frac{1}{wA_uK_{u_1}+K_{u_2}}\ln\frac{U'}{U}$$

$$=\frac{\sigma_{u_2}}{\sigma_{p_2}}\times\left\{\left[\ln\frac{P'\left(wA_p\gamma_{p_2}K_{p_1}+\gamma_{p_1}K_{p_2}\right)+\left(wA_pK_{p_1}+K_{p_2}\right)}{P\left(wA_p\gamma_{p_2}K_{p_1}+\gamma_{p_1}K_{p_2}\right)+\left(wA_pK_{p_1}+K_{p_2}\right)}\right]\right.$$

$$\times\left[\frac{\gamma_{p_1}+\gamma_{p_2}}{wA_p\gamma_{p_2}K_{p_1}+\gamma_{p_1}K_{p_2}}-\frac{1}{wA_pK_{p_1}+K_{p_2}}-\frac{\left(wA_pK_{p_1}+K_{p_2}\right)\gamma_{p_1}\gamma_{p_2}}{\left(wA_p\gamma_{p_2}K_{p_1}+\gamma_{p_1}K_{p_2}\right)^2}\right]$$

$$\left.+\frac{\gamma_{p_1}\gamma_{p_2}(P'-P)}{\left(wA_p\gamma_{p_2}K_{p_1}+\gamma_{p_1}K_{p_2}\right)}+\frac{1}{wA_pK_{p_1}+K_{p_2}}\ln\frac{P'}{P}\right\}.$$

Eq. (4.295)

It should be noted that in Eq. (4.295) the right-hand side is identical to the left-hand side, except for the factor $\sigma_{u_2}/\sigma_{p_2}$ and the obvious fact that the left-hand side refers to the fuel and the right-hand side refers to the poison.

In practice, U and P are usually known, since these are the relative loads at the beginning of a time step. Each can be taken as equal to 1.0. U' is determined by the energy requirements of the core, and P' is then given by the above transcendental relationship which may be solved by standard techniques. It should be noted that the only approximation required to obtain Eq. (4.295) was the constancy of wA_u and wA_p. This approximation is equivalent to assuming that epithermal-to-thermal absorption ratios are constant during a time step. Integration of the depletion Eq. (4.294) was made possible by fitting the self-shielding factors to the the form

$$\frac{K_p}{1+\gamma_p P}.$$

C) EXPLICIT REPRESENTATION. The equations developed in the preceding section apply to media in which the materials are either homogeneous or can be treated as homogeneous through the definition of appropriate self-shielding factors. However, this treatment requires that the time dependence of the self-shielding factors be simply expressible and that the homogenization process not seriously affect power distributions. These requirements can be met readily for the fuel and, in many cases, for the lumped poison. In general, if a large number of uniformly spaced elements are present, homogenization is acceptable. On the other hand, if lumped poison is serving as a flux suppressor in addition to its usual role and if there are only a few elements in the core, the homogenization process will clearly alter the power distributions. Furthermore, it will usually not be obvious over what regions of the core the homogenization should be carried out. Consequently, the self-shielding factors obtained will be somewhat arbitrary and their dependence will be unpredictable. For these reasons, it is sometimes desirable to avoid homogenization of the lumped poison and to treat it explicitly in the diffusion theory calculation. In the static case, the lumped poison can usually be represented adequately by blackness theory or thin region theory. For depletion, on the other hand, special techniques, which must be compatible with the overall depletion scheme, are required. The following material describes a technique associated with the constant power fuel-based depletion scheme.

In explicit lumped poison regions, no fuel is actually present, and some artifice must be found in order to extend the fuel-based method to the depletion of these regions. This extension is made possible by adding a small arbitrary amount of fuel (having negligible effect upon the reactivity of the system) to each poison region. Under the constant power assumption, this fuel will be depleted in each time step, assuming the power distribution remains unchanged during the time step. The poison depletion may then be calculated directly, using the previous depletion equations. This use of a trace of fuel in explicit poison regions is called fuel doping. In all cases, it is assumed that a method (such as blackness theory) is available for accurately predicting the poison absorption rate and the power produced by the fuel in the poison plate. It must be noted that in calculating the fuel depletion in the poison plate, the absorption cross section of the trace of fuel must be an effective cross section analogous to the effective poison absorption cross section, i.e., the blackness corrections must be applied to the fuel as well.

In many cases, the poison is homogeneously distributed within the lumped region, and the γ_2 and γ_3 of Eq. (4.295) are set equal to zero. However, lumping effects within the poison region, such as particle self-shielding, may be taken into account by setting

$$\gamma_{\text{poison}} = \frac{1}{f_1} - 1$$

where f_1 = particle self-shielding factor. The same procedure may be used to account for macroscopic effects, such as representing pin or strip combinations by a uniform plate in the explicit models. In this case, the

$$\gamma_{\text{poison}} = \frac{1}{f_2} - 1$$

where f_2 = plate-to-pin or plate-to-strip factor. The constant power assumption is again used to predict the fuel burnup. However, this assumption applied to the fuel in the explicit poison region can lead to an underestimate of poison depletion. The constant power assumption is equivalent to assuming that the flux at a given point varies inversely with the fuel fraction at that point. Thus, at points where the specific power is high (i.e., where the flux is high) the flux changes considerably during a time step. Conversely, the flux changes only a small amount in areas where the specific power or

flux is low. Since, typically, the flux is low in a poison lump, the constant power assumption leads to a small variation of flux in the lump during a time step. Such a variation is not physically reasonable, since rapid poison burnup in the lump will lead to a rapid variation in flux. Figure 4.60 illustrates typical flux variations for a lump immersed in a large homogeneous fuel region. The upper smooth curve is the average fuel flux which varies approximately as $1/U$. The true poison flux variation is shown by the lower smooth curve. It starts at a lower level than the fuel flux to represent the self-shielding of the poison. However, it must eventually approach the fuel flux when the poison is entirely depleted and, therefore, rises faster than the average fuel flux. On the other hand, as noted previously, the constant power assumption leads to a flux rise which is slower than that of the fuel. The result is a flux variation shown by the stepped curve in Fig. 4.60. This flux is always lower than the true flux and leads to poison depletion which is too slow. To minimize this error in poison depletion, the following choices (among others) are available:

1. Restrict the size of the depletion step.
2. Use an iterative procedure. After the poison is depleted, the flux distribution is recomputed and the depletion repeated, using an average of the power generation in the lump at the beginning and end of the depletion step.
3. Alter the depletion equations for the case of explicit poison. In this method, an attempt is made to estimate the variation of the flux in the poison during the time step based upon the initial self-shielding of the poison. Making such an estimate will usually introduce much smaller errors than to leave the equations unmodified.

The first choice is acceptable in circumstances where the expense of running depletion calculations is low enough that a large number of time steps can be afforded. The second choice virtually doubles the computation time required and is probably not superior to the first, in terms of accuracy, for a given amount of computation. The third choice provides good accuracy without increasing computing time. It is implemented in the following way: Consider the one-group depletion equations

$$\frac{dU}{dt} = -U\bar{f}_u\sigma_u\phi \qquad \text{Eq. (4.296)}$$

$$\frac{dP}{dt} = -P\bar{f}_p\sigma_p\phi\,. \qquad \text{Eq. (4.297)}$$

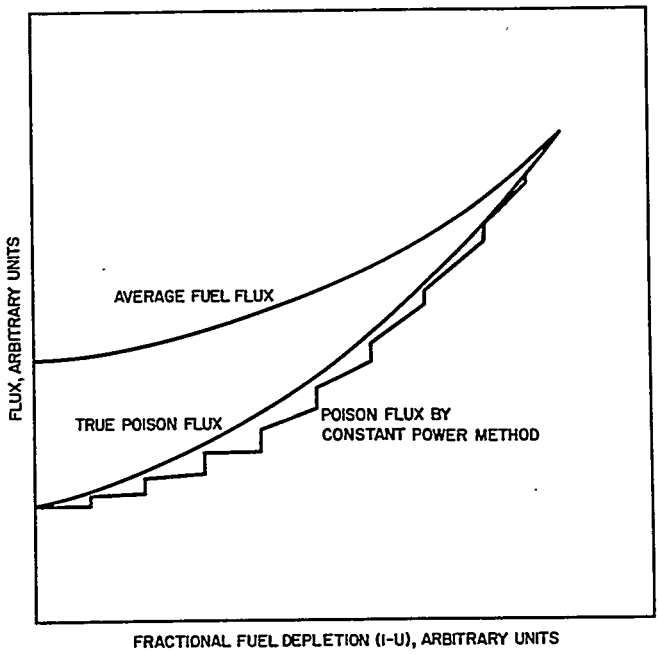

FIGURE 4.60. Flux Level in Poison Lump as Function of Fuel Depletion.

Equations (4.296) and (4.297) can be written in the form

$$\int \phi dt = -\int \frac{dU}{U\bar{f}_u\sigma_u} \qquad \text{Eq. (4.298)}$$

$$\int \phi dt = -\int \frac{dP}{P\bar{f}_p\sigma_p} . \qquad \text{Eq. (4.299)}$$

The right-hand side of Eq. (4.298) can be integrated if the fuel self-shielding is of the usual form $\bar{f}_u = \frac{K_u}{1+\gamma_u U}$, and σ_u is a constant. The result is

$$\int_{t_i}^{t_{i+1}} \phi dt = -\frac{1}{\sigma_u K_u}\left[\ln U + \gamma_u U\right]_{U_i}^{U_{i+1}} \qquad \text{Eq. (4.300)}$$

where subscript i refers to beginning of a time interval, and subscript $i+1$ refers to end of a time interval.

The constant power assumption then permits the right-hand side of Eq. (4.299) to be evaluated for the trace of fuel in the poison plate, and provides the time-integrated flux for the poison depletion via Eq. (4.299). However, as discussed above, this constant power flux does not provide sufficiently rapid poison depletion. Therefore, the flux is modified as follows:

$$\phi_E = \left[\phi_{CP}\right]\left[\frac{1+\Gamma P_i}{1+\Gamma P(t)}\right]. \qquad \text{Eq. (4.301)}$$

where

ϕ_E = the estimated flux
ϕ_{CP} = the constant power flux
Γ = an assumed constant
P_i = the poison fraction at the beginning of the time step
$P(t)$ = the variable poison fraction.

Equation (4.299) then becomes

$$-\int \frac{dP}{f_p \sigma_p P}\,\frac{1+\Gamma P}{1+\Gamma P_i} = \int \phi_{CP}\,dt\,. \qquad \text{Eq. (4.302)}$$

The left-hand side of Eq. (4.302) can be integrated over a time interval and set equal to the right-hand side of Eq. (4.300). The result, taking $f_p = \dfrac{K_p}{1+\gamma_p^P}$, is

$$\ln\frac{U_{i+1}}{U_i} + \gamma_u(U_{i+1}-U_i) = \frac{K_u}{K_p}\,\frac{\sigma_u}{\sigma_p}\,\frac{1}{1+\Gamma P_i}\left\{\ln\frac{P_{i+1}}{P_i} + (\gamma_p+\Gamma)(P_{i+1}-P_i) + \Gamma\gamma\left[(P_{i+1})^2-(P_i)^2\right]\right\}.$$

The constant Γ is a self-shielding parameter, analogous in some respects to the parameter γ_p. It represents the fitting parameter in $f_{\text{plate}} = \dfrac{1}{1+\Gamma P}$ where f_{plate} is the self-shielding

factor of the homogeneous poison plate, with respect to its surroundings. An estimate of Γ may be obtained from

$$f_{\text{plate}}^{(t=o)} = \frac{1}{1+\Gamma} = \left[f_{\text{total}}^{(t=o)}\right]\left[1+\gamma\right]$$

where $f_{total}^{(t=0)}$ is the total self-shielding factor at the beginning of life. An improved value of Γ may be obtained by analyzing results of preliminary depletion studies.

4. The Constant Flux Method

A) INTRODUCTION. The constant flux method of performing number density calculations involves solving differential equations describing point-variable isotopic densities under the assumption that the flux in each energy group and at each point remains constant during a time interval.

The basic depletion time interval (Δt) referred to in this section is the time between spatial calculations. For example, in the TURBO[83] two-dimensional depletion program, this interval would be that between two successive PDQ-type[34] iterative calculations. Since the spatial calculation is most time-consuming, there is strong incentive to make Δt as large as practicable to reduce overall computing time for the depletion study. For this reason, various calculational devices have been introduced within the basic depletion time interval to minimize the errors in fuel and burnable poison inventory which are associated with large Δt's. Each of these devices, and the reasons for their use, is discussed in the following sections.

B) DEPLETION OF U^{235}. As indicated in Sect. 4.6.C.2, the constant flux assumption leads to the solution

$$\frac{N_F(\vec{r}, t+\Delta t)}{N_F(r,t)} = \exp\left[-\left(\sum_i^G \phi_i f_i \sigma_i\right)\Delta t\right] .$$

Eq. (4.303)

Since the function $\left(\sum_i^G \phi f_i \sigma_i\right)$ in Eq. (4.303) is a function of time it is desirable to approximate its time dependence so that the time between calculations of the spatial distribution of the flux, Δt, can be large. A method which has been found useful is to break the time interval Δt into N_1 subintervals of length

$\Delta t'$. After each of these the thermal flux level is renormalized to give the same integrated power level as at the beginning of the time interval. The flux shapes in all groups and the flux levels in the higher energy groups are held constant. If the cross-sections, σ_i, or self-shielding factor, f_i, are dependent on the number densities, the subintervals $\Delta t'$ are broken into N_2 sub-subintervals of length $\Delta t''$. After each depletion for $\Delta t''$ seconds the cross sections and self shielding factors are re-evaluated using the new number densities. In the general case there will be $N_1 N_2$ calculations of new number densities during the large time interval Δt.

In approximating exponentials, as in Eq. (4.303), the constant flux method employs the approximation

$$\exp(-x) \approx \frac{2-x}{2+x} \quad (o \leq x < 1). \qquad \text{Eq. (4.304)}$$

This approximation is fast and quite accurate, since typical values of x are much less than unity. Infinite series expansions of the exponential and its approximation show the first three terms to be identical, and the error to be less than $x^3/12$.

C) DEPLETION OF HOMOGENEOUS SINGLE ISOTOPE POISONS. With one exception, the depletion of homogeneous single isotope poisons is carried out in the same way as for U^{235}. In the treatment of boron-10 poison, the thermal self-shielding factor may be constant within the basic depletion interval, or it may be strongly dependent on the fraction of boron 10 remaining. If the former is true,

$$\frac{N_{B\text{-}10}(t+\Delta t'')}{N_{B\text{-}10}(t)} = \exp\left[-\left(\sum_i^G \sigma_i f_i \phi_i\right)\Delta t''\right]. \qquad \text{Eq. (4.305)}$$

If the latter is true, Eq. (4.305) represents a first estimate of the depletion. If the epithermal factor is assumed constant over the interval, the analytic solution can be obtained in implicit form and can be used to find the effective depletion time τ, at which the fractional depletion [right-hand side of Eq. (4.305)] calculated above actually occurs. Then, an additional step of length $\Delta t'' - \tau$ with revised thermal self-shielding factor is made to give a better approximation. This procedure, which is described in complete detail in Ref. 83, is employed when the basic depletion time interval has 10 or less subintervals.

D) DEPLETION OF HOMOGENEOUS MULTIPLE ISOTOPE POISONS. In certain cases where the burnable poison is composed of several isotopes with high absorption cross sections, it has been found that the desired average values of the epithermal microscopic cross sections of U^{235} and the poison isotopes depend on the concentrations of both U^{235} and one of the poison isotopes (say P_1). For example, the epithermal microscopic cross sections of all the poison isotopes of a given chain as well as U^{235} might be approximated by functions of the form

$$\frac{1}{\sigma_a} = a_0 + a_1 N_{U^{235}} + a_2 N_{P_1} . \qquad \text{Eq. (4.306)}$$

This type of relationship, plus several thermal microscopic cross-section functions of U^{235} depletion, is incorporated into the constant flux treatment of multiple isotope poisons. Although this special approach makes the formulation of the depletion equations somewhat more complicated, the basic procedure is the same as that discussed in connection with Eq. (4.303), with the additional complication that before each sub-subinterval $(\Delta t'')$ the most recent number densities of U^{235} and principal poison isotope must be used to compute new microscopic cross sections.

When one or more of the isotopes in the multiple isotope poison chain decays radioactively at a significant rate, the decay constant λ must be included in the exponential, that is,

$$\exp\left[-\left(\sum_i^G (\sigma_i f_i \phi_i)\right) \Delta t''\right]$$

becomes

$$\exp\left[-\left(\sum_i^G (\sigma_i f_i \phi_i) + \lambda\right) \Delta t''\right] .$$

Similarly, when neutron absorption by one isotope provides the source of another poison isotope, the neutron capture rate must be factored into the solution for the latter isotope. Thus,

$$N^M(t+\Delta t'') = \frac{\left[2 - \sum_i^G \sigma_i^M f_i^M \phi_i \Delta t''\right] N^M(t)}{2 + \sum_i^G \sigma_i^M f_i^M \phi_i \Delta t''} + \frac{2N^{M-1}\left(\frac{t+\Delta t''}{2}\right) \sum_i^G \sigma_i^{M-1} f_i^{M-1} \phi_i \Delta t''}{2 + \sum_i^G \sigma_i^{M-1} f_i^{M-1} \phi_i \Delta t''}$$

Eq. (4.307)

where N^M and N^{M-1} are the poison isotope under consideration and the next lowest isotope of the same element, respectively, and the second term in the numerator is the average neutron capture rate of isotope N^{M-1} during the time interval $\Delta t''$.

The depletion of chains of isotopes having significant resonance absorption has the drawback that an estimate must be made a priori of the time-dependent history of these isotopes and the fuel, so that suitable microscopic constants may be determined and least-square fitted as functions of fuel and principal poison concentrations. The ideal situation might be one in which spectrum calculations are made each time group constants are required in the depletion calculation. However, this would be very time-consuming and has not been used in the point depletion approach. A reasonable set of microscopic constants can, in practice, be generated by using estimated depletion behavior based on an iterative procedure that employs a series of one-point-core depletion calculations and the subsequent spectrum calculations.

E) DEPLETION OF DISCRETE POISONS, SINGLE ISOTOPE. A discrete poison region may be represented in the diffusion theory description by means of fictitious (or effective) diffusion coefficients and macroscopic absorption cross sections derived from transport theory approximations (see Sect. 4.3.C).

The depletion of these special regions is calculated in the constant flux method by assuming that D_{Pd} and $\Sigma_{a,Pd}$ in each energy group are known functions of the poison number density. A single poison number density, $N_{Pd}(t)$, describes the entire discrete poison region at time t.

The depletion of the poison number density is accomplished through the following equation:

$$N_{Pd}(t + \Delta t''') = N_{Pd}(t) \exp \left[- \sum_{i}^{G} (\sigma_i \phi_i) \Delta t''' \right] \qquad \text{Eq. (4.308)}$$

where

$\Delta t'''$ = the subinterval chosen to be no more than 50 hours and the value of

$$\frac{\Sigma^{i}_{a,\,Pd}(t)}{N_{Pd}(t)} \; \bar{\Phi}^{i}_{Pd}(t)$$

is substituted for the product $(\sigma_i \phi_i)$ which is not known directly, since microscopic constants are not employed in the diffusion theory description of the discrete poison. $\bar{\Phi}^{i}_{Pd}(t)$ represents the average i^{th} group flux in the poison region.

It should be noted that a new subdivision of the basic depletion time interval has been introduced in Eq. (4.308). This refinement necessitates updating of the poison number density and macroscopic absorption cross section before each subsubinterval, so that the appropriate (larger) effective microscopic cross section will be used, thus ensuring that the depletion of the discrete poison is not underestimated.

5. *Core Subdivision*

The discussions of Sects. 4.6.C.3 and 4.6.C.4 have considered only briefly the spatial nonuniformities which come about within a reactor as a result of its operation. To account properly for the time and spatial dependence of fuel, poison, and fission product concentrations, it is necessary to apply the depletion equations derived in the preceding sections in a manner which accounts for the spatial and time dependence of the driving functions (fluxes or power). Ideally, the depletion equations would be applied to an infinitesimal volume within which the true time dependence of the fluxes or power was somehow known. This ideal cannot be achieved because of (1) the practical necessity of solving the depletion equations for a finite

number of volume units and (2) the implicit relationship between the time dependence of fluxes (or power) and the time dependence of material concentrations. The number of volume units for which the depletion equations must be solved can be limited by subdividing the core into volume units within which both materials and fluxes (or power) are assumed uniform. The implicit relationship between material concentrations and fluxes is circumvented by assuming that the flux (or power) distributions are unchanged over some interval of time. This assumption permits direct application of the depletion equations separately to each volume unit, presuming that the flux (or power) distributions are available from a few-group diffusion theory calculation.

The extent of core subdivision is determined by many considerations. Of primary importance are the requirements for accuracy in power distributions and reactivity. If design margins are small, then errors introduced by insufficient subdivision of the core cannot be tolerated. On the other hand if margins are larger, design expense can sometimes be reduced by a coarser core subdivision. The accuracy obtained with a given degree of subdivision will depend on the fraction of fuel to be depleted together with the power distribution and its variation with time. A core with a rapidly varying power distribution, and which depletes a large fraction of its fuel, must be finely subdivided to obtain accurate results.

Two distinct types of core subdivision are currently in use. These are point subdivision and region subdivision. In the point subdivision method, the changes in composition occurring in each spatial mesh element are computed according to the basic depletion equations. A mesh element is defined as the volume enclosed by lines or planes joining neighboring mesh points. These elemental volumes are approximately equal in number to the number of mesh points employed in a given problem. Therefore, the pointwise depletion method usually involves a great many solutions of the depletion equations. On the other hand, it represents the spatial variation of depletion to the same degree of detail that fluxes and power densities are represented and, consequently, produces an essentially continuous variation of concentrations with position.

An advantage of this continuity is that power distributions are also continuous, as in reality they must be. (The region depletion method does not possess this advantage.) The microscopic cross sections used in conjunction with the pointwise method must be somewhat arbitrarily chosen. If they are self-determined by the infinite medium spectrum characteristic of the composition in the single mesh element, there is an obvious question of validity. On the other hand, if they are determined

by the infinite medium spectrum characteristic of some average composition in the vicinity of the mesh element, there is a spatial variation which is not properly accounted for.

A superior technique is the use of several thermal groups to represent the spatially varying thermal neutron spectrum more accurately. The fast neutron spectrum must still be determined on an infinite medium basis, but this is not usually a serious deficiency.

The regionwise depletion method differs from the pointwise method in that the composition within a group of mesh elements rather than within a single element is assumed to remain uniform during depletion. The time variation of this uniform composition is determined by the basic depletion equations, as in the case of pointwise depletion. The regionwise method has both advantages and disadvantages with respect to the pointwise method.

One advantage is that solution of the depletion equation by groups of mesh elements rather than for single elements is less time-consuming. A further advantage of the regionwise method is that the number of compositions is small enough to permit calculation of infinite media spectra and cross sections for each composition. Thus, the gross shift of spectrum in the core can be readily calculated, although the limitations of regionwise constant spectra still apply.

A significant disadvantage of the region method is the introduction of composition discontinuities at region interfaces. These discontinuities arise because the uniform composition in each region depends directly on the average power density with which the region has been depleted. Thus, adjacent regions with the same initial composition will have different compositions at some stage of depletion if the power densities are different. The resultant discontinuities, which are not physical, give rise to power discontinuities, since the neutron fluxes are continuous.

If the core has been finely subdivided, the power discontinuities are not serious, and the average power at region interfaces can be used with confidence. However, special care must be taken in areas where power and depletion gradients are large. In these areas the assumption of uniform depletion within regions can lead to appreciable errors. These errors are manifested in the depletion patterns and power distributions. For example, in the high power density portion of a region, the uniform depletion assumption results in too little depletion, i.e., too much residual fuel. Consequently, since the fluxes are only slightly in error, the power density calculated at the beginning of the next time step is too large. The converse arguments apply to the low power density portion of a

region. These effects can usually be minimized by choosing the size of crucial regions such that the power variation within them is less than 5 percent.

Reactivity variations with depletion as calculated by the regionwise method are generally insensitive to region size. Therefore, in zones of low or fairly flat power, large regions can be employed to reduce computing time, improve utilization of program capacities, and simplify input data.

D. Depletion of Natural Uranium

While the material presented above on the depletion of U^{235} is generally applicable to depletion calculations of natural uranium, there are a number of special features regarding natural uranium depletion which require individual attention. For example, the epithermal group removal to thermal cross section is dependent on the resonance absorption in U^{238}. In addition to U^{235}, several other fissionable nuclides are present (U^{238}, Pu^{239}, and Pu^{241}), and their respective contributions to the power generation and the formation of fission fragment poisons have to be accounted for.

For depletion calculations it is customary to use fitted microscopic cross sections rather than obtain constants for each time in life. These fitted cross sections represent a best fit to a variety of conditions (i.e., inventories) likely to be encountered during the depletion. These topics are discussed below for natural uranium as used in the blanket region of the PWR reactor. It should be noted that the extension from highly enriched uranium to slightly enriched uranium would require similar considerations. The general reactivity characteristics of slightly enriched uranium systems of various enrichments are discussed in Ref. 84.

In the following discussion, four neutron energy groups are considered: thermal (0 to 0.625 ev), epithermal (0.625 ev to 5.53 kev), fast (5.53 kev to 0.821 Mev), and very fast (0.821 Mev to 10 Mev). The differential equations governing the concentrations of the time-dependent elements can be expressed in a compact form after the following definition is made. For element m in a particular mesh rectangle or region,

$$A_m = \sum_{i=1}^{3} \sigma_{A,m}^{i} \Phi^i + g_m \sigma_{A,m}^{4} \Phi^4$$

where

i = the energy group index
σ_A = the microscopic absorption cross section
g = the thermal self-shielding factor for the region containing this mesh rectangle
Φ = the average power normalized flux for the mesh rectangle.

Similar expressions can be written for C_m and F_m, in which the absorption cross section in A_m has been replaced by the capture and fission cross sections, respectively. The question of the constant power or constant flux assumptions when integrating these equations is not germane to the subsequent discussion, since the cross sections do not vary rapidly with depletion.

An additional definition is made to simplify the inclusion of the resonance absorption of U^{238}:

$$\Sigma^3_{A,r}(U^{238}) = \frac{1 - p^{28}_{r_3}}{p^{28}_{r_3}} \left[\Sigma^3_{A,s}(U^{238}) + \Sigma^3_R \right]$$

where

$\Sigma^3_{A,r}(U^{238})$ = the resonance absorption of U^{238}
$\Sigma^3_{A,s}(U^{238})$ = the smooth absorption of U^{238}
$p^{28}_{r_3}$ = the resonance escape probability for U^{238}

$$= \frac{\Sigma^3_R + \Sigma_{A,s}(U^{238})}{\Sigma^3_{A,r}(U^{238}) + \Sigma^3_{A,s}(U^{238}) + \Sigma^3_R}$$

Σ^3_R = the removal cross section

all of which are evaluated for the third group in each particular mesh rectangle.

The depletion equations for the U^{235} chain are:

$$\frac{dN_{U^{235}}}{dt} = -A_{U^{235}} N_{U^{235}}$$

$$\frac{dN_{U^{236}}}{dt} = -A_{U^{236}} N_{U^{236}} + C_{U^{235}} N_{U^{235}}.$$

Similarly, the equations for the U^{238} chain are:

$$\frac{dN_{U^{238}}}{dt} = -A_{U^{238}} N_{U^{238}} - \Sigma^{3}_{A,r}(U^{238})\Phi^{3}$$

$$\frac{dN_{Pu^{239}}}{dt} = -A_{Pu^{239}} N_{Pu^{239}} + C_{U^{238}} N_{U^{238}} + \Sigma^{3}_{A,r}(U^{238})\Phi^{3}$$

$$\frac{dN_{Pu^{240}}}{dt} = -A_{Pu^{240}} N_{Pu^{240}} + C_{Pu^{239}} N_{Pu^{239}}$$

$$\frac{dN_{Pu^{241}}}{dt} = -(\lambda_{Pu^{241}} + A_{Pu^{241}}) N_{Pu^{241}} + A_{Pu^{240}} N_{Pu^{240}}$$

where λ is the decay constant, and where the double beta decay process in the sequence

$$U^{238} \xrightarrow[\text{capture}]{\text{neutron}} U^{239} \xrightarrow[23.5 \text{ minutes}]{\beta^-} Np^{239} \xrightarrow[2.10 \text{ days}]{\beta^-} Pu^{239}$$

is assumed to occur almost instantaneously compared to the average time step lengths of from several hundred to 1500 hours.

The equations governing the concentrations of the fission products can be written in terms of an effective yield which combines the individual yields of all the fissioning isotopes. The effective yield of element m is

$$Y_m = \sum_j \bar{N}_j \cdot \gamma_{m,j} F_j$$

where m = an index on the direct fission products [Pm^{149}, I^{135}, Xe^{135}, and FP (lumped fission products)]. (The reader is referred to Sect. 4.5 for a discussion of the lumped fission products for U^{235} and Ref. 68 for U^{238}, Pu^{239}, Pu^{241}.)

The interactions of materials with neutrons of greater than thermal energies are described in terms of a set of fitted

cross sections appropriate to the material compositions. It is assumed that the fast neutron spectrum present can be described as that appropriate to homogeneous mixtures of the materials present in gross regions of the core, and within which the rate of exchange of neutrons is sufficient to permit the disregarding of local heterogeneities. In PWR, the seed and the blanket have each been designated as distinct regions, and for them appropriate spectra and spectrum-averaged cross sections have been obtained from the MUFT-5 program (see Chaps. 2 and 7). These calculations are made at both operating (535°F) and ambient (68°F) temperatures, using the fuel distributions appropriate to the beginning, the middle, and the end of core life. The middle and end-of-life number densities are those predicted by a one-dimensional core depletion, utilizing an earlier (and more approximate) set of fitted constants. These 12 conditions (seed and blanket each at three stages of depletion and two temperatures) represent the full range of material composition which will occur during the lifetime of PWR-2, Seed 1.

For each of the reactor conditions, values of σ_A, σ_F, and $\nu\sigma_F$ for each element are directly determined from a MUFT edit by elements. The fitted values for these three cross sections are simple arithmetic averages of the values obtained from the 12 cases examined, except for U^{238}, Pu^{239}, Pu^{240}, and Pu^{241}. Since significant amounts of these isotopes occur only in the blanket region, the calculation for these isotopes is restricted to the values from the six blanket cases. The fitted σ_{Tr}'s and σ_R's for each element are indirectly obtained from the results of additional MUFT problems in which the atom densities of the elements are perturbed individually, resulting in perturbed values of the overall few-group values of D and Σ_R. For differential perturbations of the atom densities about a given case, the change in D or Σ_R will be characteristic of the physical change in the atom density perturbation and the change in fast spectrum. Thus, from the results of the perturbed and unperturbed problems, σ_{Tr_i}'s and σ_{R_i}'s for each element n can be computed by the following relationships:

$$\sigma^n_{Tr_i} = \frac{\Sigma'_{Tr_i} - \Sigma_{Tr_i}}{N'_n - N_n} = \frac{D_i - D'_i}{3 D_i D'_i (N'_n - N_n)}$$

$$\sigma^n_{R_i} = \frac{\Sigma_{R'_i} - \Sigma_{R_i}}{N'_n - N_n}$$

where the primed quantities refer to the perturbed problems. These cross sections will be valid if the change in fast spectrum is small or linear. The fitted fast constants are employed in depletion codes as follows. In Groups 1 and 2 of a four-group scheme, the following relationships apply:

$$D_i = \frac{1}{3\sum_n N^n \sigma_{Tr_i}{}^n}$$

$$\Sigma_{A_i} = \sum_n N^n \sigma_{A_i}{}^n$$

$$\Sigma_{R_i} = \sum_n N^n \sigma_{R_i}{}^n$$

$$\nu\Sigma_{F_i} = \sum_n N^n (\nu\sigma_{F_i})^n$$

$$(K\Sigma_F)_i = \sum_n N^n K_i^n (\nu\sigma_{F_i})^n$$

where K_i^n = the energy release per fission neutron from a fission by element n in group i.

In the epithermal group, D_3, $\nu\Sigma_{F_3}$ and $K\Sigma_{F_3}$ are computed as above. The Σ_{R_3} and Σ_{A_3} are determined by the following expressions:

$$\Sigma_{R_3} = \frac{p_{r3}^{28}(a+1)}{p_{r3}^{28}+a}\sum_n N^n \sigma_{R_3}{}^n - \frac{a}{p_{r3}^{28}+a}\left[N^{28}\sigma_{A_3}^{28} + p_{r3}^{28}\sum_{m\neq 28} N^n \sigma_{A_3}{}^n\right]$$

$$\Sigma_{A_3} = \sum_n N^n \sigma_{a_3}^n + \frac{1-p_{r3}^{28}}{p_{r3}^{28}}\left[\Sigma_{R_3} + N^{28}\sigma_{A_3}^{28}\right]$$

where

28 identifies U^{238}

p_{r3}^{28} = the resonance escape probability for U^{238}

a = an empirically determined constant.

The TURBO [83] depletion programs can accept only one value of a and a single set of effective fast cross sections. Therefore, it is necessary in using this program to specify an average value of a that represents all cases. The defining equations for Σ_{A_3} and Σ_{R_3} are solved for a and $\sigma_{A_3}^{28}$ as a function of Σ_{A_3}, Σ_{R_3}, and p_{r3}^{28}. Values of a and $\sigma_{A_3}^{28}$ are then calculated for each of the three hot blanket cases and the averages incorporated into the fitted constants.

Next, the fitted microscopic constants are used to construct hot seed and blanket macroscopic constants at several different times in life and compared with MUFT calculations for the same times in life. Experience has shown that some alterations of the fitted σ_R's and σ_{T_r}'s can significantly improve the agreement between the fitted macroscopic constants and corresponding MUFT calculations. This is believed to be the result of nonlinear perturbations in the spectrum.

It should be pointed out that negative values of the fitted microscopic cross sections may occur because, in determining the fitted transport and removal cross sections, it is assumed that the entire change in macroscopic quantity between the perturbed and unperturbed problems can be attributed directly to the change in number density. A mere increase in the number of atoms present tends to make the macroscopic transport and removal cross sections increase for the lighter elements, but this is not necessarily true for uranium and plutonium isotopes. For the latter two elements, an increase in number density results in a relatively large increase in absorption which depresses the energy spectrum and, consequently, reduces the probability of leaking both spatially (σ_{T_r}) and in energy (σ_R) from the region. These negative cross sections present no problem as long as they are applied to regions with spectra which are similar to those from which the negative cross sections were derived. The differences between MUFT results and the fitted macroscopic constants are small, in general, considering the uncertainties both in the MUFT library and in the assumption of constant microscopic cross sections for finite regions.

E. Integrated Depletion Systems

What follows is a description of two somewhat different approaches to the problem of determining three-dimensional lifetime data, using two-dimensional and one-dimensional diffusion equation depletion programs. The KARE system $r\text{-}z$

synthesis technique is described in detail for both the undepleted core calculation as well as for depleted core calculations, since the undepleted core method has not been described elsewhere. The TURBO-ZIP technique is described for the depleted core case only, since the undepleted core calculation is the same as the PDQ-WANDA synthesis method described in Sect. 4.4.B.

1. *The KARE System*

D. F. Molino

A) INTRODUCTION. The KARE system (see Chap. 7) employs several one- and two-dimensional few-group diffusion theory programs. These programs are automatically provided with macroscopic cross-section input from a program which utilizes either of two cross-section schemes. A general depletion routine, incorporating number density calculations of fuel, homogeneous poison, and explicit poison, is used for each of the few-group diffusion programs. This general depletion routine utilizes the constant power assumption and employs region depletion.

The one-dimensional programs of the KARE system are in cylindrical and slab geometry. The two-dimensional programs utilize (x, y), (r, z), or triangular coordinate systems.

The KARE system may be used in a variety of ways to perform a depletion study. The choice of method depends on the stage of the design work and the type of reactor under investigation. Only a single technique covering the complete depletion cycle will be described in detail. The technique to be described is known as the r–z synthesis method. It is most applicable to cores which are right circular cylinders or reasonably well approximated by such cylinders.

B) THE r–z SYNTHESIS METHOD. In the design of reactor cores in which calculations are made with the conventional (i.e., single channel) synthesis technique (Sect. 4.4), each axial plane of the core is converted to a single point, having appropriate average cross sections and radial bucklings which represent the correct transverse leakage for the plane. The average cross sections are obtained by flux- and volume-weighting the cross sections from the individual regions comprising the plane. These axially dependent cross sections are then employed in a one-dimensional axial calculation to arrive at the reactivity level for the entire core. With the r–z synthesis method, on the other hand, the entire core is represented by a two-dimensional cylindrical model. This cylindrical model may be generated by normalizations of various one-dimensional radial models, as described below,

or it may be derived by homogenization with appropriate flux- and volume-weighting. These two separate approaches will be discussed concurrently in each section of the following material, since they tend to illustrate the large number of options available to the designer in his choice of model. The discussion will center on the normalized r–z model, with occasional references to the flux- and volume-weighting alternative.

Before proceeding with the discussion of r–z synthesis calculations, it should be emphasized that since the actual core geometry is altered to that of a right circular cylinder, this model can not directly yield accurate power distributions in the radial plane. Power distributions must be generated by a combination of r–z and detailed planar calculations analogous to the combination of one- and two-dimensional results in conventional synthesis.

The normalization of the r–z model to detailed planar calculations takes place in two stages: (1) beginning-of-life normalizations, (2) depletion-dependent normalizations.

1) Construction and Normalization of the Radial Models at the Beginning-of-Life. The first step in the r–z model construction is to approximate the detailed x,y geometry by a number of regions composed of concentric circles. This step usually involves considerable homogenization of the detailed geometry. Following this step, the radial models (one for each type of control rod configuration) are normalized in reactivity to appropriate detailed x,y reactivities. There are generally three beginning-of-life normalizations required: (1) initial normalization, (2) control rod normalization, (3) control rod extension normalization. Each of these normalizations, in addition to the geometry construction, is discussed below.

(a) Homogenization of Structure, Coolant, and Fuel Regions. The homogenization of the regions in the r-z model is somewhat arbitrary. In most cases, the actual geometry is such that the regions to be combined for the homogenization process can easily be distinguished. Nevertheless, there always remains some ambiguity when a detailed two-dimensional geometry is to be represented in one dimension. Hence, in choosing the model geometry, it is often convenient to leave one or more parameters undetermined, so that they can be adjusted to bring about the desired normalization of the one- and two-dimensional models. The adjustable parameters might be characteristic dimensions or perhaps compositions of nonfuel regions. However, if the core in question lends itself particularly well to cylindrical representation, it may be feasible to homogenize regions of the detailed two-dimensional model by flux-weighting and

to use the resulting effective compositions and self-shielding factors directly in the one-dimensional radial model. This procedure completely determines the radial model such that any reactivity difference between it and the detailed model must be applied as a correction to r-z model results.

As part of the homogenization and model construction process, it is sometimes necessary to deal with discrete burnable poison. Since discrete poison cannot be represented in the radial models, its homogeneous equivalent must be found and used in the radial model with appropriate self-shielding factors. The homogeneous equivalent may be found either through calculations with the detailed x,y model or through experiment.

(b) Initial Normalization. The purpose of the initial normalization is to adjust the provisional one-dimensional radial model, constructed from purely geometric considerations, to a final model which agrees in reactivity with the detailed x,y model. This normalization is generally carried out for the rod-free condition of the core at operating temperature. The adjustment makes use of the parameters which were left undetermined in the construction of the model. Once this normalization is completed, the radial geometry and the material volume fractions of nonfuel regions are fixed and used for calculations in all conditions (hot and cold, with and without xenon).

The normalized radial model at this point agrees in reactivity with the detailed model in only one specific condition. The next step is to normalize the model in other important conditions.

If the radial models have been generated by flux-weighting the initial normalization is not required.

(c) Control Rod Normalization. Control rods in the radial models may be represented either by highly absorbing shells or by homogeneously distributed absorbers. In the latter case, there is no explicit geometric representation of the rods. Instead, the effect of the rods is obtained through modification of group constants.

When the rods are represented by highly absorbing shells, the variables for the normalization are the control shell transmission probabilities in the radial model. For the case where only one control rod shell is needed, this normalization is straightforward. However, for the case where more than one shell is required to account for several rings of control rods, each individual shell of the radial model must be normalized to its respective ring of rods in the actual geometry. This method, in addition to representing the total rod bank worth correctly, attempts to allow each rod group to account for its proper fraction of the total worth. Proper representation of

individual group worths is essential if rod group programming is specified for control of the core.

The normalization for each shell is accomplished by first choosing the thermal group transmission probability arbitrarily. The value may be zero, representing a black rod, or it may be set equal to the actual thermal transmission probability. The epithermal transmission probability is then adjusted until the reactivities of the corresponding radial and detailed planar models agree. These normalizations are carried out in both the hot and cold conditions, so that a final radial model exists for each temperature.

When the rods are represented in the homogeneous manner, a normalization may or may not be performed. If the normalization is performed, it is carried out by techniques similar to those used for the shell normalizations just described. However, in this case, the adjustable parameters would be one or more group constants of the homogenized fuel regions. In some instances, a normalization as such may not be required. For example, if the r-z model were constructed by flux-weighting from the detailed planar models, the rods could be included in this flux-weighting process. Hence, no specific normalization would be necessary.

(d) Extension Normalizations, If Required. If control rod extensions are present, their reactivity effect must be accounted for in the r-z model. When the model is constructed by the flux-weighting technique, the extensions are included in determining the region compositions and self-shielding factors. This procedure is analogous to that used for including control rods in the group constants of the regions.

The extensions may also be represented by shells in a manner similar to one of the possible control rod representations. For the normalization of the extension shells, the metal fractions in the extension shells are varied until the reactivity of the extension plane of the radial model agrees with the reactivity of the detailed planar model. Individual shells can be normalized in a manner similar to that described in the above section for the control rod shells.

(e) Consideration of Axial Nonuniformities in Core Geometry or Composition. The normalization and homogenization processes discussed in the previous sections are quite straightforward for a core which is axially uniform in geometry and composition. For axially nonuniform cores, it is necessary to perform additional normalizations and, therefore, to generate additional radial models. The techniques for producing these models are identical to those already described. The number of such models is not necessarily dictated by the core characteristics, but may be dependent on the detail to which the designer wishes to represent axial variability.

(f) Construction and Utilization of the Beginning-of-Life r-z Model. When the radial models representing all the different axial zones of the core have been constructed and normalized, the next step is to join these models into a two-dimensional r-z model.

The axial geometry of the r-z model is not dependent on the radial normalizations, so that it may be specified at the discretion of the designer. However, axial core subdivisions must reflect any axial nonuniformity in geometry or composition and must have sufficient detail to describe the axial xenon distribution accurately.

Following the normalization and construction of the r-z model, it can be used for beginning-of-life calculations. Quantities which can be determined include control margin, critical rod positions, rod bank worths, and axial power distributions.

2) Depletion-Dependent Normalizations. Although each of the radial models comprising the r-z model is normalized at the beginning of life, depletion of fuel and poison may cause its reactivity to diverge from that of the corresponding detailed planar model. For preliminary design work some divergence may be acceptable. However, if the r-z model is expected to yield the best possible predictions of endurance, power distributions, and rod positions for final design, the reactivity behavior with depletion of the radial and detailed planar models must agree.

The two models are adjusted to agree as a function of depletion by one of two methods. The first method is associated with the normalized r-z model, and the second with the r-z model constructed through flux-weighting. The first method depends on altering the depletion rates of fuel and poison by adjusting their self-shielding factors. In the second method, the flux-weighting process used in constructing the beginning-of-life r-z model is continued throughout life and, in this sense, is analogous to conventional synthesis. However, the results of the flux-weighting process are depletion-dependent self-shielding factors which are fitted to simple expressions and used in the r-z model. The self-shielding factor expressions for fuel and poison are similar to those described in Sect. 4.2.

The determination of self-shielding factors, either through empirical normalization or through flux-weighting, is necessary for each of the radial models comprising the r-z model. Furthermore, these factors are generally temperature-dependent and may be dependent on xenon concentration. All these effects are accounted for by normalization or flux-weighting.

The final self-shielding factors used in the normalized r-z model are, as indicated in the preceding discussions, at least partially empirical. Hence, they may not represent flux ratios, but merely adjustable parameters which can be used to match radial and detailed planar reactivities.

C) UTILIZATION OF r-z DEPLETION RESULTS. Depletion stuides with the r-z model yield the following information:

1. Rod bank or group positions as a function of lifetime for all operating conditions of interest, i.e., hot and cold without xenon, hot with steady-state, maneuvering, or peak xenon.
2. Reactivity levels with the rods fully withdrawn at peak and maneuvering xenon.
3. Endurances for the various xenon operating conditions, i.e., steady-state, maneuvering, or peak xenon.
4. Reactivity level variation for the fully rodded shutdown condition. (Depending on the core geometry, the shutdown with one or more rods removed may also be calculated.)
5. Xenon override margin as a function of life.
6. Variation of the average core or region axial power distribution throughout life and for all operating conditions.
7. Core and region axial fuel depletion patterns as a function of lifetime.
8. Lifetime variation of temperature coefficients for all operating conditions.
9. Lifetime variation of rod worth for all operating conditions.
10. Axial flux distributions for various conditions as a function of time.

Data from the r-z model are used in conjunction with the detailed planar data to determine stuck rod reactivities and power distributions throughout life. Planar average cross sections and transverse bucklings can be obtained as a function of fuel depletion for each axial zone of interest from the detailed planar calculation in the stuck rod shutdown condition. Based on the axial depletion pattern, Item 7, these data can be combined through a standard synthesis calculation to arrive at the stuck rod reactivity at any time during life.

Axial power distributions and fuel depletion patterns as a function of time are employed in conjunction with detailed planar data to construct hot channel power distributions throughout life. Assuming separability, the power density at any point is taken to be the product of a local factor, obtained from the detailed planar model, and a gross factor taken from the r-z model. The local factor may be defined as the ratio of local power density in the plane to the plane average, or it may be the ratio of the local power density to the average of some

portion of the plane. The local factors are depletion-dependent and, in addition, vary from one axial zone to another in accordance with the presence or absence of rods, etc. The gross factors obtained from the r-z model represent the average power, at a given elevation, of the entire plane or a portion thereof. If the gross factors are taken from only a portion of the plane as represented in the r–z model, then the local factors must be taken from the corresponding portion of the plane as represented in the detailed planar model. At a particular radial location, the power density can be constructed at each axial point as described above. The integral of the resulting curve then provides the integrated radial factor

2. The TURBO-ZIP System

A) DESCRIPTION. The TURBO-ZIP system (see Chap. 7) of synthesis and depletion employs the TURBO two-dimensional (x, y) program, and the ZIP one-dimensional (z) program. For the special case of the initial, undepleted core calculation, these programs are the same as the PDQ (x,y) and WANDA (z) programs, respectively (see Chap. 7). Briefly, the assumption of separability is made, and a number of (x,y) planes are depleted in several steps throughout the expected core life. Then, by means of flux-weighting, average quantities are extracted from the radial results and are used in the z axis calculations at a number of times in core life. The three-dimensional flux and power distributions are then constructed by combining the appropriate (x, y) and (z) solutions. The effect of nonuniform fuel and burnable poison depletion and fission product buildup, burnup, and decay are accounted for in the TURBO time-dependent pointwise-variable program by means of isotopic density equations which link together two successive times in core life for which calculations are desired. In the ZIP program, the fuel and burnable poison depletion effects are accounted for by relating axial pointwise-variable fuel fractions to the flux-weighted average diffusion equation coefficients derived from the TURBO results. The buildup, burnup, and decay of fission products may also be accounted for in ZIP by means of time-dependent pointwise-variable isotopic density equations as in TURBO. The schematic of Fig. 4.61 outlines the interrelationship of the radial and axial calculations of the TURBO-ZIP synthesis depletion system. The components of this system are discussed below.

1) The TURBO Program.[79] The TURBO (x, y) program accepts as input the dimensions and compositions of a number of rectangular regions which represent a radial cross section of the core and its reflector. A nonuniform mesh, also specified

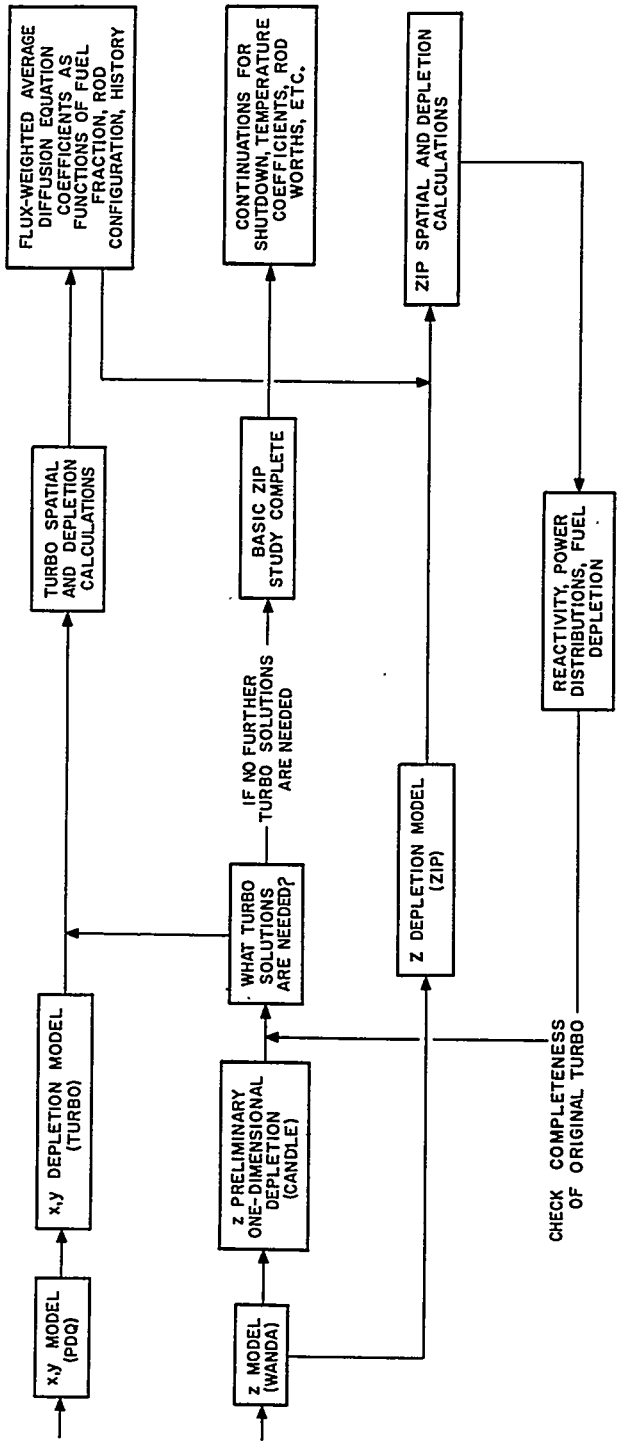

FIGURE 4.61. TURBO-ZIP Synthesis Depletion System.

by the requestor, is imposed on the core and reflector cross section, and each mesh rectangle (or mesh point) is then described by its diffusion properties, calculated on the basis of its composition, and a library of microscopic cross sections provided by the requestor. The neutron diffusion calculation is then performed, as in the PDQ program, and the neutron flux distribution and eigenvalue solution to the system are obtained.

Following the diffusion calculation, the program normalizes the flux solutions to an input power level and computes the composition changes which would take place in each mesh rectangle, if the neutron flux distribution were constant for a given time interval. At the end of each TURBO time step, a new distribution of isotopic densities is computed for use in the next time step.

At the start of the next time step, each mesh rectangle will have a different inventory of fuel, burnable poison, and fission products. Elements such as hydrogen, oxygen, and zirconium contribute to the diffusion equation coefficients but are not depleted from one step to the next (although it is possible under certain conditions to make changes in the inventories of these elements). Based on the new inventory in each mesh rectangle, the TURBO program computes new diffusion equation coefficients for each point, the diffusion solution is again calculated, and the new depletable element inventory computed for the desired time interval and power level. This procedure is carried out as many times as is necessary to describe the depletion of the radial cross section of the core being considered. In practice, the depletion of several different radial cross sections is usually calculated to distinguish, for example, between slowly depleting rods-in sections and rapidly depleting rods-out sections of the core.

2) The ZIP Program. The ZIP program accepts as input the dimensions and mesh spacing which describe the core and its axial reflectors. Specific isotopic densities are not included, however, in contrast to the TURBO program. Instead, each axial region or point is described by (1) its fuel fraction, i.e., the relative amount of fuel remaining in the radial slice represented by the axial point; (2) the number and type of control rods present; and (3) the history of the point in terms of the presence or absence of control rods during previous operation. Item (1) is computed by the program and is a stored quantity, while Items (2) and (3) are accounted for in the TURBO data (flux-weighted average diffusion equation coefficients) supplied as input and in the control rod programs which the ZIP program uses to search for a critical condition.

The TURBO data for the axial regions (supplied either in the form of a least squares fit to a polynomial in fuel fraction of the region remaining or in tabular form directly from the TURBO output) are used to determine diffusion equation coefficients for each axial point. The cross sections of any fission products described explicitly in ZIP are also added into the corresponding TURBO averaged absorption cross sections at this stage of the calculation, as well as a correction to the transverse leakage term at each point $(D_i B^2_{r,i})$. The latter correction has been found necessary in those instances where the leakages computed by the TURBO program depend not only on the rod configuration and average fuel fraction, but also on the concentration of fission products (principally xenon 135). This will be discussed further in the section dealing with xenon treatment in ZIP.

After the diffusion equation coefficients have been prepared for each axial point, a critical rod position search is made. After each unsuccessful spatial calculation (i.e., $|\lambda - \lambda_{\text{critical}}| > \epsilon$ where ϵ is a convergence criterion) the program automatically adjusts the height of the slice representing controlling rods, recomputes the diffusion equation coefficients, and then performs a new spatial calculation, eventually finding the position for which $|\lambda - \lambda_{\text{critical}}| \leq \epsilon$.

After the critical position and corresponding flux and power distribution have been calculated, the ZIP program simulates power operation of the core for a given (input) time interval by depleting each axial point according to the pointwise power distribution, which is assumed to be constant during the time step. In addition to this depletion step, fission product concentrations can be calculated for each point. The fission products which can be calculated in the ZIP program are the I^{135}, Xe^{135} chain, and the Pm^{149}, Sm^{149} chain, or any combination of two similar chains.

The above cycle is repeated as many times as requested, or until the core is depleted to the point where the desired criticality level can no longer be maintained. Figure 4.62 is a schematic of the ZIP portion of the TURBO-ZIP system.

B) USE OF TURBO-ZIP SYSTEM

1) General Discussion. It is assumed that prior to the use of the TURBO-ZIP synthesis depletion system, a three-dimensional synthesis calculational model (PDQ-WANDA system) has been developed for the undepleted core design (see Sect. 4.4.B). This model would represent the best compromise between high accuracy and low computer solution time.

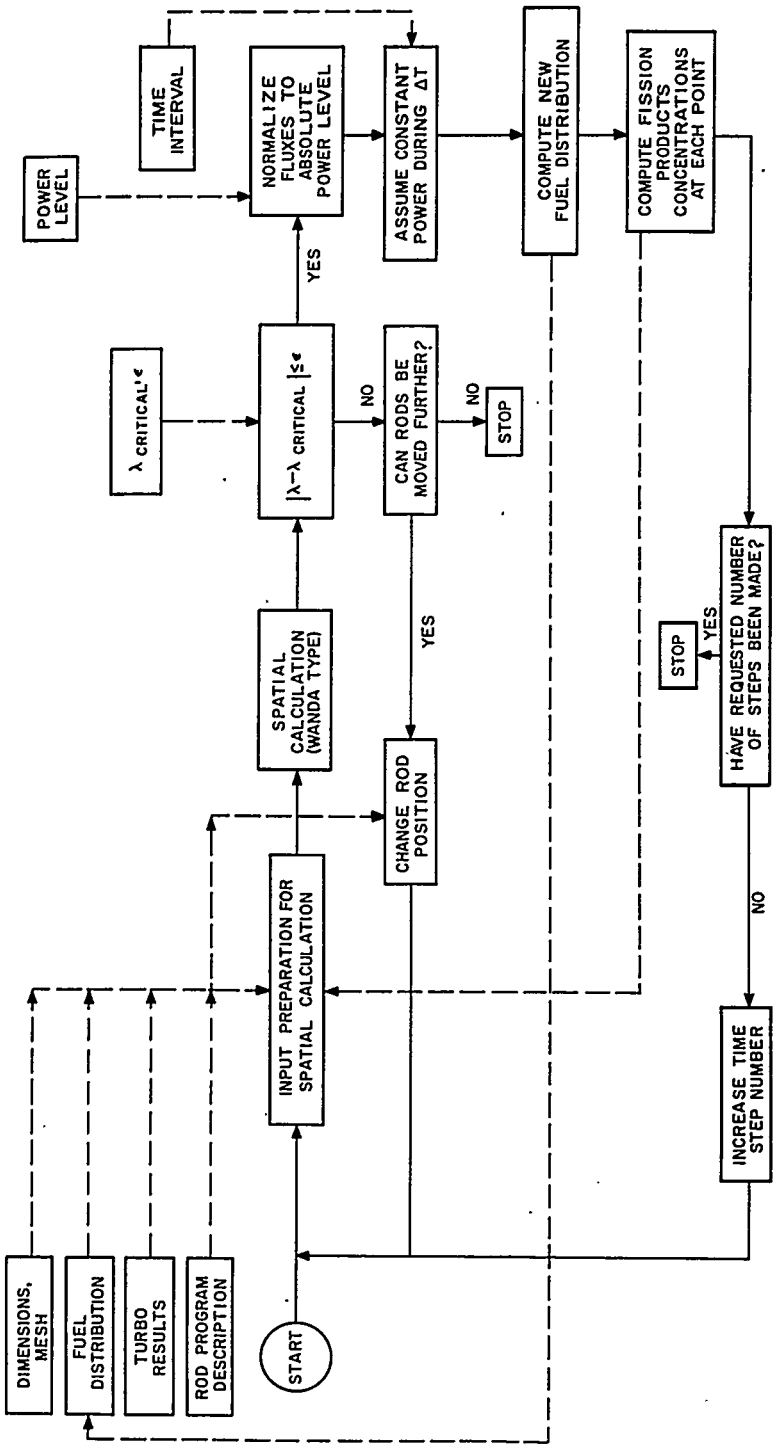

FIGURE 4.62. ZIP Program.

It is also assumed that a one-dimensional axial depletion calculation, e.g., the CANDLE program (see Chap. 7), has been performed, so that a reasonable estimate is available of the critical control rod configurations which will be obtained during power operation. These configurations will determine how the core will be depleted nonuniformly.

The first step in the procedure is to divide the core into a convenient number of axial regions (typically about five) which are distinguished one from another on the basis of the number of control rods present in each axial region and on the length of time (effective power hours) that the region contains a given group of control rods. An example of this procedure is illustrated in Fig. 4.63, which is a sketch of the results of the above-assumed one-dimensional depletion calculation. As shown in this figure, five different axial regions (which are frequently referred to as radial slices) have been selected. The first two of these regions contain both groups of control rods for the first portion of the core life, then one group of control rods for most of the remainder of the core life, and finally no control rods during the last part of core life. The fourth and fifth radial slices are somewhat simpler in that they contain either one group of rods or no rods, depending on the time in core life. The third, or middle section, has the most complicated control rod sequence, starting with only one group of rods in and progressing to two groups in, one group in, and finally no rods in.

At this point it would be necessary to approximate the smooth curves in Fig. 4.63, so as to define the exact end points of the time intervals in which each rod group configuration occurred. This additional approximation can be made by assuming that the midpoint of the slice is typical of the entire slice.

Since the axial power distribution is, in general, not uniform, the abscissa scale of Fig. 4.63 represents only the average core age and not the radial slice age. To account for this, it is necessary to examine the pointwise-variable axial fuel distribution as a function of core age in order to determine the radial slice effective power hours rather than the less useful measure of core average effective power hours. Figure 4.64 shows an example of the results of this procedure. Note that if this figure is rotated 90 degrees counterclockwise, an average power distribution curve is seen. If the rotation is 90 degrees clockwise, the curve can be thought of as a rough end-of-life axial fuel distribution curve. Using the results of Fig. 4.64, the next step is to set up with the TURBO x–y depletion program the five sequences representing radial slices 1 through 5. During this step, the equivalence of slices 1 and 2 during the first portion of core life will be noted, as well as the equivalence

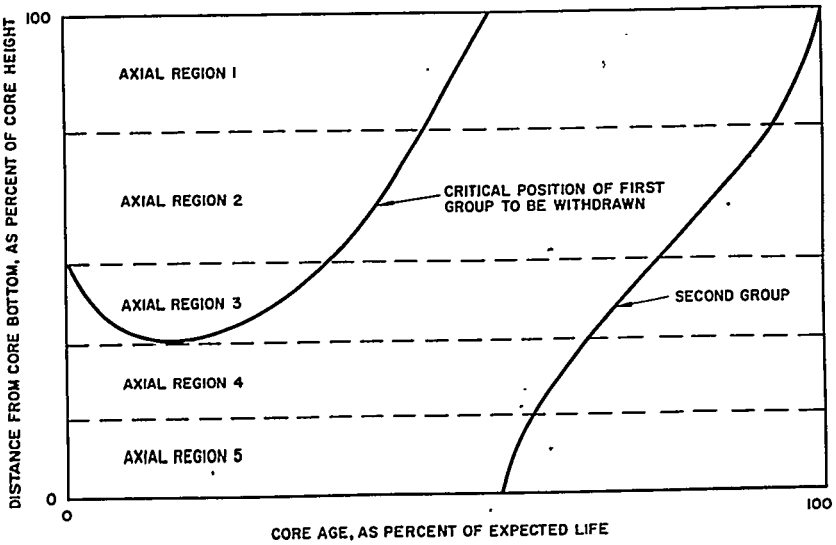

FIGURE 4.63. Results of the One-Dimensional Depletion Calculation Using the CANDLE Program.

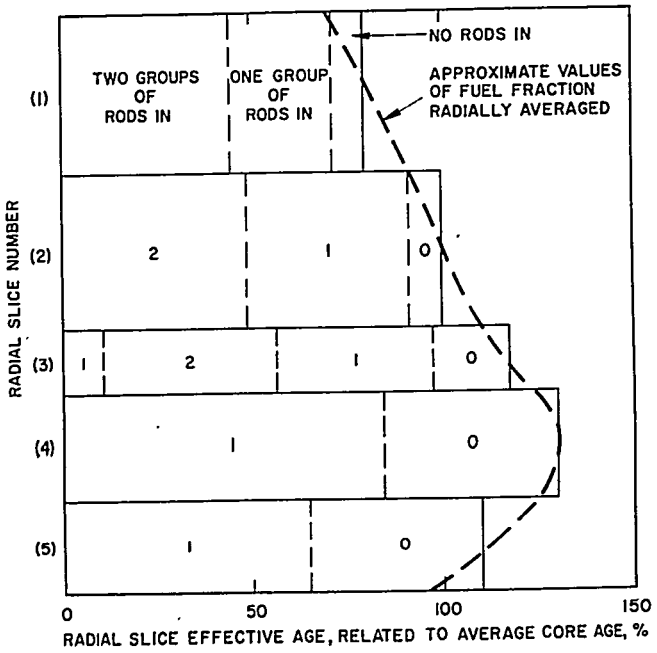

FIGURE 4.64. The Pointwise-Variable Axial Fuel Distribution as a Function of Core Age to Determine Radial Slice Effective Power Hours.

of slices 4 and 5. In addition to this early-in-life equivalence, it is possible that TURBO solutions late in life will be relatively independent of the exact time of change over from one rod configuration to the next. If this is so, it is possible that a number of the late-in-life calculations need be performed for only one radial slice rather than two.

The optimum time step length (ΔT) used in depleting each radial slice cannot be determined without considering the particular core design. Sub-time steps, which are used to renormalize the thermal flux within a long time step, and sub-sub-time steps, which are used to recalculate rapidly varying microscopic cross sections within the sub-time step, can be used to improve overall accuracy without the need for frequent spatial (i.e., PDQ type) calculations. A good starting point, however, is a ΔT corresponding to 5 to 10 percent burnup of the original fuel loading.

At this point, the two-dimensional depletion calculations are ready for solution. The calculations may be performed with a constant input buckling (B_z^2) corresponding to the axial geometric buckling value. Frequently, however, they are performed with an input buckling which will give a λ value close to the critical value. As discussed in Sect. 4.4.B, the reason for the latter approach of seeking a critical λ value in the two-dimensional solutions is that the radial buckling (B_r^2, which will be used in the axial ZIP calculation) inferred from the TURBO result may be sensitive to the value of λ. For this reason, and since it will not be possible to estimate the exact B_z^2 for criticality, it is useful to have available the results of at least one pair of two-dimensional calculations that differ only in the value of the input buckling. Knowledge of this will permit good estimates of B_z^2, and permit the output from the two-dimensional solution to be corrected to any critical λ value, or both, so as to ensure radial and axial eigenvalue agreement.

The basic* two-dimensional calculations having been completed, the computer-edited output would be assembled in a manner similar to that illustrated in Figs. 4.65 and 4.66. These figures show the dependence of typical diffusion equation parameters on core age, control rod configuration, and control rod history effect (i.e., the sequence and duration of control in the radial slice).

*Basic calculations are those sufficient to synthesize the core's normal operation out to the end of the core life. Cold shutdown calculations, hot and cold excess reactivity calculations, temperature coefficient calculations, etc., are frequently performed as continuations from the basic calculations.

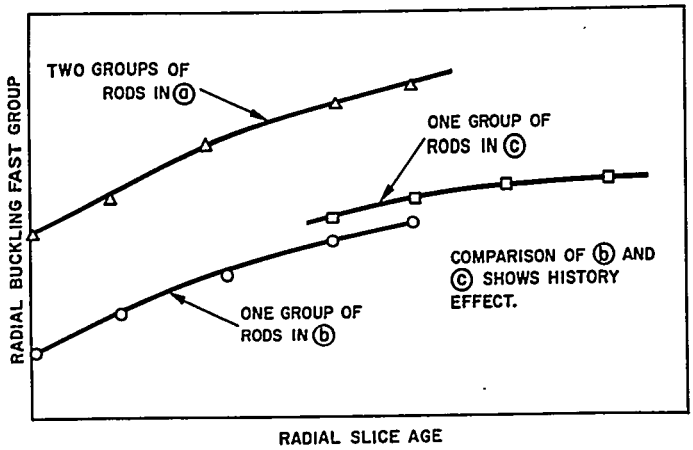

FIGURE 4.65. Fast Group Radial Buckling (from TURBO) vs Radial Slice Age.

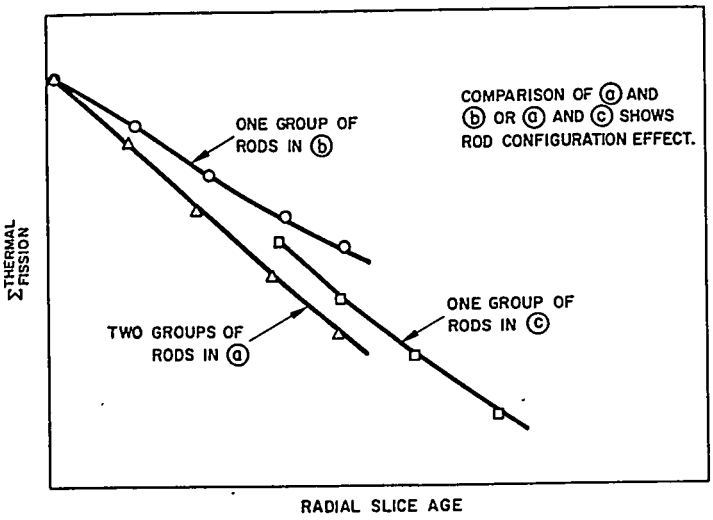

FIGURE 4.66. Flux-Weighted Average Thermal Fission Macroscopic Cross Section (from TURBO) vs Radial Slice Age.

The abscissas of Figs. 4.65 and 4.66 are radial slice age. In practice, it has been found convenient to use instead the ratio, fuel remaining in the radial slice/fuel originally in the radial slice. This ratio is labeled fuel fraction and is abbreviated by the symbols π or f. It is one of the basic variables in the ZIP program.

After it has been established that the TURBO output data are correct and complete enough to describe the most depleted radial slice, the next step is to prepare a ZIP synthesis calculation containing the results of all the TURBO calculations. This information is provided to the ZIP program either in the form of (1) polynomials, usually least-square-fitted, relating the flux-weighted average diffusion equation coefficients to the average radial fuel fraction, or preferably (2) data directly from TURBO, which the ZIP program uses to set up an interpolation table. The latter feature is available in the ZIP03 program. It eliminates the need for curve fitting and reduces the likelihood of mistakes in transcribing data. Included in the data provided to the ZIP program are depletion-independent diffusion equation constants for the core reflector regions, as well as fission product yields, decay constants, and microscopic absorption cross sections.

In addition, the control rod withdrawal sequence is provided to ZIP, with region boundaries which permit limits to be observed on rod withdrawal or insertion. Using these data, the ZIP program can automatically simulate the operation of the core from beginning to end of life. During each time interval specified by the requestor, the critical rod position and power distribution, determined at the beginning of the interval, are assumed to remain constant. The pointwise-variable fuel depletion and fission product concentrations are computed for the end of the interval, and the cycle is then repeated for the next time step, i.e., diffusion equation parameters are calculated; fission product poisoning effects are added; the spatial calculation is performed as many times as necessary to find the critical position; the fuel is depleted, and fission products are built up, burned out, or decay.

At the completion of this ZIP synthesis depletion calculation, it is essential to return to the original preliminary axial calculation (or estimated control rod histories used to divide the core axially) and compare the preliminary and final results from the point of view of expected lifetime, rod configurations, and power distributions. If the differences are such that the radial slices have been improperly depleted, a second iteration of the TURBO-ZIP system consisting of partial depletion studies would be required. It is worth noting, however, that the process converges quickly, so that a second iteration would quite probably be sufficient.

After the ZIP calculations have been completed, the three-dimensional power distributions can be constructed for all conditions of interest. Usually, attention is focused on the conditions which are believed to be most limiting as, for example, the condition yielding the maximum product of axial and radial

power factors or the maximum average radial hot channel factor.

2) Xenon Treatment in ZIP. One of the most severe problems associated with use of the TURBO-ZIP system (and for that matter, all combined depletion-synthesis systems) is that of the xenon treatment. That is, should the effect of xenon be included in the (x,y) solutions or the (z) solution? Neither course is free of difficulties. If xenon is included in the (x,y) solutions, the TURBO data then depend on the power level assumed in the TURBO solution. On the other hand, if the xenon effect is suppressed from the radial solution, then the radial bucklings derived from TURBO are inappropriate for the ZIP description with xenon.

The effect of xenon on the radial bucklings can be determined reasonably well by running a small number of pairs of TURBO problems that differ only in xenon concentration. In the ZIP program specifications, emphasis was placed on the use of xenon-free radial solutions, with xenon to be included in the axial solutions, calculated at each axial point as a function of the flux and fuel fractions appropriate to each point. (Samarium, since its effect is less than that of xenon, and not strongly power-dependent, is usually, but not necessarily, included in the TURBO solution.)

The artificial xenon weight factors for a particular model employing two neutron energy groups and group-independent radial buckling are defined as

$$W_1 = \frac{D_1(B_r^{2\prime} - B_r^2)}{N_{Xe}\,\sigma_{Xe,2}}$$

$$W_2 = \frac{D_1(B_r^{2\prime} - B_r^2)}{N_{Xe}\,\sigma_{Xe,2}} + \frac{\Sigma_a^{2\prime} - \Sigma_a^2}{N_{Xe}\,\sigma_{Xe,2}}$$

where the unprimed symbols represent quantities from TURBO solutions without xenon and the primed symbols represent quantities with xenon. The above quantities are flux-weighted averaged constants obtained from the appropriate radial TURBO's. N_{Xe} is the average xenon number density in the TURBO solutions with xenon, and $\sigma_{Xe,2}$ is the microscopic thermal absorption cross section of xenon. In the above relations B_r^2 and $B_r^{2\prime}$ must be corrected to $\lambda=1$ values if the B_r^2 terms are found to be sensitive to the eigenvalue of the radial TURBO problem. It will be noted, where xenon does not significantly

affect the core leakage, that the values of the above weight factors reduce to

$$W_1 = 0$$

$$W_2 = \frac{\Sigma_a^{2\prime} - \Sigma_a^2}{N_{Xe}\,\sigma_{Xe,2}}$$

which can be thought of simply as the spatial weight factors for xenon.

In the ZIP program, the weight factors are used to modify the macroscopic absorption cross sections of xenon (i.e., Σ_a for each energy group can be modified) as follows:

$$\Sigma_a^i(\text{ZIP}) = \Sigma_a^i(\text{input}) + W_i N_{Xe}\sigma_{Xe,\,\text{thermal}}$$

where Σ_a^i (ZIP) is the value actually used in the ZIP spatial calculation, Σ_a^i (input) is the value based on the TURBO data to ZIP, W_i is an input number depending on rod configuration and fuel fraction, $\sigma_{Xe,\text{thermal}}$ is the input thermal microscopic cross section for xenon, and N_{Xe} is the pointwise-variable xenon concentration computed within the ZIP program.

3. Illustrative Examples

Illustrative examples and some discussion of the evolution of the TURBO-ZIP method can be found in Refs. 54 and 57. A discussion of the TURBO-ZIP system in considerably greater detail may be found in Ref. 85.

4.7 BURNABLE POISONS

A. Radkowsky

A. Introduction

The major portion of this volume is devoted to the treatment of individual topics in reactor physics. This section seeks, in part, to fill a need for illustrating how the various techniques are synthesized into the conceptual design of a reactor by presenting the physics aspects of a single reactor component, burnable poisons, the optimal use of which profoundly affects the entire reactor design.

The basic principle involved in the application of burnable poisons[86,87] is to add to the reactor, in a form which is physically fixed in the core, parasitic capturing elements (i.e., the burnable poisons) which become transmuted by neutron capture into elements of low cross section. This process compensates for reactivity losses from fuel depletion and the formation of stable fission products.

The advantages obtainable through the use of burnable poisons are: (1) increased reactor endurance, (2) improved core performance through better power distribution, (3) increased safety, and (4) reduced mechanical control.

It should be borne in mind that advantages conceivable from a reactor physics viewpoint must be compatible with metallurgical and other engineering requirements.

Most work on burnable poisons has been in connection with water-moderated fixed-fuel reactors. In Vol. III, the application of burnable poisons to intermediate spectrum reactors is discussed. For convenience, the work is summarized briefly in Sect. 4.7.H.

Reactor life or endurance, as used in this section, is understood to be the period during which the core has sufficient excess reactivity to permit startup under maximum transient poisons (xenon and samarium) after shutdown, following prolonged operation at some specified power level (which may be less than the normal power output). This period is often expressed somewhat loosely as the number of equivalent full power hours of operation or in terms of the total energy production of the core.

Insofar as physics considerations are concerned, reactor life is generally determined by the amount of fuel that can be loaded into the reactor. Until the advent of burnable poisons, the initial fuel loading was limited by the amount of excess reactivity which could be controlled by mechanically positioned control rods. The feasible number of control rods is usually severely restricted, particularly in a pressurized water reactor. In addition, it is considered desirable for safety reasons to limit the initial level of excess reactivity in the core. Methods of control other than mechanical, such as use of soluble poison, require additional plant equipment and introduce the possibility of new accidents, such as the sudden introduction of clean water into the core. In contrast to other methods, the use of burnable poisons requires no plant changes, permits a large increase in core fuel loading and, consequently, endurance and at the same time enhances safety by decreasing the amount of excess reactivity in the core to approximately the minimum required to override transient xenon and samarium.

In the first applications of burnable poisons, only a modest increase in core life was sought. This could be achieved in highly enriched U^{235} fueled reactors by increasing the fuel loading a relatively small amount and adding boron uniformly to the fuel. Thus, little or no change was required in the basic core design. As nuclear power has developed, much greater increases in core endurance as well as thermal performance have been demanded. This has led to major increases of fuel loadings, with resultant significant changes during core lifetime in the neutron spectrum and fuel content and distribution, as well as to large accumulations of fission product poisons. The use of homogeneous boron alone is no longer adequate to accommodate the resultant changes in reactivity. It is, therefore, necessary to consider (1) zoning or segregating at least part of the burnable poison, so that the average flux at the poison differs from that at the fuel, (2) using materials other than boron. All these factors, in turn, lead to engineering changes in the overall power distributions and in the local power peaking, or hot spots, which may necessitate a variety of zoning schemes to produce acceptable power distributions. The effect on the core temperature coefficient of reactivity and the integrated reactivity change from room temperature to operating temperature may be large and require other adjustments. The result is that the utilization of burnable poisons and the achievement of much longer reactor life affect almost every aspect of the reactor design.

The general plan of this section is first to present the elementary theory of the application of homogeneous burnable poisons, discuss the areas in which this theory is inadequate, and indicate the modifications in reactor design arising from burnable poison utilization which must be made to obtain the desired endurance goals in various reactor types.

B. Elementary Theory of Homogeneous Burnable Poisons in Thermal Reactors

To bring out the conceptual ideas, several simplifying assumptions are made, and their validity is discussed elsewhere in this volume. The standpoint is adopted that a fixed (essentially small) amount of mechanical control, equivalent to a reactivity increment, Δk_M, is available for shimming, i.e., to compensate for the reactivity changes associated with effects due to fuel depletion. Additional mechanical control is provided for other needs, such as for the loss of reactivity due to xenon (includes samarium) and for that due to the temperature rise from room temperature to operating conditions (temperature defect). For definiteness the mechanical control is assumed to be

obtained by the movement of absorbing materials in and out of the core. One then investigates which combinations of fuel and burnable poison give maximum lifetime. It is assumed that the core is thermal with a Maxwellian spectrum, utilizes highly enriched fuel, has the burnable poison and fuel uniformly distributed and unshielded, and that burnup is uniform and is governed by the average thermal flux in the reactor. For generality, assume for the present that poison absorbers of various microscopic cross sections are available.

Consider first the core in the hot operating condition with xenon at the peak, transient value. The usual two-group expression for the effective multiplication constant will be used:

$$k_{eff} = \frac{\eta f}{(1 + L^2 B^2)(1 + \tau B^2)} \qquad \text{Eq. (4.309)}$$

where

η = the number of fission neutrons emitted per neutron absorbed by the fuel

f = the thermal utilization

τ = the age, treated as constant over the life of the core

B^2 = the geometric buckling, assumed constant with lifetime and with control rod position (this assumes constant reflector savings and flux distributions)

L = the thermal diffusion length.

The fast effect and resonance escape probability are taken as unity. The usual expressions for f and L^2 are used:

$$f = \frac{\Sigma_U}{\Sigma_U + \Sigma_M + \Sigma_X + \Sigma_{sf}} = \frac{1}{1 + \dfrac{\Sigma_M + \Sigma_X + \Sigma_{sf}}{\Sigma_U}} \qquad \text{Eq. (4.310)}$$

and

$$L^2 = \frac{D}{\Sigma_T}. \qquad \text{Eq. (4.311)}$$

(Although the above expression for the diffusion length in light water reactors is not very accurate, the product, L^2B^2, in Eq. (4.309) has only a small effect relative to τB^2.) Here Σ denotes a macroscopic absorption cross section and the subscripts

U, M, X, sf, and T, refer to fuel, moderator plus structural materials, xenon and samarium, stable fission products and parasitic fuel-capture products, and total, respectively:

$$\Sigma_T = \Sigma_U + \Sigma_M + \Sigma_X + \Sigma_{sf} \qquad \text{Eq. (4.312)}$$

D is the diffusion constant for thermal neutrons and is assumed constant over life.

The macroscopic absorption of the maximum xenon, Σ_X, is also taken as constant over reactor life, assuming a constant power level. This is a good approximation for the xenon if the thermal flux level is above 10^{14} neutrons/(cm^2 sec) and if the distribution of the xenon in the core does not change greatly throughout core life. The latter condition will usually be fulfilled if the motion of the shimming control elements is small. For flux levels less than 10^{14} neutrons/(cm^2 sec), the maximum xenon effect is relatively small.

As a result of the assumptions, and using the definitions of Eq. (4.310) and (4.311), k_{eff} can be written

$$k_{\text{eff}} = \frac{\eta}{1+\tau B^2} \quad \frac{\Sigma_U}{\Sigma_T + DB^2} \qquad \text{Eq. (4.313)}$$

It is convenient to define the parameter

$$\bar{f} = \frac{f}{1+L^2B^2} = \frac{\Sigma_U}{\Sigma_T + DB^2} \qquad \text{Eq. (4.314)}$$

which includes all the thermal group dependence. In the following discussion the function $\left(\frac{1-\bar{f}}{\bar{f}}\right)$ will be used to illustrate the properties of burnable poisons.

In the initial treatment, it is convenient to neglect the formation of the stable fission products. This effect will be considered later.

The case in which no burnable poisons are used in the core will be considered first. Starting with a fuel loading just sufficient to achieve criticality ($k_{\text{eff}} = 1$) in the hot maximum xenon-poisoned core with all absorbing rods withdrawn, one has from Eqs. (4.309) to (4.312)

$$\frac{1-\bar{f}}{\bar{f}} = \frac{\Sigma_M + \Sigma_X + DB^2}{\Sigma_U} = \frac{\eta}{1+\tau B^2} - 1 \equiv A. \qquad \text{Eq. (4.315)}$$

The value of $\left(\frac{1-\bar{f}}{\bar{f}}\right)$ satisfying Eq. (4.315) will be denoted by A.

The initial fuel loading can now be increased to have a macroscopic cross section, Σ'_U, at which the core is critical with the full available shimming control, equal to a negative reactivity, $-\Delta k_M$, inserted into the core. In this case:

$$\frac{1-\bar{f}}{\bar{f}} = \frac{\Sigma_M + \Sigma_X + DB^2}{\Sigma'_U} = \frac{\eta}{(1+\Delta k_M)(1+\tau B^2)} - 1 \equiv A' \qquad \text{Eq. (4.316)}$$

The value of $\left(\frac{1-\bar{f}}{\bar{f}}\right)$ satisfying Eq. (4.316) will be denoted by A'. Σ'_U is proportional to the maximum amount of fuel which can be loaded into the core with the available mechanical-shimming control and provides a measure of the maximum core life which can be obtained without the use of burnable poisons. With a greater fuel loading, the core could not be adequately shut down, for example, in the cold, xenon-free condition. Otherwise, there would be excess mechanical control for shutdown, which could be designated as shimming control, and an increase in the core fuel content and life accordingly. Another limitation might be that increase of fuel loading could result in too great a penetration of the control rods into the hot, xenon-free core and cause excessive flux compression and, thus, power peaking.

Note that as the core depletes and the fuel cross section becomes less than Σ'_U, the left side of Eq. (4.316) increases, indicating a decrease in reactivity.

Consider now the use of burnable poisons and a larger fuel loading. Again assume that the new reactor is just critical, with maximum xenon present, and the (absorbing) shimming rods fully inserted. On the left side of Eq. (4.316), Σ'_U will be replaced by Σ_{U_o}, and there will be an added term equal to $\Sigma_{B_o}/\Sigma_{U_o}$. The macroscopic cross sections Σ_{B_o} and Σ_{U_o} refer to the burnable poison and to the now increased fuel loading necessary to maintain criticality, respectively.

To treat effects of burnup one could, in effect, study the variations of the thermal utilization during core life. However, instead of doing this directly, it is found advantageous to study the variation of the function

$$\left(\frac{1-\bar{f}}{\bar{f}}\right)$$

divided by its value, A', which satisfies Eq. (4.316). Furthermore, for mathematical convenience the above ratio is expressed as the sum of two components:

$$\frac{1-\bar{f}(t)}{A'\bar{f}(t)} \equiv p(t) + q(t)$$

where

$$\frac{\Sigma_M + \Sigma_X + DB^2}{A'\Sigma_U(t)} \equiv p(t)$$

$$\frac{\Sigma_B(t)}{A'\Sigma_U(t)} \equiv q(t) \qquad \text{Eq. (4.317)}$$

and t is the time of equivalent full power operation that the core has run, starting with a fuel loading corresponding to Σ_{U_o} at time $t = 0$. The macroscopic cross sections of fuel and burnable poison at time t are $\Sigma_U(t)$ and $\Sigma_B(t)$, respectively.

From Eq. (4.316) a simple physical meaning can be assigned to $p(t)$:

$$p(t) = \frac{\Sigma'_U}{\Sigma_U(t)}.$$

Thus, $p(t)$ is the ratio of the beginning-of-life fuel content without burnable poison to the fuel content with burnable poison at the time, t, in core life.

Except for a constant factor, $q(t)$ is the ratio of the burnable poison to the fuel content as a function of t. At $t = 0$, using Eq. (4.315) modified, as indicated above, to include a burnable poison term:

$$p_o + q_o = 1. \qquad \text{Eq. (4.318)}$$

At the end of core life, the core being just critical with maximum xenon and with the shimming absorption control, Δk_M, completely withdrawn,

$$p + q = \frac{\frac{\eta}{1+\tau B^2} - 1}{A'} = \frac{A}{A'} > 1. \qquad \text{Eq. (4.319)}$$

It will be noted that the core reactivity is a monotonically decreasing function of $p + q$.

The time-dependent parameters on the left side of Eq. (4.317) are:

$$\Sigma_U = \Sigma_{U_o} e^{-\sigma_U \int \phi(t)dt}$$

$$\Sigma_B = \Sigma_{B_o} e^{-\sigma_B \int \phi(t)dt} \qquad \text{Eq. (4.320)}$$

Here, σ_U is the microscopic cross section of the fuel, σ_B is the microscopic cross section of the burnable poison, and $\phi(t)$ is the thermal flux as a function of time.

It is assumed, at present, that the poison element contains only one burnable isotope and that this isotope upon absorbing a neutron becomes essentially nonabsorbing. Let

$$\int \phi(t)dt \equiv T$$

then,

$$p(t) = p_o e^{\sigma_U T}$$

$$q(t) = q_o e^{(\sigma_U - \sigma_B)T} \qquad \text{Eq. (4.321)}$$

It is advantageous to use the integrated flux time, T, as the variable rather than the time, t, since T provides a direct measure of fuel utilization, i.e., the greater the value of T achieved during the core lifetime, the greater the fraction of fuel burned. There are now several cases to be considered:

Case 1. Assume that $\sigma_B \cong 0$, i.e., the burnable poison has an extremely low cross section compared with fuel. Examples of such poisons would be iron or titanium. Then, disregarding physical limitations, one can add as much fuel as desired and obtain any desired life, provided that the poison is increased sufficiently to satisfy Eq. (4.318). As fuel is increased, p_o decreases, and q_o, which is proportional to the ratio of poison to fuel cross sections, must be increased to satisfy Eq. (4.318). Since in this case the function $(p + q)$ has the same time dependence and the same initial value as the function in the case in which no burnable poison is used, the integrated flux time, T, at which the

end-of-life condition Eq. (4.319) is satisfied will also be the same as for the case of no burnable poison. This means that the same fraction of fuel will be burned as before and, therefore, the reactor life will have increased in proportion to the added fuel. While reactor life can, thus, be extended, this method is relatively wasteful of fuel inventory because of the additional fuel necessary to balance the effect of the unburned poison.

Case 2. The poison burns out at a rate less than that of the fuel ($\sigma_U > \sigma_B$). In this case q increases more slowly than in Case 1. Thus, if one starts out with the same fuel loading (therefore, the same p_o and q_o) as in Case 1, a greater value of T will be required to satisfy Eq. (4.319); therefore, a greater fractional burnup of the fuel and, consequently, a greater endurance as compared with Case 1 will be achieved. For a given core lifetime the fuel inventory is less than in Case 1 and decreases monotonically as $\sigma_B \to \sigma_U$. In contrast to Case 1 if one fixes the value of σ_B and increases the fuel loading, the final value of T, the integrated flux time throughout life also increases, indicating an improved utilization of the fuel as well as longer life (see Appendix A-1 of Ref. 86).

Case 3. The poison burns out more rapidly than that of the fuel ($\sigma_B > \sigma_U$). This case is most important from a practical standpoint. First, assume that initially the values of p_o and q_o are such that at $T = 0$

$$\frac{dp}{dT} > \left| \frac{dq}{dT} \right|$$

or

$$\sigma_U p_o > (\sigma_B - \sigma_U) q_o \, .$$

(The above condition on the derivatives remains true throughout core life, since $\frac{d^2}{dT^2}(p + q)$ is always positive.) For the same fuel loading (same p_o) as in Case 2, p will increase during core life at the same rate as before, but q will decrease instead of increasing. Hence, a larger value of T will be required for the sum of p and q to reach the end-of-life condition Eq. (4.319), with the result that a greater fuel burnup will be obtained as compared with Case 2. With the value of the fuel loading fixed, a greater fractional fuel burnup will be obtained the greater the value of the poison microscopic cross section.

If, on the other hand, σ_B is fixed, the fractional burnup again will increase as the fuel loading is increased, as in Case 2. However, as one increases the fuel investment (decrease p_o) for

a fixed value of the microscopic cross section of the poison, a point is reached at which

$$\sigma_U p_o = (\sigma_B - \sigma_U) q_o . \qquad \text{Eq. (4.322)}$$

The fuel loading cannot be permitted to increase (p_o to decrease) any further (with the control rod positions specified for maximum xenon at the beginning of life) since, if $\sigma_U p_o < (\sigma_B - \sigma_U) q_o$, the reactivity will increase initially, whereas it has been postulated that the rods cannot go into the core any further. (This implies that any greater fuel loading would impair the ability to shut down the cold clean reactor. The effect of the use of burnable poison on shutdown is discussed later in some detail.) If it is desired to increase reactor life beyond this point and to improve fuel utilization, one must choose a lower value of σ_B and increase the fuel loading to satisfy Eq. (4.322) (see Appendix A-2 of Ref. 86). Thus, as in Case 2, to obtain a longer core life one must use a poison cross section closer to that of the fuel, with the difference that now the fuel microscopic cross section is being approached from above instead of below.

In actual practice, when $\sigma_B > \sigma_U$, one usually follows another course: the choosing of core loadings of fuel and burnable poison so that the core is just slightly supercritical (by the reactivity margin required for design tolerances, etc.) in the maximum xenon condition at the beginning of life (i.e., with the control rods completely withdrawn). Specifically, the ratio of poison to fuel is so increased that reactivity increases initially with burnup, i.e., $(p + q)$ decreases. The reactivity rise must not exceed the mechanical shimming control, Δk_M, available. Mathematically, one can choose $(p + q)$ so as to satisfy at $T = 0$, the end-of-life condition, Eq. (4.319), rather than Eq. (4.318). The fuel content is now limited by the requirement that when $(p + q)$ has decreased sufficiently to satisfy Eq. (4.318) (when the shimming rods are fully inserted), then Eq. (4.322) must also be satisfied, so that reactivity will now start to decrease and the rods will be withdrawn until $(p + q)$ satisfies Eq. (4.319) a second time at the end of core life.

This procedure results in a considerable increase in lifetime and fuel utilization as compared with starting with the shimming rods inserted. Consider a fixed value of σ_B. After sufficient burnup has taken place so that Eqs. (4.318) and (4.322) are satisfied simultaneously, exactly the same quantities of fuel and burnable poison will have been left as would have been used had these conditions been satisfied to begin with and, consequently, the same increment of T remaining until the end of life. Thus, the total value of integrated flux time, T, attained by the core fuel loading has been substantially increased.

For a given value of poison cross section, σ_B, there is again a maximum permissible value of fuel loading. This fuel loading is determined by the maximum rate at which reactivity may be permitted to increase initially with burnup. A lower fuel loading and lower associated quantity of poison will have a lower value of T at end of life (see Appendix A-3 of Ref. 86). A greater fuel and poison loading will have too great a reactivity rise. Again, when the fuel loading has been increased to the maximum permissible for a given value of σ_B, the way to lengthen life is to use a higher fuel content with a smaller value of σ_R (see Appendix A-4 of Ref. 86).

Case 4. Combinations of Poisons. The use of a combination of poisons is governed by the same general principles as the use of a single poison; equations similar to Eqs. (4.318), (4.319), and (4.322) apply. A practical application of a combination of poisons would occur in a case when the amount of fuel is fixed and there is no available poison with the optimum cross section for this fuel loading. In such a case it would be necessary to use a combination of poisons with cross sections above and below the optimum, respectively. This would not, however, give as efficient a utilization of fuel as the use of the single poison of optimum cross section (see Appendix A-5 of Ref. 86).

A special case of a combination of poisons is furnished by the presence of high cross section impurities in the fuel. As long as either no burnable poison is present or the ratio of fuel to burnable poisons is such that reactivity decreases initially with depletion, there is no special disadvantage in leaving the high cross-section impurities in the fuel, provided that these impurities are not sufficient to cause the initial reactivity to be less than the minimum acceptable value. The impurities will quickly burn out, and very little fuel will be wasted. The situation is quite different when using burnable poison to the maximum extent, i.e., to obtain optimum fuel utilization. One would then have the reactivity at the lowest permissible value at the beginning of life, and any significant amounts of impurities in the fuel would render the initial reactor performance unsatisfactory. Thus, more stringent standards on fuel composition are generally necessary when burnable poisons are used. In practical reactor design, it would be necessary to set the fuel and burnable poison content such that the hot, new core with peak xenon is supercritical with all rods withdrawn by a margin equal to the reactivity effect of the impurities in addition to margins provided for other reasons. This results in less than optimum utilization of the fuel.

The effect of the stable fission products and parasitic fuel-capture products (for example, U^{236}) will now be considered. Make the usual assumption in elementary treatments, so that

each fission results in a fixed amount of absorptive cross section. The macroscopic absorption cross section, Σ_{sf}, resulting from the above processes is given by

$$\Sigma_{sf}(T) = \left(\sigma_{U^{236}} \frac{a}{1+a} + \frac{\sigma_{sf}}{1+a}\right) \frac{\left[\Sigma_{U_o} - \Sigma_U(T)\right]}{\sigma_U} \quad \text{Eq. (4.323)}$$

where the first term on the right represents the absorption of the U^{236} formed (for U^{235} fuel; Pu^{240} if the fuel is Pu^{239}, etc.), and the second term represents the absorption of the stable fission products. Here,

$\sigma_{U^{236}}$ = microscopic absorption of U^{236}
σ_{sf} = microscopic cross section of the stable fission products formed per fission
a = ratio of parasitic capture to fission
$\Sigma_{U_o}, \Sigma_U(T)$ = macroscopic fuel cross section initially and at integrated flux time, T, respectively:

$$\text{let} \qquad a \equiv \frac{\left[\sigma_{U^{236}} \frac{a}{1+a} + \frac{\sigma_{sf}}{1+a}\right]}{\sigma_U}$$

$$\text{now,} \qquad \Sigma_{U_o} = \Sigma_U(T)\, e^{\sigma_U T}$$

$$\text{hence,} \qquad \Sigma_{sf}(T) = a\Sigma_U(T) \left[e^{\sigma_U T} - 1\right].$$

Referring to Eqs. (4.315) through (4.321), the reactivity of the core at any burnup will now be characterized by

$$\left[p + \frac{a}{A'}\left(e^{\sigma_U T}\right) + q - \frac{a}{A'}\right]$$

in lieu of $(p+q)$. Defining

$$p^* \equiv p + \frac{a}{A'} e^{\sigma_U T}$$

so that p^* has the same time dependence as p, one can now study the behavior of (p^*+q) and find that there is no essential change in the mathematical structure previously used. Note that (p^*+q) moves between $(1+a/A')$ and $(A+a)/A'$ in lieu of between a/A' and A/A'. It will be found that because of the exponential time increase of the term added to p that in each case the maximum

value of T, and, therefore, both the core endurance and the fuel utilization are reduced from the previous cases in which the effects of the stable fission and parasitic fuel capture products were not included.

Equation (4.322) for the limiting case when the reactivity starts to decrease with core operation is replaced by

$$\sigma_U p_o (1 \tau a/A') = (\sigma_B - \sigma_U) q_o$$

Furthermore, the fractional fuel depletion which can be attained is now limited even with very high fuel loadings, since the ratio of fission product to fuel absorption increases rapidly with fractional fuel depletion.

Case 5. Epithermal Burnable Poisons. The previous treatment has covered only the use of thermally absorbing elements as burnable poisons. In the case of elements which have epithermal resonances, it is found that an appreciable depletion may be obtained from epithermal absorption. The efficacy of an unshielded resonance absorber as a burnable poison is given roughly by the relationship

$$\sigma_B = R \frac{\Sigma_T}{\overline{\xi \Sigma_s}} \equiv R \beta \gamma \qquad \text{Eq. (4.324)}$$

where σ_B is the microscopic cross section of an equivalent thermal absorber; R is the infinite-dilution resonance-absorption integral; $\overline{\xi \Sigma_s}$ is the value, averaged over the fast flux, of the slowing-down power of the moderator; and Σ_T is the total thermal macroscopic absorption cross section (see Appendix A-6 of Ref. 86). If the value of Σ_T falls appreciably with core life, as it will in a high burnup core, the cross section, σ_B of the thermal poison equivalent to the resonance absorber will change during the core life. For burnable poisons of high cross section, the importance of the effect is usually small, since the poison will be almost depleted by the time that Σ_T has been substantially reduced.

Primarily, the maximum xenon override conditions have been considered up to the present. It also is necessary to give attention to other operating conditions of the reactor and, particularly, to the cold shutdown condition. Consider first the reactor in the cold condition with transient poisons, i.e., xenon and samarium absent. Assume that absorption cross sections of the fuel and of the burnable poison have the same dependence on moderator temperature. For simplicity, neglect the effect of the stable fission product poisons since, as demonstrated previously, their presence does not change the mathematical structure used, so that the conclusions below are essentially unaffected.

For the available mechanical control for shutdown purposes there will be a limiting value of core excess reactivity, Δk_{ex}, in the cold condition, such that it is possible to shut down the core with a satisfactory margin of subcriticality. (This would usually imply that one or more of the control rods could be withdrawn without causing the core to become critical.) This condition is expressed by

$$\frac{\Sigma_M^* + D^* B^{2*} + \Sigma_B^*(T)}{\Sigma_U^*(T)} = \frac{\eta}{\left(1+\Delta k_{ex}\right)\left(1+\tau^* B^{2*}\right)} - 1 \,. \qquad \text{Eq. (4.325)}$$

Here room-temperature quantities are identified by asterisks. The value of η is assumed to be independent of temperature. Then, the variation of the excess reactivity in the cold clean condition may be characterized by the left side of Eq. (4.325). As the left side of Eq. (4.325) increases, the reactivity of the core decreases.

Dividing the left side of Eq. (4.325) by the constant A' from Eq. (4.316),

$$\frac{\Sigma_M^* + D^* B^{2*} + \Sigma_B^*(T)}{A' \Sigma_U^*(T)}$$

$$= \left[\frac{\Sigma_M^* + D^* B^{2*}}{\Sigma_M + \Sigma_X + DB^2}\right] \frac{\Sigma_U(T)}{\Sigma_U^*(T)} \left[\frac{\Sigma_M + \Sigma_X + DB^2}{A' \Sigma_U(T)}\right] + \frac{\Sigma_B^*(T)}{A' \Sigma_U(T)} = bp + q \qquad \text{Eq. (4.326)}$$

where

$$b \equiv \left[\frac{\Sigma_M^* + D^* B^{2*}}{\Sigma_M + \Sigma_X + DB^2}\right] \frac{\Sigma_U(T)}{\Sigma_U^*(T)}$$

is nearly constant with respect to T, and p and q are as defined in Eq. (4.317). The reactivity of the core in the cold clean condition is, then, a monotonically decreasing function of $(bp+q)$. Usually, in a power reactor, Σ_X is so large that b is less than one regardless of temperature changes in the parameters. The dependence of p and q on the integrated flux time, T, will be the same as previously, since it is the cross sections at operating temperature which are effective in the depletion of the fuel and poison.

The maximum quantity of fuel which can be loaded into the core without burnable poisons is proportional to Σ'_U of Eq. (4.316). In this case, at $T = 0$, $p_o = 1$ and $q_o = 0$.

From Eq. (4.326) the reactivity in the cold, clean condition is characterized by $bp_o+q_o=b$. When burnable poisons are added, it is still true that $p+q=1$ at T corresponding to the time of maximum reactivity in the hot maximum xenon condition. Then,

$$bp + q = b + q(1 - b) > b .$$

At any other T, the reactivity in the hot, maximum xenon condition is lower. Set $p+q\equiv 1+\delta$, $\delta>0$. Then,

$$bp + q = b(1+ \delta) + q(1 - b) > b . \qquad \text{Eq. (4.327)}$$

Thus, the core with burnable poisons is always less reactive in the cold, clean condition than the core without burnable poisons, provided that in each case the loadings are compatible with the same amount of shimming control. If the worth of the control rods remains the same, a smaller number of rods usually would be needed to shut the core down. This is discussed subsequently.

By the same reasoning it follows that in operating conditions with either no xenon, or amounts less than maximum, the core with burnable poisons will have a lower reactivity throughout life than the same core with the maximum fuel loading possible without burnable poisons. This would generally mean that the absorbing control rods would be withdrawn further from the core, which is often beneficial from a heat transfer standpoint although exceptions could occur, for example in cores controlled by moving only selected control rods (i.e., rod programming).

The principal conclusions from this elementary treatment of burnable poisons are:

1. Even absorbers of low cross section have some utility as a burnable poison. However, the fraction of fuel depletion obtainable increases as the cross section of the absorber approaches and exceeds that of the fuel.
2. With an absorber whose macroscopic cross section exceeds that of the fuel, it is generally most advantageous to arrange the proportions of fuel and poison, so that reactivity first increases and then decreases.
3. For any given poison, the obtainable fraction of fuel depletion is limited by the amount of mechanical control available for shimming. The corresponding amount of reactivity variation occurring with the use of burnable poisons is usually known as the mismatch.
4. The core in the cold, clean condition usually becomes less reactive (more shut down) through the use of burnable poisons.

It has been tacitly assumed that the worth of the control rods expressed in reactivity units is unaffected by the changes in fuel and homogeneous poison loading. If the control rod is purely a thermal absorber, it follows from the area absorption theory[87] that its worth will decrease as the fuel and poison content of the core increases and results in a reduction in the thermal diffusion length, which in a Maxwell spectrum is inversely proportional to the square root of the macroscopic absorption cross section. Actually, the heavier loadings result in a shift of the spectrum to higher energies which tend to prevent the effective diffusion length from falling rapidly. If the control rod worth depends to a considerable extent upon resonance absorption, as is the case with a hafnium rod, the worth of the rod may actually increase with increasing core absorption. In any case, changes in rod worth over a wide range of fuel and poison content do not appear to be great in many practical cases.

The following list of various areas in which the above elementary treatment is inadequate or unrealistic will be subsequently discussed in greater detail.

1. It has been assumed that burnable poisons of any desired microscopic cross section and $1/v$ energy dependence are available. Actually this is far from the case (see Sect. 4.7.C).
2. It has been assumed that the burnable poisons are uniformly mixed with the fuel. Actually, because of the limitations of available materials, the poisons must often be distributed quite differently than the fuel (see Sect. 4.7.D).
3. The nonuniformity of depletion throughout a core must be taken into account (see Sect. 4.7.E).

C. Materials Suitable for Use as Burnable Poisons

Nature is not very abundant with elements suitable as burnable poisons, i.e., that have both satisfactory engineering properties and cross sections to obtain desired fuel depletion with minimum poison residue compatible with a small amount of mechanical shimming control.

The burnable poison which has proved most useful to date is boron. For moderate fuel depletion, the use of boron results in little poison residue, yet requires only a small amount of shim control. Furthermore, physics predictions of the endurance of cores with boron are facilitated by the $1/v$ energy dependence of its cross section and the fact that no absorbing isotopes are formed. As a result of the $1/v$ energy dependence of the cross section, the depletion of the poison relative to U^{235} fuel will be

nearly independent of the shape of the thermal spectrum. Even considering epithermal fission, the ratio of the boron to U^{235} fuel cross sections, averaged over all energies of reactor interest, is almost independent of the thermal spectrum. Figure 4.67[88] shows this ratio as a function of the neutron energy corresponding to the temperature of the equivalent Maxwellian thermal distribution. While the helium resulting from the disintegration of boron 10 is objectionable metallurgically, dilute boron loadings appear to be acceptable.[87]

Table 4.18 covers the characteristics of various materials which might be considered for use as burnable poisons and summarizes the problems involved. For accurate nuclear data the compilations of the Brookhaven and Argonne Laboratories should be consulted. This table does not include data on short-lived unstable isotopes produced by neutron absorption. These must be considered in detailed calculations. The depletion effects of the burnable poison are to some extent a function of the power history of the core, since depletion of the transient isotopes by neutron absorption competes with their decay.

All materials listed involve formidable problems in calculation or in nuclear and engineering suitability. The calculation problem is intensified by the fact that the cross-section data are generally not as well known for materials having isotopic chains of absorbing elements and complicated resonance structures as for other isotopes.

Figure 4.68, taken from Ref. 87 shows the burnup relative to U^{235} fuel of two elements, dysprosium and europium, which are frequently proposed as burnable poisons. These curves are intended to show general behavior only, as they are based

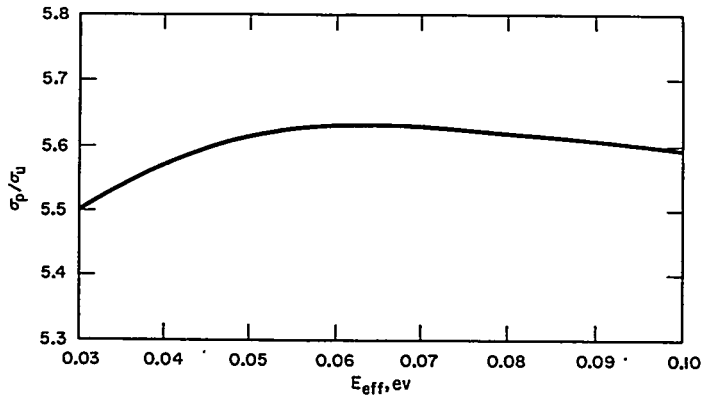

FIGURE 4.67. Ratio of Average B^{10} Absorption Cross Section to Average U^{235} Absorption Cross Section Averaging Over All Energy vs Effective Energy of Equivalent Maxwellian Thermal Distribution.

TABLE 4.18 — CHARACTERISTICS OF SOME MATERIALS POTENTIALLY USEFUL AS BURNABLE POISONS

Element	Isotope*	Isotopic Abundance (percent)	Microscopic Absorption Cross Sections† (barns)	Resonance Absorption Integral (barns)	Chain of Absorption Reaction: Isotope Produced by Neutron Absorption‡	Chain of Absorption Reaction: Thermal Absorption Cross Section of New Isotope (barns)	Remarks
Boron	B^{10}	19.78	3840 (n, α reaction)		Li^{7}	0.033	g
Silver	Ag^{107}	52	40	74	Cd^{108}		a, c
	Ag^{109}	48	84	1300	Cd^{110}	0.2	
Cadmium	Cd^{113}*	12	27,000		Cd^{114}	1.2	a, d
Indium	In^{113}	4	63	1050	Sn^{114}		a, c
	In^{115}	96	200	3210	Sn^{116}	0.006	
Samarium	Sm^{147}	15	90	1350	Sm^{148}		d, e, f
	Sm^{149}	14	41,500		Sm^{150}		
	Sm^{152}	27	220	2850	Eu^{153}	320	
Europium	Eu^{151}	48	8700	3000	Eu^{152}	7000	a, c, e, f
	Eu^{153}	52	320	1280	Eu^{154}	1400	h
Gadolinium	Gd^{155}	15	58,000		Gd^{156}		a, d, e
	Gd^{157}	16	240,000		Gd^{158}	4	
Dysprosium	Dy^{160}	2	130	20	Dy^{161}	580	a, c, f
	Dy^{161}	19	580	700	Dy^{162}	140	
	Dy^{162}	26	140	1300	Dy^{163}	220	
	Dy^{163}	25	220	640	Dy^{164}	2800	
	Dy^{164}	28	2800	450	Ho^{165}	64	
Hafnium	Hf^{174}	0.18	400	Large resonance absorption	Lu^{175}	23	b, e, f
	Hf^{177}	19	370		Hf^{178}	80	i
	Hf^{178}	27	80		Hf^{179}	65	j
	Hf^{179}	14	65		Hf^{180}	10	j
	Hf^{180}	35	10	22	Ta^{181}	21	j
Lithium	Li^{6}	7.4	950 (n, α reaction)	380			a
Erbium	Er^{166}	33	10		Er^{167}	700	c, e
	Er^{167}	29	700		Er^{168}	2	k
Iridium	Ir^{191}	37	1000	3500	Pt^{192}	16	a, b, f
					Os^{192}	1.6	
	Ir^{193}	63	120	1370	Pt^{194}	1.2	
Mercury	Hg^{196}	0.15	1300		Pt^{196}	1.0	a, l
	Hg^{199}	16.9	2000		Hg^{200}	50	

a. Unsolved metallurgical problems.
b. High residue of poison, except in very hard spectra.
c. High residue of poison.
d. Cross section is so high that homogeneous mixtures of poison and fuel may result in excessive reactivity rises.
e. Computations complicated by non-1/v behavior of cross section.
f. Computations complicated by chain of isotopes of appreciable absorption.
g. In widespread use, although the helium production is undesirable metallurgically.
h. Complex chain of isotopes with some of the cross sections not well known.
i. Attractive metallurgically.
j. Resonance absorption very important, but resonance structure is extremely complicated.
k. Useful in some cases to enhance negative temperature coefficient of reactivity.
l. Toxicity must be considered.
*Only naturally occurring isotopes with appreciable absorption are listed.
†Thermal cross section at 200 m/sec.
‡If isotope produced is short lived, the isotope after decay is listed.

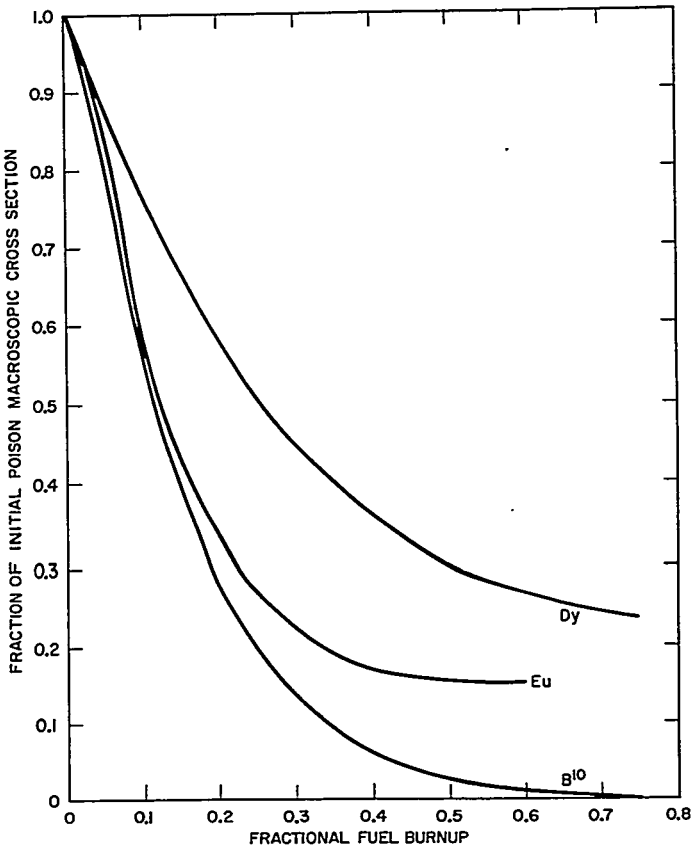

FIGURE 4.68. Fraction of Initial Poison Cross Section vs Fuel Depletion for Europium, Dysprosium, and Boron.

solely on depletion by thermal neutrons and on the available cross-section data which at this time are incomplete. For comparison purposes, data have also been included in Fig. 4.68 for boron. It will be noted that, initially, the europium tends to deplete with respect to fuel at nearly the same rate as boron, so that by the treatment of Sect. 4.7.B, nearly the same macroscopic cross section of each poison would be employed. However, unlike boron, europium has an appreciable residue which would result in lowering the endurance obtained with a given fuel loading. With dysprosium, the initial rate of absorption depletion is much less than for boron and europium, tending towards a lower reactivity mismatch, but the poison residue is even greater than for europium. For a harder spectrum, the residue of dysprosium tends to increase. This is because the lower isotopes have a relatively high resonance

capture in comparison with Dy^{164}, which has the largest thermal absorption. Thus, as the spectrum hardens, the lower isotopes transmute more rapidly into Dy^{164}, while the rate of destruction of Dy^{164} decreases. From a reactor physics standpoint, combinations of boron and dysprosium might be attractive for reactivity control.

Of the erbium isotopes, only Er^{167} has appreciable capture cross sections in the thermal and epithermal range, exhibiting a $1/v$ absorption cross section at low thermal energies, and large absorption resonances at 0.460 ev and at 0.584 ev. Studies of the use of erbium as a burnable poison have been made by P. G. Klann at the Knolls Atomic Power Laboratory. Because of the low-lying resonances, the depletion of erbium relative to fuel is very sensitive to the shape of the thermal spectrum. For well thermalized cores the depletion rate is slow, but at harder spectra the depletion rate increases rapidly. Figure 4.69 shows a comparison of reactivity changes as a function of fuel burnup for (1) erbium mixed homogeneously with the fuel; (2) unshielded boron, also homogeneous; and (3) self-shielded boron (see Sect. 4.7.D). The calculation was done for a well moderated, light water core, $\beta\gamma = 0.2$, where $\beta\gamma$ is the ratio of the macroscopic absorption of the core material at the moderator temperature to the slowing-down power. For the same fractional burnup, erbium has the lowest reactivity mismatch, although there is an appreciable erbium residue. An interesting feature of erbium is that for a core in which the neutron spectrum is highly thermal, the temperature coefficient of reactivity of the core becomes much more negative as erbium is added since, as the temperature of the moderator increases, the thermal spectrum shifts towards higher energies and the erbium resonances become more absorbing. This is important from a self-protection standpoint. Erbium is employed for this reason in the TRIGA reactor and has also been considered for superheat reactors. Since well thermalized, large water-moderated cores usually have a low leakage, the use of the erbium from the standpoint of enhancing the temperature coefficient may be highly beneficial. In this respect, the erbium residue would ensure that the coefficient would remain negative near the end of life at which the ratio of fuel-to-moderator captures is decreased. The point is illustrated by Fig. 4.70 which shows the average (from 0 to 1 ev) cross section of erbium as a function of moderator temperature. It will be noted that the erbium cross section remains nearly constant, while the U^{235} cross section decreases a little faster than $1/v$. Hence, the ratio of erbium to fuel absorptions increases with temperature, resulting in a negative increment to the temperature coefficient.

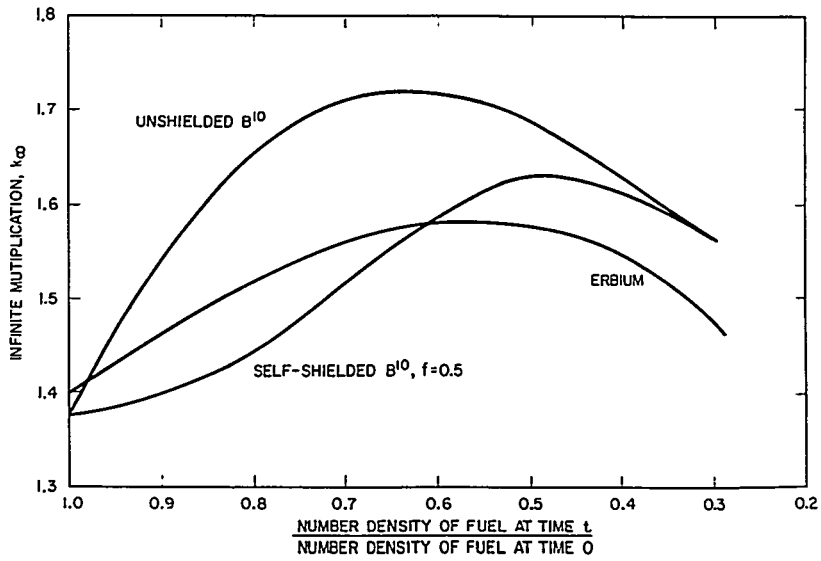

FIGURE 4.69. Reactivity as a Function of Undepleted Fuel Load for Various Poisons.

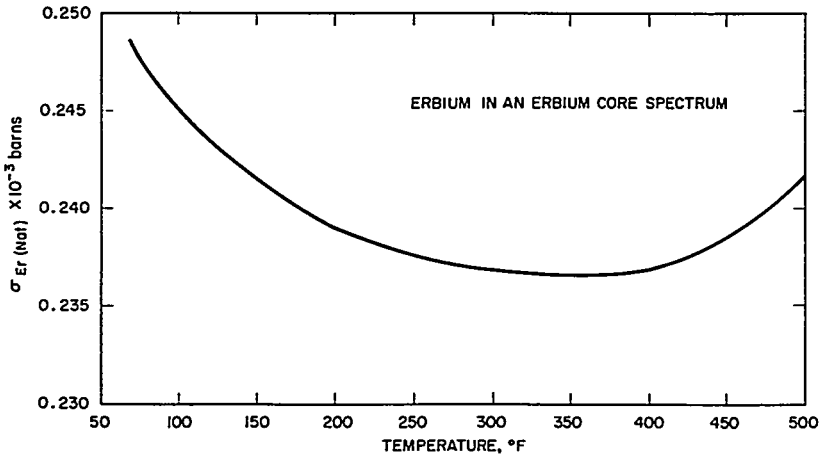

FIGURE 4.70. Averaged Microscopic Cross Section of Erbium in Indicated Spectrum as a Function of Moderator Temperature.

Very high cross-section elements, such as cadmium and samarium, are sometimes employed as supplementary burnable poisons to increase the shutdown of a new clean core by the amount of reactivity associated with permanent samarium. These materials deplete so rapidly that they are virtually gone by the time the samarium builds up. Samarium is especially

convenient in this regard and would not be expected to introduce any metallurgical problems since, in any case, it is formed in the fuel elements by fission. The method is only useful when the reactivity in the cold condition of the core at any stage of depletion, with transient xenon and samarium absent, is not appreciably greater than in the new core. Otherwise, the mechanical control must be designed to provide adequate shutdown in the cold core at the most reactive point in life, and there would already be a margin of shutdown safety at the beginning of core life.

This section concludes with a discussion of the use of hafnium as a burnable poison. Natural hafnium consists of six isotopes of appreciable absorption with a complicated resonance structure. The poison residue is of the order of 30 percent of the original microscopic cross section. On the other hand, hafnium is attractive metallurgically, particularly for water-cooled cores utilizing zirconium-clad elements. The physics properties of hafnium as a burnable poison have been investigated by I. Itkin, W. D. Kimball, R. W. Lenker, and E. Schmidt at Bettis Atomic Power Laboratory and by F. Feiner at the Knolls Atomic Power Laboratory.

An important problem in hafnium depletion is energy self-shielding. This arises from the fact that in the epithermal region the absorption by Hf^{177} and Hf^{178} is dominated by a few strong resonances. As a result, the effective epithermal microscopic absorption of the hafnium isotopes increases rapidly as concentrations of the hafnium isotopes are changed by neutron irradiation. If the hafnium is mixed homogeneously with the fuel, the spatial self-shielding appears to be negligible for the relatively low hafnium dilutions considered to date. Figure 4.71 shows the variation of the ratio of Hf/U^{235} fuel captures in a typical case for a medium having a volume of Zr/H_2O of approximately 0.95 and an Hf/U^{235} ratio of about 2.

D. Self-Shielded Burnable Poisons

The reactor designer often finds that poisons which can be mixed homogeneously with the fuel are inadequate to obtain the objectives of high burnup of fuel and long endurance with minimum mechanical control for shimming. For example, it is evident from Sect. 4.7.B that, if the poison microscopic cross section exceeds that of the fuel, there is a certain fuel loading and corresponding endurance beyond which the reactivity rise due to the relatively rapid depletion of the poison will be greater than can be handled by the available mechanical control. It would be natural to employ a poison of lower cross section. If no suitable material is available, the poison of higher

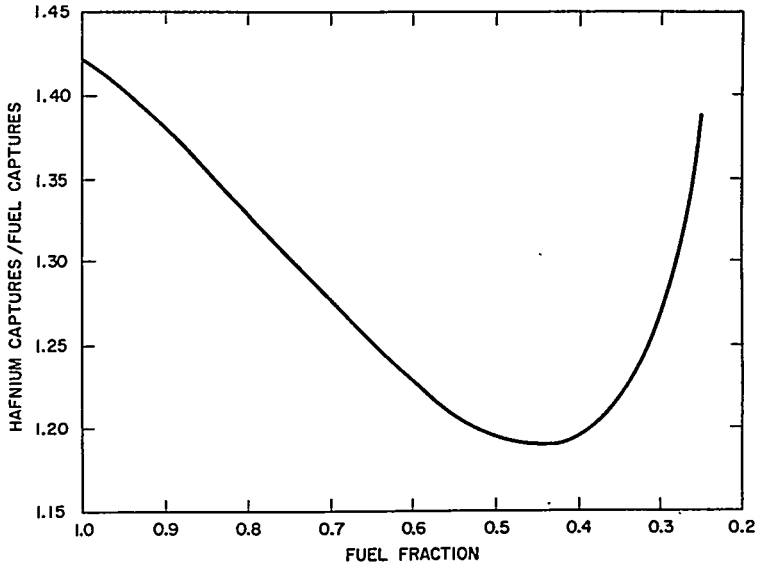

FIGURE 4.71. Variation of Hafnium to Fuel Captures with Fuel Fraction.

cross section can still be utilized by locating it apart from the fuel in such manner that the flux and statistical weight applicable to the poison relative to the fuel yield an effective poison cross section approximating that desired. While there are various ways of doing this, perhaps the most efficacious is to install the poison in lumped or spatially self-shielded form. If the fuel is unself-shielded or nearly so, the flux dip inside the poison will be such that the effective cross section of the poison is substantially reduced from its unself-shielded value at the beginning of life when it is desired to reduce the reactivity rise. As the poison depletes, the effective cross section of the poison relative to fuel will increase, which is the desired behavior to maintain reactivity as high as possible near the end of life when it would otherwise fall rapidly due to depletion of fuel and accumulation of fission product poisons.

The analytical treatment of self-shielded poisons is facilitated by use of the following approximate form for the self-shielding factor which is suggested by the transport theory solution for lumps uniformly distributed in a homogeneous medium. This formula was first introduced by H. Hurwitz, Jr. (KAPL):[2]

$$f = \frac{1}{1 + \gamma \Sigma_B} \qquad \text{Eq. (4.328)}$$

where Σ_B is the macroscopic cross section of the poison. γ is a geometric factor which provides an index of the degree of self-shielding, i.e., the greater the value of γ, the more self-shielded is the fuel. (γ here should not be confused with that used (Sect. 4.7.C) in the product $\beta\gamma$ as a measure of spectral hardness). As an approximation, $\gamma\Sigma_B$ is taken as 2ξ for $\xi > 2$ and $1.5\,\xi$ for $\xi < 2$, where

$$\xi = \frac{2V}{S}\,\Sigma_B$$

V = the volume of the lump and S its surface area
ξ = the optical thickness or number of attenuation or relaxation lengths through the lump.

The self-shielding factor f (also sometimes represented by g) is usually defined as the ratio of the average flux in the lump to that of the average flux in the outside medium. In practical situations, the formula for f is modified empirically as in Sects. 4.6.C.3 and 4.2.D.3 to the form

$$f = \frac{\overline{K}}{1 + C\Sigma_B} \qquad \text{Eq. (4.329)}$$

where $\overline{K}$ and C are fitted parameters to experiments or to transport theory calculations, and f is now the ratio of the average flux in the poison to that in the moderator. It is also useful to define a self-shielding factor of the same form, with a two-parameter fit, as the ratio of poison absorptions to fuel fissions or to fuel absorptions (see Sect. 4.2.D.3). In many cases a fit of this kind to experiment or calculation can be found for the entire range of depletion.

If one uses the procedure of Sect. 4.7.B, reactivity behavior of the core material can still be followed by the quantity $[p(T) + q(T)]$. p has the same dependence, $e^{\sigma_U T}$, as before on T, the integrated flux time, but the dependence on T of q, $e^{(\sigma_U - \sigma_B)T}$, now has σ_B equal to the effective value of the poison microscopic cross section and a rising function of T. If self-shielded sufficiently to make the initial value of σ_B less than σ_U, the reactivity will initially fall; hence, one must start with the absorbing shimming control rods inserted. As depletion proceeds, σ_B may become greater than σ_U, and the reactivity starts to increase. For an optimum case, the reactivity should start to increase when the shimming rods are nearly completely withdrawn. The rods would then be reinserted to the point of maximum insertion, at which time, for optimum choices of fuel and of poison content and self-shielding, the reactivity would start to decrease again. This

behavior is illustrated by Fig. 4.72 and results in utilization of the shimming control three times, as compared with the maximum of twice which is possible with unself-shielded poison. By using combinations of poisons of different self-shielding, it appears possible to obtain an increased number of loops in the reactivity curve and, thus, a still greater fractional depletion of the fuel.

An interesting possibility is apparent from comparison of Figs. 4.72 and 4.73 for a poison mixed homogeneously with

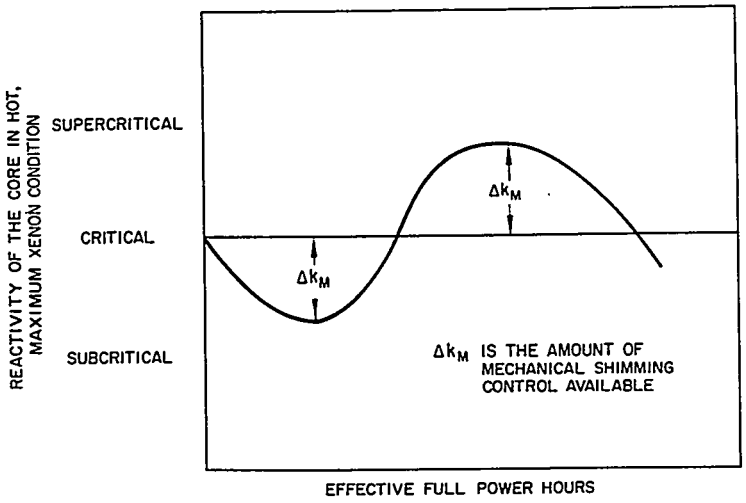

FIGURE 4.72. Variation of Reactivity Throughout Core Life for a Heavily Self-Shielded Burnable Poison.

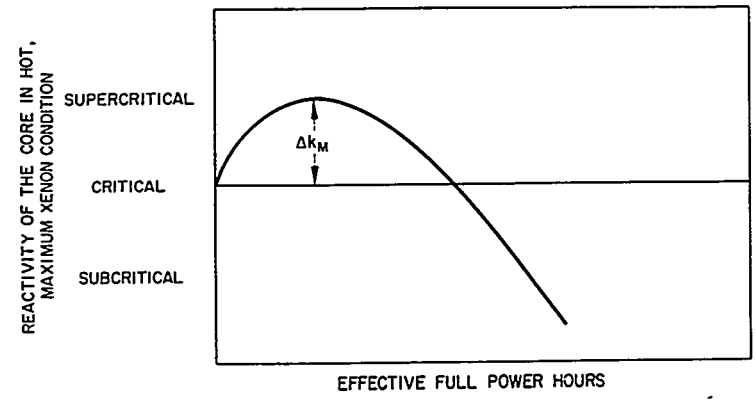

FIGURE 4.73. Variation of Reactivity Throughout Core Life for an Unself-Shielded or Lightly Self-Shielded Burnable Poison.

the fuel. If most of the burnable poison is heavily self-shielded and the remaining poison has little or no self-shielding one can arrange (1) for the reactivity rise due to depletion of the lightly shielded poison to superimpose on the initial reactivity fall resulting from the heavily shielded poison, and (2) for the sharp fall in reactivity as the lightly shielded poison becomes exhausted to coincide with the late rise in reactivity due to the heavily shielded poison. Figure 4.74 shows the result of a study made by J. H. Leonard[89] at Bettis Atomic Power Laboratory for the second Shippingport core design in which, over many thousands of hours, the effective cross section of the burnable poison matches extremely well the absorption cross section required for criticality. The thermal poison demand curve in Fig. 4.74 indicates the value of macroscopic cross section of uniform poison, distributed throughout the highly enriched seed, which would be

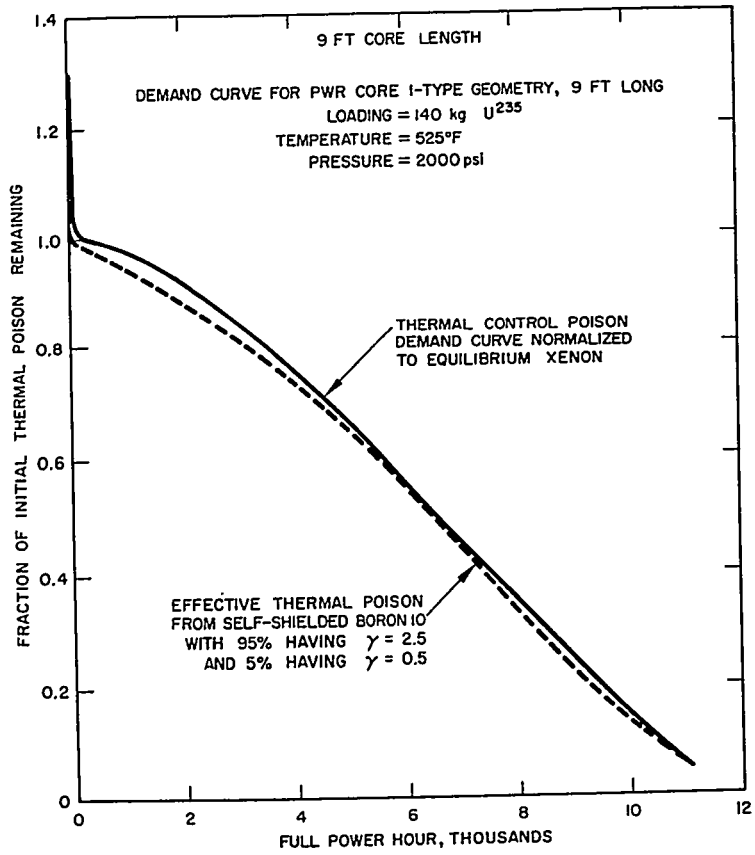

FIGURE 4.74. Comparison of Poison Demand Curve with a Typical Boron 10 Depletion Rate.

required to maintain criticality if no control rods or burnable poison were used. In this case, 95 percent of the poison was heavily shielded ($\gamma = 2.5$) and 5 percent lightly shielded ($\gamma = 0.5$). The calculation took into account fast neutron depletion of the poison and the changing ratio of fast-to-slow flux with core depletion. In some cases, the epithermal depletion of boron gives almost the same effect as a lightly self-shielded poison, and one can obtain a nearly constant value of reactivity throughout reactivity life by use of self-shielded boron alone.

From the above, it appears that in a thermal reactor by using combinations of differently self-shielded elements of boron, for example, one can minimize the reactivity mismatch for any given fuel loading and still avoid a large residue of unburned poison which would tie up considerable fuel. However, the practicalities of the situation must not be overlooked. With present uncertainties in the values of the various cross sections and other nuclear parameters, uncertainties in calculational methods, and the effects of manufacturing tolerances, an adequate reactivity allowance must be provided in the design. One can imagine a reactor with a burnable poison content calculated to be exactly critical throughout core life, at some specified xenon condition, with all control rods withdrawn. As a result of a slight error in construction, etc., the reactor might not meet its reactivity requirements for even an hour if adequate reactivity allowances had not been made in the design.

For reactor regions containing self-shielded poison elements of plate form, in which a one-dimensional treatment of the poison is adequate, diffusion theory can usually be used provided that fictitious constants are chosen for the poison elements in accordance with blackness theory (Chap. 3, Sect. 3.6). From such a diffusion theory calculation, the number of absorptions in the poison elements can be obtained and values found for the parameters of Eq. (4.329).

In many cases the poison elements are in plates of short width (as in the second Shippingport core design (Sect. 4.7.F)) or in other forms for which one-dimensional blackness theory does not apply. The best treatment of the problem is by the use of Monte Carlo, but on computers available at the present time this method is too time-consuming and expensive for configurations of practical interest. A procedure[90] (also discussed in Sect. 4.2.D) which has proved to be useful in practice is to find an equivalence for a model geometry between Monte Carlo and diffusion theory and to assume that this equivalence holds regardless of the external medium, provided that the poison characteristics and the mesh spacing of the poison region remain constant. Figure 4.75 shows a typical

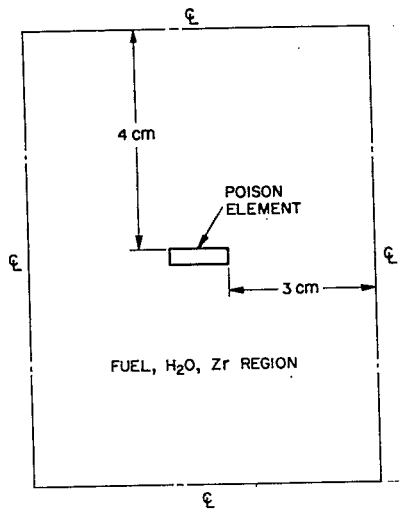

FIGURE 4.75. Model Geometry for Establishing Equivalence between Monte Carlo and Diffusion Theory.

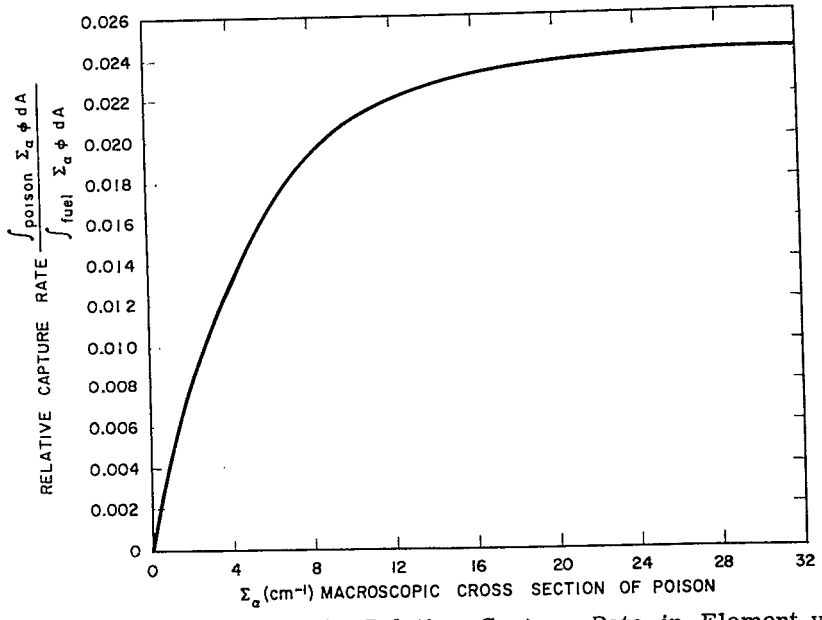

FIGURE 4.76. Monte Carlo Relative Capture Rate in Element vs Macroscopic Cross Section of Poison.

model geometry selected. Figure 4.76 shows the relative capture rate in poison to fuel, as computed by Monte Carlo, versus the macroscopic cross section of the poison. Figure 4.77 is the same for diffusion theory, with the same source

distribution as used in the Monte Carlo code, and the diffusion constant of the poison chosen arbitrarily as $1/3\,\Sigma_a$. (The results do not appear to be sensitive to the choice of D.) By comparison of Figs. 4.76 and 4.77, an effective macroscopic absorption cross section can be found which makes the diffusion theory agree with the Monte Carlo result. Using these effective constants, the Monte Carlo and diffusion theory with effective constants have been compared for another test geometry more similar to the actual core design. The results are shown in Fig. 4.78 and indicate close agreement between diffusion theory and Monte Carlo, while the one-dimensional blackness theory has a large discrepancy.

The use of lumped burnable poisons has quite different effects on the cold shutdown condition of the core than in the case of homogeneous poisons. If the poison has a $1/v$ energy dependence of the microscopic cross section, as is the case for boron, the poison microscopic cross section will be considerably higher cold than hot. This means that the lumped poison elements will be more highly self-shielded and, therefore, less effective in the cold core than in the hot core. Concomitantly, the temperature coefficient of reactivity will become more negative. The effects on the adequacy of the control system must be carefully considered. While this

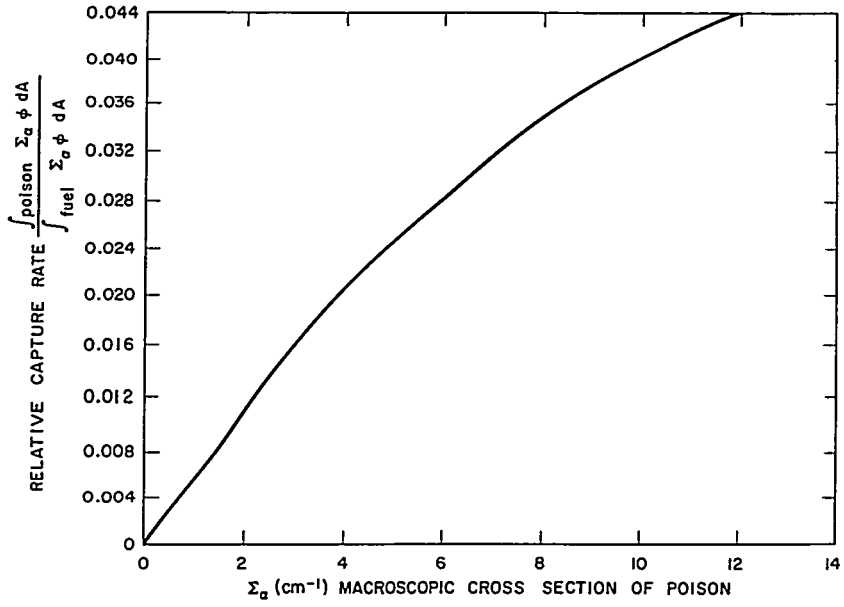

FIGURE 4.77. Diffusion Theory Relative Capture Rate in Element vs Macroscopic Cross Section of Poison.

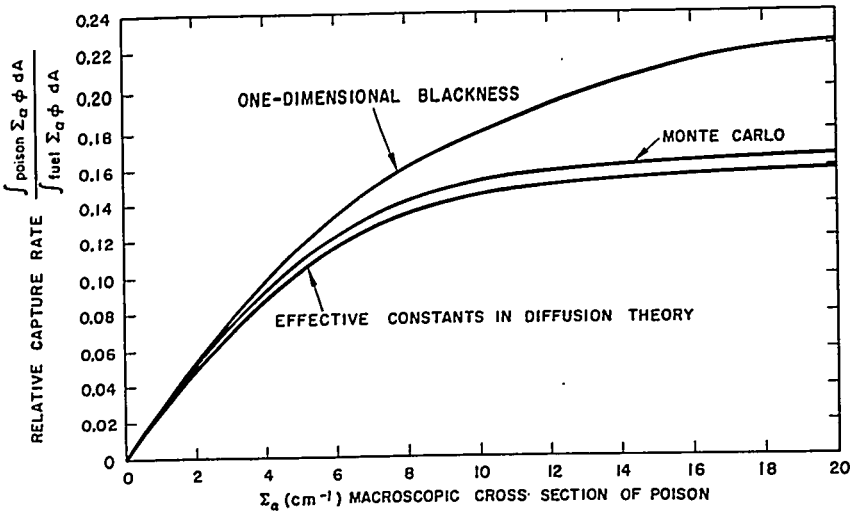

FIGURE 4.78. Comparison of Monte Carlo, One-Dimensional Blackness, and Diffusion Theory Effective Constants for a Test Geometry Similar to the Second Shippingport Seed.

phenomenon increases the reactivity of the core in the cold condition relative to the hot, there is not necessarily a corresponding increase in the reactivity of the cold core with one or more control rods withdrawn, which is the criterion usually adopted for judging adequacy of shutdown. When an absorbing control rod is withdrawn with all the other rods inserted, the criticality of the core usually depends strongly on the characteristics of the region not containing rods. If it should happen, for example, that when one rod is withdrawn the flux tends to peak near the poison elements, this would enhance the worth of the poison relative to fuel and make the core less reactive in this condition. The converse could also hold. This indicates the need for carefully correlating the location of the burnable poison elements with the overall design to include effects on control and power distribution.

Sometimes it is more convenient to make the burnable poison elements of plates which are themselves composed of separated strips, pins, or wires. It is then quite difficult to treat the strips individually. Instead, an equivalence is found,[91] either experimentally or by Monte Carlo, for the plate-to-strip ratio, which is defined as that amount of poison uniformly distributed in the plate to give the same reactivity effect as the separate strips. Since the poison in the strip is more heavily self-shielded, less boron is required in a uniform plate than in strip form to produce the same reactivity loss, the effect varying inversely with the strip poison concentration. A typical

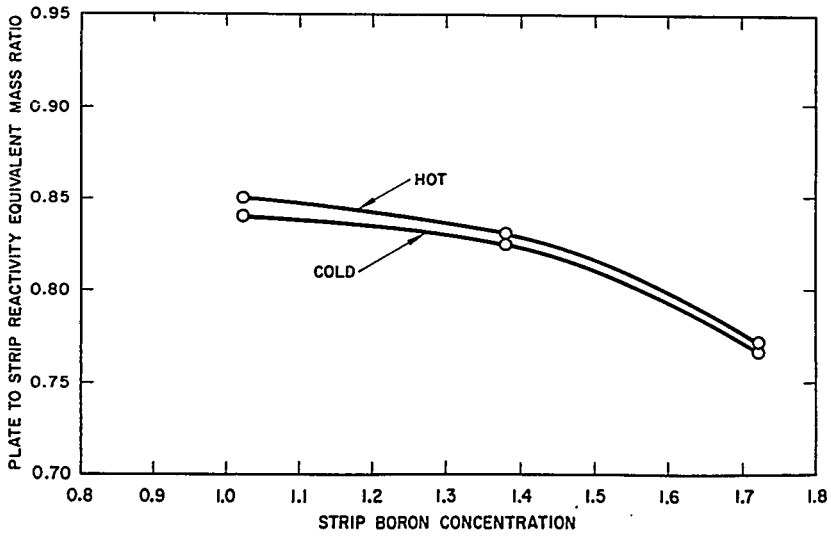

FIGURE 4.79. Plate to Strip Reactivity Equivalent Mass Ratio vs Strip Boron Concentration.

case is shown in Fig. 4.79. It would be desirable if the strip-to-plate ratio were independent of temperature and of the characteristics of the external medium. This is almost, but not exactly, true. An interesting point in Fig. 4.79 is that the plate-to-strip ratio is greater hot than cold. At first sight it would appear that there would be a bigger reduction in the self-shielding of the plates than in the strips with temperature, so that the plate-to-strip ratio should decrease. This neglects two-dimensional effects, in that the strips act like small control rods whose worth increases more rapidly than plates with an increase of diffusion length in the external medium (see Vol. II and Ref. 87).

It is frequently necessary to take into account particle self-shielding effects. This matter is treated in detail in Sects. 4.2.B and 4.2.C. For a simplified treatment, one may write the self-shielding factor of a poison element containing self-shielded particles as

$$f = f(\xi_{\text{plate}}) f(\xi_o) \qquad \text{Eq. (4.330)}$$

where $f(\xi_o)$ is the self-shielding factor of a particle [Eq. (4.328)] in terms of ξ_o, the optical thickness of the particle, and $f(\xi_{\text{plate}})$ is the self-shielding factor of the plates, assuming

that the particles (taking into account their self-shielding) are smeared out uniformly throughout the plate. Thus,

$$\xi_{\text{plate}} = 2\left(\frac{V}{S}\right)_{\text{plate}} P\Sigma_B f(\xi_o)$$

where

$\left(\frac{V}{S}\right)_{\text{plate}}$ = the volume-to-surface ratio of the plate

P = the volume fraction of the plate occupied by the poison particles

Σ_B = the macroscopic cross section of the poison in the plates.

If the inverse linear fits of Eqs. (4.328) and (4.329) are substituted in Eq. (4.330), an inverse linear fit is obtained for a plate containing finite particles.

E. Nonuniform Depletion Effects and Zoning

Up to this point only the so-called point core effects have been considered, that is, the effects of nonuniform depletion of both fuel and burnable poison which occur in a real core have not been taken into account. Nonuniform depletion has important effects on reactivity behavior, endurance, and power distribution.

In general, nonuniform depletion tends to flatten the reactivity curve, i.e., reduce the mismatch, throughout core life. The core reactivity is now effectively an average of that of different regions, each at a different stage of depletion, so that the variations in core reactivity will be appreciably less than occurring in any one region. In this respect nonuniform depletion is advantageous.

On the other hand, nonuniform depletion usually tends to reduce the endurance, since the fuel tends to burn out most in regions of high thermal flux which usually are also regions of high statistical weight. If one considers two cores of equal fuel loading, one with and the other without burnable poisons, the core without the burnable poisons will usually have a greater nonuniformity of fuel burnup, since the control rods will have to be inserted much farther in the core during most of the core life and will introduce greater flux distortions. In a burnable poison core, the poison will burn out most rapidly where the fuel does, thus, tending partly to offset the reactivity

loss due to the nonuniformity of fuel burnup. Even in a burnable poison core, nonuniformity of burnup introduces a reactivity loss as compared with uniform burnup. Physically, this is because in the parts of the core in which high flux exists the end-of-life point, as calculated by a uniform burnup assumption, has in effect been passed. At such locations, reactivity starts to fall very rapidly, since burnup of the burnable poison (which by this time is largely depleted) no longer compensates for fuel depletion effects. Furthermore, since burnable poison cores are usually designed for great endurance and high fractional fuel depletion, the effects of nonuniform depletion become much more severe than in short-lived cores. Finally, since the multiplication factor of the core material is low in cores containing burnable poisons, the regions in which control rods are present will have relatively low flux penetration, and the fuel in the region will be little used. This can be overcome to some extent by rod programming and alternation of control rods.

The effects of nonuniform depletion on power distribution may be quite severe in long-lived cores. For example, if the core is controlled by absorbing control rods moving in from the top of the core, then near the end of life the power will tend to localize near the top of the core, since the fuel elsewhere will be nearly exhausted. The presence of uniformly distributed burnable poisons will prevent this for a considerable period by keeping the value of k_∞ in each region nearly constant. However, as previously pointed out, when the burnable poisons are depleted in a region, the local reactivity decreases rapidly. There are also local power peaking effects which must be considered; for example, the phenomenon of tufting. This refers to the fact that fuel near an absorbing control rod is largely undepleted. When the rod is removed near the end of life, a water-hole will usually be present in a light water core unless fuel followers are employed. The increased density of fuel near the control rod will then increase the local peaking beyond the normal value.

It is often possible to improve core performance and overcome the deleterious effects of nonuniform depletion by zoning of the burnable poisons. This zoning may be accomplished by varying the quantity of poison per unit core volume or by self-shielding of the poison, or both.

Some interesting points in connection with nonuniform burnup and corrective action by a nonuniform poison loading are illustrated by Figs. 4.80 to 4.83, representing the results of calculations by the Knolls Atomic Power Laboratory. The illustrated phenomena are typical of those applying to small fuel elements, highly enriched in U^{235}, and boron as the burnable poison. The studies covered a wide range of fuel and poison

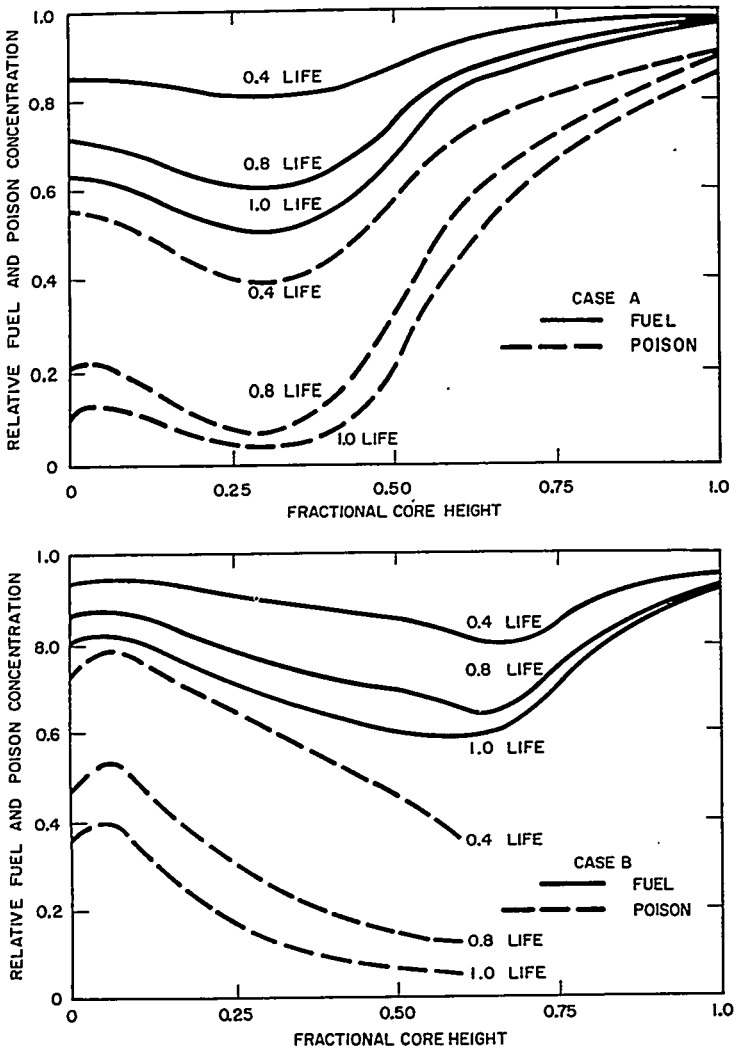

FIGURE 4.80. Fuel and Burnable Poison Distributions (Axial) for Full and Partial Length Poison.

loadings, metal-to-water ratio, and length-to-diameter ratios. Reflectors were of light water.

The calculations were performed by one-dimensional four-group codes, with provision for performing computations relating to life history and maximum xenon. Control of these cores is obtained by the movement of absorbing control rods into the top of the core to a uniform depth.

In Fig. 4.80, Case A applies to a core in which initially fuel and burnable poison are uniformly distributed. In Case B, the

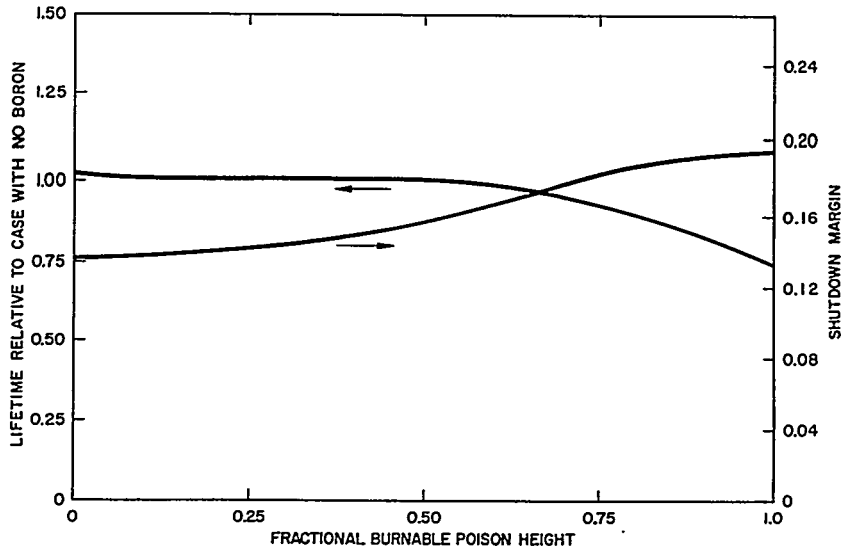

FIGURE 4.81. Effect of Height of Burnable Poison Region for Constant Fuel Loading on Endurance and Shutdown Margin.

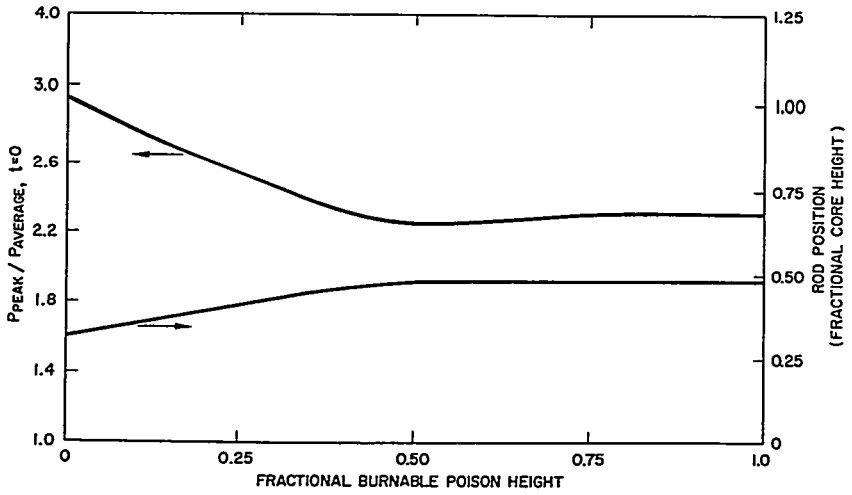

FIGURE 4.82. Initial Axial Power Factors: Rod Positions.

same amount of poison and fuel are used, but the poison extends only to 3/4 of the height of the core. It will be noted that much more uniform burnup is obtained in Case B. In Case A, the fuel and poison in the region normally occupied by control rods hardly burn out at all. In Case B almost all the poison is

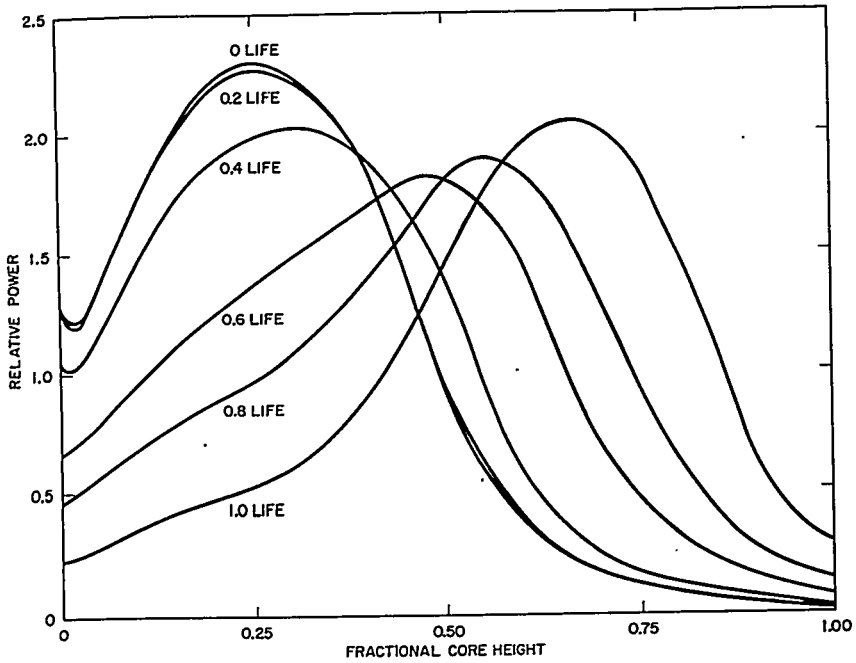

FIGURE 4.83. Time-Dependent Power Distributions, Partial Poison Length: 3/4.

depleted, thus, producing a considerably longer core life than in Case A.

The above points are further illustrated by Fig. 4.81 which shows the effect of the initial extent of the burnable poison region on endurance and shutdown. It will be noted that the optimum height of the burnable poison region is approximately 3/4 of full core height, since there is little gain in endurance in going below a 3/4 height of burnable poison, whereas the shutdown margin continues to decrease. It should be noted that shutdown requirements are set by the ability to shut down the core at room temperature with some of the control elements stuck out of the core, rather than by a numerical amount of subcriticality with all rods in, so that a reduction in burnable poison height may introduce shutdown difficulties. The core region above the burnable poison has a high multiplication factor, and the rod-free region may become critical at room temperature should some rods be stuck out. The effect would become marked as the height of the burnable poison region is decreased and as the fuel loading is increased. As the fuel loading is increased, it becomes necessary to consider more complicated patterns of burnable poison distribution, such as a high density of poison in the lower part of the core and a lower density in the upper part of the core.

Figure 4.82 shows the initial axial flux factor and the initial position of the control rods as a function of burnable poison height. The sharp peaking at very low poison heights is due to the much greater insertion required of the control rods.

Figure 4.83 shows the power distributions as a function of time in a core with 3/4 poison height. It will be noted that the value of the power-density peak-to-average is quite stable, although the position of the peak changes with burnup.

This study assumed that the control rods moved as a bank, all the rods being inserted to an equal depth. With programming of rods, some rods being inserted far into the core and others nearly all removed, the burnup is usually much more uniform. However, in extremely long-lived cores it is still possible to obtain gains in endurance and power distribution by axial zoning of the burnable poison.

Zoning of the burnable poisons is also utilized to overcome maldistribution of power even at the beginning of life. The purpose of such zoning may be (1) to improve the gross or overall power distribution and (2) to reduce local power peaks due to heterogeneities in the core structure.

The application of burnable poisons to improvement of overall power distributions in thermal reactors is essentially quite straightforward. Assuming that the fuel density is uniform, the power distribution should be such as to result in higher poison concentrations in regions of otherwise relatively high thermal flux, with the aim of obtaining as flat a thermal flux and, therefore, power distribution as practicable. An alternative is to have the poison density uniform and vary the fuel concentration so as to obtain uniform power, i.e., put low amounts of fuel in regions of high flux and vice versa. The redistribution of fuel has some apparent disadvantages. The fuel is more concentrated in regions having low flux and, usually, low statistical weight, so that extra fuel inventory is required. Secondly, the flux nonuniformity is aggravated, with the result that burnup is highly uneven and power distribution tends to be unstable with burnup. In contrast, a burnable poison redistribution wastes little fuel, since the poison is usually almost entirely consumed. The flux distributions tend to become flatter, resulting in more even burnup throughout the core. This simple picture must be modified in a practical case by considering xenon distributions and effects due to movements of control rods.

Figures 4.84 and 4.85 show some typical results at Bettis Atomic Power Laboratory of power flattening obtainable by redistribution of burnable poisons only. The work was done by P.H. Wackman. The behavior, again, is typical of a wide range of small, highly enriched reactors. In these figures it

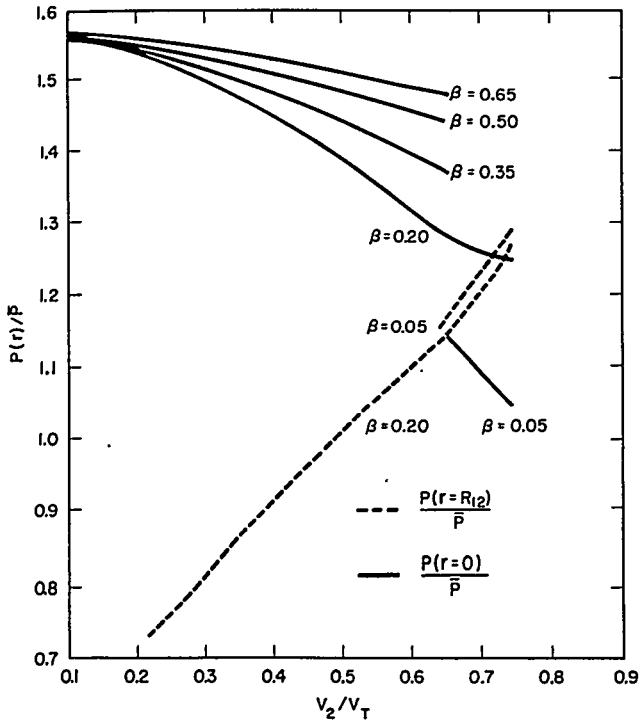

FIGURE 4.84. Peak-to-Average Power Ratio as a Function of V_2/V_T for a Nonuniformly Poisoned Core.

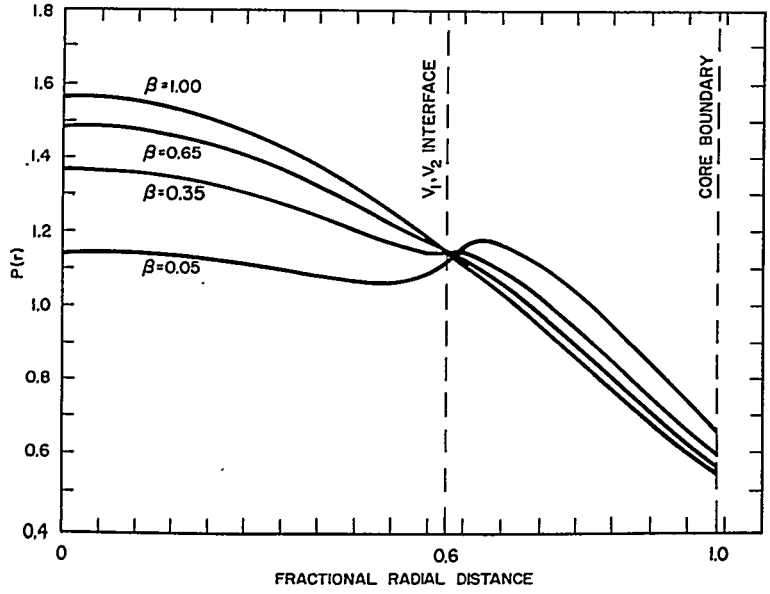

FIGURE 4.85. Power Density as a Function of Core Radius for V_2/V_T = 0.65 and Various β.

is assumed that the reactor is divided into two radial zones: V_2 is the volume of the outer zone in which the burnable poison concentration is lowered; V_T is the total core volume. Thus, V_2/V_T represents the fraction of the core having relatively low poison concentration. β is the ratio of poison density in the outer to the inner zone (not to be confused with the β used in the product $\beta\gamma$ in Sect. 4.7.C). The solid line gives an indication of the maximum power peaking at the core center, $r = 0$. The broken line indicates the peaking at the zone interface, $r = R_{1-2}$.

The aim is to make both peaks (i.e., at core center and at zone interface) equal and as small as possible. It will be noted that, in general, the peaks tend to decrease rapidly when the outer zone exceeds 60 percent of the core volume. A value of β of 0.05 gives the lowest peaks. However, with such a lightly poisoned outer zone, it would probably be difficult to shut the core down. A β of 0.20 is more practicable and results in only a slightly higher peak.

For optimal results in power flattening, it is usually desirable to use both burnable poison and fuel zoning. The poison is first distributed in such a way as to flatten the flux as much as practicable. Then the fuel is zoned to compensate for residual flux nonuniformities to obtain a flat power distribution. Since the flux is nearly uniform, the initial good power distribution will usually be well maintained throughout core life.

Local power peaks tend to be quite high in light water-moderated cores in which water channels act as strong sources of thermal neutrons to the surrounding highly absorbing areas. For cores composed of a large number of identical units, such as fuel assemblies with associated control rods, the local power peaks tend to superimpose upon the overall power distribution pattern. The local peaks can be greatly reduced by placing the burnable poisons near the water channels. Where these channels are used for control rods, a reduction in control rod effectiveness may result which must be considered in the overall control available. Near the end-of-life the burnable poisons will be depleted; at the same time, the local power peaks will be considerably improved as a result of burnup of fuel in the high flux regions. For optimum results, it appears desirable to supplement the effect of the localization of the burnable poison by some local fuel redistribution.

The investigation of local power peaks and of corrective measures is usually accomplished by making a detailed study of the power distribution in a typical unit of the core (see Sect. 4.3). However, the following study is illustrative of results which may be obtained. In this study, which utilizes a single neutron group, the slowing-down density is taken as

proportional to the moderator density homogenized over each subregion.

The present data for a one-dimensional slab case result from the work of R.S. Halgas at Bettis Atomic Power Laboratory. However, the results for the more realistic two-dimensional cases are quite similar. As shown in Fig. 4.86, a typical unit of the core would consist of Region 3 representing the water hole, Region 2 the poison strip (which is assumed thin), and Region 1 the fuel plus moderator. Region 3 and Region 1 were assumed to have uniform slowing-down densities of 1 and 0.36, respectively. By proper adjustment of the amount of poison in Region 2, essentially all the neutrons produced in Region 3 will be absorbed in Region 2, resulting in a flat power distribution in Region 1. Actually, it is often preferable to overpoison, i.e., cause the flux peak to shift initially from Region 3 to Region 1.

Figure 4.87 shows some typical results of power peaking as a function of flux time for various burnable poison microscopic cross sections. The depletion calculations were of the

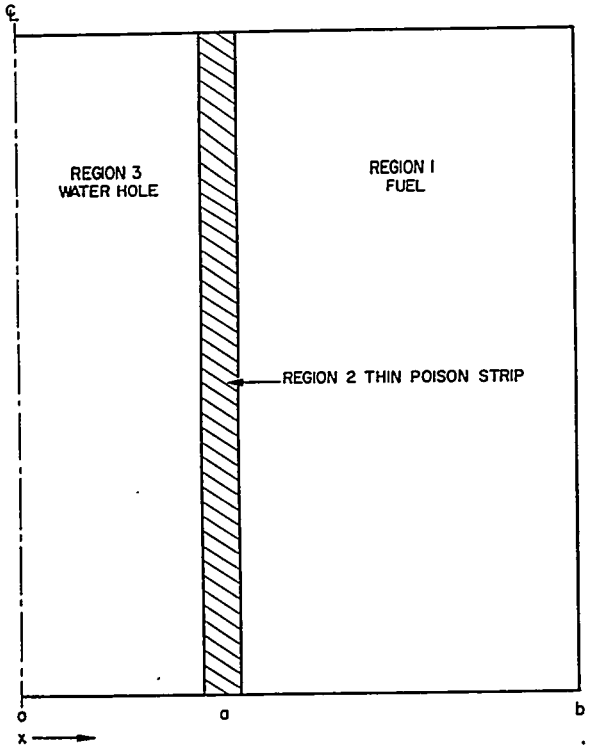

FIGURE 4.86. Geometric Arrangement, Infinite Slab Cell Having a Central Water Hole Bounded by a Thin Poison Region.

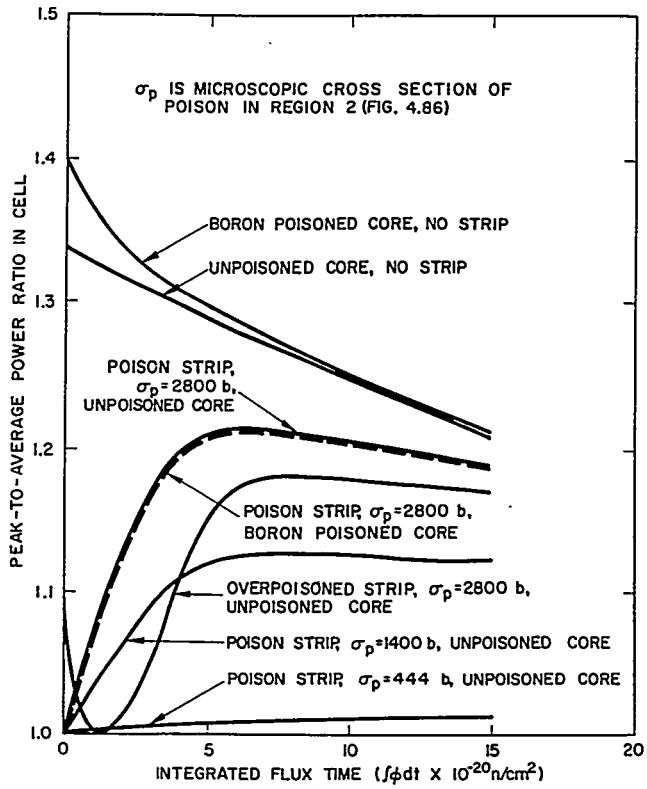

FIGURE 4.87. Peak-to-Average Power Ratio for Uniform Cell Depletion (Hot Equilibrium Xenon and Samarium).

cell type (Sect. 4.3), with each region depleted uniformly. Comparisons are given with the local peaking which occurs in cases in which the poison is uniformly distributed or in which no burnable poison is used in the fuel region. Note that an originally flat flux distribution tends to worsen with burnup, but the maximum peak during life is far lower than for the uniformly poisoned or unpoisoned core. The overpoisoned case has somewhat better power distribution over core life than the case for which the flux is flat at the beginning of life. If a finite poison strip is considered, the results do not differ qualitatively. A point-by-point depletion, in lieu of regional depletion, results in lower power peaks as a function of flux time but, again, does not change the results qualitatively.

F. Application of Burnable Poisons to Cores with High U^{238} Content Fuels

The preceding sections have dealt primarily with cores utilizing highly enriched U^{235}. Burnable poisons can also be

applied to cores utilizing fuels with large amounts of U^{238}. Such cores are of two principal types: (1) the seed-blanket design (Ref. 92 and Vol. II) in which a natural uranium blanket is driven by a highly enriched seed region; and (2) the slightly enriched types in which a uniformly low enrichment of U^{235} in U^{238} fuel is used in each region of the core.

The application of burnable poisons to a seed-blanket core is quite similar to that in a highly enriched core, since all control is concentrated in the seed with the blanket subcritical. However, the change of reactivity with fractional seed depletion may differ appreciably from a highly enriched core, depending upon the seed loading and the depletion of the blanket. For example, if the blanket properties were to remain constant, the reactivity worth of the blanket would decrease during the lifetime of a particular seed because, as the seed depletes and becomes less black, the blanket acts as a poorer reflector to the seed. On the other hand, this may be compensated during early seed loadings by a rather rapid buildup of blanket reactivity due to plutonium formation. These phenomena require careful study to ensure that the self-shielding of the burnable poison is chosen properly to match the reactivity changes of the fuel materials.

In a seed-blanket core, the amount of reactivity which must be controlled by burnable poisons is usually small relative to a highly enriched core because the seed is ordinarily designed as a highly buckled region in order to provide the maximum leakage into the blanket and, thus, increase the fraction of total core power generated from natural uranium. It is evident from Eq. (4.319), by writing the factors in terms of the buckling, B^2, that the value of T, the integrated flux time, attained at the end of life and, therefore, the fraction of fuel depleted, increase with the buckling for a given mismatch of reactivity.

Figure 4.88 shows schematically the arrangement of burnable poison in the Shippingport Core 2 design. The burnable poison was boron, located at the corner of the seed clusters in order to suppress power peaks. The power distribution in the seed was further improved by use of three regions of fuel zoning. The relatively narrow burnable poison plates made it possible, during the course of the design work, to vary independently the self-shielding of the poison (by changing the boron concentration) and the total amount of the poison by changing the width of the plates without necessitating other changes in the seed design.

In slightly enriched cores, the initial reactivity level of the core material, the variation of reactivity throughout lifetime, and the integrated flux time obtainable, increase monotonically with the enrichment. From some elementary studies, the use

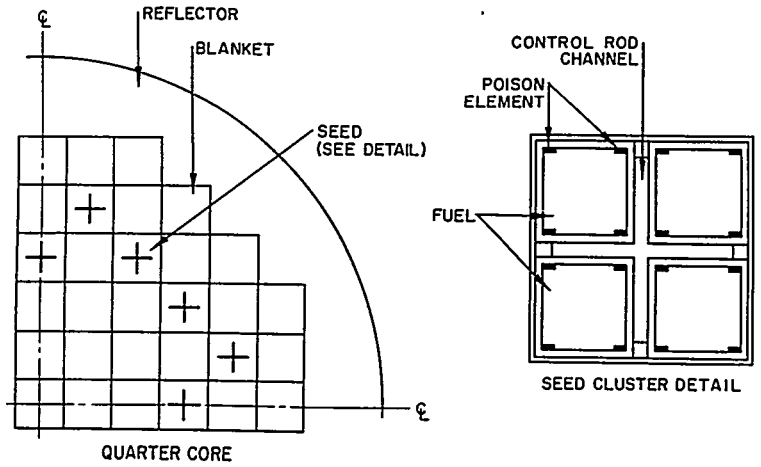

FIGURE 4.88. Schematic Arrangement of Burnable Poison in Shipping-port Core 2 Geometry.

of boron as a burnable poison appears to work out satisfactorily for slightly enriched cores, resulting in a close reactivity match and small residue of poisons. For the lower enrichments, the amount of burnable poison needed is relatively small, and a lower degree of self-shielding is acceptable. From Ref. 93, the following initial values of γ for boron as a burnable poison [(Eq. (4.326)] are optimum for various enrichments:

Enrichment (w/o U^{235})	Initial Value of γ for Burnable Poison
2	1.25
3	1.9
4	2.1

The above values assume batch loading. For cyclic loading of slightly enriched fuels, it has been assumed in present studies that the burnable poison would be replaced at each shift of fuel, although it is conceivable that a combination of burnable poisons of different self-shieldings would function satisfactorily through the complete life cycle of the fuel.

Up to the present time, the actual application of burnable poisons to slightly enriched reactors has been relatively limited. In the Dresden boiling water reactor, pellets of dysprosium oxide are used in the ends of the fuel elements.[94] In the Indian Point uranium-thorium reactor, uniform boron has been incorporated in the fuel element clad.[95]

G. Advanced Applications of Burnable Poison

The possibility of maintaining the reactivity of highly enriched thermal cores nearly constant with lifetime through the use of burnable poisons suggests the idea of leaving large sections of a reactor uncontrolled and of concentrating mechanical control in a small region of the reactor (see Fig. 4.89). This would usually permit a reduction in the total mechanical control needed.

Essentially, such reactors, while highly enriched, would be of the seed type, with the seed, a supercritical section containing all the controls, and the blanket, a subcritical region producing the major portion of the reactor power. From the control standpoint, the blanket need not be made of natural uranium. Its fuel can be of any enrichment; no fertile material is necessary. The only essential is that the blanket reactivity be so adjusted that at all times the reactor is subcritical with the control rods inserted in the seed. This involves a suitable choice of fuel, poison, and poison self-shielding in the blanket.

The division of power between seed and blanket is given approximately by:

$$\frac{\text{Power in Blanket}}{\text{Power in Seed}} = \frac{(\text{Seed Multiplication Factor} - 1)}{(\text{Seed Multiplication Factor})} \cdot \frac{(\text{Blanket Multiplication Factor})}{(1 + \text{Blanket Leakages} - \text{Blanket Multiplication Factor})} \quad \text{Eq. (4.331)}$$

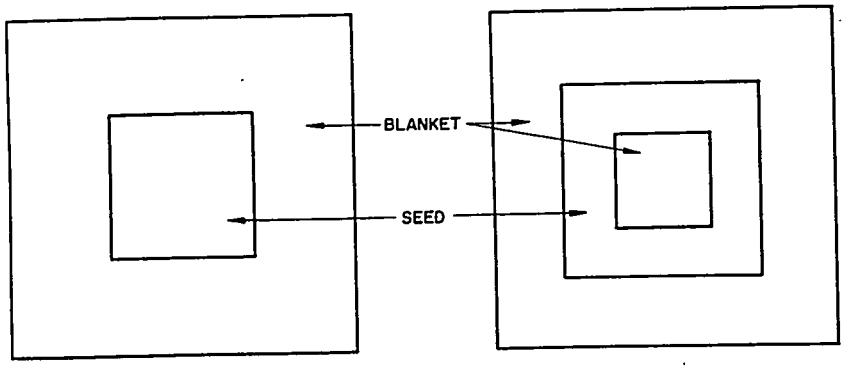

FIGURE 4.89. Seed-Blanket Cores.

In Eq. (4.331) the blanket fast effect has been treated as equal to unity, i.e., the highly enriched case. It is apparent from the formula that the power in the blanket region will be quite sensitive to the blanket multiplication factor. Thus, the use of burnable poisons, by maintaining the blanket multiplication factor nearly constant, will play a key role. Burnable poisons may also be utilized in the seed to minimize mechanical controls there. Several zones of enriched fuel can be utilized to flatten power in the blanket.

A reactor of this type has the disadvantage of relatively high power density in the rod-controlled zone. On the other hand, the use of a high buckling in the controlled zone with leakage into the uncontrolled zone should result in a large magnitude of negative temperature coefficient which is otherwise difficult to obtain in a large reactor. Furthermore, the fact that the multiplication factors in various regions of the core remain nearly constant throughout life tends to result in the power division in these regions remaining constant and favors the use of constant orificing of the coolant flow.

It is often useful to think of the two regions (rodded and unrodded) as separate cores. The unrodded region must be subcritical at room temperature and, therefore, must be subcritical during core operation by, at least, the amount of the cold-to-hot reactivity defect plus equilibrium xenon. The subcriticality of the blanket region could be reduced by the use in the blanket of suitable poisons of some material which would decrease in absorption relative to fuel with increase in neutron temperature. Such poisons could not be used in a uniform reactor because of the possibility of introducing a positive temperature coefficient of reactivity. Another possibility would be to use burnable poison materials in the blanket which had a relatively high residue. In such a location of low statistical weight, these materials would not increase the fuel loading of the core unduly.

H. Use of Burnable Poisons in Epithermal Reactors

While this subject is treated in detail in Vol. III, a brief resume is given here for completeness of discussion. In cores operating in the epithermal energy region, the chief problem in the application of burnable poisons is to find a poison of sufficiently high cross section relative to fuel to minimize the poison residue. Multigroup methods have been used to carry out the life history studies. Analytic methods have not been too fruitful because of the many complications associated with poison resonance structures and with changing spectrum during core life.

Studies have been carried out at Knolls Atomic Power Laboratory on a reactor model in which, by mechanical means, control is exercised by varying the fraction of boron in the core reflector. The following are the approximate core parameters for the studies outlined here: core radius, 40 cm; reflector radius, 58 cm; core contains $0.06 \times 10^{+24}$ nuclei/cc of beryllium; reflector contains $0.09 \times 10^{+24}$ nuclei/cc of beryllium; fuel content is approximately 50 kg highly enriched U; principal burnable poisons which have been investigated are boron, hafnium, and cadmium.

Figure 4.90 shows some typical results obtained. In each case, the relative amounts of fuel and poison were such as to maintain a constant amount of subcriticality when the same control elements were operated to shut down the core. Cadmium appears to be the most efficient burnable poison from the standpoint of increased endurance versus added fuel, i.e., cadmium had the least poison residue. The results are probably quite sensitive to the reactor spectrum.

An interesting aspect of the use of cadmium as the burnable poison is that if the added fuel exceeds about 14 kg, there appears to be a sharp drop, rather than gain, in the reactor

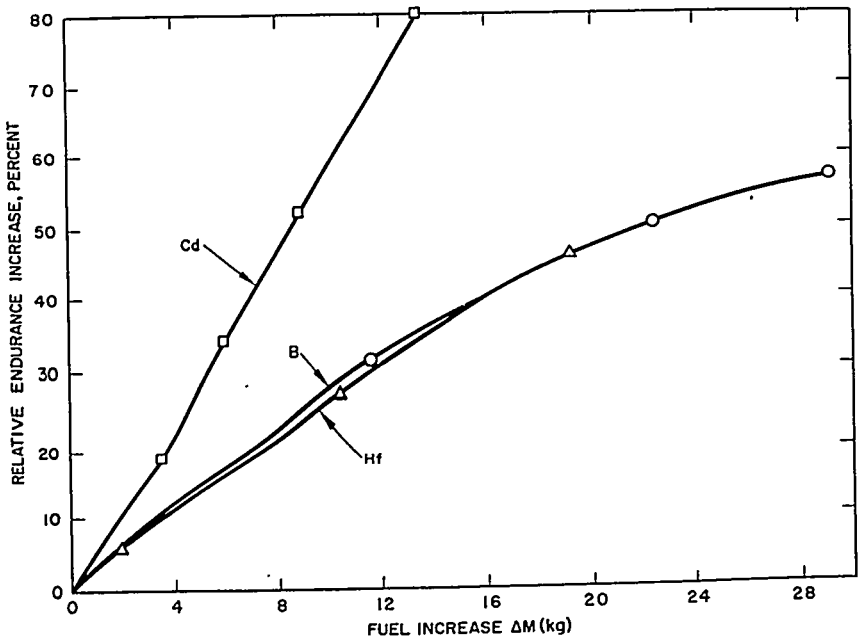

FIGURE 4.90. Variation of Endurance Increase as a Function of Fuel Increase When Unshielded Boron, Cadmium, and Hafnium are Used as Burnable Poisons in an Epithermal Reactor.

endurance. The explanation is to be found in the fact that after a sufficient concentration of cadmium is reached, the reactivity worth of the cadmium becomes very sensitive to the reactor spectrum. In the shutdown condition, the reflectors are poisoned by boron, and the core spectrum of neutrons causing fission is relatively high in energy. In the operating condition, the boron is removed from the reflector, and as a result the core spectrum becomes much more nearly thermal. The worth of the cadmium then increases markedly, so that the excess reactivity of the core is greatly reduced.

In conclusion, the use of burnable poisons appears to be feasible from physics consideration in epithermal cores, although the amount of poison residue and, consequently, the relative increase in fuel inventory for a given gain in endurance are much greater than in thermal cores.

REFERENCES

1. Naval Reactors Branch, Division of Reactor Development, U.S. Atomic Energy Commission; Westinghouse Electric Corporation, Bettis Plant; and Duquesne Light Company, "The Shippingport Pressurized Water Reactor," Addison-Wesley Publishing Company, Inc., Reading, Massachusetts, 1958.

2. H. Hurwitz, Jr., and P.F. Zweifel, "Self-Shielding of Lumped-Poison Mixtures," Nucl. Sci. Eng. 1, 438-440 (1956).

3. K. M. Case, F. de Hoffmann, and G. Placzek, "Introduction to the Theory of Neutron Diffusion, Vol. I," U.S. Government Printing Office, Washington, D.C., 1953.

4. W.R. Burrus, "How Channeling between Chunks Raises Neutron Transmission through Boral," Nucleonics 16 (1), 91-94 (1958).

5. W.R. Burrus, "Radiation Transmission through Boral and Similar Heterogeneous Materials Consisting of Randomly Distributed Absorbing Chunks," ORNL-2528, January 1960.

6. C. Eisenhart and M. Zelen, "Elements of Probability," Chapter 12 in Part 1, "Mathematics" in "Handbook of Physics," E.U. Condon and H. Odishaw, Eds., pp. 1-134 to 1-164, McGraw-Hill Book Company, Inc., New York, 1958.

7. D. Hilbert and S. Cohn-Vossen, "Geometry and Imagination," p. 47, Chelsea Publishing Company, New York, 1952.

8. V.L. Sailor, H.L. Foote, Jr., H.H. Landon, and R.E. Wood, "High Resolution Crystal Spectrometer for Neutrons," Rev. Sci, Instr. 27, 26-34 (1956).

9. B. Davison, "Neutron Transport Theory," Clarendon Press, Oxford, 1957.

10. M.S. Bartlett, "An Introduction to Stochastic Processes with Special Reference to Methods and Applications," University Press, Cambridge, England, 1955.

11. D.S. Selengut, "Variational Analysis of Multi-Dimensional Systems" in "Nuclear Physics Research Quarterly Report for October, November, December 1958," HW-59126, January 1959, pp. 89-124.

12. C.H. Randall, "The Central Problem of Dispersion Analysis," KAPL-M-CHR-4, February 1961.

13. C.H. Randall, "Microscopic Effects in Multiphase Mediums (Neutron Self-Shielding)," KAPL-M-CHR-2, May 1960.

14. C.H. Randall, "Microscopic Self-Shielding" in "Reactor Technology Report No. 15 — Physics," KAPL-2000-12, December 1960, pp. III.15-III.21.

15. C.H. Randall, "Stochastic Models for Heterogeneous Materials. I. (Large Scale Inhomogeneities and Neutron Transmission)," KAPL-M-CHR-6, August 1962.

16. M. Halperin, "Some Asymptotic Results for a Coverage Problem," Ann. Math. Statistics 31, 1063-1076 (1960).

17. H. Cramer, "Mathematical Methods of Statistics," Princeton University Press, Princeton, 1946.

18. A.F. Henry, "A Theoretical Method for Determining the Worth of Control Rods," WAPD-218, August 1959.

19. E.H. Bareiss, "Flexible Transport Theory Routines for Nuclear Reactor Design," David Taylor Model Basin Report DTMB-1030, December 1956.

20. L. Hageman, "HERD 1, 2, and 3 — IBM-704 Codes Used to Solve the One-Dimensional, One-Velocity Transport Equation with Isotropic Scattering," WAPD-TM-162, January 1959.

21. B.L. Anderson, J.A. Davis, E.M. Gelbard, and P.H. Jarvis, "FLIP — An IBM-704 Code to Solve the P_L and Double P_L Equations in Slab Geometry," WAPD-TM-134, March 1959.

22. N.C. Francis and K.R. Edgar, "Multigroup Treatment of Thermal Neutrons" in "Reactor Technology Report No. 19 — Physics," KAPL-2000-16, December 1961, pp. II.9-II.17.

23. E.L. Wachspress, "Thin Regions in Diffusion Theory Calculations," Nucl. Sci. Eng. 3, 186-200 (1958).

24. M. Goldsmith, R.T. Jones, T.M. Ryan, S. Kaplan, and A.D. Voorhis, "Theoretical Analysis of Highly Enriched Light Water Moderated Critical Assemblies" in "Proceedings of the Second United Nations International Conference on the Peaceful Uses of Atomic Energy, Geneva, 1958," Vol. 12, pp. 435-445, United Nations, Geneva, 1958.

25. W.W. Clendenin, "Resonance Escape Probability in Hydrogenous Lattices," Nucl. Sci. Eng. 5, 1-4 (1959).

26. S. Stein, "Resonance Capture in Heterogeneous Systems," WAPD-139, November 1955.

27. D.J. Hughes and J.A. Harvey, "Neutron Cross Sections," BNL-325, U. S. Government Printing Office, Washington, D. C., July 1, 1955.

28. H. Bohl, Jr., E.M. Gelbard, G.R. Culpepper, and P.F. Buerger, "P1MG — A One-Dimensional Multigroup P_1 Code for the IBM-704," WAPD-TM-135, July 1959.

29. E.M. Gelbard, G.J. Habetler, and R. Ehrlich, "The Role of Digital Computers in the Design of Water Moderated Reactors" in "Proceedings of the Second United Nations International Conference on the Peaceful Uses of Atomic Energy, Geneva, 1958," Vol. 16, pp. 473-482, United Nations, Geneva, 1958.

30. H. Bohl, Jr., and A.P. Hemphill, "MUFT-5 — A Fast Neutron Spectrum Program for the Philco-2000," WAPD-TM-218, February 1961.

31. O.J. Marlowe and M.C. Suggs, "WANDA-5 — A One-Dimensional Neutron Diffusion Equation Program for the Philco-2000 Computer," WAPD-TM-241, November 1960.

32. H. Bohl, Jr., E. Gelbard, P. Buerger, and G. Culpepper, "SLOP-1 — A Thermal Multigroup P_1 Code for the IBM-704," WAPD-TM-188, October 1960.

33. J.J. Berwind and J. Spanier, "TRAC-1 — A Monte Carlo Philco-2000 Program for the Calculation of Neutron Probabilities," WAPD-TM-229, March 1961.

34. W.R. Cadwell, "PDQ-4 — A Program for the Solution of the Neutron-Diffusion Equations in Two Dimensions on the Philco-2000," WAPD-TM-230, June 1961.

35. E.M. Gelbard, H.B. Ondis, and J. Spanier, "MARC — A Multigroup Monte Carlo Program for the Calculation of Capture Probabilities," WAPD-TM-273, May 1962.

36. M.A. Martino and W.W. Stone. "TRAM, A Monte Carlo Thermal Neutron Code for the IBM-704," KAPL-2039, June 1959.

37. R.D. Richtmyer, R. Van Norton, and A. Wolfe, "The Monte Carlo Calculation of Resonance Capture in Reactor Lattices" in "Proceedings of the Second United Nations International Conference on the Peaceful Uses of Atomic Energy, Geneva, 1958," Vol. 16, pp. 180-186, United Nations, Geneva, 1958.

38. B.L. Spinrad, "Anisotropic Diffusion Lengths in Diffusion Theory," J. Appl. Phys. 26, 548-550 (1955).

39. Ya. V. Shevelev, "Neutron Diffusion in a One-Dimensional Uranium-Water Lattice," J. Nucl. Energy 6, 132-141 (1957).

40. Ya. V. Shevelev, "The Thermal Utilization in a Close-Packed Lattice," J. Nucl. Energy 6, 121-131 (1957).

41. L. Trlifaj, "A Variational Method for the Homogenization of a Heterogeneous Medium," J. Nucl. Energy 6, 142-154 (1957); also available as AEC-tr-3349.

42. L. Trlifaj, "On the Anisotropy of a Heterogeneous Medium with Respect to the Diffusion of Neutrons. I," Czech. J. Phys. 7, 397-409 (1957).

43. L. Trlifaj, "On the Anisotropy of a Heterogeneous Medium with Respect to the Diffusion of Neutrons. II," Czech, J. Phys. 7, 523-532 (1957).

44. D.S. Selengut, "Diffusion Coefficients for Heterogeneous Systems" in "Nuclear Physics Research Quarterly Report for January, February, March 1959," HW-60220, April 1959, pp. 65-84.

45. B. Davison, "Effective Thermal Diffusion Length in a Sandwich Reactor," J. Nucl. Energy 7, 51-68 (1958).

46. K.N. Mukhin, V.K. Makar'in, and A.P. Venediktov, "Diffusion of Thermal Neutrons in Anisotropic Media," AEC-tr-4716, 1960.

47. L. Dresner, "Resonance Absorption in Nuclear Reactors," Chap. 5, Pergamon Press, Inc., New York, 1960.

48. G.N. Watson, "A Treatise on the Theory of Bessel Functions," 2nd Ed., The Macmillan Company, New York, 1944.

49. R.S. Wick, "Resonance Escape Probability Calculations in Non-Uniform Lattice Arrays" in "Bettis Technical Review, Reactor Physics and Mathematics," WAPD-BT-17, February 1960, pp. 1 - 13.

50. L. Nordheim, "The Theory of Resonance Absorption" in "Nuclear Reactor Theory. Proceedings of Symposia in Applied Mathematics, Vol. XI," G. Birkhoff and E.P. Wigner, Eds., pp. 58-88, American Mathematical Society, Providence, 1961.

51. J.J. Kepes, L.A. Mikoleit, and R.G. Serenka, "Resonance and Total Uranium-238 Activations in Thin Natural Uranium-Niobium Fuel Plates," Trans. Am. Nucl.Soc.3,210-211 (1960).

52. D.H. Jones, "Three Dimensional Flux Distributions in a Rod-Programmed Seed-Blanket Slab Reactor" in "Bettis Technical Review, Reactor Physics and Mathematics," WAPD-BT-17, February 1960, pp. 25-29.

53. "Pressurized Water Reactor (PWR) Project, Technical Progress Report for the Period August 24 to October 23, 1960," WAPD-MRP-88, p. 67.

54. J.E. Meyer, "Synthesis of Three-Dimensional Power Shapes — Flux Weighting Technique" in "Bettis Technical Review, Reactor Physics and Mathematics," WAPD-BT-4, October 1957, pp. 29-41.

55. R.B. Horst, "Synthesis Methods in R-Z Geometry" in "Bettis Technical Review, Reactor Physics and Mathematics," WAPD-BT-8, June 1958, pp. 26-38.

56. T.W. Ball, "Synthesis of Lifetime Power Distributions in R-Z Geometry" in "Bettis Technical Review, Reactor Physics and Mathematics," WAPD-BT-8, June 1958, pp. 39-45.

57. W.N. Lorentz, "Synthesis of Three Dimensional Power Shapes — Application of Flux-Weighted Synthesis Technique" in "Bettis Technical Review, Reactor Physics and Mathematics," WAPD-BT-8, June 1958, pp. 46-52.

58. E.L. Wachspress, "Digital Computation of Space-Time Variation of Neutron Fluxes," KAPL-2090, October 1960.

59. S. Glasstone and M.C. Edlund, "The Elements of Nuclear Reactor Theory," pp. 90-189, D. Van Nostrand Company, Inc., New York, 1952.

60. E.L. Wachspress, "The Numerical Solution of Boundary Value Problems" in "Mathematical Methods for Digital Computers," A. Ralston and H. S. Wilf, Eds., pp. 121-128, John Wiley and Sons, Inc., New York, 1960.

61. E.H. Auerbach, J.P. Jewett, and M.A. Ketchum, "UFO: A Three-Dimensional Neutron Diffusion Code for the IBM-704," KAPL-1999, March 24, 1959.

62. G.P. Calame and F.D. Federighi, "A Variational Procedure for Determining Spatially Dependent Thermal Spectra," Nucl. Sci. Eng. 10, 190-201 (1961).

63. L.V. Kantorovich and V.I. Kryloff, "Approximate Methods of Higher Analysis," Interscience Publishers, Inc., New York, 1959.

64. S.H. Gould, "Variational Methods for Eigenvalue Problems," University of Toronto Press, Toronto, 1957.

65. F.B. Hildebrand, "Methods of Applied Mathematics," Prentice-Hall, Inc., New York, 1952.

66. S.H. Crandall, "Engineering Analysis; A Survey of Numerical Procedures," McGraw-Hill Book Company, Inc., New York, 1956.

67. W.J. Duncan, "The Principles of the Galerkin Method," Aeronautical Research Committee Technical Report No. 1848, September 1938.

68. T.R. England, "Time Dependent Fission Product Thermal and Resonance Absorption Cross Section," WAPD-TM-333, November 1962.

69. R.W. Deutsch, "Computing 3-Group Constants for Neutron Diffusion," Nucleonics 15 (1), 47-52 (1957).

70. E.C. Hansen, "Simple Estimates of Effective Thermal and Resonance Cross Sections" in "Reactor Technology Report No. 19 - Physics," KAPL-2000-16, December 1961, pp. III.11-III.23.

71. E.L. Ince, "Ordinary Differential Equations," Dover Publications, Inc., New York, 1944.

72. S. Katcoff, "Fission Product Yields from U, Th, and Pu," Nucleonics 16 (4), 78-85 (1958).

73. D.J. Hughes and R.B. Schwartz, "Neutron Cross Sections," BNL-325 (2nd Ed.), U.S. Government Printing Office, Washington, D.C., July 1, 1958.

74. J.D. Garrison and B.W. Roos, "Fission-Product Capture Cross Sections," Nucl. Sci. Eng. 12, 115-134 (1962).

75. C.R. Greenhow and E.C. Hansen, "Thermal and Resonance Fission Product Poisoning for U^{235} Systems," KAPL-2172, October 1961.

76. W.H. Walker, "Yields and Effective Cross Sections of Fission Products and Pseudo Fission Products," CRRP-913, March 1960.

77. E.C. Hansen, "A Critical Examination of the Uncertainties in Predicted Gross Fission Product Poisoning," KAPL-M-ECH-8, March 1962.

78. E.C. Hansen and C.R. Greenhow, "An Improved Generalized Analysis of Fission Product Poisoning," Trans. Am. Nucl. Soc. 3, 403-404 (1960).

79. J.D. Callaghan, L.M. Culpepper, J.G. Fairey, E.M. Gelbard, C.M. King, T.J. Lawton, O.J. Marlowe, and D.S. McCarty, "TURBO — A Two Dimensional Few-Group Depletion Code for the IBM-704," WAPD-TM-95, November 1957.

80. R.P. Schumann and J.R. Berreth, "Neutron Activation Cross Sections of Pm^{147}, Pm^{148}, and Pm^{149}," Nucl. Sci. Eng. 12, 519-522 (1962).

81. F.D. Judge and E.C. Hansen, "Self-Shielding of Fission Product Resonances," Trans. Am. Nucl. Soc. 5, 370-371 (1962).

82. E.A. Nephew, "Thermal and Resonance Absorption Cross Sections of the U^{233}, U^{235}, and Pu^{239} Fission Products," ORNL-2869, March 1960.

83. O.J. Marlowe, "Nuclear Reactor Depletion Programs for the Philco-2000 Computer," WAPD-TM-221, January 1961.

84. W.R. Clancey, "Variation Throughout Reactor Lifetime of the Regeneration Factor, η, for Slightly Enriched Uranium," WAPD-93, December 1953.

85. C.J. Pfeifer and F.R. Urbanus, "ZIP-2 — A One-Dimensional Few-Group Synthesis Nuclear Reactor Depletion Program for the Philco-2000 Computer," WAPD-TM-228, November 1961.

86. A Radkowsky, "Theory and Application of Burnable Poisons" in "Proceedings of the Second United Nations International Conference on the Peaceful Uses of Atomic Energy, Geneva, 1958," Vol. 13, pp. 426-445, United Nations, Geneva, 1958.

87. R.W. Dayton, W.S. Hogan, W.A. Northrop, A. Radkowsky, and D.N. Schmoker, "Control Materials Theory and Calculations for Thermal Reactors" in "Neutron Absorber Materials for Reactor Control," W.K. Anderson and J.S. Theilacker, Eds., pp. 41-152, U. S. Government Printing Office, Washington, D.C., 1962.

88. R.C. Dahlberg and F.D. Judge, "The Depletion of Burnable Poison in Endurance Calculations," KAPL-2058, March 1960.

89. J.H. Leonard and P.H. Wackman, "Lumped Burnable Poisons — III: Applications," Trans. Am. Nucl. Soc. 1 (1), 132-134 (1958).

90. N.G. Demas and R.C. Shank, "Self-Shielded Boron Representation for PWR-2," WAPD-T-1384, September 1961.

91. D.A. Gavin, J.J. Bulmer, and T.F. Ruane, "Experiments and Calculations with Reactivity Equivalent Burnable Poisons," Trans. Am. Nucl. Soc. 3 (2), 494-495 (1960).

92. A. Radkowsky and R.T. Bayard, "The Physics Aspects of Seed and Blanket Cores with Examples from PWR" in "Proceedings of the Second United Nations International Conference on the Peaceful Uses of Atomic Energy, Geneva, 1958," Vol. 13, pp. 128-145, United Nations, Geneva, 1958.

93. F. Schwoerer, "Economic Potential of the Seed-Blanket Reactor," WAPD-237, December 1960.

94. "Amendment No. 1 to Preliminary Hazards Summary Report for the Dresden Nuclear Power Station," GEAP-3009, May 1958.

95. H.S. Barringer, R.B. Flickinger, and S.W. Spetz, "Consolidated Edison Thorium Reactor Physics Design," Rev. 1, BAW-120, July 1960.

Chapter 5

REACTOR KINETICS

J. N. Grace, Editor

5.1 INTRODUCTION

The design of a naval reactor plant requires thorough analysis of dynamic behavior to assure satisfactory performance. There can be no tolerance of system instabilities arising after construction, since correction might entail significant design changes. Furthermore, the design of control and protection systems requires knowledge of reactor transient response to both normal maneuvers and system malfunctions. Consequently, the objective of the kinetics effort in the Naval Reactors program has been to develop methods of analysis to predict reactor stability and transient performance.

In the ensuing review of typical analytical methods in reactor kinetics developed in the Naval Reactors program, the material is limited, wherever practical, to the nuclear aspects. However, to take into account all phenomena which feed back upon reactor behavior, it is often necessary to include analysis of heat transfer, fluid flow, and plant dynamics.

The discussion of methods of reactor stability and transient analysis begins with the derivation of basic neutron kinetics equations in Sect. 5.2. The time-dependent diffusion equations are reduced to a set of ordinary differential equations by assuming separability of the space and time solutions. These equations are applicable to most reactor kinetics problems. Certain parameters appear in the kinetics equations, and methods for determining their values are presented in the latter part of Sect. 5.2.

The reactor kinetics equations are applied in Sect. 5.3, where methods of analysis of inherent reactor stability are developed. First, in Sect. 5.3.A, the effects on reactor stability of xenon and coolant pressure variations in the presence of a negative temperature coefficient are analyzed. These analyses were developed rather early in the program

(before 1954) when self-regulation through a negative temperature coefficient of reactivity was first being exploited. Later, the effects of boiling on reactor stability were analyzed, supplementing the early experimental work done at Argonne National Laboratory. These methods for predicting performance under boiling conditions are described in Sect. 5.3.B. Finally, in Sect. 5.3.C, the inherent ability of a reactor to limit a runaway power transient is examined. Exhaustive experimental investigations of power excursions have been conducted at the SPERT facilities in Idaho for aluminum and stainless steel cores, both pressurized and unpressurized. Some progress has been made in the analysis of these transients; however, much remains to be done.

The natural stability of the power distribution within a reactor and the transient response to nonuniform perturbations are discussed in Sect. 5.4. Several methods of analysis involving either modal expansions of the power distribution or nodal divisions of the reactor into coupled regions are presented. The methods are useful in the study of flux tilt transients caused by unbalances in the power plant or nonuniform rod motion. Xenon-induced, self-sustaining oscillations of the power distribution are treated in some detail, and stability criteria are developed. The subject of space-time kinetics becomes more important as cores grow larger because of reduced neutron coupling between parts of the larger system.

In all of the foregoing sections, it is assumed that neutron population and power level are continuous functions of time. This is a valid assumption when producing significant amounts of power and even at zero power when a sufficiently large neutron source exists, whether natural or artificial. However, source strengths can be so low that the continuous treatment is no longer valid, and reactor behavior must be studied as a stochastic process, taking into account statistical fluctuations in neutron population. In Sect. 5.5, two methods of analysis of low level reactor transients are presented. One method involves direct integration of the forward stochastic equation, but depends on the assumption that the prompt neutron generation time is zero. This limitation does not exist in the other method, which involves solution of kinetics equations for the moments of the probability distribution. However, knowledge of the form of the probability distribution is required. The methods of analysis are applied to experiments performed at Los Alamos Scientific Laboratory. Section 5.5 also includes a summary of the contributions to the natural source level from spontaneous fission, (α, n) reactions, photoneutron production, and cosmic rays.

5.2 NEUTRON KINETICS

A. F. Henry

A. Derivation of the Kinetics Equations

A. F. Henry

To describe in detail the space-time behavior of the neutron flux in a reactor is difficult. The physical source of this difficulty is the fact that the prompt component of the neutrons emitted in fission reacts to changes in local environment almost instantaneously, while the component due to neutrons from delayed emitters changes relatively slowly. Thus, numerical methods for solving the equations which specify the space-time behavior must use very small time steps to account for prompt neutron behavior, yet must describe a time span sufficiently long that delayed neutron effects are included. Since the major part of the numerical difficulty is associated with the spatial part of the problem, the traditional approach has been to neglect changes in flux shape and to concentrate on describing accurately the behavior in time of the overall neutron population or power level. This neglect is justified in a great many applications, particularly if the perturbations giving rise to the transient behavior are small.

When changes in flux shape are neglected, the time-dependent transport equation and the equations specifying the behavior of the delayed neutron emitters can be integrated over all direction, position, and energy to yield differential equations in time alone. By suitable definitions of the quantities, reactivity, prompt neutron lifetime, etc. (to be discussed below), these equations can be cast into a form generally referred to as the reactor kinetics equations. In principle, a solution of the reactor kinetics equations derived in this manner leads to a complete specification of the space-time behavior of the directional flux and delayed emitter concentrations.

In practice, the fact that the flux shape is practically never constant during a transient can lead to significant errors if the derivation of the kinetics equations just outlined is actually carried out. Specifically, the theoretical expression derived for the reactivity by such a procedure can lead to errors of the same order of magnitude as the reactivity itself. To circumvent this difficulty, while still retaining the approximation of constant flux shape, an adjoint flux was introduced at an early stage[1,2] into derivations of the kinetics

equations. It has been used in the increasingly general derivations that have appeared since then.[3,4,5,6]

The derivation presented in this section is a slight generalization of that given in Ref. 7. In this particular procedure, space-time separability of the flux is not assumed. Hence, for reactor configurations involving stationary fuel, the resulting equations are formally equivalent to the time-dependent transport equation. Since, however, the actual kinetics equations which result are identical in form with those derived by approximate methods, a more precise statement of the approximations required in practical cases is possible.

For reactor systems in which the fuel is stationary, time behavior is described by the following equations:

$$-\vec{\Omega}\cdot\nabla\mathcal{F}(\vec{r},\vec{\Omega},u,t)-\Sigma(\vec{r},u,t)\mathcal{F}(\vec{r},\vec{\Omega},u,t)$$

$$+\int_{\Omega'}\int_0^\infty d\Omega'\,du'\left\{\Sigma_s(\vec{r},u',u,\vec{\Omega}'\cdot\vec{\Omega},t)\right.$$

$$\left.+\frac{1}{k}\sum_j\left[f^j(u)\nu^j(u')(1-\beta^j)\right]\Sigma_f^j(\vec{r},u',t)\right\}\mathcal{F}(\vec{r},\vec{\Omega}',u',t)+S(\vec{r},\vec{\Omega},u,t)$$

$$+\sum_i\lambda_i C_i(\vec{r},t)f_i(u)=\frac{\partial}{\partial t}\left[\frac{\mathcal{F}(\vec{r},\vec{\Omega},u,t)}{v(u)}\right] \qquad \text{Eq. (5.1)}$$

and

$$\frac{\partial C_i(\vec{r},t)}{\partial t}=\int_{\Omega'}\int_0^\infty d\Omega'\,du'\,\frac{1}{k}\sum_j\nu^j(u')\beta_i^j\Sigma_f^j(\vec{r},u',t)\mathcal{F}(\vec{r},\vec{\Omega}',u',t)-\lambda_i C_i(\vec{r},t)$$

Eq. (5.2)

where

$\mathcal{F}(\vec{r},\vec{\Omega},u,t)$ = the directional flux density at point $\vec{r}$ and time t for neutrons of lethargy u traveling in direction $\vec{\Omega}$.

$\Sigma(\vec{r},u,t)$ = the total macroscopic interaction cross section.

$\Sigma_s(\vec{r},u',u,\vec{\Omega}'\cdot\vec{\Omega},t)$ = the total macroscopic differential cross section for scattering from lethargy u' and direction $\vec{\Omega}'$ to u and $\vec{\Omega}$.

$\frac{1}{k}\sum_j \left[f^j(u)\nu^j(u')(1-\beta^j)\right]\Sigma_f^j(\vec{r},u',t)$ = the fission source term for prompt neutrons, $1/k$ being introduced for later mathematical convenience ($k = 1$ for physically realizable systems). Superscript j distinguishes the various fissionable isotopes. Thus, $\nu^j(u')$ is the total number of neutrons emitted from a fission of the j^{th} element; these have a spectrum $f^j(u)$ such that $\int_u f^j(u)du = 1$; $\Sigma_f^j(\vec{r},u',t)$ is the macroscopic fission cross section.

$S(\vec{r},\vec{\Omega},u,t)$ = the external source density.

$C_i(\vec{r},t)$ and λ_i = the concentration and decay constant of the i^{th} group of delayed neutron emitters.

$v(u)$ = the neutron speed corresponding to lethargy u.

$\frac{1}{k}\sum_j \nu^j(u')\beta_i^j\Sigma_f^j(\vec{r},u',t)$ = the source term for the i^{th} group of delayed neutron emitters. Subscript i refers to the various groups of delayed neutron emitters, the fraction of neutrons emitted from the i^{th} group due to a fission in element j being $\beta_i^j\left(\beta^j = \sum_i \beta_i^j\right)$; $f_i(u)$ represents the spectrum (normalized to unity) of delayed neutrons.

Equation (5.1) is the mathematical statement of the fact that, for an infinitesimal volume containing neutrons of lethargy u moving in direction $\vec{\Omega}$, the rate at which neutrons are removed from the volume (by leakage, scattering, or absorption) subtracted from the rate at which they are introduced (by scattering, fissioning, external source, or decay of delayed neutron emitters) equals the rate of increase of the number of this class of neutrons in the infinitesimal volume.

The time dependency allowed in the definition of the various cross sections is present primarily to account for

changes in molecular motion (temperature) and moderator density during a transient. The cross sections as written are already averages over molecular motion and, hence, in the thermal region depend on material temperatures.

The eigenvalue k provides a means of adjusting Eq. (5.1), so that time behavior predicted from it will not be merely the result of using incorrect cross sections or too gross an approximation. Thus, if Eq. (5.1) with $k = 1$ fails to predict a stationary state for a reactor known to be critical, k can be adjusted until the solution is stationary. Then, the adjusted value of k can be used in Eq. (5.1) to predict time behavior if the system is subsequently perturbed.

Equations in the time alone can be obtained from Eqs. (5.1) and (5.2) by the simple expedient of integrating over all space, direction, and lethargy. However, this procedure is impractical, since the time dependence of $\mathcal{F}(\vec{r}, \vec{\Omega}, u, t)$ is not in general separable, so that it would be necessary to know the instantaneous shape of $\mathcal{F}(\vec{r}, \vec{\Omega}, u, t)$ beforehand. Thus, a certain amount of mathematical manipulation is required to convert Eqs. (5.1) and (5.2) to a more conventional and tractable form.

It is of great practical help to introduce a source free adjoint equation[1, 4, 8] appropriate to some critical condition in the reactor (generally, the initial or asymptotic state). This equation is

$$\vec{\Omega} \cdot \nabla \psi_o^*(\vec{r}, \vec{\Omega}, u) - \Sigma_o(\vec{r}, u)\psi_o^*(\vec{r}, \vec{\Omega}, u) + \int_{\Omega'} \int_0^\infty d\Omega' \, du' \left[\Sigma_{so}(\vec{r}, u, u', \vec{\Omega}' \cdot \vec{\Omega}) + \frac{1}{k} \sum_j f_t^j(u') \nu^j(u) \Sigma_{fo}^j(\vec{r}, u) \psi_o^*(\vec{r}, \vec{\Omega}', u') \right] = 0 \qquad \text{Eq. (5.3)}$$

where subscripts zero indicate that the quantities correspond to a steady-state condition and

$$f_t^j(u') \equiv f^j(u')(1 - \beta^j) + \sum f_i(u') \beta_i^j \, .$$

The adjoint flux $\psi_o^*(\vec{r}, \vec{\Omega}, u)$ has the physical significance[4,8,9,10] of being proportional to the overall power level which will result asymptotically if neutrons of lethargy u having direction $\vec{\Omega}$ are introduced at point $\vec{r}$ in a critical reactor initially at zero power.

Next, it is convenient to partition the function $\mathcal{F}(\vec{r}, \vec{\Omega}, u, t)$ into a shape function $\psi(\vec{r}, \vec{\Omega}, u, t)$ and a time function $T(t)$, such that

$$\mathcal{F}(\vec{r}, \vec{\Omega}, u, t) \equiv \psi(\vec{r}, \vec{\Omega}, u, t) T(t) \, ; \; T(0) = 1 \qquad \text{Eq. (5.4)}$$

with the additional requirement that

$$\frac{\partial}{\partial t}\int_u \int_V \frac{\phi_o^*(\vec{r}, u)\phi(\vec{r}, u, t)}{v(u)}\,du\,dV = 0 \qquad \text{Eq. (5.5)}$$

where

$$\phi_o^*(\vec{r}, u) \equiv \int_\Omega \psi_o^*(\vec{r}, \vec{\Omega}, u)$$

$$\phi(\vec{r}, u, t) \equiv \int_\Omega \psi(\vec{r}, \vec{\Omega}, u, t)$$

and the integration is over all space and lethargy.

Mathematically, these definitions are made to permit replacement of

$$\frac{\partial}{\partial t}\int_u \int_V \frac{\phi_o^*(\vec{r}, u)\phi(\vec{r}, u, t)\,T(t)}{v(u)}\,du\,dV$$

by

$$\frac{dT(t)}{dt}\left[\int_u \int_V \frac{\phi_o^*(\vec{r}, u)\phi(\vec{r}, u, t)}{v(u)}\,du\,dV\right]$$

Physically, since $T(t)\phi(\vec{r}, u, t)/v(u)$ is just the number density of neutrons at point $\vec{r}$ having lethargy u, $T(t)$ times, the integral in Eq. (5.5) is proportional to the power level which will result asymptotically from the presence of these neutrons in the core for which ϕ_o^* is the adjoint. It follows that for a small perturbation any asymptotic change in power level is expressed by variation of the time function $T(t)$, it having been required that the factor

$$\int_u \int_V \frac{\phi_o^*(\vec{r}, u)\phi(\vec{r}, u, t)}{v(u)}\,du\,dV$$

be time-independent.

It is important to note that Eq. (5.4) is purely a definition and embodies no physical assumption. Equation (5.5) is a restrictive condition placed on the time-dependent shape function ψ and again requires no physical assumption. If the time dependence of $\mathcal{F}$ is separable (for example, if the flux is rising on an asymptotic period), ψ will be independent of time, and Eq. (5.5) will be obeyed automatically.

With the symbols <1>, <2>, and <3> representing the entire Eqs. (5.1), (5.2), and (5.3), the operations*

$$\int_V \int_u \phi_o^*(\vec{r}, u) \int_\Omega \langle 1 \rangle \, d\Omega - T(t)\phi(\vec{r}, u, t) \int_\Omega \langle 3 \rangle \, d\Omega \, dV \, du$$

and

$$\int_V \int_u \phi_o^*(\vec{r}, u) f_i(u) \langle 2 \rangle \, dV \, du$$

(integration being over all volume and lethargy), yield

$$\frac{dT}{dt} = \frac{\rho - \bar{\beta}}{\Lambda} T + \sum_i \lambda_i c_i + Q \qquad \text{Eq. (5.6a)}$$

$$\frac{dc_i}{dt} = \frac{\bar{\beta}_i}{\Lambda} T - \lambda_i c_i \qquad \text{Eq. (5.6b)}$$

where

$$\rho = \rho(t) \equiv \frac{1}{F} \int_V \int_u \left\{ -\phi_o^*(\vec{r}, u) \int_\Omega \vec{\Omega} \cdot \nabla \psi(\vec{r}, \vec{\Omega}, u, t) d\Omega \right.$$

$$- \phi(\vec{r}, u, t) \int_\Omega \vec{\Omega} \cdot \nabla \psi_o^*(\vec{r}, \vec{\Omega}, u) d\Omega - \delta\Sigma(\vec{r}, u, t) \phi_o^*(\vec{r}, u) \phi(\vec{r}, u, t)$$

$$+ \int_{u'} \delta \left[\Sigma_s^o(\vec{r}, u', u, t) + \frac{1}{k} \sum_j f_t^j(u) \nu^j(u') \Sigma_f^j(\vec{r}, u', t) \right] \phi_o^*(\vec{r}, u)$$

$$\left. \times \phi(\vec{r}, u', t) du' \right\} dV \, du \equiv \text{Reactivity} \qquad \text{Eq. (5.7)}$$

*By $\int_V \int_u \phi_o^*(\vec{r}, u) \int_\Omega \langle 1 \rangle \, d \, d\Omega$, for example, is meant: integrate both sides of Eq. (5.1) over all directions $\vec{\Omega}$; multiply the resulting equation by $\phi_o^*(\vec{r}, u)$, and integrate both sides over V and u.

$\delta\Sigma(\vec{r}, u, t)$, etc., representing the difference between the perturbed (in general, time-dependent) quantities in Eq. (5.1) and the unperturbed constants in Eq. (5.3),

$$F = F(t) \equiv \int_V \int_u \int_{u'} \sum_j f_i^j(u)\nu^j(u')\Sigma_f^j(\vec{r}, u', t) \times \phi_o^*(\vec{r}, u)\phi(\vec{r}, u', t)\, dV\, du\, du' \qquad \text{Eq. (5.8)}$$

$$\Lambda = \Lambda(t) \equiv \frac{1}{F} \int_V \int_u \frac{\phi_o^*(\vec{r}, u)\phi(\vec{r}, u, t)}{v(u)}\, dV\, du \equiv \text{Prompt neutron lifetime} \qquad \text{Eq. (5.9)}$$

$$\bar{\beta}_i = \bar{\beta}_i(t) \equiv \frac{1}{F} \int_V \int_u \int_{u'} \frac{1}{k} \sum_j \nu^j(u') f_i(u) \beta_i^j \Sigma_f^j(\vec{r}, u', t)$$

$$\times\, \phi_o^*(\vec{r}, u)\phi(\vec{r}, u', t)\, dV\, du\, du' \equiv \text{Effective delayed neutron fraction} \qquad \text{Eq. (5.10)}$$

$$c_i = c_i(t) \equiv \frac{1}{\Lambda F} \int_V \int_u C_i(\vec{r}, t) f_i(u) \phi_o^*(\vec{r}, u)\, dV\, du \qquad \text{Eq. (5.11)}$$

$$Q = Q(t) \equiv \frac{1}{\Lambda F} \int_V \int_u \int_\Omega \phi_o^*(\vec{r}, u) S(\vec{r}, \vec{\Omega}, u, t)\, dV\, du\, d\Omega\,. \qquad \text{Eq. (5.12)}$$

$\Sigma_s^o(\vec{r}, u', u, t)$ is the P_o component of $\Sigma_s(\vec{r}, u', u, \vec{\Omega}' \cdot \vec{\Omega}, t)$ expanded in Legendre functions of the cosine $\vec{\Omega}' \cdot \vec{\Omega}$.

The definition in Eq. (5.8) of F is arbitrary. That is, although the magnitudes of $\rho, \bar{\beta}$, and Λ are altered by changes in F, the kinetics Eqs. (5.6a) and (5.6b) are entirely independent of it. The particular definition used here is chosen so that the reactivity perturbation associated with fictitious alteration of the eigenvalue k is $\delta(1/k)$ [see Eq. (5.24)]. Had there been a desire to make this change equal δk, F would have been defined as Eq. (5.8) multiplied by $1/k$. This reduces to the perennial question of whether reactivity is more appropriately expressed as $(k_{\text{eff}}-1)/k_{\text{eff}}$ or as $(k_{\text{eff}}-1)$.* Evidently, it makes no difference, provided $\bar{\beta}$ and Λ are defined consistently with ρ.[11]

* The symbol, k_{eff}, here refers to the effective multiplication constant, rather loosely defined as (Production rate of neutrons due to fission) ÷ (Destruction rate by all processes).

More fundamentally, the fact that the present formalism allows an arbitrary choice of F implies that attempts to define ρ, Λ, or $\bar{\beta}$ as physical quantities have been abandoned. These quantities have an approximate significance, but it is difficult to make this precise except when the reactor system is rising or falling on an asymptotic period.

Equations (5.7) to (5.12) represent what might be called the diffusion theory form for the parameters of the kinetics equation. This terminology is not meant to imply any approximations in the expressions but rather that they have been obtained by integrating the neutron and adjoint equation over all directions before cross multiplication and subtraction, a procedure which yields results reducing in a straightforward manner to the common diffusion theory expressions. If, instead, with $\mathcal{F}(\vec{r}, \vec{\Omega}, u, t) \equiv \psi_t(\vec{r}, \vec{\Omega}, u, t) T_t(t)$, the equally valid procedure of integrating over $\vec{\Omega}$ after cross multiplication and subtraction[4] is used, expressions for ρ, Λ, c, and Q become

$$\rho_t \equiv \frac{1}{F_t} \int_V \int_u \int_\Omega \left\{ -\delta\Sigma(\vec{r}, u, t)\psi_o^*(\vec{r}, \vec{\Omega}, u)\,\psi_t(\vec{r}, \vec{\Omega}, u, t) \right.$$

$$+ \int_{u'} \int_{\Omega'} \delta \left[\Sigma_s(\vec{r}, \vec{\Omega}' \cdot \vec{\Omega}, u', u, t) + \frac{1}{k} \sum_j f_t^j(u)\nu^j(u')\Sigma_f^j(\vec{r}, u', t) \right]$$

$$\left. \psi_o^*(\vec{r}, \vec{\Omega}, u)\psi_t(\vec{r}, \vec{\Omega}', u', t)\,du'\,d\Omega' \right\} dV\,du\,d\Omega \qquad \text{Eq. (5.13)}$$

$$\Lambda_t \equiv \frac{1}{F_t} \int_V \int_u \int_\Omega \frac{\psi_o^*(\vec{r}, \vec{\Omega}, u)\psi_t(\vec{r}, \vec{\Omega}, u, t)}{v(u)}\, dV\,du\,d\Omega \qquad \text{Eq. (5.14)}$$

$$c_{it} \equiv \frac{1}{\Lambda_t F_t} \int_V \int_u \int_\Omega C_i(\vec{r}, t) f_i(u) \psi_o^*(\vec{r}, \vec{\Omega}, u)\,dV\,du\,d\Omega \qquad \text{Eq. (5.15)}$$

$$Q_t \equiv \frac{1}{\Lambda_t F_t} \int_V \int_u \int_\Omega \psi_o^*(\vec{r}, \vec{\Omega}, u) S(\vec{r}, \vec{\Omega}, u, t)\,dV\,du\,d\Omega\,. \qquad \text{Eq. (5.16)}$$

If, as has been assumed, prompt and delayed neutrons are emitted isotropically, F_t and $\bar{\beta}$ are still given by Eqs. (5.8) and (5.10). The normalization of $\psi_t(\vec{r}, \vec{\Omega}, u, t)$ is now to require $\Lambda_t F_t$, rather than ΛF see Eq. (5.5), to be time-independent.* The form of the kinetics equations and the inhour formula is the same for both sets of definitions. That is, in the transport theory form

$$\dot{T}_t = \frac{\rho_t - \bar{\beta}}{\Lambda_t} T_t + \sum_i c_{it}\lambda_i + Q_t \qquad \text{Eq. (5.17a)}$$

$$\dot{c}_{it} = \frac{\bar{\beta}_i}{\Lambda_t} T_t - \lambda_i c_{it}. \qquad \text{Eq. (5.17b)}$$

Being the same physical quantities, $T\psi = T_t\psi$. Moreover, since $\psi_o^*(\vec{r}, u) = \int \psi_o^*(\vec{r}, \vec{\Omega}, u)d\Omega$, and since any difference between F_t and F is due entirely to a difference in normalization between ψ_t and ψ, $\psi/F = \psi_t/F_t$, and $\Lambda\psi c_i = \Lambda_t\psi_t c_{it}$. Using these relationships, multiplying Eq. (5.17a) by $\Lambda_t\psi_t$, and subtracting from the product of Eq. (5.6a) and $\Lambda\psi$ yields

$$\rho = \rho_t + \Lambda\frac{\dot{T}}{T} - \Lambda_t\frac{\dot{T}_t}{T_t} + \frac{Q_t\Lambda_t F_t - Q\Lambda F}{FT}. \qquad \text{Eq. (5.18)}$$

Because of Eqs. (5.12) and (5.16), the last term in Eq. (5.18) vanishes for an isotropic source. It follows, since Λ and Λ_t are small quantities, that ρ will very nearly equal ρ_t except during a fast transient or in the presence of an external anisotropic source large in comparison with the source due to fissioning.

It may appear at first glance that the transport theory formalism [Eqs. (5.13) to (5.16)] is the more suitable. From a formal point of view, this is indeed the case, since only cross section (and not flux gradient) changes appear in the expression [Eq. (5.13)] for reactivity and since the prompt neutron lifetime and effective source are defined so that their magnitudes are affected by higher angular modes. However, in most practical cases, diffusion theory must be used to describe the reactor.

---

* F_t may differ from F because of the initial normalization $\psi_t(\vec{r}, \vec{\Omega}, u, 0) \neq \psi(\vec{r}, \vec{\Omega}, u, 0)$ (i.e., it may be inconvenient to require that $\Lambda_t F_t = \Lambda F$). However, this is the only difference between F_t and F. Also, note that $\bar{\beta}$, ρ, Λ are independent of the normalization of ψ_o^* and ψ.

The formalism of Eqs. (5.7) to (5.12) is then more convenient, since, for a P_1, Selengut-Goertzel approximation, the first two terms of Eq. (5.7) reduce to

$$\frac{1}{F}\int_V \int_u -\delta D(u,\vec{r})\nabla\phi_o^*(\vec{r},u)\cdot\nabla\phi(\vec{r},u,t)dV\,du$$

where D is the diffusion constant at lethargy u and position $\vec{r}$. With this reduction, the expression for ρ involves only P_0 components of the directional flux and adjoint. Use of Eq. (5.13) requires explicit computation of higher angular components even in a P_1 approximation.

B. Physical Interpretation of the Adjoint Flux: Iterated Fission Probability

H. Hurwitz, Jr.

Although the physical definition of the adjoint flux is stated in the preceding section, it is primarily the mathematical properties of that function which are used. Because of the very basic role of the adjoint flux in reactor theory, such a purely mathematical treatment is inadequate. Accordingly, in the present section the physical interpretation introduced in Ref. 8 will be reviewed. Specifically, the concept of iterated fission probability will be introduced, and the diffusion theory expression for reactivity derived from this definition.

A definition now follows for a function, $F(\vec{r},u)$, called the iterated fission probability, according to the following occurrences visualized for a reactor which is just critical: Let a neutron be introduced in the assembly, which is assumed to be just critical, at point $\vec{r}$ and with lethargy u. This neutron will, on the average, produce a certain number of fissions with a certain spatial distribution. Neutrons from these fissions will produce further fissions, etc., each succeeding generation having a distribution closer to the actual power distribution in the operating assembly. Furthermore, since the assembly is critical, the number of fissions produced in the n^{th} generation will approach a limit as n approaches infinity, and this limit is defined as $F(\vec{r},u)$. $F(\vec{r},u)$ is similar to the probability $P(\vec{r},u)$ that a neutron introduced at point $\vec{r}$ with lethargy u will produce a fission. There are, however, essential differences. In general, $F(\vec{r},u)$ depends more strongly on position than $P(\vec{r},u)$. This can be seen physically by observing that a neutron introduced near the edge of the reactor will tend to produce fissions near the

edge of the core, and these fissions will have less than the average chance of producing further fissions. Thus, near the edge, $F(\vec{r},u)$ is less than $P(\vec{r},u)$. By the same argument, $F(\vec{r},u)$ is greater than $P(\vec{r},u)$ near the center. For a bare pile with radius R, $F(\vec{r},u)$ will depend on position as

$$\frac{\sin\left(\frac{\pi r}{R}\right)}{r},$$

whereas $P(\vec{r},u)$ will be flatter (Fig. 5.1A). For a pile with a reflector (Fig. 5.1B), F has a more complicated shape, but the relation between F and P is still roughly the same as before. (Note that F and P are defined in all regions of the assembly, reflector, and blanket, as well as the core.) The relation between F and P can be crudely expressed by saying that F is the infinite order iteration of P. It will be seen that it is F rather than P which occurs in the formulas for the change in reactivity due to small changes in the pile composition. The function $P(\vec{r},u)$ is, however, still of interest, since it has a somewhat less involved physical interpretation than $F(\vec{r},u)$. For example, in thinking about $F(\vec{r},u)$ it is often helpful to keep in mind its relationship to $P(\vec{r},u)$. It will be seen below that $F(\vec{r},u)$ is proportional to the self-consistent adjoint function, $\phi_o^*(\vec{r},u)$, whereas $P(\vec{r},u)$ is proportional to the constant source adjoint function. Both of these functions can, in principle, be calculated by the multigroup method, although the latter can, in practice, be found more easily.

For intermediate or thermal energy assemblies it is important to consider the dependence of F on energy. Consider first the value of F at the energy of neutrons emitted in fission. Call this $F_H(\vec{r})$ (H = high). Strictly speaking, F_H is the average of $F(\vec{r},u)$ over the fission neutron spectrum. The functions F_H and P_H have the property that if they are averaged over

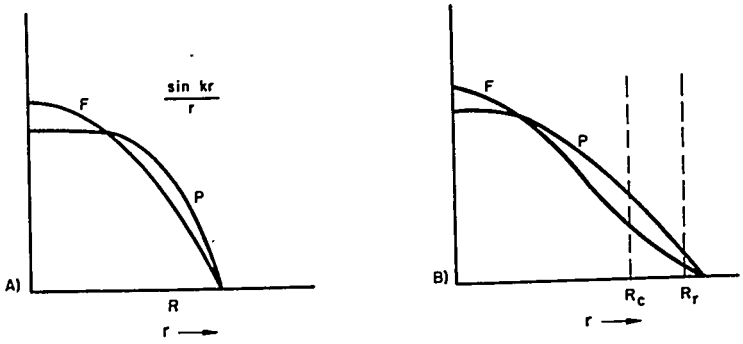

FIGURE 5.1. Core Configurations: A) Bare Pile; B) Reflected Pile.

the core with a weight function proportional to the power distribution, their average values are identical, and equal to $1/\nu = 1/2.44$ for U^{235}. Thus, at the center F_H and P_H are somewhat greater than 0.410 with $F_H > P_H$, whereas at the edge of the core the inequality $0.410 > P_H > F_H$ holds.

To get an idea of how F and P behave for lower energies, consider a crude model in which the fission cross section is assumed very small down to a certain low energy, at which point it suddenly becomes large. Thus, when the neutrons have been degraded to the low energy region, those in the core are almost all captured without having a chance to migrate very far. It would, therefore, be expected that in the core the low energy value $P_L(\vec{r})$ or $P(\vec{r}, u)$ would be almost equal to $1/(1+\alpha)$, where α is the ratio of capture cross section (including that of structural materials and other poisons) to fission cross section. At the outer edges of the core and in the reflector, $P_L(\vec{r})$ drops considerably below $1/(1+\alpha)$ owing to the fact that even low energy neutrons introduced at these points have a good chance of escaping. $P_L(\vec{r})$ is, therefore, fairly constant over the core, but drops near the core edges and in the reflector (see Fig. 5.2A). To get an idea of the behavior of $F_L(\vec{r})$ it is necessary to consider what happens to the neutrons emitted in fissions arising from the introduction of a low energy neutron into the assembly. Because of the high cross sections in the low energy region, the fissions produced by a low energy neutron will take place near the point at

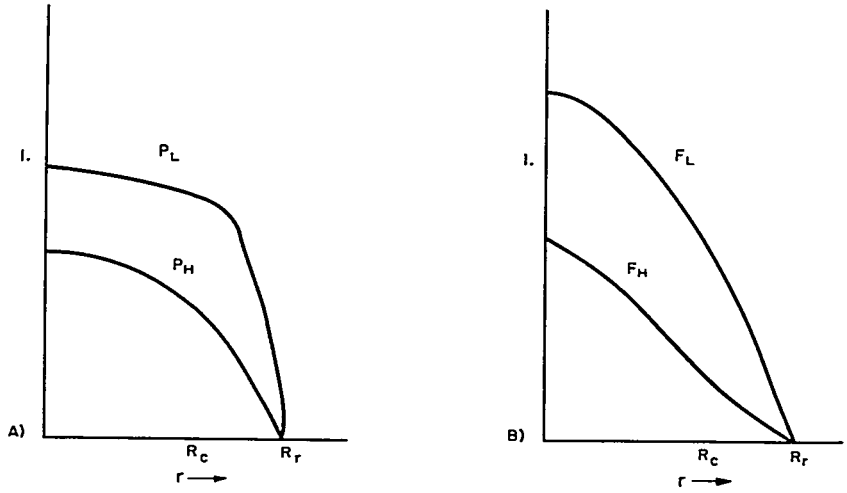

FIGURE 5.2. Core Configurations: A) Probability of Producing Fission in Reactor; B) Iterated Fission Probability in Reactor.

which the neutron was introduced. The ultimate effect of the fast neutrons emitted in these fissions in producing further fissions is determined by $F_H(\vec{r})$; it may, therefore, be concluded that in the core $F_L(\vec{r})$ is approximately $\nu P_L(\vec{r})F_H(\vec{r})$. In the reflector, $F_L(\vec{r})$ is approximately $\nu P_L(\vec{r})F_H(\vec{R}_c)$, where $\vec{R}_c$ is the core surface, since most of the fissions due to low energy neutrons introduced into the reflector occur near the outer edge of the core (see Fig. 5.2B).

It will now be shown how $F(\vec{r},u)$ can be used to find the effect on reactivity of various changes in an assembly. The diffusion theory case with one fissionable isotope will be the specific one examined. Extension to transport theory is straightforward.[4]

Imagine that the assembly is operating at critical, and then certain changes are made in it. These changes can include changes in fission cross section, $\Sigma_f(\vec{r},u)$; absorption cross section, $\Sigma_a(\vec{r},u)$, (Σ_a includes Σ_f), diffusion coefficient, $D(\vec{r},u)$, slowing-down power and inelastic scattering, $\Sigma_s^o(\vec{r},u,u')$, and finally changes in the number of neutrons emitted per fission, ν. This latter change never occurs in practice but is considered here because of the mathematical relationship $\rho=-\frac{\Delta\nu}{\nu_0}$, where ρ is the change in reactivity due to a certain change in the assembly, and $\Delta\nu$ is the change in ν which would be required to bring the assembly back to critical [see Sect. 5.2.C, Eq. (5.24)].

Assume that some or all of the changes enumerated above occur in an assembly at critical, and formulate a diffusion theory relationship between the changes which must hold if the assembly is to remain at critical. First of all, consider a change $\delta\Sigma_a(\vec{r},u)$ in the macroscopic absorption cross section. This has the effect of removing neutrons from the assembly at the rate

$$\iint dV\, du\, \phi(\vec{r},u)\,\delta\Sigma_a(\vec{r},u).$$

Each of these extra neutrons which is removed would otherwise, on the average, have led to $F(\vec{r},u)$ fissions in far future generations, so that the number of fissions in each generation is ultimately changed at the rate

$$-\iint dV\, du\, \phi(\vec{r},u)\,\delta\Sigma_a(\vec{r},u)\,F(\vec{r},u).$$

A change in fission cross section causes, in addition to the absorption change just described, a change in ultimate fissions

due to the extra neutrons produced. The ultimate fissions are increased at the rate

$$+\nu \iiint dV\, du\, du'\, \phi(\vec{r}, u)\delta\Sigma_f(\vec{r}, u)F(\vec{r}, u')f_t(u').$$

An increase in the slowing down and inelastic scattering cross section $\Sigma_s^o(\vec{r}, u, u')$ increases the ultimate fissions by moving neutrons to an energy where F is greater. The rate of increase is

$$\iiint dV\, du du'\, \phi(\vec{r}, u)\Sigma_s^o(\vec{r}, u, u')\,[F(\vec{r}, u') - F(\vec{r}, u)]\,.$$

An increase in diffusion coefficient decreases the fissions in future generations by increasing the neutron current from points of high F to points of low F. The rate of this decrease is

$$-\iint dV\, du\, \delta D \nabla\phi(\vec{r}, u)\cdot\nabla F(\vec{r}, u).$$

Finally, an increase $\delta\nu$ in the number of neutrons emitted per fission gives an ultimate increase in the number of fissions by

$$\delta\nu \iiint dV\, du\, du'\, \phi(\vec{r}, u)\Sigma_f(\vec{r}, u)F(\vec{r}, u')f_t(u') = \delta\nu\left(\frac{F}{\nu_o}\right)$$

with F defined by Eq. (5.8). If the assembly is to remain critical, the cumulative effect of all the changes on future generations must be zero. One is, therefore, led to the fundamental formula

$$\rho = -\frac{\delta\nu}{\nu_o} = -\frac{\iint dV\, du\, \phi(\vec{r}, u)\delta\Sigma_a(\vec{r}, u)F(\vec{r}, u)}{F}$$

$$+\frac{\iiint dV\, du\, du'\, \phi(\vec{r}, u)\,\delta\,\Sigma_s^o(\vec{r}, u, u')\,\left[F(\vec{r}, u') - F(\vec{r}, u)\right]}{F}$$

$$-\frac{\iint dV\, du\, \delta D(\vec{r}, u)\nabla\phi(\vec{r}, u)\cdot\nabla F(\vec{r}, u)}{F}$$

$$+\frac{\nu \iiint dV\, du\, du'\, \phi(\vec{r}, u)\delta\Sigma_f(\vec{r}, u)F(\vec{r}, u')f_t(u')}{F} \qquad \text{(eq. (5.19)}$$

Since $\delta\Sigma_a(\vec{r},u)+\int du'\delta\Sigma_s^o(\vec{r},u,u')=\delta\Sigma(\vec{r},u)$, Eq. (5.19) is the diffusion theory analog of Eq. (5.7). Thus, the adjoint flux $\phi_o^*(\vec{r},u)$, defined mathematically by Eq. (5.3), is directly proportional to the iterated fission probability, $F(\vec{r},u)$.

Since $F(\vec{r},u)$ represents the true effectiveness of a neutron of lethargy u added to the assembly at $\vec{r}$, Eq. (5.19) simply states that the effect on ρ of a change in the assembly is proportional to the number of neutrons added to the assembly per unit time by the change multiplied by the effectiveness of these neutrons. Note that the arguments leading to Eq. (5.19) could not have been carried out if the fission probability function $P(\vec{r},u)$ had been used instead of the iterated probability $F(\vec{r},u)$.

C. The Utility of the Kinetics Equations

A.F. Henry

Having been obtained without approximation from transport theory, Eqs. (5.6a) and (5.6b) are quite accurate for reactors in which fuel is stationary. Their utility depends on the possibility of computing ρ, Λ, $\overline{\beta}_i$, and Q. This problem, while very difficult in general, can for a great many practical cases be treated to a high order of accuracy by relatively simple approximations.

The formal difficulty in the way of general treatment is that of computing the time-dependent shape function $\psi(\vec{r},\vec{\Omega},u,t)$. In fact, unless ψ or some accurate approximation to it can be found readily, the recasting of Eqs. (5.1) and (5.2) into Eqs. (5.6a) and (5.6b) or (5.17) becomes a mere formality.

1. The Time Separable Case

The most fruitful approach to the investigation of ψ seems to be first to examine cases where its determination involves no formal difficulty. This is the situation whenever ψ is independent of time, that is, whenever the time behavior of the directional flux, $\mathcal{F}(\vec{r},\vec{\Omega},u,t)$, is a separable function.

The condition of time separability exists for constant values of reactivity when the source term is negligible in comparison with the fission rate. Strictly speaking, this is the only time when it exists. If these conditions are fulfilled, the neutron and delayed emitter populations will eventually behave as $e^{\omega t}$, where ω is given by the largest root of

the inhour equation, obtained from Eqs. (5.6a) and (5.6b) by taking $c_i \sim T \sim e^{\omega t}$:

$$\rho = \omega \Lambda + \sum_i \frac{\omega \bar{\beta}_i}{\omega + \lambda_i} \cdot \cdot \qquad \text{Eq. (5.20)}$$

Under such circumstances, the stationary shape function $\psi(\vec{r}, \vec{\Omega}, u)$ is from [Eqs. (5.1) and (5.2)] one of the solutions of

$$-\vec{\Omega} \cdot \nabla \psi_\omega(\vec{r}, \vec{\Omega}, u) - \left[\Sigma(\vec{r}, u) + \frac{\omega}{v}\right] \psi_\omega(\vec{r}, \vec{\Omega}, u)$$

$$+ \int_{\Omega'} \int_0^\infty d\Omega' \, du' \Sigma_s(\vec{r}, u', u, \vec{\Omega}' \cdot \vec{\Omega}) \psi_\omega(\vec{r}, \vec{\Omega}', u')$$

$$+ \sum_j \int_{\Omega'} \int_0^\infty d\Omega' \, du' \left[\nu^j(u')(1 - \beta^j) f^j(u) \right.$$

$$\left. + \sum_i \frac{\lambda_i}{\omega + \lambda_i} \nu^j(u') \beta_i^j f_i(u) \right] \Sigma_f^j(\vec{r}, u') \psi_\omega(\vec{r}, \Omega', u') = 0$$

Eq. (5.21)

where k has been set equal to unity, its physically real value.

The largest value of ω yielding a stationary solution of Eq. (5.21) is identical with the largest root of Eq. (5.20). Except for a prompt critical situation ($\rho \gtrsim \beta$), the largest value of ω is found [from Eq. (5.20)] to be such that $|\omega/v| << \Sigma(\vec{r}, u)$. Thus, except during a runaway, the stationary solution is one corresponding to a delayed neutron yield differing from the equilibrium value. The term $\lambda_i/(\omega + \lambda_i)$ shows the yield at any instant to be decreased for a supercritical situation ($\omega > 0$) and increased (generally substantially) for a subcritical situation. For very large ω (prompt critical cases), the stationary solution is one corresponding to an increase in the absorption cross section by an amount ω/v and the complete absence of any delayed neutrons ($\lambda_i/(\omega + \lambda_i) \to 0$).

If Eq. (5.21) is actually solved,* there is no need to determine ρ, since ω will already have been found.† However, because of the inconvenience of having ω as an eigenvalue, two approximate methods of computing ρ (and thence ω) are commonly employed. Careful examination of these will suggest means of obtaining the shape function for nonseparable situations.

The first method is to use in the expression of Eq. (5.7) for ρ the flux, $\psi_o(\vec{r}, \vec{\Omega}, u)$, which is the stationary solution before the perturbation. This procedure requires that the integrals in Eq. (5.7) be evaluated and becomes of questionable accuracy if, as can occasionally happen, a small change in reactivity leads to a major change in flux shape.

The second method consists of solving the stationary equation

$$-\vec{\Omega} \cdot \nabla\psi_\nu(\vec{r}, \vec{\Omega}, u) - \Sigma(\vec{r}, u)\psi_\nu(\vec{r}, \vec{\Omega}, u) + \int_{\Omega'} \int_0^\infty d\Omega' \, du' \times \left[\Sigma_s(\vec{r}, u', u, \vec{\Omega}' \cdot \vec{\Omega}) + \frac{1}{k} \sum_j f_t^j(u) \nu^j(u) \Sigma_f(r, u')\right] \psi_\nu(\vec{r}, \vec{\Omega}, u') = 0 \qquad \text{Eq. (5.22)}$$

where the constants in the equations are the perturbed ones, and the eigenvalue k is adjusted to obtain a stationary solution. For excursions in reactivity smaller in magnitude than prompt critical, ψ_ω [from Eq. (5.21)] and ψ_ν [from Eq. (5.22)] will be virtually identical, since the equations which lead to them differ only in that a small fraction of the source (roughly equal to the magnitude of the reactivity change being computed) consists in one case of prompt neutrons and in the other case of delayed neutrons. Thus, use of ψ_ν in Eq. (5.7) for the reactivity should yield almost the same result as the use of ψ_ω.

Once this fact has been established, there is no need actually to compute ψ_ω and perform all numerical integrations in Eq. (5.7), since the desired reactivity change can be found indirectly from the eigenvalue ν required to make Eq. (5.22) stationary. The argument which justifies this procedure is based on the fact that Eq. (5.22) describes a physical system differing from the one under consideration only in that

*Statements about solving the transport equation should be interpreted as meaning solving some tractable but unspecified approximation to it. One talks in terms of transport theory for the sake of generality.

†Direct integration of Eq. (5.21) yields the dynamic inhour formula of Gross and Marable[12] along with the dynamic reactivity and lifetime.

it is maintained critical by a fictitious value of ν. Since this system is stationary, the reactivity change between it and the original, critical, unperturbed system is zero. But this zero change can be thought of as made up of the reactivity change ρ which is sought and that change (designated by ρ_ν) due to the fictitious alteration of ν. Thus, $\rho = -\rho_\nu$. For a steady-state value of k of unity one finds

$$\delta\left[\frac{1}{k}\sum_j f_t^j(u)\nu^j(u')\Sigma_f^j(\vec{r},u')\right] \equiv \frac{1}{k}\left[\sum_j f_t^j(u)\nu^j(u')\Sigma_f^j(\vec{r},u')\right]$$

$$-\sum_j f_t^j(u)\nu^j(u')\Sigma_{fo}^j(\vec{r},u') = \left(\frac{1}{k}-1\right)\left[\sum_j f_t^j(u)\nu^j(u')\Sigma_f^j(\vec{r},u')\right]$$

$$+\delta\left[\sum_j f_t^j(u)\nu^j(u')\Sigma_f^j(\vec{r},u')\right].$$

Hence, from Eqs. (5.18) and (5.13),

$$\rho_\nu \simeq \rho_{\nu t} = \left(\frac{1}{k}-1\right)$$

$$\times \frac{\int_V\int_u\int_{u'}\int_\Omega\int_{\Omega'}\sum_j f_t^j(u)\nu^j(u')\Sigma_f^j(\vec{r},u')\psi_o^*(\vec{r},\vec{\Omega},u)\psi_\nu(\vec{r},\vec{\Omega}',u')\,dV\,du\,du'\,d\Omega\,d\Omega'}{\int_V\int_u\int_{u'}\int_\Omega\int_{\Omega'}\sum_j f_t^j(u)\nu^j(u')\Sigma_f^j(\vec{r},u')\psi_o^*(\vec{r},\vec{\Omega},u)\psi_\nu(\vec{r},\vec{\Omega}',u')\,dV\,du\,du'\,d\Omega\,d\Omega'}.$$

Eq. (5.23)

Thus, for small changes in reactivity, Eq. (5.7) may be replaced by

$$\rho = -\rho_\nu = 1 - \frac{1}{k} \qquad \text{Eq. (5.24)}$$

and the desired reactivity change may be computed directly from the eigenvalues k associated with the perturbed and unperturbed states.

D. Computation of Parameters in the Kinetics Equations

L. Bohl and S. G. Margolis

There are three general methods for computing the parameters ρ, $\bar{\beta}_i$, Λ, and Q which appear in the reactor kinetics equations. These are the eigenvalue method, the direct integration method, and the iterated fission probability method.

1. Eigenvalue Method

The essential feature of the eigenvalue method is its derivation of kinetics parameters from differences between the eigenvalues of steady-state solutions calculated for perturbed and unperturbed states. In situations involving a single computation of reactivity, or where only the $\bar{\beta}_i$ and Λ are required, this method is frequently the most convenient. In reactivity calculations, the eigenvalue k of the perturbed state is calculated by any suitable method, and the reactivity is then found using Eq. (5.23). The parameters β_i and Λ are calculated by introducing artificial perturbations. Equations (5.7), (5.9), and (5.10) or Eqs. (5.13), (5.14), and (5.10) show that Λ is given by the eigenvalue change associated with the perturbation $\delta\Sigma(\vec{r},u,t) \div 1/v(u)$ and that $\bar{\beta}_i$ is given by the change associated with the perturbation

$$\delta\left[\frac{1}{k}\sum_j f_i^j(u)\nu^j(u')\Sigma_f^j(\vec{r},u',t)\right] = \frac{1}{k}\sum_j \nu^j(u')f_i(u)\beta_i^j\Sigma_f^j(\vec{r},u',t).$$

Experimental measurements of $\bar{\beta}$ using this relationship are discussed in Refs. 13 and 14.

2. Direct Integration (Perturbation) Method

The essential feature of the direct integration method, frequently called the perturbation method, is its use of a direct evaluation of the volume integral in the formula for reactivity. In contrast to the eigenvalue method, explicit calculations of the eigenvalue of the perturbed states are not required.

The utility of the direct integration method is greatest in determining the reactivity associated with a number of small perturbations of a particular core configuration. Specifically, the determination of position- or region-dependent temperature and void coefficients is greatly facilitated by this scheme. One important application of position-dependent coefficients is in reactors with a strong power coefficient. In such reactors, changes in the axial distribution of moderator density as the

reactor is brought to power can create a net reactivity change, even though the average temperature of the coolant is unchanged. Moreover, the evaluation of reactivity effects from subcooled boiling requires knowledge of the void coefficient at the location of the boiling. Finally, there are sometimes particular regions in the reactor (e.g., reflectors, control rod channels, and the interstitial spaces between fuel modules) in which the local temperature and void coefficients differ markedly in magnitude or sign from the core-average values. Since the equilibrium and transient temperature of the moderator in these regions may also be quite different from that in the fuel lattice, the reactivity coefficients for these regions must be computed separately.

In principle, position- or region-dependent reactivity coefficients could be obtained by changing cross sections for an incremental change in temperature or void and recomputing the eigenvalue. This process would have to be repeated successively for each subregion of the reactor. Moreover, for fine subdivisions of the reactor, the temperature increments would have to be very large if errors due to convergence were to be avoided. In contrast to these repeated eigenvalue calculations, the direct integration (perturbation) method uses weighting functions which convert local parameter changes into reactivity effects without further iteration. The weighting functions are generated by computing the volume integral in the formula for reactivity as a sum of volume integrals over subregions, using generally the flux and adjoint associated with the unperturbed state. The complexity of the integrations depends on what particular approximation to the transport equation is being employed. Thus, for example, in the diffusion theory approximation, the expression for the temperature coefficient at constant pressure can be written

$$\left.\frac{\partial\rho}{\partial T}\right|_p \equiv \sum_i \left.\frac{\partial\rho}{\partial T}\right|_{p,i} = \frac{1}{F}\sum_i \int_{V_i}\int_u \left\{ -\left.\frac{\partial D_i(u)}{\partial T}\right|_p \nabla\phi_o^*(\vec{r},u)\cdot\nabla\phi_o(\vec{r},u) \right.$$

$$-\left.\frac{\partial\Sigma_i(u)}{\partial T}\right|_p \phi_o^*(\vec{r},u)\,\phi_o(\vec{r},u)$$

$$\left. + \int_{u'} \frac{\partial}{\partial T}\left[\Sigma^o_{s_i}(u',u) + \frac{1}{k}\sum_j f_t^j(u)\nu^j(u')\Sigma^j_{f_i}(u')\right]\right|_p \phi_o^*(\vec{r},u)\,\phi_o(\vec{r},u')\,du' \Bigg\}\, dV\, dU$$

Eq. (5.25)

where F is defined in Eq. (5.8), and it has been assumed that the partial derivatives of the reactor parameters, $D_i(u)$, $\Sigma_i(u)$,

etc., in region i are independent of position within that region. A single computation of $\phi_o(\vec{r}, u)$ and $\phi_o^*(\vec{r}, u)$ suffices to find all the individual terms of Eq. (5.25). Thereafter, the reactivity, ρ, associated with arbitrary temperature changes, δT_i, in the different regions is given by

$$\rho = \sum_i \left.\frac{\partial \rho}{\delta T}\right|_{p,i} \delta T_i . \qquad \text{Eq. (5.26)}$$

Since reactivity coefficients are defined in the limit of zero perturbation, the replacement of $\phi(\vec{r}, u, t)$ by $\phi_o(\vec{r}, u)$ in deriving Eq. (5.25) is rigorous. The validity of Eq. (5.26) depends on the magnitude of the flux shape changes associated with the finite perturbations, δT .

In the few-group diffusion approximation, the direct integration formulas for reactivity are conveniently applied with the aid of either the KARE-PSP[15] or the PDQ-FRILL code options. For a given change in reactor parameters, PSP calculates $(k_P - k_v)/k_p$ and FRILL calculates $(k_P - k_U)/k_P k_U$, where k_P is the perturbed and k_U the unperturbed eigenvalue. In either case, the change in eigenvalue may then be identified with a reactivity, using Eq. (5.24). Specifically, PSP calculates

$$\frac{k_P - k_U}{k_p} = F - (A + E + D)$$

where

$$F = \frac{1}{N}\frac{1}{k_U}\sum_{g=1}^{G}\sum_{g'=1}^{G}\int \delta\nu\Sigma^f_{g'}\left(x_g \phi^*_g \phi_{g'}\right) dV$$

$$A = \frac{1}{N}\sum_{g=1}^{G}\int \delta\Sigma^A_g\left(\phi^*_g \phi_g\right) dV$$

$$E = \frac{1}{N}\sum_{g=1}^{G-1}\int \delta\Sigma^R_g\left(\phi^*_g - \phi^*_{g+1}\right)\phi_g\, dV$$

$$D = \frac{1}{N}\sum_{g=1}^{G}\int \delta D_g\left(\nabla\phi^*_g \cdot \nabla\phi_g\right) dV$$

and

$$N = \frac{1}{k_U}\sum_{g'=1}^{G}\sum_{g=1}^{G}\int \nu\Sigma^f_{g'} x_g \phi^*_g \phi_{g'}\, dV .$$

In the above, g is the group index and G is the number of groups. Essentially the same formulas are evaluated by the PDQ-FRILL option, except that in FRILL the normalizing factor N is not divided by the unperturbed eigenvalue k_p. Note that the quantities calculated by PSP and FRILL differ by a factor k_v and that the outputs of the two programs may differ significantly if k_u is not nearly unity.

3. *Iterated Fission Probability Method*

The principal advantage of the iterated fission probability method[16] is its ability to account explicitly for the spectrum of delayed or external source neutrons. As was discussed in Sect. 5.2.B, the iterated fission probability is proportional to the fission rate (neutrons either per second or per generation) which is attained asymptotically in a critical assembly initially at zero power prior to the introduction of a neutron at position $\vec{r}$ traveling in direction $\vec{\Omega}$ with lethargy u.* Thus, such a quantity as F [Eq. (5.8)] can be interpreted for a critical reactor $[\phi(\vec{r}, u', t) = \phi_o(\vec{r}, u')]$ as the (constant) fission rate expected asymptotically if the neutrons introduced in one second by fissioning during steady-state operation are introduced instead as an initial source with the core at zero power. For the present discussion it will be convenient to normalize $\phi_o(\vec{r}, u')$ so that the total fission rate is unity, and to normalize ϕ_o^* so that F is also unity. The reactivity associated with the perturbation of, say, $\Sigma(\vec{r}, u)$ is then the asymptotic fission rate which results when a source, $\delta\Sigma(\vec{r}, u)\phi_o(\vec{r}, u)$, is introduced into the critical reactor, initially at zero power. In most computing machine procedures for solving the criticality equations there is a one-to-one correspondence between neutron generations and outer iterations.† Thus, it is possible to keep track of the fission rate simply by noting its value at the end of each outer iteration until it approaches a constant. (Any automatic normalization supplied by the machine must be removed in this procedure.) The quantities Λ, $\bar{\beta}_i$, and Q may also be computed by this method, since all the integrals involved can be interpreted as importance weighted sources.

When applied within the framework of few-group diffusion theory, this method is particularly useful for the computation

*The neutron introduced is an average one in the sense that stochastic phenomena are not considered.

†Acceleration techniques (for example, those using Chebyshev polynomials) generally destroy this correspondence and must be avoided or otherwise accounted for if the method being described is to be applied correctly.

of $\bar{\beta}_i$ and Q, since it permits the specific spectrum of the delayed or external source neutrons to be accounted for explicitly. Thus, in the delayed neutron case, the procedure is to determine two sets of few-group constants, the first appropriate to the delayed neutron spectrum and the second to the total fission spectrum. Behavior of neutrons from the source

$$\frac{1}{k}\sum_j \nu^j(u')f_i(u)\beta_i^j\Sigma_f^j(\vec{r},u')\phi_0(r,u')$$

is then computed in the first iteration (generation) by solving the few-group diffusion equations with the delayed neutron spectrum constants. A new fission source is constructed, and behavior of neutrons for this and all succeeding generations is determined using the few-group constants from the total fission spectrum. Thus, what might be called a parallel group structure is used to account, within the framework of few-group theory, for the different spectrum of delayed neutrons. For the bare core case, the procedure is equivalent to a multigroup computation. Moreover, it seems reasonable to expect it to be quite accurate for any situation in which few-group theory itself is a good approximation.

This method is readily extendible to the stationary subcritical case. However, higher modes of both the flux and adjoint are then required, and calculations become increasingly complicated. Since practical situations generally involve assemblies near critical, the higher modes usually contribute very little to the result and may be safely neglected.

5.3 REACTOR SYSTEM KINETICS

J. N. Grace

From the equations in the preceding discussion one can calculate the reactor power transient resulting from a given reactivity transient. The reactivity, however, is not easily specified, since it is, in general, the sum of a known external perturbation and other reactivity feedback effects. These other effects are functions of system variables which depend on the power level. The following discussion will develop methods of analysis of reactivity feedback phenomena and evaluate their effect on system stability. While the previous section treated reactivity-to-power, this section treats power-to-reactivity and the stability of the resultant closed-loop system.

The present investigations are limited to problems where space and time are separable, thus allowing use of the ordinary differential equations of reactor kinetics. The dynamic boundary value problems of flux tilt transients and spatial stability are treated in Sect. 5.4.

The frequency-response method of stability analysis, as applied to reactor kinetics, is introduced at the outset, followed by an analysis of two inherent reactivity feedback phenomena; the effects of variable fission product poisoning (xenon) and system pressure variations, each operating simultaneously with a negative temperature coefficient of reactivity. The section continues with an investigation of the effects of boiling on reactivity feedback and stability, including a discussion of interactions with hydrodynamic instability, and concludes with an investigation of the ability of inherent reactivity feedback mechanisms to arrest reactor power excursions resulting from large reactivity perturbations.

A. Inherent Stability

J. N. Grace

1. Introduction

A) THE TRANSFER FUNCTION. A basic technique used in the frequency response method of reactor analysis is linearization of equations by means of the small signal assumption. This assumption will be used in the development of the concept of a transfer function.

Let P and Q represent two parameters of an assumed physical system, and assume that P and Q are functionally related within the system. The frequency response method of analysis is carried out by assuming that one of the parameters (for example, P) is subjected to a sinusoidal variation of small, arbitrary amplitude $|\delta P|$ and of frequency ω. Thus, if P_o is the steady-state value of P,

$$P = P_o + \delta P = P_o + |\delta P| e^{j\omega t} \qquad \text{Eq. (5.27)}$$

where it is understood that only the real part of P is interpreted to have physical significance.

Since Q is functionally related to P by the physical system, the assumed small oscillation of P will result in a small oscillation in Q, of the same frequency ω, and of amplitude $|\delta Q|$. Thus, if Q_o is the steady-state value of Q,

$$Q = Q_o + \delta Q = Q_o + |\delta Q| e^{j(\omega t + \alpha)} \qquad \text{Eq. (5.28)}$$

where α is a phase shift which, in general, is a function of ω.

The quantity δP is called the input; it is the independent variable or the so-called driving function. The quantity δQ is the output and is the dependent variable. The ratio of output to input, as a function of frequency, is called the transfer function. Generally speaking, a transfer function is defined for a component of a system or for a coupled system of components.

In terms of this definition the transfer function, F_{QP}, is defined by the equation

$$\delta Q \equiv F_{QP}\ \delta P\,. \qquad \text{Eq. (5.29)}$$

It is important to note that the transfer function gives the output δQ, resulting from an arbitrary input δP. The transfer function is frequently designated by the notation

$$F_{QP} \equiv \left(\frac{\delta Q}{\delta P}\right).$$

Clearly, F_{QP} is a complex function of ω. Thus,

$$F_{QP} = \frac{|\delta Q|}{|\delta P|}\,\epsilon^{j\alpha}.$$

In general, F_{QP} is also a function of P_o and Q_o.

The transfer function F_{QP} can be determined from the equations of the physical system. In solving these equations to obtain F_{QP}, the assumption is made that $|\delta P| << P_o$ and $|\delta Q| << Q_o$ and that only the first-order terms in the differentials δP and δQ need be retained. This linearization process is referred to as the small-signal approximation.

The definition of transfer functions may be continued and other functions defined relating the input δP to other system output parameters. If R is another such parameter, a transfer function may be written relating R and P just as was done with P and Q. If δQ represents an input to δR, it is also possible to write a transfer function relating R and Q. Thus,

$$\delta R \equiv F_{RQ}\,\delta Q \equiv F_{RQ}F_{QP}\,\delta P$$

and

$$F_{RP} \equiv F_{RQ}F_{QP}\,.$$

Thus, the overall transfer function for a coupled system of components is the product of the transfer functions of the individual components.

B) FEEDBACK AND STABILITY. In the frequency response analysis of a system with feedback, it is important to define the transfer functions carefully. Since the system with feedback forms a closed loop, it is not simple to make a clear distinction between the input and output variables. A frequently used technique is to open the loop at some appropriate point in order to define the transfer functions. In a reactor plant, the reactor itself provides a natural point for opening the loop.

Consider a reactor coupled to a plant, and assume the reactor has negative temperature coefficient of reactivity. Assume further that the reactor is provided with means for varying the reactivity in an oscillatory way, for example, through control rod motion.

The two principal variables to be considered, so far as the reactor is concerned, are the reactivity, δk, and the power level of the reactor. The power level of the reactor is proportional to the average neutron flux in the reactor ϕ, and this parameter will be used as representative of the reactor power level. Because of the form of the equations, however, a more convenient parameter is

$$y = \log_e \phi .$$

Then, the oscillatory differential δy is

$$\delta y = \frac{1}{\phi_o} \delta \phi$$

where ϕ_o is the steady-state value of ϕ. Since the steady-state value of the reactivity, δk, is zero, the symbol δk itself will be used to represent the oscillatory differential of reactivity.

Making use of the loop-opening technique, the reactor is first considered independent of the plant. It is assumed that an oscillatory differential reactivity is induced in the reactor by a small amplitude oscillation of the control rods. The differential reactivity δk is the input or driving variable. The first transfer function defined is G, the reactor transfer function. This transfer function is defined to give the reactor oscillatory power response for an arbitrary oscillatory reactivity input:

$$\frac{\delta \phi}{\phi_o} \equiv G \, \delta k . \qquad \text{Eq. (5.30)}$$

As defined, G is a function dependent only on the kinetic properties of the reactor. It may be calculated from the reactor kinetics equations.

Next, the feedback will be considered. If the reactor power level has an oscillatory component $\delta \phi / \phi_o$, all temperatures

throughout the reactor plant will have an oscillatory component of this frequency. Since the reactor temperature itself will have an oscillatory component, there will be a reactivity feedback into the reactor as a consequence of the changing reactor temperature. Let F represent the reactivity transfer function which gives the reactivity feedback into the reactor as a consequence of the reactor power level variation:

$$\delta k = F\frac{\delta\phi}{\phi_o}. \qquad \text{Eq. (5.31)}$$

As defined, F depends on the plant parameters, namely, specific heats, flow rates, plant temperatures, etc. It is calculated by assuming the reactor power has an oscillating component of the reactor mean temperature. Note that Eq. (5.31) gives the reactivity as a function of reactor power, while Eq. (5.30) gives reactor power as a function of reactivity.

The next step is to close the feedback loop. This is accomplished by adding the reactivities at the reactor. Let δk_{IMP} represent the arbitrary impressed reactivity on the reactor due to the oscillating control rod motion. In the absence of feedback, Eq. (5.30) gives the resulting reactor response,

$$\frac{\delta\phi}{\phi_o} = G\,\delta k_{IMP}. \qquad \text{Eq. (5.30a)}$$

Due to the reactor response in power level, a reactivity feedback will occur given by Eq. (5.31). Designate the reactivity feedback as δk_{FB}:

$$\delta k_{FB} = F\frac{\delta\phi}{\phi_o}. \qquad \text{Eq. (5.31a)}$$

The net reactivity available to the reactor, δk_{NET} is the sum of the reactivities

$$\delta k_{NET} = \delta k_{IMP} + \delta k_{FB} \qquad \text{Eq. (5.32)}$$

and the resulting reactor response will correspond to the net reactivity

$$\frac{\delta\phi}{\phi_o} = G\,\delta k_{NET} = G(\delta k_{IMP} + \delta k_{FB}).$$

Substitution of Eq. (5.31a) for δk_{FB} gives

$$\frac{\delta\phi}{\phi_o} = \left(\frac{G}{1-FG}\right)\delta k_{IMP} \,. \qquad \text{Eq. (5.33)}$$

Comparison of Eq. (5.33) with Eq. (5.30a) shows that, as a consequence of feedback, the reactor response is increased by the factor

$$\left(\frac{1}{1-FG}\right).$$

The factor FG is frequently called the loop gain. If the loop gain is unity, with a phase angle of 360 degrees, the reactor response is infinite for an arbitrarily small amplitude of excitation. The stability criterion, namely, the system is stable if

$$|FG| < 1$$

for phase angles which are a multiple of 360 degrees, is derived from the form of Eq. (5.33).

If the loop gain is less than unity, but in a given frequency range approaches unity and has a phase shift which is a multiple of 360 degrees, the factor

$$\left(\frac{1}{1-FG}\right)$$

becomes large in this frequency range. The system is then said to have a resonance at the frequency ω_R where the phase shift is a multiple of 360 degrees.

C) MULTIPLE FEEDBACK LOOPS. There are a number of feedback loops in a reactor plant. The temperature feedback has been discussed. There is also a feedback effect associated with primary loop pressure. Another feedback effect is associated with xenon poisoning of the reactor. A transfer function F can be defined for each of these parameters, just as Eq. (5.31) defined the transfer function for reactor temperature. In this way, a series of transfer functions F_1, F_2, F_3, etc., may be defined. The reactivity feedback from these is a set of values $\delta k_1, \delta k_2, \delta k_3$, etc. The net reactivity is the sum of the impressed reactivity and these feedback reactivities:

$$\delta k_{NET} = \delta k_{IMP} + \delta k_1 + \delta k_2 + \delta k_3 \,. \qquad \text{Eq. (5.34)}$$

This leads to the reactor response equation

$$\frac{\delta\phi}{\phi_o} = \frac{G}{\left[1 - G\,(F_1 + F_2 + F_3)\right]}\,\delta k_{IMP}\,. \qquad \text{Eq. (5.35)}$$

The total loop gain is now the sum of the individual feedback loop gains:

$$\text{Total Loop Gain} = F_1G + F_2G + F_3G\,.$$

A useful result for the application of transfer function methods can be derived by assuming for the moment that only two feedback loops are present. From Eq. (5.35), the reactor response is given by

$$\frac{\delta\phi}{\phi_o} = \frac{G}{\left[1 - G\left(F_1 + F_2\right)\right]}\,\delta k_{IMP}\,. \qquad \text{Eq. (5.35a)}$$

By simple algebraic manipulation this can be put in the form

$$\frac{\delta\phi}{\phi_o} = \frac{\left(\dfrac{G}{1 - F_1G}\right)}{\left[1 - \left(\dfrac{G}{1 - F_1G}\right)F_2\right]}\,\delta k_{IMP}\,. \qquad \text{Eq. (5.35b)}$$

Thus, if the overall reactor response has been calculated for one feedback loop, the effect of an additional feedback loop can be readily determined. The reactor response with feedback F_1 is used (instead of the reactor transfer function) in finding the loop gain of the second loop. In this formulation the loop gain is

$$\left(\frac{G}{1 - F_1G}\right)F_2\,.$$

This can be extended to a series of feedback loops by calculating the response for addition of one feedback loop at a time.

D) REACTIVITY COEFFICIENTS. It is frequently convenient to calculate transfer functions for a plant for parameters other than the reactivity. By so doing, it is sometimes possible to generalize results by calculating dimensionless quantities or variables which might apply to a range of conditions. For example, instead of calculating the reactivity feedback due to

temperature, it may be more general to calculate the reactor temperature change. If T_R is the reactor mean temperature,

$$\delta T_R = F_T \frac{\delta \phi}{\phi_o} \qquad \text{Eq. (5.36)}$$

defines the transfer function F_T. The reactivity feedback δk_T is obtained by introducing the temperature coefficient of reactivity α_T:

$$\delta k_T = \alpha_T \, \delta T_R = \alpha_T \, F_T \frac{\delta \phi}{\phi_o} . \qquad \text{Eq. (5.37)}$$

The advantage of calculating F_T is that, once obtained, the response of the plant for a range of values of α_T may be readily computed. Similar remarks may be made concerning other variables.

E) EFFECTS OF CHARACTERISTIC TIMES ON THE ANALYSIS OF REACTOR PLANT STABILITY. A straightforward method of computing the stability characteristics of the overall reactor plant would be the application of Eq. (5.35). This would require the computation of the individual transfer functions F_1, F_2, F_3, etc., for each feedback loop in the system and the combining of these to obtain the total loop gain. The latter step is an involved procedure algebraically and is generally unnecessary because of the properties of the reactor plant feedback loops.

The stability analysis of reactor plants is made easier by the wide spread in characteristic frequencies associated with the various feedback loops. These characteristic frequencies differ by orders of magnitude, so that it is possible, in any given frequency range, to limit consideration to a few feedback loops.

The lowest frequency is that associated with fuel depletion. The characteristic time for this effect is of the order of thousands of hours. The next higher frequency of importance is associated with xenon poisoning. The characteristic time is of the order of 10 hours. Between this frequency range and the next higher characteristic frequencies, there is a large gap. The next higher characteristic frequencies above xenon are of the order of tenths of a cycle per second and are associated with primary loop circulation times and the principal delayed neutron effects. Above this, the next higher frequencies are of the order of one cycle per second. These are associated with transit time of the coolant through the reactor, transit time of the coolant through the boiler, and the pressurizer surge line cutoff frequency. Still higher frequencies of the order of 10 cycles per second are associated with the heat transfer

properties from the reactor fuel elements to the coolant. The highest frequency range, of the order of 100 to 1000 cycles per second, is associated with the lifetime of the neutrons in the reactor.

In the treatment of the reactor plant stability, in a particular frequency range, those effects which are of lower characteristic frequency by several orders of magnitude are considered to be stationary. Those effects which are of higher characteristic frequency are considered to take place instantaneously. The range between the characteristic times of the xenon effects, of the order of 10 hours, and the loop circulation and delayed neutron characteristic times, of the order of tens of seconds, is very large. In this range, the analysis of the plant stability may be carried out on a quasistationary basis. This represents a considerable simplification.

2. *The Reactor Transfer Function*

The reactor transfer function, G, is defined by Eq. (5.30) and depends only on the kinetic properties of the reactor. The reactor kinetics equations are written with the assumption of separability of the spatial and time variables (see Sect. 5.2). The equations are derived on the basis of a one-group bare reactor model.[17] If n represents the neutron density in the reactor, C_i the concentration of delayed neutron emitters, δk the reactivity, and λ the decay constant of the delayed neutron emitters, then

$$\frac{dn}{dt} = \frac{\delta k}{\Lambda} n - \sum_i \frac{dC_i}{dt} \qquad \text{Eq. (5.38)}$$

$$\frac{dC_i}{dt} = \frac{\beta_i n}{\Lambda} - \lambda_i C_i \qquad \text{Eq. (5.39)}$$

where

$\Lambda = \Lambda_o / k_{\text{eff}}$ and Λ_o may be thought of as the effective lifetime for neutrons in the reactor and k_{eff} is the multiplication factor

β_i = the yield of the i^{th} group of delayed neutrons in fission

β = the total yield of delayed neutrons in fission and is equal to $\sum_i \beta_i$.

In these equations, n can be considered to be the spatial average concentration of neutrons in the reactor or proportional to the total number; C_i must be taken in the same sense. If n is considered to be the average density of neutrons in the reactor and $\bar{v}$ the average velocity of the neutrons, the neutron flux ϕ is equal to $n\bar{v}$. Thus, Eqs. (5.38) and (5.39) could be written in terms of the neutron flux.

While Eqs. (5.38) and (5.39) represent an extremely simple model of a reactor, they may be extended to more complicated models. For example, the concept of an effective value for β can be used to take into account the fact that the delayed neutrons are emitted at lower energy than the mean energy of fission neutrons. Furthermore, the effect of a reflector can be introduced. For purposes of this discussion, however, the simple equations are adequate.

The reactor transfer function is derived by writing the neutron density as the sum of a constant n_o plus the sinusoidal component of amplitude δn. That is,

$$n(t) = n_o + \delta n\, \epsilon^{j\omega t} .$$

The delayed neutron emitter concentration is similarly written:

$$C_i(t) = C_{io} + \delta C_i\, \epsilon^{j\omega t} .$$

The expressions for $n(t)$ and $C_i(t)$ are substituted into the kinetic equations. To linearize the equations it is necessary to neglect the second-order product $\delta k\, \delta n$. The result, substituting $\delta\phi/\phi_o$ for its equal $\delta n/n_o$, is

$$\frac{\delta\phi/\phi_o}{\delta k} = \frac{1}{j\omega\left[\Lambda + \beta \sum_i \frac{1}{j\omega + \lambda_i}\right]} . \qquad \text{Eq. (5.40)}$$

Figure 5.3 shows the magnitude of the reactor transfer function, while Fig. 5.4 shows the phase of the reactor transfer function as a function of frequency with the neutron lifetime, Λ, as a parameter. The effect of the neutron lifetime on the magnitude of the transfer function is negligible for frequencies below one-half cycle per second. On the other hand, some phase shift dispersion with neutron lifetime is observed at frequencies as low as 0.05 cycle per second. Maximum phase shift occurs for frequencies around one cycle per second. At very low frequencies, the reactor transfer function increases as $1/\omega$ and has a fixed phase shift of 90 degrees.

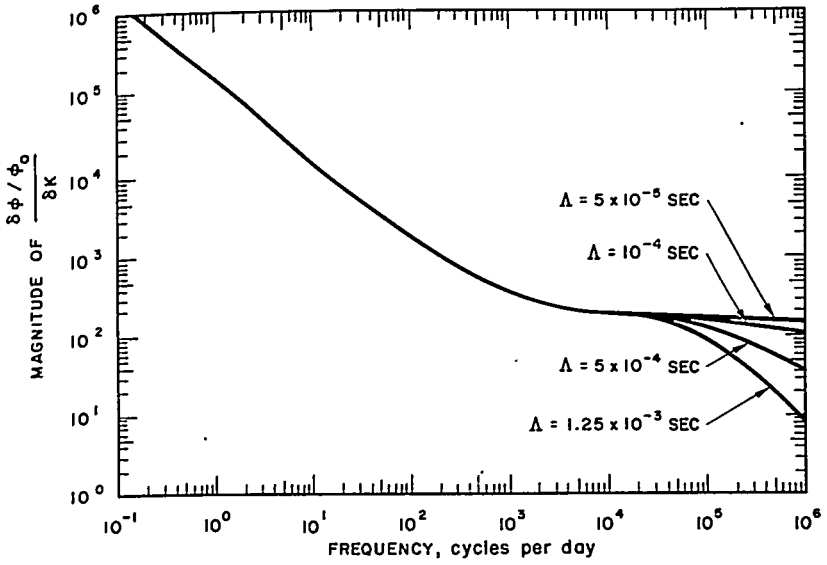

FIGURE 5.3. Magnitude of the Reactor Transfer Function.

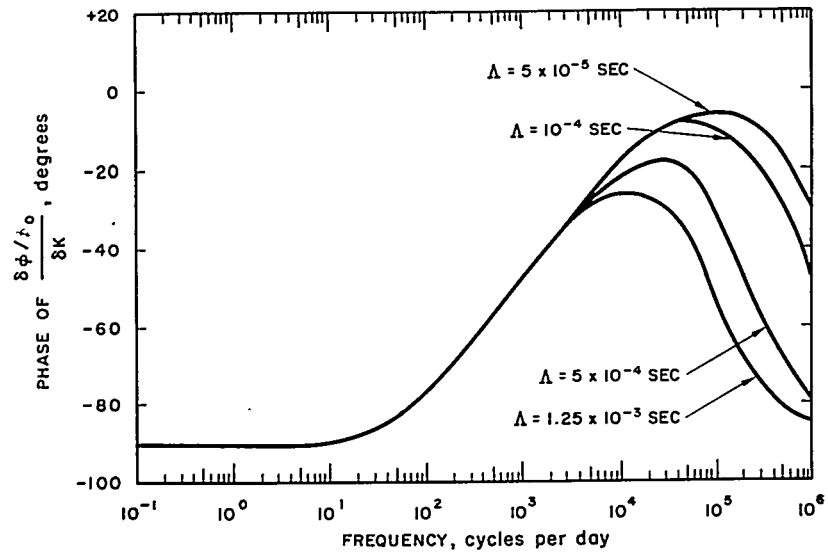

FIGURE 5.4. Phase of the Reactor Transfer Function.

3. *The Xenon Transfer Function*

The fission product poisons which are most often explicitly taken into account in reactor kinetics problems are xenon and

samarium. The well-known equations for these fission products may be found in standard texts:[17]

$$\frac{dX}{dt} = \gamma_x \Sigma_f \phi + \lambda_i I - \sigma_x \phi X - \lambda_x X \qquad \text{Eq. (5.41)}$$

$$\frac{dI}{dt} = \gamma_i \Sigma_f \phi - \lambda_i I \qquad \text{Eq. (5.42)}$$

where

Σ_f = the macroscopic cross section for fission (cm^{-1})
X = the density of xenon 135 nuclei (number/cm^3)
I = the density of iodine 135 nuclei (number/cm^3)
γ_x = the direct fractional yield of xenon 135 in fission
γ_i = the fractional yield of iodine 135 in fission
λ_i = the decay constant of iodine 135
λ_x = the decay constant of xenon 135
σ_x = the microscopic cross section of xenon
ϕ = the neutron flux density.

These equations can be considered as applying to a one-group model or as applying only to the thermal group of a multigroup model.

A similar set of equations may be written for the samarium poisons:

$$\frac{dS}{dt} = \lambda_p P - \sigma_s \phi S \qquad \text{Eq. (5.43)}$$

$$\frac{dP}{dt} = \gamma_p \Sigma_f \phi - \lambda_p P \qquad \text{Eq. (5.44)}$$

where

S = the density of samarium 147 nuclei (number/cm^3)
P = the density of promethium 147 nuclei (number/cm^3)
σ_s = the microscopic cross section of samarium 147
λ_p = the decay constant of promethium 147
γ_p = the fractional yield of promethium 147 in fission.

In Eqs. (5.41) through (5.44), the concentrations X, I, S, and P are functions of time; $X(t)$ and $S(t)$ may be considered, in circuit language, as the output variables. The driving function is the flux $\phi(t)$.

The reactor model considered in this discussion is the so-called point model in which spatial variations are not taken into account. The flux $\phi(t)$ will be considered to be an appropriate average which would yield the same reactivity changes with xenon poisoning as does the actual distribution of flux in the reactor.

For small reactivity changes around criticality in a thermal homogeneous reactor, the derivative of reactivity with respect to the nonfission macroscopic absorption cross section, Σ_a, is

$$\frac{d\delta k}{d\Sigma_a} = -\frac{1}{\Sigma_a + \Sigma_f}.$$

Thus, for an increment Σ_x

$$d\delta k = \frac{\Sigma_x}{\Sigma_a + \Sigma_f}. \qquad \text{Eq. (5.45)}$$

The feedback effect of xenon on the reactor is independent of the plant and may be calculated without taking the plant into account. The xenon transfer function which will be calculated is

$$F_{x\phi} \equiv \frac{\left(\delta\Sigma_x/\Sigma_f\right)}{\left(\delta\phi/\phi_o\right)} \equiv \frac{\left(\sigma_x/\Sigma_f\right)\delta X}{\left(\delta\phi/\phi_o\right)}. \qquad \text{Eq. (5.46)}$$

The xenon reactivity transfer function is obtained from $F_{x\phi}$ by use of Eq. (5.45). Thus,

$$\frac{\delta k_x}{\left(\delta\phi/\phi_o\right)} = \frac{\Sigma_f}{\Sigma_a + \Sigma_f} \epsilon^{j\pi} F_{x\phi} \equiv \alpha_x F_x \qquad \text{Eq. (5.47)}$$

where α_x is the xenon reactivity coefficient. This definition of $F_{x\phi}$ provides greater generality in the sense discussed under reactivity coefficients.

The xenon transfer function can be calculated using Eqs. (5.41) and (5.42). The xenon number density is expressed as

$$X(t) = X_o + \delta X\, \epsilon^{j\omega t}$$

with a similar expression for the iodine number density. It is assumed that the steady-state components, i.e., n_o, X_o, I_o, etc.,

satisfy Eqs. (5.41) and (5.42) as do the time-dependent components. Furthermore, it is again necessary to neglect second-order terms such as $\delta X \delta n$. The result of the calculation is

$$F_{x\phi} = \frac{\dfrac{\sigma_x \delta X}{\Sigma_f}}{\dfrac{\delta\phi}{\phi_o}} = \frac{\left[\dfrac{\lambda_x}{\sigma_x\phi_o}\left(\gamma_i+\gamma_x\right)+\dfrac{j\omega}{\lambda_i}\left(\dfrac{\gamma_x\lambda_x}{\sigma_x\phi_o}-\gamma_i\right)\right]}{\left[\left(1+\dfrac{\lambda_x}{\sigma_x\phi_o}\right)\left(1+\dfrac{j\omega}{\lambda_i}\right)\left(1+\dfrac{\lambda x}{\sigma_x\phi_o}+\dfrac{j\omega}{\sigma_x\phi_o}\right)\right]}. \qquad \text{Eq. (5.48)}$$

The stationary values of the xenon number density and the flux density are connected by the equation

$$X_o = \Sigma_f \phi_o \left(\frac{\gamma_i+\gamma_x}{\lambda_x+\Sigma_x\phi_o}\right). \qquad \text{Eq. (5.49)}$$

By substitution of Eq. (5.49) in Eq. (5.48) and the use of Eq. (5.47), an expression for the xenon reactivity transfer function is obtained:

$$\frac{\dfrac{\delta k}{\left(\dfrac{\delta\phi}{\phi_o}\right)}}{} = \left(\frac{\Sigma_f}{\Sigma_a+\Sigma_f}\right)\epsilon^{j\pi}\left\{\frac{\left[\dfrac{\lambda_x}{\sigma_x\phi_o}\left(\gamma_i+\gamma_x\right)+\dfrac{j\omega}{\lambda_i}\left(\dfrac{\gamma_x\lambda_x}{\sigma_x\phi_o}-\gamma_i\right)\right]}{\left[\left(1+\dfrac{\lambda_x}{\sigma_x\phi_o}\right)\left(1+\dfrac{j\omega}{\lambda_i}\right)\left(1+\dfrac{\lambda_x}{\sigma_x\phi_o}+\dfrac{j\omega}{\sigma_x\phi_o}\right)\right]}\right\}. \qquad \text{Eq. (5.50)}$$

The expression in braces is the xenon transfer function, $F_{x\phi}$, while the coefficient is α_x, the reactivity coefficient.

Figures 5.5 and 5.6 show the magnitude and phase shift of the xenon transfer function, respectively. Since ϕ_o is involved in the expression for the xenon transfer function, it is shown on the figures as a parameter.

Equation (5.50) shows that there is a phase shift of 180 degrees in the xenon reactivity coefficient. Thus, where the phase of the xenon transfer function is 180 degrees, the xenon reactivity oscillation is in phase with the disturbance causing it, and the possibility of instability is present. The phase shift necessary for instability occurs at a frequency of about one cycle per day. The question of instability due to xenon will be discussed after considering the effect of reactor temperature on reactivity.

One further point of interest deals with the samarium poisoning. It can be shown by use of Eqs. (5.43) and (5.44), with

substitution of appropriate constants, that samarium has a small effect on the reactor stability compared with xenon. For this reason, the effect of samarium will not be treated explicitly.

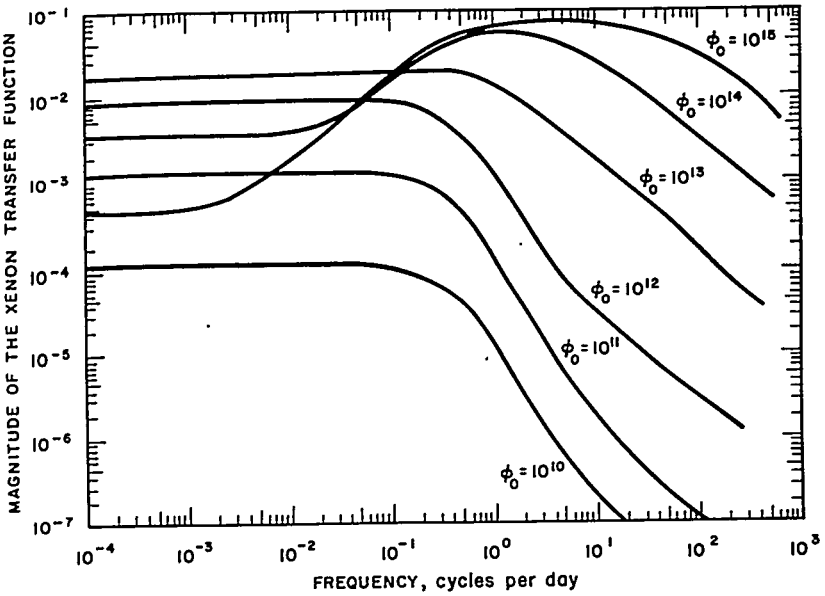

FIGURE 5.5. Magnitude of the Xenon Transfer Function.

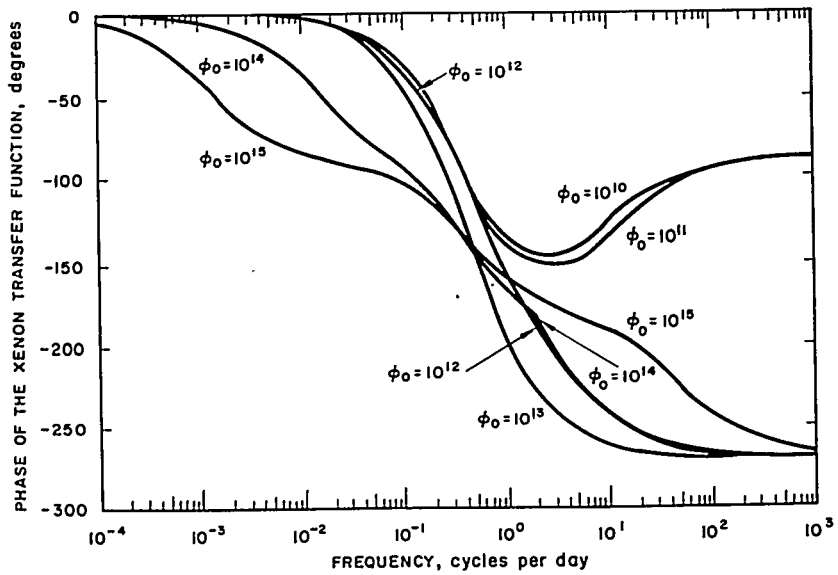

FIGURE 5.6. Phase Shift of the Xenon Transfer Function.

4. *Reactor Plant Equations*

To derive transfer functions for the temperature coefficient of reactivity and the pressure coefficient of reactivity, the plant equations must be used. These will now be discussed briefly. A simplified model of the reactor plant is shown in Fig. 5.7.

A) REACTOR HEAT TRANSFER EQUATIONS. The simplest description of heat transfer in a reactor is based on a one-section model. The use of the simple model leads to a set of ordinary differential equations which are sufficiently accurate for most problems in reactor stability and transient analysis. There is a limitation, however, on the maximum speed of reactor transients which this model can handle. Modification of the equations to include more sections for application to the analysis of fast transients is a straightforward extension of the method presented here.

In the one-section model, heat transfer in the reactor is assumed to occur at a single point; thereby, spatial variations are neglected. Two points of energy storage are included, the reactor metal and the coolant in the core. Two ordinary differential equations are obtained:

$$Q = C_{rm}\frac{dT_m}{dt} + h_r\left(T_{rm} - T_{rw}\right) \qquad \text{Eq. (5.51)}$$

and

$$h_r\left(T_{rm} - T_{rw}\right) = C_{rw}\frac{dT_{rw}}{dt} + F_w c\left(T_{r_o} - T_{r_i}\right) \qquad \text{Eq. (5.52)}$$

where

$$T_{rw} = \frac{1}{2}\left(T_{r_i} + T_{r_o}\right) \qquad \text{Eq. (5.53)}$$

$Q(t)$ = total power generated in the fuel plates (Btu/sec)
C_{rm} = total thermal capacity of reactor metal (Btu/°F)
$T_{rm}(t)$ = average reactor metal temperature (°F)
$h_r(F_w)$ = total heat transfer coefficient (Btu/sec°F)
$T_{rw}(t)$ = average reactor water temperature in coolant passes (°F)
C_{rw} = total thermal capacity of reactor water (Btu/°F)
$F_w(t)$ = total coolant flow rate (lb/sec)
c = specific thermal capacity of coolant (Btu/lb°F)
$T_{r_o}(t)$ = reactor outlet average coolant temperature (°F)
$T_{r_i}(t)$ = reactor inlet average coolant temperature (°F)

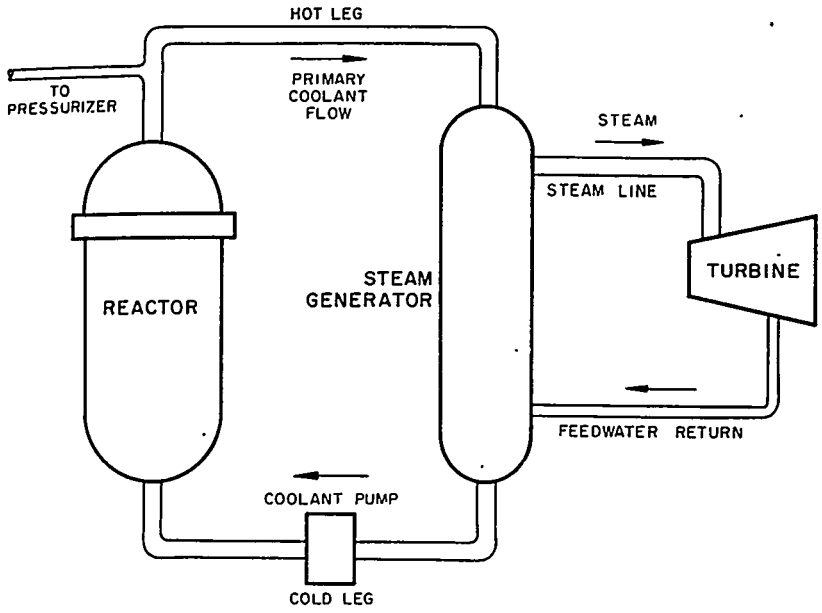

FIGURE 5.7. Simplified Schematic Diagram of the Reactor Plant.

These equations are derived directly from considerations of heat balance. They are used to derive $T_{r_o}(t)$ and $T_{rw}(t)$ for given variations of $Q(t)$, $T_r(t)$, and F_w. The variable $T_{r_o}(t)$ feeds into the primary loop, and $T_{rw}(t)$ affects reactivity feedback which, in turn, affects Q.

B) PRIMARY PIPING EQUATIONS. In circulating through the primary loop, the coolant undergoes mixing and transport delay effects. For example, a transient in coolant temperature at the core outlet does not appear at the vessel outlet until some time later and, moreover, its shape (temperature at a point vs time) is changed. It is necessary to describe these effects by means of equations, so that the filtering of temperature transients can be included in the representation of the primary loop. It is possible to approximate these filtering effects by combinations of two types of time delays: a pure transport delay and a simple mixing delay.

A pure transport delay is that which delays a transient by a fixed amount of time without altering its shape. The outlet coolant temperature T_o of a component of the primary loop causing such a delay is simply equal to the inlet temperature

displaced in time by an amount τ_t, the transport delay, expressed as

$$T_o\left(t+\tau_t\right)=T_i(t). \qquad \text{Eq. (5.54)}$$

A mixing delay is derived by assuming complete mixing in the volume concerned. Then, the outlet temperature T_o is equal to the average temperature in the volume concerned. A power balance for a particular section or component requires that the net power flowing into the volume be equal to the rate of increase in stored energy.

Consider a section into which water is flowing at the rate F_w at a temperature $T_i(t)$. The water leaves the section at the rate F_w and at a temperature $T_o(t)$. $T_o(t)$ is equal to the mixed or average temperature T_{ave} in the volume. If M_{ws} is the mass of water in the section, an energy balance over the time Δt yields the equation

$$\Delta t\, c\, F_w \left[T_i(t)-T_o(t)\right]=c\, M_{ws}\frac{dT_{ave}}{dt}\Delta t = cM_{ws}\frac{dT_o}{dt}\,\Delta t \qquad \text{Eq. (5.55)}$$

where c is the specific heat.
The resulting equation is

$$\left(\frac{M_{ws}}{F_w}\frac{dT_o}{dt}+T_o\right)=\tau_m\frac{dT_o}{dt}+T_o=T_i \qquad \text{Eq. (5.56)}$$

where $\tau_m \equiv M_{ws}/F_w$ and is called the mixing delay.

In general, the filtering effect on coolant temperature of a section of the primary loop is described by a combination of mixing and transport delays:

$$\tau_m\frac{dT_o(t)}{dt}+T_o(t)=T_i\left(t-\tau_t\right) \qquad \text{Eq. (5.57)}$$

where τ_m is now modified and is given by the equation

$$\tau_m+\tau_t=M_{ws}/F_w. \qquad \text{Eq. (5.58)}$$

The decision as to how to divide the total time delay between mixing and transport is based on the geometry of the particular section of the coolant loop and the expected flow pattern. For example, a straight pipe will cause, primarily, a transport delay with relatively little mixing delay. A more complicated geometry may cause both. Because greater filtering effects occur in the heat transfer section of the heat exchanger, the division between transport and mixing does not have to be accurately predicted. However, it is important that the sum of the two delays accurately represent the effect of the total volume in which water is transported and mixed; otherwise, the thermal capacity is not properly represented, and an error is introduced in the calculation of changes in coolant volume and pressurizer surges.

With the exclusion of the heat transfer sections of the reactor and heat exchanger, mixing and transport effects are encountered in the primary loop as follows. In the piping between the reactor vessel outlet and the heat exchanger inlet, and between the heat exchanger outlet and the reactor vessel inlet, pure transport delays may be assumed. Combined mixing and transport effects are encountered in the reactor vessel between the vessel inlet and the core inlet and between the core outlet and the vessel outlet. In two-pass cores, a combined mixing and transport delay connects the two passes. In the inlet and outlet plenums of the heat exchanger, combined mixing and transport delays may be assumed.

The thermal capacity of the coolant contained in the core is included in the reactor heat transfer equations given in the discussion of the transfer function above. Thus, the delay in the core itself is implicitly contained in these equations and should not be included again as a transport or mixing delay. Similarly, the heat transfer equations of the heat exchanger include the thermal capacity of primary water. Consequently, no additional delay should be included.

C) HEAT EXCHANGER EQUATIONS. The derivation of a set of differential equations for the heat exchanger and the secondary loop is based on the assumptions that the state of the steam produced is always dry and saturated and that the water on the secondary side is always at the saturation temperature for the existing pressure. Thus, it becomes possible to use the saturation temperature in the heat transfer equations as the temperature existing on the steam side of the heat exchanger.

As in the derivation of reactor heat transfer equations, a one-section model is used for the heat exchanger. Two points of energy storage are assumed: the primary coolant water and the water on the secondary side. The thermal capacity of the

boiler metal may be included with the secondary water, since the thermal resistance on the primary side of the heat exchanger predominates. Based on this model, the following equations are readily derived:

$$F_w{}^c \left(T_{b_i} - T_{b_o}\right) = C_{bw}\frac{dT_{bw}}{dt} + h_b\left(T_{bw} - T_s\right) \qquad \text{(Eq. 5.59)}$$

$$h_b\left(T_{bw} - T_s\right) = C_{bs}\frac{dT_s}{dt} + P_L \qquad \text{(Eq. 5.60)}$$

$$T_{bw} = \frac{1}{2}\left(T_{b_i} + T_{b_o}\right) \qquad \text{(Eq. 5.61)}$$

where

$T_{b_i}(t)$ = inlet primary water temperature (°F)

$T_{b_o}(t)$ = outlet primary water temperature (°F)

$T_{bw}(t)$ = average primary water temperature (°F)

$T_s(p)$ = saturation temperature at secondary pressure (°F)

$h_b(F_w)$ = total effective heat transfer coefficient (Btu/sec°F)

C_{bw} = total thermal capacity of primary water in heat exchanger tubes (Btu/°F)

C_{bs} = total thermal capacity of water on secondary side and boiler metal (Btu/°F)

P_L = net power delivered by the steam generator (Btu/sec).

Equation (5.61), which gives the average coolant temperature T_{bw}, is valid when the primary coolant temperature drop from inlet to outlet is small, compared with the mean temperature drop from the primary to the secondary side of the heat exchanger. In instances where this requirement is not satisfied, the equation may still be used if the heat transfer coefficient h_b is properly modified.

D) PRESSURIZER EQUATIONS. The determination of coolant surge rate is obtained by integrating the net power trans-

ferred to the coolant. The difference between the heat transfer rates at the reactor and the heat exchanger is the rate of storage of energy in the coolant. The surge rate caused by volume expansion, which must be accommodated by the pressurizer, is directly proportional to this power difference:

$$\text{Surge rate} = \frac{dV}{dt} = M_{wp} \frac{\partial v}{\partial T}\bigg|_p \frac{dT}{dt} = \frac{1}{c} \frac{\partial v}{\partial T}\bigg|_p \Delta P \qquad \text{Eq. (5.62)}$$

where

V = volume of primary coolant

M_{wp} = mass of primary coolant

$\left.\frac{\partial v}{\partial T}\right|_p$ = temperature coefficient of expansion

ΔP = rate of energy storage in coolant.

Surge rates accompanying power transients are determined by simultaneous solution of the reactor and plant equations, including Eq. (5.62), under the given transients. The pressurizer equations are treated subsequently in greater detail.

E) REACTOR VESSEL EQUATIONS. Several effects peculiar to the particular reactor vessel and core being analyzed are not included in this analysis for the purpose of simplification. Among these is the filtering effect on inlet temperature transients exerted by thermal shields through which the coolant flows before entering the core. Another is the effect of flow leakage which bypasses the heated section of the core. Such effects, when necessary, are readily taken into account.

F) SECONDARY LOOP EQUATIONS. The derivation of equations for the secondary loop is based on the assumption that the steam at the outlet of the steam generator is dry and saturated. This assumption is justified because (1) steam separators and recirculation are employed to obtain high quality steam, and (2) superheating is not used in pressurized water reactors because of the small temperature differences available.

The power delivered by the steam generator is proportional to the product of steam flow rate and the difference of enthalpy between the steam and the feedwater:

$$h_b\left(T_{bw} - T_s\right) = F_s\left(H_s - H_{fw}\right) + C_{bs} \frac{dT_s}{dt} \qquad \text{Eq. (5 .63)}$$

where

F_s = steam flow rate (lb/hr)
H_s = steam enthalpy
H_{fw} = feedwater enthalpy

and the symbols T_{bw}, T_s, and h_b have the same significance as in the heat exchanger equations above. This is based on equality between steam and feedwater flow rates and, thus, neglects any instabilities of the secondary system.

The enthalpy of saturated steam is nearly constant[18] over a wide range of pressure, varying from 1198 Btu/lb to 1204 Btu/lb over a pressure range from 200 to 800 psig. The feedwater enthalpy, which depends on condenser pressure, is usually between 50 and 100 Btu/lb. Thus, the enthalpy difference may be regarded as a constant, and the power delivered is directly proportional to the steam flow rate.

The impedance to steam flow caused by the turbine is nearly independent of turbine speed. By assuming constant back pressure, the steam flow rate is proportional to the throttle pressure at a given throttle opening:

$$F_s \equiv p_s A \qquad \text{Eq. (5.64)}$$

where

p_s = saturation pressure
A = proportionality factor which is a function of the throttle opening.

G) LIMITATIONS OF THE ONE-SECTION APPROXIMATION. The lumping of the distributed parameter heat transfer problem in the reactor and in the heat exchanger imposes limitations on the speed of transients and the frequency of oscillations which may be accurately analyzed by using the equations derived. The formulation of a rigorous set of criteria for universal application appears to be impractical because of the nonlinear nature of the equations and the wide variety of problems in transients and frequency response which must be considered. However, it is possible to obtain analytically some approximations for the limitations by frequency response methods and by analog simulation of transients. The frequency response approach leads to a criterion which requires that the angular frequency of periodic variations should not exceed $1/\tau$ for a one-section model, where τ is the coolant transport time through the heat transfer section. The maximum permissible frequency is directly proportional to the number of sections

used in the model; a one-section model is adequate for the majority of transients encountered in practice.

5. *Effect of Reactor Temperature Coefficient at Low Frequencies*

The effect of the reactor temperature coefficient will be treated as a quasistationary problem for use in the analysis of xenon instability. As noted in the discussion of effects of characteristic times on the analysis of reactor plant stability, there is a large frequency range in which such a treatment is valid. The equilibration times of the components of the reactor, i.e., fuel plates, coolant channels, etc., to temperature changes are of the order of fractions of a second. The recirculation time of the primary coolant is of the order of seconds, and the equilibration times for temperature changes in primary loop components are of the order of tens of seconds. The reactor kinetic response to a small reactivity change will have reached a steady-state condition in a matter of minutes. When the highest frequency of interest is limited to the order of cycles per hour, it is clear that a quasistationary condition will prevail.

A reactor having a negative temperature coefficient of reactivity is capable of adjusting its average temperature to compensate for reactivity changes, such as variations in xenon concentration. However, to maintain equilibrium at a new temperature, the power level is different from its original value. It is useful to know this change in power level resulting from a given reactivity change. This is called the forward reactor transfer function with temperature feedback evaluated at zero frequency, $(\delta\phi/\phi_o)/\delta k$. Since the reactivity is compensated by a temperature change,

$$\delta k = -\alpha_T \delta T_{rw}$$

it is necessary to determine the power change necessary to maintain this change in temperature, $\delta T_{rw}/(\delta\phi/\phi_o)$. To do this one takes advantage of the fact that a fractional change in reactor power produces the same fractional change in both the temperature drop from the primary-to-secondary side of the heat exchanger and the steam pressure:

$$\frac{\delta\phi}{\phi_o} = \frac{\delta\left(T_{rw} - T_s\right)}{\left(T_{rw} - T_s\right)_o} = \frac{\delta p}{p_o}.$$

It follows that

$$\frac{dT_{rw}}{\frac{d\phi}{\phi_o}} = \frac{dT_{rw}}{\frac{d(T_{rw}-T_s)}{(T_{rw}-T_s)_o}} = \left.\frac{\partial T_{rw}}{\frac{\partial (T_{rw}-T_s)}{(T_{rw}-T_s)_o}}\right|_{T_s \text{ const}} + \frac{dT_s}{\frac{dp}{p_o}}$$

or

$$\frac{dT_{rw}}{\frac{d\phi}{\phi_o}} = (T_{rw}-T_s)_o + p_o \left.\frac{dT_s}{dp}\right|_{\text{sat}}$$

where the last derivative is obtained from the saturation curve in steam tables.

The answer to the problem is

$$\frac{\delta\phi/\phi_o}{\delta k} = \frac{1}{-\alpha_T\left[(T_{rw}-T_s)_o + p_o \left.\frac{dT_s}{dp}\right|_{\text{sat}}\right]}$$

(log mean temperature difference may be used instead of $T_{rw} - T_s$).

The result may be illustrated by numerical example, using a plant having the following characteristics:

$$(T_{rw} - T_s) = 100\ F^\circ$$

$$p_s = 500 \text{ psi}$$

$$\alpha_T = -2 \times 10^{-4}/F^\circ.$$

At 500 psi, the steam tables give $\left(\partial T_s/\partial p\right)_{\text{sat}} = 0.20\ F^\circ/psi$. Substitution gives

$$\frac{\delta\phi/\phi_o}{\delta k} = \frac{10^4}{2(100 + 500 \times 0.2)} = \frac{10^4}{400} = 25.$$

This means, for example, that a reactivity change of 0.001 δk produces a power change of 2.5 percent in the steady state.

It is interesting to note that the calculated power change would be much greater if there were no recirculation of the coolant. Without recirculation the reactor inlet temperature is constant;

$$\frac{\delta T_{rw}}{\delta\phi/\phi_o} = \frac{1}{2}\left(T_{r_o} - T_{r_i}\right)_o$$

and

$$\frac{\delta\phi/\phi_o}{\delta k} = \frac{1}{-\alpha_T \frac{1}{2}\left(T_{r_o} - T_{r_i}\right)_o} = 100$$

assuming a value of 100 degrees for the temperature rise through the reactor. The effect of recirculation is to enhance the effective temperature coefficient typically by a factor of 4 or 5.

6. *Xenon Loop Stability*

The plots of the phase of the xenon transfer function shown in Fig. 5.6 indicate that for sufficiently large values of the flux, the phase shift can equal or exceed 180 degrees. Since the xenon reactivity coefficient α_x contains a phase shift of 180 degrees, the xenon poisoning can lead to a reactivity feedback with a total phase shift of 360 degrees. Thus, in the absence of stabilizing influences, a reactor could oscillate in power level because of xenon poisoning at a frequency of one to two cycles per day. The xenon instability is generally not considered troublesome, since it occurs at such a low frequency that simple external control can overcome the instability. The following discussion will treat the stabilizing effect of the negative temperature coefficient of reactivity on the xenon instability. Since the xenon instability is of very low frequency, the quasistationary analysis given in the preceding discussion on the temperature feedback effect may be used.

The temperature coefficient reactivity feedback phase is 180 degrees for all frequencies which are sufficiently low. The xenon reactivity feedback phase is 360 degrees for the critical frequency, i.e., that frequency which may be the frequency of instability. If consideration is limited to this frequency, the reactivity feedbacks may be added directly. If δk_{FB} is the net reactivity feedback,

$$\delta k_{FB} = \delta k_T + \delta k_x .$$

If δk_T exceeds δk_x in magnitude, the feedback will be degenerative, since δk_T is negative and δk_x is positive. Thus, at the critical frequency, the system is stable if

$$|\delta k_T| > \delta k_x$$

or

$$\frac{\delta k_x}{|\delta k_T|} < 1 .$$

From Eq. (5.47), the system is stable if

$$\frac{\delta k_x}{|\delta k_T|} = \frac{\alpha_x F_x}{\alpha_T \left[\left(T_{rw} - T_s \right)_o + p_o \left(\frac{\partial T}{\partial p} \right)_{sat} \right]} .$$

To examine this equation numerically, the critical frequencies, i.e., those frequencies for the various flux levels at which the xenon transfer function has a phase shift of 180 degrees, were selected from Fig. 5.6. The corresponding values of the magnitude of the xenon transfer function were selected from Fig. 5.5 and plotted as in Fig. 5.8. This plot shows that there is no possibility of instability due to xenon at flux levels below about 4×10^{11} neutrons/cm^2/sec. The tendency toward instability increases monotonically with flux level. Since the temperature coefficient of reactivity enters the stability criterion directly, any instability could, in principle, be overcome by a negative temperature coefficient of reactivity sufficiently large in magnitude.

To examine this point, consider the numerical example given in the discussion on the effect of reactor temperature coefficient at low frequencies. As a flux level, choose ϕ_o equal to 10^{14} neutrons/cm^2/sec. The magnitude of F_x is about 6.3×10^{-2} The value of $\Sigma_f/(\Sigma_f + \Sigma_a)$ must also be chosen to obtain the magnitude of α_x. Choose this to be 0.6. The limiting value of $|\alpha_T|$ for stability is then about 1.9×10^{-4} in reactivity per degree F. All values of α_T larger in magnitude than this, and negative, assure stability.

To test this analysis, the xenon reactivity problem has been simulated on the analog computer. The nonlinear terms were accurately simulated in this study to determine their influence on stability. The flux level was chosen to be 10^{14} neutrons/cm^2/sec. The temperature coefficient was chosen to be about 10 percent too low for stability, thus assuring instability, i.e., the ratio of xenon reactivity feedback to temperature reactivity feedback was 1.10. The critical frequency from Fig. 5.6 was determined to be 1.3 cycles per day.

Figure 5.9 shows the result of the computation. The observed frequency is approximately 1.2 cycles per day. The amplitude

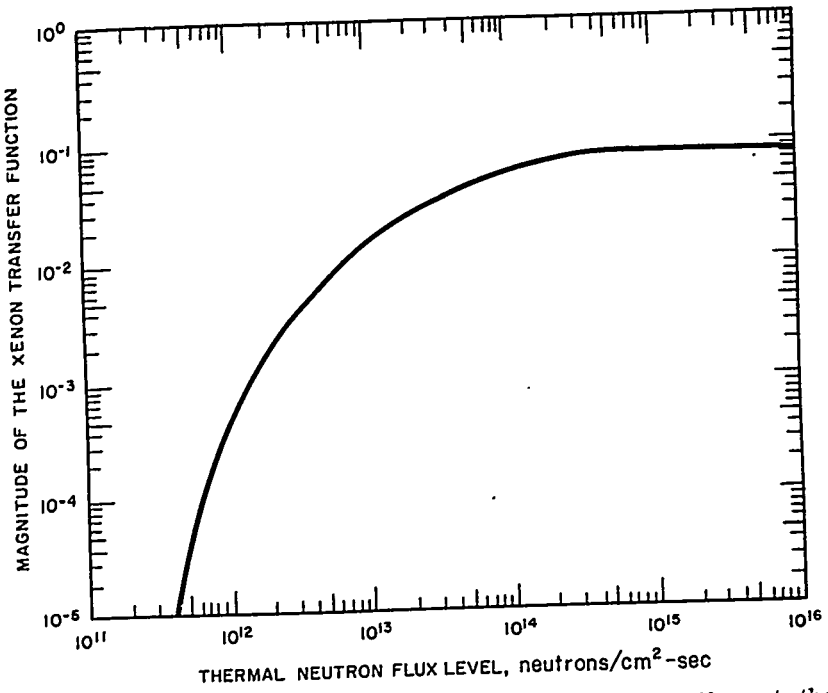

FIGURE 5.8. Magnitude of the Xenon Transfer Function at the Critical Frequency.

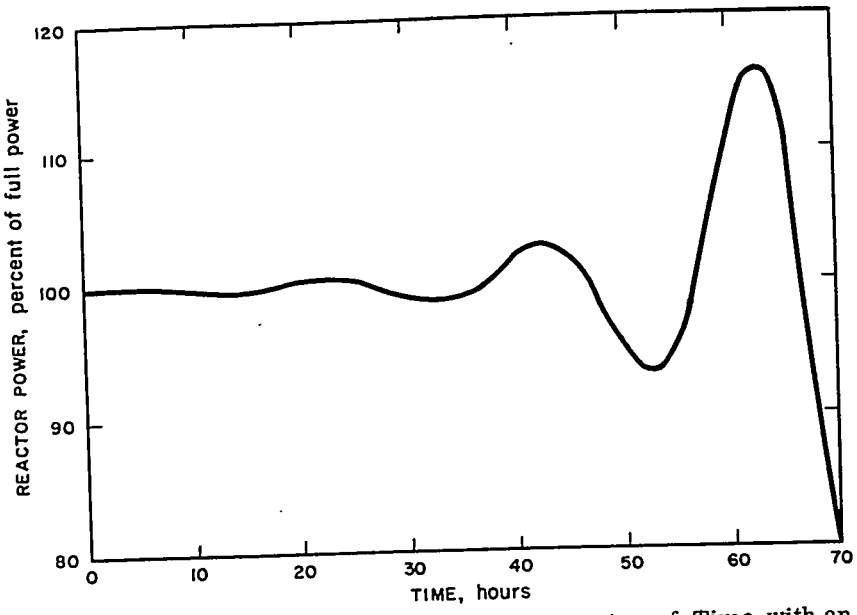

FIGURE 5.9. Reactor Power Level as a Function of Time with an Unstable Xenon Reactivity Feedback.

of the oscillation builds up rapidly in a few cycles. Nonlinearities eventually limit the amplitude, but this is of little practical value.

This analysis of xenon instability was originally reported in Ref. 19 and was restudied by Chernick who included vanishingly small values of temperature coefficient.[20]

7. *Pressurizer System Dynamics*

The remainder of this section deals with the combined effects of pressure and temperature on plant stability. First, the pressurizer system dynamic equations are derived, and then the stability problems are discussed.

The pressurizer is connected to the primary loop through a surge line. The pressurizer itself is a vessel partially filled with water; the remainder of the vessel is filled with steam. The water in the pressurizer is heated electrically to maintain the appropriate steady-state pressure in the system. The pressurizer is generally equipped with a spray which serves two purposes: the reduction of pressure maxima caused by heating of the primary loop, and the degasification of the primary water. In this discussion it will be assumed that there is a steady-state flow through the spray for degasification. The surge line may consist of sections having different flow areas. These may be heat exchangers in the line or reduced diameter sections which provide damping. A diagram of the pressurizer system is shown in Fig. 5.10.

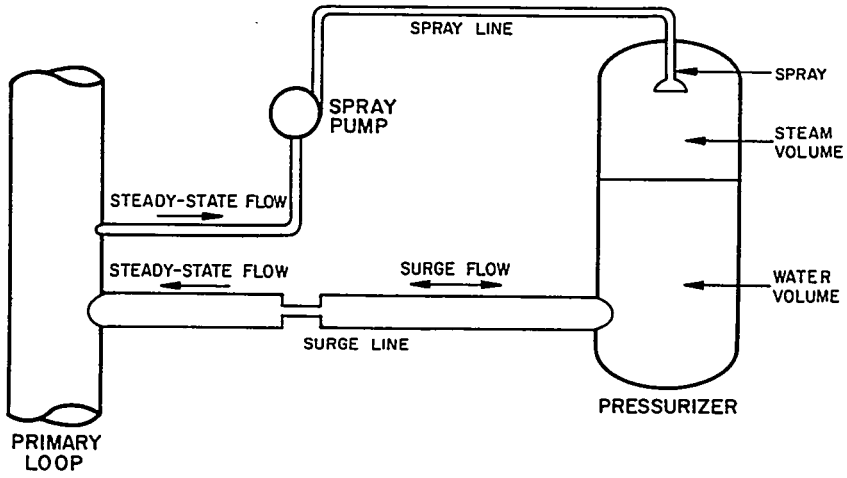

FIGURE 5.10. Diagram of the Pressurizer System

The pressure coefficient of reactivity of a pressurized water reactor is positive and, under transient conditions, detracts from the negative temperature coefficient of reactivity. When the reactor temperature increases, an important contribution to the negative temperature coefficient of reactivity comes about from the reduced density of the water in the reactor. The density can decrease, however, only if there is a net flow of water out of the primary system into the pressurizer, neglecting expansion of the piping. To produce this flow, the pressure in the reactor must rise to overcome two effects: the compression of the steam volume in the pressurizer, and the force required to produce the flow in the surge line. Thus, when an increase in reactor temperature occurs, there must be some increase in reactor pressure. Until the pressurizer reestablishes equilibrium pressure conditions, this pressure rise reduces the effectiveness of the negative temperature coefficient of reactivity.

In addition, there is a possibility of instability arising from the pressurizer system. A rise in pressure in the reactor will cause a mass flow of water toward the pressurizer. The water flow will compress the steam volume and increase the pressurizer pressure. The kinetic energy of the moving water could lead to an excess flow into the pressurizer and a transient drop in reactor pressure. This would be compensated for by a return flow of water from the pressurizer to the reactor. In the absence of adequate damping, the possibility exists of oscillation sustained by feedback to the reactor. This possibility will be examined following the derivation of the equations.

The first equation to be derived deals with the flow of water into the pressurizer under dynamic conditions. A time-dependent differential equation for the water density in the reactor is derived.

The reactor pressure is designated by p, the pressurizer pressure by p_p. The steady-state pressure difference between the pressurizer and reactor due to the degasifier flow is designated by Δp_{ss}. Thus, for the steady-state

$$p_{po} - p_o = \Delta p_{ss} \qquad \text{Eq. (5.65)}$$

where the subscript o designates the steady-state value. For a transient condition

$$p_p - p = \Delta p_{ss} + dp_p - dp \qquad \text{Eq. (5.66)}$$

where dp_p represents the change in p_p from its steady-state

value, and dp represents the change in p from its steady-state value.

The thermodynamic state of the water in the primary loop is governed by an equation of state relating the pressure p, the temperature T, and the density ρ. The pressure can be written as an explicit function of the other two variables, i.e., $p(T,\rho)$. The incremental pressure dp can be written

$$dp = \left(\frac{\partial p}{\partial T}\right)_\rho dT + \left(\frac{\partial p}{\partial \rho}\right)_T d\rho \,. \qquad \text{Eq. (5.67)}$$

The incremental change in the pressurizer pressure can be written

$$dp_p = \frac{dp_p}{dV_p} dV_p$$

where V_p is the pressurizer steam volume, and dp_p/dV_p is a constant of the pressurizer. The change in pressurizer steam volume is just equal to the increase in volume of the coolant in the primary system. The fractional increase in primary loop density $d\rho/\rho$ times the primary loop volume V_o is the decrease in volume of coolant in the primary system. Thus,

$$dp_p = \frac{dp_p}{dV_p} \frac{d\rho}{\rho} V_o \,. \qquad \text{Eq. (5.68)}$$

Equation (5.66) can then be written:

$$p_p - p = \Delta p_{ss} - \left(\frac{\partial p}{\partial T}\right)_\rho dT - \left[\left(\frac{\partial p}{\partial \rho}\right)_T \rho + V_o \frac{dp_p}{dV_p}\right] \frac{d\rho}{\rho} \,. \qquad \text{Eq. (5.69)}$$

The pressure difference across the surge pipe is responsible for the flow of water in the surge line. Suppose the surge line has two sections in series. Section 1 has a flow area A_1, a total mass of water M_1, and an average water velocity v_1. Section 2 has characteristic values A_2, M_2, and v_2. Density changes in the surge line are neglected. (This was assumed implicitly above when the increase in primary loop coolant volume was set equal to the decrease in pressurizer steam volume.) The flow equation for the surge line is

$$p_p - p = \frac{M_1}{A_1}\frac{dv_1}{dt} + \frac{M_2}{A_2}\frac{dv_2}{dt} + f_1(v_1) + f_2(v_2) \qquad \text{Eq. (5.70)}$$

where $f_1(v_1)$ and $f_2(v_2)$ are the friction pressure drops in the pipe sections 1 and 2, respectively. The form of the friction pressure drop is assumed to be a proportionality factor times the velocity squared with the proportionality factor varying as $v^{-0.2}$. Thus,

$$f_1(v_1) = a_1 |v_1|^{1.8} \qquad \text{Eq. (5.71a)}$$

$$f_2(v_2) = a_2 |v_2|^{1.8} \qquad \text{Eq. (5.71b)}$$

where a_1 and a_2 are constants.

Because of the steady flow into the spray system, v_1 and v_2 have steady-state values plus a time-dependent portion:

$$v_1 = v_{1_o} + v_1(t) \qquad \text{Eq. (5.72a)}$$

$$v_2 = v_{2_o} + v_2(t). \qquad \text{Eq. (5.72b)}$$

The mass flow through pipe section 1 is equal to the mass flow in pipe section 2, since they are in series. Thus,

$$\rho v_1 A_1 = \rho v_2 A_2 . \qquad \text{Eq. (5.73)}$$

Since the time-dependent portion of the mass flow is equal to the increase in the mass of water in the primary loop,

$$\rho v_1(t) A_1 = \rho v_2(t) A_2 = V_o \frac{d\rho}{dt}. \qquad \text{Eq. (5.74)}$$

Differentiating Eq. (5.74) with respect to time yields

$$\rho \frac{dv_1}{dt} A_1 = \rho \frac{dv_2}{dt} A_2 = V_o \frac{d^2\rho}{dt^2} . \qquad \text{Eq. (5.75)}$$

The total friction pressure drop is the sum of f_1 and f_2. If the steady-state flow volume is designated as F_o, adding Eqs. (5.71a) and (5.71b) and substituting from Eqs. (5.65), (5.72a), (5.72b), and (5.74) give the result

$$f_1(v_1) + f_2(v_2) = \left[1 + \frac{V_o}{\rho F_o} \frac{d\rho}{dt}\right]^{1.8} \Delta p_{ss} . \qquad \text{Eq. (5.76)}$$

Substitution of Eqs. (5.75) and (5.76) in Eq. (5.70) yields

$$p_p - p = \left[\frac{M_1}{A_1^2} + \frac{M_2}{A_2^2}\right] \frac{V_o}{\rho} \frac{d^2\rho}{dt^2} + \left[1 + \frac{V_o}{\rho F_o} \frac{d\rho}{dt}\right]^{1.8} \Delta p_{ss}. \qquad \text{Eq. (5.77)}$$

To obtain Eq. (5.78), Eq. (5.77) is combined with Eq. (5.69):

$$\left(\frac{\partial p}{\partial T}\right)_\rho dT = -\left[\left(\frac{\partial p}{\partial \rho}\right)_T \rho + V_o \frac{dp_p}{dV_p}\right] \frac{d\rho}{\rho} - \left[\frac{M_1}{A_1^2} + \frac{M_2}{A_2^2}\right] \frac{V_o}{\rho} \frac{d^2\rho}{dt^2}$$

$$- \left\{\left[1 + \frac{V_o}{\rho F_o} \frac{d\rho}{dt}\right]^{1.8} - 1\right\} \Delta p_{ss}. \qquad \text{Eq. (5.78)}$$

Equation (5.78) provides a relationship between the thermodynamic variables p, T, and ρ. Through this relationship, an explicit value can be obtained for the total derivative of the pressure with respect to the temperature. To make Eq. (5.78) more tractable, the friction term is linearized by expanding it and taking the first term.

Next, the time-dependent variables are assumed representable by a steady-state value plus an oscillatory component of frequency ω:

$$\rho = \rho_o + \delta\rho\, \epsilon^{j\omega t}$$

$$p = p_o + \delta p\, \epsilon^{j\omega t}$$

$$T = T_o + \delta T\, \epsilon^{j\omega t}.$$

Substituting these, Eq. (5.78) can be solved for $\delta\rho/\delta T$:

$$\frac{\delta\rho}{\delta T} = -\frac{\rho\left(\frac{\partial p}{\partial T}\right)_\rho}{\left\{\left[\left(\frac{\partial p}{\partial \rho}\right)_T \rho + V_o \frac{dp_p}{dV_p}\right] - \omega^2 V_o \left[\frac{M_1}{A_1^2} + \frac{M_2}{A_2^2}\right] + j\omega\, 1.8\, \frac{V_o}{F_o} \Delta p_{ss}\right\}}$$

Eq. (5.79)

Equation (5.67) may be rewritten for the oscillatory condition

$$\frac{\delta p}{\delta T} = \left(\frac{\partial p}{\partial T}\right)_\rho + \left(\frac{\partial p}{\partial \rho}\right)_T \frac{\delta\rho}{\delta T}.$$

Using Eq. (5.79) and the modified form of Eq. (5.67), the following expression for $\delta_p/\delta T$ is obtained:

$$\frac{\delta p}{\delta T} = \left(\frac{\partial p}{\partial T}\right)_\rho \left\{ 1 - \frac{\rho\left(\frac{\partial p}{\partial \rho}\right)_T}{\left\{\left[\left(\frac{\partial p}{\partial \rho}\right)_T \rho + V_o \frac{dp_p}{dV_p}\right] - \omega^2 V_o \left[\frac{M_1}{A_1^2} + \frac{M_2}{A_2^2}\right] + j\omega\, 1.8 \frac{V_o}{F_o} \Delta p_{ss} \right\}} \right\}$$

Eq. (5.80)

This is the required relation to carry out the stability analysis.

A numerical example has been calculated with the following values for the parameters in the equations:

$$\left(\frac{\partial p}{\partial T}\right)_\rho = 1.6 \times 10^4 \text{ lb/ft}^2 \text{ °F}$$

$$\rho\left(\frac{\partial p}{\partial \rho}\right)_T = 1.6 \times 10^7 \text{ lb/ft}^2$$

$$\left[\left(\frac{\partial p}{\partial \rho}\right)_T \rho + V_o \frac{dp_p}{dV_p}\right] = 1.7 \times 10^7 \text{ lb/ft}^2$$

$$V_o \left[\frac{M_1}{A_1^2} + \frac{M_2}{A_2^2}\right] = 4.1 \times 10^5 \text{ slugs/ft}$$

$$\frac{V_o}{F_o} = 1.2 \times 10^4 \text{ sec}$$

$$\Delta p_{ss} = 1.2 \text{ lb/ft}^2$$

These values are representative of a typical plant design.

The result, in Fig. 5.11, shows a resonance behavior at a frequency of approximately 0.2 cycle per sec. Resonance occurs when the coefficient of $(\partial p/\partial T)_\rho$ in Eq. (5.80) vanishes. A second resonance occurs when the real part of the denominator in Eq. (5.80) vanishes at a frequency slightly over one cycle per sec. At frequencies above this, the pressurizer cannot respond to the oscillations in the reactor; the value of $\delta p/\delta T$ takes on

the value for solid water, approximately 1.6×10^4 lb/ft^2°F, and the reactor cannot change the water density by a temperature rise. At resonance, the value of $\delta p/\delta T$ is 100 times the value for solid water.

8. *Combined Reactivity Effect of Pressure Coefficient and Temperature Coefficient: Slow Variations*

The plant stability is now considered, taking both pressure and temperature effects into account, and limiting the treatment to the quasistationary case. The reactor temperature coefficient of reactivity applies to the mean reactor water temperature, T_{rw}. This temperature may differ substantially from the mean primary loop temperature T of Eq. (5.80). The pressure of the primary system is determined by T rather than by T_{rw}. In the primary system, the pressure p is uniform for the frequencies being considered. Thus, the combined reactivity effect of temperature and pressure is given by Eq. (5.81):

$$\delta k = \left(\frac{\partial \delta k}{\partial T_{rw}}\right)_p \delta T_{rw} + \left(\frac{\partial \delta k}{\partial p_{rw}}\right)_{T_{rw}} \frac{\delta p}{\delta T} \delta T \qquad \text{Eq. (5.81)}$$

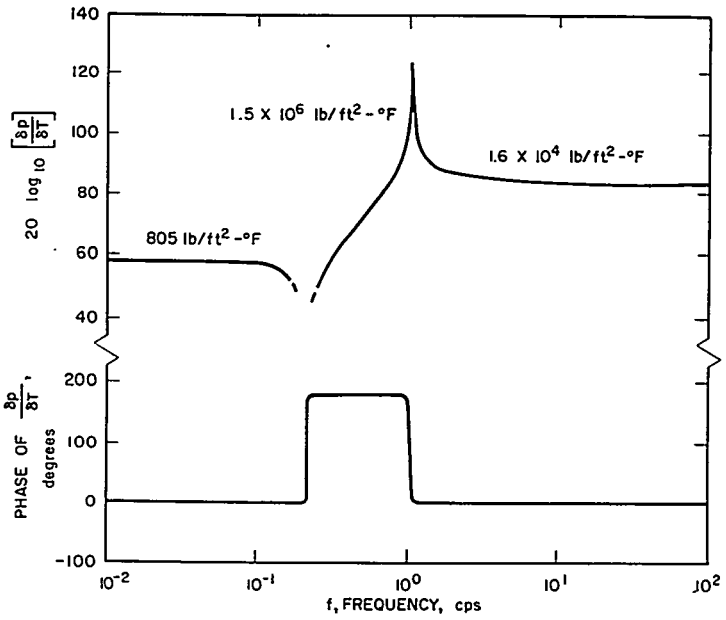

FIGURE 5.11. Magnitude and Phase of $\delta p / \delta T$ for Example.

where $\delta p/\delta T$ is the transfer function derived above. This may be written

$$\delta k = \alpha_T \, \delta T_{rw} + \alpha_p \frac{\delta p}{\delta T} \delta T \qquad \text{Eq. (5.81a)}$$

since, by definition,

$$\alpha_T \equiv \left(\frac{\partial \delta k}{\partial T_{rw}}\right)_p$$

and

$$\alpha_p \equiv \left(\frac{\partial \delta k}{\partial p_{rw}}\right)_{T_{rw}} .$$

In general, δT_{rw} and δT differ in both magnitude and phase. However, for sufficiently slow oscillations of the order of a few cycles per hour, they are essentially equal if the cold and hot legs of the system are of equal volume. Under these conditions,

$$\delta k = \left(\alpha_T + \alpha_p \frac{\delta p}{\delta T}\right) \delta T . \qquad \text{Eq. (5.82)}$$

This is the relation which holds for the quasistationary case. For these slow oscillations, Eq. (5.80) may be simplified. The mass of the water in the surge line will not affect the pressure. The pressure will be determined primarily by the pressurizer characteristics. Dropping the terms in ω and ω^2 in Eq. (5.80) and noting further that for practical designs

$$\left(\frac{\partial p}{\partial \rho}\right)_T \quad \rho >> V_o \frac{dp_p}{dV_p}$$

then,

$$\frac{\delta p}{\delta T} \cong \frac{1}{\rho} \frac{\left(\frac{\partial p}{\partial T}\right)_\rho}{\left(\frac{\partial p}{\partial \rho}\right)_T} \; V_o \frac{dp_p}{dV_p} . \qquad \text{Eq. (5.83)}$$

To complete the treatment of the quasistationary case it is necessary to derive an expression for δT, the amplitude of the average primary loop temperature variation. Assuming the average loop temperature equals the average core (coolant) temperature, which implies equal hot and cold leg volumes,

the results previously derived for slow temperature variation can be applied:

$$\delta T = \frac{\delta\phi}{\phi_o}\left[\left(T - T_s\right)_o + p_o\left(\frac{\partial T}{\partial p}\right)_{sat}\right].$$

The above transfer functions, $\delta p/\delta T$ and $\delta T/(\delta\phi/\phi_o)$, may be multiplied together with the pressure coefficient, α_p, to determine reactivity feedback due to pressure variations. Since none of these expressions involves a phase shift, the effect of the positive pressure coefficient of reactivity is to reduce the effectiveness of the negative temperature coefficient of reactivity in providing stability. The reduction of the effectiveness is relatively small, however. In the example given in the discussion on pressurizer system dynamics, the value of $|\delta p/\delta T$ at low frequencies was shown to be approximately 800 lb/ft^2/°F. The pressure coefficient α_p has a magnitude of about 1 to 3×10^{-8} in reactivity per lb per sq. ft. Thus, the pressure contribution, $\alpha_p(\delta p/\delta T)$, is about 1 to 2×10^{-5} in reactivity per °F. Values of the temperature coefficient are generally 10 times larger.

9. *Reactivity Effects of Pressure and Temperature: Rapid Variations*

The analysis of the plant response to combined temperature and pressure variations becomes considerably more complicated when the frequencies considered are sufficiently high to introduce phase differences in the response of various units. Because of the complicated algebraic expressions which are involved in a quantitative discussion, only a qualitative discussion is presented. Typical results are used to illustrate the discussion.

The first transfer function to be considered is that of the reactor water temperature without recirculation of the primary loop water. With no recirculation of the primary coolant taken into account, there is no coupling of the plant load to the reactor. The reactor inlet temperature, T_{ri}, is therefore constant. The mean reactor temperature, T_{rw}, is calculated using the equations given in the discussion on reactor heat transfer equations. The oscillatory component of the reactor power results in an oscillatory component of the reactor metal and reactor coolant temperatures. To derive the equivalent transfer function with recirculation, all of the reactor plant equations given in Sect. 5.3.A.4 must be introduced.

Figure 5.12 shows the transfer function for mean reactor water temperature with recirculation (the feedback transfer

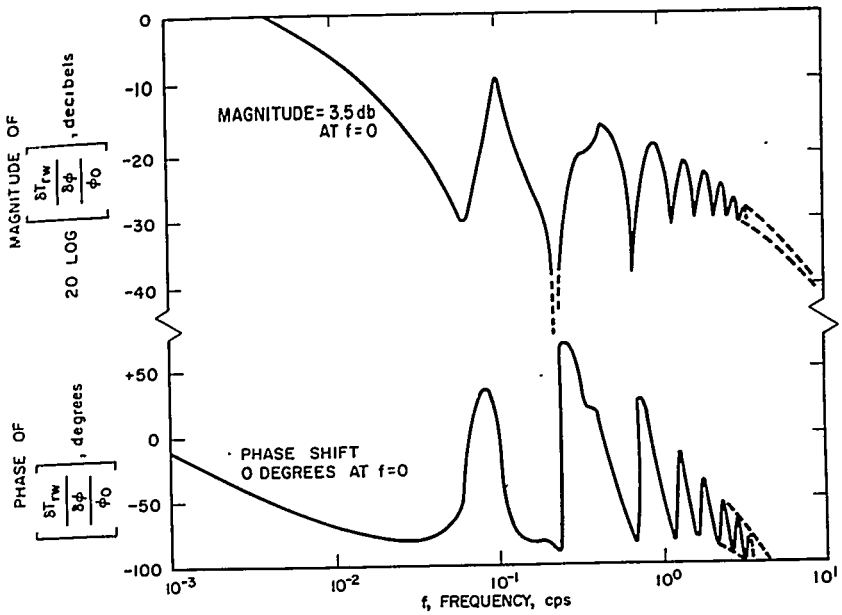

FIGURE 5.12. Magnitude and Phase of the Transfer Function for Reactor Water Temperature with Primary Water Recirculation.

function). The variable magnitude of this transfer function at frequencies greater than 0.1 cycle per sec is very pronounced. These resonances are due to coolant recirculation. At lower frequencies, the time delays are unimportant. At very high frequencies, the oscillatory nature of the transfer function persists, but the range of magnitude is limited.

The reactivity feedback associated with the reactor water temperature is

$$\delta k_T = \alpha_T \left(\frac{\delta T_{rw}}{\delta\phi/\phi_o} \right) \frac{\delta\phi}{\phi_o} \equiv F \frac{\delta\phi}{\phi_o}$$

where α_T is the temperature coefficient of reactivity, and F is the transfer function for reactivity. The overall response of the reactor with feedback is given by Eq. (5.33)

$$\frac{\delta\phi}{\phi_o} = \left(\frac{G}{1 - FG} \right) \delta k_{IMP} \qquad \text{Eq. (5.33)}$$

where G is the reactor transfer function. The magnitude and phase of G are given in Figs. 5.12 and 5.13, respectively. If the transfer function G is multiplied by α_T times the transfer function for reactor water temperature, the overall loop gain

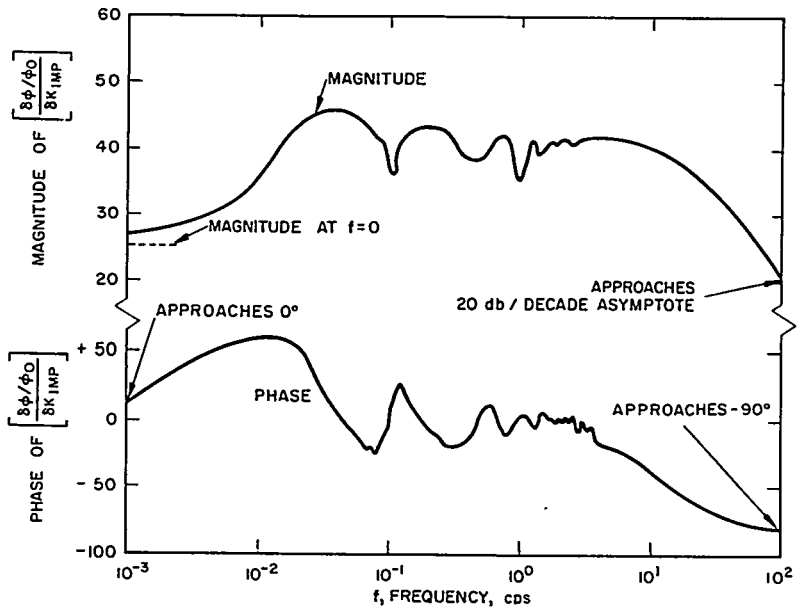

FIGURE 5.13. Magnitude and Phase of the Overall Reactor Transfer Function with Temperature Feedback and Recirculation.

FG for temperature feedback may be obtained. Introducing this into Eq. (5.33), the overall reactor response with temperature feedback and recirculation may be calculated. As an example, Fig. 5.13 gives this overall response function, assuming a reactor temperature coefficient of -3×10^{-4} per degree F. The response is relatively smooth and free of resonances. It is interesting to note that the magnitude of the response rises significantly above the zero frequency value at a frequency in the neighborhood of 0.01 cycle per sec or 36 cycles per hour. At 10 cycles per hour, the response is only slightly higher than the zero frequency level. Thus, this calculation confirms the range in which the quasistationary approach was assumed to be valid. At high frequencies the temperature coefficient is ineffective, and the transfer function is the same as that of the reactor without feedback.

To take pressure effects into account, it is necessary to calculate the response of the average primary loop temperature. This can be done using the reactor and plant equations of Sect. 5.3.A.4. The result of the computation for a typical plant is shown in Fig. 5.14. The transfer function is relatively smooth and free of resonances. The resonance at 0.1 cycle per sec is associated with the primary loop circulation time. The variations between 0.1 and 1 cycle per sec are associated with the

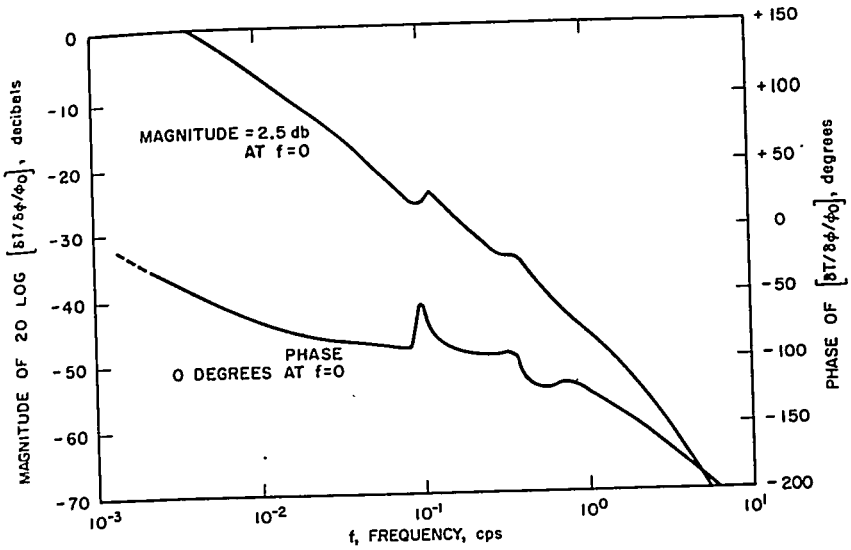

FIGURE 5.14. Magnitude and Phase of the Transfer Function for Average Primary Loop Water Temperature.

transit times of the coolant through the reactor and steam generator units and harmonics of the loop circulation frequency.

The transfer function for the reactivity feedback can be calculated, once the water temperature is calculated, by the use of Eq. (5.82) with the pressurizer equation, Eq. (5.80), providing the value of $(\delta p/\delta T)$. Since the effect of the temperature feedback has already been calculated, it is convenient to add the pressurizer effect by the method given by Eq. (5.81). The loop gain, with the pressurizer taken into account, is shown in Fig. 5.15. The effect of the pressurizer resonance, shown in Fig. 5.11, is of considerable importance. The loop gain calculated is slightly over unity at one cycle per sec, and the example calculated might be expected to be unstable at this frequency, i.e., self-sustaining oscillations of all system variables can spontaneously develop at one cycle per sec. The overall system is quite stable, however, at all other frequencies. Thus, corrective measures to assure stability need only be applied to this one resonant frequency. This particular instability is easily corrected by increasing the functional damping in the surge line, e.g., by adding an orifice.

B. Boiling Induced Reactivity Feedback

J. E. Meyer and J. V. Reihing, Jr.

Large changes in coolant density occur during periods of boiling operation of a water-cooled and moderated reactor core

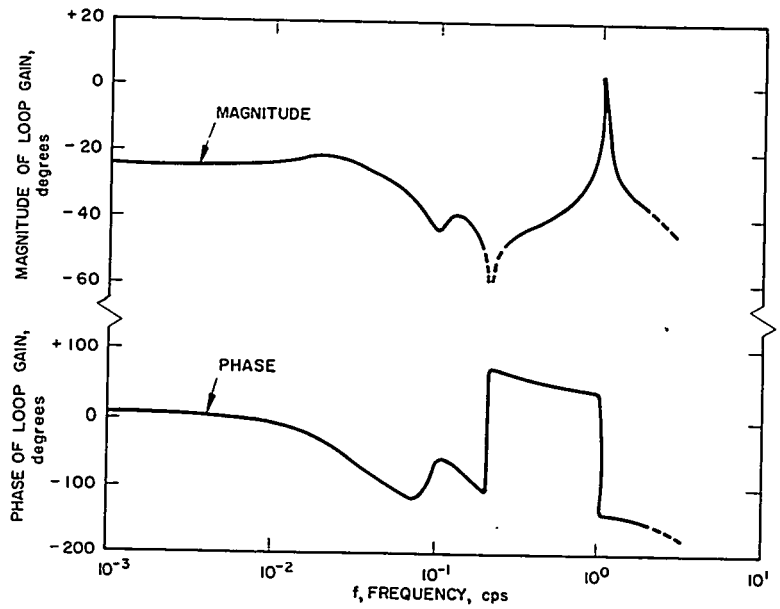

FIGURE 5.15. Overall Loop Gain with Both Pressure Feedback and Temperature Feedback with Recirculation.

which increase the possibility of reactor power level reactivity instabilities over that experienced in nonboiling operation. The boiling effect is primarily manifested by a marked increase in the magnitude of the feedback reactivity within the reactor core. As a consequence, the degree of stability of the closed loop reactor kinetics (core heat transfer) reactivity system is ordinarily reduced under boiling conditions. Boiling operation also enhances the likelihood of oscillatory hydrodynamic phenomena which are often interrelated with the core reactivity effects and, therefore, influence the system stability.

The following discussion is devoted to (1) operation of the core in boiling and nonboiling situations; (2) equations describing the heat transfer-fluid flow reactivity system under boiling conditions; (3) examples of computational methods of examining the stability or transient characteristics of the system, or both; (4) selected results of both in- and out-of-pile experiments that illustrate boiling reactivity feedback effects or boiling hydrodynamic effects, or both.

1. Reactivity Mechanisms

The discussion will now be confined to three reactivity mechanisms predominantly affecting the core neutron population and, hence, core power on a short-term basis (times less

than one minute). These are (1) motion of control rods, (2) changes in water density, and (3) changes in water temperature. The term changes in water density means that this reactivity mechanism arises from an alteration of the moderator number density at constant temperature. Analogously, the term changes in water temperature means that reactivity is induced by alterations of moderator temperature at constant density. Computations have indicated that for most pressurized water-cooled and moderated reactors the density induced reactivity mechanism is several times larger than the temperature mechanism.

2. Importance of Boiling

The magnitude of the inherent feedback reactivity under boiling conditions may be contrasted to that under nonboiling conditions by means of a numerical example illustrated in Fig. 5.16 in which water density (ρ_w) and water temperature (T_w) as a function of water enthalpy at a system pressure of 2000 psi are plotted. It is postulated that the reactor coolant conditions are characterized by a single mean enthalpy, H_R (a one-point reactor model). Further, it is assumed that the reactivity induced by changes in coolant conditions is given by

$$\left[\begin{matrix}\text{Feedback}\\ \text{reactivity}\end{matrix}\right] = \left[\begin{matrix}\text{Density coefficient}\\ \text{of reactivity}\\ \text{at constant}\\ \text{temperature}\end{matrix}\right] \left[\begin{matrix}\text{Change in}\\ \text{coolant}\\ \text{density}\end{matrix}\right] + \left[\begin{matrix}\text{Temperature coefficient}\\ \text{of reactivity}\\ \text{at constant}\\ \text{density}\end{matrix}\right] \left[\begin{matrix}\text{Change in}\\ \text{coolant}\\ \text{temperature}\end{matrix}\right]$$

where the following typical coefficients are chosen for illustration:

$$\left[\text{Density coefficient}\right]_{\substack{\text{Constant}\\ \text{temperature}}} = +47.0 \times 10^{-4}/\text{lb/ft}^3$$

$$\left[\text{Temperature coefficient}\right]_{\substack{\text{Constant}\\ \text{density}}} = -0.73 \times 10^{-4}/{}^\circ\text{F} \ .$$

Two hypothetical experiments are illustrated in Fig. 5.16 in terms of the functional dependence of the coolant density and

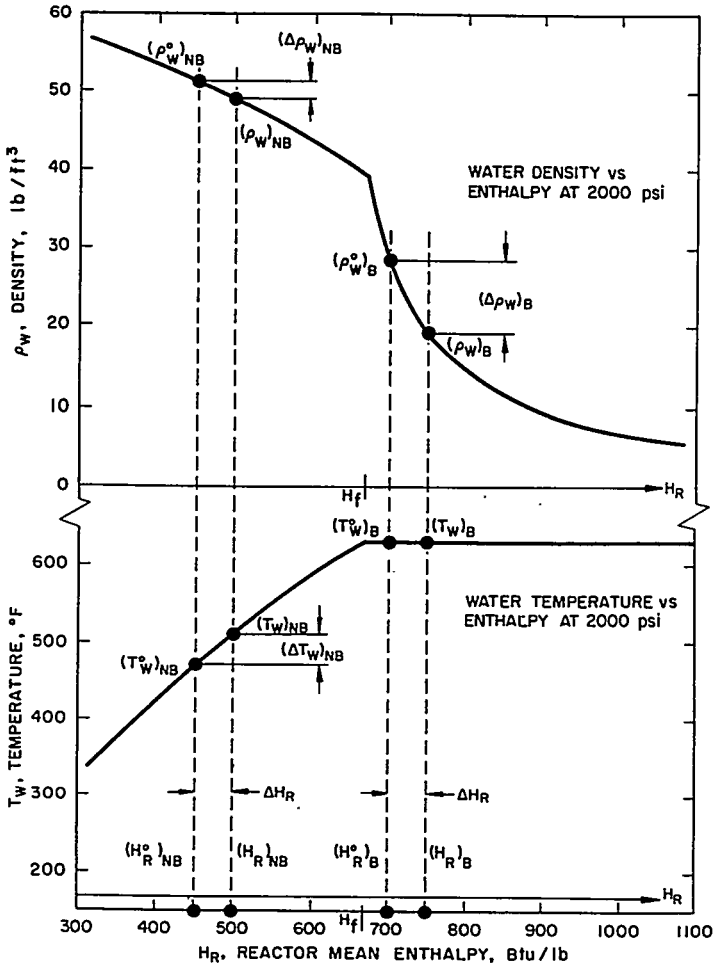

FIGURE 5.16. A Contrast of Boiling and Nonboiling Operation.

temperature upon mean reactor enthalpy. In the first experiment the reactor is initially situated in a nonboiling steady-state characterized by an enthalpy $(H_R^o)_{NB}$. Assuming that the reactivity feedback loop is open, the reactor heat is increased, so that the reactor mean enthalpy increases by an amount ΔH_R to a value $(H_R)_{NB}$. There is, as shown in Fig. 5.16, an attendant reduction in the coolant density and an increase in the coolant temperature. In the second experiment, the reactor is caused to experience the same mean enthalpy increase, ΔH_R, but the initial steady-state enthalpy, $(H_R^o)_B$, is situated in the boiling regime. As in the first case, there occurs an attendant density reduction. No change, however, takes place in the coolant temperature. Table 5.1 summarizes the results of these

TABLE 5.1 — RESULTS OF BOILING AND NONBOILING EXPERIMENTS

Initial Enthalpy H_R^o (Btu/lb)	Enthalpy Addition ΔH (Btu/lb)	Density Change Δp_w (lb/ft^3)	Temperature Change ΔT_w (°F)	Feedback Reactivity $\Delta \delta k_{fb}$ Reactivity
Nonboiling 450	50	-2.24	+43.7	-0.0137
Boiling 700	50	-9.27	0.0	-0.0436

hypothetical experiments in terms of the density and temperature changes and the resulting feedback reactivity.

The table shows that the feedback reactivity induced by a 50 Btu/lb enthalpy addition under boiling conditions is more than three times that induced under nonboiling conditions despite the fact that the coolant temperature remains unchanged at the saturation value. As previously indicated, this difference in feedback magnitude is due primarily to the large coolant density changes which accompany boiling.

To assess adequately the nuclear-thermal stability of a reactor core and to examine the transient behavior of a reactor, particularly under boiling conditions, a mathematical model more elaborate than a one-point model is required. The development which follows forms such a model and generates the describing equations.

3. *Theory*

The effects on average core neutron level of changes in rod position, water density, and water temperature may be calculated by use of a reactivity δk expressed as follows:

$$\delta k = \delta k_R + \delta k_D + \delta k_T \qquad \text{Eq. (5.84)}$$

where

δk_R = reactivity introduced by changes in position of control rods from some reference position

δk_D = reactivity introduced by changes in water density distribution (within and near the core) from some reference distribution

δk_T = reactivity introduced by changes in water temperature distribution (within and near the core) from some reference distribution.

The quantities δk_D and δk_T may be expressed by

$$\delta k_D(t) = \int_{V_c} K_D(\vec{r}) \left[\rho_w(\vec{r}, t) - \rho_{wo}(\vec{r})\right] dV \qquad \text{(Eq. 5.85)}$$

$$\delta k_T(t) = \int_{V_c} K_T(\vec{r}) \left[T_w(\vec{r}, t) - T_{wo}(\vec{r})\right] dV . \qquad \text{(Eq. 5.86)}$$

In these expressions, the volumetric integration with respect to dV is taken over the entire coolant volume V_c in and near the core. The functions K_D and K_T are functions of space, $\vec{r}$, (and reference conditions) which give the local importance of changes in density and temperature, respectively. The quantities ρ_w and T_w are, respectively, coolant density and temperature, and are functions of space. The quantities ρ_{wo} and T_{wo} are the reference distributions of density and temperature and are also functions of space.

Typically, the coolant passes through the core in a number of flow channels. A discussion follows of the equations required to describe one such channel and to predict for that channel a distribution of density ρ_w and temperature T_w for insertion in the integrals of Eqs. (5.85) and (5.86).

Consider the single flow channel illustrated in Fig. 5.17. A flow channel passing between two parallel flat plate metallic fuel elements is illustrated. Cartesian (x, y, z) coordinates are used with the z axis parallel to the predominant direction of fluid flow and with the x axis normal to the plate surface. The flow area $(A = 2\ell_1 w)$ is considered to be constant throughout the length, L, of the channel. The distance ℓ_m is measured from the plate surface to the plate centerline. All heat generated within the volume illustrated in Fig. 5.17 is assumed to be removed by the coolant passing through the volume or to be stored in the metal and coolant within the channel. All heat generated outside the volume illustrated in Fig. 5.17 is assumed to be removed by other coolant or to be stored in other coolant or other metal. The coolant enters the channel from a core inlet plenum region and is discharged into a core exit plenum region.

Equations expressing conservation of mass, momentum, and energy in the coolant are required for prediction of coolant velocity, density, and temperature. The z component of coolant velocity is denoted by V_w; x and y components of velocity are assumed to be small. The coolant velocity (V_w), density (ρ_w), and temperature (T_w) vary with position in the channel and with

time. That is, each must be considered a function (density may be a discontinuous function) of x, y, z, and time t. For example:

1. The velocity V_w is largest near the center of the channel and becomes very small near the channel wall.
2. At some axial positions in the channel (at which the plate surface temperature exceeds the coolant saturation temperature) boiling may be taking place at the plate surface, with the temperature of the liquid in center of the channel considerably below saturation. In this case (local boiling), the low density vapor will be located predominantly in the immediate neighborhood of the plate surface.
3. At other axial positions in the channel, a large fraction of the flow area may be occupied by vapor, and all liquid in the channel will be close to saturation temperature. In this case (bulk boiling), the low density vapor may be located predominantly in the center of the channel. A portion of the high density liquid may be contained in a slow moving film on the channel walls. The remainder of the liquid may be dispersed as droplets being carried along by the stream of vapor.

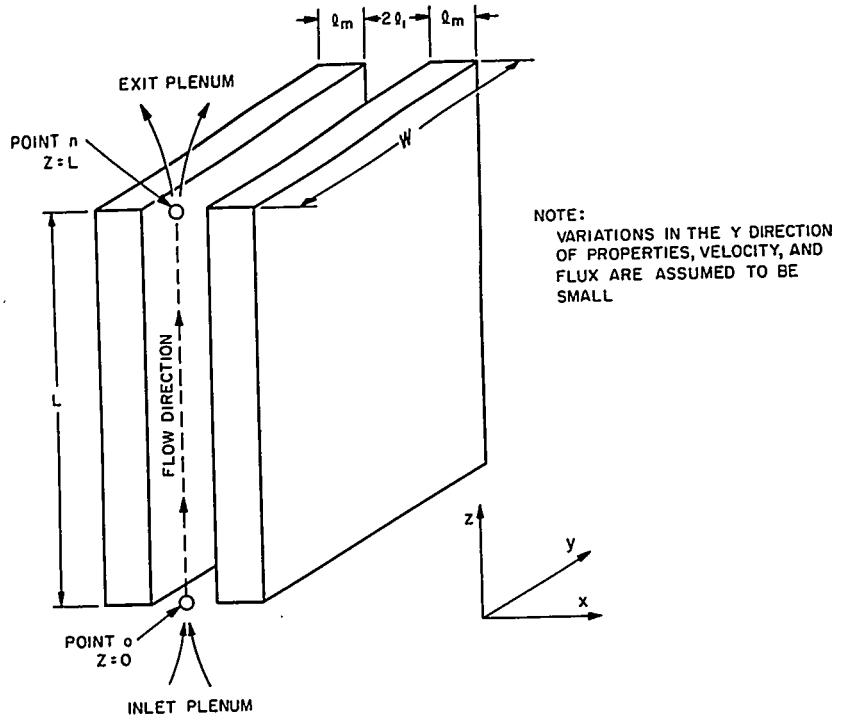

FIGURE 5.17. Flow Channel Schematic.

As is evident by the above discussion, the variation of V_w, ρ_w, and T_w across the thickness (x) direction of the channel can be quite large and detailed behavior fairly difficult to describe. The mean length of travel of neutrons through the coolant is generally much larger than $2\ell_1$, so that a detailed description in the x direction is not required for reactor kinetics calculations. An integration of the conservation laws over the area A at each axial position yields equations in the form required for density-temperature predictions. A complete description of this integration is contained in Ref. 21. The equations resulting from the application of conservation of mass will be derived here for illustrative purposes.

Consider the portion of coolant bounded by the plate surfaces and by the planes $z = z_1$ and $z = z_2$. A description of the conservation of mass applied to this volume is

$$\left[\begin{array}{l}\text{Time rate of increase}\\ \text{of mass within the}\\ \text{volume}\end{array}\right] + \left[\begin{array}{l}\text{Net rate at which}\\ \text{mass is flowing out}\\ \text{of the volume}\end{array}\right] = 0 .$$

An equivalent integral equation is

$$\frac{d}{dt}\left\{\int_{z_1}^{z_2}\left[\int_A \rho_w\, dA\right] dz\right\} + \left[\int_A \rho_w V_w\, dA\right]_{z=z_2} - \left[\int_A \rho V_w\, dA\right]_{z=z_1} = 0 . \qquad \text{Eq. (5.87)}$$

Define the following averages over the channel cross section:

$$\bar{\rho}_w = \frac{1}{A}\int_A \rho_w\, dA \qquad \text{Eq. (5.88)}$$

and

$$G = \frac{1}{A}\int_A \rho_w V_w\, dA. \qquad \text{Eq. (5.89)}$$

Substitute Eqs. (5.88) and (5.89) into Eq. (5.87), divide the resulting equation by $A(z_2 - z_1)$, and take the limit as z_2 approaches z_1. The resulting form for the conservation of mass equation is

$$\frac{\partial \bar{\rho}_w}{\partial t} + \frac{\partial G}{\partial z} = 0 . \qquad \text{Eq. (5.90)}$$

where

$\bar{\rho}_w$ = an area-averaged mean density

G = the total mass flow rate per unit flow area, or the mass velocity.

A similar derivation of the conservation of energy equation yields (with certain physical approximations discussed in Ref. 21):

$$\frac{\partial}{\partial t}\left(\bar{\rho}_w \bar{H}\right) + \frac{\partial}{\partial z}\left(GH'\right) = \left(\frac{\phi}{\ell_1}\right) + q'_w \qquad \text{Eq. (5.91)}$$

where

ϕ = the heat transferred from the plate to the coolant per unit plate surface area (heat flux)

q'_w = the time rate of direct heat input to the coolant per unit coolant volume (heat is from gamma-ray attenuation and neutron thermalization).

The quantities $\bar{H}$ and H' represent two additional averages over the flow area:

$$\bar{H} = \frac{1}{\bar{\rho}_w A}\left[\int_A \left(\rho_w H\right) dA\right] \qquad \text{Eq. (5.92)}$$

and

$$H' = \frac{1}{GA}\left[\int_A \left(\rho_w V_w H\right) dA\right] \qquad \text{Eq. (5.93)}$$

where

H = the local value of enthalpy (heat content per unit mass).

Equations (5.90) and (5.91) form a set of equations from which x direction details have been eliminated. However, such details still appear in the definition for the quantities $\bar{\rho}_w$, G, $\bar{H}$, and H', so that further information is required. This information is generally obtained experimentally from out-of-pile electrically heated test sections.[21, 22] It is assumed that such experiments have been conducted and that the experimental information is adequately represented by equations of the following functional form (for a given system pressure and geometry):

$$\left.\begin{aligned} \bar{\rho}_w &= \bar{\rho}_w(H') \\ \bar{T}_w &= \bar{T}_w(H') \\ \bar{H} &= \bar{H}(H') \end{aligned}\right\} \qquad \text{Eq. (5.94)}$$

that is, the mean density $\bar{\rho}_w$, mean temperature $\bar{T}_w$, and the mass-weighted enthalpy $\bar{H}$ are assumed to be known (and probably nonlinear) functions of the flow-weighted enthalpy H'.

The experimental information of Eq. (5.94) permits the conservation of mass and energy to be expressed in the following convenient forms for computational purposes:

$$\rho_w'' \frac{\partial H'}{\partial t} + G \frac{\partial H'}{\partial z} = \left(\frac{\phi}{\ell_1}\right) + q_w' \qquad \text{Eq. (5.95)}$$

and

$$\frac{\partial G}{\partial z} = -\frac{1}{\rho_w''} \left(\frac{d\bar{\rho}_w}{dH'}\right) \left[\left(\frac{\phi}{\ell_1}\right) + q_w' - G \frac{\partial H'}{\partial z}\right]. \qquad \text{Eq. (5.96)}$$

In these equations, the quantity ρ_w'', which has the same units as density, is relatable to the previously defined quantities of Eq. (5.94) by

$$\rho_w'' = \bar{\rho}_w \left(\frac{d\bar{H}}{dH'}\right) + (\bar{H} - H') \left(\frac{d\bar{\rho}_w}{dH'}\right) \qquad \text{Eq. (5.97)}$$

and, hence, is also a known function of H'.

4. Example: Feedback Behavior of a Single Coolant Channel

The use of Eqs. (5.85), (5.86), (5.94), (5.95), and (5.96) to obtain a reactivity contribution from changes in heat input occurring in one channel may be illustrated by considering the following simple situation: (1) The heat input to the channel is varying sinusoidally in time at an angular frequency, ω, about some mean level, Q_o, with an amplitude, Q_1. That is,

$$\left[\left(\frac{\phi}{\ell_1}\right) + q_w'\right] = Q_o + Q_1 \sin \omega t \qquad \text{Eq. (5.98)}$$

where Q_o and Q_1 are spatially invariant. (2) The channel inlet enthalpy H_o' is constant in time. (3) The channel inlet mass velocity, G_o, is constant in time. (4) The reactivity importance functions K_D and K_T are constant in space.

Numerical methods, such as those described in Ref. 23, may be applied to the resulting integro-differential equation system and transient solutions obtained. Figures 5.18 and 5.19 illustrate typical boiling and nonboiling results. Figure 5.18 indicates the time behavior of the reactivity introduced by

changes in the core* water temperature and density (commonly called the feedback reactivity) for two primary system pressures. Also shown in Fig. 5.18 is the sinusoidal heat input (the forcing function), so that the phase relationship between heat input and feedback reactivity may be seen.† Figure 5.19 shows axial plots of the water enthalpy, density, and mass velocity at four instances of time within a single period of the heat input oscillation. These plots illustrate the undulating within-channel behavior of these variables, particularly under boiling conditions (low pressure).

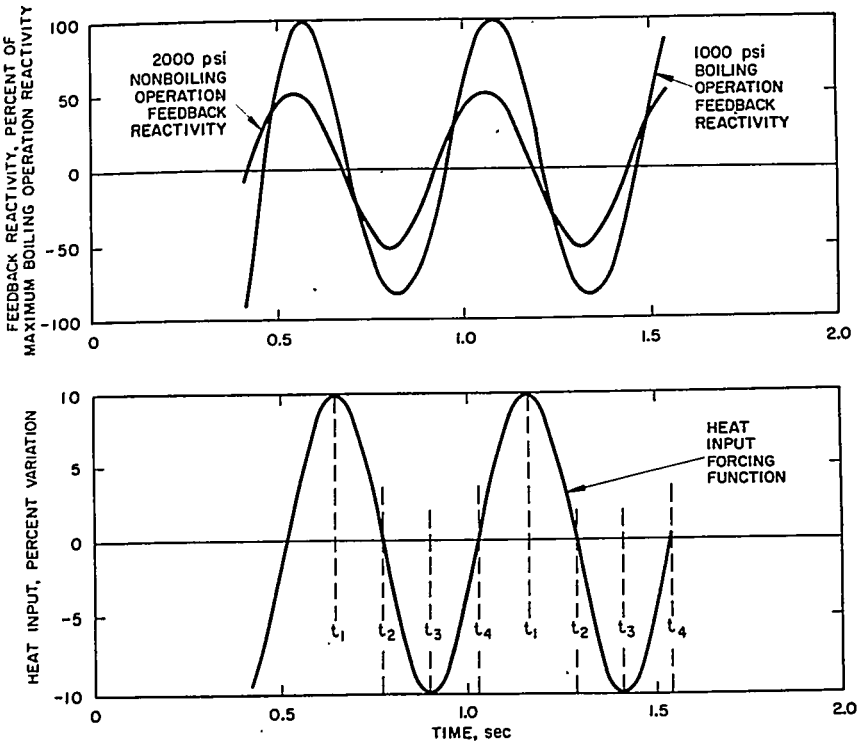

FIGURE 5.18. A Contrast of Boiling and Nonboiling Performance, Feedback Reactivity Response to Sinusoidal Variations in Heat Input.

*It is assumed that the transients experienced by this single coolant channel adequately characterize the behavior of the entire core.

† Because of the inherent heat capacity of the cooling water and the fluid transport phenomena occurring in the flowing water, a change in heat input to the stream does not instantaneously induce a change in the integrated stream temperature and density. Rather, this process operates with a time constant which is dependent upon the heat capacity and transport effects. This time constant gives rise to the phase lag of feedback reactivity relative to heat input.

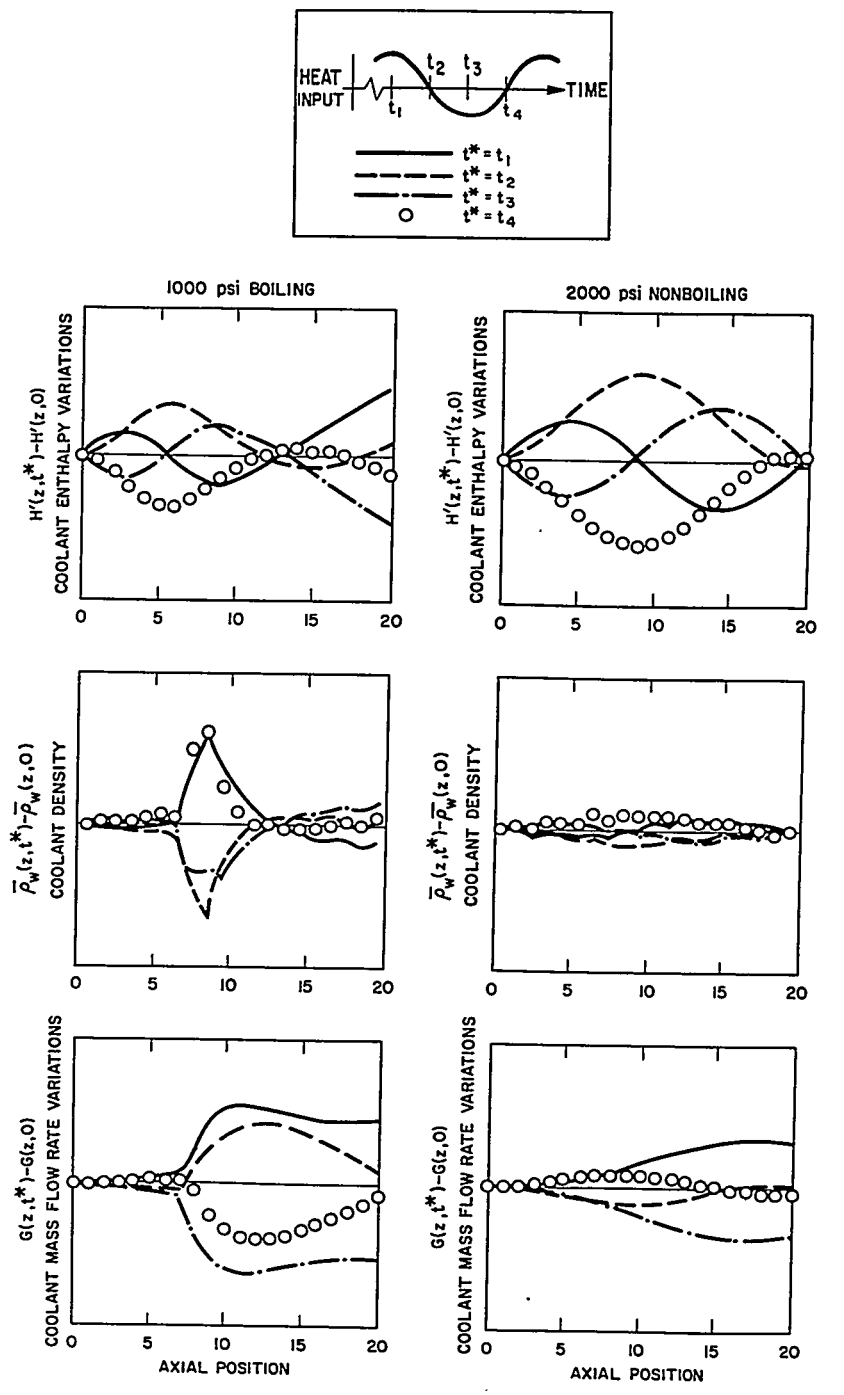

FIGURE 5.19. A Contrast of Boiling and Nonboiling Operation, Axial Profiles of Coolant Conditions.

5. *Stability Considerations*

The reactor transfer function relating the oscillatory reactor power response to an arbitrary oscillatory reactivity input (previously discussed and illustrated in Sect. 5.3.A) can now be examined in conjunction with the feedback reactivity relationship (Fig. 5.18) in order to investigate the inherent nuclear-thermal stability of the reactor core. Consider the following qualitative stability argument:

1. Postulate that an arbitrary (but small) oscillatory reactivity input of magnitude δk_I and angular frequency ω is imposed upon the reactor system, i.e.,

$$\delta k_I(t) = \delta k_I \sin \omega t . \qquad \text{Eq. (5.99)}$$

   The $\delta k_I(t)$ time-varying signal may be thought of as the sum of the time-varying rod motion reactivity $\delta k_R(t)$ and time-varying feedback reactivity $\delta k_{fb}(t)$.
2. The nature of the reactor transfer function (dependent only upon nuclear core parameters, Sect. 5.3.A) indicates that an oscillatory reactor power response of magnitude $\phi(\omega)$ about a steady-state mean level ϕ_o and phase relationship (relative to the imposed reactivity) of $\theta_\phi(\omega)$ results.
3. Assume that this reactor heat is released instantaneously in the fuel-bearing portions of the reactor plates, but that further phase shift, $\theta_m(\omega)$, is experienced in traversing the fuel plate cladding and the clad-coolant interface film.* Therefore, the coolant heat input is given by

$$Q(t) = Q_b + Q_{1(\omega)} \sin \left[\omega t + \theta_\phi(\omega) + \theta_m(\omega) \right] . \qquad \text{Eq. (5.100)}$$

4. The transient results shown in Fig. 5.18 indicate that this oscillatory heat input induces a feedback reactivity $\delta k_{fb}(t) = \delta k_D(t) + \delta k_T(t)$ (dependent upon nuclear, thermal, and hydraulic core parameters) of magnitude $\delta k_{fb}(\omega)$ and phase relationship (again, relative to the imposed reactivity) of $\theta_\phi(\omega) + \theta_m(\omega) + \theta_{fb}(\omega)$, i.e.,

$$\delta k_{fb}(t) = \delta k_{fb}(\omega) \sin \left[\omega t + \theta_\phi(\omega) + \theta_m(\omega) + \theta_{fb}(\omega) \right] . \qquad \text{Eq. (5.101)}$$

*Phase shift arises from the time constants associated with the conductive-convective heat transfer processes. For example, phase shift is proportional to the heat capacity of the metal plate and clad and inversely proportional to the thermal conductivity of the metal.

5. Since the density and temperature-induced feedback reactivity is an inherent mechanism (in contrast to rod reactivity), the reactor core system will experience self-sustaining or divergent (within the limits of the linearized analysis) oscillatory transients, even though the imposed reactivity disturbance be removed, if the feedback reactivity is equal to or greater than the imposed reactivity,

$$\delta k_{fb}(\omega) \geq \delta k_I \qquad \text{Eq. (5.102)}$$

at a frequency where the total phase shift is equal to an integral multiple of 2π radians,

$$\theta_\phi(\omega) + \theta_m(\omega) + \theta_{fb}(\omega) = 2n\pi \; ; \; n = 1,2,3 \ldots \qquad \text{Eq. (5.103)}$$

In this event, the feedback reactivity returns to reinforce (and, in fact, takes control over) the imposed disturbance, so that the oscillations continue undamped or grow within a diverging envelope. Equations (5.102) and (5.103), therefore, form a stability criterion.

The assumptions employed in the above qualitative argument influence the system analysis in various ways. For example, nonuniformities in the axial power shape as well as reactivity importance shapes can markedly influence both feedback magnitude and phase relationships, particularly in boiling situations.

6. Inlet Enthalpy Variations

Implied in the assumption that the channel inlet enthalpy is constant in time is the fact that the reactor plant components other than the reactor core have negligible influence upon stability. This assumption is only valid at excitation periods considerably smaller than the times required to traverse loop piping, plenums, steam generators, etc. The illustrative example under consideration can, therefore, be termed a core only stability examination. Even though the stability of the core only system is neither a necessary nor sufficient condition for overall reactor plant stability, reliable plant operation is best achieved if both the overall system and all major subsystems (e.g., core only) exhibit stability.

7. Inlet Flow Variations

The assumption that the inlet mass velocity is constant in time precludes certain hydrodynamic effects which may

significantly influence the transient behavior and inherent nuclear-thermal reactivity stability of the core. Examples of such interacting hydrodynamic phenomena are total reactor plant flow oscillations (loop oscillations) and parallel reactor core channel flow oscillations. Since both of these oscillatory flow phenomena may occur at constant reactor power, the combined effects of what will be called the thermal-hydraulic system and the nuclear-thermal system for a given reactor plant design could be markedly different than either effect operating alone. The experiments and analysis of Mendler, et al.,[24] demonstrate the total reactor plant flow oscillation process in which, at constant reactor power, the mass velocity in the reactor core and the reactor plant vary with time in an oscillatory manner.

E. R. Quandt reports the analysis and experimental measurement of parallel channel flow oscillations.[25] This process can take place under conditions of constant reactor power and constant total core mass flow rate. The channel (or channels) under consideration is in parallel with a large group of channels whose pressure drop characteristic remains invariant in time (e.g., total core pressure drop constant). In this situation, if flow oscillations occur in this parallel channel, and if the channel is in a position of significant reactivity worth, the resulting temperature and density-induced reactivity attributable to this channel takes on importance.

8. *Computational Methods*

Several computational methods exist for determining the nature of the boiling density and temperature feedback reactivity functional relationship and its influence on reactor core dynamics. Three methods and specific examples of each are cited here.

A) TRANSIENT RESPONSE METHODS. The first are those computational methods which yield direct transient solutions to the closed loop equation system. The transient solutions so obtained reflect the simultaneous effects of rod reactivity, density and temperature feedback reactivity, and the reactor kinetics equations. Since these closed loop transient computational methods include the effects of the nonlinear as well as the linear system phenomena, they are useful in obtaining both the small and large signal behavior of the reactor system.

An example of this first method of analysis is the ART digital program,[26] which is based on the solution of describing equations similar to Eqs. (5.85), (5.86), (5.94), (5.95), and

(5.96) for a multichannel core together with the reactor kinetics equations. Numerical differencing techniques are applied to these equations to yield difference equations in time and space, and the program operates with these resulting difference equations to compute the transient core behavior.

Two further examples of the first method of analysis are based upon mathematical models that describe the entire reactor plant, including the plant piping, steam generators, steam loads, etc. The TANK digital computer program is of this type.[27] Analog computers are also often employed to solve this class of problems. An example of an analog computer simulation of a reactor plant that includes a reasonably detailed spatial description of the reactor core is reported in Ref. 28.

B) FREQUENCY RESPONSE FROM THE TRANSIENT RESPONSE METHODS. The second are those analysis methods specifically designed to obtain the complex frequency domain characteristics (in contrast to time domain or transient characteristics) of the reactivity feedback system through the use of transient solutions. This method is an open-loop technique commonly employed in the study of feedback control systems (see, for example, Sect. 5.3.A and Ref. 29). The analysis method makes use of a thermal transient program such as the previously described ART program,[26] and proceeds in the following way:

1. A small step change in the heat input to the core is imposed upon the system (e.g., input to the ART program). The heat input disturbance is made small, so that the reactor system response is approximately linear.
2. The program computes from the difference equations the resulting feedback reactivity transient (each of the reactor kinetics equations is made inoperative).
3. The program evaluates the Laplace transform of the time derivative of the feedback reactivity function at a number of selected frequencies. Because of the unique form of the input, i.e., a step function, this process yields the value of the desired feedback transfer function, $\overline{\delta k}_{fb}(j\omega)/\overline{Q}(j\omega)$.
4. The feedback transfer function, when taken together with the forward transfer function (derivable from the reactor kinetics equations, Sect. 5.3.A), provides sufficient information to assess core stability and to compute closed loop performance throughout the frequency spectrum. A more complete treatment of the theory underlying this second method can be found in Ref. 30.

C) FREQUENCY RESPONSE METHODS. The third method is also directed toward obtaining the frequency domain characteristics of the feedback system. In this technique, the analysis proceeds directly from the feedback system describing equations to the feedback system transfer function without obtaining time domain information. Essentially a small perturbation method, the procedure is as follows:

1. The feedback system describing equations are formed similar to those expressed in Eqs. (5.85), (5.86), (5.94), (5.95), and (5.96). This equation system includes nonlinear partial differential equations in space and time.
2. Spatial differencing techniques are applied, resulting in difference equations in space and nonlinear differential equations in time.
3. Small perturbation theory is next applied to the system to remove temporal nonlinearities. Small perturbations about a steady state are assumed, and resulting second and higher order terms are neglected.
4. Finally, Laplace transform theory is employed to form the desired quotient, $\overline{\delta k}_{fb}(j\omega)/\overline{Q}(j\omega)$.

A specific example of this method is that reported by Margolis and Kaplan,[31] in which they divide the single coolant channel representation of the reactor core into two axial regions to accomplish the analysis. The first of these is called the nonboiling region and extends from the channel inlet to the position of the single-phase two-phase interface in the channel coolant stream. The second or boiling region includes the rest of the channel.

9. *In-Pile Experiments*

Experimental evidence of the influence of boiling upon the interrelated nuclear thermal-hydraulic behavior of reactor plants exists. Two examples of such in-pile experiments conducted on pressurized water power reactors will be described.

The first set of experiments was performed by inserting oscillatory reactivity perturbations into a reactor at power by mechanically moving a reactor control rod. At various fixed primary system pressures, the frequency of oscillation of the control rod reactivity was varied in order to develop the reactor closed loop frequency response. Shown in Fig. 5.20 are the results of these experiments in terms of the measured closed loop gain of the system as a function of frequency. Also indicated in Fig. 5.20 are the results of calculations of the closed loop gain obtained from the method outlined in the discussion on frequency response from the transient

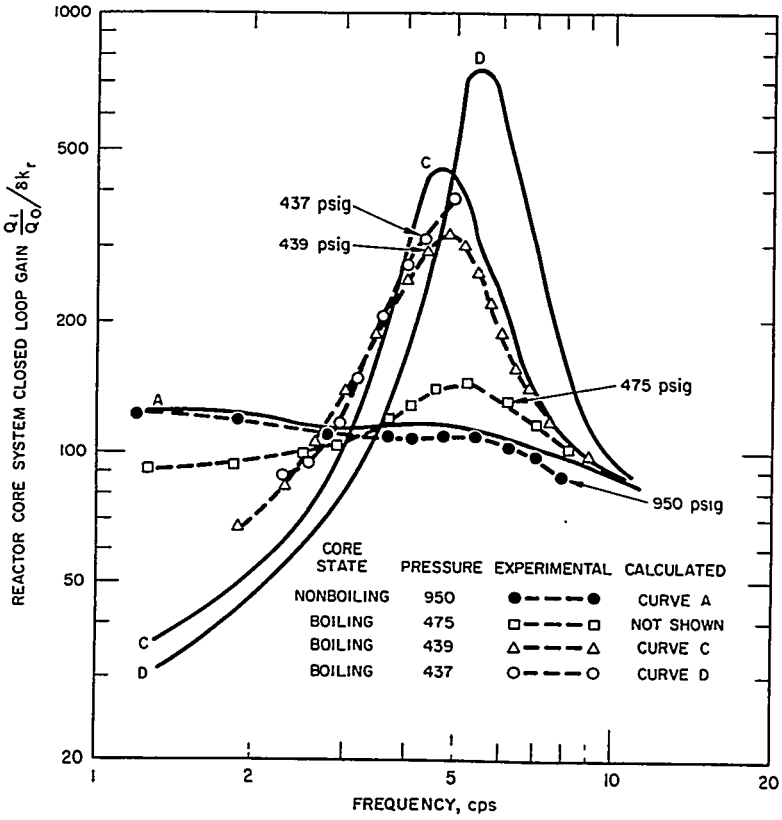

FIGURE 5.20. Comparison of Measured and Calculated Closed Loop Gain for Boiling and Nonboiling Operation.

response methods. Both the experimental and calculational evidence demonstrate the marked increase in closed loop gain experienced as the core operation point is shifted from nonboiling to boiling conditions by a reduction of primary system pressure. At a sufficiently low system pressure (large amounts of boiling), a condition of self-sustaining power oscillations was reached experimentally, i.e., even with the rod motion stopped (perturbation removed) the core power continued to oscillate.

Reference 32 reports the second set of experiments in which flow oscillations were observed to occur in highly instrumented subassemblies under boiling conditions. These experiments were carried out under a large variety of power-flow-pressure configurations. In those situations in which significant boiling occurred in the channels of the hot subassembly (even though no boiling existed outside of the

subassembly), the flow and temperature instrumentation indicated flow oscillations. In some extreme cases, the parallel hot channel flow actually reversed, i.e., fluid was expelled from the inlet of the channel. Such boiling-induced flow oscillations undoubtedly influence the reactivity feedback system and, consequently, the thermal-nuclear core stability. Two examples of small signal perturbation methods of analysis of these hydrodynamic phenomena are reported in Refs. 33 and 34.

10. Summary

1. The presence of significant amounts of boiling in a reactor core could cause an unstable or oscillatory power behavior in a core that operates stably under nonboiling conditions.
2. The analysis of experiments has indicated large changes in stability characteristics with fairly small changes in power, flow, or pressure.
3. This analysis has also indicated that a detailed spatial description of the boiling and feedback effects is required to predict this phenomenon in an adequate manner.
4. Interrelations with effects of flow oscillations also caused by boiling are potentially important stability considerations. Methods to couple the hydrodynamic and reactivity phenomena are in a period of vigorous analytical and experimental development.

C. Self-Shutdown of Reactor Power Excursions

K. J. Chock

A necessary phase of reactor design is the analysis of the behavior of a reactor and associated power plant during power excursions induced by positive reactivity insertions. This analysis is required for both safety and design considerations.

Reactor power transients can be divided into two categories distinguishable by the magnitude of the reactivity insertion:

1. Insertions of reactivity in small steps or slow rates, resulting in power excursions that are limited by the negative temperature coefficient or by normal reactor protection systems, or both.
2. Insertions of reactivity in such large steps or fast rates that the reactor becomes prompt critical. Because of the rapidity of the power and fuel plate temperature rise, this class of accidents precludes limitation by the reactor

protection systems and must be terminated by inherent self-shutdown mechanisms, such as fuel plate expansion, steam void formation, or core disassembly.

The first category, covering maneuvering transients and most of the operational accidents, is studied with analytical models which are reasonably well understood, readily described, and generally accepted (see Sects. 5.3.A and 5.3.B).

Considerable differences have existed among investigators as to the proper model upon which to base the analysis of the faster transients. This stems from the lack of a detailed knowledge of the nature of heat transfer and void formation during transient boiling. To guard against uncertainties, the earliest model[35] required that all initial reactivity perturbation be compensated before the transient terminated and that no feedback occur before final termination. In addition, void formation was assumed to be the exclusive shutdown mechanism. These assumptions ensure conservatism. An extension of this model employing the same basic assumptions has been used for safeguards evaluations of critical assemblies at Bettis Atomic Power Laboratory.[36] More recently, the actual reactivity feedback required to terminate power excursions and the importance of feedback mechanisms other than void formation have been studied along with the development of an improved understanding of the heat transfer process. The development of all theoretical models is based on comparisons with experimental transients performed by Phillips Petroleum personnel on the SPERT reactors.

In this section, the reactivity required to terminate power excursions is derived analytically. Next, the relative importance of several inherent feedback mechanisms is discussed, followed by analog simulator results and comparisons with SPERT transients (pressurized and unpressurized). Finally, the analytical models used in the analog studies are described.

1. Reactivity Requirements for Terminating a Fast Excursion

A sustained power rise can always be stopped momentarily without reducing the initial reactivity perturbation to zero because of the presence of delayed neutrons. In fact, for reactor periods in the usual range of interest (5 to 35 msec), the required reactivity change is only a small fraction of the initial reactivity. If the reactivity change is terminated after dn/dt first becomes zero, the reactor power will later rise again and asymptotically approach a new stable period. If reactivity is reduced to zero, the reactor will attain a constant power level. Depending upon the rate at which the reactivity is reduced to zero, the final level may be either higher or

lower than that at which dn/dt was first caused to be zero. If the reactor eventually becomes subcritical, the power will decay to source level. Thus, the calculation of the reactivity requirements for terminating a fast power excursion involves two considerations: (1) the amount of reactivity change necessary to stop the initial power rise and (2) the reactivity feedback rate required to prevent a subsequent power rise.

A) TERMINATION OF THE INITIAL POWER RISE. Consider the reactor kinetics equations of Sect. 5.2:

$$\frac{dn(t)}{dt} = \frac{\delta k(t)}{\Lambda} n(t) - \frac{\bar{\beta}}{\Lambda} n(t) + \sum_i \lambda_i c_i(t) \qquad \text{Eq. (5.104)}$$

and

$$\frac{dc_i(t)}{dt} = \frac{\bar{\beta}_i}{\Lambda} n(t) - \lambda_i c_i(t) \ . \qquad \text{Eq. (5.105)}$$

It is assumed here that extraneous sources of neutrons may be neglected. In the steady state,

$$\lambda_i c_i = \frac{\bar{\beta}_i}{\Lambda} n \qquad \text{Eq. (5.106)}$$

and

$$\sum_i \lambda_i c_i = \frac{\bar{\beta}}{\Lambda} n \qquad \text{Eq. (5.107)}$$

so that the last two terms of Eq. (5.104) cancel, and $\delta k(t) = 0$. Thus, if the reactor is in the steady state, a positive reactivity addition will cause dn/dt to be positive, and a negative reactivity will cause dn/dt to become negative. Now, consider a reactor in which the power level has been increasing for some time $(dn/dt > 0)$. From Eq. (5.105),

$$\lambda_i c_i(t) < \frac{\bar{\beta}_i}{\Lambda} n(t) \qquad \text{Eq. (5.108)}$$

and hence,

$$\sum_i \lambda_i c_i(t) < \frac{\bar{\beta}}{\Lambda} n(t) \ . \qquad \text{Eq. (5.109)}$$

The sum of the last two terms of Eq. (5.104) is now negative, and dn/dt is positive only because

$$\frac{\delta k(t)}{\Lambda}\, n(t) > \left[\frac{\bar{\beta}}{\Lambda}\, n(t) - \sum_i \lambda_i c_i(t)\right] . \qquad \text{Eq. (5.110)}$$

To make dn/dt negative, it is sufficient to decrease $\delta k(t)$, so that

$$\frac{\delta k(t)}{\Lambda}\, n(t) < \left[\frac{\bar{\beta}}{\Lambda}\, n(t) - \sum_i \lambda_i c_i(t)\right] . \qquad \text{Eq. (5.111)}$$

Therefore, during a power excursion, dn/dt can be made zero or negative without reducing $\delta k(t)$ to zero.

The change in reactivity (initial reactivity minus reactivity when $dn/dt = 0$) required to arrest momentarily a power excursion can be bounded by rather simple considerations. From Eq. (5.104), the reactivity at the time, t^*, of peak power is determined by setting $dn/dt = 0$ and solving for $\delta k(t^*)$.

$$\delta k(t^*) = \bar{\beta} - \Lambda \sum_i \lambda_i \frac{c_i(t^*)}{n(t^*)} . \qquad \text{Eq. (5.112)}$$

The bounds on $\delta k(t^*)$ are set by the limits chosen for $n(t)$, since $c_i(t^*)$ is likewise limited by $n(t)$.

Figure 5.21 shows a convenient set of bounds on $n(t)$. The lower limit is expressed as

$$n(t) \geq n_o \qquad o \leq t \leq t_1$$

$$n(t) \geq n_1 \epsilon^{\omega t} \qquad t_1 \leq t \leq t^* .$$

The upper limit is described by

$$n(t) \leq n_o \epsilon^{\omega t} \qquad 0 \leq t \leq t_1$$

$$n(t) \leq n(t^*) \qquad t_1 \leq t \leq t^* .$$

To determine the resulting bounds on $c_i(t^*)$, the solution of Eq. (5.105) is written in the integral form,

$$c_i(t) = \frac{\bar{\beta}_i}{\Lambda}\, \epsilon^{-\lambda_i t} \int_o^{t^*} n(t)\, \epsilon^{\lambda_i t}\, dt + \frac{\bar{\beta}_i}{\Lambda \lambda_i}\, n(o)\, \epsilon^{-\lambda_i t} . \qquad \text{Eq. (5.113)}$$

Employing the lower bound in Eq. (5.113) and performing the required integrations yield

$$c_i(t^*) \geq \frac{\bar{\beta}_i}{\Lambda} \frac{n_1 \epsilon^{\omega t^*}}{(\omega+\lambda_i)} + \frac{\bar{\beta}_i n_o \epsilon^{-\lambda_1(t^*-t_1)}}{\Lambda\lambda_i}\left(\frac{\omega}{\omega+\lambda_i}\right) . \quad \text{Eq. (5.114)}$$

To evaluate (t^*-t_1), define

$$r = \frac{n_o \epsilon^{\omega t^*}}{n_1 \epsilon^{\omega t^*}} = \frac{n_o}{n_1} \quad \text{Eq. (5.115)}$$

where

$n_o \epsilon^{\omega t^*}$ = the extrapolated exponential power at the time of peak power

$n_1 \epsilon^{\omega t^*}$ = the actual peak power.

From Figure 5.21,

$$n(t^*) = n_o \epsilon^{\omega t_1} = n_1 \epsilon^{\omega t^*} \quad \text{Eq. (5.116)}$$

or

$$t^* - t_1 = \frac{\ln r}{\omega} . \quad \text{Eq. (5.117)}$$

Expressing the lower bound on $c_i(t^*)$ in terms of the relationships inherent in Eqs. (5.116) and (5.117) yields

$$c_i(t^*) \geq \frac{\bar{\beta}_i n_1 \epsilon^{\omega t^*}}{\Lambda(\omega+\lambda_i)} + \frac{\bar{\beta}_i n_o}{\Lambda\lambda_i}\left[\frac{\omega}{(\lambda_i+\omega)} r^{-\lambda_i/\omega}\right] . \quad \text{Eq. (5.118)}$$

Similarly, the upper bound on $c_i(t^*)$ is derived from Eq. (5.113), using the appropriate limits on $n(t)$. Upon performing the required integrations and eliminating $n(t^*)$ by means of Eq. (5.116),

$$c_i(t^*) \leq \frac{\bar{\beta}_i}{\Lambda} \frac{n_o \epsilon^{\omega t_1}}{\omega+\lambda_i} \epsilon^{-\lambda_i(t^*-t_1)} - \frac{\bar{\beta}_i n_o \epsilon^{-\lambda_i t^*}}{\Lambda(\omega+\lambda_i)} + \frac{\bar{\beta}_i n_1 \epsilon^{\omega t^*}}{\Lambda\lambda_i}$$

$$- \frac{\bar{\beta}_i}{\Lambda\lambda_i} n_1 \epsilon^{\omega t^*} \epsilon^{-\lambda_i(t^*-t_1)} + \frac{\bar{\beta}_i}{\Lambda\lambda_i} n_o \epsilon^{-\lambda_i t^*} . \quad \text{Eq. (5.119)}$$

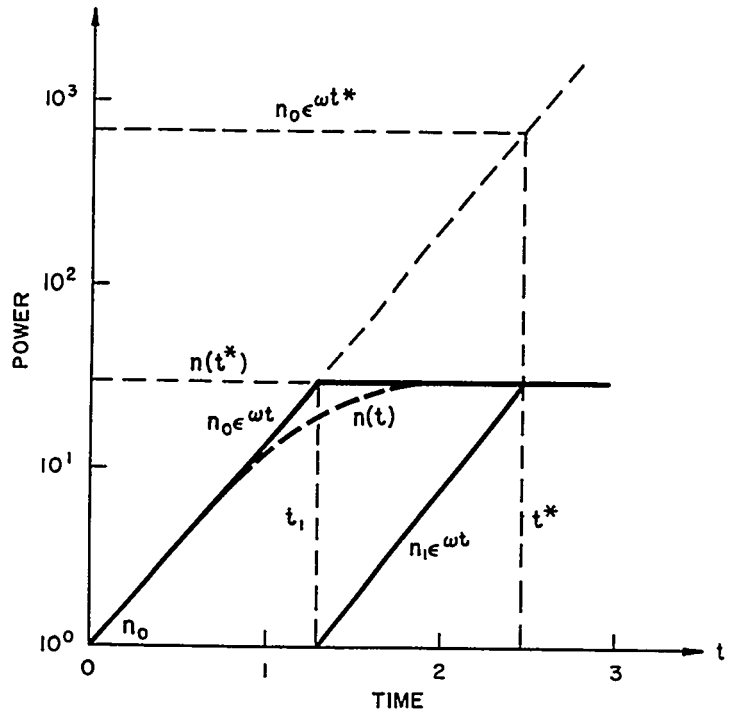

FIGURE 5.21. A Set of Bounds on $n(t)$.

Restating Eq. (5.119) in terms of the parameter r [see Eq. (5.117)],

$$c_i(t^*) \leq \frac{\overline{\beta}_i}{\Lambda}\frac{n_1\epsilon^{\omega t^*}}{\lambda_i} - \frac{n_1\epsilon^{\omega t^*}}{\Lambda}\frac{\omega\overline{\beta}_i}{\lambda_i(\omega+\lambda_i)}r^{-\lambda_i/\omega}$$

$$+\frac{n_o\epsilon^{-\lambda_i t_1}}{\Lambda}\frac{\omega\overline{\beta}_i}{\lambda_i(\omega+\lambda_i)}r^{-\lambda_i/\omega} \quad \text{Eq. (5.120)}$$

Substituting Eq. (5.116) and the upper and lower bounds on $c_i(t^*)$ into Eq. (5.112) results in the following inequalities:

$$\sum\frac{\omega\overline{\beta}_i}{\omega+\lambda_i}\left[1-\epsilon^{-\lambda_i t^*}\right] \geq \delta k(t^*) \geq \sum_i\left[\left(\frac{\omega\overline{\beta}_i}{\omega+\lambda_i}r^{-\lambda_i/\omega}\right)\left(1-\epsilon^{-(\omega+\lambda_i)t_1}\right)\right].$$

Eq. (5.121)

The exponential term on the left-hand side of the inequality may be omitted without destroying the inequality. The exponential on the right-hand side of the inequality may be neglected by noting that the power excursion of interest usually originates in the source range and extends through the power range, so that $\epsilon^{-\omega t_1}$ ranges from 10^{-5} through 10^{-15}. Therefore, the bounds on the reactivity present at the time of peak power ensure that

$$\sum_i \frac{\omega\bar{\beta}_i}{\omega+\lambda_i} \geq \delta k(t^*) \geq \sum_i \frac{\omega\bar{\beta}_i}{\omega+\lambda_i} r^{-\lambda_i/\omega} \quad \text{Eq. (5.122)}$$

The initial step reactivity which produces an exponential power rise of period $1/\omega$ is given by the inhour formula as

$$\delta k_o = \omega\Lambda + \sum_i \frac{\omega\bar{\beta}_i}{\omega+\lambda_i} \quad \text{Eq. (5.123)}$$

The bounds on the change in reactivity (compensating reactivity) required to stop the power rise are obtained by subtracting the initial reactivity [Eq. (5.123)] from the reactivity present at the time of peak power [Eq. (5.122)]:

$$-\omega\Lambda \geq \delta k(t^*) - \delta k_o \geq -\omega\Lambda - \sum_i \left[\frac{\omega\beta_i}{\omega+\lambda_i}\left(1-r^{-\lambda_i/\omega}\right)\right] \quad \text{Eq. (5.124)}$$

or

$$\omega\Lambda \leq \delta k_o - \delta k(t^*) \leq \omega\Lambda + \sum_i \left[\frac{\omega\beta_i}{\omega+\lambda_i}\left(1-r^{-\lambda_i/\omega}\right)\right] \quad \text{Eq. (5.125)}$$

Thus, the magnitude of the required change in reactivity must be at least equal to $\omega\Lambda$ but is never greater than the right-hand side of Eq. (5.125). Provided that at least an upper limit on r is known, the bounds on the compensating reactivity at the power peak have been determined.

Evidently, r may have any value greater than unity and can be expected to be a function of the various thermal time constants of the reactor, the reactivity coefficients, and the reactor period. The analytic determination of r for a given period in a given reactor would require the solution of the exact nonlinear problem. Experimental evidence, however, indicates that the range of practical values for r is relatively small. For a SPERT 1-A core,[37] r varied from a maximum of 5 for low

values of ω (~ 0.1 sec^{-1}) to a minimum of 1.5 for high values of ω (~ 100 sec^{-1}). It is expected that large values of r are realized only when the inherent shutdown mechanisms are very weak, so that the compensating reactivity is introduced slowly, and that strong reactivity feedback effects, resulting in rapid compensation, produce small values of r. Thus, the variation of r with period observed in the SPERT experiments is qualitatively explained by the fact that no boiling occurred at small inverse periods, but at larger inverse periods boiling augmented the reactivity feedback. Evidently, r approaches infinity only if the reactivity coefficients approach zero, and only an instantaneous introduction of negative reactivity can produce an r value equal to unity.

Figure 5.22 is a graph of the maximum compensated reactivity at peak power for various values of r. The upper curve, for $r = \infty$, is identical with the inhour curve and, therefore, represents the initial reactivity. Thus, in the range of inverse periods of interest (10^{-2} to 10^{3} sec^{-1}), only for extremely large values of r is it required that the reactivity be reduced to zero in order to stop the power rise. For inverse periods of greatest interest to safeguards analyses (10 to 100 sec^{-1}), only a small fraction of the initial reactivity is compensated at peak power. As shown in Fig. 5.23, even for $r = 10{,}000$, the maximum fraction of the initial reactivity compensated at peak power in this inverse period range is less than 0.26.

B) BEHAVIOR AFTER PEAK POWER. The behavior of the reactor after dn/dt has been reduced to zero depends on the rate of reactivity feedback. If the reactivity is held constant at the value required instantaneously to stop the power rise, the power will again rise and asymptotically approach a new stable period, as given by the inhour equation [Eq. (5.123)]. If it is reduced to zero, the reactor will attain some constant power level. Depending upon the rate at which the reactivity is reduced, the final level can be either higher or lower than that at which dn/dt was first caused to be zero. If the reactor eventually becomes subcritical, the power will decay to source level.

If the power level is to remain constant at the peak value, $n(t^*)$, then

$$\frac{\delta k(t) - \bar{\beta}}{\Lambda} n(t^*) + \sum_i \lambda_i c_i(t) = 0 \qquad \text{Eq. (5.126)}$$

and

$$\frac{dc_i(t)}{dt} = \frac{\bar{\beta}_i}{\Lambda} n(t^*) - \lambda_i c_i(t) \ . \qquad \text{Eq. (5.127)}$$

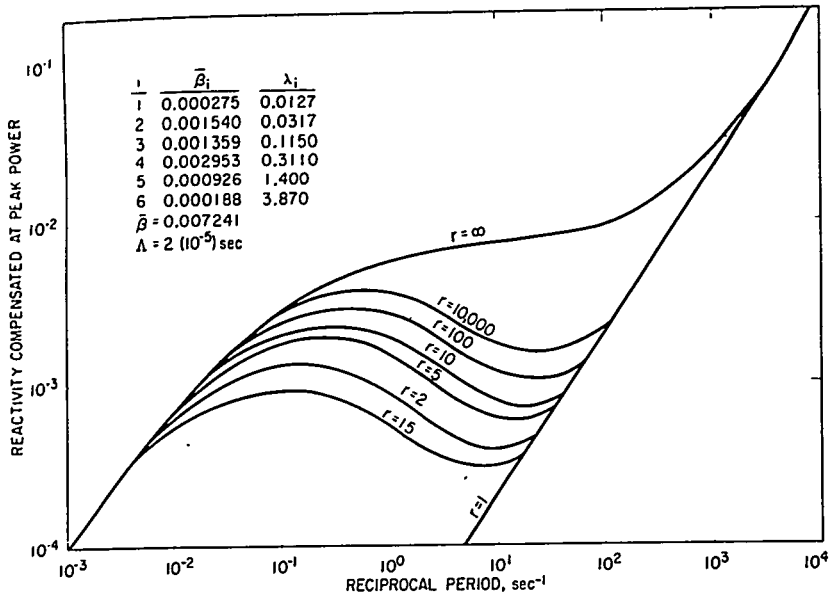

FIGURE 5.22. Maximum Reactivity Compensated at Peak Power for Various Values of r.

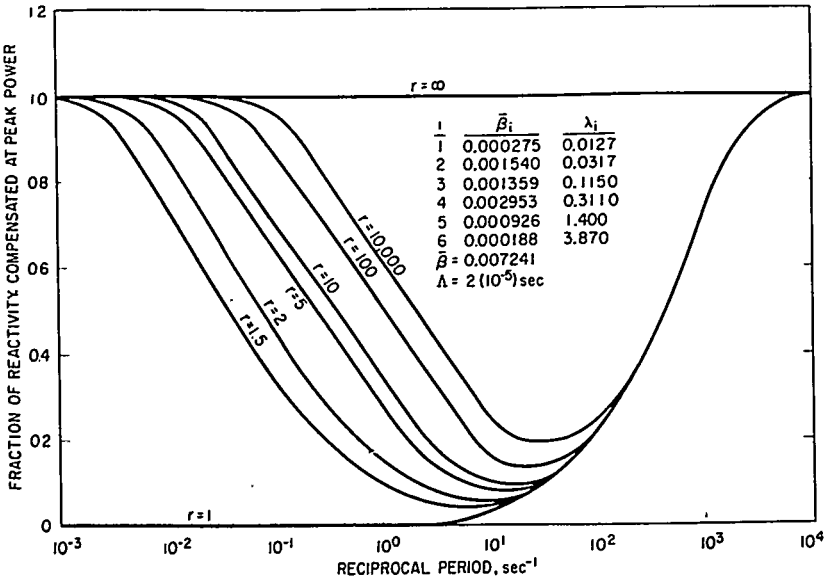

FIGURE 5.23. Maximum Fraction of Initial Reactivity Compensated at Peak Power for Various Values of r.

The solution of Eq. (5.127) in integral form is

$$c_i(t) = \frac{\bar{\beta}_i}{\Lambda} \epsilon^{-\lambda_i t} \int_o^t n(t^*)\, \epsilon^{\lambda_i t}\, dt + c_i(o)\, \epsilon^{-\lambda_i t} \quad . \qquad \text{Eq. (5.128)}$$

The limits on the delayed neutron precursor concentration at time zero are now specified by inequalities [Eqs. (5.114) and (5.120)]. As shown previously, the last exponential term on the right side of each inequality may be omitted without destroying the inequalities. Noting that $n_1 \epsilon^{\omega t^*} = n(t^*)$ yields the limits on $c_i(o)$ as

$$\frac{\bar{\beta}_i n(t^*)}{\Lambda(\omega+\lambda_i)} \leq c_i(o) \leq \frac{\bar{\beta}_i n(t^*)}{\Lambda} \left[\frac{1}{\lambda_i} - \frac{\omega}{\lambda_i(\omega+\lambda_i)}\, r^{-\lambda_i/\omega} \right]. \qquad \text{Eq. (5.129)}$$

Performing the required integration in Eq. (5.128) and using the limits on $c_i(o)$ as prescribed by inequality [Eq. (5.129)] bounds the time behavior of the i^{th} precursor concentration for the assumed condition of constant peak power, $n(t^*)$.

Thus,

$$\frac{\bar{\beta}_i n(t^*)}{\Lambda} \left[1 - \frac{\omega}{\omega+\lambda_i}\, \epsilon^{-\lambda_i t} \right] \leq \lambda_i c_i(t) \leq \frac{\bar{\beta}_i n(t^*)}{\Lambda} \left[1 - \frac{\omega}{\omega+\lambda_i}\, r^{-\lambda_i/\omega}\, \epsilon^{-\lambda_i t} \right].$$

Eq. (5.130)

Substituting this inequality into Eq. (5.126) yields the limits on the reactivity behavior required to maintain the power constant at its maximum value,

$$\sum_i \frac{\omega \bar{\beta}_i}{\omega+\lambda_i}\, \epsilon^{-\lambda_i t} \geq \delta k(t) \geq \sum_i \frac{\omega \bar{\beta}_i}{\omega+\lambda_i}\, r^{-\lambda_i/\omega}\, \epsilon^{-\lambda_i t} \qquad \text{Eq. (5.131)}$$

The limits on the rate at which the reactivity must change in order to maintain constant power after a sustained exponential rise are thus:

$$\sum_i \frac{\lambda_i \bar{\beta}_i \omega}{\omega+\lambda_i}\, \epsilon^{-\lambda_i t} \geq -\frac{d\,\delta k(t)}{dt} \geq \sum_i \frac{\lambda_i \bar{\beta}_i \omega}{\omega+\lambda_i}\, r^{-\lambda_i \omega}\, \epsilon^{-\lambda_i t} \quad . \qquad \text{Eq. (5.132)}$$

Note that the reactivity rate required to keep the power constant decreases with time as the delayed neutrons approach their equilibrium value. If the reactivity rate after peak

power always exceeds the left-hand side of Eq. (5.132), the power will drop. If it is always less than the right-hand side of Eq. (5.132), the power will rise.

The maximum reactivity rate of decrease required to prevent the power from rising above $n(t^*)$ is given by the left-hand side of Eq. (5.132) evaluated at time zero:

$$-\left.\frac{d\delta k}{dt}\right|_{\max} = \sum_i \frac{\lambda_i \bar{\beta}_i \omega}{\omega+\lambda_i} \qquad \text{Eq. (5.133)}$$

If the reactivity rate of decrease exceeds this value, the power must drop. It is apparent from Eq. (5.133) that for very small ω the maximum initial rate necessary to prevent a power rise is equal to $\bar{\beta}\omega$. For large ω, however, the rate becomes independent of ω. Thus, if

$$-\frac{d\delta k}{dt} > \sum_i \lambda_i \bar{\beta}_i \qquad \text{Eq. (5.134)}$$

the power must decrease after time zero. This ultimate maximum rate is roughly 0.35 percent δk/sec.

Equation (5.133), which gives the maximum initial reactivity rate required to prevent a power increase after dn/dt is first made zero, applies strictly for $r=1$, the condition in which the deficiency in delayed neutrons at time zero is the greatest. For larger values of r, the delayed neutron deficiency is smaller and, hence, the reactivity rate required to prevent a power increase after time zero is smaller. Because of the way in which the bounds have been formulated, the reactivity rate required to prevent a power rise can be expected to be nearer to the lower bound of Eq. (5.132) than to the upper bound. However, conservatism dictates the use of the upper bound. In many cases, it will not differ greatly from the lower bound.

2. *Inherent Self-Shutdown Mechanisms*

The variation in moderator density following a change in coolant temperature is the primary mechanism of reactivity feedback during normal power operations. If the reactor were subjected to a fast high power excursion, additional reactivity feedback would result from fuel plate expansion and void formation. Reactivity effects originating from the temperature dependence of nuclear cross sections (Doppler coefficients) or a change in geometric buckling with attendant core growth are significant in some core designs.

In a reactor exhibiting a negative temperature coefficient, the reactivity effects due to changes in moderating ability

are inherent self-shutdown mechanisms. However, changes in nuclear characteristics (buckling and Doppler coefficients) may aid or impede the termination of a power excursion, depending on the particular core materials and structural design.

A) CHANGE IN MODERATOR DENSITY. In safeguards analyses, the power excursion is generally initiated from no-flow and ambient temperature conditions. Under these conditions, the reactivity feedback resulting from a decrease in moderator density with increasing coolant temperature is no longer the major source of reactivity. First of all, the heat transfer with static coolant conditions is significantly less effective than under nominal forced circulation condtions. Secondly, the temperature coefficient at ambient conditions is much less than that for hot conditions. Thus, for a given heat generation rate within the fuel plates, the coolant experiences both a smaller density change and smaller reactivity feedback worth.

With the drastic reduction in conduction heat transfer from the fuel plates to the coolant, the process of direct (radiation) heating of the coolant becomes important. In all water-moderated reactors a fraction of the total heat generation occurs from dissipation of neutron kinetic energy and fission gamma energy in the coolant. For an enriched core, this fraction may be estimated from a table[38] illustrating the distribution of energy in slow-neutron fission of U^{235}. In a typical zirconium core having a metal-to-water ratio of unity, approximately 3 percent of the instantaneous energy released per fission is dissipated directly in the coolant. Since the power at which a fast excursion terminates is considerably higher than the nominal design power, this fraction represents a significant amount of heat dissipated directly in the coolant. Moreover, this medium of heat transfer is instantaneous when compared with the time-dependent conduction of heat from the fuel plates through the clad and to the coolant.

B) STEAM VOID FORMATION. The boiling phenomenon during fast power excursions is not well understood. The characteristic (stable or unstable) and the mode of boiling (nucleate or film), the mechanism and amount of heat transfer, and the degree of superheat, if any, are areas of uncertainty. Numerous experimental programs are currently being conducted in the area of transient boiling. Preliminary results indicate that this phenomenon may be amenable to description by correlations. Until such correlations are available, conservatism must form the basis for the design of any analytical

model employing void formation as one of its shutdown mechanisms.

C) FUEL PLATE EXPANSION. The relative importance of fuel plate expansion as a shutdown mechanism is somewhat obscured by the fact that a reactor changes its reactivity by several percent in going from cold critical to hot critical conditions. Yet, the reactivity change due to fuel plate expansion is only a small fraction of the total change. Consider a reactor with the following characteristics:

Temperature difference between hot and cold critical	400°F
Average temperature coefficient at hot critical	-2×10^{-4} $\delta k/°F$
Ratio of fuel plate thickness to water channel thickness	1
Thermal expansion coefficient of fuel plates	5×10^{-6} ft/ft-°F
Average void coefficient	5×10^{-3} δk/% void

The change in reactivity due to coolant expansion (from cold to hot critical) is,

$$-2 \times 10^{-4}\ \delta k/°F \times 400°F = 8\%\ \delta k.$$

The corresponding change due to fuel plate expansion in the thickness direction is only

$$5 \times 10^{-6}\ \text{ft/ft-°F} \times \frac{\text{Fuel plate thickness}}{\text{Water channel thickness}} \times 100\%$$

$$\times\ 400°F \times 5 \times 10^{-3}\ \delta k/\%\ \text{void} = 0.1\%\ \delta k,$$

or 1.2 percent of the total change in reactivity.

During a fast power excursion, the large difference in per unit temperature worth between coolant expansion and fuel plate expansion is offset by the fact that only a small percentage of the energy generated in the fuel plates reaches the coolant. In a severe transient, the fuel plates may experience a temperature excursion of several thousand degrees, while the average coolant temperature changes only a few degrees. Moreover, the reactivity required momentarily to arrest a fast power excursion constitutes only a small fraction of the initial reactivity perturbation (see Sect. 5.3.C.1). Thus, the effects of fuel plate expansion must be considered in analyzing fast power excursions.

When considering the effects of fuel plate expansion, care should be exercised that positive reactivity feedback contributions are not overlooked. If appreciable axial expansion can occur, the resulting core growth affects the geometric buckling and produces a positive or negative reactivity feedback, depending on whether the growth is into or out of the rodded region. In general, the support structures of conventional plate-type reactors are so designed that thermal expansion of the fuel plates can occur only in the thickness direction. Under these conditions, radial expansion need only be considered, and the reactivity feedback results from the displacement of moderator from the active core with no attendant core growth.

D) NUCLEAR EFFECTS.* The energy distribution of thermal neutrons in a reactor is determined by its absorption and leakage properties and by the kinetic energy of the nuclei with which the neutrons undergo scattering collisions. This last (and very important) contribution to the nature of the thermal neutron spectrum depends, in turn, on the temperature of the scattering materials and, in particular, on the temperature of the material with which the neutrons collide most frequently. Hence, in light water-moderated systems the kinetic energy of the water molecule is of considerable importance in determining the thermal neutron energy distribution. As the average energy of this distribution increases, the absorption rate in U^{235} relative to that in other materials generally decreases, since the absorption cross section of U^{235} (because of a negative energy resonance) falls faster than $1/v$, whereas that of most other materials falls either as $1/v$ or (because of low energy resonances) more slowly. Thus, an increase in moderator temperature for a light water-moderated core produces a nuclear temperature effect on reactivity which is negative. It follows that during a very rapid excursion this mechanism for terminating the transient will be effective mostly to the extent that the energy generated appears as an increase in water temperature during the time duration of the excursion. (The neutron distribution will come into equilibrium with a changed moderator temperature in 10^{-5} or 10^{-6} seconds.) Thus, this nuclear shutdown mechanism is not very effective.

The increase in the resonance capture rate of neutrons can be a far more important mechanism in tending to terminate a prompt excursion. In this case, it is primarily the fuel material temperature that matters. The kinetic energy of fission

*D. R. Harris

fragments is transmitted almost instantly to this material. Hence, resonances in U^{235}, U^{238}, fission products, and any alloying material are broadened almost immediately. For slightly enriched or much depleted reactors there is a consequent decrease in reactivity due to the extra parasitic capture in the Doppler-broadened resonances. For temperature increases in the neighborhood of 500°C this decrease contributes significantly to the termination of the excursion.

For undepleted highly enriched cores the Doppler effect if smaller, since the fission resonances broaden along with the capture resonances. It is thought that the capture rate is increased slightly more than the fission rate by this process. However, the uncertainty in the resonance parameters for U^{235} makes it impossible to guarantee this behavior under all conditions. Thus, the best estimate is that Doppler broadening in highly enriched, undepleted reactors contributes a small negative fuel temperature coefficient.

3. *Analytical Models and Applications*

K. J. Chock

A) ANALOG SIMULATOR RESULTS. The foremost difficulty in analyzing the behavior of water-moderated and cooled reactors undergoing rapid power excursions is the description of the heat transfer and void formation phenomena that occur during transient boiling. A high degree of subcooling obviates this problem. SPERT 3 results[39] indicate that at high pressures (high subcooling) essentially no boiling occurs during the initial power burst. Thus, a pressurized water reactor may be rigorously represented by a subcooled model in which all boiling effects are neglected, and the compensating reactivities are derived from thermal expansion of the fuel plates and the coolant. Such a model tends to be most conservatiye at low subcooling, becoming less conservative as the subcooling is increased.

Figure 5.24 gives a relative measure of the degree of conservatism (inherent in neglecting the boiling effects) as a function of the initial subcooling. These results were obtained from an analog representation of the SPERT 3 reactor. At high pressures, where essentially no boiling occurred during the initial power burst, the energy released at the time of peak power is less than a factor of 2 greater than that attained at atmospheric pressure conditions (lowest subcooling). This result has been substantiated by experiments at the SPERT 3 Facility.[39]

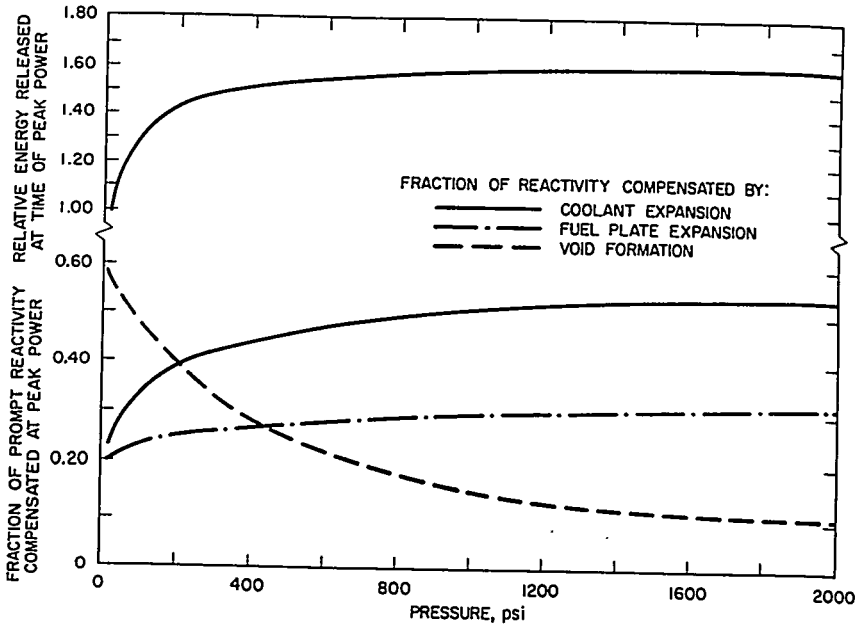

FIGURE 5.24. Analog Results for 10-msec Period Transient Using SPERT 3 Parameters.

In the analysis of an unpressurized reactor the subcooled model may yield results which are too conservative to demonstrate the self-shutdown ability of the reactor. This is especially true in those instances where the prompt feedback effects are very weak, and void formation is the primary shutdown mechanism. The SPERT 1 unpressurized aluminum-clad core and the SPERT 3 pressurized stainless steel-clad core exhibit marked differences in their shutdown characteristics. The higher heat conductivity of the aluminum-clad results in better heat transfer to the coolant and a greater dependence on void formation as the shutdown mechanism. Figure 5.25 shows the comparison of the analog results with the SPERT 1 experimental data. Though the SPERT 1 reactor vessel is unpressurized, simulated pressurized conditions were also examined using the subcooled model. The results indicate that the peak power under simulated subcooled conditions is more than a factor of 5 greater than that attained at atmospheric conditions. The corresponding difference for the SPERT 3 reactor is less than a factor of 2. Thus, the subcooled model may be used to analyze the SPERT 3 type reactors, but the boiling model should be used in the analysis of the SPERT 1 type cores to avoid excessive conservatism. Since Zircaloy has an even lower heat conductivity than stainless steel, the subcooled model may be readily applied to such cores.

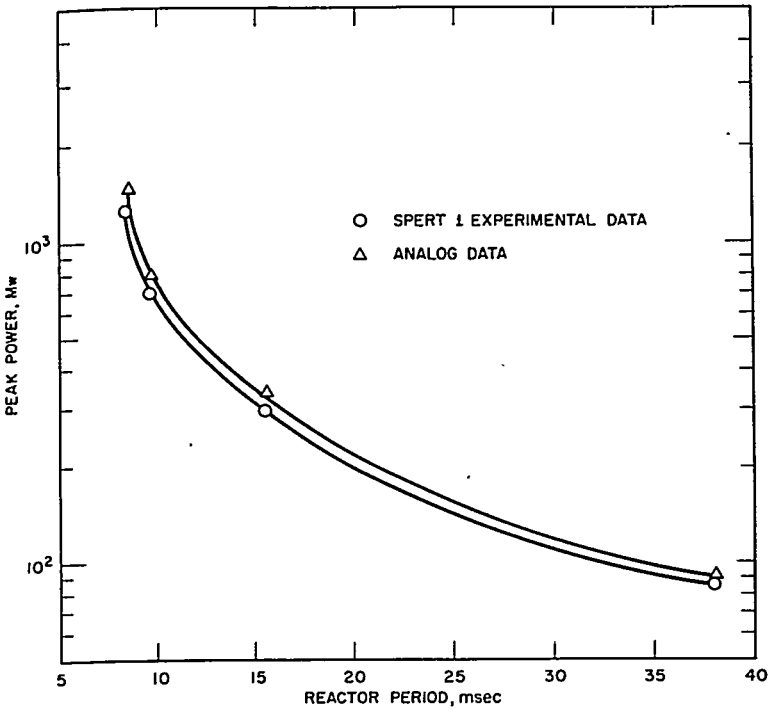

FIGURE 5.25. Comparison of Analog Model and SPERT 1 Experimental Data.

B) SUBCOOLED MODEL. The subcooled model is based on the following assumptions:

1. No boiling occurs, and reactivity compensation results from fuel plate and coolant expansion only. In most cases, this assumption is conservative. However, care should always be exercised in determining the effective expansion of the fuel plates, since an axial expansion could result in a reactivity increase. In addition, Doppler effects in U^{235} could, in some core designs, yield a positive reactivity contribution of sufficient magnitude to be important.
2. No heat is transferred by convection. For initial periods less than ~ 35 msec and for reasonable flow rates and core dimensions, convection has essentially no effect on the initial power burst.[40] The equilibrium power level following the burst is approximately proportional to the flow rate. The fuel plate surface temperatures decrease with increasing flow velocities.
3. Conduction of heat in directions other than that normal to the fuel plate surface is neglected. This is a reasonable

assumption, in view of the fact that the fuel plates are relatively thin.

4. Delayed neutrons remain at their initial levels, so that the kinetics equations reduce to

$$\frac{dn}{dt} = \frac{\delta k - \bar{\beta}}{\Lambda} n \ . \qquad \text{Eq. (5.135)}$$

This equation is valid for describing the initial power burst resulting from periods shorter than ~ 35 msec (Sect. 5.3.C.1). If reactor periods beyond this range or the resultant equilibrium power rises are of interest, the delayed precursor contributions should be included. They have been omitted here to eliminate unnecessary computations when considering power excursions of safeguards interest (5 to 35 msec period transients) and to simplify hand calculations.

Based on the foregoing assumptions, the reactivity as a function of time is described by

$$\delta k = \delta k_o + \left[\gamma_m \psi_m \bar{T}_m(t) + \gamma_c \psi_c \bar{T}_c(t)\right] \frac{\alpha_v}{\psi_w} + \alpha_T \bar{T}_w(t) \qquad \text{Eq. (5.136)}$$

where

δk_o = the initial step reactivity insertion
γ_m and γ_c = the equivalent coefficients of thermal expansion for the meat and clad, respectively
ψ_m = the half-thickness of the meat
ψ_c = the clad thickness
ψ_w = the half-thickness of the water channel
$\bar{T}_i$ = the change in average temperature of the respective medium
α_v = the void coefficient of reactivity of the water (δk/unit void)
α_T = the temperature coefficient of reactivity of the water (void coefficient multiplied by volumetric expansion coefficient of water).

The temperatures are obtained from the one-dimensional heat conduction equation,

$$\frac{\partial T_i(t)}{\partial t} = \frac{K_i \partial^2 T_i(t)}{\rho_i c_i \partial x^2} + \frac{S_i n(t)}{\rho_i c_i} \qquad (i = m, c, w) \qquad \text{Eq. (5.137)}$$

where

ρ = the density
c = the specific heat
K = the conductivity
S = the power density per unit power
n = the per unit power obtained from Eq. (5.135)

with the boundary conditions,

$$\frac{\partial T_M}{\partial x} = 0 \text{ at the fuel plate centerline} \qquad \text{(Eq. 5.138)}$$

$$K_m \frac{\partial T_m}{\partial x} = K_c \frac{\partial T_c}{\partial x} \text{ and } T_m = T_c \text{ at the meat-clad interface} \qquad \text{(Eq. 5.139)}$$

$$K_c \frac{\partial T_c}{\partial x} = K_w \frac{\partial T_w}{\partial x} \text{ and } T_c = T_w \text{ at the clad-water interface} \qquad \text{(Eq. 5.140)}$$

$$\frac{\partial t_w}{\partial x} = 0 \text{ at the water channel centerline .} \qquad \text{(Eq. 5.141)}$$

Average temperatures for use in Eq. (5.136) are computed from

$$\overline{T}_i(t) = \frac{1}{x_i - x_{i-1}} \int_{x_{i-1}}^{x_i} T_i(x, t)\, dx \qquad \text{Eq. (5.142)}$$

The above equations are readily solvable by standard computing machine techniques. For analog computation, Eq. (5.137) is reduced to a set of ordinary difference equations by replacing $\partial^2 T/\partial x^2$ by the three-point difference formula. Equation (5.142) then becomes a sum rather than an integral.

C) SIMPLIFIED SUBCOOLED MODEL. It is sometimes desirable to estimate upper bounds for the energy release, the maximum power, and the maximum temperatures attained during a prompt excursion. A simplified model amenable to hand calculations is readily developed by assuming that adiabatic boundaries exist at the meat-clad and clad-water interfaces of the subcooled model, i.e., no heat is transferred by conduction. This assumption is highly conservative, since a transfer

of energy from the fuel plates to the water increases the amount of water ejected from the core per unit energy released. In addition, the adiabatic boundaries ensure conservative fuel temperature calculations.

With the elimination of conduction heat transfer, Eq. (5.137) simplifies to

$$\frac{\partial T_i(t)}{\partial t} = \frac{S_i n(t)}{\rho_i c_i} \quad . \qquad \text{Eq. (5.143)}$$

Equations (5.135), (5.136), and (5.143) may be combined to form Eq. (5.144):

$$\frac{dn}{dt} = \frac{A_n}{\Lambda} \int_o^t n\,dt + \frac{\delta k_o - \bar{\beta}}{\Lambda} n \qquad \text{Eq. (5.144)}$$

where

$$A = \left[\frac{\gamma_m \psi_m S_m}{\rho_m c_m} + \frac{\gamma_c \psi_c S_c}{\rho_c c_c}\right] \frac{\alpha_v}{\psi_w} + \frac{\alpha_T S_w}{\rho_w c_w} \quad . \qquad \text{Eq. (5.145)}$$

Bright, et al.,[41] have obtained the following analytic solutions for Eq. (5.144): (It is assumed that the initial reactivity is inserted at a very low initial power level, n_o, so that a stable period is achieved before appreciable heating occurs.)

$$n(t) \simeq \frac{4\alpha^4}{b^2 n_o} \frac{e^{-\alpha t}}{\left(\frac{2\alpha^2}{b n_o} e^{-\alpha t} + 1\right)^2} \qquad \text{Eq. (5.146)}$$

$$\int_o^t n(t)\,dt \simeq \frac{2\alpha}{b} \frac{(1 - e^{-\alpha t})}{\left(\frac{2\alpha^2}{b n_o} e^{-\alpha t} + 1\right)} \qquad \text{Eq. (5.147)}$$

where

$$\alpha = \frac{\delta k_o - \bar{\beta}}{\Lambda}$$

the initial inverse period, and

$$b = -\frac{A}{\Lambda} \quad .$$

The peak power is

$$n_{max} = \frac{\alpha^2}{2b} \qquad \text{Eq. (5.148)}$$

and the total energy release is

$$\int_o^\infty n(t)dt = \frac{2\alpha}{b} \; . \qquad \text{Eq. (5.149)}$$

From Eq. (5.143), the maximum temperatures are

$$T_{i_{max}} = \frac{S_i}{\rho_i c_i} \cdot \frac{2\alpha}{b} + T_i(o) \; . \qquad \text{Eq. (5.150)}$$

Thus, this model affords a very simple means of estimating the energy release, the maximum power, and the maximum temperatures.

Hurwitz[42] has developed a simple formula for estimating the total energy yield during a startup incident in which the reactivity is brought above critical linearly in time rather than instantaneously. When the reactivity has reached the neighborhood of prompt critical, it is supposed that the power has risen to a sufficiently high level to cause a reactivity reduction which is a linear function of the total energy generated. It is further assumed that the power is arrested in a cyclic fashion. Initially, the reactivity is reduced below prompt critical by the high power level. However, when the power level falls sufficiently, the external mechanism which is causing the incident again dominates, and the reactivity increases. The power soon rises to a high level again, and the reactivity again begins to fall, and so on. This cyclic process continues until the externally produced reactivity increase ceases and the power falls monotonically to zero. Under the assumed conditions, the total energy yield is

$$\lim_{t \to \infty} E = \int_o^\infty P(t)dt = \left(\Delta K_m + \sqrt{2\Delta K_m - 1}\right) \Big/ \gamma \qquad \text{Eq. (5.151)}$$

where

E = the total energy generated
$P(t)$ = the instantaneous power
ΔK_m = the amount of reactivity (in dollars) above critical
γ = the proportionality constant relating the reactivity feedback and total energy generated.

D) BOILING MODEL. The boiling model is an extension of the subcooled model wherein the reactivity feedback from void formation is considered. This is assumed to begin when the fuel plate surface temperature reaches the saturation temperature of the coolant.

The analog results previously discussed were obtained with the model described in Ref. 43. The salient feature of this model is its treatment of the boiling region immediately adjacent to the plate. The conduction process in this region is actually dominated by turbulent convection through the steam bubbles themselves and through the surrounding water, agitated by the stirring action of the bubbles. The heat transfer mechanism is, nevertheless, treated mathematically as a conduction process through a region of variable thickness δ. The effects of convection and agitation are accounted for by treating the conductivity of the boiling region as a fitted parameter. Specifically, heat conduction through the steam region is represented by

$$\frac{\partial T_S}{\partial t} = \frac{K_s}{\rho_s c_s} \frac{\partial^2 T_s}{\partial x^2} \,. \qquad \text{Eq. (5.152)}$$

Boundary condition [Eq. (5.140)] is replaced by

$$K_c \frac{\partial T_c}{\partial x} = K_s \frac{\partial T_s}{\partial x} \qquad \text{Eq. (5.153)}$$

and

$$T_c = T_s \,.$$

The following applies at the steam-water interface:

$$T_s = T_w = T_{\text{sat}} \qquad \text{Eq. (5.154)}$$

and

$$h_{fg} \rho_s \frac{d\delta}{dt} = - K_s \frac{\partial T_s}{\partial x} + K_w \frac{\partial T_w}{\partial x} \qquad \text{Eq. (5.155)}$$

where

δ = the steam region thickness
h_{fg} = the latent heat of vaporization of the water
ρ_s = the density of steam.

An alternate approach, recently introduced, treats the boiling heat transfer in a more realistic manner. This approach is similar to the familiar Jens-Lottes treatment of steady-state nucleate boiling, and is based on the experimental observation that during nucleate boiling the appropriate boundary condition at the clad-coolant interface is

$$T_c = T_{sat}(P) + \Delta T(\phi, P) \qquad \text{Eq. (5.156)}$$

where ϕ is the heat flux from clad to channel, given by

$$\phi = -K_c \frac{\partial T_c}{\partial x} . \qquad \text{Eq. (5.157)}$$

At atmospheric pressure, the wall superheat ΔT is of order 50°F. Since the heat flux is not required to satisfy the continuity condition [Eq. (5.153)], the heat fluxes given by Eq. (5.157) account realistically for the improved heat transfer observed experimentally at the inception of boiling.

In place of Eq. (5.155), the void volume is calculated by an empirical equation of the form

$$h_{fg}\rho_s \frac{d\delta}{dt} = \alpha\phi - \frac{h_{fg}\rho_s \delta}{\tau} . \qquad \text{Eq. (5.158)}$$

The fraction α, determined empirically from in-pile or out-of-pile data,[44;45] accounts for the fact that because of competition between bubble growth and bubble collapse only a small fraction of the nucleate boiling heat flux contributes to net growth of the void volume. The time constant τ accounts for convection of bubbles out of the channel and bubble collapse. Typical values for τ are of order 50 to 100 msec, while α ranges from 0.0005 at atmospheric pressures to 0.01 or more at 1000 psia.

In new work, the treatment just described replaces the quasiconduction model of Ref. 43. In addition, the momentum integral treatment of hydrodynamics[46] is incorporated.

5.4 SPACE-TIME KINETICS

S. Kaplan

A. Introduction

The preceding sections have dealt with the separable cases of reactor kinetics, i.e., with those cases in which the spatial shape of the neutron flux remains constant while the amplitude

varies. However, there are many practical cases in which the distortion of the spatial shape during transients is quite significant. For an illustration of such a case consider a reactor, each side of which is cooled by a separate coolant loop. A perturbation in one loop can affect the moderator temperature on one side of the reactor differently from the other. This causes a distortion or tilting of the flux shape. Flux tilts, in general, are undesirable because they worsen the peaking factors.

To determine whether tilting effects will be a problem in a given reactor, two main questions must be answered. First, what disturbances in the nuclear properties are likely to occur which will stimulate a flux tilt? Second, for any given disturbance, how much tilt will result? Here the general observation may be made that reactors which are large in number of mean free paths and poorly coupled (as, for example, an annular configuration) tend to be more susceptible to tilt phenomena.

In answering these two questions it is important to consider feedback, i.e., the effects of a flux tilt upon the original disturbance of the nuclear properties. Therefore, as in separable reactor kinetics, the equations describing neutron flux, delay precursors, and other nuclear phenomena must be solved simultaneously with those governing the temperature and flow conditions throughout the systems. Since an exact solution is not attainable, it is necessary to construct tractable yet realistic approximate models. For the reactor-plant thermal-hydraulic equations, this is accomplished (see Sect. 5.3) by breaking the system into segments and solving for averaged quantities over each segment. The result is an example of a finite model, i.e., one in which continuous independent variables have been replaced by discrete variables.

The main concern of the present section is the construction of finite models describing the nuclear phenomena in the few-group diffusion theory approximation. As discussed in Chap. 4, present digital computers can handle the geometrical complexity of a power reactor reasonably well in static problems. However, they are not yet adequate for this complexity together with time dependence. Accordingly, the natural plan of attack is to attempt to separate the neutron space-time equations into space equations and time equations, the space equations to be solved by digital computer, the time equations to be added to reactor-plant thermal-hydraulic models, and the combined set solved either by analog or, by discretizing the time variable, digital computer.

Three methods are discussed which have been proposed for accomplishing this separation: nodal analysis, modal

analysis, and the instantaneous tilt method. In the nodal method, the spatial configuration of the reactor is represented by a limited set of points or nodes, each representing a certain portion of the reactor volume. With this representation the neutron space-time equations reduce to a set of coupled ordinary differential equations, with time as the only independent variable and with the dependent variables being the average fluxes in the regions corresponding to the nodes. In this set of time-dependent equations there are coupling coefficients which represent the diffusion of neutrons from one node to another. The coupling coefficients are inferred from detailed spatial calculations.

In the modal method, the flux is represented by a linear combination of space-dependent basis functions, or modes, with time-dependent coefficients of combination. With this representation, the space-time problem again reduces to a set of ordinary differential equations in which the unknowns are the coefficients of combination. The modes themselves generally have to be found by digital calculation.

In the instantaneous tilt method, an adiabatic[47] approximation is made which allows the flux shape at any instant to be related to the nuclear properties at that instant. A series of static spatial calculations are performed to specify this relation. The time equations in this method are the conventional reactor kinetics equations.

The three methods identified above are described in this section and sample applications are presented for the no-xenon feedback case. In addition, several variations of the modal method are applied to the xenon problem.

B. The Instantaneous Tilt Method

N. J. Curlee

This method is an application of the analysis of Sect. 5.2.A. There the time-dependent directional flux was expressed rigorously as the product of a time-dependent normalized shape function (ψ) and an amplitude function (T) of time only. T rigorously satisfies the reactor kinetics equations

$$\frac{dT}{dt} = \frac{\rho - \bar{\beta}}{\Lambda} T + \sum_i \lambda_i c_i + Q \qquad \text{Eq. (5.159)}$$

and

$$\frac{dc_i}{dt} = \frac{\bar{\beta}_i}{\Lambda} T - \lambda_i c_i \qquad \text{Eq. (5.160)}$$

where the definitions of $\rho, \bar{\beta}, \Lambda, c_i$, and Q involve the shape function and are given by Eqs. (5.7) through (5.12).

This formulation requires that the shape function ψ be normalized such that

$$\frac{\partial}{\partial t}\int_u \int_V \frac{\phi_o^*(\vec{r}, u)\phi(\vec{r}, u, t)}{v(u)}\, du\, dV = 0 \qquad \text{Eq. (5.161)}$$

where

$$\phi_o^*(r, u) \equiv \int_\Omega \psi_o^*(\vec{r}, \vec{\Omega}, u)\, d\Omega \qquad \text{Eq. (5.162)}$$

$$\phi(r, u, t) \equiv \int_\Omega \psi(\vec{r}, \vec{\Omega}, u, t)\, d\Omega \qquad \text{Eq. (5.163)}$$

and the integration is over all space and lethargy.

In transients where the flux shape does not change with time, the reactor kinetics equations are the only nuclear equations which need be solved simultaneously with the reactor-plant thermal-hydraulic equations. This is not true, however, when the shape function (ψ in transport theory and ϕ in diffusion theory) does change with time. In this situation, the reactor kinetics equations do not change in form, but it is necessary, in addition, to find the instantaneous shape function. At this point, the principal approximation of this method is made. The true shape function is replaced by the static flux shape corresponding to the instantaneous values of the nuclear properties of the reactor.* This replacement is referred to as the instantaneous tilt approximation, since it assumes in effect that the flux shape responds instantaneously to changes in nuclear properties. In actual fact, the presence of delayed neutrons causes the shape change to lag somewhat behind the change in properties.[48†]

The instantaneous tilt assumption allows the space-time problem to be separated into a space part and a time part, and permits the space part to be solved before the time part is begun. The following are the steps in using the method.

Recall that the reactor-plant thermal-hydraulic equations produce as output the temperature and density distribution in the form of average values in discrete regions of the reactor. In any given problem, the possible combinations of temperature and density values for the regions are contained within some

*The instantaneous reactor must be made critical by adjustment of some designated parameter.

†A method for including the delayed neutron effect on the shape function has been proposed[49] but has not yet been applied.

finite range. The first step in using the method is to calculate the static shape functions appropriate to various combinations spaced throughout this range. Next, one sets up a scheme for interpolating between these calculations, thus, in effect, obtaining shape functions appropriate to all combinations within the range. Similarly, an interpolation scheme must be set up for the values of the parameters in the kinetics equations [Eqs. (5.159) and (5.160)] which are by Eqs. (5.7) through (5.12) functionals of the instantaneous flux shape. This completes the spatial part of the problem. The time part consists in solving the kinetics equations simultaneously with the reactor-plant thermal-hydraulic equations and incorporating the interpolation scheme. Thus, at any instant one takes the output of the reactor-plant thermal-hydraulic equations and, making the instantaneous tilt assumption, enters the interpolation scheme to determine the shape function ϕ at that instant and the values of the parameters in the kinetics equations. The output of the kinetics equations and the shape function determine the power distribution input to the reactor-plant thermal-hydraulic equations, thus closing the loop.

The following example, taken from Ref. 50, illustrates the application of the method to a two-dimensional shape problem in a large power reactor (the Shippingport reactor). As shown in Fig. 5.26, the reactor consists of an annulus (seed) of highly enriched core material (U^{235}, Zr, and H_2O) surrounded inside and out by a natural uranium blanket. For simplicity, this example does not take account of the time dependence of the flux within the blanket region. The seed is considered to be broken into four segments, two of which are numbered the same because of symmetry about the line A-A. The problem is to compare the transient behavior of the reactor when the inlet temperature to all parts of the seed is dropped with the behavior when the inlet temperature in Region 1 only is dropped. For the first step of the method, a series of static flux shapes must be obtained. In Ref. 50 these consisted of seven solutions of the diffusion equations for different sets of average coolant temperatures in each of the three regions. The solutions were obtained with a two-energy group two-dimensional code (PDQ).

The scheme for interpolating between these seven shapes consists of the following algebraic form:

$$\bar{\phi}_1 = 0.25 + \alpha_1(T_3 - T_1) + \alpha_2(2T_2 - T_1 - T_3)$$

$$\bar{\phi}_2 = 0.5 - 2\alpha_2(T_2 - T_1 - T_3) \qquad \text{Eq. (5.164)}$$

$$\bar{\phi}_3 = 0.25 - \alpha_1(T_3 - T_1) + \alpha_2(2T_2 - T_1 - T_3)$$

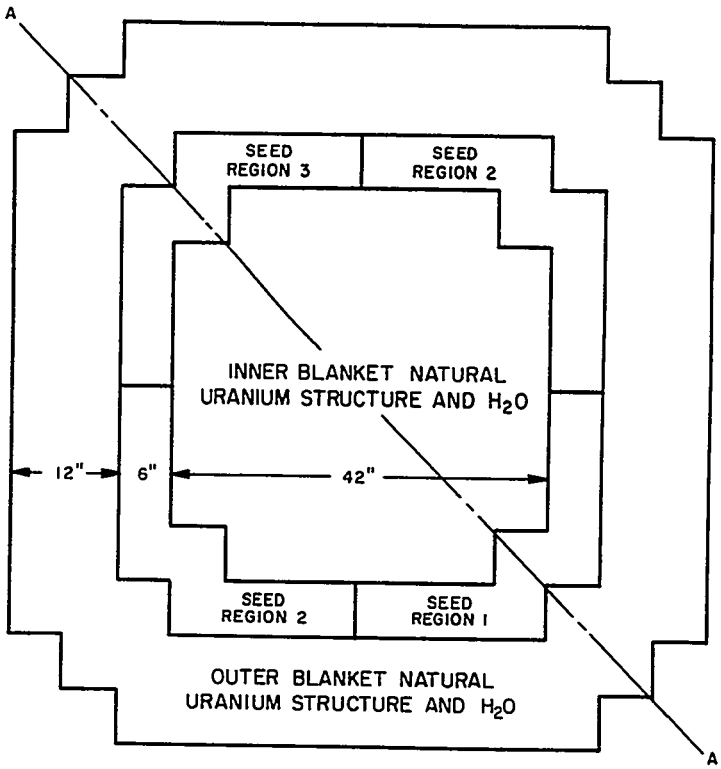

FIGURE 5.26. Seed-Blanket Configuration.

Here $\bar{\phi}_i$ is the integral of the flux over the i^{th} seed region when the flux is so normalized that its integral over the whole seed is unity. This algebraic form was developed from symmetry considerations but can be interpreted in terms of the azimuthal modes of the unperturbed reactor. The nontemperature dependent terms represent the fundamental azimuthal mode which is uniform. The α_1 terms represent the first azimuthal overtone which has a maximum in Region 1, zeros in the Regions 2, and a minimum in Region 3. The α_2 terms represent the second azimuthal overtone with maxima in Regions 1 and 3 and minima in the Regions 2.

The interpolation formula chosen for the reactivity parameter is

$$\rho = \sum_{i=1}^{3} \bar{\phi}_i \left[\alpha \delta T_i + \beta (\delta T_i)^2 \right] . \qquad \text{Eq. (5.165)}$$

The effects of variation of the other parameters in the kinetics equation are ignored in this example, since they are small compared to the effect of reactivity change.

These reactivity and shape equations, when combined with the conventional reactor kinetics equations and the heat transfer equations, form a set of simultaneous equations suitable for solution on an analog computer. Figure 5.27 shows a block diagram of the analog computer solution. Results are shown in Fig. 5.28 for a typical solution in which the initially uniform flux shape changes during the transient.

C. Nodal Analysis

S. Kaplan

The nodal analysis method treats the nuclear equations in the same way that the reactor-plant thermal-hydraulic equations are treated, i.e., the reactor is divided into regions, or nodes, and a set of time equations found involving the average fluxes at each node. In doing this, the main point of difficulty is to account for the diffusion of neutrons from node to node. In Refs. 51 and 52, where the nodes are separated by an intervening nonfissioning medium, the leakage between two nodes (say the i^{th} and j^{th}) is approximated by a term of the form

$$D\,\frac{[\phi_i - \phi_j]}{\ell_{ij}}$$

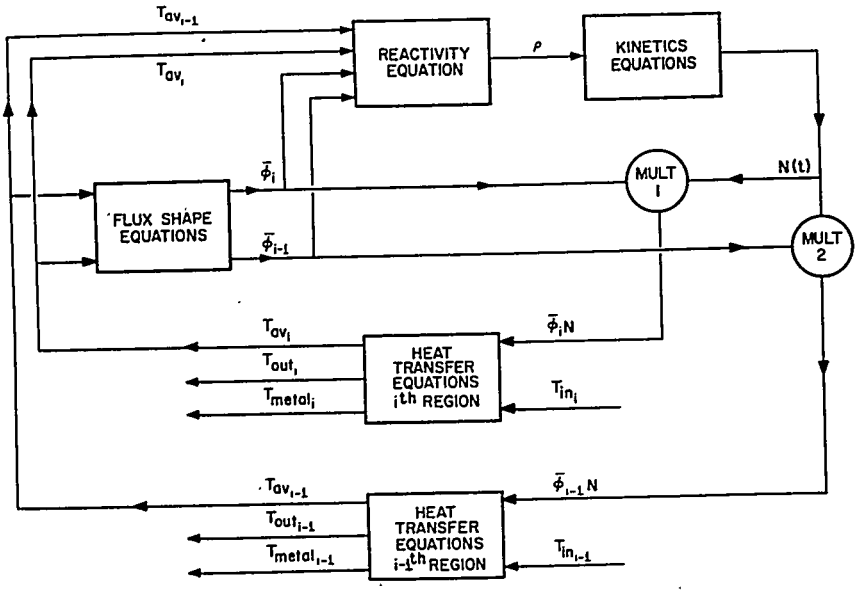

FIGURE 5.27. Diagram of Analog Computer Solution.

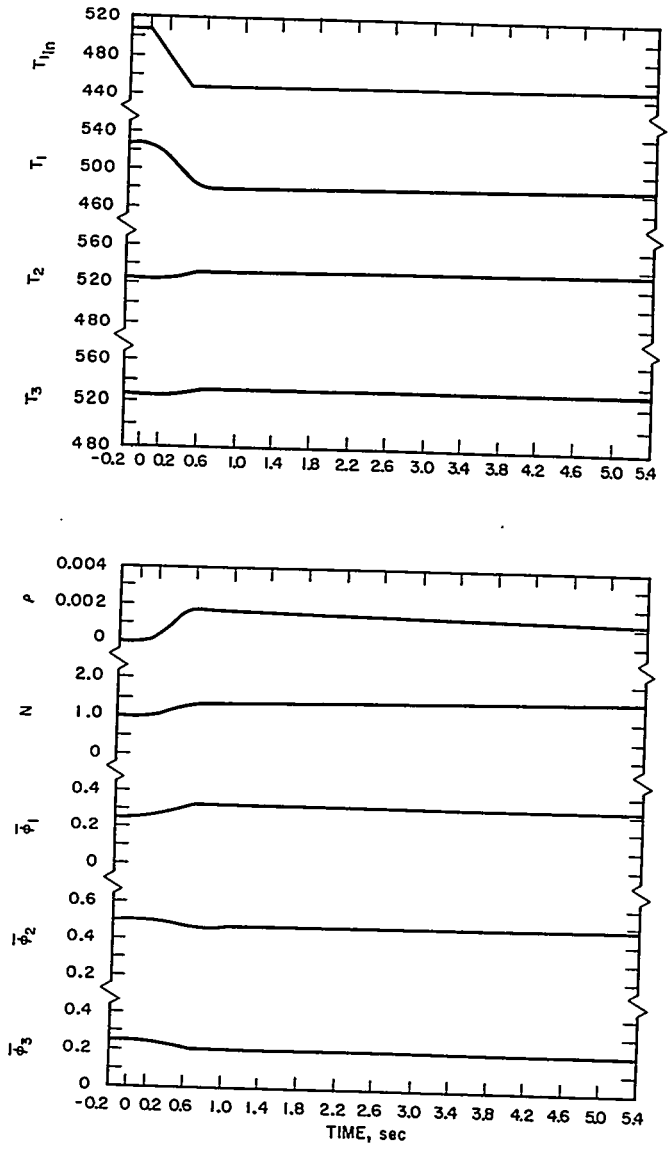

FIGURE 5.28. Reactor Variables vs Time Following a 60°F Inlet Drop in Region 1 of the PWR Seed.

where D is the diffusion constant of the intervening material and ℓ_{ij} is some average distance between the nodes. Another method is to apply the gross coupling[53] concept used in the multichannel synthesis technique (see Chap. 4).

The latter application is outlined here. For simplicity, one energy and one delay group will be used, i.e., a nodal approximation will be constructed for

$$\nabla \cdot D\nabla\phi - \left[\Sigma_a - \frac{\nu\Sigma_f}{\lambda_0}(1-\beta)\right]\phi + \lambda c = \frac{\dot{\phi}}{v}$$

$$\beta\frac{\nu\Sigma_f}{\lambda_0}\phi - \lambda c = \dot{c} \ . \qquad \text{Eq. (5.166)}$$

Denote the reactor volume by R and the subregions or nodes by R_i, and let S_i denote the surface of each node. Also, for later convenience, let R_o denote the region exterior to the reactor.

The first step in arriving at the nodal representation is to integrate Eqs. (5.166) over each R_i:

$$\oint_{S_i} D\nabla\phi \cdot \vec{N}_i\, dS - \int_{R_i}\left[\Sigma_a - \frac{\nu\Sigma_f}{\lambda_0}(1-\beta)\right]\phi\, dR + \lambda\int_{R_i} c\, dR = \frac{1}{v}\int_{R_i}\dot{\phi}\, dR$$

$$\beta\int_{R_i}\frac{\nu\Sigma_f}{\lambda_0}\phi\, dR - \lambda\int_{R_i} c\, dR = \int_{R_i}\dot{c}\, dR \ . \qquad \text{Eq. (5.167)}$$

Defining,

$$V_i = \oint_{R_i} dR \ ,$$

$$\phi_i = \frac{1}{V_i}\int_{R_i}\phi\, dR \ , \qquad c_i = \frac{1}{V_i}\int_{R_i} c\, dR \qquad \text{(Eq. (5.167a)}$$

$$\Sigma_{ai} = \frac{1}{\phi_i V_i}\int_{R_i}\Sigma_a\phi\, dR \ , \quad \Sigma_{fi} = \frac{1}{\phi_i V_i}\int_{R_i}\Sigma_f\phi\, dR \ . \qquad \text{Eq. (5.167b)}$$

Equations (5.167) become

$$\oint_{S_i} D\nabla\phi \cdot \vec{N}_i\, dS - \left[\Sigma_{ai} + \frac{\nu\Sigma_{fi}}{\lambda_0}(1-\beta)\right]\phi_i V_i + \lambda c_i V_i = \frac{1}{v}\dot{\phi}_i V_i$$

$$\beta\frac{\nu\Sigma_{fi}}{\lambda_0}\phi_i V_i - \lambda c_i V_i = \dot{c}_i V_i \qquad \text{Eq. (5.168)}$$

which is just a statement of neutron balance for region i. If the R_i were small parallelepipeds and if in the surface integral of Eq. (5.168) the gradient on a face separating two adjacent parallelepipeds is approximated by the difference of the average fluxes on either side divided by the center-to-center distance, then Eq. (5.168) reduces to the usual rectangular finite-difference equations. For general R_i the gross coupling concept is invoked as follows:

Let

$$\oint_{S_i} D\nabla\phi \cdot \vec{N}_i \, dS = \sum_{j=0}^{J} \oint_{S_{ij}} D\nabla\phi \cdot \vec{N}_i \, dS \qquad \text{Eq. (5.169)}$$

where S_{ij} denotes the interface between R_i and R_j. At each point on S_{ij} let

$$-D\nabla\phi \cdot \vec{N}_i = j_i^+ - j_i^- \qquad \text{Eq. (5.170)}$$

where $j_i^+ (j_i^-)$ is the partial neutron current in direction $\vec{N}_i (-\vec{N}_i)$, and define

$$j_{ij}^+ = \oint_{S_{ij}} j_i^+ \, dS = j_{ji}^-$$

$$j_{ij}^- = \oint_{S_{ij}} j_i^- \, dS = j_{ji}^+ \quad . \qquad \text{Eq. (5.171)}$$

The gross coupling hypothesis is that the one way leakage from region R_i to R_j is proportional to the average flux in region R_i, i.e.,

$$j_{ij}^+ = p_{ij} \phi_i \quad . \qquad \text{Eq. (5.172)}$$

Putting Eqs. (5.169) through (5.172) into Eq. (5.168) one obtains

$$-\left[p_i + \Sigma_{ai} - \frac{\nu\Sigma_{fi}}{\lambda_0}(1-\beta)\right]\phi_i V_i + \sum_{j=1}^{J} p_{ji}\phi_j + \lambda c_i V_i = \frac{1}{v}\dot{\phi}_i V_i$$

$$\beta \frac{\nu\Sigma_{fi}}{\lambda_0} \phi_i V_i - \lambda c_i V_i = \dot{c}_i V_i \qquad \text{Eq. (5.173)}$$

where

$$p_i = \frac{1}{V_i} \sum_{j=0}^{J} p_{ij} \qquad \text{Eq. (5.174)}$$

and the summation in Eq. (5.173) starts at $j = 1$, since $\phi = 0$ in R_o (a way of saying that no neutrons return from outside the reactor).

Equations (5.173) are the nodal representation of the nuclear equations for the present model. They constitute the time part of the space-time breakdown. The space part consists of finding the parameters p_{ij}, Σ_{ai}, Σ_{fi} in Eqs. (5.173). This is done by solving a static problem for the detailed flux distribution, denoted by ψ, for a nominal or average set of conditions. The p_{ij} are deduced from this distribution using the diffusion theory relation[17]

$$j^+ \text{ (in direction } \vec{N}) = \frac{\psi}{4} - \frac{D}{2} \vec{N} \cdot \nabla \psi \qquad \text{Eq. (5.175)}$$

so that

$$j_{ij}^+ = \frac{1}{4} \oint_{S_{ij}} \psi \, dS - \frac{1}{2} \oint_{S_{ij}} D \nabla \psi \cdot \vec{N}_i \, dS \, . \qquad \text{Eq. (5.176)}$$

From Eq. (5.172)

$$p_{ij} = \frac{1}{\psi_i} \left\{ \frac{1}{4} \oint_{S_{ij}} \psi \, dS - \frac{1}{2} \oint_{S_{ij}} D \nabla \psi \cdot \vec{N}_i \, dS \right\} \qquad \text{Eq. (5.177)}$$

and the Σ_{ai} and Σ_{fi} are calculated from Eqs. (5.167a) and (5.167b) with ψ replacing ϕ.

Thus, the procedure for this analysis is first to do a static calculation to obtain the function ψ. Then, at any instant, the temperatures and densities coming from the reactor-plant thermal-hydraulic equations are converted to nuclear constants D, Σ_a, $\nu\Sigma_f$. These are combined with the predetermined ψ through Eqs. (5.177) and (5.167b) to produce input to the nodal Eqs. (5.173). The output of these ϕ_i are the input to the reactor-plant

thermal-hydraulic equations, thus closing the loop. This can be represented schematically as follows:

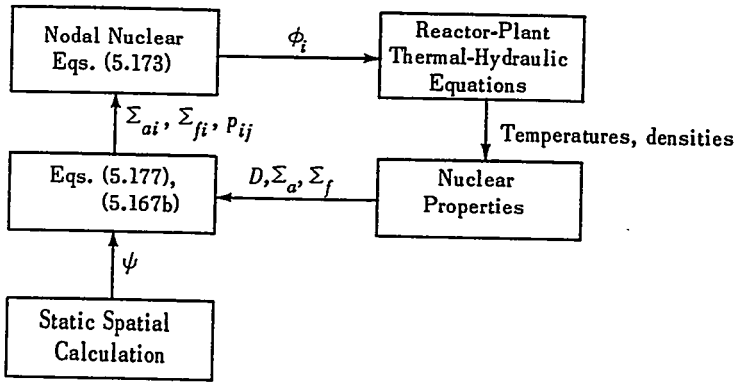

This nodal method is conceptually simple and has the attractive feature that the neutron equations are treated in the same way as the reactor-plant thermal-hydraulic equations. A numerical example illustrating the calculation of the coupling coefficients is given in Chap. 4, Sect. 4.4.C.

D. Modal Analysis

S. Kaplan

1. *Introduction*

The central idea of modal analysis is to approximate the unknown functions of space and time by a linear combination of known space functions with time-dependent coefficients.* There are two major steps in such an analysis: the selection of the space functions and, subsequently, the determination of the coefficients. There are a great many versions of modal analysis corresponding to different ways of handling these two steps.

In this discussion several versions will be described corresponding to different methods of choosing the space functions. Once functions are chosen, however, the coefficients of combination are found in the same way. The assumed form of solution is substituted into the governing differential equation, this equation is then multiplied through by other space functions,

*These space functions are referred to as modes, but this usage is not intended to imply that the space functions are necessarily eigenfunctions or vibration modes of any particular problem.

termed weighting functions, and the result is integrated over space and set equal to zero. This yields a set of ordinary differential equations which have the coefficients of combination as unknowns.

The substitute-integrate process can be motivated by variational principles,[54,55,56] and this motivation suggests that the weighting functions should be chosen to approximate the time-dependent adjoint flux. In principle, many other types of weighting functions may be used. Here, however, the adjoint type will be used exclusively.

For the sake of definiteness, consider a two-energy group model with one delayed precursor group:

$$\begin{pmatrix} \frac{1}{v_F} & 0 \\ 0 & \frac{1}{v_S} \end{pmatrix} \begin{pmatrix} \dot{\phi}_F \\ \dot{\phi}_S \end{pmatrix} + \begin{pmatrix} -\nabla \cdot D_F + \Sigma_F & 0 \\ -\Sigma_R & -\nabla \cdot D_S \nabla + \Sigma_S \end{pmatrix} \begin{pmatrix} \phi_F \\ \phi_S \end{pmatrix}$$

$$= +\Lambda \begin{pmatrix} C \\ 0 \end{pmatrix} + (1-\beta) \begin{pmatrix} \nu\Sigma_{fF} & \nu\Sigma_{fS} \\ 0 & 0 \end{pmatrix} \begin{pmatrix} \phi_F \\ \phi_S \end{pmatrix} \qquad \text{Eq. (5.178)}$$

$$\begin{pmatrix} \dot{C} \\ 0 \end{pmatrix} = \beta \begin{pmatrix} \nu\Sigma_{fF} & \nu\Sigma_{fS} \\ 0 & 0 \end{pmatrix} \begin{pmatrix} \phi_F \\ \phi_S \end{pmatrix} - \Lambda \begin{pmatrix} C \\ 0 \end{pmatrix} \qquad \text{Eq. (5.179)}$$

where the subscripts F and S indicate fast and slow group quantities. Denoting the square matrices, in order of appearance, by T, L, and M, and letting the flux and precursor column matrices be denoted by Φ and Γ, respectively, Eqs. (5.178) and (5.179) can be shortened to

$$T\dot{\Phi} + L\Phi = \Lambda\Gamma + (1-\beta)M\Phi \qquad \text{Eq. (5.180)}$$

$$\dot{\Gamma} = \beta M\Phi - \Lambda\Gamma \ . \qquad \text{Eq. (5.181)}$$

Here L and M are in general time-dependent. It is convenient to express these in terms of their steady-state or reference values, denoted by circumflexes:

$$L(t) = \hat{L} + L_1(t)$$

$$M(t) = \hat{M} + M_1(t) .$$

Then, Eqs. (5.180) and (5.181) become:

$$T\dot{\Phi} + \hat{L}\Phi - (1-\beta)\hat{M}\Phi - \Lambda\Gamma = -L_1\Phi + (1-\beta)M_1\Phi \qquad \text{Eq. (5.182)}$$

$$\dot{\Gamma} + \Lambda\Gamma - \beta\hat{M}\Phi = \beta M_1\Phi \ . \qquad \text{Eq. (5.183)}$$

2. Omega Modes

One possible attack on Eqs. (5.182) and (5.183) is to approximate the dependent variables by a series of base vectors ψ_n as follows:

$$\Phi(\vec{r},t) \cong \sum_{n=0}^{N} a_n(t)\psi_n(r) \qquad \text{Eq. (5.184)}$$

$$\Gamma(\vec{r},t) \cong \sum_{n=0}^{N} c_n(t)\hat{M}\psi_n(r) \ , \qquad \text{Eq. (5.185)}$$

where the ψ_n are the eigenvectors of the equation

$$\left[\hat{L} - \hat{M}\right]\psi_n = \omega_n T\psi_n \ . \qquad \text{Eq. (5.186)}$$

These ψ_n are referred to as omega modes. These eigenvectors, together with those of the adjoint equations,*

$$\left[\hat{L} - \hat{M}\right]^{\mathrm{T}}\psi_n^* = \omega_n T\psi_n^* \qquad \text{Eq. (5.187)}$$

have the biorthogonality property,

$$(\psi_m^*, T\psi_n) = 0 \qquad \omega_n \neq \omega_m \ . \qquad \text{Eq. (5.188)}$$

*It is shown in Ref. 57 that the set of eigenvalues (ω_n) of Eq. (5.186) is the same as the set of eigenvalues from the adjoint Eq. (5.187).

Ordinary differential equations relating the coefficients $a_n(t)$ and $c_n(t)$ are found by substituting the approximations [Eqs. (5.184) and (5.185)] into Eqs. (5.182) and (5.183), multiplying by the adjoint vectors, and integrating over the reactor. The result is

$$\dot{a}_n + \omega_n a_n + \beta \sum_k a_k M_{nk} - \Lambda \sum_k c_k M_{nk} = \frac{\left(\psi_n^*, \left(-L_1 + (1-\beta) M_1\right)\Phi\right)}{\left(\psi_n^*, T\psi_n\right)}$$

Eq. (5.189)

$$\sum_k \left(\dot{c}_k + \Lambda c_k - \beta a_k\right) M_{nk} = \beta \left(\psi_n^*, M_1 \Phi\right) \qquad \text{Eq. (5.190)}$$

where

$$M_{nk} = \frac{\left(\psi_n^*, \hat{M}\psi_k\right)}{\left(\psi_n^*, T\psi_n\right)}.$$

If one now makes the perturbation theory approximation of replacing Φ by the reference value $\hat{\Phi}$ in the terms on the right side of Eqs. (5.189) and (5.190), then these terms become known quantities. Equations (5.189) and (5.190) are then inhomogeneous equations. The exponentials appearing in the solution are characteristic of the unperturbed reactor. Alternatively, if the perturbation approximation is not made, the representations of Eqs. (5.184) and (5.185) may be substituted on the right side of Eqs. (5.189) and (5.190), yielding a set of homogeneous equations whose solution contains exponentials which are characteristic of the perturbed reactor.

Note that in Eqs. (5.189) and (5.190) the equations for any given n value are coupled to those for all other values by the M_{nk} terms.

3. *Lambda Modes*

Another possible set of base vectors[58] are the eigenvectors of:

$$\hat{L}\psi_n = \frac{1}{\lambda_n} \hat{M}\psi_n \qquad \text{Eq. (5.191)}$$

which are referred to as lambda modes. These, together with the eigenvectors of the adjoint equation,

$$\hat{L}^T \psi_n^* = \frac{1}{\lambda_n} \hat{M}^T \psi_n^* \qquad \text{Eq. (5.192)}$$

have the biorthogonality property,

$$\left(\psi_m^*, \hat{M}\psi_n\right) = 0, \ \lambda_n = \lambda_m \ .^* \qquad \text{Eq. (5.193)}$$

The approximate solution again has the form of Eqs. (5.184), (5.185), and the coefficients $a_n(t)$ and $c_n(t)$ are found by the same substitution-integration procedure as before:

$$\sum_{n=0}^{N} \dot{a}_n T_{kn} + a_k \left[\frac{1}{\lambda_k} - (1-\beta)\right] - \Lambda c_k = \frac{\left[\psi_k^*, \left(-L_1 + (1-\beta)M_1\right)\Phi\right]}{\left(\psi_k^*, \hat{M}\psi_k\right)} \qquad \text{Eq. (5.194)}$$

$$\dot{c}_k + \Lambda c_k - \beta a_k = \frac{\beta\left(\psi_k^*, M_1 \Phi\right)}{\left(\psi_k^*, \hat{M}\psi_k\right)} \qquad \text{Eq. (5.195)}$$

where

$$T_{kn} = \frac{\left(\psi_k^*, T\psi_n\right)}{\left(\psi_k^*, \hat{M}\psi_k\right)} \qquad \text{Eq. (5.196)}$$

Referring back to Eq. (5.186) one sees that the omega modes may be interpreted as the natural modes of the unperturbed reactor with no delayed neutrons. Similarly, the lambda modes may be interpreted as natural modes of the reactor with delayed neutrons. To see this, let $\Phi = \Phi e^{\omega t}$ and $\Gamma = \Gamma e^{\omega t}$ in Eqs. (5.168) and (5.169). Then, from Eq. (5.169),

$$\Lambda\Gamma = \frac{\Lambda}{\Lambda + \omega} \beta M \Phi \qquad \text{Eq. (5.196a)}$$

and substituting this in Eq. (5.168) yields

$$\hat{L}\Phi - \left(1 - \frac{\beta\omega}{\Lambda + \omega}\right)\hat{M}\Phi + \omega T \Phi = 0 \ . \qquad \text{Eq. (5.196b)}$$

*Again, the equivalence of the spectra of Eqs. (5.191) and (5.192) may be shown to follow from the result of Ref. 57.

The ω eigenvalues of Eq. (5.196b) can be divided into two types: (1) those having large values associated with prompt neutron lifetimes and (2) those of small magnitude associated with delayed neutrons. For the small magnitude roots the term $\omega T \Phi$ in Eq. (5.196b) is negligible, so that by the identification

$$\frac{1}{\lambda_n} = \left(1 - \frac{\beta\omega}{\Lambda + \omega}\right)$$

these modes are seen to be the same as the lambda modes.

4. Other Types of Modes

The two modal analyses just described use eigenfunctions of the unperturbed problem as the basis functions. Another interesting possibility is to use eigenfunctions of the perturbed problem. For example, suppose that the operators $L(t)$ and $M(t)$ vary monotonically from their time zero values $\hat{L}$, $\hat{M}$ to final values L_f, M_f. One might expect that the flux during the transient could be well approximated by a linear combination of the flux shapes corresponding to the initial and final operators. Similarly, the transient precursor concentrations could be approximated by a linear combination of the initial and final shapes. Symbolically, one assumes

$$\Phi(\vec{r}, t) = \hat{a}(t)\hat{\Phi}(\vec{r}) + a_f(t)\Phi_f(\vec{r}) \qquad \text{Eq. (5.197)}$$

$$\Gamma(\vec{r}, t) = \hat{c}(t)\hat{\Gamma}(\vec{r}) + c_f(t)\Gamma_f(\vec{r}) \qquad \text{Eq. (5.198)}$$

where

$$\left[\hat{L} - (1-\beta)\hat{M}\right]\Phi - \Lambda\hat{\Gamma} = -\hat{\omega}T\Phi \qquad \text{Eq. (5.199)}$$

$$-\beta\hat{M}\hat{\Phi} + \Lambda\hat{\Gamma} = -\hat{\omega}\hat{\Gamma} \qquad \text{Eq. (5.200)}$$

$$\left[L_f - (1-\beta)M_f\right]\Phi_f - \Lambda\Gamma_f = \omega_f\Gamma\Phi_f \qquad \text{Eq. (5.201)}$$

$$-\beta M_f\Phi_f + \Lambda\Gamma_f = \omega_f\Gamma_f \qquad \text{Eq. (5.202)}$$

and $\hat{\omega}$ and ω_f denote the most positive eigenvalues, respectively, of the problems in Eqs. (5.199) to (5.200) and Eqs. (5.201) to (5.202).

Using the substitution-integration procedure, one now obtains the following set of ordinary differential equations:

$$\begin{bmatrix} (\hat{\Phi}^*, \mathfrak{L}\hat{\Phi}) & (\hat{\Phi}^*, \mathfrak{L}\Phi_f) & \Lambda(\hat{\Phi}^*, \hat{\Gamma}) & \Lambda(\hat{\Phi}^*, \hat{\Gamma}_f) \\ (\Phi_f^*, \mathfrak{L}\hat{\Phi}) & (\Phi_f^*, \mathfrak{L}\Phi_f) & \Lambda(\Phi_f^*, \hat{\Gamma}) & \Lambda(\hat{\Phi}^*, \hat{\Gamma}_f) \\ \beta(\hat{\Gamma}^*, M\hat{\Phi}) & \beta(\hat{\Gamma}^*, M\Phi_f) & -\Lambda(\hat{\Gamma}^*, \hat{\Gamma}) & -\Lambda(\hat{\Gamma}^*, \Gamma_f) \\ \beta(\Gamma_f^*, M\hat{\Phi}) & \beta(\Gamma_f^*, M\Phi_f) & -\Lambda(\Gamma_f^*, \hat{\Gamma}) & -\Lambda(\Gamma_f^*, \Gamma_f) \end{bmatrix} \begin{bmatrix} \hat{a}(t) \\ a_f(t) \\ \hat{c}(t) \\ c_f(t) \end{bmatrix}$$

$$= \begin{bmatrix} (\hat{\Phi}^*, T\hat{\Phi}) & (\hat{\Phi}^*, T\Phi_f) & 0 & 0 \\ (\Phi_f^*, T\hat{\Phi}) & (\Phi^*, T\Phi_f) & 0 & 0 \\ 0 & 0 & (\hat{\Gamma}^*, \hat{\Gamma}) & (\hat{\Gamma}^*, \hat{\Gamma}_f) \\ 0 & 0 & (\Gamma_f^*, \hat{\Gamma}) & (\Gamma_f^*, \Gamma_f) \end{bmatrix} \begin{bmatrix} \dot{\hat{a}}(t) \\ \dot{a}_f(t) \\ \dot{\hat{c}}(t) \\ \dot{c}_f(t) \end{bmatrix} \qquad \text{Eq. (5.203)}$$

where the abbreviation

$$\mathfrak{L}(t) = -L(t) + (1-\beta)M(t) \qquad \text{Eq. (5.204)}$$

has been used.

Another interesting type of mode has been suggested by Dougherty and Shen.[55] To obtain these modes, one divides the reactor into regions and sets the fission cross section everywhere equal to zero. One then inserts a distributed fission source, obtained from the unperturbed source distribution, into one of these regions and solves for the resulting flux shape. This process is repeated for each region, thus generating a set of spatial shapes which Dougherty and Shen refer to as "Green's function modes." The use of this type of mode can be motivated by casting Eqs. (5.168) and (5.169) into an integral form.

While numerical experience with the four types of modes just described is not extensive, all have been used successfully in limited cases. From their physical interpretations, one might expect that the lambda modes would yield somewhat better results than the omega modes. Also the lambda modes are easier to calculate with existing codes than are the omega

modes. For the third and fourth types of expansion, the modes are not only easy to find, but they have the attractive feature that they can be tailored to the particular problem at hand.

5. An Example

To illustrate the application of modal analysis more concretely and in more detail, consider as a final example[59] a modal analysis of an initially uniform bare reactor using the eigenfunctions of the Helmholtz equation

$$\left[\nabla^2 + B_{gn}^2\right]\psi_n = 0$$

in the reactor geometry where B_{gn}^2 is the geometric buckling of the n^{th} mode. Since these ψ_n are scalar functions, one writes the expansions in the form

$$\Phi(\vec{r},t) = \begin{pmatrix} \phi_F \\ \\ \phi_S \end{pmatrix} = \sum_n \begin{pmatrix} a_n(t) \\ \\ b_n(t) \end{pmatrix} \psi_n(\vec{r}) \equiv \sum_n A_n(t)\psi_n(\vec{r}) \qquad \text{Eq. (5.205)}$$

$$\Gamma(\vec{r},t) = \begin{pmatrix} C \\ \\ 0 \end{pmatrix} = \sum_n \begin{pmatrix} c_n(t) \\ \\ 0 \end{pmatrix} \psi_n(\vec{r}) \equiv \sum_n \xi_n(t)\psi_n(\vec{r}) \,. \qquad \text{Eq. (5.206)}$$

The coefficient vectors are given in terms of the unknowns by

$$A_n(t) = \int_{\text{core}} \psi_n \Phi \, dV$$

$$\xi_n(t) = \int_{\text{core}} \psi_n \Gamma \, dV \,. \qquad \text{Eq. (5.207)}$$

It now remains to find the coefficient vectors $A_n(t)$ and $\xi_n(t)$ in terms of known quantities. To do this, multiply Eqs. (5.182) and (5.183) by ψ_n and integrate over the reactor. One needs the identities:

$$\int \psi_n T\dot{\Phi} \, dV = T\int \psi_n \dot{\Phi} \, dV = T\dot{A}_n \qquad \text{Eq. (5.208)}$$

$$\int \psi_n \hat{M}\Phi \, dV = \hat{M}\int \psi_n \Phi \, dV = \hat{M} A_n \qquad \text{Eq. (5.209)}$$

since for a uniform bare reactor the unperturbed operator $\hat{M}$ is not a function of position; and lastly,

$$\int \psi_n \hat{L} \Phi_1 \, dV = \hat{L}_n' A_n \qquad \text{Eq. (5.210)}$$

where $\hat{L}_n'$ is the matrix

$$\begin{pmatrix} \hat{D}_F B_{gn}^n = \hat{\Sigma}_F & 0 \\ -\hat{\Sigma}_R & \hat{D}_S B_{gn}^2 = \hat{\Sigma}_S \end{pmatrix} .$$

Carrying out this procedure and making the perturbation approximation yields for the coefficient vectors:

$$T\dot{A}_n = \hat{L}_n' A_n - (1-\beta)\hat{M} A_n - \Lambda \xi_n = \int \psi_n \left[-L_1 + (1-\beta) M_1 \right] \hat{\Phi} \, dV$$

Eq. (5.211)

$$\dot{\xi}_n - \beta \hat{M} A_n + \Lambda \xi_n = \beta \int \psi_n M_1 \hat{\Phi} \, dV \; . \qquad \text{Eq. (5.212)}$$

Equations (5.211) and (5.212) are a set of ordinary differential equations. For any given perturbation (L_1, M_1) they can be solved for the A_n and ξ_n. To first order then, the final solution is:

$$\Phi(\vec{r}, t) = \Phi(\vec{r}) + \sum_n A_n(t) \psi_n(\vec{r})$$

$$\Gamma(\vec{r}, t) = \hat{\Gamma}(\vec{r}) + \sum_n \xi_n(t) \psi_n(\vec{r}) \; . \qquad \text{Eq. (5.213)}$$

A) ASYMPTOTIC RESULTS. It is of some interest to combine Eqs. (5.211) and (5.212) and to examine the asymptotic values. Combining,

$$T\dot{A}_n + \sum_{j=1}^{6} \dot{\xi}_{jn} + \hat{L}_n' A_n - \hat{M} A_n = \int \psi_n \left[-L_1 + M_1 \right] \hat{\Phi} \, dV \; .$$

Eq. (5.214)

For the asymptotic result, set the time derivatives equal to zero, giving

$$\left[\hat{L}_n' - \hat{M} \right] A_{n\infty} = \int \psi_n \left[-L_1 + M_1 \right] \hat{\Phi} \, dV \equiv \begin{pmatrix} P_{nF} \\ P_{nS} \end{pmatrix} \qquad \text{Eq. (5.215)}$$

where it has been assumed that the integral of the perturbations is not a function of time. If the determinant of $\left[\hat{L}_n' - \hat{M}\right]$ does not vanish, Eq. (5.215) may be solved by Cramer's rule:

$$a_{n\infty} = \frac{P_{nF}\left[\hat{D}_S B_{gn}^2 + \hat{\Sigma}_S\right] + \nu\hat{\Sigma}_{fS} P_{nS}}{\left|\hat{L}_n' - \hat{M}\right|}$$

$$b_{n\infty} = \frac{P_{nS}\left[\hat{D}_F B_{gn}^2 + \Sigma_{FF} - \hat{\nu}\Sigma_{fF}\right] + \hat{\Sigma}_R P_{nF}}{\left|\hat{L}_n' - \hat{M}\right|} \quad \text{Eq. (5.216)}$$

These may be simplified by using the notation

$$\left[\hat{S}_n\right] \equiv \left[\hat{D}_S B_{gn}^2 + \hat{\Sigma}_S\right]$$
$$\left[\hat{F}_n\right] \equiv \left[\hat{D}_F B_{gn}^2 + \hat{\Sigma}_F\right]$$

and noting that the denominator determinants

$$\left|\hat{L}_n' - \hat{M}\right| = \left[\hat{S}_n\right]\left\{\left[\hat{F}_n\right] - \nu\hat{\Sigma}_{fF}\right\} - \hat{\Sigma}_R \nu\hat{\Sigma}_{fS}$$

$$= \left[\hat{S}_n\right]\left[\hat{F}_n\right]\left\{1 - \left[\frac{\nu\hat{\Sigma}_{fF}}{\left[\hat{F}_n\right]} + \frac{\hat{\Sigma}_R \nu\hat{\Sigma}_{fS}}{\left[\hat{S}_n\right]\left[\hat{F}_n\right]}\right]\right\} \quad \text{Eq. (5.217)}$$

are expressible in terms of the eigenvalue of the n^{th} mode of the steady-state equation,

$$\hat{L}\psi_n = \frac{1}{\lambda_n}\hat{M}\psi_n \ .$$

In the present uniform bare geometry these eigenvalues are

$$\lambda_n = \nu\left\{\frac{\hat{\Sigma}_{fF}}{\left[\hat{F}_n\right]} + \frac{\hat{\Sigma}_R\hat{\Sigma}_{fS}}{\left[\hat{S}_n\right]\left[\hat{F}_n\right]}\right\} \quad \text{Eq. (5.218)}$$

so that Eq. (5.217) becomes

$$\left|\hat{L}_n' - \hat{M}\right| = \left[\hat{S}_n\right]\left[\hat{F}_n\right]\left\{\frac{\lambda_o - \lambda_n}{\lambda_o}\right\} . \qquad \text{Eq. (5.219)}$$

Then from Eq. (5.216)

$$a_{n\infty} = \frac{\lambda_o}{\lambda_o - \lambda_n}\frac{1}{\left[\hat{F}_n\right]\left[\hat{S}_n\right]}\left\{P_{nF}\left[\hat{S}_n\right] + \nu\hat{\Sigma}_{fS}P_{nS}\right\}$$

$$b_{n\infty} = \frac{\lambda_o}{\lambda_o - \lambda_n}\frac{1}{\left[\hat{F}_n\right]\left[\hat{S}_n\right]}\left\{P_{nF}\hat{\Sigma}_R + P_{nS}\left(\left[\hat{F}_n\right] - \nu\hat{\Sigma}_{fF}\right)\right\}$$

Eq. (5.220)

which shows that the asymptotic amplitude of any mode is inversely proportional to the eigenvalue difference, $\lambda_o - \lambda_n$, for that mode.

B) NUMERICAL EXAMPLE. Solutions to Eqs. (5.211) and (5.212) for the first overtone, $n = 1$, have been obtained by an electrical analog for three special cases. These cases are for bare uniform ring reactors (Fig. 5.29) in which an antisymmetric step temperature change has been made.

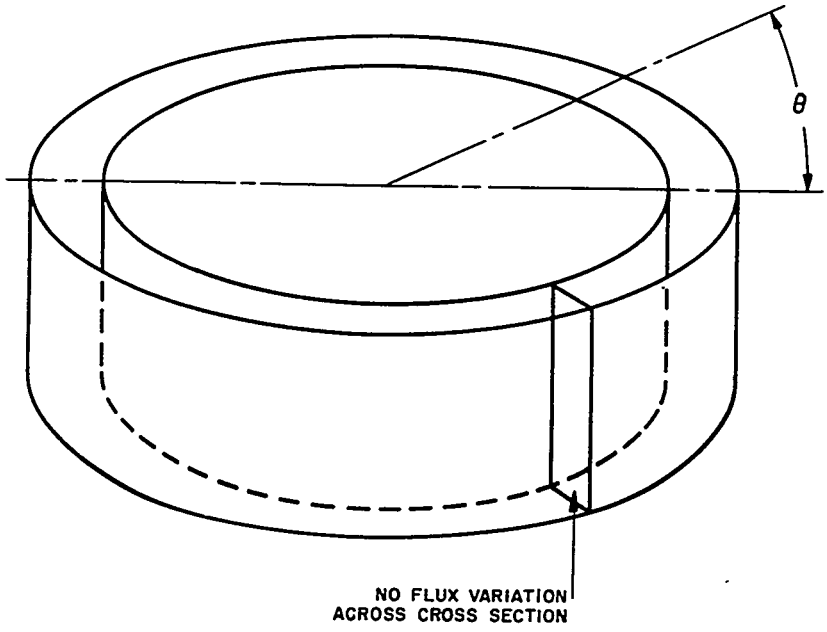

FIGURE 5.29. Uniform Ring Model.

Results are shown in Fig. 5.30 for three ring reactors having different eigenvalue differences between fundamental and first overtone modes. The values of the first mode coefficient in the flux expansion have been interpreted in terms of the power tilt peaking factor that would result if all higher mode contributions were negligible. This is used as the ordinate in Fig. 5.30. This figure also shows, for comparison, the time behavior of the peaking factor that would be predicted by a model using only one group of delayed neutron precursors.

It is seen in Fig. 5.30 that part of the tilt takes place in the order of prompt neutron lifetimes and part in the order of delayed neutron lifetimes. This behavior may be understood physically by thinking of the perturbed reactor as being subcritical and containing a distributed delayed neutron source.

E. Modal Analyses of Xenon Stability

S. Kaplan

Reactivity feedback through xenon concentration can cause oscillations of the spatial flux shape in the same way that it can cause oscillations of the overall flux level. Physically, imagine that a small reactivity unbalance has caused a flux tilt. On the side where the flux is high the xenon burnup rate will

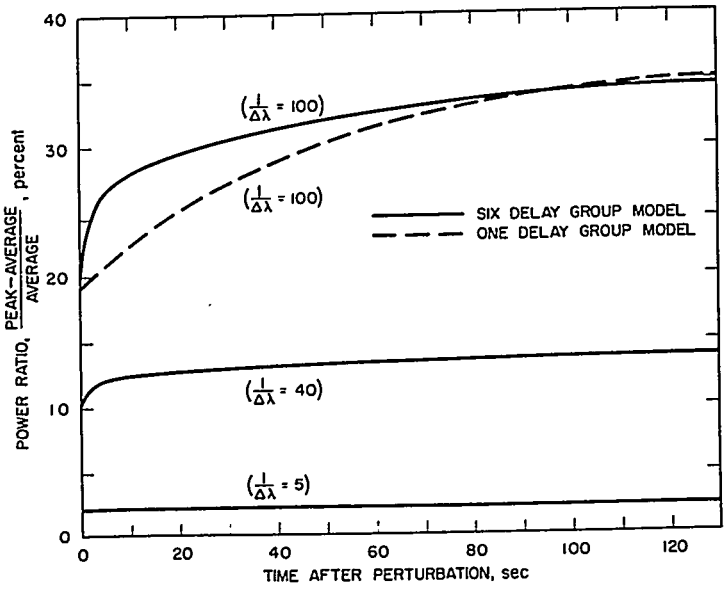

FIGURE 5.30. Transient Flux Tilt in Annular Core Caused by Step Temperature Unbalance (490°F to 510°F).

be higher, causing a diminished xenon concentration and, thus, worsening the original reactivity unbalance. Like the flux level oscillations, the spatial oscillations have characteristically long periods and, therefore, there is ample time for the reactor operator to take corrective action. However, to counteract a spatial oscillation, it is necessary to provide instrumentation all around the core to detect the oscillation; secondly, the reactor control system must be designed to allow rods on different sides of the core to move independently. Thus, it is desirable to design the reactor to be inherently stable against such oscillations.

The phenomenon of xenon spatial instability was first analyzed using a modal method by Ward[60] and a nodal method by Henry and Germann.[51] The modal method has been pursued by Randall and St. John,[61] Wick,[52] Stewart,[62] Harris and Lacy,[63] and Mochizuki and Takeda.[64] The nodal method has been extended also by Wick.[52] In the present section several treatments of the problem are presented from the modal analysis point of view. These treatments have been influenced strongly by the work of the preceding authors, particularly by that of Ward and Stewart.

The equations governing xenon oscillations are nonlinear. However, within a small neighborhood of the equilibrium point a linear approximation may be used. The first three topics discuss treatments which use the linear approximation. Of these three, the first two, which are designated the p and μ mode treatments, are concerned with determining the time behavior of individual modes of oscillation through calculation of the associated frequencies and damping factors. On the other hand the treatment of the λ–modes, using the Nyquist criterion, considers the question of whether any unstable modes exist without examining the modes individually.

These discussions are followed by an examination of the effects of nonlinearity on the transient flux. In a uniform ring geometry it is found that nonlinearity limits the amplitude of the spatial oscillations and causes a precession effect in which the position of peak flux rotates around the ring.

Before describing the analyses it may be worthwhile to discuss the meaning of stability as used here, since there are several kinds of stability, and usage is not completely uniform in the literature. Discussion will deal with equations of the form

$$\frac{d}{dt}\,\delta y = \text{linear terms in } \delta y + \text{higher order terms in } \delta y \qquad \text{Eq. (5.221)}$$

where δy represents the deviation of a system from a steady-state operating point. This operating point will be called stable

if, given an initial nonzero δ_γ one has that $\lim_{t\to\infty} \delta\gamma = 0$. Thus, this usage is in the sense of asymptotic stability rather than orbital or limit cycle type stability. According to Liapunov's theorem on stability,[65] if the higher order terms in Eq. (5.221) become negligible as $\delta_\gamma \to 0$ then these terms may be omitted in Eq. (5.221) and the stability tests applied to the remaining linear system.

1. Natural or p-Modes

For algebraic simplicity, consider the case of two neutron energy groups, one delay precursor group, and no fast xenon capture. In this model the governing equations are:

1. Iodine balance:

$$\dot{I} = -\lambda_I I + \gamma_I \left[\Sigma_{fS}\phi_S + \Sigma_{fF}\phi_F\right] . \qquad \text{Eq. (5.222)}$$

2. Xenon balance:

$$\dot{X} = \lambda_I I - \lambda_X X + \gamma_X \left[\Sigma_{fF}\phi_F + \Sigma_{fS}\phi_S\right] - \sigma_X X \phi_S . \qquad \text{Eq. (5.223)}$$

3. Fast flux balance:

$$\dot{\phi}_F = v_F \nabla \cdot D_F \nabla \phi_F - v_F \Sigma_F \phi_F + v_F(1-\beta)\left[\nu\Sigma_{fF}\phi_F + \nu\Sigma_{fS}\phi_S\right] + v_F \lambda C . \qquad \text{Eq. (5.224)}$$

4. Slow flux balance:

$$\dot{\phi}_S = v_S \nabla \cdot D_S \nabla \phi_S - v_S \Sigma_S \phi_S - v_S \sigma_X X \phi_S + v_S \Sigma_R \phi_F . \qquad \text{Eq. (5.225)}$$

5. Precursor balance:

$$\dot{C} = -\lambda C + \beta\left[\nu\Sigma_{fS}\phi_S + \nu\Sigma_{fF}\phi_F\right] . \qquad \text{Eq. (5.226)}$$

Along with these equations, one has as boundary conditions that I, X, ϕ_F, ϕ_S, and C vanish on the surface of the reactor.

It is assumed that at time zero the reactor is just critical, and quantities evaluated at that time are indicated by the circumflex. Now, to shorten the writing, define the matrices:

$$\Phi \equiv \begin{pmatrix} I \\ X \\ \phi_F \\ \phi_S \\ C \end{pmatrix} \qquad \text{Eq. (5.227)}$$

$$\mathfrak{L} \equiv \begin{pmatrix} -\lambda_I & 0 & \gamma_I \Sigma_{fF} & \gamma_I \Sigma_{fS} & 0 \\ \lambda_I & -\lambda_X & \gamma_X \Sigma_{fF} & \gamma_X \Sigma_{fS} & 0 \\ 0 & 0 & v_F\left[\nabla \cdot D_F \nabla - \Sigma_F + (1-\beta)\nu\Sigma_{fF}\right] & v_F\left[1-\beta\right]\nu\Sigma_{fS} & v_F \lambda \\ 0 & 0 & v_S \Sigma_R & v_S\left[\nabla \cdot D_S \nabla - \Sigma_S\right] & 0 \\ 0 & 0 & \beta\nu\Sigma_{fF} & \beta\nu\Sigma_{fS} & -\lambda \end{pmatrix}$$

Eq. (5.228)

$$H \equiv \begin{pmatrix} 0 & 0 & 0 & 0 & 0 \\ 0 & 0 & 0 & -\sigma_X & 0 \\ 0 & 0 & 0 & 0 & 0 \\ 0 & 0 & 0 & -\sigma_X v_S & 0 \\ 0 & 0 & 0 & 0 & 0 \end{pmatrix}$$

Eq. (5.229)

With this notation, Eqs. (5.222) to (5.226) become

$$\dot{\Phi} = \mathfrak{L}\Phi + XH\Phi \ . \qquad \text{Eq. (5.230)}$$

The corresponding steady-state equation is

$$0 = \hat{\mathfrak{L}}\hat{\Phi} + \hat{X}\hat{H}\hat{\Phi} \ . \qquad \text{Eq. (5.231)}$$

Expressing the operator $\mathfrak{L}$ and the dependent variables as sums of steady-state and perturbed parts,

$$\mathfrak{L} = \hat{\mathfrak{L}} + \delta\mathfrak{L}, \quad \Phi = \hat{\Phi} + \delta\Phi, \quad X = \hat{I} + \delta X \ . \qquad \text{Eq. (5.232)}$$

Equation (5.230) becomes

$$\dot{\Phi} = \left[\hat{\mathfrak{L}} + \delta\mathfrak{L}\right]\left[\hat{\Phi} + \delta\hat{\Phi}\right] + \left[\hat{X} + \delta X\right]\hat{H}\left[\hat{\Phi} + \delta\Phi\right] \qquad \text{Eq. (5.233)}$$

and subtracting the steady-state part

$$\delta\dot{\Phi} = \left[\hat{\mathfrak{L}} + \hat{X}\hat{H}\right]\delta\Phi + \hat{H}\hat{\Phi}\,\delta X + \delta\mathfrak{L}\hat{\Phi} + \delta X\hat{H}\,\delta\Phi + \delta\mathfrak{L}\,\delta\Phi. \qquad \text{Eq. (5.234)}$$

Now, rearranging, one has

$$\hat{H}\hat{\Phi}\,\delta X = \hat{\phi}_S \hat{H}'\,\delta\Phi \qquad \text{Eq. (5.235)}$$

where

$$\hat{H}' \equiv \begin{pmatrix} 0 & 0 & 0 & 0 & 0 \\ 0 & -\sigma_X & 0 & 0 & 0 \\ 0 & 0 & 0 & 0 & 0 \\ 0 & -\sigma_X \nu_S & 0 & 0 & 0 \\ 0 & 0 & 0 & 0 & 0 \end{pmatrix} \qquad \text{Eq. (5.236)}$$

Defining the operator $\hat{\mathfrak{L}}'$,

$$\hat{\mathfrak{L}}' \equiv \hat{\mathfrak{L}} + \hat{X}\hat{H} + \hat{\phi}_S \hat{H}' \ . \qquad \text{Eq. (5.237)}$$

Equation (5.234) becomes

$$\delta\dot{\Phi} = \hat{\mathfrak{L}}'\,\delta\Phi + \delta\mathfrak{L}\hat{\Phi} + \left[\delta\mathfrak{L} + \delta X \hat{H}\right]\delta\Phi \qquad \text{Eq. (5.238)}$$

where the last term on the right is the nonlinear (and second order for small perturbations) term.

Let Ψ_n represent the eigenvectors (which will be called the p-modes) and p_n the eigenvalues of the operator $\hat{\mathfrak{L}}'$ (assuming they exist). Then,

$$\hat{\mathfrak{L}}'\Psi_n = p_n \Psi_n \ . \qquad \text{Eq. (5.239)}$$

Similarly, let Ψ_n^* and p_n^* represent the eigenvectors and eigenvalues of the transpose of $\hat{\mathfrak{L}}'$. Then,

$$\hat{\mathfrak{L}}'^T\Psi_n^* = p_n^* \Psi_n^* \ . \qquad \text{Eq. (5.240)}$$

Now, suppose one conjectures that the Ψ_n form a complete set. Then it follows that the set of eigenvalues $\{p_n\}$ is the same as the set $\{p_n^*\}$, and one may then expand $\delta\Phi$:

$$\delta\Phi(\vec{r}, t) = \Sigma a_n(t)\Psi_n(\vec{r}) \qquad \text{Eq. (5.241)}$$

where, in view of the biorthogonality, the expansion coefficients are given explicitly in terms of the unknown $\delta\Phi$ by

$$a_n(\Psi_n^*, \Psi_n) = (\Psi_n^*, \delta\Phi) \ . \qquad \text{Eq. (5.242)}$$

One may find equations determining a_n from the implicit definition of $\delta\Phi$, Eq. (5.238), by taking the inner product of both sides of that equation with Ψ_n^*:

$$\left(\Psi_n^*, \Psi_n\right)\dot{a}_n = \left(\Psi_n^*, \hat{\mathfrak{L}}'\delta\Phi\right) + \left(\Psi_n^*, \delta\mathfrak{L}\hat{\Phi}\right) + \left(\Psi_n^*, \left[\delta\mathfrak{L} + \delta X\hat{H}\right]\delta\Phi\right) \ . \qquad \text{Eq. (5.243)}$$

Now,

$$\left(\Psi_n^*, \hat{\mathfrak{L}}'\delta\Phi\right) = \left(\delta\Phi, \hat{\mathfrak{L}}'^{T}\Psi_n^*\right) = p_n\left(\Psi_n^*, \delta\Phi\right) \ . \qquad \text{Eq. (5.244)}$$

Defining the first-order driving term, R_n,

$$R_n \equiv \left(\Psi_n^*, \delta\mathfrak{L}\hat{\Phi}\right)\left(\Psi_n^*, \Psi_n\right)^{-1} \qquad \text{Eq. (5.245)}$$

Equation (5.243) becomes in the linear approximation,

$$\dot{a}_n = p_n a_n + R_n \ . \qquad \text{Eq. (5.246)}$$

Solving this,

$$a_n(t) = e^{p_n t}\int_o^t e^{-p_n \tau} R_n(\tau)\, d\tau + e^{p_n t} a_n(0) \ . \qquad \text{Eq. (5.247)}$$

This equation gives the time dependence of the expansion coefficients. Note that in the linear model there is finality [66, 67] in the determination of the coefficients, i.e., each coefficient is independent of the others and of the number of modes retained in the expansion.

For the case where R_n, and hence $\delta\mathfrak{L}$, is not a function of time,

$$a_n(t) = \frac{-R_n}{p_n}\left[1 - e^{p_n t}\right] + e^{p_n t} a_n(0) \ . \qquad \text{Eq. (5.248)}$$

Since the term $<\delta X H \delta\Phi>$ in Eq. (5.243) is negligible as $\delta\phi \to 0$ for the case of time-independent $\delta\mathfrak{L}$, it is justified to infer a stability criterion from the linear approximation. To do this, return to Eq. (5.239) and note that in general the eigenvalues and eigenvectors are complex. However if, say, p_j and Ψ_j are complex, then since $\hat{\mathfrak{L}}'$ is real there exists another eigenvalue, call it $p_{\bar{j}}$, and corresponding eigenvector, $\Psi_{\bar{j}}$, which are the complex conjugates of p_j and Ψ_j, respectively. The same is true for the adjoints. Therefore, from Eq. (5.242), if a_j is complex then $a_{\bar{j}}$ is its conjugate. Thus, in the series [Eq. (5.241)] complex terms appear in conjugate pairs, so that for every complex p_n, $\delta\Phi$ will have a component equal to the real part of $a_n \Psi_n$. From Eq. (5.248) one sees that this component of $\delta\Phi$ will oscillate with period related to the imaginary part of p_n and will diverge or converge according to whether the real part is positive or negative. Therefore, the condition for stability in a given mode is that the eigenvalue of that mode have a negative real part.

In arriving at this stability criterion, it was required that $\delta\mathfrak{L}$ not be a function of time. This is equivalent to requiring that there be no temperature feedback. If temperature feedback is present it can, in principle, be treated by linearizing, i.e., by replacing $\delta\mathfrak{L}\,\hat{\Phi}$ by $\delta\mathfrak{L}'\delta\Phi$, where $\delta\mathfrak{L}'$ is constant, and then adding $\delta\mathfrak{L}'$ to $\hat{\mathfrak{L}}'$ to form a new p-mode operator, $\hat{\mathfrak{L}}' + \delta\mathfrak{L}'$. The eigenvalues of this new operator indicate whether or not a given mode is stable with temperature feedback present.

In requiring $\delta\mathfrak{L}$ to be constant in Eq. (5.248), one has also in effect required that there be no feedback via any control mechanism. Without control or temperature feedback, however, the fundamental mode is unstable (see Sect. 5.3), and in this circumstance the question of higher mode stability is not too interesting. The question arises: If the reactor is kept critical at all times by a control device, does this alter the conclusion that higher mode stability is determined by the real part of the eigenvalue? To answer this question in any given case one must know the exact nature of the control device. However, the following observation may be made in general. In Eq. (5.245), let $\delta\mathfrak{L}$ now represent the change in the $\mathfrak{L}$ operator due to action of the control device. Suppose one is interested in the stability of a mode for which Ψ_n^* is antisymmetric as a function of space. Suppose further that $\hat{\Phi}$ is symmetric and that $\delta\mathfrak{L}$ is such that $<\Psi_n^*, \delta\mathfrak{L}\,\hat{\Phi}> = 0$ (for example if $\delta\mathfrak{L}$ represents a uniform control poison). Then the term containing $\delta\mathfrak{L}$ vanishes from Eq. (5.247) for this mode and the presence of this type of control does not alter the previously derived stability criterion.

In connection with the conjecture of completeness of the p-modes, it may be shown at least in one very simple reactor

geometry (the uniform ring) that they do indeed form a complete set in the sense that an arbitrary five-element column vector may be expanded in a series of p-modes, with the series converging in the mean. A second useful fact which can be demonstrated on the uniform ring is that if the $\hat{\mathfrak{L}}'$ operator in Eq. (5.239) be modified by omitting those terms resulting from the $\dot{\phi}_F$ and $\dot{\phi}_S$ terms and from the delayed neutrons, then this omission has negligible effect upon the calculation of those p-eigenvalues which reflect the long term xenon transients. Intuitively, one would expect this same conclusion to hold also for reactors of more complicated geometry. Therefore, making these omissions, the stability criterion becomes that the eigenvalues, p_n, of the equation

$$0 = \begin{bmatrix} -\lambda_I - p_n & 0 & \gamma_I \Sigma_{fF} & \gamma_I \Sigma_{fS} \\ \lambda_I & -\lambda_X - \hat{\phi}_S \sigma_X - p_n & \gamma_X \Sigma_{fF} & \gamma_X \Sigma_{fS} - \sigma_X \hat{X} \\ 0 & 0 & \nabla \cdot D_F \nabla - \Sigma_F - \nu\Sigma_{fF} & \nu\Sigma_{fS} \\ 0 & -\hat{\phi}_S \sigma_X & \Sigma_R & \nabla \cdot D_S \nabla - \Sigma_S - \sigma_X \hat{X} \end{bmatrix} \begin{bmatrix} I_n \\ X_n \\ \phi_{Fn} \\ \phi_{Sn} \end{bmatrix} \quad \text{(Eq. 5.249)}$$

have negative real parts. From a practical standpoint, the xenon spatial stability analysis requires the calculation of the overtone eigenvalue with the largest (most positive) real part. This eigenvalue is complex in cases of interest, i.e., in cores which are neither very stable nor very unstable.

A digital computer code called XEP has been prepared which may be used to find the complex eigenvalues and corresponding eigenvectors of Eq. (5.249) for slab geometry. It uses the Wielandt iteration scheme described in Chap. 7 and, thus, requires as input an estimate of the eigenvalue sought. All numerical operations in XEP employ complex arithmetic. A brief description of the code is included in Chap. 7.

To discuss the location in the complex plane of the least stable overtone eigenvalue, it is desirable to consider first an approximate analysis in which Eq. (5.249) is replaced by a real eigenvalue problem involving only the flux components of the p-mode eigenvector. This method, termed the μ-mode approximation, was originally suggested by D. R. Harris and P. S. Lacy.[63] It is described below and compared with p-mode results from the XEP code. In this way, the essential features of the p-mode spectrum in the range of complex eigenvalues are readily established. For a p-mode analysis, the μ-mode approximation may be used to obtain input eigenvalue estimates

for the XEP code. However, in most instances studied the μ-mode approximation appears to be good enough to replace the p-mode formulation. The μ-mode method is of particular interest because of its simplicity and the range of calculational tools available for its application.

2. *μ-Mode Approximation*

R.L. Ewen

The major assumptions of the μ-mode treatment are most clearly seen by considering for the present that Σ_{fF} is zero and solving the iodine and xenon component equations of Eq. (5.249) for $\sigma_X \hat{\phi}_S X$ in terms of ϕ_S. Note that $\sigma_X \hat{\phi}_S X$ appears as a term in the slow group neutron balance and is the only modification to the usual form of the neutron balance equations necessary to represent the xenon dynamics. This term may be written in the form

$$\sigma_X \hat{\phi}_S X = N(p, \eta) \Sigma_{fS} \phi_S \qquad \text{Eq. (5.250)}$$

in which

$$\eta = \sigma_X \hat{\phi}_S / \lambda_X$$

and

$$N(p, \eta) = \frac{-\lambda_I \left(\gamma_I + \gamma_X\right) - p\left(\gamma_I \eta - \gamma_X\right)}{\left(1 + \eta + \frac{p}{\lambda_X}\right)\left(\lambda_I + p\right)\left(1 + \eta^{-1}\right)} \qquad \text{Eq. (5.251)}$$

which, in general, is a complex, space-dependent function.

The μ-mode approximation grew from the observation that for a uniform ring reactor, in which η is constant and overtones have a sinusoidal space dependence, $N(p, \eta)$ is a negative real quantity for each harmonic. Therefore, xenon and slow flux perturbations are 180 degrees out of phase at every point, and since all other coefficients in the neutron equations are real, the two flux components are in phase with each other, and the phase is constant spatially throughout the reactor. From detailed examination of the $N(p, \eta)$ function, it is reasonable to expect that complex modes in nonuniform reactors will also approximate a 180-degree phase difference between the xenon and slow flux components. Furthermore, a limited amount of XEP code data for complex modes have verified that xenon is usually within 10 or 15 degrees of being 180 degrees out of phase with respect to the flux components and that typical flux phase variations spatially are very small.

These observations are the motivation for the basic postulate of the μ-mode approximation, namely, that $N(p, \eta)$ is real and negative. As a result of this postulate, the flux components may be chosen as real quantities. Since the condition that the imaginary part of $N(p, \eta)$ vanish implies a given fixed η, $N(p, \eta)$ is further assumed to be a constant (not space-dependent), with η based on the average $\hat{\phi}_S$ in the fueled regions of the core. Consequently,

$$N(p, \eta) = -\mu \qquad \text{Eq. (5.252)}$$

with μ a positive real constant for each overtone. In view of Eqs. (5.250) and (5.252), the neutron balance equations of Eq. (5.249) become

$$-\nabla \cdot D_F \nabla \phi_F + \Sigma_F \phi_F - \nu\Sigma_{fF} \phi_F - \nu\Sigma_{fS} \phi_S = 0$$

$$-\Sigma_R \phi_F + \nabla \cdot D_S \nabla \phi_S + \left(\Sigma_S + \sigma_X \hat{X}\right) \phi_S = \mu \Sigma_{fS} \phi_S \qquad \text{Eq. (5.253)}$$

or, for short,

$$[L - M]\Phi = \mu Q \Phi \qquad \text{Eq. (5.253a)}$$

where

$$Q \equiv \begin{pmatrix} 0 & 0 \\ 0 & \Sigma_f \end{pmatrix} \qquad \text{Eq. (5.253b)}$$

in which μ is the eigenvalue.

The quantity $\mu_u \Sigma_{fS}$ represents a slow group poison which must be removed to make the n^{th} mode critical. Fast fission may be treated in an approximate manner by letting

$$"\Sigma_{fS}" = \Sigma_{fS} + \Sigma_{fF} \frac{\hat{\phi}_F}{\hat{\phi}_S} \quad .$$

Note that if $\sigma_X \hat{X}$ is omitted in the problem [Eq. (5.253)], which omission normally introduces little error and is conservative, then the eigenvalue μ becomes independent of power level.

A method of correcting the μ-eigenvalues for the effects of temperature feedback has been suggested by S. G. Margolis.

For small perturbations the corrected eigenvalue and eigenvector, identified by μ' and Φ', satisfy

$$[L-M]\,\Phi' + \delta T\,\frac{\partial (L-M)}{\partial T}\,\hat{\Phi} = \mu' Q\,\Phi' \quad . \qquad \text{Eq. (5.253c)}$$

Here the temperature change δT is given by

$$\delta T = K\Phi' \qquad \text{Eq. (5.253d)}$$

where K is a row matrix which usually contains integral operators (see Sect. 5.4.E.3). Now applying perturbation theory to Eq. (5.253c) one obtains

$$\mu' = \mu + \frac{\int \Phi^{*T} K\Phi\,\frac{\partial}{\partial T}\,(L-M)\hat{\Phi}\,dV}{\int \Phi^{*T} Q\Phi\,dV} \quad . \qquad \text{Eq. (5.253e)}$$

In a uniform ring reactor μ_n has the interpretation

$$\mu_n = \frac{\lambda_o - \lambda_n}{\lambda_o}\,\frac{\Sigma_S + \sigma_X \hat{X} + D_S B_n^2}{\Sigma_{fS}}$$

in which λ_o is the fundamental λ-mode eigenvalue, λ_n is the eigenvalue of the n^{th} harmonic, and B_n^2 is the buckling of the n^{th} harmonic. This expression is exact for no fast fission and is a very good approximation when there is fast fission.

Equations (5.251) and (5.252) yield a quadratic in p which may be written as

$$p^2 - 2bp + c = 0 \qquad \text{Eq. (5.254)}$$

in which

$$b = -\frac{\lambda_X}{2}\left[1 + \eta + \frac{\lambda_I}{\lambda_X} - \frac{\gamma_I \eta - \gamma_X}{\mu\left(1+\eta^{-1}\right)}\right] \qquad \text{Eq. (5.255)}$$

$$c = \lambda_I \lambda_X \left[1 + \eta + \frac{\gamma_I + \gamma_X}{\mu\left(1+\eta^{-1}\right)}\right] \qquad \text{Eq. (5.256)}$$

Therefore, p is complex when $c > b^2$, and if a complex p is written as $\alpha \pm i\omega$,

$$\alpha = b \qquad \text{Eq. (5.257)}$$

$$\omega = \left(c - b^2\right)^{1/2} . \qquad \text{Eq. (5.258)}$$

Regardless of whether the roots of Eq. (5.254) are real or complex, they are stable if $b < 0$; c can be expressed as a linear function of b from Eqs. (5.255) and (5.256). When this is substituted into Eq. (5.258) the equation for a circle in the complex plane is obtained. That is, as μ varies for a given flux level, the complex p-eigenvalues follow a circular path in the complex plane. Several of these circular paths for various values of η are indicated in Fig. 5.31, which has been prepared using the values

$$\lambda_I = 2.88 \times 10^{-5} \text{ sec}^{-1}$$

$$\lambda_X = 2.11 \times 10^{-5} \text{ sec}^{-1}$$

$$\gamma_I = 0.06$$

$$\gamma_X = 0.003$$

In discussing Fig. 5.31 and the roots of Eq. (5.254), it may be considered that variations in μ arise from variation in core design, such as core size, which change μ for a given overtone, or from consideration of different overtones for a given core. For very small values of μ, a pair of positive real roots is obtained. As $\mu \to 0$, one root approaches

$$p = \frac{\lambda_I(\gamma_I + \gamma_X)}{\gamma_I \eta - \gamma_X} \qquad \text{Eq. (5.259)}$$

and the other becomes very large, so that it cannot be realistically determined without including delayed neutron dynamics. As μ is increased for a given η, these roots merge and branch out on a circular path as indicated. Only the path of one of the conjugate pair is indicated in Fig. 5.31. Further increases in μ cause the pair of roots to merge again and branch out on the negative real axis, one approaching $-\lambda_I$ as $\mu \to -\infty$, the other going to a limit of $-\lambda_X(1 + \eta)$. The centers of the circles followed by the complex eigenvalues are on the positive real axis at the locations marked on the figure and given by Eq. (5.259).

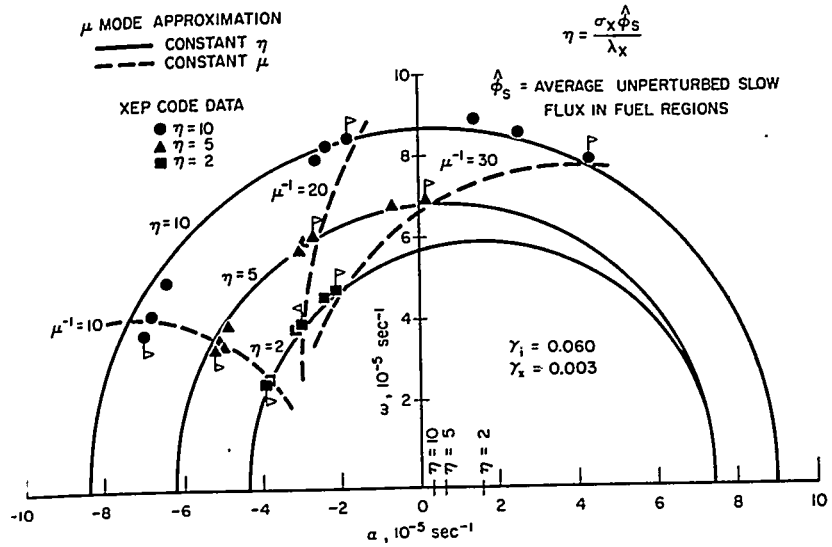

FIGURE 5.31. Location of Xenon Natural Mode Eigenvalues in the Complex Plane.

Lines of constant μ are also indicated, for μ^{-1} equal to 10, 20, and 30.

Complex eigenvalues for various nonuniform cores which have been calculated exactly using the XEP code are also shown in Fig. 5.31 and follow fairly closely the circular pattern of the μ approximation. The largest deviation appears to be at high flux levels for very stable cores.

A stability characteristic for a particular core may be defined as the curve of damping factor, $-\alpha$ for the least stable overtone, vs flux level η. Figure 5.32 shows such characteristics computed from Eq. (5.255) for several μ values, along with XEP data for comparison. Note that increasing flux level may either increase or decrease the damping factor, depending on the particular core in question. A value of $\mu = \gamma_I$ gives a flat characteristic at high fluxes. For larger values, the core is stable at all flux levels. In the region of complex eigenvalues, α is linear in μ^{-1} for fixed η.

Figure 5.33 shows the curves of μ vs η which define the stability boundary, $\alpha = 0$, and the region in which the p-eigenvalues are complex (i.e., $c > b^2$). Typically, only one or perhaps two pairs of p-eigenvalues will be complex. It is apparent that the μ-mode approximation is generally not valid for negative real p-eigenvalues, since regions of the core in which X_n is in phase with the flux components are then possible. However, this is not a problem in the stability analysis of cores which are not extremely stable.

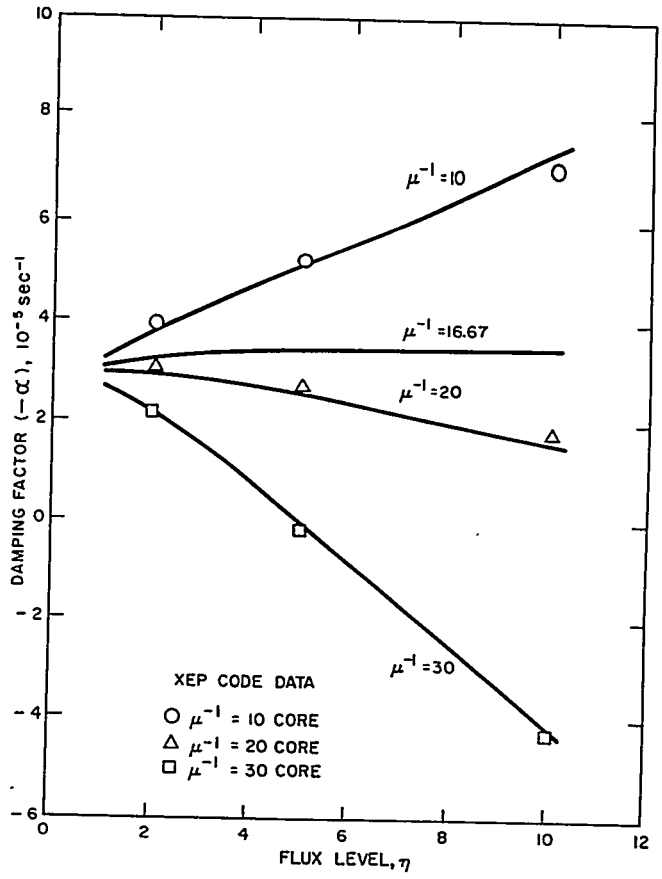

FIGURE 5.32. Xenon Spatial Stability Characteristics, Damping Factor vs Flux Level.

An alternate μ approximation may be made which appears to be slightly more accurate than that outlined above in the limited cases tested. It is not quite as easily applied, however. The alternate is based on the fact that Eq. (5.250) may be rewritten as

$$\sigma_S \hat{\phi}_S X = N'(p, \eta) \sigma_X \hat{X} \phi_S \qquad \text{Eq. (5.260)}$$

and the basic approximation of Eq. (5.252) modified to

$$N'(p, \eta) = -\mu_X \ . \qquad \text{Eq. (5.261)}$$

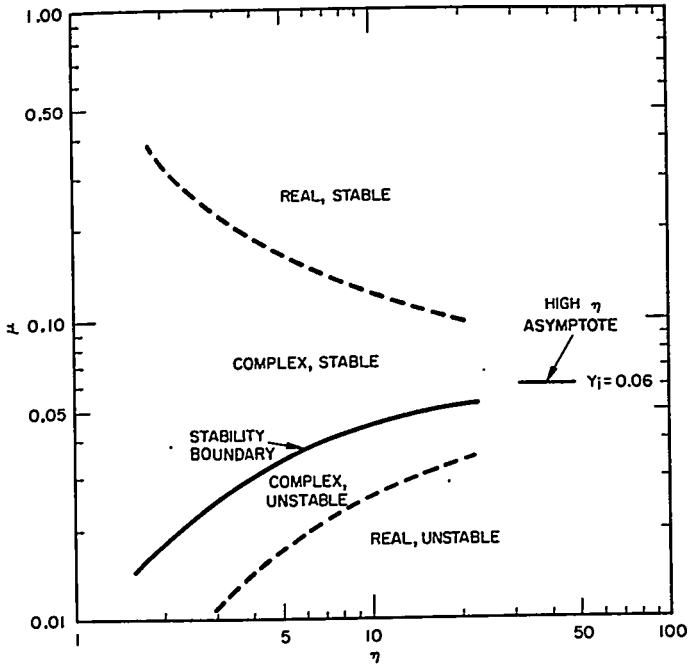

FIGURE 5.33. Regions of the $\mu - \eta$ Plane for Xenon Spatial Stability.

In this way, some of the space dependence of $N(p, \eta)$, namely the $1 + \eta^{-1}$ in the denominator, is expressed explicitly in $\sigma_X \hat{X}$. The effective thermal absorption cross section in Eq. (5.253) becomes

$$\Sigma_S + \sigma_X \hat{X}\left(1 - \mu_X\right)$$

and the previous μ-eigenvalues are related to the μ_X's by

$$\mu = \frac{\left(\gamma_I + \gamma_X\right)\mu_X}{1 + \eta^{-1}} \,. \qquad \text{Eq. (5.262)}$$

The disadvantage of the μ_X approximation is the variation of μ_X with power level.

Existing diffusion theory codes designed for the fundamental λ-mode problem such as WANDA and PDQ (see Chap. 7) may be used for the μ and μ_X approximations, provided that core symmetry allows the appropriate overtone mode to be calculated by specification of the boundary conditions. The μ-eigenvalue search requires a series of calculations, except in very special

cases, for which the automatic poison search feature of WANDA is applicable. A special code called MULE (see Chap. 7) will do the μ and μ_X overtone eigenvalue problems directly for slab geometry and for cylindrical cores which are uniform azimuthally.

3. λ-*Modes and the Use of Nyquist's Criterion*

S. G. Margolis

Thus far, the use of p-modes and μ-mode approximations to them has been considered.

The following discussion makes use of an expansion in λ-modes. A linearized form of temperature feedback is included, and the analysis shifts over to Laplace transform space in order to handle this feedback conveniently and to demonstrate the use of Nyquist's criterion.

It is assumed as part of the model that the reactor is controlled by varying the number of neutrons emitted per fission in such a way that on the xenon time scale the reactor is always critical and the fundamental λ-mode component of the transient flux is held constant. For algebraic simplicity, and since they are unimportant, consideration of prompt or delayed neutron dynamics is neglected and one assumes in effect that the flux adjusts instantaneously to a shape consistent with the materials properties at that instant. With this assumption, the neutron equations are, in the notation of Sect. 5.4.D,

$$L\Phi = \frac{1}{\lambda} M\Phi \qquad \text{Eq. (5.263)}$$

where λ now includes the effect of the control. Making the perturbation approximation yields as the equation governing the first order flux perturbation

$$\left[\hat{L} - \frac{1}{\hat{\lambda}}\hat{M}\right]\delta\Phi = \left[\frac{\delta M}{\hat{\lambda}} - \delta L - \frac{(\delta\lambda)}{\hat{\lambda}^2}\hat{M}\right]\hat{\Phi} \,. \qquad \text{Eq. (5.264)}$$

This is an inhomogeneous equation with the driving term on the right-hand side. The corresponding homogeneous adjoint equation has a nontrivial solution, namely Ψ_0^*, the fundamental adjoint mode of the steady state. It follows from this (Ref. 68, p. 45) that Eq. (5.264) has a solution only if the right side is orthogonal to Ψ_0^*

$$\left(\dot{\Psi}_0^*, \left[\frac{\delta M}{\hat{\lambda}} - \delta L - \frac{(\delta\lambda)}{\hat{\lambda}^2}\hat{M}\right]\hat{\Phi}\right) = 0 \quad . \qquad \text{Eq. (5.265)}$$

This condition is the perturbation theory expression for the change in λ required to maintain criticality following changes δL and δM.

An attempt is now made to solve Eq. (5.264) with an expansion in λ-modes

$$\delta\Phi = \sum_{n=1}^{\infty} b_n \Psi_n \quad . \qquad \text{Eq. (5.266)}$$

where b_o is omitted by the hypothesis on the type of control. Assuming the λ-modes to be normalized, so that

$$\left(\Psi_j^*, M\Psi_j\right) = 1 \qquad \text{Eq. (5.267)}$$

one determines the b_j by operating on Eq. (5.264) with Ψ_j^*

$$\left[\frac{1}{\lambda_j} - \frac{1}{\hat{\lambda}}\right] b_j = \left(\Psi_j^*, \left[\frac{\delta M}{\hat{\lambda}} - \delta L\right]\hat{\Phi}\right) \quad . \qquad \text{Eq. (5.268)}$$

Since $\delta\lambda$ does not appear one concludes that this type of control does not affect the stability of any higher mode. Denoting the Laplace transform by the symbol $\mathcal{L}\{\ \}$ and letting $\mathcal{L}\{b_j\} = B_j$, the transform of Eq. (5.268) is

$$\left[\frac{1}{\lambda_j} - \frac{1}{\hat{\lambda}}\right] B_j = \left(\Psi_j^*, \mathcal{L}\left\{\left[\frac{\delta M}{\hat{\lambda}} - \delta L\right]\hat{\Phi}\right\}\right) \quad . \qquad \text{Eq. (5.268a)}$$

One next spells out exactly what is contained in the matrices δL and δM. For analytical purposes, δL will be treated as the sum of four operators. The first two represent feedback through the coolant enthalpy, the third represents the effects of xenon poisoning, and the fourth represents all external forced disturbances:

$$\delta L = \delta L_1 + \delta L_2 + \delta L_3 + \delta L_4 \qquad \text{Eq. (5.269)}$$

where, with primed quantities representing derivatives with respect to coolant enthalpy,

$$\delta L_1 = \begin{bmatrix} -\nabla \cdot \delta h D_F' \nabla & 0 \\ 0 & -\nabla \cdot \delta h D_S' \nabla \end{bmatrix} \qquad \text{Eq. (5.270)}$$

$$\delta L_2 = \delta h \begin{bmatrix} \Sigma_F' & 0 \\ -\Sigma_R' & \Sigma_S' \end{bmatrix} \qquad \text{Eq. (5.271)}$$

$$\delta L_3 = \begin{bmatrix} 0 & 0 \\ 0 & \sigma_x \delta x \end{bmatrix} \qquad \text{Eq. (5.272)}$$

$$\delta L_4 = \begin{bmatrix} -\nabla \cdot \delta_E D_F \nabla + \delta_E \Sigma_F & 0 \\ -\delta_E \Sigma_R & -\nabla \cdot \delta_E D_S \nabla + \delta_E \Sigma_S \end{bmatrix}. \qquad \text{Eq. (5.273)}$$

Similarly, δM is broken into two matrices, representing enthalpy feedback and external forced disturbances, respectively:

$$\delta M = \delta M_1 + \delta M_2 \qquad \text{Eq. (5.274)}$$

$$\delta M_1 = \delta h \begin{bmatrix} \nu\Sigma_{fF}' & \nu\Sigma_{fF}' \\ 0 & 0 \end{bmatrix} \qquad \text{Eq. (5.275)}$$

$$\delta M_2 = \begin{bmatrix} \delta_E \nu\Sigma_{fF} & \delta_E \nu\Sigma_{fS} \\ 0 & 0 \end{bmatrix} . \qquad \text{Eq. (5.276)}$$

A) ENTHALPY FEEDBACK. It will be assumed that all δ quantities and all primed quantities are space-dependent, i.e., $\delta h = \delta h(x, y, z)$, $\Sigma_F' = \Sigma_F'(x, y, z)$, etc.

The perturbations in enthalpy, δh, are calculated, using a static heat-balance

$$h(x, y, z) - h_{in}(x, y) = \frac{1}{G(x, y)} \int_0^z (K\Sigma_{fF}\phi_F + K\Sigma_{fS}\phi_S)\, dz' \qquad \text{Eq. (5.277)}$$

where $G(x, y)$ is the coolant mass flow rate and K the energy release per fission.

For simplicity, it will be assumed in Eq. (5.277) that the fission cross sections Σ_{fF} and Σ_{fS} are independent of temperature.* Then one finds

$$\delta h\,(x, y, z) = \frac{1}{G(x, y)} \int_0^z (K\Sigma_{fF}\,\delta\phi_F + K\Sigma_{fS}\,\delta\phi_S)\, dz' \,. \qquad \text{Eq. (5.278)}$$

Define

$$P_n = K\Sigma_{fF}\psi_{Fn} + K\Sigma_{fS}\psi_{Sn} \qquad \text{Eq. (5.279)}$$

where ψ_{Fn} and ψ_{Sn} are the components of Ψ_n and define

$$W_n(x, y, z) = \int_0^z P_n(x, y, z')\, dz' \,. \qquad \text{Eq. (5.280)}$$

Then, from Eqs. (5.266) and (5.278)

*In other words, one neglects $K\delta\Sigma_f\hat{\phi}$ in comparison to $K\hat{\Sigma}_f\delta\phi$.

$$\delta h(x,y,z) = \frac{1}{G(x,y)} \sum_{n=0}^{N} b_n W_n(x,y,z) \qquad \text{Eq. (5.281)}$$

One must perform one more preliminary step before evaluating the coolant-enthalpy-feedback terms of Eq. (5.268), namely, factor out δh from the operator δL_1. This is done as follows: Since

$$\int_V \psi^* \nabla \cdot \delta h D' \nabla \hat{\phi} \, dV = \int_V \nabla \cdot (\psi^* \delta h D' \nabla \hat{\phi}) \, dV - \int_V \delta h D' \nabla \hat{\phi} \cdot \nabla \psi^* \, dV$$

$$= \int_S (\psi^* \delta h D' \nabla \hat{\phi}) \cdot dS - \int_V \delta h D' \nabla \hat{\phi} \cdot \nabla \psi^* \, dV \qquad \text{Eq. (5.282)}$$

If ψ^* vanishes on the reactor boundary, the first integral is zero. One can now evaluate the enthalpy-feedback contributions to Eq. (5.268):

$$\left(\Psi_j^*, \left[\frac{\delta M}{\hat{\lambda}} - \delta L_1 - \delta L_2 \right] \hat{\Phi} \right) = \sum_{n=0}^{N} \alpha_{jn} b_n \qquad \text{Eq. (5.283)}$$

$$\left(\Psi_j^*, \mathfrak{L} \left\{ \left[\frac{\delta M}{\hat{\lambda}} - \delta L_1 - \delta L_2 \right] \hat{\Phi} \right\} \right) = \sum_{n=0}^{N} \alpha_{jn} B_n \qquad \text{Eq. (5.283a)}$$

$$\alpha_{jn} = \int \frac{W_n(x,y,z)}{G(x,y)} \left\{ -\left(D_F' \nabla \psi_{Fj}^* \cdot \nabla \hat{\phi}_F + D_S' \nabla \psi_{Sj}^* \cdot \nabla \hat{\phi}_S \right) \right.$$

$$\left. + \psi_{Fj}^* \left[\left(\frac{\nu \Sigma_{fF}'}{\hat{\lambda}} - \Sigma_F' \right) \hat{\phi}_F + \frac{\nu \Sigma_{fS}'}{\hat{\lambda}} \hat{\phi}_S \right] + \psi_{Sj}^* \left(\Sigma_R' \hat{\phi}_F - \Sigma_S' \hat{\phi}_S \right) \right\} dV .$$

Eq. (5.284)

B) XENON FEEDBACK. From the iodine and xenon balance equations, if the series representation of Eq. (5.266) and Laplace transform are used, one obtains

$$\delta X = \sum_{n=1}^{N} B_n \left\{ G_1 \left(\hat{\Sigma}_{fF} \psi_{Fn} + \Sigma_{fS} \psi_{Sn} \right) - G_2 \psi_{Sn} \right\} + G_3 + G_4$$

Eq. (5.285)

where

$$G_1 = \frac{\gamma_X (s + \lambda_I) + \gamma_I \lambda_I}{\left(s + \lambda_X + \hat{\phi}_S \sigma_X \right) \left(s + \lambda_I \right)}$$

Eq. (5.286)

$$G_2 = \frac{\hat{X} \sigma_X}{s + \lambda_X + \hat{\phi}_S \sigma_X}$$

Eq. (5.287)

$$G_3 = \frac{\lambda_I \, \delta I(0^+)}{\left(s + \lambda_I \right) \left(s + \lambda_X + \hat{\phi}_S \sigma_X \right)}$$

Eq. (5.288)

$$G_4 = \frac{\delta X(0^+)}{s + \lambda_X + \hat{\phi}_S \sigma_X}$$

Eq. (5.289)

One can now evaluate the xenon-feedback contributions to Eq. (5.268a):

$$\left(\psi_j^*, \mathfrak{L} \left[-\delta L_3 \right] \hat{\Phi} \right) = - \sum_{n=0}^{N} G_{jn} B_n - C_j$$

Eq. (5.290)

where

$$G_{jn} = \sigma_X \int \psi_{Sj}^* \left(G_1 \left(\hat{\Sigma}_{fF} \psi_{Fn} + \hat{\Sigma}_{fS} \psi_{Sn} \right) - G_2 \psi_{Sn} \right) \hat{\phi}_S dV$$

Eq. (5.291)

$$C_j = \sigma_X \int \psi_{Sj}^* \left(G_3 + G_4 \right) \hat{\phi}_S dV$$

Eq. (5.292)

C) EXTERNALLY FORCED DISTURBANCES. It will be assumed that the disturbances are applied as steps at time $t = 0$ and remain constant thereafter. For brevity, denote the external disturbance term

$$\left(\Psi_j^*, \left[\frac{\delta M_2}{\hat{\lambda}} - \delta L_4\right]\hat{\Phi}\right) = F_j \ . \qquad \text{Eq. (5.293)}$$

D) SOLUTION FOR THE MODAL EXPANSION COEFFICIENTS. At this point, one has all the information required to evaluate the right-hand side of Eq. (5.268). To review: the perturbed flux $\delta\Phi$ is represented by a series in Eq. (5.266), the perturbed operators δL and δM were specified by Eqs. (5.269) to (5.276), and the connection between the perturbed flux and perturbed operators was given by Eqs. (5.283a), (5.284), (5.290), (5.291), and (5.292). Thus, one arrives at the following N equations for the N unknowns $B_1, \cdots, B_N$:

$$\left(\frac{1}{\hat{\lambda}} - \frac{1}{\lambda_j}\right)B_j + \sum_{n=0}^{N}\left(\alpha_{jn} - G_{jn}\right)B_n = -\left(F_j - C_j\right)$$

$$(j = 1, 2, \ldots, N) \ . \qquad \text{Eq. (5.294)}$$

Equation (5.294) can be written more compactly as

$$[A]\ [B] = -\left\{[F] - [C]\right\} \ . \qquad \text{Eq. (5.295)}$$

Stability of the system [Eq. (5.295)] is controlled by the zeros of Δ, where

$$\Delta = det\ [A] \qquad \text{Eq. (5.296)}$$

with typical element

$$\Delta_{jn} = \left(\frac{1}{\hat{\lambda}} - \frac{1}{\lambda_j}\right)\delta_{jn} + \alpha_{jn} - G_{jn} \ . \qquad \text{Eq. (5.297)}$$

Briefly, the manner in which the zeros of Δ control the stability of the system [Eq. (5.295)] is as follows:

$$[B] = -[A^{-1}]\left\{[F] - [C]\right\} = -\frac{[adj\,A]}{\Delta}\left\{[F] - [C]\right\} .$$

Eq. (5.298)

Thus, $\Delta\,(=\Delta(S))$ appears in the denominator of the expression for each element of B. Recall that B_j is the Laplace transform of the time function b_j. The two are related by the inverse transform

$$b_j(t) = \frac{1}{2\pi_i}\int_{c-i\infty}^{c+i\infty} B_j(s)e^{ts}\,ds \qquad \text{Eq. (5.299)}$$

where the contour of integration lies to the right of any singularities of the integrand. When the integral is evaluated as a sum of residues, any right-half-plane singularities will contribute divergent exponential terms. If such terms occur, the system is unstable. Since, according to Eq. (5.298), any zero of Δ is a singularity of $[B]$, Δ must have no zeros in the right-half-plane if the system [Eq. (5.295)] is to be stable.

E) USE OF THE NYQUIST CRITERION TO TEST FOR STABILITY. Through G_{jn}, the determinant Δ is likely to be a rather complicated function of the transform variable s. Thus, it appears to be a formidable task to find the complex zeros of a Δ directly, say by solving the equation $\Delta(s) = 0$. On the other hand, inspection of G_1 and G_2 shows that G_{jn} is analytic in the right-half-plane. If the parameter s is allowed to traverse a closed contour in the right half of its own complex plane, the function $\Delta(s)$ will assume a sequence of complex values which trace out another closed contour in the Δ-plane. That is, the closed contour C_1 in the s-plane is mapped onto the closed contour C_2 in the Δ-plane. As shown, for example in Ref. 69, the contour C_2 will wind around the origin of the Δ-plane once for every zero of Δ in C_1. Since Δ reduces to a constant for sufficiently large $|s|$, an evaluation of Δ along the imaginary axis from $s = -i\infty$ to $s = +i\infty$ is equivalent to evaluation of Δ on a contour surrounding the right-half-plane. As a consequence:

If a plot of $\Delta(s)$ for purely imaginary s ranging from $-i\infty$ to $+i\infty$ does not enclose the origin, then Δ has no zeros in the right-half-plane and the flux shape is stable.

F) USE OF A SINGLE MODE. In some cases the perturbed flux may be adequately represented by the first overtone λ-mode. In that case, Eq. (5.294) takes the simple form

$$\left[\left(\frac{1}{\hat{\lambda}}-\frac{1}{\lambda_1}\right)+\alpha_{11}-G_{11}\right]B_1=-(F_1-C_1). \qquad \text{Eq. (5.300)}$$

Here the expression in brackets plays the role of $\Delta(s)$. Since both the reciprocal eigenvalue difference $\left(\frac{1}{\hat{\lambda}}-\frac{1}{\lambda_1}\right)$ and the enthalpy feedback coefficient α_{11} are purely real, the effect of a unit increase in either of these quantities is merely to translate a plot of $\Delta(s)$ one unit to the right. This property is useful because it allows the designer to determine by inspection the effect on stability of a proposed change in either the second-mode eigenvalue or the enthalpy feedback coefficient.

G) RESULTS. Calculations have been performed using the test geometry shown in Fig. 5.34. This is a core consisting of rodded and unrodded slabs. Periodic boundary conditions were imposed so as to represent circumferential diffusion around an annular seed. The fundamental and first four overtone modes calculated by the MULE code are also shown in Fig. 5.34. To test the validity of stability calculations based on a single-mode representation of the perturbed flux, the first overtone p-mode was calculated for this same geometry, using an average unperturbed flux level of 8.4×10^{13}. This value was chosen to put the system on the borderline between stable and unstable conditions. As found by the XEP code, the eigenvalue was $s_p = (0.0011 + i\ 0.7975)\,10^{-4}$.

One would thus expect $\Delta(s)$ to have a zero in the right-half-plane. Plots of $\Delta(s)$, as a function of $Im(s)$ with $Re(s)$ as a parameter, are shown in Fig. 5.35. These effectively map a portion of the s-plane onto the Δ-plane. A zero of Δ occurs at $s = (0.0010 + i\ 0.7970)10^{-4}$, in close agreement with the p-mode result.

In the example cited above, a zero of $\Delta(s)$ was found by explicit graphical solution of $\Delta(s) = 0$. The use of the Nyquist plot is illustrated in Fig. 5.36, which shows typical complex plane plots of the determinant Δ, with average thermal flux $\bar{\phi}_s$ as parameter. At a thermal flux of 5×10^{13}, the system is stable, since the locus of $\Delta(s)$ does not encircle the origin. The loci for average thermal fluxes of 1.0×10^{14} and 1.5×10^{14} do encircle the origin, indicating instability at these levels.

Inspection of Fig. 5.36 shows that the locus for $\bar{\phi}_s = 1.0 \times 10^{14}$ would just graze the origin if it were shifted 0.00164 units to the left. This indicates that for stability at the $\bar{\phi}_s = 1.0 \times 10^{14}$ flux level, the value of $\left(\frac{1}{\hat{\lambda}}-\frac{1}{\lambda_1}\right)$ should be increased from its initial value of 0.02355 to 0.02519.

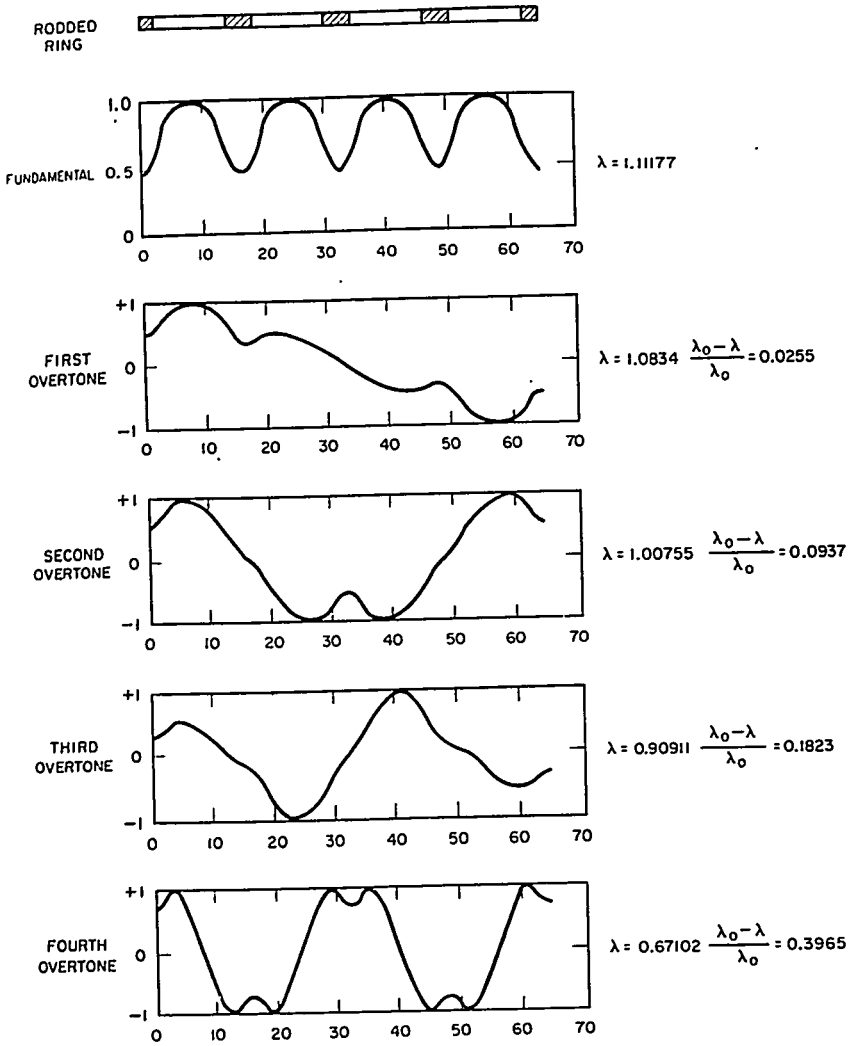

FIGURE 5.34. Fundamental and First Four Overtone Modes for Rodded Ring.

4. *Nonlinear Effects*

S. G. Margolis

This section describes a modal analysis of xenon oscillations in a uniform ring reactor with nonlinear terms retained. This permits an evaluation of the effect of nonlinearities on transient flux behavior and, in particular, of their effect in limiting the amplitude of xenon spatial oscillations. Since this analysis is

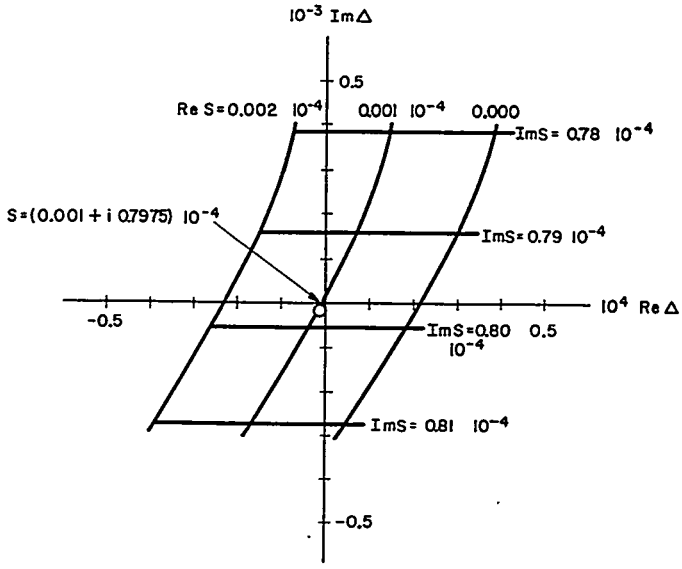

FIGURE 5.35. Map of the s-Plane on the Δ-Plane.

rather lengthy, only the procedure will be outlined and the results briefly discussed. A fuller discussion which includes temperature feedback is contained in Ref. 70.

The analysis starts with the set of balance equations of Sect. 5.4.E.1, except that delayed neutrons are neglected and, as part of the model, a uniform thermal group poison representing control rods is added in such an amount that the reactor is critical at every instant and such that the total power level is held constant. Then, the iodine, xenon, and flux variables are expanded in truncated Fourier series:

$$I = I_o(t)\psi_o(\theta) + I_1(t)\psi_1(\theta) + I_2(t)\psi_2(\theta)$$

$$X = X_o(t)\psi_o(\theta) + X_1(t)\psi_1(\theta) + X_2(t)\psi_2(\theta)$$

$$\phi_F = a_o\psi_o(\theta) + a_1(t)\psi_1(\theta) + a_2(t)\psi_2(\theta)$$

$$\phi_S = b_o\psi_o(\theta) + b_1(t)\psi_1(\theta) + b_2(t)\psi_2(\theta)$$

where $\psi_o = \frac{1}{\sqrt{2\pi}}$, $\psi_1 = \frac{1}{\sqrt{\pi}}\sin\theta$, $\psi_2 = \frac{1}{\sqrt{\pi}}\cos\theta$. These expansions are substituted into the balance equations, and these equations are then integrated over θ with weight functions ψ_o, ψ_1, and ψ_2.

This process yields the following set of coupled ordinary differential equations relating the expansion coefficients:

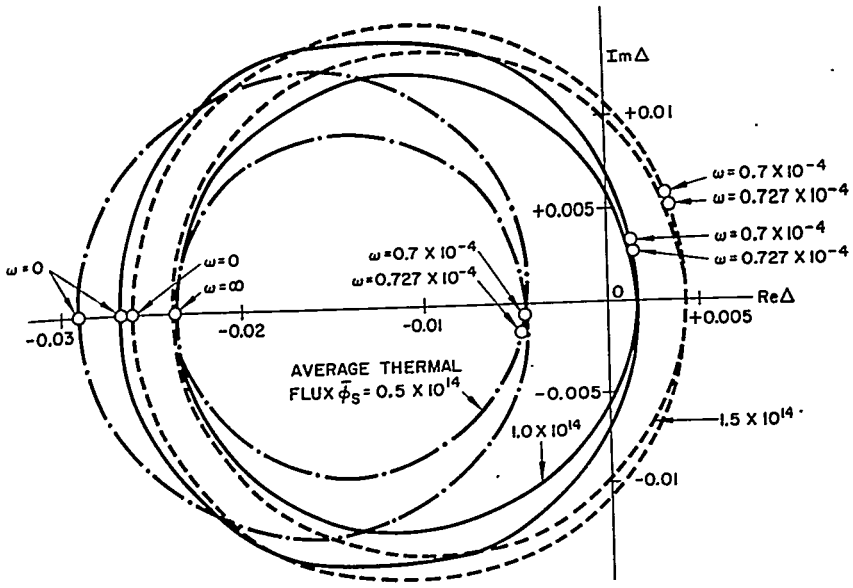

FIGURE 5.36. Nyquist Plots for Slab Reactor as a Function of Thermal Flux.

A) IODINE EXPANSION COEFFICIENTS:

$$\frac{dI_n}{dt} = \gamma_I\left(\Sigma_{fF}\, a_n + \Sigma_{fS}\, b_n\right) - \lambda_I I_n \quad (n = 0, 1, 2) \quad . \qquad \text{Eq (5.301)}$$

B) XENON EXPANSION COEFFICIENTS:

$$\frac{dX_o}{dt} = \lambda_I I_o - \lambda_X X_o + \gamma_X\left(\Sigma_{fF}\, a_o + \Sigma_{fS}\, b_o\right)$$

$$-\sigma_{XS}\left[X_o b_o \int \psi_o^3\, d\theta + X_1 b_1 \int \psi_o \psi_1^2\, d\theta + X_2 b_2 \int \psi_o \psi_2^2\, d\theta\right]$$

Eq. (5.302)

$$\frac{dX_1}{dt} = \lambda_I I_o - \lambda_X X_o + \gamma_X\left(\Sigma_{fF}\, a_1 + \Sigma_{fS}\, b_2\right)$$

$$-\sigma_{XS}\left[X_o b_1 \int \psi_1^2 \psi_o\, d\theta + X_1 b_o \int \psi_1^2 \psi_o\, d\theta\right] \qquad \text{Eq. (5.303)}$$

$$\frac{dX_2}{dt} = \lambda_I I_2 - \lambda_X X_2 + \gamma_X\left(\Sigma_{fF}\, a_2 + \Sigma_{fS}\, b_2\right)$$

$$-\sigma_{XS}\left[X_o b_2 \int \psi_2^2 \psi_o\, d\theta + X_2 b_o \int \psi_2^2 \psi_o\, d\theta\right] \qquad \text{Eq (5.304)}$$

C) TWO-GROUP NEUTRON FLUX EXPANSION COEFFICIENTS:

$$\left.\begin{aligned} a_o &= \text{Constant} \\ b_o &= \text{Constant} \end{aligned}\right\} \qquad \text{Eq. (5.305)}$$

$$\left(-D_F B_{g1}^2 - \Sigma_F + \gamma\Sigma_{fF}\right)a_1 + \nu\Sigma_{fS} b_1 = \frac{1}{v_F}\,\dot{a}_1 \Sigma_R a_1 + \left(-D_S B_{g1}^2 - \Sigma_S\right)b_1 = \frac{1}{v_S}\, b_1$$

$$+\psi_o \sigma_{XS}\left[X_o b_1 + X_1 b_o\right] + \int \psi_1\, \delta\Sigma_S \phi_S\, d\theta \qquad \text{Eq. (5.306)}$$

$$\left(-D_F B_{g1}^2 - \Sigma_F + \nu\Sigma_{fF}\right)a_2 + \nu\Sigma_{fS} b_2 = \frac{1}{v_S}\,\dot{a}_2$$

$$\Sigma_R a_2 + \left(-D_S B_{g1}^2 - \Sigma_S\right)b_2 = \frac{1}{v_S}\,\dot{b}_2 \quad + \psi_o \sigma_{XS}\left[X_o b_2 + X_2 b_o\right] + \int \psi_2\, \delta\Sigma_S \phi_S\, d\theta$$

Eq. (5.307)

where $\delta\Sigma_S$ is the sum of the control cross section and any arbitrary other perturbation which may be present; B_{g1}^2 is the buckling of the ψ_1 and ψ_2 modes.

Equation (5.302) shows that the assumption of a constant fundamental mode component of neutron flux does not imply a constant fundamental mode of xenon number density. Oscillations in the overtone flux modes contribute to the driving function of Eq. (5.302) and excite oscillations in the fundamental xenon mode. In turn, the fundamental xenon mode coefficient appears in the driving functions of Eqs. (5.306), (5.307), (5.303), and (5.304) and contributes to oscillations in the overtone modes of both flux and xenon.

D) RESULTS. Equations (5.301) through (5.307) have been solved with an analog computer for various combinations of the two most important parameters, steady-state flux, $\hat{\phi}_S$, and overtone buckling B_{g1}^2. For presenting the results it is more convenient to use the dimensionless parameter $(\lambda_o - \lambda_1)/\lambda_o$, the

eigenvalue difference between fundamental and first overtone λ modes, than it is to use the buckling parameter B_g^2. Now consider the plane formed by the parameters $\hat{\phi}_S$ and $(\lambda_o - \lambda_1)/\lambda_o$. One may divide this plane into stable and unstable regions by setting the real part of the first overtone p-mode equal to zero.

According to the linear theory, when the core operating point is stable but close to the stability boundary, small perturbations in cross sections produce large transient swings in power distribution, which eventually approach a steady-state flux tilt condition. On the other hand, if the operating point is on the unstable side, the linear theory predicts oscillations of exponentially increasing amplitude.

E) EFFECTS OF NONLINEARITIES. For initial operating points on the stable side of the boundary (such as points 1 and 2 of Fig. 5.37), nonlinearity does not change the qualitative transient behavior. The principal effect of nonlinearity is to limit the amplitude of flux tilt. Typically, this limitation becomes important when the flux tilt exceeds 50 percent of the core average flux. When a transient is initiated (by unbalancing the thermal absorption, for example), the flux tilts and overshoots but eventually settles down to a steady state. When the thermal absorption is made uniform again, the flux returns to its original unperturbed state.

For initial operating points on the unstable side of the stability boundary, however, the effects of nonlinearity do produce changes in the qualitative transient behavior. Operating point 3 of Fig. 5.37 is typical of the unstable region. As shown in Fig. 5.38, with the fundamental mode of flux held constant, the spontaneous buildup of the overtones is exponential at first. Eventually, however, nonlinearity causes the oscillation to settle into a periodic, almost sinusoidal time-dependence with constant amplitude.

Owing to the azimuthal symmetry of the ring model, the flux tilt has no preferred orientation. Instead, the position of peak flux precesses around the core with a period of roughly 24 hours. This behavior is shown by the polar flux plots of Fig. 5.39, which are plotted for successive times during the cycle. The positions of minimum and maximum flux are located on opposite sides of the core, as the position of the line joining them rotates around the core.

In the particular example shown (point 3, Fig. 5.37), one effect of nonlinearity is to limit the amplitude, so that the peak flux is 170 percent of the average, and the minimum flux 30 percent of the average. For less stable operating conditions, the limiting amplitude is larger, e.g., for point 4 of Fig. 5.37, the maximum is nearly 200 percent of the average, and the

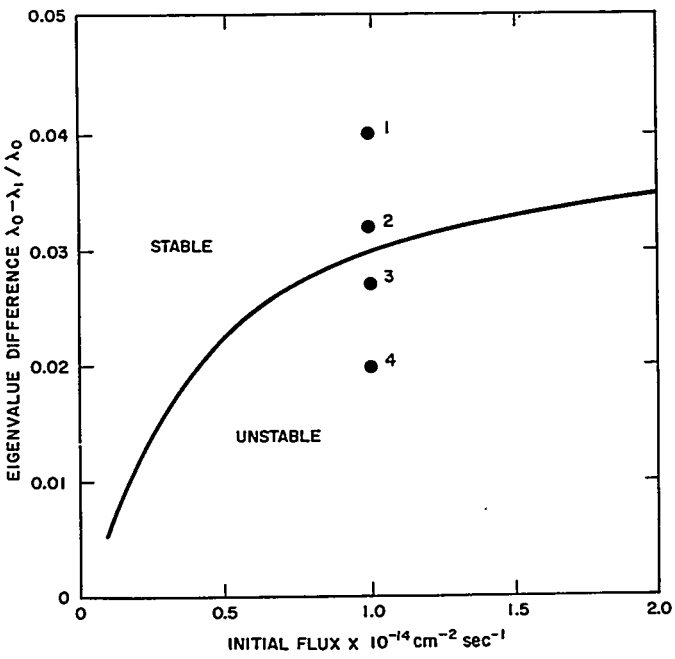

FIGURE 5.37. Effects of Nonlinearity.

minimum is nearly zero. It is clear that, although the nonlinearity limits the amplitude, it is not a strong effect, and one would not rely on it in core design.

A second effect of nonlinearity is brought out by the modal analysis, namely, that nonlinearity leads to a definite phase relationship between the $\sin\theta$ and $\cos\theta$ modes (determined by initial conditions in the linear case). The locking of the sine and cosine modes causes the observed precession of the flux peak.

F) LIMIT CYCLE AMPLITUDE. Making use of the precession phenomenon observed in the computer solutions, it is possible to return to Eqs. (5.301) through (5.307) and obtain an approximate analytic expression for the limiting amplitude of the oscillation. This expression is

$$\frac{B}{b_o}=\left[\frac{\frac{C^*}{C}-1}{\left(\frac{C^*}{C}-1\right)+\left(1-\frac{\left(\phi_{S0}\sigma_X\right)^2}{\left(\lambda_1+\lambda_X+\phi_{S0}\sigma_X\right)\left(\lambda_X+\phi_S\sigma_{XS}\right)}\right)}\right]^{1/2} \qquad \text{Eq. (5.308)}$$

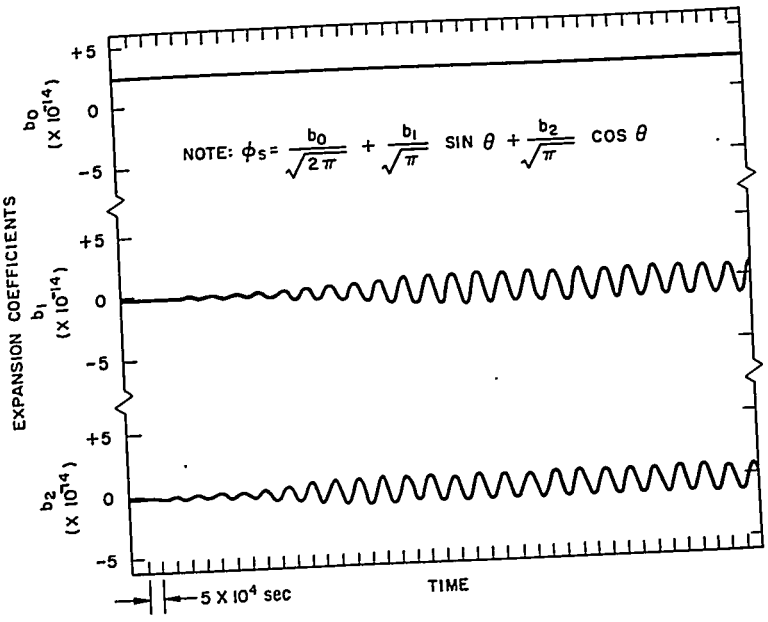

FIGURE 5.38. Effects of Nonlinearity.

where B is the maximum value of $b_1(t)$, C is a coupling parameter which for no temperature feedback is equal to $(\lambda_o - \lambda_1)/\lambda_o$, and C^* is the minimum value of C required for stability as given by Fig. 5.37. Figure 5.40 shows the limiting amplitude as calculated from Eq. (5.308) in comparison with amplitudes obtained from analog solutions.

F. Summary

S. Kaplan

Three methods have been outlined for attacking reactor kinetics problems where space and time are not separable: instantaneous tilt, nodal analysis, and modal analysis. The three methods have been described for the case of no xenon feedback. The case including xenon feedback was then discussed from a modal analysis standpoint, although the nodal analysis can also be applied to this case. Numerical experience with the methods has not yet been extensive enough to allow very definite conclusions about relative accuracy and feasibility. However, several observations may be made about the advantages and disadvantages stemming from the general features of the methods.

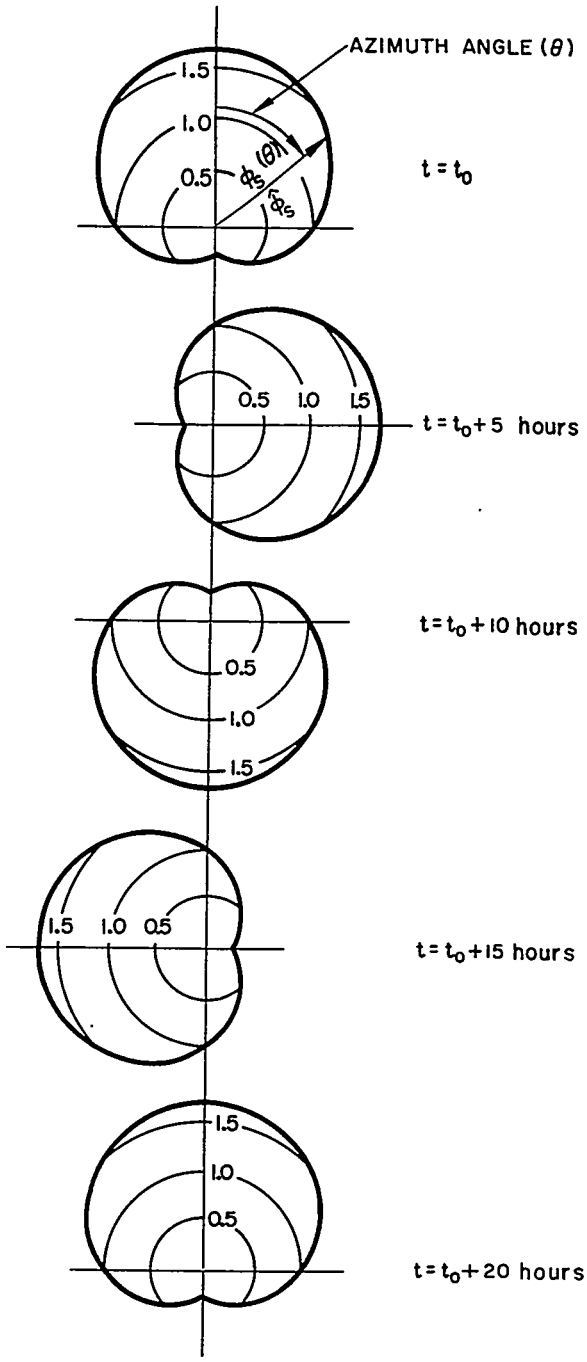

FIGURE 5.39. Polar Flux Plots at Various Times in 20-Hour Period.

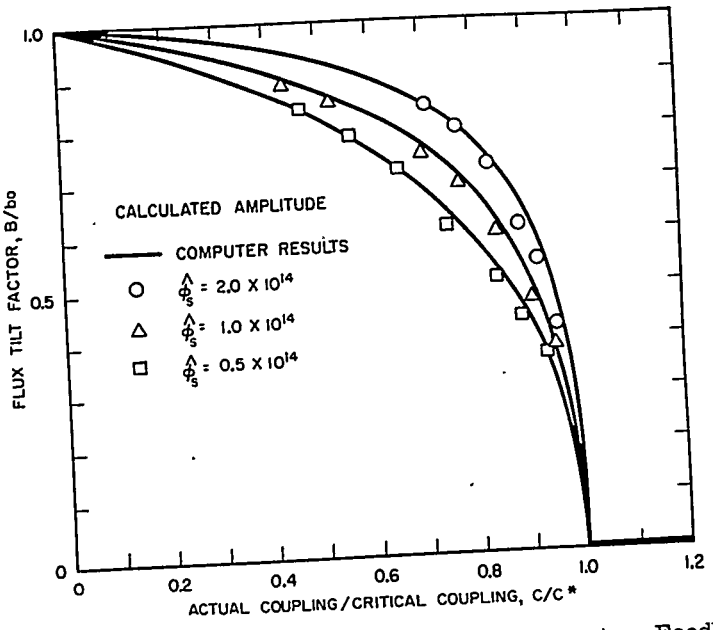

FIGURE 5.40. Limit Cycle Amplitude without Temperature Feedback.

The principal virtue of the instantaneous tilt method is that it uses the conventional reactor kinetics equations and is a natural extension of the treatment which is used in the case of separable reactor kinetics. It has the disadvantage that, when applied to complicated geometries, the interpolation schemes required become unwieldy and the number of static calculations needed becomes large. Furthermore, the basic assumption of instantaneous tilting is not rigorously valid, whereas the solutions given by the nodal and modal methods approach the exact solutions as more nodes or modes are used.

The advantages of the nodal method are its simplicity and the fact that the neutron equations are treated in the same way as the reactor-plant thermal-hydraulic equations. The adequacy of the approximations used in calculating the leakage coefficients is the major unknown factor.

The modal method has been used more often than the other two methods and, generally, seems to give satisfactory results. An advantage is that at any instant, a spatial power shape can be found which is detailed and continuous. Disadvantages are that in some cases it is difficult to calculate the modes and that sometimes a large number of modes are required. However, the idea of using perturbed eigenfunctions gives promise of improving both these defects.

In Sect. 5.4.E, four modal treatments of the xenon spatial stability problem are described. The first, p-mode, treatment

identifies the natural modes of oscillation of the linearized problem. The eigenvalues associated with these modes indicate stability or instability by the sign of their real part. The second, μ-mode, treatment represents an approximation to the natural mode formulation which is of particular interest because of its simplicity and the range of calculational tools available for its application. A series of comparisons of μ- and p-mode results showed excellent agreement in both damping factor and frequency and indicates that for practical purposes the μ-mode approximation can replace the p-mode analysis.

The third treatment utilizes an expansion in more readily available λ-modes, followed by an examination of the roots of the secular determinant via Nyquist's criterion. This formulation readily includes temperature feedback and, in the one-mode truncation, displays the effect of this feedback in a very simple and useful way.

The fourth treatment is a modal analysis in a very simple core but retaining the nonlinear terms resulting from the product of the xenon concentration and the neutron flux. It is found that nonlinearity limits the amplitude of the xenon oscillation but that it is not a strong effect, and one would not rely on it for design purposes.

5.5 KINETICS OF LOW SOURCE LEVEL

A. Introduction

D. R. Harris

The neutron level in a reactor fluctuates as a result of the probabilistic nature of the processes of neutron loss and production. For example, all of a set of neutrons present in a reactor at a certain time conceivably could induce fissions, and from each of these fissions a larger than average number of neutrons could arise. The consequence would be a large fluctuation in neutron level.

Fluctuations in a multiplicative system, such as a reactor, differ qualitatively from those ordinarily encountered. Many nonmultiplicative physical systems which contain fluctuating numbers of component particles can be described by a grand canonical ensemble, and in such systems the magnitude of the fluctuations relative to the expected number of particles becomes negligible as the expected number becomes large. In consequence, the kinetic behavior of such systems can be treated deterministically, entirely ignoring fluctuations. In a stationary multiplicative process without feedback, however, the magnitude of the fluctuations relative to the expected number

of component particles does not approach zero when the expected neutron number increases as a result of increasing multiplication. When the reactor power level is sufficiently large, fluctuations are diminished as a result of negative reactivity feedback, for example. Conventional deterministic kinetics methods subsequently describe reactor behavior correctly.

Deterministic studies of reactor behavior are not sufficient in some other situations. When a reactor is started up with a weak neutron source, there is an interval when the multiplication is large but the expected neutron level still is sufficiently low, so that fluctuations in neutron level are large. If fluctuations are large, it is conceivable that the neutron level in the reactor remains low, and perhaps unobserved, while more and more reactivity is introduced in the startup procedure. Eventually, so much reactivity is introduced that the presently rising neutron transient damages the reactor. On the other hand, if the neutron source were strong, fluctuations would be less important and the safety probability would be correspondingly increased.

The analysis of reactor startup as a stochastic process is the primary aim of this section, and its several divisions comprise a rather complete treatment of both the methodology and data required. As already implied, a basic problem lies in the calculation of probabilities that power levels may be different from the levels predicted by standard deterministic kinetics equations. Important nondeterministic features of systems, such as random fission neutron multiplicity and decay of delayed neutron progenitors, are introduced in the theory in Sect. 5.5.B.1. The derivation of a general mathematical formulation, from which required probabilities can be calculated, is accompanied by simple examples to illustrate application of the formalism.

Two methods are then presented for the statistical analysis of startup or other reactor operation. Both are approximate treatments of the forward stochastic equation of Sect. 5.5.B.1. The first method,[71] to be described in Sect. 5.5.B.2, represents a straightforward extension of the already existing deterministic analysis of reactor kinetic behavior. The forward stochastic equation is used to show in some cases, and it is conjectured for other cases, that the distribution in probabilities that various numbers of neutrons are in the reactor can be approximated by a gamma distribution. This distribution is specified by its mean and variance which are computed from equations similar to the usual reactor kinetics equations. In the second method, to be described in Sect. 5.5.B.3, the same probability distribution is computed by a numerical integration

of the forward stochastic equation in a modified form.[72,73] The modification arises from the reasonable simplifying assumption that any chain of prompt fission events occurs in a negligibly short time in a subprompt-critical reactor. The mathematical model which can then be developed for the quasi-independent treatment of prompt chains, and of slower events like reactivity changes and progenitor decay, is also described in those details which are required for numerical application. Many pertinent numerical results are included, as well as a possible extension of the model to improve on the assumption of zero prompt generation time. Results from a set of fast experimental changes in reactivity are compared with the predictions of the methods of both Sects. 5.5.B.2 and 5.5.B.3.

Section 5.5.C examines the effects of feedback on the statistical behavior of a multiplicative system. The preceding discussion neglected, for instance, the interdependence of neutron capture time and the neutron level through the mechanism of a temperature coefficient. A model is developed to include such relations, and its predictions for the perturbation of mean values and dispersions of probability distributions are exhibited.

Section 5.5.D is a detailed discussion of origins of reactor source neutrons, an accurate knowledge of (weak) source strengths being required for computation of reactor fluctuations.

It is possible that study of the reactor as a stochastic process has practical application to reactor phenomena other than start-up. Studies of reactor kinetic behavior usually are based on solution of the time-dependent neutron transport equation which describes the expected (average) number $\langle N(\vec{r},\vec{p})\Delta\vec{r}\Delta_p\rangle$ of neutrons in an element $\Delta\vec{r}\Delta\vec{p}$ of geometric and momentum space. Some terms in the transport equation represent expected rates, e.g., of neutron absorption, and take the form $\langle\Sigma(\vec{r},\vec{p},t)N(\vec{r},\vec{p})\Delta\vec{r}\Delta\vec{p}\rangle$, where $\Sigma(\vec{r},\vec{p},t)$ represents a cross section. In usual derivations of the transport equation an expected rate is approximated by the product of the expected cross section and the expected neutron number $\langle\Sigma\rangle\ \langle N\Delta\vec{r}\Delta\vec{p}\rangle$. In fact, however,

$$\langle\Sigma N\Delta\vec{r}\Delta\vec{p}\rangle = \langle\Sigma\rangle\ \langle N\Delta\vec{r}\Delta\vec{p}\rangle + \text{covariance}\ (\Sigma, N\Delta\vec{r}\Delta\vec{p})$$

and, if Σ is related to $N\Delta\vec{r}\Delta\vec{p}$ by some feedback process, the covariance may not be negligible. It is inferred that the usual deterministic reactor kinetic equations which ignore the covariance terms are not complete. Of interest is an examination of conditions under which the covariance terms can be ignored and, if these conditions are not met, the consequences

of the more general stochastic theory. That the stochastic theory can lead to results which are qualitatively different from the deterministic theory is illustrated in Sect. 5.5.C by examination of the stability of a simple model of a reactor with a positive temperature coefficient.

B. Analysis of Low Source Startup

1. *Derivation of the Forward Stochastic Equation*

D. R. Harris

The multiplicative process occurring in a reactor is a special case of the general multiplicative process which has been studied by statisticians, biologists, and others, and the reactor process can be analyzed by techniques largely developed in other applications. Of these techniques, the most comprehensive is the study of the so-called forward stochastic equation[74, 75] which is derived and discussed in this section. The mathematical description is illustrated by certain simple examples which clarify the physical significance of the analysis and which in some cases have been useful in testing approximate solutions.

It is supposed that the neutrons in the reactor are indistinguishable as by location or velocity and that the probability that any particular neutron produces a fission in the time interval t to $t + \delta t$ is $\delta t / \tau_f(t)$. Similarly, the probability that the neutron is lost during δt by capture or leakage is $\delta t / \tau_c(t)$. In this section feedback is assumed absent, so that the means times τ_f and τ_c do not depend on the number of neutrons which happen to be present. Moreover, the nuclei comprising the reactor and determining τ_f and τ_c are assumed not to be fluctuating for any other reason, such as random thermal motion or a randomly moving control rod, so that $\tau_f(t)$ and $\tau_c(t)$ are given single-valued functions of time. There are present delayed neutron precursors with various decay constants $\lambda_1, \lambda_2, \ldots, \lambda_J$, each precursor decaying to produce just one neutron. The precursors of each type are indistinguishable as by location. Source events, such as spontaneous fissions, occur with a probability $S\,\delta t$ in the interval δt, and in a source event $\nu_p\,(= 0, 1, \ldots)$ prompt neutrons and $\nu_j\,(= 0, 1, \ldots)$ precursors of type j are injected into the reactor with probability $p_s(\nu_p, \nu_1, \ldots, \nu_J)$. It is easy, although cumbersome, to generalize subsequent results to include more than one type of source event. Similarly, only one sort of neutron-induced fission is considered, each fission giving rise to ν_p neutrons and ν_j precursors of type j with probability $p_f(\nu_p, \nu_1 \ldots, \nu_J)$.

The probabilities $P(N, C_1, C_2, \ldots, C_J, t)$ that at time t there are in the reactor $N (= 0, 1, 2, \ldots)$ neutrons and $C_j (= 0, 1, 2, \ldots)$ delayed neutron precursors of type j, $j = 1, 2, \ldots, J$, change in time according to the equations

$$\frac{dP(N, C_1, \ldots, t)}{dt} = \sum_{\nu_p=0}^{\infty} \sum_{\nu_1=0}^{\infty} \cdots \sum_{\nu_J=0}^{\infty} p_f(\nu_p, \nu_1, \ldots, \nu_J)$$

$$\cdot P(N + 1 - \nu_p, C_1 - \nu_1, \ldots, C_J - \nu_J, t)(N + 1 - \nu_p)\tau_f^{-1}$$

$$-(\tau_f^{-1} + \tau_c^{-1}) NP(N, C, t) + \tau_c^{-1} NP(N + 1, C, t)$$

$$+ \sum_{j=1}^{J} \lambda_j C_j [P(N-1, C_1, \ldots, C_j + 1, \ldots, C_J, t) - P(N, C_1, \ldots, t)]$$

$$+ S \sum_{\nu_p=0}^{\infty} \sum_{\nu_1=0}^{\infty} \cdots \sum_{\nu_J=0}^{\infty} p_s(\nu_p, \nu_1, \ldots, \nu_J)$$

$$\cdot P(N - \nu_p, C_1 - \nu_1, \ldots, C_J - \nu_J, t) - SP(N, C_1, \ldots, t) \cdot \qquad \text{Eq. (5.309)}$$

The statement of the problem is completed variously, for example, by specifying values for the probability set at an initial time. The infinite set of Eqs. (5.309) can be rephrased concisely by a transformation from the function $P(N, C_1, \ldots, C_J, t)$ defined over the discrete space of variables $N, C_1, \ldots, C_J$, to the probability generating function

$$G(u, v_1, \ldots, v_J, t) = \sum_{N=0}^{\infty} \sum_{C_1=0}^{\infty} \cdots \sum_{C_J=0}^{\infty} P(N, C_1, \ldots, C_J, t) u^N v_1^{C_1} \cdots v_J^{C_J}$$

Eq. (5.310)

which is defined over the continuous space of the dummy variables $u, v_1, \ldots, v_J$. Multiplying each of Eqs. (5.309) by $u^N v_1^{C_1} \cdots v_J^{C_J}$ and summing over $N, C_1, \ldots,$ and C_J, the forward stochastic equation is obtained:

$$\frac{\partial G}{\partial t}=\left\{\tau_f^{-1}\left[g_f\left(u, v_1, \ldots, v_J\right)-u\right]+\tau_c^{-1}\left[1-u\right]\right\}\frac{\partial G}{\partial u}$$

$$+\sum_{j=1}^{J}\lambda_j\left(u-v_j\right)\frac{\partial G}{\partial v_j}+S\left[g_s\left(u, v_1, \ldots, v_J\right)-1\right]G \quad .$$

Eq. 5.311)

Here g_f and g_s are probability generating functions defined by

$$g_f\left(u, v_1, \ldots, v_J\right) \equiv \sum_{\nu_P=0}^{\infty}\sum_{\nu_1=0}^{\infty}\cdots\sum_{\nu_J=0}^{\infty} p_f\left(\nu_P, \nu_1, \ldots, \nu_J\right) u^{\nu_P} v_1^{\nu_1}\cdots v_J^{\nu_J}$$

Eq. (5.312)

and by an analogous expression for g_S. The forward equation can be derived directly, without recourse to Eqs. (5.309).[74,75] The forward equation is supplemented, for example, by specifying the probability set, and hence $G(u, v_1, \ldots, v_J, t)$, at some initial time. In addition, if the set $P(N, C_1, \ldots, C_J, t)$ represents actual probabilities, then the sum of all probabilities must equal unity, so that the generating function is constrained at all times by

$$G(1, 1, \ldots, 1, t)=\sum_{N=0}^{\infty}\sum_{C_1=0}^{\infty}\cdots\sum_{C_J=0}^{\infty} P(N, C_1, \ldots, C_J, t)=1 \quad .$$

Eq. (5.313)

The probability generating function and the dummy variables $u, v_1, \ldots, v_J$ are introduced as mathematical tools and have no immediate physical significance. On the other hand, the probability generating function involves all the probabilities $P(N, C_1, \ldots, C_J, t)$, and the physically significant probability set can be recovered from it. If the probability generating function is known as a solution to the forward equation, the probability set can be computed from

$$P(N, C_1, \ldots, C_J, t)=\frac{1}{N!\,C_1!\cdots C_J!}\frac{\partial^{N+C_1+\cdots+C_J}}{\partial u^N\,\partial v_1^{C_1}\cdots\partial v_J^{C_J}}G\Bigg|_{u=v_1=\cdots=v_J=0} \quad .$$

Eq. (5.314)

Moments of the probability distribution also can be calculated directly from the probability generating function. The expected number of neutrons, $\bar{N}(t)$, is defined by

$$\bar{N}(t) = \sum_{N=0}^{\infty} \sum_{C_1=0}^{\infty} \cdots \sum_{C_J=0}^{\infty} N P(N, C_1, \ldots, C_J, t) \quad \text{Eq. (5.315a)}$$

and can be calculated from the expression

$$\bar{N}(t) = \left. \frac{\partial G(u, v_1, \ldots, v_J, t)}{\partial u} \right|_{u=v_1=\ldots=v_J=1} . \quad \text{Eq. (5.315b)}$$

The expected number of precursors of j^{th} type, $\bar{C}_j(t)$, is similarly defined and calculated, as are higher moments. The variance of the neutron number, $\sigma_N^2(t)$, and the covariance of the neutron number with the number of precursors of j^{th} type, $\mu_{NC_j}(t)$, are defined and calculated from the probability generating function by the expressions

$$\sigma_N^2(t) \equiv \sum_{N=0}^{\infty} \cdots \sum_{C_J=0}^{\infty} (N-\bar{N})^2 P(N, C_1, \ldots, C_J, t)$$

$$= \left[\frac{\partial^2 G}{\partial u^2} + \frac{\partial G}{\partial u} - \left(\frac{\partial G}{\partial u} \right)^2 \right]_{u=v_1=\ldots=v_J=1} \quad \text{Eq (5.316)}$$

$$\mu_{NC_j}(t) \equiv \sum_{N=0}^{\infty} \cdots \sum_{C_J=0}^{\infty} (N-\bar{N})(C_j - \bar{C}_j) P(N, C_1, \ldots, C_J, t)$$

$$= \left[\frac{\partial^2 G}{\partial u \, \partial v_j} - \frac{\partial G}{\partial u} \frac{\partial G}{\partial v_j} \right]_{u=v_1=\ldots=v_J=1} . \quad \text{Eq (5.317)}$$

In the absence of feedback, the forward equation always is of first order and first degree and can be solved in principle by integration of the associated Lagrange equations. For example, if only neutrons (or bacteria) are present, if in each fission only two offspring are formed, and if no source is present, then ε_f is just u^2 and the forward equation reduces to

$$\frac{\partial G}{\partial t} = \left[\tau_f^{-1}(u^2-u)+\tau_c^{-1}(1-u)\right]\frac{\partial G}{\partial u}\,. \qquad \text{Eq. (5.318)}$$

The associated Lagrange equations are

$$dt + \frac{du}{\tau_f^{-1}(u^2-u)+\tau_c^{-1}(1-u)} = 0 \qquad \text{Eq. (5.319)}$$

with integral

$$\frac{h(t)}{u-1} - \int_0^t \tau_f^{-1}(t')h(t')dt' = \text{constant} \qquad \text{Eq. (5.320)}$$

where $h(t)$ represents $\exp \int_0^t dt'\left[\tau_c^{-1}(t') - \tau_f^{-1}(t')\right]$. The solution to Eq. (5.318) is any function of the left-hand side of Eq. (5.320). The functional relation is determined if the probability distribution $P(N,O)$ is known at time zero; then

$$G(u,t) = \sum_{N=0}^{\infty} P(N,O)\left[1 + \frac{1}{\frac{h(t)}{u-1} - \int_0^t \tau_f^{-1}(t')h(t')dt'}\right]^N.$$

Eq. (5.321)

The general solution is known for this case, the case of binary fission, even when a source is present.[74] A numerical integration of associated Lagrange equations has been adapted for computer calculations (see Sect. 5.5.B.3).

An indirect solution of the forward equation has been developed (see Sect. 5.5.B.2) which proceeds in two steps. First, it is shown that the probability distribution is approximated by a gamma distribution when the multiplication is large, as is usually the case in a reactor application.[71] The gamma distribution is characterized by two parameters which can be chosen as the expected neutron number $\bar{N}(t)$ and the variance $\sigma_N^2(t)$. Second, $\bar{N}(t)$ and $\sigma_N^2(t)$ are calculated from equations which are derived in Sect. 5.5.B.2 from the forward equation and which are similar to the ordinary kinetics equations.

The latter method, which is useful only when the multiplication is large, is complemented by another indirect solution which holds at low multiplication. When the multiplication is low, the probability distribution is approximated by a Poisson

distribution, which is characterized by a single parameter, the easily computed expected number. When fissions are absent, the forward equation reduces to

$$\frac{\partial G}{\partial t} = \tau_c^{-1}(1-u)\frac{\partial G}{\partial u} + S(u-1)G \quad . \qquad \text{Eq. (5.322)}$$

This equation is solved by $G(u,t)$ equal to $\exp[(u-1)\bar{N}(t)]$, the generating function[76] for the Poisson distribution

$$P(N,t) = e^{-\bar{N}}\bar{N}^N/N! \qquad \text{Eq. (5.323)}$$

if and only if the expected number satisfies the usual neutron balance equation

$$\frac{d\bar{N}(t)}{dt} = -\tau_c^{-1}(t)\bar{N}(t) + S(t) \qquad \text{Eq. (5.324)}$$

This result establishes the connection between the analysis of reactor fluctuations and the conventional treatments of counting losses, particle densities, etc., which assume the Poisson distribution. For example, if a Po-Be neutron source is placed in a water bath, neutrons are produced singly in $Be^9(\alpha,n)$ reactions, diffuse independently of one another, and are captured or leak out of the bath without producing descendants. The situation is described by Eqs. (5.322) through (5.324), and the probability set $P(N,t)$, that $N(=0,1,2,\ldots)$ neutrons are in the bath at time t, is a Poisson distribution consistent with the usual assumption.

2. *Approximate Analytic Solution of the Forward Equation: Distribution Method*

D. R. Harris

The first method for analysis of reactor fluctuations, as has been mentioned earlier, provides an extension of deterministic analysis of reactor kinetic behavior. The neutron level which is computed in a usual deterministic transient analysis is identified, in the absence of feedback, with the mean (expected value) of the probability distribution of neutron number. The variance in the number of neutrons present also can be computed by standard techniques from equations which

are similar to the equations for the mean (discussed below in probability distributions in multiplicative process). It is also shown that the probability distribution of neutron level in a stationary process, i.e., one in which the probability distribution is independent of time, approaches a standard gamma distribution in the limit of large multiplication. It is conjectured that the probability distribution of neutron number in a reactor can be approximated by a gamma distribution when the multiplication is large and the process is not varying rapidly with time. A gamma distribution is specified by two parameters, here taken to be the mean and variance which can be computed as outlined above. Finally, useful probabilities can be read from tables of the incomplete gamma function.[77]

This use of the gamma distribution in analysis of highly multiplicative processes is analogous to the use of the normal distribution in describing the cumulative effect of many independent random errors or displacements. Moreover, just as this application of the normal distribution is based on proof of the central limit theorem, which is stated explicitly in the discussion on probability distributions in multiplicative processes, so the present use of the gamma distribution depends on the demonstration in that discussion that the gamma distribution is approached in the limit of large multiplication.

Both the normal and gamma distributions require specification of two parameters, such as the mean and variance. It is fortunate that the gamma distribution, which turns out to be appropriate for highly multiplicative systems, requires no more moments for its specification because computation of higher moments could be very tedious. Equations describing the time behavior of the first and second moments of the neutron and delayed neutron precursor distributions are obtained below. A description is also given of the application of the distribution method to analysis of startup of a reactor with a weak source, and the distribution method is tested later (analysis of experimental transients) by comparison with measurements on the GODIVA reactor of fluctuations in transient development.

A) DESCRIPTION OF METHOD. Early in a startup the expected neutron level is low, so that feedback effects are negligible. In this case, withdrawal of control rods according to some startup schedule increases the reactivity of the reactor in a deterministic fashion, i.e., the reactivity is a known single-valued function of time, $\rho(t)$. The neutron and delayed neutron precursor populations fluctuate, however, and at a time t there is a certain probability $P(N, C_1, \ldots, C_j, t)$ that there are $N(=0,1,2,\ldots)$ neutrons and $C_j(=0,1,2,\ldots)$ precursors of type $j(=1,2,\ldots,J)$ in the reactor. It would seem at first glance that

the safety probability during startup is to be identified with the sum of probabilities that at some time t_H, when the reactivity has attained a large value, the neutron and precursor levels are not low, i.e.,

$$\text{Safety probability} = 1 - \sum_{N \text{ low}} \sum_{C_1 \text{ low}} \cdots \sum_{C_j \text{ low}} P(N, C_1, \ldots, C_j, t_H) \ . \qquad \text{Eq. (5.325)}$$

This identification will in fact be made, although its justification is somewhat involved and is delayed until the end of the section. For the moment it is assumed that reactivity feedback is not operative at times before t_H.

The so-called distribution method permits approximate calculation of the safety probability in the sense of Eq. (5.325). In describing this method it is convenient to treat all delayed neutron precursors as being of a single type with decay constant λ. It is assumed that subsequent to the chosen time t_H, when the reactivity has attained the value $\rho(t_H)$, the neutron and precursor levels vary deterministically, i.e., according to the usual reactor kinetics equations. Thus, the fluctuations in neutron and precursor levels are assumed to be confined to times before t_H. In a particular reactor history, any pair of values of N and C can be realized at time t_H, but subsequent to time t_H a neutron and precursor transient is supposed to develop deterministically from each possible initial pair of values (N, C) realized at time t_H.

This assumption is not strictly valid, but it introduces little error in the present application. Analog simulation or other computation of the deterministic transients including feedback effects then shows that transients initiated at time t_H with certain values of initial neutron and precursor levels (N, C) are acceptable and lead to no reactor damage, while other pairs (N, C) are unacceptable in that they initiate transients which may lead to reactor damage. The acceptable and unacceptable ranges of possible initial values (N, C) are separated by a curve of marginal acceptability in the (N, C) plane. The curve of marginal acceptability is chosen conservatively, taking into account uncertainties in the deterministic transient analysis.

As is illustrated in Fig. 5.41A, transient studies show that the curve of marginal acceptability is roughly parallel to the N axis (only the initial precursor level is significant) when the reactor is subprompt-critical at time t_H, while the curve of marginal acceptability is roughly parallel to the C axis (only the initial neutron level is significant) when the reactor is

superprompt-critical at time t_H (Fig. 5.41B). In either case, the unacceptable cases are contained in the union of two strips in the (N, C) plane, $N < N'$ and $C < C'$, where (N', C') is chosen to be anywhere on or to the right of the curve of marginal acceptability as is illustrated in Fig. 5.41C. The safety probability in the sense of Eq. (5.325) is taken to be unity minus the sum of the probabilities of values (N, C) to the left of the curve of marginal acceptability and, thus, is greater than unity minus the sum of the probabilities of values (N, C) in the two strips $N < N'$ and $C < C'$. This choice is also conservative, i.e.,

$$\text{Safety probability} > 1 - \sum_{N=0}^{N'} P_N(N, t_H) - \sum_{C=0}^{C'} P_C(C, t_H) \qquad \text{Eq. (5.326a)}$$

where $P_N(N, t_H)$ represents the probability that $N(=0,1,2,\dots)$ neutrons are in the reactor at time t_H independent of the number of precursors present, while $P_C(C, t_H)$ is the probability that C precursors are in the reactor at time t_H independent of the neutron number present.

Actually, the neutron and precursor numbers are strongly correlated, so that most probability is associated with pairs (N, C) lying near a certain curve called the curve of regression which passes through the pair of expected values $(\bar{N}(t_H), \bar{C}(t_H))$. If one chooses the pair (N', C') of Eq. (5.326a) to be on the intersection of the curve of regression with the curve of marginal acceptability, then either strip $N < N'$ or $C < C'$ contains most of the dots representing unacceptable pairs (N, C), and the approximation evidently is even better if the strip parallels the curve of marginal acceptability. For example, in the typical case where the reactor is superprompt-critical at time t_H, choose the strip $N < N'$ which roughly parallels the curve of marginal acceptability (Fig. 5.41B). In this case,

$$\text{Safety probability} \approx 1 - \sum_{N=0}^{N'} P_N(N, t_H) \quad . \qquad \text{Eq. (5.326b)}$$

If the reactor is subprompt-critical at the chosen time t_H, then by analogy

$$\text{Safety probability} \approx 1 - \sum_{C=0}^{C'} P_C(C, t_H) \quad . \qquad \text{Eq. (5.326c)}$$

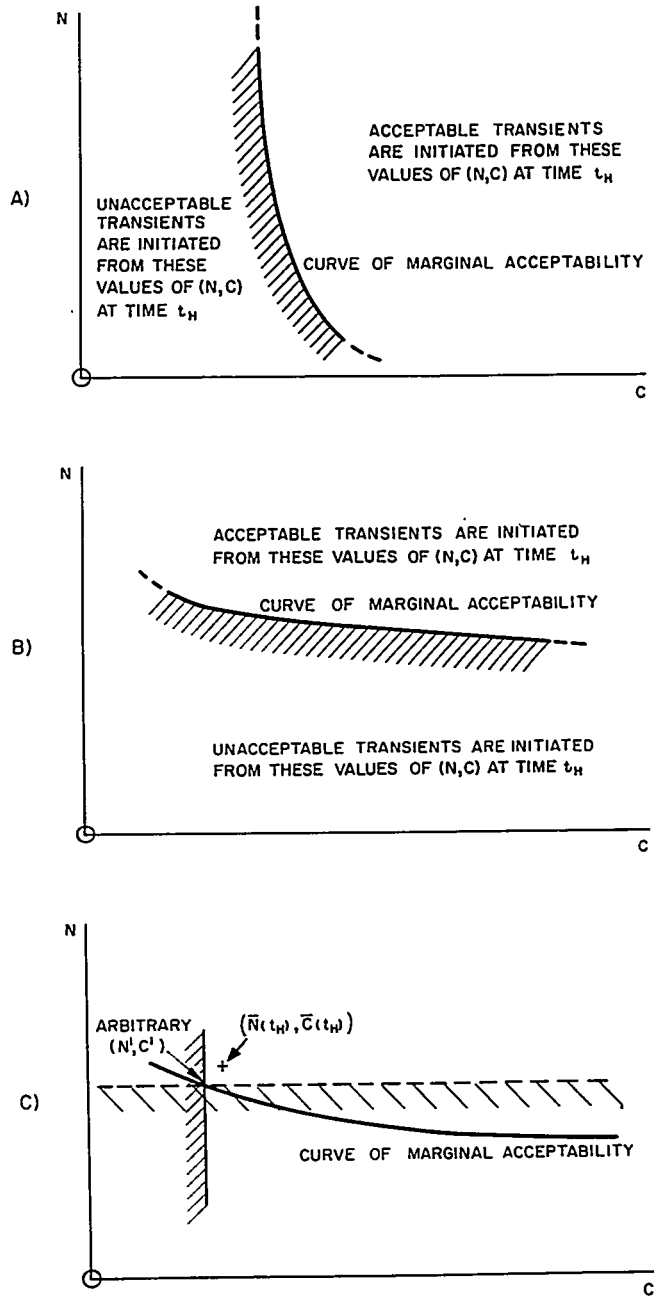

FIGURE 5.41. Curves of Marginal Acceptability: A) Reactor Subprompt-Critical at Time t_H; B) Reactor Superprompt-Crtical at Time t_H; C) Unacceptable Cases Contained by Two Strips $N < N'$ and $C < C'$

The analysis to be presented describes the computation of safety probability in the sense of Eq. (5.326c), but the computation can be applied immediately to determine safety probability in the general, conservative sense of Eq. (5.326a), which is that used in practice.

The distribution method now provides a technique for calculation of $P(N,t)$ or $P(C,t)$, or more generally of the probability distribution of a single variate in any highly multiplicative process. It is proposed in the next section from a study of the forward stochastic equation that at a time such as t_H during a reactor startup, at which time the process parameters are slowly varying, the multiplication is large, and reactivity feedback is assumed inoperative prior to t_H, then the probability distribution $P_N(N,t)$ or $P_C(C,t)$ is approximated by a gamma distribution.[71] More precisely, the probability that N takes on a value in the range $\delta N (\delta N >> 1)$ is approximated by the continuous gamma distribution,[76]

$$P_N(N,t)\,\delta N \approx \frac{r^{-1/r}}{\Gamma(r^{-1})}\left(\frac{N}{\bar{N}(t)}\right)^{r^{-1}-1} e^{-r^{-1}N/\bar{N}(t)}\,\delta\left(\frac{N}{\bar{N}(t)}\right) . \qquad \text{Eq. (5.327)}$$

In evaluating the right-hand side of Eq. (5.327), the reduced variable $N/\bar{N}(t)$ is treated as continuously varying between zero and infinity (this requires $\bar{N}(t) >> 1$, which typically is valid). The gamma distribution is characterized by the relative standard deviation $r(t)$ in Eq. (5.327):

$$r(t) \equiv \frac{\sigma_N(t)}{\bar{N}(t)} . \qquad \text{Eq. (5.328)}$$

The sums of probabilities related to the safety probability by Eqs. (5.326a), (5.326b), or (5.326c) are evaluated as the tabulated integral[77]

$$\int_0^{N'/N} d\xi\, \frac{r^{-1/r}}{\Gamma(r^{-1})}\, \xi^{r^{-1}-1} e^{-r^{-1}\xi} .$$

The expected value $\bar{N}(t)$ and the relative standard deviation $r(t)$ are calculated from equations, analogous to the ordinary kinetic equations, which are derived from the forward stochastic

equation. These equations include the effects of any number of groups of delayed neutrons in moderating fluctuations and provide the expected precursor level and the relative standard deviation of precursor number as well. The latter quantities then permit the evaluation of safety probability, using the gamma distribution. The forward stochastic equation, Eq. (5.311), is differentiated with respect to u, v_1, etc., in turn, and each resulting equation is evaluated at the point $u = 1$, $v_1 = 1$, etc. Derivatives of the generating function G, evaluated at the unit point, are replaced by mean values $\bar{N}(t)$, $\bar{C}_1(t)$, etc., as illustrated in Eq. (5.315b). In the case of a single type of precursors and ignoring precursors from the source, the following first moment equations result:

$$\dot{\bar{N}} = \bar{\nu}_f \tau_f^{-1} (\rho - \beta) \bar{N} + \lambda \bar{C} + S \bar{\nu}_s$$

$$\dot{\bar{C}} = \bar{\nu}_f \tau_f^{-1} \beta \bar{N} - \lambda \bar{C} . \qquad \text{Eq. (5.329)}$$

Here, $\bar{\nu}_f$ and $\bar{\nu}_s$ represent the mean number of neutrons (prompt plus delayed) emitted in fissions and in source events, respectively, while β is the delayed neutron fraction $\bar{\nu}_d/\bar{\nu}_f$, and ρ is the reactivity $(\bar{\nu}_f \tau_f^{-1} - \tau_f^{-1} - \tau_c^{-1}) / \bar{\nu}_f \tau_f^{-1}$.

Next Eq. (5.311) is differentiated twice with respect to u or twice with respect to v_1, or with respect to u and v_1, etc., and each resulting equation is evaluated at the unit point. Again derivatives of G, evaluated at the unit point, are replaced by moments as illustrated in Eqs. (5.316) and (5.317). It is convenient to use as second moments the quantities

$$\mu_{NN}(t) \equiv \sigma_N^2(t) - \bar{N}(t)$$

$$\mu_{CC}(t) \equiv \sigma_C^2(t) - \bar{C}(t) \qquad \text{Eq. (5.330)}$$

and the covariance $\mu_{NC}(t)$ defined in Eq. (5.317). The second moment equations are

$$\dot{\mu}_{NN} = 2\bar{\nu}_f \tau_f^{-1} (\rho - \beta) \mu_{NN} + 2\lambda \mu_{CC} + \tau_f^{-1} \overline{\nu_p (\nu_p - 1)}_f \bar{N} + S \overline{\nu(\nu - 1)}_s$$

$$\dot{\mu}_{NC} = \bar{\nu}_f \tau_f^{-1} \beta \mu_{NN} + \left[\bar{\nu}_f \tau_f^{-1} (\rho - \beta) - \lambda \right] \mu_{NC} + \lambda \mu_{CC} + \tau_f^{-1} \overline{\nu_p \nu_{df}} \bar{N}$$

$$\dot{\mu}_{CC} = 2\bar{\nu}_f \tau_f^{-1} \beta \mu_{NC} - 2\lambda \mu_{CC} + \tau_f^{-1} \overline{\nu_d(\nu_d - 1)}_f \bar{N}.$$

Eq. (5.331)

Equations (5.329) are the usual deterministic reactor kinetic equations without feedback, and the second moment Eqs. (5.331) are similar in form and can be solved by similar methods.

It is necessary now to return to the identification of safety probability, with the probability that the neutron level is not low at a chosen time t_H. For simplicity, the discussion will ignore the presence of delayed neutron precursors. Having classified all neutron levels at time t_H as acceptable or unacceptable, the probability that the neutron level is not less than some value N' at time t is taken to be the safety probability. But, there actually is no physical mechanism to quench fluctuations after a particular time t_H, and in fact a supposedly unacceptable trajectory initiated below N' at time t_H may fluctuate upward and become acceptable, while a supposedly acceptable history initiated above N' at time t_H may fluctuate downward and become unacceptable. Thus, Eq. (5.325) does not have the desired significance in a strict sense. The same ambiguity arises in computation of safety probability by the numerical method described in Sect. 5.5.B.3.

While there is no physical mechanism which can eliminate fluctuations after some particular time t_H, negative reactivity feedback is shown in Sect. 5.5.C to diminish fluctuations. Moreover, even when feedback is ignored, it appears that transients initiated from some particular level tend to develop more deterministically when the initial level is raised. Suppose the initial level is so large that the source can be neglected, and suppose the system is supercritical in the absence of delayed neutrons. Then, from Eqs. (5.329) and (5.331) the relative standard deviation can be computed as a measure of the dispersion of levels eventually obtained. One finds

$$\frac{\sigma_N^2}{\bar{N}^2} \xrightarrow[t \to \infty]{} \left[\frac{\nu(\nu - 1)}{\bar{\nu}\rho} - 1 \right] \frac{1}{N_{(0)}}$$

which is inversely proportional to the initial level $N(0)$.

Thus, there are indications that the choice of safety probability in the sense of Eq. (5.325) is adequate. It should be recalled that the selection of a curve of marginal acceptability and the use of Eq. (5.326a) are both conservative. Conservatism is also applied in determining that a computed safety probability is satisfactory for a practical application. This

conservatism reflects practical considerations as well as the choice of safety probability in the sense of Eq. (5.325) and the uncertainties in computation of probability distributions described below and in Sect. 5.5.B.3.

B) PROBABILITY DISTRIBUTIONS IN MULTIPLICATIVE PROCESSES. The exact probability distribution $P(N,t)$, that just N elements are present at time t in a multiplicative process, is known for only a few special processes. It is of interest to determine approximate forms for the probability distribution, and this is most conveniently accomplished by determining the limiting probability distributions approached when certain process parameters, such as reactivity or source strength, become small or large. One such limiting distribution has been derived in Sect. 5.5.B.1. It was shown there that the Poisson distribution[76] is the limiting distribution attained when multiplication approaches zero, i.e., reactivity ρ approaches $-\infty$,

$$\lim_{\rho \to -\infty} P(N,t) = e^{-\bar{N}} \frac{\bar{N}^N}{N!} \qquad \text{Eq. (5.332)}$$

It is now proposed to show the useful and apparently new results that the limiting distributions attained when the source strength or the multiplication increase without limit are the normal and gamma distributions, respectively.[71] The limiting case of large multiplication is the case of interest in the analysis described in the previous section, startup of a reactor with a weak source.

The central limit theorem as formulated by Levy (Ref. 76, p. 215) states that if $\xi_1, \xi_2, \ldots$ are independent random variables, all having the same probability distribution with finite mean and variance, then the distribution for the variable $\xi_1 + \xi_2 + \ldots + \xi_n$ approaches normality as n increases without limit. Now suppose the random variable ξ_1 is the number of neutrons (taking on particular value $N\,(=0,1,2,\ldots)$) in a reactor when a neutron source of unit strength is present. If the source strength is doubled, $\xi_1 + \xi_2$ is the number of neutrons (again taking on values $N\,(=0,1,2,\ldots)$) in the reactor. The random variables ξ_1 and ξ_2 are independent because the source events are independent and because feedback effects are ignored. As the source strength increases without limit, the random number of neutrons in the reactor is $\xi_1 + \xi_2 + \xi_3 \ldots$, a sum of independent random variables, each with the same probability distribution which approaches normality according to the central limit theorem. While this result can be regarded as a special case of the central limit theorem, it is useful to give an independent proof so as to relate this proof with the proof for the case of large multiplication.

Proofs of the central limit theorem typically utilize properties of the characteristic function

$$\phi(\zeta, t) \equiv \sum_{N=0}^{\infty} P(N,t)\, e^{N\zeta} \qquad \text{Eq. (5.333)}$$

where ζ is pure imaginary, but it is more convenient to use here and in later sections the generalized cumulant function

$$K(\zeta, t) \equiv \ln \sum_{N=0}^{\infty} P(N,t)\, e^{N\zeta} \qquad \text{Eq. (5.334)}$$

where ζ is complex. Assuming that moments of all orders exist, it can be shown that the cumulants $K_j(t)$ which appear in the power series expansion of $K(\zeta, t)$,[76]

$$K(\zeta, t) = \sum_{j=1}^{\infty} \frac{K_j(t)}{j!}\, \zeta^j \qquad \text{Eq. (5.335)}$$

are equal to important moments of the probability distribution, in particular to the mean and variance,

$$\begin{aligned} K_1(t) &= \bar{N}(t) \\ K_2(t) &= \sigma_N^2(t) \\ &\vdots \end{aligned} \qquad \text{Eq. (5.336)}$$

A continuous variable which is normally distributed with mean zero and unit variance has the probability distribution[76]

$$P(N)\,\delta N = \frac{1}{\sqrt{2\pi}}\, e^{-N^2/2}\, \delta N \qquad \text{Eq. (5.337)}$$

with the cumulant function (the sum in Eq. (5.334) is replaced by an integral)

$$K(\zeta) = \frac{\zeta^2}{2} \,. \qquad \text{Eq. (5.338)}$$

The following lemmas now are required and are proved in the references indicated:

Lemma 1. The cumulant function of a sum of independent random variables is the sum of the cumulant functions of each of the variables (Ref. 76, p. 188).

Lemma 2. A necessary and sufficient condition for convergence of a sequence of distributions $P_1(N), P_2(N), \ldots$ to a distribution $P(N)$ is that for every imaginary ζ, the corresponding sequence of cumulant functions $\underline{\overline{K}}_1(\zeta), \underline{\overline{K}}_2(\zeta), \ldots$ converges to a limit $\overline{K}(\zeta)$ which is continuous for the special value $\zeta = 0$ (Ref. 76, p. 96).

These lemmas usually are expressed replacing the probability function $P(N)$ by the so-called distribution function and replacing the cumulant function by the characteristic function. The slight restrictions necessary for the above expressions of the lemmas are satisfied in their application below (Ref. 76, p. 218). The following theorem now is proven.

Theorem 1. Any one-variable multiplicative process without feedback approaches a normal process as the source strength increases without limit.

If the process is not empty then a source of strength $S(t)$, perhaps time-dependent, must have been present at some time. Let $P(N,t)$ represent the probability that N neutrons are in the system at time t, while $p(N,t)$ represents the probability that N neutrons are in the system at time t if the source had the same time dependence as $S(t)$ but strength less by a constant factor C. Let $\underline{\overline{K}}(\zeta,t)$ and $k(\zeta,t)$ be cumulant functions corresponding to $P(N,t)$ and $p(N,t)$, respectively, with cumulants $\underline{\overline{K}}_j(t)$ and $K_j(t)$, respectively. Then, by Lemma 1,

$$\underline{\overline{K}}(\zeta,t) = Ck(\zeta,t) \qquad \text{Eq. (5.339)}$$

or equating each term in the power series expansion of $\underline{\overline{K}}$ and k,

$$\underline{\overline{K}}_j(t) = CK_j(t). \qquad \text{Eq. (5.340)}$$

Let $\underline{\overline{K}}'(\zeta,t)$ represent the cumulant function of the standardized variable which takes on values $(N - \underline{\overline{K}}_1)/\underline{\overline{K}}_2^{1/2}$. That is,

$$\underline{\overline{K}}'(\zeta,t) = \ln \sum_{N=0}^{\infty} P(N,t) \exp\left(\frac{N - \underline{\overline{K}}_1}{\underline{\overline{K}}_2^{1/2}}\right)\zeta. \qquad \text{Eq. (5.341)}$$

Factoring out $\exp(-\underline{\overline{K}}_1\zeta/\underline{\overline{K}}_2^{1/2})$ and rewriting,

$$\underline{\bar{K}}'(\zeta, t) = -\frac{\underline{\bar{K}}_1}{\underline{\bar{K}}_2^{1/2}}\zeta + \underline{\bar{K}}\left(\frac{\zeta}{\underline{\bar{K}}_2^{1/2}}, t\right) . \qquad \text{Eq. (5.342)}$$

Expanding $\underline{\bar{K}}$ in a power series

$$\underline{\bar{K}}'(\zeta, t) = -\frac{\underline{\bar{K}}_1}{\underline{\bar{K}}_2^{1/2}}\zeta + \sum_{j=1}^{\infty}\frac{1}{j!}\underline{\bar{K}}_j\frac{\zeta^j}{\underline{\bar{K}}_2^{j/2}} \qquad \text{Eq. (5.343)}$$

and introducing Eq. (5.340),

$$\underline{\bar{K}}'(\zeta, t) = -C^{1/2}\frac{K_1}{K_2}\zeta + \sum_{j=1}^{\infty}\frac{1}{j!}C^{1-j/2}\frac{K_j}{K_2^{j/2}}\zeta^j$$

$$= \frac{1}{2!}\zeta^2 + \frac{1}{3!}\frac{1}{C^{1/2}}\frac{K_3}{K_2^{3/2}}\zeta^3 + \frac{1}{4!}\frac{1}{C}\frac{K_4}{K_2^2}\zeta^4 + \cdots .$$

Eq. (5.344)

As the source strength increases without limit, $C \to \infty$, and for every ζ

$$\lim_{C\to\infty}\underline{\bar{K}}'(\zeta, t) = \frac{1}{2}\zeta^2 \qquad \text{Eq. (5.345)}$$

which corresponds to a normal probability distribution according to Eq. (5.338). The limiting cumulant function $\zeta^2/2$ is continuous at $\zeta = 0$; therefore, according to Lemma 2, the probability distribution of the standardized variable which takes on values $N - \underline{\bar{K}}_1/\underline{\bar{K}}_2^{1/2}$ approaches normality as the source strength increases without limit. Hence, the random neutron number is in the high source limit distributed normally with mean $\underline{\bar{K}}_1$ and variance $\underline{\bar{K}}_2$.

Theorem 2. The time-independent probability distribution of a variate in a stationary multiplicative process approaches a gamma distribution as the multiplication increases without limit.

The demonstration of this theorem is not at first restricted to the stationary case, in order that some of the expressions below can be used in discussion of the nonstationary case. If

only a single variate, e.g., neutrons or precursors, takes part in a multiplicative process then the forward stochastic equation, Eq. (5.311), becomes

$$\frac{\partial G(u,t)}{\partial t} = \left\{\tau_f^{-1}\left[g_f(u) - u\right] + \tau_c^{-1}\left[1 - u\right]\right\} \frac{\partial G(x,t)}{\partial u} + S\left\{g_s(u) - 1\right\} G(u,t).$$

Eq. (5.346)

If the random variable represents neutron or bacteria number, the meanings of the time-independent process parameters $\tau_f, \tau_c, g_f(u), g_s(u)$, and S are as described in Sect. 5.5.B.1. If the random variable represents precursor number, with the prompt neutron cascade assumed instantaneous (Sect. 5.5.B.3), then $g_f(u) = g_s(u)$ is the probability generating function for the number of precursors formed in a prompt neutron cascade, τ_c^{-1} is zero, and τ_f^{-1} is replaced by the precursor decay constant. In any case, Eq. (5.346) can be transformed to one involving the cumulant function $\bar{K}(\zeta, t)$,

$$\frac{\partial \bar{K}(\zeta,t)}{\partial t} = J(\zeta) \frac{\partial \bar{K}(\zeta,t)}{\partial \zeta} + SH(\zeta) \qquad \text{Eq. (5.347)}$$

using the transformation [see Eq. (5.334)]

$$\bar{K}(\zeta,t) = \ln F(e^{\zeta},t) \ . \qquad \text{Eq. (5.348)}$$

The functions $J(\zeta)$ and $H(\zeta)$ are time-independent here because the process parameters are assumed time-independent. Definitions of J and H and their power series expansions are

$$J(\zeta) \equiv \tau_f^{-1}\left[g_f(e^{\zeta})e^{-\zeta} - 1\right] + \tau_c^{-1}\left[e^{-\zeta} - 1\right] \equiv \sum_{j=1}^{\infty} \frac{1}{j!} J_j \zeta^j$$

$$H(\zeta) \equiv g_s(e^{\zeta}) - 1 \equiv \sum_{j=1}^{\infty} \frac{1}{j!} H_j \zeta^j \ . \qquad \text{Eq. (5.349)}$$

The coefficients J_j and H_j are calculated by expanding the functions in Eqs. (5.349) in Taylor series. J_0 and H_0 vanish, and

$$J_j = \tau_f^{-1}\overline{(\nu_f - 1)^j} + \tau_c^{-1}(-1)^j \; ; \; j = 1, 2, \ldots$$

$$H_j = \overline{\nu_S^j} \qquad \text{Eq. (5.350)}$$

where indicated moments of the number of progeny in a fission $\nu_f = 0, 1, 2 \ldots$ and in a source event $\nu_s = 0, 1, 2, \ldots$ appear. The coefficient J_1 is proportional to the reactivity ρ, viz.,

$$J_1 = \tau_f^{-1}(\bar{\nu}_f - 1) - \tau_c^{-1} = \bar{\nu}_f \, \tau_f^{-1} \, \rho \; .$$

The power series expansions for J, H, and for $\underline{\bar{K}}'$ [Eq. (5.335)] are substituted into Eq. (5.347) and coefficients of ζ^j are equated. Thus, the forward stochastic equation is rephrased as an infinite set of equations in the cumulants $K_j(t)$:

$$\frac{dK_j(t)}{dt} = \sum_{n=1}^{j} \binom{j}{n-1} J_{j-n+1} K_n(t) + SH_j \; ; \qquad j = 1, 2, \ldots$$

Eq. (5.351)

where $\binom{j}{n}$ is the binomial coefficient $j!/n!(j-n)!$.

Let $k_n(t)$ represent the Laplace transform of $K_n(t)$,

$$k_n(p) \equiv \int_0^\infty dt \, e^{-pt} K_n(t)$$

and transform Eqs. (5.351), obtaining

$$\left[p - \binom{j}{1} J_1\right] k_j(p) - \sum_{n=1}^{j-1} \binom{j}{n-1} J_{j-n+1} k_n(p) = SH_j \frac{1}{p} + K_j(0) ; \qquad j = 1, 2, \ldots$$

Eq. (5.352)

with solutions

$$k_1(p) = \frac{SH_1 p^{-1} + K_1(0)}{p - J_1}$$

$$k_2(p) = \frac{SH_2 p^{-1} + K_2(0)}{p - \binom{2}{1} J_1} + \binom{2}{2} J_2 \frac{k_1(p)}{p - \binom{2}{1} J_1}$$

$$\vdots$$

$$k_j(p) = \frac{SH_j p^{-1} + K_j(0)}{p - \binom{j}{1} J_1} + \binom{j}{j} J_j \frac{k_1(p)}{p - \binom{j}{1} J_1}$$

$$+ \ldots + \binom{j}{2} J_2 \frac{k_{j-1}(p)}{p - \binom{j}{1} J_1} \quad . \qquad \text{Eq. (5.353)}$$

$$\vdots$$

Suppose first that the system is subcritical, i.e., ρ and hence J_1 are negative. Inverting the Laplace transforms by the method of residues it is seen that all contributions from poles at $p = \binom{j}{1} J_1$ contain factors $\exp\left\{\binom{j}{1} J_1 t\right\}$ indicating transients which die out after sufficient time. Only the residues from the pole at $p = 0$ then contribute, and in this stationary case

$$K_1 = \frac{SH_1}{-\binom{1}{1} J_1}$$

$$K_2 = \frac{SH_2}{-\binom{2}{1} J_1} + \frac{\binom{2}{2} J_2}{-\binom{2}{1} J_1} K_1$$

$$\vdots$$

$$K_j = \frac{SH_j}{-\binom{j}{1} J_1} + \frac{\binom{j}{j} J_j}{-\binom{j}{1} J_1} K_1 + \ldots + \frac{\binom{j}{2} J_2}{-\binom{j}{1} J_1} K_{j-1} .$$

Eq. (5.354)

As the multiplication increases, ρ and hence J_1 approach 0^-. All terms in Eqs. (5.354) increase, but the last term on the right-hand side of each equation increases most, so that K_j is of the order $0\left[1/(-J_1)^j\right]$. Thus,

$$\lim_{\rho \to 0-} K_j = \frac{\binom{j}{2} J_2}{-\binom{j}{1} J_1} K_{j-1} \; ; \; j = 2, 3, \ldots \quad . \qquad \text{Eq. (5.355)}$$

The parameters J_1 and J_2 can be eliminated by introducing the limiting values of K_1 and K_2, and in the limit

$$K_j = \frac{j-1}{2} \frac{J_2}{-J_1} K_{j-1} = (j-1) \frac{K_2}{K_1} K_{j-1} = (j-1)(j-2) \left(\frac{K_2}{K_1} \right)^2 K_{j-2} = \cdots \quad .$$

Eq. (5.356)

Finally,

$$\lim_{\rho \to 0-} K_j = (j-1)! \left(\frac{K_2}{K_1} \right)^{j-1} K_1 \; ; \quad j = 3, 4, 5, \ldots \quad .$$

Eq. (5.357)

It can be shown that this is the relation among cumulants which is required for the gamma distribution defined by Eq. (5.327) (Ref. 2, p. 126). It has been assumed throughout that the cumulants exist, so it can be inferred that the limiting function (or at least its power series expansion) is that of the gamma distribution and is continuous at $\zeta = 0$. Hence, by Lemma 2, the limiting probability distribution is the gamma, and Theorem 2 has been demonstrated.

Next suppose the system is supercritical, i.e., ρ and hence J_1 are positive. Inverting the transforms, Eqs. (5.353), by residues it is seen that $K_j(t)$ is ultimately dominated by the contribution from the pole $p = \binom{j}{1} J_1$ which contains the factor $\exp \binom{j}{1} J_1 t$ and which increases faster than the contribution from any other pole. It follows that $K_j(t)$ and $(j-1)! \left[K_2(t)/K_1(t) \right]^{j-1} K_1(t)$ have the same time dependence as is required for a gamma distribution. It would appear that if the probability distribution were gamma at a particular time, then at a later time this would still be so.

C) ANALYSIS OF EXPERIMENTAL TRANSIENTS. G. Hansen and T. Wimett of Los Alamos have observed the fluctuation in rise time of 89 transients following assembly of the GODIVA fast reactor to a reactivity of \$0.70.[78] From an initially stationary condition at a reactivity of -\$5, reactivity was inserted in 0.5 sec to -\$0.20 and held at -\$0.20 for 2 sec. Then a transient rod penetrated the GODIVA sphere, bringing the

reactivity to \$0.70, and the time required for the power level to rise to 1.48×10^{11} fissions per second was measured. At power levels of the order of 10^{11} fissions per second, the transients were observed to rise deterministically, i.e., exponentially, and the period was measured for each transient. The scatter in measured periods contributes negligibly to the observed dispersion in rise times. The measurements are shown in Fig. 5.42.

From the moment Eqs. (5.329) and (5.331), the mean and relative standard deviation can be calculated for step reactivity rises. For GODIVA the Rossi-α parameter $\bar{\nu}_f \tau_f^{-1} \beta$ has been measured to be 1.03×10^6 sec^{-1}, and the effective delayed neutron fraction is 0.68. A mean lifetime λ^{-1} for a single group of delayed neutron precursors is chosen so as to yield the measured period, and with these data one computes from the moment equations that the mean power level attained 30 seconds after final assembly should be $7 \times 1.48 \times 10^{11}$ fissions per second, and the calculated relative standard deviation is 1.8. Here the actual reactivity insertion was approximated by a pair of steps. Values of mean and relative standard deviation inferred from the sample of 89 transients are shown in Fig. 5.42. Gamma distributions computed with various combinations of mean relative standard deviation (r.s.d.) are shown in Fig. 5.42 and appear to be consistent with the measurements in view of the rather small sample of 89 members.[71] Much more experimental data must be obtained before significant conclusions may be drawn.

That the sample is small, even for computation of mean and variance, is indicated by the computed values of the estimated errors in inferred mean and r.s.d. which are shown in Fig. 5.42. The computation of these errors illustrates the utility of an assumed probability distribution, in this case the gamma distribution. Given a sample of n members $N_1, N_2, \ldots, N_n$ drawn from a population with mean m and variance σ^2, the unbiased estimates of mean and variance are $\bar{N} = n^{-1} \sum_j N_j$ and $\Sigma^2 = n(n-1)^{-1} \sum_j (N_j - \bar{N})^2$, respectively. The variances of $\bar{N}$ and Σ^2 are measures of error in inference of m and σ^2 from the sample:[76]

$$\operatorname{var} \bar{N} = \frac{\sigma^2}{n} \qquad \text{Eq. (5.358)}$$

$$\operatorname{var} \Sigma^2 = \frac{n^2}{(n-1)^2} \left[\frac{\mu_4 - \sigma^4}{n} - \frac{2(\mu_4 - 2\sigma^4)}{n^2} + \frac{\mu_4 - 3\sigma^4}{n^3} \right]. \qquad \text{Eq. (5.359)}$$

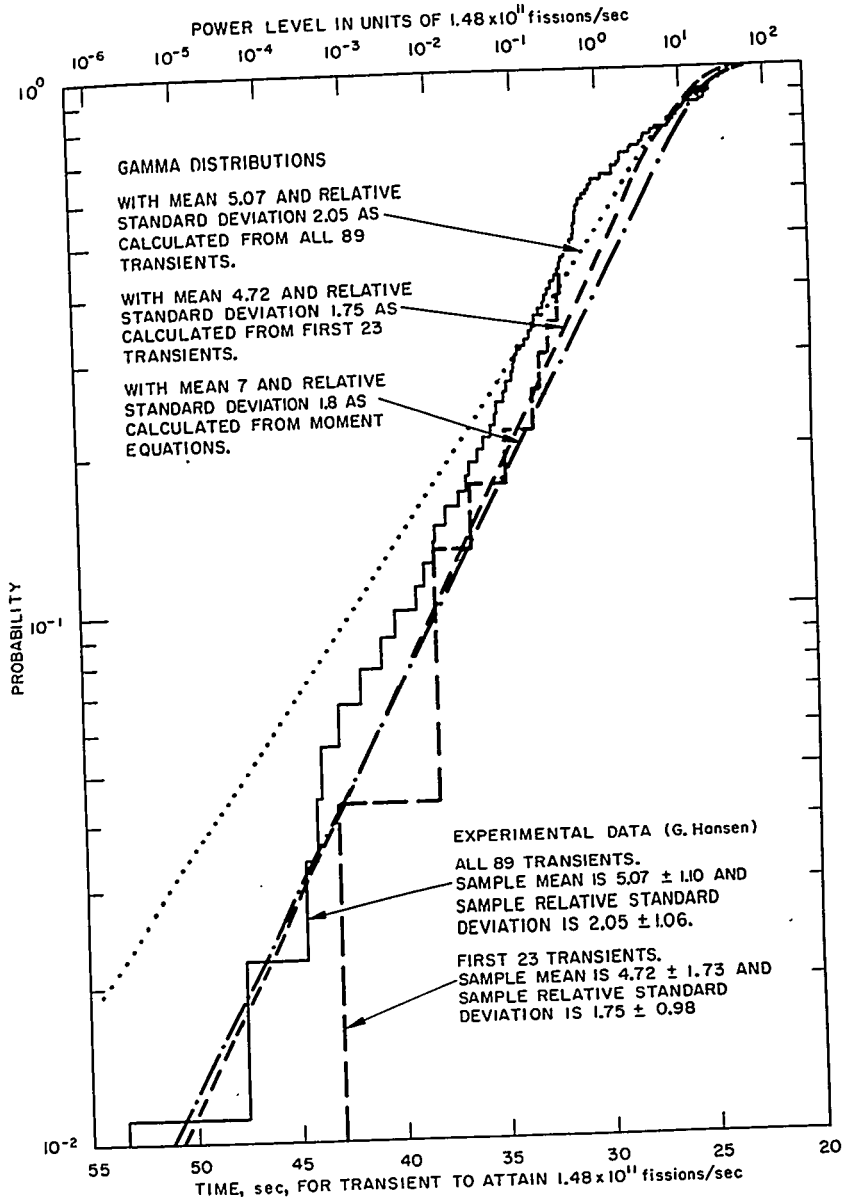

FIGURE 5.42. Probability That Indicated Power Level Is Not Exceeded at a Time 30 Seconds after Step Insertion of $0.7 Reactivity in GODIVA.

For a gamma variate the fourth central moment, μ_4, is $3\sigma^4(1+2\sigma^2/m^2)$, so that Eq. (5.359) becomes

$$\text{var}\,\Sigma^2 = \frac{2\sigma^4}{n-1}\left[1+3\,\frac{\sigma^2}{m^2}\,\frac{n-1}{n}\right]. \qquad \text{Eq. (5.360)}$$

To a first approximation the unknown population moments in Eq. (5.360) can be replaced by their unbiased sample estimates $\bar{N}$ and Σ^2. Finally, an estimate of uncertainty in inference of the r.s.d. σ/m is, ignoring correlation between $\bar{N}$ and Σ,

$$\text{var}\,\frac{\Sigma}{\bar{N}} \simeq \frac{\Sigma^2}{\bar{N}^2}\left[\frac{\text{var}\,\bar{N}}{\bar{N}} + \frac{1}{4}\,\frac{\text{var}\,\Sigma^2}{\Sigma^4}\right]. \qquad \text{Eq. (5.361)}$$

Equations (5.358), (5.360), and (5.361) provide the error estimates shown in Fig. 5.42, e.g., for all 89 transients the sample mean is 5.07 ± 1.10, the latter value being the square root of var $\bar{N}$ from Eq. (5.358).

3. *Numerical Solution of the Forward Equation*

H. Hurwitz, Jr., D.B. MacMillan, J.H. Smith, and M.L. Storm

The second method for analysis of population fluctuations and their possible effects on reactor operation is developed in Sects. 5.5.B.3 and 5.5.B.4. Direct integration of the general forward stochastic equation to determine probability information is quite difficult and time-consuming, so that an approximation to the equation permitting a direct numerical approach has been developed on physical grounds. Following a derivation of the approximate equation, methods are described for its numerical integration, and subsequently the application of numerical results is made to operational problems. Although the general equation has already been obtained in Sect. 5.5.B.1, this separate presentation illustrates a useful way of viewing the connections between prompt and delayed nondeterministic events in a multiplying system so as to simplify the forward stochastic equation.

A) DERIVATION OF ZERO PROMPT LIFETIME EQUATIONS. Restricting attention to situations in which the reactivity does not greatly exceed delayed critical makes possible a considerable simplification of the calculations, namely, the

neglect of the prompt neutron generation time. When the reactivity is close to delayed critical, the insertion of a single source or delayed neutron into the assembly will cause a chain of prompt fissions which will persist for the order of magnitude of 100 generations. The prompt chain duration time is, thus, of order of magnitude 10^{-3} seconds. During this time there will be little change in reactivity, and furthermore the population of delayed neutron progenitors will change almost exclusively by virtue of the fact that additional progenitors may be produced in the course of the prompt fission chain. It is, therefore, legitimate to make the assumption that the prompt fission chain occurs in an infinitesimally short time. This is equivalent to the assumption that the prompt generation time is zero, and it is well known that this assumption does not influence the pile reactor kinetics equations when the reactivity is in the neighborhood of delayed critical.

The procedure is to carry out the statistical analysis on the basis that the elementary event is the chain of prompt fissions caused by a single source or delayed neutron. The statistical quantity to be calculated is the population of delayed neutron progenitors. For convenience, it will be assumed that only one type of progenitor exists, i.e., there is only one delayed neutron group, and its lifetime has the typical value of about 10 seconds. To perform the analysis, it is necessary to know the statistical distribution of the number of progenitors produced in a single prompt fission chain. The distribution can be calculated in terms of the prompt reactivity at the time when the prompt fission chain occurs. It can then be used in the calculation of the progenitor population in very much the same manner that the distribution of neutrons per fission is used to calculate the reactor neutron population when the reactivity exceeds prompt critical. In the following sections there is given a detailed discussion of the manner of carrying out this program.

1) Distribution Function for Delayed Neutron Progenitors in a Single Prompt Neutron Chain. Let $P(n,m,t)$ be the probability that at time t after the introduction of a single neutron there are n neutrons present, and m delayed neutron progenitors have been produced. If the reactor is below prompt critical and the emission of a further neutron from the source or from a delayed neutron progenitor is not considered, $P(n,m,t)$ will approach zero as t becomes infinite unless $n=0$. It is desired to calculate $P(0,m,\infty)$.

The events which change n and m and their probabilities per unit time are as follows:

Event	Result	Probability/unit time
Neutron loss without fission	$n \to n-1$ $m \to m$	$\frac{n}{\tau}\left(1-\frac{k_p}{\nu_p}\right)$
Fission with emission of prompt neutrons and no delayed neutron progenitors	$n \to n+\nu-1$ $(\nu = 0, 1, \ldots.)$ $m \to m$	$\frac{n}{\tau}\frac{k_p}{\nu_p}(1-\beta\nu_p)\,p(\nu)$
Fission with emission of prompt neutrons and one delayed neutron progenitor	$n \to n+\nu-1$ $m \to m+1$	$\frac{n}{\tau}\beta k_p\,p(\nu)$

Here τ is the generation time, k_p is the prompt reactivity, ν_p is the average number of prompt neutrons per fission, $p(\nu)$ is the probability of emission of ν prompt neutrons in a fission, and β is the average ratio of delayed neutrons to prompt neutrons.

The differential equation satisfied by $P(n,m,t)$ is

$$\frac{dP(n,m,t)}{dt} = -\frac{nP(n,m,t)}{\tau} + \frac{n+1}{\tau}\left(1-\frac{k_p}{\nu}\right)P(n+1,m,t)$$

$$+\sum_{\nu=0}^{\infty}\frac{n+1-\nu}{\tau}\frac{k_p}{\nu_p}(1-\beta\nu_p)\,p(\nu)\,P(n+1-\nu,m,t)$$

$$+\sum_{\nu=0}^{\infty}\frac{n+1-\nu}{\tau}\beta k_p\,p(\nu)\,P(n+1-\nu,\,m-1,t)\,. \qquad \text{Eq. (5.362)}$$

Equation (5.362) is to be solved subject to the initial condition

$$P(n,m,0) = \delta_{n,1}\,\delta_{m,0}\,. \qquad \text{Eq. (5.363)}$$

Equation (5.362) may be most conveniently solved by using the generating function $G(u,v,t)$, which is defined in terms of the dummy variables u and v by

$$G(u,v,t) = \sum_{n,m=0}^{\infty} P(n,m,t)\,u^n v^m\,. \qquad \text{Eq. (5.364)}$$

It follows from Eqs. (5.363) and (5.364) that

$$G(1,1,t) = 1;$$

$$\left.\frac{\partial G}{\partial u}\right]_{u,\,v=1} = \bar{n}; \qquad \left.\frac{\partial G}{\partial v}\right]_{u,\,v=1} = \bar{m} \quad . \qquad \text{Eq. (5.365)}$$

The auxiliary generating function $g(u)$ is defined by

$$g(u) = \sum p(\nu)\, u^{\nu} \qquad \text{Eq. (5.366)}$$

which implies

$$g(1) = 1$$

$$\left.\frac{dg}{du}\right]_{1} = \sum \nu p(\nu) = \nu_p \, . \qquad \text{Eq. (5.367)}$$

If Eq. (5.362) is multiplied by $u^n v^m$ and summed over n and m, there is obtained, using Eqs. (5.364) and (5.366),

$$\frac{\partial G}{\partial t} = -\frac{u}{\tau}\frac{\partial G}{\partial u} + \frac{1}{\tau}\left(1 - \frac{k_p}{\nu_p}\right)\frac{\partial G}{\partial u} + \frac{k_p}{\nu_p}\frac{(1-\beta\nu_p)}{\tau} g(u)\frac{\partial G}{\partial u}$$

$$+ \frac{\beta k_p}{\tau}\, g(u)\, v\, \frac{\partial G}{\partial u} \quad . \qquad \text{Eq. (5.368)}$$

Note that Eq. (5.368) is a special case of the general forward equation [Eq. (5.311)].

From Eq. (5.363) the boundary condition is

$$G(u,v,0) = u \, . \qquad \text{Eq. (5.369)}$$

To solve Eq. (5.368) it is convenient to use the method of Laplace transforms.

Let

$$\mathcal{G}(u,v,\eta) = \int_0^{\infty} e^{-\eta t}\, G(u,v,t)\, dt \, . \qquad \text{Eq. (5.370)}$$

Then, from Eqs. (5.368) and (5.369),

$$\eta \mathcal{G} = -\frac{u}{\tau}\frac{\partial \mathcal{G}}{\partial u} + \frac{1}{\tau}\left(1 - \frac{k_p}{\nu_p}\right)\frac{\partial \mathcal{G}}{\partial u} + \frac{k_p}{\nu_p}\frac{\left(1-\beta\nu_p\right)}{\tau} g(u)\frac{\partial \mathcal{G}}{\partial u} + \frac{\beta k_p}{\tau} g(u)\, v \frac{\partial \mathcal{G}}{\partial u} + u\,.$$

Eq. (5.371)

From Eqs. (5.365) and (5.370)

$$\mathcal{G}(1,1,\eta) = 1/\eta\,. \qquad \text{Eq. (5.372)}$$

If Eq. (5.371) is differentiated with respect to u, for u and v equal to unity,

$$\left.\frac{\partial \mathcal{G}}{\partial u}\right]_{1,1} = \frac{1}{\eta + \dfrac{1-k_p}{\tau}}\,. \qquad \text{Eq. (5.373)}$$

Since the left side of this equation is the Laplace transformation of $\bar{n}(t)$, it is concluded that

$$\bar{n}(t) = \exp\left(-\frac{1-k_p}{\tau}\, t\right)\,. \qquad \text{Eq. (5.374)}$$

Similarly, differentiating Eq. (5.371) with respect to v gives, for u and v equal to unity,

$$\eta \left.\frac{\partial \mathcal{G}}{\partial v}\right]_{u,v=1} = \frac{\beta k_p}{\tau}\left.\frac{\partial \mathcal{G}}{\partial u}\right]_{u,v=1} \qquad \text{Eq. (5.375)}$$

or

$$\frac{d\bar{m}}{dt} = \frac{\beta k_p}{\tau}\,\bar{n}. \qquad \text{Eq. (5.376)}$$

Equations (5.374) and (5.376) express the results which would be obtained by the application of the standard reactor kinetics equations to the problem under consideration. (This could have been seen earlier by considering the partial derivatives of Eq. (5.368) with respect to u and v at $u = v = 1$.)

From Eq. (5.376),

$$\bar{m}\Big]_{t=\infty} = \frac{\beta k_p}{1-k_p} \cdot \qquad \text{Eq. (5.377)}$$

Thus, if k_p is equal to $1/1+\beta)$, $\bar{m}$ will be equal to unity, i.e., the prompt fission chain resulting from a single neutron will produce on the average one delayed neutron progenitor, so that the reactor is just critical when delayed neutrons are considered.

From Eqs. (5.364) and (5.370) together with the fact that $P(n,m,t)$ approaches zero if n is greater than zero but remains finite if n is equal to zero,

$$\lim_{\eta \to 0} \mathcal{G}(u,v,\eta) \approx \frac{\mathcal{G}_1^{(\nu)}}{\eta} + \mathcal{G}_2(u,v) . \qquad \text{Eq. (5.378)}$$

Furthermore,

$$\mathcal{G}_1(1) = 1$$

$$\mathcal{G}_2(1,1) = 0$$

$$\mathcal{G}_1(v) = \sum_{m=0}^{\infty} P(0,m,\infty)\, v^m . \qquad \text{Eq. (5.379)}$$

Equation (5.371) becomes

$$\mathcal{G}_1(0,v) = \frac{1}{\tau}\left[1 - \frac{k_p}{\nu_p} - u + \frac{k_p}{\nu_p}\left(1-\beta\nu_p\right)\; g(u) + \beta k_p\, g(u)\, v\right]\frac{\partial \mathcal{G}_2}{\partial u} + u . \qquad \text{Eq. (5.380)}$$

Now, for each value of v, the coefficient of $\partial\mathcal{G}_2/\partial u$ becomes zero for a certain value of u. Since G, and hence $\mathcal{G}_2$, has no singularities for u and v between zero and one,

$$\mathcal{G}_1(v) = u_1(v) \qquad \text{Eq. (5.381)}$$

where $u_1(v)$ is defined by the relationship

$$\left[1 - \frac{k_p}{\nu_p} - u + \frac{k_p}{\nu_p}\left(1-\beta\nu_p\right)\; g(u) + \beta k_p\, g(u)\, v\right] = 0 . \qquad \text{Eq. (5.382)}$$

In the neighborhood of $u = v = 1$, Eq. (5.382) becomes

$$\left[-1 + k_p \left(1 - \beta\nu_p\right) + \beta k_p \nu_p \right] \delta u_1 + \beta k_p \, \delta v = 0 .$$

Eq. (5.383)

Therefore,

$$\frac{\delta u}{\delta v} = \left[\frac{d \, \mathcal{G}_1(v)}{dv} \right]_{v=1} = \frac{\beta k_p}{1 - k_p} .$$

Eq. (5.384)

By Eq. (5.380) this is the average value of m at infinite time and is, thus, in agreement with Eq. (5.377).

Another check on Eqs. (5.381) and (5.382) is furnished by a consideration of $P(0,0,\infty)$ which is the probability that no delayed neutron progenitors are produced in the chain of fissions. This is the value of $\mathcal{G}_1(v)$ when v is zero and, accordingly, is the root of the equation

$$\left[1 - \frac{k_p}{\nu_p} - u_1 + \frac{k_p}{\nu_p} \left(1 - \beta\nu_p\right) g\left(u_1\right) \right] = 0 .$$

Eq. (5.385)

It is possible to derive this same relationship for $P(0,0,\infty)$, (abbreviated by the letter Z) in the following fashion.

Consider that a neutron has been introduced in the assembly and ask how it could fail to produce a delayed neutron progenitor. The possibilities are as follows:

Possibility	Probability
No fissions are produced	$1 - \frac{k_p}{\nu_p}$
A fission is produced, but no progenitors arise, and furthermore none of the ν neutrons which are emitted in the fission produce progenitors	$\frac{k_p}{\nu_p}\left(1 - \beta\nu_p\right) \Sigma_{p(\nu)} Z^{\nu}$

Hence, the equation for Z is

$$Z = 1 - \frac{k_p}{\nu_p} + \frac{k_p}{\nu_p}\left(1 - \beta\nu_p\right) g(Z) \ . \qquad \text{Eq. (5.386)}$$

This equation agrees exactly with Eq. (5.385).

It is in principle possible to calculate as many of the numbers $P(0, m, \infty)$ as desired by expanding the solution of Eq. (5.382) in a power series in ν. Thus, for example,

$$P(0, 1, \infty) = \frac{\beta k_p g(Z)}{\left[1 - \frac{k_p}{\nu_p}\left(1 - \beta\nu_p\right) g'(Z)\right]} \ . \qquad \text{Eq. (5.387)}$$

In performing further calculations it is generally more informative to work with the moments of the probability distribution $P(0, m, \infty)$. These may be obtained by expanding the solution of Eq. (5.382) around $\nu = 1$ rather than $\nu = 0$. For instance,

$$\overline{m(m-1)} = \left.\frac{d^2 \mathcal{G}_1}{d\nu^2}\right]_{\nu=1} = \frac{1}{\nu_p}\left(\frac{k_p \beta}{1-k_p}\right)^2 \frac{k_p\, \overline{\nu(\nu-1)} + 2\nu_p^2\left(1-k_p\right)}{1-k_p} \ .$$

Eq. (5.388)

Note that this involved $\left.\frac{d^2 g}{du^2}\right]_{u=1}$ which is equal to $\overline{\nu(\nu-1)}$. In a similar fashion the higher values of m will involve higher moments of ν.

2) Behavior of Delayed Neutrons in a Startup. The above calculation must now be repeated, in essence, with the function $\mathcal{G}_1(\nu)$ playing the role of $g(u)$ in Eq. (5.368). The calculation is simpler than the previous calculation in that it is necessary to consider only the population of delayed neutron progenitors. On the other hand, it is necessary to take into account the fact that the distribution of delayed neutron progenitors from a single prompt neutron charge depends on the value of prompt reactivity which varies with time.

Let $P_d(m, t)$ be the distribution function for the number of delayed neutron progenitors, m, at time, t, and let $P_d(m,t) = P(0,m,\infty)$ be the distribution of delayed neutron progenitors produced in a prompt neutron chain which occurs at time t. (It is assumed that the time duration of such a chain is small compared to the time in which the prompt reactivity changes appreciably and

delayed neutron progenitors decay.) If all delayed neutron progenitors have the same decay constant, λ, the equation for $P_d(m,t)$ is

$$\frac{dP_d(m,t)}{dt} = -\lambda m P_d(m,t) + \lambda \sum_{n=0}^{\infty} (m-n+1)\, p_d(n,t)\, P_d(m-n+1,t)$$

$$- s\, P_d(m,t) + s \sum_{n=0}^{\infty} p_d(n,t)\, P_d(m-n,t) \; ; \qquad \text{Eq. (5.389)}$$

s is the rate at which prompt neutrons are introduced in the reactor by mechanisms other than delayed neutrons. As before, introduce generating functions defined by

$$G_d(v,t) = \Sigma P_d(m,t)\, v^m$$

$$g_d(v,t) = \Sigma p_d(m,t)\, v^m = \mathcal{G}_1(v)\Big]_{k_p = k_p(t)} \; . \qquad \text{Eq. (5.390)}$$

Thus,

$$G_d(1,t) = g_d(1,t) = 1 \; . \qquad \text{Eq. (5.391)}$$

If Eq. (5.389) is multiplied by v^m, one finds

$$\frac{\partial G_d(v,t)}{\partial t} = \lambda (g_d(v,t) - v) \frac{\partial G_d(v,t)}{\partial v} + s(g_d(v,t) - 1)\, G_d(v,t) \; .$$

Eq. (5.392)

As with Eq. (5.368), this is a special case of the forward equation [Eq. (5.311)]. In both Eqs. (5.368) and (5.392), the restriction to one type of delayed event reduces the number of variables.

If $g_d(v,t)$ were independent of time, there would exist a stationary solution of Eq. (5.392) given by

$$G_d(v,t) = \exp\left[-\frac{s}{\lambda} \int_v^1 \frac{\left(-g_d(v',t) + 1\right)}{\left(g_d(v',t) - v'\right)} dv' \right] \; . \qquad \text{Eq. (5.393)}$$

This solution can be used as the initial condition for a problem in which the reactivity is held constant for a long time

and then caused to increase. If the initial reactivity is initially far below delayed critical, $P_d(m, t)$ will initially be unity for m equal to zero, and zero for m greater than zero, so that $g_d(v, t)$ is equal to unity. Then, by Eq. (5.393) $G_d(v,t)$ will also be equal to unity, which means that $P_d(m, t)$ is unity for m equal to zero, and zero otherwise.

If $g_d(v, t)$ has a sufficiently simple dependence on t, it may be possible to obtain useful analytic solutions to Eq. (5.392).* Alternatively, it may be possible numerically to integrate Eq. (5.392) with respect to time. If one starts well below delayed critical, $G_d(v, t)$ will initially be equal to unity. As the reactivity rises, $G_d(v, t)$ will decrease toward zero for small v (i.e., the probability that m is a small number will be small). When the reactivity is above delayed critical, $G_d(v, t)$ will become increasingly steep in the neighborhood of $v = 1$, i.e., the entire increase in $G(v, t)$ from a small number, when v is zero, to unity, when v is unity, will take place for v slightly less than unity. Thus, the behavior of $G_d(v, t)$ in the neighborhood of $v =$ unity is crucial in determining the behavior of delayed neutron progenitor concentration and, hence, power in a reactor startup.

Another way of treating Eq. (5.392) is to consider successively higher derivatives of this equation with respect to v at $v = 1$. Since the coefficient of $\partial G_d/\partial v$ in this equation vanishes when v is unity, it is possible by this method to obtain a series of linear differential equations in time for the quantities

$$\frac{\partial^n G_d(v, t)}{\partial v^n}$$

These equations may be integrated successively starting with $n = 1$ and working to successively higher values of n. For $n = 1$ (i.e., by differentiating Eq. (5.392) once with respect to v) the standard reactor kinetic equation is obtained:

$$\frac{d}{dt}\bar{m} = -\lambda\left(\frac{-\beta k_p}{1-k_p} + 1\right)\bar{m} + s\,\frac{\beta k_p}{1-k_p}\,. \qquad \text{Eq. (5.394)}$$

The relations of Eq. (5.377),

* W. B. Jordan (KAPL) and G. I. Bell (LASL) have both obtained approximate solutions for generating functions and probabilities for special problems. Their results agree fairly well with the more general studies to be described later, and parts of their work (especially that of W. B. Jordan) have been very useful in the development and checking of the more general numerical approach.

$$\bar{m}(t) = \left.\frac{\partial G_d}{\partial v}\right]_{v=1}$$

and

$$\left.\frac{\partial g_d}{\partial v}\right]_{v=1} = \frac{\beta k_p}{1-k_p} \qquad \text{Eq. (5.395)}$$

have been used to establish Eq. (5.394). Equations for the higher moments of m can be obtained in a similar fashion.

One somewhat useful calculation is that of the probability that a single delayed progenitor will lead to a diverging chain of fissions if the reactivity is held at a value between delayed and prompt critical. This probability can be calculated by elementary methods, but it is instructive to proceed by means of Eq. (5.392). Consider the case in which $g_d(v,t)$ is constant and s is zero. The initial condition is that $P(m,0)$ is equal to $\delta_{m,0}$ or

$$G_d(v,0) = v \quad . \qquad \text{Eq. (5.396)}$$

The method of Laplace transforms yields

$$\eta \mathcal{G}_d(v,\eta) = \lambda\left(g_d(v) - v\right)\frac{\partial \mathcal{G}_d(v,\eta)}{\partial v_1} + v \quad . \qquad \text{Eq. (5.397)}$$

By analogy to Eq. (5.378),

$$\lim_{\eta \to 0} \mathcal{G}_d(v,\eta) = \frac{\mathcal{G}_{d_1}(v)}{\eta} + \mathcal{G}_{d_2}(v) \quad . \qquad \text{Eq. (5.398)}$$

At infinite time, m is either zero or infinite. Hence,

$$\mathcal{G}_{d_1}(v) = P(0,\infty) \quad . \qquad \text{Eq. (5.399)}$$

By an argument similar to that leading to Eq. (5.381),

$$P(0,\infty) = v^{\dagger} \qquad \text{Eq. (5.400)}$$

where

$$g_d(v^\dagger) - v^\dagger = 0 \quad . \qquad \text{Eq. (5.401)}$$

This is the result which would be obtained by an argument similar to that leading to Eq. (5.386).

B) NUMERICAL SOLUTION OF ZERO LIFETIME EQUATIONS.

1) Computation of Probabilities. As described earlier in this chapter, a system may be judged safe if it is sufficiently unlikely that a power level be anomalously low in the presence of a high reactivity and short period. If $m_1(t)$ is a specific precursor population,

$$Q\left[m_1, t\right] = \sum_{m=0}^{m_1-1} P_d(m, t) \qquad \text{Eq. (5.402)}$$

is the probability that, whatever the population, it is less than m_1. Evidently, Q should be small for m_1 somewhat less than the value predicted by usual deterministic techniques. These ideas will be made more quantitative in later presentation of results. From the definition of the generating function [Eq. (5.390)],

$$Q = \sum_{m=0}^{m_1-1} \frac{1}{m!} \left[\frac{\partial^m G_d(v, t)}{\partial v^m} \right]_{v=0} \qquad \text{Eq. (5.403)}$$

and from the theory of residues, this is also

$$Q = \frac{1}{2\pi i} \oint G_d(z, t) \sum_{0}^{m_1-1} z^{-m-1} dz \qquad \text{Eq. (5.404)}$$

where the integration contour lies within the unit circle. When this finite sum is evaluated, and use is made of the fact that $G_d/(1-z)$ is analytic inside the unit circle, there results

$$Q = \frac{1}{2\pi i} \oint \frac{G_d(z, t)}{z^{m_1}(1-z)} \, dz \quad . \qquad \text{Eq. (5.405)}$$

The integrand in Eq. (5.405) has a saddle point on the real axis between 0 and 1, and when the method of steepest descents is applied to obtain Q, it is found that

$$Q = \frac{1}{\sqrt{2\pi\sigma_o}} \frac{v_o^{-m_1} G_d(v_o, t)}{1 - v_o} \qquad \text{Eq. (5.406)}$$

with

$$\sigma_o = \frac{\partial^2}{\partial v^2} \ln \frac{v^{-m_1} G_d(v, t)}{1 - v}\Bigg]_{v = v_o} \qquad \text{Eq. (5.407)}$$

and v_o satisfies

$$\frac{\partial}{\partial v} \ln \frac{v^{-m_1} G_d(v, t)}{1 - v}\Bigg]_{v = v_o} = 0$$

or

$$\frac{m_1}{v_o} = \frac{1}{1 - v_o} + \frac{\partial \ln G_d}{\partial v}\Bigg]_{v = v_o} \qquad \text{Eq. (5.408)}$$

Thus, to evaluate the probability for the occurrence of anomalous levels (far from the expected value) in the course of reactor operation, it is necessary to have detailed knowledge of the generating function. However, it is still much simpler to determine the behavior of G_d than to work directly with the original coupled differential equations for the many individual probabilities $P_d(m, t)$ typically required.

Note that the only cases in which the method of steepest descent must fail, in principle, of application are those for which Q is zero. From the power series definition of G_d, it follows that unless $P_d(m, t) = 0$ for all $m \leq m_1$, the integrand in Eq. (5.405) has singularities as $v \to 0^+$ and $v = 1$. With the exception noted, there is a minimum on the real axis in $(0, 1)$. Furthermore, saddle points of interest will be expected to be located near $v = 1$. (The monotonic function G_d is small for v near zero, rising rapidly to unity only as $v \to 1$. The function $v^{-m_1}(1-v)^{-1}$ has a minimum at $v = \frac{m_1}{1 + m_1} \to 1 - \frac{1}{m_1}$ for $m_1 >> 1$. This point will be considered in more detail later.) In anticipation of the importance of a range of v close to 1, there is made the substitution

$$x = -\ln(1 - v) \qquad \text{Eq. (5.409)}$$

or

$$v = 1 - e^{-x}$$

to extend the numerical range of a computational parameter.

The accuracy of the method of steepest descents in determining Q can be established for certain generating functions. For a probability distribution of the Poisson type, for example, with

$$P(m) = \frac{e^{-\bar{m}}(\bar{m})^m}{m!}$$

and

$$G(v, \bar{m}) = e^{-\bar{m}(1-v)}$$

the exact value of $Q(m_1)$ is obtained from Eq. (5.362) as

$$Q = 1 - \frac{\gamma(m_1, \bar{m})}{\Gamma(m_1)}$$

where γ and Γ are, respectively, the incomplete and complete gamma functions. Two cases can be examined readily: $\bar{m} >> m_1$ and $m_1 >> \bar{m}$. The leading terms in developments in $m_1/\bar{m}$ and $\bar{m}/m_1$ are

$$Q = \begin{cases} \dfrac{1}{\bar{m}} \sqrt{\dfrac{m_1}{2\pi}}\, e^{-(\bar{m} - m_1)} \left(\dfrac{\bar{m}}{m_1}\right)^{m_1}, & \bar{m} >> m_1 \\ 1, & m_1 >> \bar{m} \end{cases}.$$

The steepest descents technique yields, to the same orders,

$$Q = \begin{cases} \dfrac{1}{\bar{m}} \sqrt{\dfrac{m_1}{2\pi}}\, e^{-(\bar{m} - m_1)} \left(\dfrac{\bar{m}}{m_1}\right)^{m_1}, & \bar{m} >> m_1 \\ e/\sqrt{2\pi} = 1.08 \end{cases}.$$

While this Poisson generating function does not have the same shape in detail as that for the present physical problem, the above results lend confidence to the use of steepest descents in this probability determination.

Another method of obtaining a value of $Q_{m_1} = \sum_{m < m_1} P(m, t)$ was proposed by Hurwitz.[72] It is derived by the use of Laplace transform techniques, leading to the expression of Q_{m_1} as an integral which is (as in the method described above) evaluated

by the method of steepest descents. It was used in the early stages of these studies, until the residue method was developed and was found to be superior. One can compute for each of the two methods a second term in the steepest descents expansion, involving $\partial^3 G_d/\partial x^3$ and $\partial^4 G_d/\partial x^4$. The second term becomes large compared to the first term for the Laplace transform method when $\bar{m}/m_1$ is small (i.e., less than or not much greater than one) and when s is small (e.g., $s/\lambda = 250$). In all cases that have been computed to date by the residue method, the second term has been small (less than 8 percent of the first term). In all cases where the second terms are small for both methods, they give essentially identical results. The two methods are different enough in derivation, so that this fact lends credibility to the calculations. When the second term is large for the Laplace transform method, the results of the two methods differ.

2) The Generating Function Equation. It has been shown that the generating function, G_d, satisfies

$$\frac{\partial G_d(v,t)}{\partial t} - \lambda\left[g_d(v,t) - v\right]\frac{\partial G_d}{\partial v} = s\left(g_d - 1\right)G_d \quad . \qquad \text{Eq. (5.410)}$$

The substitution of

$$L = -\ln G \qquad \text{Eq. (5.411)}$$

$$V = \lambda e^x\left[1 - g_d - e^{-x}\right]$$

$$S = s\left(1 - g_d\right)$$

$$v = 1 - e^{-x}$$

into Eq. (5.410) leads to

$$\frac{\partial L}{\partial t} + V\frac{\partial L}{\partial x} = \frac{DL}{Dt} = S \qquad \text{Eq. (5.412)}$$

defining the operator D/Dt; λ, s, and g_d have all been previously defined in terms of constant or time-dependent reactor parameters. Use of L amplifies the numerical range of G encountered when $v \approx 1$.

In terms of the large variable x, the quantities, L, V, and S have the expansions

$$L = e^{-x}\bar{m} - \frac{e^{-2x}}{2}\left[\overline{m(m-1)} - \bar{m}^2\right] + \cdots$$

$$V = \lambda\left[\frac{\beta k_p}{1-k_p} - 1\right] - \frac{e^{-x}}{2}\left[\frac{d^2\mathcal{G}_1}{dv^2}\right]_{v=1} + \cdots$$

$$S = \frac{e^{-x} s \beta k_p}{1-k_p} - \frac{e^{-2x} s}{2}\left[\frac{d^2\mathcal{G}_1}{dv^2}\right]_{v=1} \qquad \text{Eq. (5.413)}$$

where $\left[d^2\mathcal{G}_1/dv^2\right]_{v=1}$ is given by Eq. (5.388). These will be useful in later developments.

If now one defines a characteristic curve in (x, t) space as a curve along which

$$\frac{dx}{dt} = V(x, t) , \qquad \text{Eq. (5.414)}$$

then one observes that ordinary differentiation with respect to time along such a curve is equivalent to application of the operator D/Dt defined in Eq. (5.412), so that $L(x, t)$ satisfies an ordinary differential equation [Eq. (5.412)] along the curve and may be computed by techniques used for solving ordinary differential equations. Although introduction of the characteristic curves appears to be artificial in terms of the underlying physical problem, it will be seen that both conceptual and numerical advantages accrue from consideration of the behavior of the functions along such curves.

To make an evaluation of m_1 and the corresponding Q, values of L, $\partial L/\partial x$, and $\partial^2 L/\partial x^2$ must be known at a point in (x, t) space. The latter two quantities also satisfy ordinary differential equations along the characteristic curves:

$$\frac{D}{Dt}\left(\frac{\partial L}{\partial x}\right) + \frac{\partial V}{\partial x}\frac{\partial L}{\partial x} = \frac{\partial S}{\partial x} \qquad \text{Eq. (5.415)}$$

$$\frac{D}{Dt}\left(\frac{\partial^2 L}{\partial x^2}\right) + 2\frac{\partial V}{\partial x}\frac{\partial^2 L}{\partial x^2} = \frac{\partial^2 S}{\partial x^2} - \frac{\partial L}{\partial x}\frac{\partial^2 V}{\partial x^2} . \qquad \text{Eq. (5.416)}$$

These equations are derived by operating on Eq. (5.412) with $\partial/\partial x$ and $\partial^2/\partial x^2$, respectively, followed by interchange of $\partial/\partial x$ and $\partial/\partial t$ where necessary.

The behavior of m_1 and Q on these special paths will now be examined for large x. As noted previously, saddle points of interest lie near $v=1$ and, hence, correspond to large x. In numerical results to be considered later, the smallest value of x of interest is about 5 and, hence, $e^x >> 1$. From Eqs. (5.408), (5.409), and (5.411),

$$m_1 = \left(e^x - 1\right)\left(1 - \frac{\partial L}{\partial x}\right) . \qquad \text{Eq. (5.417)}$$

Operating on both sides of Eq. (5.417) with D/Dt gives, in conjunction with Eqs. (5.414) and (5.415),

$$\frac{Dm_1}{Dt} = Ve^x\left(1 - \frac{\partial L}{\partial x}\right) - \left(e^x - 1\right)\frac{D}{Dt}\left(\frac{\partial L}{\partial x}\right)$$

$$= Ve^x\left(1 - \frac{\partial L}{\partial x}\right) - \left(e^x - 1\right)\left[\left(1 - \frac{\partial L}{\partial x}\right)\frac{\partial V}{\partial x} + \frac{\partial S}{\partial x} - \frac{\partial V}{\partial x}\right] .$$

Substitution from Eq. (5.417) and rearrangement yield

$$\frac{Dm_1}{Dt} = \left(\frac{e^x}{e^x - 1}V - \frac{\partial V}{\partial x}\right)m_1 - \left(e^x - 1\right)\left(\frac{\partial S}{\partial x} - \frac{\partial V}{\partial x}\right) . \qquad \text{Eq. (5.418)}$$

It is seen from Eq. (5.413) that for large values of x, $\frac{e^x}{e^x - 1}V \to V >> \frac{\partial V}{\partial x}$ and the inhomogeneity $-\left(e^x - 1\right)\left(\frac{\partial S}{\partial x} - \frac{\partial V}{\partial x}\right)$ has a leading term which is independent of x. The homogeneous solution of this equation grows with an approximate instantaneous period of V^{-1} and eventually dominates the particular integral. The shape of the function m_1 is then given by the solution of*

$$\frac{Dm_1}{Dt} = Vm_1 = \lambda\left[\frac{\beta k_p}{1 - k_p} - 1\right] m_1 . \qquad \text{Eq. (5.419)}$$

*Note that the solution of Eq. (5.419) is $m_1 \propto e^{\int v dt} = e^x$. The demonstration that $m_1 e^{-x}$ becomes constant along a characteristic makes quantitative an earlier statement that the saddle point differs from $v=1$ only by an amount of order m_1^{-1}. It now follows from Eq. (5.417) that $1 - \partial L/\partial x$ is equally constant, and

$$v_{sp} = 1 - e^{-x} = 1 - \frac{1 - \partial L/\partial x}{m_1} .$$

As t increases and m_1 is calculated for values of x along a characteristic, its behavior becomes that of the average level of progenitors, $\bar{m}$, as obtained from

$$\frac{d\bar{m}}{dt} = \lambda\left(\frac{\beta k_p}{1-k_p} - 1\right)\bar{m} + \frac{s\beta k_p}{1-k_p}. \qquad \text{Eq. (5.420)}$$

Thus, the ratio $\bar{m}/m_1$ will be constant when the $\bar{m}$ and m_1 levels are sufficiently large. However, $\bar{m}/m_1$ is usually different from unity, as is seen from comparison of Eqs. (5.418) and (5.420).

A second important phenomenon associated with the characteristics method is that Q also becomes constant on such a path as x becomes large. In showing this to be true, reference will be made to the kinetic behavior of m_1 just demonstrated. Note also that $m_1 \propto e^x$ implies that $\partial L/\partial x$ approaches a constant value under these conditions.

To show the constancy of Q, start with Eq. (5.406) in the form

$$\ln\sqrt{2\pi}\,Q = -\frac{1}{2}\ln\sigma' - \left\{ m_1 \ln\left(1-e^{-x}\right) + L \right\} \qquad \text{Eq. (5.421)}$$

where

$$\sigma' = (1-v)^2 \frac{\partial^2}{\partial v^2} \ln \frac{v^{-m_1} G_d}{1-v}$$

$$= \frac{m_1}{\left(e^x-1\right)^2} + 1 - \frac{\partial L}{\partial x} - \frac{\partial^2 L}{\partial x^2} \qquad \text{Eq. (5.422)}$$

in which $x = -\ln(1-v)$ is to be evaluated at the saddle point. In evaluating $D\ln Q/Dt$, the $\ln\sigma'$ term and the bracket $\{\}$ will be treated separately.

Since $e^{-x} << 1$,

$$\frac{D}{Dt}\left\{ L + m_1 \ln\left(1-e^{-x}\right)\right\} \approx \frac{DL}{Dt} - e^{-x}\frac{Dm_1}{dt} + e^{-x} V m_1$$

$$= S - e^{-x}\left(\frac{Dm_1}{Dt} - V m_1\right)$$

S is of order e^{-x} and $\frac{Dm_1}{Dt} = V m_1 + e^x\left(\frac{\partial V}{\partial x} - \frac{\partial S}{\partial x}\right) + \ldots$ so that $\frac{D\{\}}{Dt}$ is a small quantity of order e^{-x}. For the σ' term,

$$\sigma' \approx e^{-x}\left(e^{-x} m_1\right) + 1 - e^{-x}\frac{\partial}{\partial x}\left(e^x \frac{\partial L}{\partial x}\right)$$

so that

$$\frac{D\sigma'}{Dt} \approx -e^{-x} V \left(e^{-x} m_1\right) + e^{-x} \frac{D}{Dt}\left(e^{-x} m_1\right) - \frac{D}{Dt} e^{-x} \frac{\partial}{\partial x}\left\{e^{x} - m_1\right\}$$

using Eq. (5.417). Since the steepest descents method gives the ultimate behavior described by $m_1 = (\text{constant})\, e^{x}$ along a characteristic, all terms in this expression of $D\sigma'/Dt$ are no larger than $0(e^{-x})$.

The constancy of $\bar{m}/m_1$ and Q along characteristics in the region of large x has been verified numerically with accuracy of four or more significant figures. Note, however, that such behavior is not observed on all characteristics, but only on those along which x eventually becomes large.

Somewhere near $k_p = 1$ it becomes a poor approximation to neglect the prompt neutron lifetime and to disregard the change in progenitor level during a chain of prompt fissions. This model can compute ultimate probability distribution only when the distribution stops changing (matures) while the approximation is still good. Probability distributions for high reactivity insertion rates mature later than those for low rates. The high $\bar{m}/m_1$ part of a given distribution matures later than the low $\bar{m}/m_1$ part. Possibilities of employing a more accurate model will be considered in the discussion of extension of the model to nonzero lifetime.

3) Some Calculational Details. To solve Eqs. (5.412), (5.415), and (5.416) for the required mathematical and physical information, appropriate boundary conditions in both x and t must be established. The formalism to be developed for setting starting values will also permit a discussion of the probability for the progenitor population to be very high in a shut down reactor.

All time-dependent reactivity cases to be considered are understood to originate $(t = 0)$ after a long period of reactor shutdown. In the latter static situation, the generating function is given by the solution of Eq. (5.410) when $\partial G_d / \partial t = 0$:

$$G_d = \exp\left[\int_x^{\infty} \frac{S}{V}\, dx'\right] . \qquad \text{Eq. (5.423)}$$

This satisfies the boundary condition

$$\lim_{\substack{x \to \infty \\ v \to 1}} G_d = 1$$

which states merely that there certainly are zero or more progenitors in the reactor.

From this, a simple result may be derived for the probability that a system with low multiplication and a weak source contains more than some large number, m_1, of progenitors. Suppose that $m_1 \gg \bar{m}$, the expected static number. For large x, Eq. (5.423) becomes [using Eqs. (5.413) and (5.420)]

$$L = \bar{m}\, e^{-x} = \bar{m}(1 - v)$$

and

$$G_d = e^{-\bar{m}(1-v)}.$$

The probability that there be m_1 or more progenitors in the reactor is exactly

$$1 - Q(m_1) = \frac{\gamma(m_1, \bar{m})}{\Gamma(m_1)} \approx \frac{(\bar{m})^{m_1} e^{-m}}{(m)!}$$

$$\approx \frac{\exp\left\{-m_1\left[\ln(m_1/\bar{m}) - 1 + \bar{m}/m_1\right]\right\}}{\sqrt{2\pi m_1}}, \text{ for } m_1 \gg \bar{m}$$

and this is a very small number.

Returning to the matter of boundary conditions, one notes that Eq. (5.423) specifies $G_d(x, t = 0)$ completely in terms of the known functions $S(x)$ and $V(x)$. Choice of x amounts to choosing the characteristic curve in the (x, t) plane along which G_d and its derivatives will be computed. The values of G_d and its derivatives will, in turn, be used to compute by the steepest descents method values of $\bar{m}/m_1$ and corresponding values of $\log Q$. It has been found that the paths that give rise to useful calculations have initial x values in a narrow range. It is desirable in practice to be able to estimate the location of this range. These paths of interest typically have x values in roughly the range $5 < x < 8$ when delayed critical is passed. Use of this fact and of the large x approximation in the characteristic Eq. (5.414) will provide adequate estimates of the range of useful initial values.

Thus, for example, if reactivity $\frac{k_p(1+\beta)-1}{\beta k_p}$ increases linearly from a D dollar shutdown at a rate R, then solution of Eq. (5.414) yields approximately

$$x_o - x_m \approx \frac{\lambda D}{R} - \frac{\lambda}{R}\ln(1 + D) \qquad \text{Eq. (5.424)}$$

where x_m is the value of x on the characteristic at time $t = D/R$ (delayed critical), and x_o is the value of x on the characteristic at $t = 0$. Then,

$$x_o = 5 + \frac{\lambda D}{R} - \frac{\lambda}{R} \ln (1 + D)$$

is a good number to try as an initial value for x. Experimental calculations with several nearby initial values of x will locate the range more exactly.

In this connection, Fig. 5.43 shows some typical characteristics for a constant rate of reactivity insertion. The characteristics of interest are those which are high enough so that they rise before prompt critical is reached rather than having a negative slope to the end, and yet are low enough so they pass through a region in which x is small enough so that the large x approximation is invalid. As indicated in a previous discussion, the lower paths yield larger values of $\bar{m}/m_1$ and the corresponding small values of Q_{m_1}.

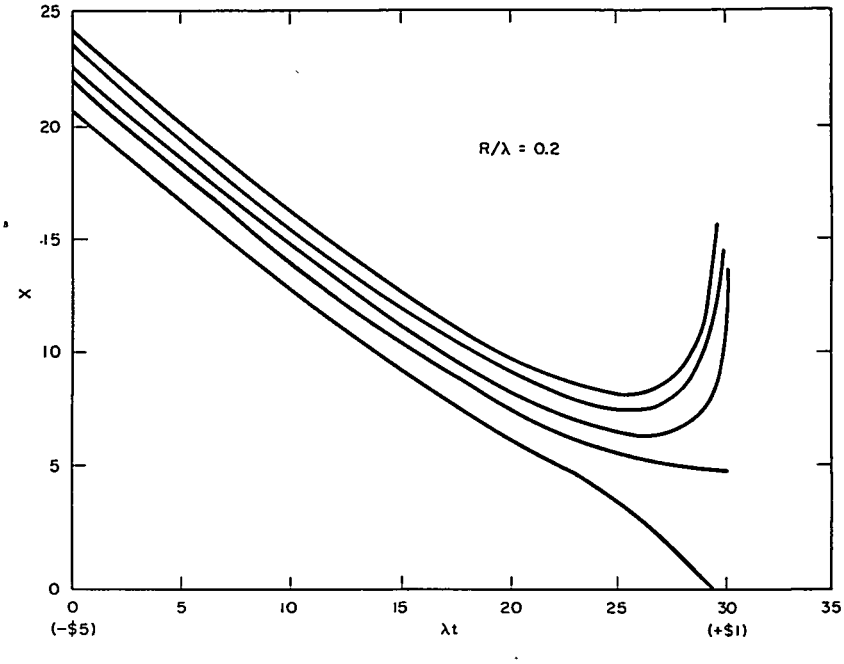

FIGURE 5.43. Characteristics for Steady Reactivity Insertion from Shutdown of $D = 5$.

To obtain detailed numerical information on progenitor levels and probabilities, there has been written a FORTRAN program for the Philco-2000 to solve the following set of equations:

$$\frac{dx}{d(\lambda t)} = e^{x}(1-u_1) - 1 \qquad \text{Eq. (5.425a)}$$

$$\frac{d}{d(\lambda t)}\left[\frac{\lambda L}{s}\right] = 1 - u_1 \qquad \text{Eq. (5.425b)}$$

$$\frac{d}{d(\lambda t)}\left[\frac{\partial}{\partial x}\frac{\lambda L}{s}\right] = -e^{x}\left[(1-u_1) - \frac{\partial u_1}{\partial x}\right]\left[\frac{\partial}{\partial x}\frac{\lambda L}{s}\right] - \frac{\partial u_1}{\partial x} \qquad \text{Eq. (5.425c)}$$

$$\frac{d}{d(\lambda t)}\left[\frac{\partial^2}{\partial x^2}\frac{\lambda L}{s}\right] = -2e^{x}\left[(1-u_1) - \frac{\partial u_1}{\partial x}\right]\left[\frac{\partial^2}{\partial x^2}\frac{\lambda L}{s}\right] - \frac{\partial^2 u_1}{\partial x^2}$$

$$- e^{x}\left[(1-u_1) - 2\frac{\partial u_1}{\partial x} - \frac{\partial^2 u_1}{\partial x^2}\right]\left[\frac{\partial}{\partial x}\frac{\lambda L}{s}\right] \qquad \text{Eq. (5.425d)}$$

and

$$\frac{d}{d(\lambda t)}\left[\frac{\lambda \bar{m}}{s}\right] = G' - (1-G')\left(\frac{\lambda \bar{m}}{s}\right), \qquad \text{Eq. (5.425e)}$$

where

$$(1-u_1) = \frac{k_p}{\nu_p}\left[(1-g)(1-\beta\nu_p e^{-x}) + \beta\nu_p e^{-x}\right] \qquad \text{Eq. (5.426a)}$$

$$\frac{\partial u_1}{\partial x} = \frac{\beta k_p e^{-xg}}{1 - \frac{k_p}{\nu_p}\left[1 - \beta\nu_p e^{-x}\right]\frac{\partial g}{\partial u_1}} \qquad \text{Eq. (5.426b)}$$

$$\frac{\partial^2 u_1}{\partial x^2} = -\frac{\partial u_1}{\partial x} + \frac{2}{g}\frac{\partial g}{\partial u_1}\left(\frac{\partial u_1}{\partial x}\right)^2 + \frac{e^{x} - \beta\nu_p}{\beta\nu_p g}\frac{\partial^2 g}{\partial u_1^2}\left(\frac{\partial u_1}{\partial x}\right)^3 \qquad \text{Eq. (5.426c)}$$

$$k_p = \frac{1}{1 + \beta\left[1 + D - \frac{R}{\lambda}\lambda t\right]} \qquad \text{Eq. (5.426d)}$$

$$\nu_p = 2.473 \qquad \text{Eq. (5.426e)}$$

$$1-g = 2.473(1-u_1) - 2.432(1-u_1)^2 + 1.217(1-u_1)^3 - 0.323(1-u_1)^4 + 0.038(1-u_1)^5 \qquad \text{Eq. (5.426f)}$$

$$\frac{\partial g}{\partial u_1} = 2.473 - 4.864(1-u_1) + 3.651(1-u_1)^2 - 1.292(1-u_1)^3 + 0.190(1-u_1)^4 \qquad \text{Eq. (5.426g)}$$

$$\frac{\partial^2 g_2}{\partial u_1} = 4.864 - 7.302(1-u_1) + 3.876(1-u_1)^2 - 0.760(1-u_1)^3 \qquad \text{Eq. (5.426h)}$$

$$G' = \frac{1}{1 + D - \frac{R}{\lambda}\lambda t} \; .$$

D and R may be step functions of time, so that arbitrary combinations of step changes and linear reactivity variations are permitted. Note that Eqs. (5.425a) through (5.425e) are simply Eqs. (5.412), (5.414), (5.415), (5.416) and (5.420), with time and $\ln G$ scaled in terms of the delayed neutron time constant and source strength in order to make the solutions as general as possible. Physically, $u_1(v)$ is the generating function for the probability distribution of progenitors arising immediately on introduction of a single neutron into a static system; as discussed in derivation of zero prompt lifetime equations, $u_1(v)$ is the unique root between 0 and 1 of Eq. (5.426a). The polynomial g is the generating function for the probability distribution of neutron multiplicity in fission. Constants for this multiplicity description were obtained from the work of Diven, et al.[79]

Numerical solution of the equations must be carried out with care, first because e^{-x} may be very small, and second because $1 - k_p$ may be very small. For example, if a computing machine is instructed to compute

$$\eta = \log(1 - e^{-x})$$

it will get few significant figures when x is large (e.g., $x > 15$), so that an alternative calculation such as

$$\eta = -e^{-x} - \frac{e^{-2x}}{2} - \frac{e^{-3x}}{3}$$

should be used for large x.

The early portions of many trajectories lie in regions of x large enough so that e^{-x} is exceedingly small. It is then true to a good approximation that

$$\frac{\lambda L}{s} = -\frac{\partial}{\partial x}\frac{\lambda L}{s} = \frac{\partial^2}{\partial x^2}\frac{\lambda L}{s} = e^{-x}\frac{\lambda \bar{m}}{s}$$

so that one need solve only the equations for x and $\bar{m}$, which are then

$$\frac{dx}{d(\lambda t)} = G' - 1 = -\frac{D - Rt}{1 + D - Rt}$$

$$\frac{d}{d(\lambda t)}\frac{\lambda \bar{m}}{s} = G' - (1 - G')\frac{\lambda \bar{m}}{s} .$$

C) EXTENSION OF MODEL TO NONZERO LIFETIME. The discussion now turns briefly to the mathematical model obtained when the assumption of zero neutron lifetime is dropped. Let $P_1(n, m, t)$ be the probability that at time t there are n neutrons and m progenitors in the reactor, and let τ be neutron lifetime. Then, corresponding to Eq. (5.311),

$$\begin{aligned}\frac{dP_1(n,m,t)}{dt} &= -\lambda m P_1(n,m,t) + \lambda(m+1)P_1(n-1, m+1, t) \\ &\quad - s P_1(n,m,t) + s P_1(n-1, m, t) \\ &\quad - \frac{n P_1(n,m,t)}{\tau} + \frac{n+1}{\tau}\left(1 - \frac{k_p}{\nu_p}\right)P_1(n+1, m, t) \\ &\quad + \sum_{\nu}\frac{n+1-\nu}{\tau}\frac{k_p}{\nu_p}(1 - \beta\nu_p)\,p(\nu)P_1(n+1-\nu, m, t) \\ &\quad + \sum_{\nu}\frac{n+1-\nu}{\tau}\beta k_p\, p(\nu)\,P_1(n+1-\nu, m-1, t) .\end{aligned} \qquad \text{Eq. (5.427)}$$

Let

$$G_1(u, v, t) = \sum_n \sum_m P_1(n, m, t)\, u^n v^m .$$

Then,

$$\frac{\partial G_1}{\partial t} = \lambda(u-v)\frac{\partial G_1}{\partial v} - s(1-u)G_1 + \frac{1}{\tau}\left[-u+1-\frac{k_p}{\nu_p}+g(u)\left(\frac{k_p}{\nu_p}(1-\beta\nu_p)+\beta k_p v\right)\right]\frac{\partial G_1}{\partial u} \quad .$$

Let

$$L_1(u,v,t) = -\ln G_1(u,v,t) \quad .$$

Then,

$$\frac{\partial}{\partial(\lambda t)}\frac{\lambda L_1}{s} = (u-v)\frac{\partial}{\partial v}\frac{\lambda L_1}{s} + 1 - u\,\frac{1}{\lambda\tau}\left[-u+1-\frac{k_p}{\nu_p}+g(u)\frac{k_p}{\nu_p}(1-\beta\nu_p) + \beta k_p v\right]\frac{\partial}{\partial u}\frac{\lambda L_1}{s} \quad . \qquad \text{Eq. (5.428)}$$

New independent variables w and x are now defined by

$$u = 1 - e^{-w}$$
$$v = 1 - e^{-x} \quad . \qquad \text{Eq. (5.429)}$$

In terms of them, the equation is

$$\frac{\partial}{\partial(\lambda t)}\frac{\lambda L_1}{s} - (1-e^{x-w})\frac{\partial}{\partial x}\frac{\lambda L_1}{s} - \frac{1}{\lambda\tau}\left[1-e^{w}\frac{k_p}{\nu_p}(1-g)-e^{w-x}\beta k_p g\right]\frac{\partial}{\partial w}\frac{\lambda L_1}{s} = e^{-w} \quad . \qquad \text{Eq. (5.430)}$$

As with the case of two variables, a characteristic path in (x, w, t) space can be found along which the function L_1 satisfies an ordinary differential equation. With the notation

$$\mathfrak{L} = \frac{\lambda L_1}{s}$$
$$\mathcal{F} = \frac{1}{\lambda\tau}\left[1-e^{w}\frac{k_p}{\nu_p}(1-g)-e^{w-x}\beta k_p g\right] \qquad \text{Eq. (5.431)}$$

the defining partial differential equation becomes

$$\frac{\partial \mathfrak{L}}{\partial \lambda t} - (1-e^{x-w})\frac{\partial \mathfrak{L}}{\partial x} - \mathcal{F}\frac{\partial \mathfrak{L}}{\partial w} = e^{-w} \quad . \qquad \text{Eq. (5.432)}$$

The characteristic is defined by

$$\frac{dw}{d\lambda t} = -\mathcal{F}$$
$$\frac{dx}{d\lambda t} = -(1-e^{x-w}) \,. \qquad \text{Eq. (5.433)}$$

Along this path, $\mathfrak{L}$ satisfies

$$\frac{d\mathfrak{L}}{d\lambda t} = e^{-u} \qquad \text{Eq. (5.434)}$$

where d is now the three-dimensional operator analogous to that of Eq. (5.412).

It is desired now to compare the behavior of this model to the behavior of the zero neutron lifetime model described above. The key to this comparison is a study of the behavior of the characteristic. Observe that

$$\frac{\partial}{\partial w}\left(\frac{dw}{d\lambda t}\right) = \frac{\partial}{\partial w}(-\mathcal{F}) = \frac{1}{\lambda\tau}\left[\left(1-g-\frac{\partial g}{\partial w}\right)+e^{w-x}\beta k_p\left(g+\frac{\partial g}{\partial w}\right)\right] \,. \qquad \text{Eq. (5.435)}$$

Further, recall that

$$g = 1-2.473\ e^{-w}+2.432\ e^{-2w}-1.217\ e^{-3w}+\cdots$$

and, hence, as long as w is not small,

$$\frac{\partial}{\partial w}\left(\frac{dw}{d\lambda t}\right) \approx \frac{1}{\lambda\tau}\left[2.432\frac{k_p}{\nu_p}\ e^{-w}+e^{w-x}\beta k_p\right] \,. \qquad \text{Eq. (5.436)}$$

That is, this derivative is positive and, since $\lambda\tau$ is small (of the order of 10^{-6} for water-moderated reactors), the derivative is large. This being the case, if a point on a characteristic be selected at some positive time and followed backwards through time, it will be found that the values of w on it will tend to become and remain close to the values that would make

$$\frac{dw}{d\lambda t} = -\mathcal{F} = 0 \,.$$

But this condition, that $\mathcal{F}=0$, is precisely the condition that defines u along the characteristic in the zero neutron lifetime model. Moreover, when w satisfies $\mathcal{F}=0$, the equations of this model reduce to the equations of the zero neutron lifetime model. When w is close to the solution of $\mathcal{F}=0$, it follows from Eq. (5.431) that

$$e^{-w} \approx \frac{\beta k_p}{1-k_p}\ e^{-x}$$

and from Eq. (5.435) that

$$\frac{\partial}{\partial w}\left(\frac{dw}{d\lambda t}\right) \approx \frac{1-k_p}{\lambda\tau} \quad .$$

The lower the reactivity, the larger this derivative, and the more closely w on the characteristic in (x, w, t) space will approximate the solution of $\mathcal{F} = 0$.

Thus, one is led by another route to the observation made earlier that the zero neutron lifetime model is a good approximation to the nonzero neutron lifetime model for low reactivities: the lower, the better.

While it is necessary to compute the time behavior of the two-parameter probability distribution $P_1(m, n, t)$ for this model, the desired end result is still a one-parameter probability distribution of reactor power at a given time. When reactivity is below prompt critical, it is the precursor concentration that governs reactor behavior, so that one is interested in abstracting information about the precursor distribution alone. Let

$$P_1(m, t) = \sum_n P_1(m, n, t) \quad .$$

Then,

$$G_1(1, v, t) = \sum_m \sum_n P_1(m, n, t)\, 1^n v^m$$

$$= \sum_m P_1(m, t)\, v^m \quad .$$

A characteristic which passes through $u = 1$ will yield values of $G_1(1, v, t)$ and its partial derivatives with respect to v, which may be used in Eqs. (5.406), (5.407), and (5.408) to obtain a value of m_1 and a corresponding Q_m. In x, w, t space this corresponds to a characteristic on which w becomes very large, approximating $w = \infty$.

It appears to be practical to use this nonzero lifetime model to compute probability distributions. Such calculations will, however, be much more cumbersome and expensive than calculations with the zero lifetime model, and their use will probably be chiefly to determine the limitations of the assumption of zero neutron lifetime. The problems connected with

computing the nonzero neutron lifetime model arise from the fact that some of the differential equations (for example, the one for w) have time constants proportional to $\lambda\tau$, so that very small time intervals will have to be used for numerical integration, and from the fact that for each physical startup situation there now is a two-parameter family of characteristics to explore, while in the zero lifetime model there was only a one-parameter family of characteristics.

One could also define a zero lifetime six-delay group model in which the probability generating function would be defined over a seven-dimensional space (one dimension for time, and one for each group of delayed neutron precursors), or a one-group model with spatial dependence in which the dimensionality of the probability generating function space would be one more than the number of spatial nodes. However, exploration of the resulting many-parameter families of paths would be quite expensive, and it is not now anticipated that calculations of this sort will be practical.

4. *Application of Forward Equation Solution to Low Source Startup.*

H. Hurwitz, Jr., D. B. MacMillan, J. H. Smith, and M. L. Storm

To relate probability considerations to reactor design specifications, discussion turns first to a nonstatistical method used in setting the source strength and the maximum reactivity shim rate.

If control rod insertion or scram is produced by a trip at a fixed power level, the power excursion following the trip should not cause plant damage. Suppose that the maximum available shim rate is accidentally employed in the startup of two systems which are identical except for having unequal sources. Then, the reactor with the smaller source will reach the scram level later, in the presence of higher reactivity and a shorter period, and will experience a more severe power transient.

In nonstatistical analysis of such transients, the kinetics calculations have two phases. One may be called a linear phase. It is conducted with the standard time-dependent equations for average levels of neutrons and progenitors, and covers the part of the transient in which the power generated is insignificant. The second phase continues the first into the power range, taking account of temperature changes

and their effects on kinetic behavior. The total analysis can prescribe, for a given maximum shim rate, the minimum source strength which may be used without danger of too large a power excursion. These are referred to as R_M and S_m.

When very low source strengths are being studied, probability considerations necessitate the addition of another phase to such calculations. This statistical phase covers the part of the transient in which the power level is so low that behavior is statistical rather than deterministic. Suppose that a non-statistical calculation indicates S_m and R_M to be a just safe source strength and shim rate combination. Since there is a possibility occasioned by fluctuations that these are not safe, a larger source $S > S_m$ may be contemplated for use. What degree of certainty exists with S that an excessively large power transient will be avoided?

With the source strength S, it is possible in principle to do characteristic calculations until one of them is characterized by a constant ratio $\bar{m}/m_1$ which is equal to the value of S/S_m. Solutions for average progenitor levels scale directly with whatever source is employed. The pair $\bar{m}$ and m_1 are, therefore, the average levels corresponding to sources S and S_m. In addition, the constant probability which is simultaneously obtained, $Q(m_1)$, gives specifically the likelihood for the time-dependent power to be less than a level already classified as a borderline case. Depending on the actual value of Q and safeguards criteria in use, the source S may or may not be considered effective enough in guarding against a level trip at too short a period.

To facilitate application of the theory, the results of a large number of characteristic calculations for ramp reactivity increases are recorded graphically in Figs. 5.44 to 5.51 ($ = 0.008 was used throughout). In those cases in which two distinct curves are labeled with one parametric value, the two curves show the results of the two methods for calculating Q described in computation of probabilities. Except in the region of weak sources, and probabilities not much less than 1, the two methods are equally accurate.[73]*

*The numerical results for ramp insertions were obtained using the Laplace transform formulation of Q. However, as illustrated in the figures, differences between the two formulations for Q occur only for Q's not much less than unity. Hence, the two formulations are equally applicable in assessing the feasibility of startup procedures where the obvious interest is to set design parameters, so that the probability of experiencing a transient more severe than a predefined limiting transient is exceedingly small.

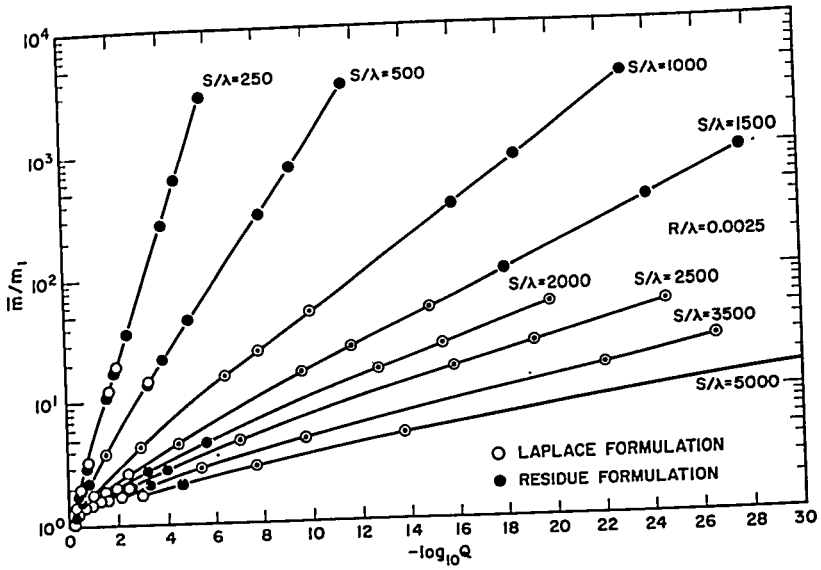

FIGURE 5.44. Relative Progenitor Levels vs Log_{10} of Associated Probabilities, $R/\lambda = 0.0025$.

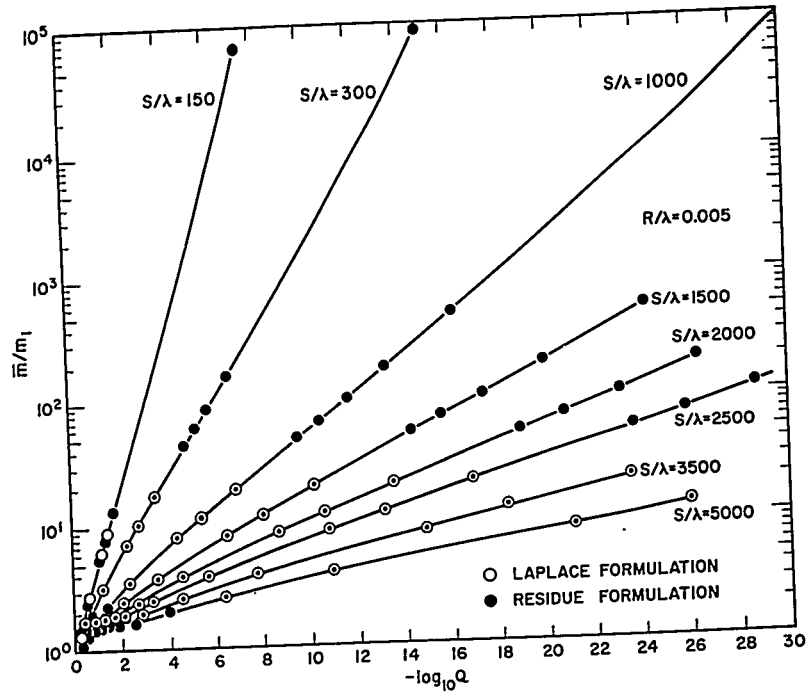

FIGURE 5.45. Relative Progenitor Levels vs Log_{10} of Associated Probabilities, $R/\lambda = 0.005$.

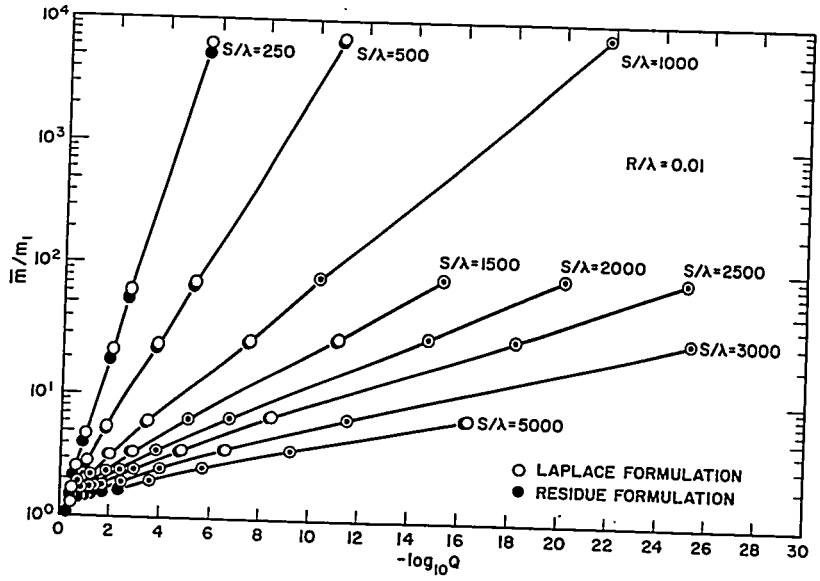

FIGURE 5.46. Relative Progenitor Levels vs Log_{10} of Associated Probabilities, $R/\lambda = 0.01$.

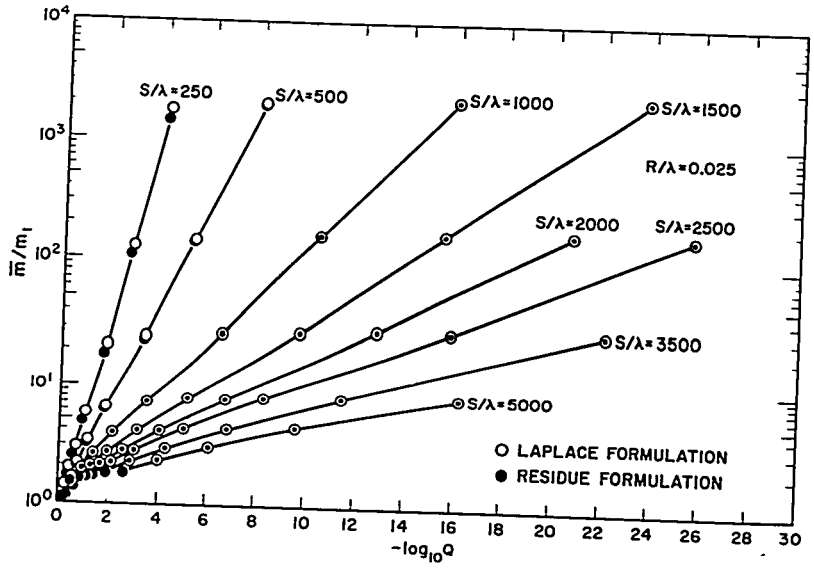

FIGURE 5.47. Relative Progenitor Levels vs Log_{10} of Associated Probabilities, $R/\lambda = 0.025$.

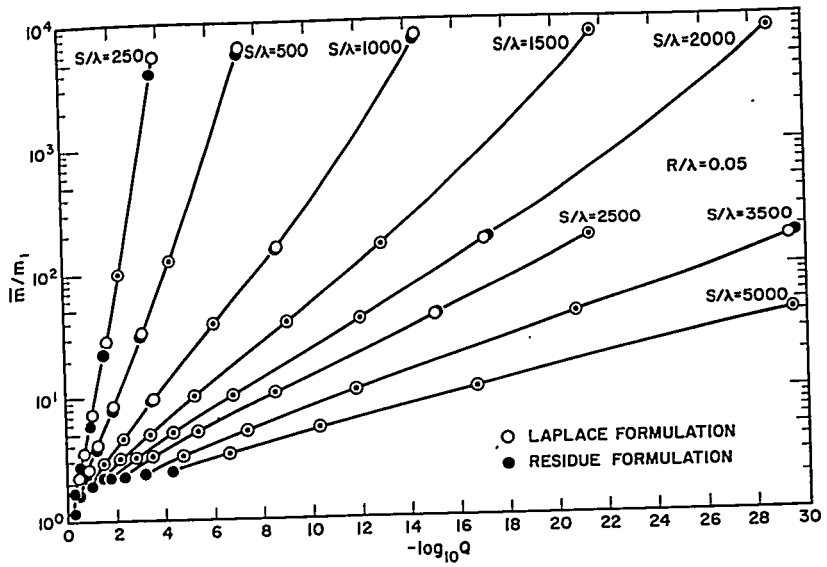

FIGURE 5.48. Relative Progenitor Levels vs Log_{10} of Associated Probabilities, $R/\lambda = 0.05$.

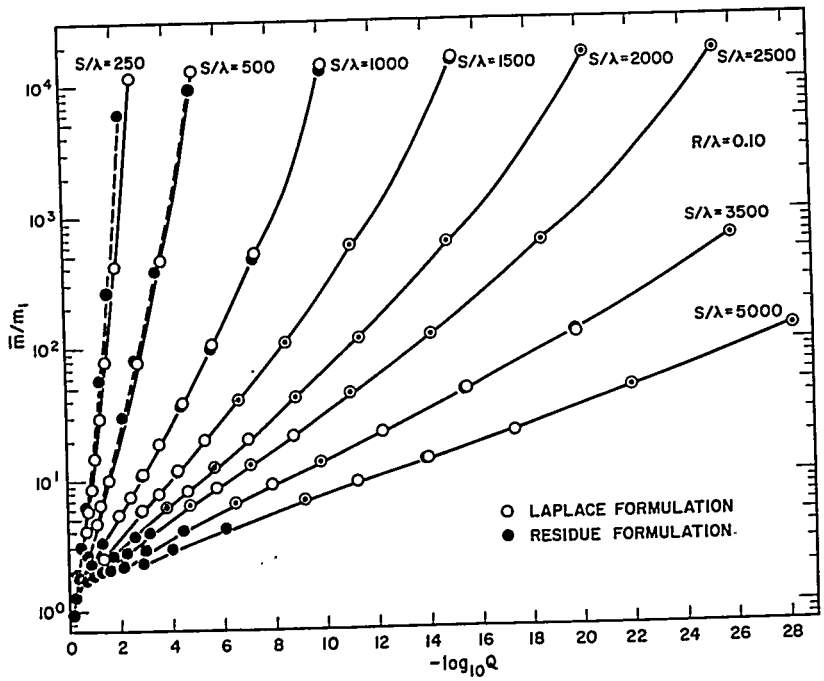

FIGURE 5.49. Relative Progenitor Levels vs Log_{10} of Associated Probabilities, $R/\lambda = 0.10$.

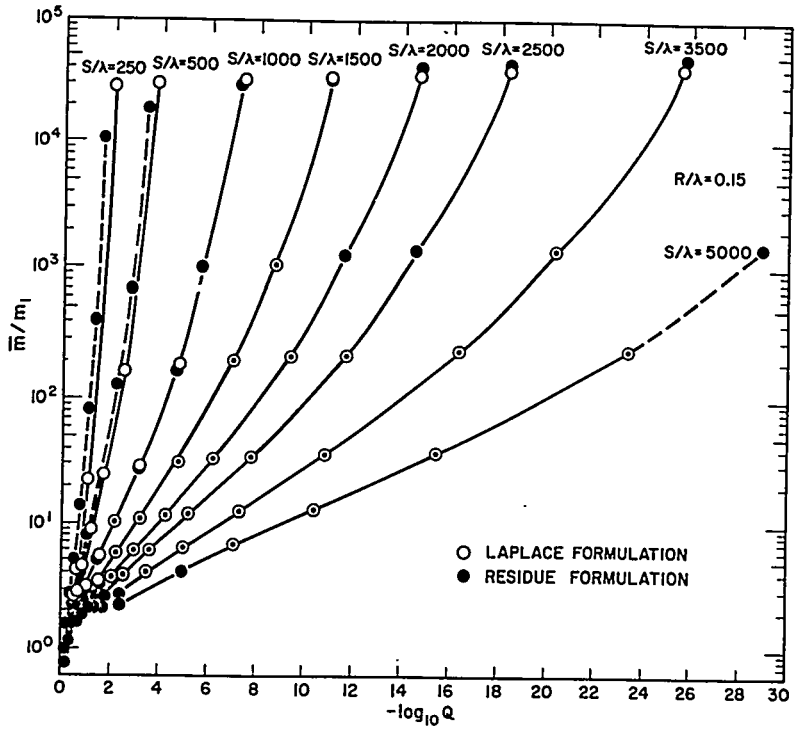

FIGURE 5.50. Relative Progenitor Levels vs Log_{10} of Associated Probabilities, $R/\lambda = 0.15$.

In applying the above results which were obtained as functions of the parameters R/λ and S/λ, it is necessary to choose an equivalent one-group λ. This choice can be made by fitting single group kinetic calculations to six-group kinetic calculations. This is simply done for step changes of reactivity, but the choice is not unique for ramp insertion of reactivity. However, this fact is mitigated by the following observation. If these data are replotted with actual source and shim rate as parameters (not S/λ and R/λ), it is found that there is not a strong dependence on the choice of λ for the faster shim rates of interest in accident considerations. For example, with R = 0.02 \$/sec and $50 < S < 700$ neutrons/sec, changing λ from 0.1 to 0.2 sec^{-1} causes only about an order of magnitude change in Q. The difference in probabilities obtained when λ is varied from 0.2 to 0.1 sec^{-1} can be larger for smaller shim rates, but the available data show that the larger value for λ is conservative in the sense that for a given ratio $\bar{m}/m_1$ the associated value of -log Q is smaller when λ=0.2 than when λ= 0.1 sec^{-1}. Thus, the associated probability of having a more severe transient is greater.

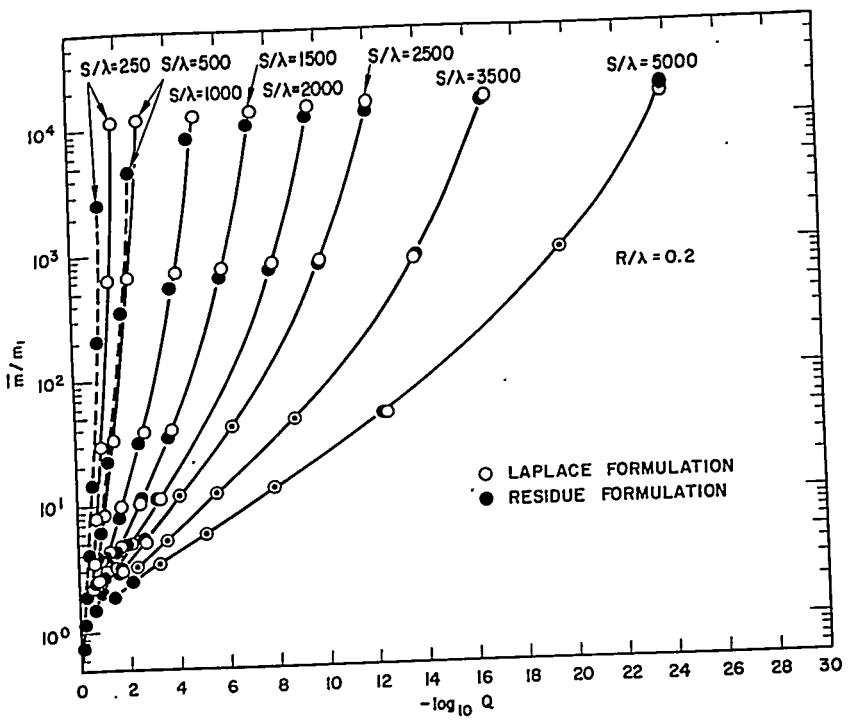

FIGURE 5.51. Relative Progenitor Levels vs Log_{10} of Associated Probabilities, $R/\lambda = 0.2$.

To illustrate the use of these graphs, consider a system in which preliminary nonstatistical studies indicate that a shim rate of 0.1¢/sec and a source strength of 20 neutrons/sec are just safe. Will use of a stronger source of 100 neutrons/sec give a firm assurance that the level during startup will not fall below a value for which reactor integrity is assumed? For $\lambda = 0.1$ sec^{-1}, refer to Fig. 5.46 for $S/\lambda = 1000$. For $\bar{m}/m_1 = S/S_m = 100/20$, $Q = 10^{-3}$. Note that providing an increased source of $S \approx 200$ neutrons/sec would give $Q \approx 10^{-6}$, which might be more satisfactory. This illustrates the sensitivity of probability to source strength which can be observed in all the results.

For R/λ less than or equal to \$0.2, the statistical distributions are for practical purposes independent of the reactivity pattern before the reactor arrives at ΔK =\$0.50 (assuming the reactor has been shut down long enough that the remaining delayed neutron precursors are due to source activity rather than

This is based on calculations done for R/λ = \$0.2 in which it was observed that, for any source strength and $\bar{m}/m_1$, the values of log Q computed, when one starts from equilibrium at to previous power operation).

-\$0.50 (equivalent to coming up to -\$0.50 infinitely slowly) and proceeds from there at a ramp of $R/\lambda = \$0.2$, and when one starts at equilibrium at -\$10, jumps to -\$0.50 (thus, coming up to -\$0.50 infinitely quickly), and then proceeds at $R/\lambda = \$0.2$, are both within 10 percent of the computed value of log Q for the case of coming up from a many-dollar shutdown at a steady ramp of $R/\lambda = \$0.2$. The effect of the reactivity pattern before reaching $\Delta K = -\$0.50$ will be even smaller when the ramp rate used after reaching $\Delta K = \$0.50$ is slower than $R/\lambda = \$0.2$. Further calculations were also done starting with a \$10 shutdown and changing the rate of linear increase in reactivity from one value to another before attainment of delayed criticality. Results for ln Q were observed to change by no more than 10 percent (usually much less) over a wide range of reactivity insertion patterns.

The numerical results discussed above were obtained for constant reactivity insertion rates (ramps). The distributions obtained for various step approximations to some selected ramps will next be described.

The ramps considered were $R/\lambda = \$0.005$ and $R/\lambda = \$0.05$, and the step approximations consisted of 10-cent steps or 40-cent steps with appropriate waiting times between successive steps. For example, for $R/\lambda = \$0.005$ and taking $\lambda = 0.2$ sec^{-1} (so that $R = 0.1$ cent/sec), the 10-cent steps were separated by 100-second intervals or by values of $\lambda(\Delta t) = 20$.

For reactivity increments as large as 40 cents, the details of crossing criticality should be considered. That is, startups in which one of the steps makes the reactor exactly critical can have a different distribution from startups where, for example, one of the steps carries the reactor from 20 cents below critical to 20 cents above critical. To assess this effect, initial shutdowns for the 40-cent steps were varied from -\$10.0 to -\$9.8.

Figures 5.52 and 5.53 compare the distributions obtained for the above step sequence procedures with ramp data calculated for the Laplace formulation of Q for a range of source strengths (S/λ neutrons). The distributions obtained using 10-cent steps are for practical purposes indistinguishable from the previous ramp data. For $R/\lambda = \$0.05$, the details of crossing criticality in a 40-cent step do not have a significant effect. For $R/\lambda = \$0.005$, the details of the crossing are more pertinent, and the shaded bands of data shown in Fig. 5.52 depict the ranges in which the distribution may fall.

It is seen from the figures that, on a relative basis, the values of -log Q for the 40-cent steps are less than the corresponding ramp values. However, it is felt that the differences

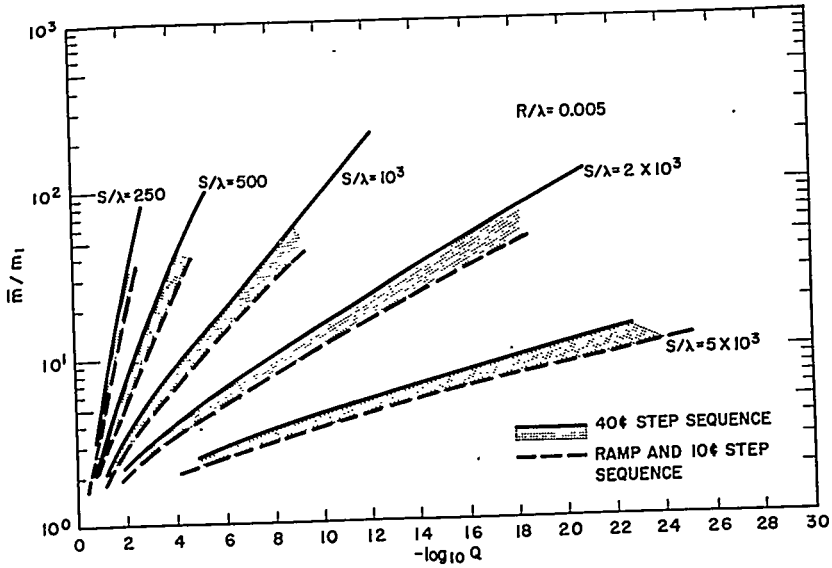

FIGURE 5.52. Statistical Distribution of Startups for Step Sequence Approximation, $R/\lambda = 0.005$.

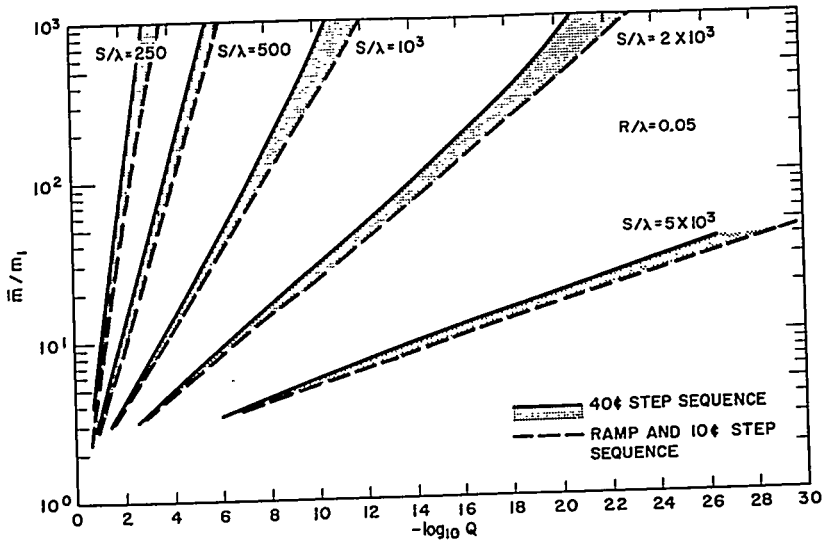

FIGURE 5.53. Statistical Distribution of Startups for Step Sequence Approximation, $R/\lambda = 0.05$.

between these step sequence calculations and the corresponding ramp calculations are not sufficient to yield different design conclusions as to regions of acceptable probability values.

It is to be expected that, when a strong enough source is provided, fluctations in power levels can be disregarded and reactor transients calculated reliably by the relatively simple techniques for predicting time behavior of the average level. Thus, one can ask for the required minimum source strength which is such that the effect of fluctations are insignificant, and there is a negligible probability of reaching a given power level with a significantly higher reactivity than that predicted by the pile kinetics equations. In terms of the mathematical formalism, this is equivalent to seeking the source strength for a given R/λ at which the probability corresponding to $\bar{m}/m$ greater than one is extremely small. A precise answer to this question is limited by the subjective element involved in the choice of small probabilities. However, numerical studies with the present statistical model have shown that for $R/\lambda \lesssim \$0.2$, and a source of 10^4 neutrons/sec, there is about one chance in 10^{10} that values of $\bar{m}/m_1$ greater than two will be obtained. As the source is increased, it is found that for a given $\bar{m}/m_1$ the corresponding values of -log Q scale directly with S/λ. Accordingly, the previously mentioned values of -log Q increase to about 100 when the source is increased to 10^5 neutrons/sec. Thus, for the ramp rates considered here, large fluctuations are not probable for sources greater than 10^4 neutrons/sec and are certainly improbable for sources as large as 10^5 neutrons/sec.

Moment calculations offer additional insight into the way in which transient behavior becomes deterministic when a sufficiently high power is reached. For example, one may take as initial condition that $m = m_o$ with probability 1, and compute the first two moments of the probability distribution as functions of time. The normalized variance

$$\mu(t) = \frac{\overline{\left(m(t) - \bar{m}(t)\right)^2}}{\left(\bar{m}(t)\right)^2}$$

satisfies the equation [derived from Eq. (5.392)]

$$\frac{d\mu}{dt} = \frac{1}{\bar{m}} \left\{ \lambda(G'' - G') + \frac{(G'' + G')s}{\bar{m}} - 2G's\mu \right\}$$

where G' and G'' are the derivatives of $\mathcal{G}_1(v)$ at $v = 1$. Concern is especially with the case of increasing (steadily or by steps) reactivity during startup. In this case, $\bar{m}$ increases faster than some exponential, so that $\int(dt/\bar{m})$ is bounded. Hence, μ has a finite limiting value even in the case of zero source.

An upper bound on μ may be used, in the absence of any other information about the distribution, to obtain a very conservative upper bound on the probability of a specific deviation. For fixed reactivity and zero source, with initial condition $m = m_o$, the limiting value of μ is easily computed and provides the following upper bounds on the probability that the precursor number, $m(t)$, will at any time after the initial time be out of the range $0.5\ \bar{m} < m < 1.5\ \bar{m}$ (if p is the probability of being out of that range, then $p < 4\mu$):

m_o \ ΔK	\$0.20	\$0.35	\$0.50	\$0.65	\$0.80
10^5	8×10^{-2}	7×10^{-2}	8×10^{-2}	1×10^{-1}	3×10^{-1}
10^7	8×10^{-4}	7×10^{-4}	8×10^{-4}	1×10^{-3}	3×10^{-3}
10^9	8×10^{-6}	7×10^{-6}	8×10^{-6}	1×10^{-5}	3×10^{-5}

5. *Comparison with Experiment and Implications for Startup Calculations*

H. Hurwitz, Jr., D. B. MacMillan, J. H. Smith, and M. L. Storm

Consideration is now turned to a comparison of the predictions of this theory with the only experimental data currently available: the GODIVA weak source transient data obtained by G. E. Hansen[78] and T. E. Wimett, and discussed in Sect. 5.5.B.2.

The reactivity pattern used in the experiments brought GODIVA as quickly as possible from shutdown to \$0.70 above delayed critical. The quantities measured are the waiting time for the power to reach a specified level and the period. If this experiment is repeated N times, one can order the experimentally observed waiting times $t_1, \ldots, t_N$ where $t_1 \leq t_2 \ldots \leq t_N$. Then, the empirical probability $Q_N(t)$ of observing a waiting time greater than or equal to t is obtained as

$$Q_N(t) = 1 \text{ for } t < t_1$$

$$= 1 - \frac{j}{N} \text{ for } t_j \leq t_{j+1},\ j = 1, 2 \ldots, N-1$$

$$= 0 \text{ for } t_N \leq t$$

The results of the statistical calculations can be compared directly with the above empirical probability distribution of waiting times. As mentioned previously, the values of m_1 determined along each trajectory eventually follow the kinetics

equation and are characterized by a constant value of $Q(m_1, t)$. Thus, the time at which each such trajectory reaches the reference power level defines a waiting time together with the associated probability $Q(m_1, t)$. This calculated probability distribution can then be compared directly with the empirical distribution $Q_N(t)$.

There were 89 experiments done, i.e., 89 startups for which waiting time and period were measured. In the first 23 experiments the fiducial level was 2.73×10^{11} fissions/sec; in the other 66, it was 1.48×10^{11} fissions/sec. The first 23 experiments were extrapolated back to the 1.48×10^{11} fissions/sec fiducial level by subtracting from their waiting times (after the waiting times had been reduced to period units) the time in periods required to go from 1.48×10^{11} to 2.73×10^{11} fissions/sec, namely, $\ln (2.73/1.48)$.

As an indication of the uncertainty in the experimental cumulative frequency distribution due to the uncertainties in time and period measurements, the experimental data have been analyzed in various ways, and the results are presented as the three probability histograms in Fig. 5.54. The time scale is presented in period units, and zero time represents the arrival of the average transient at the fiducial level. The highest histogram is obtained by omitting experiments 1 to 23, on the hypothesis that they come from a different population, and reducing the remaining experiments to the period time scale by means of the individual periods T. The lowest histogram is obtained by reducing all 89 experiments by the average period T. The nominal histogram is obtained by reducing all experiments by the individual periods T. For simplicity of representation, only the low probability portions of the extreme histograms are shown. The time at which the average fission rate over all experiments reached the fiducial level of 1.48×10^{11} fissions/sec was found to be 15.41 (periods) and 15.65 for the highest and lowest histograms, and 15.36 for the nominal histogram. These values all agree to within 0.3. Thus, the zero on the period time scale is well defined.

Initial calculations were performed for the following nominal experimental parameters:

1. Reactivity Insertion Pattern: Steady state at -$5, then a step to -$0.30, and one second later a final step to $0.70.
2. Effective source of 90 neutrons/sec.
3. Effective delayed neutron fraction of 0.0066.
4. One-group decay constant of 0.2459 sec^{-1}. This was chosen, on the basis of the inhour equation for the model, to yield a period equal to the observed average period of 1.743 sec for the 89 runs. On this basis, the calculated arrival time of the average fission rate at the 1.48×10^{11}

fiducial level was 14.36 periods from the time at which reactivity came to \$0.70, in good agreement with the previously mentioned values derived from experiment.

5. Average number of neutrons emitted per fission (ν_p) of 2.59.

The results of this calculation are also shown in Fig. 5.54.

Subsequent studies were designed to test the sensitivity of the calculations to variations in the individual parameters. It was found that the results were not significantly affected by the following changes:

1. Change in shutdown from -\$5 to -\$8.
2. Changes in the detailed nature of the reactivity insertion pattern; instead of the nominal pattern, reactivity was brought directly from -\$5 to +\$0.70.
3. Change in β_{eff} from 0.0066 to 0.0062.
4. Change in $\overline{\nu}$ from 2.59 to 2.47.

In this regard it is mentioned that for $\overline{\nu} = 2.59$, the values for the probabilities of emitting ν neutrons were based on Ref. 80. This required minor changes in the original program which employs $\overline{\nu} = 2.47$ and the experimental probabilities for neutron emission given in Ref. 80.

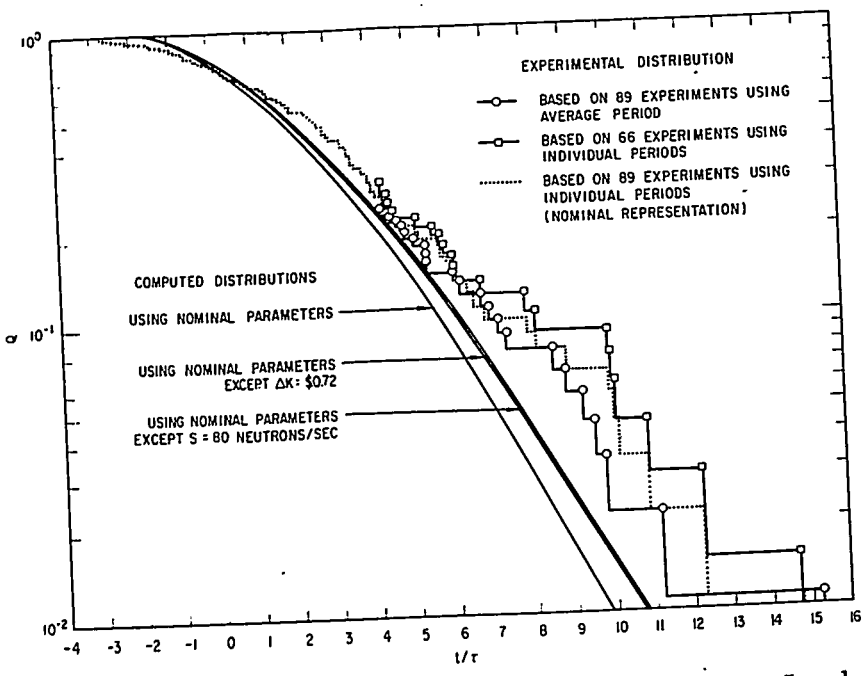

FIGURE 5.54. Probabilities for Delayed Attainment of Power Level vs Delayed Time.

The calculations were found to be sensitive to variations in source strength and to the magnitude of the reactivity step. Figure 5.54 shows the distribution obtained by changing the source to 80 neutrons/sec, keeping everything else fixed, and the distribution obtained by changing the step to \$0.72, keeping everything else fixed.

In regard to the latter change, the directly measured periods show that the experiments all lie in a 4-cent range in reactivity, and that all but 8 of them lie in a 2-cent range within which they are fairly uniformly distributed. The effect of this variation should then be rather smaller than the difference between the computed distribution for Δk = \$0.70, S = 90 neutrons/sec and the computed distribution for Δk = \$0.72, S = 90 neutrons/sec. Thus, the effect of this variation is not important in view of the statistical uncertainties inherent in having no more than 89 experiments.

These computed results use only the first term in the saddle point expansion. The second term is about minus 6 percent of that, indicating that the computed results are higher than they should be by a few percent. This brings the computation closer to the experiment near Q = 1, where a few percent is a significant absolute difference; but it has no important effect on the tail end of the distribution.

One final point which is mentioned briefly is the possible use of the empirical distribution as a guide for suitably changing the input parameters to the calculation in accordance with an intended application. Specifically, the primary interest is in adjusting the reactivity input parameter, since it provides a convenient means for introducing conservatism into accident analyses.

There may be a significant difference between the experimental distribution based on the small number of experiments and the true distribution for infinitely many experiments. For safeguards applications, one must take account of the possibility that the true distribution is more pessimistic than the empirical distribution, that is, it may show a larger probability of arriving at the fiducial level later than a given waiting time. Thus, an appropriate safeguards normalization should yield higher probabilities than the empirical distribution by an amount governed by a statistical estimate of the possible difference between the experimental and true distributions. From this point of view, it is seen from Fig. 5.54 that the model predictions with nominal parameters are nonconservative over most of the data range.

With regard to possible differences between the experimental and true distributions given an experimental cumulative frequency distribution based on 89 experiments, one can

assert with 95 percent confidence that the true distribution from which the experiments were drawn lies everywhere below a histogram which is 0.13 higher (on the probability scale) than the experimental distribution. For 99.99 percent confidence, the corresponding upper bound histogram is 0.23 higher than the experimental distribution.

Figure 5.55 shows the best estimate experimental distribution and the 95 percent and 99.99 percent confidence upper bound histograms. It also shows the model predictions for the nominal parameters and the model predictions when the nominal step is replaced by a step to a 10 percent higher reactivity (Δk = \$0.77) and to a 20 percent higher reactivity (Δk = \$0.84). It is seen that the computed distribution for reactivity 20 percent high lies above the 95 percent confidence upper bound at many points and even above the 99.99 percent confidence upper bound at some points. (The fact that this computed distribution lies under the upper bounds at the tail end of the distribution is not surprising, since the criterion used is distribution-free.) If it is assumed that in the monotonically related family of computed curves generated by reactivity modifications alone there is one that is a good fit to the unknown true distribution, then it follows that the calculation using reactivity 20 percent high is conservative even at the 99.99 percent confidence level. At any rate, for the step change experiments, increases in reactivity by about 10 to 20 percent of nominal value swing the predictions of the model from reasonable agreement to plausible conservatism with respect to the available data. Moreover, as indicated by Fig. 5.54, comparable reductions in nominal source strength would produce similar changes in calculated probabilities.

The probabilities of interest in reactor designs, which are inherently conservative in intent, lie in a range of small values (such as 10^{-6} and less) where experimental confirmation is unavailable. The extent to which calculational models normalized to experiment in the available data range of relatively large probabilities (greater than about 10^{-2}) can be relied on for design is a matter of judgment, since the limitations of a point reactor model with a single delayed group remain to be evaluated. In this regard, it should be noted that a given degree of success of a point reactor probability model for a closely coupled fast reactor such as GODIVA does not guarantee that the same degree of success will be attained for a loosely coupled thermal reactor, although the differences may be outside of the range observable in a small number of experiments.

A) SUMMARY AND DISCUSSION. The methods considered permit evaluation of the probability that, for a given weak source

and shim rate, a reactor will experience a more severe power transient than some predefined limiting transient. The choice of probability values for any situation is a highly subjective factor. Extreme probability values can be selected which are uncontroversial. For example, one chance in two of experiencing a damaging transient is unacceptably large, while one chance in 10^{20} is acceptably small. After a design probability has been set, the limitations in the model must be taken into account to ensure that the minimum desired probability is achieved. These limitations, the assumption of space-time separability, and the use of zero neutron lifetime and only one delayed neutron precursor group, require that one allow for a substantial percentage uncertainty in the predicted values of log Q. While this is of no consequence when the calculated probabilities are very small (e.g., $Q \simeq 10^{15}$), it is obviously pertinent when the calculated probabilities are disconcertingly large.

The GODIVA experiments, while markedly different from typical applications to thermal power reactors, are the only data currently available for normalization of the statistical model. The model predictions using the nominal parameters

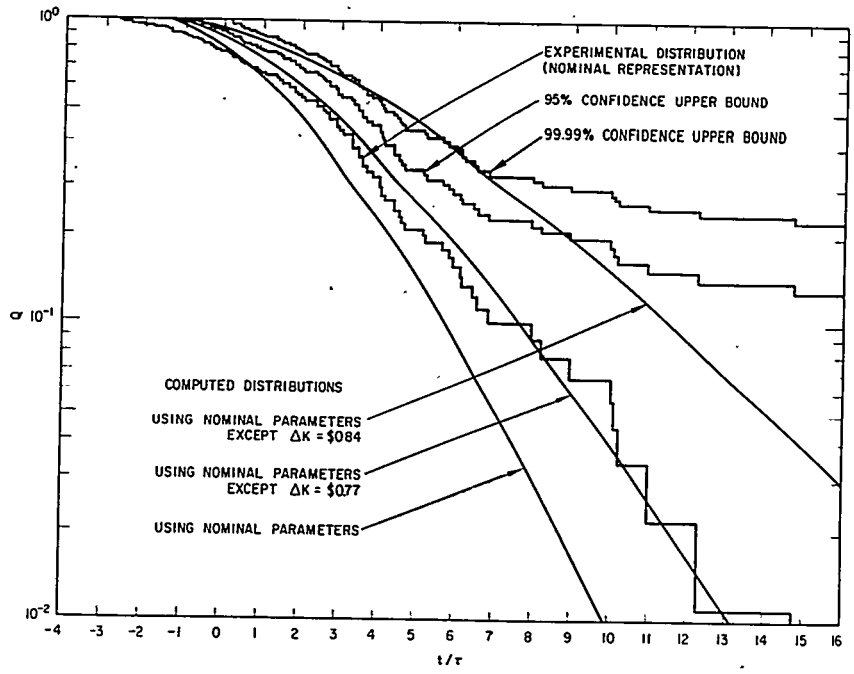

FIGURE 5.55. Probabilities for Delayed Attainment of Power Level vs Delay Time.

were obviously nonconservative, predicting $-\log_{10} Q$ too low by around 30 percent.

At the present state of knowledge, it is felt that the normalizations necessary to yield reasonable agreement with the GODIVA experiment should be employed for other reactivity insertion patterns. That is, the reactivity insertion rate should be increased from 10 to 20 percent in any design application. In addition, an overall conservative approach should be employed and a minimum expected source strength should be used.

Various deficiencies in the calculational model have been pointed out. As a final remark, it should be repeated that the lack of experimental data inherently prevents a completely thorough critique of the methods as applied in the prediction of uncommon but important deviations from average kinetic behavior.

C. Multiplicative Process with Feedback

D. R. Harris

The qualitative effects of feedback on the multiplicative process can be most clearly discussed by study of a simple model. It is assumed that delayed neutron precursors are absent and that all reactor parameters are constant except for the neutron capture time which is related to the neutron level by

$$\tau_c^{-1} = \tau_{c_1}^{-1} - A(N-1) \ . \qquad \text{Eq. (5.437)}$$

Here the parameter A can be regarded as being proportional to a temperature coefficient of reactivity for a system with negligible heat capacity, so that the temperature follows the instantaneous neutron level. A more realistic model in which system temperature and delayed neutron precursors are treated explicitly is described elsewhere.[81]

When the inverse capture time of Eq. (5.437) is inserted into Eq. (5.309), the derivation leading to the forward stochastic equation yields

$$\frac{\partial G}{\partial t} = Au(u-1)\frac{\partial^2 G}{\partial u^2} + \left\{ \tau_f^{-1}\left[g_f(u) - u\right] + \tau_{c_1}^{-1}(1-u) \right\} \frac{\partial G}{\partial u} + S\left[g_s(u) - 1\right] G \qquad \text{Eq. (5.438)}$$

the $\partial^2 G/\partial u^2$ term being the consequence of the linear feedback assumed above. Had feedback involving N^j been assumed, the forward stochastic equation would have been of order $j+1$.

As was described in Sect. 5.5.B.1, moments of the neutron distribution are related to derivatives of G with respect to u evaluated at $u = 1$. In particular, the mean neutron number $\bar{N}$, the variance K_2, and the third central moment K_3 are

$$\bar{N}(t) = \left.\frac{\partial G(u,t)}{\partial u}\right|_{u=1}$$

$$K_2(t) = \left.\frac{\partial^2 G(u,t)}{\partial u^2}\right|_{u=1} - \bar{N}^2(t) + \bar{N}(t)$$

$$K_3(t) = \left.\frac{\partial^3 G(u,t)}{\partial u^3}\right|_{u=1} - 3(\bar{N}^2 + K_2)(\bar{N} - 1) + 2\bar{N}(\bar{N}^2 - 1) \ . \qquad \text{Eq. (5.439)}$$

By taking derivatives of Eq. (5.438) with respect to u and evaluating at $u = 1$, an infinite set of moment equations is obtained of which the first two are

$$d\bar{N}/dt = \left[\tau_f^{-1}(\bar{\nu}_f - 1) - \tau_{c_1}^{-1} + A(\bar{N} - 1)\right]\bar{N} + S\bar{\nu}_s + AK_2 \qquad \text{Eq. (5.440a)}$$

$$dK_2/dt = 2\left[\tau_f^{-1}(\bar{N} - 1) - \tau_{c_1}^{-1} + A(\bar{N} - 1)\right]K_2 - \left[\tau_f^{-1}(\bar{\nu}_f - 1) - \tau_{c_1}^{-1} + A(\bar{N} - 1)\right]\bar{N} + \overline{\nu_f(\nu_f - 1)}\,\tau_f^{-1}\bar{N} + \overline{\nu_s(\nu_s - 1)}\,S + S\bar{\nu}_s + A(2K_3 + 2\bar{N}K_2 - K_2) \ . \qquad \text{Eq. (5.440b)}$$

These equations cannot be solved directly because there are only two equations in the three variables $\bar{N}$, K_2, and K_3. (Higher moment equations would also be fewer than the number of unknown moments.)

Suppose, first, that there is no feedback, that the process is stationary, and that a desired neutron level $\bar{N}$ is attained by control rod adjustment, i.e., by varying $\tau_{c_1}^{-1}$. Then, setting $\dot{\bar{N}}$ and $\dot{K}_2$ equal to zero,

$$0 = \left[\tau_f^{-1}(\bar{\nu}_f - 1) - \tau_{c_1}^{-1}\right]N + S\bar{\nu}_s$$

$$0 = 2\left[\tau_f^{-1}(\bar{\nu}_f - 1) - \tau_{c_1}^{-1}\right](K_2 - \bar{N}) + \overline{\nu_f(\nu_f - 1)}\,\tau_f^{-1}\bar{N} + \overline{\nu_s(\nu_s - 1)}\,S \ .$$

Eq. (5.441)

The mean stationary neutron level is just

$$\bar{N} = \frac{S\bar{\nu}_s}{-\left[\tau_f^{-1}(\bar{\nu}_f - 1) - \tau_{c_1}^{-1}\right]} . \qquad \text{Eq. (5.442)}$$

The requirement that $\bar{N}$ is nonnegative imposes a condition on permissible values of $\tau_f^{-1}, \tau_{c_1}^{-1}$, and $\bar{\nu}_f$; that the reactor must be subcritical. A measure of the dispersion of the probability distribution is the relative standard deviation (r.s.d.) the square of which is, from Eqs. (5.441),

$$(K_2^{1/2}/\bar{N})^2 = 1/\bar{N} + \overline{\nu_f(\nu_f - 1)}\,\tau_f^{-1}/2S\bar{\nu}_s + \overline{\nu_s(\nu_s - 1)}/2\bar{N}\bar{\nu}_s . \qquad \text{Eq (5.443)}$$

Because the factorial moments $\overline{\nu(\nu-1)}$ are nonnegative, the right-hand side of Eq. (5.443) is nonnegative, as is required of the r.s.d. As $\bar{N}$ increases by adjustment of $\tau_{c_1}^{-1}$, i.e., by increasing multiplication, the r.s.d. decreases only to a point, then becomes constant at $\overline{\nu_f(\nu_f - 1)}\,\tau_f^{-1}/2S$. This property, that the r.s.d. does not approach zero when the multiplication increases without limit, is a special feature of a multiplicative process.

Now suppose that the stationary process with $A = 0$, just described, is modified by turning on a nonzero temperature coefficient. If, after some transient interval a stationary process eventually develops, the mean and r.s.d. would be given by

$$\bar{N} = \frac{S\bar{\nu}_s + AK_2}{-\left[\tau_f^{-1}(\bar{\nu}_f - 1) - \tau_{c_1}^{-1} + A(\bar{N} - 1)\right]} \qquad \text{Eq. (5.444)}$$

$$(K_2^{1/2}/\bar{N})^2 = (K_2^{1/2}/\bar{N})_o^2 \frac{1}{1 + \dfrac{AK_2}{S\bar{\nu}_s}} + \frac{AK_2}{S\bar{\nu}_s}\,\frac{1 + K_3/K_2\bar{N}}{1 + \dfrac{AK_2}{S\bar{\nu}_s}} . \qquad \text{Eq. (5.445)}$$

Here $(K_2^{1/2}/\bar{N})_o$ represents the r.s.d. for zero temperature coefficient given by Eq. (5.443). The nonzero value of A modifies the mean $\bar{N}$ by shifting the reactivity at the mean level, and this effect accounts for the A in the denominator of Eq. (5.444). This effect would exist even if fluctuations were neglected. In addition, a nonzero value of A shifts the mean by a factor $1 + AK_2/S\bar{\nu}_s$, the increase or decrease depending on the sign of A. It would be expected, for a probability distribution symmetrical about the mean neutron level, that a positive (negative)

value of A would make the distribution more disperse (less disperse) without changing the mean. The distribution is not symmetrical about the mean, however, and the nonzero A results in a shift of the mean value.

The effect of nonzero temperature coefficient on the dispersion of the distribution, i.e., on the r.s.d., is intuitively clear, although Eq. (5.445) is somewhat involved. It is convenient to introduce N_M, defined by

$$N_M \equiv \sqrt{S\bar{\nu}_s / |A|} \qquad \text{Eq. (5.446)}$$

where N_M is noted later to be a marginal level for stability in deterministic analysis of the reactor, assuming a positive temperature coefficient. If the effect of the temperature coefficient on the probability distribution is not large, then the third central moment K_3 can be eliminated by assuming the distribution to be normal, or gamma, in character (see Sect. 5.5.B.2):

$$K_3 = \begin{cases} 0 \text{ if normal distribution} \\ 2K_2^2 / \bar{N} \text{ if gamma distribution} \end{cases} \qquad \text{Eq. (5.447)}$$

Equation (5.445) can be rearranged for greater clarity:

$$\left(K_2^{1/2}/\bar{N}\right)^2 = \left(K_2^{1/2}/\bar{N}\right)_o^2 + \frac{A}{|A|}\left(\frac{\bar{N}}{N_M}\right)^2 \cdot \left(K_2^{1/2}/\bar{N}\right)^2 \left[1 \pm \left(K_2^{1/2}/\bar{N}\right)^2\right].$$

Eq. (5.448)

The plus (minus) sign holds for the assumption of a gamma (normal) distribution. If the distribution is to be approximated by a normal distribution, the r.s.d. must be small compared with unity (Sect. 5.5.B.2). Thus, for assumption of either gamma or normal distribution a positive temperature coefficient increases the r.s.d., while a negative coefficient decreases the r.s.d.

It has been assumed above that there exists a stationary process when the temperature coefficient is nonzero. It is shown below that no stationary process exists, in fact, when the temperature coefficient is positive (and only two neutrons are emitted in a fission), and the connection between this fact and the stability of a reactor with a positive temperature coefficient will now be discussed.

In the classical deterministic theory of stability of a physical system, the existence of fluctuations plays only a tacit role.

Specifically, if $\vec{N}(t)$ is a time-dependent vector describing the state of the system, and if the stability of the equilibrium state $\vec{N}_o$ (where $\vec{N}(t) = 0$) is in question, then the Liapunov criterion for stability is: The state of equilibrium $\vec{N}_o$ is stable whenever, given in the state space $\vec{N}$ any region ϵ containing $\vec{N}_o$, there is another region δ in ϵ such that every trajectory $\vec{N}(t)$ starting in δ and developing deterministically remains in ϵ.[82] Thus, stability of the state $\vec{N}_o$ is examined in terms of trajectories initiated in the neighborhood of $\vec{N}_o$, it being tacitly assumed that small fluctuations or disturbances exist to alter the system from the state $\vec{N}_o$; whereupon stability follows if deterministic trajectories remain in the vicinity of $\vec{N}_o$.

It is conceivable that a physical process is stable in the Liapunov sense but is actually unstable when examined as a stochastic process. To investigate this possibility, it is necessary first to have a usable criterion for stability of a stochastic process. If at an initial time t_o the probability set $P(\vec{N}, t_o)$ is specified, where $P(\vec{N}, t)$ is the probability that the system is in state $\vec{N}$ at time t, then the notion of stability must be associated with the future development of the set $P(\vec{N}, t)$. Because instability is intuitively associated with a tendency for a system to depart further and further from its initial state $\vec{N}_o$, it is natural to associate instability with the nonexistence of a stationary process (i.e., one for which the entire probability set $P(\vec{N}, t)$ is time-independent) which might eventually be attained. The nonexistence of a stationary process is sometimes easy to prove, and stationarity can be satisfactorily associated with stability for special cases such as the one examined here. That stationarity is neither necessary nor sufficient to satisfy intuitive conceptions of stability in general can be shown by examples.

In a deterministic treatment, the neutron level N in the reactor model discussed above satisfies Eq. (5.440a) with the variance K_2 set equal to zero:

$$dN/dt = \left[\tau_f^{-1}(\bar{\nu}_f - 1) - \tau_{c_1}^{-1} + A(N - 1)\right] N + S\bar{\nu}_s . \qquad \text{Eq. (5.449)}$$

If temperature coefficient, source strength, τ_f^{-1}, and $\bar{\nu}_f$ are fixed, then any equilibrium neutron level N_o can be attained by adjustment of τ_c^{-1}, e.g., for some control rod position:

$$0 = \left[\tau_f^{-1}(\bar{\nu}_f - 1) - \tau_{c_1}^{-1} + A(N_o - 1)\right] N_o + S\bar{\nu}_s . \qquad \text{Eq. (5.450)}$$

Subtracting the two equations and rearranging,

$$dN/dt = \frac{S\bar{\nu}_s}{N_o}\left[\frac{A}{|A|}\frac{N N_o}{N_M^2} - 1\right](N - N_o). \qquad \text{Eq. (5.451)}$$

Here the marginal level N_M defined by Eq. (5.446) has been introduced. It is seen from Eq. (5.451) that if $A \gtrless 0$ the reactor is stable in that $\dot{N}$ always has the opposite sign of the deviation $(N - N_o)$, and the neutron level always returns to N_o after a disturbance. If the temperature coefficient is positive and $N_o < N_M$, then the reactor is stable in the limited sense that increasing the neutron level by a factor less than N_M^2/N_o^2 results in the neutron level's returning to N_o. If too many neutrons are present initially, the neutron level will increase without limit even if $N_o < N_M$. If $N_o \geq N_M$, then the reactor is unstable.

The equivalent stochastic process is described by the forward stochastic Eq. (5.438). It is convenient to simplify the discussion by assuming just two neutrons are emitted in a fission, and only one neutron is emitted in a source event. Then,

$$\frac{\partial G}{\partial t} = Au(u-1)\frac{\partial^2 G}{\partial u^2} + \left[\tau_f^{-1}(u^2 - u) + \tau_{c_1}^{-1}(1-u)\right]\frac{\partial G}{\partial u} + S(u-1)G\,.$$

Eq. (5.452)

For a stationary process, $\partial G/\partial t = 0$. In this case, the point $u = 0$ is a singular but regular point of the total differential equation, Eq. (5.452), and one can seek solutions in powers of u.[83] When A is positive, one solution turns out to involve nonintegral powers of u, and the only other solution is in integral powers of u but with some negative coefficients $P(N)$, whereas probabilities must be positive. Thus, neither solution is a probability generating function, and no stationary process exists when the temperature coefficient is positive. It is conjectured that this occurs because the neutron level in the reactor ultimately fluctuates to a large value, whereupon the consequent large positive reactivity tends to increase the neutron level ever further.

For the simple model examined here the neutron capture probability τ_c^{-1} becomes negative for positive reactivity coefficient A and for sufficiently large neutron level N, as may be seen from Eq. (5.437). This behavior contributes to the large positive reactivity at large neutron levels. When the dependence of capture probability on neutron level is altered from Eq. (5.437) to one for which τ_c decreases to zero when

N increases to N' and remains zero for $N \geq N'$, it is found that the conclusions noted above are unaltered.

To summarize, when the stability of this simple reactor model with a positive reactivity coefficient is examined from the usual deterministic point of view, it is found to be stable unless the disturbances from equilibrium are larger than a certain threshold level. However, when the same system is examined as a stochastic process, it is found that with any initial probability distribution $P(N,t_o)$ of neutron number, the probability distribution does not eventually attain a time-independent (stationary) condition because no stationary condition can exist. This behavior may occur because in the random process it is always possible (though perhaps improbable) that the neutron number exceeds the deterministic threshold level and is unlikely to diminish thereafter.

D. Natural Reactor Sources

D. R. Harris

It has been determined that the weaker the source the more severe the fluctuations in neutron populations. Indeed, the probabilities which have been calculated in Sects. 5.5.B.2 and 5.5.B.3 depend in a sensitive exponential way on the source strength. This feature of possible undesirable excursions emphasizes the need for accurate knowledge of weak sources, and what follows is a discussion of that problem.

When an artificial neutron source is either absent or has decayed to a low level, the natural neutron source in the reactor, although weak, may be predominant. Determination of the natural neutron source is conveniently divided according to whether the reactor is new (when neutrons arise largely from spontaneous fissions, (α, n) reactions, and the cosmic radiation) or has a history of power operation (when (γ,n) reactions usually dominate). Not only are the neutron source mechanisms and, thus, the techniques for calculating source strength different for new and used reactors, but also source strength measurements are more convenient and more plentiful for new reactors than after power operation. Calculation of the natural neutron source in a new reactor is described first, together with experimental verification of the calculations. Calculation of the post-operation (γ,n) source is next discussed. Attention is focused throughout on reactors fueled by uranium, but the source mechanisms and methods of calculation are applicable to any fuel.

1. *Natural Neutron Source in New Reactors*

Calculation of the neutron yields from spontaneous fission, (α,n) reactions and the cosmic radiation will be described in turn, followed by comparisons between calculations and measured neutron source strengths for certain typical reactor types. Methods of calculation of neutron source strength in a new reactor are described in more detail in Refs. 84 and 85, where the energy spectra of source neutrons and their multiplicities are also treated.

A) SPONTANEOUS FISSION OF URANIUM. The spontaneous fission rates listed in Table 5.2 were measured by counting pulses produced in an ionization chamber by fission fragments emerging from a thin deposit of uranium, or by counting fission fragment tracks in nuclear emulsions containing uranium. The neutron emission rate in spontaneous fission of U^{238} has been measured a number of times (Table 5.2), usually by comparing the count rates of a neutron detector in a nearly critical, natural uranium fueled reactor with and without a calibrated neutron source. The assumption that nearly all source neutrons in such natural uranium systems result from spontaneous fission of U^{238} has been reviewed and confirmed.[84,85]

Reference to Table 5.2 shows that calculation of the neutron emission rate in spontaneous fission of other uranium isotopes requires estimates of the mean neutron yield per spontaneous fission, $\bar{\nu}$. A semiempirical theory of neutron emission in fission has been developed and applied with considerable success by Leachman[86] and Terrell.[80] In this analysis it is assumed that $\bar{\nu}$ varies linearly with the excitation energy of the fissioning compound nucleus. The experimental data obtained before 1960 are compatible with the assumed linear relation as is illustrated in Fig. 5.56 for the compound nuclei U^{236}, U^{239}, and Pu^{240}. Extrapolation of the observed linear relation for U^{236} to the ground state of U^{236} gives $\bar{\nu} \simeq 1.5$ for spontaneous fission of U^{236}. Leachman's calculated value of $d\bar{\nu}/d$ (energy) for U^{234}, combined with the measured $\bar{\nu}$ for thermal neutron induced fission of U^{233}, yields $\bar{\nu} \simeq 1.7$ for spontaneous fission of U^{234}. The theory[86] similary suggests $\bar{\nu} \simeq 1.8$ for spontaneous fission of U^{235}. In view of the large uncertainties, a single estimate $\bar{\nu} \simeq 1.7$ is employed here for spontaneous fission of U^{234}, U^{235}, and U^{236}.

Measurements of spontaneous fission rate and neutron yield are critically reviewed in Refs. 84 and 85, and best estimates of specific spontaneous fission neutron yields for natural and enriched uranium are listed in Table 5.3. About 60 percent of the spontaneous fission neutron yield from enriched uranium results from the 5 percent of U^{238} which is present.

TABLE 5.2 — MEASURED SPONTANEOUS FISSION RATES IN URANIUM

Nuclide	Spontaneous Fission Rate per Gram of Nuclide or Mixture ($kg^{-1}\ sec^{-1}$)	Neutron Emission Rate from Spontaneous Fission ($kg^{-1}\ sec^{-1}$)	Mean Neutron Yield ($\bar{\nu}$)
U^{232}	16,000 ± 10,000 (Ref. 87)		
U^{233}	0.2 (Ref. 87)		1.7 (est.)
U^{234}	< 9 (Ref. 87)		
	3.6 ± 1.5 (Ref. 88)		1.8 (est.)
U^{235}	0.3 ± 0.17 (Ref. 87)		1.5 (est.)
U^{236}	3 (Ref. 89)		
U^{238}	6,90 ± 0:24 (Ref. 87)		
	8.6 ± 0.4 (Ref. 92)	18.0 ± 0.6 (Ref. 92)	2.1 ± 0.1 (Ref. 92)

TABLE 5.2 —MEASURED SPONTANEOUS FISSION RATES IN URANIUM (Continued)

Nuclide	Spontaneous Fission Rate per Gram of Nuclide or Mixture (kg^{-1} sec^{-1})	Neutron Emission Rate from Spontaneous Fission (kg^{-1} sec^{-1})	Mean Neutron Yield ($\bar{\nu}$)
$U^{natural}$	4.4 ± 0.5 (Ref. 90)	15 (Ref. 87, p. 27)	
	6.7 ± 0.4 (Ref. 91)	17.5 (Ref. 93)	
		15.4 (Ref. 94)	
		16.0 (Ref. 95)	
		15.2 ± 0.5 (Refs. 96, 97)	
		15.3 ± 0.6 (Ref. 98)	
		15.6 ± 1.2 (Ref. 99)	

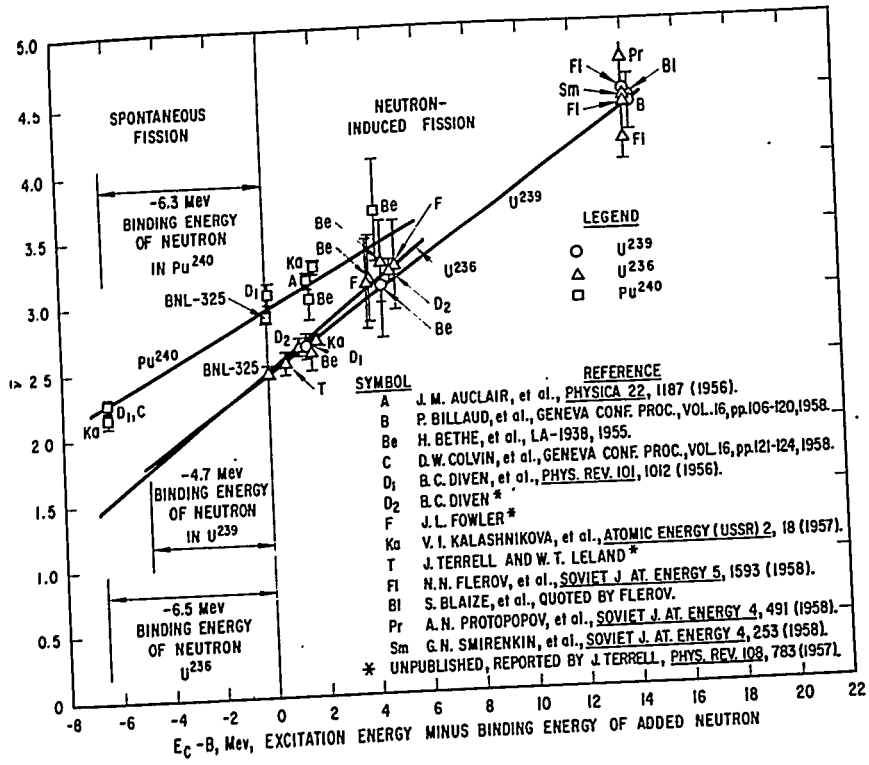

FIGURE 5.56. Neutron Yield ($\bar{\nu}$) in Fission vs Excitation Energy (E_o) of Pu^{240}, U^{236}, and U^{239}.

TABLE 5.3 — NEUTRON YIELD PER KILOGRAM OF URANIUM PER SECOND FROM SPONTANEOUS FISSION

Natural Uranium† (kg^{-1} sec^{-1})	Enriched Uranium‡ (kg^{-1} sec^{-1})
16 ± 1	1.5 ± 0.3

†Weighted mean of measurements of Refs. 92, 96, 97, 98, and 99 of Table 5.2.

‡Calculated as described in the text, using the isotopic composition listed in Table 5.4. The quoted error reflects the uncertainty in $\bar{\nu}$ for $U^{234-236}$.

B) (α, n) REACTIONS. Alpha particles emitted in natural radioactivity of uranium can produce neutrons by (α, n) reactions with light nuclei. Measured α-particle energies and emission rates in uranium radioactivity are shown in Table 5.4. The α-particle emission rate from U^{234} is strikingly large.

The α group of highest energy, E_α=4.77 Mev from U^{234}, has a range of order 10^{-3} cm in solid metals or ceramics. As a result, in heterogeneous reactors the α particles are confined in the uranium-bearing fuel elements and do not penetrate into the coolant. The (α,n) neutron production is affected also by grain structure of characteristic dimension 10^{-3} cm in the fuel element. This microstructure effect will be discussed later; for the moment it is supposed that the α particle slows down by atomic collisions in a homogeneous fuel element. In penetrating a distance between x cm and $x+dx$ cm, the alpha slows from energy E_α ev to $E_\alpha - dE_\alpha$ and produces a neutron with probability $N_j\sigma_j(E_\alpha)dx$, where N_j represents the number of target nuclei of j^{th} type per cubic centimeter and $\sigma_j(E_\alpha)$ represents the cross section for (α,n) reaction with the target nucleus. Transforming from the x variable to the E_α variable, the probability P_j that an alpha produces a neutron in j^{th} type reactions while slowing down from an initial energy E_o is

$$P_j = \int_0^{E_o} dE_\alpha \left|\frac{dx}{dE_\alpha}\right| N_j\sigma_j(E_\alpha) \ . \qquad \text{Eq. (5.453)}$$

Measured rates of energy loss are reviewed, and best values are fitted by Whaling[100] in terms of the stopping cross section per atom ϵ defined by

$$\epsilon \equiv \frac{1}{N_S}\left|\frac{dE}{dx}\right| \ \text{ev cm}^2/\text{atom} \ . \qquad \text{Eq. (5.454)}$$

Here N_S represents the number of stopping atoms or molecules per cubic centimeter. Combining these relations, the probability that an alpha produces a neutron in reactions of j^{th} type in the homogeneous medium is

$$P_j = \frac{N_j}{N_S}\int_0^{E_o} dE_\alpha \frac{\sigma_j(E_\alpha)}{\epsilon(E_\alpha)} \ . \qquad \text{Eq. (5.455)}$$

In terms of the weight fraction $w_j = N_jA_j/N_SA_S$ of target material, where A represents atomic weight, a convenient expression is

$$P_j = w_j\int_0^{E_o} dE_\alpha \frac{A_S}{A_j}\frac{\sigma_j(E_\alpha)}{\epsilon(E_\alpha)} \ . \qquad \text{Eq. (5.456)}$$

TABLE 5.4 — URANIUM α-RADIOACTIVITY

Nuclide	Half-Life* for α-Decay (yr)	Energy* of α (Mev)	Relative* Frequency of Energy Group (%)	Relative Amount of Nuclide in Natural Uranium (w/o)	α-Decay Rate per kg of Natural Uranium (kg^{-1} sec^{-1})	Relative Amount of Nuclide in Enriched Uranium † (w/o)	α-Decay Rate per kg of Enriched Uranium (kg^{-1} sec^{-1})
U^{234}	2.48×10^5	4.77	72	0.0058	1.2×10^7	1.0	2.2×10^9
		4.72	28				
U^{235}	7.13×10^8	4.58	10	0.720	5.4×10^5	93.2	7.1×10^7
		4.47	3				
		4.40	83				
		4.20	4				
		4.50	73				
U^{236}	2.39×10^7	4.45	27	--	--	0.3	6.8×10^6
U^{238}	4.51×10^9	4.19	77	99.274	1.2×10^7	5.5	6.5×10^5

*Ref. 103, p. 230.
†Typical values are listed.

In Refs. 84 and 85 the integral in Eq. (5.456) is referred to as the yield integral and is calculated in the variety of ways indicated below. In all cases, the stopping power per atom $\epsilon(E_\alpha)$ is obtained from Whaling's review[100] or is interpolated according to the Bloch formula between values for stopping materials of similar charge.

1. When $\sigma_j(E_\alpha)$ has been measured,[101] as is the case for Al and Mg (Fig. 5.57), numerical integration of σ_j/ϵ gives the yield integrals for Al and Mg listed in Table 5.5 for various initial alpha energies E_o.
2. Measurements of the yield integral have been made when alphas of various initial energies are stopped in thick targets of boron and beryllium.[102] If the boron or beryllium were homogeneously distributed in a matrix, for example of zirconium, then the yield integral for alphas stopping in the mixture can be approximated by, for example for boron,

$$\int_0^{E_o} dE_\alpha \frac{A_{Zr}\sigma_B(E_\alpha)}{A_B \epsilon_{Zr}(E_\alpha)} \approx \frac{A_{Zr}\epsilon_B(E'_\alpha)}{A_B \epsilon_{Zr}(E'_\alpha)} \int_0^{E_o} dE_\alpha \frac{\sigma_B(E_\alpha)}{\epsilon_B(E_\alpha)} \qquad \text{Eq. (5.457)}$$

where E'_α is a fixed energy. This is a good approximation because $\epsilon_B(E_\alpha)/\epsilon_{Zr}(E_\alpha)$ is a very slowly varying function compared with $\sigma(E_\alpha)$, which increases sharply with alpha energy (see Fig. 5.57). The integral $\int dE_\alpha \sigma_B/\epsilon_B$ in Eq. (5.454) is the thick target yield integral for boron measured as noted above, and the ratio $\epsilon_B(E'_\alpha)/\epsilon_{Zr}(E'_\alpha)$ is insensitive to choice of some average E'_α. The yield integrals in Table 5.5 for boron and beryllium in low density in zirconium are calculated in this way.

3. Measurements have been made of the yield integral when alphas emitted at energy 5.3 Mev from polonium slow down in thick targets.[102,104,105] Extrapolation of the measurements to lower initial alpha energies E_o is accomplished by calculating $\sigma(E_\alpha)$ according to the continuum theory,[106] calculating the yield integrals as in method 1 above for E_o = 5.3 Mev and the desired E_o, and setting.

$$\int_0^{E_o} dE_\alpha \frac{A_S}{A_j}\frac{\sigma_j(E_\alpha)}{\epsilon(E_\alpha)} \approx \left(\int_0^{5.3\ \text{Mev}} dE_\alpha \frac{A_S}{A_j}\frac{\sigma_j(E_\alpha)}{\epsilon(E_\alpha)}\right)_{\text{Measured}} \left[\frac{\displaystyle\int_0^{E_o} dE_\alpha \frac{A_S}{A_j}\frac{\sigma_j(E_\alpha)}{\epsilon(E_\alpha)}}{\displaystyle\int_0^{5.3\ \text{Mev}} dE_\alpha \frac{A_S}{A_j}\frac{\sigma_j(E_\alpha)}{\epsilon(E_\alpha)}}\right]_{\substack{\text{Calculated}\\ \text{continuum}\\ \text{theory}}}$$

Eq. (5.458)

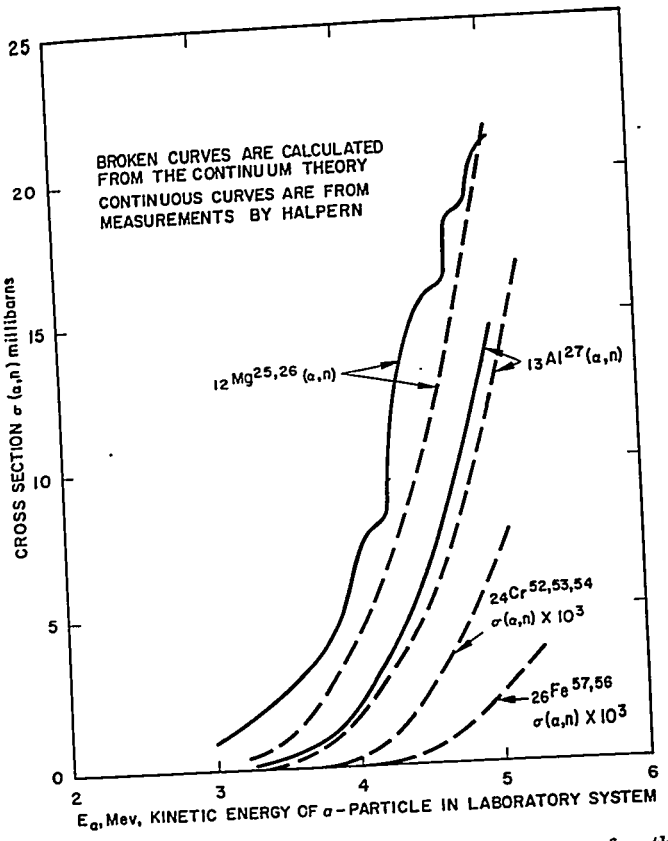

FIGURE 5.57. Measured and Calculated Cross Sections for the (α,n) Reaction in Mg, Al, Cr, and Fe.

The continuum theory reasonably reproduces the measured energy variation of $\sigma(E_\alpha)$ as is shown in Fig. 5.57, although the normalization of the calculated $\sigma(E_\alpha)$, which is removed in the extrapolation, may be questionable. The yield integrals for dilute sodium dissolved in zirconium, which are listed in Table 5.5, are determined in this way.

4. The extrapolation of the measured yield integral for alphas of initial energy 5.3 Mev to infer yield integrals for lower initial alpha energies gains in confidence when there are measurements of the differential (α, n) cross section for neutron emission in a particular direction. Because the (α, n) neutrons may be emitted with a complex angular distribution, a measured differential (α, n) cross section in a particular direction provides only an approximation for the energy dependence of $\sigma(E_\alpha)$, the angle-integrated cross section. Nevertheless, when a measured cross section for neutron emission in a particular

TABLE 5.5 — (α,n) YIELD INTEGRAL* $\int_0^{E_o} dE_\alpha \frac{A_S}{A_j} \frac{\sigma_j(E_\alpha)}{\epsilon(E_\alpha)}$

Reacting Nuclide	Stopping Material	E_o (Mev)				
		5.3	4.8	4.6	4.4	4.2
$_{13}Al^{27}$	Al	0.46, 0.74 (Ref. 104)	0.17	0.11	0.064	0.035
$_{13}Al^{27}$	Zr	--	0.26	0.18	0.10	0.062
$_{12}Mg$	Zr	--	0.84	0.60	0.41	0.26
$_5B$	B	19 (Refs. 102, 105) 24 (Ref. 104)	14 (Ref. 102)	12 (Ref. 102)	10 (Ref. 102)	9 (Ref. 102)
$_5B$	Zr	39	29	25	21	19
$_8O$	O_2	0.070 (Ref. 104) 0.063 (Ref. 107)	0.05	--	--	--

TABLE 5.5 — (α, n) YIELD INTEGRAL* $\int_0^{E_o} dE_\alpha \frac{A_S}{A_j} \frac{\sigma_j(E_\alpha)}{\epsilon(E_\alpha)}$ (Continued)

Reacting Nuclide	Stopping Material	E_o (Mev)				
		5.3	4.8	4.6	4.4	4.2
$_8O$	UO_2	0.20	0.14	--	--	--
$_{11}Na^{23}$	Na	1.5 (Ref. 104)	--	--	--	--
$_{11}Na^{23}$	Zr	--	1.6	1.1	0.8	0.5
$_6C$	C	0.11 (Ref. 104)	0.07	--	--	--
$_6C$	Zr	0.24	0.16	--	--	--
$_4Be$	Be	76 (Ref. 102)	53 (Ref. 102)	43 (Ref. 102)	39 (Ref. 102)	32 (Ref. 102)
$_4Be$	Zr	--	142	115	104	86

*Measured values are referenced. All other values of yield integral in the table are calculated as described in the text and in Refs. 84 and 85.

direction is known as a function of alpha energy, as is the case for O^{18} (α,n) and C^{12} (α,n),[108] this measured differential cross section is used in place of the calculated (α,n) cross section in the extrapolation of the yield integral from one initial alpha energy to another, as described above.

The alpha particle emission rates of Table 5.3, the yield integrals of Table 5.5, and the weight fractions of target materials in various slowing-down materials are combined according to Eq. (5.456) to calculate the (α,n) neutron production rates listed in Table 5.6. The fuel elements which are considered contain natural uranium or highly enriched uranium dissolved in low concentration in aluminum or Zircaloy-2 or are present as the compound UO_2. Of the many nuclides present in uranium-Zircaloy-2 alloy, some have negligible (α,n) cross sections because of high nuclear charge, as illustrated in Fig. 5.57 for Cr and Fe. Other nuclides have (α,n) energy thresholds above 4.8 Mev, as is the case for C^{12}, N^{14}, N^{15}, and O^{16}. Those nuclides which contribute nearly all of the (α,n) reactions in Zircaloy-2 are O^{18}, C^{13}, Na^{23}, Al^{27}, and Mg as listed in Table 5.6. Addition of boron or beryllium to the Zircaloy-2 fuel element greatly augments the neutron yield.

C) COSMIC RADIATION. Entering a reactor from above are cosmic radiation collision products, a penetrating μ-meson beam and a strongly-interacting cascade of nucleons and π-mesons.[84,85,109] If a nucleus in the reactor is struck by a fast nucleon or π-meson, it may remain intact but excited or it may undergo spallation or fission. Neutron emission occurs in de-excitation processes in all three cases, the yield increasing with atomic number of the nucleus. In addition, a negative μ-meson, absorbed by a nucleus, excites the nucleus and neutrons are emitted. The attenuation of the μ-meson beam and the nucleon π-meson cascade, and the consequent neutron production, are a complex process; estimation of the local neutron production rate is best accomplished by extrapolation from measured production rates (Fig. 5.58).

It is important to recognize that few neutrons diffuse into the reactor from the atmospheric pool of low energy neutrons because their average migration length in reactor shielding material is small. For example, the average migration length in water for neutrons with the atmospheric spectrum measured by Hess, et al.[110] is less than 4 cm. Thus, background neutrons of interest, those produced with energies of order 1 or 10 Mev, are produced locally in the reactor.

TABLE 5.6 — NEUTRON YIELD PER GRAM OF URANIUM PER SECOND FROM (α,n) REACTIONS IN VARIOUS FUEL ELEMENTS

(Homogeneous or Fine Random Mixture of Phases)

Fuel Element		Natural Uranium* (kg^{-1} sec^{-1})	Enriched Uranium* (kg^{-1} sec^{-1})
U-Al		2.4	350
U-Zircaloy-2	O (1200 ppm)	24×10^{-4}	37×10^{-2}
	C (270 ppm)	8×10^{-4}	9×10^{-2}
	Na (20 ppm)	5×10^{-4}	7×10^{-2}
	Al (75 ppm)	3×10^{-4}	4×10^{-2}
	Mg (20 ppm)	5×10^{-4}	0.8×10^{-2}
	Sum	4.5×10^{-3}	0.6
U-Zircaloy-2-Natural Boron (500 ppm)			
	O, C, Na, Al, Mg	4.5×10^{-3}	0.6
	B	0.29	32
	Sum	0.29	32.6
U-Zircaloy-2-Beryllium (500 ppm)			
	O, C, Na, Al, Mg	4×10^{-3}	0.5
	Be	1.1	120
	Sum	1.1	120.5
UO_2		0.28	36

*Isotopic contents as listed in Table 5.4.

The rate of production of low energy neutrons in the reactor will be determined by extrapolation from measured production rates in nonfissionable materials. Typical of these measurements is that of Cocconi and Cocconi Tongiorgi.[111] These experimenters surrounded a large mass of material, hereafter called the neutron producer, with a layer of paraffin about 3 in. thick in which were embedded a number of BF_3 counters. The assembly was enclosed in a watertight container and submerged at various depths in a lake. The efficiency with which the counters detected a neutron born in the producer was determined by use of a calibrated Ra-Be source. The neutron detection rate with producer in place, minus the detection rate without producer, corrected for detection efficiency, and

divided by the producer mass, gives the specific neutron production rate. Such rates in lead, aluminum, and paraffin producers measured at various depths in the lake are shown in Fig. 5.58. These data points are labeled C. Neutron production rates are not given by the Cocconis but were calculated for the present study from the published rates of production of 0, 1, 2, . . . neutrons.

Three physical processes are involved here. First, the μ-meson beam and the nuclear π-meson cascade have been attenuated by all material above the producer. If such attenuation were approximately proportional to a fixed cross section per nucleon, then equal attenuations would be observed for each g cm^{-2}. The abscissa of Fig. 5.58 represents the thickness of attenuating material in units of g cm^{-2}. Second, for a given beam the neutron yield per gram of producer

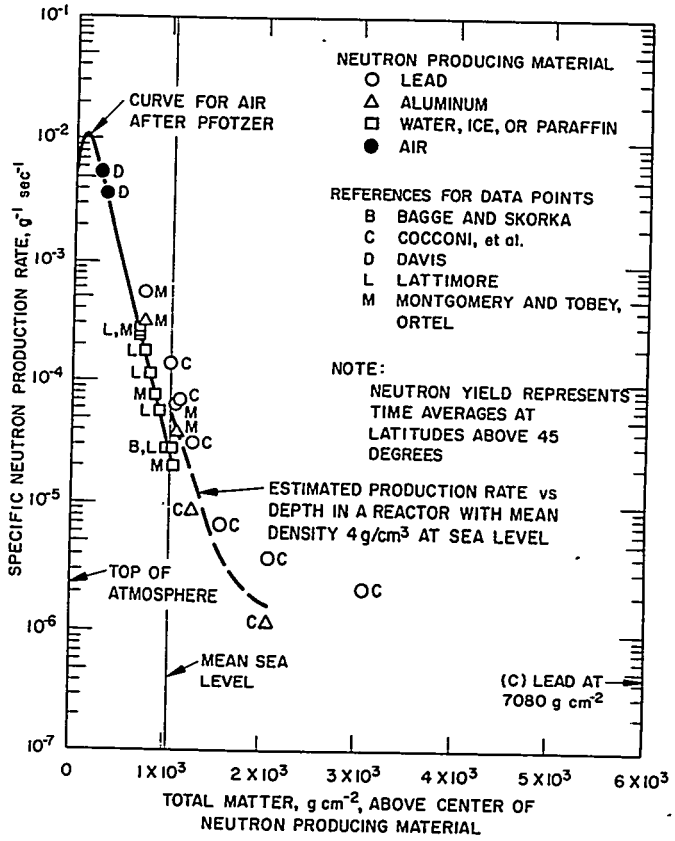

FIGURE 5.58. Production by Cosmic Rays of Neutrons with 1 Mev to 10 Mev Energies in Various Materials at Various Depths.

increases with the atomic number of the producer.[84,85] Third, the neutrons so produced are slowed down by the producer and adjacent materials and, perhaps, captured before detection. In the Cocconi and Cocconi Tongiorgi experiment,[111] the attenuating material comprised about 10^3 g cm^{-2} of air, various thicknesses of water, and up to 100 g cm^{-2} of lead, paraffin, steel, etc. Also, the producing material and the surrounding paraffin comprised the slowing-down material. In another experiment, Lattimore[112] exposed boron-loaded photographic emulsions at various depths in a glacier. Here the small mass of the emulsion ensures that except for air attenuation the attenuating, producing, and slowing-down materials all were identical: ice. In general, the slowing-down material is not very important in the measurement of specific neutron yield because of the manner of detector calibration. The slowing-down material properties do not appear as variables in Fig. 5.58.

The expected increase in specific neutron yield with increasing atomic number of the producer is well illustrated by the data of Fig. 5.58. The specific yields in water, aluminum, and lead are in approximate ratio 1:2:5 near sea level. In all cases shown in Fig. 5.58, data points obtained by the same group using the same neutron producing material differ only in the thickness of waterlike attenuating material (water, ice, air, or paraffin) above the producer.

For depths below sea level z such that $-300 \text{ g cm}^{-2} < z < 3000 \text{ g cm}^{-2}$ the data of Fig. 5.58 are approximated by the relation

$$Y_j = A_j e^{-z/L_{H_2O}} + B_j e^{-z/\lambda_{H_2O}} . \qquad \text{Eq. (5.459)}$$

Here Y_j represents the neutron yield per second per gram of the j^{th} producing material, L_{H_2O} is the attenuation length for the nucleon cascade in water, and λ_{H_2O} is the attenuation length for the μ-meson beam in water at moderate depths. Also, A_j and B_j are the specific neutron yields in the j^{th} producing material at sea level resulting from the nucleon cascade and from the μ-meson beam, respectively.

The nucleon π-meson cascade and the μ-meson beam which penetrate into the core of a reactor have been attenuated by the steel, water, lead, etc. above the core together with the layer of core material above the observed point. The attenuation length of the nucleon π-meson cascade varies for different materials. Thus, $L \simeq 150$ g cm^{-2} for water (Fig. 5.58), $L \simeq 200$ g cm^{-2} for aluminum,[113] and $L \simeq 300$ g cm^{-2} for lead.[113,114] Suppose the mean density of core material and of the pipes, control rods, etc., above the core is about 4 g cm^{-3}, a not

unreasonable figure. Then, the constants A and B of Eq. (5.459) take on values of 5×10^{-5} g^{-1} sec^{-1} and 3×10^{-6} g^{-1} sec^{-1}, respectively, as interpolated between aluminum and lead data of Fig. 5.58. Assume a cascade attenuation length $L \simeq 200$ g cm^{-2} for the hypothetical material of density 4 g cm^{-3}. The choice of an attenuation length for the μ-meson beam is not very important at moderate depths. It is taken to be $\lambda \simeq 2500$ g cm^{-2}. Then, the specific neutron yield in the reactor is given approximately by the relation

$$Y \simeq 5 \times 10^{-5} e^{-z/200} + 3 \times 10^{-6} e^{-z/2500} \text{ g}^{-1} \text{ sec}^{-1} \qquad \text{Eq. (5.460)}$$

and this relation is plotted in Fig. 5.58. This relation ignores the complicated transition effects which occur when the cascade passes from one material to another when above the reactor are layers of differing materials. For example, Bernardini, et al., [113] found an increase in the rate of cascade induced nuclear reactions in the first several centimeters in lead, followed by exponential attenuation. Such little understood transitions are assumed not to affect the gross behavior described by Eq. (5.460).

Production of low energy neutrons by the cosmic radiation varies with geomagnetic latitude, being least near the equator and increasing to about 50 degree latitude, where the production rate at sea level flattens out for further latitude increase at a value about 2.5 times that at the equator.[115] The data of Fig 5.58 were obtained at geometric latitudes between about 45 degrees north and 60 degrees north, and the numerical yields in Eqs. (5.459) and (5.460) refer to such latitudes as well as to higher latitudes.

The cosmic ray neutron yield decreases with increasing atmospheric pressure, but the variation is not large (-1 percent/mm Hg). A variety of time variations have been observed in the cosmic ray neutron production rate including a diurnal variation (about ±1/2 percent), a 27-day variation (about ±2 percent), decreases associated with magnetic storms (up to about 10 percent), and increases associated with solar flares (up to about 3200 percent).[115] Large increases associated with solar flares are rare, five such events being observed in 17 years.[115]

D) OTHER BACKGROUND SOURCES. In $U^{234-236}$ and U^{238} radioactivity a number of gammas are emitted, most having energies of order 50 kev, and all having energies less than 250 kev. But photoneutron thresholds in most naturally occurring nuclides exceed 6 Mev, the exceptions being deuterium

and beryllium which have (γ, n) thresholds 2.2 Mev and 1.7 Mev, respectively. Thus, photoneutron production by gammas from uranium radioactivity is impossible. By the same token, the 1.5 Mev gamma emitted in some K^{40} decays does not yield photoneutrons.

E) CALCULATED AND MEASURED NATURAL NEUTRON SOURCES. Calculated natural neutron source strengths in certain typical uranium-fueled reactors are listed in Table 5.7. Spontaneous fission neutron yields and (α, n) yields in homogeneous media are taken from Tables 5.2 and 5.6, respectively. Yields of neutrons from the cosmic radiation are interpolated from Fig. 5.58 according to the properties of the materials which attenuate the cosmic ray beam above the core or which act as targets for the beam.

It has been pointed out that the natural neutron source resulting from (α, n) reactions is affected by the microstructure of some fuel elements. While the range of a 4.8 Mev alpha is about 20 μ in a fuel plate, the sharp decrease of (α, n) cross section with decreasing alpha energy (Fig. 5.58) requires that most neutrons be produced in the first 5 μ of the alpha track. Microstructure with characteristic dimension about 5 μ then affects the (α, n) yield. For example, microphotographs of polished and etched specimens U-Al fuel show many grains of UAl_4, the uranium-bearing phase, most having longest dimension about 2 μ and shortest dimension about 1 μ, while a very few have longest dimension ranging up to 25 μ. If all alphas slowed in a homogeneous medium of UAl_4, the neutron yield would only be 58 percent of the yield in pure aluminum because of the augmented slowing down of the alpha particle by uranium in UAl_4. However, a representative alpha of initial energy 4.75 Mev emerges from the parent UAl_4 grain with energy about 4.6 Mev, corresponding to a track of length 1 μ in UAl_4. Then, from the yield integrals of Table 5.5, the (α, n) neutron yield in the U-Al fuel element relative to that in pure aluminum is $2/3 + 0.58 \times 1/3$, or 0.86. The (α, n) neutron yield for U-Al fuel listed in Table 5.7 is 86 percent of the homogeneous yield. It has been assumed that no uranium is dissolved in the aluminum phase.

Similarly, when about 600 ppm of boron are added to a uranium-Zircaloy fuel element, up to about 200 ppm of the boron go into homogeneous solution, and the remainder forms ZrB_2 grains with shortest dimensions about 3 μ. About 18 percent of the uranium also is in solution, while the rest is concentrated in a thin uranium-rich phase surrounding grains of nearly pure zirconium. The ZrB_2 grains usually appear to be separated from the uranium-rich phase by sheaths of zirconium

TABLE 5.7 — NATURAL NEUTRON SOURCES IN TYPICAL REACTORS

Fuel Material	Reactor Type	Spontaneous Fission Neutron Yield per kg U/sec	Cosmic Radiation*			(α, n) Neutron Yield per kg U/sec		Total Calculated Neutron Yield per kg U/sec	Measured Neutron Yield per kg U/sec
			kg Core Material per kg U	Condensed Material above Core Center (kg/cm^2)	Neutron Yield per kg U/sec	Homo-geneous	With Micro-structure Effect		
$U^{nat}O_2$	GLEEP	16	10	1000	0.02	0.24	0.24	16 ± 1	15.2 ± 0.5 (Ref. 97)
U^{enr}metal	GODIVA	1.5	1	120	0.3	--†	--	>1.8	2.4 ± 0.1
U^{enr}-Al	SPERT	1.5	20	200	2	350	300	300 ± 100	360 ± 100 (Ref. 116)
$U^{enr}O_2$	Water Moderated Critical Facility	1.5	20	200	0.5	36	36	38	
U^{enr}-Zirc-2	Water Moderated Critical Facility	1.5	20	200	0.5	0.5	0.5	2.5 ± 1	3 ± 1 (Ref. 117)
	Water Moderated Power Facility			500	0.1	0.5	0.5	2.1 ± 1	
U^{enr}-Zirc-2 (with added 640 ppm B)	Water Moderated Critical Facility	1.5	20	200	0.5	41	31	33 ± 8	37 ± 7 (Ref. 117)
	Water Moderated Power Facility			500	0.1	41	31	33 ± 8	

*Reactors assumed at sea level, except for GODIVA and SPERT.
†Trace element contents not known.

of order 3 μ thick. Examination of a model composed of infinite slabs of ZrB_2, Zr, and U of appropriate thicknesses has indicated that the (α,n) neutron yield is 25 to 30 percent less in the heterogeneous fuel element than in the homogeneous case. The (α,n) neutron yield is correspondingly decreased for the last case listed in Table 5.7.

Natural neutron sources in new reactors have been measured by comparison with standard sources, and such measurements are listed in Table 5.7. The measurements are in reasonable agreement with calculated values, in view of the roughly 20 percent uncertainties in experiment and calculation. Comparison of calculations and measured values for U-Al fuel and U-Zircaloy-2-boron fuel suggests that the diminution in (α,n) yield resulting from fuel element microstructure is overestimated, such as might result if a larger fraction of uranium is in solution than has been assumed. However, such a conclusion is questionable, in view of the large uncertainties.

Perhaps the most striking aspect of the natural neutron source is the large contribution from (α, n) reactions when low-Z target nuclei are present in sufficient abundance. In other cases, such as the GODIVA uranium sphere and the critical assembly with U-Zircaloy-2 fuel elements, the neutron source contributions from spontaneous fission, cosmic radiation, and (α,n) reactions are comparable.

2. *Photoneutron Source in Uranium-Water Reactors after Power Operation*

A) INTRODUCTION. After substantial power operation of a reactor, a variety of natural neutron source mechanisms become operative. If the reactor contains deuterium or beryllium, a natural neutron source arises from $D(\gamma,n)$ and $Be^9(\gamma,n)$ reactions, and this source is temporarily much larger than that in the new reactor. These threshold reactions are induced by hard gammas de-exciting delayed fission products, by de-excitation gammas emitted in decay of neutron capture reaction products, and by bremsstrahlung gammas produced by delayed beta activity. Such delayed gammas are not sufficiently energetic to induce photoneutron reactions with any naturally occurring nuclides other than D or Be^9. A minor additional neutron source arises in photofission of fuel nuclei by delayed gammas. It is possible that the natural neutron source is augmented by delayed neutrons emitted directly in decay of fission products. However, sufficient nuclear mass data exist that render unlikely any delayed neutron activity with a half-life longer than 15 m. The same nuclear mass data also rule out the interesting possibility that some neutron-rich fission product

or neutron capture reaction product might have a (γ,n) threshold lower than the maximum energy of the delayed gammas.

In summary, then, the delayed natural neutron source consequent to power operation of a reactor containing deuterium or beryllium results mainly from photodisintegration of these nuclides. Calculations will be described of the $D(\gamma,n)$ photoneutron source strength at times greater than 2 hours and less than 70 hours after power operation of uranium-water reactors,[118] and these calculations will be tested by comparison with the measurements of S. Bernstein, et al.[119]

The central problem in calculation of the delayed photoneutron source is the determination of the delayed emission rate of hard gammas with energies above the thresholds of the $D(\gamma,n)$ and $Be^9(\gamma,n)$ reactions, 2.23 Mev and 1.67 Mev, respectively. In 1951, W. K. Ergen[120] was able to reproduce Bernstein's measured photoneutron decay curve at times later than 10 hours after irradiation by calculating the number of $D(\gamma,n)$ reactions produced by hard gammas accompanying decays of the fission products Rb^{88}, I^{135}, and La^{140}, together with a large inferred yield of hard gammas accompanying decay of Te^{131}. Since that time, improved gamma spectrometry has resulted in qualitative changes in the decay schemes of these nuclides. For example, Te^{131} is not considered now to emit hard gammas. Moreover, other nuclides have been discovered which decay accompanied by significant hard gammas. It is to be expected that delayed hard gammas exist which have not yet been observed, and that some adopted gamma yields are in error. Nevertheless, the comparison of the calculated photoneutron yield in D_2O with Bernstein's measurements suggests that the photoneutron yield can be calculated with some confidence for a day or so after brief reactor operation.

B) PHOTOREACTIONS. Most unstable nuclei formed as a result of reactor operation emit betas and gammas as decay products, and such delayed betas and gammas can produce neutrons by a variety of processes. Beta particles can induce neutron-emitting reactions by virtual photon creation in the Coulomb field of the target nucleus, followed by nuclear absorption of the photon. This process is less likely than is production of bremsstrahlung by the beta particle, followed by a (γ,n) reaction, and will be ignored.

Beta or other decay of an unstable nucleus may leave the residual nucleus in an excited state which de-excites by gamma emission. Of the known de-excitation gammas which are emitted from fission products in a reactor more than 30

minutes after shutdown, the 4.87 Mev gamma from Rb^{88} is highest in energy.

In emerging through the Coulomb field of the parent nucleus, a beta emits gamma radiation with a continuous spectrum of energies up to the beta energy. In contrast to this inner bremsstrahlung, the radiation emitted when the beta passes through the Coulomb field of another nucleus is referred to as outer bremsstrahlung. The bremsstrahlung formed in a reactor more than 30 minutes after shutdown is less energetic than 5.2 Mev, the maximum beta energy (from Rb^{88}). The production of photoneutrons by hard bremsstrahlung is important only after the decay of La^{140}, perhaps 3000 hours after shutdown, and when the betas are slowed in high Z material, such as a fuel plate. Neither condition is satisfied in analysis of the Bernstein experiment, and bremsstrahlung is ignored here.

The photoreactions of present interest are those which can be induced by gammas of energies about 5 Mev or less.

1) Photofission. The absorption of a hard gamma in U^{235}, U^{238}, Pu^{239}, or other heavy nucleus results in fission or in neutron emission. For gamma energies below the neutron binding energy, greater than or equal to 5.2 Mev, the photofission cross section has been measured[121,122] for gamma energies as low as 4.6 to 4.7 Mev; and that photofission has no true threshold is shown by the existence of spontaneous fission. The $U^{235}(\gamma, f)$, $U^{238}(\gamma, f)$, and $Pu^{239}(\gamma, f)$ cross sections[121,122] increase very rapidly with energy from about 1 mb at 4.6 Mev to about 100 mb at 5.2 Mev, as is illustrated for U^{238} in Fig. 5.59. The observed strong energy dependence is characteristic of a Coulomb barrier penetration phenomenon. Hence, at lower gamma energies the photofission cross section must be very small and, assuming some deuterium or beryllium is present, is negligible. In consequence, photofission is of interest only for the 4.87 Mev gamma from decay of Rb^{88} and for the accompanying bremsstrahlung. Because of the small cross sections involved, photofissions augment the neutron source appreciably only when uranium or plutonium nuclei are perhaps 100 times as numerous as deuterium nuclei, as is in fact the case in a typical reactor with high uranium content.

2) Photoneutron Reactions with Stable Nuclides. Thresholds for photoneutron reactions with stable nuclides other than D or Be^9 are above 5.3 Mev, and these reactions are not induced by delayed gammas. The thresholds for the $Be^9(\gamma, n)$ and $D(\gamma, n)$ reactions are 1.67 Mev and 2.23 Mev, respectively. Because

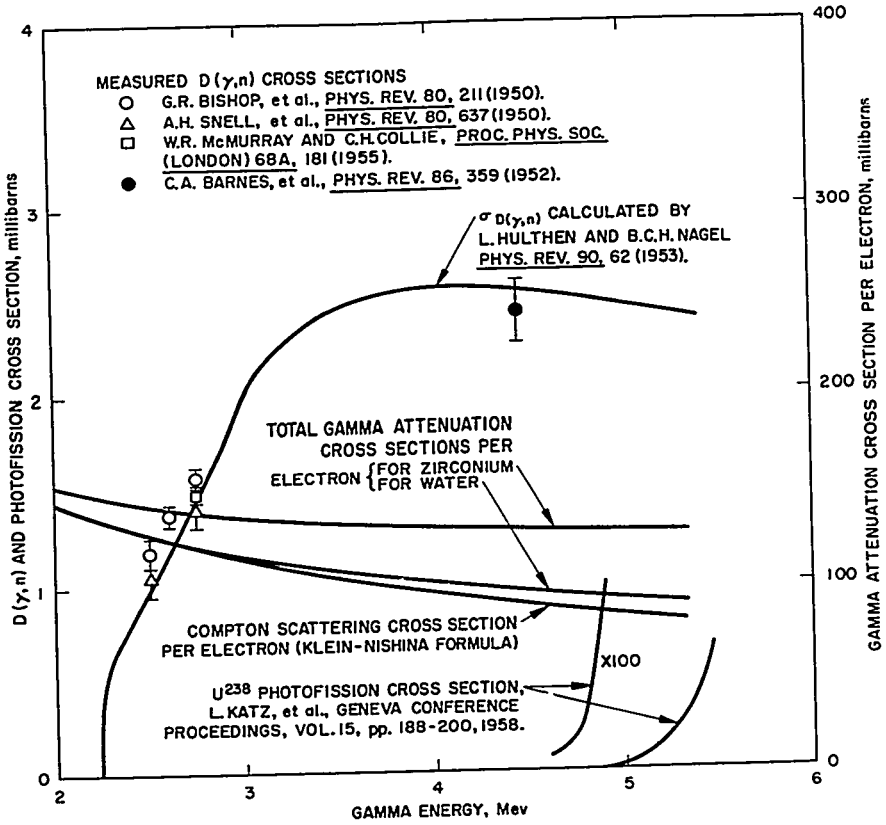

FIGURE 5.59. Gamma Reaction Cross Sections.

gammas of lower energy are more plentiful in decay of long-lived nuclides, beryllium is more effective in neutron production than is deuterium. It is desired to focus attention on the photoneutron source in water-moderated reactors which contain deuterium in the water but which may or may not contain beryllium. It will be assumed that beryllium is not present, even in quantities as low as a few ppm.

Suppose that the weight fraction of beryllium in core metal is W_{ppm}, that the water-to-metal volume ratio is R, and that a beryllium nucleus is five times more likely to yield a photoneutron in the delayed gamma flux than is a deuterium nucleus.* Then, the numbers of photoneutrons from Be^9 (γ, n) and $D(\gamma, n)$ reactions are in approximate ratio $W/4R$, so that the Be^9 (γ, n) and $D(\gamma, n)$ yields are comparable when R is of order unity and

*P. F. Fox measured this relative effectiveness for gammas emitted in a U-Zr-water reactor 10 days after shutdown, following lengthy power operation. The Be/D effectiveness ratio is expected to increase at later times after shutdown.

only a few ppm of beryllium are present. This surprising result arises because the deuterium content of ordinary water is very small, only about 30 ppm by weight.

C) CALCULATION OF PHOTONEUTRON PRODUCTION BY GAMMAS OF ARBITRARY ENERGY. The mean length for attenuation of a typical delayed gamma of energy 2.6 Mev is 23.5 cm in water, 4.0 cm in zirconium, or 1.2 cm in uranium. Most delayed gammas in a reactor are born within fuel elements composed of uranium, UO_2, Zircaloy, etc., and in many cases these fuel elements are thin, compared with a gamma attenuation length. Repeating arrays of fuel elements and coolant channels can be homogenized in calculations of photoneutron production. The calculation of photoneutron production in infinite homogeneous media is treated first; then heterogeneous effects are considered.

1) Photoneutron Production in Infinite Homogeneous Media

(a) Gamma Reaction Rates

(1) $D(\gamma,n)$ Cross Section. Most delayed gammas of interest for this study have energies between the $D(\gamma,n)$ threshold, 2.23 Mev, and about 3.5 Mev. In this energy interval the $D(\gamma,n)$ cross section increases rapidly with increasing energy, as is illustrated in Fig. 5.59, and a few measured values of the cross section are available. Hulthen and Nagel have calculated the $D(\gamma,n)$ cross section using accurate approximations for the neutron and proton wave functions for a Yukawa nuclear potential parameterized by the mass of the π-meson. The calculated cross section illustrated in Fig. 5.59 and used in this study corresponds to an assumed π-meson mass $286.4\, m_e$. Earlier experiments of Bishop, et al.,[123] seem to indicate that the calculated cross section is about 10 percent too low near 2.5 to 2.8 Mev, but the more recent experiment of McMurray and Collie[124] is in excellent agreement with the calculated cross section. At higher energies not shown in Fig. 5.59, the measured cross sections are in substantial agreement with the calculated cross section. In the absence of detailed measured values, the $D(\gamma,n)$ cross section calculated by Hulthen and Nagel, and displayed in Fig. 5.59, is used for this study. The uncertainty in the assumed $D(\gamma,n)$ cross section is estimated to be about 10 percent.

(2) Gamma Attenuation Cross Sections. While gammas of energies 2.23 to 5 Mev can induce $D(\gamma,n)$ reactions and photofission, they are much more likely to experience photoelectric

absorption, pair production or, most important, Compton scattering. Other gamma absorption processes can be ignored. Photoelectric absorption and pair production result in the total absorption of the gamma, but Compton scattering does not degrade all scattered gammas below 2.23 Mev (see Table 5.8). Only those gammas which are scattered through an angle greater than Θ, defined by

$$\frac{0.511}{E_{\text{final}}} - \frac{0.511}{E_{\text{initial}}} = 1 - \cos\Theta$$

TABLE 5.8 — PROBABILITY FOR COMPTON SCATTERING WITH FREE ELECTRON TO A GAMMA ENERGY ABOVE 2.23 Mev*

E_γ(Mev)	Θ	p(E), Probability that $0 \leq$ Scattering Angle $\leq \Theta$
2.4	10.3°	0.056
2.8	17.5°	0.15
3.2	21.4°	0.22
3.6	24.1°	0.26
4.0	25.8°	0.29

*Adapted from tabulated Klein-Nishina formula of Ref. 125.

with E_{final} = 2.23 Mev, will be degraded below 2.23 Mev. Secondary electrons produced in any of these gamma interactions can produce further gammas by bremsstrahlung, but this second order process can be ignored. The fluorescent radiation sometimes emitted during absorption of a gamma is weak and can be ignored.

Cross sections for gamma attenuation are given by Evans,[125] Grodstein,[126] McGinnies,[127] and Storm, et al.,[128] the last tabulation including all elements of interest. The somewhat uncertain effects of electron binding and of coherent scattering on the Compton cross section are to be ignored in the present application because the combined effect is to increase the forward scattering[125] for which the change in gamma energy is small, thus leaving the gamma practically unaffected. When these effects are ignored, the Compton scattering cross section, given by the Klein-Nishina formula, is the same for each

electron in the target atoms, and this cross section is shown in Fig. 5.59. Pair production and photoelectric absorption augment the attenuation cross section more for heavier targets, as is illustrated for water and zirconium in Fig. 5.59. Gamma attenuation coefficients in the energy range 2 to 5 Mev are believed to be accurate within 1 or 2 percent.[125]

(3) Abundance of Deuterium. It is appropriate to point out that the deuterium content of natural water, which is taken in the present study to be in ratio N_D/N_H to hydrogen of 150×10^{-6}, is only an average value. Extensive measurements of this ratio are reviewed by Kirshenbaum[129] and range from 118×10^{-6} to 185×10^{-6}, although such extreme values are exceptional. The vapor pressure of light water exceeds that of heavy water, and it appears that heavy water condenses and falls as rain from clouds more readily than does light water. Where local rain falls from clouds which have undergone much prior condensation, as is the case at many inland sites, the local N_D/N_H ratio is expected to be low.[129]

(b) Calculation of Photoneutron Production Probability by Method of Successive Flights. A method of successive flights will now be applied to calculate the probability $P_\infty(E_o)$ that a gamma of initial energy E_o produces a neutron by the $D(\gamma, n)$ reaction in an infinite homogeneous medium containing N_D deuterons and N_j atoms of type $j = 1, 2, \ldots$ per cm^3. The additional effects of the actual heterogeneous structure of the reactor are considered later. Let $\sigma_{\gamma,n}(E)$ represent the $D(\gamma, n)$ cross section, let $\sigma_{cj}(E)$ represent the cross section per j^{th} atom for Compton scattering, and let $\sigma_{tj}(E)$ represent the total gamma attenuation cross section for an atom of j^{th} type. Then, the associated linear attenuation coefficients (macroscopic cross sections) are

$$\Sigma_{\gamma,n}(E) = N_D \sigma_{\gamma,n}(E)$$

$$\mu_c(E) = \sum_j N_j \sigma_{cj}(E) \qquad \text{Eq. (5.461)}$$

$$\mu_t(E) = \sum_j N_j \sigma_{tj}(E) .$$

Let $p(E)$ represent the probability that Compton scattering at energy E does not degrade the gamma below 2.23 Mev. Thus,

$p(E)\mu_c(E)/\mu_t(E)$ is the probability that the gamma has energy above 2.23 Mev following a collision at energy E. Then,

$$P_\infty(E_o) = \frac{\Sigma_{\gamma,n}(E_o)}{\mu_t(E_o)} + \left[\frac{\mu_c(E_o)}{\mu_t(E_o)}\,p(E)\right]\frac{\Sigma_{\gamma,n}(E_1)}{\mu_t(E_1)}$$

$$+\left[\frac{\mu_c(E_o)}{\mu_t(E_o)}\,p(E_o)\right]\left[\frac{\mu_c(E_1)}{\mu_t(E_1)}\,p(E_1)\right]\frac{\Sigma_{\gamma,n}(E_2)}{\mu_t(E_2)} + \ldots \qquad \text{Eq. (5.462)}$$

where the successive terms represent contributions from successive flights. Those gammas which remain above 2.23 Mev after the first Compton scattering have a nearly uniform distribution in energy.[125] To simplify the calculation, the gammas all are supposed to have the mean energy E_ℓ after the ℓ^{th} scattering

$$E_\ell = 0.48\,(E_{\ell-1} + 2.23)\,. \qquad \text{Eq. (5.463)}$$

The total gamma attenuation cross sections for various nuclides for use in Eq. (5.462) are obtained from Refs. 126, 127, and 128, the Compton scattering cross sections are obtained from Ref. 125, and the probability $p(E)$ is tabulated in Table 5.8. The $D(\gamma,n)$ reaction cross section used is that of Hulthen and Nagel, as noted previously.

If the photoelectric and pair production cross sections were negligible then, because σ_c is just proportional to the number of electrons in the atom, the quantity $P_\infty(E)N_e/N_D$ would not vary from medium to medium (N_e is electron density). While this is not quite true even for light elements, the parameter $P_\infty(E)N_e/N_D$ is convenient for comparing calculations of Eq. (5.462). Figure 5.60 shows this function as calculated for H_2O (or D_2O), for lead, for zirconium, and for a reactor medium with zirconium-to-water volume ratio 5:3. The function evidently decreases with increasing competition from photoelectric absorption and pair production in the heavier atoms. Contributions from flights after the first are of order 10 percent, as is displayed for the case of water. For moderate water-to-zirconium ratios the plotted function $P_\infty(E)N_e/N_D$ is insensitive to the value of the water-to-metal ratio, and the function can be interpolated conveniently for particular zirconium-water systems from Fig. 5.60.

2) Photoneutron Production in Finite or Heterogeneous Systems. The calculation of gamma flux in and near a reactor has

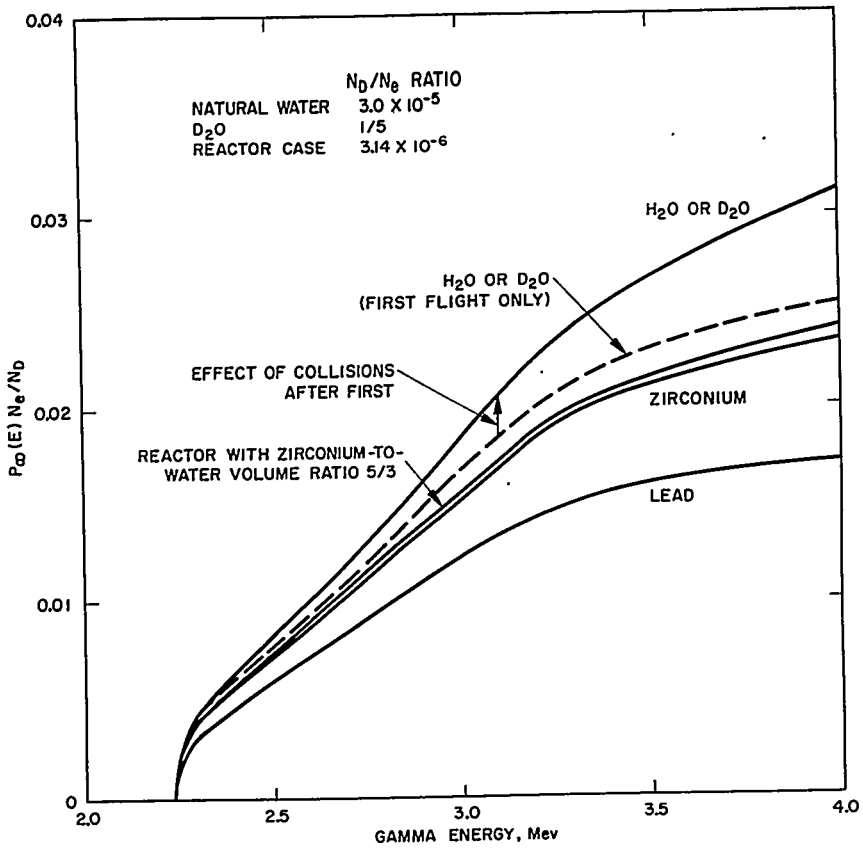

FIGURE 5.60. Probability $P_\infty(E)$ That Gamma of Initial Energy E Produces a Neutron in an Infinite Homogeneous Medium Times Electron to Deuteron Number Ratio.

been performed by many techniques, of which perhaps the most convenient is a multienergy-group digital computer calculation in a low transport approximation. In and near the reactor, the gamma flux is more nearly isotropic than is the case farther from the reactor, e.g., in shielding material, and a low transport approximation is more appropriate than in shielding problems. However, there are situations where calculation of (γ, n) reaction rate requires more care, as in the calculation of $D(\gamma, n)$ reaction rate in water surrounding a thick fuel element, or requires less care, as in calculation of $D(\gamma, n)$ reaction rate in a simply buckled homogeneous reactor. In some of these cases, the equivalent first flight calculation to be described finds application.

If from Compton collisions no gammas emerged with energy above 2.23 Mev, the threshold for the $D(\gamma, n)$ reaction, then in

calculating the $D(\gamma, n)$ reaction rate each gamma would make only a single flight, followed by effective absorption. A few delayed gammas do survive Compton scattering with energy above 2.23 Mev, but in such cases the scattered gamma is not greatly deflected (see Table 5.8) nor is its energy greatly altered. It is natural to regard the second and subsequent flights as prolongations of the first flight and to increase the attenuation length for the first flight accordingly.

It will be shown that a suitable choice for the decreased attenuation coefficient $\mu'(E_o)$ is given by the expression

$$\frac{1}{\mu'(E_o)} = \frac{1}{\mu_t(E_o)} \left\{ 1 + \left[\frac{\mu_c(E_o)}{\mu_t(E_o)} p(E_o) \right] \frac{\Sigma_{\gamma,n}(E_1)}{\mu_t(E_1)} \Big/ \frac{\Sigma_{\gamma,n}(E_o)}{\mu_t(E_o)} + \dots \right\} = \frac{P_\infty(E_o)}{\Sigma_{\gamma,n}(E_o)}$$

Eq. (5.464)

in the notation of the previous section. For suppose that the primary gamma is moving along the x axis and that after a Compton scattering the gamma, if it has not been degraded below 2.23 Mev, still is moving along the x axis. Then, the (γ, n) reaction rate between x and $x + dx$ is

$$R_{\gamma,n}(x)dx = e^{-\mu_t(E_o)x} \Sigma_{\gamma,n}(E_o)dx$$

$$+ \int_0^x dx' \mu_c(E_o) p(E_o) e^{-\mu_t(E_o)x'} e^{-\mu_t(E_1)(x-x')} \Sigma_{\gamma,n}(E_1)dx + \dots \quad \text{Eq. (5.465)}$$

or

$$R_{\gamma,n}(x)dx = e^{-\mu_t(E_o)x} \Sigma_{\gamma,n}(E_o)dx$$

$$+ \frac{\mu_c(E_o)p(E_o)}{\mu_t(E_1) - \mu_t(E_o)} \left[e^{-\mu_t(E_o)x} - e^{-\mu_t(E_1)x} \right] \Sigma_{\gamma,n}(E_1)dx + \dots \quad . \quad \text{Eq. (5.466)}$$

It is proposed to approximate $R_{\gamma,n}(x)$ by a single exponential corresponding to a single flight

$$R_{\gamma,n}(x)dx \sim e^{-\mu'(E_o)x} \Sigma_{\gamma,n}(E_o)dx . \quad \text{Eq. (5.467)}$$

When $R_{\gamma,n}(x)$ is integrated from zero to infinity, the infinite medium reaction rate for a single gamma, $P_\infty(E_o)$ of Eq. (5.462) is obtained. If it is required that

$$\int_0^\infty e^{-\mu'(E_o)x} \Sigma_{\gamma,n}(E_o)dx$$

take on the same value, Eq. (5.464) is obtained. Alternatively, in a least squares approximation,

$$\frac{\delta}{\delta\mu'}\int_0^\infty dx\left[e^{-\mu' x}\Sigma_{\gamma,n}-R_{\gamma,n}\right]^2=0. \qquad \text{Eq. (5.468)}$$

From Eq. (5.468) it follows that

$$\frac{1}{4\mu'^2}=\frac{1}{\left[\mu'+\mu_t(E_o)\right]^2}+\frac{\mu_c(E_o)p(E_o)\Sigma_{\gamma,n}(E_1)}{\Sigma_{\gamma,n}(E_o)}\,\frac{2\mu'+\mu_t(E_o)+\mu_t(E_1)}{\left[\mu'+\mu_t(E_o)\right]^2\left[\mu'+\mu_t(E_1)\right]^2}$$

Eq. (5.469)

which again yields Eq. (5.464) in the present approximation where $\mu_t(E_o)\approx\mu_t(E_1)$, and where second and subsequent flights contribute few (γ,n) reactions compared with the first flight. Finally, the expression, Eq. (5.464), for $\mu'(E_o)$ ensures that Eq. (5.467) is approximately satisfied for small x. Thus, the equivalent first flight reaction rate approximates the actual rate at low x, in general shape as ensured by the least squares criterion, and in total integral. The approximation is poor at large x, a region which may be of little interest. In the equivalent first flight approximation, the gamma moves as in a fully absorbing medium, a situation which has been analyzed in great detail.[130]

D) HARD GAMMA FORMATION AFTER REACTOR OPERATION

1) Delayed Hard Gammas from Fission Products. In Table 5.9 are listed delayed fission products which decay with accompanying hard gammas and betas with energies above 2.23 Mev. By focusing attention on delay times of order 1h or greater, it is possible to reduce all chains to one or two members such that the sum of half-lives is greater than 30m. Chains such as the 106 chain which are delayed longer than the mass 140 chain are ignored here. The nuclear decay data in Table 5.9 are largely taken from or in agreement with the Nuclear Data Sheets of K. Way, et al.;[131] exceptions are discussed below.

Yields of various nuclides in U^{235} fission are taken in most cases from the reviews of Katcoff.[132,133] Measured cumulative or direct yields are underlined in Table 5.9, but in other cases cumulative chain yields are apportioned to the various nuclides by application of the theory of equal charge displacement, together with Wahl's empirical curve of most probable charge.[134]

For example, the cumulative yield to Te^{132} has been measured directly to be ~4.7 percent, but a more precise yield for the whole mass 132 chain is 4.38 percent. The theory of equal charge displacement indicates little direct yield after Te^{132}. The cumulative yield to Te^{132} is, thus, taken to be 4.38 percent (not underlined) in Table 5.9.

The mass 128 chain is altered in accordance with new nuclide identifications,[131] and the ground state branch of Sn^{128} has been assigned the yield previously assigned to the 9h Sn activity in the mass 126 chain.[131]

The number of photoneutrons produced per decay in an infinite medium of D_2O, as well as in an infinite homogeneous medium of Zr and water in volume ratio 5:3, are listed in Table 5.9.

Cross sections for the (n, γ) reaction with 2200 mps neutrons are indicated in the few cases for which these are known. A more detailed discussion of important decay schemes is now given.

La^{140}: Measurements of the yield of high energy gammas in the decay of La^{140} are listed in Table 5.10. A very extensive series of measurements by Dzhelepov, et al., using a 180-degree Compton spectrometer, has yielded the first two columns of Table 5.10. Less accurate measurements by Coleman and by Bolotin, et al., also are listed. All results, except those of Bolotin, et al., are in agreement with the gamma yields and energies measured by Dzhelepov, et al., and the latter are adopted. The $D(\gamma, n)$ and $D(\gamma, p)$ measurements assume 2.5 Mev as the principal gamma energy. The detailed gamma spectrum of Dzhelepov, et al., produces a number of $D(\gamma, n)$ reactions equal to that of 2.5 Mev gammas in yield 3.99 percent.

I^{132}, I^{134}, I^{135}: The hard gammas listed for these nuclides have not been identified from gamma spectrometry[143] but have been inferred from $D(\gamma, n)$ measurements.[144-147] These nuclides emit few if any hard betas, so that there is no bremsstrahlung contribution. It was concluded in the preceding discussion on photoneutron reactions with stable nuclides that delayed neutron emission following decay of I^{135} is possible but unlikely.*

*Recently, the high energy gammas from I^{132} decay have been observed (H. G. Devare, quoted in Ref. 131) in quantity 0.43 percent at various energies above 2.23 Mev. These gammas produce the same number of $D(\gamma, n)$ neutrons as a 0.49 percent yield of 2.4 Mev gammas, in good agreement with the $D(\gamma, n)$ measurements.

TABLE 5.9 — DELAYED FISSION PRODUCT GAMMAS ABOVE 2.23 Mev

Precursor Half-Life U^{235} Fission Yield Cross Section for 2200 mps Neutron	Nuclide Half-Life U^{235} Fission Yield Cross Section for 2200 mps Neutron	Energy of Transition (Mev)	Beta Energy (Mev) Yield per Decay	De-excitation Gamma Energies (Mev), and Quanta per Decay	Photoneutrons per Decay, $\sum_j y_j P_j$	
					In D_2O	Zr-Water Reactor
10h Sm^{156} (0.013%)	15d Eu^{156} (0.001%)	2.455	2.455 (50%)	None observed	Ignore	Ignore
12.8d Ba^{140} (6.44%) (12b)	40.2h La^{140} (0%) (3.1b)	3.80	None	2.343, 2.515, 2.915 (0.7%) (3.2%) (0.07%) 3.110, 3.380 (0.029%) (0.013%)	6.57×10^{-3}	9.15×10^{-10}
				+		
	9.7d Sn^{125} (0.013%)	2.33	2.33 (95%)	None observed	Ignore	Ignore
77h Te^{132} (4.38%)	2.3h I^{132} (0%)	3.57	2.92 (0.03%)	2.4 from D(γ, n) (0.5%)	6.20×10^{-6}	8.93×10^{-11}
49h Zn^{72} (1.6×10^{-5}%)	14h Ga^{72} (0%)	4.00	2.529 (5%) 3.166 (5%)	2.49, 2.51 (8.9%) (16.8%) 2.69, 3.34 (0.068%) (0.017%)	4.09×10^{-4} Ignore	6.08×10^{-9} Ignore
23m Sb^{131} (0.39%) (To Te^{131m})	30h Te^{131m} (0.05%) (0.44% Cumulative)	2.46	2.46 (3.8%)	2.24 (0.7%)	1.40×10^{-6}	2.20×10^{-11}

TABLE 5.9 — DELAYED FISSION PRODUCT GAMMAS ABOVE 2.23 Mev (Continued)

Precursor Half-Life U^{235} Fission Yield Cross Section for 2200 mps Neutron	Nuclide Half-Life U^{235} Fission Yield Cross Section for 2200 mps Neutron	Energy of Transition (Mev)	Beta Energy (Mev) Yield per Decay	De-excitation Gamma Energies (Mev), and Quanta per Decay	Photoneutrons per Decay, $\sum_j y_j P_j$	
					In D_2O	Zr-Water Reactor
21.0h Pd^{112} (0.010%)	3.2h Ag^{112} (0%)	4.04	2.57 (1.6%) 2.63 (0.9%) 2.73 (2.8%) 3.42 (18%) 4.04 (56%)	2.24, 2.54, 2.71 (0.9%) (1.0%) (0.4%) 2.83, 2.95, 3.10 (0.65%) (0.06%) (0.032%K) 3.28 (0.02%)	6.16×10^{-5}	8.72×10^{-10}
	17.0h Zr^{97} (5.9%)	2.66	None	2.58 (0.7%)	1.36×10^{-5}	1.91×10^{-10}
	11.3h Ge^{77} (0.0031%)	2.75	2.27 (14%)	2.32 (0.72%)	Ignore	Ignore
	10.3h Y^{93} (6.45%)	2.89	2.62 (3.9%) 2.89 (90%)	2.43 (0.05%)	7.90×10^{-7}	1.31×10^{-11}
	9.7h Sr^{91} (5.81%)	2.67	2.67 (27%)	None observed	Ignore	Ignore

TABLE 5.9 — DELAYED FISSION PRODUCT GAMMAS ABOVE 2.23 Mev (Continued)

Precursor Half-Life U^{235} Fission Yield Cross Section for 2200 mps Neutron	Nuclide Half-Life U^{235} Fission Yield Cross Section for 2200 mps Neutron	Energy of Transition (Mev)	Beta Energy (Mev) Yield per Decay	De-excitation Gamma Energies (Mev), and Quanta per Decay	Photoneutrons per Decay, $\sum_j y_j P_j$	
					In D_2O	Zr-Water Reactor
57m Sn^{128} (0.37%)	9.6h Sb^{128m} (0.05%)	~4.6	None	None observed	Ignore	Ignore
	6.7h I^{135} (6.1%)	2.68	None	2.4 from D (γ, n) (1.1%)	1.36×10^{-5}	1.97×10^{-10}
	5.5h Pd^{111m} (~0.0002%)	2.37 IT to Ag^{111}		None observed	Ignore	Ignore
2.6h Sr^{92} (5.3%)	3.60h Y^{92} (0.7%)	3.60	3.60 (88%)	2.40 (0.15%)	3.75×10^{-6}	1.015×10^{-10}
18m Ba^{141} (6.3%)	3.7h La^{141} (0.1%)	2.43	2.43 (95%)	None observed	Ignore	Ignore
2.9h Cd^{117m} (0.011% x 0.6)	50m Cd^{117}	2.6	2.3 (<100%)	None observed	Ignore	Ignore
	2.8h Kr^{88} (3.57%)	2.73	2.7 (20%)	2.40 (35%)	4.34×10^{-4}	6.27×10^{-9}

TABLE 5.9 — DELAYED FISSION PRODUCT GAMMAS ABOVE 2.23 Mev (Continued)

Precursor Half-Life U^{235} Fission Yield Cross Section for 2200 mps Neutron	Nuclide Half-Life U^{235} Fission Yield Cross Section for 2200 mps Neutron	Energy of Transition (Mev)	Beta Energy (Mev) Yield per Decay	De-excitation Gamma Energies (Mev), and Quanta per Decay	Photoneutrons per Decay, $\sum_j y_j P_j$	
					In D_2O	Zr-Water Reactor
2.8h Kr^{88} (3.57%)	17.7m Rb^{88} (0%) (1.0b)	5.2	2.5 (14%) 3.4 (4%) 5.2 (76%)	2.68, 3.01, 3.24 (2.5%) (0.32%) (0.32%) 3.52, 3.68, 4.87 (0.26%) (0.09%) (0.32%)	1.40×10^{-4}	1.86×10^{-9} (Includes 0.17×10^{-9} from U^{235} (γ, f) with $N_{U235}/N_D = 100$)
86m Ge^{78} (0.019%)	91m As^{78} (0.002%)	4.27	2.96 (9.7%) 3.65 (19%) 4.27 (47%)	2.24, 2.42 (1.0%) (<1%) 2.65 (1.4%)	Ignore	Ignore
	2.9h Cd^{117m} (0.011%)	2.6		2.5 (Weak)	Ignore	Ignore
44m Te^{134} (6.9%)	53m I^{134} (0.9%)	4.2	2.5 (30%) 3.9 (< 1%)	2.4D(γ, n) (1%)	1.24×10^{-5}	1.79×10^{-10}

TABLE 5.9 — DELAYED FISSION PRODUCT GAMMAS ABOVE 2.23 Mev (Continued)

Precursor Half-Life U^{235} Fission Yield Cross Section for 2200 mps Neutron	Nuclide Half-Life U^{235} Fission Yield Cross Section for 2200 mps Neutron	Energy of Transition (Mev)	Beta Energy (Mev) Yield per Decay	De-excitation Gamma Energies (Mev), and Quanta per Decay	Photoneutrons per Decay, $\sum_j y_j P_j$	
					In D_2O	Zr-Water Reactor
9.5m Cs^{139} (6.47%)	85m Ba^{139} (0.08%) (4b)	2.38	2.25 (66%) 2.34 (15%)	None observed	Ignore	Ignore
11m Ba^{142} (5.35%)	81m La^{142} (0.6%)	4.5	4.5 (<100%)	2.40, 2.57, 3.00 (11%) (3%) (4%) 3.30, 3.65 (0.7%) (1.2%)	4.42×10^{-4}	5.99×10^{-9}
	78m Kr^{87} (2.49%) (<600b)	4.2	3.3 (≤10%) 3.8 (≥65%)	2.57 (22%)	4.18×10^{-4}	5.86×10^{-9}
57m Sn^{128} (0.37%)	10.7m Sb^{128} (0.32%)	~4.6	2.9 (<100%)	None observed	Ignore	Ignore
	60m Eu^{158} (0.002%)	~3.2	2.65 (100%)	None observed	Ignore	Ignore
	53m Te^{133m} (4.9%)	~3	2.4 (17%)	None observed	Ignore	Ignore

TABLE 5.9 — DELAYED FISSION PRODUCT GAMMAS ABOVE 2.23 Mev (Continued)

Precursor Half-Life U^{235} Fission Yield Cross Section for 2200 mps Neutron	Nuclide Half-Life U^{235} Fission Yield Cross Section for 2200 mps Neutron	Energy of Transition (Mev)	Beta Energy (Mev) Yield per Decay	De-excitation Gamma Energies (Mev), and Quanta per Decay	Photoneutrons per Decay, $\sum_j y_j P_j$	
					In D_2O	Zr-Water Reactor
17m Xe^{138} (5.49%)	32.2m Cs^{138} (0.25%)	4.83	2.3-3 (67%) 3.40 (21%)	2.63, 3.34 (9%) (0.5%)	2.18×10^{-4}	3.01×10^{-9}
14m Ce^{146} (2.77%)	25m Pr^{146} (0.3%)	4.2	2.3 (44%) 3.7 (56%)	None observed	Ignore	Ignore
3.3m Se^{84} (0.87%)	31.8m Br^{84} (0.03%) (0.90% Cumulative)	4.68	2.80 (15%) 3.83 (14%) 4.68 (32%)	2.47, 2.82, 3.03 (8%) (2%) (3%) 3.28, 3.93 (2.5%) (11%)	1.065×10^{-3}	1.36×10^{-8}

TABLE 5.10 — HIGH ENERGY GAMMAS ACCOMPANYING La^{140} DECAY

Gamma Energy	Compton Spectrometer (%)	D(γ, n) Measurements (%)	D(γ, p) Measurements (%)	Scintillator (%)	Three Crystal Pair Spectrometer (%)
2343 ± 15	0.7 (Refs. 135, 136)				
2515 ± 15	3.2 (Refs. 135, 136)	1-10 (Ref. 138) 5 (Ref. 139)	4 (Ref. 140)	4 (Ref. 141)	1 (Ref. 142)
2915 ± 30	0.07 (Refs. 135, 136)		0.1 (Ref. 140)		0.04
3110 ± 50	0.029 (Ref. 137)				
3380 ± 70	0.0013 (Ref. 137)				
Sum	4.0	5	4.1	4	1

Zr^{97}: The yield of the 2.58 Mev gamma from decay of Zr^{97} is determined as having $1/2 \pm 1/4$ of the area (corrected for spectrometer efficiency) of the 2.2 Mev gamma, according to data of Delyagin, et al.,[148] the yield of the latter being 1.5 percent. Way, et al.,[131] give a yield ≤ 1 percent for the 2.58 Mev gamma. It is suggested later that improvement between measured and calculated photoneutron yields is obtained for a gamma yield about 1.1 percent per Zr^{97} decay, which value is consistent with the data of Delyagin, et al.[148] On the other hand, there is some doubt[131] as to the assignment of the 2.58 Mev gamma to Zr^{97}.

Te^{131m} and Te^{131}: It was pointed out in the introduction that Ergen[120] suggested that Bernstein's photoneutron data[119] could be fitted if one assumed a strong Te^{131} gamma above 2.23 Mev. The 24.8m Te^{131} decay would be delayed following 30h Te^{131m} decay. Subsequently, Parker[147] observed a weak gamma above 2.23 Mev of yield ~ 0.6 percent following 30h Te^{131m}. Ferguson and Tomnovec[149] observed no gamma harder than 1.13 Mev from Te^{131} decay, while Bedesen, et al.,[149] observed a 2.24 Mev gamma of yield 0.7 percent de-exciting I^{131} following beta decay of Te^{131m}. It appears that the hard gamma activity follows decay of Te^{131m}, not Te^{131}, and is weak.

Y^{92}: The 2.4 Mev state of Zr^{92} is populated by 9 percent of Y^{92} beta decays, and is de-excited by gammas of energies and relative yields 2.40 Mev (0.8), 1.44 Mev (42), 0.54 Mev (5).[131] The absolute yield of the 2.40 Mev gamma is $9\% \times 0.8/47.8 = 0.15\%$ according to this decay scheme.

Rb^{88}: The gamma energies and yields of N. H. Lazar, et al.,[150] are adopted here as by Way, et al.,[131] but there remains some question because S. Thulin[151] reported these gammas to be less than half as strong.

La[142]: The gamma energies and yields reported by R. P. Schuman, et al.,[152] are adopted here. These are consistent with the earlier gamma energies and relative yields of Ryde and Herrlander.[153] Way, et al.,[131] give only relative yields.

2) Delayed Hard Gammas from Products of Neutron Capture Reactions. These are unimportant. Even for Cs^{136}, which has been considered in the past to be a hard gamma emitter, Girgis and van Lieshout[151] have measured the yields of the 2.35 Mev and 2.49 Mev gammas to be less than 0.05 percent per Cs^{136} decay.

E) CALCULATION OF DELAYED PHOTONEUTRON SOURCE STRENGTH

1) Buildup, Reaction, and Decay of Hard Gamma Emitters. The mass 140 fission product chain provides a typical example of a source of delayed gammas capable of inducing the $D(\gamma,n)$ reaction. The energetic delayed gammas are emitted in decay of La^{140}, as discussed in the hard gamma formation after reactor operation:

$$16s_{54}Xe^{140} \xrightarrow{\beta^-} 16s_{55}Cs^{140} \xrightarrow{\beta^-} 12.8d_{56}Ba^{140} \xrightarrow{\beta^-} 40.2h_{57}La^{140} \xrightarrow{\beta^-} \text{Stable}_{58}Ce^{140} . \quad \text{Eq. (5.470)}$$

In computation of the photoneutron source at times well after irradiation one can suppose quick decays, such as the first two in Eq. (5.470), to be instantaneous. After all such simplifications, all decay chains of present interest can be displayed as

$$\underset{(Y_{Z-1,A})}{\tau_{ZH,A}(Z-1,A)} \xrightarrow{\beta^-} \underset{(Y_{Z,A})}{\tau_{Z,A}(Z,A)} \xrightarrow{\beta^-} \begin{cases} \text{Gammas} \\ E_1, \gamma_{Z,A,1} \\ E_2, \gamma_{Z,A,2} \end{cases} . \quad \text{Eq. (5.471)}$$

Had it been desired to compute the (γ,n) source sooner than 2 hours after reactor operation, some decay chains would require three nuclide links. Here $\tau_{Z,A}$ represents the mean life of the nuclide (Z,A), $Y_{Z,A}$ represents the direct yield of the nuclide (Z,A) in the reactor per fission in the reactor, and $\gamma_{Z,A,j}$ represents the yield of the gamma of energy E_j following beta decay of (Z,A). If the nuclides in the chain also are produced by neutron capture reactions then such yields, per reactor fission, are included in $Y_{Z,A}$.

Let $F(t)$ represent the fission rate in the reactor as a whole, let $N_{Z,A}(t)$ represent the number of $[Z,A]$ nuclei in the reactor, and, as before, let $P_{Z,A}(E)$ represent the probability that a gamma which is born with energy E and with the spatial distribution of $[Z,A]$ decays produces a photoneutron anywhere in the reactor. Let $I_{Z,A}(E_j)$ represent the importance to the fundamental reactor mode or to the photoneutron detector of such neutrons. Then, $S_{Z,A}(t)$ the photoneutron source from $[Z,A]$ decays to the fundamental mode or to the detector is determined by

$$\dot{N}_{Z+1,A} = Y_{Z+1,A}F - \tau^{-1}_{Z+1,A}N_{Z+1,A} \quad \text{Eq. (5.472a)}$$

$$\dot{N}_{Z,A} = Y_{Z,A}F - \tau_{Z,A}^{-1}N_{Z,A} + \tau_{Z+1,A}^{-1}N_{Z+1,A} \qquad \text{Eq. (5.472b)}$$

$$S_{Z,A} = \tau_{Z,A}^{-1}N_{Z,A}\sum_j \gamma_{Z,A,j}P_{Z,A}(E_j)I_{Z,A}(E_j). \qquad \text{Eq. (5.472c)}$$

In particular, at a time t following constant power operation at fission rate F for a time T,

$$\tau_{Z+1,A}^{-1}N_{Z+1,A}/F = Y_{Z+1,A}\left(1 - e^{-T/\tau_{Z+1,A}}\right)e^{-t/\tau_{Z+1,A}} \qquad \text{Eq. (5.473a)}$$

$$\tau_{Z,A}^{-1}N_{Z,A}/F = \left[Y_{Z,A} + Y_{Z+1,A}\frac{1}{1-\frac{\tau_{Z+1,A}}{\tau_{Z,A}}}\right]\left(1 - e^{-T/\tau_{Z,A}}\right)e^{-t/\tau_{Z,A}}$$

$$+ Y_{Z+1,A}\frac{1}{1-\frac{\tau_{Z,A}}{\tau_{Z+1,A}}}\left(1 - e^{-T/\tau_{Z+1,A}}\right)e^{-t/\tau_{Z+1,A}}. \qquad \text{Eq. (5.473b)}$$

Loss and gain of gamma emitters by neutron absorption is unimportant.

2) Comparison of Photoneutron Calculations with Measurements of Bernstein, et al. S. Bernstein, et al.,[119] irradiated a small sample of enriched uranium oxide in the Oak Ridge reactor, then quickly transferred the irradiated sample to the center of a sphere of D_2O. Photoneutrons produced in the D_2O by delayed gammas as well as by delayed neutrons from the sample were moderated in the D_2O and in a tank of oil in which the D_2O sphere was immersed, then captured largely by hydrogen in the oil. The moderated neutron flux in the oil was measured by a U^{235} fission chamber as a function of position at a particular time after irradiation. The spatially integrated neutron flux was taken to be proportional to the photoneutron plus delayed neutron yield at the time, independent of the energy or spatial distribution of the photoneutrons or delayed neutrons at birth. By repeating the measurement, decay curves of neutron yield were obtained. The D_2O was then drained from the system, and decay curves of delayed neutrons alone were measured. The difference between the two decay curves represents a decay curve for photoneutrons alone. The measured decay

curves for delayed neutrons alone and for delayed photoneutrons alone were decomposed into sums of simple exponentials of the form of Eq. (5.473a)

$$c(t) = \sum_j A_j \left(1 - e^{-T/\tau_j}\right) e^{-t/\tau_j}. \qquad \text{Eq. (5.474)}$$

In Table 5.11 are listed for the photoneutron decay the longer half-lives $\tau_{1/2\,j}$ and the yields A_j relative to the 22-second delayed neutron group which are reported by Bernstein, et al. [119]

The measured photoneutron decay curves, with certain corrections, will be compared with calculated decay curves. The measurements are reported as though the gamma emitting nuclides were produced directly in fission, leading to decay equations of the type of Eqs. (5.473a) or (5.474). Because this is not generally true, as is illustrated by the mass 140 fission product chain, it is necessary to reconstruct the composite photoneutron decay curve for irradiation and waiting times used in the experiment. In the measurements, the yields and half-lives of the longer lived photoneutron groups were determined from 3.75h irradiation and up to 70h counting time, so that these values are used in reconstructing the observations.

Bernstein, et al., inferred absolute photoneutron yields from yields relative to the 22-second delayed neutron group by assuming for the latter a yield of 0.44 percent per U^{235} fission. For the 22-second group Hughes, et al.,[154] and Keepin, et al.,[155] have reported yields of 0.41 percent and 0.346 percent, respectively. Both values will be used to determine absolute photoneutron yields from the measurements. The 22-second delayed neutron group is itself a composite of simple exponential decays, and its effective yield depends to some extent on the analysis of the total delayed neutron decay.

Bernstein, et al., computed from their data the photoneutron yield for an infinite medium of D_2O. In the experiment, a gamma emerging from the small irradiated uranium dioxide sample passed successively through 0.475 cm of plastic, 0.428 cm of Al, 23.3 cm of D_2O, then more aluminum and oil. The probability of interaction in the D_2O is

$$\exp\left(-0.475\mu'_{\text{plastic}} - 0.428\mu'_{\text{Al}}\right)\left[1 - \exp\left(-23.3\mu'_{D_2O}\right)\right] \qquad \text{Eq. (5.475)}$$

The attenuation coefficients μ' are taken to be equivalent first flight coefficients. To infer photoneutron yields in an infinite D_2O medium from yields measured in the finite D_2O sphere, the latter are multiplied by the reciprocal of Eq. (5.475). Details of the calculation are given in Table 5.12 for three gamma

TABLE 5.11 — MEASURED PHOTONEUTRON DECAY PARAMETERS

Measurements by Bernstein, et al.[119]		Analysis by Bernstein, et al.[119]		Present Analysis		
$\tau_{1/2}$	Yield Relative to 22-sec Delayed Neutron Group	Assumed Energy (Mev)†	Yield per Fission Infinite D_2O*	Assumed Energy (Mev)†	Correction Relative to Bernstein's	Yield per Fission Infinite D_2O*
53h	0.00038	3	3.26×10^{-6}	2.5	0.898	2.31×10^{-6}
4.4h	0.00119	3	10.1×10^{-6}	2.6	0.912	7.27×10^{-6}
1.65h	0.0093	2.62	74.2×10^{-6}	2.6	0.986	57.7×10^{-6}
27m	0.0082	2.60	65.6×10^{-6}	2.5	0.962	49.8×10^{-6}
7.7m	0.0124	3	106.5×10^{-6}	3	1	83.8×10^{-6}

*Assumed yield of 22-second delayed neutron group, 0.44 percent.
†Assuming Keepin's yield of 22-second delayed neutron group, 0.346 percent.

TABLE 5.12 — CORRECTIONS FOR GAMMA ATTENUATION*

Gamma Energy (Mev)	μ_{D_2O} (cm^{-1})	μ_{Al} (cm^{-1})	I $\exp(-\mu_{Al} \times 0.428\ cm)$	II $\exp(-\mu_{Plastic} \times 0.475\ cm)$	$p(E_o)$	$p(E_o)p(E_1)$	μ'_{D_2O} $[\mu_{D_2O}/1 + p(E_o)]$	III $1-\exp(-\mu'_{D_2O} \times 23.3\ cm)$	$\frac{1}{I \times II \times III}$ Correction Factor
2.5	0.044	0.103	0.957	0.979	0.085	0.00035	24.7	0.610	1.75
2.6	0.043	0.100	0.958	0.980	0.105	0.00063	25.75	0.596	1.78
2.9	0.040	0.094	0.961	0.981	0.175	0.0031	29.9	0.542	1.96

*From experiment by Bernstein, et al.[119]

energies: 2.5 Mev, 2.6 Mev, and 2.9 Mev. The equivalent first flight attenuation coefficient $\mu'_{D_2O}(E_o)$ is less than the uncorrected coefficient $\mu_{D_2O}(E_o)$ by the factor $1 + p(E_o) + p(E_o)p(E_1) + \ldots$ where $p(E)$ is the probability that a Compton scattered gamma remains above the $D(\gamma,n)$ threshold. It is evident from the magnitude of $p(E_o)$ and $p(E_o)\,p(E_1)$ that only the second flight correction is appreciable, being of order 10 percent.*

The infinite medium correction is energy-dependent, and Bernstein, et al., assumed for the gamma energies predominant in the photoneutron groups the values listed in Table 5.11. For the 1.65h, 27m, and 7.7m groups the energies were taken by Bernstein, et al., to be those measured by Spatz, et al.,[156] while for the longer-lived groups the choice was arbitrary. The presently assumed group energies are listed in Table 5.11 and are inferred from the gamma emitters calculated to dominate photoneutron production in the various time intervals. Ratios of correction factors calculated here and listed in Table 5.11 to correction factors used by Bernstein are given in Table 5.11. Finally, the photoneutron group yields corrected for an infinite D_2O medium and using Keepin's delayed neutron group yield are also listed in Table 5.11. The total photoneutron decay curve calculated from these parameters is displayed in Fig. 5.61.

Calculated photoneutron decay curves also are shown in Fig. 5.61. The decay rate of each fission product which emits hard gammas is calculated from Eqs. (5.473a) or (5.473b), using the decay parameters and fission yields listed in Table 5.9. The flux level in the Oak Ridge reactor was much less than 10^{14} cm^{-2} sec^{-1} at the location of the measurement, so that no correction for nuclide production or loss by neutron capture is necessary. Gamma yields per nuclear decay, γ_j, are listed in Table 5.9, and photoneutron yields in D_2O per gamma, $P(E_j)$, are computed using Fig. 5.60. The photoneutron yield per decay of a particular nuclide is calculated as $\sum_j \gamma_j P_j$ and is listed in Table 5.9. The product of the fission product decay rate and the photoneutron yield per decay are plotted in Fig. 5.61 for each important nuclide, assuming an irradiation of one fission per second for 3.75h.

At times greater than about 30h after irradiation, the nuclides La^{140}, Zr^{97}, and I^{132} dominate the production of photoneutrons. The gammas emitted by these nuclides have principal energies 2.5 Mev, 2.6 Mev, and 2.4 Mev, respectively, and it is for this

*Second flight corrections of order 10 percent also were applied by Bernstein, et al.,[119] these being obtained in an undescribed way by E. Greuling and H. Soodak.

reason that the effective gamma energies for Bernstein's 53h and 4.4h groups are taken to be 2.5 Mev and 2.6 Mev, respectively, rather than 3 Mev as assumed by Bernstein, et al. (see Table 5.11).

Errors in measurement and in the correction of measured photoneutron yields to the infinite D_2O medium are estimated at 3 to 5 percent, but the uncertainty in the yield of the 22-second delayed neutron composite group appears to be much larger, of order 10 to 20 percent. Uncertainties in the calculation other than in gamma yields are associated with the $D(\gamma,n)$ cross section, about 10 percent, and with fission product yields, 5 to 15 percent.

F) CONCLUSIONS. With these uncertainties in mind, the calculated and measured photoneutron curves of Fig. 5.61 may be compared. The only marked disagreement, about 25 percent, is at times greater than about 25 hours after irradiation, when most photoneutron production is by gammas emitted in decay of La^{140}, Zr^{97}, I^{132}, and I^{135}. The gamma yields per decay of I^{132} and I^{135} were determined from $D(\gamma,n)$ measurements,[143-147] which would appear to be a reliable method for present purposes. Very large increases in I^{132} and I^{135} gamma yields would be required to match the measurements. The gamma yields from Zr^{97} and La^{140} might be larger than listed in Table 5.9. It is found that a 25-percent increase in the La^{140} gamma yield alone does not produce agreement between calculation and experiment. However, a small increase in yield of La^{140} gammas plus a larger (but still in agreement with spectrometric observations[148]) increase in Zr^{97} gamma yield results in a close agreement between experiment and calculation.

The suggested increase in the yield of the 2.58 Mev gamma from Zr^{97} from 0.7 percent to 1.1 percent is highly speculative, particularly in view of the questionable nuclear assignment of this gamma.[131] The suggested increase in the gamma yield of La^{140}, about 17 percent, finds some confirmation in the study of Hansen and Wilsky[157] who point out that the yield of the 0.513 Mev gamma, relative to which all spectrometric gamma yields are referred, should be 96.1 ± 0.8 percent rather than the 88.2 percent previously assumed.

These calculations are expected to be applicable to much longer irradiation and cooling times. Eventually, the La^{140} activity decays until it is dominated by a small uncertain yield of photoneutrons produced by hard de-excitation and bremsstrahlung gammas from 30-second Rh^{106} following decay of 1y Ru^{106}. The Rh^{106} contribution has not been observed in any photoneutron experiment.

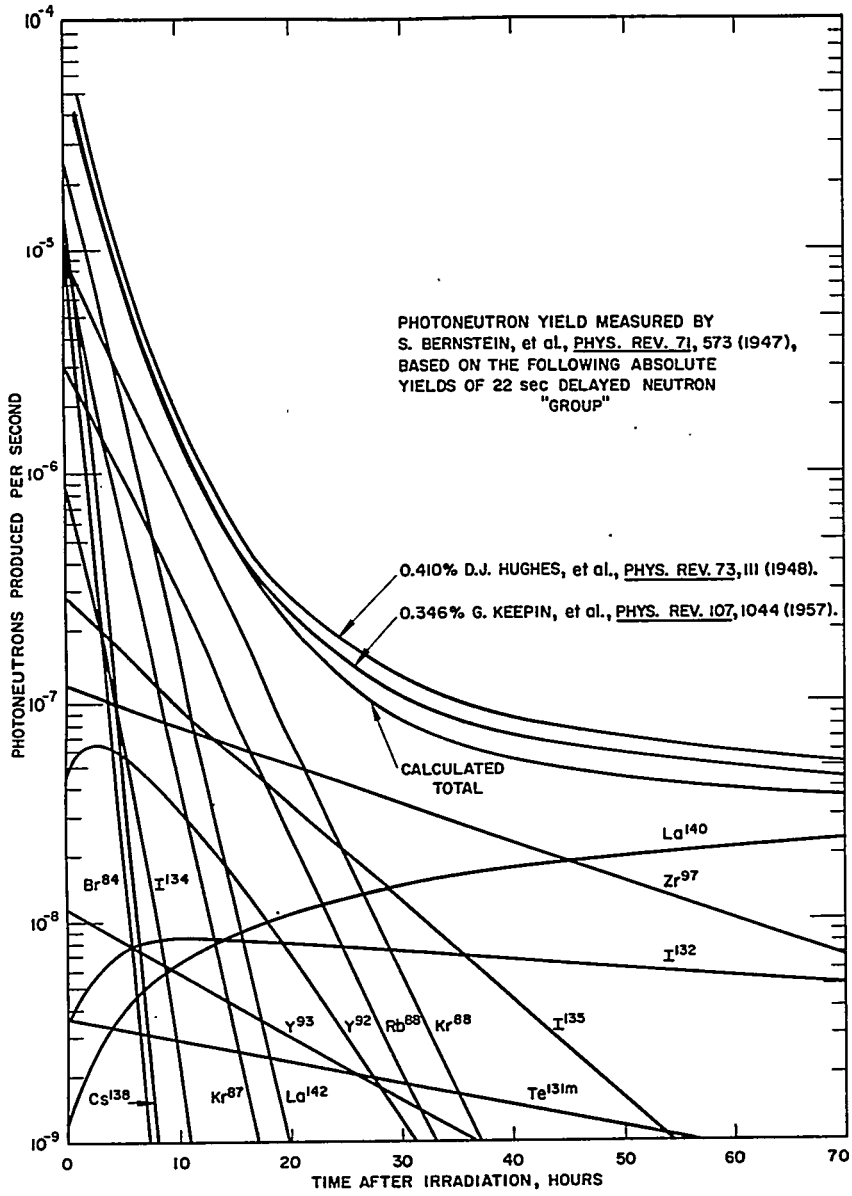

FIGURE 5.61. Photoneutrons Produced per Second in Infinite Medium of D_2O by Delayed Gammas following Irradiation of U^{235} for 3.75 Hours at Power Level of One Fission per Second.

REFERENCES

1. L. W. Nordheim, "Weight Factors and Period Relations for Composite Piles" in "Physics Section Monthly Report for Period Ending May 31, 1945," CP-2824, 1945, pp. 9-17..

2. H. Brooks, "Perturbation Methods in Multi-Group Calculations," KAPL-71, May 25, 1948.

3. L. W. Nordheim, "Pile Kinetics," MDDC-35, June 1946.

4. L. N. Ussachoff, "Equation for the Importance of Neutrons, Reactor Kinetics and the Theory of Perturbation" in "Proceedings of the International Conference on the Peaceful Uses of Atomic Energy, Geneva, 1955," Vol. 5, pp. 503-510, United Nations, New York, 1956.

5. H. Hurwitz, Jr., "Derivation and Integration of the Pile-Kinetic Equations," Nucleonics 5 (1), 61-67 (1949).

6. J. Lewins, "The Reduction of Time-Dependent Equations for Nuclear Reactors to a Set of Ordinary Differential Equations," Nucl. Sci. Eng. 9, 399-407 (1961).

7. A. F. Henry, "The Application of Reactor Kinetics to the Analysis of Experiments," Nucl. Sci. Eng. 3, 52-70 (1958).

8. H. Hurwitz, Jr., "Note on the Theory of Danger Coefficients," KAPL-98, Sept. 18, 1948.

9. D. S. Selengut, "Variational Analysis of Multi-Dimensional Systems" in "Nuclear Physics Research Quarterly Report for October, November, December 1958," HW-59126, January 1959, pp. 89-124.

10. J. Lewins, "The Time-Dependent Importance of Neutrons and Precursors," Nucl. Sci. Eng. 7, 268-274 (1960).

11. J. Lewins, "The Use of the Generation Time in Reactor Kinetics," Nucl. Sci. Eng. 7, 122-126 (1960).

12. E. E. Gross and J. H. Marable, "Static and Dynamic Multiplication Factors and Their Relation to the Inhour Equation," Nucl. Sci. Eng. 7, 281-291 (1960).

13. S. Kaplan and A. F. Henry, "An Experiment to Measure Effective Delayed Neutron Fractions," WAPD-TM-209, February 1960.

14. T. F. Ruane, D. J. Anthony, P. Buck, D. A. Gavin, and H. B. Stewart, "A Measurement of the Effective Delayed Neutron Fraction by the Substitution Method," Trans. Am. Nucl. Soc. 1 (2), 142-144 (1958).

15. J. A. Archibald, Jr., and J. L. Fletcher, "KARE Input. Revision IV," KAPL-M-JA-6 (Rev. IV), August 15, 1962.

16. D. R. Harris, "A Method of Calculating Neutron Importance Using Few-Group Codes," Trans. Am. Nucl. Soc. 3, 396-397 (1960).

17. S. Glasstone and M. C. Edlund, "The Elements of Nuclear Reactor Theory," D. Van Nostrand Company, Inc., New York, 1952.

18. J. H. Keenan and F. G. Keyes, "Thermodynamic Properties of Steam," Table 4, John Wiley and Sons, Inc., New York, 1936.

19. J. N. Grace, M. A. Schultz, and T. E. Fairey, "Inherent Reactor Stability" in "Proceedings of the 1955 Conference on Nuclear Engineering, Held at the University of California, Los Angeles, April 27-29, 1955," pp. B-1 — B-21, California Book Co., Ltd., Berkeley, California, 1955.

20. J. Chernick, "The Dynamics of a Xenon-Controlled Reactor," Nucl. Sci. Eng. 8, 233-243 (1960).

21. J. E. Meyer, "Conservation Laws in One-Dimensional Hydrodynamics" in "Bettis Technical Review, Reactor Technology," WAPD-BT-20, September 1960, pp. 61-72.

22. G. W. Maurer, "A Method of Predicting Steady-State Boiling Vapor Fractions in Reactor Coolant Channels" in "Bettis Technical Review, Reactor Technology," WAPD-BT-19, June 1960, pp. 59-70.

23. J. E. Meyer and J. S. Williams, Jr., "A Momentum Integral Model for the Treatment of Transient Fluid Flow" in "Bettis Technical Review, Reactor Technology," WAPD-BT-25, May 1962, pp. 47-72.

24. O. J. Mendler, A. S. Rathbun, N. E. Van Huff, and A. Weiss, "Natural-Circulation Tests with Water at 800 to 2000 psia under Nonboiling, Local Boiling, and Bulk Boiling Conditions," ASME Paper No. 60-HT-36.

25. E. R. Quandt, "Analysis and Measurement of Flow Oscillations" in "Heat Transfer-Buffalo," Chem. Eng. Progr. Symposium Ser. 57, No. 32, 111-126 (1961).

26. J. E. Meyer, R. B. Smith, H. G. Gelbard, D. E. George, and W. D. Peterson, "ART — A Program for the Treatment of Reactor Thermal Transients on the IBM-704," WAPD-TM-156, November 1959.

27. M. A. Ketchum, "TANK. Power Plant Transient Analysis Program," KAPL-M-EC-9, July 6, 1961.

28. W. J. Gallagher, "Analysis of a Simulated Cold Water Incident in PWR" in "Bettis Technical Review, Reactor and Plant Engineering," WAPD-BT-9, August 1958, pp. 39-50.

29. J. G. Truxal, "Automatic Feedback Control System Synthesis," McGraw-Hill Book Company, Inc., New York, 1955.

30. J. V. Reihing, Jr., and W. G. Clarke, "An Appraisal of the MIM and ART Differencing Methods Employing M0076, A Digital Frequency Analysis Program," WAPD-TM-286, December 1961.

31. S. G. Margolis and S. Kaplan, "Transfer Functions for Boiling Reactor Stability Calculation" in "Bettis Technical Review, Reactor Technology," WAPD-BT-21, November 1960, pp. 1-21.

32. W. H. Esselman, I. H. Mandil, S. J. Green, P. C. Ostergaard, and R. A. Fredrickson, "Thermal and Hydraulic Experiments for Pressurized Water Reactors" in "Proceedings of the Second United Nations International Conference on the Peaceful Uses of Atomic Energy, Geneva, 1958," Vol. 7, pp. 758-773, United Nations, Geneva, 1958.

33. A. B. Jones, "Hydrodynamic Stability of a Boiling Channel," KAPL-2170, October 2, 1961.

34. J. E. Meyer and R. P. Rose, "Application of a Momentum Integral Model to the Study of Parallel Channel Boiling Flow Oscillations," ASME Paper No. 62-HT-41; WAPD-T-1363, November 1961.

35. S. E. Golian, T. A. Bergstrahl, E. G. Harris, and R. C. O'Rourke, "Transient Response of Plane Parallel Fuel Assemblies to Exponential Power Excursions," NRL-4495 (Del.), January 1955.

36. B. H. Noordhoff, C. E. Foreman, and J. W. Haskins, "Comparison of Two Methods for Analyzing Accidental Power Transients," WAPD-TM-31, January 1957.

37. G. O. Bright, Ed., "Quarterly Progress Report for July, August, September 1958," IDO-16512, May 6, 1959.

38. J. F. Hogerton and R. C. Grass, Eds., "The Reactor Handbook. Vol. I. Physics," AECD-3645, U. S. Government Printing Office, Washington, D. C., March 1955.

39. F. Schroeder and C. R. Toole, "The Effect of System Pressure on Room Temperature Power Excursions in SPERT III," Trans. Am. Nucl. Soc. 3, 434 (1960).

40. C. R. Toole and F. Schroeder, "The Effect of Forced Coolant Flow on Room Temperature Power Excursions in SPERT III," Trans. Am. Nucl. Soc. 3, 433-434 (1960).

41. G. O. Bright, S. G. Forbes, W. E. Nyer, and F. Schroeder, "An Elementary Model for Reactor Burst Behavior," IDO-16393, August 2, 1957.

42. H. Hurwitz, Jr., "Approximate Analysis of Reactor Start-Up Incidents," Nucl. Sci. Eng. 6, 11-17 (1959).

43. W. A. Vogele and S. O. Johnson, "Simulation of Prompt-Critical Excursions in Water-Moderated Reactors," WAPD-T-1059, September 1959.

44. A. J. Martenson, "Transient Boiling in Small Rectangular Channels," Ph.D. Thesis, University of Pittsburgh, 1962.

45. H. A. Johnson, V. E. Schrock, S. Fabic, and F. B. Selph, "Transient Boiling Heat Transfer and Void Volume Production in Channel Flow," SAN-1007, March 1963.

46. J. E. Meyer and R. P. Rose, "Application of a Momentum Integral Model to the Study of Parallel Channel Boiling Flow Oscillations," Trans. Am. Soc. Mech. Engr. 85, Series C, 1-9 (1963).

47. L. I. Schiff, "Quantum Mechanics," McGraw-Hill Book Company, Inc., New York, 1949.

48. S. Kaplan and S. G. Margolis, "Delayed Neutron Effects During Flux Tilt Transients," Nucl. Sci. Eng. 7, 276-277 (1960).

49. A. F. Henry and R. S. Willey, "Determination of Reactor Transients When Space and Time Are Not Separable," Trans. Am. Nucl. Soc. 2 (2), 63-64 (1959).

50. N. J. Curlee, Jr., "Nonseparable Space-Time Transients Resulting from Changes in Inlet Coolant Temperature," Nucl. Sci. Eng. 6, 1-10 (1959).

51. A. F. Henry and J. D. Germann, "Oscillations in the Power Distribution Within a Reactor," Nucl. Sci. Eng. 2, 469-480 (1957).

52. R. S. Wick, "Space- and Time-Dependent Flux Oscillations (And Instability) in Thermal Reactors Due to Nonuniform Formation and Depletion of Xenon," WAPD-TM-138, August 1958.

53. E. L. Wachspress, "Digital Computation of Space-Time Variation of Neutron Fluxes," KAPL-2090, October 1, 1960.

54. S. Kaplan and J. A. Bewick, "Space and Time Synthesis by the Variational Method" in "Bettis Technical Review, Reactor Technology," WAPD-BT-28, March 1963, pp. 27-44.

55. D. E. Dougherty and C. N. Shen, "The Space-Time Neutron Kinetic Equations Obtained by the Semidirect Variational Method," Nucl. Sci. Eng. 13, 141-148 (1962).

56. J. Lewins, "The Approximate Separation of Kinetics Problems into Time and Space Functions by a Variational Principle," J. Nucl. Energy: Pt. A 12, 108-112 (1960).

57. M. A. Martino, "Concerning the Multigroup Diffusion Operator," KAPL-1867, September 20, 1957.

58. D. R. Harris, S. Kaplan, and S. G. Margolis, "Modal Analysis of Flux Tilt; Transients in a Nonuniform Reactor," Trans. Am. Nucl. Soc. 2 (2), 178-179 (1959).

59. S. Kaplan, S. G. Margolis, and D. R. Harris, "Transient Response of the Spatial Flux Distribution in an Initially Uniform Bare Reactor to Arbitrary Non-Uniform Changes in Materials Properties" in "Bettis Technical Review, Reactor Physics and Mathematics," WAPD-BT-17, February 1960, pp. 69-83.

60. A. G. Ward, "The Problem of Flux Instability in Large Power Reactors," CRRP-657, July 26, 1956.

61. D. Randall and D. S. St. John, "Xenon Spatial Oscillations," Nucleonics 16 (3), 82-86, 129 (1958).

62. J. C. Stewart, "A Generalized Criterion for Xenon Instability," KAPL-M-JS-4, December 18, 1958.

63. D. R. Harris and P. S. Lacy, "A Simple Approximate Test for Spatial Xenon Stability," Trans. Am. Nucl. Soc. 3, 437-438 (1960).

64. K. Mochizuki and A. Takeda, "An Analysis of Neutron Flux Spatial Oscillation Due to Xenon Build-Up in a Large Power Reactor Core," Nucl. Sci. Eng. 7, 336-344 (1960).

65. R. Bellman, "Introduction to Matrix Analysis," p. 243, McGraw-Hill Book Company, Inc., New York, 1960.

66. A. Sommerfeld, "Partial Differential Equations in Physics," Academic Press, Inc., New York, 1949.

67. S. Kaplan, "The Property of Finality and the Analysis of Problems in Reactor Space-Time Kinetics by Various Modal Expansions," Nucl. Sci. Eng. 9, 357-361 (1961).

68. B. Friedman, "Principles and Techniques of Applied Mathematics," John Wiley and Sons, Inc., New York, 1956.

69. E. A. Guillemin, "The Mathematics of Circuit Analysis," p. 325, John Wiley and Sons, Inc., New York, 1949.

70. S. G. Margolis and S. Kaplan, "Nonlinear Effects on Spatial Power Distribution Transients and Oscillations with Xenon Reactivity Feedback" in "Bettis Technical Review, Reactor Technology," WAPD-BT-21, November 1960, pp. 23-27.

71. D. R. Harris, "Analysis of Reactor Fluctuations," Trans. Am. Nucl. Soc. 4, 317-318 (1961).

72. H. Hurwitz, Jr., "Reactor Startup with Statistical Fluctuations," General Electric Company Research Laboratory Report No. 60-RL-(2405E), April 1960.

73. D. B. MacMillan, J. H. Smith, and M. L. Storm, "Effects of Neutron Population Fluctuations on Reactor Design" in "Reactor Technology Report No. 15 — Physics," KAPL-2000-12, December 1960, pp. IV.14-IV.26.

74. M. S. Bartlett, "An Introduction to Stochastic Processes with Special Reference to Methods and Applications," University Press, Cambridge, England, 1955.

75. E. D. Courant and P. R. Wallace, "Fluctuations of the Number of Neutrons in a Pile," Phys. Rev. 72, 1038-1048 (1947).

76. H. Cramér, "Mathematical Methods of Statistics," Princeton University Press, Princeton, N. J., 1946.

77. K. Pearson, Ed., "Tables of the Incomplete Γ-Function," University Press, Cambridge, England, 1957.

78. G. E. Hansen, "Assembly of Fissionable Material in the Presence of a Weak Neutron Source," Nucl. Sci. Eng. 8, 709-719 (1960).

79. B. C. Diven, H. C. Martin, R. F. Taschek, and J. Terrell, "Multiplicities of Fission Neutrons," Phys. Rev. 101, 1012-1015 (1956).

80. J. Terrell, "Distributions of Fission Neutron Numbers," Phys. Rev. 108, 783-789 (1957).

81. D. R. Harris, "Stochastic Fluctuations in a Power Reactor," WAPD-TM-190, November 1958.

82. A. A. Andronov and C. E. Chaikin, "Theory of Oscillations," Princeton University Press, Princeton, N. J., 1949.

83. E. T. Whittaker and G. N. Watson, "A Course of Modern Analysis," p. 194, et seq., University Press, Cambridge, England, 1946.

84. D. R. Harris, "Calculation of the Background Neutron Source in New, Uranium-Fueled Reactors," WAPD-TM-220, March 1960.

85. D. R. Harris, "Natural Neutron Sources in New Uranium Fueled Reactors," Trans. Am. Nucl. Soc. 3, 534-535 (1960).

86. R. B. Leachman, "Emission of Prompt Neutrons from Fission," Phys. Rev. 101, 1005-1011 (1956).

87. E. Segre, "Spontaneous Fission," Phys. Rev. 86, 21-28 (1952).

88. A. Ghiorso, G. H. Higgins, A. E. Larsh, G. T. Seaborg, and S. G. Thompson, "Spontaneous Fission of U^{234}, Pu^{236}, CM^{240}, and Cm^{244}," Phys. Rev. 87, 163-164 (1952).

89. A. H. Jaffey and A. Hirsch, "Spontaneous Fission of U^{236}" in "Chemistry Division, Section C-1 Summary for April, May, and June 1949," ANL-4326 (Del.), August 3, 1949.

90. N. A. Perfilov, "Half-Life Periods of the Spontaneous Fission of Uranium and of Thorium," J. Exptl. Theoret. Phys. (U.S.S.R.) 17, 476-484 (1947).

91. W. J. Whitehouse and W. Galbraith, "Energy Spectrum of Fragments from the Spontaneous Fission of Natural Uranium," Phil. Mag. [7] 41, 429-443 (1950).

92. B. D. Kuz'minov, L. S. Kutsaeva, V. G. Nesterov, L. I. Prokhorova, and G. P. Smirenkin, "Some Features of the Spontaneous Fission of U^{238}," Soviet Phys. JETP 10, 290-294 (1960).

93. G. Scharff-Goldhaber and G. S. Klaiber, "Spontaneous Emission of Neutrons from Uranium," Phys. Rev. 70, 229 (1946).

94. H. Pose, "Spontaneous Neutron Emission of U and Th," Z. Physik 121, 293-297 (1943).

95. A. O. Hanson, M. B. Fischer, S. L. Friedman, E. D. Klema, and J. H. Williams, "Capture and Inelastic Scattering in Spheres of Various Metals," LA-276, May 12, 1945.

96. D. J. Littler, "A Determination of the Rate of Emission of Spontaneous Fission Neutrons by Natural Uranium," Proc. Phys. Soc. (London) 65A, 203-208 (1952).

97. D. J. Littler, "The Rate of Emission of Spontaneous Fission Neutrons by Natural Uranium," J. Nucl. Energy: Pt. A 11, 34 (1959/60).

98. A. W. Waltner and B. E. Leonard, "Measurement of the Spontaneous Fission Neutron Yield of Natural Uranium," J. Nucl. Energy: Pt. A 11, 1-7 (1959/60).

99. R. D. Edge, "Neutron Experiments with a Sensitive Szilard-Chalmers Detector," Australian J. Phys. 9, 429-435 (1956).

100. W. Whaling, "The Energy Loss of Charged Particles in Matter" in "Encyclopedia of Physics," Vol. XXXIV, S. Flugge, Ed., pp. 193-217, Springer-Verlag, Berlin, 1958.

101. I. Halpern, "The (α,n) Cross Sections of Beryllium, Magnesium, and Aluminum," Phys. Rev. 76, 248-250 (1949).

102. E. Segre and C. Wiegand, "Thick-Target Excitation Functions for Alpha Particles," MDDC-185, September 15, 1944.

103. G. C. Hanna, "Alpha-Radioactivity" in "Experimental Nuclear Physics," Vol. III, E. Segre, Ed., pp. 54-257, John Wiley and Sons, Inc., New York, 1959.

104. J. H. Roberts, "Neutron Yields of Several Light Elements Bombarded with Polonium Alpha Particles," MDDC-731, 1944.

105. R. L. Walker, "The (α,n) Cross Section of Boron," Phys. Rev. 76, 244-247 (1949).

106. J. M. Blatt and V. F. Weisskopf, "Theoretical Nuclear Physics," John Wiley and Sons, Inc., New York, 1952.

107. A. G. Khabakhpashev, "The Spectrum of Neutrons from a Po-α-O Source," J. Nucl. Energy: Pt. A 13, 81-82 (1960/61).

108. T. W. Bonner, A. A. Kraus, Jr., J. B. Marion, and J. P. Schiffer, "Neutrons and Gamma Rays from the Alpha-Particle Bombardment of Be^9, B^{10}, B^{11}, C^{13}, and O^{18}," Phys. Rev. 102, 1348-1354 (1956).

109. B. Rossi, "High Energy Particles," p. 491 et seq., Prentice-Hall, Inc., New York, 1952.

110. W. N. Hess, H. W. Patterson, R. Wallace, and E. L. Chupp, "Cosmic-Ray Neutron Energy Spectrum," Phys. Rev. 116, 445-457 (1959).

111. G. Cocconi and V. Cocconi Tongiorgi, "Nuclear Disintegrations Induced by μ-Mesons," Phys. Rev. 84, 29-36 (1951).

112. S. Lattimore, "Rate of Production of Neutrons in Ice by Cosmic Rays," Phil. Mag. [7] 42, 331-337 (1951).

113. G. Bernardini, G. Cortini, and A. Manfredini, "On the Nuclear Evaporation in Cosmic Rays and the Absorption of the Nucleonic Component. I," Phys. Rev. 76, 1792-1797 (1949).

114. E. P. George and A. C. Jason, "Nuclear Disintegrations in Photographic Plates Exposed to Cosmic Rays under Lead Absorbers," Proc. Phys. Soc. (London) 62A, 243-252 (1949).

115. J. A. Simpson, W. Fonger, and S. B. Treiman, "Cosmic Radiation Intensity-Time Variations and Their Origin. I. Neutron Intensity Variation Method and Meteorological Factors," Phys. Rev. 90, 934-950 (1953).

116. J. G. Crocker and G. O. Bright, "Determination of Intrinsic Neutron Source Levels in Enriched Uranium-Aluminum Cores," Trans. Am. Nucl. Soc. 3, 534 (1960).

117. W. B. Doub and S. Milani, "Measurement of the Natural Neutron Source in Two Cores," WAPD-TM-254, November 1960.

118. D. R. Harris, "Photoneutron Source in Uranium-Water Reactors after Power Operation," Trans. Am. Nucl. Soc. 5, 138-139 (1962).

119. S. Bernstein, W. M. Preston, G. Wolfe, and R. E. Slattery, "Yield of Photo-Neutrons from U^{235} Fission Products in Heavy Water," Phys. Rev. 71, 573-581 (1947).

120. W. K. Ergen, "Hard Gamma Emitters Among Fission Fragments," ANP-59, May 3, 1951.

121. L. Katz, A. P. Baerg, and F. Brown, "Photofission in Heavy Elements" in "Proceedings of the Second United Nations International Conference on the Peaceful Uses of Atomic Energy, Geneva, 1958," Vol. 15, pp. 188-201, United Nations, Geneva, 1958.

122. E. J. Winhold and I. Halpern, "Anisotropic Photofission," Phys. Rev. 103, 990-1000 (1956).

123. G. R. Bishop, C. H. Collie, H. Halban, A. Hedgran, K. Siegbahn, S. du Toit, and R. Wilson, "The Cross Section for Photo-Disintegration of the Deuteron at Low Energies," Phys. Rev. 80, 211-222 (1950).

124. W. R. McMurray and C. H. Collie, "The Radium Equivalent of ^{24}Na Sources and the Photodisintegration Cross Section of Deuterium," Proc. Phys. Soc. (London) 68A, 181-188 (1955).

125. R. D. Evans, "Compton Effect" in "Encyclopedia of Physics," Vol. XXXIV, S. Flugge, Ed., pp. 218-298, Springer-Verlag, Berlin, 1958.

126. G. W. Grodstein, "X-ray Attenuation Coefficients from 10 kev to 100 Mev," National Bureau of Standards Circular 583, U. S. Government Printing Office, Washington, D. C., 1957.

127. R. T. McGinnies, "X-ray Attenuation Coefficients from 10 kev to 100 Mev," National Bureau of Standards Supplement to Circular 583, U. S. Government Printing Office, Washington, D. C., 1959.

128. E. Storm, E. Gilbert, and H. Israel, "Gamma-Ray Absorption Coefficients for Elements 1 through 100 Derived from the Theoretical Values of the National Bureau of Standards," LA-2237, April 1957.

129. I. Kirshenbaum, "Physical Properties and Analysis of Heavy Water," p. 381, et seq., McGraw-Hill Book Company, Inc., New York, 1951.

130. K. M. Case, F. de Hoffmann, and G. Placzek, "Introduction to the Theory of Neutron Diffusion, Vol. I," U. S. Government Printing Office, Washington, D. C., 1953.

131. K. Way, et al., "Nuclear Data Sheets," National Academy of Sciences — National Research Council, Washington, D. C., 1958-1961.

132. S. Katcoff, "Fission-Product Yields from U, Th, and Pu," Nucleonics 16 (4), 78-85 (1958).

133. S. Katcoff, "Fission-Product Yields from Neutron-Induced Fission," Nucleonics 18 (11), 201-208 (1960).

134. A. C. Wahl, "Nuclear-Charge Distribution in Fission: Cumulative Yields of Short-Lived Krypton and Xenon Isotopes from Thermal-Neutron Fission of ^{235}U," J. Inorg. Nucl. Chem. 6, 263-277 (1958).

135. V. P. Prikhodtseva and Yu. V. Khol'nov, "γ-Spectrum of Lanthanum-140," Izvest. Akad. Nauk S. S. S. R., Ser. Fiz. 22, 176-178 (1958).

136. B. S. Dzhelepov, V. P. Prikhodtseva, and Yu. V. Khol'nov, "$0^+ \rightarrow 0^+$ Transition in Ce^{140}," Soviet Phys. "Doklady" 3, 803-805 (1958).

137. B. S. Dzhelepov, B. A. Emel'yanov, K. P. Kupriyanova, and Yu. N. Podkopaev, "The Gamma Spectrum of La^{140} in the Energy Range 2300-3900 kev," Soviet Phys. JETP 11, 205-206 (1960).

138. A. Wattenberg, "Photo-Neutron Sources and the Energy of the Photo-Neutrons," Phys. Rev. 71, 497-507 (1947).

139. V. A. Arkhipov, "The Absolute Intensity of the 2.5 Mev ^{140} La Gamma-Radiation," J. Nucl. Energy 8, 252-253 (1958/59).

140. G. R. Bishop, R. Wilson, and H. Halban, "Measurement of Some Weak γ-Ray Intensities," Phys. Rev. 77, 416-417 (1950).

141. C. F. Coleman, "The Decay Scheme of ^{140} La," Phil. Mag. [7] 46, 1132-1134 (1955).

142. H. H. Bolotin, C. H. Pruett, P. L. Roggenkamp, and R. G. Wilkinson, "Excited States of Ce^{140}," Phys. Rev. 99, 62-67 (1955).

143. H. L. Finston and W. Bernstein, "Decay Scheme of I^{132}," Phys. Rev. 96, 71-74 (1954).

144. L. S. Goldring, "Chlorine^{36,38} (Carrier-Free)" in "Quarterly Progress Report, July 1 - September 30, 1951," BNL-132, December 1951, p. 125.

145. H. A. Levy and M. H. Feldman, "Hard Gamma Emitters in Fission" in "Chemistry Division Quarterly Progress Report for Period Ending June 30, 1949," ORNL-286 (Del.), pp. 71-83.

146. H. A. Levy and M. H. Feldman, "Hard Gamma Emitters in Fission: - 54-Minute Iodine$^{(134)}$" in "Chemistry Division Quarterly Report for the Months December, 1948, January and February, 1949," ORNL-336, May 4, 1949, pp. 46-51.

147. G. W. Parker; "Photoneutrons from Energetic Gamma Rays Emitted by Fission Product Radionuclides" in "Chemistry Division Quarterly Progress Report for Period Ending March 31, 1951," ORNL-1053, October 5, 1951, pp. 46-48.

148. N. N. Delyagin, A. A. Sorokin, N. V. Forafontov, and V. S. Shpinel, "Decay Scheme for Zr^{97} and Nb^{97}," Nucl. Phys. 2, 687-705 (1956/57).

149. J. M. Ferguson and F. M. Tomnovec, "Gamma-Ray Spectrum of Te^{131}," USNRDL-TR-490, December 12, 1960.

150. N. H. Lazar, E. Eichler, and G. D. O'Kelley, "Nuclear Levels in Sr^{88} from the Disintegration of Rb^{88} and Y^{88}," Phys. Rev. 101, 727-732 (1956).

151. S. Thulin, "Studies in Nuclear Spectroscopy with Electromagnetically Separated Gaseous Isotopes. II. Disintegration of Some Krypton and Xenon Isotopes," Arkiv Fysik 9, 137-195 (1955).

152. R. P. Schuman, E. H. Turk, and R. L. Heath, "Decay of Short-Lived Barium and Lanthanum Fission Products," Phys. Rev. 115, 185-187 (1959).

153. H. Ryde and C. J. Herrlander, "Gamma Transitions in the Decay of La^{142}," Arkiv Fysik 13, 177-183 (1958).

154. D. J. Hughes, J. Dabbs, A. Cahn, and D. Hall, "Delayed Neutrons from Fission of U^{235}," Phys. Rev. 73, 111-124 (1948).

155. G. R. Keepin, T. F. Wimett, and R. K. Zeigler, "Delayed Neutrons from Fissionable Isotopes of Uranium, Plutonium, and Thorium," Phys. Rev. 107, 1044-1049 (1957).

156. W. D. B. Spatz, D. J. Hughes, and A. Cahn, "Photo-Neutrons Produced in D_2O and Beryllium by Fission Product Gamma-Rays," Phys. Rev. 72, 163 (1947).

157. P. G. Hansen and K. Wilsky, "High Energy Gamma Rays in the Decay of La^{140}," Nucl. Phys. 30, 405-408 (1962).

GENERAL REFERENCES

H. Chestnut and R. W. Mayer, "Servomechanisms and Regulating System Design," Vol. I, John Wiley and Sons, Inc., New York, 1951.

G. A. Korn and T. M. Korn, "Electronic Analog Computers," McGraw-Hill Book Company, Inc., New York, 1952.

M. A. Schultz, "Control of Nuclear Reactor and Power Plants," McGraw-Hill Book Company, Inc., 2nd Ed., New York, 1961.

M. F. Gardner and J. L. Barnes, "Transients in Linear Systems," Vol. I, John Wiley and Sons, Inc., New York, 1942.

Chapter 6

COMPARISONS OF INTEGRAL EXPERIMENTS WITH THEORY

D. R. Connors, Editor

6.1 INTRODUCTION

Before an analytical model can be used for the design of a nuclear reactor core its adequacy must be tested against experimental data and the degree of its reliability established. This chapter describes some of the tests to which the analytical models are subjected in the continuing attempts to establish the scope of their validity and the areas where improvements are required. In the design of a reactor core, calculations must be relied upon to predict many characteristics of the core's performance. Thus, the capability of the model to predict each individual characteristic must be determined, since each characteristic can affect the ultimate design of the core. Some of the performance areas which must be tested include the ability of the model to predict the criticality of the core, the rod positions and rod worths, the temperature coefficients, shutdown, local power peaking, gross power sharing, the depletion of the various materials in the core, and the buildup of the poisons as a result of this depletion. The final test of the adequacy of a specific analytical model lies in actual performance of the reactor core at initial operation and throughout its operating lifetime. Much can be done, however, prior to the construction and operation of the final product to determine the limitations of the model and to establish the margins for error which must be built into the core because of these limitations.

Several types of experiments can be performed to test each of the various aspects of the reactor design technique. Some of these experiments are aimed at the development or verification of the basic physical parameters inherent in the model, for example, the measurement of the neutron absorption and scattering cross sections as a function of energy or the determination of the resonance parameters of the various materials used in the construction of the core. Other experiments are

aimed at testing the methods in which these basic physical parameters are coalesced in order to obtain a description of the thermal or epithermal neutron distributions in the core in space, time, and energy, for example, experiments to measure the low energy neutron spectrum in hydrogenous media. Some of the experiments provide a test of how successful the overall analytical model, which includes the many fundamental component parts, has been in predicting the gross reactivity and neutron distributions of a comparatively simple geometric system, for example, the clean critical type of experiment. Each of the experiments serves an important role in establishing the level of confidence in the analytical model. Not all of these types of experiments are described in this chapter. Rather the material has been confined to certain integral types of experiments more directly connected with the verification of the overall analytical model. It should be recognized that one of the problems associated with this integral approach is the difficulty of detecting compensating errors which could be made in two or more parts of the overall analytical model.

Zero power critical experiments are an excellent example of the integral type of experiment against which the basic model can be tested. In this chapter the term critical experiment refers to the assemblies of various geometric sizes and shapes which are operated in a self-sustaining or critical condition. Since the reactor can be critical at any neutron level from the very low levels up to the high heat producing levels, it is necessary to restrict further the term zero power critical experiment to those experiments at low neutron levels in which little heat is produced by neutron fissioning, thus resulting in a negligible change in the materials inventory of the core during the experiment and in the formation of a negligible number of fission product poisons. These experiments are typified by rapid access to the core following critical operations, so that geometric changes can be easily made without the complication of the high radiation levels characteristic of reactors operating at higher power levels. These critical experiments usually operate at power levels no higher than about 1000 watts and are constructed of an accurately known inventory of materials whose composition can be carefully controlled. The construction features of the critical experiments are highly flexible and, thus, usually not suited to high power operation. The zero power critical experiment has provided much of the data against which the analytical techniques used in the design of reactor cores have been tested, and several types of these critical experiments are discussed in this chapter.

One major aspect of the analytical model that will not be discussed explicitly is the ability of the model to predict the

lifetime performance of the core, i.e., the depletion of materials such as the U^{235} fuel or the B^{10} burnable poison or the buildup of fission product poisons as a result of operation at power. Instead it will be seen that the model is tested under various conditions of fuel and poison loading, and its capability to represent each of these conditions is determined. However, certain assumptions can be made about the depletion characteristics from the critical data at various loading conditions. If each of these fuel and poison loading conditions can be successfully predicted by the analytical model, then depletion becomes a problem of determining the changes in the fuel and poison loadings from the loading at an initial condition to that which is present after some amount of power operation. From the ability of the model to predict the relative neutron distribution in the core for an arbitrary materials composition, confidence in the ability to calculate the relative depletion of various regions in the core can be established. This is particularly true if the relative neutron distributions are measured at high temperature, since it is at the high temperatures that the core will actually be depleted. Further confirmation of depletion can be obtained from these low power critical experiments if the relative number of neutron captures in fuel and poison are actually measured. Final verification of the depletion aspect of the model, however, comes with the lifetime operation of the designed core. A performance analysis then establishes the extent to which the model has accurately predicted the core depletion.

Two basic types of critical experiments are commonly utilized in the integral testing of the analytical model. These have been categorized as clean critical experiments and mockup experiments. Clean critical experiment refers to that class normally run in a simplified geometry, which is clean of an axial inhomogeneity due, for example, to the partial withdrawal of the safety control rods. In these experiments some parameter, such as geometric size, fuel or poison loading, or temperature, is adjusted so that the core is critical with the control rods fully withdrawn or nearly so. In general, this simplifies the analysis of the experiment, since the importance of the axial dimension is reduced, particularly if it is large compared with at least one of the other major axes in the core. Clean critical experiments which are run in a narrow slab type geometry are amenable to a one-dimensional type of analysis, since the most important dimension is the narrow one.

The role of the clean critical experiment in both slab and more complex two- and even three-dimensional geometries is one of uncovering major problem areas in the analytical models.

This is accomplished by investigating a wide variety of experimental cases, each of which may emphasize a particular portion of the analytical model more than the others while still retaining careful control of the experimental conditions. By carefully varying one of the parameters under investigation, for example, the poison concentration, some insight is gained into the degree of validity of the model in representing that variable parameter. However, it is important to note that the parameter under investigation is merely being emphasized, since criticality is retained by varying some other parameter. Thus, care must be taken in the interpretation of the results, since compensating errors could be made in the representation of both parameters. Several types of clean critical experiments at both ambient and high temperatures are discussed in this chapter.

Mockup experiments are the class of critical experiments in which the nuclear properties of the design core are very closely matched in the critical assembly except that the operation is restricted to low power. One of the major functions of the mockup is to identify a difference between experiment and theory, which it is assumed will also exist for the design core when actually manufactured and operated. In addition to furnishing this difference, the mockup also provides the designer with a certain limited amount of engineering information about the core characteristics, such as critical rod positions and rod worths, shutdown margins, and temperature coefficients in the zero power condition, depending upon how closely the mockup did indeed represent the nuclear features of the design core. Mockup operations and comparisons with analysis, although extremely important in providing final overall verification of the analytical model, are not discussed in this chapter mainly because of the difficulty of isolating through a mockup experiment a particular fault of a portion of the model. Rather, the emphasis of this chapter will be placed upon confirming the aspects of the analytical techniques which can be accentuated or isolated, since it is in this manner that the need for specific improvements can be established. Thus, in the first part of this chapter (Sects. 6.2, 6.3, 6.4, and 6.5), the emphasis is placed on critical experiments of relatively simple geometry where a major attempt is made to obtain results which can be readily interpreted and understood. Critical experiments will be discussed here for systems which are fueled with uranium. In Sects. 6.2, 6.3, and 6.4 the uranium discussed is highly enriched in the U^{235} isotope. In Sect. 6.5 several experiments are discussed which have been performed on slightly enriched uranium systems. Here the difficulties associated with the resonance absorption will be emphasized as well as certain

aspects of the thermal neutron problem in the high uranium content systems.

In addition to the class of reactor experiments which are operated at critical, a significant amount of confirmation of calculational techniques can be obtained through the analysis of certain subcritical systems. Sections 6.6 and 6.7 are concerned with these subcritical systems. Again, only a few selected types of experiments in this category are described. One of the types of particular interest is the pulsed neutron experiment in which a burst or pulse of high energy neutrons is injected into a subcritical assembly, and the time rate of decay of the prompt neutrons generated by this burst is measured. Information on the degree of subcriticality can be obtained through an analysis of the decay rate and, in particular, can be compared with calculations of the subcritical system, thus extending the range over which the calculational models can be tested. In addition to these measurements of the degree of subcriticality of a system, the pulsed neutron technique can also be utilized as a means of isolating certain problem areas in the analytical model. An example of this arises from the fact that the decay constant of the fundamental mode prompt neutrons can be made to depend strongly upon the neutron leakage in the far subcritical region. Thus, comparisons of the measured prompt decay rates with calculations may provide a test of the adequacy of parameters which describe the leakage, a test even more sensitive than can be made through critical experiments.

In Sect. 6.7 another type of subcritical experiment is described. In this example the thermal neutron spectrum from a subcritical assembly was studied with the aid of a slow neutron chopper in which neutrons of different velocities were separated by their different times of arrival at a detector after having been chopped into pulse bursts by a rotating shutter. Comparisons are then made between the measured and calculated neutron energy distributions, using the calculational techniques developed to design the core. This type of experiment adds further confirmation of the calculational model by testing the basic physical theories developed to describe the interaction of the neutrons with matter and their distribution in space and energy.

In summary, this chapter attempts to give the reader some insight into a few of the extensive experimental tests to which the various portions of the nuclear design methods are subjected. Because of their detailed and complex nature, many of these experiments may seem to require a special theory of their own as an aid in their interpretation. Wherever possible, however, the attempt has been made to maintain a terminology consistent with the other chapters in this volume and to refer

the reader to sections where the theory is more adequately described.

6.2 HIGHLY ENRICHED CLEAN CRITICAL EXPERIMENTS AT AMBIENT TEMPERATURES

A. Clean Slab Experiments with Small Bundle Box Geometry

D. R. Connors

1. Introduction

The practical use of an analytical model to describe reactor behavior dictates that the model be a compromise between accuracy and simplicity. Simplicity is required because of the computing costs in the application of a model and the limted capacity of the computer codes themselves. Because of the simplifications that are required, it is necessary to compare any specific analytical model with more accurate theoretical standards, where these standards are available, and with a wide range of experimental configurations in order to establish the limitations of the model. Examples of the extensive testing of practical analytical techniques against higher order theoretical approximations have been given in the preceding chapters. In this section, the capabilities and limitations in the reactivity and power distributions predicted by certain of the various methods previously described are tested against the results from a large number of experimental critical assemblies which have been analyzed with these models. Four sets of experiments in slab geometry and their associated analyses are described here. The emphasis is upon comparisons between theory and relatively simple experiments, in the belief that a thorough understanding of simple experiments is required before proceeding to the more complex types.

The major purpose of the slab critical experiments is to provide a body of data against which the total or overall analytical model could be tested. This total model includes many fundamental component parts, such as the thermal neutron scattering kernel or the inelastic scattering cross sections of the various materials. In general, the experiments do not provide a test of any of the individual fundamental components even though, in many cases, they can emphasize one particular feature more than others. Instead, the analysis of the experiments brings together all of these components of the model and, thus, the results are subject to compensating errors which could be made in the various portions of this total model. Through the analysis of a large number of experiments of

different types with a particular analytical method, a degree of confidence can be gained that, if errors do exist in the various portions of that method, they are at least in balance over the range of experiments considered. This degree of confidence is necessary before the model can be used to evolve the nuclear design of a reactor.

A description is given of the results for several types of clean critical slab experiments which used fuel elements constructed from pieces of Zircaloy* and a metal alloy fuel shim containing enriched uranium. With these metallic fuel elements, experimental information has been obtained and comparisons with theory are reported for a set of slab assemblies in which the metal-to-water volume ratio and the U^{235} fuel density were the major variable parameters. This set of experiments was designed to test the adequacy of the overall analytical model for treating systems composed mainly of U^{235}, zirconium, and water in the absence of a large amount of neutron absorption from control rods or a nuclear poison. As such, this set of clean slabs should emphasize the portions of the model dealing with the slowing down of neutrons into the thermal group due mainly to scattering collisions with hydrogen and the subsequent absorption of neutrons in U^{235}. However, the narrowness of these slabs makes them highly sensitive to the treatment of the neutron leakage into the reflector. Thus, although the set emphasizes certain portions of the model more than others, the results are mainly a test of the total analytical technique.

For the second set of experiments and analyses, several slab assemblies are reported which contained septa of lumped boron poison in which the metal-to-water ratio, the fuel density, and the boron optical thickness were the major variable parameters. This set of experiments was designed to emphasize the portion of the calculational model which describes the self-shielding of a thermal neutron absorber as well as the competition for neutrons between the discrete absorber and the fuel region. By comparison of the calculated result for a nearly identical slab without a poison septum with the result for the poisoned slab, a degree of confidence can be obtained in the portion of the model which treats the lumped poison. This will be true even if the calculations for both the unpoisoned and the poisoned cores are not in exact agreement with the experiment. As long as the two calculations are consistent with one another, even though both may disagree somewhat with the

*Zircaloy is the trade name of an alloy of zirconium which contains tin, iron, chromium, and nickel as alloying ingredients coupled with certain impurities in the parts per million concentration range. A typical sample is listed in the footnote of Table 6.1.

experiment, confidence can be obtained in the portion of the model which represents the lumped poison. However, since compensating effects could mask the results, one must be careful to accept the results as a test of the total model in which this area is merely emphasized rather than viewing the results as a final test of the poison representation itself.

In the third set of experiments, slab criticals containing a lumped epithermal absorber in the form of hafnium septa are described. The intent was to emphasize the portion of the total model dealing with the treatment of resonance self-shielding in a typical epithermal absorber. Both a single blade septum and a dual, water-filled blade type are described.

Finally, a set of slab experiments is described which contained large amounts of distributed epithermal absorbers, hafnium, and iridium. These experiments are designed to emphasize portions of the total model which deal with the neutron slowing-down as well as with the treatment of resonance absorption.

In summary, the purpose of these comparisons is to provide an overall test of specific analytical techniques while at the same time emphasizing various portions of the model. The results of the comparisons will show that the overall model used for the analyses has been reasonably successful in predicting both reactivity and power distributions over the wide range of experiments presented here. In particular, the importance of including such effects as the inelastic scattering in zirconium and oxygen and an explicit treatment of the fission resonances in U^{235} will be demonstrated. The results will also indicate the sensitivity of certain homogenization techniques, particularly near fuel-water interfaces, and point out the need for a fairly exact treatment of spectrum and transport effects near lumped absorbers.

2. *Description of Experiments*

Before proceeding with a description of the results obtained for each set of experiments, a description of the general properties of the assemblies is in order. The experimental assemblies can best be described with the aid of Figs. 6.1, 6.2, and 6.3. The basic slab geometry used in these experiments has, as a unit building block, a hollow 1.1-in. square zirconium module box which is about 45 in. high. An array of these hollow boxes is mounted upon a base structure within a floodable tank. In Fig. 6.1 such an array of boxes is shown arranged in a simple rectangular geometry. In Fig. 6.2, a closeup of one of the module boxes shows the U^{235} fuel contained in the form of 19.8 weight percent uranium-zirconium metal alloy fuel shims which are each about 20 mils thick. These fuel shims were held against

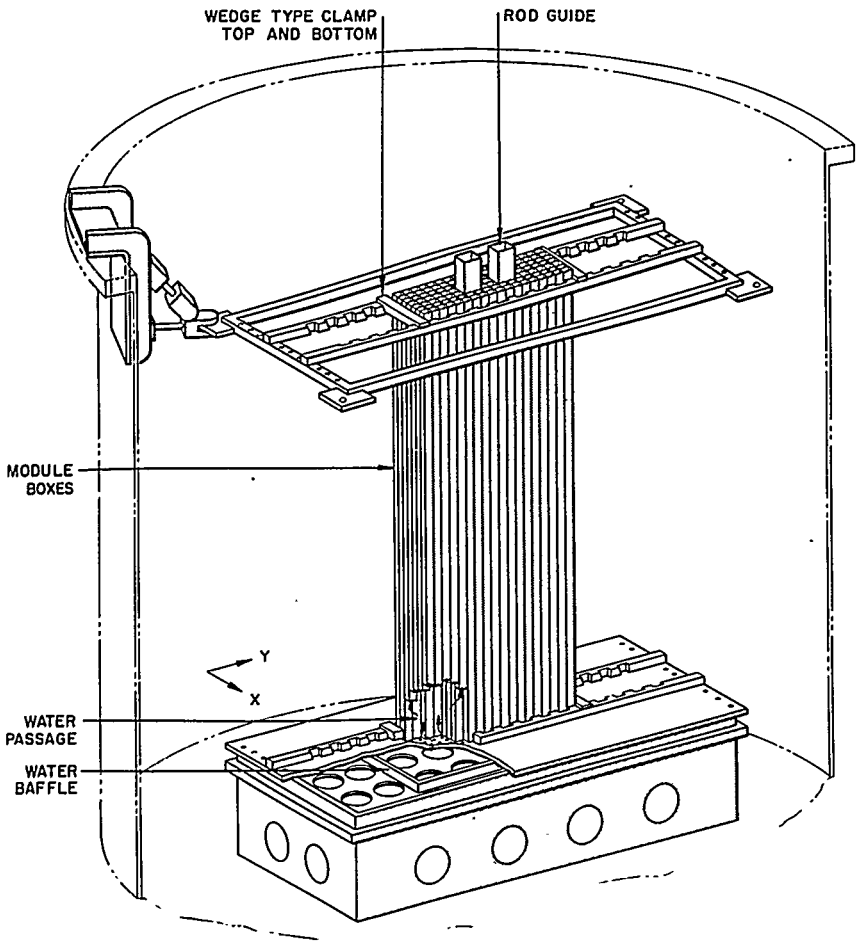

FIGURE 6.1. Perspective View of Metal Slab Assembly of Small Module Box Construction Showing the Highly Flexible Nature of the Construction.

the sides of the central Zircaloy strip by small aluminum clips. The central Zircaloy strips shown in Fig. 6.2 are represented as being 60 mils thick although strips with thicknesses of 70 and 110 mils were also used in these experiments. By varying the number of fuel shims or the number of Zircaloy strips within the module boxes, or both, a variation can easily be made in either or both the fuel density or metal-to-metal volume ratio in the slab. The unit module box shown in Fig. 6.2 contains what has been designated as the 4×8 array, i.e., eight fuel shims clipped to four Zircaloy strips such that

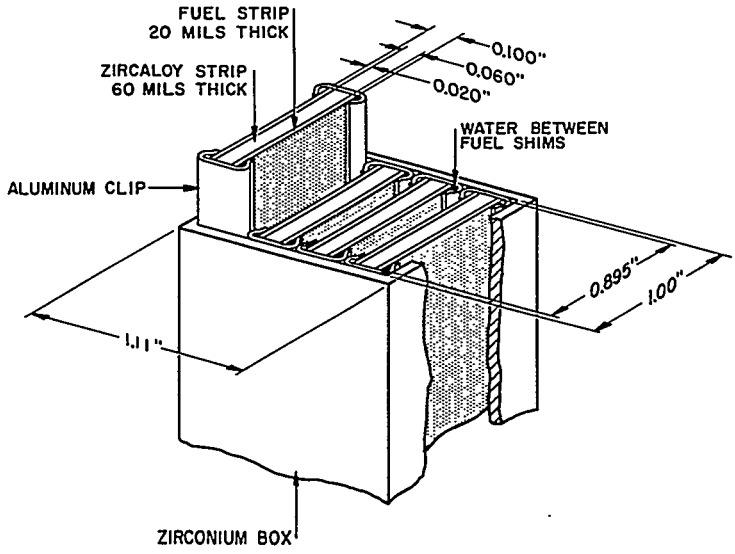

FIGURE 6.2. Detail of Small Module Box Construction Showing a 4×8 Array of Fuel Elements.

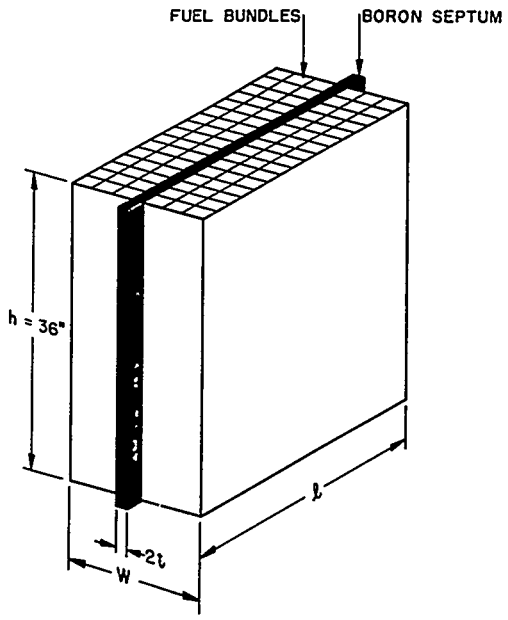

FIGURE 6.3. Orientation of Lumped Absorber Septum in Small Module Box Slabs. (In this figure, the 36-in. height of the active fuel region does not include the upper and lower reflector regions.)

two fuel shims are clipped to each Zircaloy strip. In a designation of 4 × 4, only one fuel shim would be clipped to each of the four Zircaloy strips, while for the 3 × 3 designation only three fuel shims and Zircaloy strips would be within the box.

When a uniform fuel density was desired throughout the slab, such as the first set of clean slabs reported here, each module box throughout the slab contained the same number of fuel shims and Zircaloy strips. Nonuniform distributions could be obtained by a selective loading of the module boxes. In all experiments in which the module box was used, each slab reactor was fueled to an axial height of 36 in. Thus, since the module boxes were 45 in. high (and since the Zircaloy strips were also 45 in. high or more), a metal-water reflector existed above and below the fueled region. These reflectors contained the same materials as the fuel region, except that the fuel shims were replaced by their equivalent volume in the form of 20-mil thick aluminum strips. The entire assembly was flooded with water within the confines of the floodable tank, yielding a water reflector on each side of the slab array in addition to the metal-water reflectors above and below the fueled region. Table 6.1 lists the dimensions and material compositions of the major components used in the construction of the slabs.

The movable mechanical reactivity control for each experiment was generally provided by two hollow, square, control rod boxes which had walls composed of a boron-impregnated stainless steel. Each of these rods had a horizontal cross-sectional area equivalent to the area of four of the zirconium module boxes. Four fueled module boxes, nearly identical to those in the rest of the slab, were attached to the lower end of each control rod, so that when the rods were withdrawn they pulled up the fueled boxes into the slab to form a nearly uniform array of the boxes. In each experiment, the size of the assembly was adjusted to the rectangular size closest to being critical with these fuel-bearing rods completely withdrawn and the fuel brought up into the slab. The excess or subcriticality associated with this rectangular size (usually within 1/2 percent of a k_{eff} value of unity) was determined by using either rod calibration techniques or by a measurement of the reactor period with the rods completely withdrawn. The reactivity with the control rods withdrawn and the fuel bundles drawn up into the slab is called the all-rods-out reactivity.

All calculations listed in this section have been performed in the all-rods-out condition. These calculated results are tabulated as being normalized to experimental values of k_{eff} of 1.00. An example can best illustrate how this normalization

TABLE 6.1 — MAJOR COMPONENTS IN METAL SLAB EXPERIMENTS

Unit	Dimensions in Inches (in a horizontal cross section)	Area (in. ^{2})	Major Material Components	Density (g/cc)
Fuel shim	0.020 x 0.895	0.018 ± 0.001	19.8 w/o uranium (enriched to 93.14% in U^{235} and containing 5.72% U^{238}) 80.2 w/o zirconium*	7.52 ± 0.03
60-mil Zircaloy strip	0.059 x 0.895	0.053 ± 0.001	Mainly Zircaloy-2 although several elements were fabricated from Zircaloy-3†	6.55 ± 0.03
70-mil Zircaloy strip	0.0714 x 0.908	0.064 ± 0.001	Zircaloy-2	6.58 ± 0.03

TABLE 6.1 — MAJOR COMPONENTS IN METAL SLAB EXPERIMENTS (Continued)

Unit	Dimensions in Inches (in a horizontal cross section)	Metal Area (in. ^{2})	Major Material Components	Density (g/cc)
110-mil Zircaloy strip	0.110 x 0.910	0.098 ± 0.002	Zircaloy-2	6.56 ± 0.03
Module boxes	1.109 x 1.109	0.266 ± 0.001	Zirconium	6.49 ± 0.03
Aluminum clips				
4 x 8 type 4 x 4 type	0.621 x 0.0146	0.0082 ± 0.0001	Type 52S aluminum	2.79 ± 0.014
3 x 5 type 3 x 6 type	0.759 x 0.015	0.0100 ± 0.0001	Type 52S aluminum	2.78 ± 0.014

*In the construction of the slabs, many individual fuel shims are used to create the full fuel loading. Including the uncertainty in the chemical analyses and a statistical sampling uncertainty which is due to the fact that chemical analyses are performed only on a selected number of elements, it is concluded that the uranium loading is 19.83 w/o with a standard deviation of ± 0.16 w/o. Thus, the total fuel loading in each slab is known with an accuracy of about ± 0.8%.

†The Zircaloy-2 alloy contained 98.2 w/o zirconium, 1.35 w/o tin, 0.13 w/o iron, 0.09 w/o chromium, and 0.05 w/o nickel. The Zircaloy-3 is similar, except that it contained only 1/6 to 1/8 as much tin.

is performed. Suppose that at a certain rectangular size the experimentally determined value of k_{eff} with all rods out were 1.001, thus indicating a slightly supercritical reactor. This value of k_{eff} would be inferred from the measurements of the reactor period with all rods withdrawn or from the rod calibration technique. If the calculation for this core, again performed for the all-rods-out condition, yielded an eigenvalue of 1.003, then the calculation is also indicating a slightly supercritical reactor, but more supercritical than the experiment. The calculation for a just critical experimental condition would be expected to be 1.002, which is found by subtracting the experimental excess of 0.001 from the calculated value of 1.003. This manner of normalization of the eigenvalue calculations has been used where possible throughout this chapter, so that the various experimental-analytical comparisons can be observed simply by comparing the deviations of the analysis results from a value of 1.000.

For the second and third sets of experiments, which contained lumped poison septa in the form of boron or hafnium, the orientation of the poison septum was as shown in Fig. 6.3. For the experiments with boron septa, the boron was contained in the form of a thin plastic tape (Mylar) on which was deposited a layer of boron which was highly enriched (~95 percent) in the B^{10} isotope. Layers of this plastic tape were built up to the desired lumped boron concentration and then encased between two aluminum envelope plates (each about 1/32 in. thick type 2S aluminum) for mounting between the rows of module boxes in the slab. Variations in the number of layers of the plastic tape provided the desired flexibility for varying the optical thickness $2t\Sigma_a$ of the boron, where t is defined as the half thickness of the boron region. Each layer of the B^{10} enriched boron tape was about 0.001 in. thick and was loaded to about 5.5 mg B^{10}/in.^{2} of area. The tape density, loaded with boron, was about 1.4 g/cm^3 and, except for the boron, had a chemical composition of $C_{10}H_8O_4$.

Experiments were also performed with the boron contained in the form of a boron-stainless steel plate with no aluminum envelope plates as well as with the boron contained in a polyethylene matrix sandwiched between aluminum plates. In the polyethylene case, the hydrogen content of the tape was roughly ten times that of the plastic tape results reported here. Analysis of these additional experiments with lumped boron is not reported here, but it showed that effects due to the particular type of boron carrier, such as the neutron scattering in the hydrogen of the polyethylene or the plastic, would have to be represented in the calculation but, once represented, would have little effect on the conclusions drawn from the results.

In the case of the lumped hafnium experiments, metallic hafnium plates, containing about 98 weight percent natural hafnium with the remainder mainly zirconium, were available in thicknesses of 0.060 in. and 0.204 in. The hafnium septa were mounted between rows of module boxes in the slab without the need for additional envelope plates. Both a single blade type and a water-filled box type of hafnium septa are included in this set of experiments, with the variations in the box types being in the hafnium blade thickness and in the thickness of the interior water gap. (The designation, "Box, 0.120-1.26-0.120 in.," means a septum composed of two 0.120-in. thick hafnium septa separated by 1.26 in. of water.) In each experiment, the poison septum was oriented in the slab in a manner similar to that shown for the boron septum in Fig. 6.3. The fuel density and metal-to-water volume ratio of the core fuel region into which the hafnium septa were installed were equivalent to that of one of the cores in the first set of clean slab experiments, Core 32. The core size was adjusted for criticality with the septum installed in place. Further experimental details for these septum experiments, such as the dimensions of the poison materials, are listed in tables following the analytical-experimental comparisons.

In each experiment which contained a distributed epithermal absorber, the resonance absorber was inserted into the slab reactor in a stepwise manner; that is, the absorber concentration was increased in several discrete steps. The hafnium was contained in the form of hafnium oxide which was deposited upon a thin Mylar tape. Each HfO_2-Mylar tape was about 0.001 mil thick and had the same surface area as one of the 20 weight percent fuel strips. The HfO_2-bearing tape was positioned beneath the fuel strips and held against the Zircaloy strip (see Fig. 6.2) by the fuel strip which, in turn, was held by the clips. In the full hafnium loading (Core 52 in Table 6.11), an HfO_2-Mylar tape was positioned beneath each of four fuel strips in each module box in the slab. Thus, the absorber was distributed in the same manner as the fuel in the slab. Partial hafnium loadings were attained by replacing HfO_2-Mylar tapes under some of the fuel strips with dummy Mylar tapes which contained no hafnium. Thus, the loading identified as two hafnium tapes per bundle box (Core 47 in Table 6.11) consisted of a dummy Mylar tape under one of the fuel strips on two of the Zircaloy bars and the HfO_2-Mylar tapes on the other two Zircaloy bars in each module box. Each module box in this core contained four Zircaloy bars and eight fuel elements in the standard 4 × 8 loading method.

A similar method of distributing the iridium absorbers throughout the slab was used, with the exception that the iridium

was contained as a very fine powder distributed in a polyethylene tape. In this case, the tape was 0.005 in. thick. In both types of absorber experiments, a control slab containing a full loading of the dummy absorber tapes was run such that the most significant effect due to the absorber could be isolated. This control slab was simply a slab of the same fuel density and metal-to-water ratio which contained no distributed resonance absorber but which contained the dummy Mylar or polyethylene tapes in their place.

In many of the experimental systems described above, the activation distribution of enriched uranium wire detectors was measured along typical lines of interest in the slab. For nearly one-dimensional slabs, such as the sets of experiments reported in this section, the major line of interest is a plot parallel to the narrow dimension of the slab.

Experimental uranium activation plots were obtained by irradiating uranium-Zircaloy wire detectors, each about 0.030 in. in diameter and about 1/2 in. long, which were placed at small intervals along the line in question. The wires were oriented with their axes aligned in the vertical direction. Each wire contained about 6 weight percent of enriched uranium with the remainder Zircaloy. The wire detectors were dropped into holes drilled into small Zircaloy wands (1/2 in. high by 0.050 in. thick by variable length), which slipped tightly into a horizontal slot (about 1/2 in. high by 0.050 in. wide) between the module boxes. This slot was formed by the appropriate alignment of several module boxes, each of which had a small horizontal notch cut into one wall of the box at about the mid-height of the slab. For activation measurements in water channels or in the reflector, the wand material was changed from Zircaloy to plastic in order to keep the perturbation caused by the wand to a minimum. In comparing measured and calculated activation distributions, it is important to note that the position of the activation plots lay experimentally between the walls of abutting module boxes.

3. *General Analytical Model*

The basic framework of the analytical model used to obtain the following results is four-group diffusion theory. Many portions of this model have been tested against more exact theoretical standards for the specific geometries and range of parameters characteristic of these sets of slab experiments. Some of these comparisons are described below.

A) FAST GROUP CONSTANTS. The fast neutrons have been described with three energy groups: Group 1, 10 Mev to 0.821

Mev; Group 2, 0.821 Mev to 5.53 kev; Group 3, 5.53 kev to 0.625 ev. Group 3 in this scheme has been called the epithermal group, with the first two groups being designated as fast groups. Constants for these three fast groups were obtained with the MUFT Code,[1] which solves the P_1 slowing-down equations where the spatial dependence is separated by representing the flux by its Fourier transform. This method of generation of the few-group constants is discussed in Chap. 2, Sect. 2.8, and a description of the MUFT computer program is presented in Chap. 7. For most of the analyses discussed here, the cross-section library[2] used in MUFT included an inelastic scattering matrix in Group 1 for zirconium and absorption cross sections for zirconium yielding a resonance integral of 1.1 barns. Identification of the actual cross sections used in this library can be obtained from Table 6.2 which refers to the elements listed in Ref. 2. Certain calculations used an earlier version of the cross-section library, which did not include such effects as the inelastic scattering in zirconium and oxygen nor an

TABLE 6.2 — IDENTIFICATION OF CROSS SECTIONS USED IN THE ANALYSES OF SLAB EXPERIMENTS*

Element	MUFT Code Identification Symbol	Tape 5 Schematic Symbol
H	001	1
O	102	72
Zr	103	73
C	104	74
Al	009	9
Hf	014	14
U^{235}	118	85
U^{238}	120	88
B^{10}	129	35

*Analyses performed with this library used the identification symbols associated with Tape 5. The actual cross sections are tabulated in Ref. 2.

explicit treatment of the fission resonances in U^{235}. This earlier version can be identified with the aid of Table 6.3.

One other difference between these libraries lies in the treatment of aluminum. Cross sections are included for aluminum in the later version of the library, as discussed in Ref. 2. However, in the earlier version aluminum was treated in the fast neutron groups by assuming that the aluminum could be replaced by an equivalent amount of zirconium obtained from

$$N_{\text{equiv Zr}} = 0.365\, N_{\text{Al}}$$

where N = nuclei/cm^3. This equivalence was only necessary for the fast group treatment of the aluminum, since cross-section data were available for the thermal group. This equivalence relationship was developed as a method of duplicating the measured age in an aluminum-water mixture by the MUFT calculation, using zirconium in place of aluminum in the calculation. Since the experiments reported below did not contain an appreciable amount of aluminum, the contribution of the

TABLE 6.3 — EARLY CROSS SECTIONS USED FOR SOME COMPARISONS OF RESULTS IN ANALYSIS OF SLAB EXPERIMENTS*

Element	MUFT Code Identification Symbol	Tape O Schematic Symbol
H	001	1
O	002	2
Zr	003	3
Hf	014	14
U^{235}	018	18
U^{238}	020	20
B^{10}	129	35

*Analyses performed with this earlier library tape used the identification symbols associated with Tape O. The actual cross sections are tabulated in Ref. 2.

aluminum treatment to the difference between the fast group libraries is small.

The three-fast group approximation has been tested against a 54-fast group representation in one-dimensional spatial calculations using the P1MG Code.[3] For simple cores (no internal water gaps or absorbing septa) the comparisons show that the few-group representation gives excellent agreement in activation shapes and eigenvalues with the multigroup calculations. Examples of this are shown in Figs. 6.4 and 6.5. Although the few-group calculations do not simulate in detail the characteristics of the multigroup calculation, such as the source to thermal group at core reflector interfaces, the gross properties are retained.

B) THERMAL GROUP CONSTANTS. The analyses described in this section used one of two schemes for the representation of the thermal neutron energy group (0.625 ev to 0) in the four-group diffusion theory model. In several cases differences are pointed out by a comparison of the results obtained with each of these schemes. The group constants generated by one of these

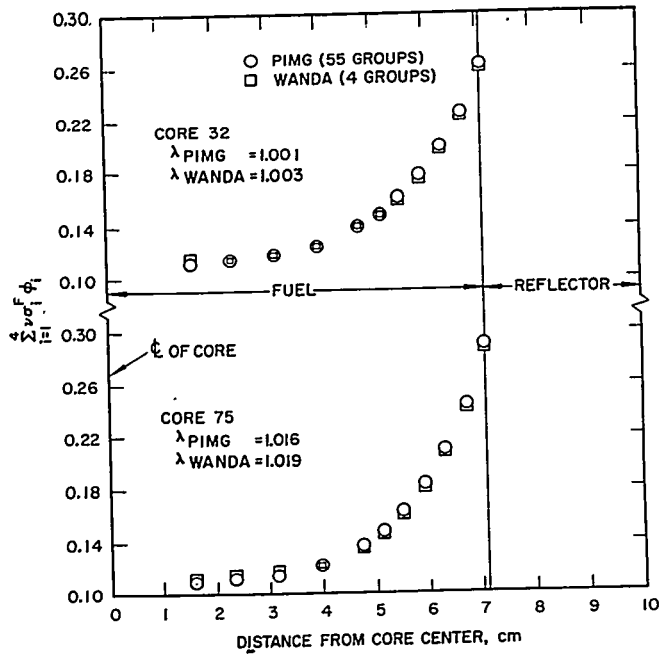

FIGURE 6.4. Comparison of Fission Sources from P1MG and Four-Group WANDA Calculations.

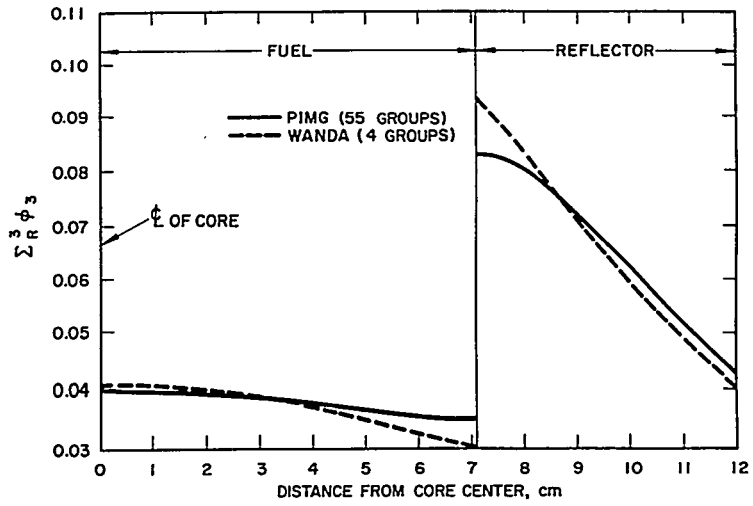

FIGURE 6.5. Comparison of Source to Thermal from P1MG and Four-Group WANDA Calculations for Core 75.

schemes can be designated as hardened constants. For this case, the hardening of the neutron energy spectrum because of the preferential absorption of lower energy neutrons has been treated by using a Wigner-Wilkins energy distribution for the averaging of the cross sections. This manner of generating thermal group constants is discussed in Chap. 3, Sect. 3.2, for the case of the spectrum calculated with the Wigner-Wilkins kernel of mass 1. This spectrum hardening and the contribution of a $1/E$ tail arising from the slowing down of higher energy neutrons into the thermal group through hydrogen moderation are treated analytically in the SOFOCATE[4] or KATE[5] codes described in Chap. 7. In each of the given analyses, the Radkowsky[6] prescription has been used for the representation of the thermal neutron scattering kernel.

The second scheme for treating the thermal group has been to use mixed constants, as described in Chap. 3, Sect. 3.7. In this case the thermal group diffusion coefficient is averaged over a Maxwellian spectrum, while the absorption and fission cross sections are averaged over the hardened Wigner-Wilkins spectrum. In all cases where these mixed constants have been used, the boundary condition applied at the interface between regions of different group constants has been continuity of the neutron current and density. The coupling of this boundary condition with the use of mixed constants yields the thermal group model which has been designated as the mixed number density model[7] (MND).

Where the hardened or Wigner-Wilkins constants have been used, the boundary condition applied at region interfaces has been continuity of the neutron flux. This method leads to a discontinuity in the activation $(\sigma\phi)$ of an absorber at boundaries between dissimilar media, since the microscopic cross section may have an abrupt change at the boundary. On the other hand, the mixed number density model yields a continuous activation distribution across region boundaries for a $1/v$ absorber. The mixed number density model, in essence, combines the thermal utilization typical of a hardened spectrum with a diffusion length characteristic of a Maxwellian spectrum.

C) THERMAL GROUP HETEROGENEITY CORRECTION FACTORS (PLATE DISADVANTAGE FACTORS). Thermal group heterogeneity correction factors were applied in the process of homogenizing the fuel bundle boxes and their contents into a uniformly distributed mixture. Correction factors are necessary because the neutron exposures of the various components of the bundle box are not at the same flux level as in a uniformly distributed mixture. The correction factors (flux-weighting factors) were generated from detailed one-dimensional double-P_3 approximations to the neutron transport equation using the FLIP[8] code on the IBM-704. For each type of module box construction used experimentally, cell calculations were run for a geometry which represented a one-dimensional array of a few of the module boxes and their contents explicitly in a direction normal to the fuel shims. Microscopic cross sections used as input parameters to the double-P_3 calculations were obtained from averages over the Wigner-Wilkins spectrum of the homogenized bundle box constituents. The detailed double-P_3 flux distributions through the cell were then used to flux-weight and homogenize the materials over the appropriate regions.

D) HOMOGENIZATION GEOMETRY. One of the more difficult problems, both in the design of a reactor core and in the analysis of experimental results, is the precise definition of the geometry over which the explicit fuel element components are homogenized into a uniformly distributed mixture. Homogenization is necessary because of the limited capacity of the computer codes available and the basic limitation of diffusion theory itself in representing the detailed flux distributions (see Chap. 4). To show the sensitivity of the calculated results to this definition, three methods were used for homogenizing the components of the module boxes (see Fig. 6.6). In the first method, all components of the module boxes are homogenized up to the outer surface of the walls. Thus,

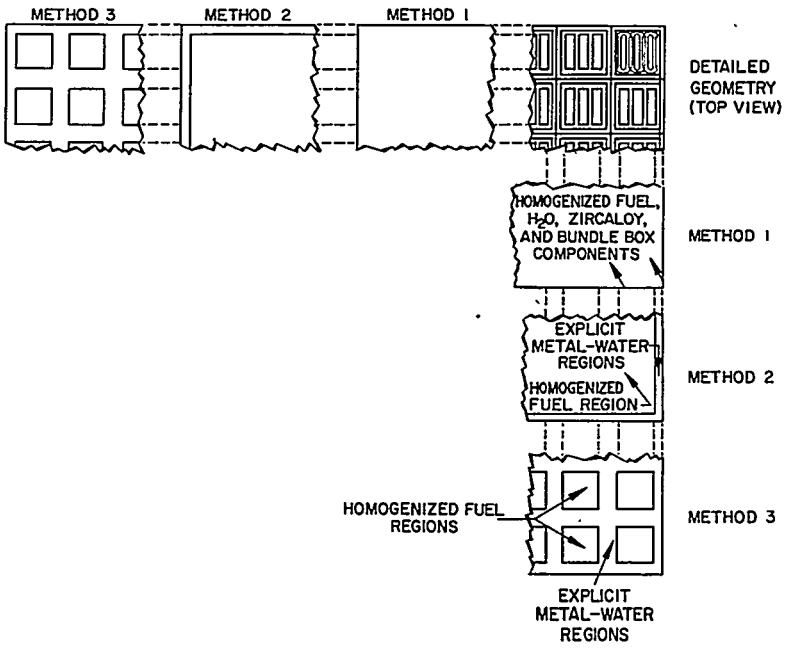

FIGURE 6.6. Description of Various Homogenization Methods in Small Bundle Box Slabs.

the region interface in the calculation is one between a homogenized fuel region and a water reflector region. This common method of homogenization is particularly desirable because it requires a minimum number of different regions in the diffusion calculation and, in general, a minimum number of spatial mesh points.

One of the difficulties experienced with Method 1 homogenization lies in the comparison of experimental activation measurements with calculation. This difficulty is caused by the transient in the activation distribution which occurs near the interface between dissimilar regions, such as the fuel region-water reflector interface in the slab criticals. Since an activation wire detector located at such an interface is actually within a small metal-to-water region, it is normally exposed to a higher flux level than exists in the fuel region. Calculationally, however, the homogenization process has moved fuel into this small metal-water region, which results in too large an absorption in this region and, thus, a depression of the calculated flux level. Method 1 can also result in a motion of fuel into a region of different reactivity worth and, thus, affect the criticality calculation.

To overcome these objections, a second method of defining the homogenization technique was evolved in which the fuel in the bundle boxes near large water regions is homogenized only to the point at which the fuel shims actually end within the bundle box. Thus, for Method 2, an explicit region of homogenized metal and water (which has a metal-to-water volume ratio of about 1.0 and is about 0.100 in. in extent) was included in the calculation between the homogenized fuel region and the large water channel.

Comparisons with detailed neutron activation distributions pointed out the necessity of utilizing a third method of homogenizing the fuel region in the analysis of these experiments: The fuel region was homogenized only within the rectangular location over which it extends within each module box (see Fig. 6.6). Thus, in Method 3, the small metal-to-water regions, made up of both the abutting module box walls and the remaining water, were explicitly represented as separate regions in the calculations. A comparison between the one- and two-dimensional geometries of Method 2 and Method 3 is shown in somewhat more detail in Fig. 6.7. It can be observed in this figure that the location of the experimental activation measurements is within these small metal-to-water regions. The effect of this gridwork of small metal-to-water regions upon the calculated activation distribution is to cause a slight additional flux peaking at the intersections of these regions. In essence, this raises the average flux level at locations which are away from the fuel region-water reflector interface over that calculated with the one-dimensional homogenization technique of Method 2.

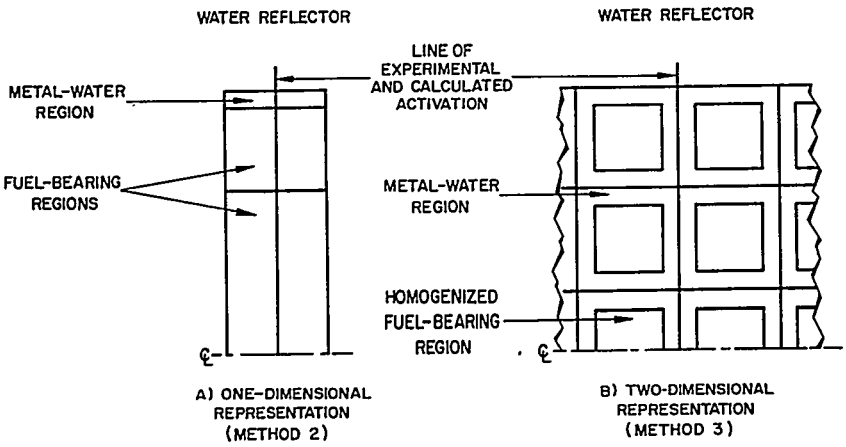

FIGURE 6.7. Comparison of Two Geometrical Representations Used in Homogenizing Core Materials.

The raising leads to lower local peak-to-average ratios at the fuel region-reflector interface in Method 3 than are calculated by Method 2.

E) BASIC DIFFUSION THEORY GEOMETRY. For the analyses discussed, two-dimensional diffusion theory calculations were performed to obtain all the tabulated results using the PDQ[9] code. These radial PDQ calculations were run in the horizontal plane of each slab. The technique used for the synthesis of the radial and axial dimensions was similar to the single channel synthesis described in Chap. 4, Sect. 4.4. In the synthesis technique as it was used here, the radial results are pieced together by means of a one-dimensional diffusion theory calculation run in the axial direction to yield the effective three-dimensional results. The one-dimensional axial calculations were run on the WANDA[10] code using diffusion theory constants which were obtained by flux-weighting over the fuel regions of the radial problems. The axial reflector regions were represented by constants obtained by homogenizing all of the materials in the reflector.

For the following results the buckling synthesis method used group-dependent bucklings in most of the axial fuel region. Group-independent bucklings were used in fueled zones, called transition regions, which were 1 in. in height and which were located near the top and bottom reflector regions of the axial problem. The same group-independent bucklings of these transition zones were also used in the adjacent top and bottom reflector regions.

The group-independent buckling used in the axial diffusion theory problem is obtained from the radial PDQ calculation in the following manner: First a radial calculation is made in which the axial dimension is represented by an initial estimate of the transverse leakage term, DB_z^2, appropriate to the axial height of the fuel and the top and bottom reflectors. After solution of the radial PDQ problem, a set of flux-weighted four-group constants is obtained by averaging over all of the explicit fuel regions of the PDQ problem. A radial buckling term is then obtained from the relation

$$B_r^2(\lambda_o) = B_t^2(\lambda_o) - B_z^2(\lambda_o)$$

where $B_t^2(\lambda_o)$ is the total buckling of the system and is obtained from the four-group criticality equation at the eigenvalue λ_o of the radial problem, and $B_z^2(\lambda_o)$ was the initial estimate used in the radial problem. This expression yields the group-independent leakage used in the axial reflector regions and the transition zones. The group-dependent bucklings used in

the major portion of the fueled region in the axial problem are obtained directly from the integrals of $D\nabla^2\phi$ for each group over the radial fueled regions of the core. These integrals are calculated directly in the radial PDQ problem. The constants and the radial leakage term are next used in the axial diffusion calculation, from which a second estimate is obtained of the transverse leakage B_z^2. The entire process of radial and axial calculations is repeated until this synthesis procedure yields the same eigenvalue from both the radial and axial results. While this may seem somewhat cumbersome, in practice this procedure is relatively easy to complete after some experience with it. No more than two radial and two axial calculations are usually required.

Before commencing the PDQ studies a series of transport calculations was made to determine the adequacy of solutions in the P_1 approximation and of the specific mesh chosen for the problem layout. A series of one-dimensional problems was run for each of the basic problems represented by different directions in the proposed PDQ calculation. This series of one-group one-dimensional calculations, which was run with the FLIP[8] routine, compared solutions in P_1, P_3, and double-P_3 transport approximations for a mesh spacing matching the PDQ problem. The results were also compared with a double-P_3 problem having a very fine mesh for effect due to mesh and for any differences between the P_1, P_3 and double-P_3 effects in either direction. It was found that the mesh effect was negligible and that P_3 was a reasonable approximation of the transport effects in one-dimension. A two-dimensional one-group comparison was next made to compare the results of the PDQ calculation with those obtained in a P_3 approximation using TRIP-1.[11] This comparison was performed, using Method 3 for the homogenization technique. It showed that along nonfueled traverses, such as the locations where the neutron activation distributions were measured, the P_1 solution of PDQ was equivalent to the P_3 solution; but along traverses which cross fuel-bearing regions there was a difference of 6 percent in peak to asymptotic activation ratio at the fuel-nonfuel interfaces. Thus, the P_1 approximation using Method 3 for the homogenization technique should be adequate for the comparison between the calculated and measured activation distributions for the sets of experiments discussed here, since the activation detectors were located between the abutting module box walls.

Subsequent to the analysis of the results with methods described above, the multigroup Monte Carlo technique using the MARC[12] routine became available for theoretical comparisons in the thermal neutron group. This technique has

been applied to the module box geometry used in the discussed sets of experiments. MARC calculations, using the Radkowsky prescription[6] for the representation of the thermal neutron scattering kernel (see also Chap. 3, Sect. 3.2), have been performed for a module box cell (similar to a cell of Core 32) in which the detailed geometry of the module box walls, fuel shims, Zircaloy bars, clips, and water channels was explicitly represented. The MARC calculations were then compared with one-group PDQ cell calculations which used the mixed number density model for the single group in the homogenization geometry of Method 3. A comparison of the thermal utilization of the cell showed that the PDQ agreed with the MARC result to within about 0.1 percent. This indicates that for systems of high thermal utilization, such as the set of clean slabs reported below, the use of the flux-weighted homogenized constants in the geometry of Method 3 should be a reasonable approximation to the more exact treatment of the thermal neutron problem.

F) REPRESENTATION OF LUMPED BORON REGIONS. For the analyses of the slab experiments which contained septa of lumped boron, an explicit geometric representation for the boron region was used in the diffusion calculations. This region included both the boron-impregnated Mylar tape and the aluminum cover plates.

Two methods were used for the boron representation in the thermal neutron group. In one method, the mixed number density scheme was coupled with a basic one-dimensional P_1 blackness theory model.[13] The blackness method is, in essence, a technique of modifying a low-order approximation, such as the basic diffusion model used in the analyses described here, in regions where a higher transport approximation is required (see Chap. 3, Sect. 3.6). The blackness coefficients, $\alpha(E)$ and $\beta(E)$, are defined as linear combinations of the fluxes and currents at the surfaces of the lumped boron absorber and are shown to be functions of the neutron transmission and reflection coefficients peculiar to the lumped absorber. It should be noted that they are energy-dependent functions. Thus, averages of the blackness coefficients must be obtained prior to their use in the four-group diffusion model used for the analyses reported here. The group-averaged values were obtained from the relation:

$$\langle \alpha \rangle = \frac{\int \frac{\alpha(E)\,\phi(E)\,dE}{1 + C\alpha(E)}}{\int \frac{\phi(E)\,dE}{1 + C\alpha(E)}} \qquad \text{Eq. (6.1)}$$

$$\langle\beta\rangle = \frac{\int \frac{\beta(E)\,\phi(E)\,dE}{1 + C\beta(E)}}{\int \frac{\phi(E)\,dE}{1 + C\beta(E)}} \qquad \text{Eq. (6.2)}$$

where the averages extend over the energy range associated with the particular group in question, in this case, the thermal neutron group. The flux energy spectrum, $\phi(E)$, was assumed to be that generated for the homogenized core fuel region and, thus, represented the hardened spectrum peculiar to an infinite medium of the fuel region constituents. The value of C in Eqs. (6.1) and (6.2) was taken as zero.

From the group-averaged blackness coefficients, $\langle\alpha\rangle$ and $\langle\beta\rangle$, fictitious diffusion theory coefficients, D and Σ_a, are defined for the lumped boron region such that in a diffusion calculation (flux continuity) the ratio of neutron current to flux at the lumped boron surface is consistent with the ratio required by the blackness coefficient. In coupling this blackness method to the mixed number density model, these fictitious constants are divided by the average reciprocal of the neutron velocity in the fuel region. The calculation of these fictitious diffusion theory coefficients as well as a discussion of the basic techniques of group averaging of the blackness coefficients is presented in Chap. 4, Sects. 4.2.D and 4.3.C. The results of applying this thermal group representation for the boron are listed under the heading "Blackness Theory Boron Constants" in later tables. It should be noted that this method does not take into account any local perturbations in the infinite medium flux spectrum which are due to the presence of the boron.

In the second method of representing the thermal neutron absorption in the lumped boron region, the boron region constants were fitted to one-dimensional multienergy group thermal calculations which were run in the double-P_1 approximation (SLOP-1).[14] Thus, the thermal absorption rate in the boron was adjusted from a pure blackness value in order to force the diffusion calculation to generate the same absorption rate as that predicted by the detailed multigroup transport approximation. This second method takes into account the effect of the boron on the spectrum at its surface as well as the effect of higher order transport effects. Results obtained by applying this method are listed under the heading "Spectrum-Fitted Boron Constants" in Table 6.7.

In the epithermal neutron group, the blackness method described above was used for the representation of the lumped boron region. In this case, the group averages were taken

over the neutron energy spectrum, $\varphi(E)$, generated for the homogenized core fuel region using the MUFT routine. For averaging over the epithermal group, a value of $C = \sqrt{3}$ was used in Eqs. (6.1) and (6.2) to take some account for suppression of the infinite medium flux at the surface of the boron absorber at energies where absorption is important.[13]

In the two highest energy fast groups, the boron regions were represented as being normal P_1 diffusion regions, using constants obtained directly from a MUFT calculation of the homogenized boron region constituents. Since these lumped absorber regions represent very small fractions of the core volume and since the major portion of the absorption in the boron occurs at lower energies, the specific choice of constants in these two highest energy groups is not particularly important in the experiments reported here.

G) REPRESENTATION OF LUMPED HAFNIUM REGIONS. In the experiments which contained lumped hafnium, each hafnium septum was represented as an explicit region in the diffusion calculation. In cases where two hafnium septa were separated by a water channel, the water was also represented as an explicit region.

In the epithermal neutron energy range, 0.625 ev to 5.53 kev, where resonance absorption in the hafnium isotopes is most important, the hafnium septum was treated by the P_1 blackness theory method. For these calculations, the epithermal range was divided into 402 lethargy groups. Within each of these lethargy groups the microscopic cross section was obtained by averaging the energy-dependent cross section in the group with a $1/E$ spectrum. For the hafnium, the energy-dependent cross sections were calculated with the aid of a computer routine which obtained at each energy the sum of the contributions resulting from the application of the Breit-Wigner single level formula to each of 59 known resonances in hafnium and adding the $1/v$ contribution to these Breit-Wigner shapes resulting from the unresolved resonances. For the energy range in which resonance parameters were not known, the energy-dependent cross sections were obtained from a statistical model. Using the average cross sections in each of the 402 lethargy groups, the blackness coefficients, $\alpha(u)$ and $\beta(u)$, were next evaluated for each lethargy group. Finally, a single group-averaged value of the blackness coefficients for the epithermal energy range was evaluated by averaging the coefficients in each of the 402 lethargy groups over a $1/E$ flux spectrum, according to Eqs. (6.1) and (6.2), using a value of $C = \sqrt{3}$ for the surface suppression factor.

Two types of representations were used for the lumped hafnium regions in the thermal neutron group. In the first method, the blackness theory treatment was used. In this blackness theory method, the group-averaged values of $\langle\alpha\rangle$ and $\langle\beta\rangle$ were obtained by averaging over either a hardened spectrum peculiar to the fuel region of the core or a Maxwellian spectrum. The purpose of investigating the use of a Maxwellian spectrum for averaging the thermal group constants was to attempt to take account of the softening effect of the internal water region on the flux at the inner surfaces of the box-type septa. In the second method of treating the hafnium in the thermal group, spectrum-fitted hafnium region constants were obtained by fitting the explicit hafnium regions to multigroup thermal transport calculations, again using the double-P_1 approximation on the SLOP code as was found to be required for the lumped boron set of experiments.

The following effective diffusion theory constants were used for the representation of hafnium in the two highest energy groups of the four-group diffusion calculations:

Energy Range	Diffusion Coefficient	Absorption Coefficient
Group 1	0.926 cm	0.003 cm^{-1}
Group 2	0.833 cm	0.0395 cm^{-1}

H) REPRESENTATION OF DISTRIBUTED EPITHERMAL ABSORBERS. The final set of experiments discussed in this section contained distributed neutron absorbers which had strong neutron absorption characteristics in the epithermal energy range (0.625 ev to 5.53 kev). The purpose of this set was to emphasize that portion of the total calculational model in which the neutron absorption in the epithermal group competes heavily with the slowing down of the neutrons into the thermal group. In this set of experiments, two types of absorbers have been used, namely, hafnium and iridium. As noted previously, hafnium has a very complex structure for its resonance absorption cross section in this energy range with some 59 known and resolved resonances. It has a thermal absorption cross section[15] of 105 barns at 2200 m/sec and a resonance integral[16] of 1900 barns. Iridium, on the other hand, has a relatively simple resonance absorption cross section, with nearly all of its resonance absorption coming from three large resonances. The thermal absorption cross section[15] of iridium is listed as 430 barns at 2200 m/sec with a resonance integral[17] of about 2000 barns.

In the analysis of the experiments containing the distributed epithermal absorbers, these materials were represented directly in the thermal and fast group calculations of the fuel region constants. Hafnium was represented as a natural element using the cross-section library which can be identified through Table 6.3. In the case of iridium, an isotopic representation was used for the two naturally occurring isotopes, Ir^{191} and Ir^{193}. In the calculation of the thermal group constants, the distributed absorbers were represented explicitly in transport calculations of the plate disadvantage factors in the manner discussed above. Since these absorbers have significant absorption in the epithermal group, a correction was made for the resonance self-shielding effects in the epithermal groups in homogenizing the fuel element constituents.

4. *Comparison of Calculated and Experimental Results for Reactivity*

A) SET 1, CLEAN, UNPOISONED SLAB CORES. The first set of experiments against which the previously described model has been tested is designated as the clean slab series. The results for calculated reactivity, applying the analytical model described above to this set of experiments, are presented in Table 6.4. This set of experiments is free of such items as large internal water channels, poison materials, or rod septum materials. The fuel density varied from 52.5 g of U^{235}/liter to 232 g of U^{235}/liter of core volume and the metal-to-water volume ratio varied from 0.95 to 2.70 over the range of slabs considered (see Table 6.4). Further experimental details, such as the type of fuel element construction and the critical size of each slab, are listed in Table 6.5.

To indicate the effect of different methods for treating the thermal neutron group, results of applying both the hardened flux continuity model and the mixed number density model in the analysis of these experiments are listed in Table 6.4 for the complete set. In addition, all three homogenization techniques have been used with the mixed number density model, and the results are listed to show the difference between these techniques. The results show that the difference between homogenization Method 1 and Method 2 was about 0.8 percent in the eigenvalue calculated for each slab in the series with the exception of the high fuel density slab (Core 75) and the high zirconium slab (Core 83). The large sensitivity of the reactivity due to the homogenization technique in the case of the high fuel density slab (1.7 percent) is probably

TABLE 6.4 — CLEAN SLAB SERIES*

Description of Cores				Calculated Eigenvalues k_{calc}			
				Wigner-Wilkins Flux Continuity Model	Mixed Number Density Model		
Core Number	Fuel Density (g U^{235}/liter)	Metal/Water Ratio	Critical Core Size (Number of module boxes, width x length)	Homogenization Method 1	Homogenization Method 1	Homogenization Method 2	Homogenization Method 3
1	58.1	1.17	7 x 20	1.001	1.007	1.000	1.003
11	77.5	1.75	7 x 23	0.998	1.003	0.995	1.001
15	96.8	1.32	6 x 19	0.994	0.998	0.990	0.998
24	52.5	0.95	6 x 26	1.000	1.006	0.998	1.005
26	106	1.13	5 x 22	0.996	0.999	0.991	1.005
30	116	1.40	6 x 19	1.000	1.003	0.995	1.001
32	155	1.38	5 x 27	0.998	0.998	0.990	0.991
75	232	1.41	5 x 23	1.014	1.013	0.996	1.004
83	58.1	2.70	11 x 19	0.991	0.995	0.992	-
			Average †	0.999	1.002	0.995	1.001
			Spread ‡	0.023	0.018	0.010	0.014

*Four-group calculations with hardened flux model and mixed number density model, eigenvalues normalized to $k_{exp} = 1.000$.
†Average of calculated eigenvalues.
‡Spread between maximum and minimum eigenvalue in series.

TABLE 6.5 — SOME EXPERIMENTAL DETAILS OF CLEAN SLAB SERIES

Core Number	Fuel Element Designation (No. of Zircaloy strips x No. of fuel shims)	Type of Zircaloy Strip (mils)	Fuel Density (g U^{235}/liter)	Metal/Water Ratio	Critical Size (Number of bundle boxes, width x length)	k_{eff} † All Rods Out	Temperature (°F)
1	3 x 3	110	58.1	1.17	7 x 20	1.005	--
11	4 x 4	110	77.5	1.75	7 x 23	0.9996	72
15	3 x 5	110	96.8	1.32	6 x 19	0.9999	74
24	3 x 3	110	52.5	0.95	6 x 26	1.003	77
26	3 x 6	110	106	1.13	5 x 22	1.003	78
30	3 x 6	110	116	1.40	6 x 19	1.005	71
32	4 x 8	70	155	1.38	5 x 27	1.003	75
75	3 x 12	70	232	1.41	5 x 23	1.002	111
83	*	70 110	58.1	2.70	11 x 19	1.005	67

*Seven 0.070-in. Zircaloy bars and one 0.110-in. bar were used for this experiment and coupled into three elements with three fuel shims.
†The uncertainty in the measurement of k_{eff} is about ± 0.002.

due to two facts. First, the fuel shims were aligned parallel to the narrow dimension of the slab, leading to a larger metal-to-water zone than the normal 0.100-in. zone. In the other slabs the fuel shims were oriented perpendicular to the narrow dimension of the slab. A second contributing factor to this large effect was probably the increased importance of this zone due to the large thermal flux peaking which occured at the reflector. Because of the high fuel density and narrow size, Core 75 had the most severe gradient in the thermal flux at the reflector. On the other hand, in Core 83, the small homogenization effect (0.3 percent) between Methods 1 and 2 was probably due to a combination of the large slab size, which should have reduced the importance of the zone near the outer reflector, coupled with the lower fuel density which yielded a smaller gradient at the interface.

In addition to the comparisons listed in Table 6.4, where the sensitivity of the calculated results to thermal group model and to the homogenization technique is displayed, the results of two approximations in the fast group representation are listed in Table 6.6 for one of the experiments in the series. The results listed compare the two versions of the cross-section libraries available in the MUFT routine previously identified in Tables 6.2 and 6.3.

The particular experiment for which results for the two fast group libraries are reported in Table 6.6 is the slab

TABLE 6.6 — COMPARISON OF FAST GROUP LIBRARIES FOR HIGH ZIRCONIUM SLAB (CORE 83)*

Analysis Model (Homogenization Method 1)	k_{calc}
Hardened Flux Continuity Thermal Model	
Later MUFT library tape (Table 6.2)	0.991
Earlier MUFT library tape (Table 6.3)	0.959
Mixed Number Density Thermal Model	
Later MUFT library tape (Table 6.2)	0.995
Earlier MUFT library tape (Table 6.3)	0.961

*Eigenvalues normalized to $k_{exp} = 1.000$.

containing an appreciable amount of zirconium as well as a fairly low fuel density (Core 83). This experiment was intended to emphasize the difference between these fast group treatments in the test of the total analytical model. Because of the high metal-to-water ratio of the experiment and because of the differences in the MUFT cross-section libraries, most of the differences in the analysis results are due to treatment of the inelastic scattering in zirconium. The results in Table 6.6 show that, with either thermal group model, the later MUFT library version yields results about 3 percent higher than the earlier version. A much smaller increase (about 1.5 percent) occurred in the calculated results for the other slabs in the set which had substantially lower metal-to-water ratios.

B) SET 2, SLABS POISONED WITH LUMPED BORON. In the second set of experiments against which the total calculational model was tested, several slab criticals were constructed which contained a single one-dimensional septum of a self-shielded $1/v$ absorber, lumped boron. The boron septum controlled from 0 to 15 percent in reactivity, depending upon the optical thickness $2t\Sigma_a$ of the septum and the type of core in which the septum was installed. Details of this second set of experiments are listed in Tables 6.7 and 6.8.

Table 6.7 lists the results of applying the analysis model, in which the mixed number density scheme was used for the thermal group representation, to the analysis of this set of experiments. Results are presented for both methods of representing the boron region in the thermal neutron group.

It can be seen that all calculations lie within ±1 percent of the experimental results. However, there is some indication in the basic blackness theory results of an increasing discrepancy between theory and experiment as the boron optical thickness (or boron worth) is increased. The strongest indication of this trend is for Cores 11, 12, and 13, in which the calculated eigenvalues increase by 1 percent as the boron worth is increased. A similar indication of this occurs for Cores 5, 7, and 10. These results indicate that the neutron absorption rate in the thermal group blackness method is being underestimated by the calculation by an amount equivalent to about 7 percent of the boron worth (i.e., 1 percent out of 14 percent). These results prompted further theoretical investigations which ultimately led to the specification of the spectrum-fitted method. Comparisons with SLOP-1 problems which contained boron septa indicated that the thermal group blackness method coupled with the mixed number density model underestimated the neutron capture rate in the boron by about 10 percent. For this reason, the boron thermal constants were adjusted to yield results consistent with multigroup

TABLE 6.7 — BORON SLAB SERIES*

Core Number	Critical Core Size	Fuel Region Data		Approximate Boron Optical Thickness $2t\Sigma_a$ (2200 m/sec)	Approximate Boron Worth (Percent Δk)	k_{calc} (Mixed Number Density)	
		g U^{235}/liter	Metal/Water Ratio			Blackness Theory Boron Constants (Homogenization Method 2)	Spectrum-Fitted Boron Constants (Homogenization Method 3)
1	7 x 20	58.1	1.17	0	--	1.000	1.003
5	9 x 18	58.1	1.17	1.0	8	0.995	
7	9 x 25	58.1	1.17	1.4	12	0.999	
10	10 x 23	58.1	1.17	2.0	15	1.006	
11	7 x 23	77.5	1.75	0	--	0.995	1.001
12	10 x 20	77.5	1.75	1.0	11	1.001	1.005
13	10 x 25	77.5	1.75	2.0	14	1.005	1.003
32	5 x 27	155	1.38	0	--	0.990	0.992
43	7 x 18	155	1.38	1.0	12	0.994	
75	5 x 23	232	1.41	0	--	0.996	1.004
84	7 x 18	232	1.41	2.0	14	0.994	1.002

*Four-group two-dimensional calculations with mixed number density continuity, eigenvalues normalized to $k_{exp} = 1.000$.

TABLE 6.8 — FURTHER EXPERIMENTAL DETAILS OF BORON SLAB SERIES

Core Number	Fuel Region Parameters	Boron Plate Parameters*				Results	
		Total Thickness of Boron-Mylar Region (in.)	Total Thickness of Plate Region Including Al Sandwich Plates	Surface Density of B^{10} (mg $B^{10}/in.^2$)	Plate Location	Critical Size	k_{eff}† All Rods Out
5	Same as Core 1	0.005	0.071	11.0	Between 4th and 5th box rows	9 x 18	1.000
7	Same as Core 1	0.010	0.076	27.6	Between 4th and 5th box rows	9 x 25	1.003
10	Same as Core 1	0.015	0.081	55.2	Centered	10 x 23	1.004
12	Same as Core 11	0.010	0.076	27.6	Centered	10 x 20	1.004
13	Same as Core 11	0.015	0.081	55.2	Centered	10 x 25	1.004
43	Same as Core 32	0.010	0.076	27.6	Between 3rd and 4th box rows	7 x 18	1.001
84	Same as Core 75	0.010	0.076	56.8	Between 3rd and 4th box rows	7 x 18	1.002

*The boron plate extended over the entire fueled height of 36 in. and for the entire slab length. The plate location was roughly at the center of the narrow dimension but in all cases between bundle boxes. Thus, for a slab with an odd number in width (e.g., 9 boxes) the septum was 1/2 box off center.

†The uncertainty in the measurement of k_{eff} is about ±0.002.

double-P_1 calculations (using SLOP-1). These results are listed in the table under the heading "Spectrum-Fitted Boron Constants." No indication of a trend is apparent in the fitted results.

C) SET 3, SLABS POISONED WITH LUMPED HAFNIUM. The third set of experiments, which reports results obtained from slab criticals containing septa of a lumped epithermal absorber, hafnium, emphasized those portions of the total calculational model dealing with the treatment of the self-shielding of a complex resonance absorber as well as with the competition for neutrons between the lumped absorber and the fuel region. Experimental results from these lumped hafnium slabs are presented in Table 6.9, while the analytical results are listed in Table 6.10. Included in the results listed in Table 6.10 is that obtained for the core of identical fuel loading and metal-to-water ratio but which did not contain a hafnium septum. For all results listed in Table 6.10, the mixed number density model was used for the representation of the thermal neutron group. It is seen that the reactivity compensation for the insertion of the septum into this type of fuel material was accomplished by substantial increases in the width of the slabs. The worth of the septum, ranging from 19 to 27 percent Δk, was calculated by determining the increase in the calculated eigenvalue which would result if the septum were removed from the slab.

The results of two different homogenization schemes are also presented in Table 6.10, and it is observed that the changes due to homogenization are consistent with those seen in the set of clean slab experiments.

D) SET 4, SLABS POISONED WITH DISTRIBUTED EPITHERMAL ABSORBER. Table 6.11 compares the experimental and calculated results for the final set of experiments which contained the distributed epithermal absorbers, hafnium or iridium. Further details of the experiments are presented in Table 6.12. The calculated results for this set of experiments were obtained with the earlier version of the cross-section library in MUFT (Table 6.3). In addition, these results were obtained with the hardened Wigner-Wilkins thermal group representation, using Method 1 for the homogenization technique. The results show that as much as 20 percent Δk is held down by the hafnium or iridium absorbers. A large fraction of this reactivity is due to absorption in the epithermal neutron group.

TABLE 6.9 — SOME EXPERIMENTAL DETAILS OF LUMPED HAFNIUM SLAB SERIES

Core Number†	Hafnium Plate Region Parameters*				Critical Size	k_{eff}‡ All Rods Out	Approximate Temperature (°F)
	Thickness of One Plate (in.)	Thickness of Water Gap between Plates (in.)	Thickness of Other Plate (in.)	Location of Hafnium Region			
33	0.204	None	None	Between 4th and 5th box rows	9 x 18	1.002	75
38	0.059	1.990	0.204	Between 5th and 6th box rows	11 x 25	1.001	70
56	0.120	1.26	0.120	Between 5th and 6th box rows	11 x 21	1.004	82
57	0.120	0.510	0.120	Between 5th and 6th box rows	10 x 21	1.004	80
60	0.060	1.38	0.060	Between 5th and 6th box rows	10 x 25	1.003	80

*The hafnium metal used for these experiments contained 98 percent hafnium, with the remainder mainly zirconium.
†Fuel region parameters for these experiments are the same as for Core 32.
‡The uncertainty in the measurement of k_{eff} is about ± 0.002.

TABLE 6.10 — LUMPED HAFNIUM SLAB SERIES*

Core Number	Description of Core†			Calculated Eigenvalues‡			
				Blackness Theory Hafnium Constants			Spectrum-Fitted Hafnium Constants (Homogenization Method 3)
	Critical Core Size	Hafnium Septum Type	Approximate Septum Worth	1/E, Hardened (Homogenization Method 1)	1/E, Hardened (Homogenization Method 2)	1/E, Maxwellian (Homogenization Method 2)	
32	5 x 27	None—control	0	1.000	0.992	0.992	0.992
33	9 x 18	Single 0.204 hafnium	19%	1.004	0.997	0.996	0.991
38	11 x 25	0.204-2.0-0.060 box	24%	1.002	0.995	0.990	--
56	11 x 21	0.120-1.26-0.120 box	27%	1.002	0.995	0.991	--
57	10 x 21	0.120-0.51-0.120 box	27%	0.996	0.990	0.987	0.990
60	10 x 25	0.060-1.38-0.060 box	26%	1.004	0.993	0.984	0.985
			Average**	1.001	0.994	0.990	0.990
			Spread††	0.7%	0.8%	1.2%	0.7%

*Eigenvalues normalized to $k_{exp} = 1.000$.
†Fuel Region Description; 155 g U^{235}/liter, M/W = 1.38.
‡Blackness coefficients for the septum region were averaged either over a 1/E fast spectrum and a hardened fuel region thermal spectrum (Wigner-Wilkins) or over a 1/E fast spectrum and a Maxwellian, as noted.
**Average of calculated eigenvalues.
††Spread between largest and smallest eigenvalues.

TABLE 6.11 — DISTRIBUTED RESONANCE ABSORBER SERIES*

	Description of Cores						Results
Core Number	Type of Resonance Absorber	Number of Absorber Tapes per Bundle Box	Absorber Density (g/liter)	Fuel Density (g U^{235}/liter)	Metal-Water Ratio	Approximate Absorber Worth (%Δk)	Calculated Eigenvalues (k_{calc})
15	None (Iridium control)	0	0	96.8	1.32	0	0.983
16	Iridium	1	4.0	96.8	1.32	5.2	0.983
17	Iridium	2	8.0	96.8	1.32	10.4	0.984
21	Iridium	3	12.0	96.8	1.32	16.3	0.983
22	Iridium	4	16.0	96.8	1.32	21.3	0.987
45	None (Hafnium control)	0	0	155	1.38	0	1.000
46	Hafnium	1	7.25	155	1.38	5	0.987
47	Hafnium	2	14.6	155	1.38	10	0.990
51	Hafnium	3	21.9	155	1.38	15	0.993
52	Hafnium	4	29.0	155	1.38	20	0.995

*Four-group calculations with hardened Wigner-Wilkins thermal group constants, eigenvalues normalized to $k_{exp} = 1.000$.

TABLE 6.12 — SOME EXPERIMENTAL DETAILS OF THE DISTRIBUTED RESONANCE SERIES OF EXPERIMENTS

Number	Absorber Type	Fuel Parameters		Critical Size (No. of Boxes)	k_{eff}†	Approximate Temperature (°F)
		Fuel Element Designation	Type of Zircaloy Strip (mil)			
15	None	3 x 5	110	6 x 20	1.007	76
16	1 Ir tape/element containing 60.4 w/o	3 x 5	110	7 x 18	1.000	82
17	2 Ir tapes/element containing 60.4 w/o	3 x 5	110	7 x 28	1.001	78
21	3 Ir tapes/element containing 60.4 w/o	3 x 5	110	9 x 20	1.003	79
22	4 Ir tapes/element containing 60.4 w/o	3 x 5	110	10 x 23	1.001	81
45	None	4 x 8	70	6 x 17	1.000	71
46	1 HfO_2 tape at 6.9 g Hf per bundle box	4 x 8	70	6 x 25	1.000	73
47	2 HfO_2 tapes at 13.8 g Hf per bundle box	4 x 8	70	7 x 23	0.999	73
51	3 HfO_2 tapes at 20.7 g Hf per bundle box	4 x 8	70	8 x 23	0.999	71
52	4 HfO_2 tapes at 27.6 g Hf per bundle box	4 x 8	70	9 x 24	1.001	73

† The uncertainty in the measurement of k_{eff} is about ±0.002.

5. *Comparisons of Calculated and Experimental Activation Distributions*

In addition to the comparisons between the calculated and measured reactivity presented for each of the four sets of experiments, a second major test of the total calculational model is obtained through the comparison of neutron activation distributions. A few typical activation distributions obtained from the four sets of slab experiments will be discussed. It is important to note the normalization between experiment and analysis in the comparisons presented below. The normalization extends only over the fuel region of the calculation and of the experiment and requires that the integral of the activity over these regions be the same in each case. This type of normalization is used mainly because of applicability to nuclear design considerations, where the distribution of heat production is a prime consideration. Finally, it will be seen that extreme care must be taken to calculate exactly what is measured in the experiment, even to the extent of including an explicit geometrical representation of the experimental details, else a misleading conclusion may be drawn. This will be particularly apparent in interpreting the results of Figs. 6.8 and 6.9, where the differences between the hardened thermal group model and the mixed number density model are apparent but could easily have been masked by the effect of the homogenization method selected for the comparison with the experimental results.

A) CLEAN SLAB. Figure 6.9 shows a comparison between the measured U^{235} fission activation distribution and that calculated by either the hardened Wigner-Wilkins thermal model or the mixed number density model for a slab in the clean, unpoisoned set of slab experiments, Core 32. In this comparison, the homogenization scheme designated as Method 3 has been used. Figure 6.8 shows a comparison of different homogenization schemes for the same experiment. The values plotted are the local peak-to-core average activation. The calculated values plotted here are the calculated activations of a bare unshielded uranium fission detector of uniform density at each position in the slab. The experimental results are the activations of the uranium wire detectors. The accuracy associated with the experimental results is about ±6 percent.

Figure 6.8 indicates the strong sensitivity of the calculated activation distribution to the homogenization technique. Indeed, it would have indicated that the mixed number density model substantially overestimated the experimental distribution, if

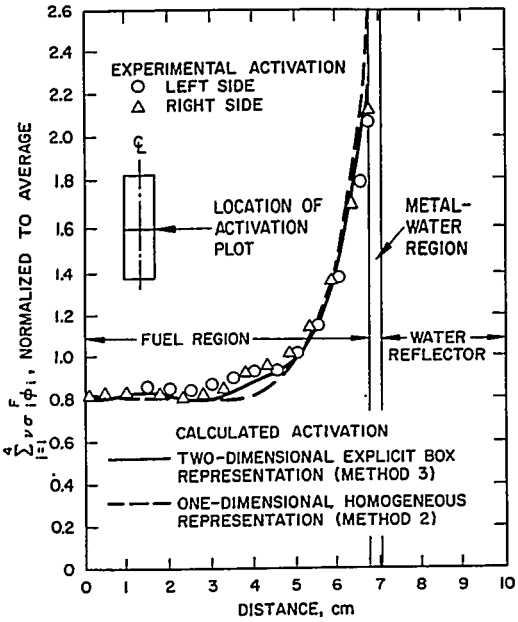

FIGURE 6.8. Total U^{235} Fission Activation Shapes through the Thin Dimension of a Clean Slab (Core 32), Using the Mixed Number Density Model in Thermal Group. (These results show the sensitivity of the calculated values to the core representation method.)

only the results of Method 2 were available. However, it was found by more detailed calculations that the experimental values should not be directly compared with the calculation performed with homogenization Method 2 in order to draw a valid conclusion in regard to the thermal spectrum treatment. The reason is that the experimental reflector peaks tend to become smoothed out or reduced in magnitude when considered on a peak-to-average basis because of the presence of smaller peaks which occur at each intersection of the metal-to-water regions formed by the abutting bundle boxes. It is noted in Fig. 6.8 that a small ripple occurs in the calculated result using Method 3 and apparently is also present in the experimental results with a period of 2 to 3 cm. This ripple is due to the peaking caused by the explicit representation of the intersecting metal-to-water regions as indicated in Fig. 6.7. When the ripple does not result from the calculation, as was the case for Method 2 on Fig. 6.8 where the metal-to-water regions were not represented explicitly, a higher peaking is calculated.

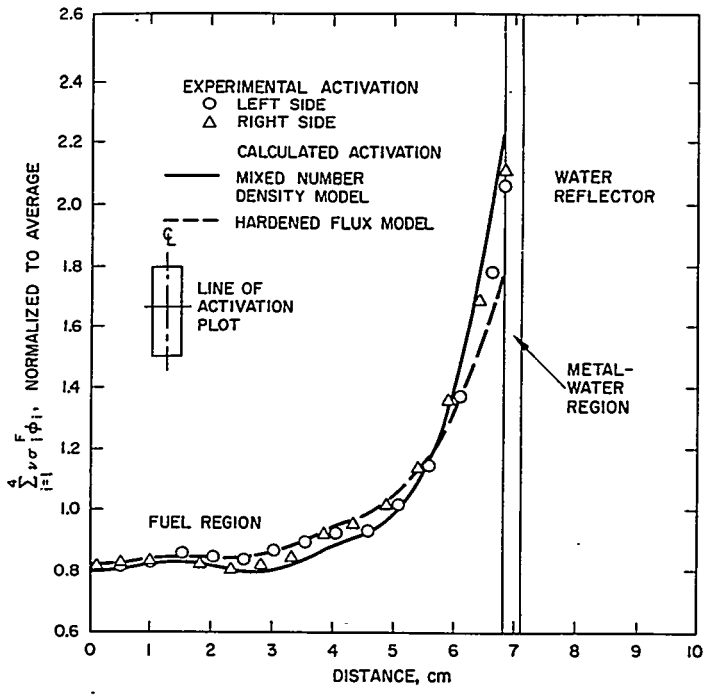

FIGURE 6.9. Total U^{235} Fission Activation Shapes through the Thin Dimension of a Clean Slab (Core 32), Comparing Two Types of Thermal Group Constants. (These results show the sensitivity of the calculated values to the thermal neutron treatment.)

To determine which thermal neutron spectral description (hardened or mixed number density) better represents the physical system, the more explicit bundle box homogenization technique of Method 3 must be used. This comparison shows that the mixed number density description leads to a slight overestimate of the reflector peaking by about 5 to 7 percent, whereas the hardened description underestimates the reflector peaking by 15 to 20 percent. This result is typical of comparisons of either water hole peaking or reflector peaking obtained throughout the sets of slab experiments and has led to the conclusion that the total model using the mixed number density description for the thermal neutron group yields a reasonably adequate description of water hole peaking. It should be pointed out that a Maxwellian thermal group description would have yielded a result almost identical to the mixed number density result for the activation peaking.

B) LUMPED BORON SLAB. Figure 6.10 shows a comparison between the measured and calculated uranium activation

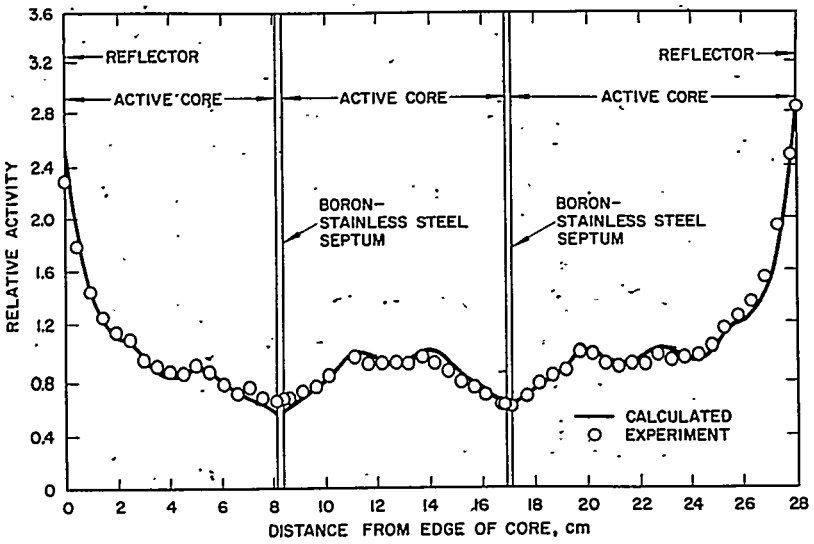

FIGURE 6.10. Slab Containing Self-Shielded Boron and Internal Water Gaps; Experimental and Calculated Activation Shapes for Traverse E Noted on Figure 6.11. (These comparisons are for bare U^{235} wires at 464°F.)

distribution for a slab containing two internal septa of lumped boron, slab Core 86. The geometry of this particular slab experiment is shown in Fig. 6.11. A plot through the dimension parallel to the boron in this slab is given in Fig. 6.12. These plots were taken at an elevated temperature (464° F). For these cases, Method 3 was used for the homogenization in combination with the mixed number density model and with boron thermal group absorption coefficients which were spectrum-fitted to the multigroup thermal calculations in the manner described above. Figure 6.10 shows that the calculated distribution near the water reflector region again is in substantial agreement with the experimental result. In addition, the calculation deviates only slightly from the experimental result near the boron absorber. In obtaining the experimental results with the small wire detectors contained within the flux plot wands, the wand was inserted through a small hole cut through the boron-stainless steel septum which was located at the 8-cm position shown in Fig. 6.10. This hole was required in order to insert the wand into the fuel region between the two boron septa. No such hole was cut in the other boron septum, since a second wand could be inserted from the right side of the slab and butted against the septum. This probably explains the slight

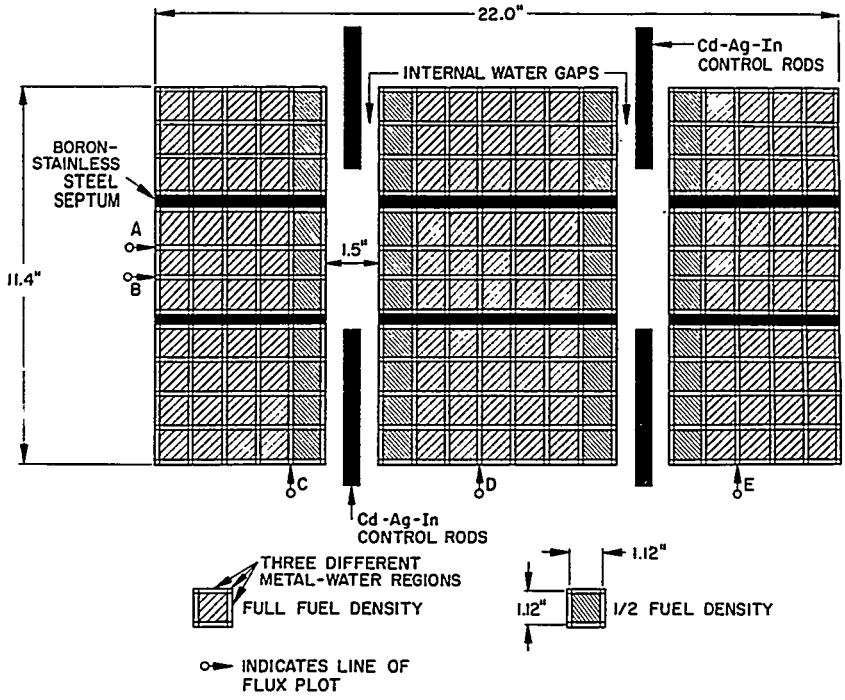

FIGURE 6.11. Geometric Layout for Calculations on Slab Containing Self-Shielded Boron and Internal Water Gaps.

difference in the experimental results shown in Fig. 6.10. Since no allowance was made in the calculation for the reduced boron content at the location of the left septum, the calculation yields a lower result. Finally, the large internal water channel peaks indicated in Fig. 6.12 seem to be well represented by the total analytical model.

C) DISTRIBUTED IRIDIUM SLAB. Figures 6.13 and 6.14 compare calculated flux distributions with measured activation distributions for a slab core which contained a distributed epithermal absorber, iridium. The comparisons shown are for Core 22 (Table 6.11), which contained about 16 g of iridium per liter distributed throughout the slab. The result in Table 6.11 gives the worth of the resonance absorber as about 21 percent Δk. About one-half of this worth is due to absorption in the three major resonances which occur in the epithermal group. Figure 6.13 compares the shape of the calculated epithermal group (Group 3) flux with the activation distribution measured with cadmium-covered neutron detectors. Since the 0.020-in. thick cadmium covers have an

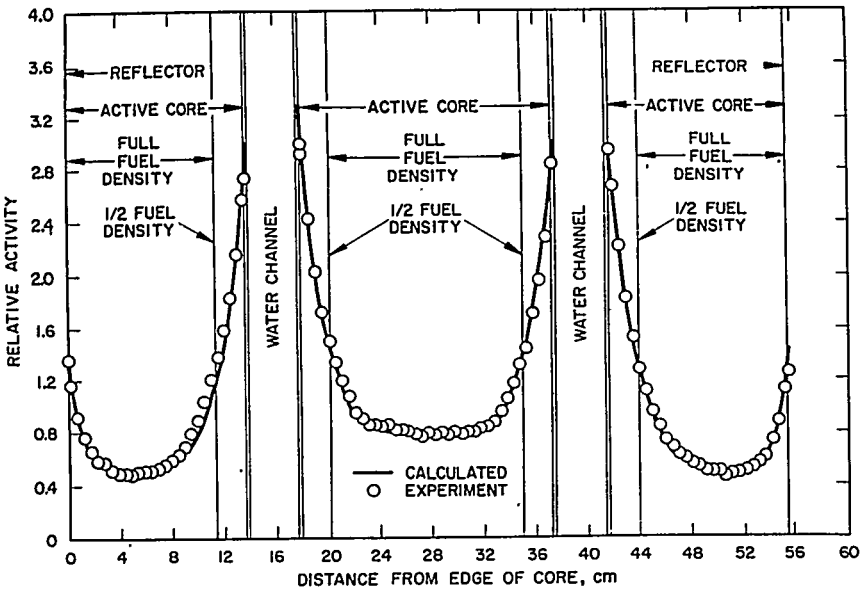

FIGURE 6.12. Slab Containing Self-Shielded Boron and Internal Water Gaps; Experimental and Calculated Activation Shapes for Traverse A Noted on Figure 6.11. (These comparisons are for bare U^{235} wires at 464°F.)

effective cutoff energy of about 5 ev, the activation of the cadmium-covered detectors should be due mainly to neutrons in the epithermal group (0.625 ev to 5.53 kev). In the comparison shown in Fig. 6.13, the calculated fast flux shape is somewhat flatter than the experimental result in the core fuel region. This is probably due to the use of the earlier MUFT library (Table 6.3) for this experiment, which neglected such effects as the zirconium resonance absorption. In addition, P_3 effects would probably yield steeper calculated gradients at the reflector interface in the epithermal group.

Figure 6.14 compares the calculated thermal group flux with the equivalent activation distribution which is obtained by subtracting the cadmium contribution from the activity of uncovered or bare detectors. The experimental error associated with this difference is about ±8 percent. The calculated thermal (Group 4) flux lies below the experimental points at the location of the peak in the fuel region at the core-reflector interface. The calculations for both Figs. 6.13 and 6.14 were made with the hardened thermal group constants and homogenization Method 1. The use of a softer

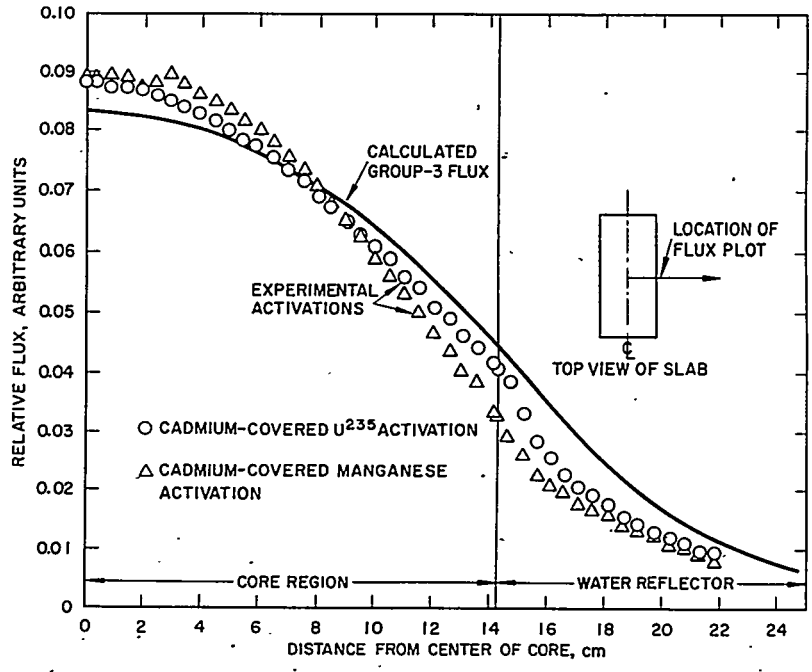

FIGURE 6.13. Comparison between Experiment and Theory for the Fast Group Flux for a Slab Containing a Large Amount of Distributed Iridium (Core 22).

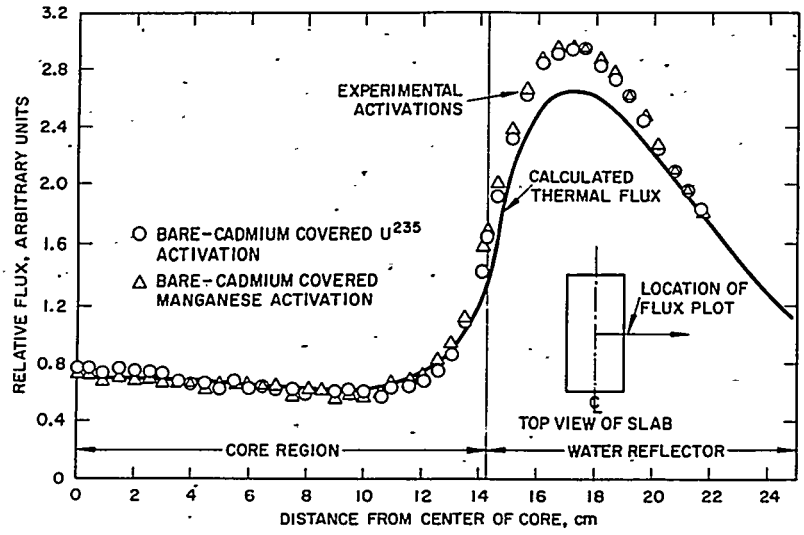

FIGURE 6.14. Comparison between Experiment and Theory for the Thermal Group Flux for a Slab Containing a Large Amount of Distributed Iridium (Core 22).

spectrum, such as a Maxwellian spectrum, or the use of the mixed number density model would tend to increase the calculated peak values.

6. Summary and Conclusions

Several conclusions may be drawn from the results presented for the first set of experiments on clean slabs. First, in regard to the thermal neutron representation, both the hardened flux continuity model and the mixed number density model have yielded consistent reactivity results over the wide range of fuel densities and metal-to-water ratios considered. In particular, the spread in the calculated results (maximum to minimum) for homogenization Method 2 coupled with the mixed number density model is reduced to about 1 percent in reactivity, with the eigenvalues centered about 1/2 percent below the experimental results. This consistency in the calculated reactivity was expected, since both the hardened thermal model and the mixed number density model yield approximately the same thermal utilization in an infinite medium. The major reactivity difference between these thermal neutron representations occurs because each yields a different flux peaking at the reflector interface and, thus, a small difference occurs because of the different reactivity worth of the fuel along this edge.

A second conclusion which can be drawn from the clean slab results listed in Table 6.4 is that the reactivity calculation is fairly sensitive to the homogenization technique used, particularly at the fuel-reflector interface. Coupled with the results on the power distributions which are also sensitive to this definition, as noted in Fig. 6.8, it is concluded that homogenization Method 3 yields the best overall approximation for the definition of the homogenization technique required for the analysis of experiments such as those reported here.

The power distribution results both from the first set of experiments as well as from the later experiments lead to the conclusion that the hardened thermal model substantially underestimates the neutron peaking near large water regions. It is concluded, however, that the mixed number density model yields a reasonable prediction of the neutron distributions in the fuel regions even in the presence of large water reflector regions or internal water channels.

The comparison of the results for the earlier and later versions of the MUFT library tape shows clearly the need to include effects such as inelastic scattering in zirconium and oxygen and to treat explicitly of resonance fissioning in U^{235}. These refinements seem to be required from a basic

theoretical viewpoint. Thus, it is reassuring that the inclusion of such refinements seems to lead to a more consistent set of results with the total analytical model, subject as it is to many compensating errors.

The conclusions which can be drawn from the comparisons between experiment and theory reported for the second set of experiments lie mainly in the demonstration that the large amounts of reactivity tied up in the lumped thermal absorbers can be reasonably well represented by the analysis model which represents the boron as an explicit geometric region. In addition, the results show that a fairly exact method of representing the thermal neutron spectrum and transport effects at the surface of the boron is necessary. This observation indicates how particular portions of the analysis model can be emphasized in a set of slab experiments, such as those reported here. The trend of the analysis results as a function of boron density, when looked at in a comparison with the first core (nonpoisoned) in the sequence, indicated a possible error in the boron capture rates predicted by the basic thermal group blackness model when coupled to the mixed number density model. A closer examination of this problem with the theoretically more exact multigroup spectrum transport approximation performed with the SLOP code revealed that the blackness method was underestimating the boron capture rates by about 10 percent. Thus, even though the absolute eigenvalues obtained from slab experiments may change as the gross analytical model changes, the ability to isolate individual effects, such as the boron representation, is retained by an examination of the consistency among the various results.

Several conclusions can also be drawn from the third set of experiments. First, from the results listed in Table 6.10, the total analytical method, which used the mixed number density scheme for the representation of the fuel regions, yields reasonably consistent eigenvalues over the range of lumped hafnium septum experiments considered. It is further noted that either a hardened (Wigner-Wilkins) spectrum or a Maxwellian spectrum for averaging the thermal group rod blackness coefficients yields about the same order of results, with the possible exception of Core 60. In Core 60, the two very thin hafnium blades (0.060 in.) are quite sensitive to the spectrum used in the thermal group averaging process. Finally, it is concluded that corrections to the thermal neutron spectrum at the surface of the hafnium septa do not seem to be necessary for these lumped hafnium experiments, whereas this correction apparently was necessary for the lumped boron experiments. This is probably due to the fact that the

hafnium is more important as an epithermal neutron absorber than the boron and, thus, a correction in the thermal group is less important.

The major significance in the results of the final set of experiments containing distributed epithermal absorbers lies in the difference between the result calculated for the control core and that calculated for the absorber. A difference in the eigenvalue calculated for an absorber slab, as compared to the calculated value for the control slab, can be attributed to a misrepresentation of the epithermal absorber. Thus, the conclusion drawn from the results listed in Table 6.11 is that a reasonably good representation has been obtained for the epithermal absorption of either hafnium or iridium, even though as much as 20 percent in reactivity is held down by the resonance absorber.

Recent results indicate that a Δk increase in the calculated reactivity of about a 1/2 to 1 percent would be obtained by a P_3 calculation of the first set of experiments. The consistency from slab to slab should not be significantly affected by the inclusion of the P_3 approximation. The absolute eigenvalue around which this set of analyses is centered, however, will probably change as newer analytical models are employed. The tabulated results do indicate, on the other hand, that no large errors, sensitive to fuel loading or metal-to-water ratio, are being made by the approximations of the analytical model which lead to the calculated results.

B. Clean Slab Experiments with Repeating Plane Geometry

D. R. Connors

1. Introduction

The preceding section discussed an analysis of four sets of experiments in which the fuel element construction was in the form of small fuel shims inserted into small Zircaloy module boxes. Difficulty was encountered in the interpretation of the results because of this type of fuel element construction. While the specific homogenization technique developed for the analysis of these sets appears to have been successful, both when compared with fairly rigorous theoretical standards (such as the multigroup Monte Carlo technique MARC) and with experimental results, the possibility remains that the results may be subject to experimental error due to this highly flexible manner of construction. It is, therefore, appropriate to present an analysis of several slab experiments in which a much simpler fuel element construction was utilized.

These results will extend the range over which the total analytical model has been tested as well as add to confidence that the interpretation of the small module box experiments has been correct.

Several experiments have been performed with a slab assembly, using a fuel element construction which had the form of a semi-infinite plane of a uranium-Zircaloy metal alloy. Repeating planes of these semi-infinite fuel plates were held parallel to one another in a slab array, and the assembly was flooded with water and brought to criticality. With this simple geometry, several experiments have been performed at low metal-to-water volume ratios. First, a simple, clean, unpoisoned slab assembly was constructed and operated. Following this, regions of reduced hydrogen density were incorporated into this slab to simulate the presence of void regions. Finally, a septum of lumped hafnium poison was introduced into the slab both in the presence of, and apart from, the simulated voided regions.

2. *Description of Experiments*

Figure 6.15 shows a perspective view of the type of critical assembly construction which was used for this series of experiments. Each critical assembly was constructed in the shape of a slab core. The fuel plates were oriented with their long dimension parallel to the base plate. The individual fuel plates, 2.6 in. high and 48. in. long, were stacked above each other and butted together along the 48-in. dimension to form vertical planes of uranium-zirconium fuel material with a thickness of about 0.140 in. Each fuel plate was effectively composed of a 4 weight percent U^{235}-Zircaloy alloy, spaced to provide vertical water channel planes of 0.350-in. thickness between the fuel planes, and yielding a metal-to-water volume ratio of about 0.4. Grooved aluminum end-spacing plates with vertical slots were used to position the fuel plates at each end of their long dimension. Small plastic spacer wands were employed at about 10-in. intervals to maintain a parallel orientation between layers of fuel planes (by preventing the bowing of fuel plates). The entire core structure was enclosed in a gridwork of steel horizontal tie bars and vertical support bars, as shown in Fig. 6.15. Plastic buttress plates provided support between the outer planes of fuel elements and the steel gridwork. The steel gridwork was attached to the base plate at the bottom of the core and to the top frame above the core. The base plate and top frame were secured to the reactor tank.

Control for the series of experiments was furnished by four silver-cadmium-indium blade-type control rods which

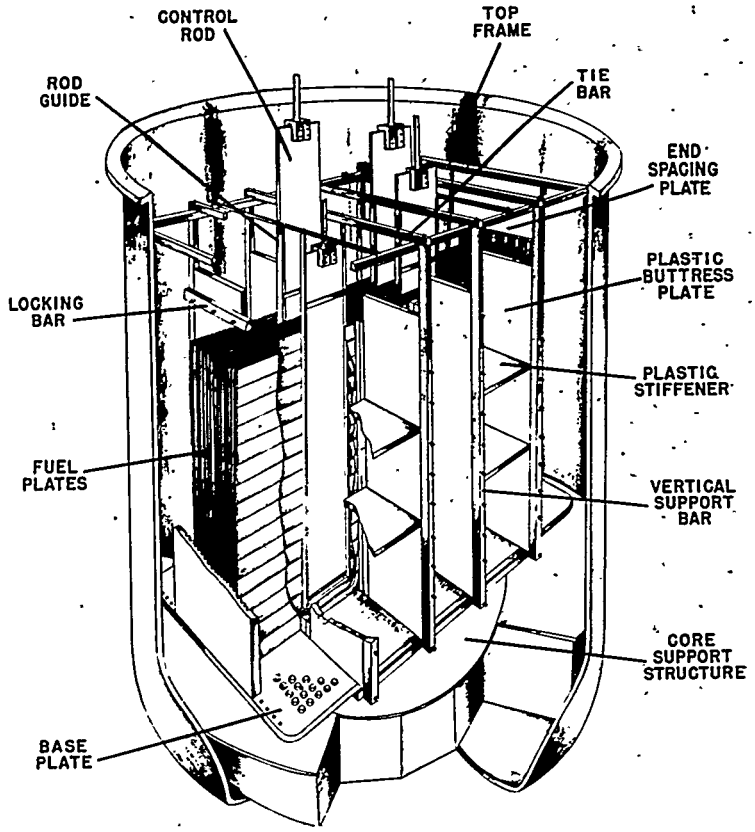

FIGURE 6.15. Perspective View of the Construction of Repeating Plane Slab Experiments Which Were Run at Low Metal-to-Water Ratios.

had a blade thickness of about 0.173 in. and a span of about 5 in. The rods traveled vertically within the 0.350-in. water channels formed by the separation of the fuel planes, so that when the rods were fully withdrawn from the core a nearly uniform array of fuel planes and water-channel planes was present in the slab.

In each experiment in this series, two basic types of experimental data were obtained. The first type was the effective multiplication factor for an assembly having the control rods removed from the core (clean critical). The second type was the thermal and epithermal neutron activation distributions. These fission activation distributions were obtained from the irradiation of uranium-Zircaloy wires, 0.030 in. in diameter and 0.5 in. high, which were positioned within the 0.350-in. water channels between the fuel plate planes. Both bare and cadmium-covered activations were obtained.

Further details of the construction of each of the experiments in the series can be obtained through an examination of Figs. 6.16 through 6.20. These figures show that the first experiment in the series was a clean slab which consisted simply of a repeating array of the planes of fuel plates and water channels. The particular dimensions of 0.140 in. for the U^{235}-Zircaloy fuel plates and 0.350 in. for the water channels were retained constant throughout the series of experiments. The metal-to-water volume ratio resulting from these dimensions is about 0.4. For the second and third experiments in this series, the hydrogen content in certain water channels in the central region was reduced by the introduction of Styrofoam (expanded polystyrene) strips in the manner shown in Figs. 6.17 and 6.18. The Styrofoam sheets were approximately 0.250 in. thick and extended over the full core height in the manner illustrated. Since the density of the Styrofoam plane was 0.195 g/cm^3, the overall hydrogen concentration in the low hydrogen density channels was reduced to 39 percent of its normal value at ambient temperature. In the final two experiments in the series, a lumped hafnium septum 0.240 in. thick was introduced into the low metal-water system in the presence and absence of the voided regions of reduced hydrogen density.

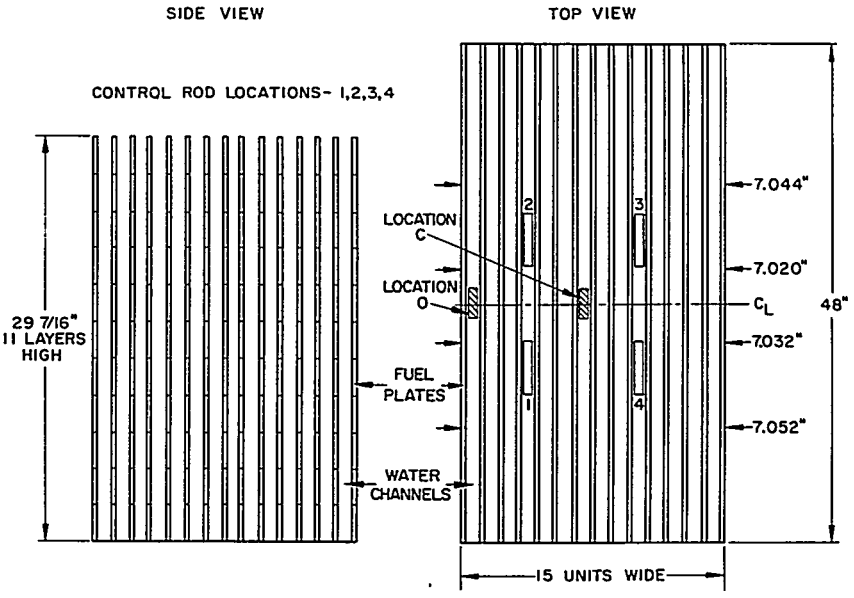

FIGURE 6.16. Arrangement and Dimensions for Core 1 of the Repeating Plane Series, a Clean Slab.

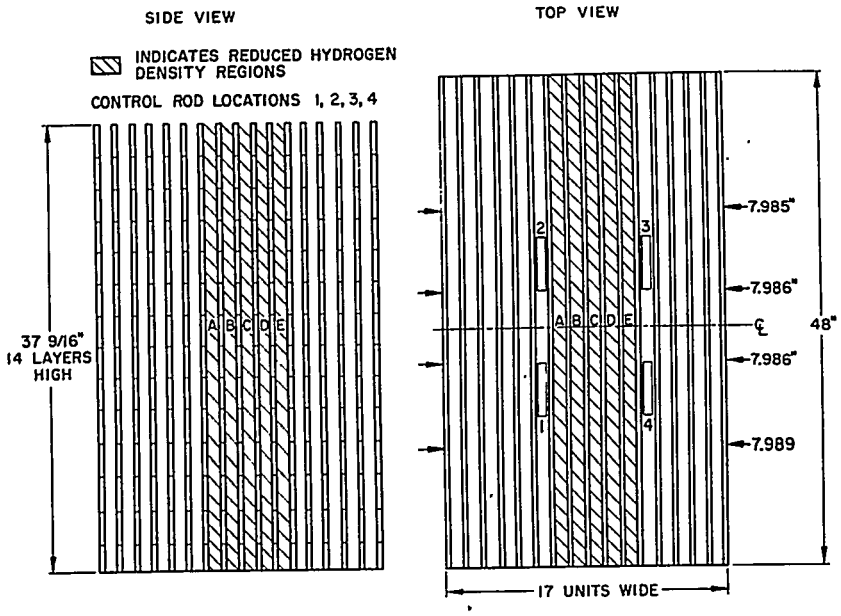

FIGURE 6.17. Arrangement and Dimensions for Core 2 of the Repeating Plane Series. (This core contained a central region of reduced hydrogen density formed by inserting foamed polystyrene into the indicated channels.)

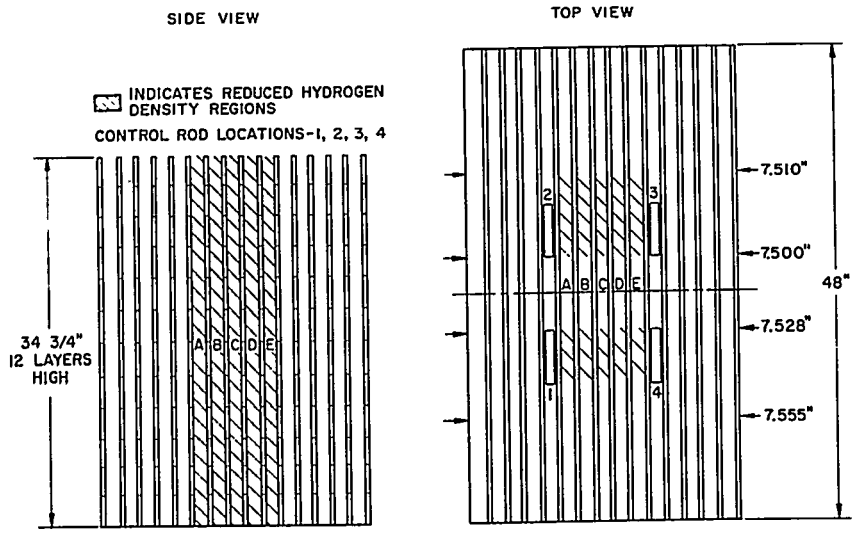

FIGURE 6.18. Arrangement and Dimensions for Core 3 Containing Isolated Regions of Reduced Hydrogen Density.

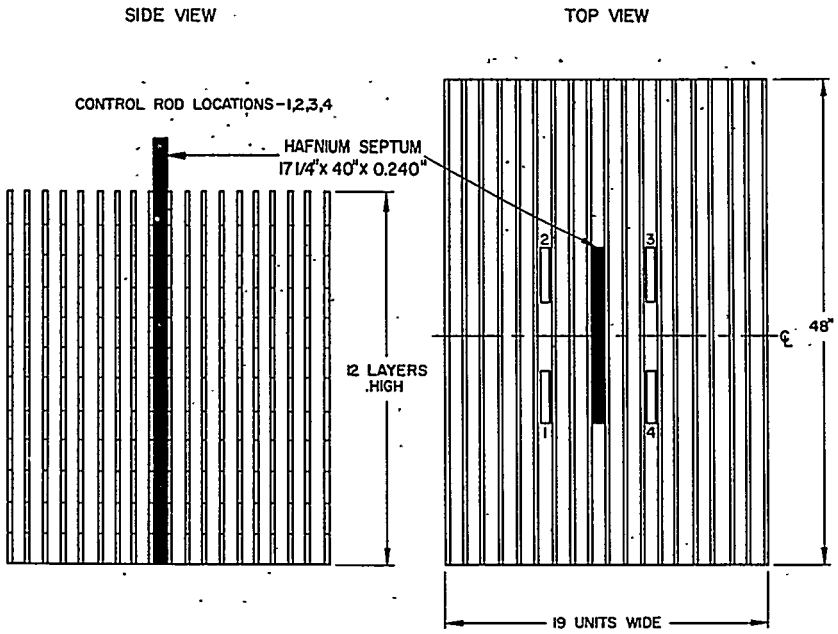

FIGURE 6.19. Core 4 Arrangement and Dimensions for the Lumped Hafnium Septum Experiment in the Repeating Plane Series of Slab Experiments.

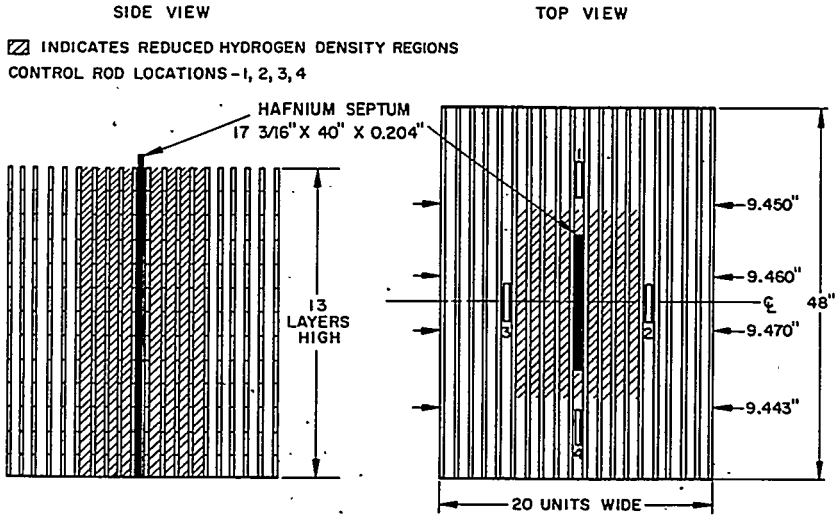

FIGURE 6.20. Arrangement and Dimensions for Core 5 in Which the Hafnium Septum Was Surrounded by a Region of Reduced Hydrogen Density.

3. *Analytical Model*

In the analysis of this series of experiments, the same analytical model as that described in Sect. 6.2.A.3 was used with a few minor exceptions. Again, a four-group two-dimensional analysis was performed, using the PDQ code for the basic diffusion theory calculations in the horizontal plane. The group structure was identical to that previously described. Fast group constants, however, were obtained from MUFT calculations which used the earlier MUFT library tape (Table 6.3). Thus, such fast group effects as inelastic scattering in zirconium and oxygen were not explicitly represented in the calculation. The use of the more recent library tape (Table 6.2) in the analysis of this set of experiments would probably yield results not much different from those reported here. This speculation is based on the low metal-to-water ratio in the experiments, with the resulting reduced importance of zirconium and fuel in the fast groups.

The thermal group representation used in this analysis was the hardened (Wigner-Wilkins) spectrum-averaged constants coupled with the boundary condition of continuity of neutron flux across region interfaces. For Cores 1 and 2, calculations were also made, using thermal group constants averaged over a Maxwellian spectrum. The use of the Maxwellian constants resulted in eigenvalues which were only 0.4 percent and 0.2 percent higher than the hardened results for Cores 1 and 2, respectively. This is indicative of the relatively soft spectrum of the series of experiments due to the combination of low metal-to-water ratio and the fairly light fuel density. It also indicates that the mixed number density thermal model would yield nearly identical results as either the Maxwellian or the hardened constants for these experiments.

Thermal group plate disadvantage factors or heterogeneity correction factors were again generated by the double-P_3 approximation, as described in the general analytical model. Because of the simple experimental arrangement of repeating parallel planes of fuel plates and water channels, the homogenization technique was somewhat different from that used for the analysis of the small module box slab experiments. For these analyses, the fuel region at the outer reflector boundaries was homogenized to a point beyond the edge of the last fuel plate by a distance of one-half of a water channel (1/2 x 0.350 in.). Thus, the homogenized fuel region extends over the range formed by cells of fuel plates and water channels. For Core 1, a comparison was made of the sensitivity of this method of homogenization by comparing calculations in which the fuel was homogenized only to the outer edge of

the last fuel plate, and the additional distance of one-half water channel was not included. For this core, it was found that the calculated eigenvalue would be reduced by about 1.1 percent if the fuel were smeared only to the outer edge of the last fuel plate. Thus, just as in the analyses of the small module box experiments described in Sect. 6.2.A, a large sensitivity of the calculated result to the method of homogenizing the fuel at interfaces near large water regions is noted in this series of analyses.

4. Comparison of Calculated and Experimental Results for the Low Metal-to-Water Series of Experiments

Table 6.13 lists the reactivity results obtained in the analysis of this series of experiments with the simple repeating planes of fuel plates and water channels. In Figs. 6.21 and 6.22, a comparison is given between the measured neutron activation distribution and the calculated fluxes for Core 2 obtained with the hardened thermal model described above. In these figures, the experimental points were obtained from the activation of the bare and cadmium-covered uranium-Zircaloy. Figure 6.21 compares the calculated thermal flux (Group 4 of the four-group calculation) with the equivalent thermal group activation which was obtained by subtracting the epicadmium activity from the bare activity. In Fig. 6.22, the epicadmium activity is compared with the calculated Group 3 flux.

The results presented in Table 6.13 show that the reactivity of the slab cores in this low metal-to-water volume ratio range of 0.4 can be calculated satisfactorily with the four-group diffusion theory model. It is noted in the results that the method of treating the low hydrogen density region, which was represented as a region of reduced hydrogen density, adequately predicted the reactivity effect of the simulated void. In addition, the blackness theory treatment used for the representation of the hafnium region in the lumped hafnium septum experiments (Cores 4 and 5) yielded a satisfactory prediction of the criticality of these cores even when the hafnium was in the presence of the low hydrogen density region.

The power distribution results presented in Figs. 6.21 and 6.22 show that the model predicts the shape of both the thermal and the epithermal distributions reasonably well. It should be noted that either a Maxwellian model or a mixed number density treatment of the thermal neutron group would yield peaking factors at the reflector interface which are slightly higher than, but quite similar to, the results calculated on Fig. 6.21.

TABLE 6.13 — EXPERIMENTS WITH REPEATING PLANES OF FUEL ELEMENTS AND WATER CHANNELS*

Core Number	Core Type	Fuel Density (g U^{235}/liter)	Metal/Water Ratio	Calculated Worth of Low Hydrogen Density Region (%Δk)	Calculated Worth of Rod Septum (%Δk)	Calculated Eigenvalue
Core 1	Clean slab	34.6	0.4	---	---	0.995
Core 2	Slab with a one-dimensional voided region	34.6	0.4	5.7	---	0.991
Core 3	Slab with a two-dimensional voided region	34.6	0.4	2.8	---	0.995
Core 4	Slab with an internal hafnium rod septum	34.6	0.4	---	8.7	1.001
Core 5	Slab with the internal hafnium rod septum in a voided region	34.6	0.4	---	11.2†	0.993

*Four-group two-dimensional calculations with hardened flux continuity model, calculated eigenvalues normalized to $k_{exp} = 1.000$.
†11.2% Δk represents the total worth of the rod septum and the voided region in Core 5.

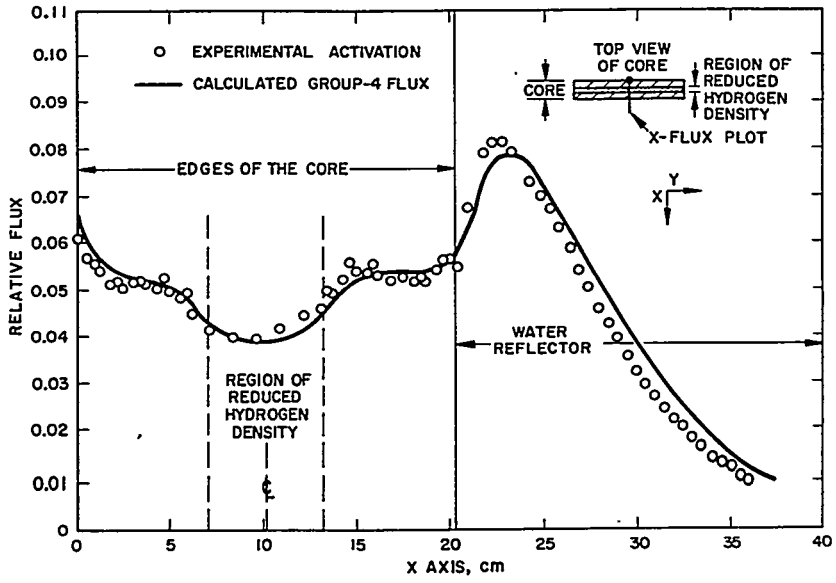

FIGURE 6.21. Thermal Group (Subcadmium) Comparison for Core 2 Which Contained the Central Region of Reduced Hydrogen Density.

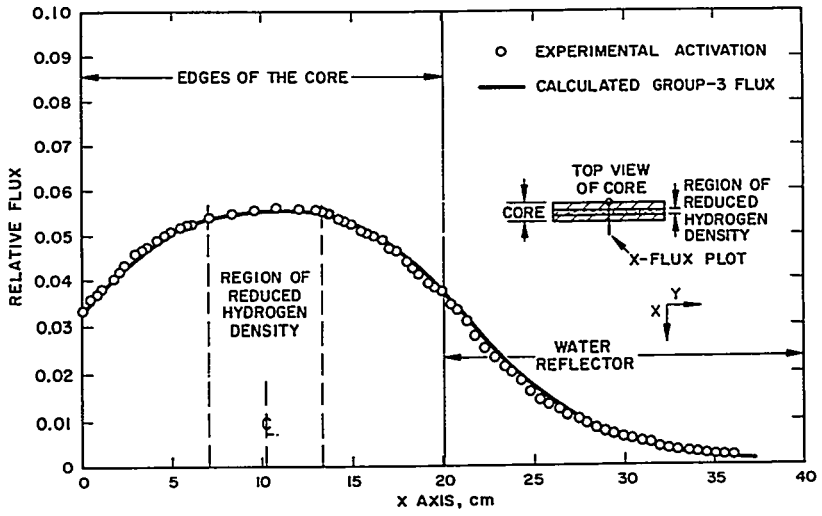

FIGURE 6.22. Epithermal Group Comparison for Core 2 Which Contained the Central Region of Reduced Hydrogen Density.

This is because of the relatively soft spectrum of the experiment.

It can be concluded, from the results listed in Table 6.13 coupled with the activation measurements typified by Figs. 6.21 and 6.22, that the basic group diffusion theory model is capable of representing these low metal-to-water ratio clean critical experimental systems with a high degree of consistency. Thus, these results add to the confidence in the model generated through the analysis of the previously described sets of experiments at the higher metal-to-water ratios which used the small module box geometry.

C. Plastic-Moderated Critical Experiments

T. F. Ruane

1. Introduction

In addition to the water-moderated experiments described in Sects. 6.2.A and 6.2.B, plastic-moderated critical assemblies have played an important role in the development of the technology of water-moderated power reactors. A key feature of the plastic-moderated system is the ease with which the concentration of the moderator within a coolant channel can be changed in order to simulate the density variation from the low ($\sim 70°$ F) to the high ($\sim 500°$ F) temperatures. In addition, the dry critical assembly can be made extremely stable and yield highly reproducible results because of the rigid clamping of the component parts and the precise control of moderator composition and density. Thus, the dry assembly is ideal for the measurement of the reactivity coefficients of various samples, especially when the perturbation yields a small reactivity change.

There is no provision in the plastic critical facility for a rapid safety scram feature in the form of a moderator dump in which the opening of a large drain valve allows the moderator to be discharged rapidly. Instead, the core is normally assembled in two sections, and these sections are brought together with remote controls to form the uniform moderated array from which the control rods are subsequently withdrawn to approach critical. The rapid separation of these sections upon initiation of a scram provides the required shutdown comparable to the moderator dump of the wet assemblies. The rapid section separation is accomplished either by spring loading in a horizontal assembly or by gravitational force in a vertical assembly, of which the Plastic Mockup Assembly (PMA) is an example. Figure 6.23 illustrates this mode of

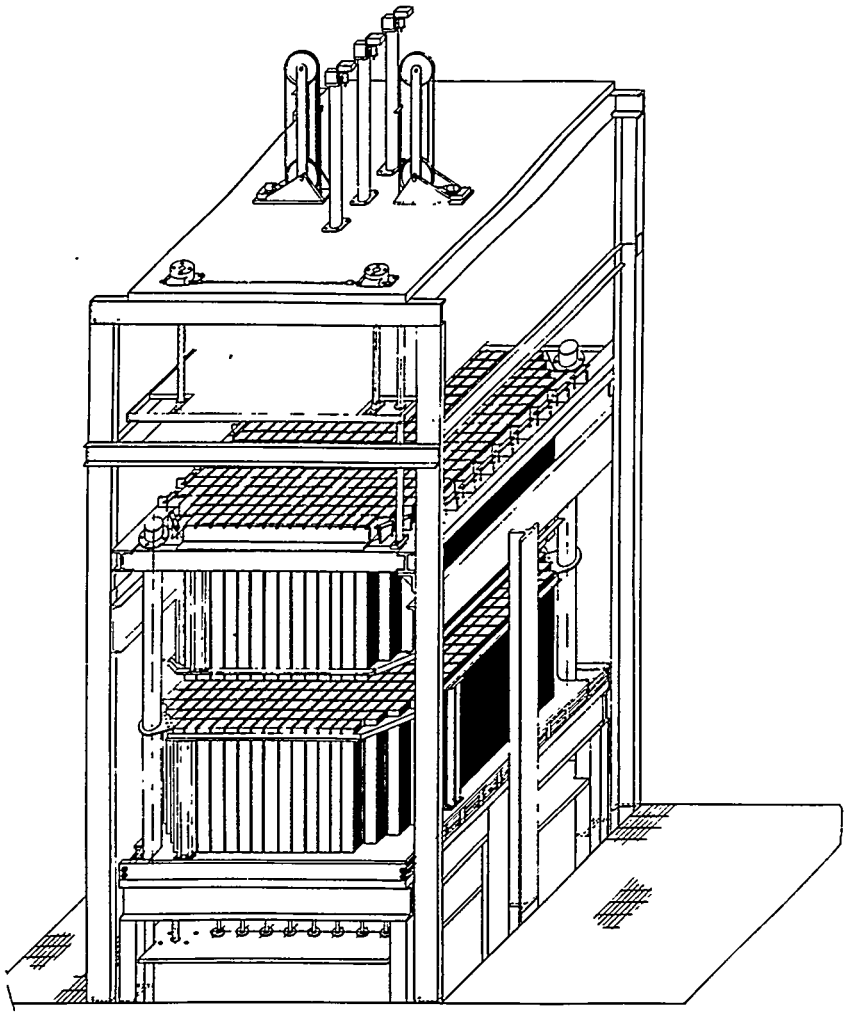

FIGURE 6.23. Perspective View of the Plastic Mockup Assembly (PMA) Showing the Safety Scram Feature by Rapid Separation of the Lower Half of the Dry Assembly Downward from the Upper Half.

operation for the case of the Plastic Mockup Assembly, a plastic-moderated dry critical assembly.

This section describes two representative types of experiments which have been performed in one of the plastic-moderated assemblies. Another type of experiment on a plastic assembly, the measurement of flux transients near interfaces between discontinuous media, is discussed in Sect. 6.4. In the first experiment described here, a comparison

is made between the power peaking measured in a light water-moderated system and that measured in a plastic (polyethylene) moderated system. The comparison of the experimental results demonstrates that the water-gap peaking can be simulated in a plastic assembly. This is important, since the power producing reactor cores of interest to the nuclear designer are normally moderated with light water. Thus, the equivalence of both the reactivity characteristics and the peaking characteristics of the plastic assembly with a water assembly must be demonstrated before the dry assembly can be of practical use in mockup type experiments. In addition to this experimental comparison, the analysis of these peaking experiments can yield information concerning the validity of the calculational models. Again, however, it must be noted that the data, including the effect of the plastic, must be amenable to calculations and analysis by the regular nuclear design technique.

The second example of the use of a plastic-moderated assembly presented here is in the measurement of reactivity coefficients, the reactivity worth of a small change in the concentration of a particular material in the core. Measurements have been made for several materials, such as polyethylene, zirconium, aluminum, and stainless steel. Perturbation theory, coupled with a group diffusion model somewhat similar to that discussed in the general calculational model (Sect. 6.2.A.3), has been used to analyze these results. This type of experiment is intended to emphasize the portions of the analytical model which deal with the properties of these individual materials.

2. *Substitution of Hydrocarbons for Water*

A significant feature of the plastic-moderated dry critical assembly, as compared to the water assembly, is the relative ease with which the hydrogen density of the moderator may be varied. Thus, a core equivalent to a hot water condition may be studied without the attendant temperature limitations of water, in particular, the corrosive action of high temperature water as discussed in Sect. 6.3.A. However, to utilize a dry assembly for confirmation of the analytical techniques to be used in the design of a water-moderated reactor, some understanding must first be gained of the relationship of plastic and water. Hurwitz and Smith[18] considered the case of organic fluids and proposed the construction of three-dimensional criticality surfaces upon which the reactivity effects of a moderator change are regarded as a linear

function of the change in moderator composition. This three-dimensional surface is obtained by the experimental measurement of the reactivity equivalence of various organic fluids under identical conditions. Each point on the surface represents an amount of organic with a particular chemical composition of carbon, hydrogen, and oxygen, which is equivalent in reactivity to all other points on the surface.

Early experimental comparisons at Knolls Atomic Power Laboratory by S. W. Kitchen indicated that for water (H_2O), polyethylene (CH_2), and polystyrene (C_8H_8), the hydrogen atoms contribute more than 99 percent of the measured reactivity effect in a predominantly thermal spectrum, i.e., the reactivity coefficient of hydrogen was essentially constant for these three materials. Later measurements by MacKinney[19] included the above materials as well as the liquid hydrocarbons, monoisopropyldiphenyl ($C_{15}H_{16}$) and methyl alcohol (CH_3OH). MacKinney's measurements showed that the equal reactivity surface developed by Hurwitz and Smith for hydrogenous liquids could be extended to include the plastics. Figure 6.24 is an example of a criticality surface generated in this manner and illustrates that it is possible to obtain by experimental methods those moderator compositions which are equivalent to water at various temperatures.

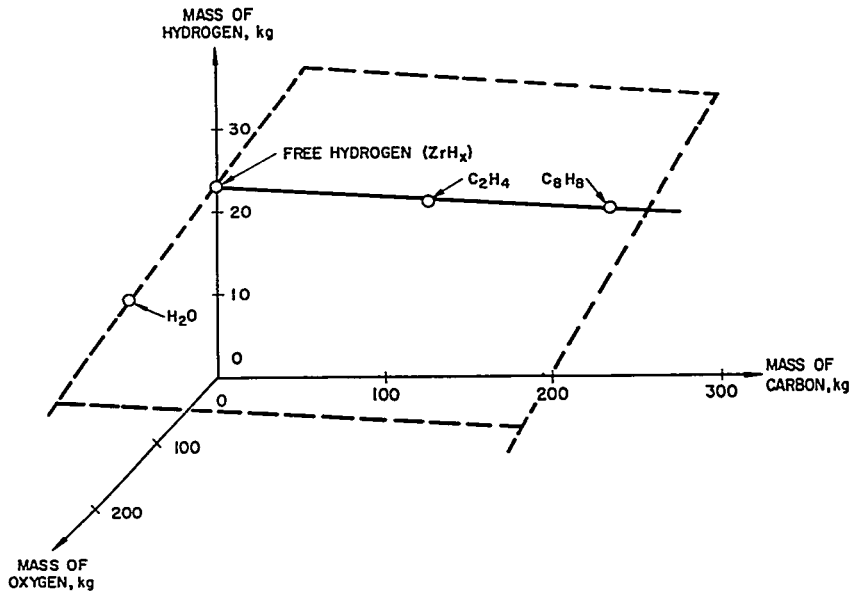

FIGURE 6.24. Equal Reactivity Plane Analysis of Reactivity-Coefficient Data from the Plastic Mockup Assembly. (Each point lying in the plane represents the same reactivity effect.)

More recent independent measurements were made by T. F. Ruane and D. R. Bach with emphasis on the comparison of polyethylene and water. These experiments agree, in general, with the conclusion of the earlier work that hydrogen is the predominant constituent insofar as reactivity effects are concerned when it is desirable to equate a plastic to water. However, it was also found that second-order effects, such as chemical binding or the differences between carbon and oxygen, become important when thick water gaps or very thermal spectra are involved. Since the reactivity effect is predominantly associated with the hydrogen and since the current nuclear design techniques have models for representing hydrogen in both free and bound states, comparisons based on plastic-moderated experimental results are useful in confirming the design techniques.

3. *Comparison of Theory and Experiment*

Two examples of the types of experiments which are performed in a plastic assembly to aid in the evaluation of analytical design techniques are discussed in this section. These examples include comparisons between experiment and theory for several cases of power peaking near simulated water gaps and then compare several measured and calculated reactivity coefficients.

A) WATER GAP PEAKING EXPERIMENTS. A series of experiments was performed in the Plastic Mockup Assembly to measure the power peaking next to thick moderator channels.[20] The purpose was twofold: (1) The power peaking was thus measured in a moderator channel which alternately contains water or polyethylene to simulate the water. The adequacy of the moderator substitution method described above, which is based upon reactivity equivalence, was evaluated as it pertains to power peaking. (2) The adequacy of an approximate design model in predicting power peaking next to moderator channels was evaluated. This type of experiment serves an important role in the design of power reactors by providing confidence limits for the design calculations which, in the interest of urgency and economy, have utilized a simpler model. In some cases, this type of experiment can also be used to indicate the direction in which refinements and improvements must be made in the design techniques.

The peaking experiments were conducted in a slab core 12-3/4 in. wide, 45-1/4 in. long, and 48 in. high. The basic PMA matrix box is a 3-in. × 3-in. aluminum can with 0.060-in.

walls. These cans were separated by a 1/4-in. polyethylene channel. The fuel plates were of enriched uranium-aluminum alloy, the structural material was aluminum, and the moderator was polyethylene. The reflectors were of polyethylene, except for a small amount of aluminum structure. The central plane of this slab core, which is the top face of the lower section of the assembly, is shown in Fig. 6.25. This figure also shows the central test region and the polyethylene side reflectors.

From this basic core, the central eight matrix cans were removed, and a watertight aluminum cell was inserted. The cell contained a region of the core 6 in. × 12 in., with the 12-in. dimension aligned with the 12-in. width of the whole core, as shown in Fig. 6.25. The core components were inserted into this box so as to maintain a U^{235} density of 110 g/liter and a metal-to-water (in this case metal-to-nonmetal) volume ratio of 1.8. The composite fuel elements were assembled in the box so as to maintain a coolant channel of 0.060 in. which could be filled with either polyethylene or water. The cladding plates were either aluminum or, for certain experiments, steel which was used to increase the neutron absorption of the system. When polyethylene was used as the moderator, the proper hydrogen density was maintained by the use of polyethylene strips thinner than the 0.060-in. channel, with an air gap in the remaining portion of the channel.

The experiments were performed for both slab and cruciform water channels. The slab channels were varied in both thickness and moderator density. In general, these slab channel experiments should be amenable to calculation by standard one-dimensional diffusion theory techniques, since the channel was oriented so as to bisect the narrow dimension of the slab similar to the method shown in Fig. 6.3 for the boron septum. The cross gaps accommodated a 6-in. × 8-in. cruciform control rod. In this case, both the cross-gap thickness and the moderator density as well as the moderator type were varied. In addition to the changes in gap composition and size, the effect of the test cell, i.e., fuel plates and gap liner, was investigated for both aluminum and zirconium. A summary of some of the experimental data and some associated calculational results is given in Tables 6.14, 6.15, and 6.16.

The power distribution measurements were made in a horizontal plane near the center of the core. The relative power at a point was determined by measurement of the gamma activity of small uranium-aluminum tabs (1 in. × 3/8 in. × 0.070 in.) which were of identical composition as the fuel plate and which were inserted into holes punched from the

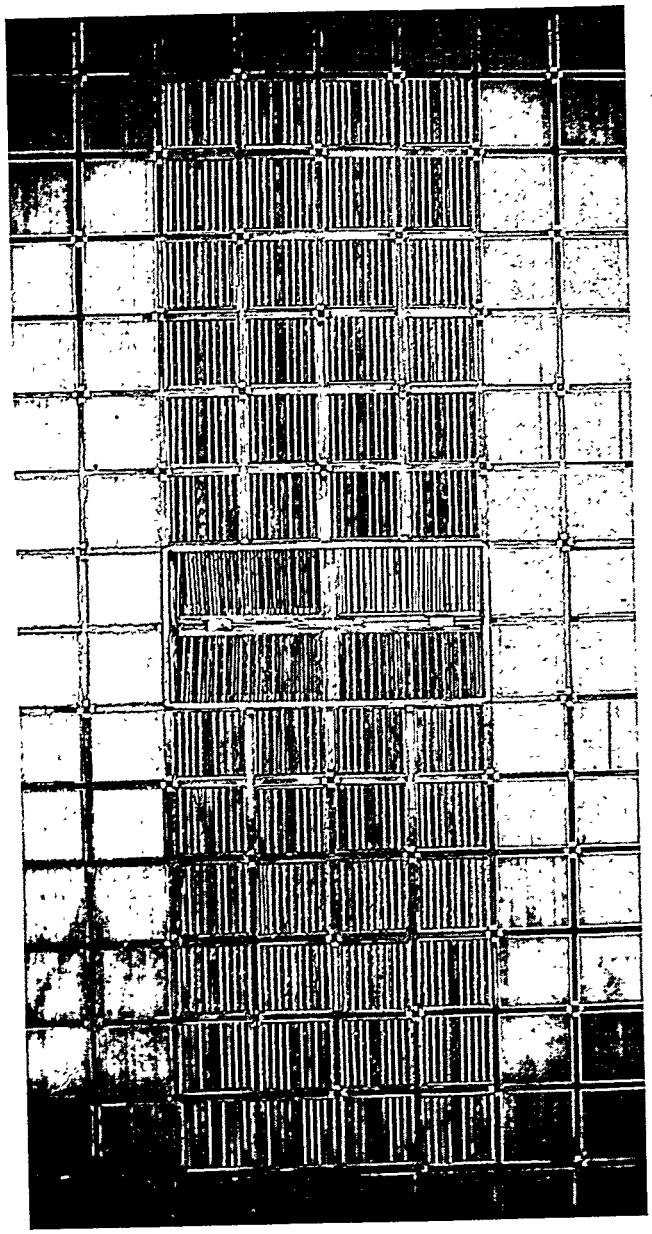

FIGURE 6.25. Top View of the Central Region of the PMA 4-C Slab Core Showing the Slab Fuel Region, the Outer Polyethylene Reflectors, and the Watertight Aluminum Can in Which the Detailed Flux Measurements Were Made.

TABLE 6.14 — POWER PEAKING FOR ALUMINUM-POLYETHYLENE SLAB GAP CORE

Gap Thickness (in.)	Temperature* (°F)	Poison (Steel) (volume percent)	Peaking Ratio†	
			Experimental	Calculated† (one-dimensional)
0.400	~ 70	12	1.79	1.74
0.400	~500	12	1.51	1.58
0.200	~500	12	1.24	1.36
0.800	~500	12	1.81	1.99
0.200	~500	24	1.40	1.40
0.400	~500	24	1.60	1.64

*Equivalent hydrogen density.
†Ratio of power at gap to asymptotic value on activation line.

TABLE 6. 15 — POWER PEAKING FOR ALUMINUM-POLYETHYLENE CROSS GAP CORE

Gap Thickness (in.)	Temperature* (°F)	Poison (Steel) (volume percent)	Experimental Peaking Ratio†
0.200	~70	24	1.73
0.400	~70	24	2.41
0.200	~500	12	1.57
0.400	~500	12	2.24
0.200	~500	24	1.64
0.400	~500	24	2.34

*Equivalent hydrogen density.
†Ratio of power at gap to asymptotic value in plane.

TABLE 6.16 — POWER PEAKING FOR CROSS GAP CORES

Gap Thickness (in.)	Moderator	Poison (Steel) (volume percent)	Structure	Experimental Peaking Ratio*
0.400	Water (cold)	24	Zirconium	2.81
0.400	Polyethylene (cold water equivalent)	24	Zirconium	2.89†
0.400	Polyethylene (cold water equivalent)	24	Aluminum	2.41
0.400	Water (cold)	24	Aluminum	2.43†

*Ratio of power at gap to asymptotic value in plane.
†Contains a correction for structural material based upon calculation.

particular fuel plate at the points of interest. Figure 6.26 shows several fuel plate sections loaded with the activation detectors.

The calculated results listed in Table 6.14 followed a method similar to that of Sect. 6.2.A.3, with the exception of the means employed to determine the macroscopic group

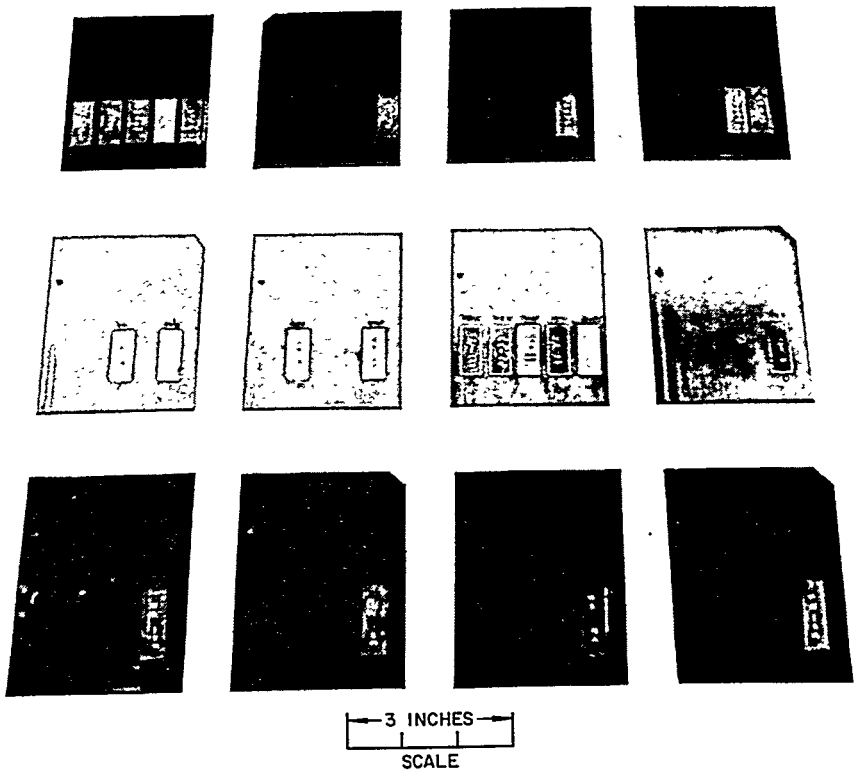

FIGURE 6.26. Punched Fuel Plate Sections with Tabs in Place Used for Obtaining the Detailed Measurements of Flux Peaking in the Plastic Mockup Assembly.

constants and the homogenization model. Sections 6.2.A and 6.2.B used a method for the generation of few-group constants which can be identified as the MUFT-SOFOCATE method. In those cases, the few-group constants for the fast neutron groups were obtained by solving the P_1 slowing-down equations, assuming that the spatial dependence can be separated by representing the flux by its Fourier transform using the MUFT routine. In addition, the thermal group constants, for the cases which used hardened constants, were generated by averaging energy-dependent cross sections over a Wigner-Wilkins energy distribution using the SOFOCATE routine. This section discusses results obtained by using a second method for the generation of few-group constants. This second method, called the WOXX technique, which is relatively simple, also has been successfully used in the design of power reactors. However, this advantage is obtained by means

of certain simplifying approximations which will limit its range of applicability to a larger degree than do the approximations inherent in the MUFT-SOFOCATE technique. To evaluate this particular method in its ability to predict power peaking at water channels, the three-group WOXX routine was used in the analysis of the peaking experiments.

The WOXX code for the calculation of group constants is based upon the method of Deutsch.[21] The WOXX routine is based upon a three-energy group structure. The fast group extends from 10 Mev to 180 kev, and the epithermal group ranges from 180 kev to the thermal group cutoff. The thermal group cutoff is a variable which is taken as four times an effective temperature. This effective temperature is that temperature of a Maxwellian distribution of neutron velocities which will have the same average neutron velocity as that predicted by a Wigner-Wilkins spectrum for an unbound hydrogen gaseous moderator. Thus, the thermal group of WOXX approximates the Wigner-Wilkins hardening of the spectrum due to absorption but retains the format of a Maxwellian distribution for ease of calculation. The thermal group cutoff is taken as four times the effective temperature after the thermal spectrum has been smoothly joined to a $1/E$ spectrum. This cutoff energy also represents a calculational convenience. These two approximations, which are related, of the hardened Maxwellian and thermal cutoff lead to the basic limitations of this method and restrict its application to relatively thermal reactors.

The fast and epithermal group constants in the WOXX method are obtained by averaging over a $1/E$ spectrum for the energy ranges listed above. An additional factor which is included in the calculations is the age-to-indium value for a fission neutron source in water. An experimentally measured value was used for the total age. Thus, the neutron age, as well as the basic isotopic or elemental microscopic parameters, is dependent upon experimental measurements. As a result, there are different versions of WOXX which contain different values of the neutron age as well as containing different sets of microscopic cross-section information for the elements. It should be noted that different sets of cross-section data are also used with MUFT-SOFOCATE method. Thus, in many cases, it is difficult to compare directly these two methods for generating the few-group constants, since differences in the cross-section data could mask the comparison. The particular version of WOXX which was used for the calculations illustrated here had an age-to-indium value of 30.9 cm^2, treated the zirconium absorption as $1/v$ in the epithermal group, and did not take into account such

effects as the resonance absorption in oxygen or uranium and, thus, represents an early version of the routine.

The homogenization technique chosen for the analyses presented here was similar to the method noted as Method 1 described in the general calculational model (Sect. 6.2.A.3). Thus, the fuel was homogenized right up to the edge of the slab channel. As noted in that discussion, this method moves fuel into a region close to the gap where it does not actually exist in the experiment. It was also noted there that one of the effects of this type of homogenization, while it is desirable in order to minimize the number of spatial mesh points and regions, is to cause a depression in the calculated peaking at the gap interface by putting absorption in the calculation into a region where it does not actually exist in the experiment.

The one-dimensional slab experiments were analyzed using the one-dimensional few-group diffusion theory routine (WANDA[10]) run along a line through the narrow dimension of the slab. The results listed in Table 6.14 show that the particular calculational scheme chosen represented the experimental power peaking fairly well for the one-dimensional gap cases. Over the range of gap thicknesses, moderator concentrations, and poison loadings considered, the calculated results were within about 10 percent of experiment and, in general, fell above the experimental values. It should be emphasized that this apparent agreement has been obtained by using the particular set of cross-section data described above, where it was noted that these data represented an early version. In addition, the homogenization scheme chosen should tend to depress the calculated peaking values below those which would be obtained from a theoretically more accurate scheme. Thus, the agreement for this one-dimensional case over the range of these experiments should not be interpreted as indicating general agreement with this model over a broad range. Further improvement in the agreement of calculated and experimental peaking can only be accomplished by use of more refined calculational models, as set forth in Chap. 4 of this volume.

A result important to the development and design of pertinent experiments is illustrated in Table 6.16, where results comparing the direct substitution of polyethylene for water are given. The data given in Table 6.16 illustrate that the power peaking at a water gap can be duplicated within the experimental uncertainty of ±5 percent when polyethylene is substituted for the water, in the manner described at the beginning of this section, by maintaining the hydrogen density constant. A further observation from these data is the significant effect of the structural material (aluminum vs

zirconium) on the observed peaking which is attributed to the difference of the two scattering cross sections.

To summarize the conclusions from these experiments and calculations: (1) The reactivity equivalent substitution method of polyethylene for water, which is essentially a maintenance of the hydrogen density, yields comparable results for power peaking to within about ±5 percent. (2) Calculation of power peaking by the particular calculational model described agrees to within 10 percent of experiment for the simple slab moderator gap cases considered, with the calculation lying above the experimental result. This agreement probably results from the compensating errors due to the use of the particular cross-section data and the WOXX group constant technique coupled with the particular homogenization scheme chosen for the analysis.

B) REACTIVITY COEFFICIENT EXPERIMENTS. The second type of experiment on the dry critical assembly discussed here is the measurement of the reactivity worth of samples of various materials in the reactor. The measurement, in reactors of simple geometry, of small reactivity changes associated with a uniform regional change in reactor composition can provide useful data for comparison against calculational techniques. In particular, in certain cases the evaluation of the distributed reactivity coefficients can provide a more stringent test of the validity of a given calculational procedure than can be provided by the determination of criticality alone. Apparently satisfactory agreement between experiment and calculations for gross core criticality in some cases may be misleading because of cancellations stemming from errors in the various portions of the total model. For this reason, it is necessary that a large number of critical assemblies be analyzed for gross core criticality before a realistic conclusion can be reached regarding the adequacy of a particular calculational technique. The reactivity coefficient analysis, on the other hand, can examine the adequacy with which the individual reactor constituents are treated in the total calculational scheme.

A series of core distributed reactivity coefficient measurements of moderator and structural materials was made in a polyethylene-moderated and reflected slab reactor. A core distributed reactivity coefficient is defined here as the reactivity change per unit mass in which the small material change is made uniformly throughout the core. The dry core assembly, similar to the one described previously, was approximately 12 in. wide, 45 in. long, and 48 in. high and contained about 41 kg of U^{235}, 300 g of natural boron, and a

metal-to-water ratio of about 1.8. (The spectral hardness parameter, $\beta\gamma$, was 0.45. This parameter is defined in Sect. 6.4 as the ratio between thermal absorption and slowing-down power.) The experiments were analyzed in a manner similar to that described in the previous section in the discussion of the general calculational model, with the exception that perturbation theory was used for the calculation of the reactivity coefficients. In regard to the actual measurement of distributed reactivity coefficients, it should be noted that the plastic reactor, in general, yields results which are more easily reproducible than a water assembly and offers no particular problems in making measurements relative to void. Since the PMA assembly used in these experiments separates into two halves, as indicated in Fig. 6.23, the slab core has eightfold symmetry. This symmetry reduces the degree of sampling needed to measure the core-distributed reactivity coefficients.

For the calculations of the reactivity coefficients presented here, two cross-section methods were utilized: the WOXX[22] method and a version of the MUFT-SOFOCATE technique. The group constants obtained from MUFT[23] and SOFOCATE[4] that were used in the comparisons described here were based upon a three-group neutron energy structure. This group structure was that characteristic of the WOXX and was used for the purpose of comparison rather than the four-group diffusion model described in detail in the discussion of the general calculational model. In addition, the MUFT calculations used the early library (Table 6.3) which did not include such effects as the inelastic scattering in zirconium or oxygen or an explicit treatment of resonance fissioning in U^{235}.

Since aluminum was not available in this early MUFT library, the treatment of aluminum in the fast neutron groups was to relate it to an equivalent amount of zirconium by means of the empirical relationship

$$N_{\text{equiv Zr}} = 0.365\, N_{\text{Al}}$$

where N = nuclei/cm^3. This equivalence was only necessary for the fast group treatment of the aluminum, since cross-section data were available for the thermal group. This equivalence relationship was developed as a method of duplicating the measured age in an aluminum-water mixture by the MUFT calculation, using zirconium in place of aluminum in the calculation.

The calculations were performed by means of the IBM-704 two-dimensional diffusion theory code CURE,[24] with the cross

sections derived either from the WOXX or from the MUFT-SOFOCATE (three-group) routine. The transverse dimension was represented by the leakage term. For each set of cross sections, both flux and adjoint flux distributions were obtained from the two-dimensional calculation. These were then used in standard first-order perturbation theory calculations to determine the reactivity changes of interest. It should be noted that the primary purpose of these experiments and analyses is to study the methods and techniques that are in use for power reactor design. When disagreements are found between calculated and measured criticality, comparison of the subsequent reactivity coefficient measurement calculations of the individual core components may then serve to point the direction which should be taken as regards improvement of the calculational method.

The calculated values of the reactivity coefficients of polyethylene and some of the structural materials that are used in experimental assemblies are summarized in Table 6.17 with their experimental values. The experimental uncertainty for these data is ±5 percent, so that calculations which do not fall within this range are deficient in some manner.

Some general conclusions which can be drawn from the results of this particular study are as follows: The MUFT-SOFOCATE method used resulted in the best overall values. In particular, the polyethylene agreement is excellent, while the WOXX result indicates a basic limitation in its approximation. Along these lines, later experimental information indicates a lower value for the age-to-indium than that used in this version of WOXX which, however, would tend to decrease the calculated reactivity coefficient and, thus, increase the

TABLE 6.17 — REACTIVITY COEFFICIENTS (cents/kg), CALCULATED AND EXPERIMENTAL

Material	WOXX*	Three-Group MUFT-SOFOCATE*	Experimental
Polyethylene	37.3	44.7	43.6
Aluminum	1.27	0.54	0.73
Zirconium	1.10	0.83	0.74
Stainless steel	3.39	2.69	3.40
Magnesium	--	2.92	1.83

* $\beta_{eff} = 0.0078$.

disagreement with experiment. Another noteworthy example is zirconium. As stated previously, neither cross-section method contained resonance absorption or inelastic scattering. However, the MUFT-SOFOCATE gives reasonable agreement with experiment; in fact, later inclusion of these effects did not significantly alter the calculated value. In the case of WOXX, the inclusion of these effects does bring it into reasonable agreement with experiment.

In summary, there are many aspects of the calculational model which must be considered by the core designer, for example, the group structure, the selection of a method of generating group constants, the selection of cross-section data, and the homogenization method. Many times these selections cannot be made independently. Experiments and analyses, such as the one discussed here, which point out the limitations of certain approximations in the overall model play an important role in the development of reactor technology. As a result of the studies reported here and others of comparable nature, many of the shortcomings of the various design techniques can be brought to light and attention focused upon those areas most in need of improvement.

6.3 HIGHLY ENRICHED CLEAN CRITICAL EXPERIMENTS AT ELEVATED TEMPERATURES

L. O. Herwig and W. Skolnik

A. Introduction

One of the more important reactivity effects in a water-moderated power reactor is that resulting from the temperature change from ambient to operating conditions. Over this range the density of water changes by 20 to 25 percent. The resulting change in the concentration of hydrogen has two important consequences: alteration of the neutron slowing-down behavior and alteration of the scattering properties at thermal energies. Unpressurized critical assemblies, such as those discussed in Sect. 6.2, are limited in temperature range to values below the boiling point of water at atmospheric pressure. Thus, a direct measurement of the temperature-dependent properties of reactors had not been possible until the design core was actually manufactured and installed into the reactor plant pressure vessel and initial tests performed. It should be noted that these high temperature measurements previously did not take place until after the core design effort had been completed and the financial investment in the construction of the core itself had been made. Many attempts

to simulate high temperature conditions were made in the unpressurized critical facilities; for example, the reduction of the hydrogen density in the water channels through the introduction of a plastic material. Although these attempts were useful, it was apparent that a significant contribution could be made by expanding the range over which critical experiments are performed to include high temperature conditions. The operation of mockups of the design core at high temperature prior to the actual manufacture of the design core is highly desirable, since this may detect some characteristic of the core that could be improved by a change in the design. The measurement of relative neutron distributions and the capture rates in fuel and burnable poison regions are particularly important at high temperatures in obtaining confidence in the portion of the model which depicts core depletion. In addition to the mockup experiments, the high temperature operation of simplified experiments, such as the clean slab experiments described in Sect. 6.2, extends the range over which the total calculational model can be tested.

To satisfy the need for both mockup and simplified experimental measurements at high temperature, critical facilities have been constructed which are capable of operating at elevated temperatures and pressures. This section describes results from two such facilities. One of these high temperature facilities, designated the PTR (Pressurized Test Reactor), can operate assemblies to 560° F at pressures to 1200 psi. The second high temperature facility, designated the HTTF (High Temperature Test Facility), can operate larger assemblies to 490° F and 655 psi. These facilities are similar in most respects to the unpressurized critical assemblies in which the experiments described in the previous section were conducted. The major difference lies in the pressure vessel containment and the water heating, cooling, and circulating equipment. The experimental techniques used in the high temperature facilities are similar to those developed for the low temperature assemblies. However, they are complicated by the necessity of suitably choosing materials which are capable of withstanding the corrosive effect of high temperature water.

In these high temperature facilities several experiments have been performed on clean cores in addition to the large number of experiments performed on the mockups. Comparison between experiment and theory for a few of these clean cores is discussed in this section. By clean cores are meant the cores of relatively simple geometry, where the experiments are expressly designed to provide checks on the calculational methods. These experiments have been analyzed by different methods in an attempt to emphasize various portions of the

overall calculational model. Comparison is made both between calculated and experimental reactivity and between calculated and measured power distributions or neutron activation shapes. Experimental results from both the PTR and the HTTF are discussed in this section and compared with the analytical results.

B. Description of Experiments

1. PTR Experiments

To obtain the required flexibility of geometrical arrangement in the PTR facility, the experimental cores are constructed of cans 2 by 4 in. in cross section. Water gaps and absorbing septum gaps may be inserted by spacing can rows. A typical arrangement is shown in Fig. 6.27.

The core components, which are inserted into the core cans, consist of a comb arrangement for spacing the fuel plates,

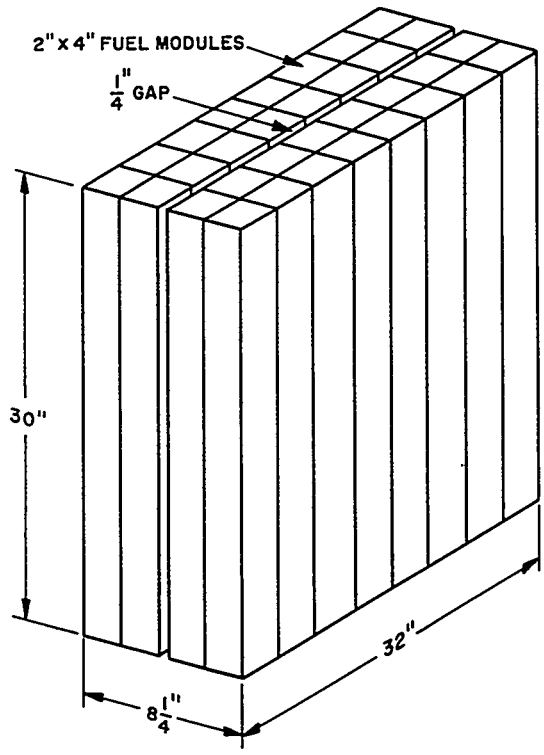

FIGURE 6.27. Schematic Drawing of a Typical Slab Arrangement for High Temperature Experiments in The PTR Facility.

absorber plates, and additional blank plates for establishing the desired ratio of metal-to-water volumes. Figure 6.28 shows a typical arrangement. Figure 6.29 is a detailed drawing of a portion of the can with a typical loading and shows the detailed dimensions of the fine structure. A close examination of the figures shows that the teeth of the comb structure are Zircaloy plates which extend outward from the central region in each direction. The spacing between these Zircaloy plates is fixed by the thickness of the Zircaloy pieces which form the center of the comb. It should be noted that the fuel and any additional plates are only loosely held between the Zircaloy plates, so that the dimensions shown are average spacings. Other arrangements are easily effected by changing the thickness of the spacers at the centerline of the comb. For the experiments to be described here, the can, the comb center, and plates were made of Zircaloy-3, while the fuel cladding and the additional loose plate added within the structure to adjust the metal-to-water ratio were made of Zircaloy-2. The fuel consisted of a solid uranium center foil, approximately 1.5 mils thick, clad on each side with about 10 mils of Zircaloy-2. The use of solid uranium fuel greatly increases the accuracy with which the fuel content of each plate is known, since each fuel plate is individually weighed. Table 6.18 lists the properties of the average fuel plate.

Several types of experiments have been performed in the PTR using the basic core construction features described above. The experimental method was simply to adjust the water temperature until the core was slightly supercritical with all rods out. The excess reactivity with all rods out was determined by period measurements or from standard rod calibration techniques in the same manner as given in the description of the clean slab experiments with small bundle box geometry. Then foils or tabs or the fuel elements themselves were activated in a critical run where a rod was reinserted to maintain criticality. The temperature was ordinarily maintained constant to within 1°F during the activation. In each case, the height of the fuel in the core was fixed at 30 in.

High temperature experiments in simple slab geometry have been performed in the PTR to investigate the temperature dependence of several parts of the analytical model. These experiments have included sets of clean slabs which were free of deliberately inserted nuclear poisons as well as experiments poisoned with lumped boron septa and with homogeneously distributed boron. Of the several types of experiments which have been performed, two sets have been selected for discussion here as yielding typical temperature-dependent results.

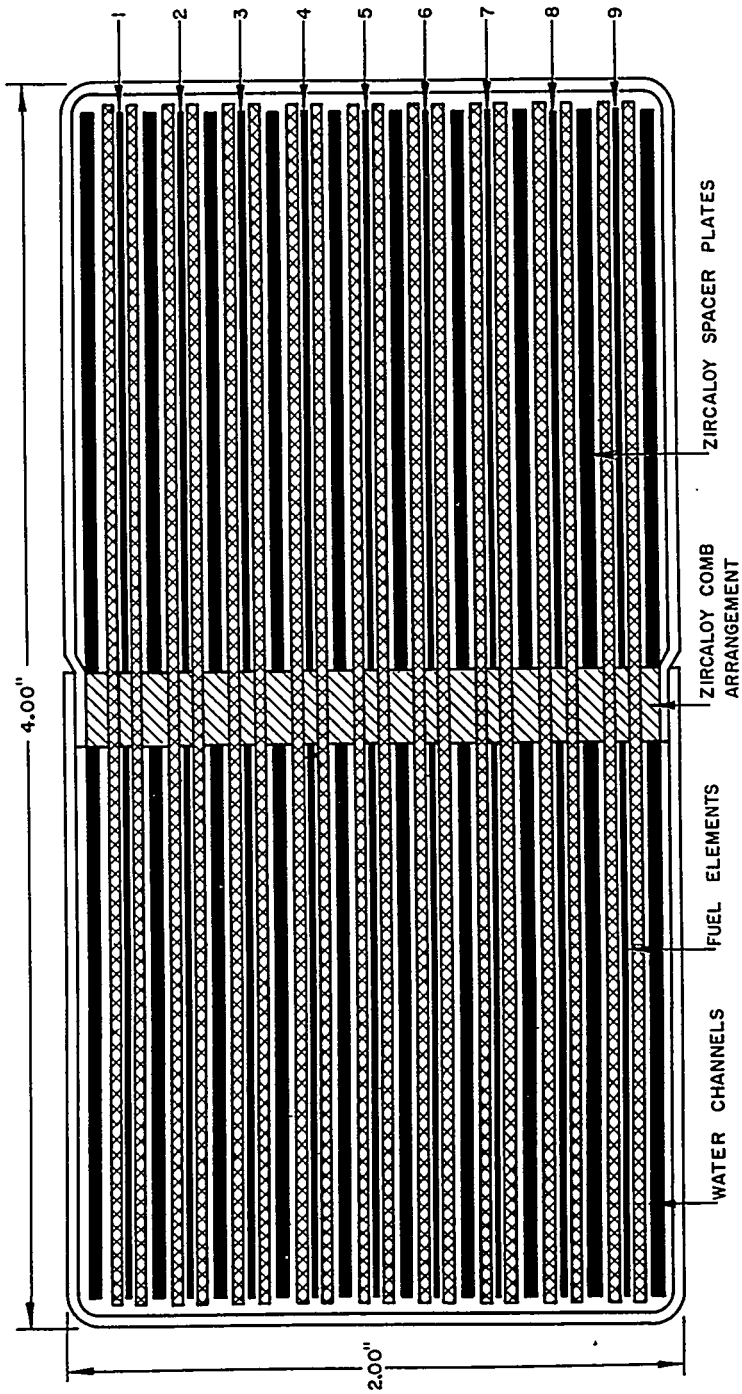

FIGURE 6.28. PTR Fuel Module Construction Showing Zircaloy Comb Arrangement, Fuel Elements, and Zircaloy Spacer Plates.

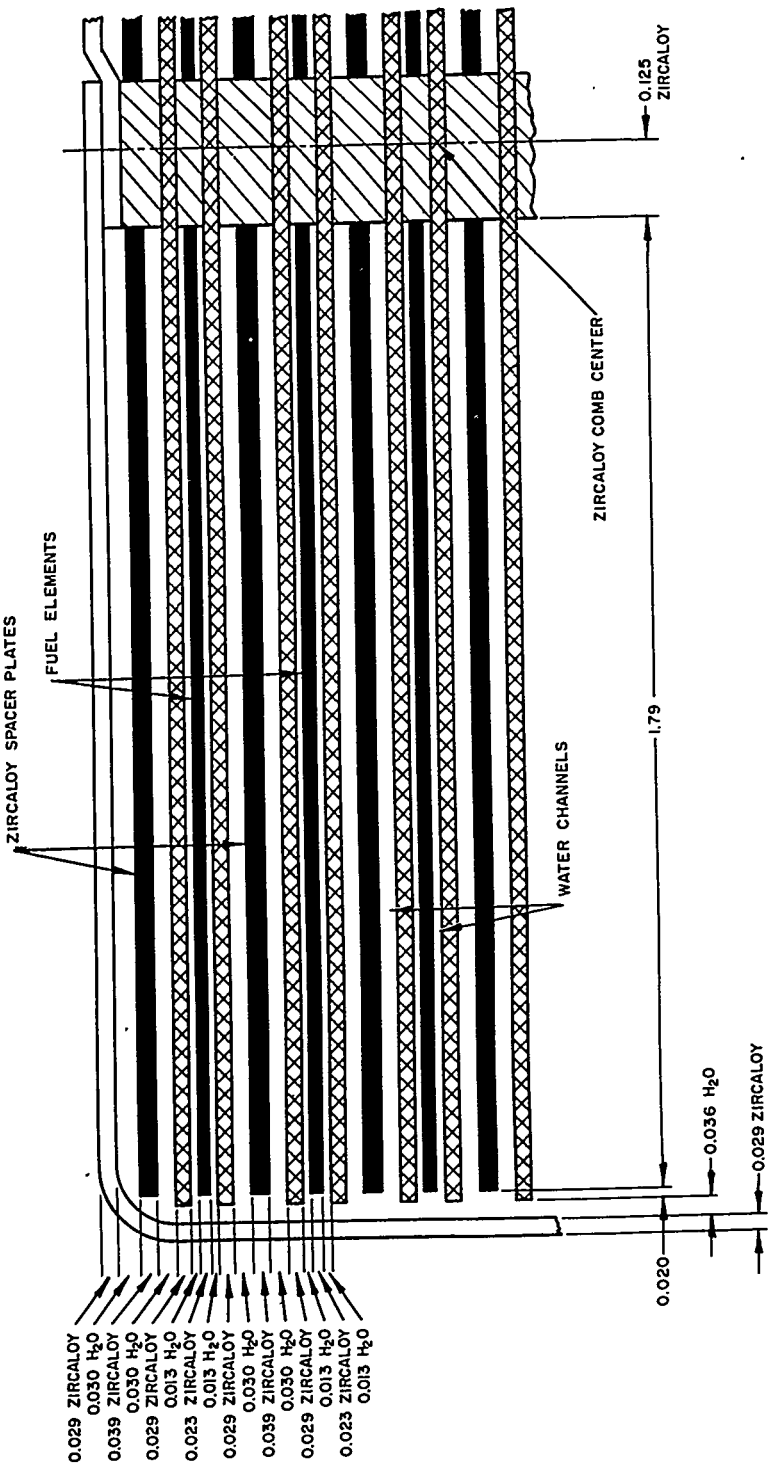

FIGURE 6.29. Detailed Construction of PTR Fuel Module. (Dimensions in inches.)

TABLE 6.18 — PROPERTIES OF AVERAGE FUEL PLATE

Isotopic constitution*	U^{234}, 0.234 g U^{235}, 21.507 g U^{236}, 0.111 g U^{238}, 1.236 g
Lateral dimensions of fuel†	29.77 in. high 1.61 in. wide
Derived fuel meat thickness‡	0.00157 in.

*The total uranium weight of each fuel strip was measured prior to cladding. From the Oak Ridge determined isotopic constitution, the individual isotopic weights for each fuel plate were calculated and the averages for many fuel plates were found.

† The outer dimensions of the clad fuel plate are 1.79 in. wide and 30 in. long; the differences in dimensions are due to a Zircaloy border around the edge of the fuel meat region.

‡ Found by assuming the fuel is of full uranium density, 18.7 g/cm^3, and with the lateral dimensions given in the table.

Table 6.19 lists the experimental parameters of a set of clean slab experiments containing just fuel, Zircaloy, and water. In this series the variable parameters were the core size, the metal-to-water volume ratio, the fuel density, and the temperature at which the control rods were nearly completely withdrawn. As noted in Sect. 6.2, experiments of this type emphasize the portion of the total calculational model which deals with the neutron slowing down into the thermal group and the subsequent absorption of neutrons in U^{235}. For each experiment in this series, the critical size over a range of temperatures was determined in an effort to emphasize the temperature-dependent parameters in the model.

These experiments were performed at several slab widths ranging from about 6 in. wide up to about 24 in. In general, the increased width from core to core, which would lead to a more reactive core due to the same values of k_∞ in a larger fuel region, has been compensated for by reducing the fuel loading density to maintain a critical array. At any particular slab width the fuel density is increased in order to maintain criticality at higher temperatures (see Table 6.19). The variation in the width of these slabs should emphasize the portion of the model which treats the neutron leakage into the reflector. This variation is then observed as a function of temperature.

TABLE 6.19 — DESCRIPTION OF PTR CLEAN CORE EXPERIMENTS

Core Number	Description	Dimensions* (in.) (horizontal plane)	Metal-Water Volume Ratio	Fuel Density (g/liter)	Temperature (°F)	Excess Reactivity with All Rods Out (cents)
1	Clean cores (6" wide)	6 x 32	1.72	218	331.0	12.7
		6 x 32	1.72	317	478.0	16.7
2	Clean cores (8" wide)	8 1/4 x 32	1.54	53.2	79.0	0
	with 1/4" water gap bisecting the narrow dimension	8 1/4 x 32	1.54	54.6	265.1	10.4
		8 1/4 x 32	1.54	56.6	334.0	7.4
		8 1/4 x 32	1.54	61.5	403.0	15.4
		8 1/4 x 32	1.54	73.8	506.0	10.1
3	Clean cores (8" wide)	8 x 24	1.54	76.5	267.5	12.4
		8 x 28	1.54	76.5	382.2	10.8
		8 x 40	1.54	76.5	502.0	25.0
4	Clean cores (14" wide)	14 x 32	1.54	26.0	119.0	8.6
		14 x 32	1.54	27.3	245.5	0
		14 x 32	1.54	29.4	414.0	5.1
		14 x 32	1.54	30.1	465.0	0
		14 x 32	1.54	31.5	501.0	0

TABLE 6.19 — DESCRIPTION OF PTR CLEAN CORE EXPERIMENTS (Continued)

Core Number	Description	Dimensions* (in.) (horizontal plane)	Metal-Water Volume Ratio	Fuel Density (g/liter)	Temperature (°F)	Excess Reactivity with All Rods Out (cents)
5	Clean cores (24" wide)	24 x 32 24 x 32 1/2† 24 x 32 1/2†	1.54 1.54 1.54	19.1 20.5 21.2	224.5 399.3 548.0	6.4 9.0 0
6	Clean cores (24" wide) with 1/4" gap	24 1/4 x 24 1/4 24 1/4 x 24 1/4 24 1/4 x 24 1/4	2.38 2.38 2.38	24.3 25.5 32.8	237.5 299.0 551.5	5.8 6.4 210.0
7	Clean core, (8" wide)	8 x 32 8 x 32 8 x 32	1.148 1.148 1.148	52.0 54.6 65.7	203.5 374.5 500.5	20.4 18.0 7.5

*In each case the core height was 30 in. for the PTR slab experimental series.
†A 1/2-in. water channel was introduced in this dimension to allow penetration of control rods.

In water reflected cores, the higher slowing-down density in the reflector causes the thermal flux to increase near the core reflector interface. By introducing metal into the reflector, the thermal flux may be flattened near the reflector. Table 6.20 lists results for a set of experiments in which metal was introduced into the reflector region. These experiments were intended to emphasize further the portions of the model which deal with the leakage of core neutrons into the reflector and with the effect of the reflector on core reactivity. It is noted that Core 12 had a Zircaloy water reflector while Cores 13 and 14 had stainless steel reflectors.

2. *HTTF Experiments*

In addition to the PTR experiments, several clean slab experiments have been performed in the HTTF, one of which is discussed here. The major difference in this HTTF experiment from those discussed for the PTR was in the method of construction of the fuel element. The HTTF core was made up of square Zircaloy module boxes with an effective outside dimension of 1.563 in. with an effective wall thickness of 0.053 in. Figure 6.30 shows a detailed cross section of this module box construction. The actual outside dimension of the box is 1.537 in. with a wall thickness of 0.040 in. A Zircaloy-2 shim, 0.026 in. thick, was inserted between module boxes, thus resulting in the above effective dimensions. The module box design is seen to be quite similar to the type of fuel element used in the experiments described in Sect. 6.2.A. The fuel plates were 9 weight percent enriched U-Zr alloy fuel meat which was 0.060 in. × 1.386 in. × 30 in. and which was clad on each face with 0.015 in. of Zircaloy-2. The fuel elements were held in place by Zircaloy-2 clips welded to the two opposite sides of the module box. The average metal-to-water ratio was 1.2 with an average U^{235} density of 168 g/liter. Control for this experiment was maintained with four fuel-bearing control rods in the manner described in clean slab experiments with small bundle box geometry for the low temperature experiments. In this case, each rod was the size of a single module box. Two cores, each four module boxes wide but of different lengths, were assembled using the Zircaloy-2 module boxes in a closely packed array. Water temperature was varied to bring the cores close to critical, and the excess reactivity was determined from a period measurement in the rods-out condition or from a rod-bank calibration. The results are listed in the Table 6.21 for the series of clean slab experiments described here.

TABLE 6.20 — DESCRIPTION OF PTR REFLECTOR EXPERIMENTS

Core Number	Description	Fuel Region Dimensions (in.)	Core Metal-Water Volume Ratio	Reflector Metal-Water Volume Ratio	Core Fuel Density (g U^{235} /liter)	Temp. (°F)	Excess Reactivity (cents)
12	Clean core with Zircaloy water reflector 6" wide on each side of slab	14 x 32 1/2*	1.54	1.54	25.2	151.4	5.5
					25.9	284.3	13.1
					27.9	441.7	10.2
					30.6	544.1	6.6
13	Same as 12 except with stainless steel reflector	14 x 32 1/2*	1.54	0.325	30.0	104.8	11.2
					32.0	293.2	17.4
					34.0	410.0	10.6
					38.1	499.4	0
14	Same as 13 with stainless steel reflector	14 x 32 1/2*	1.54	4.30	27.9	109.2	12.8
					29.9	266.2	10.4
					32.6	413.7	11.2
					36.7	505.4	12.6

*Two parallel 1/4-in. control rod water gaps are included in this dimension, each 18 in. from the centerline.

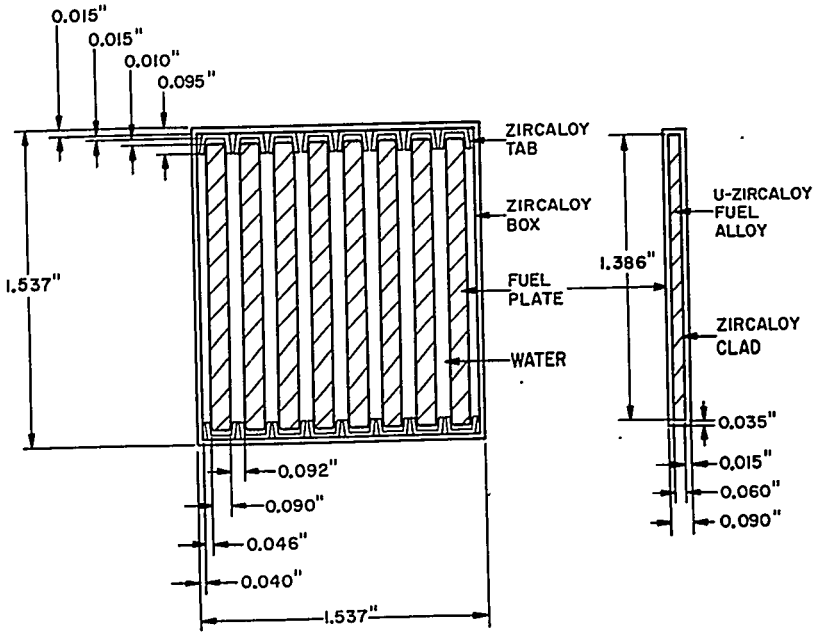

FIGURE 6.30. Schematic Arrangement of Fuel Module and Fuel Element for High Temperature Slab Experiments in the HTTF.

TABLE 6.21 — DESCRIPTION OF HTTF CLEAN SLAB EXPERIMENTS

Temp. (°F)	Core Size, thickness x height x length (in.)	Experimental k_{eff} with All Rods Out*	Fuel Density (g/liter)	Metal-Water Ratio
65	6.28 x 30 x 17.3	1.007	168.0	1.2
232	6.28 x 30 x 17.3	1.004	168.0	1.2
459	6.28 x 30 x 23.6	1.002	168.0	1.2

*The uncertainty in the measurement of k_{eff} is about ±0.002.

C. Calculational Model

In general, the same type of group diffusion theory model described in clean slab experiments with small bundle box geometry was used for both types of experiments discussed here. However, while the model is basically the same, several

notable differences exist in the application, particularly for the analyses obtained for the PTR experiments. In addition to presenting the dependence of the reactivity calculations on the temperature of the system, the results will compare two basic methods or techniques which have been used for the calculation of group-averaged cross sections. To understand the difference between these two techniques, it is worthwhile to separate the calculation of group-averaged cross sections into two distinct phases. First, a set of energy-dependent microscopic cross sections are required to represent the absorption, fission, and scattering properties of each material in the reactor. Secondly, these microscopic cross sections must be energy-averaged to obtain the group-dependent values. This second phase is where the basic difference in the two techniques becomes apparent. For want of a better means of identification, the two techniques used for the group-averaging process are referred to here as the WOXX method and the MUFT-SOFOCATE method. The WOXX technique was described in some detail in Sect. 6.2.C where it was the method used to obtain most of the calculated results. The MUFT-SOFOCATE method was described in detail in the general analytical model for the small bundle box geometry clean slab experiments and was the method used extensively to obtain the low temperature results of Sects. 6.2.A and 6.2.B.

It should be emphasized that several sets of microscopic cross-section data may be used with either technique. However, even if the same microscopic data are used in both methods, the two techniques, in general, will yield different results for the group-averaged values. Because of the use of the several sets of cross-section data, it is sometimes difficult to draw conclusions from comparisons of the results obtained from each method. However, it has been observed that for a particular set of cross-section data the MUFT-SOFOCATE technique will yield results which are more consistent over a wider range of experiments than are the results obtained with the WOXX technique. This observation is reassuring, since the MUFT-SOFOCATE technique is more sophisticated theoretically than is the WOXX method. Over a narrow range of experimental conditions, however, the choice of a particular set of cross sections can be made such that the WOXX method yields reasonably consistent results. For this reason, as well as because of its relative simplicity, the WOXX method has had some historical importance in reactor design activities; hence, results are presented here and compared with the MUFT-SOFOCATE method. The specific differences from the model described in Sect. 6.2.A.3 are briefly itemized below.

1. Group Structure

It will be seen in an examination of the results that both three- and four-group diffusion calculations have been made in the analysis of the PTR experiments. A three-group structure is common to the WOXX method, as discussed in Sect. 6.2.C. In this three-group structure, Group 1 extends from 10 Mev to 180 kev, with Group 2 ranging from 180 kev down to the energy equivalent of four times the effective temperature of the assembly ($4T_{eff}$). The thermal neutron group then extends from this cutoff energy down to 0 ev in the WOXX system. The effective temperature of the assembly, T_{eff}, is defined by Deutsch[21] to be higher than the physical temperature of the system by the amount required to take into account the hardening of the spectrum due to neutron absorption.

For the MUFT-SOFOCATE results listed for the PTR experiments, both four-group and three-group results are tabulated. The four-group structure is identical to that defined in Sect. 6.2.A.3 for the analysis of the low temperature experiments. Thus, Group 1 ranges from 10 Mev to 0.821 Mev, Group 2 from 0.821 Mev to 5.53 kev, Group 3 from 5.53 kev to 0.625 ev, and the thermal group from 0.625 ev down to 0 ev. The three-group structure used with the MUFT-SOFOCATE method involved the coalescing of Groups 1 and 2 of the four-group scheme into a single group. Thus, the three-group structure used for these calculations is not the same as the three-group WOXX method described above.

For the parameters of the HTTF experiments, a 55-group structure was also used in which one thermal group was coupled to the 54 fast groups used in the MUFT multigroup calculation. This was accomplished using the P1MG routine. Comparisons with the four-group model showed a difference of about 0.3 percent in reactivity, indicating that the four-group model was a reasonable approximation to the multigroup system for the set of HTTF experiments discussed here.

2. Fast Group Constants

For the PTR experiments two methods of generating the fast group constants were investigated in the first analyses performed on these experiments. The three-group WOXX calculations used the Deutsch[21] prescription in which the fast spectrum is treated as a $1/E$ spectrum. The four-group MUFT-SOFOCATE calculations used the slowing-down treatment of the MUFT prescription with the earlier library[23] of cross sections (Table 6.3), which did not include such items as an explicit treatment of the inelastic scattering in zirconium or oxygen. The cross-section data for these two methods are

comparable and, thus, a comparison of these results points out the differences between the techniques rather than emphasizing the differences in the cross-section data.

The three-group MUFT-SOFOCATE analyses show the differences that have been obtained with another set of cross-section data[2] coupled with the MUFT routine. These recent calculations were performed with the aid of the FICS[25] routine which performs a least square fit to the results of group cross sections that are obtained from MUFT in the fast group and KATE[5] (a later version of the SOFOCATE routine) for the thermal group. The cross-section data[2] used for the three-group MUFT-SOFOCATE calculations contain the most recent information on zirconium, oxygen, and U^{235} (Table 6.22). It should be noted that these data are slightly different from the data used in the analyses of the low temperature experiments of Sect. 6.2.A.

For the analysis of the HTTF experiments, the MUFT routine was also used for the generation of the fast group constants. In this case, the cross-section library used was that identified[2] as including the inelastic scattering in zirconium and oxygen as well as an explicit treatment of the resonance fission in U^{235} (Table 6.2). These cross sections were identical to those used in the analyses of the cold experiments discussed in Sect. 6.2.A.

TABLE 6.22 — CROSS SECTIONS USED IN FICS ANALYSIS OF THE PTR HIGH-TEMPERATURE EXPERIMENTS*

Element	Transac Identification Symbol
H	001
O	102
Zr	970
U^{235}	218
B^{10}	029

*Actual cross sections are tabulated in Ref. 2. While the zirconium library is not listed in the reference, it is similar to the zirconium element identified as 103, with the exception of the inelastic scattering terms which are based on a Hauser-Feshbach fit.

3. *Thermal Group Constants*

Hardened Maxwellian constants are used in the three-group Deutsch prescription associated with the WOXX routine for one set of the PTR calculations. The term hardened Maxwellian means that the cross sections are averaged over a Maxwellian spectrum which is evaluated at the effective temperature of the system. This effective temperature is defined by Deutsch[21] as that temperature of a Maxwellian distribution of velocities which yields the same average neutron velocity as a Wigner-Wilkins distribution. Thus, this technique will yield results similar to those obtained by using a Wigner-Wilkins (hardened) spectrum. For the PTR four-group MUFT-SOFOCATE results, the thermal group constants were directly averaged over the hardened (Wigner-Wilkins) spectrum using the SOFOCATE[4] routine. For the PTR three-group MUFT-SOFOCATE results, the mixed number density model,[7] discussed in Sect. 6.2.A and in Chap. 3, was used in the thermal group. Three types of thermal group constants were compared in the HTTF analyses, and the results are tabulated. Model 1 used the hardened (Wigner-Wilkins) constants, whereas in Model 2 Maxwellian constants were used. In Model 3, the mixed number density model[7] was used.

In all other respects, the calculational model was quite similar to that used for the cold analyses described in Sect. 6.2.A.3. Again thermal group plate disadvantage factors (see Chap. 4, Sect. 4.2) were obtained from one-dimensional one-velocity calculations which used a high order transport approximation (TRANVAR[26] in the case of the PTR experiments and FLIP[8] in the HTTF analyses). For these transport calculations, the fuel region was divided into naturally recurring regions called cells; within a cell each core component, be it a fuel plate, a Zircaloy plate, or interstitial water, was explicitly represented. The effective fuel load or the fuel plate disadvantage factors were found by flux- and volume-weighting the fuel cross section with the fluxes determined from the transport calculation. Thus, the homogenized equivalent to the fuel region was determined, where the fuel region was considered to extend up to the core-reflector or core-gap interface. The method described is similar to Method 1 as shown in Fig. 6.4. (Homogenization techniques are discussed in detail in Chap. 4, Sect. 4.3.)

For the PTR experiments the analyses were performed by the two-dimensional diffusion theory routine, CURE,[24] while the PDQ[27] routine was used for the HTTF experiments. As before, a transverse buckling represented the effect of the axial dimension in these two-dimensional radial calculations.

D. Results of Core Reactivity Calculations

Comparisons of the eigenvalues calculated for the just critical experimental condition are listed in Tables 6.23, 6.24, and 6.25 for the PTR experiments and for the HTTF experiments. Since these results have been normalized to just critical values, all calculated results would be 1.000 if in exact agreement with experiment. Table 6.23 lists the results obtained for the set of clean core experiments performed in the PTR facility. Table 6.24 presents the results obtained for the various PTR reflector experiments. The comparison of the two alternate techniques for the calculation of group constants yields some interesting results when the experiments presented in Tables 6.23 and 6.24 are considered as a whole. First, the total spread (difference between the largest and smallest eigenvalues) in the calculated eigenvalues for critical is 6.2 percent Δk for the WOXX method. Using comparable cross-section information in the four-group MUFT-SOFOCATE method, the total spread is reduced to 4.5 percent Δk. When the cross-section data have been improved to include the more recent information, as has been done in the three-group MUFT-SOFOCATE results, this spread is reduced to 2.5 percent over all of the experimental conditions listed. This improvement with both the technique used and with the cross-section data is expected, since the MUFT-SOFOCATE technique is more sophisticated theoretically and since the more recent cross-section information should be more accurate.

A further examination of Tables 6.23 and 6.24 indicates that with either cross-section technique little evidence of a temperature dependence exists in the results. At best, there is a slight indication that as the temperature was increased the calculated values of k_{eff} decreased slightly. For the most recent cross-section information, this decrease is slight, with the indication that, in general, the calculated values decrease by about 0.5 percent Δk from 80°F to 500°F.

The results obtained on the HTTF experiments are presented in Table 6.25. The difference between the three types of thermal group treatments is apparent and shows how the mixed number density model closely approximates the hardened (Wigner-Wilkins) model reactivity calculation. The fuel region homogenization technique used in obtaining the results in Tables 6.23, 6.24, and 6.25 has been to homogenize the fuel region up to the reflector interface. This technique was identified as homogenization Method 1 in Sect. 6.2.A. For the HTTF experiments, the sensitivity of the calculated value of k_{eff} to the homogenization method was determined for each of the temperatures considered. When the fuel region was homogenized

TABLE 6.23 — COMPARISON OF EXPERIMENT AND CALCULATION FOR THE PTR CLEAN CORE EXPERIMENTS

Core Number	Temp. (°F)	k_{calc}*		
		WOXX	MUFT-SOFOCATE	
		(three-group) Early Cross Sections	(four-group) Early Cross Sections	(three-group) Recent Cross Sections
Core 1 (6" wide)	331.0	1.013	0.991	1.024
	478.0	1.012	0.977	1.019
Core 2 (8" wide, 1/4" gap)	79.0	0.990	0.985	1.018
	265.1	0.981	0.975	1.012
	334.0	0.982	0.969	1.011
	403.0	0.983	0.972	1.016
	506.0	0.980	0.963	1.014
Core 3 (8" wide)	267.5	0.995	0.985	1.022
	382.2	0.994	0.982	1.020
	502.0	0.992	0.978	1.019
Core 4 (14" wide)	119.0	1.012	0.988	1.014
	245.5	1.009	0.983	1.029
	414.0	1.004	0.977	1.004
	465.0	1.002	0.971	1.007
	501.0	1.000	0.971	1.008

TABLE 6.23 — COMPARISON OF EXPERIMENT AND CALCULATION FOR THE PTR CLEAN CORE EXPERIMENTS (Continued)

Core Number	Temp. (°F)	k_{calc}*		
		WOXX	MUFT-SOFOCATE	
		(three-group) Early Cross Sections	(four-group) Early Cross Sections	(three-group) Recent Cross Sections
Core 5 (24" wide)	224.5	1.034	1.008	1.014
	399.3	1.032	1.004	1.014
	548.0	1.023	0.988	1.009
Core 6 (24" wide, 1/4" gap)	237.5	1.036	0.990	1.018
	399.0	1.038	0.985	1.013
	590.0	1.033	0.966	1.012
Core 7 (8" wide)	203.5	0.996	--	1.022
	374.5	0.988	--	1.016
	500.5	0.989	--	1.018

*Eigenvalues normalized to $k_{exp} = 1.000$.

TABLE 6.24 — COMPARISON OF EXPERIMENT AND CALCULATION FOR THE PTR METAL-WATER REFLECTOR EXPERIMENTS

Core Number	Temp. (°F)	k_{calc}*		
		WOXX	MUFT-SOFOCATE	
		(three-group) Early Cross Sections	(four-group) Early Cross Sections	(three-group) Recent Cross Sections
Core 12	151.4	1.040	0.993	1.022
Zr reflector	284.3	1.042	0.987	1.019
(M/W = 1.54)	441.7	1.043	0.982	1.021
	544.1	1.037	0.972	1.021
Core 13	104.8	1.016	--	1.011
stainless steel	293.2	1.011	--	1.005
reflector	410.0	1.007	--	1.004
(M/W = 0.325)	499.4	1.006	--	1.004
Core 14	109.2	1.018	--	1.006
stainless steel	266.2	1.015	--	1.015
reflector	413.7	1.013	--	1.010
(M/W = 4.3)	505.4	1.010	--	--

*Eigenvalues normalized to k_{exp} = 1.000.

TABLE 6.25 — COMPARISON WITH CALCULATION FOR HTTF CLEAN SLAB EXPERIMENTS

Temp. (°F)	Calculated Eigenvalue for Critical		
	Model 1	Model 2	Model 3
65	1.000	1.003	1.000
232	1.001	1.006	1.002
459	1.001	1.007	1.003

Experimental and Calculated Temperature Coefficient (10^{-4} $\Delta k/°F$)

Temp. (°F)	Experimental	Calculated Model 1
65	+1.10 ±0.05	+1.19
232	--	--
459	-3.82	-3.82

NOTES:

Model 1: Four-group, MUFT (new library), hardened Wigner-Wilkins.
Model 2: Four-group, MUFT (new library), Maxwellian.
Model 3: Four-group, MUFT (new library), Mixed Number Density.

only to the point where the fuel elements actually end, and a small metal-water region was included between the fuel region and the reflector in the manner identified as homogenization Method 2 in Sect. 6.2.A, a reduction of 0.6 percent Δk was observed in each of the HTTF calculations. Thus, the same degree of sensitivity to the homogenization method as was observed in the low temperature experiments is seen also in these high temperature results.

A comparison of calculated and experimental temperature coefficients is also presented in Table 6.25 for the HTTF experiments. The results are in excellent agreement with the experimental values for this particular experiment.

E. Results of Activation Distribution Comparisons

In addition to the comparisons discussed above between the calculated and experimental values of k_{eff} for these slab

experiments, several results have been obtained comparing the neutron activation distributions throughout the slabs as a function of temperature. The set of experiments performed in the HTTF is described here in order to present typical examples of the results which have been obtained in comparing the measured and calculated neutron activations. In the HTTF, the activation distributions were made with U^{235}-zirconium (6 weight percent) wires approximately 0.030 in. in diameter and 0.500 in. long. After the irradiation the wires were β-counted in order to determine the resulting fission product activity. Two means of holding the wires in the core were utilized. They were either placed in holes drilled in the fuel elements or they were strung in ladder fashion on parallel stainless steel wires and located in water gaps between the fuel elements. The method of holding the wire within the fuel plate itself is illustrated in Fig. 6.31. The wire activation data were corrected for (1) the departure of the activation of an individual point from the module box average which was due to activation peaking in and around lumped core materials such as fuel plates and module box structure, including peaking effects in both thermal neutron flux and thermal neutron spectrum; (2) the departure of each measured wire activation from the true activation assuming no perturbation of the activation distributions due to the presence of the wire detectors, including the effects of adjacent wires at any given position; and (3) other effects such as the integration effect of a finite-sized wire in an activation gradient, the effects of recoil fission products collecting on activation wires placed in fuel plates as opposed to positions in water channels, and differences in weight groups of wires used in various activation measurements.

Experimental results for the clean slab experiments performed in the HTTF are presented in Figs. 6.32 through 6.35. In Fig. 6.32 a comparison is shown of the experimental results and the calculated values for the total activation of the bare or unshielded uranium loaded detectors. These results include the contribution to the total activation of neutrons of all energies. The experimental results were obtained by the ladder method, as discussed above; the actual points were measured in the water channels between the fuel elements and a correction then applied. Calculated values are presented for three methods of representing the thermal neutron group, the mixed number density model, a Maxwellian spectrum model, or the hardened spectrum model of Wigner-Wilkins. The low temperature results (65.6° F) are shown in Fig. 6.32 for the HTTF clean slab experiment. These results show that either the mixed number density

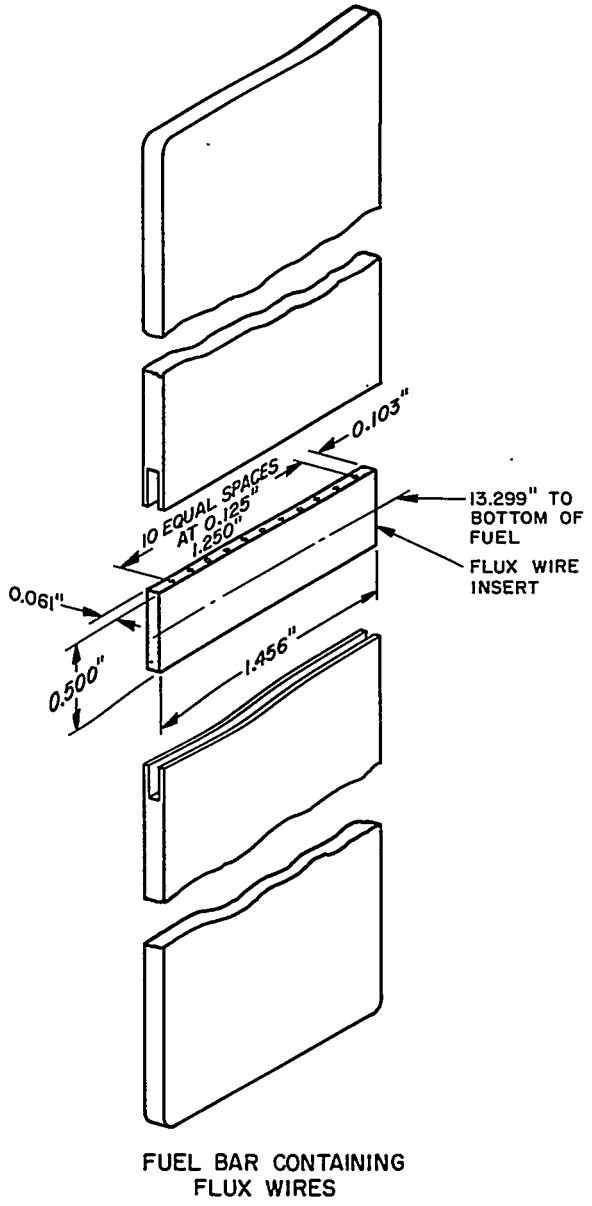

FIGURE 6.31. Method of Holding Flux Wires for Activation Measurements within Fuel Elements in the HTTF Experiments.

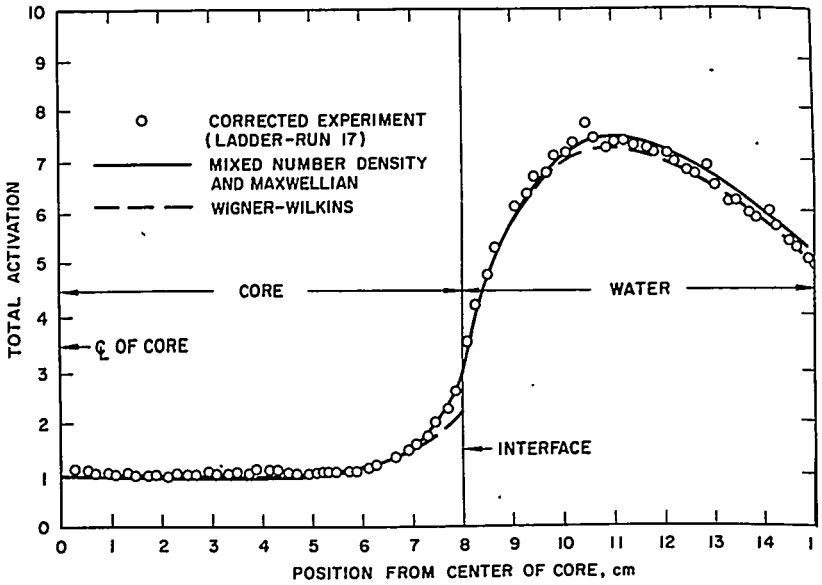

FIGURE 6.32. Comparison of Calculated and Measured Total Activations for HTTF Core 1 at 65.6°F.

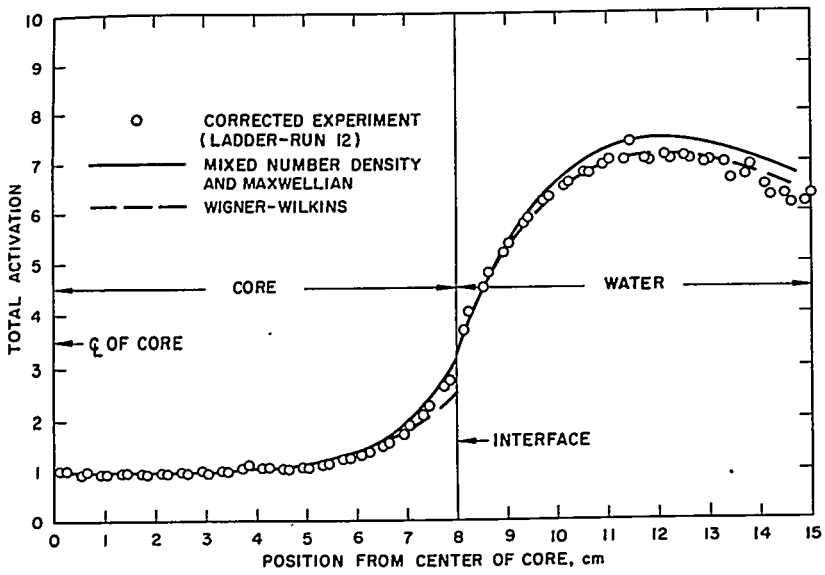

FIGURE 6.33. Comparison of Calculated and Measured Total Activations for HTTF Core 1 at 459°F.

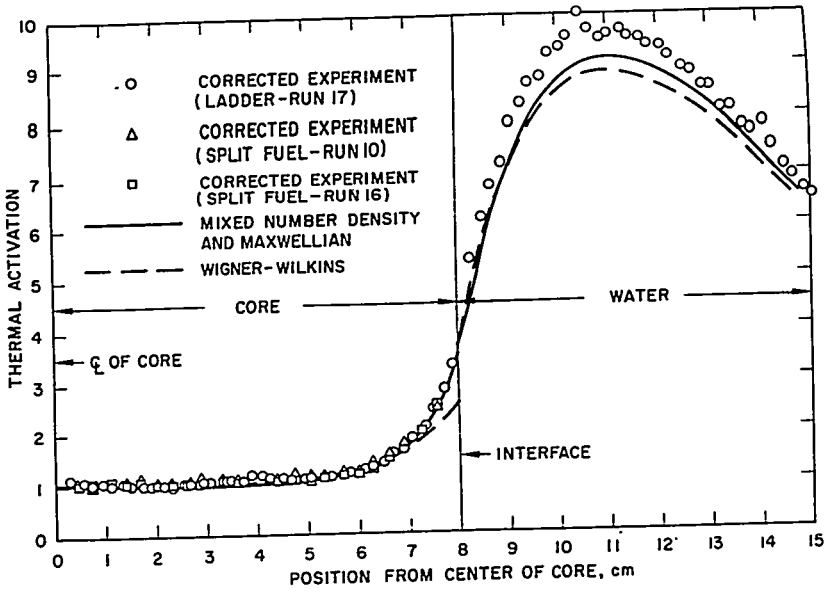

FIGURE 6.34. Comparison of Calculated and Measured Thermal Activation for HTTF Core 1 at 65.6°F.

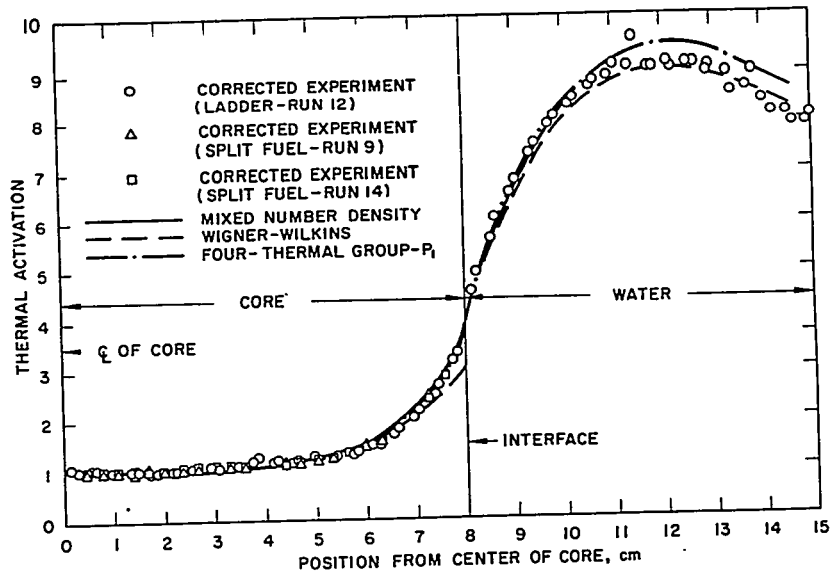

FIGURE 6.35. Comparison of Calculated and Measured Thermal Activations for HTTF Core 1 at 459°F.

model or the Maxwellian model is in reasonable agreement with experiment for describing the activation shape in the fuel region and, in particular, the activation peaking near the fuel-reflector interface. However, it is observed that the use of the hardened (Wigner-Wilkins) spectrum substantially underestimates the peaking at the interface. In Fig. 6.33 these same trends are apparent at high temperature (459° F). In this case, the mixed number density model slightly overestimates the peaking at the interface, while the underestimate of the hardened spectrum model is not as severe as at the lower temperatures. In Figs. 6.34 and 6.35 the portion of the activation due to thermal neutrons only are compared for these same low and high temperature cases. These results again demonstrate the agreement of the mixed number density model or a Maxwellian model in describing the interface peaking and show the disagreement obtained with the hardened spectrum. It should also be noted that none of the models is particularly successful in describing the thermal neutron peaking in the water reflector region itself. This mismatch is not particularly significant to a nuclear designer who will be concerned mainly with the distribution in the fuel region where most of the captures are occurring and where the identification of peaking is necessary to assure adequate cooling of the fuel elements. This mismatch does point out, however, that basic limitations do exist in the overall calculational model even though the prediction of the distribution in the fuel region seems adequate.

Comparisons are also presented in Figs. 6.34 and 6.35 between the activations measured with the wires located within the fuel plates themselves, in the manner shown in Fig. 6.31, as compared with the results obtained from the ladder method. These comparisons show the close agreement between the two experimental methods.

F. Conclusions

The comparisons between calculations and experiments given in the tables are the result of several years of effort to develop analytical methods for treating pressurized water reactors. This discussion has presented only one of the many extensive comparisons which have been made to test the adequacy of the overall calculational model. The early results obtained for the PTR series, based on the Deutsch three-group scheme and on the four-group hardened thermal model using the earlier MUFT cross-section library, showed little consistency over the range of experiments studied. It was observed, with the same cross-section information, that the MUFT-SOFOCATE

method yielded more consistent results over a wide range of experiments that those obtained with the WOXX method. However, no consistent trend with any single parameter, such as metal-to-water ratio or temperature, was exhibited. Hence, it was difficult to use the experiments to indicate where improvements in the analytical methods should be made, even though in some cases they pointed out the areas of the model which should be investigated. However, when better basic cross-section data became available, such as was used in the three-group MUFT-SOFOCATE results as approximated by the FICS routine, a definite improvement appeared in the consistency of the comparison over the range of experiments studied.

Even though consistency has been obtained there remains the matter of the absolute level of the calculated reactivity. The PTR experiments give a calculated reactivity 1 to 2 percent above unity, based on the later cross-section information, while the HTTF calculations based on Model 3 (the model most similar to the later PTR results) show calculated values of k_{eff} very close to unity. It is somewhat difficult to compare the results described here with those presented in Sect. 6.2. There it was noted that the reactivity of a wide range of experiments was capable of being predicted to within about 1 percent $\Delta\rho$ when using the mixed number density model coupled with a fast group description based on the newer cross-section library. The closest overall analytical model here to the one used in Sect. 6.2 is the model used on the HTTF analyses, and the HTTF results agree quite well with the low temperature experiments. The analyses of the PTR experiments, using an even later set of cross sections[2] (Table 6.22), are similar to the model used in the low temperature analyses with the only other apparent differences being in the coalescing of the four-group structure into a three-group scheme as well as the use of an homogenization technique noted previously as Method 1. The use of this model in the analysis of the PTR experiment leads to consistent results even though the absolute eigenvalue is above unity. Whether the difficulty lies with the analytical methods or with the experimental results, such as materials inventory or core dimensions, is not known at this time.

These results do point out, however, some facts that the core designer must be careful to observe. Not only must a calculational technique yield consistent results, so that predictions made with the model can be accepted with a certain degree of confidence, but these consistent results must also fall reasonably near a k_{eff} value of 1.000. This is because the value of k_{eff} for a critical reactor experimentally is exactly

unity. Thus, while the deviations from unity can (and indeed must) be treated as a bias, they still should remind the designer of the approximations inherent in the model which are causing the differences between experiment and theory. On the other hand, faced with an understanding of the approximations necessary in the overall model, the designer must be just as cautious not to place too much emphasis on obtaining calculated eigenvalues of exactly unity lest he be lulled into a false sense of overconfidence in the calculational model, containing as it does a delicate balance between many compensating effects. Finally, the designer must make enough careful comparisons with experiment to establish where the absolute eigenvalue falls with the specific set of cross-section data that he is using.

6.4 INVESTIGATIONS OF NEUTRON PEAKING IN HIGHLY ENRICHED CLEAN CRITICAL EXPERIMENTS

F. Feiner, S. Weinstein, and W. B. Wright

A. Introduction

In Sects. 6.2 and 6.3, critical assembly experiments on simple idealized geometries were shown to be excellent means of obtaining information on basic reactor physics phenomena. Data so obtained are extremely important in stimulating and guiding the development of improved analytical techniques which may subsequently be incorporated into practical reactor design methods. This section discusses another type of critical reactor experiment which investigates in detail the transient behavior of the neutron flux in a central test lattice region of a reactor. The analysis of the experiment indicates how the interaction of theory and experiment can lead to improvements in the overall calculational model.

The particular experiment discussed here is concerned with the behavior of the neutron flux near medium discontinuities in the central lattice region of a reactor. It has been noted previously that calculations are generally performed by assuming that a neutron energy distribution peculiar to an infinite medium exists within a given region and that the group constants obtained from this spectrum can be applied up to the boundary of the region. This is the usual approximation followed, for example, in the use of region-dependent constants as calculated by the SOFOCATE or KATE thermal group constant routines and the MUFT fast group prescription. Physically, such an abrupt change in spectrum is not realistic.

For this reason approximate methods have been developed to represent more closely the transition in the spectrum from one region to another. For example, in Sects. 6.2 and 6.3 it was noted that considerable use has been made of the mixed number density model as an approximation to a more accurate representation of the position-dependent spectrum in the thermal neutron group. With this model, which was discussed in Chap. 3, one boundary condition required across region interfaces, in addition to continuity of neutron current, is that of continuity of the neutron density rather than the neutron flux. This requirement forces the activation of a $1/v$ absorber to be smooth across an interface between dissimilar media. In addition, the use of the mixed constants (Maxwellian averaged diffusion coefficient coupled with Wigner-Wilkins averaged absorption and fission coefficients) in the mixed number density model is recognition of the fact that the spectrum of the gradient of the flux is close to a Maxwellian, at least near a water gap, whereas the spectrum of the flux seems to be close to a hardened Wigner-Wilkins.

This section describes comparisons which have been made with experiment for two other approximate methods developed to describe the change in the neutron energy spectrum near discontinuities in the medium. To formulate a theory or even a prescription to describe the phenomena encountered, a large amount of experimental data should be compared with calculational results. The plastic-moderated dry critical assembly designated as the Preliminary Pile Assembly (PPA), with its test lattice geometry, was considered to be well suited for a study of a number of lattices differing significantly in composition. To ease the performance of a large number of experiments, the size of the test lattice region was made just large enough so that, at its center, spectra characteristic of a full size core of the lattice compositions were achieved. The reactivity effect of the lattice on the whole reactor, however, was small, so that lattice changes could be made easily and safely.

B. Experimental Arrangement

As shown in Fig. 6.36, the PPA is a four-region assembly consisting of: (I) the central test lattice region, (II) the main part of the core, (III) a booster region, and (IV) a reflector. The central region is approximately 8.4 in. in diameter. In hydrogen-moderated lattices, this is sufficient to achieve the infinite medium spectrum of the lattice in question at the center, provided a number of restrictions are observed: (1) If the metal-to-moderator volume ratio is low, i.e., less than

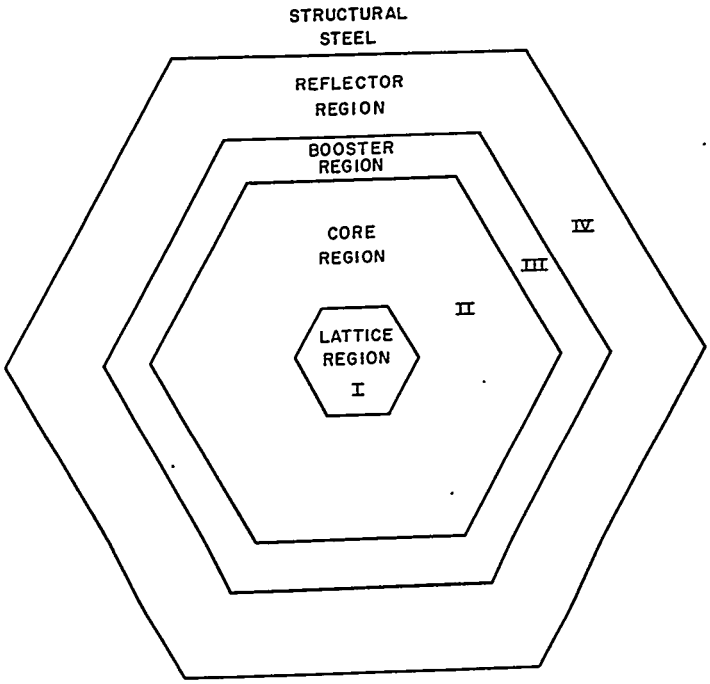

FIGURE 6.36. Geometry of the PPA Reactor Showing the Central Test Lattice Region in Which the Flux Transients Were Measured.

0.5, the k_∞ of the test lattice region should be between 0.9 and 1.2. (2) If the metal-to-moderator volume ratio is greater than 1, k_∞ may be as great as 1.4, but care must be taken that no slabs of material are inserted into the test lattice region which would allow significant neutron streaming in from the core region (II). When these conditions are satisfied, one can show experimentally and analytically that the infinite medium spectrum peculiar to the lattice region composition is achieved. Experimentally, this is seen by performing a radial flux traverse and noting that the buckling near the axis of the lattice region is very small, indicating very slight leakage into or out of the region. Calculationally, one can compare the flux ratios obtained from calculations for an infinite medium of this composition with that for simple one-dimensional radial calculations of the experiment. Results so obtained are shown in Table 6.26 for a number of lattices studied. The condition imposed on k_∞ of the lattices studied means that it is not possible to study directly all compositions of practical interest. However, since the neutron spectrum is determined by the ratio of absorption to scattering, it is possible to produce spectra of interest by replacing some fuel with poison materials and,

thus, lower the k_∞ to acceptable values without affecting the physics of the problem.

TABLE 6.26 — PPA LATTICE AND INFINITE MEDIUM EPITHERMAL TO THERMAL FLUX RATIOS

Lattice*	$(FR)_{PPA}$†	$(FR)_{\text{infinite medium}}$
L-3	2.45	2.39
L-4	0.72	0.68
L-5	1.29	1.26
L-7	4.27	4.32

*See Table 6.28 for characteristics of the lattices.
†$(FR)_{PPA}$ = Ratio of epithermal to thermal flux from a four-group one-dimensional diffusion calculation.

The core region (II) of the PPA consists of slugs (Fig. 6.37) held in a hexagonal matrix of steel tubes. Two-inch diameter discs of enriched uranium-aluminum alloy, aluminum, and polyethylene are threaded on 3/16-in. diameter steel rods to form a repeating array of cells each 1.3 in. long. The smeared or homogenized atom densities of the elements in the core, both actual and effective (i.e., flux-weighted), are presented in Table 6.27. The booster region (III) is similarly constructed. The fuel density in this region is roughly twice as great as in the core and serves to flatten the radial flux shape. The reflector region (IV) is composed of polyethylene cylinders inserted into the matrix tubes.

The control rods are located in the interstices between matrix tubes in the booster region (III). In this region, for certain experiments, cadmium slivers are inserted as reactivity shims, so that activations may be performed with the control rods essentially all out of the reactor.

Figure 6.38 exhibits some of the component materials of the test lattice region. Hexagonal slabs of polyethylene, iron, fuel, and aluminum form the building blocks from which the lattices are constructed. These are stacked into the test lattice region drawer as shown in Fig. 6.39. A repeating array of small unit cells of the order of 0.1 to 0.2 in. thick is placed in the drawer in this manner.

TABLE 6.27 — PPA REGIONAL ATOM DENSITIES*

Region	Elements	Actual Atom Densities	Effective (Flux-weighted) Atom Densities
Core (II)	H	0.05160	0.05160
	C	0.02580	0.02580
	U^{235}	0.782×10^{-4}	0.483×10^{-4}
	U^{238}	0.56×10^{-5}	0.35×10^{-5}
	Al	0.00902	0.00556
	Fe	0.00537	0.00494
Booster (III)	H	0.03958	0.03958
	C	0.01979	0.01979
	U^{235}	0.223×10^{-3}	0.183×10^{-3}
	U^{238}	0.163×10^{-4}	0.134×10^{-4}
	Al	0.00422	0.00395
	Fe	0.00360	0.0033
	Zr	0.0111	0.0078
Reflector (IV)	H	0.0696	0.0696
	C	0.0348	0.0348
	Fe	0.00297	0.00297

*Atoms/barn-cm

Medium discontinuities are introduced into the lattices by substituting either moderator slabs or absorber plates for part of the lattice region. Substituting a moderator slab leads to a flux peaking transient, whereas the substitution of an absorbing slab leads to a flux depressing transient. Pure polyethylene and polyethylene plus absorbers were used for the moderator gaps, while hexagonal plates of cadmium and boron-loaded glass were used for the absorber experiments. Activation profiles were measured by activating small foils of materials with different energy responses to neutrons. In Fig. 6.40 are shown the hex plates which are especially equipped to have foils mounted in them, as well as an example of a detector foil. The foils, made of fuel, manganese, indium, and gold, were 7/16 in. in diameter and a few mils thick. They are mounted so as to minimize the

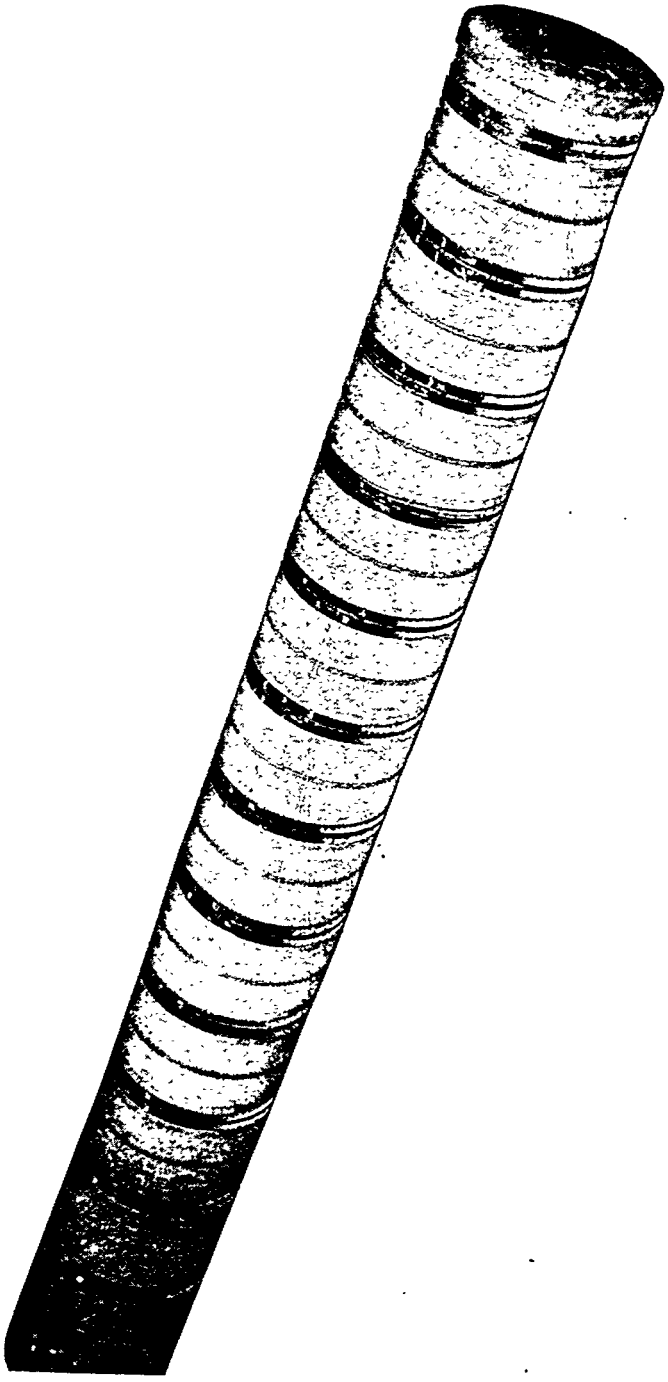

FIGURE 6.37. Core Slugs Consisting of 2-in. Diameter Discs of Uranium-Aluminum, Aluminum, and Polyethylene Which Formed the Core Region of the PPA.

FIGURE 6.38. Some Components of the Central Test Lattice Region for the Flux Transient Experiments in the PPA.

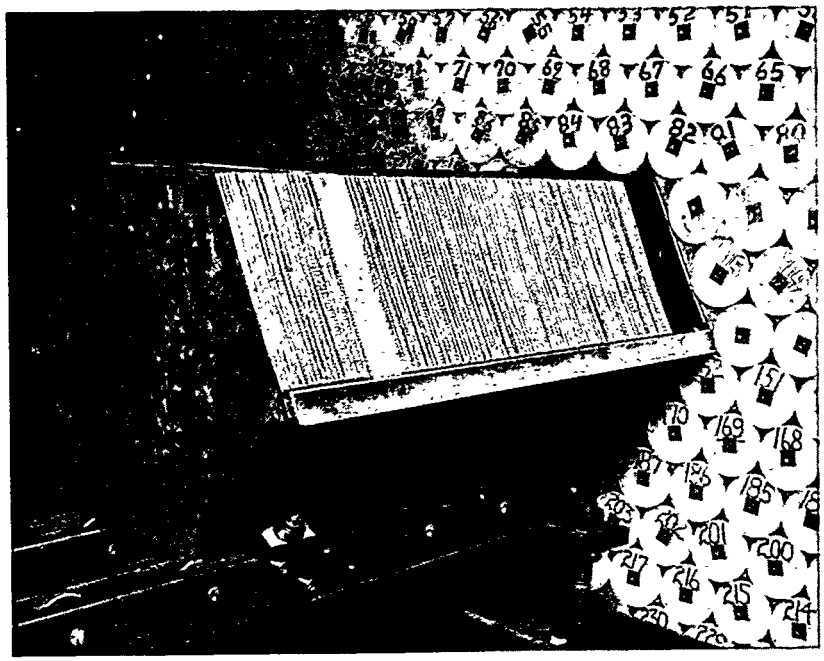

FIGURE 6.39. The Test Lattice Region of the PPA Being Inserted into the Core Region.

perturbing effects which they would impose on the lattice configuration. Measurements were also made with cadmium covers surrounding the foils in order to separate the sub-cadmium and epicadmium contribution to the activity. Figure 6.41 is a schematic representation of the arrangement of the foils for a measurement.

C. Characteristics of Lattices

The characteristics and salient parameters of the lattices studied are presented in Table 6.28. The metal-to-water ratios listed refer to the effective ratios had the moderator been in the form of water. These experiments span a sizable range both in metal-to-water ratio and in spectrum hardness which is characterized by

$$\beta\gamma = \frac{\Sigma_a (kT)}{\xi \Sigma_s}.$$

FIGURE 6.40. Method of Mounting Detector Foils within Hexagonal Plates of the Central Test Lattice Region.

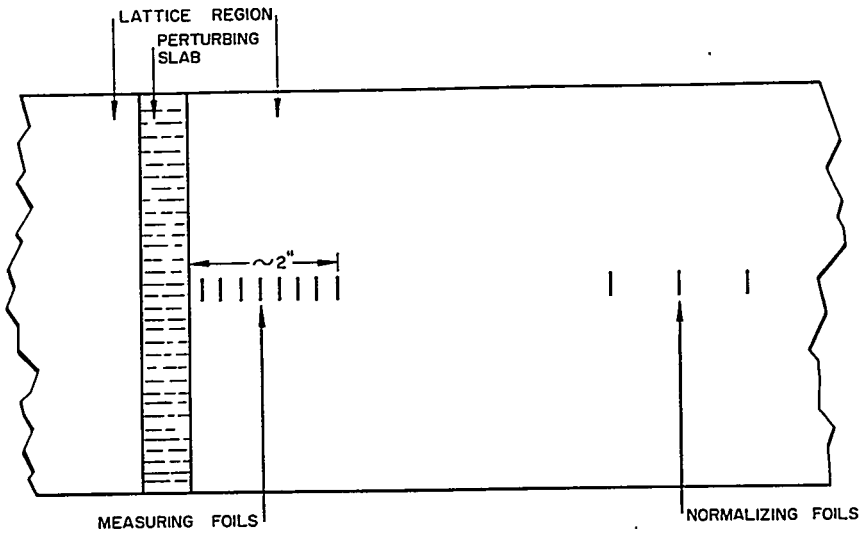

FIGURE 6.41. Arrangement of Detector Foils near the Discontinuity in the Central Test Lattice Region.

For the experiments, which were performed at room temperature, the $\beta\gamma$ was determined by evaluating Σ_a at 0.025 ev and $\xi\Sigma_s$ at 1 ev.

In Fig. 6.42, the unit cell construction of the lattices studied is shown schematically, as well as the construction of the moderator gaps.

D. Experimental Results

Figure 6.43 presents a schematic representation of the results obtained. By performing suitably normalized measurements with and without the perturbing absorber or moderator in place, two types of quantities can be obtained from the data: (1) The peaking or flux depression near or at the medium boundary, defined as the ratio of activity with the perturbation present to that without; and (2) the shape of the spatial transient, defined as the activity with perturbation minus activity without the perturbation. These quantities may be obtained for a number of detectors with and without cadmium covers.

A striking feature of the basic results is that, within the experimental uncertainty, the spatial transients could be represented by single exponentials, i.e., $A(x) = A_o e^{-x/L}$. In this relation, $A(x)$ is the position-dependent transient activity, A_o is an amplitude factor, x is the distance of the foil from the lattice-perturbation interface, and L is a characteristic length termed the

TABLE 6.28 — CHARACTERISTICS OF THE LATTICES

Lattice	Thermal k_∞	$\Sigma_a(kT)$ (cm^{-1})	$\beta\gamma=\frac{\Sigma_a(kT)}{\xi\Sigma_s}$	$\left(\frac{\Sigma_a}{\Sigma_T}\right)^*$	$\frac{\Sigma_a(kT)}{\Sigma_s}$	Hydrogen to U^{235} Atom Ratio	Fractional Metal Volume	Equivalent Metal-to-Water Ratio
L-3	1.03	0.146	0.43	0.119	0.213	147	0.71	3.4
L-4	1.13	0.062	0.096	0.039	0.078	632	0.73	2.3
L-5	1.11	0.074	0.19	0.069	0.133	316	0.57	1.1
L-7	1.02	0.30	0.78	0.167	0.295	79	0.74	2.7

*Maxwellian averages:

Σ_a = macroscopic absorption cross section
Σ_T = macroscopic total cross section
Σ_s = macroscopic epithermal scattering cross section
ξ = logarithmic energy decrement
= $\frac{2}{A+2/3}$ for $A > 10$
= 1 for $A = 1$

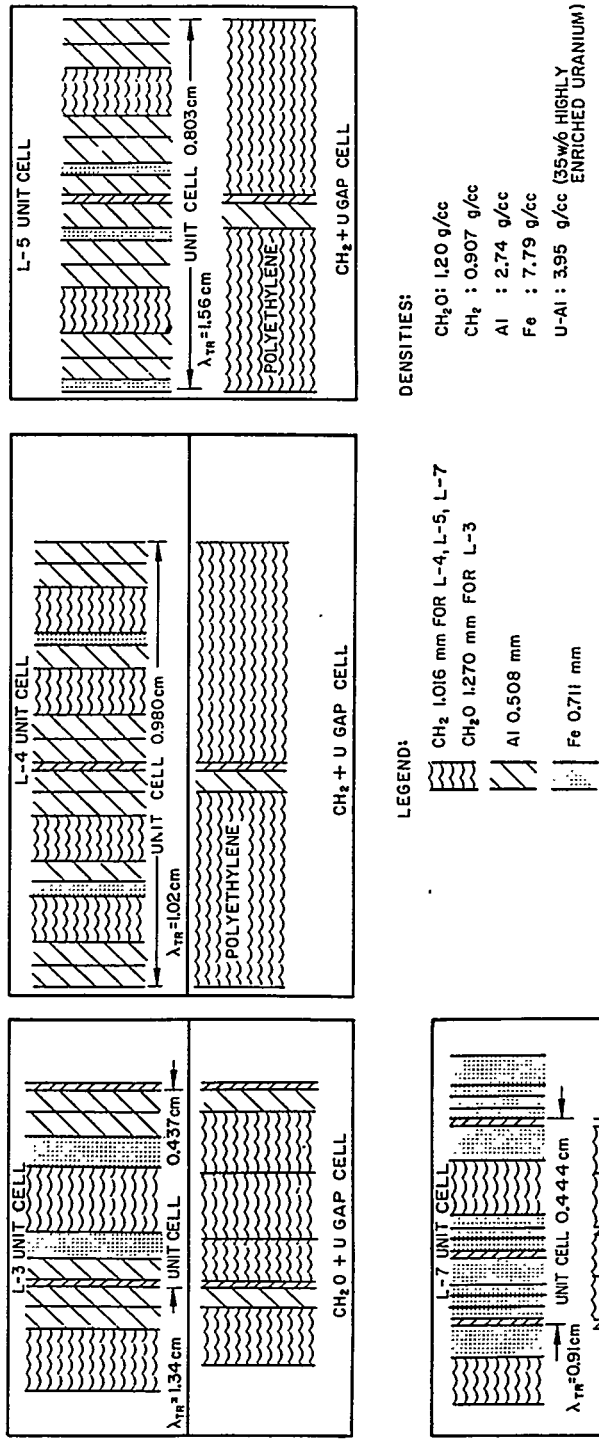

FIGURE 6.42. Details of the Unit Cell and Fuel Gap Construction for the Flux Transient Experiments.

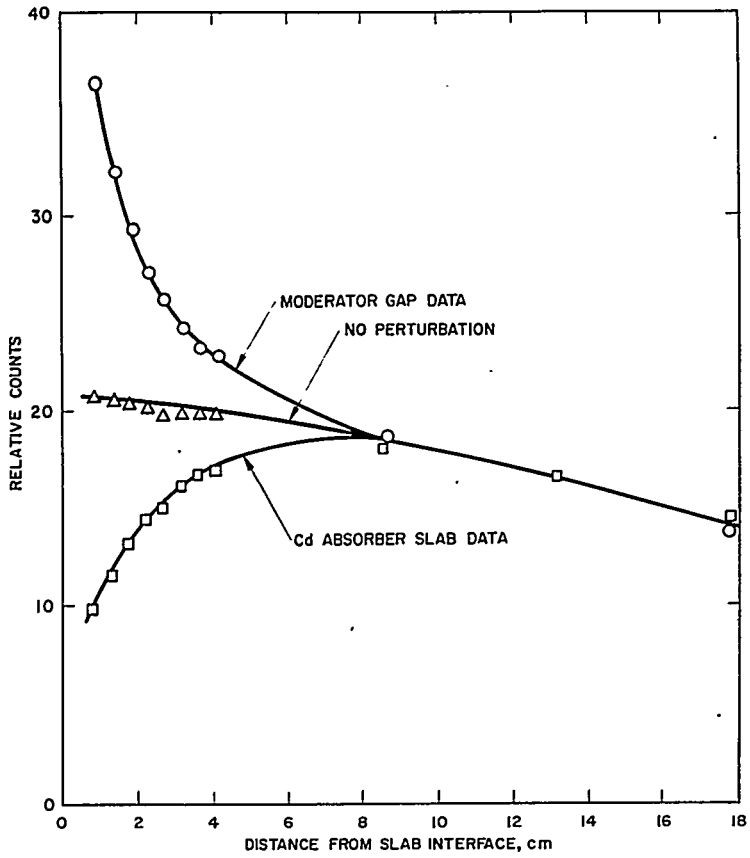

FIGURE 6.43. Measured Flux Transients for Both Moderator Gap Peaking and Absorber Gap Depression.

relaxation length of the transient. Figure 6.44 is a graph of $\lambda(x)$ versus x for a representative case. Table 6.29 presents the relaxation lengths for the moderator gap measurements and Table 6.30 those for the absorber plates. For the 20-mil cadmium plate measurement in Lattice L-7, a simple exponential was not obtained, so that no relaxation length is listed. The neutron activation measurements listed in Tables 6.29 and 6.30 were performed with 2-mil thick manganese foils.

In Tables 6.31 and 6.32 are listed the experimental peaking values, as determined with both manganese foils and with fuel foils ($\Sigma_a t = 0.03$ at 0.025 ev). The fuel values for the quantity (peaking -1) are from 25 to 40 percent higher than the manganese values. This is probably a consequence of the relatively smaller epithermal contribution to the fuel activity as compared with manganese.

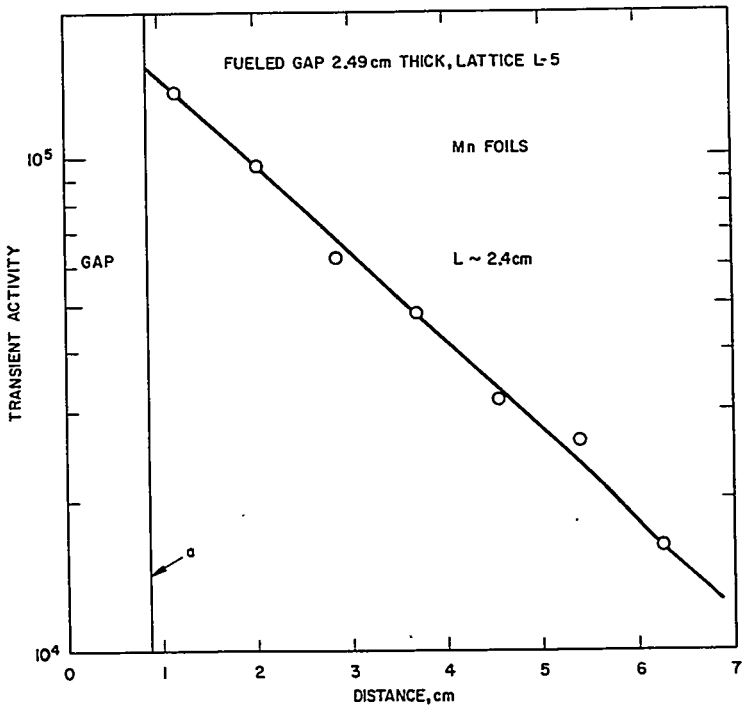

FIGURE 6.44. A Plot of the Transient Activity, $A(x)$, as a Function of Distance, x, from the Perturbation Interface Showing the Exponential Shape of the Transient.

The errors quoted in the tables are arrived at by analyzing the individual components of error entering into the measurements, such as counting statistics, foil weight, and power level normalization uncertainties, as well as from reproducibility checks made in a fairly large number of instances.

In Fig. 6.45 epicadmium traverses taken in Lattice L-7 are plotted both for the case of a 1-in. moderator gap and for a boron absorber plate with a value of $\Sigma_{at} = 1$. The results indicate an epithermal source dip of 10 to 15 percent. For the case of a cadmium slab the dipping is less severe.

E. Analysis

1. Spectrum-Independent Model

A comparison of the experiments has been made with a common regionwise constant spectrum technique (using a hardened Wigner-Wilkins spectrum for the thermal group constants; for

TABLE 6.29 — RELAXATION LENGTHS FROM MODERATOR GAPS*

Lattice	Gap Type	Gap Thickness (cm)	Experimental Relaxation Length	SOFOCATE† $L = \sqrt{D/\Sigma_a}$ 0.3 ev Cutoff	SOFOCATE† $L = \sqrt{D/\Sigma_a}$ 0.625 ev Cutoff	γ(E) Model	SWAKRAUM‡
L-3	CH_2O+U	0.828	1.71 ± 0.10	2.08	2.28	1.708	1.590
	CH_2O+U	1.722	1.75 ± 0.06	2.08	2.28	1.703	1.625
	CH_2O+U	2.616	1.78 ± 0.05	2.08	2.28	1.700	1.640
	CH_2O	0.381	1.82 ± 0.16	2.08	2.28	1.689	1.620
	CH_2O	2.667	1.64 ± 0.04	2.08	2.28	1.685	1.575
L-4	CH_2+U	2.037	2.14 ± 0.08	2.53	2.68	2.360	2.125
L-5	CH_2+U	2.490	2.35 ± 0.06	2.89	3.15	2.563	2.330
L-7	CH_2	0.826	1.23 ± 0.05	1.23	1.42	0.998	0.96
	CH_2	1.638	1.10 ± 0.03	1.23	1.42	0.994	0.935
	CH_2	2.451	1.00 ± 0.01	1.23	1.42	0.992	0.925

*Manganese foils. Dimensions in cm.
† Hardened (Wigner-Wilkins) thermal group constants.
‡ Flat epithermal source.

TABLE 6.30 — RELAXATION LENGTHS 20-MIL CADMIUM PLATES*

Lattice	Experimental Relaxation Length	SOFOCATE† $L = \sqrt{D/\Sigma_a}$		γ (E) Model	SWAKRAUM‡
		0.3 ev Cutoff	0.625 ev Cutoff		
L-3	2.29	2.08	2.28	2.26	2.14
L-4	2.75	2.53	2.68	2.68	2.41
L-5	2.99	2.89	3.15	3.18	2.78

*Manganese foils. Dimensions in cm.
†Hardened (Wigner-Wilkins) thermal group constants.
‡Flat epithermal source.

TABLE 6.31 — MODERATOR GAP PEAKING

Lattice	Gap Type	Gap Thickness (cm)	Experimental Peaking		Spectrum Independent Model* (Mn)	γ (E) Model		SWAKRAUM† (Mn)
			Manganese	Fuel		Mn	Fuel	
L-3	CH_2O +U	0.821	1.390 ± 0.012	--	1.260	1.340	--	1.389
	CH_2O +U	1.772	1.646 ± 0.020	--	1.482	1.590	--	1.672
	CH_2O +U	2.616	1.852 ± 0.025	--	1.627	1.749	--	1.820
	CH_2O	0.381	1.209 ± 0.012	--	1.227	1.286	--	1.305
	CH_2O	2.667	2.483 ± 0.025	--	2.085	2.758	--	2.881
L-4	CH_2+U	2.037	1.373 ± 0.014	--	1.292	1.371	--	1.382
L-5	CH_2+U	2.490	1.750 ± 0.022	--	1.601	1.796	--	1.819
L-7	CH_2	0.826	2.090 ± 0.025	2.37 ± 0.04	1.600	2.098	2.35	2.138
	CH_2	1.638	3.000 ± 0.030	3.64 ± 0.04	2.012	3.061	3.54	3.141
	CH_2	2.451	3.650 ± 0.040	4.18 ± 0.05	2.350	3.888	4.54	3.988
	CH_2+U	0.889	1.847 ± 0.018	2.07 ± 0.03	1.452	1.702	1.86	1.770
	CH_2+U	1.740	2.186 ± 0.022	2.66 ± 0.03	1.733	2.056	2.30	2.145
	CH_2+U	2.629	2.560 ± 0.030	3.02 ± 0.04	1.901	2.236	2.52	2.320
	CH_2+Fe	2.778	2.636 ± 0.030	--	1.850	2.780	--	--
	CH_2+Dy	1.968	1.898 ± 0.025	--	--	1.884	--	2.038
	CH_2+Al	1.956	2.093 ± 0.025	--	1.597	2.076	--	2.135

*Regionwise constant hardened (Wigner-Wilkins) thermal group constants and MUFT fast group constants in a four-group diffusion theory calculation.
†Flat epithermal source.

TABLE 6.32 — ABSORBER PLATE ACTIVITY DEPRESSION

Lattice	Absorber Type	Absorber Thickness (mil)	Experimental Activity Depression	(γE) Model	Flat Epithermal Source	
					SWAKRAUM† Blackness	SWAKRAUM† Double-P_1
L-3	Cd	3	0.517	0.522	0.504	0.460
	Cd	20	0.421	0.402	--	0.397
L-4	Cd	3	0.312	0.302	0.299	0.261
	Cd	20	0.230	0.209	--	0.202
L-5	Cd	3	0.396	0.396	0.389	0.345
	Cd	20	0.317	0.285	--	0.284
L-7	Cd	3	0.632	--	0.609	0.569
	Cd	3	0.420*	--	0.409*	0.350*
	Cd	20	0.615	0.507	--	0.503
	Boron $\Sigma_a t = 1$ at 0.025 ev		0.455*	--	--	0.425*
	Boron $\Sigma_a t = 2$ at 0.025 ev		0.365*	--	--	0.305*

*Subcadmium depression only.
†Flat epithermal source. The epicadmium contributions to the calculated values have been determined rather crudely. Since they amount to 30 to 50 percent of the total activity with absorber, the quoted calculated values are uncertain to 10 to 20 percent.

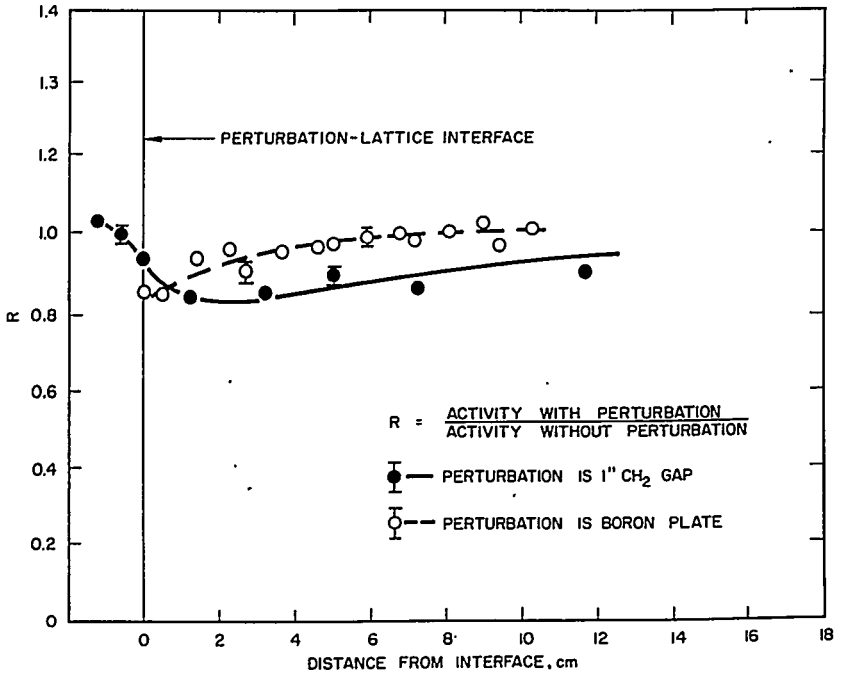

FIGURE 6.45. Cadmium-Covered 0.1-mil Gold Traverses in Lattice L-7.

the latter the SOFOCATE[4] routine was used, and for the fast group constants the MUFT[23] routine). For these calculations, the spatial effects were taken into account with one-dimensional few-group diffusion theory calculations using the WANDA[10] routine. In Tables 6.29 and 6.30, hardened (Wigner-Wilkins) diffusion lengths, $L = \sqrt{D/\Sigma_a}$, are listed for two values of the cutoff energy in the SOFOCATE calculation. It is seen that L calculated with the more or less normal 0.625 ev cutoff agrees reasonably well with the measured cadmium relaxation lengths. However, for the moderator gaps, a cutoff energy of about 0.3 ev is required to give agreement, which is unsatisfactory.

For the peaking values, MUFT-SOFOCATE group constants were obtained for the gap and lattice regions, again using a hardened Wigner-Wilkins spectrum for averaging the thermal constants. Four-group diffusion theory calculations were then performed using the WANDA routine. From the results, the manganese peaking factors listed in Table 6.31 were calculated. The results show that this procedure underestimates the peaking markedly. These results are in agreement with the comparisons made on the slab experiments of simple geometry discussed

in Sects. 6.2 and 6.3, where it was seen that the use of a region-wise constant hardened spectrum resulted in an underestimate of the water gap or reflector peaking.

2. Space-Energy Separable Transient Model, $\gamma(E)$

A) RELAXATION LENGTHS. As mentioned before, a striking feature of the basic experimental results is that within the accuracy of the experiments, the spatial transients measured could be represented by single exponentials. That such a simple behavior should be found in a region of rapidly changing spectrum seemed quite surprising. The simplest form of diffusion theory predicts that there should be only one characteristic diffusion length

$$L^2 = \frac{\int \phi(E) D(E)\, dE}{\int \phi(E) \Sigma_a(E)\, dE},$$

where $D(E)$ is the energy-dependent diffusion constant for the lattice composition and $\Sigma_a(E)$ the macroscopic absorption cross section. This, however, is too simple, since it was observed that the characteristic length, L, depended on whether the perturbation was a moderator or absorber.

In this attempt at analysis of the data, use was made of the two striking experimental observations: (1) The transients are characterized by a single exponential; (2) their characteristic length depends on the nature of the perturbation. Number (1) suggests that the analysis be made in terms of a spatially independent transient spectrum, $\phi_t(E)$. Number (2) suggests that $\phi_t(E)$ must be a function of the perturbation. Since the experiment emphasizes primarily the thermal region, it was possible to choose $\phi_t(E)$ to be a Maxwellian for the moderator gaps and a transmission modified Wigner-Wilkins spectrum for the absorbers. Thus, for the moderator gaps

$$L_t^2 = \int_0^\infty \frac{D(E)\phi_t(E)\, dE}{\Sigma_a(E)\phi_t(E)\, dE} \qquad \text{Eq. (6.3)}$$

$$\phi_t(E) = \phi_{\max}(kT_{\text{eff}}) .$$

Here it is noted that the Maxwellian is evaluated at a hardened energy given by

$$kT_{\text{eff}} = (kT)(1 + \beta\gamma_{\text{gap}}) .$$

For absorber plates, the transient spectrum is given by

$$\phi_t(E) = \frac{\phi_\infty(E)}{1 + \frac{2\bar{D}}{\bar{L}}\left(\frac{1+T(E)}{1-T(E)}\right)} \qquad \text{Eq. (6.4)}$$

where $\phi_\infty(E)$ = Wigner-Wilkins spectrum for the lattice. $\bar{D}$ and $\bar{L}$ are averages taken over this Wigner-Wilkins spectrum

$$T(E) = 2E_3[\xi(E)]$$

where $\xi(E) = \Sigma_a(E)t$ for the plate and E_3 is the standard E function. The results obtained with this model are given in Tables 6.29 and 6.30 and indicated substantial agreement with the experiments. It should be noted that the value of L obtained from Eq. (6.3) is insensitive to the spectrum used to obtain $\frac{\bar{D}}{\bar{L}}$ in Eq. (6.4).

B) PEAKING MEASUREMENT. To apply this simple model to the peaking measurement, it must be extended to provide the relative amplitudes of $\phi_t(E)$ and $\varphi_\infty(E)$. To do this the following assumptions can be made: (1) There is an energy, E^*, not too far above thermal such that for $E \geq E^*$ the flux, $\phi(E)$, is essentially unperturbed by the absorber plates and moderator gaps. (2) The spectrum, $\phi(E,x)$ for $E < E^*$, in the gaps as well as in the lattice is a superposition of the infinite medium Wigner-Wilkins spectrum of the respective regions plus a spatially varying component separable in space and energy.

These assumptions plus the physically reasonable requirement of flux and current continuity at all energies permit the calculation of the peaking. The derivation proceeds as follows: Consider an infinite medium A that has a well defined neutron spectrum $\phi_A(E)$ everywhere. Insertion of a region B of different cross sections into A will result in a position-dependent spectrum in A near the A–B boundary. In the diffusion theory approximation, this spectrum will satisfy the equation

$$-D_A(E)\nabla^2\phi_A(E,r) + \Sigma^A_{\text{total}}(E)\phi_A(E,r) = S(E,r) + \int_0^{E^*} \phi_A(E',r)\Sigma_A(E'\to E)dE' \qquad \text{Eq. (6.5)}$$

where $S(E,r)$ is the source term,

$$S(E,r) = \int_{E^*}^{\infty} \phi_A(E',r)\Sigma_A(E'\to E)dE'$$

and E^* is some cutoff energy. If $\frac{\Sigma_a(E)}{\Sigma_{tot}(E)} \ll 1$ for $E > E^*$ in both A and B, then the source will be independent of position and $S(E,r) = S(E)$.

Asymptotically in A the spectrum becomes stationary and will satisfy the equation

$$\Sigma^A_{\text{total}}(E)\phi_A(E) = S(E) + \int_0^{E^*} \phi_A(E')\Sigma_A(E' \to E)dE' \quad . \qquad \text{Eq. (6.6)}$$

Defining $\gamma(E,r) = \phi_A(E,r) - \phi_A(E)$ and subtracting Eq. (6.6) from Eq. (6.5),

$$-D_A(E)\nabla^2\gamma(E,r) + \Sigma^A_{\text{total}}(E)\gamma(E,r) = \int_0^{E^*} \gamma(E',r)\Sigma_A(E' \to E)dE' \qquad \text{Eq. (6.7)}$$

which is an equation for the transient introduced in A by the insertion of B. As pointed out before, experimentally it was observed that in a large number of cases the spatial transients were exponential, i.e.,

$$\int \gamma(E,x)\sigma_{\text{foil}}(E)dE \sim e^{-kx} \quad .$$

A solution of Eq. (6.7) which would lead to this result is

$$\gamma(E,x) = \gamma(E)f(x) \, .$$

Noting that

$$\Sigma_{\text{total}}(E) = \Sigma_a(E) + \int_0^{E^*} \Sigma_A(E \to E')dE'$$

since energies above E^* are not perturbed, the insertion of the separable solution into Eq. (6.7) yields

$$-\frac{\nabla^2 f(x)}{f(x)} D_A(E)\gamma(E) + \Sigma_a(E)\gamma(E)$$

$$= \int_0^{E^*} \left[\gamma(E')\Sigma_A(E' \to E) - \gamma(E)\Sigma_A(E \to E')\right] dE' \qquad \text{Eq. (6.8)}$$

Letting

$$\frac{\nabla^2 f}{f} = \frac{1}{L_\gamma^2}$$

and integrating Eq. (6.8) over energy

$$-\frac{1}{L_\gamma^2}\int_0^{E^*} D_A(E)\,\gamma(E)\,dE + \int_0^{E^*} \Sigma_a^A(E)\,\gamma(E)\,dE$$

$$= \int_0^{E^*}\int_0^{E^*}\left[\gamma(E')\Sigma_A(E'\to E) - \gamma(E)\Sigma_A(E\to E')\right] dE\,dE' = 0 \qquad \text{Eq. (6.9)}$$

so that

$$L_\gamma^2 = \frac{\int_0^{E^*} D_A(E)\,\gamma(E)\,dE}{\int_0^{E^*} \Sigma_a^A(E)\,\gamma(E)\,dE} \,. \qquad \text{Eq. (6.10)}$$

To obtain $\gamma(E)$, the spectrum equation in region B can be considered:

$$-D_B(E)\nabla^2\phi_B(E,r) + \Sigma_{\text{total}}(E)\phi_B(E,r) = S_B(E)$$

$$+\int_0^{E^*} \phi_B(E',r)\Sigma_B(E'\to E)\,dE' \,. \qquad \text{Eq. (6.11)}$$

Again, $S_B(E)$ is independent of position because of the choice of E^*. There exists an asymptotic spectrum characteristic of the cross sections of B and the source $S_B(E)$ satisfying the equation

$$\Sigma_{\text{total}}^B(E)\,\phi_B(E) = S_B(E) + \int_0^{E^*} \phi_B(E')\Sigma_B(E'\to E)\,dE' \,. \qquad \text{Eq. (6.12)}$$

If the dimensions of B are small, an asymptotic spectrum actually never exists. However, one can be defined, as in Eq. (6.12) and subtracted from Eq. (6.11) yielding

$$\beta(E,r) = \phi_B(E,r) - \phi_B(E)$$

and

$$-D_B(E)\nabla^2\beta(E,r)+\Sigma^B_{\text{total}}(E)\,\beta(E,r)=\int_0^{E^*}\beta(E',r)\Sigma_B(E'\to E)dE' \quad .$$

It can be assumed that $\beta(E,x)$ is separable in energy and position for the case of a slab gap. Then, writing the energy-dependent flux explicitly for the lattice A and the gap B as

$$\phi_A(E,x)=\phi_A(E)+\gamma(E)e^{-(x-a)/L_\gamma} \qquad \text{Eq. (6.13)}$$

and

$$\phi_B(E,x)=\phi_B(E)+\beta(E)\cosh x/L_\beta \qquad \text{Eq. (6.14)}$$

the flux and current can be equated at the gap boundary $(x=a)$ so that

$$\gamma(E)=\frac{\phi_B(E)-\phi_A(E)}{1+\dfrac{D_A(E)}{D_B(E)}\dfrac{L_\beta}{L_\gamma}\coth a/L_\beta} \qquad \text{Eq. (6.15)}$$

and

$$\beta(E)=-\gamma(E)\frac{D_A(E)}{D_B(E)}\frac{L_\beta}{L_\gamma}\operatorname{csch} a/L_\beta \qquad \text{Eq. (6.16)}$$

where a is the half gap thickness, $\varphi_A(E)$ and $\phi_B(E)$ are normalized at energies $E>E^*$, and L_β is defined analogously to L_γ. For small gap thicknesses

$$\lim_{a\to 0}\gamma(E)\to 0$$

$$\lim_{a\to 0}\beta(E)\to\phi_A-\phi_B; \qquad \varphi_B(E,x)\to\phi_A(E) \quad .$$

For large gap thickness

$$\phi_B(E,x)=e^{-a'/L_\beta}\gamma(E)\frac{D_A(E)}{D_B(E)}\frac{L_\beta}{L_\gamma}\operatorname{csch} x/L_\beta+\phi_B(E)$$

so that $\varphi_B(E,a/L_\beta>>1)\to\varphi_B(E)$.

These relations indicate that the spectrum in the gap varies in hardness between the spectrum of the lattice and that of an infinite gap region, whereas the spectrum in the lattice is softened by the presence of the gap. In calculations of $\gamma(E)$, $\phi_A(E)$ and $\phi_B(E)$ were taken to be the Wigner-Wilkins spectra for the lattice and gap, respectively, normalized in the $1/E$ region. At high $\beta\gamma$, a 2-ev cutoff is necessary in the Wigner-Wilkins calculation to ensure $1/E$ behavior in the high energy tail.

Figure 6.46 compares the $\gamma(E)$ for a pure moderator gap in L-7 with a Maxwellian spectrum at an effective temperature given by

$$T_{\text{eff}} = \left[1 + (\beta\gamma)_{\text{gap}}\right] T$$

and the L-7 Wigner-Wilkins spectrum. The comparison shows that Maxwellian averages will be in good agreement with averages taken over $\gamma(E)$.

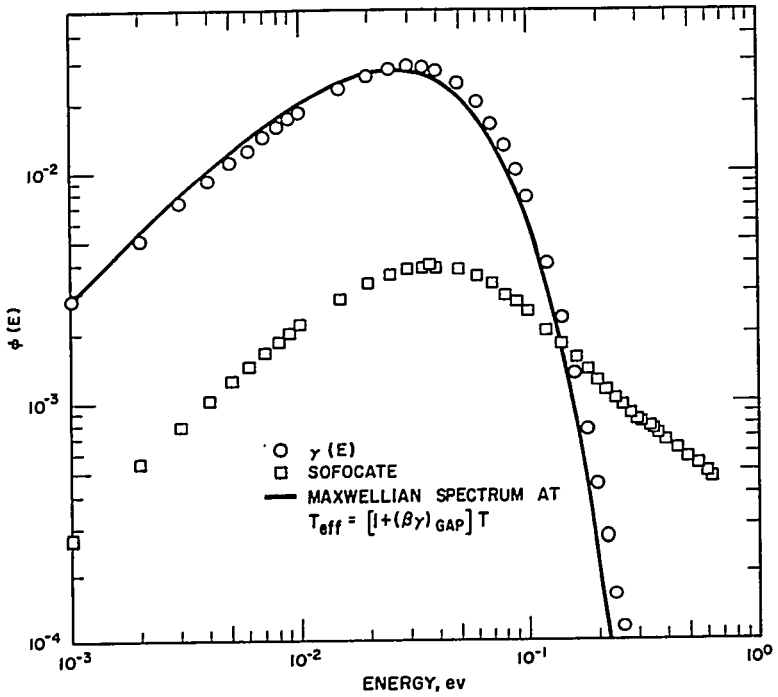

FIGURE 6.46. Comparison of the $\gamma(E)$ Spectrum with a Maxwellian Evaluated at a Hardened Temperature and with a Wigner-Wilkins for a Moderator Gap in Lattice L-7.

From Eqs. (6.13) and (6.15), the experimental peaking measured by a foil of cross section $\sigma_{foil}(E)$ corresponds to

$$\text{Peaking} = 1 + \frac{\int_0^\infty \gamma(E)\sigma_{foil}(E)dE}{\int_0^{E_{co}} \phi_{SOF}^{lattice}(E)\sigma_{foil}(E)dE + \phi(E_{co}) \int_{E_{co}}^\infty \sigma_{foil}(E)\, d\ln E}$$

Eq. (6.17)

Using the present terminology and applying transmission theory boundary conditions to the case of absorber plates leads to

$$\gamma(E) = \frac{-\phi_\infty}{1 + \frac{2D_A(E)}{L_\gamma}\left(\frac{1+T(E)}{1-T(E)}\right)}$$

quite similar to Eq. (6.4).

In Tables 6.29 through 6.32, the peakings and relaxation lengths calculated with the above model, called the $\gamma(E)$ model, are presented. This simple space-dependent spectrum model produces significantly better agreement with experiment than the use of the hardened (Wigner-Wilkins) regionwise constant diffusion theory calculation discussed above. Moreover, agreement within 10 percent in both the peaking and relaxation lengths is obtained for nearly all the cases studied. This good agreement is surprising in view of the crudity of the approximations of the model, in particular that of the spatially independent epithermal source and the strict space-energy separability of the transient spectrum.

3. *SWAKRAUM Variational Approach*

Further analysis of the experiments has been performed with the SWAKRAUM variational approach[28] which was discussed in Chap. 3, Sect. 3.7. In the $\gamma(E)$ model discussed above, it was noted that:

$$\phi(E, x) = \phi_\infty(E) + \phi_t(E)e^{-x'L}$$

where $\phi_\infty(E)$ is the infinite medium Wigner-Wilkins lattice spectrum and $\phi_t(E)$ is a Maxwellian for the gap effective temperature. The SWAKRAUM approach generalizes this formulation to

$$\phi(E, x) = \sum_{i=1}^{N} \chi_i(x)\,\Psi_i(E) \qquad N \leq 4$$

where the $\Psi_i(E)$ (base spectra) may be arbitrarily chosen and the $\chi_i(\infty)$ are found from a variational principle.

In its simplest form, P_1 calculations are performed using a flat epithermal source, the mass 1 scattering kernel, and the Radkowsky-Esch[29] prescription for $D(E)$. The results of these calculations, using the variational approach, are also presented in Tables 6.29 through 6.32. The values obtained are quite similar to those from the $\gamma(E)$ model.

4. *Additional Effects*

Although the previous results indicate agreement to within about 10 percent, several additional effects can be investigated with the aid of the SWAKRAUM program. These effects have been investigated for the case of a 1-in. polyethylene gap in Lattice L-7 for two reasons: The most reliable data exist for this lattice, and the lattice itself, being the hardest one studied, exhibits the most pronounced spectrum-dependent effects.

The sensitivity of the calculations to the following approximations have been investigated:

1. Choice of trial spectra, $\Psi_i(E)$
2. Number of spectra used, 2, 3, 4
3. Transport approximation used, P_1, double-P_1, P_3
4. Spatial distribution of the epithermal source
5. Scattering kernel
   a. Radkowsky — water } mass 1
   b. Radkowsky-Esch — polyethylene }
   c. Goldman[30] — polyethylene

The results are presented in Table 6.33 and reflected in Figs. 6.47 and 6.48. Each of the effects is seen to be a magnitude of a few percent, and their relative importance depends on the particular case studied.

Since SWAKRAUM is a thermal neutron group program, the most meaningful comparison with experiment can be made with subcadmium activations. Figures 6.47 and 6.48 show such a comparison for the case of the boron plate absorber and a polyethylene gap in Lattice L-7. For these two quite different cases agreement to within a few percent is achievable for the subcadmium energy region.

F. Conclusions

The experiments and methods discussed have been shown to yield a significant improvement in the ability to calculate spatial flux transients. Differences of 30 percent between experiment and a space-independent spectrum calculation, which used

TABLE 6.33 — EFFECT OF VARIOUS QUANTITIES ON THE PEAKING (L-7)

Quantity	Relative to	Case	Effect (%)
Experimental epithermal source	Flat source	1" moderator gap Boron plate absorber	-4.6 -7.8 (thermal)
Approximation			
Double-P_1	P_1	1" moderator gap 0.1" moderator gap	+1.0 +3.9
P_3	P_1	1" moderator gap 0.1" moderator gap	+0.7 +2.8
No. of Spectra			
3	2 spectra	1" moderator gap	-0.4 (thermal peaking)
4	2 spectra	1" moderator gap	+0.2 (thermal peaking)
Kernel			
Radkowsky-water	Radkowsky-Esch[29] polyethylene	1" moderator gap	-1.6
Goldman-Federighi[30] polyethylene	Radkowsky-Esch[29] polyethylene	1" moderator gap	-5.7

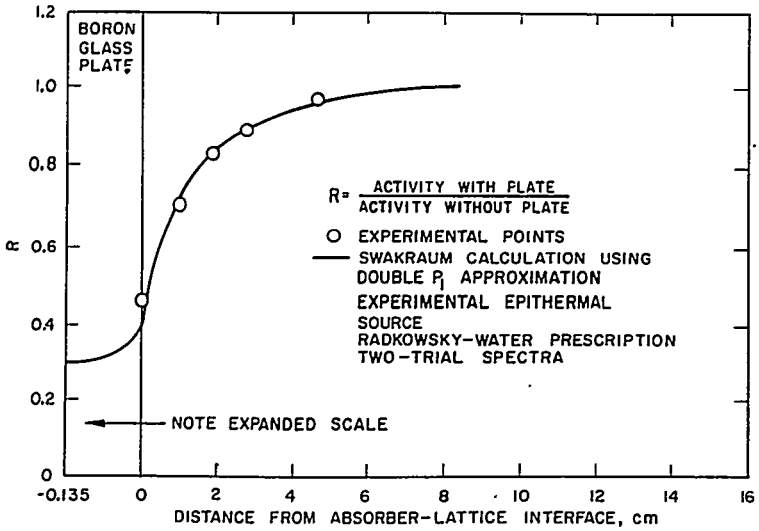

FIGURE 6.47. Comparison of SWAKRAUM Variational Calculation with the Subcadmium Manganese Activity for a Boron Glass Plate in Lattice L-7.

regionwise constant hardened (Wigner-Wilkins) thermal group constants, have been reduced to about 10 percent. (This is the same order of improvement observed after introduction of the mixed number density model, as was noted in Sects. 6.2 and 6.3.) The improvement is especially striking for the case of moderator gap peaking in which the thermal effects are emphasized. For absorber plates significant differences still exist, however, because most of the measurable interactions are due to epithermal neutrons which have not yet been adequately treated.

Once the bulk of the discrepancies has been removed by use of a rather simple position-dependent spectrum prescription, such as the method described in this section or the mixed number density model, a number of other effects still remain. Since their magnitude is individually in the range of only a few percent, it is very difficult to arrive at unambiguous conclusions concerning them from a comparison with experiment. It is possible, however, to note the following points:

The effect on moderator peaking of the choice of approximation (P_1, P_3, double-P_1) is less than 1 percent for thick gaps and less than 4 percent for thin gaps. The choice of thermal scattering model gives as much as a 6 percent effect in peaking. The difference between assuming a flat epithermal source distribution and using a measured one amounts to about 5 percent in peaking.

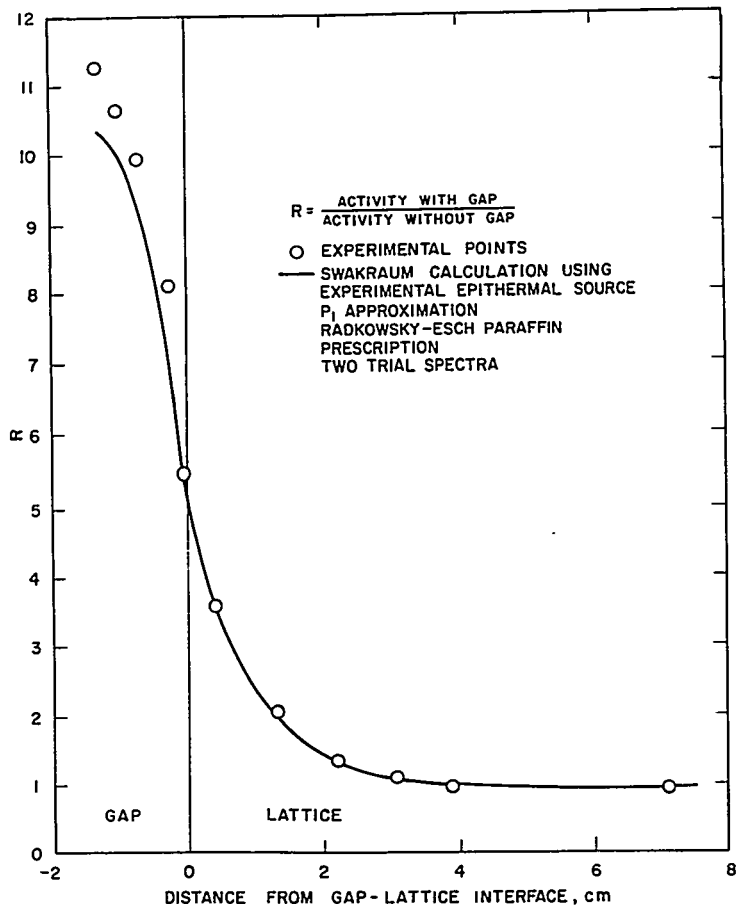

FIGURE 6.48. Comparison of SWAKRAUM Variation Calculation with the Subcadmium Manganese Activity for a CH_2 Gap in Lattice L-7.

For the case of activity depression induced by absorber plates, the difference between the P_1 blackness and double-P_1 approximations is generally about 10 percent. The difference between assuming a flat epithermal source and using a measured one is about 10 percent.

In summary, simple position-dependent spectrum models, such as the $\gamma(E)$ model and the SWAKRAUM variational model discussed here as well as the mixed number density model discussed in the previous sections, have been developed to approximate the change in the neutron energy spectrum near discontinuities in the medium. These approximate models may

be used in diffusion theory to describe adequately the thermal activations near core-moderator interfaces if the epithermal source is known. Near core-absorber interfaces, where the thermal spectrum effects are not dominant, other effects must be taken into account in order to yield accurate predictions.

6.5 HIGH U^{238} CONTENT CRITICAL EXPERIMENTS AT AMBIENT TEMPERATURE

D. Klein

A. Introduction

Discussion to this point has been concerned with experiments performed on highly enriched uranium fueled assemblies. Attention is now turned to systems containing low enrichment of U^{235} and high concentration of U^{238}. High uranium content (slightly enriched) lattices have been discussed extensively in the literature.[31-33] Recent improvements have been made in cross sections, resonance parameters, and in calculational techniques resulting in a corresponding improvement in the ability to predict reactor parameters. Criticality can now be predicted to better than about 1 percent in k_{eff}. The uncertainty in the U^{238} resonance absorption has been reduced to about one barn for single rods and for lattices. This has resulted from extensive theoretical and experimental studies of resonance absorption in recent years. There is still a 0.5-barn uncertainty in the high energy capture, and more work must be done on the Dancoff interaction. However, improvements have been made in the U^{238} fast fission calculation by the inclusion of heterogeneous effects. The value of α^{25} in the epithermal region still remains uncertain, but additional measurements of the U^{235} resonance parameters or direct measurements of α^{25} itself must be made before the problem can be resolved. The thermal neutron problem has recently attracted more attention. Calculated disadvantage factors using multigroup transport codes disagree with the measured values by 6 percent in cylinders and 3 percent in slabs. This discrepancy exists regardless of the kernel used in the calculation (Radkowsky or Nelkin), and indicates that more theoretical and experimental work is required.

Measurements[31,34] of critical size, bucklings, reflector savings, migration areas, resonance escape probability, fast effects, and thermal utilization have been reported in the literature. Two of these subjects are emphasized here. The

first part of this section discusses the problem of resonance absorption and measurements of effective U^{238} capture integrals in rods of uranium and UO_2 which are compared with Hellstrand's experimental results and Nordheim's theoretical predictions. Within the experimental errors it will be shown that the agreement is good. Also discussed are certain equivalence relations which allow the correlation of isolated rod and lattice resonance integrals. The correlation is made in the last part of the section using the experimental results. It will be seen that, except for very tight lattices, the formulation appears to work well.

The last two parts of this section deal with one aspect of the thermal neutron problem in the high uranium content systems. A discussion is given of reaction rates which were measured with different detectors, such as U^{235}, Pu^{239}, and Pu^{241}, and in the case of U^{235} different detector shields, such as cadmium, boron, and gadolinium. A simple calculational model is used to analyze the results, and it will be seen that it yields good results considering the simplicity of the model. However, to give a complete analysis of the results would require accurate knowledge of the energy and spatial-dependent flux in the fuel and moderator. At present, this cannot be determined calculationally with the required degree of confidence, since the thermal scattering kernel is still not known and since higher order transport calculations are only now becoming available.

B. Effective U^{238} Resonance Capture Integrals in Rods and Lattices

J. Hardy, Jr., D. Klein, G. G. Smith, and S. Stein

Theoretical calculations[35-37] of U^{238} resonance absorption in isolated rods and lattices have suggested certain equivalence relations. These equivalence relations are dependent upon the use of the Wigner rational approximation to the escape probability. In this framework, lattices are characterized by an effective surface-to-mass ratio which allows correlation of isolated rod and lattice resonance integrals.

This section deals with the measurement of U^{238} resonance neutron capture in isolated uranium metal and UO_2 rods and with Monte Carlo calculations of the resonance integrals. The study was made to investigate the range of validity of the equivalence relations under idealized conditions. Resonance integrals are inferred from measurements of the resonance escape probability, p^{28}, for a number of different lattices. These results are then correlated with the isolated rod

measurements by using two of the suggested equivalence relations.

1. Measurements in Isolated Rods

The effective U^{238} resonance neutron capture integrals of uranium metal and UO_2 rods of a variety of diameters have been measured by an activation technique. The experiment employed 10-cm long sections of fuel rod irradiated in a cadmium can, as shown in Fig. 6.49. The can was located in a water hole at the center of the TRX, a water-moderated, slightly enriched, heterogeneous critical facility.[34] In this water hole, the overall spectrum of the epithermal neutron flux is very nearly proportional to $1/E$ up to an energy of approximately 25 kev, above which there appears a flux peak characteristic of water-moderated reactors.

Each measurement of the effective resonance integral for a particular rod consisted of two irradiations. After the first irradiation, called the fuel rod run, a uniform sample of uranium atoms was extracted from the irradiated fuel rod and made into thin deposits. The U^{238} capture activity of these deposits was then measured. In the second irradiation, called

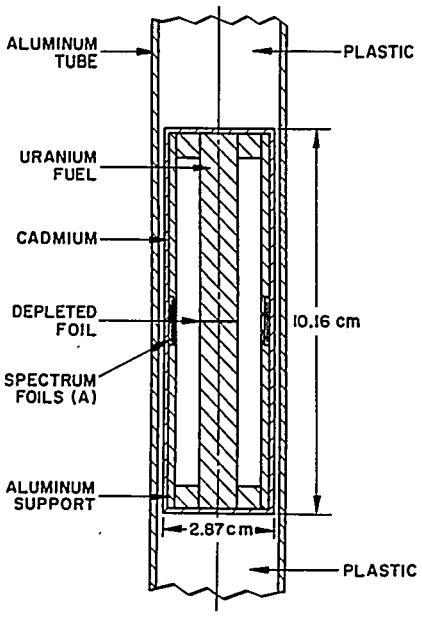

FIGURE 6.49. Test Fuel Loading.

the normalizing run, the deposits were placed in the otherwise empty cadmium can, irradiated, and their activities measured exactly as before. With some corrections (for background activity, flux spectrum, etc.) the ratio of activity from the fuel rod run to that from the normalizing run is just the ratio of the effective resonance integral per U^{238} atom of the fuel rod to the dilute resonance integral of U^{238}.

Table 6.34 lists the characteristics of the fuel rods for which measurements were done. The cadmium can, containing the 10-cm long section of fuel rod, was mounted between plastic rods in an aluminum tube and positioned at the center of a 12-cm diameter water hole. The cadmium can was 10 cm high, with a wall thickness of 0.076 cm. Its diameter was 2.87 cm for all except the largest metal rod, which required a can of 4.10-cm diameter. To ensure that no error was caused by this change, measurements on the 2.16-cm diameter metal rod were done in both cadmium cans. The results were indistinguishable within the experimental uncertainty.

For each of the five metal rods, a circular uranium metal foil, depleted to 190 ppm U^{235} and of the same diameter as the fuel, was carefully positioned at the center of the fuel section in the cadmium can. After an irradiation of one hour, the foil was removed and dissolved in dilute HCl. A small amount of H_2O_2 was then added, and individual drops of the solution placed on blotter paper. The blotter paper was dried and circular foils punched from the spots made by the drops

TABLE 6.34 — FUEL DESCRIPTION

Fuel	Enrichment	Diameter (cm)	Density (g/cm^3)	$\sqrt{S/M}$ ($cm/g^{1/2}$)
U Metal	Natural	3.175	18.9	0.259
	Natural	2.159	18.9	0.313
	Natural	1.524	18.9	0.373
	1.3% U^{235}	0.983	18.9	0.464
	1.3% U^{235}	0.686	18.9	0.558
UO_2	Natural	2.210	10.5	0.414
	1.3% U^{235}	1.524	7.5	0.590
	1.3% U^{235}	0.975	10.5	0.623
	1.3% U^{235}	0.986	7.5	0.734

of solution. The uranium concentration in the deposits appeared to be quite uniform. The effective uranium thickness of the deposits was about 0.3 mg/cm^2 in every case.

The 74-kev gamma activity resulting from the decay of U^{239} (half-life, 23.5 min.) was counted on a NaI scintillation spectrometer from 25 to 70 minutes after the irradiation.

In addition, there was a depleted uranium metal foil acting as a reactor power monitor. It was placed in a standard reference position where the spectrum was unaffected by the contents of the cadmium can. The 74-kev gamma activity of this foil (undissolved) was counted on the scintillation spectrometer from 70 to 90 minutes after the irradiation.

The normalizing run was made approximately two days after the fuel rod run. It was an exact duplicate of the first, except that the cadmium can now contained only the deposits mounted on a thin aluminum support plate. After irradiation, the activities of the deposits and the monitor foil were counted exactly as before. A small background on the foils was measured immediately before the irradiation and subtracted from the observed counts.

The UO_2 fuel rods were made up of cylindrical pellets with a height-to-diameter ratio of approximately unity. One of these pellets was used as the primary detector of U^{238} capture. Because the UO_2 pellets would not dissolve rapidly in acid, it was necessary to develop a somewhat different method of preparing the thin deposits. After irradiation, the central pellet was crushed to a fine powder which was then fused with molten potassium pyrosulfate. After the reaction was complete, approximately 1 ml of the molten salt was introduced into 10 ml of warm dilute HNO_3 where it dissolved rapidly. Deposits were then prepared as before from this solution. With some practice, the entire procedure from initial crushing to completion of the deposits took less than 10 minutes. Except for this modification, the UO_2 resonance integral measurements proceeded exactly as did those for metal rods.

The first significant correction to the measured activities was removal of the fission product gamma counts appearing in the window at 74 kev. This was done by the following method which has been reported in the literature.[38,39] First, the pulse height spectrum of the fission product gamma activity of a U^{235} foil from 50 to 300 kev is measured. Then, the γ pulse height spectrum from the U^{238} deposits is similarly measured. The two spectrum shapes are normalized in the energy range from 174 to 264 kev where, a few minutes after irradiation, the activity is due entirely to fission products. Assuming that the fission product γ pulse height

spectrum of U^{235} is close to that of U^{238} from 50 to 300 kev, one can obtain the amount of fission product background appearing in the 74-kev window along with the capture activity.

As a check on this method, in several cases a more direct but more involved technique was also used which consisted of a chemical separation of the uranium from fission products. After the regular deposits were made, the remaining solution was combined with a mixture of ammonium nitrate and hexone (methyl isobutyl ketone) and shaken vigorously for 5 minutes. It was then allowed to stand for 1 minute, so that the hexone layer separated out at the top. Deposits were made from drops of the hexone, which contained a large fraction of the uranium and was strongly depleted in fission products. These deposits were subsequently handled exactly as described in the case of the regular deposits, except that no fission correction was applied. The resulting resonance integral values obtained by the two methods were in good agreement within the precision with which each could be repeated. It was concluded that uncertainty of the fission correction could not introduce more than a 0.2-barn error into the results.

The percent fission correction varies with rod size because epicadmium fission is nearly independent of rod size, whereas the U^{238} resonance integral is not. Also, the correction was greater for the UO_2 rods than for the metal rods because depleted foils were used in the metal rods, whereas the UO_2 pellets were slightly enriched. The fission correction ranged from 2 to 4 percent for the metal rods, and from 5 to 6 percent for the UO_2 rods. The percent fission correction was nearly constant during the counting time from 30 to 70 minutes after shutdown. (For a typical metal rod, the correction factor might range from 0.96 to 0.98 during the counting period.)

No fission correction was applied to the counts from the normalizing run, since the correction was much less than 1 percent in this case.

The power normalized ratio of U^{238} activity from the first run to that from the second is, except for spectrum corrections, just the ratio of the rod effective resonance integral to the infinitely dilute resonance integral. Thus,

$$R_U = \frac{U_A^*}{U_A} \times \frac{U_B}{U_B} \times 280 \qquad \text{Eq. (6.18)}$$

where

U_A^* = U^{238} capture activity of the uranium deposit after the fuel rod run

U_A = U^{238} capture activity of the uranium deposit after the normalizing run

U_B^* = activity of the depleted uranium power monitor foil after the fuel rod run

U_B = activity of the depleted uranium power monitor foil after the normalizing run

The value of 280 barns is used for the dilute resonance capture integral[40] of U^{238}. It is in close agreement with the value 282 barns measured by a separate experiment at the Bettis Atomic Power Laboratory.

The choice of a depleted uranium foil as the monitor and the fact that its 74-kev activity was counted on the same counter as the deposits tend to cancel any slight drift in counting electronics or variation in the timing of the irradiations.

R_U as defined above is very nearly the effective resonance integral which is sought. It contains, however, a normalization to the same reactor power level as measured in a remote reference position, whereas it should be normalized to the same resonance neutron flux incident on the cadmium can, as measured by suitable monitors. The detectors chosen to monitor the resonance flux were indium and molybdenum foils placed against the inner surface of the cadmium can as shown in Fig. 6.49 (labeled Spectrum Foils, Position A). These foils were 1 cm in diameter and 0.013 cm thick. The indium was alloyed with tin to give 0.1 percent indium by weight; the molybdenum foil was 99.98 percent pure molybdenum.

The experimental results are shown in Table 6.35. The column labeled R_U lists the average measured uranium activation ratios multiplied by 280 barns. These values are already corrected for fission product activity. The columns headed R_{In} and R_{Mo} list the corresponding indium and molybdenum monitor foil activation ratios. Except for the larger diameter metal rods, these ratios were indistinguishable from unity. The presence of a slight flux dip and spectrum shift for the larger pieces of metal fuel is not surprising.

TABLE 6.35 — EXPERIMENTAL RESULTS

Fuel	$\sqrt{S/M^*}$ ($cm/g^{1/2}$)	$R_U^{\dagger}$ (barns)	$R_{In}^{\ddagger}$	R_{Mo}	R_{Mon}^{**}	$I^{\dagger\dagger}$ (barns)
U Metal	0.259	11.28 ± 0.17	0.962	0.990	0.976	10.96
	0.313	13.19 ± 0.11	0.974	0.990	0.982	12.83
	0.373	14.70 ± 0.03	0.990	0.994	0.992	14.22
	0.464	17.43 ± 0.16	1.00	1.00	1.00	16.83
	0.558	19.99 ± 0.09	1.00	1.00	1.00	19.39
UO_2	0.414	16.95 ± 0.15	1.00	1.00	1.00	16.35
	0.590	21.47 ± 0.50	1.00	1.00	1.00	20.87
	0.623	22.10 ± 0.07	1.00	1.00	1.00	21.50
	0.734	24.91 ± 0.05	1.00	1.00	1.00	24.31

*M is mass of uranium metal or of UO_2.

$\dagger R_U = \frac{U_A^*}{U_A} \times \frac{U_B}{U_B^*} \times 280$ barns.

$\ddagger R_{In} = \left(\frac{In_A^*}{In_B^*}\right) \div \left(\frac{In_A}{In_B}\right) = \left(\frac{In_A^*}{In_A}\right) \times \left(\frac{In_B}{In_B^*}\right)$, etc.

$^{**}R_{Mon} = 1/2\,(R_{In} + R_{Mo})$.

$\dagger\dagger I = \frac{R_U}{R_{Mon}} - 0.6$ barn.

Uncertainty of 0.6 barn applies to all the results.

The average of R_{In} and R_{Mo} (called R_{Mon}) was used to correct the measured R_U values. Finally, this was reduced by 0.6 barn to account for a departure of the spectrum from $1/E$. Thus, the effective resonance integral is

$$I = (R_U/R_{Mon}) - 0.6 \text{ barn} . \qquad \text{Eq. (6.19)}$$

The error estimates listed for R_U are standard deviations representing the reproducibility of the measurements. An uncertainty of 1 percent is assigned to the values of R_{Mon}, which is conservative for the smaller rods. In the case of largest metal rod ($\sqrt{S/M} = 0.259$), the magnitude of the spectrum shift makes an uncertainty of 2 percent more realistic.

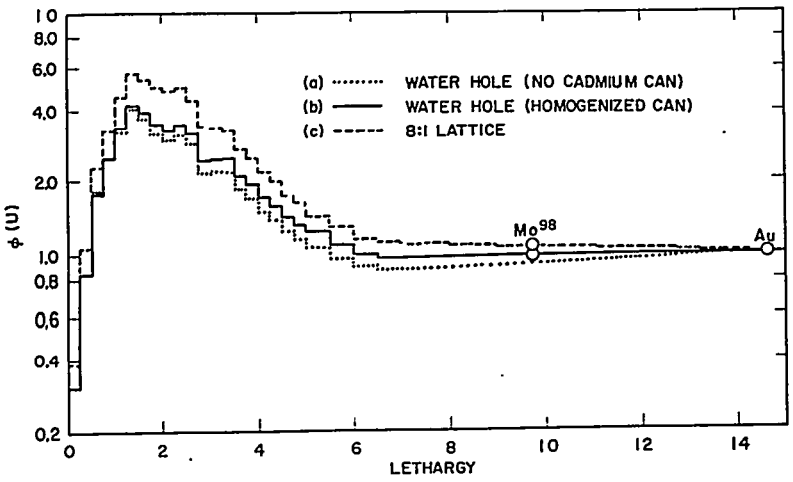

FIGURE 6.50. Calculated Flux Spectra.

In addition, the fission correction to R_U is uncertain to about 0.2 barn. Any error here would systematically affect all rod sizes. The fission correction and the self-shielding correction to the uranium activity observed in the normalizing run were neglected, since both were considerably less than 1 percent and opposed each other.

The remaining source of uncertainty is the flux spectrum in the cadmium can. Calculations of the resonance flux spectrum were done using a 54-group, one-dimensional P_1 program for the IBM-704, P1MG.[3] The first calculation was for the case of a central water hole filled with water (i.e., without the cadmium can). The resulting spectrum is shown by the dotted line in Fig. 6.50. In addition to the flux peak at small values of the lethargy* (due mostly to the decrease of the hydrogen cross section above about 25 kev), $\phi(u)$ rises by about 15 percent from lethargy 7 to 15. This rise is due to the cumulative effects of the flow of neutrons into the water hole at every lethargy. However, this calculation is not realistic because the cadmium can displaced a large portion of the water in the center of the water hole. The effect of this is to flatten $\varphi(u)$ at lethargies greater than 7.

A somewhat more realistic calculation was done in which the can was treated as infinitely long (to preserve the requisite one-dimensional nature of the system). In addition, the can and its uranium fuel rod were homogenized, and resonance capture in the uranium was ignored. The resulting spectrum (solid line) was indeed much flatter, as was expected.

*Lethargy u=0 corresponds to 10 Mev.

Because of the uncertainties involved in treating the heterogeneities, a second approach was used, namely to measure the ratio of U^{238} capture in the can to that in a reference configuration where the spectrum was known. One could then calculate the ratio of U^{238} capture in the known reference spectrum to that in a flat spectrum ($\phi(u)$ constant). It would be advantageous for the reference spectrum to be as flat as possible.

The reference configuration chosen was a hexagonal lattice of 0.983-cm diameter, 1.3 percent enriched uranium metal fuel rods at a lattice pitch of 2.88 cm (water-to-uranium volume ratio 8:1). The fuel rods were clad with aluminum, having an outer diameter of 1.153 cm. The spectrum appropriate to this lattice is shown as (c) in Fig. 6.50. This spectrum, calculated by P1MG, gave a resonance escape probability, $p = 0.929$, whereas the corresponding measured value was $p = 0.928 \pm 0.001$.

The measurements were made with metal foils of uranium (depleted to 5 ppm U^{235}), molybdenum, and gold as shown in Fig. 6.51. In case (b), the fuel rod loading was placed in the cadmium can and irradiated in the same manner as a standard resonance integral measurement. The reference measurements (c) employed the same fuel loading and the same foils, with a 0.6-cm high cadmium sleeve. The foils were placed in the central rod of the 8:1 lattice.

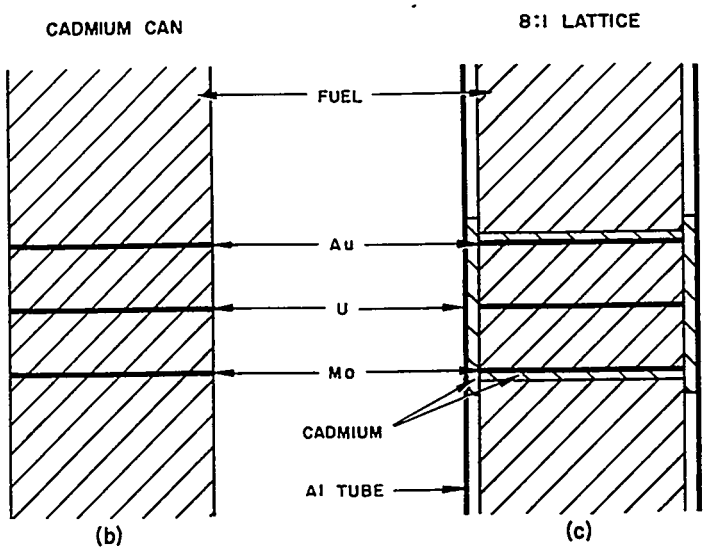

FIGURE 6.51. Foil Loadings for Spectrum Check.

Normalized to the same gold activation, the measured ratio of activation in the 8:1 lattice to activation in the cadmium can was 1.084 ± 0.008 for U^{238} capture and 1.083 ± 0.008 for Mo^{98} capture. (The equality of these numbers is not significant.) The calculated ratio of U^{238} capture in a flat flux spectrum $(\phi(u) = 1)$ to capture in spectrum (c) was 0.894. Thus, the ratio of capture in a flat flux spectrum to capture in the cadmium can spectrum was 0.9680 for the 0.983-cm diameter uranium metal rod. Since the directly measured value was 17.43 barns, the correction amounts to a subtraction of 0.56 barn.

From the spectra (b) and (c) of Fig. 6.50, the Mo^{98} ratio is 1.096, in good agreement with the measured value of 1.084. The calculated U^{238} capture ratio in these two spectra was 1.079, also in good agreement with the measured value of 1.083. It is concluded from this agreement that spectrum (b) represents the can spectrum accurately.

To calculate these ratios from the spectra of Fig. 6.50, it was necessary to assume that the Mo^{98} capture occurs predominantly at an energy of 480 ev, and that depression of the gold capture due to interference by the 6.7 ev resonance of U^{238} was the same in the lattice as in the cadmium can and could, thus, be ignored.

To calculate the U^{238} capture in the several spectra of Fig. 6.50, it was also necessary to have values for the effective U^{238} resonance capture integral of the rod in small lethargy groups. These values were obtained from Nordheim's calculations[41] up to 1000 ev. From 1000 ev to 30,000 ev values were obtained from Vernon.[42] Above 30,000 ev, the directly measured cross section values from BNL-325 were used.[43]

Most of the correction to the measured resonance integral is contributed by the flux peak below lethargy 7. For the 0.983-cm rod, the peak contributes an excess of 0.7 barn, whereas the flux dip for $u > 7$ causes a deficit of ~0.1 barn. It was decided to apply a flat 0.6-barn correction to the resonance integral for every rod. This should introduce no more error than the uncertainty inherent in the entire spectrum correction procedure. An uncertainty of 0.3 barn is assigned to this correction.

The final effective resonance integral values are listed in the last column of Table 6.35. The estimated errors are as follows (average for all rod sizes):

1. Reproducibility of the raw measurements . . . 1 percent
2. Uncertainty of the monitor ratio (due to spectrum shift) . . . . . 1 percent

3. Uncertainty of the fission correction . . . . . 0.2 barn
4. Uncertainty of the spectrum correction . . . . 0.3 barn

An overall uncertainty of 0.6 barn is felt to be reasonable.

A least squares fit to the measured points yielded the following expressions for the effective resonance integrals (including $1/v$ capture):

$$UO_2 \quad I = 6.09 + 24.8\sqrt{S/M}_{UO_2}, \quad 0.4 < \sqrt{S/M}_{UO_2} < 0.75 \qquad \text{Eq. (6.20)}$$

$$U_{metal} \quad I = 3.91 + 27.8\sqrt{S/M}_{U}, \quad 0.2 < \sqrt{S/M}_{U} < 0.6 \qquad \text{Eq. (6.21)}$$

Figures 6.52 and 6.53 show the measured effective resonance integrals for metal and UO_2 plotted against $\sqrt{S/M}$. These also compare the results with the calculations of Nordheim,[41] which have been done for the resolved resonances up to 1000 ev and unresolved s-wave resonances above 1000 ev. In addition, the following contributions are added to Nordheim's results:

	I (Barns)	
1. $1/v$ capture (all S/M)	+1.1	+1.7
2. All capture above 30 kev (all S/M)	+0.8	
3. S-wave capture above 30 kev (all S/M)	-0.2	

4. P-wave capture below 30 kev:

	S/M	
Metal	0.259	+0.79
	0.558	+0.96
UO_2	0.414	+0.90
	0.734	+1.10

1. is calculated using a U^{238}capture cross section of 2.71 barns at $E = 0.0253$ ev and assuming a cadmium cutoff energy of 0.5 ev.
2. is obtained directly from measured capture cross sections in BNL-325.[43]
3. is calculated assuming unshielded capture.[35]

4. is obtained from calculations reported by Chernick and Vernon[37] which assume a p-wave strength function twice that for s-wave resonances. Lack of knowledge of this strength function contributes appreciable uncertainty to these numbers.

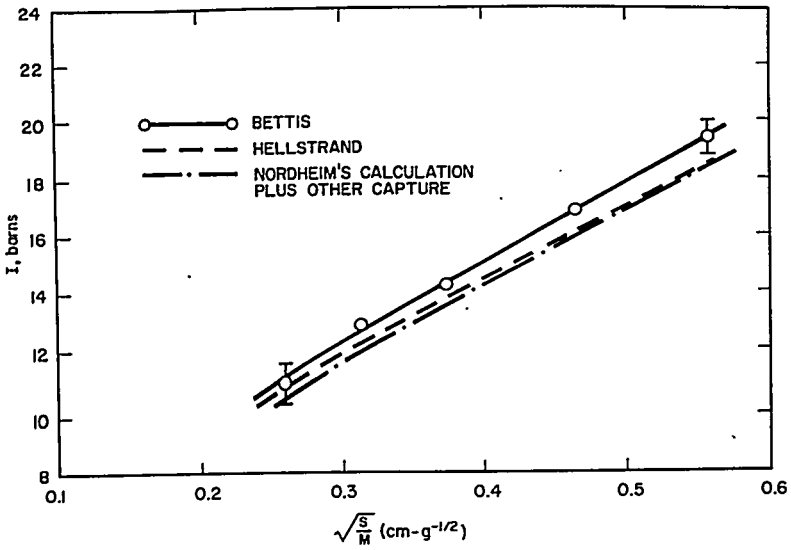

FIGURE 6.52. Results for Isolated Uranium Metal Rods.

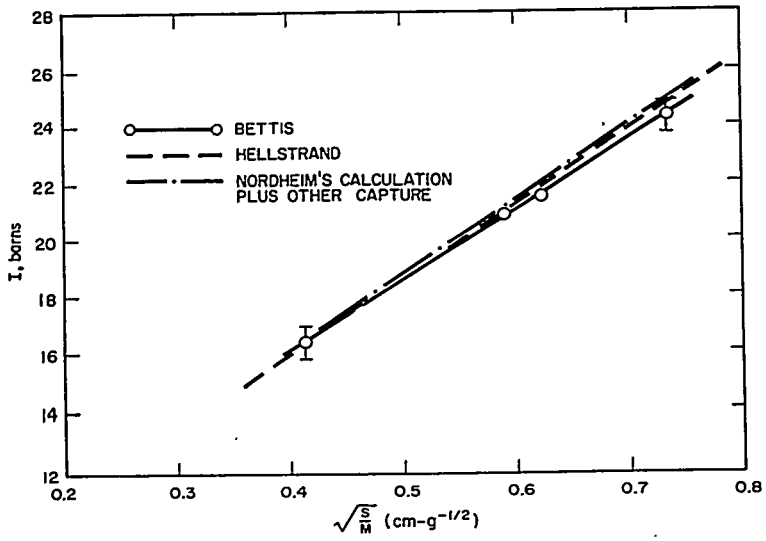

FIGURE 6.53. Results for Isolated UO_2 Rods.

It should be pointed out that a direct comparison such as this of resonance integrals (calculated) with resonance integrals (measured) is not entirely unambiguous. The ambiguity is introduced by the fact that the nuclear data used in Nordheim's calculations yield an infinitely dilute resonance integral of only 268 barns,[41] whereas the measured value is 280 barns. The effect on the rod calculations of this 12±4 barn discrepancy depends strongly on its origin.

Also shown in Figs. 6.52 and 6.53 are Hellstrand's results for U metal and UO_2 rods,[44] to which he assigns an overall uncertainty of 5 percent, including uncertainty of the gold resonance integral standard. The UO_2 results are in excellent agreement. Agreement is not as good for the metal results, but is still within the overall uncertainties.

2. *Monte Carlo Study of Equivalence Relations*

The equivalence relations deduced by several authors[35-37, 45,46] are statements connecting lattices with the same resonance integral. Descriptions of the theory are abundant, and there is no need to add still another. The result is simply stated in the form: The resonance integrals of lattices of a fixed absorber composition and temperature depend only on the effective surface-to-mass ratio, given by

$$(S/M)^* = (S/M)(1-C) \qquad \text{Eq. (6.22)}$$

and do not otherwise depend on geometry and moderator.

Here, (S/M) is the surface-to-mass ratio of the absorber lump, and $(1-C)$ is the familiar Dancoff factor, defined as the probability that a neutron leaving an absorber lump will collide in the moderator before entering another lump. This equivalence may be derived by use of the Wigner rational approximation to the region-averaged collision probabilities, together with the assumption that each resonance is either broad or narrow with respect to all the scattering materials in the lattice.

The use of the rational approximation to estimate $(1-C)$ leads to a simpler form for the effective surface-to-mass ratio, due to Bell:[45]

$$(S/M)^*_{\text{Bell}} = (S/M)\left[1 + \frac{S_1}{4V_1\Sigma_1}\right]^{-1} \qquad \text{Eq. (6.23)}$$

where S_1/V_1 is the surface-to-volume ratio of the moderator, and Σ_1 is the scattering cross section of the moderator. The factor multiplying (S/M) in the above equation will be referred to as the Bell-Dancoff factor, $(1-C)_{\text{Bell}}$.

A more general equivalence relation has been stated that links lattices in which the absorber contains varying quantities of internal moderator. This statement requires that the resonances all be narrow with respect to the internal moderator, a condition not met for oxygen in U^{238}. To anticipate later results, the more general equivalence is not as valid as the form given above.

The equivalence relations can be used to predict resonance integrals in a wide variety of configurations on the basis of determinations in a relatively small number of lattices or, perhaps, isolated rods. Although the rational approximation is subject to large errors, there is reason to believe that the equivalence relation is better than the approximations leading to it. In particular, for isolated lumps of absorber, the equivalence connects various shapes with the same surface-to-mass ratio. Examination of the actual collision probabilities for slabs, spheres, and cylinders[47] reveals differences of only a few percent, whereas the rational approximation predicts no difference but may be 20 percent in error. Thus, the rational approximation is inadequate for calculation of resonance integrals, but the equivalence relation is still useful in predicting resonance integrals for cylinders, say, from accurate calculations for slabs.

In the hope that the extension to lattices would also be reliable, an investigation of the equivalence relations was undertaken using Monte Carlo results for resonance escape probabilities. A large number of existing calculations were used, together with some new ones, so that three different sets of resonance parameters are used, corresponding to different stages of parameter measurement. Only resolved resonances were included in the calculations because the major uncertainties associated with the use of the narrow-resonance or narrow-resonance infinite-absorber approximations occur in these resonances. No corrections for spectrum effects, leakage, or competing absorption are required. Resonance integrals were computed from the expression

$$I = (-\ln p^{28}) \frac{\overline{\xi\Sigma_s} V_{\text{cell}}}{N_u V_o} \tag{6.23a}$$

where $\overline{\xi\Sigma_s}$ is the slowing-down power of the homogenized cell, N_u the U^{238} atom density, V_o the volume of the fuel, and V_{cell} the cell volume.

The measurements on isolated rods suggest that a plot of resonance integral versus $\sqrt{(S/M)^*}$ should be very nearly linear. Figure 6.54 shows results for a group of 15 metal-water lattices at 293°K and consisting of hexagonal arrays of cylindrical rods. Resonance parameters used in these calculations were essentially those in Ref. 15. No $1/v$ absorption was included. Rod diameters ranged from 0.25 in. to 2.0 in., and $\sqrt{(S/M)^*_{\text{Bell}}}$ from 0.2 cm/g$^{1/2}$ to 0.5 cm/g$^{1/2}$. Within 0.2 barn they are represented by the least squares fit

$$I = -0.41 + 23.44 \sqrt{(S/M)^*_{\text{Bell}}} \quad . \qquad \text{Eq. (6.24)}$$

(The negative volume term can be explained by assuming a departure from linearity at small $(S/M)^*$.) The scatter is just about that expected from Monte Carlo uncertainties. The tightest lattice considered has a Bell-Dancoff factor of 0.43, compared to 0.94 in the most open lattice.

The resonance integrals for a group of UO_2 lattices are exhibited in Fig. 6.55. In most of these cases the geometry was alternating slabs of UO_2 and water. Thirty-nine resolved resonances were included,[2] the temperature was again 293°K. The tightest lattices shown (one a slab, the other a cylinder lattice) depart significantly from the rest of the data; their Bell-Dancoff factor is 0.37. The rest of the calculations are represented, to the accuracy of the Monte Carlo, by

$$I = 1.79 + 26.69 \sqrt{(S/M)^*_{\text{Bell}}} \quad . \qquad \text{Eq. (6.25)}$$

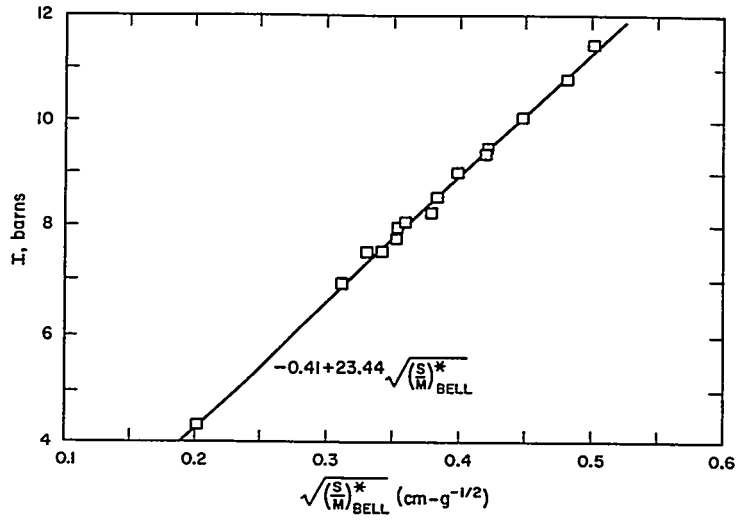

FIGURE 6.54. Monte Carlo Resonance Integrals (18 Resonances) for U-H_2O Lattices in Terms of the Bell Equivalence Parameter.

These range in Bell-Dancoff factor between 0.64 and 0.82. They exhibit a root mean square error of 0.2 barn.

The slab lattices used in the straight line fit in Fig. 6.55 were also calculated at an absorber temperature of 553° K. With the same accuracy, the results were represented by the expression

$$I = 1.44 + 28.98 \sqrt{(S/M)^*_{\text{Bell}}} \,. \qquad \text{Eq. (6.26)}$$

The exact Dancoff factors were computed for the cold slab lattices in this group, and the results are shown in Fig. 6.56. There is improvement in the agreement obtained, but the tightest lattice remains out of line. The use of $(S/M)^*$ does extend somewhat the useful range of the equivalence relation. This advantage is to some extent offset by the greater complexity of this calculation for rod lattices.

Two other UO_2 lattices also suggest that the Dancoff factor may be a better approximation in tight lattices. The lattice descriptions are given in Table 6.36 together with the results of the Monte Carlo calculations which used 27 resonances,

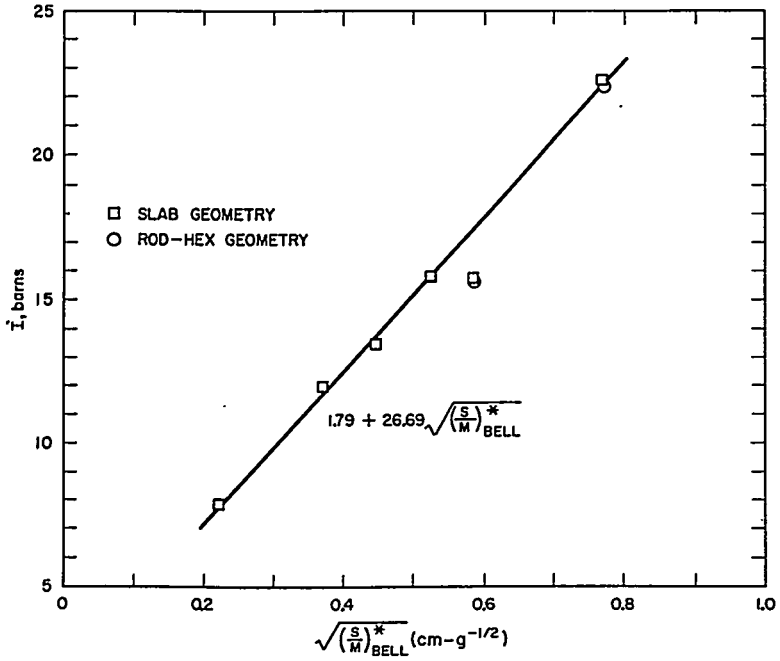

FIGURE 6.55. Monte Carlo Resonance Integrals (39 Resonances) for UO_2-H_2O Lattices in Terms of the Bell Equivalence Parameter.

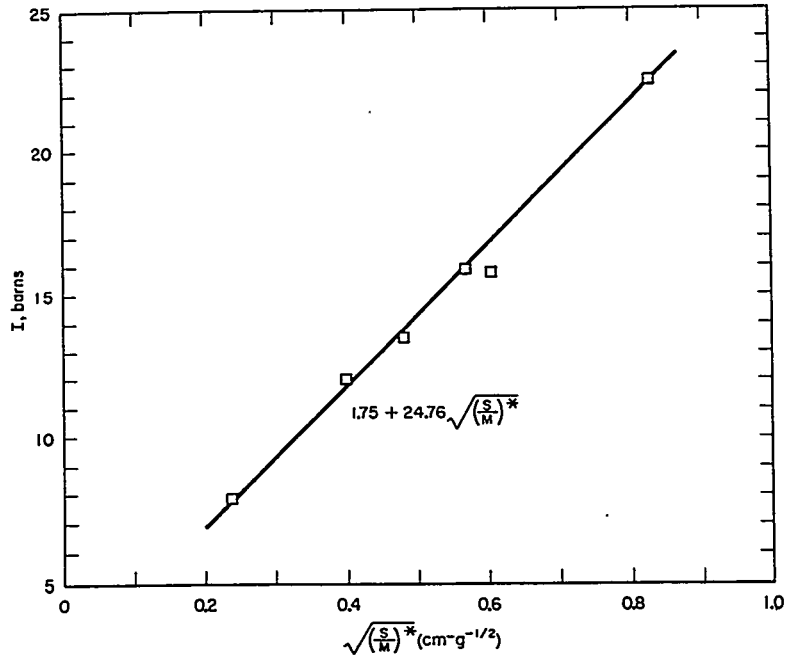

FIGURE 6.56. Monte Carlo Resonance Integrals (39 Resonances) for UO_2-H_2O Lattices in Terms of the Dancoff Equivalence Parameter.

TABLE 6.36 — SOME MONTE CARLO RESULTS FOR TIGHT LATTICES

Geometry	Moderator	S/M	$\sqrt{(S/M)^*}_{Bell}$	$\sqrt{(S/M)^*}$	I (barns)
Cylinder, hex. array	H_2O	0.381	0.513	0.544	14.9
Slab	H_2O	0.762	0.513	0.527	14.3
Cylinder, hex. array	D_2O	0.381	0.513	--	14.8

essentially those in Ref. 43. The probable error in the resonance integral is ≈0.15 barn. The lattices have the same $(S/M)^*_{Bell}$, 0.263 cm^2/g, and the temperature is 293°K. The resonance integral for the close-packed slab lattice falls

somewhat low. For this lattice, $(S/M)^*$ is also somewhat lower than for the other and by an amount consistent with the expected slope of 25 to 30 $g^{1/2}$-barns/cm.

Included in Table 6.36 is a deuterium-moderated lattice which shows that the equivalence holds well under a change of moderator. The Dancoff factor, in this case, could not be calculated with the necessary precision.

In conclusion, both formulations give a linear dependence on the square root of the effective surface-to-mass ratio over a wide range of lattices. The lines are distinct, being separated by as much as two barns. In principle, isolated rod calculations could permit a selection, since in that limit

$$(S/M)^* = (S/M)^*_{\text{Bell}} = S/M.$$

These wide lattice calculations would be extremely costly. The following experimental study makes such a comparison.

3. *Experimental Results Using Equivalence Relations*

Experimental tests of the equivalence relations can be extracted from TRX measurements of U^{238} resonance escape probability, p^{28}, for lattices and measurements of the effective resonance integrals described above. The lattices in question were hexagonal, water-moderated, and composed of cylindrical, aluminum-clad fuel rods of slightly enriched uranium metal or UO_2.

Table 6.37 lists the measured values of p^{28} from which the lattice effective resonance integrals have been computed. Cases 1 to 6 and 12 to 19, as well as the measurement technique, were reported previously.[31] In case 7, p^{28} is a recently remeasured value; cases 8 to 11 are new. The measured values of ρ, the ratio of epithermal-to-thermal U^{238} radiative capture, are also listed in the table.

The resonance integrals were computed from the expression

$$I' = (-\ln p^{28}) \frac{\overline{\xi \Sigma_s} V_{\text{cell}}}{N_u V_o}. \qquad \text{Eq. (6.27)}$$

A correction to account for the effects on p^{28} of leakage and U^{235} absorption was determined as follows. In each case, a 54-energy group P_1 calculation of resonance capture was done for a homogenized lattice by means of the MUFT

TABLE 6.37. LATTICE RESULTS

Case	Rod Diameter (in.)	Fuel	Enrichment (w/o U^{235})	W/U†	ρ‡	p^{28}	$\frac{\overline{\xi\Sigma_s}V_{cell}}{N_U V_U}$ (barns)	I′ (barns)	ΔI_1 (barns)	ΔI_2 (barns)	I (barns)	$\sqrt{(S/M)^*_{Bell}}$** (cm/$g^{1/2}$)	$\sqrt{(S/M)^*}$
1	0.600		1.3	1.5	1.80 ±0.18	0.720 ±0.014	44.25	14.54	1.10	1.05	12.39 ±0.9	0.324	0.350
2	0.600		1.3	2.0	1.24 ±0.12	0.794 ±0.016	58.89	13.59	1.00	1.05	11.54 ±1.2	0.334	0.359
3	0.600		1.3	3.0	0.89 ±0.09	0.850 ±0.017	87.85	14.28	0.84	1.05	12.39 ±1.8	0.346	0.367
4	0.600		1.15	2.0	1.20 ±0.03	0.785 ±0.005	58.81	14.24	0.79	1.05	12.40 ±0.4	0.334	0.359
5	0.600		1.15	3.0	0.93 ±0.04	0.833 ±0.007	87.72	16.03	0.66	1.07	14.30 ±0.8	0.346	0.367
6	0.387	U metal	1.3	2.0	1.59 ±0.03	0.747 ±0.005	59.11	17.26	1.05	1.07	15.14 ±0.4	0.393	0.424
7	0.387		1.3	3.0	1.066 ±0.012	0.8233 ±0.0028	88.06	17.15	0.82	1.08	15.25 ±0.29	0.412	0.441
8*	0.387		1.3	1.0	3.13 ±0.20	0.589 ±0.015	29.26	15.49	1.46	1.09	12.94 ±0.8	0.346	0.382
9*	0.387		1.3	2.4	1.37 ±0.02	0.779 ±0.004	68.62	17.14	0.98	1.07	15.08 ±0.4	0.402	0.432
10	0.387		1.3	2.4	1.41 ±0.06	0.772 ±0.008	68.62	17.75	0.98	1.07	15.70 ±0.7	0.402	0.432
11*	0.387		1.3	8.1	0.484 ±0.02	0.9284 ±0.0010	236.08	17.53	0.25	1.10	16.18 ±0.23	0.443	0.459
12	0.600		1.3	3.0	1.19 ±0.04	0.805 ±0.006	90.95	19.73	0.82	1.04	17.87 ±0.7	0.489	
13	0.600	UO_2	1.3	4.0	0.994 ±0.013	0.838 ±0.003	118.83	21.00	0.73	1.06	19.21 ±0.4	0.508	
14	0.600	7.53 g/cm^3	1.3	5.0	0.807 ±0.014	0.869 ±0.003	148.14	20.80	0.60	1.07	19.13 ±0.5	0.522	
15	0.388		1.3	4.0	1.04 ±0.05	0.832 ±0.007	117.53	21.61	0.71	1.07	19.83 ±1.0	0.585	
16	0.388		1.3	5.0	0.901 ±0.02	0.853 ±0.004	146.61	23.31	0.64	1.08	21.59 ±0.7	0.608	
17	0.384	UO_2	1.3	2.9	1.43 ±0.01	0.775 ±0.004	86.18	21.97	0.93	1.04	20.00 ±0.4	0.498	
18	0.384		1.3	3.6	1.15 ±0.01	0.815 ±0.004	107.16	21.92	0.81	1.06	20.05 ±0.5	0.517	
19	0.384	10.53 g/cm^3	1.3	4.9	0.934 ±0.010	0.850 ±0.004	143.86	23.38	0.68	1.07	21.63 ±0.7	0.540	

* Measured in sublattice at center of two-region core.

† Water-to-uranium volume ratio. For UO_2 rods, uranium volume is the volume of a uranium metal rod with the same number of uranium atoms as the UO_2 rod.

‡ ρ = (Epicadmium U^{238} Radiative Capture) ÷ (Subcadmium U^{238} Radiative Capture).

** M is mass of uranium metal or of UO_2.

code.*[1] The resonance shielding factor (L factor) used was such that the calculated value of p^{28} very closely approximated the corresponding measured value. A second calculation was also done which differed from the first only in that the U^{235} was omitted and the lattice buckling was reduced by a factor of 100. The difference between the resonance integrals inferred from the two calculations, ΔI_1, was used to correct $(I)'$ to the value appropriate to an infinite lattice without U^{235}.

In addition, in these water-moderated lattices $\overline{\xi \Sigma_s(u)}$ decreases rapidly with increasing energy greater than 10 kev. This causes a peaking of the flux in this interval and leads one to infer too large a value for the effective resonance integral from Eq. (6.27). The error can be corrected adequately by simply removing the excess capture contributed by the flux peak. This was done, using the calculated multigroup flux values for groups 1 to 25, which just span the lethargy region of the flux peak

$$\Delta I_2 = \sum_{i=1}^{25} (\phi_i - 1)\, \bar{\sigma}_i^{28} \Delta u_i \qquad \text{Eq. (6.28)}$$

where $\phi_{25} = 1$. The U^{238} capture cross sections were obtained from experimental values listed in Ref. 43. Errors quoted were calculated from those for the p^{28} values.

The equivalence parameter for the Bell formulation, $(S/M)^*_{\text{Bell}}$, was calculated from Eq. (6.23) for each lattice. Figures 6.57 and 6.58 show the results for uranium metal and UO_2, respectively. Included are the measured isolated rod resonance integrals to which an overall uncertainty of 0.6 barn is assigned. In addition, there is a resonance integral inferred from a Monte Carlo calculation of p^{28} for case 8.[48] This calculation was done for an infinite lattice without U^{235}; 30,000 histories were run, the neutrons being started at 10 kev. The result was p^{28} (10 kev→3 ev) = 0.6925 ± 0.0027, yielding a resonance integral of 10.75 ± 0.11 barn. To this were added 2.9 barns to account for the remaining capture.

The metal rod results are perfectly consistent with the assumed equivalence relation. Except for the three high density lattice cases, the UO_2 results show good consistency also. Part of the discrepancy among the UO_2 lattices can probably be attributed to the use of uranium metal foils in the older UO_2 measurements.[38]

*For the two-region lattices, a 54-energy group, radially dependent, P_1 problem was done instead, by means of the PIMG code.[3]

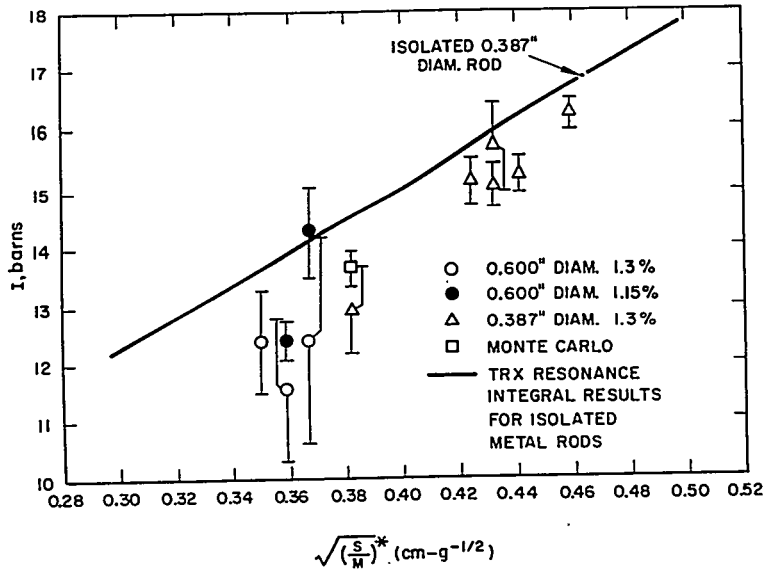

FIGURE 6.57. Comparison of Measured Isolated Rod and Lattice Resonance Integrals for Metal Rods in Terms of the Bell Equivalence Parameter.

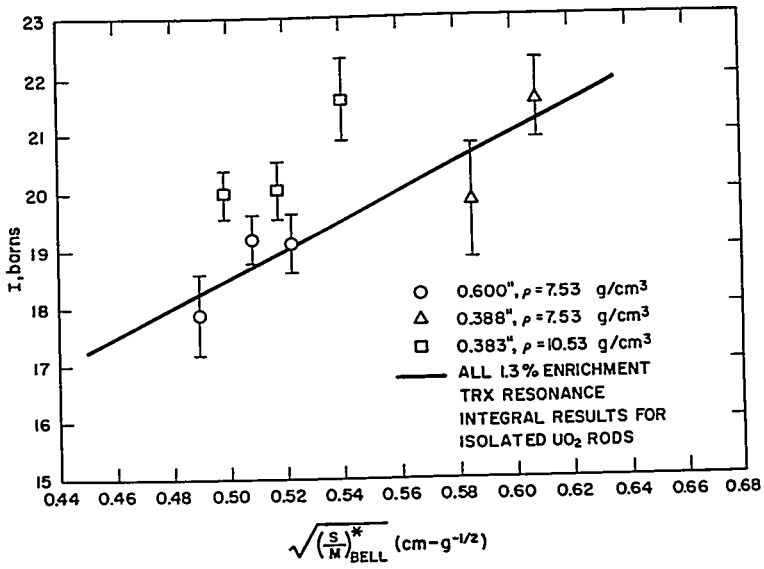

FIGURE 6.58. Comparison of Measured Isolated Rod and Lattice Resonance Integrals for UO_2 Rods in Terms of the Bell Equivalence Parameter.

The metal results were replotted in terms of the Dancoff equivalence parameter $\sqrt{(S/M)^*}$ (see Fig. 6.59). Although there is some uncertainty involved in properly calculating $(1-C)$, particularly in the tighter lattices, our lattice results fall below the isolated rod values when plotted against $\sqrt{(S/M)^*}$. The overall agreement is still considered good.

The more general equivalence[36] among lattices of uranium metal and of UO_2 in terms of one parameter does not appear to work as well. The equivalence parameter is, in this case,

$$\lambda_e^{1/2} = \left[\left(\frac{4N}{A^{28}}\right)\sigma_{ps} + \left(\frac{S}{M_U}\right)\right]^{1/2} \qquad \text{Eq. (6.29)}$$

where

S = surface of fuel (cm^2)
M_U = mass of uranium in fuel (g)
N = Avogadro's number
A^{28} = 238
σ_{ps} = admixed oxygen potential scattering cross section per uranium atom (barns).

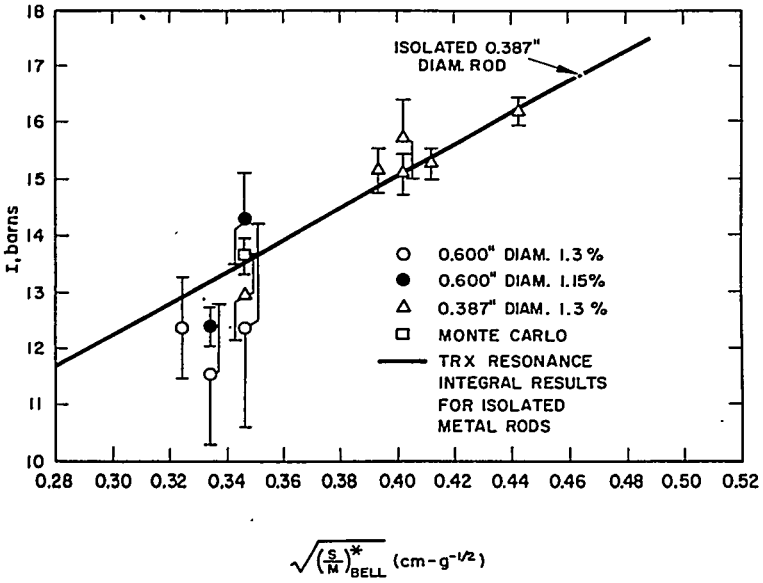

FIGURE 6.59. Comparison of Measured Isolated Rod and Lattice Resonance Integrals for Metal Rods in Terms of the Dancoff Equivalence Parameter.

On this basis, all of the data should form a single straight line. Referring to Fig. 6.60, it can be seen that the oxide results are about two barns lower than the metal results. To obtain better agreement it would be necessary to reduce the admixed oxygen moderating cross section in Eq. (6.29). Such a reduction is qualitatively consistent with the fact that the treatment of oxygen in the narrow resonance approximation is not strictly correct for the lowest resonances in U^{238}.

In summary, the equivalence relations, using either the Dancoff factor or the Bell approximation to it, have been tested over a wide range of surface-to-mass ratios by Monte Carlo calculations. In tight lattices, some breakdown appears in both formulations, but the Dancoff treatment shows somewhat better agreement than the Bell approximation. Both formulations were also tested experimentally over a smaller range of surface-to-mass ratios; the Bell approximation is favored in these comparisons. Within the precision of all the information cited, no clear cut preference is indicated. Both formulations appear to work well.

C. The Relative U^{235} Fission Activation as a Function of Energy in Slightly Enriched Uranium–Water Lattices

D. Klein and J. J. Volpe

While Sect. 6.5.B emphasized the resonance problem in the slightly enriched uranium systems, the succeeding two sections will discuss one aspect of the thermal problem. A quantity of interest in the investigation of thermal reactor characteristics is the relative amount of thermal and epithermal activations, which is usually expressed in terms of the cadmium ratio. An experimental study of the relative U^{235} fission activation as a function of energy has been made for the TRX facility, a heterogeneous, light water-moderated and reflected critical assembly.[34] The parameter directly obtained from the experiments is the ratio of the fission activation of a bare U^{235} detector to that of a similar detector covered by a shield of absorbing material which is either cadmium, boron, or gadolinium. The results are compared with those obtained from a theoretical model.

For the comparisons discussed here, the fuel making up the critical assembly was in the form of cylindrical rods, 48 in. long, clad in an aluminum jacket 0.028 in. thick. A radial air gap of 0.005 in. existed between the cladding and fuel. The fuel rods were arranged in a hexagonal array in a stainless steel lattice plate with the outer boundary of

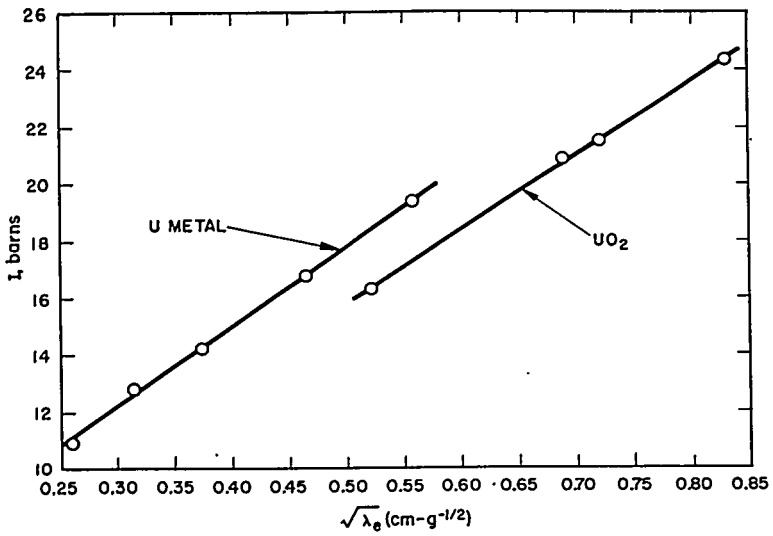

FIGURE 6.60. Comparison of Measured Resonance Integrals for Isolated Metal and UO_2 Rods in Terms of the Generalized Equivalence Parameter λ_e.

the fuel region filled to approximate a cylindrical core. The measured activation ratios were obtained for a critical core consisting of 0.387-in. diameter uranium metal rods enriched to 1.3 weight percent U^{235} and spaced such that the water-to-uranium volume ratio was 2.4. This type of fuel rod is typical of the type found in certain power reactors and, thus, was considered to provide an appropriate test of the theory.

1. *Experimental Investigations*

The experimentally measured quantity is the ratio of the fission activation of a bare U^{235} foil to that of a similar foil enclosed in a box made of either cadmium, boron, or gadolinium. This quantity is designated as the cadmium, boron, or gadolinium ratio, respectively. The foils were circular, 0.005 in. thick and 0.387 in. in diameter, and made of a uranium-aluminum alloy. The uranium was enriched to greater than 90 weight percent U^{235} and alloyed at 10 weight percent with 2S aluminum. This concentration is such that the U^{235} atom density in any foil is approximately the same as that in the fuel. The foils were positioned between sections of a split fuel rod, as shown in Fig. 6.61, and irradiated within a small central region of the core. After irradiation, fission product γ radiation from the foils was measured by scintillation counter techniques and background corrections

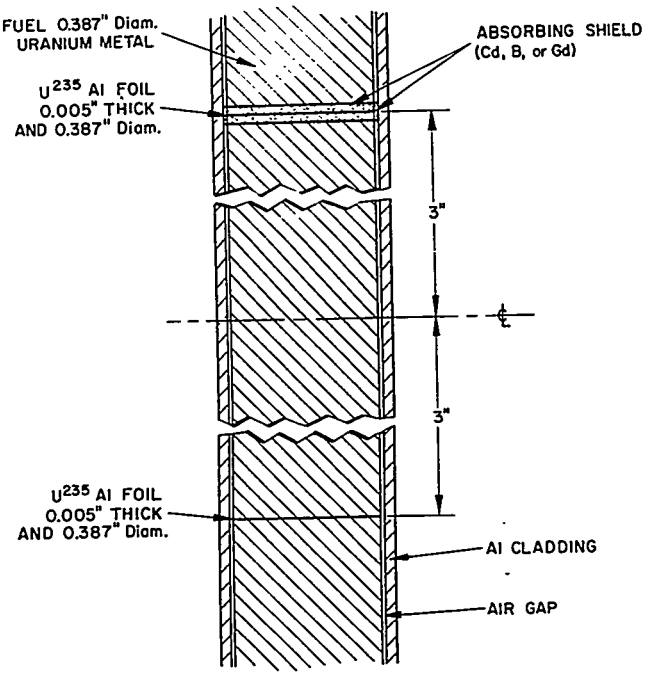

FIGURE 6.61. Foil Arrangement for Irradiation.

applied. The technique is similar to that used in the integral measurement of thermal utilization.[31]

In general, the various shield materials used on the covered foil were in the form of two cylindrical wafers plus a ring of the same thickness as one wafer and a height equal to that of the entire package. A typical covered foil is shown in Fig. 6.62. One cadmium box was made with a thickness of 437 mg per cm^2 obtained by using cadmium that was 0.020 in. thick. Two types of boron covers were used. One set was constructed from tape composed of finely ground boron adhering to a 0.0005-in. Mylar backing. The thickness of boron 10 on the tape was 0.80 ± 0.04 mg per cm^2 yielding a range of boron-10 thicknesses of 1.6 ± 0.08 mg per cm^2 to 28 ± 1.4 mg per cm^2 when using 2 to 35 tapes. The second set was constructed from sintered boron giving boron 10 thicknesses in the range of 21.5 ± 0.20 mg per cm^2 to 41.1 ± 0.40 mg per cm^2. All the boron utilized was enriched to 91 weight percent boron-10. The gadolinium boxes were made from sintered material consisting of natural Gd_2O_3. The range of natural gadolinium thicknesses obtained was from 6.5 ± 0.30 mg per cm^2 to 130 ± 3.0 mg per cm^2.

The activity of the covered foil, when measured as described above, is expected to be too high because of edge effects.

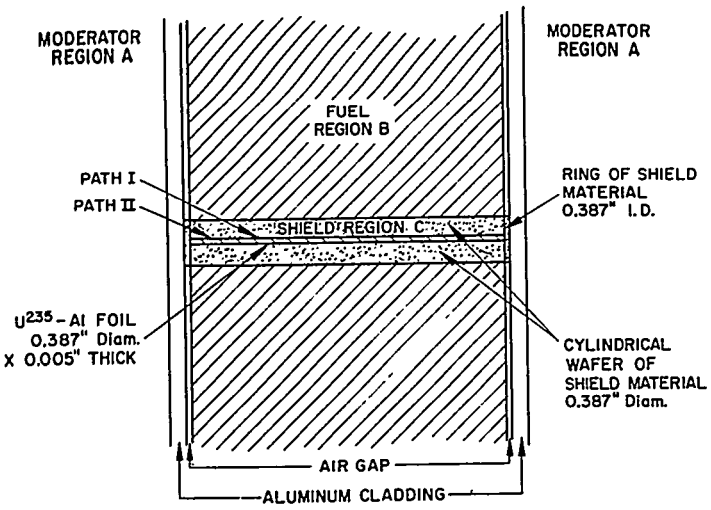

FIGURE 6.62. Typical Covered Foil When Irradiated.

This arises from the fact that neutrons activating the detector have shorter path lengths when traversing the side of the ring portion of the shield material than when passing through the wafer portion at the same incident angles. Furthermore, the contribution of the resulting additional activity tends to occur mainly at the outer edge of the foil where the greater area per element of radius is located. Hence, it was felt that the overall correction could not be neglected. An example of this situation is shown on Fig. 6.62, with the path lengths designated as I and II.

An attempt to account for edge effects experimentally was made by increasing the thickness of the ring surrounding the covered foils in the case of the boron and gadolinium shields. It was felt that the boron shields would be more sensitive to this effect due to the $1/v$ cross-section behavior than the gadolinium or cadmium shields. The measured boron-covered activities with the normal size rings were found to be too high and were decreased by amounts varying from 1 percent to 15 percent, the higher corrections being applied to the smaller thicknesses. All the measured gadolinium-covered activities were found to be too high by approximately 3 percent, whereas the cadmium-covered result was too high by about 4 percent.

The experimental results for boron and gadolinium, corrected for edge effects, are plotted versus shield thickness in Figs. 6.63 and 6.64.

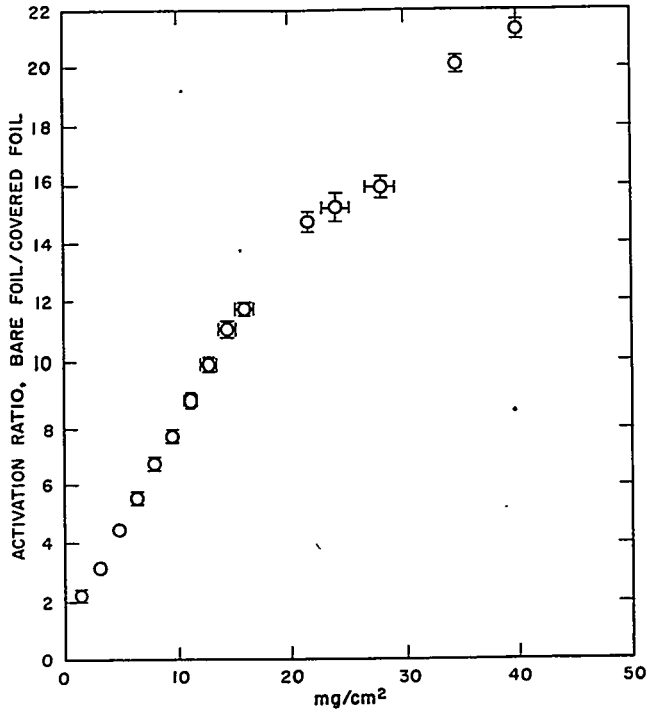

FIGURE 6.63. Experimental Activation Ratio (Bare Foil/Covered Foil) vs mg/cm² of Boron-10.

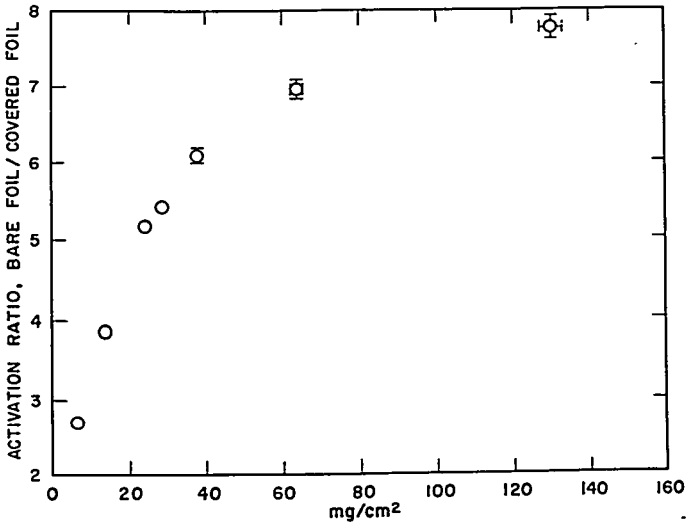

FIGURE 6.64. Experimental Activation Ratio (Bare Foil/Covered Foil) vs mg/cm² of Gadolinium.

2. *Theoretical Investigations: Description of Model*

Calculated values of the relative fission activations can be obtained if the flux impinging upon the bare and covered detectors is known as a function of energy, position, and direction. In view of the lack of such detailed information, the following model was constructed (see Fig. 6.62). The flux in the moderator (Region A) was assumed to be isotropic and have a 20° C Maxwellian energy distribution plus essentially a $1/E$ component. This latter part of the spectrum was obtained from a multigroup Fourier transform code (MUFT) written for the IBM-704 in which the spectrum from 10 Mev to 0.625 ev was calculated for an infinite homogeneous mixture of the materials in the core.[23]

The flux in the fuel (Region B) was obtained by modifying the assumed moderator spectrum with a fuel self-shielding factor in the energy range of 0 to 0.625 ev. This factor is defined as the ratio of the spatially averaged flux in the fuel to the flux on the surface, assuming that the fuel rod is immersed in a bath of monoenergetic neutrons whose magnitude is constant and angular distribution isotropic at every point. The self-shielding factor is related to the problem of the first collision probability for a uniformly distributed source of monoenergetic neutrons within a homogeneous medium.[47] This relationship is given by

$$f' = 1 - P_c$$

where f' is the self-shielding factor and P_c is the collision probability within the medium. Tabulated values of P_c for a pure absorber in cylindrical geometry are given in Ref. 47 as a function of the optical thickness R/λ_a, where R is the radius of the cylinder and λ_a is the absorption mean free path.

In view of the fact that the scattering in the fuel is not negligible in the thermal range for the low enriched uranium used ($\Sigma_s/\Sigma_a \sim 0.7$ at 0.025 ev), a first-order correction was made on the self-shielding factor obtained for a pure absorber. If it is assumed that the spatial distribution of higher generation collisions is uniform, then this correction[49] is given by

$$f_o = \frac{f'}{1 - \frac{\Sigma_s}{\Sigma_t}(1 - f')}$$

where f' is the self-shielding factor computed without scattering in the fuel, and Σ_s/Σ_t is the ratio of scattering to total cross section in the fuel.

The joining of the $1/E$ component to the Maxwellian flux in the case of the moderator region and to the moderator flux modified by f_o in the case of the fuel region was accomplished by satisfying the following two conditions. The energy-dependent flux was required to be continuous and, at the same time, the total absorption rate in the cell below 0.625 ev was set equal to the number of neutrons slowing down past this energy. This can be expressed as

$$q_{0.625} = C\int_o^{0.625\ \mathrm{ev}} \Sigma_a^{\mathrm{fuel}}(E) f_o(E)\phi(E)dE + C\int_o^{0.625\ \mathrm{ev}} \Sigma_a^{\mathrm{mod}}(E)\phi(E)dE$$

where

$q_{0.625}$ = slowing-down density at 0.625 ev in units of neutrons/cm^3/ sec

$\Sigma_a^{\mathrm{fuel}}, \Sigma_a^{\mathrm{mod}}$ = macroscopic absorption cross sections of the fuel and moderator, respectively.

C = normalizing constant.

Thermal leakage was ignored on the basis that this contribution is small for this system. A plot of the moderator and fuel flux spectra is given in Fig. 6.65.

Having thus established a representation of the energy spectrum of the flux in the fuel, the cadmium, boron, and gadolinium ratios were obtained by calculating the relative value of the fission activation integral $\int \sigma_f^{235}(E)\phi(E)dE$ for the bare and covered foils. The quantity $\phi(E)$ denotes the flux impinging upon the respective detectors. For the case of the bare foil, $\phi(E)$ was chosen to be the flux in the fuel as developed in the model above, i.e., the moderator flux modified by f_o. However, for the case of the covered foil, transmission through the shield material must be accounted for. Assuming slab geometry with no edge effects, thin detectors, and the flux impinging upon the shield material isotropic (Fig. 6.62, Region C), then the fission activation integral for the covered foil is given by $\int \sigma_f^{235}(E) f_o(E) E_2(\xi)\phi(E)dE$.[50] The quantity designated as $E_2(\xi)$ is a member of the tabulated (Appendix A of Ref. 34 and Ref. 51) set of functions expressed as

$$E_n(\gamma) = \int_o^1 u^{n-2} e^{-\gamma/u} du \ .$$

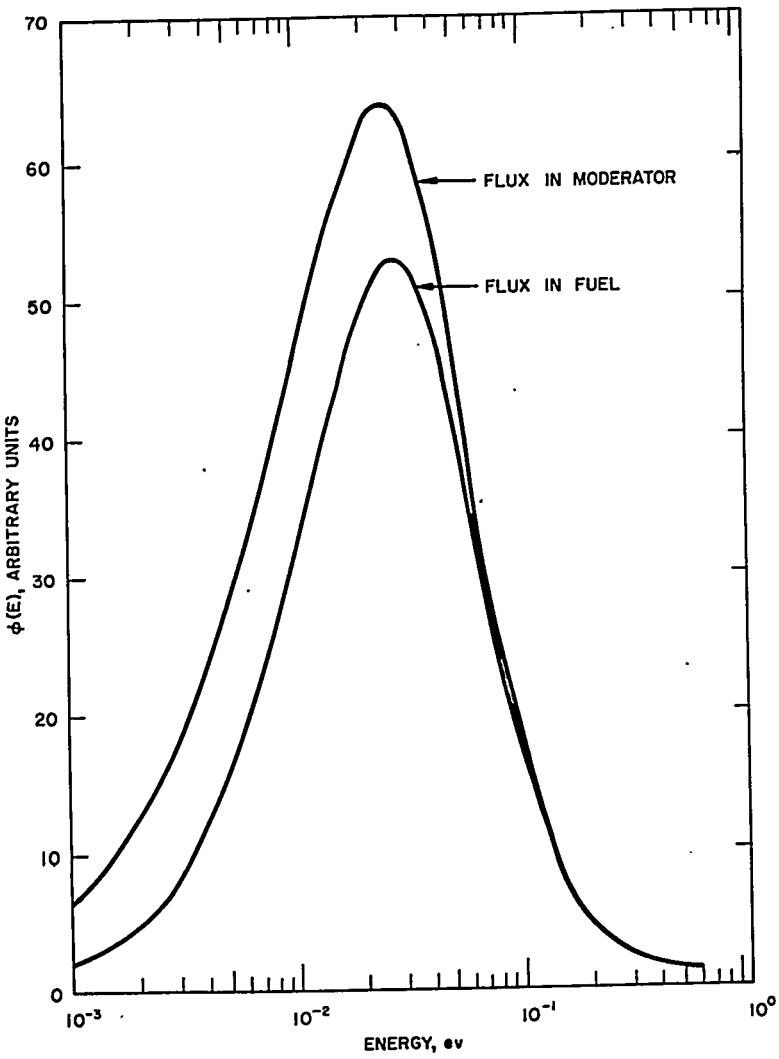

FIGURE 6.65. $\phi(E)$ vs Energy.

The energy-dependent argument denoted as ξ is the shield thickness measured in units of mean free path. Both activation integrals were integrated over the energy range of 0 to 10 Mev.

A) CUTOFF ENERGY. A convenient method for comparing on one graph all the experimental and theoretical results obtained is to introduce an effective cutoff energy for the shield of absorbing material surrounding the covered detector. This quantity is defined[52] as the cutoff energy of a perfect

filter that permits the same total activation rate in a detector as the shield material surrounding the detector allows. Thus, in place of any of the shield materials used, a filter with the following characteristic is substituted:

$$\sigma_a = \infty \text{ for } 0 \leq E < \epsilon$$

$$\sigma_a = 0 \text{ for } \epsilon \leq E \leq \infty .$$

The effective cutoff energy ϵ, for the model discussed here, is obtained by satisfying the following relationship:

$$\int_o^{10\ \text{Mev}} \sigma_f^{235}(E) f_o(E) E_2(\xi) \phi(E) dE = \int_\epsilon^{10\ \text{Mev}} \sigma_f^{235}(E) f_o(E) \phi(E) dE .$$

The approximate range of cutoff energies calculated in this fashion is the following:

ϵ = 0.04 ev to 25 ev for boron shields

ϵ = 0.07 ev to 0.3 ev for gadolinium shields

ϵ = 0.55 ev for the cadmium shield

The cutoff energy in the case of boron is quite sensitive to the shield thickness due to the $1/v$ behavior of the boron cross section. This is reflected in the extensive range of ϵ values obtained for this material. In contrast, the gadolinium cross-section behavior is somewhat like cadmium, except that it covers a lower portion of the energy spectrum and does not decrease quite as rapidly. Hence, the values of ϵ for the gadolinium shields are not as sensitive to thickness and tend to lie in a much narrower range.

B) CROSS-SECTION DATA. The microscopic cross sections used in the calculation of the activation integrals and cutoff energies were obtained from various sources. In the case of the fission cross section of U^{235}, the following values were used: from 0 to 5.1 ev, BNL-325, Second Edition; from 5.1 ev to 10 Mev, average group cross sections from the multigroup Fourier transform code discussed previously (MUFT). These group-averaged cross sections were obtained at each of the 54 energy groups peculiar to the MUFT routine. Since little self-shielding exists in the samples, effects such as Doppler broadening could be ignored. Values were

obtained for cadmium from BNL-325, Second Edition, for the range 0 to 0.060 ev and the Breit-Wigner formula for the range 0.060 ev to 5.1 ev utilizing the resonance parameters in BNL-325; for boron, from 0 to 15 kev, BNL-325, Second Edition; for gadolinium, from 0 to 0.034 ev, BNL-325, Second Edition; for the range 0.034 ev to 0.28 ev, measurements[53] from Brookhaven; and for 0.28 ev to 101 ev, BNL-325, Second Edition. The later measurements for gadolinium are lower than the previous Brookhaven results shown in BNL-325 by as much as 40 to 50 percent in the energy range mentioned.

3. *Discussion of Results*

The experimental and theoretical results are shown in Fig. 6.66 as a function of cutoff energy. Also shown are two auxiliary curves representing the fact that the theoretical values were obtained utilizing a measured U^{235} resonance fission integral of 270 barns as a normalization for the epithermal fission cross section. Since this value currently has approximately a 10 percent experimental error associated with it, the upper curve in Fig. 6.66 represents the calculated results using 245 barns and the lower curve using 295 barns.

The horizontal errors shown on the experimental points are due to the uncertainties in the thickness of the various shields used. The vertical errors are a combination of

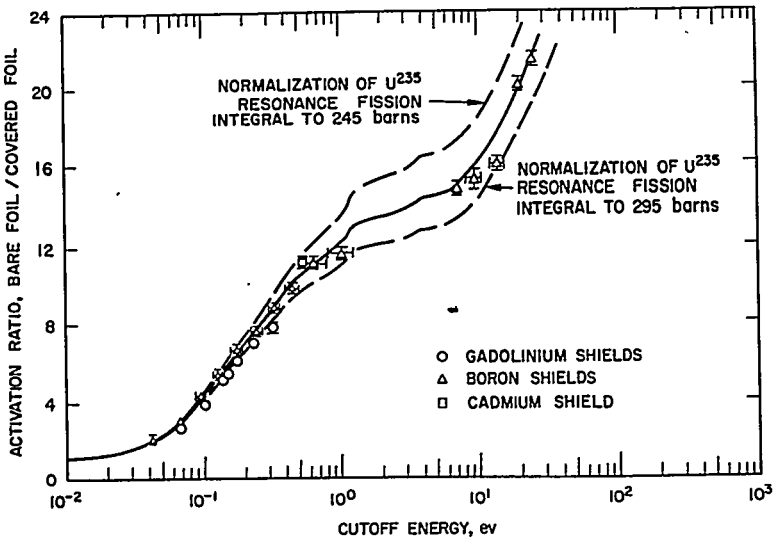

FIGURE 6.66. Experimental and Theoretical Activation Ratios as a Function of Cutoff Energy.

statistical and edge correction uncertainties. No attempt has been made to associate any errors with the calculated results, aside from the 10 percent uncertainty in the measured resonance fission integral. Part of the discrepancy between the measured activations using boron and gadolinium covers may be the result of the current uncertainty in the isotopic concentration of boron 10 in the natural boron. The activation results reported here are based on a value of 19.8 percent as given in BNL-325, Second Edition.

The disagreement between the boron and gadolinium results may also be partially due to the details of the assumed flux spectrum in the transition region (about 0.1 ev to 0.3 ev) between the thermal and epithermal ranges. The gadolinium cutoff energies are more sensitive to the detailed spectrum in this range than the boron values due to the sharply decreasing behavior of the gadolinium cross section at these energies.

As a check of the sensitivity of the results to the assumed overall flux spectrum used in the model, two other fluxes were constructed representing softer and harder spectrums. The softer spectrum was obtained from an IBM code (SOFOCATE) which solves for the Wigner-Wilkins distribution in the range 0 to 0.625 ev of an infinite homogeneous mixture of the materials in the core.[4] The harder spectrum was constructed by modifying this softer spectrum with the self-shielding factor f_o. Both fluxes were normalized to the $1/E$ component used in the model by satisfying the same conditions previously discussed. A comparison of the three distributions is shown in Fig. 6.67 where the notation $f_o\varphi_{MAX}$ indicates the spectrum used in the model, ϕ_{SOF} and $f_o\phi_{SOF}$, the softer and harder spectrums, respectively. Various results utilizing these fluxes are compared in Table 6.38. It is seen that, in general, the results are not very sensitive to the choice of spectrum made.

It is concluded that the agreement between calculated and measured values is adequate in view of the simplified model used and the existing uncertainties in both the theoretical and experimental results.

D. Relative Pu and U^{235} Fission Rates in Water–Uranium Reactor Spectra

This section deals with measurements of Pu^{239} and Pu^{241} fission rates relative to U^{235} in the 1.3 percent enriched uranium metal fueled lattice previously discussed. Experimental results were obtained in lattices having the 0.387-in. diameter rods and with water-to-uranium ratios of 2.35 to 1 or 1 to 1.

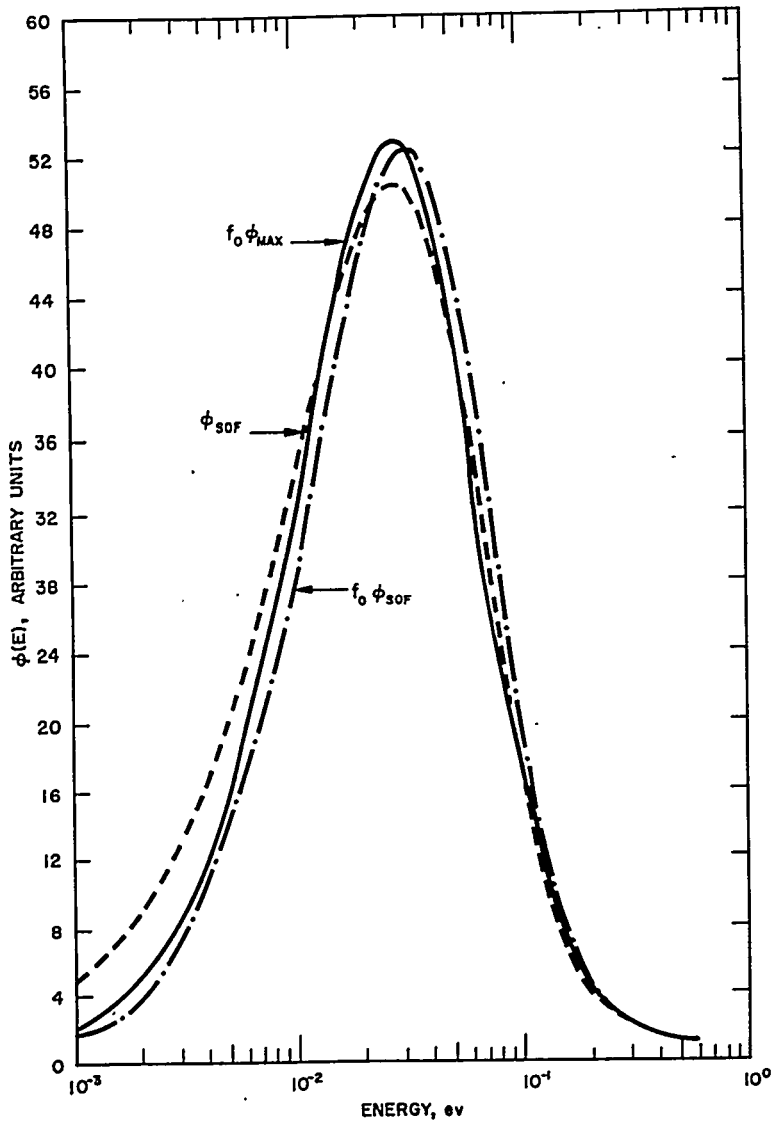

FIGURE 6.67. Comparison of Various Flux Spectra.

1. Description of Experiment

The Pu was in the form of 1 mg/cm^2 deposits on highly pure nickel foils 0.010 in. thick. The U^{235} was in the form of uranium-aluminum foils 0.005 in. thick alloyed at 10 weight percent uranium. The enrichment of the uranium was greater

TABLE 6.38 — COMPARISON OF RESULTS USING VARIOUS FLUX SPECTRA

Shield Material	$\frac{mg}{cm^2}$	$\phi(E) = \phi_{SOF}(E)$		$\phi(E) = f_o(E)\phi_{MAX}(E)$		$\phi(E) = f_o(E)\phi_{SOF}(E)$		Experimental Bare-to-Covered Foil Activation Ratio
		ϵ (ev)	$\frac{\int_0^{10\ Mev} \sigma_f^{235}(E)\phi(E)dE}{\int_\epsilon^{10\ Mev} \sigma_f^{235}(E)\phi(E)dE}$	ϵ (ev)	$\frac{\int_0^{10\ Mev} \sigma_f^{235}(E)\phi(E)dE}{\int_\epsilon^{10\ Mev} \sigma_f^{235}(E)\phi(E)dE}$	ϵ (ev)	$\frac{\int_0^{10\ Mev} \sigma_f^{235}(E)\phi(E)dE}{\int_\epsilon^{10\ Mev} \sigma_f^{235}(E)\phi(E)dE}$	
Boron-10	1.60	0.041	2.02	0.041	1.99	0.044	1.96	2.21 ± 0.18
	4.80	0.090	4.18	0.092	4.09	0.092	4.00	4.42 ± 0.12
	8.00	0.168	6.59	0.168	6.46	0.162	6.34	6.77 ± 0.20
	11.2	0.323	9.06	0.316	8.89	0.300	8.80	8.86 ± 0.15
	14.4	0.656	11.3	0.637	11.1	0.582	11.1	11.0 ± 0.3
	21.5	7.09	15.3	7.04	15.1	6.58	15.2	14.8 ± 0.3
	28.0	13.09	18.0	13.8	17.8	13.7	18.0	15.9 ± 0.3
	40.1	24.7	21.7	24.7	21.4	24.6	21.8	21.3 ± 0.3
Gadolinium	6.48	0.067	3.15	0.067	3.08	0.069	2.99	2.67 ± 0.03
	23.9	0.137	5.86	0.138	5.71	0.136	5.67	5.17 ± 0.08
	37.6	0.175	6.75	0.174	6.59	0.171	6.60	6.08 ± 0.10
	63.6	0.233	7.70	0.229	7.57	0.224	7.62	6.96 ± 0.12
	130	0.320	9.01	0.316	8.89	0.315	9.01	7.75 ± 0.15
Cadmium	437	0.525	10.7	0.526	10.6	0.526	10.8	11.3 ± 0.4

than 90 percent. The isotopic concentrations of the Pu deposits are given in Table 6.39. It is noted that two types of samples were used such that the deposits either had a high concentration of Pu^{239} or a high concentration of Pu^{241}. All foils and deposits were 0.387 in. in diameter.

The measured total fission product activity of the Pu^{239} and U^{235} foils can be expressed in terms of the isotopic fission rates as follows:

$$A^{49}_{\text{TRX}}(t) = K_2(t) N^{49} \int_o^\infty \sigma_f^{49} \phi(E) dE$$

$$A^{25}_{\text{TRX}}(t) = K_1(t) N^{25} \int_o^\infty \sigma_f^{25} \phi(E) dE$$

where $A(t)$ is the activity at time t of a plutonium or uranium foil irradiated in the TRX, N is the atom density, and $K_1(t)$ and $K_2(t)$ are functions which reflect the time of irradiation, the time from shutdown, and the efficiency of counter. Since the plutonium deposit is almost entirely Pu^{239}, the higher isotopes are ignored in the equations.

To eliminate the time functions $K_1(t)$ and $K_2(t)$, the foils were also irradiated in the Brookhaven National Laboratory (BNL) thermal column where the following equations apply:

$$A^{49}_{\text{BNL}}(t) = K_2(t) N^{49} \bar{\sigma}_{th}^{49} \phi_{th}$$

$$A^{25}_{\text{BNL}}(t) = K_1(t) N^{25} \bar{\sigma}_{th}^{25} \phi_{th}$$

where $\bar{\sigma}_{th}$ is the fission cross section of Pu^{239} or U^{235} averaged over a Maxwellian spectrum, and ϕ_{th} is the total Maxwellian flux.

TABLE 6.39 — ISOTOPIC CONCENTRATIONS OF Pu DEPOSITS

	Pu^{239}	Pu^{240}	Pu^{241}	Pu^{242}
Pu^{239} deposit	99.36%	0.63%	0.01%	
Pu^{241} deposit	9.02%	31.01%	57.96%	2.01%

If all the equations are combined, the Pu^{239} fission rate relative to U^{235} can be expressed in terms of the measured activities:

$$\frac{\int_o^\infty \sigma_f^{49}\,\phi(E)\,dE}{\int_o^\infty \sigma_f^{25}\,\phi(E)\,dE} = \left\{\frac{A^{49}(t_1)}{A^{25}(t_2)}\right\}_{\text{TRX}} \left\{\frac{A^{25}(t_2)}{A^{49}(t_1)}\right\}_{\text{BNL}} \frac{\bar{\sigma}_{th}^{49}}{\bar{\sigma}_{th}^{25}}$$

Eq. (6.30)

where t_1 and t_2 indicate that it is not necessary to measure the uranium and plutonium activities at the same time, but it is necessary to measure A^{49}_{TRX} and A^{49}_{BNL} with the same elapsed time after the irradiation. The latter condition is also necessary for the uranium foils. Implicit in the derivation is the assumption that the time decay due to irradiation by epithermal neutrons is the same as the decay due to thermal activation. Since the cadmium ratios were greater than 5 to 1, it is not considered to be an important effect. No time dependence was detected in the activation ratios or in the cadmium ratios.

For the Pu^{241} fission rates relative to Pu^{239}, the equations are similar to those given above. The activations in the TRX can be expressed as

$$A^{41}_{(t)\,\text{TRX}} = K_3(t)N_{41}^{41}\int_o^\infty \sigma_f^{41}\,\phi(E)\,dE + K_2(t)N_{41}^{49}\int_o^\infty \sigma_f^{49}\,\phi(E)\,dE$$

$$A^{49}_{(t)\,\text{TRX}} = K_2(t)N_{49}^{49}\int_o^\infty \sigma_f^{49}\,\phi(E)\,dE$$

where A^{41} is the activity of the Pu^{241} deposit and A^{49} is the activity of the Pu^{239} deposit, and N_k^i is the number of atoms of isotope i in deposit k. Thus, N_{41}^{49} would be the number of Pu^{239} atoms in the sample which was enriched in Pu^{241}. For the activation in the BNL thermal column, the following equations apply:

$$A^{41}_{(t)\,\text{BNL}} = K_3(t)N_{41}^{41}\bar{\sigma}_{th}^{41}\,\phi_{th} + K_2(t)N_{41}^{49}\bar{\sigma}_{th}^{49}\,\varphi_{th}$$

$$A^{49}_{(t)\,\text{BNL}} = K_2(t)N_{49}^{49}\bar{\sigma}_{th}^{49}\phi_{th}\ .$$

Combining the above equations leads to the final expression

$$\frac{\left[\left(\frac{A^{41}(t)}{A^{49}(t)}\right)_{TRX} - \frac{N_{41}^{49}}{N_{49}^{49}}\right]}{\left[\left(\frac{A^{41}(t)}{A^{49}(t)}\right)_{BNL} - \frac{N_{41}^{49}}{N_{49}^{49}}\right]} \frac{\bar{\sigma}_{th}^{41}}{\bar{\sigma}_{th}^{49}} = \frac{\int_o^\infty \sigma_{(E)}^{41} \phi(E)dE}{\int_o^\infty \sigma_{(E)}^{49} \phi(E)dE} \qquad \text{Eq. (6.31)}$$

where it is necessary to use activities measured at the same time. Equation (6.31) has ignored the contribution from the Pu^{240}. Similar expressions can easily be derived which include the Pu^{240} contribution, but its effects are negligible for these foils.

The relative fission rates in the thermal and epithermal energy regions can be obtained from Eqs. (6.30) or (6.31) by the use of measured cadmium ratios:

$$\frac{\int_o^\epsilon \sigma_f^{49} \phi(E)dE}{\int_o^{\epsilon'} \sigma_f^{25} \phi(E)dE} \left(\frac{CR^{25}}{CR^{49}}\right)\left(\frac{CR^{49}-1}{CR^{25}-1}\right)\frac{\int_o^\infty \sigma_f^{49} \phi(E)dE}{\int_o^\infty \sigma_f^{25} \phi(E)dE} \qquad \text{Eq. (6.32)}$$

$$\frac{\int_\epsilon^\infty \sigma_f^{49} \phi(E)dE}{\int_{\epsilon'}^\infty \sigma_f^{25} \phi(E)dE} = \left(\frac{CR^{25}}{CR^{49}}\right) \times \frac{\int_o^\infty \sigma_f^{49} \phi(E)dE}{\int_o^\infty \sigma_f^{25} \phi(E)dE} \qquad \text{Eq. (6.33)}$$

where CR is the cadmium ratio and ϵ is an effective cutoff energy of a cadmium shield. As discussed in the previous section, the cutoff energy is a function of the flux, cross sections, and shield material. It is not necessary that $\epsilon = \epsilon'$. Similar expressions for Pu^{241} relative to Pu^{239} result if Eq. (6.31) is used in place of Eq. (6.30).

Since the isotopic abundance of Pu^{239} in the Pu^{241} deposit is not negligible, the measured cadmium ratio of the Pu^{241} deposit must be corrected to yield the cadmium ratio of Pu^{241}. This correction is applied by the use of the following expression:

$$CR^{41} = \frac{"CR^{41}"}{1 + \delta_{41}^{49}\left(1 - \frac{"CR^{41}"}{CR^{49}}\right)} \qquad \text{Eq. (6.34)}$$

where "CR^{41}" is the cadmium ratio of the Pu^{241} deposit, and

$$\delta_{41}^{49} = \frac{N_{41}^{49}}{N_{41}^{41}} \frac{\int_o^\infty \sigma_f^{49} \phi(E) dE}{\int_o^\infty \sigma_f^{41} \phi(E) dE}.$$

The foils and deposits were first irradiated in the BNL thermal column. A nickel blank was included in the irradiation. The nickel blank was identical to the nickel planchets on which the plutonium was deposited and was used to correct for the nickel activation of the planchets. The foils and deposit activities were counted approximately 24 hours later at the Bettis Atomic Power Laboratory. The foils and deposits were subsequently irradiated in the TRX facility at flux symmetric positions in a split fuel rod, as shown in Fig. 6.68, and the activities counted at the same time from shutdown as the BNL irradiations.

Fission product γ radiation from the foils was measured by scintillation counter techniques. The equipment consisted of the following components: a sodium-iodide crystal 1-3/4 in. in diameter by 2 in. thick mounted on an RCA 5819 photomultiplier, a regulated H. V. power supply, a linear amplifier, and a scaler. The activities as well as the background were counted with a bias set at 400 kev. Since the activities decayed as a function of time, the foils and deposits were counted in turn for one minute. Data were taken for approximately 5 hours. Decay curves were drawn and activation ratios taken at the same time. A complete run with one set of foils consisted of two BNL irradiations in addition to the TRX irradiation. This procedure eliminated the need for knowing the weights of the deposits very accurately, since the activation ratios in Eq. (6.31) are much larger than the ratio of atom densities.

The cadmium ratios were measured in a split fuel rod, as shown in Fig. 6.68. A complete run consisted of two irradiations, one with the cadmium in the lower position and one with the cadmium in the upper position. By taking the square root of the product of the cadmium ratios from the two runs, a result is obtained which is independent of the relative foil calibration and any flux asymmetry. The thickness of the cadmium pill box was 0.020 in. The cadmium ratio is a function of the cadmium thickness and geometry as well as the flux and detector. Since the calculations discussed below assumed an infinite slab, this was approximated experimentally by the pill box. It was determined experimentally that the edge effect correction amounts to 4

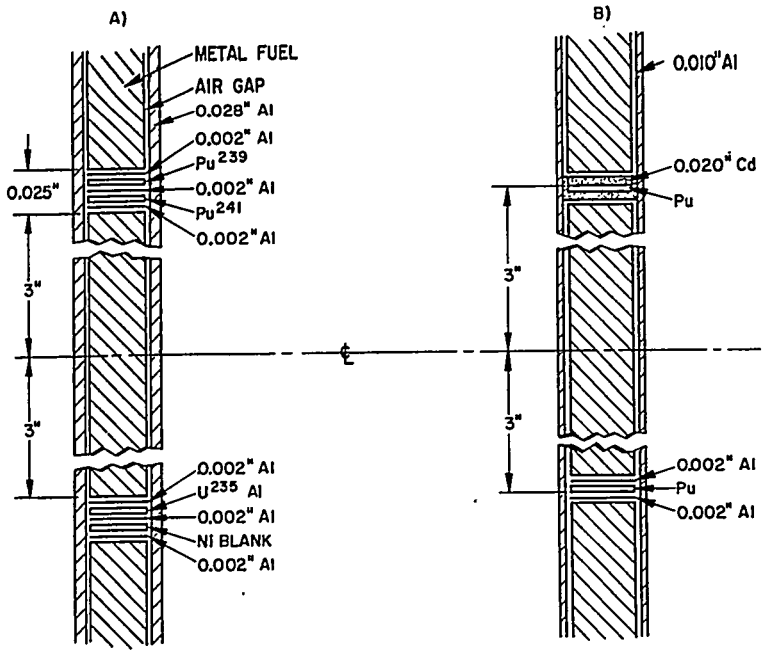

FIGURE 6.68. Foil Loading Schematic.

percent for U^{235} and Pu^{239}. It is estimated that the correction is about 4 percent for Pu^{241}.

The effect of self-shielding in the Pu deposits was investigated by comparing the activity of a Pu deposit, shielded by a Pu deposit on both sides, with the activity of a deposit which was unshielded. The ratio was 1.00 ± 0.01.

In the case of Pu^{241}, it was necessary to correct for the decay due to the 13-year half-life, since the experiment ran several months.

2. *Results and Discussion*

The experimental results for both lattices are given in Tables 6.40 and 6.41. The cross sections were obtained from BNL-325, Second Edition. The uncertainties listed reflect only statistical uncertainties, since the theoretical results to which they are compared use the same thermal cross sections. The measured cadmium ratios reflect a 2-percent uncertainty for the edge effect correction.

Table 6.40 also shows the sensitivity of the cadmium ratio of Pu^{239} to a change in the cadmium thickness.

TABLE 6.40 — Pu and U^{235} REACTION RATES IN THE 2.35-TO-1 LATTICE

	Experimental	Calculated
$\dfrac{\int_o^\infty \sigma_f^{49}\,\phi(E)dE}{\int_o^\infty \sigma_f^{25}\,\phi(E)dE}$	1.95 ± 0.03	1.80
$\dfrac{\int_o^{0.43} \sigma_f^{49}\,\phi(E)dE}{\int_o^{0.53} \sigma_f^{25}\,\phi(E)dE}$	2.00 ± 0.03	1.84
$\dfrac{\int_{0.43}^\infty \sigma_f^{49}\,\phi(E)dE}{\int_{0.53}^\infty \sigma_f^{25}\,\phi(E)dE}$	1.49 ± 0.08	1.35
$\dfrac{\int_o^\infty \sigma_f^{41}\,\phi(E)dE}{\int_o^\infty \sigma_f^{49}\,\phi(E)dE}$	1.18 ± 0.03	
$\dfrac{\int_o^{0.44} \sigma_f^{41}\,\phi(E)dE}{\int_o^{0.43} \sigma_f^{49}\,\phi(E)dE}$	1.15 ± 0.03	1.15
$\dfrac{\int_{0.44}^\infty \sigma_f^{41}\,\phi(E)dE}{\int_{0.43}^\infty \sigma_f^{49}\,\phi(E)dE}$	1.51 ± 0.07	--

TABLE 6.40 — Pu and U^{235} REACTION RATES IN THE 2.35-TO-1 LATTICE (Continued)

	Experimental	Calculated
CR^{25}	11.3 ± 0.3	10.6
CR^{49}	14.9 ± 0.5	14.1
CR^{41}	11.6 ± 0.3	--
CR^{49*}	16.6 ± 0.6	15.6

*Measured with 0.030 in.; all others have 0.020 in. of cadmium.

TABLE 6.41 — Pu and U^{235} REACTION RATES IN THE 1-TO-1 LATTICE

	Experimental	Calculated
$\dfrac{\int_o^\infty \sigma_f^{49}\,\phi(E)dE}{\int_o^\infty \sigma_f^{25}\,\phi(E)dE}$	2.16 ± 0.02	2.14
$\dfrac{\int_o^{0.43} \sigma_f^{49}\,\phi(E)dE}{\int_o^{0.53} \sigma_f^{25}\,\phi(E)dE}$	2.37 ± 0.02	2.35
$\dfrac{\int_{0.43}^\infty \sigma_f^{49}\,\phi(E)dE}{\int_{0.53}^\infty \sigma_f^{25}\,\phi(E)dE}$	1.33 ± 0.05	1.31

TABLE 6.41 — Pu and U^{235} REACTION RATES IN THE 1-TO-1 LATTICE (Continued)

	Experimental	Calculated
$\dfrac{\int_o^\infty \sigma_f^{41}\phi(E)dE}{\int_o^\infty \sigma_f^{49}\phi(E)dE}$	1.05 ± 0.02	--
$\dfrac{\int_o^{0.44} \sigma_f^{41}\phi(E)dE}{\int_o^{0.43} \sigma_f^{49}\phi(E)dE}$	0.991 ± 0.020	1.02
$\dfrac{\int_{0.44}^\infty \sigma_f^{41}\phi(E)dE}{\int_{0.43}^\infty \sigma_f^{49}\phi(E)dE}$	1.46 ± 0.07	--
CR^{25}	5.14 ± 0.15	4.94
CR^{49}	8.35 ± 0.25	8.04
CR^{41}	6.02 ± 0.20	--

To calculate the reaction rates for comparison with the above measurements, it is necessary to know the energy and spatially dependent flux as well as the cross sections. The thermal cross sections were obtained from BNL-325, Second Edition. The MUFT code,[23] which was used to compute the epicadmium activations, is normalized to a measured resonance integral for U^{235} of 270 barns.[26] The resonance integral for Pu^{239} was estimated to be 250 barns to a cutoff at 2.0 ev.[54] The uncertainty in these numbers was given as 10 percent.

The calculational model which is used here is discussed in Sect. 6.5.C. It is felt that the lack of adequate cross-section data in the epicadmium region and an inadequate detailed energy spectrum in the thermal region are responsible for the small disagreement between measured and calculated reaction rates.

The disagreement is not bad in view of these inadequacies. It is not known why the agreement is better in the case of the 1-to-1 lattice.

As for the relative reaction rates between the two lattices, the results indicate the effect of the hardened spectrum in the 1-to-1 lattice. The reaction rates of Pu^{241} and U^{235} relative to Pu^{239} decrease in going from the 2.35-to-1 lattice to the 1-to-1 lattice. Although Pu^{241} also has a resonance at 0.3 ev, it is not as dominant as the one in Pu^{239}. The fission reaction rates of Pu^{241} relative to U^{235} do not change, within experimental error, in going from the 2.35-to-1 lattice to the 1-to-1 lattice.

6.6 PULSED NEUTRON SOURCE MEASUREMENTS

D. R. Bach, S. I. Bunch, R. J. Cerbone, K. S. Quisenberry, B. E. Simmons, and R. E. Slovacek

A. Introduction

This section presents a description of techniques developed for obtaining reactor design information by using the pulsed neutron source method. In this type of experiment, the time decay of the neutron flux in a critical or subcritical assembly is observed following the introduction of a burst of fast neutrons into the assembly.

The pulsed neutron technique [55,56] is primarily useful in cases where the k_{eff} value of the assembly is below about 0.995, since in these cases the conventional reactivity measurement methods tend to become unreliable. For example, the conventional methods in some cases rely upon the measurements of the reactivity worth of control rods as a function of position followed by an integration of the worth over the control rod motion to the desired subcritical position. However, the rod worth measurements must be made in a critical configuration and, thus, are not pertinent in far subcritical situations. Other conventional methods, such as the rod drop technique where the control rods are rapidly inserted from a critical position and the decay of the neutron flux is then followed as a function of time, also become less reliable in far subcritical conditions because of the large change in power distribution caused by the rod insertion. On the other hand, in the pulsed neutron technique, the degree of subcriticality is interpreted directly from the rate of decay of the prompt neutrons, following their introduction into the core, and it can be interpreted as either the density change in $1/v$ poison, which would make the reactor critical, or as a reactivity.

The pulsed neutron technique is distinct from a Swedish pulsed method,[57] reported in 1955, which employs a relatively slowly varying, periodic neutron source. The pulsed technique discussed in this section uses a burst of neutrons of about 10 to 50 μsec in pulse width, whereas the Swedish method employed a source which was about 250 to 500 msec in length with a repetition time of about twice the pulse length. Thus, the interpretation of the Swedish reactivity technique depends upon a detailed knowledge of the buildup of the delayed neutron emitters. More closely related to the type discussed here is the Rossi-α experiment and its variations,[58] in which statistical analysis of reactor noise results in the determination of a prompt flux decay constant, α, just as is measured directly in the pulsed technique described here. The Rossi-type measurement method has been of considerable use in the fast-reactor design field, although adequate noise observations are difficult to obtain except near critical.

Considerable work has been carried out with the pulsed technique to measure the reactivity of multiplying media. These measurements[55,59-65] were limited to the reactivity region near delayed critical and have been carried out in heavy water, light water, graphite moderators, and in bare uranium systems. Campbell and Stelson[66] have extended the range of the pulsed technique to obtain decay constants of bare assemblies from critical to far subcritical. In these cases, subcriticality was effected by reducing the size of the system. Since the systems were already quite small, the measured decay constants were quite sensitive to the leakage probability.

In the discussion of the clean critical experiments (Sects. 6.2, 6.3, 6.4, and 6.5) it was indicated that, to a large extent, the validity of analytical methods currently in use has been determined by comparisons with critical assembly measurements. In some cases, however, the far subcritical assembly could provide a more sensitive measure of certain parameters used in reactor calculations. However, it is not the intent of this section to propose that the pulsed method replace the critical experiments, but rather to show how it complements critical experimentation. Some of the work to be described here will provide experimental data and associated analyses in an attempt to evaluate the validity of the pulsed source technique.

The theory of the pulsed neutron technique is presented first. This is followed by a discussion of the application of the method to subcritical assemblies for the case in which a calibration in a critical configuration is required. The calibration relates the prompt neutron decay rate in the critical and subcritical configurations in order to determine the degree of subcriticality. An area of considerable interest that is also described below

is the measurement of reactivity made without the delayed critical calibration. This can be accomplished by means of an observation of the delayed as well as the prompt portion of the decay following the introduction of a very intense burst of neutrons into a critical or subcritical assembly.

B. Theory

In the pulsed neutron method, a pulse or burst of high energy neutrons is injected into a subcritical reactor. After the introduction of this burst of neutrons, as many prompt-neutron generations elapse, the injected flux will tend to settle into a stable, decaying distribution in the reactor. In addition, shortly after the burst, the delayed neutrons created by the decaying flux comprise but a small fraction of the total neutron flux. It is possible that there is a time interval, suitable for data recording, which occurs after the flux has stabilized and, thus, forgotten its pulsed origin, yet before daughter delayed neutrons constitute an appreciable fraction of it.

The advantages of the pulsed neutron technique stem basically from the occurrence in practice of just such a pure flux mode, i.e., time separability of the reactor flux, in the absence of any significant effects due to delayed neutron emitter behavior. These conditions are sufficient to yield accurately an exponential form for the time behavior of that flux. Substitution of a separable vector flux

$$\Psi(\vec{r}, u, \vec{\Omega}, t) = f(\vec{r}, u, \vec{\Omega})\, T(t) \qquad \text{Eq. (6.35)}$$

into the transport equation for prompt neutrons

$$Q\Psi = \frac{1}{v}\frac{\partial \Psi}{\partial t} \qquad \text{Eq. (6.36)}$$

gives immediately the relation

$$T(t) = e^{-\alpha t} \qquad \text{Eq. (6.37)}$$

where the separability constant α is the flux decay rate referred to earlier, and the transport operator Q is defined to have no delayed neutron contributions. Here $\vec{r}, u, \vec{\Omega}$, and t represent position, lethargy, direction, and time, respectively, and $v(u)$ is the neutron speed.

1. Interpretation of α

Before considering further the actual achievement of the pure modal condition, it is convenient to develop the two primary subcriticality interpretations of α. The first stems directly from the time-independent equation resulting from the separation of Eq. (6.36):

$$Qf(\vec{r}, u, \vec{\Omega}) = -\frac{\alpha}{v} f(\vec{r}, u, \vec{\Omega}). \qquad \text{Eq. (6.38)}$$

This expression has the eigenvalue α and, with the assumption of modal purity, is the exact representation of the pulsed reactor.

Equation (6.38), if rewritten as

$$(Q + \frac{\alpha}{v}) f(\vec{r}, u, \vec{\Omega}) = 0 \qquad \text{Eq. (6.39)}$$

is mathematically equivalent to a prompt critical reactor. This prompt critical reactor differs in composition from the initial physical reactor by the uniform poison cross-section change

$$\delta\Sigma_a = -\frac{\alpha}{v}. \qquad \text{Eq. (6.40)}$$

Clearly, α is interpretable numerically as an atomic removal density for a hypothetical atom having a microscopic capture cross section

$$\sigma_a = \frac{1}{v} \qquad \text{Eq. (6.41)}$$

Hence, α is numerically an atomic removal density which will make the given physical reactor exactly prompt critical.

The second possible interpretation of α is that of reactivity. The conventionally calculated reactivity, as measured from prompt critical, is defined as $\frac{\nu - \nu_c}{\nu}$; where ν is the physical value for the mean prompt neutron yield per fission, and ν_c is the ν eigenvalue for solution of the equation

$$Qf_\nu(\vec{r}, u, \vec{\Omega}) = 0. \qquad \text{Eq. (6.42)}$$

Although Eq. (6.42) does not represent the pulsed reactor, i.e., $f_\nu(\vec{r}, u, \vec{\Omega})$ is in general distinct from the experimentally occurring flux $f(\vec{r}, u, \vec{\Omega})$ of Eq. (6.38), it is of practical interest to relate $\frac{\nu-\nu_c}{\nu}$ to α.

This relationship can be analytically based upon the following expression, derivable[67] by multiplying the adjoint to Eq. (6.39) by $f_\nu(\vec{r}, u, \vec{\Omega})$, multiplying Eq. (6.42) by the solution $F(\vec{r}, u, \vec{\Omega})$ of the adjoint of Eq. (6.39), subtracting, and integrating over all variables:

$$\frac{\nu-\nu_c}{\nu} = -\alpha \left\{ \frac{\int d\vec{\Omega} du dV f_\nu(\vec{r}, u, \vec{\Omega}) v^{-1}(u) F(\vec{r}, u, \vec{\Omega})}{\int d\vec{\Omega} du dV f_\nu(\vec{r}, u, \vec{\Omega}) \nu \Sigma_f(\vec{r}, u) F^H(\vec{r})} \right\}. \qquad \text{Eq. (6.43)}$$

Here

$$F^H(\vec{r}) \equiv \int d\vec{\Omega} du \frac{\chi(u)}{4\pi} F(\vec{r}, u, \vec{\Omega}) \qquad \text{Eq. (6.44)}$$

$\chi(u)$ is the fission spectrum, and Σ_f is the fission cross section. Equation (6.43) is mathematically exact; its validity is not limited to small changes about critical.

The direct use of Eq. (6.43) to convert a measured α into $\frac{\nu-\nu_c}{\nu}$ is not very attractive, especially since the solution of not only Eq. (6.42) but also the adjoint of Eq. (6.39) would be required to evaluate the bracketed factor. However, in practice, this factor may often be evaluated by inference from the experimental solution of another (but parallel) problem. The latter will now be outlined in terms of a prompt generation time ℓ and a so-called dynamic reactivity ΔK.

According to perturbation theory, the asymptotic decay constant α of a reactor slightly below prompt critical (with no delayed neutrons present) can be used[63] to define a prompt generation time ℓ by

$$\left(\frac{\nu-\nu_c}{\nu}\right)_{\nu_c \to \nu} = -\ell\alpha. \qquad \text{Eq. (6.45)}$$

Comparing this with Eq. (6.43), it is seen that in the limit $\nu_c \to \nu$ and $\alpha \to 0$, $f_\nu(\vec{r}, u, \vec{\Omega}) \to f(\vec{r}, u, \vec{\Omega})$ and hence

$$\ell = \frac{\int d\vec{\Omega} du dV f(\vec{r}, u, \vec{\Omega}) v^{-1}(u) F(\vec{r}, u, \vec{\Omega})}{\int d\vec{\Omega} du dV f(\vec{r}, u, \vec{\Omega}) \nu \Sigma_f(\vec{r}, u) F^H(\vec{r})}. \qquad \text{Eq. (6.46)}$$

The dynamic reactivity will be defined by retaining the form of both Eqs. (6.45) and (6.46) outside the perturbation limit (i.e., for finite, large values of α):

$$\Delta K \equiv -\ell\alpha. \qquad \text{Eq. (6.47)}$$

It is noteworthy that this ℓ is not the prompt generation time of a subcritical reactor but rather that of neutrons in the equivalent prompt critical reactor of Eq. (6.39).

Clearly, ΔK coalesces with $\frac{\nu - \nu_c}{\nu}$ in the perturbation limit near prompt critical. Thus, for a reactor which is physically delayed critical, it is generally a good approximation that

$$\begin{aligned} \beta_{\text{eff}} &\cong \Delta K \\ &= \alpha_d \ell_d \end{aligned} \qquad \text{Eq. (6.48)}$$

where β_{eff} is the effective delayed neutron fraction and the subscript d denotes delayed criticality.

Suppose that a subcritical reactor is pulsed and α obtained, and that this reactor is somehow made delayed critical and α_d measured. Combining Eqs. (6.47) and (6.48),

$$\frac{\Delta K}{\beta_{\text{eff}}} = -\frac{\alpha\ell}{\alpha_d \ell_d}. \qquad \text{Eq. (6.49)}$$

To obtain ΔK from this relation, knowing α and α_d, and assuming that β_{eff} is independently calculable as a correction to the actual delayed neutron fraction, the ratio ℓ/ℓ_d still must be evaluated.

The evaluation of ℓ/ℓ_d will be considered here only for the broadly practical case where criticality is attained by control rod withdrawal. It will be shown with the aid of certain experimental results that often $\ell/\ell_d \cong 1$. Combining this with the assumption that $\Delta K \cong \frac{\nu - \nu_c}{\nu}$, one obtains

$$\frac{1}{\beta_{\text{eff}}} \frac{\nu - \nu_c}{\nu} \cong \frac{\alpha}{\alpha_d} \qquad \text{Eq. (6.50)}$$

where the reactivity is still defined as being relative to prompt critical.

To gain some insight into the assumptions made above, it is worthwhile to consider two versions of Eq. (6.39), representing equivalent prompt critical reactors, which determine ℓ and ℓ_d. These two versions will differ only in the exchange of uniform poison for the insertion of a lumped control rod absorber. Thus, to approximate $\ell/\ell_d \cong 1$ one must determine, for a reactor under constraint of prompt criticality, whether the prompt generation time is appreciably affected by poison rearrangements which leave the fuel and moderator compositions unaltered.

Such ℓ sensitivity can be tested experimentally by poison rearrangement under constraint of delayed criticality. If α_d is observed to be invariant when shifts in poison induce large changes in the flux distribution, and if it can be postulated that β_{eff} is concomitantly insensitive, then by Eq. (6.48) ℓ_d must also be insensitive to these shifts. But ℓ corresponds to a special case of such poison shifts and, hence, it would follow that

$$\ell \cong \ell_d . \qquad \text{Eq. (6.51)}$$

Experimentally, it has been observed[63] for a number of hydrogen-moderated reactors that configuration changes in groups of large control rods do not significantly affect α_d. It is estimated that any corresponding variation in β_{eff} is less than the 2 percent measurement uncertainty in α_d. Thus, poison redistribution within these cores affects ℓ_d at most by a few percent.

However, the poison redistribution distinguishing ℓ and ℓ_d includes an effective poison in the reflector as well as in the core. Experiments[68] with a highly buckled reactor indicate that complete destruction of the thermal-neutron-return properties of the reflector produces a change in ℓ_d of about 30 percent. It is a reasonable assumption that the partial inhibition of these properties arising in the distinction between ℓ and ℓ_d would cause considerably less than a 30 percent change. This is particularly likely for a less highly buckled reactor. It would seem that where α_d is obtained for a highly enriched hydrogenous reactor which has a buckling characteristic of a power reactor, Eq. (6.51) is valid to within a few percent over a control rod induced reactivity swing of many dollars.

Under these same restrictions, it can be inferred that $\Delta K \cong \frac{\nu - \nu_c}{\nu}$. This inference rests upon the similarity of Eqs. (6.43) and (6.45), which differ only in that the bracketed quantity in the former is not quite ℓ in the latter, as given by Eq. (6.46). Denoting the bracketed quantity by ℓ_ν, it is sufficient to show

that $\ell \cong \ell_\nu$. The same experimental arguments will be utilized as in comparing ℓ to ℓ_d.

Since the same flux adjoint occurs in both ℓ and ℓ_ν, they are more alike in that respect than ℓ and ℓ_d. The sole distinction is that arising from the difference between $f(\vec{r},u,\vec{\Omega})$ and $f_\nu(\vec{r},u,\vec{\Omega})$. The flux f represents a criticality condition achieved by removal of pure absorber from both reflector and core, whereas f_ν represents criticality achieved by increasing the mean neutron yield per fission. Thus, f_ν is likely to differ from f primarily in the enhancement of the core flux with respect to the reflector flux, with a secondary difference in the neutron energy spectrum.

But flux shifting between core and reflector, so long as it is not too violent and the reactor buckling is not too large, seems experimentally to produce small changes in the prompt generation time. Also, over a reactivity range of many dollars, the spectral effect on the prompt generation time is not likely to be large. Within these restrictions, to an accuracy of perhaps a few percent, $\ell \cong \ell_\nu$.

2. Achievement of the Pure Modal Condition

Establishment of the time separability condition of Eq. (6.35) can be studied adequately under the assumption of multigroup diffusion theory for a bare, uniform reactor in the shape of a rectangular parallelepiped. Delayed neutron effects are represented by just one precursor group.

Many fast neutron slowing-down times after introduction of the neutron burst into the reactor, the neutron velocity spectrum will have more or less stabilized, and the neutron density can be expressed as a modal expansion:

$$\rho(\vec{r},t) \cong \sum_n A_n \sin\frac{n\pi x}{X} T_n(t) \qquad \text{Eq. (6.52)}$$

where for simplicity only one space dimension has been retained. Here X is the distance between one set of reactor extrapolated boundaries; x is position in the reactor as measured from one X-boundary; n is the modal number; and A_n is adequately interpretable as a Fourier amplitude of the neutron density at a time just after occurrence of the burst, when $T(0) = 1$.

It can be shown that the time dependence can be expressed as

$$T_n(t) \cong e^{-\alpha_n t} + \frac{\lambda}{\alpha_d}\left(\frac{1}{\alpha_n/\alpha_{1d}}\right)^2 e^{-\lambda t\left(\frac{\alpha_n/\alpha_{1d}-1}{\alpha_n/\alpha_{1d}}\right)} \qquad \text{Eq. (6.53)}$$

at the times of interest, omitting consideration of any steady-state flux existing prior to the neutron burst. Here

$\alpha_n \equiv$ prompt decay constant, with α_1 being identical with that referred to earlier;

$\alpha_{1d} \equiv$ prompt decay constant of mode 1 with the reactor adjusted to delayed critical by poison removal;

$1/\lambda =$ mean life of delayed-neutron precursor nuclei. A suitable value of $1/\lambda$ to represent all delayed neutron groups is about 10 seconds.

The second term in Eq. (6.53) represents the previously ignored delayed neutron contribution to the decay rate. The ratio α_n/α_{1d} appearing there will be recognized from Eq. (6.50) as approximately the reactivity relative to prompt critical of the n^{th} mode. This reactivity is expressed in dollars. In the term amplitude, this ratio appears as the inverse square, one power being relatable to the number of precursors created during the prompt decay of the flux and the remaining power to the multiplication accorded each delayed neutron at its birth.

In the exponent of the delayed neutron term, the ratio of α_n/α_{1d} occurs in a factor which modifies λ. This factor is nearly unity when the reactor is far subcritical. At delayed critical this factor completely vanishes for the fundamental mode, leading to a permanent rise in power level when a delayed critical reactor is pulsed.

The magnitude of this permanent rise is small relative to the instantaneous power level rise occurring immediately after burst injection, being of the fractional amount λ/α_d,

$$\frac{\lambda}{\alpha_d} \sim \frac{10^{-1}\ \text{sec}^{-1}}{150\ \text{sec}^{-1}} \sim 10^{-3}$$

for a typical hydrogenous reactor. Any delayed neutron correction to the measured prompt rate of flux decay will depend upon the time location of the data recording interval, which is determined primarily by the desirability of letting higher flux modes die out. Modal suppression depends upon relative values of both initial modal amplitudes A_n and modal decay rates α_n. Overall convergence of the A_n is in general slow, as may be found by Fourier expansion of reasonable guesses at the flux as it exists immediately following the neutron burst. However, individual A_n may vanish entirely, depending upon source placement relative to the reactor. For instance, if the source is on the line of x symmetry, no asymmetric modes will be excited and $A_n \neq 0$ only for odd n.

Assuming that $A_n/A_1 \sim 1$, the appropriate time delay between the burst and data recording interval can be estimated from the relative decay rates α_n. Consider the usual four-factor formula

$$k_\infty = \eta p \epsilon f \qquad \text{Eq. (6.54)}$$

where the notation is standard.[67] In particular,

$$f = \frac{\overline{\Sigma}_u}{\overline{\Sigma}_a} \qquad \text{Eq. (6.55)}$$

$\overline{\Sigma}_u$, being the fuel absorption cross section and $\overline{\Sigma}_a$ the total (physical) absorption cross section including $\overline{\Sigma}_u$. The n^{th} modal reproduction factor is

$$k_{\text{eff}\,n} = \frac{k_\infty}{1 + M^2\left(B_n^2 + B_y^2 + B_z^2\right)} \qquad \text{Eq. (6.56)}$$

which is unity at delayed critical. This contains the y and the z dimensional fundamental mode buckling terms as well as the x dimensional buckling

$$B_n^2 = \frac{\pi^2 n^2}{X^2}. \qquad \text{Eq. (6.57)}$$

The migration area for fission neutrons is denoted by M^2.

According to the arguments of the preceding section, α_n/v is the change in absorption cross section required to achieve prompt criticality, so that

$$1 + \beta_{\text{eff}\,n} = \frac{\eta \epsilon p \overline{\Sigma}_u / (\overline{\Sigma}_a - \alpha_n/\overline{v})}{1 + M^2\left(B_n^2 + B_y^2 + B_z^2\right)} \qquad \text{Eq. (6.58)}$$

with $\overline{v}$ denoting the mean neutron velocity in this one-group approximation. In the equivalent prompt critical reactor of Eq. (6.58) the prompt generation time is

$$\ell_n = 1/(\Sigma_a \overline{v} - \alpha_n) \qquad \text{Eq. (6.59)}$$

ignoring a small finite-medium correction. From Eqs. (6.56) and (6.58),

$$k_{\text{eff } n} = (1 + \beta_{\text{eff } n})(\Sigma_a - \alpha_n/\overline{v})\Big/\overline{\Sigma}_a \qquad \text{Eq. (6.60)}$$

so that the reactivity relative to prompt critical can be expressed as

$$\frac{(\Delta k_n)_p}{k_{\text{eff } n}} = -\frac{\alpha_n/\overline{v}}{\overline{\Sigma}_a - \alpha_n/\overline{v}} = -\alpha_n \ell_n \equiv \Delta K_n \qquad \text{Eq. (6.61)}$$

where ΔK_n is the dynamic reactivity of the n^{th} mode.

Utilizing Eqs. (6.56) and (6.61), the behavior of α_n with n can be expressed as

$$\frac{\alpha_n \ell_n}{\alpha_1 \ell_1} = 1 + \left(\frac{M^2 B_1^2 (n^2 - 1)}{1 + M^2 \ (B_1^2 + B_y^2 + B_z^2)}\right)\left(\frac{1 + \beta_{\text{eff } 1}}{1 + \beta_{\text{eff } 1} - k_{\text{eff } 1}}\right). \qquad \text{Eq. (6.62)}$$

Decay rates for the first few modes relative to that of the fundamental may often be obtained to adequate accuracy by setting $\ell_n = \ell_1$ evaluating the right-hand side of Eq. (6.62). Iterative correction for the lifetime ratio may be made if desired. Plots of the right-hand side of Eq. (6.62) as a function of reactivity for $n = 2$ and $n = 3$ are given in Figs. 6.69 and 6.70 for reactors of various critical bucklings. In these figures, curves are plotted for various values of $B^2 M^2$. The change from one value of $B^2 M^2$ to the next can be made by varying the physical size of the system while keeping the composition the same (called B^2 variation on the figures) or by varying the materials composition while keeping the physical B^2 constant (called k_∞ variation). It is noted that the manner of the variation affects the relative decay rates of the higher modes in a different manner.

Assuming $A_n/A_1 = 1$, a suitable time delay to permit higher flux modes to die out can be obtained from the foregoing. Suppose it is required that during the data recording interval the maximum ratio of the second mode to the fundamental is g. If the data interval is begun at time t_o, then

$$g = \exp\left[-\frac{t_o}{1/\alpha_{1d}}\left\{\frac{\alpha_1}{\alpha_{1d}}(\xi - 1)\right\}\right] \qquad \text{Eq. (6.63)}$$

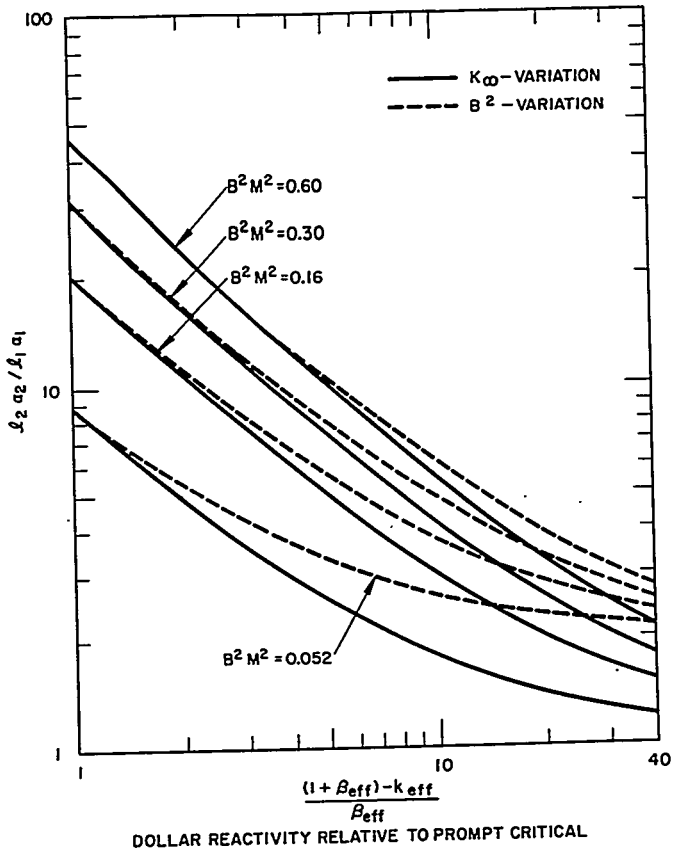

FIGURE 6.69. The Relative Decay Rate of the Second Flux Mode with Respect to the First as a Function of Reactivity.

where

$$\xi = \alpha_2/\alpha_1 \ . \qquad \text{Eq. (6.64)}$$

For most cases of practical relevance, $1 \geq k_{eff} \gtrsim 0.88$. Over this subcriticality range it can be seen that the portion within the braces of the exponent in Eq. (6.63) is roughly constant for k_∞ changes, and increases somewhat as B^2 increases above the critical value. Taking the less favorable case, for a specified value of g, t_o is reactivity-independent and may be evaluated at delayed critical:

$$t_o \cong \frac{1}{\alpha_{1d}} \left[\frac{\ln g^{-1}}{\xi} \right] . \qquad \text{Eq. (6.65)}$$

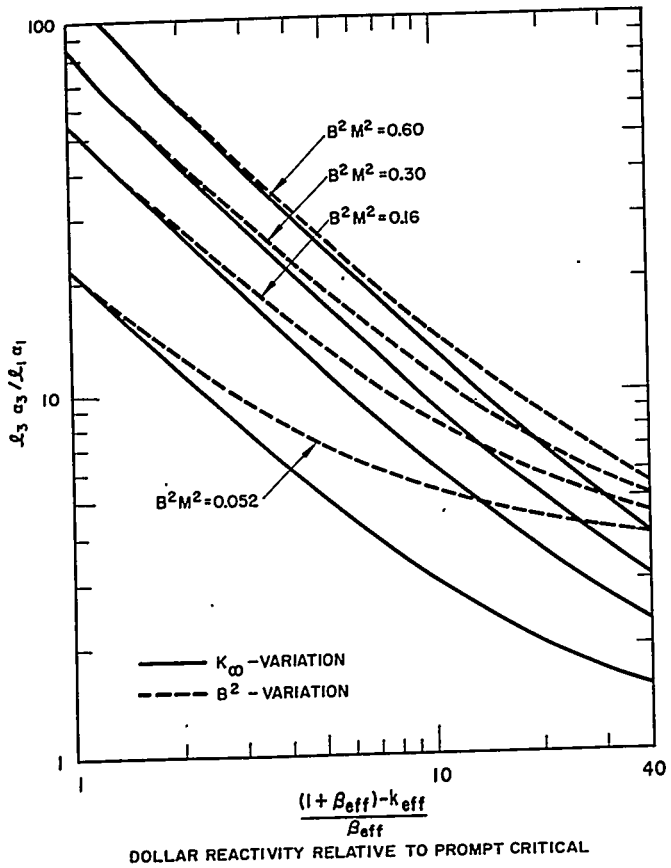

FIGURE 6.70. The Relative Decay Rate of the Third Flux Mode with Respect to the First as a Function of Reactivity.

If $\beta = 0.001$ and $B^2M^2 = 0.30$, for instance, t_o is about 1/4 the mean life of the fundamental flux mode in the delayed critical reactor.

Far subcritical, the fundamental mode may go through several mean lives during the delay time t_o. This might result in unwanted effects from delayed neutron buildup. In these cases, the delayed neutron background must be treated carefully.

For many reactors it may be found that t_o cannot be kept constant as a function of reactivity because of difficulty in obtaining counts far subcritical. Decreasing t_o for such reasons tends to minimize any delayed neutron problem at the expense of modal interference. However, a satisfactory compromise may still be reached by use of careful detector and source placement to eliminate particularly troublesome modal effects.

C. Experimental Method

The equipment needed to carry out a pulsed neutron experiment is relatively simple. A pulsed neutron source, a neutron detection system, and some sort of multichannel time analyzer are required. Other than the continuing problem of compromising detection efficiency and resolving time, the experimental problems are typical.

The data taken with the time analyzer are background and count loss corrected and then fit to a single exponential by a least squares method adapted from that of Behrens.[69] It is convenient to use a digital computer to accomplish this data reduction.

In practice, however, two major difficulties exist in a pulsed neutron experiment. First, because the prompt decay of the neutron flux is the measured quantity, interference from delayed neutron effects must be minimized. Second, since the initial source neutron distribution is essentially a point source distribution and different from the distribution of the persistent mode, higher spatial modes are excited and cause interference with the fundamental mode measurement. An additional problem in the very far subcritical experiment is the assurance of a stable neutron spectrum during the exponential decay.

The delayed neutron interference to the measurement of the prompt decay is most easily estimated by examining the experimental counting rate just previous to the neutron burst and also after the prompt decay has terminated. The increase in background after the burst gives a measure of the delayed neutron contribution to the experiment. This background is a strong function of the reactivity and the pulse repetition rate, so that decreased repetition rates are required as the system becomes closer to critical.

The interference of higher spatial modes is necessarily dependent on each experimental situation. That is, the position of the neutron source and detectors, the geometry of the system under observation, and the reactivity all influence the contamination of the persistent mode decay. For these reasons, it is important to emphasize that each experimental situation must be examined independently and that there are no simple rules which can be applied to assure that the persistent mode has been adequately measured. It is perhaps easier to point out the method by describing a typical experimental situation.

Because the higher spatial harmonics decay more rapidly than the fundamental mode, in principle it is possible to measure the fundamental mode decay constant by waiting a sufficiently long time after the end of the neutron burst. The upper curve of Fig. 6.71 shows the data as a function of channel

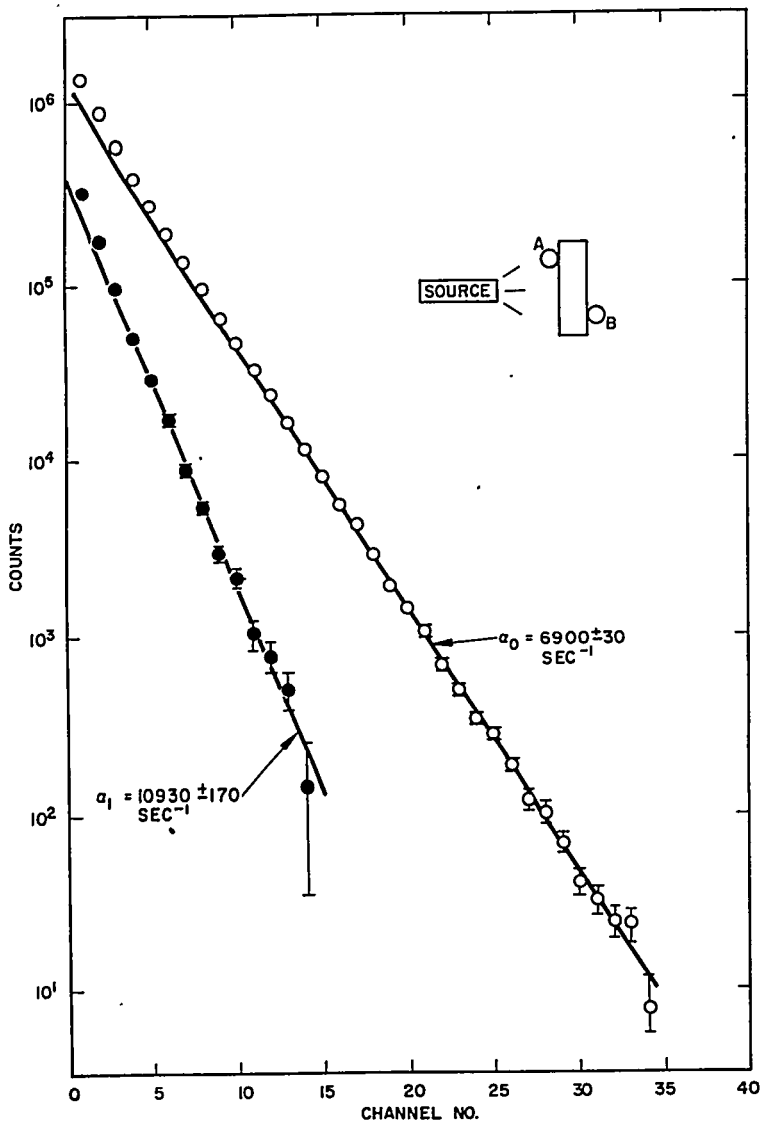

FIGURE 6.71. Harmonic Analysis of Data Obtained from 6-in. × 12-in. × 18-in. Polyethylene.

number of the time analyzer as obtained for a moderating slab (6-in. × 12-in. × 18-in. polyethylene). These data were obtained with a counter placed between the source and the slab as seen in the small sketch in the figure. The straight line was obtained by least squares fitting of the data past channel 15. The lower curve was then obtained by subtraction of the straight line from

the data points and, thus, should represent the decay of the first harmonic except for early times where still higher modes exist.

A more convenient way of studying the contribution of higher mode contamination can be made by varying the start channel in the data analysis. Figure 6.72 shows the result of such a study for the 6-in. polyethylene slab using the counters shown at locations A and B and the source position shown in the small sketch. Data were obtained with both counters connected in parallel as well as from each counter. Even after 5 mean lives of the persistent mode, as measured by the paired counters, the single counter data differ by almost 2 percent.

In contrast to the pure moderator, it is seen for the bare subcritical assembly data shown in Fig. 6.73 that a difference of 2 percent exists about 2-1/2 mean lives after the burst, and no detectable variation of decay constant with counter position is observed after 3-1/2 mean lives. The situation is changed upon the addition of a 4-in. reflector as is indicated in Fig. 6.74. The time required to achieve the persistent mode decay is greater than that for a bare system and less than that for a pure moderator, as is expected. Even with a 4-in. reflector, the

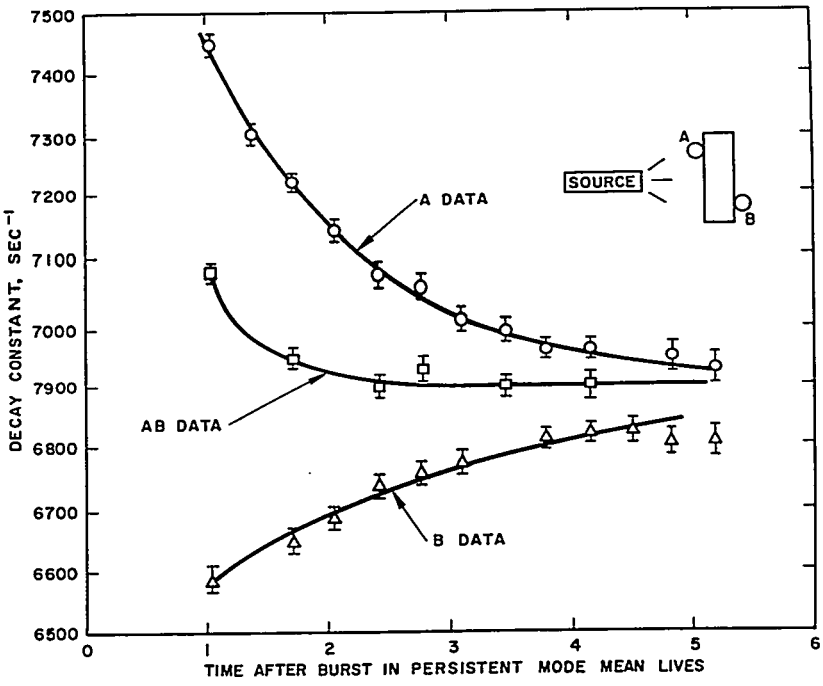

FIGURE 6.72. Variation of Decay Constant with Data Analysis Start Time; 6-in. × 12-in. × 18-in. Polyethylene.

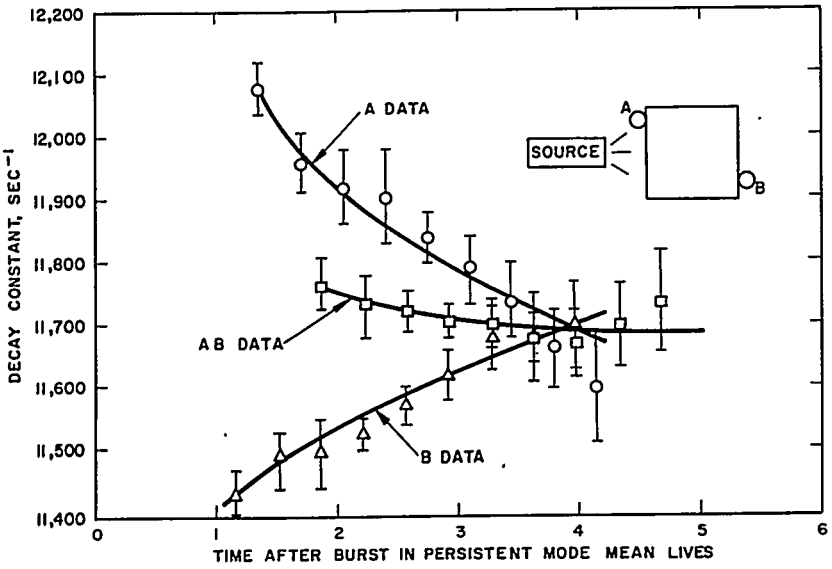

FIGURE 6.73. Variation of Decay Constant with Data Analysis Start Time; FPR-13 Composition 7 in. × 7 in. × 18 in. Bare.

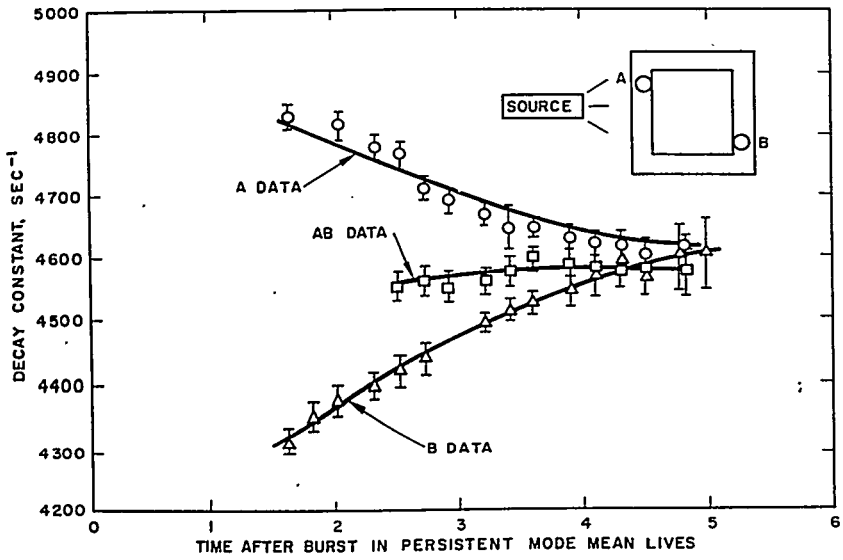

FIGURE 6.74. Variation of Decay Constant with Data Analysis Start Time; FPR-13 Composition 7 in. × 7in. × 18 in. with4-in.Reflector.

measurement of the decay constant of a multiplying medium is easier to obtain experimentally than that of a pure moderating medium of the same physical size. It should be emphasized that the quantitative results depend strongly on the source and detector placement.

In conclusion, the most stringent test for spatial modal purity lies in the determination that the decay constant is independent of detector position in the system under observation. A similar statement can be made concerning the stability of the neutron spectrum. If the decay constants as measured with bare and cadmium-covered detectors are the same, then the spectrum can reasonably be assumed to be the asymptotic spectrum.

One of the standard difficulties in a pulsed neutron measurement is the existence of room-scattered background neutrons. In most experiments in which the source is exterior to the medium under observation, only a fraction of the neutrons enter the medium. Since detectors are placed exterior to the system, adequate shielding must be provided. In the case of reflected systems, detectors are usually placed at the reflector-core interface, resulting in no particular problem. In bare systems, particularly in systems far subcritical, it has been found that cadmium and about 1 in. of boron-carbide powder surrounding the system are adequate.

D. The Far Subcritical Pulsed Neutron Technique

Numerous studies have been made using the pulsed neutron technique to obtain the thermal neutron diffusion parameters of moderating materials. A description will be given of some preliminary work which has been carried out to determine the applicability of the far subcritical pulsed neutron method for the determination of reactor design parameters. Essentially, the work discussed is concerned with systems which have been made subcritical by virtue of their size (i.e., roughly one-eighth of the size of a typical hydrogenous core).

The experiments described here were conducted in both the far subcritical and critical region for bare and reflected systems using assemblies that contained enriched uranium, aluminum, and polyethylene moderator in a near homogeneous mixture. Four different hydrogen-to-uranium ratios were used. The decay constant for each system was also determined from a few-group diffusion calculation using the $1/v$ poison removal method mentioned earlier. A cursory investigation of the neutron spectrum existing during the decay of the persistent mode is also described.

Two different experimental arrangements were used to obtain the decay constants. For the measurements on assemblies at or

near critical, a conventional critical assembly facility, Flexible Plastic Reactor (FPR), was used. The fuel element for the FPR is contained by 1-in. square aluminum tubes having a 0.025-in. thick wall, and is made up of strip elements of polyethylene, aluminum, 0.002-in. thick enriched uranium, and boron or erbium-coated Mylar tape. These elements were arranged to distribute the poison, fuel, and moderator in as homogeneous a manner as possible.

For the 6-in. thick polyethylene reflected assemblies, it was found that the room-scattered neutrons did not affect the measurements significantly when the detectors were located at the core-reflector interface. In the case of the bare assemblies, at least 1/32 in. of cadmium was used to provide a thermal neutron barrier at the surface of the system in order to shield against neutrons scattered from the surroundings. A portable neutron source was placed on the surface of the core region to provide a pulse of about 10^7 neutrons at a maximum repetition rate of two pulses per second. The neutrons had an energy of 14 Mev. NE 401 boron scintillators and Dumont 6292 photomultipliers were used for detection of the core leakage flux.

Figure 6.75 shows the second arrangement which was used for systems far from critical. The small assemblies are constructed from the identical fuel elements that were used in the critical assembly facility. A *(d, T)* source was used which provided a neutron burst of 10^6 neutrons with a repetition rate up to 120 pulses per second. One inch of boron carbide surrounded the assembly to shield against room-scattered neutrons. A sheet of 1/32-in. cadmium was used for shielding directly on the surface of the system. BF_3 proportional counters were used as detectors of the leakage flux.

The compositions of the various subcritical assemblies are given in Table 6.42. The densities are quoted in atoms/cm^3 $\times$ 10^{-20}. The last column in the table lists the infinite medium spectral index $\beta\gamma = \dfrac{\Sigma_a(kT)}{\xi\Sigma_s(\infty)}$. Consistent with the other sections of this chapter, the values presented in Table 6.42 for $\beta\gamma$ have been evaluated for Σ_a (0.025 ev) and for $\xi\Sigma_s$ (1 ev).

1. *Calculation of Decay Constants*

In the interpretation of measured decay constants of non-multiplying media, a thermal neutron spectrum is assumed to exist at times long compared to the slowing-down time. Therefore, one can assume a unique extrapolated boundary and assign

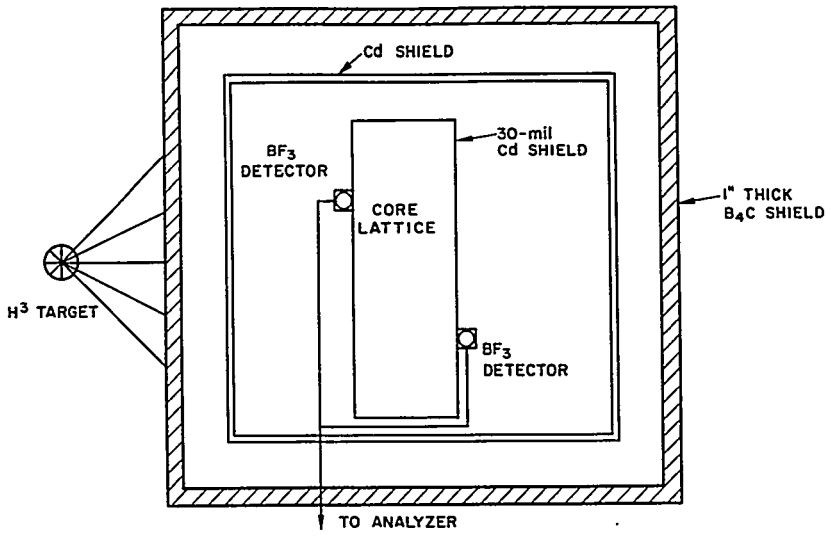

FIGURE 6.75. Experimental Arrangement for Far Subcritical Systems.

TABLE 6.42 — COMPOSITION OF SUBCRITICAL ASSEMBLIES

Assembly	Number Density in Atoms/cm^3 x 10^{-20}							$B\gamma$
	H	C	O	Al	U^{235}	Er	B^{10}	
FPR-13	417	209		166	0.822			0.063
FPR-14	355	197	14.9	187	4.93	1.72		0.48
FPR-15	323	172	7.4	299	1.64	0.817		0.18
FPR-16	274	142		258	4.10		0.224	0.68

a geometric buckling to the system. The validity of this assumption for pure moderators is discussed by Nelkin.[70] However, in multiplying media, the asymptotic spectrum is no longer a thermal spectrum. Consequently, the assumption of a unique extrapolation length to define the boundaries is a poor one, and one must take into account the variation of extrapolation length with neutron energy. The validity and usefulness of using a one-velocity analysis is questionable.

The decay constant, α, is calculated by the $1/v$ poison removal method discussed previously. The calculational procedure consists of finding that value of Σ_a for which the calculated $k_{eff} = \beta_{eff} + k_{eff}$ (critical). In this equation, the term k_{eff} (critical) is the value of k_{eff} which is calculated by the model for a just critical configuration. Thus, it represents the bias or the mismatch between calculation and experiment. In the event

that the calculational technique used were exact, then no bias would have been used and the k_{eff} value for prompt criticality would have been just, $k_{eff} = \beta_{eff} + 1.000$. Four-group diffusion theory calculations in one or two dimensions were used to obtain k_{eff} for each medium. The group-averaged cross section used in these calculations was obtained from the SOFOCATE[4] and MUFT[23] codes. The thermal group in these calculations was represented by the hardened (Wigner-Wilkins) spectrum. The MUFT calculations used the earlier library of cross sections which was discussed in Sect. 6.2 and, thus, did not take into account such effects as the inelastic scattering in oxygen or an explicit treatment of the fission resonances in U^{235}. Since the difference between decay constants calculated using infinite medium spectra and finite medium spectra was only 2 percent in the worst case, infinite medium group constants were used in most cases.

Due to the small physical size of the bare assemblies, it is important to define properly the boundary of the system for each group. For example, using the thermal group extrapolation length for all groups, the error in the decay constant would be 20 percent for the 9-in. × 4-in. × 18-in. FPR-13 system. Therefore, in the diffusion calculation, a zero flux boundary condition was imposed at the physical boundary plus 0.71 λ_t where the transport mean free path, λ_t, was obtained from the MUFT and SOFOCATE output for each group.

The determination of the boundary for a reflected system is somewhat more involved and less precise than that for the bare system. Zero flux for all groups was imposed at the outer reflector surface; the transverse buckling was determined from the central flux shape given by a preliminary calculation using estimated extrapolated end points in the transverse direction.

2. *Interpretation of Experimental Investigations of the 1/v Poison Removal*

It is possible to investigate experimentally the $1/v$ poison removal method for calculating decay constants in multiplying media. If N_B is the boron atom density which must be removed from an assembly having the decay constant α sec^{-1} to make it prompt critical $(\alpha = 0)$, then from Eq. (6.40)

$$\alpha = \sigma_o v_o N_B \qquad \text{Eq. (6.66)}$$

where $\sigma_o V_o$ = product of the boron thermal cross section and thermal neutron velocity. To gain experimentally some further

understanding of this poison removal interpretation, two independent methods were used: (1) the determination of the reactivity coefficient for boron (using period calibrated control rods) in a critical assembly; (2) the measurement of the change in decay constant upon a uniform change in boron density in a subcritical assembly. The results of each of these methods can then be compared with actual measurements of the decay constant, α, using the pulsed technique.

In method (1), N_B is calculated from the reactivity worth of boron as simply the amount of boron required to make the system prompt critical. This is then used in Eq. (6.66) to obtain decay constants which are compared (Table 6.43) to the decay constants obtained by the actual pulsed neutron technique.

The agreement between method (1) and the direct results of pulsing the assembly is surprisingly good in view of the standard problems of homogenization. The macroscopic boron cross section is certainly not $1/v$ due to the finite thickness of the foils. To correct for the self-shielding effect of the foil, a Placzek self-shielding factor (0.87) at thermal energy was used. This is also an approximation.

In method (2), a differential form of Eq. (6.66) was used:

$$\Delta\alpha = \sigma_o v_o \Delta N_B \qquad \text{Eq. (6.67)}$$

where ΔN_B is the physical change in boron density made in a subcritical assembly.

It should be noted from Eq. (6.67) that the change in decay constant should be independent of the medium for a given

TABLE 6.43 — DECAY CONSTANTS FROM PULSED NEUTRON TECHNIQUE

Critical Assembly	α (Pulsed Neutron Technique, sec^{-1})	α (Reactivity Coefficient Technique, sec^{-1})
FPR-13 bare	104 ± 2	110 ± 13
FPR-13 reflected	95 ± 2	100 ± 6
FPR-14 reflected	315 ± 4	323 ± 19
FPR-15 reflected	176 ± 2	185 ± 11
FPR-16 reflected	369 ± 5	415 ± 20

change in boron density. (This is similar to the method discussed in the literature[71,72] to obtain thermal cross sections in nonmultiplying media.) Thus, the ratio $\Delta\alpha/\Delta N_B$ should be constant according to Eq. (6.67). The measured value of the decay constant before inserting boron, the measured change in the decay constant upon inserting boron into the assembly, and the ratio of $\Delta\alpha$ to the physical change in boron density, ΔN_B, are given in Table 6.44 for several experimental assemblies. (In this table, "module vertical" means that the plane of the fuel elements is parallel to the plane formed by the 18-in. × 18-in. dimensions of the core.) The indicated error on the value of $\Delta\alpha/\Delta N_B$ was obtained by propagating the error in the decay constant (standard deviation based on counting statistics) and the error in the boron density determination. The assemblies are listed in the table in the approximate order of increasing hardness of the neutron spectrum at the center of the assembly.

It is seen that the measured values of $\Delta\alpha/\Delta N_B$ are all less than the value of $\sigma_o V_o = 1.65 \times 10^{-16}$ cm^3/sec, which is the value for natural boron. Since the boron was inserted in the form of discrete elements (with an optical thickness at 2200m/sec of ~ 0.075), the effective cross section should be reduced somewhat because of self-shielding. The change in the self-shielding factor due to the change in neutron spectrum encountered in these experiments is less than 2 percent. It should be further noted that the spread from the mean of the measured values of $\Delta\alpha/\Delta N_B$ is less than 8 percent. This spread is not unreasonable in view of the uncertainties involved in using lumped boron elements in the somewhat heterogeneous systems. Although the initial values of the decay constant (depending on the composition and size of the medium) vary by a factor of 3, $\Delta\alpha/\Delta N_B$ is approximately constant.

3. *The Decaying State Spectrum*

A direct measurement of the energy spectrum during the decay of the persistent spatial mode would be desirable, but it is difficult to obtain with presently existing pulsed source intensities. To gain some understanding of this problem, an attempt has been made to obtain an indication of the decaying spectrum by making measurements of relative control rod worths such as are made in critical experiments.[73] The relative worth of a thermal and epithermal absorber (e.g., 4-in. × 18-in. × 0.200-in. thick hafnium) compared to a thermal absorber (e.g., 4-in. × 18-in. × 0.027-in. cadmium) has been found to be a sensitive function of the spectrum in the range of $\beta\gamma$ from 0.08 to 0.7. The corresponding subcritical relative worth determination consisted of measuring the change in the decay constant

TABLE 6.44— BORON EFFECT UPON DECAY CONSTANTS

Assembly	$\alpha(sec^{-1})$	$\Delta\alpha(sec^{-1})$	$\Delta N_B \times 10^{-19}$ (Atoms/cm^3)	$\Delta\alpha/\Delta N_B \times 10^{16}$ (cm^3/sec)
4 in. x 18 in. x 18 in. Al + polyethylene				
Module vertical	8800 ± 29	4631 ± 59	3.50 ± 0.18	1.32 ± 0.07
Module horizontal	9313 ± 35	4456 ± 64	3.50 ± 0.18	1.27 ± 0.07
6 in. x 18 in. x 18 in. Al + polyethylene				
Module vertical	6613 ± 25	4593 ± 50	3.50 ± 0.18	1.31 ± 0.07
Module horizontal	6881 ± 20	4443 ± 47	3.50 ± 0.18	1.27 ± 0.07
6 in. x 18 in. x 18 in. FPR-13 bare				
Module vertical	9252 ± 32	4907 ± 95	3.50 ± 0.18	1.40 ± 0.08
Module horizontal	9247 ± 18	4953 ± 38	3.50 ± 0.18	1.42 ± 0.07
10 in. x 12 in. x 18 in. FPR-14 with 4 in. side reflector	5225 ± 33	2258 ± 53	1.75 ± 0.09	1.29 ± 0.07
6 in. x 17 in. x 18 in. FPR-15 bare	19100 ± 100	4340 ± 110	3.50 ± 0.18	1.24 ± 0.07
			Mean	1.31

upon the insertion of 9-in. × 18-in. slabs in the center of a subcritical assembly. Such measurements were made with the FPR-15 composition (6 in. × 17 in. × 18 in.) and are compared with those made in the critical assembly in Table 6.45.

The relative worths in a critical assembly indicate a spectrum with a spectral hardness index of $\beta\gamma = 0.2$ which is in good agreement with the value calculated from the composition of the core. However, the subcritical measurements indicate that $\beta\gamma$ is approximately 0.04, which is significantly different. This indicates that either a large diffusion cooling effect is present or that the epicadmium and thermal adjoint ratio is different than in the critical assembly, or that both of these effects exist to some extent.

Small diffusion cooling effects have been observed in pure moderating systems because the spectrum is essentially Maxwellian, and the velocities are thereby limited to the thermal range. In a multiplying medium, however, neutron velocities extend to fission neutron velocities and, therefore, large diffusion cooling effects are to be expected. It is possible to show by a simple two-group analysis that a measurable diffusion cooling effect should be present. That is, one can write, neglecting the delayed neutron contribution,

$$\frac{dN_2}{dt} = -\left(\Sigma_{a2} v_2 N_2 + v_2 D_2 B_2^2 N_2\right) + \Sigma_{s1} v_1 N_1 \qquad \text{Eq. (6.68)}$$

$$\frac{dN_1}{dt} = -\left(\Sigma_{s1} v_1 N_1 + \Sigma_{a1} v_1 N_1 + v_1 D_1 B_1^2 N_1\right) + \nu \Sigma_{f2} v_2 N_2 \qquad \text{Eq. (6.69)}$$

TABLE 6.45 — COMPARISON OF CHANGE IN FPR-15 COMPOSITION DECAY CONSTANTS WITH CRITICAL ASSEMBLY

Type of Rod	$\Delta\alpha(\text{sec}^{-1})$	$\Delta\alpha/\Delta\alpha_{cd}$	Critical Assembly Relative Worth
0.027 in. Cd	4818 ± 97	1.0	1.0
0.200 in. Ag	5264 ± 93	1.08 ± 0.03	1.34 ± 0.03
0.100 in. Hf	4728 ± 104	0.98 ± 0.03	1.23 ± 0.02
0.200 in. Hf	5696 ± 133	1.18 ± 0.04	1.52 ± 0.03

where the subscripts 1 and 2 refer to fast and thermal groups, respectively, and N is the neutron density. Since concern is only with measurements obtained when the decay appears to follow a single exponential, one has

$$\alpha = -\frac{1}{N_2}\cdot\frac{dN_2}{dt} = -\frac{1}{N_1}\frac{dN_1}{dt}\,. \qquad \text{Eq. (6.70)}$$

This assumption has been verified by measuring the decay constant as a function of detector position (spatial equilibrium) and with and without a cadmium screen on the detector (spectral equilibrium). The decay constant as measured for this assembly is 18,175 ±44 with the bare counter, and 18,185 ±80 with cadmium-covered counters after waiting three persistent mode mean lives. The relative worth measurements listed in Table 6.45 were also made after waiting this time. Noting that $\phi_i = N_i v_i$, Eqs. (6.68) and (6.69) become

$$\phi_2\left(\Sigma_{a2} + D_2 B_2^2 - \frac{\alpha}{v_2}\right) - \phi_1\Sigma_{s1} = 0 \qquad \text{Eq. (6.71)}$$

$$\phi_2\left(\nu\Sigma_{f2}\right) - \phi_1\left(\Sigma_{s1} + \Sigma_{a1} + D_1 B_1^2 - \frac{\alpha}{v_1}\right) = 0\,. \qquad \text{Eq. (6.72)}$$

The solution of these equations for the eigenvalue, α, is

$$\frac{\alpha}{v_2} = \Sigma_{a2} + D_2 B_2^2 - \frac{\nu\Sigma_{f2}\,\Sigma_{s1}}{\Sigma_{s1} + \Sigma_{a1} + D_1 B_1^2} \qquad \text{Eq. (6.73)}$$

if one neglects terms of second order and higher in (v_2/v_1) since (v_2/v_1) is of the order of 10^{-3}. This approximation is essentially the same as dropping the α/v_1 term in Eq. (6.72). The negative root was chosen to give the lowest eigenvalue for a physical system. Equation (6.73) is similar to that used by Campbell and Stelson[66] (and later Purohit[74]) in the analysis of their data to obtain a value for the age. In the present analysis, the usual assumption[66,74-76] of a unique buckling value for all energies is not made.

From Eq. (6.72), one obtains for the decaying state spectrum

$$\frac{\phi_1}{\phi_2} = \frac{\nu\Sigma_{f2}}{\Sigma_{s1} + \Sigma_{a1} + D_1 B_1^2} \equiv \left(\frac{\phi_1}{\phi_2}\right)_{\text{d.s.}}\,. \qquad \text{Eq. (6.74)}$$

The same expression would be obtained from Eq. (6.71) upon insertion of the eigenvalue obtained from Eq. (6.73).

In spite of the obvious crudity of a two-group analysis, Eqs. (6.73) and (6.74) can be used to gain some insight into the behavior of the spectrum in multiplying systems. Rewriting Eq. (6.73) as

$$\frac{\alpha}{v_2} = \Sigma_{s1}\left[\frac{\Sigma_{a2} + D_2 B_2^2}{\Sigma_{s1}} - \frac{\nu\Sigma_{f2}}{\Sigma_{s1} + \Sigma_{a1} + D_1 B_1^2}\right] \qquad \text{Eq. (6.75)}$$

one can identify each term inside the bracket with spectrum. That is,

$$\frac{\alpha}{v_2} = \Sigma_{s1}\left[\left(\frac{\phi_1}{\phi_2}\right)_{\text{s.s.}} - \left(\frac{\phi_1}{\phi_2}\right)_{\text{d.s.}}\right] \qquad \text{Eq. (6.76)}$$

where $(\varphi_1/\varphi_2)_{\text{s.s.}}$ is recognized as the spectral index, $\beta\gamma$, for a steady-state system. Physically, this describes the spectrum of a critical system or of a subcritical system excited by a steady-state source. It is also the spectrum one observes in a pulsed source spectrum measurement where the time of flight of a neutron that leaves the medium at any time during the burst is measured. The $(\varphi_1/\varphi_2)_{\text{d.s.}}$ is identified with Eq. (6.74) and describes the neutron spectrum that exists during the decay of the persistent mode. The steady-state spectrum can be measured explicitly, while the decaying state spectrum can be inferred crudely, from the relative rod worth type measurement, and it can also be measured explicitly in a pulsed source type spectrum measurement if one limits observation to neutrons which leave the system only during the persistent mode decay.

Equation (6.74) shows that for a medium of a given composition, the decaying state spectrum is cooled as the physical size is decreased. For the FPR-15 lattice mentioned above, the value of $(\varphi_1/\varphi_2)_{\text{d.s.}}$ given by Eq. (6.74) is 0.10, which is in fair agreement with the relative rod worth estimate of $(\varphi_1/\varphi_2)_{\text{d.s.}}$. Equation (6.74) also shows that within the approximation $\alpha/v_1 << \Sigma_{s1} + \Sigma_{a1} + D_1 B_1^2$, which is true for all of the systems, the decaying spectrum is independent of changes in the thermal absorption. More rigorously, Eqs. (6.71) and (6.72) show that the decaying spectrum is not altered on the addition or removal of a $1/v$ poison, although the decay constant must change under these conditions.

The calculation of a decay constant by the $1/v$ poison removal method involves a calculation of a steady-state system having

a fictitious absorption cross section. The steady-state spectrum of this fictitious system when prompt criticality is attained is identical to the decaying state spectrum of the actual subcritical system. This can be seen more clearly from Eq. (6.75). Σ_{a2}, the actual thermal absorption cross section, is adjusted to Σ'_{a2}, a fictitious absorption cross section, until $\alpha = 0$. When $\alpha = 0$, this means that the steady-state spectrum of the fictitious medium is the same as the physical decaying state spectrum. In Figure 6.76 are shown the SOFOCATE steady-state and decaying state spectra as obtained for the FPR-15 lattice.

4. Comparison of Measured and Calculated Results

The decay constants for a series of subcritical assemblies having a variety of compositions and physical sizes were measured and calculated. The thermal absorption cross sections vary from 0.075 to 0.39 cm^{-1}. The range in leakage with change in physical size for a given assembly of a given composition is indicated by the range in calculated k_{eff} (0.20 to 1.0). Table 6.46 includes the calculated decay constants and the measured values with errors based on counting

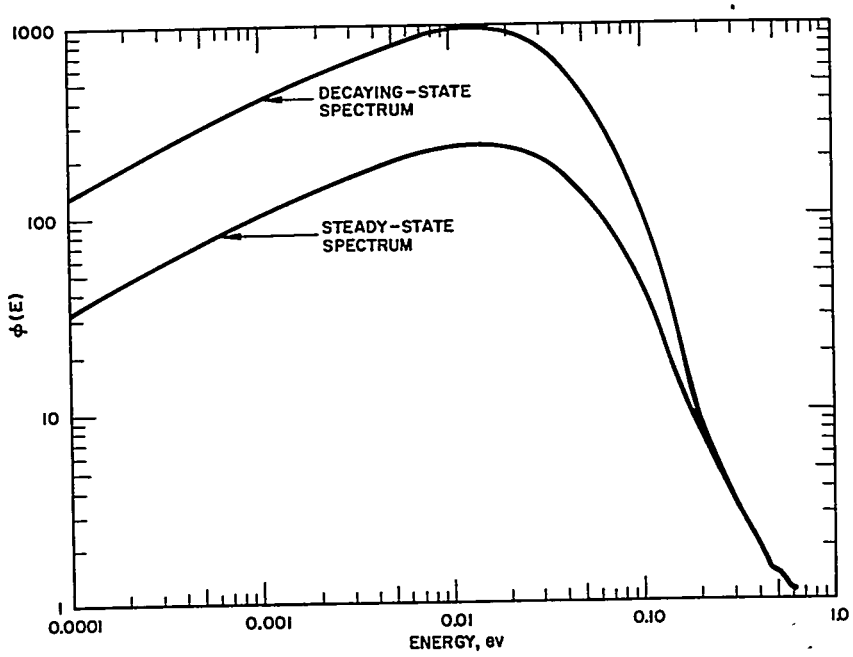

FIGURE 6.76. Steady and Decaying State Spectra.

TABLE 6.46 — CALCULATED DECAY CONSTANTS AND MEASURED VALUES

Assembly Composition	Size (in.)	Measured α (sec^{-1})	Calculated α (sec^{-1})	Calculated k_{eff}
FPR-13, bare	20 x 20 x 36	104 ± 2	97	1.021
	19 x 19 x 36	405 ± 7	406	0.994
	18 x 18 x 36	789 ± 48	799	0.964
	17 x 17 x 36	1186 ± 54	1241	0.931
	17 x 16 x 36	1416 ± 31	1497	0.911
	17 x 14 x 36	2043 ± 98	2132	0.864
	17 x 10 x 36	4513 ± 350	4210	0.716
	17 x 6 x 36	7000 ± 1100	8707	0.440
	17 x 6 x 18	8870 ± 23	9358	0.402
	7 x 7 x 18	11680 ± 60	11203	0.308
	6 x 6 x 18	13110 ± 110	13191	0.232
	9 x 4 x 18	14705 ± 82	15355	0.179
	7 x 7 x 18*	21710 ± 345	19350	
FPR-13, 6 in. reflected	17 x 16 x 36	95 ± 1.5	91	1.036
	17 x 15 x 36	194 ± 2	185	1.022
	17 x 14 x 36	398 ± 33	378	1.005
	17 x 12 x 36	909 ± 9	833	0.966
	17 x 10 x 36	1409 ± 25	1332	0.914
	17 x 6 x 36	2623 ± 93	2720	0.750
	6 x 6 x 18	4000 ± 400	4215†	0.504
FPR-14, bare	10 x 15 x 18	27100 ± 50	27263	
	8 x 15 x 18	32850 ± 105	35165	
FPR-14, 6 in. reflected 4 in. reflected	15 x 15 x 36	315 ± 4	430	
	10 x 12 x 18	5224 ± 33	5914	
FPR-15, 6 in. reflected	22 x 22 x 36	176 ± 2	159	

*First harmonic.
†Two-dimensional diffusion calculation.

statistics alone. No errors are indicated for the calculated results, although errors in the cross sections and method of calculation certainly exist.

Most of the measured decay constants agree to within ±8 percent of the calculated values. The one large discrepancy occurs for the FPR-14 critical assembly measurement. Since for this assembly the reactivity coefficient method gives a value for the decay constant (Table 6.43) that is in good agreement with the value obtained with the pulsed method, the validity of the calculated value is in question. Moreover, the core reactivity coefficient calculation[70] is within 10 percent of the measured value and, since the reflector peaking is large in this reactor, the difficulty in the calculation apparently lies in the determination of the reactivity coefficient of boron in the reflector region.

It is interesting to note that a higher mode decay constant can be measured and calculated with fair agreement (7-in. × 7-in. × 18-in. FPR-13, bare). The calculation of the first harmonic decay constant is carried out by imposing a zero flux condition for all energy groups at the midplane of the slab assembly. That is, a fundamental mode decay constant is calculated for an assembly whose boundaries are determined by the midplane and extrapolated end point of the outer boundary of the actual assembly.

A plot of the decay constant versus calculated buckling is the usual method for presentation of pulsed neutron data. Since the buckling dependence on energy must be included in the analysis of decay constants for multiplying media, it is more reasonable to display the present data as a function of calculated k_{eff} rather than B^2. Figures 6.77 and 6.78 show the measured and calculated decay constants for a bare and a reflected system with FPR-13 composition. It should be emphasized that the k_{eff} is calculated for a system having a steady-state source distributed in the persistent spatial mode. The relationship between this unphysical steady-state system and the pulsed system is rather tenuous.

5. *Discussion of Results and Conclusions*

The concept of the criticality factor has been used extensively at or near delayed critical in describing the reactivity condition of a multiplying medium. The decay constant can be related to the criticality factor[77] in the following manner:

$$-(1/n)\frac{dn}{dt} = \alpha = (1 - C)(\text{fractional neutron density loss per unit time}) \qquad \text{Eq. (6.77)}$$

where

$$C = \frac{\text{Average no. of neutrons produced in reactor per unit time}}{\text{Average no. of neutrons lost to reactor per unit time}}$$

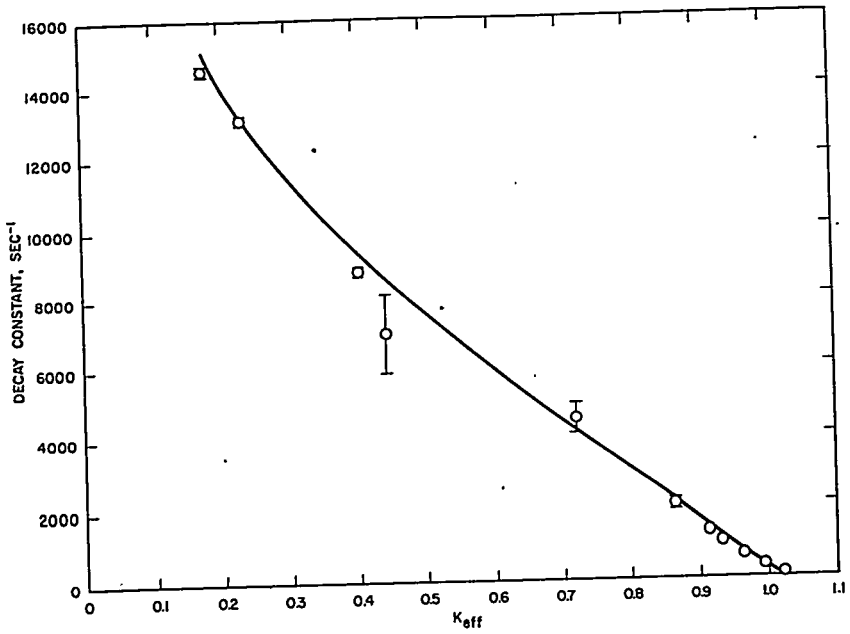

FIGURE 6.77. Bare System Decay Constants.

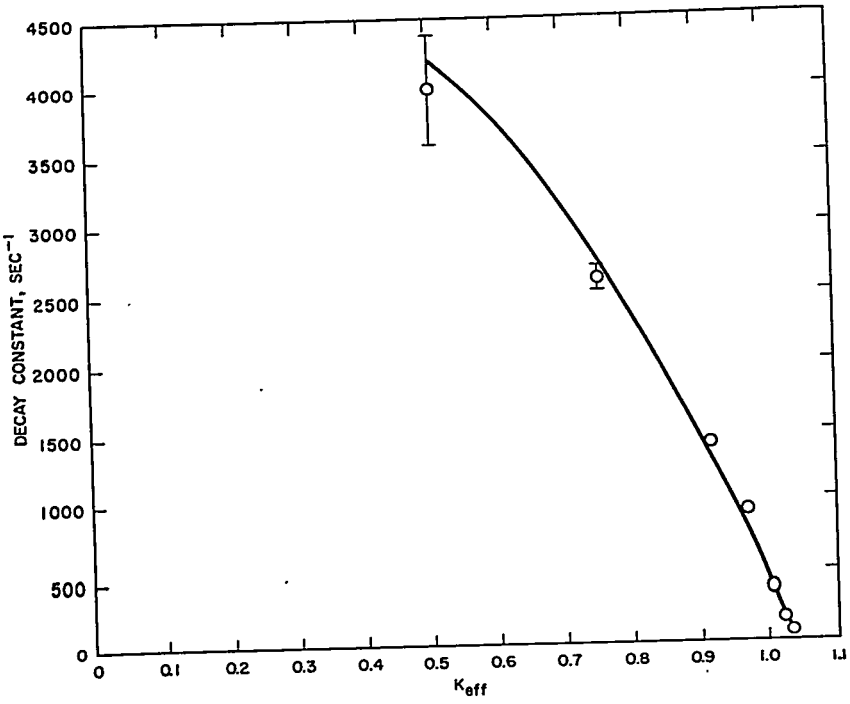

FIGURE 6.78. Reflected System Decay Constants (6-in. Reflector).

and n is the neutron density in the assembly. The criticality factor is never actually measured but must be inferred from the results of period, rod drop, or multiplication measurements in terms of the delayed neutron fraction. The extension of these measurements to far subcriticality is difficult; consequently, in general, calculations and measurements have only been compared near critical. One should note that the criticality factor C is used to characterize a dynamic physical system as contrasted to the k_{eff} factor, mentioned above, which pertains to a steady-state system.

On the other hand, measurements of the fundamental mode prompt neutron decay constant can be performed successfully on assemblies whose reactivity ranges from critical to far subcritical, provided that subcriticality is achieved by decreasing the size from the critical size rather than by addition of poison to the critical size assembly. The results presented here indicate that the decay constant can be calculated to within 10 percent with rather crude methods. Therefore, it is more useful to characterize a subcritical system by its decay constant rather than its criticality factor, since the former is directly observable.

It would appear, therefore, that the pulsed neutron technique in the far subcritical region will yield information regarding parameters and calculational methods which will complement the comparisons presently made using critical experiments. In the far subcritical region, decay constants can depend strongly on the leakage, and comparisons with calculations should provide a better measure of the adequacy of parameters which describe the leakage. Two extensions of the present investigation are indicated: first, the study of fundamental constants, such as absorption and scattering cross sections, by means of using a truly homogeneous medium; second, the evaluation of the subcritical method for measuring the homogenization equivalence of lumped poisons in complex geometries.

The apparently large diffusion cooling effect on the spectra of small multiplying media limits the unreserved application of pulsed measurements for measurements presently carried out in critical assemblies. By this is meant that one cannot simply extrapolate measurements made in the far subcritical region to the critical region without taking into account spectrum and adjoint differences between the critical and subcritical systems. On the other hand, since the spectrum is strongly leakage-dependent, an explicit measurement of the decaying state spectrum should be of considerable experimental and theoretical interest.

E. Reactivity without Critical Calibration

It has been shown in the above discussion that the reactivity of a subcritical assembly may be determined by the pulsed neutron method, provided the decay constant at delayed critical α_d is known. The reactivity R, in dollars, is then given by

$$R = \frac{\alpha}{\alpha_d} - 1. \qquad \text{Eq. (6.78)}$$

The requirement that α_d be known limits this method to situations wherein the reactor has been critical at some time.

Additional information concerning the reactivity is contained in the delayed part of the neutron flux from a pulsed assembly. Normally, the delayed neutron flux constitutes an undesirable background. If, however, a strong pulsed neutron source is used, it becomes possible to make measurements of this flux. In particular, an integral over a portion of the delayed flux may be used with the prompt data to provide a reactivity value directly in dollars.

1. Theory

The equations describing the kinetic behavior of the neutron flux in a reactor may be written as follows in the absence of a steady-state source:

$$\dot{n} = \frac{k-1}{\ell} n - \frac{k\beta}{\ell} n + \sum_{i=1}^{6} \lambda_i C_i \qquad \text{Eq. (6.79)}$$

$$\dot{C} = -\lambda_i C_i + \frac{k\beta_i}{\ell} n \qquad \text{Eq. (6.80)}$$

The notation is standard. A solution is given in the literature[78] of the form

$$n(t) = n_o \sum_{i=1}^{7} A_i(p_i) e^{p_i t} \qquad \text{Eq. (6.81)}$$

where the exponents p_i are the roots of

$$\frac{p\ell}{k\beta} - \frac{k-1}{k\beta} + 1 - \sum_{i=1}^{6} \frac{b_i \lambda_i}{(p + \lambda_i)} = 0 \qquad \text{Eq. (6.82)}$$

and the coefficients $A(p)$ are given by

$$A(p) = \frac{1 + \sum_{i=1}^{6} \frac{C_{io}}{n_o} \frac{\lambda_i}{(p + \lambda_i)}}{1 + \frac{k\beta}{\ell} \sum_{i=1}^{6} \frac{b_i \lambda_i}{(p + \lambda_i)^2}} \quad . \qquad \text{Eq. (6.83)}$$

It is desired to solve these equations in terms of dollars of reactivity only. To do so, introduce the usual prompt decay constant and dollars of subcritical reactivity R.

Examination of Eq. (6.79) gives

$$\alpha = \frac{k - 1 - k\beta}{\ell} \quad . \qquad \text{Eq. (6.84)}$$

The dollar of reactivity R is defined in terms of α, k, β, and ℓ as

$$R = \left[\alpha - \frac{k\beta}{\ell}\right] \Big/ \left[\frac{k\beta}{\ell}\right] \qquad \text{Eq. (6.85)}$$

where R is measured from delayed critical. This gives

$$\alpha = (1 + R)\frac{k\beta}{\ell} \quad . \qquad \text{Eq. (6.86)}$$

Substitution of Eq. (6.86) into Eq. (6.82) gives

$$(p - \alpha) + \frac{k\beta}{\ell} \sum_{i=1}^{6} \frac{b_i \lambda_i}{(p + \lambda_i)} = 0 \, . \qquad \text{Eq. (6.87)}$$

One solution to Eq. (6.87) is that a good approximation is $p = \alpha$. The right term is of order $k\beta/\ell\alpha$ (note $k\beta/\ell\alpha \leq 1$) times a small number (about $\sum_{i=1}^{6} b_i \lambda_i = 0.39$) when $p = \alpha$ and may be neglected since $|\alpha| << 1$. For the six other solutions p_i is of order 1, so p may be neglected relative to α in $(p - \alpha)$. This gives on substituting the definition of the dollar from Eq. (6.85),

$$\sum_{i=1}^{6} \frac{b_i \lambda_i}{(p + \lambda_i)} - (1 + R) = 0 \, . \qquad \text{Eq. (6.88)}$$

The expression for the $A(p)$, Eq. (6.83), may be simplified by assuming that the initial concentration of the i^{th} precursor, C_{io}, is given by

$$C_{io} = n_o\beta_i = n_o\beta b_i . \qquad \text{Eq. (6.89)}$$

Substitution of Eq. (6.89) into Eq. (6.83) gives

$$A(p) = \frac{1 + \beta \sum_{i=1}^{6} \frac{b_i\lambda_i}{(p+\lambda_i)}}{1 + \frac{k\beta}{\ell} \sum_{i=1}^{6} \frac{b_i\lambda_i}{(p+\lambda_i)^2}} . \qquad \text{Eq. (6.90)}$$

For the case $p \doteq \alpha$ both sum terms are much less than 1, so that the approximation $A(\alpha) = 1$ is good. For the six other coefficients Eq. (6.90) is simplified, using Eq. (6.88), to give

$$A(p) = \frac{1 + \beta(1+R)}{1 + \frac{k\beta}{\ell} \sum_{i=1}^{6} \frac{b_i\lambda_i}{(p+\lambda_i)^2}} . \qquad \text{Eq. (6.91)}$$

To simplify this expression further, note that for $p \approx 1$ the sum term in the denominator is very large compared to 1. Defining $B(p)$ as

$$B(p) \equiv \sum_{i=1}^{6} \frac{b_i\lambda_i}{(p+\lambda_i)^2} \qquad \text{Eq. (6.92)}$$

and substituting, $A(p)$ becomes

$$A(p) = \frac{[1 + \beta(1+R)]}{\frac{k\beta}{\ell}} \frac{1}{B(p)} . \qquad \text{Eq. (6.93)}$$

Substituting for $k\beta/\ell$ from Eq. (6.86),

$$A(p) = \frac{[1 + \beta(1+R)]}{\alpha} \frac{(1+R)}{B(p)} . \qquad \text{Eq. (6.94)}$$

To calculate the p_i and $B_i(p_i)$ as functions of R, a value of β must be chosen. A good choice is $\beta = 0.008$. Any disparity between this choice and the correct one for the system under

consideration will be a second-order error and may be ignored. For simplicity define $K(R)$ as

$$K(R) = [1 + 0.008(1 + R)]\ (1 + R). \qquad \text{Eq. (6.95)}$$

Finally,

$$A(p) = \frac{K(R)}{\alpha} \frac{1}{B(p)}. \qquad \text{Eq. (6.96)}$$

An integral over the delayed flux may be taken between times T_1 and T_2 after the pulse, T_1 being chosen so that the prompt contribution to the flux has vanished. Such an integral ϕ_d is given by

$$\phi_d = n_o \sum_{i=1}^{6} \frac{A_i(p_i)\left(e^{p_i T_2} - e^{p_i T_1}\right)}{p_i}. \qquad \text{Eq. (6.97)}$$

Substituting Eq. (6.96) into Eq. (6.97), one has for the delayed flux integral

$$\frac{\alpha\phi_d}{n_o} = K(R) \sum_{i=1}^{6} \frac{\left(e^{p_i T_2} - e^{p_i T_1}\right)}{p_i B_i(p_i)} \qquad \text{Eq. (6.98)}$$

where the right-hand side may be calculated as a function of reactivity and the left-hand side determined experimentally. Thus, a plot of the calculated value of $(\alpha\phi_d)/n_o$ as a function of dollars may be used to obtain a reactivity value from the experimental results. Such a plot is shown in Fig. 6.79 for an integration time of 1.0 to 21.0 seconds after the neutron pulse.

The term α/n_o is the same as the total integral of the prompt flux ($t = 0$ to $t = \infty$). Thus, the physical quantity related to reactivity is the ratio of a delayed flux integral to the total integral of the prompt flux associated with this delayed flux. If modal effects were insignificant so that $e^{-\alpha t}$ accurately described the prompt flux over all times 0 to ∞, then two simple integrals would adequately determine the reactivity. This has not been tried as yet because of the problems associated with the measurement of the flux at times immediately after the neutron pulse. It is to be noted that the reactivity result found by this method depends upon the values of β and ℓ at the time of measurement and not upon their values at delayed critical.

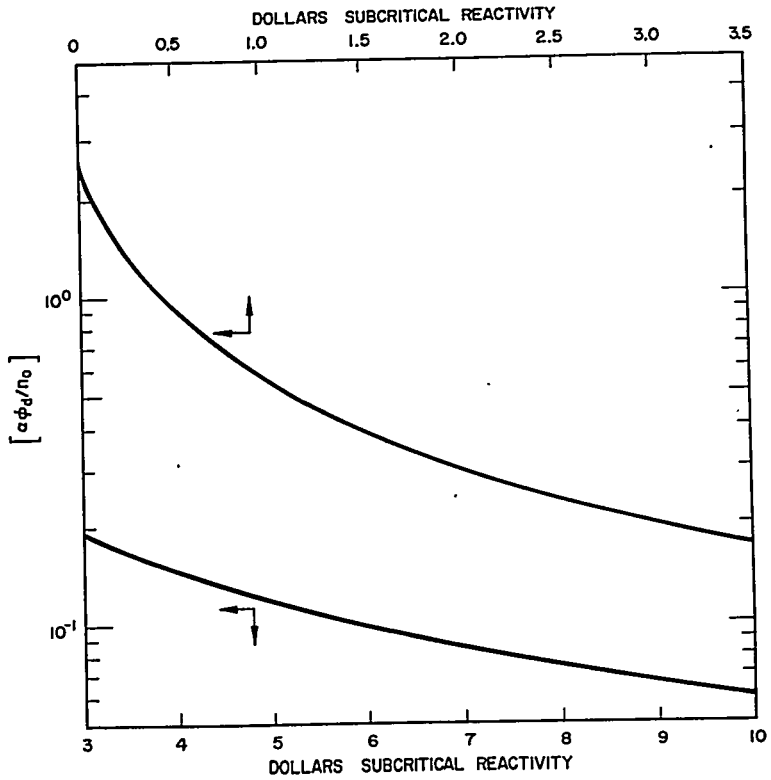

FIGURE 6.79. A Plot of $(a\phi_d/n_o)$ as Given by Eq. (6.84) a Function of Shutdown Reactivity for an Integration Time of 1.0 to 21.0 Seconds after the Burst.

2. *Experimental Procedure*

The delayed neutron integral method has been used to measure the reactivity of a subcritical reactor as follows. A conventional pulsing system was modified by the addition of an intense neutron-pulse source and a single-gated scaler connected in parallel to the regular detection system. Before each neutron pulse, the background is measured for a time interval equal to that used for the delayed neutron integral. Then the prompt data analyzer and pulse source are triggered in the usual manner. After the prompt flux has decayed, the scaler is gated on for the integral time, after which the process is repeated as many times as is necessary to collect adequate statistics.

The prompt data are analyzed in the standard way to obtain a and n_o, subtracting the delayed neutron background from

the prompt data. This background is treated as being level during the prompt decay. Because a high pulse source intensity is necessary to make the delayed neutron flux observable, the prompt data must be accumulated at very high counting rates, and the counting loss due to the finite resolution of the detection system must be corrected carefully. This count loss correction is probably the largest single source of error present in this technique. After α and n_o are obtained, the product $\alpha\phi_d/n_o$ is evaluated, and from this a reactivity is obtained using the appropriate graph.

3. *Results*

Some preliminary results are shown in Fig. 6.80. The reactivity by normal critical facility techniques was determined by conventional pulsed neutron methods and by rod-drop and multiplication measurements. These are compared on Fig. 6.80 with the results of the delayed integral pulsed technique discussed here. The errors shown in the delayed integral reactivity are those found from the spread in results over several different determinations or the statistical spread within one determination, whichever is larger. Different integration times were used for the delayed neutron integral to maintain accuracy over the interval. Near critical, a time of 1.0 to 21.0 seconds after the pulse is convenient. When the delayed flux becomes much lower in intensity (at more subcritical settings) an integral time of 0.05 to 10.05 seconds is more suitable. These times may be adjusted for experimental convenience.

4. *Discussion*

This method is of interest in that no value for α_d is required to determine a reactivity. However, the precision obtainable with present apparatus makes the conventional pulsing technique a much more desirable method when making design studies. As mentioned above, the largest single source of uncertainty appears to be in the determination of n_o from the prompt decay data. The flux value changes over a range of several decades following the pulse, and present equipment limits observation to a range not much over one decade. If a neutron counting system with a capability considerably better than that of the three-megacycle system used for the results presented here becomes available, it should be possible to improve significantly the accuracy and reliability of the results obtained by this method.

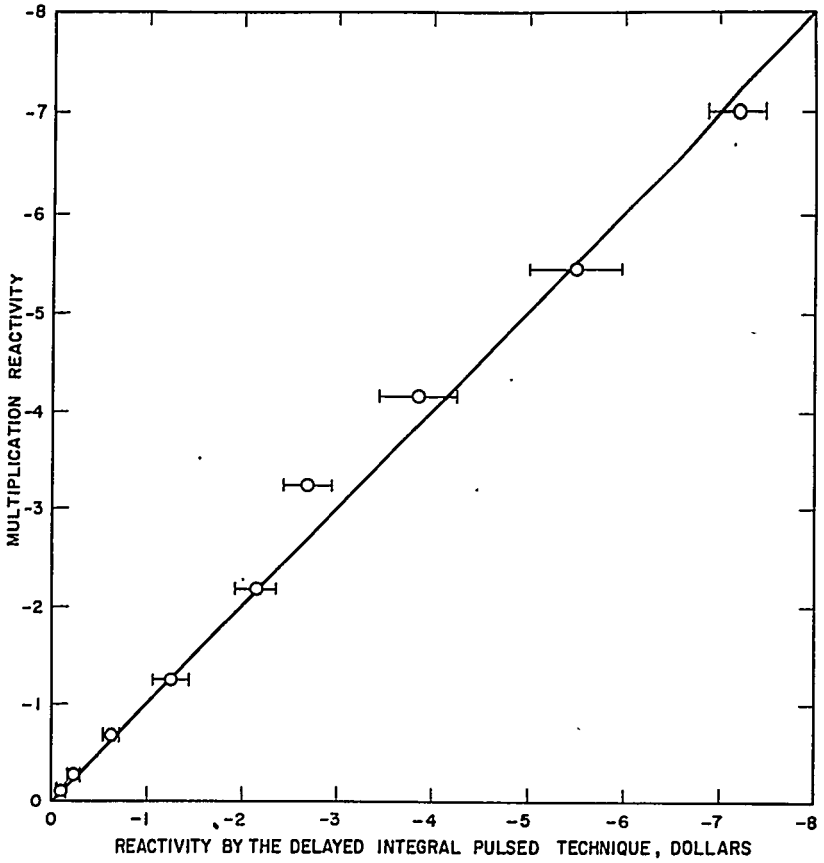

FIGURE 6.80. Comparison of Subcritical Reactivity as Determined by the Pulsed Neutron Technique without a Critical Calibration and That Determined by Conventional Critical Facility Methods (e.g., Rod Drop, Rod Calibration, Normal Pulsed Neutron, etc.).

6.7 LOW ENERGY MEASUREMENTS OF THE NEUTRON SPECTRUM

S. I. Bunch, J. R. Roesser, and R. E. Slovacek

A. Introduction

It has been noted in Sect. 6.2 that present critical assembly techniques do not lend themselves to the detailed study of the low energy spectra in reactor cores. The thermal neutron spectrum in a finite medium containing fuel and hydrogen as moderator is of considerable interest in reactor design and in

the understanding of neutron thermalization. Knowledge of the neutron spectrum in a reactor is important in many aspects of reactor design. Interpretation of such measurements as reactivity coefficients, power, or temperature coefficients, and the prediction of such reactor characteristics as control and lifetime are intimately related to the neutron spectrum in a reactor core. The neutron thermalization problem was discussed in detail in Chap. 3. In addition, a rather complete summary of the theory and measurement of reactor spectra can be found in the literature.[79, 80]

In this section, a method is described to simulate the flux at a given point within the core by means of a small, fuel-loaded assembly in the thermal column of a test reactor. This subcritical assembly served as a source for a neutron beam which could be spectrum analyzed using a time-of-flight spectrometer. The small assembly was equipped with the necessary heating elements and pressure vessel, so that the spectrum could be investigated under elevated conditions of temperature and pressure. It should be noted that the spectrum of the neutron beam current is actually measured in these experiments rather than the spectrum of the neutron flux itself at the origin of the beam. The spectrum of the neutron flux is then obtained from the measured current spectrum using a diffusion theory approximation.

Results are given on measurements which have been made on both water- and polyethylene-moderated assemblies. Six spectra were obtained from water-moderated media located in the small pressure vessel. In addition, two water spectra were obtained in which the water was poisoned with absorbers dissolved in solution at room temperature. Results are also given on neutron spectrum measurements made on four polyethylene-moderated subcritical assemblies. Polyethylene has been used extensively as a moderating material, particularly as a substitute for water in critical assembly experiments. An example of this use was discussed in Sect. 6.2.C. Since the hydrogen atom is bound differently in the polyethylene molecule than in the water molecule, one might expect the neutron spectra to be different.

Many investigators have used essentially three techniques to measure the neutron energy spectra in the thermal energy range. The crystal spectrometer method, which was the first used to measure reactor spectra, produces a monochromatic neutron beam, while the pulsed-beam and slow-chopper methods measure neutron energies by their time of flight.

In the crystal spectrometer method, a monoenergetic neutron beam is produced from selected planes in a crystal by Bragg reflection of neutrons from an incident beam emerging from

a reactor or other similar neutron source. The reflected neutron beam is detected by a counter located at the proper angle with respect to the incident beam direction such as to satisfy the Bragg condition. The incident beam spectrum can be scanned by changing the Bragg angle and recording the Bragg beam intensity as a function of angle or neutron wave length. The reflected beam intensity is then related to the incident beam neutron spectrum after correcting it for many effects. The effects which must be corrected include the reflections in the collimators, the higher order reflections from the selected set of planes in the crystal, the crystal reflectivity, the transmission of the materials in the beam path between the source region and the counting volume, the spectrometer resolution, and the detector efficiency. The crystal spectrometer technique has been applied to the measurement of spectra,[81] but large dips in the measured spectra apparently caused by extinction effects of planes other than those supplying the Bragg beam[82] make the interpretation of the data difficult.

The slow chopper technique [80,85-87] has been used almost exclusively up to the present time in the measurement of spectra in multiplying media. In this technique a neutron beam is obtained from a subcritical spectrum source region that is excited by a steady-state neutron source such as a reactor. A slow neutron chopper is placed in the beam to measure the neutron energy by time of flight. The counts registered in the time analyzer are related to the beam spectrum after making corrections for the transmission of materials in the beam between the source and detector, the detector efficiency, the system resolution, and the chopper transmission function. This technique, which was applied in obtaining the data for the measurements to be described in this section, will be discussed more completely below. The spectral hardness index for the media under investigation was extended (maximum $\beta\gamma \approx 1$) beyond any previous measurements on multiplying media.

Of the three techniques, the pulsed-beam method is unique in that it utilizes the pulsed nature of the primary neutron source as a means of determining the neutron energy. An electron linear accelerator is usually used with a tungsten target to provide a pulsed photoneutron source ($\sim 10^{11}$ neutrons/burst) of high energy neutrons. These high energy neutrons are then allowed to enter the neutron spectrum source region. By making the thermal die-away time of the spectrum source region small compared to the drift time of these thermal neutrons over a long flight path to a detector, one can measure the steady-state neutron spectrum in that region that would

be established with a steady-state source having energy and spatial characteristics similar to the pulsed source. The time distribution of neutron counts are related to the neutron beam spectrum leaving the region after correcting for the transmission of materials in the beam between the source and detector, the detector efficiency, and the system resolution (which is usually designed to give a negligible correction). An advantage of this method is that one does not have a quantity equivalent to the crystal reflectivity or the chopper transmission to determine.

The pulsed-beam time-of-flight method was first used by Poole[83] to study thermal neutron spectra in poisoned water solutions having no multiplication present. These measurements have been extended to poisoned water, polyethylene, and zirconium hydride systems by Beyster, et al.,[84] and have demonstrated conclusively that the chemical binding of the moderator must be taken into account in order to calculate the neutron spectra in these media. Measurements in subcritical assemblies having an appreciable source multiplication (a factor of 2 to 5) are more difficult to perform, since the burst width is increased when multiplication is present and longer flight paths are required to obtain sufficient resolution. The only measurement with this technique in an enriched fuel subcritical assembly is that of Beyster, et al., which had a spectral hardness index of $\beta\gamma \approx 0.12$. In that case the scalar spectrum measured was in excellent agreement with the calculated spectra using Nelkin's bound atom kernel.

B. Experimental Method

In a critical assembly, the spectrum data for a particular region of a reactor core normally consist of relative neutron activation measurements at various energies obtained by means of the activation of foil detectors which have different absorption characteristics at different energies. In addition, it is possible to obtain a relative measurement of the integral of the flux, below the cadmium cutoff energy, weighted by the cross section of material used for these activations. However, critical assembly techniques have not yet been developed for a detailed study of the low energy spectrum with a spectrometer within the assembly itself.

In the experiments discussed here, to obtain a spectrum source for spectrometer measurements, an assembly was placed behind a plate of fissionable material located in a reactor thermal column. The size of the assembly was designed to be a fraction of the size of a critical assembly, resulting in a subcritical assembly with a source multiplication of

approximately three or less. By means of activation techniques, the flux as a function of energy and position was studied in the subcritical assembly and compared with similar measurements in the critical assembly. Within the experimental error, the spectra in the center of the two assemblies were identical. The power density for a spectrum measurement was of the order of 2 watts/ft^3, and the measurement of a spectrum required about 20 hours at this level.

It is possible to extract a neutron beam from the source point within the assembly by means of a re-entrant hole. This beam can then be collimated by a collimation system in the thermal column shield. The collimated beam is then chopped by a rotating shutter and, after a given flight path length, is detected by a counter. The signal pulses from the counter are time separated into different channels corresponding to different neutron velocities. The background counting rates for the various channels can be obtained by turning on similar channels at a time in the equipment cycle when no spectrum neutrons are in the vicinity of the detector.

The arrangement of experimental equipment is shown schematically in Fig. 6.81 for the pressure vessel experiments. The thermal neutron flux from the test reactor at operating power was about 10^{10} neutrons/cm^2-sec incident on the plate. The high-energy neutrons which result from fission in this plate are transmitted through the pressure vessel wall more easily than the thermal neutrons. These neutrons excite the 16-in. long and 10-in. diameter experimental volume of the subcritical assembly which is formed by the penetration of the pressure vessel into the edge of the thermal column.

A 2-in. diameter re-entrant hole penetrates 8 in. deep into the forward end of this subcritical assembly. The hole is filled with a thin-walled helium tank to provide a method of extracting a neutron beam from the bottom of the hole with small perturbation to the medium. The beam leaves the high-pressure region through a 0.030-in. thick stainless steel high-pressure rupture disk and is collimated by a 1-meter long boron carbide collimator assembly.

Two types of media were investigated in the experimental volume, which could also be called the beam source region, since the neutron beam which served as the source for the chopper originated in this volume. In one arrangement, the 16-in. long, 10-in. diameter experimental volume in the rear of the pressure vessel was filled with pure water. For the second type of source region, a multiplying medium was used. Since chemical binding effects on spectra were not well understood even at room temperature, it was of interest to observe their variation, if any, with temperature. Facilities

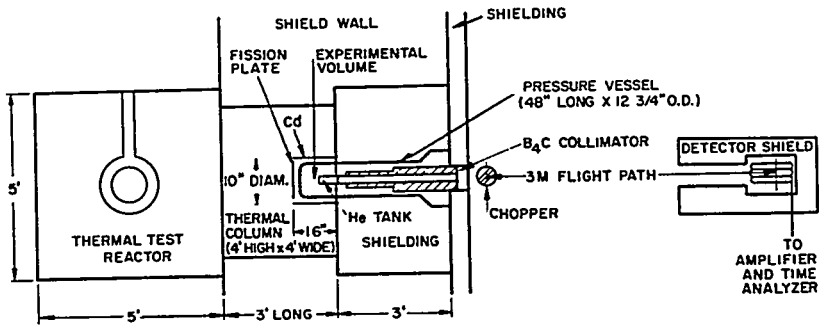

FIGURE 6.81. Experimental Arrangement.

were available to raise the temperature of the source region up to 600° F.

The multiplying medium or lattice consisted of an array of alternate planes of light water, zirconium, enriched uranium, and stainless steel. The fuel was 0.0013 in. thick and was clad with Zircaloy to enable operation of this subcritical assembly at elevated temperatures.

The composition of the multiplying medium could be changed by changing the fuel density or the metal-to-water volume ratio. In this manner, three different multiplying media were obtained. The compositions of the assemblies were chosen so that the spectral hardness index for the assemblies at room temperature was

$$\beta\gamma = \frac{\Sigma_a(0.025\ \text{ev})}{\xi\Sigma_s(1\ \text{ev})} = 0.27 \text{ to } 0.94.$$

Since the spectral hardness index is, in general, dependent upon the temperature of the system, at temperatures higher than ambient the expression $\beta\gamma = \frac{\Sigma_a(kT)}{\xi\Sigma_s(1\ \text{ev})}$ was used yielding slightly different values of $\beta\gamma$ at low and high temperatures for the same materials composition. Over the entire range in $\beta\gamma$ with $\Sigma_a >> DB^2$, the measured spectrum should well represent the spectrum in an infinite medium of this absorption with a small leakage correction.

The lateral surface of the cylindrical experimental volume was bounded by a 1 1/4-in. thick carbon steel pressure vessel

wall which was covered by a 2-in. layer of thermal lagging and cadmium sheet. Since the buckling would be difficult to calculate under the existing source and boundary conditions, activation experiments were conducted with manganese or fuel strips to measure the axial and radial flux traverses within the 16-in. long, 10-in. diameter subcritical region.

The results of these activations yielded the following information. The perturbation of the axial gradient by the re-entrant hole was found to be < 3 percent. In the case of a room temperature matrix, bare and cadmium-covered strip measurements of the activation distribution in both the radial and axial directions were obtained. The shapes of the thermal and epicadmium activation distributions in the central portion of the 10-in. diameter, 16-in. long experimental volume were found to be quite similar. By this is meant that if the thermal and epicadmium distributions were normalized at the center of the region, then the difference in the relative values was less than 6 percent at a distance of 2 to 3 mean free path lengths from the center. This indicated that the spectrum was a rapidly varying function of position only near the boundaries of a lattice. In the central portion of the experimental volume, the flux was found to be represented, to a good approximation, by the function

$$\phi(E, r, z) = \phi_o(E)\, e^{-\gamma z}\, J_o(\alpha r) \qquad \text{Eq. (6.99)}$$

where $J_0(\alpha r)$ is the Bessel function of argument αr. The buckling will then be given by $B^2 = \alpha^2 - \gamma^2$.

The measured values of α, γ, and B^2 with their estimated errors are shown in Table 6.47. The values of $D(E_o)B^2$ and $\Sigma_a(E_o)$ are also included for each medium where E_o is the neutron energy corresponding to the ambient moderator temperature. The values of α and γ were obtained from a least squares fit to the activation data for a distance of three thermal diffusion lengths about the source center. (Because of experimental difficulties, measurements were not obtained for Lattice III. The leakage effect on the spectrum was small and less than that for Lattices I and II. Since the flux gradient correction factors for Lattices I and II were nearly identical, the corrections for Lattice II were used for Lattice III. The estimated error involved in this procedure is much less than the experimental error.)

The magnitude of the measured buckling was used to determine the leakage correction DB^2, which was added to the absorption cross section in calculating the spectrum for the lattices other than the pure water cases. As a consequence of the bare and cadmium-covered activations in the lattice,

TABLE 6.47 — MEASURED VALUES OF α, γ, AND B^2

Medium	T (°K)	E_o (ev)	$\alpha(cm^{-1})$	$\gamma(cm^{-1})$	B^2 (cm^{-2})	$D(E_o)B^2$ (cm^{-1})	$\Sigma_a(E_o)$ (cm^{-1})
Water	298	0.0257	$i(0.172 \pm 0.020)$	0.166 ± 0.001	-0.057 ± 0.010	-0.0064	0.0220
Water	586	0.0505	0.112 ± 0.010	0.098 ± 0.001	0.003 ± 0.002	0.0007	0.0115
Lattice I	298	0.0257	0.093 ± 0.006	0.056 ± 0.001	0.0055 ± 0.0011	0.0011	0.193
Lattice I	586	0.0505	0.056 ± 0.004	0.036 ± 0.001	0.0018 ± 0.0014	0.0007	0.138
Lattice II	298	0.0257	0.107 ± 0.007	0.062 ± 0.002	0.0077 ± 0.0015	0.0010	0.406
Lattice II	586	0.0505	0.063 ± 0.005	0.053 ± 0.002	0.0011 ± 0.0007	0.0003	0.290
Lattice III	298	0.0257	--	--	--	0.001	0.448
Lattice III	586	0.0505	--	--	--	0.0005	0.320

where it was observed that the shape of the epicadmium and thermal distributions were nearly identical in the central region, it was assumed that no variation of B^2 occurred with energy. Thus, the energy variation of the DB^2 term was assumed to be due only to the variation of D with energy. The axial flux measurement was also used in relating the measured beam current to the flux in the source region.

In the case of pure water, Σ_a is not large compared to DB^2 for all energies of interest. Therefore, the calculated spectrum will be very sensitive to the variation of both Σ_a and DB^2 with energy. However, it was not possible to measure the variation of B^2 with energy. This was because the absorption of the detector foils, particularly when cadmium covered, was quite high relative to the absorption of the pure water. Since the foils caused a significant perturbation in the flux distributions in the water, the buckling as a function of energy could not be obtained. Thus, no leakage correction was applied to the absorption cross sections in calculating the spectrum in water, even though it was recognized that the calculations would be sensitive to this correction. The pure water results should be viewed in the light of this admittedly poor assumption and serve as an indication of the type of difficulty encountered in this type of measurement.

The compositions in terms of material atom densities (not self-shielded) for each of the media studied in the pressure vessel system are listed in Table 6.48. The spectral hardness index $\beta\gamma$, calculated using an estimated self-shielding factor, is also included in the last column of the table.

For the cases in which the experimental volume contained the poisoned water solutions or the polyethylene moderator, the experimental arrangement was modified somewhat. The pressure vessel was removed from the thermal column, and the source region was imbedded about 2 ft. inside the thermal column. The shape of the source region was changed to that of a cube, 1 ft. on edge, and was enclosed by a 100-mil thick zirconium box. A significant increase in source intensity was achieved in these cases by removing the fission plate as well as the cadmium sheets that had previously surrounded the experimental volume. For the poisoned water solutions the thermal column neutrons are absorbed near the surfaces of the experimental volume, and the thermal spectrum is quickly converted (because of the small diffusion length in the poisoned water region) to the infinite medium spectrum characteristic of the source region. Activation experiments indicate that the leakage effects on the spectrum are small. In addition, the flux gradient has been reduced by a factor of ~2, reducing the transport correction to the beam current by a factor of two.

TABLE 6.48 — PROPERTIES OF MEDIA STUDIED IN THE MEASUREMENT OF NEUTRON SPECTRA

		Number Density in Atoms/cm^3 x 10^{-20}						
Medium	Temp.	H	O	U^{235}	U^{238}	Fe	Zr	$\beta\gamma$
Water	78°F	669	335	--	--	--	--	0.016
Water	595°F	461	231	--	--	--	--	0.016
Lattice I	78°F	321	161	2.37	0.18	69.8	182	0.27
Lattice I	595°F	222	111	2.37	0.18	69.8	182	0.28
Lattice II	78°F	357	179	4.74	0.35	292	47.3	0.51
Lattice II	595°F	247	123	4.74	0.35	292	47.3	0.53
Lattice III	78°F	211	106	4.74	0.35	480	47.3	0.94
Lattice III	595°F	146	72.9	4.74	0.35	480	47.3	0.97

(This correction is discussed in Sect. 6.6.D.) The increase in intensity also allowed the re-entrant hole to be reduced to a 1/2-in. by 1-in. rectangular hole, reducing the possible perturbations caused by the hole on the spectrum.

The two poisoned water solutions contained fuel elements of the same Zircaloy clad fuel that was used in the pressure vessel experiments. The two poisons which were investigated were boron and erbium. The boron was used as $1/v$ poison which has most of its absorption in the thermal group, while erbium was used for an absorber which has resonances near the thermal energy region. The first solution studied was obtained by dissolving erbium nitrate, $Er(NO_3)_3 \cdot 5H_2O$, in water to a concentration of about 0.8 saturation. After the erbium solution measurement was completed, the solution was drained and the region refilled with a boron acid solution. Since the erbium nitrate solution was not completely removed, this residue appeared as a contaminant in the boron solution. Table 6.49 lists the self-shielded material atom densities for the two solution experiments.

Activation experiments were also performed with the erbium nitrate solution to obtain the spatial flux distribution. Since the absorber concentration was made approximately the same for the boron solution as for the erbium solution, these activations were not repeated for the boron case. The solution activations yielded the following results when a least squares fit to the data was made to the function

$$\phi(E,x,y,z) = \phi_o(E)\, e^{-\gamma Z}\,(1 - b^2x^2)(1 - b^2y^2) \qquad \text{Eq. (6.100)}$$

where

$$\gamma = 0.059 \text{ cm}^{-1}$$

$$b = i(0.081) \text{ cm}^{-1}$$

$$B^2 = 2b^2 - \gamma^2 = -0.0165 \text{ cm}^{-2}.$$

Comparing $D(E_o)B^2 \approx -0.002$ cm^{-1} to the absorption $\Sigma_a(E_o) \approx 0.25$ cm^{-1}, one sees that the leakage effects on the spectra are small (< 1 percent).

Measurements were also made on assemblies using polyethylene as moderator. In this case the spectrum source region was constructed of fuel elements that are used in the FPR (Flexible Plastic Reactor). This assembly was used previously in the pulsed neutron shutdown measurements

TABLE 6.49 — PROPERTIES OF MEDIA STUDIED IN THE MEASUREMENT OF NEUTRON SPECTRA

Medium	Number Density in Atoms/cm^3 x 10^{-20}								$\beta\gamma$
	H	O	N	Er	B^{10}	Zr	U^{238}	U^{235}	
Lattice VIII at 78°F	600	346	9.89	4.61	--	22.4	0.12	1.72	0.17
Lattice IX at 78°F	625	322	0.25	0.11	0.364	22.4	0.12	1.72	0.21

described in Sect. 6.6. The fuel element of the FPR is contained by 1-in. square aluminum tubes having a 0.025-in. thick wall. Within this hollow box layers of polyethylene, aluminum, 0.002-in. thick enriched uranium, and boron or erbium-coated Mylar tape are arranged as strips extending for the full length of the box. These elements were arranged so as to distribute the poison, fuel, and moderator in as homogeneous a manner as possible.

Table 6.50 contains the material atom densities of the four polyethylene moderator systems that were investigated. All measurements were made at room temperature (24° C). The last column in the table gives the spectral hardness index for each assembly obtained after these atom densities are corrected for self-shielding.

Measurements were made on the polyethylene matrices using both the pressure vessel and the zirconium box spectrum source experimental arrangement. For these polyethylene lattices, radial and axial activation measurements were again made within the experimental volume. For Lattices IV, V, and VI which were located within the pressure vessel, the parameters to be used in Eq. (6.99) are listed in Table 6.51. Lattice VII was not located within the pressure vessel but was used in the zirconium box described for the poisoned water solution experiments. For Lattice VII, the parameters for fitting the flux are to be used in Eq. (6.100). These parameters are also listed in Table 6.51. The leakage effects on the polyethylene spectra are 1 percent or less for every lattice. The spectrum in the central region represents the infinite medium spectrum rather closely, as was the case for each of the water-moderated media with multiplication present.

C. Details of the Chopper Design

Aside from the mechanical characteristics of a rotor, the three considerations that determine the design are the type of background likely to be encountered, the intensity, and the energy resolution desired. The latter two factors determine the shape and size of the slit and the rotor diameter, as well as the angular velocity of the rotor. In measuring the spectrum in a subcritical assembly, the beam will contain neutrons whose energies range up to fission neutron energies. With the rotor in the closed position, the high energy neutrons penetrating the rotor will contribute to the background that exists during the time-of-flight measurements. It is desirable that the rotor attenuate this high energy flux by a factor of at least 10^{-3} to 10^{-4}.

TABLE 6.50 — PROPERTIES OF MEDIA STUDIED IN THE MEASUREMENT OF NEUTRON SPECTRA

Polyethylene Medium	Number Density in Atoms/cm^3 x 10^{-20}								
	H	C	O	Al	U^{235}	U^{238}	Er	B^{10}	$\beta\gamma$
Lattice IV	342	171	--	204	5.43	0.207	--	0.207	0.65
Lattice V	417	208	--	166	0.633	0.043	--	--	0.068
Lattice VI	300	150	--	247	2.02	0.135	--	0.141	0.30
Lattice VII	376	208	14.8	173	4.55	0.326	1.70	--	0.46

TABLE 6.51 — POLYETHYLENE SOURCE REGION PARAMETERS

Medium	γ (cm^{-1})	α (cm^{-1})	b (cm^{-1})	B^2(cm^{-2})	$D(E_o)B^2$ (cm^{-1})	$\Sigma_a(E_o)$ (cm^{-1})
Lattice IV	0.051 ± 0.002	0.074 ± 0.005	--	0.0029 ± 0.0008	0.0005	0.47
Lattice V	0.059 ± 0.002	~ 0	--	-0.0035 ± 0.0002	-0.0005	0.061
Lattice VI	0.054 ± 0.002	~ 0	--	-0.0029 ± 0.0002	-0.0006	0.19
Lattice VII	0.021 ± 0.001	--	0.036 ± 0.006	0.0022 ± 0.0013	0.0004	0.37

To determine the proper materials for the construction of a chopper, the transmission of various materials has been measured. Figure 6.82 is a plot of the ratio of sample-in to sample-out beam counts as a function of sample thickness. Most of the low energy part of the spectrum is removed from the beam by the first inch or so of material. This is shown by the nearly constant slope of all curves for the first inch. The design problem thus becomes one of picking a material with a high removal cross section for neutrons with energies above 0.1 ev. For this reason, the transmission measurements shown in Fig. 6.82 were made using a source region which had a $\beta\gamma$ of about 4.8. These experiments were performed over the integrated spectrum with a $1/v$ detector.

As expected, the hydrogenous materials are more effective for neutron removal than the pure metals. The hydrogen density in the phenolic resin is not as great as that of polyethylene, but its mechanical properties are superior in maintaining the slit width dimensions at a given angular velocity. In a hydrogenous material, high energy neutrons that are slowed down in the rotor and emitted in the direction of the counter would increase the neutron background. Since the rotor is not a solid cylinder, these moderated neutrons may yield a time-dependent background which would have to be determined in order to interpret the measurements properly. This effect may be minimized by using a borated hydrogenous material. From Fig. 6.82 it may be seen that the transmission of both borated polyethylene and borated phenolic is slightly lower than that of the pure materials. This, however, does not assure that the time-dependent background has been removed. If the rotor construction is symmetric about a plane passed through the center of its plate stack, the time-dependent background as a result of transmission through the shutter will also be symmetric about flight time equal to zero. One can obtain, therefore, signal counting rates corrected for background by reflecting the data about the time when the burst occurs and subtracting.

The first rotor that was constructed for the measurement of the pressure vessel spectra consisted of a 2-in. high stack of 6-in. square by 1/16-in. thick phenolic plates separated by 2S aluminum window frames of the same size and thickness. The phenolic resin contained uniformly distributed enriched B^{10} (2 percent by weight). The mechanical construction of the partially assembled rotor is shown in Fig. 6.83, while Fig. 6.84 shows the aluminum window frames which were designed to give a constant aluminum thickness in the beam even for off-axis slits. The neutron beam direction is indicated by the arrow and is parallel to the plane of the aluminum when the

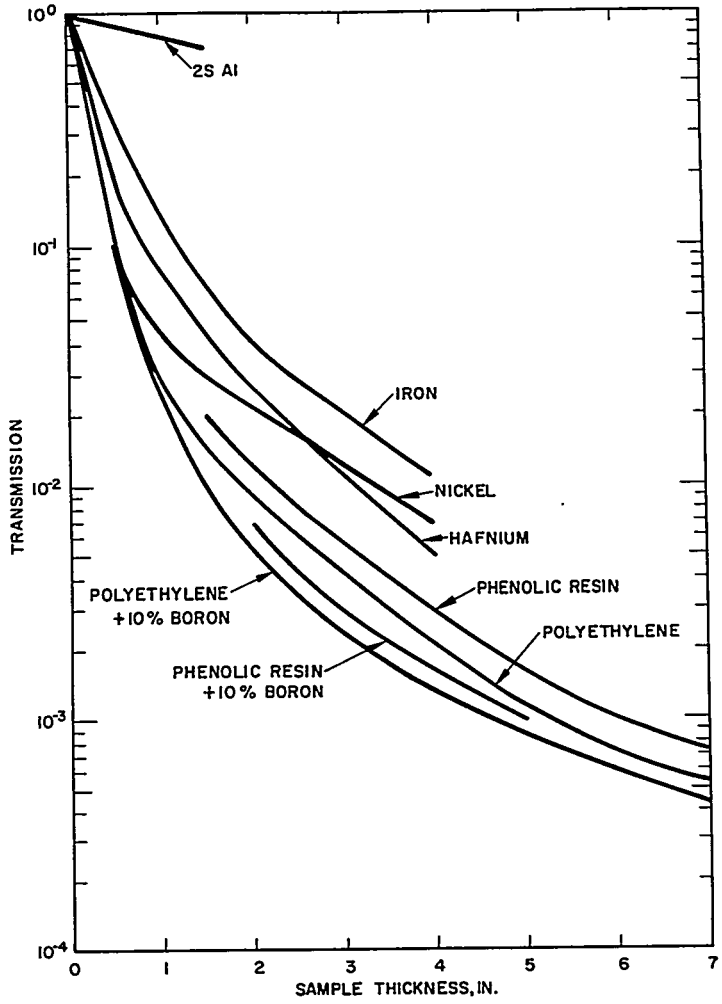

FIGURE 6.82. Transmission of Rotor Materials.

rotor is in the open position. End caps of 2-in. thickness were placed on each side of this stack and the whole assembly was turned down to a 6-in. diameter cylinder as shown in Fig. 6.85. This phenolic cylinder was shrunk-fit into a 40-mil stainless steel shell that is supported by a hub assembly. The rotor is driven by a synchronous motor through a series of timing belts which provide for a speed range of 540 to 15,000 revolutions per minute.

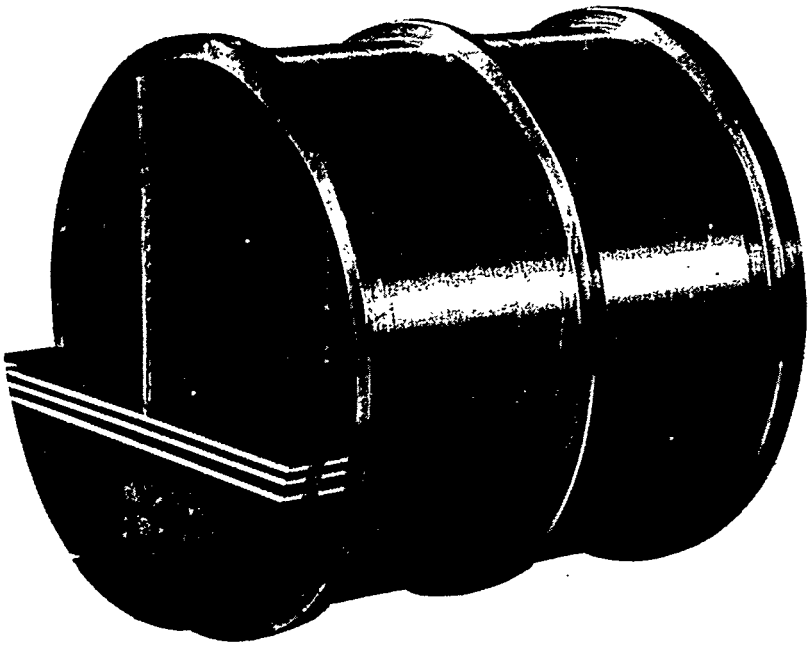

FIGURE 6.83. Partially Assembled Rotor.

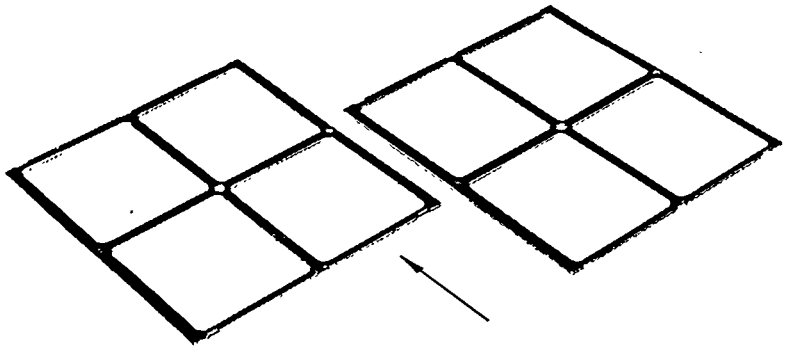

FIGURE 6.84. Aluminum Window Frames.

For a 6-in. diameter rotor and a 1/16-in. slit width, the overlap distance* for the rotor is 11.5 meters. At the highest angular velocity, the shutter would yield a burst of 13 μsec .

*The overlap distance is defined as the maximum distance of the flight path before the fast neutrons (up to 10 Mev) of a burst overtake the slow neutrons of the preceding burst. The lowest energy slow neutrons that will pass through the rotor are determined by their transit time through the rotor.

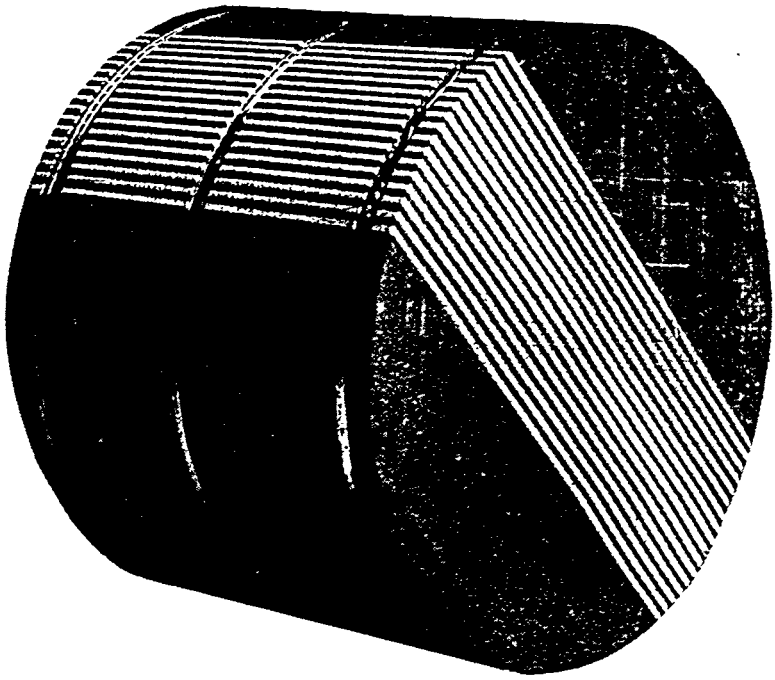

FIGURE 6.85. Stacked Plate Rotor Assembly.

Under these conditions, the shutter resolution $(\Delta E/E)$ is approximately 5 percent at 2 ev. Since this high resolution was not needed in the measurement of the pressure vessel spectra, the flight path was shortened to 3 meters and the angular velocity decreased to give a resolution of 100 percent at 2 ev and about 10 percent at 0.025 ev in the actual experiment. This was necessary to give reasonable counting rates.

With this type of chopper which utilizes straight slits on the centerline of the rotor, two neutron bursts per revolution are obtained. Because of an anisotropy in the rotor construction, the spectra measured from the two bursts were different. This anisotropy was discovered several years after the rotor construction and was due to a slight twisting of the phenolic and aluminum plates. The difference in rotor transmission was measurable only for neutron energies below 0.02 ev, and it increased with increased rotor angular velocity. For the measurements of the pressure vessel spectra, the effect on the measurement was less than other uncertainties in the experiment.

For the poison solution spectra, a second rotor was designed and constructed. This rotor was designed in such a way as to

position the neutron slits in an accurate and reliable fashion. The design of this rotor is shown in Fig. 6.86. It consists of two aluminum hubs held together by two dural 2-in. pins. Slots are cut in these hubs to fit exactly rectangular pieces of phenolic resin which are used to position the neutron slits. The rest of the center section between the two hubs is filled with polyethylene, and this section is enclosed by a 1/8-in. band of stainless steel. As the slit width is 25 percent larger for this chopper than for the previous one, $\Delta E/E$ for a given angular velocity and flight-path length is 25 percent larger. Further, a higher resolution is now desired, so that the effect of the erbium resonances on the spectrum may be seen. For these reasons, the flight path was increased to 6 meters and the angular velocity increased to give a resolution of about 10 percent at 0.5 ev for the fuel-lattice poison-solution measurements. To maintain a reasonable counting rate, the source region was moved closer to the reactor core, and the flight path and collimator were enclosed and evacuated.

The detector consisted of an array of proportional counters. These counters (2-in. diameter) were filled with $B^{10}F_3$ to one atmosphere. The active length of the counters was 7 in., and they were aligned with their axes parallel to the beam direction. The ends of the counters were made of aluminum oxide ceramic, the measured transmission of which was nearly energy-independent over the range of interest. The counter

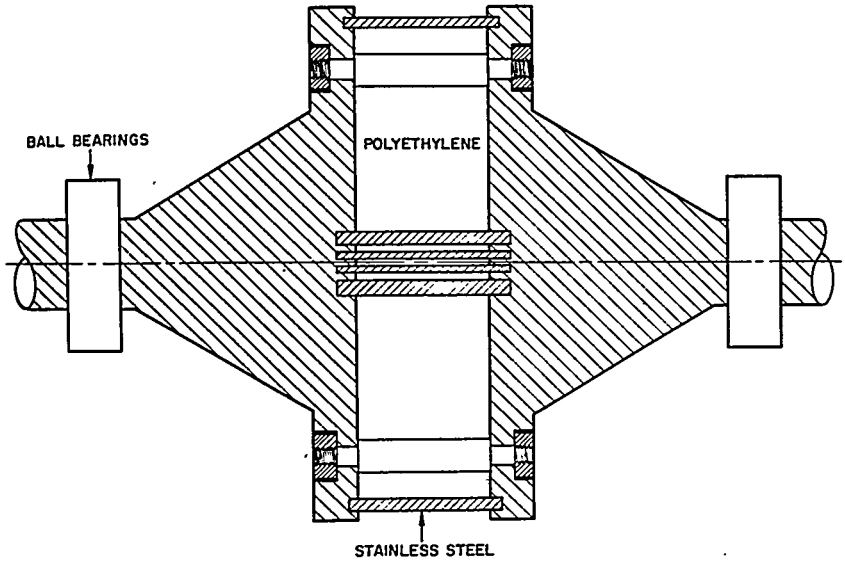

FIGURE 6.86. Clamped Plate Rotor Assembly.

assembly was housed in a large beam catcher, the walls of which were composed of 6-in. thick borated paraffin.

The output pulses from the counter were amplified and recorded as to time of arrival in a 256-channel time analyzer.[88] The time analyzer was turned on by a light pulse projected onto a mirror rotating with the chopper and reflected back into a photo-multiplier tube. The angular difference between this light trigger and the neutron burst was measured to give the time delay between the turning on of the analyzer and the time zero of the neutron burst.

The data stored in each of the 256 channels are printed out on punched cards and form part of an input deck for a computer. The computer has been programmed to reduce the data and yields as an output the flux per electron volt as a function of energy. This program corrects for background, energy-dependent system transmission, and system resolution.

D. Experimental Corrections

Since several energy-dependent corrections must be applied to the experimental data, they will be considered here for completeness, although some have been discussed in the literature.[86]

The experimental data corrected for background can be considered to be a function of the flight time, t, of the form $C(t)$. The time of flight, t, uniquely specifies the neutron energy, E, through the relation

$$E = mL^2/2t^2 \qquad \text{Eq. (6.101)}$$

where E is the neutron energy, m its mass, L the flight-path length, and t the flight time. Thus, the function $C(t)$ specifies the related function $C(E)$ uniquely. However, the change of metric from unit time to unit energy implies that

$$C(E) = C(t)\frac{dt}{dE} \qquad \text{Eq. (6.102)}$$

or

$$C(E) = C(t)\left[\frac{-t^3}{mL^2}\right] \approx t^3 C(t). \qquad \text{Eq. (6.103)}$$

That is, the count per unit energy is proportional to the count per unit flight time times the neutron flight time cubed.

1. *Beam Attenuation*

A correction to the experimental data must be made for the attenuation effect of the materials in the beam. If the neutron beam current density in the region of the source is $J_s(E)$ and the observed neutron beam current density at the detector is $J_d(E)$, these two current densities will be related by the removal cross section of the materials in the beam. That is,

$$J_s(E) = J_d(E)\, e^{[\Sigma_{t1}(E)\, X_1 + \Sigma_{t2}(E)\, X_2 + \dots]} \qquad \text{Eq. (6.104)}$$

where $\Sigma_{ti}(E)$ is the total cross section of the i^{th} material in the beam and X_i is the corresponding thickness.

2. *Shutter Transmission*

The transmission of a rotating flat-plate neutron shutter is a function of neutron energy. This energy dependence is discussed in detail in the literature.[86] If one defines the quantity $\beta = v_{co}/v$ as being equal to the ratio of the shutter cutoff neutron velocity to the neutron velocity under consideration, then the relative shutter transmission is given by

$$\tau(\beta) = 1 - \frac{8}{3}\beta^2 \;; \quad 0 \le \beta \le 1/4 \qquad \text{Eq. (6.105)}$$

$$\tau(\beta) = \frac{8}{3}\beta^2 - 8\beta + \frac{16}{3}\sqrt{\beta} \;; \quad 1/4 \le \beta \le 1\,. \qquad \text{Eq. (6.106)}$$

The adequacy of Eqs. (6.105) and (6.106) can be determined by measurements of a typical spectrum carried out at several rotor speeds. On the other hand, by providing a monoenergetic source of neutrons the transmission can be measured directly for that particular energy.[89] The transmission curve can then be obtained experimentally by performing similar measurements at several incident neutron energies.

3. *Counter Efficiency and Effective Flight-Path Length*

Two additional corrections must be made to the observed data for the variation with energy of counter efficiency and mean stopping position within the counter.

The counter efficiency as a function of energy is given by

$$\epsilon(E) = 1 - e^{-\Sigma_a(E)\ell} \qquad \text{Eq. (6.107)}$$

where $\Sigma_a(E)$ is the macroscopic absorption cross section of the counter filling gas and ℓ the length of the counter.

The mean stopping position of a neutron of energy E as measured from the front of the counter is given by

$$\bar{\lambda}(E) = \frac{\int_o^\ell \lambda \Sigma_a(E)\, e^{-\Sigma_a(E)\lambda} d\lambda}{\int_o^\ell \Sigma_a(E)\, e^{-\Sigma_a(E)\lambda} d\lambda} . \qquad \text{Eq. (6.108)}$$

The effective flight-path length is then given by

$$L(E) = L' + \bar{\lambda}(E) \qquad \text{Eq. (6.109)}$$

where L' is the flight path from the center of the chopper to the front of the active counting volume.

4. Flux-Gradient Correction

Since it is the spectrum of the neutron-beam current rather than the spectrum of the neutron flux at the origin of the beam that is measured, an additional correction must be made. The energy dependence of the flux and the beam current are related in the diffusion theory approximation by the following relationship.

$$J_+(E) = \Phi_o(E) - \lambda_T(E) \frac{d\Phi}{dz}\bigg|_{z=o} . \qquad \text{Eq. (6.110)}$$

The transport mean free path, $\lambda_T(E)$, in the medium can be obtained from a knowledge of the material cross sections in the assembly, and the flux gradients in the beam direction can be obtained from the activation experiments. One can then calculate an energy-dependent correction term to the observed current spectrum of the following form:

$$\Phi_o(E) = \frac{J_+(E)}{1 - \lambda_T(E) \frac{d}{dz} \ln \Phi(E) \Big|_{z=o}} . \qquad \text{Eq. (6.111)}$$

Since this correction in itself is small, the use of diffusion theory to approximate the flux gradient correction is considered adequate.

5. Resolution Corrections

A detailed discussion of the resolution of neutron time-of-flight spectrometers is given in the literature[86] where it was

assumed that the time-of-flight spectrum of the beam was slowly varying over the instrumental time resolution range. Frost[90] has shown that an additional correction should be made for the effect of finite resolution in the range where the slowly varying condition does not apply. If one defines the input time-of-flight spectra to the spectrometer as $I(t)$, the observed spectra as $O(t)$, and the spectrometer resolution function as $R(t)$, then

$$O(t) \int_{-\infty}^{\infty} R(\lambda) I(t+\lambda) d\lambda . \qquad \text{Eq. (6.112)}$$

If $I(t)$ is a continuous function with continuous derivatives, it can then be expanded in terms of a Taylor's expansion:

$$O(t) = \int_{-\infty}^{\infty} R(\lambda) \sum_{n=o}^{\infty} \frac{\lambda^n}{n!} \frac{d^n I(t)}{dt^n} d\lambda . \qquad \text{Eq. (6.113)}$$

If the series is uniformly convergent, then

$$O(t) = \sum_{-\infty}^{\infty} \frac{1}{n!} \frac{d^n I(t)}{dt^n} \int_{-\infty}^{\infty} \lambda^n R(\lambda) d\lambda . \qquad \text{Eq. (6.114)}$$

The function $R(\lambda)$ can be shown to be even in its argument, and the integral of the function can be normalized to unity. Under these conditions, one may rewrite, neglecting fifth and higher order derivatives,

$$O(t) = I(t) + \frac{1}{2} \frac{d^2 I(t)}{dt^2} \int_{-\infty}^{\infty} \lambda^2 R(\lambda) d\lambda + \frac{1}{24} \frac{d^4 I(t)}{dt^4} \int_{-\infty}^{\infty} \lambda^4 R(\lambda) d\lambda . \qquad \text{Eq. (6.115)}$$

By differentiating with respect to time, and again neglecting fifth and higher order derivatives, one obtains

$$\frac{d^2 O(t)}{dt^2} = \frac{d^2 I(t)}{dt^2} + \frac{1}{2} \frac{d^4 I(t)}{dt^4} \int_{-\infty}^{\infty} \lambda^2 R(\lambda) d\lambda \qquad \text{Eq. (6.116)}$$

and

$$\frac{d^4 O(t)}{dt^4} = \frac{d^4 I(t)}{dt^4} . \qquad \text{Eq. (6.117)}$$

By substituting these two results in Eq. (6.113) and by rearranging terms, one obtains

$$I(t) = O(t)\left[1 - \frac{1}{2O(t)}\frac{d^2O(t)}{dt^2}\int_{-\infty}^{\infty}\lambda^2 R(\lambda)d\lambda + \left\{\frac{1}{4}\left(\int_{-\infty}^{\infty}\lambda^2 R(\lambda)d\lambda\right)^2 - \frac{1}{4!}\int_{-\infty}^{\infty}\lambda^4 R(\lambda)d\lambda\right\}\frac{d^4O(t)}{O(t)dt^4}\right]. \quad \text{Eq. (6.118)}$$

The even moments of the resolution function can be obtained from the analytic expression derived in Ref. 86. The output function and its derivatives can be obtained directly from the experimental data. Therefore, a numerical correction can be calculated with Eq. (6.118) that will correct for variation of the input spectrum over the range of the resolution function. In the case of the pure water spectra where the counting rate increases sharply between the dE/E region and the thermal region of the spectrum, the resolution correction was as large as 20 percent. In Lattices VII, VIII, and IX this correction was not applied, since it did not change the shape of the spectra.

E. Comparison of Calculated and Measured Spectra

1. Spectra Calculations

Two methods exist for the calculation of the steady-state spectrum in a finite fuel-hydrogenous medium. The essential difference is in the energy exchange kernel used for the hydrogen atom.

The first method is that of Wigner and Wilkins[91] who calculated the steady-state spectrum in a partially absorbing infinite homogeneous medium with a monatomic gaseous moderator, the scattering nuclei of which have a Maxwellian energy distribution. The scattering nuclei were assumed to have a constant scattering cross section and a mass equal to that of the neutron, while the absorption cross section was assumed to vary as $1/v$. The effects of molecular binding and intermolecular forces were not considered. This calculation has been extended by Amster,[4] so that the neutron spectrum can be calculated for a finite homogeneous medium with the absorption cross section varying arbitrarily as a function of neutron energy. The transition from an infinite medium to a finite medium is made by adding the leakage term DB^2 to the absorption cross section to obtain an effective absorption cross section for the medium. These calculations have been

applied to water- or polyethylene-moderated assemblies. However, hydrogen in water or polyethylene does not completely fulfill the assumptions made on the scatterer in the calculations.

The second calculational procedure uses a differential neutron scattering cross section which is obtained from considerations of the intermolecular and molecular binding effects. For the case of slow neutron scattering by water, Nelkin[92] computed a differential scattering cross section, taking into account vibrations, hindered rotations, and translations of the H_2O molecule. Beyster, et al.,[84] have used Nelkin's differential cross section to calculate several spectra to compare with their measured spectra. Goldman and Federighi[93] have computed a bound scattering kernel to be used for the case of a polyethylene moderator.

In the present investigation, the bound spectrum was calculated with the SWAK code for each water medium using the Nelkin kernel and by using the Goldman kernel for each polyethylene-moderated medium. For the sake of comparison, each free atom spectrum was also calculated using the SWAK code with the mass 1 free atom kernel.

In each case, a finite medium spectrum was obtained by making a leakage correction, $D(E)B^2$, to the absorption cross section, $\Sigma_a(E)$. This leakage correction was less than 1 percent for every assembly. For the case of polyethylene, the Esch prescription[29] was used to compute the diffusion length in making the leakage correction. For the water-moderated cases, the diffusion length was computed from the Radkowsky prescription.[6]

The spectra calculations treat only an equivalent homogeneous assembly with the same average composition as the heterogeneous experimental assembly. The approximation is good over most of the energy range above 0.2 ev. Below this energy, self-shielding effects would tend to reduce the effective homogeneous Σ_a value obtained from the material composition. In Lattices V, VII, VIII, and IX a self-shielding factor was calculated from a high-order one-dimensional, one-group, transport approximation using the TRANVAR code,[26] which computes the average flux in the fuel and in the moderator regions. In the other assemblies, the mean value of Σ_a for the fuel was determined by evaluating Σ_a at the most probable energy of the system. The self-shielding factor for this value of Σ_a was then determined by using Bohl's result for a repeating slab array.[94] This self-shielding factor was then applied throughout the thermal range in the calculations. This procedure could produce errors in the calculated spectra, since a single self-shielding factor over the entire energy range of interest is not correct. A better treatment of the self-shielding effect

could be accomplished by changing the effective absorption cross sections as a function of energy. However, this was not done in the results discussed in this section. Table 6.52 lists all of the self-shielding factors that were calculated and used in the spectrum calculations.

TABLE 6.52 — SELF-SHIELDING FACTORS

Lattice	Temp. (°K)	Fuel	Boron Strip
I	298	0.90	--
I	586	0.94	--
II	298	0.92	--
II	586	0.95	--
III	298	0.93	--
III	586	0.95	--
IV	298	0.95	0.70
V	298	0.77	--
VI	298	0.90	0.80
VII	298	0.93	--
VIII	298	0.91	--
IX	298	0.91	--

2. Measured Results

Figures 6.87 thru 6.100 present the results of the experimental measurements of the thermal neutron spectra. In addition to the experimental results shown on these figures, the calculated values are also presented for both the free atom calculation of the Wigner-Wilkins method or the bound atom calculation of the Nelkin model (for water) or the Goldman model (for polyethylene). These calculations were performed for energies below 1.0 ev. For energies greater than 1.0 ev, a dE/E spectrum was assumed in the calculations. The small crosses are the measured values of the flux, with the vertical extent of the cross indicating the probable error in the relative flux as determined from the counting statistics for each channel. The measured and calculated spectra were normalized

to give the same slowing-down flux by fitting the experimental data to a dE/E spectrum above 1 ev in each case.

The two neutron spectra obtained from a pure water medium at 298°K and at 586°K in the pressure vessel experiments are shown in Figs. 6.87 and 6.88. As seen in Table 6.47, for pure water Σ_a is not large compared to DB^2 over the entire energy

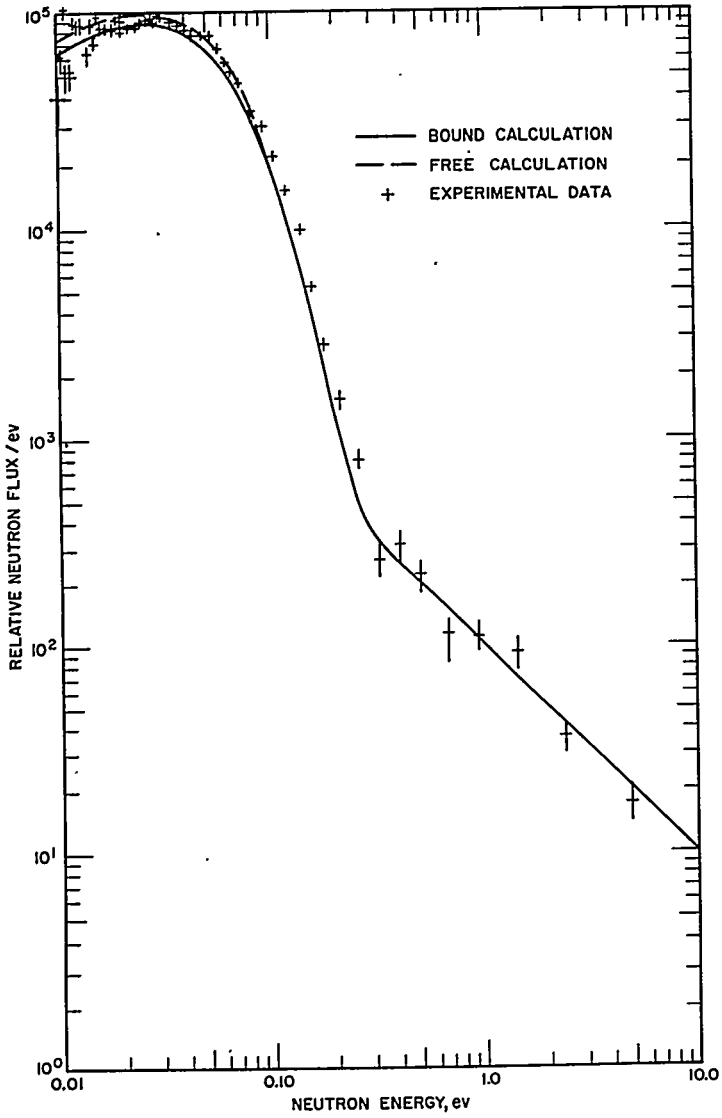

FIGURE 6.87. Neutron Spectra in Water at 298°K. (The calculations have assumed that $B_T^2 = 0$.)

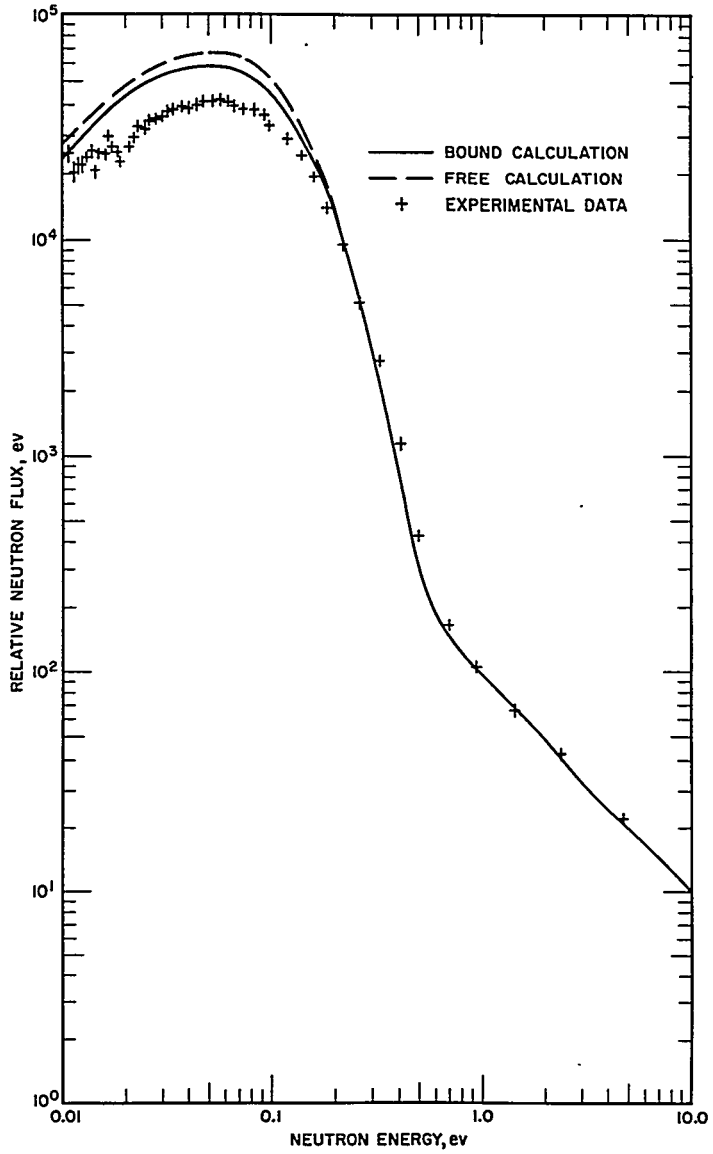

FIGURE 6.88. Neutron Spectra in Water at 586°K. (The calculations have assumed that $B_T^2 = 0$.)

range of interest. The calculated spectrum will then be very sensitive to $B^2(E)$ as well as $D(E)$. For the particular pure water spectrum source used, it is quite likely that the fast leakage is different from the thermal leakage. Since the measurement of $B^2(E)$ could not be made, the leakage correction to Σ_a was not

made in the pure water spectra calculations. The agreement between the measurement and the free calculation is fortuitous at room temperature, since the DB^2 term is negative and is about 30 percent of Σ_a at an energy of 0.0257 ev, whereas the flux leakage into the source region at 1 ev as measured by cadmium-covered foils is only about 2.5 percent of the slowing-down flux at an energy of 1 ev. For the hot water, the DB^2 term is positive and is only about 6 percent of Σ_a at 0.0505 ev. The high temperature epicadmium buckling was not measured, but one would estimate that the leakage at 1 ev compared to the slowing down would not change as much with temperature as did the thermal leakage to thermal absorption ratio. If this were the case, then the measured spectrum would be expected to be harder (ratio of thermal to slowing-down flux is smaller) than the calculated infinite medium spectrum for the higher temperature case.

The results of the measurements on water-moderated multiplying media at room temperature are shown in Figs. 6.89, 6.90, and 6.91. As seen from Fig. 6.89, in a water-moderated medium with a spectral hardness index $\beta\gamma = 0.26$, the bound spectrum calculation agrees better with the measured spectrum

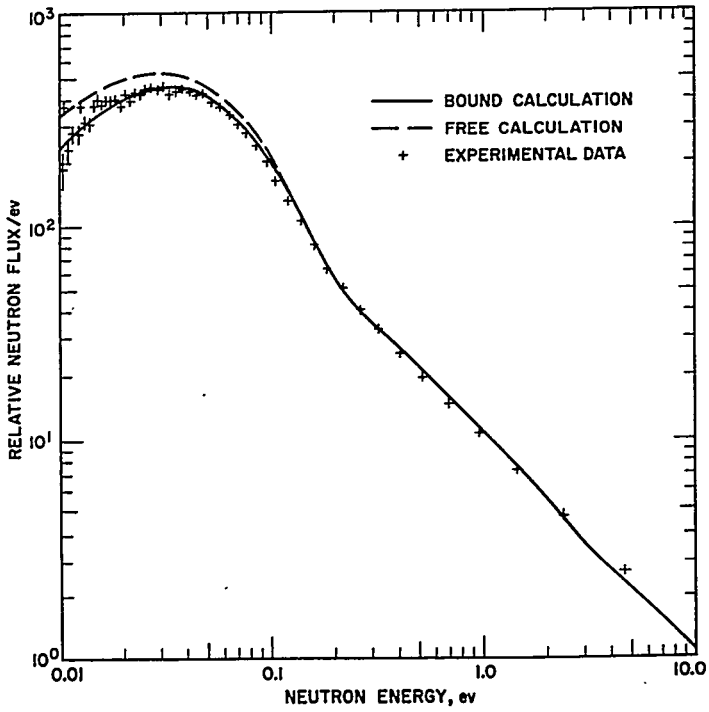

FIGURE 6.89. Water-Moderated Lattice I at 298°K for $\beta\gamma = 0.26$.

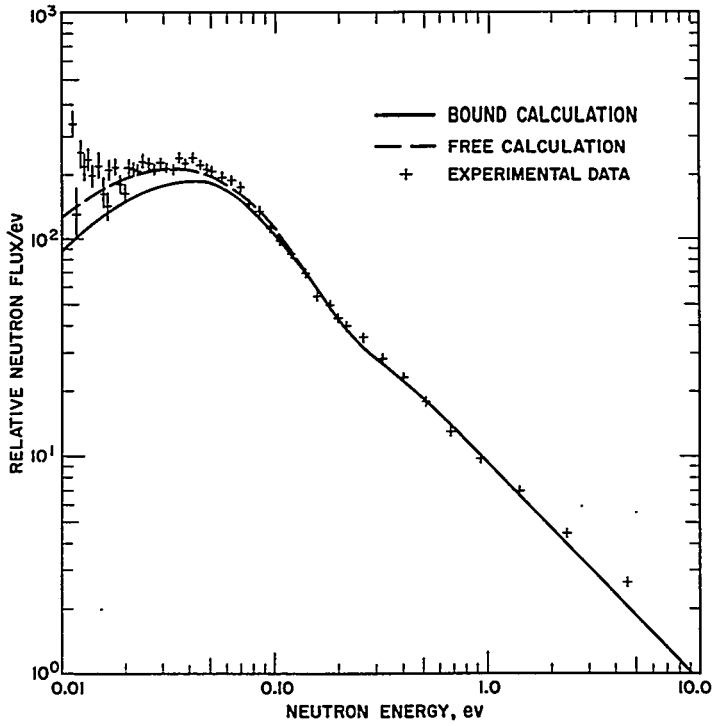

FIGURE 6.90. Water-Moderated Lattice II at 298°K for $\beta\gamma = 0.50$.

than does the free atom calculation. This result was also found by Beyster, et al.,[84] to be true for $1/v$ poison solutions with spectral hardness indices in the range $0.02 \lesssim \beta\gamma \lesssim 0.3$ and for the enriched fuel multiplying medium with a hardness index $\beta\gamma \simeq 0.12$. However, when the hardness index is increased ($\beta\gamma \simeq 0.5$ and 0.93), the free atom calculated spectra fit the present data better. No other experimental data are available at the present time in this spectral hardness range with which to make a comparison.

Calculated spectra were obtained also in which the self-shielding factor was taken as unity. These results are not shown in any of the figures, but the effect on the spectra is given approximately by decreasing the hardened thermal peak relative to the slowing-down flux by a factor equal to the self-shielding factor. It is interesting to note that the difference between the free atom and bound spectra calculations for a medium with a $1/v$ absorber shows a discrepancy of the order of the self-shielding factor in this hardened thermal energy range. The best spectrum calculation would be one which takes into account the change in the self-shielding as a function

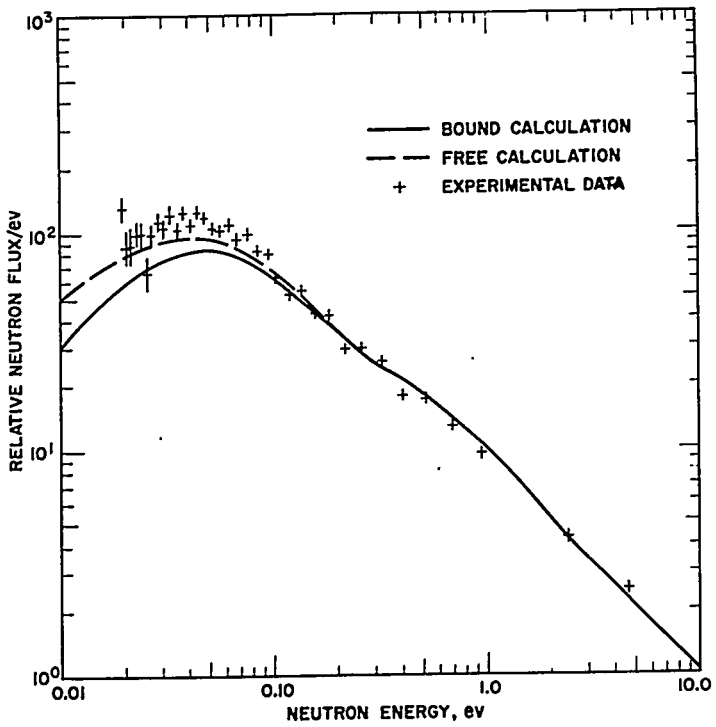

FIGURE 6.91. Water-Moderated Lattice III at 298°K for $\beta\gamma = 0.93$.

of energy as well as the chemical binding effects of the moderator.

To observe any large changes in spectrum with moderator temperature, the medium in the pressure vessel was heated up to a temperature of 586°K. The measured results are similar to those obtained at room temperature. For low $\beta\gamma \simeq 0.28$, the bound calculation agrees with the measured spectra as seen in Fig. 6.92, while the higher $\beta\gamma$ spectra are fitted better with the free atom calculations as shown in Figs. 6.93 and 6.94. There appears to be some tendency for disagreement at high $\beta\gamma$ values at both high and low temperatures.

The two poison solution results are shown in Figs. 6.95 and 6.96. In both of these cases the measurements lie between the bound and free atom calculations, with a slightly better agreement with the bound calculation. However, the $\beta\gamma$ for both assemblies is small ($\lesssim 0.2$) and the difference between the two calculations is small. The erbium result indicates what one might expect for a spectrum using a fuel with a large resonance such as plutonium.

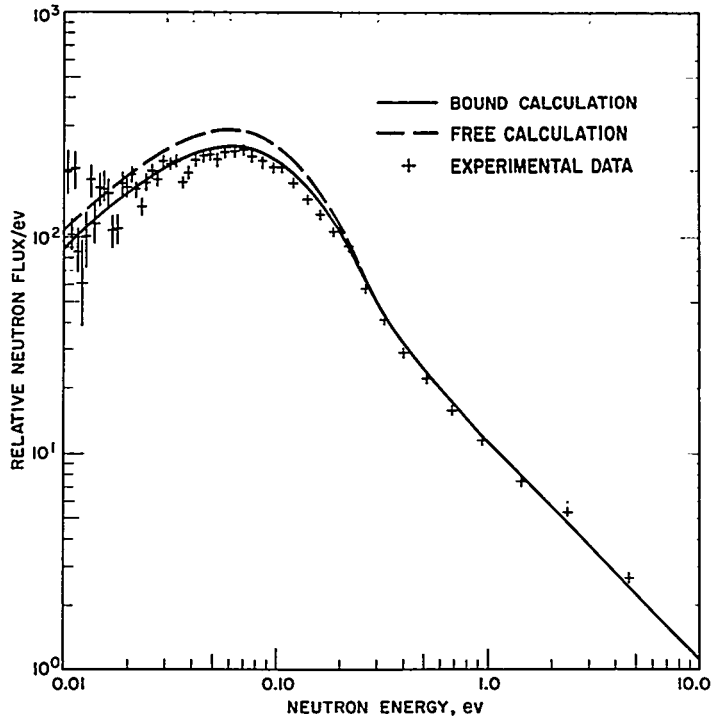

FIGURE 6.92. Water-Moderated Lattice I at 586°K for $\beta\gamma = 0.28$.

The spectra obtained for the polyethylene-moderated media are shown in Figs. 6.97 to 6.100 and indicate a consistent agreement between the bound calculations and the measurements over the spectral hardness range $0.06 \lesssim \beta\gamma \leq 0.65$. The poisoned polyethylene measurements of Beyster have also indicated this agreement with the bound calculations up to a spectral hardness of $\beta\gamma \approx 0.5$. No other polyethylene spectrum measurements are available for comparison, particularly in a multiplying medium. For a given ratio of thermal absorption to slowing-down power in a medium, it is interesting to note that the spectrum in a polyethylene medium is considerably harder than that in a water medium. These results obtained for the polyethylene-moderated media do indicate, however, a consistent deviation from the free atom calculation. Further experimental work, particularly with regard to comparing the experimental results for the chopper and the pulsed-beam type of spectrum measurements, seems to be desirable.

It is possible to obtain a quantitative comparison between measured and calculated spectra by calculating various energy moments of the two spectra. The energy moment which is used most frequently for this comparison is that which can be

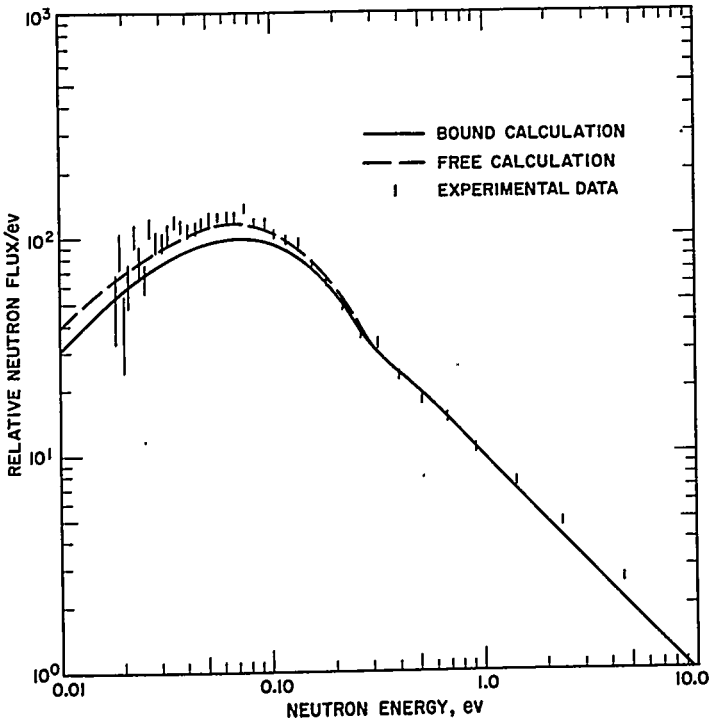

FIGURE 6.93. Water-Moderated Lattice II at 586°K for $\beta\gamma = 0.53$.

related to a $1/v$ absorber. In this case, the average of a $1/v$ cross section over the spectrum is calculated using

$$\left(\frac{\bar{\sigma}}{\sigma_o}\right) = \frac{E_o^{1/2} \int_{E_1}^{E_2} E^{-1/2}\, \Phi(E)dE}{\int_{E_1}^{E_2} \Phi(E)dE}$$

where σ_o is the thermal cross section at energy E_o. For the cases discussed here the energy range of the comparison corresponded to the energy limits of the measurement and calculation, namely, $E_1 = 0.020$ to $E_2 = 1.00$ ev. Table 6.53 lists these results for all of the assemblies for which $(\bar{\sigma}/\sigma_o)$ was calculated as well as the estimated errors of this ratio for some of the measurements made in the pressure vessel. The error in the ratio using the measured spectrum is based on counting statistics, the error in the energy calibration, and the error

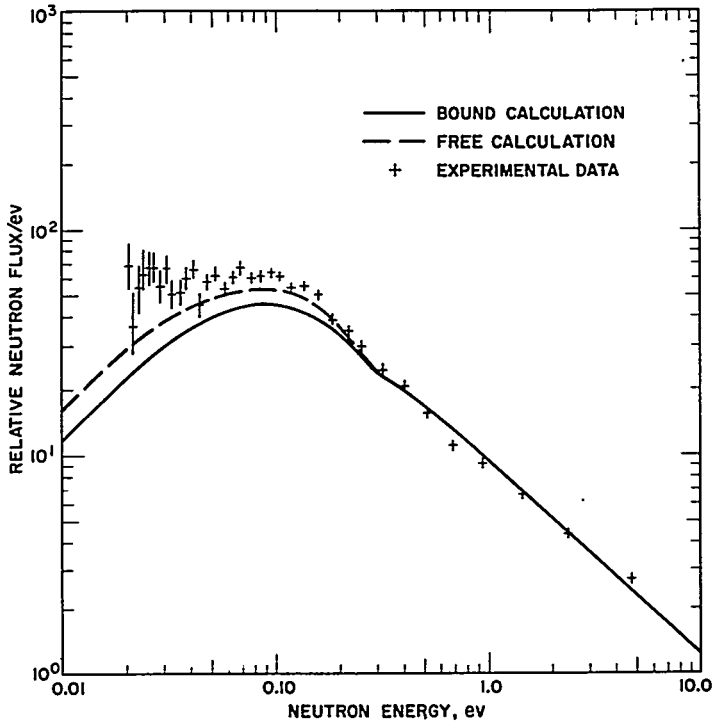

FIGURE 6.94. Water-Moderated Lattice III at 586°K for $\beta\gamma = 0.97$.

in the transmission correction for materials in the beam. The error in the ratio using the calculated spectrum is based on the uncertainties in the composition cross sections and on the errors in the measured temperatures of the media. Figure 6.101 is a plot of the data listed in Table 6.53.

The results given in Table 6.53 lead to the same observations that were made in examining the spectra presented in the figures. For both 78°F and 595°F in the water-moderated lattices, the measured spectra average cross sections agree with the bound atom calculation for low $\beta\gamma$ and with the free atom calculation for large $\beta\gamma$. For polyethylene there is agreement with the bound calculation for all the measured values of $\beta\gamma$.

F. Conclusions

The slow chopper technique for studying neutron spectra in subcritical assemblies has been developed. The multiplying medium results obtained with this technique are in general agreement, particularly at low $\beta\gamma$, with the results obtained with poisoned systems using the Poole pulsed-beam technique.

TABLE 6.53 — AVERAGE 1/v CROSS SECTIONS

Lattice	Temp. (°F)	$\beta\gamma$	$\left(\frac{\bar{\sigma}}{\sigma_o}\right)$ Exp	$\left(\frac{\bar{\sigma}}{\sigma_o}\right)$ Cal Free Atom	$\left(\frac{\bar{\sigma}}{\sigma_o}\right)$ Cal Bound
Water-Moderated					
I	78	0.26	0.518 ± 0.004	0.540 ± 0.008	0.514
I	595	0.28	0.438 ± 0.006	0.455 ± 0.006	0.440
II	78	0.50	0.463 ± 0.002	0.469 ± 0.008	0.455
II	595	0.53	0.399 ± 0.003	0.407 ± 0.006	0.380
III	78	0.93	0.409	0.401	0.388
III	595	0.97	0.365	0.353	0.341
Poisoned Water					
VIII	78	0.175	0.57	0.588	0.57
IX	78	0.215	0.55	0.56	0.55
Polyethylene-Moderated					
IV	78	0.65	0.403	0.44	0.41
V	78	0.068	0.623	0.658	0.63
VI	78	0.30	0.46	0.518	0.481
VII	78	0.46	0.45	0.484	0.448

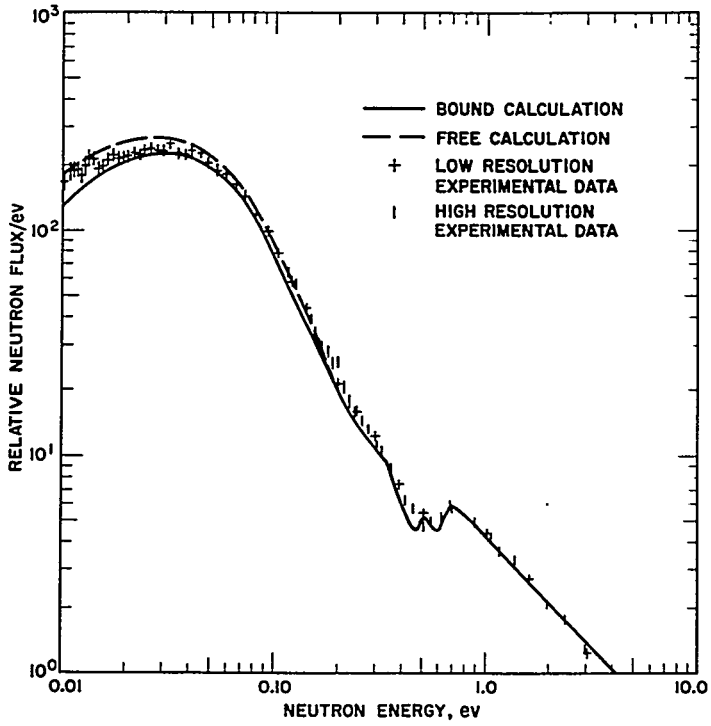

FIGURE 6.95. Poisoned Water Lattice VIII (Erbium Solution) for $\beta\gamma = 0.175$.

The polyethylene measurements are in excellent agreement with the Goldman polyethylene kernel calculations over the entire spectral hardness range ($0.06 \leq \beta\gamma \leq 0.65$) considered.

A discrepancy exists between the measurements and calculations for water-moderated media with large spectral hardness ($0.5 \leq \beta\gamma \leq 1$). The present measurements indicate good agreement between the Nelkin water kernel calculations and measurements in a water-moderated subcritical assembly when the spectral hardness $\beta\gamma \leq 0.3$. However, the measurements agree better with the free atom calculation when the spectral hardness is in the range $0.5 \leq \beta\gamma \leq 1$. This is of particular concern, since significant extensions in the lifetime of reactor cores will lead to the addition of more fuel and poison absorption and, thus, result in a harder spectrum with high $\beta\gamma$ values. In addition, since the calculated spectra are more sensitive to the kernel when larger absorption is present, it is of both practical and theoretical interest to resolve this discrepancy for high $\beta\gamma$. Further measurements using both techniques at high $\beta\gamma (\approx 1)$ should be made to ensure that a systematic error does not exist in the present measurement. If the discrepancy

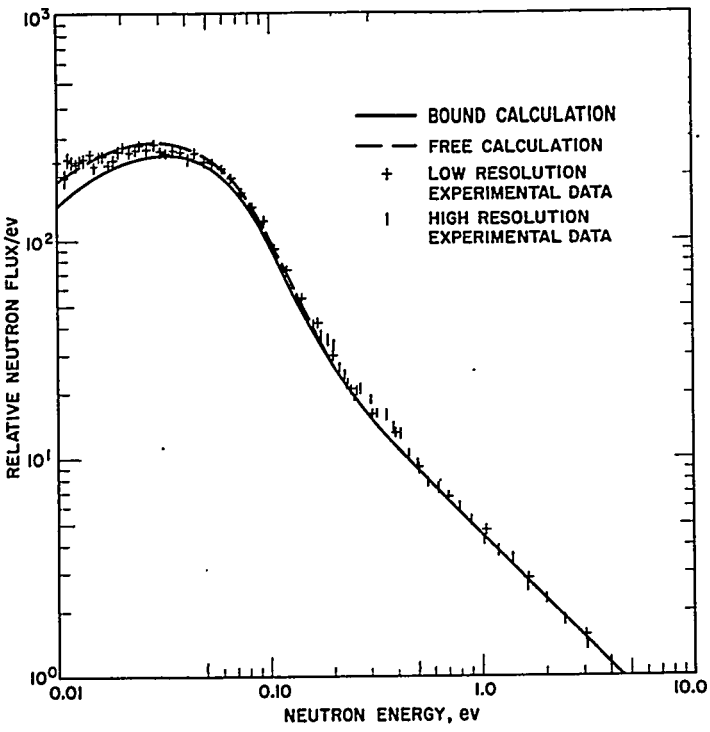

FIGURE 6.96. Poisoned Water Lattice IX (Boron Solution) for $\beta\gamma = 0.215$.

still exists, the water kernel may need to be determined more accurately.

In any heterogeneous fuel system, the absorber self-shielding dependence on energy can have almost as large an effect on the calculated spectrum as does the type of kernel that is used. Thus, improvements in the calculated results could be made by taking into account the change in self-shielding as a function of energy.

In comparing the average $1/v$ cross section, it is again observed that good agreement exists between the measured polyethylene values and the values calculated with the bound kernel. Except for high $\beta\gamma$, the water-moderated media average cross sections as determined with the measured spectrum agree better with the bound calculation. Finally, it is noted that the temperature of the moderator does not seem to introduce any particular difficulty into the comparison between experiment and theory for the thermal neutron spectrum.

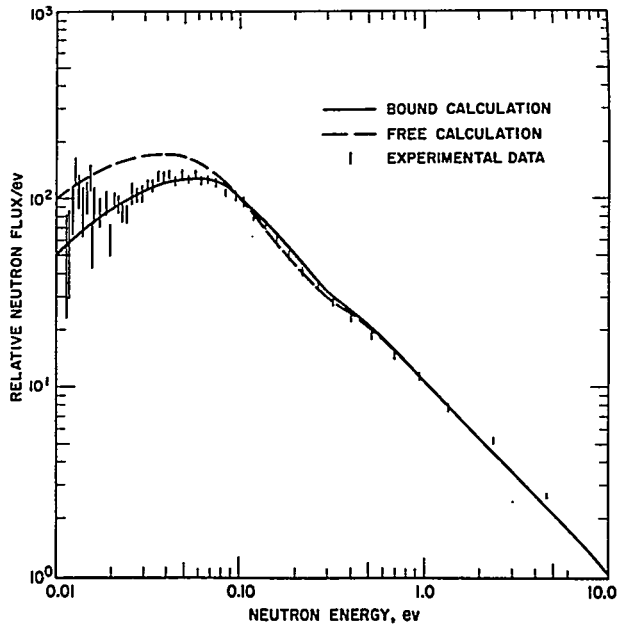

FIGURE 6.97. Polyethylene Lattice IV for $\beta\gamma = 0.65$.

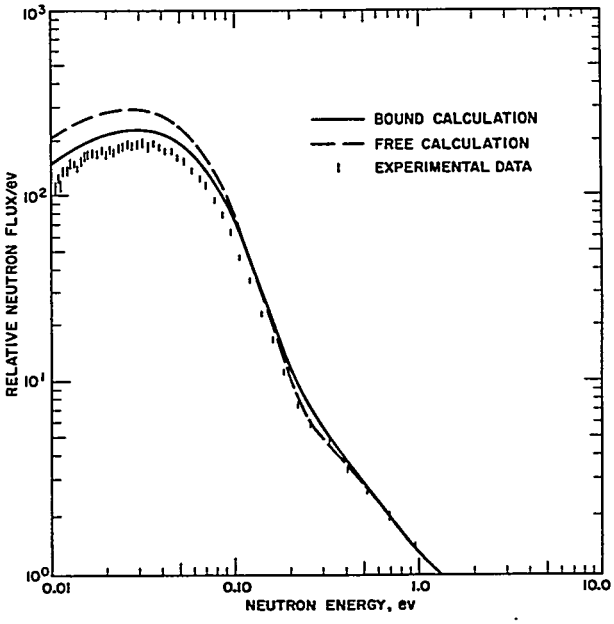

FIGURE 6.98. Polyethylene Lattice V for $\beta\gamma = 0.068$.

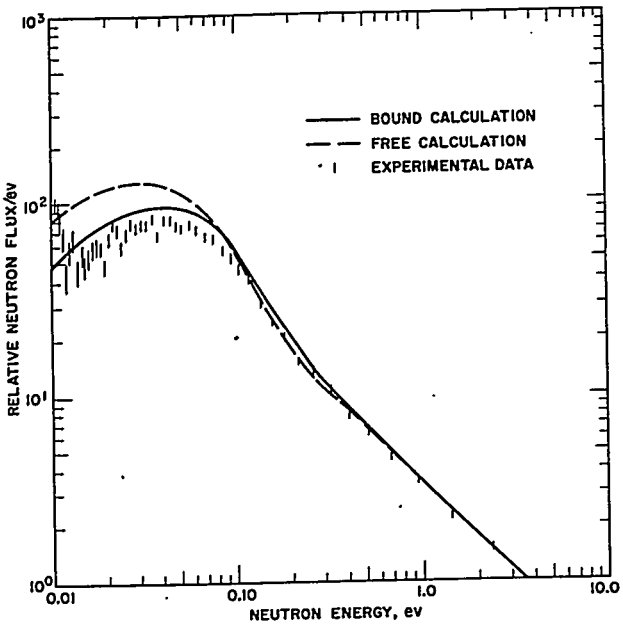

FIGURE 6.99. Polyethylene Lattice VI for $\beta\gamma = 0.30$.

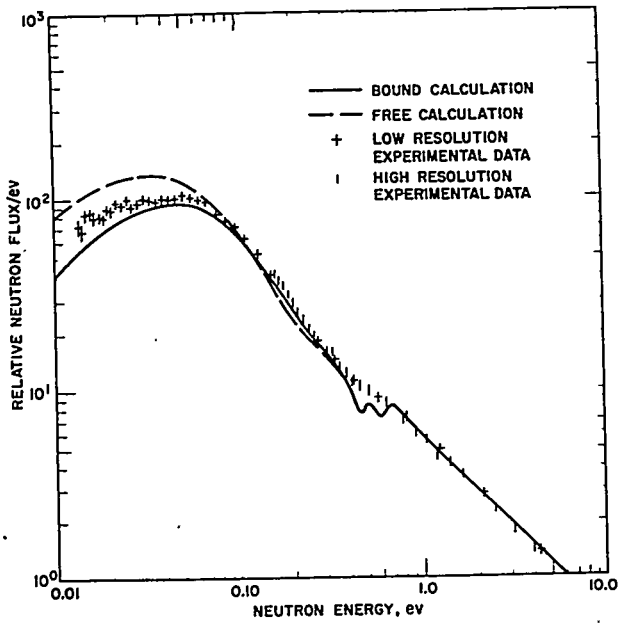

FIGURE 6.100. Polyethylene Lattice VII for $\beta\gamma = 0.46$.

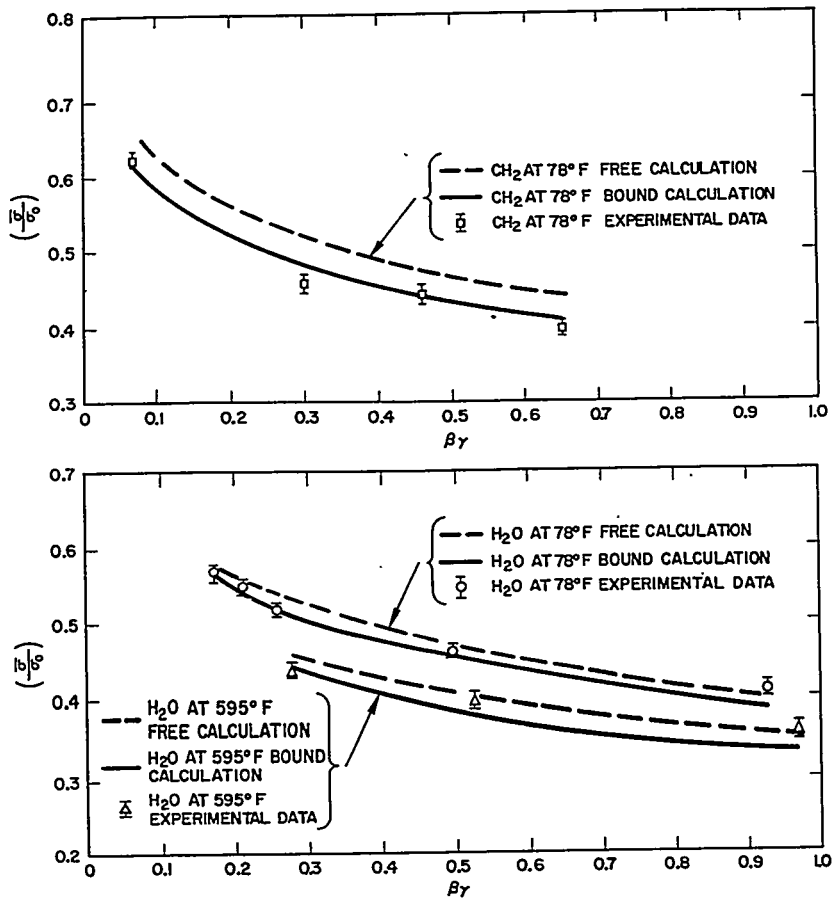

FIGURE 6.101. Average 1/v Cross Sections.

REFERENCES

1. H. Bohl, Jr., and A. P. Hemphill, "MUFT-5 — A Fast Neutron Spectrum Program for the PHILCO-2000," WAPD-TM-218, February 1961.

2. A. F. Henry, "54 Group Library for P-1 Programs," WAPD-TM-224, April 1960.

3. H. Bohl, Jr., E. M. Gelbard, G. R. Culpepper, and P. F. Bueŕger, "P1MG — A One-Dimensional Multigroup P_1 Code for the IBM-704," WAPD-TM-135, July 1959.

4. H. J. Amster and R. Suarez, "The Calculation of Thermal Constants Averaged over a Wigner-Wilkins Flux Spectrum: Description of the SOFOCATE Code," WAPD-TM-39, January 1957.

5. H. J. Amster and J. B. Callaghan, "KATE-1 — A Program for Calculating Wigner-Wilkins and Maxwellian Averaged Thermal Constants on the PHILCO-2000," WAPD-TM-232, October 1960.

6. A. Radkowsky, "Temperature Dependence of Thermal Transport Mean Free Path" in "Physics Division Quarterly Report for April, May, and June 1950," A. Wattenberg, F. C. Hoyt, and L. A. Turner, Eds., ANL-4476, July 5, 1950, pp. 89-100.

7. R. J. Breen, "A One-Group Model for Thermal Activation Calculations," Nucl. Sci. Eng. 9, 91-93 (1961).

8. B. L. Anderson, J. A. Davis, E. M. Gelbard, and P. H. Jarvis, "FLIP - An IBM-704 Code to Solve the P_L and Double- P_L Equations in Slab Geometry," WAPD-TM-134, March 1959.

9. W. R. Cadwell, "PDQ-4 — A Program for the Solution of the Neutron-Diffusion Equations in Two Dimensions on the PHILCO-2000," WAPD-TM-230, June 1961.

10. O. J. Marlowe, C. P. Saalbach, L. M. Culpepper, and D. S. McCarty, "WANDA — A One-Dimensional Few Group Diffusion Equation Code for the IBM-704," WAPD-TM-28, November 1956.

11. E. Gelbard, J. Davis, J. Dorsey, H. Mitchell, and J. Mandel, "TRIP-1 — A Two-Dimensional P-3 Program in X-Y Geometry for the IBM-704," WAPD-TM-217, July 1960.

12. E. M. Gelbard, H. B. Ondis, and J. Spanier, "MARC — A Multigroup Monte Carlo Program for the Calculation of Capture Probabilities," WAPD-TM-273, May 1962.

13. M. Goldsmith, R. T. Jones, T. M. Ryan, S. Kaplan, and A. D. Voorhis, "Theoretical Analysis of Highly Enriched Light Water Moderated Critical Assemblies" in "Proceedings of the Second United Nations International Conference on the Peaceful Uses of Atomic Energy, Geneva, 1958," Vol. 12, pp. 435-445, United Nations, Geneva, 1958.

14. H. Bohl, E. Gelbard, P. Buerger, and G. Culpepper, "SLOP-1 — A Thermal Multigroup Program for the IBM-704," WAPD-TM-188, October 1960.

15. D. J. Hughes and J. A. Harvey, "Neutron Cross Sections," BNL-325, U. S. Government Printing Office, Washington, D. C., July 1, 1955.

16. I. Itkin, "Analysis of the Neutron Capture Cross Section and Resonance Integral of Hafnium," WAPD-TM-324, August 1962.

17. V. B. Klimentov and J. M. Griazev, "Some Neutron Resonance-Absorption Integrals," J. Nucl. Energy 9, 20-27 (1959).

18. H. Hurwitz, Jr., and J. H. Smith, "The Use of Organic Fluids in Simulating Hot Reactor Conditions," KAPL-M-HH-10, November 13, 1956.

19. A. L. MacKinney, "Hydrogenous Moderator Measurements in the ACME and PMA," KAPL-M-ALM-4, July 1957.

20. P. Buck and R. J. Roseberry, "Water Gap Peaking," KAPL-M-PHB-1, March 6, 1959.

21. R. W. Deutsch, "Computing 3-Group Constants for Neutron Diffusion," Nucleonics 15 (1), 47-51 (1957).

22. J. A. Archibald, Jr., "Equations for the WOXX Cross-Section Routine of the KARE System," KAPL-M-JA-8, May 31, 1960.

23. H. Bohl, Jr., E. M. Gelbard, and G. H. Ryan, "MUFT-4 — Fast Neutron Spectrum Code for the IBM-704," WAPD-TM-72, July 1957.

24. E. L. Wachspress, "CURE: A Generalized Two-Space-Dimension Multigroup Coding for the IBM-704," KAPL-1724, April 30, 1957.

25. G. P. Calame, F. D. Federighi, and P. A. Ombrellaro, "A Two-Mode Variational Procedure for Calculating Thermal Diffusion Theory Parameters," Nucl. Sci. Eng. 10, 31-39 (1961).

26. F. D. Judge, "Variational Method in the Calculation of Reactor Neutron Flux Density," KAPL-2151, February 21, 1961.

27. G. G. Bilodeau, W. R. Cadwell, J. P. Dorsey, J. G. Fairey, and R. S. Varga, "PDQ — An IBM-704 Code to Solve the Two-Dimensional Few-Group Neutron-Diffusion Equations," WAPD-TM-70, August 1957.

28. G. P. Calame and F. D. Federighi, "A Variational Procedure for Determining Spatially Dependent Thermal Spectra," Nucl. Sci. Eng. 10, 190-201 (1961).

29. L. J. Esch, "Temperature Dependence of the Neutron Transport Cross Section in Paraffin and Polyethylene" in "Reactor Technology Report No. 19 — Physics," KAPL-2000-16, December 1961, pp. III. 23-III. 32.

30. D. T. Goldman and F. D. Federighi, "The Calculation of Neutron Spectra for Perfect Gas, Water, and Polyethylene-Moderated Systems" in "Reactor Technology Report No. 19 — Physics," KAPL-2000-16, December 1961, pp. II. 2-II. 8.

31. D. Klein, A. Z. Kranz, G. G. Smith, W. Baer, and J. DeJuren, "Measurements of Thermal Utilization, Resonance Escape Probability, and Fast Effect in Water-Moderated, Slightly Enriched Uranium and Uranium Oxide Lattices," Nucl. Sci. Eng. 3, 403-427 (1958).

32. S. J. Lukasik, "Summary of TRX Analysis Calculations," WAPD-TM-75, July 1957.

33. H. Kouts, R. Sher, J. R. Brown, D. Klein, S. Stein, R. L. Hellens, H. Arnold, R. M. Ball, and P. W. Davison, "Physics of Slightly Enriched, Normal Water Lattices (Theory and Experiment)" in "Proceedings of the Second United Nations International Conference on the Peaceful Uses of Atomic Energy, Geneva, 1958," Vol. 12, pp. 446-482, United Nations, Geneva, 1958.

34. J. R. Brown, D. G. Harris, F. S. Frantz, J. J. Volpe, J. C. Andrews, and B. H. Noordhoff, "Kinetic and Buckling Measurements on Lattices of Slightly Enriched Uranium and UO_2 Rods in Light Water," WAPD-176, January 1958.

35. L. Dresner, "Resonance Absorption in Nuclear Reactors," Pergamon Press, Inc., New York, 1960.

36. L. W. Nordheim, "The Theory of Resonance Absorption" in "Nuclear Reactor Theory. Proceedings of Symposia in Applied Mathematics. Volume XI," G. Birkhoff and E. P. Wigner, Eds., pp. 58-88, American Mathematical Society, Providence, 1961.

37. J. Chernick and R. Vernon, "Some Refinements in the Calculation of Resonance Integrals," Nucl. Sci. Eng. 4, 649-672 (1958).

38. G. G. Smith, J. Hardy, D. Klein, and J. A. Mitchell, "Experimental Studies of U^{238} Resonance Neutron Capture in UO_2 Fuel Rods," Nucl. Sci. Eng. 9, 421-429 (1961).

39. J. Hardy, Jr., G. G. Smith, J. A. Mitchell, and D. Klein, "Measurement of the Dancoff Correction," Nucl. Sci. Eng. 12, 301-308 (1962).

40. E. Hellstrand, "Measurements of the Effective Resonance Integral in Uranium Metal and Oxide in Different Geometries," J. Appl. Phys. 28, 1493-1502 (1957).

41. L. W. Nordheim, "A Program of Research and Calculations of Resonance Absorption," GA-2527, August 28, 1961.

42. A. R. Vernon, "Calculation of the Effective Resonance Integral of U^{238}," Nucl. Sci. Eng. 7, 252-259 (1960).

43. D. J. Hughes and R. B. Schwartz, "Neutron Cross Sections," BNL-325 (2nd Ed.), U. S. Government Printing Office, Washington, D. C., July 1, 1958.

44. E. Hellstrand and G. Lundgren, "The Resonance Integral for Uranium Metal and Oxide," Nucl. Sci. Eng. 12, 435-436 (1962).

45. G. I. Bell, "A Simple Treatment for Effective Resonance Absorption Cross Sections in Dense Lattices," Nucl. Sci. Eng. 5, 138-139 (1959).

46. L. W. Nordheim and J. B. Sampson, "The Effect of Small Inhomogeneities on Resonance Absorption," Trans. Am. Nucl. Soc. 2 (1), 84-85 (1959).

47. K. M. Case, F. de Hoffmann, and G. Placzek, "Introduction to Theory of Neutron Diffusion, Vol. I," U. S. Government Printing Office, Washington, D. C., 1953.

48. G. Smith, J. Hardy, Jr., and D. Klein, "Comparison of Measurements with a Monte Carlo Calculated Spatial Distribution of Resonance Neutron Capture in a Uranium Rod," Nucl. Sci. Eng. 8, 449-451 (1960).

49. J. C. Stewart and P. F. Zweifel, "Self-Shielding and Doppler Effects in the Absorption of Neutrons" in "Physics and Mathematics," Vol. 3 of "Progress in Nuclear Energy, Series I," D. J. Hughes, J. E. Sanders, and J. Horowitz, Eds., pp. 331-359, Pergamon Press, Inc., New York, 1959.

50. J. J. Volpe and D. Klein, "An Experimental Study of the Relative U^{235} Fission Activation as a Function of Energy and Slightly Enriched Uranium-Water Lattices," Nucl. Sci. Eng. 8, 416-425 (1960).

51. D. K. Trubey, "A Table of Three Exponential Integrals," ORNL-2750, July 2, 1959.

52. E. D. Clayton, "Epi-Cadmium Fission in U-235," AECD-4167, March 7, 1955.

53. D. J. Hughes, B. A. Magurno, and M. K. Brussel, "Neutron Cross Sections. Second Edition, Supplement No. 1," BNL-325 (2nd Ed.) (Suppl. 1), U. S. Government Printing Office, Washington, D. C., January 1, 1960.

54. R. L. Macklin and H. S. Pomerance, "Resonance Capture Integrals" in "Physics and Mathematics," Vol. 1 of "Progress in Nuclear Energy, Series I," R. A. Charpie, J. Horowitz, D. J. Hughes, and D. J. Littler, Eds., pp. 179-189, McGraw-Hill Book Company, Inc., New York, 1956.

55. B. E. Simmons and J. S. King, "A Pulsed Neutron Technique for Reactivity Determination," Nucl. Sci. Eng. 3, 595-608 (1958).

56. B. E. Simmons, "The Dynamic Reactivity Interpretation of Pulsed Neutron Measurements," Nucl. Sci. Eng. 5, 254-256 (1959).

57. N. G. Sjöstrand, "Measurements on a Subcritical Reactor with a Pulsed Neutron Source" in "Proceedings of the International Conference on the Peaceful Uses of Atomic Energy, Geneva, 1955," Vol. 5, pp. 52-54, United Nations, New York, 1956.

58. J. D. Orndoff, "Prompt Neutron Periods of Metal Critical Assemblies," Nucl. Sci. Eng. 2, 450-460 (1957).

59. A. V. Antonov, A. I. Isakoff, I. D. Murin, B. A. Neupocoyev, I. M. Frank, F. L. Shapiro, and I. V. Shtranich, "A Study of Neutron Diffusion in Beryllium, Graphite and Water by the Impulse Method" in "Proceedings of the International Conference on the Peaceful Uses of Atomic Energy, Geneva, 1955," Vol. 5, pp. 3-12, United Nations, New York, 1956.

60. N. G. Sjöstrand, "Measurements on a Subcritical Reactor Using a Pulsed Neutron Source," Arkiv Fysik 11, 233-246 (1956).

61. J. Bengston and L. Passell, "Pulsed Neutron Experiments with Fast Assemblies," UCRL-4998, October 31, 1957.

62. P. J. Bendt, H. J. Karr, and F. R. Scott, "Prompt Neutron Periods of a Critical Assembly Measured with a Pulsed Source," Nucl. Sci. Eng. 4, 703-708 (1958).

63. J. Bengston, "Determination of Prompt Neutron Decay Constants of Multiplying Systems" in "Proceedings of the Second United Nations International Conference on the Peaceful Uses of Atomic Energy, Geneva, 1958," Vol. 12, pp. 63-71, United Nations, Geneva, 1958.

64. F. A. Kloverstrom and T. T. Komoto, "Pulsed Neutron Source Studies of Graphite-Enriched Uranium Systems," UCRL-5477, February 5, 1959.

65. S. C. Fultz, "The Time-Dependent Thermal Neutron Flux from a Pulsed Subcritical Assembly," Nucl. Sci. Eng. 6, 313-319 (1959).

66. E. C. Campbell and P. H. Stelson in "Physics Division on Semiannual Progress Report for Period Ending September 10, 1956," ORNL-2204, February 12, 1957, p. 34.

67. H. Brooks, "Perturbation Theory for Boltzmann Equation," KAPL-304, February 27, 1950.

68. B. E. Simmons, L. S. Bohl, and D. R. Wehner, "Prompt Generation Times in Highly-Enriched Hydrogenous Reactors," Trans. Am. Nucl. Soc. 1 (1), 116-117 (1958).

69. D. J. Behrens, "Some Notes on the Nature of Experiments, on the Statistics of Counting, and on the Fitting of Exponential Decay Curves to the Results of Counting Experiments," AERE T/R 629, January 1951.

70. M. Nelkin, "The Decay of a Thermalized Neutron Pulse," Nucl. Sci. Eng. 7, 210-216 (1960).

71. F. R. Scott, D. B. Thomson, and W. Wright, "Thermal Neutron Capture Cross Sections of Hydrogen, Boron, and Silver," Phys. Rev. 95, 582-584 (1954).

72. G. von Dardel and N. G. Sjöstrand, "Absorption Cross Section of Boron for Thermal Neutrons," Phys. Rev. 96, 1566-1567 (1954).

73. D. R. Bach and M. E. Way, "The Worth of Single Control Rods in Hydrogenous Reactors," KAPL-M-DRB-2, July 28, 1958.

74. S. N. Purohit, "Neutron Thermalization and Diffusion in Pulsed Media," Nucl. Sci. Eng. 9, 157-167 (1961).

75. T. J. Krieger and P. F. Zweifel, "Theory of Pulsed Neutron Experiments in Multiplying Media," Nucl. Sci. Eng. 5, 21-27 (1959).

76. N. G. Sjöstrand, "On the Theory Underlying Diffusion Measurements with Pulsed Neutron Sources," Arkiv Fysik 15, 147-158 (1959).

77. A. M. Weinberg and E. P. Wigner, "The Physical Theory of Neutron Chain Reactors," p. 170, University of Chicago Press, Chicago, 1958.

78. G. Goertzel, "Reactor Dynamics" in "Reactor Handbook: Physics," pp. 531-616, McGraw-Hill Book Company, Inc., New York, 1955.

79. M. J. Poole, M. S. Nelkin, and R. S. Stone, "The Measurement and Theory of Reactor Spectra" in "Physics and Mathematics," Vol. 2 of "Progress in Nuclear Energy, Series I," D. J. Hughes, J. E. Sanders, and J. Horowitz, Eds., pp. 91-164, Pergamon Press, Inc., New York, 1958.

80. V. I. Mostovoy, V. S. Dikarev, M. B. Egiasarov, and Yu. S. Saltykov, "Measurement of Neutron Spectra in Uranium-Water Lattices" in "Physics and Mathematics," Vol. 3 of "Progress in Nuclear Energy, Series I," D. J. Hughes, J. E. Sanders, and J. Horowitz, Eds., pp. 247-260, Pergamon Press, Inc., New York, 1959.

81. D. A. O'Connor and J. Sosnowskii, "Measurement of the Slow Neutron Spectrum of a Neutron Beam from the W. W. R. S. Reactor by Means of a Crystal Neutron Spectrometer," Acta Phys. Polon. (Poland) 19, No. 3, 329-338 (1960).

82. R. R. Spencer and J. R. Smith, "Competitive Extinction in Neutron Monochromating Crystals," Nucl. Sci. Eng. 8, 393-399 (1960).

83. M. J. Poole, "Measurement of Neutron Spectra in Moderators and Reactor Lattices—I," J. Nucl. Energy 5, 325-341 (1957).

84. J. R. Beyster, J. L. Wood, W. M. Lopez, and R. B. Walton, "Measurements of Neutron Spectra in Water, Polyethylene, and Zirconium Hydride," Nucl. Sci. Eng. 9, 168-184 (1961).

85. V. I. Mostovoi, M. I. Pevzner, and A. P. Tsitovich, "A Mechanical Neutron Velocity Selector" in "Proceedings of the International Conference on the Peaceful Uses of Atomic Energy, Geneva, 1955," Vol. 4, pp. 12-21, United Nations, New York, 1956.

86. R. S. Stone and R. E. Slovacek, "Reactor Spectrum Measurements Using a Neutron Time-of-Flight Spectrometer," KAPL-1499, March 15, 1956.

87. R. S. Stone and R. E. Slovacek, "Neutron Spectra Measurements," Nucl. Sci. Eng. 6, 466-474 (1959).

88. E. J. Wade and D. S. Davidson, "Transistorized Time of Flight Analyzer with Ferrite Core Memory," IRE Nat. Conv. Record, Part 9, 89-94 (1957).

89. E. Maliszewski, "The Optical Properties of Slow Chopper and Time-of-Flight Device," Nucl. Instr. Methods 9, 341-346 (1960).

90. R. T. Frost, "Correction of Measured Flux Scans for Finite Resolution Effects," KAPL-M-RTF-5, October 5, 1956.

91. E. P. Wigner and J. E. Wilkins, Jr., "Effect of the Temperature of the Moderator on the Velocity Distributions of Neutrons with Numerical Calculations for H as Moderator," AECD-2275, September 14, 1944.

92. M. Nelkin, "Scattering of Slow Neutrons by Water," Phys. Rev. 119, 741-746 (1960).

93. D. T. Goldman and F. D. Federighi, "The Calculation of the Differential and Integral Cross Section for the Scattering of Thermal Neutrons from Water and Polyethylene Moderators" in "Reactor Technology Report No. 19 — Physics," KAPL-2000-16, December 1961, pp. I.47-I.53.

94. L. S. Bohl, "Application of the Variational Method to the Calculation of Flux Ratios in Repeating Slab Arrays," KAPL-M-LSB-2, June 27, 1957.

Chapter 7

REACTOR PHYSICS COMPUTATIONS

G. J. Habetler and B. H. Mount, Editors

7.1 INTRODUCTION

The importance of the digital computer in the design of nuclear reactors is evidenced by the many references to computer programs in the earlier chapters of this volume. With the aid of the computer, the nuclear designer may examine many different designs quickly and appraise their relative merits. Of particular importance is the ability to predict theoretically the lifetime behavior of a given design, thereby minimizing prototype experimentation. Rather than attempt to assess the role that computers have played and will continue to play in reactor design, detailed information will be given concerning mathematical methods applied to nuclear reactor problems, characteristics of the digital computers, programming methods used, and the major nuclear design programs developed by the Naval Reactors laboratories for the IBM-704 and Philco-2000 computers.

Efficient utilization of a computer as a design tool requires (1) careful specification of the physical and mathematical models of the problem to be solved, (2) careful selection of computer and computer configuration to be used, (3) application of the most appropriate numerical techniques, and (4) application of efficient programming methods. Item (1) has been the subject matter of the earlier chapters of this volume. Items (2) and (4) will be dealt with in this section. Sections 7.2 and 7.3 will present the mathematical theory behind the numerical techniques currently used in the programs listed in Sect. 7.4.

A. Digital Computers

Most reactor physics programs fall into one of four categories: (1) preparation of nuclear constants, (2) solution of few-group diffusion equations, (3) solution of the depletion equations for lifetime performance, (4) solution of some

approximation to the neutron transport equation. The programs in category (1) have required a relatively small amount of computer time and, therefore, relatively little numerical analysis. The significant amounts of computer time required by multidimensional diffusion and depletion problems and by approximate transport solutions have dictated that considerable mathematical and programming effort be expended in these areas. Furthermore, the most significant measure of a digital computer for the work of the laboratories has been its ability to perform multidimensional diffusion calculations.

The earliest two-dimensional digital calculations performed by the Naval Reactors laboratories were performed on the UNIVAC using the programs MUG and AML-54. Subsequent calculations were performed on the NORC computer at the U.S. Navy Weapons Laboratory, Dahlgren, Virginia, using another version of the AML-54 program. Further calculations were performed by the laboratories using QED-1 (now obsolete), CURE, PDQ-2, PDQ-3, REM, OBSCURE, and FLEER on the IBM-704 and KARE and PDQ-4 on the Philco-2000. These programs are described in Sect. 7.4.

A measure of the progress that has been made in the solution of the two-dimensional problem by mathematical advances (see Sect. 7.2), improvement in programming techniques, and faster computing equipment may be obtained from a tabulation (Table 7.1) of the approximate time required to solve a typical two-group 2500-point $x-y$ problem with each of several programs. Table 7.1 also lists the maximum numbers of energy groups and mesh points permitted by these two-dimensional programs. As progress in numerical methods, in programming, and in hardware has enabled faster solution of a problem of given size so also may larger and larger problems be run on the newer computers.

In Table 7.1, 704-8K refers to the IBM-704 with 8192 words of core store, 704-32K refers to the IBM-704 with 32,768 words, and 211-10 refers to the Philco-2000 with model 211 mainframe and 10-microsecond core store. The laboratories have experienced a 50 percent increase in computing speed when the 10-microsecond stores were replaced by 2-microsecond stores.

Table 7.1 seems to indicate a tremendous step-down in capability when going from the NORC to the 704-8K. It should be observed that problems in excess of 2500 points would have required very large amounts of time on either the UNIVAC or NORC, so that the maximum capabilities of the programs on these computers were rarely utilized.

The large number of points is required by the complexity of geometric detail and the large flux gradients appearing in high power-density reactors. A two-dimensional program,

TABLE 7.1 — APPROXIMATE TIME REQUIRED TO SOLVE A TYPICAL TWO-GROUP 2500-POINT x-y PROBLEM WITH EACH OF SEVERAL PROGRAMS

Program	Computer	Max No. Groups	Max No. Points	Time Required (hours)
MUG	UNIVAC	99	5,900	12.0
AML-54	UNIVAC	2	6,962	25.0
ACE	NORC	2	18,720	5.0
QED-1	704-8K	2	2,500	1.0
PDQ-2	704-32K	4	6,500	0.8
PDQ-3	704-32K	4	7,500	0.6
CURE	704-32K	3	3,300	0.6
PDQ-4	211-10	4	20,000	0.2
KARE	211-10	5	20,000	0.2

PDQ-5, will allow at least 50,000 mesh points and up to five energy groups.

The need for increased detail exists in three dimensions as well. To date, this demand has not been satisfied, the largest permissible number of points being 100,000 in the TNT-1 program described in Sect. 7.4. While some thought has been given to specifying a program to permit up to 1,000,000 points in three dimensions, such a program has not yet been specified. As indicated in earlier chapters, however, methods for synthesizing three-dimensional solutions have been developed and are being improved.

In Table 7.1 the large capacity (in mesh points) on the UNIVAC and NORC was observed. This capability was used infrequently because of the relatively long computing time on these machines. On the IBM-704 good computing speed was experienced, but the number of points permitted was restricted. Table 7.1 indicates that with the Philco-2000 the gain is not only in computing speed but also in capacity. Why? The answer to this question requires an understanding of the method of solution and of the characteristics of the computer as well.

In Sect. 7.2 the details of the mathematical treatment of multidimensional diffusion problems will be given. In this

subsection the method of solving the two-dimensional neutron-diffusion problem is discussed. The concepts extend readily to three dimensions. The first assumption is made that the diffusion problem is solved over a rectangular region such that either the flux is zero or the relation between the flux and its normal derivative is known over the boundary of the rectangle. A network of straight lines parallel to the sides of the bounding rectangle is imposed over the region. The mesh lines intersect in mesh points, and the objective is to compute the few-group fluxes and the fission source at each of these mesh points. Since the problem is a homogeneous one, an eigenvalue is also calculated. The partial differential equations over the the region of solution and the boundary conditions are replaced by difference equations over the set of mesh points within the region. For each neutron group one gets a system of n linear equations in n unknown fluxes where n is the number of internal mesh points.

The process of solving the multidimensional problem consists of guessing an eigenvalue and a source distribution, computing the flux in each group at each point, and recomputing the source and eigenvalue. If the recomputed source and eigenvalue are not considered adequate this computation, referred to as an outer iteration, is repeated. Within this outer iteration occurs the operation referred to as computing the flux. For the large value of n dealt with there is no known way to solve directly n equations in n unknowns. Thus, an iterative method of solution, consisting of inner iterations, is generally required in each neutron group.

Mathematical methods of improving the rates of convergence of the inner and outer iterations are discussed in Sect. 7.2. Here the basic arithmetic involved is discussed along with its effect upon programming strategy and the selection of computers. In each inner iteration, or mesh sweep, the computer evaluates at each point an expression of the form

$$\phi_o = S_o + \sum_{i=1}^{4} C_i \phi_i$$

relating the flux at any point to the source at that point and to the fluxes at four neighboring points. It is this calculation which is repeated literally millions of times in one large two-dimensional problem.

From the above formula it appears that ten numbers need to be stored in the computer for each point in the mesh. Four words of core store per mesh point are all that are needed, however; one flux, since the newly computed flux at a point replaces the previous value of the flux; one source; and because of symmetry, two rather than four coefficients per point. It seems reasonable, then, to have 7500 fluxes, 7500 sources, and 15,000 coefficients in a 32,768-word core store, allowing the program to occupy the remaining 2768 locations.

This is essentially the way memory was laid out for the inner-iteration section of the PDQ-3 program on the IBM-704. When the inner iterations in a group were completed, the fluxes would be written out on magnetic tape and the fluxes, sources, and coefficients for the next group would be read into core store. After the last group, fluxes and fission cross sections would be read from tape and the new fission source calculated.

On the IBM-704 it was important, for reasons of computing speed or program efficiency, that tapes should not move during inner iterations. On this machine a floating-multiply-add operation requires about 400 microseconds. To transfer one number between core store and tape (in either direction) requires 400 microseconds. Further, only one tape at a time can be used. For these reasons, problem size was limited to at most 7500 mesh points.

Mention has been made of the floating-multiply-add operation in connection with the transfer of one number between tape and main store. For brevity this will be referred to as the multiply-add-fetch operation. The time to compute at a point is approximately equal to five times the multiply-add-fetch time, where the fetch component of this time may be essentially zero if all the data are in the main store. However, for problems larger than 7500 points on 32K computers something must be brought into the main store from the secondary store for the calculations at each point.

Consider problems of up to 20,000 points. For these it is reasonable to keep the 20,000 fluxes in core store and to bring the sources and coefficients in from tapes (or other secondary store). The remaining 12,768 locations in the main store are used for program and for buffers into which the sources and coefficients are delivered from the tapes. Machines of the generation of the IBM-704 were not able to compute while reading or writing tapes. The multiply-add-fetch time for the IBM-704 would, therefore, be 400 plus 400 or 800 microseconds. If a program like PDQ-3 were written to allow 20,000 points on the IBM-704, the effective computing speed would have been halved.

More recent computers, the Philco-2000 and the IBM-7090 for example, provide what is commonly called buffered computation: the ability to compute while reading or writing tapes. It was this capability which enabled the laboratories, with the KARE and PDQ-4 programs, to increase maximum problem size to 20,000 with little sacrifice in speed.

As computing speeds increase it is possible to allow still larger problems to be solved. This is accompanied, obviously, by increased data flow between the main store of the computer and its auxiliary store. Present hardware development provides for this increased data-flow requirement either by high-speed rotating magnetic devices, drums or disc files, or by increasing the number of tapes which can be accessed simultaneously. It is by the use of four tapes moving simultaneously that the PDQ-5 program will function efficiently on large problems.

To illustrate future needs, an existing machine with the ability to do a floating-point multiply-add in 75 microseconds, simultaneously reading one number from tape into its fast store, requires 5 hours to do a 20,000-point, three-group, two-dimensional problem. To solve a 1,000,000-point, five-group, three-dimensional problem in the same time would require a computer with about 100 times the capability of existing commercially available computers. That is, it would require a multiply-add-fetch time of about one microsecond.

This section has stressed the relationship between the computing hardware and the two-, and to some extent, three-dimensional diffusion problems because it has been the experience and judgment of the computing personnel of the Naval Reactors laboratories that the machine configuration best suited to these problems was the most desirable one for all the digital problems of the laboratories. The multiply-add-fetch criterion is, then, useful as a measure of speed of a computer while total capacity of the computer in various echelons of storage is relatively easy to measure.

B. Programming Techniques

The importance of computer speed and of the data flow between auxiliary storage and the main store of the computer was emphasized in the preceding pages. When writing a program to solve multidimensional diffusion problems it is essential to use a good numerical technique, to program very carefully, and to provide for efficient flow of data. Concurrently with the development of new programs and hardware, new numerical techniques were developed (see Sect. 7.2).

To provide efficient use of buffered tapes on the Philco-2000 computer the XACT routine was specified and written. This

routine does most of the work of reading, writing, and checking tapes, thus enabling the applications programmer to concentrate on the problem he is trying to solve while assured that XACT will keep the tapes moving at maximum efficiency.

Up to this time big problems have been stressed, but the computer must also be prepared to handle a very large number of small problems, each having a running time of from a few seconds to a few minutes. If handled poorly this multitude of small problems could waste many hours of computer time each day. This problem becomes more acute with larger, more expensive computers.

As computers become progressively faster it becomes increasingly important to reduce the time they spend waiting idly for some human operation to take place. One solution to the problem of idle time is based on the concept that the human operator should be notified in advance of a function which he should perform, thereby allowing him time to perform this function while the computer is busy. This concept was basic to the design of the BKS system for the Philco-2000.[1]

Programs of the Naval Reactors laboratories for the IBM-704 operated independently of each other so that there generally was some idle (set-up) time between problems on the computer. Most programs allowed a number of problems to be run successively, thus reducing the frequency of machine stops. However, with the IBM-704 programs described in Sect. 7.4 there was no arrangement for automatic sequencing or switching from one program to another.

BKS was written to utilize fully the computing-speed advantage of the Philco-2000. It provides for nonstop operation of the computer from job to job as well as from one input tape to the next. It allows the operator to signal when additional tape transports are available, when he wishes to monitor the progress of a problem, when he desires to remove an output tape, or when he wishes to terminate a problem.

All programs written by the Naval Reactors laboratories for the Philco-2000 have been designed to operate within BKS. Each program uses symbolic designations for the magnetic tapes it uses. A single control card with each program informs BKS of the symbolic designation and function (input, output, scratch, file, etc.) of each of the tapes it uses. This information allows BKS to make advance assignment of tape transports and to give advance notice to the operator of the need to mount a specific input file tape. When the operator has readied the input file tape he signals to BKS (via a toggle switch on the console) that he has complied.

During the past decade of use of large digital computers there have been significant improvements in the process of

writing instructions (coding) for computers. Programs written 10 years ago — those for the UNIVAC, for example — consisted of thousands of instructions, each one fitting into the main store of the computer in a location carefully chosen by the programmer and each one referring to another location, or address, in the store. This method of fixed-location, absolute-address coding led to enormous numbers of errors, each one difficult to correct, each correction being likely to cause other errors.

A significant advance was that which led to using mnemonic, symbolic languages for communicating with the computer. The computer itself was programmed to convert this symbolic coding into the actual absolute numerical code of the machine. The machine then does the clerical job with speed and accuracy.

Algebraic languages, for example FORTRAN, in addition to being relatively independent of the characteristics of specific computers, have the advantage of allowing programming to be done more rapidly. This is accomplished by having much of the clerical work done by the compiler, a computer program which translates from the algebraic language to that of the computer. Early compilers yielded object programs which were relatively inefficient. For this reason, algebraic languages were most economical when applied to programs which would be used a small number of times.

More recent versions of algebraic compilers have generated more efficient object programs. Since one can write large programs in an algebraic language and have these programs complied to run on any of several computers with reasonable efficiency, and, thus, be independent of any particular computer, the use of algebraic programming languages for these programs is increasing.

C. Role of Analysis

The role which computers will continue to play in the field of nuclear design will depend on how well their new capabilities are used. The availability of computers inspired the creation of many mathematical models and the development of refined numerical techniques.[2] It can be anticipated that as computers continue to grow, there will be a corresponding amount of progress in numerical analysis.

As mentioned earlier, the finite-difference approximation to the multidimensional diffusion equation is a large system of simultaneous linear algebraic equations. The solution to this system of equations, obtained by means of iterative techniques, is the (approximate) neutron flux at each point of a finite difference mesh superimposed over the model. Over the last

decade, there have been significant advances in the techniques used in solving these equations. This is inherent in the figures presented in Table 7.1 of this section. Since mathematical advances have decreased the number of iterations required to solve a neutron-diffusion problem, we have been able to take advantage of the growth of fast store size and do larger problems at reasonable costs.

The first important interplay between numerical analysis and computing costs in nuclear design work was the use of the theory behind successive overrelaxation to optimize the inner-iteration strategy. This took place with the early MUG and AML-54 programs. The use of successive overrelaxation rather than some simpler iterative technique reduced the number of iterations on some of the problems by almost an order of magnitude. There have been extensions of this technique as computers have grown larger and as reactors have grown more complicated. Smaller spacing between mesh points has led to newer iterative techniques, called the implicit alternating direction methods. For some problems these have led to another appreciable factor of savings. For $r-z$ problems, the KARE program (see Sect. 7.4) realizes an average factor of 2 by this means. Section 7.2 describes some of the iterative methods currently employed successfully in the various programs described in Sect. 7.4.

As computers continue to develop, the methods for solving the diffusion equations approximately may change radically. The entire concept of inner and outer iterations is, to some extent, tailored to a computer for which it is impossible to get more than one group into the fast store at the same time and for which tape reading time is relatively expensive. Buffered tapes and large fast stores have given impetus to new analytical studies in optimum ways of solving the entire problem.

The Monte Carlo method applied to the neutron transport equation involves performing a large but finite number of numerical experiments, each of which corresponds to simulating the motion of a neutron in a medium. The amount of detail in geometry and in nuclear interactions can be as much as can be given readily and can be held in memory in some workable form. This is the converse of what happens in the numerical methods described above where the number of particles is considered to increase without limit while the phase space with which they interact is considered to be a coarse network of discrete points. From the life histories followed in the Monte Carlo method, estimates of desired physical parameters are formed. Variances of these estimators are also calculated giving a measure of the expected error of the estimators.

From the nature of the Monte Carlo method, it is seen that it can readily be extended to higher dimensions (three, for instance, instead of the usual two used in diffusion calculations) and higher order approximations to nuclear behavior (transport theory rather than diffusion theory). Of course, it introduces its own mathematical difficulties. For some problems, the solution time required to reduce the variances obtained is prohibitively large. Here analytical schemes are used either to vary the mechanics of the process or to form the estimate differently. One method uses expected values to obtain efficient unbiased estimators. Another device is the application of the adjoint transport equation to obtain approximate importance functions. Section 7.3 presents a mathematical theory which provides a unified approach to the determination of these devices.

7.2 ITERATION PROCEDURES IN NEUTRON-DIFFUSION CALCULATIONS

G. J. Habetler and L. A. Hageman

A. Introduction

The group equations used in neutron-diffusion theory[3] have the form

$$\frac{1}{v_g}\frac{\partial \phi_g(\vec{r}, t)}{\partial t} = \nabla \cdot D_g(\vec{r})\nabla\phi_g(\vec{r}, t) - \sigma_g(\vec{r})\phi_g(\vec{r}, t)$$

$$+ \sum_{g' \neq g} \sigma_{g' \to g}(\vec{r})\,\phi_{g'}(\vec{r}, t) + \chi_g \sum_{g'} f_{g'}(\vec{r})\,\phi_{g'}(\vec{r}, t) \quad (g = 1, 2, \ldots, G)$$

Eq. (7.1)

where $\phi_g(\vec{r}, t)$ is the neutron flux in the g^{th} group, $D_g(\vec{r})$ is the diffusion coefficient in the g^{th} group, $\sigma_g(\vec{r})$ is the total removal cross section in the g^{th} group, $\sigma_{g' \to g}(\vec{r})$ is the scattering cross section from group g' to group g, χ_g is the fission neutron spectrum, $f_g(\vec{r})$ is the g^{th} group fission cross section times the average number of neutrons released per fission, v_g is the velocity of g^{th} group neutrons, G is the total number of

groups, and $\vec{r}$ is the position vector. It is assumed that the following conditions are satisfied:

1. The reactor is finite in extent.
2. The reactor is composed of a finite number of simply connected subregions, in each of which the coefficients possess sufficiently high derivatives.
3. $\phi_g(\vec{r}, t)$ and the normal component of $D_g(\vec{r})\nabla\phi_g(\vec{r}, t)$ are continuous across interfaces between subregions.
4. On the outer boundary of the reactor, the boundary condition is

$$\alpha_g(\vec{r})\phi_g(\vec{r}, t) + \beta_g(\vec{r})\frac{\partial\phi_g(\vec{r}, t)}{\partial n} = 0$$

$$\alpha_g(\vec{r}) \geq 0, \quad \beta_g(\vec{r}) \geq 0, \quad \alpha_g(\vec{r}) + \beta_g(\vec{r}) > 0 \qquad \text{Eq. (7.1a)}$$

where $\partial\phi_g(\vec{r}, t)/\partial n$ is the derivative in the direction of the outward going normal to the boundary.

One of the fundamental problems of reactor design is to determine whether a steady-state solution to Eq. (7.1) exists and, if it does, to find its shape in space. In solving this problem, it has been convenient to consider instead of Eq. (7.1) the time-independent equation

$$-\nabla \cdot D_g(\vec{r})\nabla\phi_g(\vec{r}) + \sigma_g(\vec{r})\phi_g(\vec{r}) - \sum_{g' \neq g} \sigma_{g' \to g}(\vec{r})\phi_{g'}(\vec{r})$$

$$= \frac{1}{\lambda}\chi_g \sum_{g'} f_{g'}(\vec{r})\phi_{g'}(\vec{r}) (g = 1, 2, \ldots, G) \qquad \text{Eq. (7.1b)}$$

with conditions 1 through 4 still to be satisfied. The question is then asked: For what values of λ (note that in order for $\phi_g(\vec{r})$ to be a steady-state solution to Eq. (7.1), λ must be equal to unity) do solutions to Eq. (7.1b) exist, and if $\lambda = 1$ what is the shape of $\phi_g(\vec{r})$ satisfying Eq. (7.1b)? For arbitrary (but physically meaningful) coefficients $D_g(\vec{r})$, $\sigma_g(\vec{r})$, $\sigma_{g' \to g}(\vec{r})$, and $f_g(\vec{r})$, Eq. (7.1b) does not posses a solution for $\lambda = 1$. However, for physically reasonable systems, there will be a value of λ (the fundamental eigenvalue) close to unity for which the corresponding solution to Eq. (7.1b), $\phi_g(\vec{r})$, can be taken as everywhere positive.[4] The subcriticality or the supercriticality of the reactor model on which the equations are based can be ascertained by noting whether λ is less than unity or greater than unity, respectively. Moreover, the shape of the solution $\phi_g(\vec{r})$ for λ close to unity will, in general, be close to the shape

of the solution to the problem where a specific parameter is slightly modified so as to make the new fundamental eigenvalue exactly equal to unity. Thus, finding the fundamental solutions to system [Eq. (7.1b)] with boundary condition [Eq. (7.1a)] is of great interest to the nuclear engineer and will be the major concern here. The time-dependent problem will be treated in Sect. 7.2.D.

For complicated reactor designs, one can only hope to find an approximate solution to this problem. One way of doing this is by the use of numerical methods. The coupled differential equations given by Eq. (7.1b) are approximated by a coupled system of linear algebraic equations obtained by standard finite difference techniques. Basically, such a technique consists of imposing a mesh on the region of the reactor under investigation and then for each mesh point replacing the differential equation by a certain algebraic expression. There are many ways of obtaining a finite difference approximation to a differential equation.[5,6,7] For the two-dimensional problem in a rectangle, the standard five-point finite difference approximation for Eq. (7.1b) at a general interior mesh point P (Fig. 7.1) is given by[5]

$$-a\phi_{g,N} - b\,\phi_{g,S} - c\phi_{g,E} - d\phi_{g,W} + (a+b+c+d+e)\phi_{g,P} = \sum_{g' \neq g} s_{g,g'}\,\phi_{g',P} + \frac{1}{\lambda}\chi_g \sum_{g'} t_{g'}\,\phi_{g',P}$$

where

$$a = \frac{D_{g,R_1} h_W + D_{g,R_4} h_E}{2h_N}, \qquad b = \frac{D_{g,R_2} h_W + D_{g,R_3} h_E}{2h_S}$$

$$c = \frac{D_{g,R_4} h_N + D_{g,R_3} h_S}{2h_E}, \qquad d = \frac{D_{g,R_1} h_N + D_{g,R_2} h_S}{2h_W}$$

$$e = \frac{\sigma_{g,R_1} h_N h_W + \sigma_{g,R_2} h_S h_W + \sigma_{g,R_3} h_E h_S + \sigma_{g,R_4} h_E h_N}{4}$$

$$s_{g,g'} = \frac{\sigma_{g'\to g,R_1} h_N h_W + \sigma_{g'\to g,R_2} h_S h_W + \sigma_{g'\to g,R_3} h_E h_S + \sigma_{g'\to g,R_4} h_E h_N}{4}$$

$$t_{g'} = \frac{f_{g',R_1} h_N h_W + f_{g',R_2} h_S h_W + f_{g',R_3} h_E h_S + f_{g',R_4} h_E h_N}{4}.$$

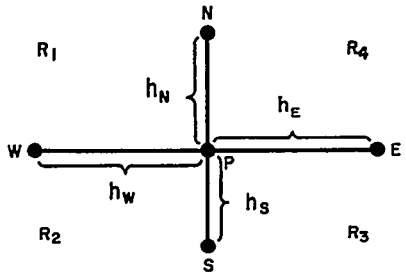

FIGURE 7.1. Schematic Representation of the Standard Five-Point Finite Difference Approximation.

The resulting algebraic equations can be written in the matrix form

$$A_g\vec{\phi}_g = \sum_{g'\neq g} S_{gg'}\vec{\phi}_{g'} + \frac{1}{\lambda}\chi_g \sum_{g'=1}^{G} F_{g'}\vec{\phi}_{g'}, \quad (g = 1, \ldots, G).$$

Eq. (7.2)

Here $\vec{\phi}_g$ is a vector whose components are the approximations for $\phi_g(\vec{r})$ at the N prescribed points in space associated with the finite difference mesh. If the finite difference approximation for $\phi_g(\vec{r})$ at the n^{th} mesh point is defined as $\phi_{g,n}$ then

$$\vec{\phi}_g = \left\{ \phi_{g,1}, \phi_{g,2}, \ldots, \phi_{g,N} \right\}.$$

The $N \times N$ matrix A_g in Eq. (7.2) is obtained by the finite difference technique from the g^{th} group diffusion and total removal terms in Eq. (7.1b). It is assumed that the finite difference technique used is such that A_g is a real positive definite* matrix whose off-diagonal elements are nonpositive and that F_g and $S_{gg'}$ are nonnegative diagonal matrices of order N. It can be shown[8] that the inverse of A_g has all positive elements. Normally, the techniques used are such that the A_g are very sparse, i.e., most of the elements of A_g are zero.

*A matrix A is said to be positive definite if for any nonzero vector $\vec{x}$ with complex coefficients the usual scalar product $\vec{x}^*A\vec{x}$ is positive, where $\vec{x}^*$ is the complex conjugate transpose of $\vec{x}$. It follows from this definition that the eigenvalues of a positive definite matrix are all positive. It also follows from this definition that a positive definite matrix with real elements is symmetric. Physically, A_g in Eq. (7.2) being positive definite means that no matter what the flux shape there will be a net loss of g^{th} group neutrons as a result of diffusion and absorption.

Thus, the discrete problem is to find the fundamental eigenvalue, if one exists, and corresponding eigenvector of Eq. (7.2). Birkhoff and Varga[9] established the result that the eigenvalue problem given by Eq. (7.2), under the conditions specified, possesses such a unique positive, largest (in modulus) fundamental eigenvalue. The eigenvector corresponding to this eigenvalue can be chosen to have positive elements. This eigenvalue and eigenvector correspond to the ones sought for the continuous case given by Eq. (7.1b). As the separation between space points becomes smaller, the assumption is made that the fundamental solution [λ and $\vec{\phi}$] of Eq. (7.2) approaches the solution of Eq. (7.1b).

Some numerical iterative techniques for solving Eq. (7.2) will be examined in the next section.

B. Source Iterations

Equation (7.2) is rewritten in the following matrix form:

$$\lambda M \vec{\Phi} = F \vec{\Phi} \qquad \text{Eq. (7.3)}$$

where

$$M \equiv \begin{pmatrix} A_1 & -S_{12} & \cdots & -S_{1G} \\ -S_{21} & A_2 & \cdots & -S_{2G} \\ \vdots & & & \vdots \\ -S_{G1} & -S_{G2} & \cdots & A_G \end{pmatrix}$$

$$F \equiv \begin{pmatrix} \chi_1 F_1 & \chi_1 F_2 & \cdots & \chi_1 F_G \\ \chi_2 F_1 & \chi_2 F_2 & \cdots & \chi_2 F_G \\ \vdots & & & \vdots \\ \chi_G F_1 & \chi_G F_2 & \cdots & \chi_G F_G \end{pmatrix}$$

Eq. (7.4)

and

$$\vec{\Phi} = \left\{ \vec{\phi}_1, \vec{\phi}_2, \ldots, \vec{\phi}_G \right\} \quad . \qquad \text{Eq. (7.5)}$$

The matrices A_g, $S_{gg'}$, F_g, and the vectors $\vec{\phi}_g$ are those defined in Sect. 7.2.A. It can be shown that M possesses a nonnegative inverse, i.e., all elements of its inverse are nonnegative.[9] Assume for the purposes of this section that this inverse can be easily obtained, and consider Eq. (7.3) in the form

$$M^{-1} F \vec{\Phi} = \lambda \vec{\Phi} .$$

To solve for the largest (in modulus) eigenvalue of such a system, the so-called power method can be used, i.e., given an arbitrary positive guess $\vec{\Phi}^{(o)}$ for $\vec{\Phi}$ one generates successive guesses by means of the iterative process

$$\begin{aligned} \vec{\Theta}^{(t)} &= M^{-1} F \vec{\Phi}^{(t)} \\ \lambda^{(t)} &= \frac{\| \vec{\Theta}^{(t)} \|}{\| \vec{\Phi}^{(t)} \|} \\ \vec{\Phi}^{(t+1)} &= \frac{1}{\lambda^{(t)}} \vec{\Theta}^{(t)} \end{aligned} \qquad \text{Eq. (7.6)}$$

where by $\|\Phi\|$ is meant the Euclidean norm of the vector $\vec{\Phi}$, i.e.,

$$\|\vec{\Phi}\|^2 = \sum_{g,n} (\phi_{g,n})^2 .$$

As a consequence of Birkhoff and Varga's work,[9] it follows that the power iteration method [Eq. (7.6)] is a convergent process and, independent of the initial positive guess $\vec{\Phi}^{(o)}$, converges to the fundamental eigenvalue and eigenvector of Eq. (7.3). Thus, for an arbitrary positive initial vector $\vec{\Phi}^{(o)}$,

$$\lim_{t \to \infty} \lambda^{(t)} = \lambda_o \qquad \lim_{t \to \infty} \vec{\Phi}^{(t)} = \vec{\Phi}_o$$

where λ_o is the fundamental eigenvalue of Eq. (7.3), i.e.,

$$\lambda_o > |\lambda_i| \text{ for } i \neq 0, \qquad \vec{\Phi}_o > 0$$

and

$$M^{-1}F\vec{\Phi}_i = \lambda_i\vec{\Phi}_i \ .$$

In practice, only a finite number of iterations are performed, say T, stopping when it is felt that $\lambda^{(T)}$ is close enough to λ_o. The rate of convergence of the power method, Eq. (7.6), depends on how well separated the fundamental eigenvalue λ_o is from the other eigenvalues of $M^{-1}F$. In other words, the convergence depends directly on the dominance ratio

$$\rho = \max_{i \neq 0} \frac{|\lambda_i|}{\lambda_o}; \qquad \text{Eq. (7.7)}$$

the smaller the ratio, the faster the convergence.[10,11,12]

For many practical problems the dominance ratio may be very close to unity. For example, a reactor composed of two loosely coupled (as far as neutrons are concerned) and otherwise identical fuel regions will have a second eigenvalue close to the fundamental eigenvalue. Besides the obvious trouble such problems will present, i.e., the slow convergence of the process [Eq. (7.6)], another more subtle difficulty occurs. When the process is a slowly converging one, the iterates $\lambda^{(t)}$ and $\vec{\Phi}^{(t)}$ change slowly from one iteration to another. If one pays attention only to the change in $\lambda^{(t)}$, i.e.,

$$\Delta\lambda^{(t)} \equiv |\lambda^{(t+1)} - \lambda^{(t)}| \ ,$$

one might be tempted to assume that $\lambda^{(t)}$ has converged to λ_o when $\Delta\lambda^{(t)}$ is less than some preassigned positive number. $\Delta\lambda^{(t)}$ being less than $\epsilon > 0$ implies very little concerning $\lambda^{(t)} - \lambda_o$. This problem of pseudoconvergence can be handled using other convergence criteria besides the one requiring that $\Delta\lambda^{(t)}$ be small.[7,8]

Since problems with ρ close to unity occur frequently, one is forced to find ways to accelerate the convergence of the

power method [Eq. (7.6)]. One such method is to replace $\vec{\Phi}^{(t)}$ by a linear combination of the initial guess and the first t iterates, $\vec{\Phi}^{(i)}\ (i = 0, \ldots, t)$,

$$\vec{\Psi}^{(t)} = \sum_{p=0}^{t} a_{tp}\, \vec{\Phi}^{(p)} \qquad \text{Eq. (7.8)}$$

as the t^{th} guess of the solution $\vec{\Phi}_o$. By suitable choice of the constants a_{tp}, $p = 0, \ldots, t$, one might be able to get $\vec{\Psi}^{(t)}$ much closer in shape to $\vec{\Phi}_o$ than $\vec{\Phi}^{(t)}$ is.

One can determine near optimum a_{tp} for this problem under the assumption that the eigenvalues of $M^{-1}F$, λ_i are uniformly distributed over their range, are real and nonnegative, and that the corresponding eigenvectors are complete. This last assumption is equivalent to assuming that the arbitrarily chosen initial guess $\vec{\Phi}^{(o)}$ can be expanded in terms of the eigenvectors of $M^{-1}F$, i.e.,

$$\vec{\Phi}^{(o)} = \sum c_i \vec{\Phi}_i \qquad \text{Eq. (7.9)}$$

for some c_i. If it is now assumed that all the eigenvalue estimates $\lambda^{(t)}$, obtained by means of the power method [Eq. (7.6)], are approximately equal to λ_o, then from Eqs. (7.6), (7.8), and (7.9) one obtains

$$\begin{aligned} \vec{\Psi}^{(t)} &\cong \sum c_i \sum_{p=0}^{t} a_{tp} \left(\frac{\lambda_i}{\lambda_o}\right)^p \vec{\Phi}_i \\ &= c_o P_t(1)\, \vec{\Phi}_o + \sum_{i \neq 0} c_i P_t \left(\frac{\lambda_i}{\lambda_o}\right) \vec{\Phi}_i \end{aligned} \qquad \text{Eq. (7.10)}$$

where

$$P_t(z) = \sum_{p=0}^{t} a_{tp}\, z^p .$$

Since $\vec{\Phi}^{(o)}$ is arbitrary, the c_i are arbitrary and, hence, an optimum strategy would be to find a $P_t(z)$ such that $P_t(1) = 1$ and the maximum of $|P_t(z)|$ is minimized over the range $0 \leq z \leq \rho$,

where ρ is the dominance ratio given by Eq. (7.7). The solution to this problem is well known[13] and is given explicitly in terms of Chebyshev polynomials as

$$P_t(z) = \frac{C_t\left(\frac{2}{\rho}z - 1\right)}{C_t\left(\frac{2}{\rho} - 1\right)} \qquad \text{Eq. (7.11)}$$

where the $C_t(x)$ are the Chebyshev polynomials of degree $t \geq 0$

$$C_t(x) = \begin{cases} \cos\left(t \cos^{-1} x\right) & |x| \leq 1 \\ \cosh\left(t \cosh^{-1} x\right) & |x| \geq 1 \end{cases} \qquad \text{Eq. (7.12)}$$

Because of the well-known recurrence relation that the Chebyshev polynomials satisfy

$$C_{t+1}(x) = 2xC_t(x) - C_{t-1}(x) \qquad t \geq 1$$
$$C_1(x) = x; \qquad C_0(x) = 1 \qquad \text{Eq. (7.13)}$$

it is possible to reformulate the extrapolated power method [Eq. (7.8)] in terms of the $\vec{\Psi}^{(t)}$ instead of the $\vec{\Phi}^{(t)}$. One obtains[7]

$$\vec{\Theta}^{(t)} = M^{-1}F\vec{\Psi}^{(t)} \qquad \vec{\Psi}^{(0)} \text{ arbitrary positive vector}$$

$$\lambda^{(t)} = \frac{\|\vec{\Theta}^{(t)}\|}{\|\vec{\Psi}^{(t)}\|}$$

$$\vec{\Psi}^{(t+1)} = \vec{\Psi}^{(t)} + \frac{4}{\rho}\alpha_{t+1}\left(\frac{\vec{\Theta}^{(t)}}{\lambda^{(t)}} - \vec{\Psi}^{(t)}\right) + \beta_{t+1}\left(\vec{\Psi}^{(t)} - \vec{\Psi}^{(t-1)}\right)$$

Eq. (7.14)

where

$$\alpha_1 = \frac{\rho}{2(2-\rho)}, \qquad \beta_1 = 0$$

$$\alpha_{t+1} = \frac{\cosh t\sigma}{\cosh (t+1)\sigma}; \qquad \beta_{t+1} = \frac{\cosh (t-1)\sigma}{\cosh (t+1)\sigma} \quad t \geq 1$$

$$\sigma = \cosh^{-1}\left(\frac{2}{\rho} - 1\right).$$

The method outlined above, the so-called method of Chebyshev extrapolation, requires a knowledge of ρ, the dominance ratio of the problem. In general, this is not known. However, techniques exist for estimating ρ and using this estimate in performing the iterations outlined in Eq. (7.14).[12] One such technique consists in performing several (of the order of 4) iterations using the power method [Eq. (7.6)]. The behavior of the eigenvalue or eigenvector estimates from iteration to iteration is used to estimate the dominance ratio. The iteration method [Eq. (7.14)] may then be used in place of Eq. (7.6) for further iteration. The few beginning iterations with the method of Eq. (7.6) are also useful for assuring that the $\lambda^{(t)}$ will be close to λ_o, thus meeting one of the assumptions necessary to the successful use of Eq. (7.14).

The other assumption that all the eigenvalues are real and nonnegative has not been shown to be valid except for very special cases.[14] However, the method as outlined above is currently being used quite successfully in many programs. This seems to indicate zero (or relatively small) imaginary parts for the eigenvalues.

Another way of accelerating the convergence of the power method as applied to a specific problem would be to reduce the dominance ratio associated with the problem. One method for accomplishing this is the following: Let λ_e be an approximation to λ_o satisfying $\lambda_e > \lambda_o$. Then rewrite Eq. (7.3) as

$$\left(M - \frac{1}{\lambda_e} F\right)\vec{\Phi} = \left(\frac{1}{\lambda} - \frac{1}{\lambda_e}\right) F\vec{\Phi} \,. \qquad \text{Eq. (7.15)}$$

One can apply the power method to this equation when it is rewritten in the form

$$\mu\vec{\Phi} = \left(M - \frac{1}{\lambda_e} F\right)^{-1} F\vec{\Phi}$$

where μ is defined by

$$\frac{1}{\mu} = \frac{1}{\lambda} - \frac{1}{\lambda_e} .$$

One obtains the iterative process

$$\vec{\Theta}^{(t)} = \left(M - \frac{1}{\lambda_e} F\right)^{-1} F \vec{\Phi}^{(t)}$$

$$\mu^{(t)} = \frac{\|\vec{\Theta}^{(t)}\|}{\|\vec{\Phi}^{(t)}\|} \qquad \text{Eq. (7.16)}$$

$$\vec{\Phi}^{(t+1)} = \frac{1}{\mu^{(t)}} \vec{\Theta}^{(t)} .$$

As $\lambda_e \to \infty$ Eq. (7.16) becomes Eq. (7.6). As with Eq. (7.6) it can be shown[15,16] that as long as $\lambda_e > \lambda_o$ and $\vec{\Phi}^{(o)} > \vec{0}$, Eq. (7.16) defines a convergent iterative process and

$$\lim_{t \to \infty} \frac{1}{\mu^{(t)}} = \frac{1}{\mu_o} = \frac{1}{\lambda_o} - \frac{1}{\lambda_e} ; \qquad \lim_{t \to \infty} \vec{\Phi}^{(t)} = \vec{\Phi}_o .$$

The dominance ratio associated with this method is given by

$$\rho = \max_{i \neq 0} \frac{\frac{1}{\lambda_o} - \frac{1}{\lambda_e}}{\left| \frac{1}{\lambda_i} - \frac{1}{\lambda_e} \right|} .$$

and with $\lambda_e > \lambda_o$ one has

$$\rho \leq \max_{i \neq 0} \frac{\frac{1}{\lambda_o} - \frac{1}{\lambda_e}}{\left| \frac{1}{\lambda_i} \right| - \frac{1}{\lambda_e}} < \max_{i \neq 0} \frac{|\lambda_i|}{\lambda_o}$$

so that this method for $\lambda_o < \lambda_e < \infty$ is an improvement over the regular power method ($\lambda_e = \infty$). In general, even the crudest guess at λ_o reduces the dominance ratio considerably. The iteration scheme defined by Eq. (7.16) is, in essence, Wielandt's inverse power method.[16]

The only possible drawback to using Eq. (7.16) rather than Eq. (7.6) is that perhaps $M - \frac{1}{\lambda_e} F$ is much more troublesome to invert than is M. For one-dimensional few-group calculations such is not the case, and Eq. (7.16) has been used successfully.[15,17] The method may also be applied to three-dimensional problems with few points in planes perpendicular to one axis. Such reactor calculation models are used in flux synthesis techniques. In two- and three-space dimensional problems, direct inversion of $M - \frac{1}{\lambda_e} F$ (or, for that matter, M) is impractical and, as will be seen in the next section, iterative techniques are used in performing the first step in the power methods of Eqs. (7.6) and (7.16). The use of a finite λ_e makes the iterative scheme used for the approximation of $\left(M - \frac{1}{\lambda_e} F\right)^{-1} F\vec{\Phi}$ more complicated and, in general, will reduce its rate of convergence. Thus, whatever gains are obtained in reducing the iterations in $\vec{\Phi}^{(t)}$ by using Eq. (7.16) rather than Eq. (7.6) may be vitiated by the increase in the work necessary to perform the equivalent of inverting $M - \frac{1}{\lambda_e} F$ rather than M.

In this section it has been assumed that direct inversions of M are possible. For most two- and three-dimensional problems, however, direct inversions of M are not feasible, so that the equations $M\vec{\Theta}^{(t)} = F\vec{\Phi}^{(t)}$ must be solved for $\vec{\Theta}^{(t)}$ by some iterative process. The source iterations described in this section are called outer iterations and the iterations used to obtain an approximation to $\vec{\Theta}^{(t)}$ are called inner iterations. The term strategy is applied to the interrelationship between inner and outer iterations. An optimum strategy between inner and outer iterations is that which will minimize the computer running time required to solve the problem. The general problem of strategy appears to be very complex and will not be explored in this volume.

The iterative techniques currently in use to obtain an approximation to $\vec{\Theta}^{(t)}$ are described in the next section.

C. Solution of the Group Equations

As mentioned previously, in two and three dimensions, when the power method of Eq. (7.6) is used, direct inversion of M for use in Eq. (7.6) or Eq. (7.14)

$$\vec{\Theta}^{(t)} = M^{-1} F \vec{\Phi}^{(t)}$$

is not practical. In some problems the order of M may be as high as 50,000. For this reason, iterative techniques will be examined for solving the equation

$$M\vec{\Theta}^{(t)} = F\vec{\Phi}^{(t)}$$

for $\vec{\Theta}^{(t)}$. When there is no up-scattering permitted in the reactor model, $S_{gg'} = 0$ for $g < g'$ (see Eq. (7.4) for definition of $S_{gg'}$). In this case, M is lower block diagonal and, consistent with the notation in Eq. (7.4),

$$M = \begin{pmatrix} A_1 & 0 & \cdots & 0 \\ -S_{21} & A_2 & \cdots & 0 \\ \cdot & \cdot & & \cdot \\ \cdot & \cdot & & \cdot \\ \cdot & \cdot & & \cdot \\ -S_{G1} & -S_{G2} & \cdots & A_G \end{pmatrix}$$

so that the equation $M\vec{\Theta}^{(t)} = F\vec{\Phi}^{(t)}$ may be solved for $\vec{\Theta}^{(t)}$ by solving successively the system of group equations

$$\left\{ A_g \vec{\Theta}_g^{(t)} = \sum_{g' < g} S_{g,g'} \vec{\Theta}_{g'}^{(t)} + X_g \sum_{g'=1}^{G} F_{g'} \vec{\Phi}_{g'}^{(t)} \right\}_{g=1}^{G}$$

Eq. (7.17)

Thus, in solving $M\vec{\Theta}^{(\iota)} = F\vec{\Phi}^{(\iota)}$ for $\vec{\Theta}^{(\iota)}$ one encounters equations of the form

$$A\vec{\phi} = \vec{k} \qquad \text{Eq. (7.18)}$$

where A represents one of the A_g in the definition of M, and $\vec{\varphi}$ and $\vec{k}$ are vectors of order N, the number of space points in the finite difference mesh. For these problems A is positive definite, has diagonal dominance, and its off-diagonal elements are nonpositive.[8]

First, a short discussion on the mechanics of iterative techniques for solving Eq. (7.18) will be given. Starting with an initial guess, $\vec{\varphi}^{(o)}$, of the solution of Eq. (7.18), procedures for determining an infinite sequence of vectors $\vec{\varphi}^{(\iota)}$, $(\iota = 1, 2, \ldots)$, which will tend to the unique solution $\vec{\varphi}$ will be examined.

A single step iterative process is one in which the iterates $\vec{\varphi}^{(\iota)}$ are related by

$$P_\iota\vec{\varphi}^{(\iota)} = (P_\iota - A)\vec{\varphi}^{(\iota-1)} + \vec{k} \qquad (\iota = 1, 2, \ldots)$$

Eq. (7.19)

for some matrices P_ι, $(\iota = 1, 2, \ldots)$.[18] In order that Eq. (7.19) be useful, it is necessary that it can be solved easily for $\vec{\Phi}^{(\iota)}$. Thus, it is reasonable to require that the P_ι be easily invertible. The case where $P_\iota = P$ for all ι is called a stationary single-step iterative process. If $\vec{\phi}$ is the unique solution of Eq. (7.18), one defines the error vector after ι steps as $\vec{E}^{(\iota)} = \vec{\varphi}^{(\iota)} - \vec{\phi}$. Then from Eqs. (7.18) and (7.19) one finds that

$$\vec{E}^{(\iota)} = \left[I - P_\iota^{-1}A\right]\vec{E}^{(\iota-1)}$$

$$= \prod_{k=1}^{\iota}\left[I - P_k^{-1}A\right]\vec{E}^{(o)} \qquad \text{Eq. (7.20)}$$

where $\vec{E}^{(o)} = \vec{\varphi}^{(0)} - \vec{\phi}$. By convergence of the iterative process Eq. (7.19) it is meant that $\|\vec{E}^{(\iota)}\|$ approaches zero as ι grows, where $\|\vec{E}^{(\iota)}\|$ is the usual Euclidean norm of the error vector

$\vec{E}^{(t)}$ defined earlier. One way to ensure convergence of the process governed by Eq. (7.19) is to require the existence of a $T_o \geq 0$ such that $\|\vec{E}^{(t)}\| < \|\vec{E}^{(t-1)}\|$ for all $t > T_o$. From Eq. (7.20) one has

$$\|\vec{E}^{(t)}\| = \|\left[I - P_t^{-1} A\right] \vec{E}^{(t-1)}\| .$$

From the definition of the Euclidean norm it follows[11] that for any matrix B and any vector $\vec{x}$

$$\|B\vec{x}\| \leq \|B\|_s \|\vec{x}\|$$

where $\|B\|_s$, called the spectral norm of B, is the positive square root of the largest eigenvalue of B^*B (B^* is the complex conjugate transpose of B). From this and the equation above it follows that

$$\|\vec{E}^{(t)}\| \leq \|I - P_t^{-1} A\|_s \|\vec{E}^{(t-1)}\|$$

Hence, convergence of the iterative process given by Eq. (7.19) is guaranteed if there exists a T_o such that $\|I - P_t^{-1} A\|_s < 1$ for all $t > T_o$.

Clearly, for a given set of Eq. (7.18), one would like to know what optimum $P_t, (t = 1, 2, \ldots)$ to use in Eq. (7.19). By optimum is meant that set of $P_t, (t = 1, 2, \ldots)$, all easily invertible, which cause $\|\vec{E}^{(t)}\|$ to drop below some preassigned small value for as low a value of t as possible. This general problem has no easy solution. For a more tractable problem and one in which analysis can be used to ensure certain convergence rates, restriction to stationary processes might be imposed.* In this case, Eqs. (7.19) and (7.20) become

$$P\vec{\varphi}^{(t)} = [P - A]\vec{\varphi}^{(t-1)} + \vec{k}$$

$$\vec{E}^{(t)} = [I - P^{-1} A]^t \vec{E}^{(o)} \qquad \text{Eq. (7.21)}$$

*Note that an iterative process where the $P_t (t = 1, 2, \ldots)$ repeat in some cyclic fashion, i.e., $P_{t+k} = P_t (t = 1, 2, \ldots)$ for some fixed k, can be stated in terms of a stationary process by considering a cycle as a single step.

A necessary and sufficient condition that a stationary single-step iterative process converge (i.e., that $\vec{E}^{(t)}$ tends to the null vector) is that the eigenvalues of $I - P^{-1} A$ be less than unity in magnitude.[11] The spectral radius $\bar{\mu}(B)$ of an arbitrary matrix B is defined as the magnitude of the eigenvalue of B of largest modulus. Clearly, then, a necessary and sufficient condition that a stationary single-step iterative process be convergent is that $\bar{\mu}[I - P^{-1} A] < 1$. Also note that $\bar{\mu}(B) \leq \| B \|_s$ for any B, equality holding for B symmetric.

The spectral radius of $I - P^{-1}A$, $\bar{\mu}[I - P^{-1} A]$, can also be used as a measure of the effectiveness of the process, the smaller the $\bar{\mu}$ the faster the process will converge. The asymptotic rate of convergence of a stationary iterative process is defined as

$$R[I - P^{-1} A] \equiv - \ln \bar{\mu}\ [I - P^{-1} A] \qquad \text{Eq. (7.22)}$$

The significance of this definition is that the number of iterations required to reduce the norm of the error vector to a prespecified fraction of the norm of the initial error vector is approximately (in a certain asymptotic sense) inversely proportional to the asymptotic rate of convergence.[19] Thus, if one process has an asymptotic rate of convergence twice as big as another, it will require roughly half as many iterations for the same degree of convergence.

Some particular iterative processes currently in use will now be examined with the intention of comparing their asymptotic rates of convergence.

If P_o is the diagonal part of A then the simplest scheme would be to take $P = P_o$. This scheme will be referred to as point relaxation. Since the matrix A in Eq. (7.18) is positive definite and has diagonal dominance, it follows[6] that point relaxation for these equations will always converge. The asymptotic rate of convergence is given by Eq. (7.22) with $P = P_o$.

One can accelerate the convergence by use of block relaxation.[20] Assume that Eq. (7.18) is the result of the usual five-point finite difference approximation for Eq. (7.1b).[8] Assume further that the problem is being solved in a rectangular region (approximately square) and that the boundary conditions are of the usual Dirichlet type. Then one may consider various partitionings and resulting choices of P for A. Let

P_1 be the diagonal block matrix corresponding to the partitioning of A into blocks corresponding to mesh points on a single horizontal mesh line. Thus, one can write

$$A = \begin{bmatrix} A_{11} & A_{12} & & & \\ A_{21} & A_{22} & A_{23} & & 0 \\ & \ddots & \ddots & \ddots & \\ & 0 & & \ddots & A_{M-1,M} \\ & & A_{M,M-1} & & A_{MM} \end{bmatrix}$$

$$P_1 = \begin{bmatrix} A_{11} & & & \\ & A_{22} & & 0 \\ & & \ddots & \\ & 0 & & A_{MM} \end{bmatrix} \qquad \text{Eq. (7.23)}$$

where the A_{ii} $(i = 1, \ldots, M)$ are square and $A_{i,i+1} = A_{i+1,i}$ correspond to the coupling between points on mesh line i and mesh line $i+1$. Let P_2 be the diagonal block matrix corresponding to the partitioning of the matrix A into blocks corresponding to blocks of mesh points on successive pairs of horizontal mesh lines. The iterative technique associated with P_o is point relaxation, (PR); that associated with P_1 is called line relaxation, (LR); and that associated with P_2 is called double-line relaxation, (2LR). It can be shown[21] that the line relaxation methods converge. For the numerical solution of the Dirichlet problem on the unit square with uniform mesh spacing $h = 1/N$, the asymptotic rates of convergence of these schemes for small h can be approximately tabulated[6,22] as shown in Table 7.2.*

*For small h, $r \sim \pi^2 h^2/2$.

TABLE 7.2 — ASYMPTOTIC RATES OF CONVERGENCE FOR SMALL h

	PR	LR	2LR
R	r	2r	4r

The numerical work associated with inverting P_1 and P_2 may be larger than that associated with inverting P_o. However, effective methods currently available for inverting tridiagonal and similar matrices allow the LR iterations to be performed in roughly the same time as PR iterations, and 2LR iterations in roughly 20 percent more time than the PR iterations.[21] Thus, one is assured gains in going to line relaxation wherever it is applicable.*

Once a particular partitioning of A has been decided upon, i.e., a particular P chosen, there are ways of improving upon the convergence of the iterative scheme [Eq. (7.21)] associated with it. Assume that matrix A can be written in the form

$$A = P - (R + R^T) \qquad \text{Eq. (7.24)}$$

where R^T is the usual transpose of R. (Note that this requires P to be symmetric, a condition that is satisfied by P_o, P_1, and P_2.) Assume also that $\overline{\mu}\,[P^{-1}(R + R^T)] < 1$. The relaxation equations then have the form

$$P\vec{\phi}^{(t)} = (R + R^T)\vec{\phi}^{(t-1)} + \vec{k} \qquad (t = 1, 2, \ldots) \ .$$

Overrelaxation or extrapolation consists of the following iterative scheme

$$(P - \omega R)\vec{\phi}^{(t)} = (1 - \omega) P\vec{\phi}^{(t-1)} + \omega (R^T \vec{\phi}^{(t-1)} + \vec{k}) \qquad (t = 1, 2, \ldots)$$

Eq. (7.25)

*As examples, see the PDQ and FLEER programs in Sect. 7.4.

for some constant ω, as yet to be determined. Note that it is desirable for $P - \omega R$ to be readily invertible. One way of accomplishing this for A is to take R to be the strictly lower triangular matrix formed by deleting from $P - A$ the upper triangular elements. Since A is symmetric, Eq. (7.24) is applicable.

If, as before, one defines the error in the t^{th} step of Eq. (7.25) to be

$$\vec{E}^{(t)} = \vec{\phi}^{(t)} - \vec{\phi}$$

where $\vec{\phi}$ is the unique solution of $A\vec{\phi} = \vec{k}$, then successive errors are related by

$$\vec{E}^{(t)} = \mathfrak{L}_\omega \vec{E}^{(t-1)} \qquad \text{Eq. (7.26)}$$

$$\mathfrak{L}_\omega = (I - \omega P^{-1}R)^{-1}\,[\omega P^{-1}R^T + (1-\omega)I]\,.$$

If $P^{-1}R$ is a strictly lower triangular matrix, then by considering the determinant of $\mathfrak{L}_\omega$, one may easily show that $\bar{\mu}(\mathfrak{L}_\omega) \geq |\omega - 1|$ for all real ω,[23] so that overrelaxation diverges for $\omega \leq 0$ and $\omega \geq 2$. If P is positive definite, it can be shown [18,24] that the method converges for $0 < \omega < 2$. For the case when $P = P_0$, the method is called successive overrelaxation (SOR);[19] for $P = P_1$, successive line overrelaxation (SLOR); for $P = P_2$, successive two-line overrelaxation (S2LOR).[21]

For $\omega = 1$, Eq. (7.25) reduces to

$$P\vec{\phi}^{(t)} = R\vec{\phi}^{(t)} + R^T\vec{\phi}^{(t-1)} + \vec{k} \qquad (t = 1, 2, \ldots)\,.$$

Thus, if R is a strictly lower triangular matrix, as an iteration proceeds the latest calculated values of the unknowns are used. This method is sometimes referred to, for historical reasons, as a Gauss-Seidel method.[25]

Under certain conditions, which will be presently defined, the optimum ω (in the sense of maximum asymptotic rate of convergence) for use in Eq. (7.25) can be determined.

For reasons of brevity*, it will be said that the matrix $P^{-1}(R+R^T)$ is cyclic of index 2 and is consistently ordered if it can be written as

$$P^{-1}(R+R^T) = \begin{pmatrix} 0 & C_1 \\ C_2 & 0 \end{pmatrix} \qquad \text{Eq. (7.27)}$$

where the null diagonal submatrices are square. With the concept of a consistent ordering for a matrix which is cyclic of index 2, Young[19] showed that the eigenvalues λ of $\mathfrak{L}_\omega$ and μ of $P^{-1}(R+R^T)$ are related by

$$(\lambda+\omega-1)^2 = \lambda\omega^2\mu^2$$

and that the optimum, ω_b, is given by

$$\omega_b = \frac{2}{1+\sqrt{1-\bar{\mu}^2\,[P^{-1}(R+R^T)]}} \,. \qquad \text{Eq. (7.28)}$$

The corresponding asymptotic rate of convergence is $-\ln(\omega_b-1)$.[6] If r is the asymptotic rate of convergence of the relaxation scheme [Eq. (7.21)] without overrelaxation, then it can be shown that the rate of convergence of $\mathfrak{L}(\omega_b)$ is approximately given by

$$R(\mathfrak{L}_\omega) \sim 2\sqrt{2}\,\sqrt{r} \,. \qquad \text{Eq. (7.29)}$$

For large scale problems (i.e., problems with a fine finite difference mesh) it follows from Eq. (7.29) that overrelaxation can be considerably faster than relaxation. The improvement is especially evident when the asymptotic rate of convergence of the relaxation scheme [Eq. (7.21)] is very small.

*The class of matrices which is cyclic of index 2 and is consistently ordered is much larger than that given here. For a more detailed discussion of cyclic matrices and consistent orderings the reader is referred to Refs. 6, 8, 19, and 20.

An estimate of ω_b can be obtained by using the power method (as outlined in Sect. 7.2.B) on the matrix $P^{-1}(R+R^T)$ for enough iterations to obtain an approximation for $\bar{\mu}[P^{-1}(R+R^T)]$.[6,26,27,28]

If $P^{-1}(R+R^T)$ is not cyclic of index 2 or is not consistently ordered, overrelaxation may still be used, but in general a precise formula for the optimum value of ω is not known. However, if P is a positive definite matrix with nonpositive off-diagonal elements and if R is a nonnegative matrix, then with ω_b [defined by Eq. (7.28)] used for ω it can be shown that

$$\bar{\mu}(\mathfrak{L}_{\omega_b}) \leq \sqrt{\omega_b - 1} \qquad \text{Eq. (7.30)}$$

The importance of Eq. (7.30) is that it gives a lower bound on the asymptotic rate of convergence for the successive overrelaxation method when $P^{-1}(R+R^T)$ is not cyclic of index 2 or is not consistently ordered.

Another method for extrapolating the relaxation results is based on the Chebyshev extrapolation method explained in Sect. 7.2.B as it is used in source iterations. Consider the relaxation equation written as

$$P\vec{\phi}^{(t)} = (R+R^T)\vec{\phi}^{(t-1)} + \vec{k} \qquad (t = 1, 2, \ldots) \qquad \text{Eq. (7.31)}$$

for some arbitrary initial vector $\vec{\phi}^{(o)}$. To accelerate the convergence of this method consider in place of the $\vec{\phi}^{(t)}$ linear combinations of them, i.e.,

$$\vec{\Psi}^{(t)} = \sum_{s=o}^{t} a_{ts}\,\vec{\phi}^{(s)}, \qquad \sum_{s=o}^{t} a_{ts} = 1 \ . \qquad \text{Eq. (7.32)}$$

As in Sect. 7.2.B, if one considers expansions of the error vector $\vec{E}^{(t)} = \vec{\Psi}^{(t)} - \vec{\phi}$ in terms of the eigenvectors $\vec{u}_\sigma$ of $P^{-1}(R+R^T)$,

$$\vec{E}^{(t)} = \sum c_\sigma^{(t)} \vec{u}_\sigma$$

it is seen that

$$c_\sigma^{(t)} = Q_t(\lambda_\sigma)\, c_\sigma^{(o)}$$

where

$$Q_t(x) = \sum_{s=o}^{t} a_{ts}\, x^s \qquad \text{Eq. (7.33)}$$

and

$$P^{-1}(R + R^T)\,\vec{u}_\sigma = \lambda_\sigma \vec{u}_\sigma \,.$$

Assuming no control over the $c_\sigma^{(o)}$, i.e., the initial error vector's dependence on the eigenvectors of $P^{-1}(R + R^T)$, it is seen that an excellent choice for the a_{ts} would be to take them such that the maximum modulus of $Q_t(x)$ over the range of eigenvalues of $P^{-1}(R + R^T)$ is a minimum. The solution to this problem is to take the a_{ts} $(s = o, \ldots, t)$ such that $Q_t(x)$ becomes

$$Q_t(x) = \frac{C_t(x/\bar{\mu})}{C_t(1/\bar{\mu})} \qquad (t = 1, 2, \ldots) \qquad \text{Eq. (7.34)}$$

where $\bar{\mu}$ is the spectral radius of $P^{-1}(R + R^T)$ and $C_t(z)$ is the Chebyshev polynomial of degree t. Since the Chebyshev polynomials satisfy a recurrence relationship, one can also be derived for the $\vec{\Psi}^{(t)}$ in Eq. (7.32). It can be written as

$$P\vec{\Psi}^{(t)} = \omega_t \left[(R + R^T)\vec{\Psi}^{(t-1)} + \vec{k} - P\vec{\Psi}^{(t-2)}\right] + P\vec{\Psi}^{(t-2)} \qquad t \geq 2$$

$$\omega_t = \frac{1}{1 - \dfrac{\omega_{t-1}}{4}\bar{\mu}^2} \qquad (t \geq 3)$$

$$\omega_2 = \frac{2}{2 - \bar{\mu}^2}$$

Eq. (7.35)

These relations are to be used in place of Eqs. (7.31) and (7.32) after $\vec{\Psi}^{(1)} \equiv \vec{\phi}^{(1)}$ is calculated.[29] Note that $\lim_{i \to \infty} \omega_i = \omega_b$, the optimum ω for use in overrelaxation. Because of this result, it turns out that the asymptotic rate of convergence of this method is

$$R(C) \cong \sqrt{2} \sqrt{r} \qquad \text{Eq. (7.36)}$$

where r is the asymptotic rate of convergence of the relaxation scheme [Eq. (7.31)]. Equation (7.30) shows that this is the lower bound of the asymptotic rate of convergence of the overrelaxation scheme. Thus, in general, extrapolation applied to the relaxation scheme is better than the Chebyshev extrapolation scheme.

If $P^{-1}(R + R^T)$ is of the form of Eq. (7.27), then overrelaxation is apparently twice as fast as Chebyshev extrapolation [see Eq. (7.29)]. However, in this case, special formulas for use in the Chebyshev extrapolation scheme making use of the special form of $P^{-1}(R + R^T)$ are available. The asymptotic rate of convergence for the two methods are then the same, but Golub and Varga[30] have shown, using spectral norms as a basis for comparison, the Chebyshev method to be superior.

The special form of $P^{-1}(R + R^T)$ in Eq. (7.27) may be exploited even further. With $A = P - (R + R^T)$, Eq. (7.18) may be written as

$$[I - P^{-1}(R + R^T)]\vec{\phi} = P^{-1}\vec{k} \qquad \text{Eq. (7.37)}$$

which may be expressed, assuming now that $P^{-1}(R + R^T)$ is in the form of Eq. (7.27), as

$$\begin{pmatrix} I_{1,1} & -C_1 \\ -C_2 & I_{2,2} \end{pmatrix} \begin{pmatrix} \vec{\phi}_1 \\ \vec{\phi}_2 \end{pmatrix} = \begin{pmatrix} \vec{g}_1 \\ \vec{g}_2 \end{pmatrix} \qquad \text{Eq. (7.38)}$$

where $I_{1,1}$ and $I_{2,2}$ are, respectively, the p by p and q by q identity matrices with $p + q = N$, $P^{-1}\vec{k} = \begin{pmatrix} \vec{g}_1 \\ \vec{g}_2 \end{pmatrix}$, and $\vec{\phi} = \begin{pmatrix} \vec{\phi}_1 \\ \vec{\phi}_2 \end{pmatrix}$.

If Eq. (7.38) is premultiplied by the matrix

$$\begin{pmatrix} I_{1,1} & C_1 \\ C_2 & I_{2,2} \end{pmatrix},$$

one obtains

$$\begin{pmatrix} I_{1,1} - C_1 C_2 & 0 \\ 0 & I_{2,2} - C_2 C_1 \end{pmatrix} \begin{pmatrix} \vec{\varphi}_1 \\ \vec{\varphi}_2 \end{pmatrix} = \begin{pmatrix} I_{1,1} & C_1 \\ C_2 & I_{2,2} \end{pmatrix} \begin{pmatrix} \vec{g}_1 \\ \vec{g}_2 \end{pmatrix}. \qquad \text{Eq. (7.39)}$$

Equation (7.39) is called the cyclic reduction of the matrix equation [Eq. (7.38)] by Varga.[6] Matrix Eq. (7.39) represents two uncoupled systems of equations, so that the solution to the original matrix problem given by Eq. (7.37) may be obtained by solving a lower order matrix equation. For example, the solution to Eq. (7.37) may be determined by first solving the reduced system of q equations

$$(I_{2,2} - C_2 C_1)\vec{\varphi}_2 = \vec{g}_2 + C_2 \vec{g}_1 \qquad \text{Eq. (7.40)}$$

and then obtaining the remaining p unknowns explicitly from

$$\vec{\varphi}_1 = C_1 \vec{\varphi}_2 + \vec{g}_1 . \qquad \text{Eq. (7.41)}$$

Hence, the number of unknowns which must be determined by an iterative process has been reduced from $(p + q)$ to q. If P is taken to be the main diagonal of A, then the matrix $I_{2,2} - C_2 C_1$ may be explicitly determined, and one is free to use any of the previously described iterative methods on the cylically reduced system of Eq. (7.40).

If Eq. (7.18) is obtained from the usual five-point finite difference approximation for Eq. (7.1b) in two dimensions, then it can be shown[31] that the asymptotic rate of convergence of the S2LOR method applied to the cyclically reduced system [Eq. (7.40)] is greater than that of the S2LOR method applied

to the original system [Eq. (7.18)]. Furthermore, each iteration on the original system requires 40 percent more computer time than does each iteration on the cyclically reduced system. The successive three-line overrelaxation (S3LOR) method may also be used very efficiently on the cyclically reduced system.[31]

Besides the extrapolation methods, one other family of iterative techniques is currently being used. These are the implicit alternating direction methods (IAD).[32-38] A description of an extension of one of these, the Peaceman-Rachford method follows.[38] It is assumed, in this method, that A can be written as

$$A = H + V + B \qquad \text{Eq. (7.42)}$$

where H, V, and B are symmetric and nonnegative definite. For two-dimensional diffusion calculations, this can be accomplished, for example, by taking H, V, and B to be the symmetric finite difference analogues of the operators $-\frac{\partial}{\partial x} D \frac{\partial}{\partial x}$, $-\frac{\partial}{\partial y} D \frac{\partial}{\partial y}$, and Σ_a, respectively. The boundary conditions assumed in the introduction give assurance that H an V are nonnegative definite.

Consider the following iterative scheme for solving $A\vec{\phi} = \vec{k}$:

$$\vec{\phi}^{(t-1/2)} = -(H + B + \omega_t I)^{-1}\left[(V - \omega_t I)\vec{\phi}^{(t-1)} - \vec{k}\right] \qquad (t = 1, 2, \ldots)$$

$$\vec{\phi}^{(t)} = -(V + B + \omega_t I)^{-1}\left[(H - \omega_t I)\vec{\phi}^{(t-1/2)} - \vec{k}\right]$$

Eq. (7.43)

where $\vec{\phi}^{(o)}$ is an arbitrary initial guess. It can be shown that the method will converge to the solution of $A\vec{\phi} = \vec{k}$ when the ω_t are independent of t, $\omega_t = \omega$, for any positive ω. For the general problem, there is no formula similar to Eq. (7.28) for calculating the optimum iteration-independent ω. Thus, no general statement can be made comparing this version of IAD and SOR. However, for a large homogeneous square problem with little absorption, the asymptotic rate of convergence of this method will be approximately $2\sqrt{2}\sqrt{r}$ where r is the asymptotic rate of convergence of point relaxation as is given in Table 7.2.

When the matrices H, V, and B commute with one another (as is the case for a homogeneous rectangular problem with zero flux boundary conditions), excellent convergence can be obtained by varying the ω's used in Eq. (7.43).[38] The optimum ω_t (assuming a uniform spread of eigenvalues of H and V over

an interval to the right of the origin) can be determined.[37] Using these, the implicit alternating direction method has an asymptotic rate of convergence $R_{IAD} \cong -c/\ln r$, for some constant c of order magnitude unity, where r is the asymptotic rate of convergence of the point relaxation method.

In Table 7.3 are given the asymptotic rates of convergence for the various methods described above in the numerical solution of the Dirichlet problem in a square domain with small uniform mesh spacing. As in Table 7.2, r is the asymptotic rate of convergence of the point relaxation method. If n is the number of iterations required to reduce the Euclidean norm of the initial error vector of the point relaxation method to a prespecified amount, then the corresponding number of iterations required by the other methods is given in the second row of Table 7.3.

For large homogeneous problems the savings with implicit alternating direction methods can be very large. For the general problem likely to be encountered in two-dimensional neutron diffusion, the matrices H, V, and B do not commute, and care must be exercised when using iteration number dependent ω_t. The convergence properties based on the commutation of the matrices may be destroyed and divergence may even ensue. While the analysis of IAD for the general problem has not been completed, the method has proved successful for a large variety of reactor problems.[38]

D. The Time-Dependent Problem

So far, only time-independent problems have been considered, seeking a steady-state solution to the diffusion equations. Occasionally, there is need for solutions to time-dependent problems. A few problems of this form can be solved by using existing programs and methods outlined earlier for the steady-state problems.

One such problem is the calculation of the asymptotic behavior of a reactor system after an initial pulsing. If the same finite differencing method in space is used on Eq. (7.1) that was used on Eq. (7.1b) to obtain Eq. (7.3), one obtains

$$(M-F)\vec{\Phi}(t) = -V\frac{\partial\vec{\Phi}(t)}{\partial t} \qquad \text{Eq. (7.44)}$$

where M and F are the matrices appearing in Eq. (7.3) and V is a diagonal matrix of reciprocal group velocities. The problem then is given $\vec{\Phi}(o)$ find $\vec{\Phi}(t)$ for large t. It can be shown that asymptotically

$$\vec{\Phi}(t) \sim ae^{\omega_o t}\vec{\Phi}_o \qquad \text{Eq. (7.45)}$$

TABLE 7.3 — ASYMPTOTIC RATES OF CONVERSION IN THE NUMERICAL SOLUTION OF THE DIRICHLET PROBLEM IN A SQUARE DOMAIN WITH SMALL UNIFORM MESH SPACING

	Point Relaxation	S2LOR with $\omega = \omega_b$	S3LOR Applied to Cyclically Reduced System With $\omega = \omega_b$	IAD Optimum Constant ω	IAD Optimum Varying ω_t
R	r	$4\sqrt{2}\sqrt{r}$	$5.47\sqrt{2}\sqrt{r}$	$2\sqrt{2}\sqrt{r}$	$-\frac{c}{\ln r}$
N	n	$\frac{1}{4\sqrt{2}}\sqrt{r}\,n$	$\frac{1}{5.47\sqrt{2}}\sqrt{r}\,n$	$\frac{1}{2\sqrt{2}}\sqrt{r}\,n$	$-\frac{r\ln r}{c}\,n$

where $\vec{\Phi}_o$ and ω_o are the eigensolutions to the eigenvalue problem

$$(M - F)\vec{\Phi}_j = -\omega_j V\vec{\Phi}_j \qquad (j = 0, 1, \ldots) \qquad \text{Eq. (7.46)}$$

for which $\omega_o > Re\,\omega_j$ $(j \neq 0)$ and for which $\vec{\Phi}_o$ may be taken as normalized and as having all positive elements.[39]

For one-space dimensional problems, there are programs available for solving for ω_o. For higher dimensions, there are no programs currently available for solving directly for ω_o. The time-independent programs, where the solution is for λ_o,

$$(\lambda_i M - F)\vec{\Phi}_i = 0 \ , \qquad \text{Eq. (7.47)}$$

can be used for solving for ω_o. The following iterative scheme can be used:

1. With a guess ω_e for ω_o, substitute $M + \omega_e V$ for M in Eq. (7.47).
2. Use the available programs for solving Eq. (7.47) with the new M, and call the resulting largest eigenvalue $\lambda_o(\omega_e)$.
3. If $\lambda_o|(\omega_e) = 1$, then $\omega_e = \omega_1$; and if $\lambda_o(\omega_e) \gtrless 1$, then $\omega_e \lessgtr \omega_o$.
4. Using this information, form another guess for ω_o by interpolation, or by some other means, and repeat steps 1 to 4 until ω_o is known to some preassigned accuracy.

It can be shown that this process will converge provided the initial guess for ω_o is not too much smaller than ω_o.

7.3 THE MATHEMATICS OF MONTE CARLO FOR REACTOR CALCULATION

J. Spanier

A. Introduction

The term Monte Carlo method refers to any calculation which involves the use of random sampling in at least some of its stages. More precisely one has in mind an experiment of some kind: By repeatedly drawing samples according to the probability laws which describe the experiment and by collecting statistical data on the sample population one is able to estimate values of parameters associated with the parent population. In

particle transport problems, with which this section is concerned, the experiment is described by the transport equation. This equation embodies the behavior of an idealized average system of particles in a certain environment. Monte Carlo methods applied to such problems involve the examination of a large number of random walks in phase space undergone by typical particles in order to predict the behavior of the aggregate as a whole. The range of problems solved by such methods is as diverse as transport theory itself, and the number of sampling procedures one can imagine to solve these problems is equally broad. It would seem appropriate, therefore, to attempt to describe Monte Carlo methods from a unified mathematical point of view. The hope in such an undertaking is to uncover the fundamental concepts common to most or all Monte Carlo sampling methods, at least as they apply to the solution of particle transport problems. Once these fundamental ideas are understood it is easier to generalize results and to explain why the better devices work more efficiently than the poorer ones. The object of this section is to outline such a unified approach. Applications of some of these ideas to the creation of Monte Carlo programs have previously been discussed in Chap. 3, Sect. 3.5.

It should be emphasized here that the task of deciding, for a given problem, which of several variance reduction techniques to use is not easily solved. This is because it is very difficult to obtain a priori estimates of the variance and also because a technique which may work well for one problem may actually increase the variance in another problem. Frequently, many variance reduction devices are used simultaneously, and it may be difficult to assess the improvement due to any single part of the program. As one might expect from these remarks, experience plays an important role in determining optimal or nearly optimal sampling procedures. The theory presented here is nevertheless essential in ensuring that the calculation shall be unbiased and that the statistical analysis shall be valid.

B. Random Walk Processes

Two ideas borrowed from the mathematical theory of probability are of fundamental importance in any unified discussion of Monte Carlo methods. These are the ideas of sample space, or probability space, and random variable. To define these terms precisely it is necessary to begin with a review of elementary measure-theoretic concepts. (See Ref. 40 for further details.)

Let Ω denote any abstract set of points. The notation $\omega \epsilon \Omega$ is read, "ω is a point of Ω."

Definition 1. A class F of subsets of a space Ω is called a field if

(a) $\Omega \in F$;

(b) if $\Lambda \in F$, then $\Omega - \Lambda \in F \cdot (\Omega - \Lambda)$ is the set complementary to Λ in Ω, i.e., the set points of Ω which does not belong to Λ;

(c) if $\Lambda_1, \ldots, \Lambda_n \in F$, then

$$\bigcup_{i=1}^{n} \Lambda_i \in F \quad \text{and} \quad \bigcap_{i=1}^{n} \Lambda_i \in F ,$$

where $\bigcup_{i=1}^{n} \Lambda_i$ is the set consisting of those points $\omega \in \Omega$ which belong to some Λ_i and $\bigcap_{i=1}^{n} \Lambda_i$ is the set consisting of those points $\omega \in \Omega$ common to all Λ_i.

Definition 2. A field F of subsets of Ω is called a Borel field if it is a field and if, whenever $\Lambda_1, \Lambda_2, \ldots$ is a countable sequence of sets of F, then

$$\bigcup_{i=1}^{\infty} \Lambda_i \in F \quad \text{and} \quad \bigcap_{i=1}^{\infty} \Lambda_i \in F$$

Definition 3. Let F be a field of subsets of Ω. A real-valued set function μ on the sets of F is called completely additive if, whenever $\Lambda_1, \Lambda_2, \ldots$ are disjoint sets of F with

$$\bigcup_{i=1}^{\infty} \Lambda_i \in F ,$$

then

$$\mu\left(\bigcup_{i=1}^{\infty} \Lambda_i\right) = \sum_{i=1}^{\infty} \mu(\Lambda_i).$$

Definition 4. If F is a field of subsets of Ω, a real-valued function μ on the sets of F is called a measure if it is nonnegative and completely additive. It is called a probability measure if it is a measure and if $\mu(\Omega) = 1$.

Definition 5. Let F be a Borel field of subsets of Ω and let ξ be a real-valued function on Ω. The function ξ is measurable with

respect to F if, for every real number c, the set $\{\omega\epsilon\Omega|\xi(\omega) \leq c\}$ belongs to F. (The notation $\{\omega\epsilon\Omega|\xi(\omega) \leq c\}$ means the set of all points ω in Ω for which $\xi(\omega) \leq c$.)

Definition 6. A sample space, or probability space, is a triple (Ω, F, μ) consisting of a space Ω, a Borel field F of subsets of Ω, and a probability measure μ on F.

Definition 7. A random variable is a real-valued function ξ on the points of a sample space (Ω, F, μ) which is measurable with respect to the Borel field F.

In what follows, the sample space is to be regarded as a mathematical realization of the physical experiment being studied. First, the space Ω itself is the collection of individual events whose aggregate makes up the experiment. For particle transport problems, each point C of Ω describes the random walk of a particle life history, from birth until death. Second, the Borel field F is the class of subsets of Ω to which the term likelihood may be applied. Typical among such subsets, for transport problems, are those sets Λ_k consisting of all random walks C which make exactly k collisions before terminating. Finally, the probability measure μ, defined on the class of measurable sets F, describes how likely each measurable subset is by assigning a nonnegative number $\mu(\Lambda)$, $0 \leq \mu(\Lambda) \leq 1$, to every $\Lambda\epsilon F$. The random variables which occur in the discussion are functions on Ω which assign to each random walk C of Ω a real number, to be regarded as the weight of the random walk C.

It is now appropriate to define the sample space (Ω, F, μ) for the particle transport problems to be considered. The basic construction is due to G. E. Albert.[41] The space Ω is the space of all possible random walks in phase space. Specifically, Ω consists of all chains $C = \{\alpha_0, \alpha_1, \ldots\}$ where α_i is a pair (x_i, P) or (x_i, Q), x_i being a point of phase space, and P and Q designating distinguished states corresponding to termination and nontermination, respectively, of the random walk. Heuristically, the typical chain

$$C = \left\{(x_0, Q), (x_1, Q), (x_2, Q), (x_3, P), (x_3, P) \ldots\right\}$$

denotes a random walk originating at the point x_0 of phase space, passing next to the state x_1, then to x_2, and finally to x_3 where it terminates. Formally, if R denotes the phase space, and $\{P, Q\}$ the two point space with elements P, Q, then the space

$X = R \times \{P, Q\}$. Thus, the space Ω is the infinite product space (space of all infinite sequences)

$$\Omega = \prod_{i=0}^{\infty} X_i \quad \text{where} \quad X_i = X, \quad i = 0, 1, 2, \ldots$$

The definition of the class F of measurable subsets of Ω is too complicated for detailed treatment here, but it will, perhaps, be more illuminating to display basic elements of F. To do this it is necessary to digress for a moment in order to define the length of a random walk chain.

Definition 8. For any chain $C = \{\alpha_0, \alpha_1, \alpha_2, \ldots\} \in \Omega$, let $n(C)$ be the smallest integer k such that the element α_k of C has the form $\alpha_k = (x_k, P)$. Then $n(C)$ is called the length of the random walk chain C. The discrete function $n(C)$ on the sample space Ω represents the number of collisions made to termination of the random walk C.

Let $\Lambda_k = \{C \in \Omega \mid n(C) = k\}$, $k = 0, 1, 2, \ldots$, and let $\Lambda_\infty = \{C \in \Omega \mid n(C) = \infty\}$, i.e., the chains of infinite length. The sets Λ_k for k finite and Λ_∞ are basic elements of F, and it is intuitively clear that

$$\Omega = \left(\bigcup_{k=0}^{\infty} \Lambda_k \right) \cup \Lambda_\infty . \qquad \text{Eq. (7.48)}$$

Furthermore, the sets Λ_k, Λ_∞ are mutually disjoint, so that they form a decomposition of the sample space Ω.

The measure μ on subsets of Ω is constructed from what has been called a random walk process in Ref. 42.

Definition 9. If R again denotes the phase space, and R^N is the space of all N-tuples of points of R, a random walk process $\{f_N, p_N\}$, is a sequence $f_N(x_0, \ldots, x_N)$, $N = 0, 1, 2, \ldots$, of probability density functions on R^{N+1} together with a sequence $p_N(x_0, \ldots, x_N)$, $N = 0, 1, 2, \ldots$, of functions on R^{N+1} with the properties

$$F_N(x_0, \ldots, x_k, \infty, \ldots, \infty) = F_k(x_0, \ldots, x_k), \; k < N, \; N > 1, \qquad \text{Eq. (7.49)}$$

where

$$F_N(x_0, \ldots, x_N) \equiv \int_{-\infty}^{x_N} \cdots \int_{-\infty}^{x_0} f_N(x'_0, \ldots, x'_N) \, dx'_0 \cdots dx'_N$$

is the distribution function of f_N and

$$0 \leq p_N(x_0, \ldots, x_N) \leq 1, \qquad N = 0, 1, 2, \ldots, \qquad \text{Eq. (7.50)}$$

for all $(x_0, \ldots, x_N)$.

Intuitively, $f_N(x_0, \ldots, x_N)$ represents the probability density of a random walk chain involving the sequence of states $(x_0, \ldots, x_N)$, and $P_N(x_0, \ldots, x_N)$ is the probability of terminating the random walk at x_N. Then $q_N = 1 - p_n$ is the probability of continuing the random walk beyond the state x_N.

The probability measure μ is derived from the random walk process $\{f_N, p_N\}$ making use of a rather technical theorem of Tulcea.[43] For the discussion to follow it will not be necessary to go through that entire development; this is done in Ref. 42. It will suffice to observe that

$$\mu(\Lambda_k) = \int_R \cdots \int_R f_k(x_0, \ldots, x_k) \prod_{i=0}^{k-1} q_i(x_0, \ldots, x_i) p_k(x_0, \ldots, x_k) dx_0 \cdots dx_k . \qquad \text{Eq. (7.51)}$$

The number $\mu(\Lambda_k)$ is the measure assigned to the set of all random walks of length exactly k. In the integral on the right f_k gives the probability density of an arbitrary chain $(x_0, \ldots, x_k)$, $\prod_{i=0}^{k-1} q_i$ guarantees that the walk does not terminate at $x_0, \ldots, x_{k-1}$, and p_k assures the termination of the chain at x_k. Thus, the measure μ is a natural consequence of the random walk process.

From a practical point of view it is important to satisfy conditions on the random walk process which guarantee that $n(C)$ is finite with probability one, i.e.,

$$\sum_{k=0}^{\infty} \mu(\Lambda_k) = 1 . \qquad \text{Eq. (7.52)}$$

In view of Eq. (7.48), this is equivalent to

$$\mu(\Lambda_\infty) = 0 . \qquad \text{Eq. (7.53)}$$

Thus, in practice, assumptions are made, so that

$$\mu(\Lambda_\infty) = \lim_{m\to\infty} \int_R \cdots \int_R f_m(x_0,\ldots,x_m) \prod_{i=0}^{m} q_i(x_0,\ldots,x_i)\,dx_0 \cdots dx_m = 0 \,. \qquad \text{Eq. (7.54)}$$

The probability model of the experiment is now complete. The space Ω contains all of the random walk chains which are the objects of study by the Monte Carlo process. A point of Ω will be identified with a sample from the parent population Ω. The subsets Λ_k provide a convenient decomposition of the space Ω according to the number of collisions suffered until termination. Finally, the measure μ derived from the random walk process $\{f_N, P_N\}$ describes the likelihood of certain aggregates of random walk chains.

This model enables one to construct typical random walks in a manner consistent with the measure μ. This is done as follows: first a state x_0 of R is chosen from the density function $f_0(x_0)$ according to well known sampling procedures. Then a decision is made to terminate the walk at x_0 with probability $p_0(x_0)$ or to continue with probability $q_0(x_0) = 1 - p_0(x_0)$. If the decision is made to continue, a state x_1 of R is chosen from the conditional density function $f_1(x_1 \mid x_0) \equiv \dfrac{f_1(x_0, x_1)}{f_0(x_0)}$, where x_0 is the previously determined initial chain point. In general, if the sequence $x_0, \ldots, x_{n-1}$ of chain points has previously been specified, and if it has been decided not to terminate the walk at x_{n-1} with probability $q_{n-1}(x_0, \ldots, x_{n-1})]$, the next chain point x_n is chosen from the conditional density function $f_n(x_n \mid x_0,\ldots,x_{n-1}) \equiv \dfrac{f_n(x_0,\ldots,x_n)}{f_{n-1}(x_0,\ldots,x_{n-1})}$. This process is repeated until termination of the walk at some point x_k of R. The random walk chain which results from this process is the chain

$$C = \{(x_0, Q), (x_1, Q), \ldots, (x_{k-1}, Q), (x_k, P), (x_k, P), \ldots\}.$$

The measure μ constructed on Ω is the appropriate measure to associate with subsets of Ω relative to this method of constructing samples from the parent population.

With the sample space fixed, it is necessary to define the basic estimating random variable on the sample space. As a function on Ω, the random variable must assign to each point of Ω, i.e., to each random walk chain C, a real number to be thought of as the weight associated with that particle history.

This weight provides a way of mathematically assessing the contribution of each history to the unknown quantity being estimated; it is the basic statistical variable of the problem.

In general, the problem is to estimate some population parameter I, usually expressible as a definite integral involving the solution to the transport equation in the integrand. The random variable ξ performs the estimation by associating with each particle history C of Ω the weight $\xi(C)$, to be regarded as the C-estimate of I. In practice a finite number N of random walks $C_1, \ldots, C_N$ are generated, and the statistical estimate of I is a function of the N-tuple $(C_1, \ldots, C_N)$. Thus, it may be described by a random variable ξ_N on the space Ω^N of all N-tuples of points of Ω. The expectation $E[\xi_N]$ of such a random variable represents the theoretical average of its values over all possible N-tuples. It seems natural to require that this average be equal to the parameter I being estimated: in the language of probability theory, that ξ_N be unbiased.

Finally, the variance of ξ_N, defined as the quantity

$$\sigma^2[\xi_N] \equiv E[\xi_N^2] - E^2[\xi_N] = E[\xi_N^2] - I^2 \quad , \qquad \text{Eq. (7.55)}$$

provides a measure of the fluctuation of the values of ξ_N from N-tuple to N-tuple, hence a measure of the expected error based on a sample of size N. Theoretically, the object is to use random variables ξ_N for which $\sigma^2[\xi_N]$ is as small as possible, for this will result in a calculation in which the number of particle histories needed to obtain a given statistical accuracy is minimized. Practically, this theoretical efficiency must be balanced against possible increases in the cost of generating each random walk C of Ω and of evaluating the random variable ξ_N. It is frequently true that efficient random variables ξ_N are more complicated than less efficient ones and involve more machine time to evaluate and analyze. Thus, in the last analysis, the most efficient random variable is the one that leads to the smallest computing time, rather than the smallest sample size, for a fixed error.

C. Analog Processes

For the transport problems discussed in this section the starting point for all of the calculations is the integral form of the transport equation

$$\phi(x) = \int_R K(x, y)\, \varphi(y)\, dy + S(x), \; x \in R \, , \qquad \text{Eq. (7.56)}$$

where R is the phase space. It is further assumed that

$$\left.\begin{aligned} &S(x) \geq 0 \quad \text{and} \quad \int_R S(x)\,dx \neq 0 \\ &K(x,y) \geq 0, \qquad 0 \leq \int_R K(x,y)\,dx \leq 1 \quad \text{for all} \quad y \in R \end{aligned}\right\} \qquad \text{Eq. (7.57)}$$

In Eq. (7.56), $S(x)$ represents the density of first collisions in phase space, $K(x,y)$ the (nonnormalized) density function for transitions from state y to state x, and $\varphi(x)\ \Sigma_t(x)\Psi(x)$ the collision density, where Σ_t is the total cross section and $\Psi(x)$ is the flux.

This subsection will deal with analog random walk processes. Heuristically, an analog process is one which is a faithful simulation of the physical process. In transport problems, since the transport equation describes a physical process, it should be possible to describe an analog random walk process based on this equation alone; i.e., using only the source S and kernel K. This is done as follows:

$$f_0(x_0) \equiv \frac{S(x_0)}{\int_R S(x)\,dx} \qquad \text{Eq. (7.58)}$$

$$\left.\begin{aligned} f_N(x_o,\ldots,x_N) &\equiv f_N(x_1,\ldots,x_N \mid x_0) f_0(x_0) \\ &= \left[\prod_{\ell=1}^{N} \frac{K(x_\ell, x_{\ell-1})}{1 - p_{\ell-1}(x_0,\ldots,x_{\ell-1})}\right] f(x_0) \\ &= \left[\prod_{\ell=1}^{N} \frac{K(x_\ell, x_{\ell-1})}{q_{\ell-1}(x_0,\ldots,x_{\ell-1})}\right] f_0(x_0) \end{aligned}\right\} \qquad \text{Eq. (7.59)}$$

where it is assumed that the denominator does not vanish and

$$\left.\begin{aligned} p_i(x_0, \ldots, x_i) &\equiv 1 - \int_R K(x, x_i)\,dx \\ q_i(x_0, \ldots, x_i) &= \int_R K(x, x_i)\,dx\,, \qquad i \geq 0 \end{aligned}\right\} \qquad \text{Eq. (7.60)}$$

In Eq. (7.59), the quantity $f_N(x_1, \ldots, x_N | x_0)$ is the conditional probability density of $x_1, x_2, \ldots, x_N$ given x_0.

Quite commonly, one attempts to estimate definite integrals of the form

$$I = \int_R g(x)\phi(x)\,dx \qquad \text{Eq. (7.61)}$$

where $g(x)$ is a given (usually nonnegative) function and $\phi(x)$ satisfies Eq. (7.56). For a wide class of functions $g(x)$, such integrals I may be represented as

$$I = \mu(\Lambda) \qquad \text{Eq. (7.62)}$$

where Λ is a given measurable subset of the space Ω of all random walks, and μ is the analog measure on Ω, based on the analog random walk process defined by Eqs. (7.58), (7.59), and (7.60). Thus, the problem is to estimate the analog measure of Λ by defining a random variable on Ω whose expected value is $I = \mu(\Lambda)$. This is easily accomplished through the definition

$$\xi(C) \equiv \begin{cases} 1 \text{ if } C \in \Lambda \\ 0 \text{ if } C \notin \Lambda \end{cases} . \qquad \text{Eq. (7.63)}$$

Then,

$$\begin{aligned} E[\xi] \equiv \int_\Omega \xi\,d\mu &= 1 \cdot \mu(\Lambda) + 0 \cdot \mu(\Omega - \Lambda) \\ &= I \end{aligned} \qquad \text{Eq. (7.64)}$$

so that ξ is an unbiased estimator of I. The random variable ξ is nothing more than the binomial estimator of an event with probability I for success and $1-I$ for failure.

Now, if $C_1, \ldots, C_N$ are N random walk chains, the N-tuple $(C_1, \ldots, C_N)$ is a point of the product space Ω^N. On the space Ω^N, N mutually independent random variables ξ_i, $1 \leq i \leq N$, are defined by

$$\xi_i(C_1, \ldots, C_N) \equiv \xi(C_i), \qquad 1 \leq i \leq N \qquad \text{Eq. (7.65)}$$

where ξ is defined by Eq. (7.63). Taking as the measure on Ω^N the product μ^N of the measures μ on each factor Ω allows the conclusion

$$E[\xi_i] \equiv \int_{\Omega^N} \xi_i \, d\mu^N = E[\xi] = I, \qquad 1 \leq i \leq N. \qquad \text{Eq. (7.66)}$$

If one now forms the random variable $\bar{\xi}_N$ on Ω^N defined by

$$\bar{\xi}_N \equiv \frac{1}{N} \sum_{i=1}^{N} \xi_i \qquad \text{Eq. (7.67)}$$

then it follows that

$$E[\bar{\xi}_N] = E[\xi_i] = I, \qquad 1 \leq i \leq N, \qquad \text{Eq. (7.68)}$$

so that $\bar{\xi}_N$ is also an unbiased estimator of I. A computation shows that the variance of ξ is

$$\sigma^2[\xi] = I(1 - I) \qquad \text{Eq. (7.69)}$$

while the variance of $\bar{\xi}_N$ is

$$\sigma^2[\bar{\xi}_N] = \frac{1}{N} I(1 - I). \qquad \text{Eq. (7.70)}$$

The decision as to how large N (the number of sample chains processed) should be before the calculation is terminated is usually based on the size of the relative error defined by

$$\sigma_r \equiv \frac{\sqrt{\sigma^2[\bar{\xi}_N]}}{I} = \sqrt{\frac{1-I}{I \cdot N}}. \qquad \text{Eq. (7.71)}$$

From this expression for the relative error of the estimator $\bar{\xi}_N$ it is seen that if I is very small, N would have to be very large before σ_r is small enough for the estimate to be useful. One's intuition suggests that an accurate estimation of an extremely rare event by direct simulation techniques will require an extremely large sample size. Thus, it becomes apparent that the simple binomial estimator $\bar{\xi}_N$ defined by Eq. (7.67) is not good enough for many problems, e.g., in shielding problems where very small transmission probabilities are sought. This motivates the search for alternative unbiased estimators with smaller variances. The problem of finding such estimators is really the central problem of Monte Carlo.

It is usually not possible to predict in advance the reduction in variance that will arise through the use of one estimator in place of another. In practice the variances themselves are very much dependent on the problem being solved, so that for one problem a certain estimator will be preferred while for another problem another estimator will be preferred. Hence it is impossible to make unqualified statements about improvements obtained through the use of one estimator in place of another. It is possible only to indicate that for a particular class of problems one estimator will have smaller variance than another and roughly how much.

One method which has proved extremely useful in applications is that involving the use of expected values or statistical estimation as it is more frequently identified. Stated briefly, the philosophy of this method dictates that no part of the calculation shall be done through the use of random choices if it can be done analytically by using the expected value of a random variable in place of a sample value. As an example of this technique consider the following problem: Suppose it is desired to estimate the absorption rate

$$I_V \equiv \int_R \frac{\Sigma_a(x)}{\Sigma_t(x)} \chi_V(x)\varphi(x)\,dx \qquad \text{Eq. (7.72)}$$

where $\frac{\Sigma_a(x)}{\Sigma_t(x)}$ is the ratio of absorption to total cross section, $\phi(x)$ is the collision density, and $\chi_V(x)$ is defined by

$$\chi_V(x) = \begin{cases} 1 \text{ if } x \text{ belong to the subregion } V \text{ of } R \\ 0 \text{ otherwise} \end{cases}$$

Then the product $g(x) = \frac{\Sigma_a(x)}{\Sigma_t(x)} \chi_V(x)$ represents the probability of absorption in the state x of V, and $g(x)\phi(x)$ is the absorption rate in the volume V. The use of expected values would give rise to an unbiased random variable on the space Ω of analog random walk chains defined by

$$\xi(C) \equiv \sum_{i=0}^{n(C)} g(x_i) \qquad \text{Eq. (7.73)}$$

where

$$C = \{(x_0, Q), (x_1, Q), \ldots, (x_{n(C)-1}, Q), (x_{n(C)}, P), \ldots\}$$

and $n(C)$ is the length of the chain C. The estimator of Eq. (7.73) can be motivated somewhat by the observation that at each collision point x_j, the expected contribution to I_V is $g(x_i)$. Thus, I_V is estimated by a sum of conditional contributions made at each collision point of C. The variance of Eq. (7.73) is, in general, difficult to examine analytically, but it can be many factors smaller than the variance $I_V(1 - I_V)$ of the variable defined by Eq. (7.63). A variation of Eq. (7.73), the track length estimator, has been applied to all of the Monte Carlo programs discussed in Chap. 3, Section 3.5, with a resulting reduction in variance over the simple binomial estimator of factors of 20 or more in some problems.

In Ref. 42 it is shown that this result is actually valid for much more general nonnegative functions $g(x)$ on R. To state this theorem precisely it is necessary to discuss Neumann series associated with the transport equations.

Again, let

$$\phi(x) = \int_R K(x, y)\phi(y)\,dy + S(x) \qquad \text{Eq. (7.74)}$$

be the integral transport equation for the collision density, and assume the integral

$$I = \int_R g(x)\varphi(x)\,dx \qquad \text{Eq. (7.75)}$$

is being estimated. The equation adjoint to Eqs. (7.74) and (7.75) is

$$\varphi^\dagger(x) = \int_R K(y, x)\phi^\dagger(y)\,dy + g(x) \qquad \text{Eq. (7.76)}$$

whose solution $\phi^\dagger(x)$ is the so-called importance function for this problem.

The Neumann series for the collision density $\varphi(x)$ is the infinite series

$$\varphi(x) = S(x) + \sum_{\ell=1}^{\infty} I_\ell(x) \qquad \text{Eq. (7.77)}$$

where

$$I_\ell(x) \equiv \int_R \cdots \int_R K(x, u_\ell)K(u_\ell, u_{\ell-1})\cdots K(u_2, u_1)S(u_1)\,du_1 \cdots du_\ell$$

Eq. (7.78)

while the Neumann series for the importance function $\phi^\dagger(x)$ is, by analogy,

$$\varphi^\dagger(x) = g(x) + \sum_{\ell=1}^{\infty} J_\ell(x) \qquad \text{Eq. (7.79)}$$

where

$$J_\ell(x) \equiv \int_R \cdots \int_R K(u_\ell, x)K(u_{\ell-1}, u_\ell)\cdots K(u_1, u_2)g(u_1)\,du_1 \cdots du_\ell .$$

Eq. (7.80)

The Neumann series relates the transport equation to the collision number, for the k^{th} term of the series consists of those particles which have collided exactly k times. It is, therefore, to be expected that the Neumann series would play a role in determining conditions under which the use of expected values would be valid. That this is so is reflected in the basic theorem which is stated here without proof.

Theorem 1. Assume that $\phi(x)$ satisfies the transport equation [Eq. (7.74)] with the condition

$$\int_R S(x)\,dx = 1.$$

Assume further that the Neumann series, Eqs. (7.77) and (7.79), converge to $\phi(x)$ and $\phi^\dagger(x)$, respectively, for all $x \in R$. Then the random variable

$$\xi(C) = \sum_{i=0}^{n(C)} g(x_i) \qquad \text{Eq. (7.81)}$$

is an unbiased estimator of the integral I.

D. Importance Sampling and Related Methods

Stated briefly, the notion of importance sampling involves a distortion of the actual physical transition probabilities (i.e., analog random walk process as defined in the previous section) with the net result that events of interest in the calculation occur more frequently than normally. This distortion is then compensated for in the estimating random variable by weighting it so as to remove any bias from the estimates. One of the interesting and important features of the method is the existence, for a large class of problems, of a zero variance sampling scheme, i.e., a scheme such that one sample yields precisely the correct estimate. This fact is important not because it is achievable in practice (for this would involve the a priori knowledge of the solution to the transport equation or to the adjoint equation) but because it points the way to devising schemes which make use of approximations to the perfect scheme.

Because of the possibility of approximating zero variance schemes using approximate solutions, the importance sampling method indicates at least one way in which full use may be

made of a good guess at the solution. This ability to use a good guess to advantage is not present in most analog methods but is characteristic of many semi-analytic techniques such as iterative finite difference methods for solving partial differential equations. Indeed, this appears to be one of the major advantages of such finite difference methods. It is, thus, desirable to investigate similar possibilities for Monte Carlo methods.

The idea of applying importance sampling to transport problems and the existence of zero variance estimators appears to go back to Goertzel.[44] More recently, Kahn has given expositions of the method.[45,46] G. E. Albert has discussed a method for estimating Neumann series and terms of Neumann series at a point which bears a strong resemblance to importance sampling.[41] The point of view here presented unifies the results of Kahn and Albert.

Consider the transport equation

$$\varphi(x) = \int_R K(x, y)\varphi(y)dy + S(x) \qquad \text{Eq. (7.82)}$$

together with the conditions of Eq. (7.57). The general problem to be solved is the estimation of

$$I = \int_R g(x)\,\varphi(x)dx, \qquad g(x) \geq 0 \qquad \text{Eq. (7.83)}$$

where $g(x)$ is a given function. It has been shown that the estimation of I is replaced in an analog calculation by the estimation of the integral

$$E[\xi] = \int_\Omega \xi\, d\mu \qquad \text{Eq. (7.84)}$$

where Ω is the sample space, μ is the analog measure on Ω, and ξ is a suitable unbiased random variable. Formally, a change of variable may be made and the integral [Eq. (7.84)] rewritten in the form

$$E[\xi] = \int_\Omega \left[\xi \frac{d\mu}{d\mu'}\right] d\mu'. \qquad \text{Eq. (7.85)}$$

Then if

$$\xi'(C) \equiv \xi(C)\frac{d\mu}{d\mu'} \qquad \text{Eq. (7.86)}$$

one has

$$E[\xi] = \int_{\Omega} \xi'(C)\,d\mu'. \qquad \text{Eq. (7.87)}$$

This shows that the random variable ξ' is an unbiased estimator of $I = E[\xi]$ with respect to the measure μ' on Ω. This is precisely the idea behind importance sampling. The new measure μ' on Ω is defined using an arbitrary random walk process $\{f_N, p_N\}$, and the new estimator ξ' is defined to be the product of the old estimator ξ with the generalized derivative $d\mu/d\mu'$ of the old measure with respect to the new.

To discuss a specific estimator, suppose $\{f_N, p_N\}$ is an arbitrary random walk process and μ' is the probability measure on Ω constructed by the general theory. Let ξ' be defined on chains of length $n(C)$ by

$$\xi'(C) \equiv \frac{g(x_{n(C)})K(x_{n(C)}, x_{n(C)-1})\cdots K(x_2, x_1)K(x_1, x_0)S(x_0)}{f_{n(C)}(x_0, \ldots, x_{n(C)})p_{n(C)}(x_0, \ldots, x_{n(C)})\prod_{i=0}^{n(C)-1} q_i(x_0, \ldots, s_i)}$$

Eq. (7.88)

provided the denominator does not vanish. Then, under the additional assumptions that the Neumann series for the collision density converges and that the related series

$$g(x)S(x) + \sum_{\ell=1}^{\infty} l_\ell(x)g(x) \qquad \text{Eq. (7.89)}$$

converges uniformly, it may be shown that ξ' is an unbiased estimator of I with respect to the measure μ'.

The existence of zero variance estimators will now be indicated. To define the zero variance process, it is necessary

to know the importance function, i.e., the solution of the equation

$$\phi^\dagger(x) = \int_R K(y, x)\phi^\dagger(y)\,dy + g(x) \qquad \text{Eq. (7.90)}$$

which is adjoint to Eqs. (7.82) and (7.83). If $\phi^\dagger(x)$ is assumed known, define a random walk process $\{f_N, p_N\}$ by

$$f_0(x_0) = \frac{\phi^\dagger(x_0)S(x_0)}{\int_R \phi^\dagger(x)S(x)\,dx}; \qquad K^*(x, y) = \frac{K(x, y)\phi^\dagger(x)}{\phi^\dagger(y)} \qquad \text{Eq. (7.91)}$$

$$f_k(x_0, \ldots, x_k) = f_k(x_1, \ldots, x_k | x_0) = \left[\prod_{\ell=1}^{k} \frac{K^*(x_\ell, x_{\ell-1})}{q_{\ell-1}(x_0, \ldots, x_{\ell-1})}\right] f_0(x_0) \qquad \text{Eq. (7.92)}$$

where

$$q_i(x_0, \ldots, x_i) = \int_R K^*(x, x_i)\,dx = 1 - \frac{g(x_i)}{\phi^\dagger(x_i)}. \qquad \text{Eq. (7.93)}$$

Defining

$$p_i(x_0, \ldots, x_i) = 1 - q_i(x_0, \ldots, x_i) = \frac{g(x_i)}{\phi^\dagger(x_i)} \qquad \text{Eq. (7.94)}$$

completes the description of the random walk process.

Theorem 2. With respect to the measure $\mu_\phi{}^\dagger$ induced on Ω by the above random walk process, the estimator ξ' of Eq. (7.88) is a zero variance estimator of I. The proof of this result may be found in Ref. 42.

It is now desirable to establish a type of duality theory for importance sampling. As before let Eqs. (7.82) and (7.83) define the original transport estimation problem. Let

$$\phi^\dagger(x) = \int_R K(y, x)\phi^\dagger(y)dy + g(x) \qquad \text{Eq. (7.95)}$$

and

$$I^\dagger = \int_R S(x)\phi^\dagger(x)dx \qquad \text{Eq. (7.96)}$$

be the pair of equations adjoint to Eqs. (7.82) and (7.83). Then, it is easy to establish that $I^\dagger = I$. Thus, the problem of estimating I is the same as the problem of estimating $I^\dagger$ and whatever theory is developed for the pair, Eqs. (7.82) and (7.83), applies equally well to the pair, Eqs. (7.95) and (7.96).

In particular, with respect to an arbitrary random walk process $\{f_N, p_N\}$ the estimator, Eq. (7.88), may be dualized to yield

$$\xi^\dagger(C) = \frac{S(x_{n(C)})K(x_{n(C)-1}, x_{n(C)}) \cdots K(x_0, x_1)g(x_0)}{f_{n(C)}(x_0, \ldots, x_{n(C)})p_{n(C)}(x_0, \ldots, x_{n(C)} \prod_{i=0}^{n(C)-1} q_i(x_0, \ldots, x_i)}$$

Eq. (7.97)

Then, since the series

$$S(x)g(x) + \sum_{\ell=1}^{\infty} J_\ell(x)S(x) \qquad \text{Eq. (7.98)}$$

where $J_\ell(x)$ is the ℓ^{th} term of the Neumann series for the importance function $\phi^\dagger(x)$ coincides with the series [Eq. (7.89)], the assumption of uniform convergence of this series leads to Theorem 3.

Theorem 3. The dual importance sampling estimator $\xi^\dagger$ of Eq. (7.97) is an unbiased estimator of $I^\dagger = I$.

Analogous to Theorem 2, zero variance estimators for the dual process also exist. They are based on a knowledge of the dual importance function, that is, the collision density ϕ. Assuming ϕ known, the dual zero variance random walk process is obtained by dualizing Eqs. (7.91) through (7.94), viz.:

$$f_0(x_0) = \frac{\phi(x_0)g(x_0)}{\int_R \phi(x)g(x)\,dx}, \qquad K^*(x,y) = \frac{K(y,x)\phi(x)}{\phi(y)}$$

Eq. (7.99)

$$f_k(x_0,\ldots,x_k) = f_k(x_1,\ldots,x_k|x_0) = \left[\prod_{\ell=1}^{k} \frac{K^*(x_\ell, x_{\ell-1})}{q_{\ell-1}(x_0,\ldots,x_{\ell-1})}\right] f_0(x_0)$$

Eq. (7.100)

where

$$q_i(x_0,\ldots,x_i) = \int_R K^*(x,x_i)\,dx = 1 - \frac{S(x_i)}{\phi(x_i)}.$$

Eq. (7.101)

The last equality follows from Eqs. (7.82) and (7.99). Then, with

$$p_i(x_0,\ldots,x_i) = \frac{S(x_i)}{\phi(x_i)}$$

Eq. (7.102)

the functions $\{f_N, p_N\}$ define a dual random walk process and yield a theorem dual to Theorem 2.

Theorem 4. With respect to the measure μ_ϕ induced on Ω by the above dual random walk process, the estimator $\xi^\dagger$ of Eq. (7.97) is a zero variance estimator of $I^\dagger = I$.

The importance of this dual theory may be seen as follows: While approximations to the importance function $\phi^\dagger$ are generally difficult to obtain, approximations to the collision density ϕ are more readily available in the form of diffusion theory solutions or transport solutions of simplified problems. Many digital programs exist for obtaining such approximations, and these may be used, in turn, to provide approximations to the dual zero variance importance sampling process defined above. This implies using a random walk model based on the adjoint equation [Eq. (7.95)] rather than the transport equation [Eq. (7.82)]. This idea has other advantages for a class of rather special problems, and has been used successfully in the programs TRAC-1 and MARC which are described in Chap. 3, Section 3.5.

7.4 DIGITAL COMPUTER PROGRAMS FOR REACTOR PHYSICS CALCULATIONS

B. H. Mount and G. J. Habetler

A. Introduction

This section contains brief descriptions of most of the major programs which have been developed for physics calculations on the IBM-704 and Philco-2000 computers by the Naval Reactors laboratories. All programs currently in use by the Naval Reactors laboratories, primarily those operating on the Philco-2000, are constantly subject to minor and occasionally major modifications.

All programs on the Philco-2000 computer are designed to operate within the framework of the BKS System (see Sect. 7.1). Estimated problem running times given in this section are based on a model 211 main-frame with 10-microsecond core store.

B. Few-Group One-Dimensional Diffusion Theory

1. WANDA-4 (IBM-704)

W. R. Cadwell

The WANDA-4[47,48] program solves the one-dimensional neutron-diffusion equations with two, three, or four lethargy groups in rectangular, cylindrical, or spherical geometry. Typical problem running time is three minutes. The computer requirements include 8192 words of core storage, one to four

tape units, and an on-line printer. The program may also make use of an on-line card reader and on-line punch as well as peripheral card-to-tape and tape-to-printer equipment. The maximum problem size is increased if additional core storage is available.

For the approximate solution to the differential equations, a maximum of N mesh points may be distributed nonuniformly in a maximum of 35 regions. The value of N depends upon the number of groups G, the number of regions R, and the amount of core storage C, according to the inequality $5247 + (5G + 3)(N + R) + GR \leq C$. The boundaries of the mesh and all region interfaces must occur at mesh points. The mesh size must be constant within each region, and the number of intervals within each region must be even, so that Simpson's Rule may be used. The diffusion coefficients and macroscopic cross sections which are required as input are also constant within each region. At each boundary of the mesh either a zero flux or a zero derivative condition may be applied.

As an option the program will vary one of several parameters to search for a specified critical eigenvalue. These parameters are the buckling or the poison cross section in all regions, or in a subset of regions, or the boundary separating two regions. In the boundary search, an input poison cross section is used at all points above the boundary and zero poison at all points below the boundary. The boundary is then moved in an attempt to achieve criticality, with the restriction that it cannot cross a region interface or delete a region.

A variable field input card format is used to reduce keypunching and verifying effort. The input is arranged so that when a series of problems is run in which the later problems are nearly the same as the first, only the data to be changed need be specified for those later problems. In such cases, the converged source of a previous problem may also be used as the initial guess.

The items available for printing include an input edit, the sequence of eigenvalues leading to the converged value, the control parameter value for each sequence of eigenvalues in a search, pointwise values of the flux and source, and region integrals of the flux and source. As an option, the flux and source may be plotted between specified points of the mesh.

2. WANDA-5 (Philco-2000)

W. R. Cadwell

The WANDA-5[49,50] program represents an extension to the Philco-2000 computer of the WANDA series of programs for

the solution of the one-dimensional few-group neutron-diffusion equations. The program is designed to operate on a computer having 32K core storage and at least three tape units, but it can easily be reassembled to operate on a 16K computer with suitable restrictions on problem size.

WANDA-5 is quite similar in character to WANDA-4. The difference equations were derived in a different manner, however, so that the restrictions on constant mesh size and an even number of mesh intervals within a region could be removed. The region dependence of the input diffusion coefficients and macroscopic cross sections has also been removed, and these quantities may vary by mesh rectangle. From one to four lethargy groups are allowed with up to 500 mesh points distributed in at most 100 regions. Typical running time is one minute.

3. BOX (IBM-704)

BOX is a one-dimensional few-group diffusion theory program written primarily for depletion calculations. A program description is given in Sect. 7.4.E.6.

4. KARE 1D Calculation (Philco-2000)

A one-dimensional option is included in the KARE System and is described in Sect. 7.4.C.9.

C. Few-Group Two-Dimensional Diffusion Theory

1. PDQ-2 (IBM-704)

W. R. Cadwell

PDQ-2[51] solves the neutron-diffusion equations with two, three, or four lethargy groups over a rectangular region of the x–y or r–z plane. The region of solution may be composed of a large number of subregions of differing nuclear properties, with the restriction that all interfaces between subregions must be parallel to the outer boundaries of the rectangle. A logarithmic derivative boundary condition may be applied at control rod boundaries, and the flux or the normal derivative of the flux may be set to zero on the external boundary.

A nonuniform grid of mesh lines is imposed on the rectangle, each mesh line being parallel to a boundary line and extending from one boundary to the opposite boundary. The mesh intervals must be chosen in such a way that all interfaces

coincide exactly with mesh lines. The maximum number of mesh points permitted depends upon the amount of core and drum storage available as follows:

		Mesh Points			
Drum Size	0	----	1000	2500	5250
	8K	1250	2500	3750	6500
		4K	8K	16K	32K
		Core Size			

The group equations which result from a standard five-point difference approximation are solved using successive point overrelaxation with an iterative technique used to obtain an estimate of the optimum overrelaxation factor for each group. The power method is used in the source iterations to converge to the largest eigenvalue and corresponding source vector. These iterations are accelerated by a Chebyshev polynomial scheme, with the required extrapolation factors calculated by the program.

For typical values of the convergence parameter, a fairly good estimate of the running time is provided by the formula

$$T = \frac{GN}{100}$$

where T is the time in minutes, G is the number of groups, and N is the number of points. A typical two-group, 2500-point problem thus requires less than one hour. If an x–y problem possesses symmetry about a diagonal, this running time can be almost halved. The running time may also be decreased by using the output flux of one problem as input to a similar problem.

Input to the program includes a number of control parameters, values of the diffusion coefficient and macroscopic cross sections by group and region, the sequence of mesh intervals in each coordinate direction, and a description of the placement of regions in the mesh. The region description is accomplished in a very simple manner using a rectangular overlay process. The output of the program consists of a complete edit of the input, a picture of the mesh with all regions and interfaces indicated, region integrals of the flux and source, and pointwise flux and source values.

In addition to the core and drum requirements listed above, the program requires an IBM-704 equipped with at least six tape units, an on-line card reader, and an on-line printer.

2. *PDQ-3 (IBM-704)*

W. R. Cadwell

PDQ-3[52] is the second program in the PDQ series for the IBM-704 computer. It solves the neutron-diffusion equations with two, three, or four lethargy groups over a rectangular region of the $x-y$ plane containing up to 7500 mesh points. The program requires a computer with 32K core storage and at least eight tape units, but drum storage is not used.

PDQ-3 has a number of special features not present in PDQ-2, but its chief advantage is speed. The increased speed is achieved primarily through the use of a successive line overrelaxation iteration scheme rather than the successive point overrelaxation of PDQ-2. Fewer iterations are required in all cases, with the most notable reduction occurring in cell problems. PDQ-3 does not make obsolete PDQ-2, however, since it requires a larger computer and does not treat $r-z$ geometry.

Features of the program not present in PDQ-2 include region-dependent input χ values with nonzero values in the thermal group, permitting adjoint calculations in two, three, or four groups; region-dependent input source values in one-group, fixed-source problems; integration of the flux and source over rectangular regions specified in the input; selective editing of pointwise flux and source values; calculation of flux-weighted average values of the region-dependent parameters; and a preliminary input edit.

3. *PDQ-4 (Philco-2000)*

W. R. Cadwell

PDQ-4[50,53] represents an extension of the PDQ series of programs to the Philco-2000 computer. It solves the neutron-diffusion equations with one to four lethargy groups over a rectangular region in either Cartesian or cylindrical coordinates. Computer requirements include 32K core storage capacity, 8 or 16 index registers, at least 12 tape transports, and auxiliary card-to-tape and tape-to-printer equipment.

A 16K version can easily be created by redefining certain assembly parameters and reassembling the program.

PDQ-4 will solve any problem that can be solved by PDQ-2 or PDQ-3. In addition, PDQ-4 allows a maximum of 20,000 mesh points and 255 regions as compared with the 7500 mesh points and 35 regions of PDQ-3. PDQ-4 also makes use of a successive two-line overrelaxation iteration technique which is significantly faster in most cases than the successive one-line overrelaxation of PDQ-3. Other added features include an optional 180-degree rotational symmetry boundary condition, contour plotting of the flux, one-dimensional plotting of the source along mesh lines specified in the input, and provision for including region areas in the input which are checked before the problem is run.

Running time depends upon the number of groups and points, the accuracy of the initial flux guess, the convergence criterion, and the physical properties of the problem. A rough estimate of running time may be obtained from the formula

$$T = \frac{GN}{400}$$

where T is the time in minutes, G is the number of groups, and N is the number of mesh points. Four-group, 20,000-point problems have been observed to run as long as five hours.

4. TIP-1 (Philco-2000)

W. R. Cadwell

TIP-1[50] is a general coupling program for the study of few-group thermal descriptions in two dimensions. The program makes use of PDQ-4 to provide solutions to neutron-diffusion problems with up to three fast and six thermal groups. The number of mesh points is restricted to 7500 and the number of regions in the mesh to 50.

In general, a PDQ-4 problem with a single thermal group is first iterated to convergence. The removal from the epithermal group provides the source for a thermal iteration of from two to six thermal groups. Upon convergence, the source and eigenvalue are recalculated using all groups, and the fast groups of the PDQ-4 problem are iterated again. If the epithermal group changes significantly, another thermal iteration must be performed, and the process is continued until convergence is achieved.

5. *CURE (IBM-704)*

E. D. Reilly, Jr.

CURE[7] is a two-space dimensional few-group neutron-diffusion program. A nonuniform mesh in either (x, y), (r, z) or (r, θ) geometry may be used. The maximum number of points allowed is approximately 3300 for a 32K IBM-704 depending on the version used.

The following boundary conditions are allowed:

1. flux zero
2. current zero
3. given ratio of current to flux
4. azimuthal periodicity in $r-\theta$ geometry
5. 90-degree periodicity on top and right boundaries of a square.

Except for the periodic options, the outer boundary may be irregular with boundary conditions that vary from point to point.

Flux iterations in CURE are performed according to the alternating direction Peaceman-Rachford method. Source iterations are accelerated according to the three-term formula

$$S^t = S^{t-1} + \alpha(t)(S^{*t} - S^{t-1}) + \beta(t)(S^{t-1} - S^{t-2})$$

where S^{*t} is the source calculated after the t^{th} source iteration, S^t is the extrapolated source after the t^{th} iteration, and $\alpha(t)$ and $\beta(t)$ are iteration-dependent parameters developed as functions of Chebyshev polynomials (see Sec. 7.2).

CURE may be used with precalculated group constants for one- to four-group calculations, or with three-group constants calculated from basic constituent materials according to the WOXX scheme (see Sect. 7.4.F.3). Up to 57 different material regions are allowed.

Without a good source guess, typical running times for CURE are

$$T = \frac{GN}{200} \text{ for } r-z \text{ problems}$$

$$T = \frac{GN}{100} \text{ for } x-y \text{ problems}$$

$$T = \frac{GN}{80} \text{ for 90-degree periodic problems}$$

where T = machine time in minutes, G = number of groups, and N = number of flux points. The running time for $r-z$ problems is especially favorable because of the empirical discovery that in this geometry only a very few Peaceman-Rachford double sweeps (one in most cases) are necessary in the inner or flux iteration.

6. *REM (IBM-704)*

E. D. Reilly, Jr.

REM is a modification of CURE which will allow diagonal material interfaces to be drawn between mesh points in $x-y$ geometry.

In REM geometry, all eight octants surrounding a point may contain different materials. As a version of CURE, REM shares the same features and limitations of CURE. Although mesh spacing is variable, the requirement that diagonals pass through mesh points quickly generates many flux points beyond those actually desired. Because of this, use of REM has been largely superseded by that of the FLEER type geometry.

7. *FLEER (IBM-704)*

E. D. Reilly, Jr.

FLEER[54] is a two-space dimensional three-group neutron-diffusion program. A uniformly spaced triangular mesh of up to 14,000 mesh points is allowed. The outer boundary of the reactor problem must be a parallelogram whose left and bottom sides are inclined at 120 degrees to each other.

Boundary conditions allowed are:

1. flux zero
2. current zero
3. given ratio of current to flux
4. 120-degree periodicity on left and bottom boundaries.

Because of the necessity of treating the 120-degree periodic boundary condition, the inner or flux iteration is accomplished by accelerated Liebmann bent line relaxation.

Source acceleration is performed according to the Chebyshev polynomial method described under CURE. The $\alpha(t)$ and $\beta(t)$ are related to a parameter a_s for which the program will attempt to calculate an optimum value to minimize running time (see Sect. 7.2).

Although precalculated group constants may be supplied and although one- and two-group problems can be run artificially (by supplying group constants which force three groups to degenerate into two or one), FLEER is actually built around the WOXX three-group scheme. Fissions are allowed only in groups two and three.

Up to 250 basically different material regions are allowed, but up to 500 different region numbers are allowed for editing purposes.

FLEER requires a 32K IBM-704 with seven tape units and four logical drums. Its approximate running time is 40 minutes per 1000 points for a three-group problem.

8. OBSCURE (IBM-704)

E. D. Reilly, Jr.

OBSCURE is a two-dimensional thermal-spectra program which will solve the diffusion equation for two coupled energy groups. The equation to be solved is

$$-\nabla \cdot D\nabla\phi + A_{\phi} = S$$

where D and A are two-by-two matrices, ϕ and S are two-by-one.

OBSCURE is designed to work in conjunction with CURE in the following way. A pseudo four-group CURE problem is run up through the calculation of pointwise coefficients only. Each group actually represents an element in the two-by-two A or D matrix. The input to this preliminary problem includes the mesh description and precalculated thermal group constants.

The pseudo problem is immediately followed by the actual CURE problem whose mesh description must agree with that of the pseudo problem. After the actual problem is run to convergence in the normal fashion, transfer of control is made to OBSCURE. OBSCURE discards the old thermal group but uses the same slowing-down source which produced it, split into two components, as a source for the new coupled groups. The two coupled groups are then solved simultaneously by line relaxation; the usual three-term elimination method is used on each row of the mesh, with matrix multiplication and inversion replacing the usual scalar operations of multiplication and division, respectively.

Several mesh sweeps are performed until the flux passes a specified convergence test; the criticality and power distribution are then recalculated and edited. No further recycling is possible.

OBSCURE requires a 32K IBM-704 with ten tape units. It is limited to 2500 mesh points and cannot be used with 90-degree periodic geometry. Running time averages about 0.03 minute per point.

9. *KARE (Philco-2000)*

E. D. Reilly, Jr.

KARE is a system of one- and two-dimensional diffusion theory programs for the Philco-2000. Group constants may be calculated for up to 511 material regions by either the three-group WOXX scheme (see Sect. 7.4.F.3) or the two-, three-, or four-group FICS routine (see Sect. 7.4.F.4). Precalculated group constants may be supplied for up to five energy groups. Several geometry options may be chosen:

1. r–z (r in one dimension)
2. x–y (x in one dimension)
3. x–y with diagonal lines (REM)
4. uniform triangular mesh (FLEER).

Up to 20,000 mesh points are allowed. Mesh spacing may be variable in all except FLEER geometry. Boundary conditions allowed are:

1. flux zero
2. current zero
3. given ratio of current to flux
4. 90-degree periodic in x–y geometry, i.e., the entire model can be constructed by 90-degree rotations of the original about the top right-hand point
5. 120-degree periodic in FLEER geometry, i.e., the entire model can be constructed by 120-degree rotations of the original about the bottom left-hand point
6. double 120-degree periodic in FLEER geometry, i.e., the entire model is infinite in extent and can be constructed by 120-degree rotations about the bottom left-hand point and the top right-hand point and points that these rotate into, etc.

Automatic criticality searches are made by having the program move rods in r–z or adjust buckling in x–y or FLEER until a desired eigenvalue is reached.

Material regions are specified by describing the contour of their boundaries. Provisions are made to allow splitting of a region into many parts and to allow only one-fourth or one-third of a mesh to be described for problems that are almost 90-degree or 120-degree periodic. The program will rotate the partial input to complete a full core and then

allow amendments to be made which describe deviations from true periodicity, such as the pulling or inserting of a rod in any third or quarter.

In the course of an automatic life study, KARE transfers information from time step to time step by means of a history tape. In addition to masses from each steady-state xenon problem, complete source and flux meshes are also saved. During a life study, each problem is furnished with a source and flux guess from the last problem of that type done during the study.

The depletion routine used in all classes of KARE problems is essentially identical to that used in CUREBO and is described in more detail under that heading (Sect. 7.4.E.7).

A provision for splitting the thermal group into two coupled groups which are solved simultaneously is available for 5000-point x–y and r–z calculations. This capability is similar to that of the IBM-704 program OBSCURE, but is more powerful in the sense that recycling through any number of source iterations is possible.

Multichannel flux synthesis calculations[55] can be done with KARE by running a series of x–y cuts whose results are stored on a history tape. From each detailed x–y problem, coupling constants are calculated for each of a small number of channels, each of which will be represented numerically by a line of points in the z direction. These lines are then solved, simultaneously for all energy groups, by the CLAG program (which is an inherent part of KARE).

At any time during a life study, or at any later time if so desired, adjoint problems corresponding to any previously done flux problem can be obtained. The flux and adjoint results can then be fed automatically to the PSP perturbation option of KARE. This procedure is especially useful in obtaining regionwise temperature coefficients at any stage in life.

A wide variety of edits is furnished with each problem, depending on the options chosen. Preiteration edits include a topological material mesh picture, a summary of cross-section input information, and group constant output data. Postiteration output consists of pointwise flux and peak power edits, and regionwise flux and absorption integral edits. In addition, special edits can be requested over any number of arbitrary combinations of regions that may be desired.

All of the input-output features of KARE also pertain to a one-dimensional option contained in the same system. Up to 200 mesh points are allowed in either slab or radial geometry. All energy groups, up to a limit of five, are solved simultaneously. Up-scattering is possible from any group, but only to the next higher energy group. One-dimensional

life studies and perturbation calculations can also be done.

FLEER has been written for the Philco-2000 as part of the KARE System. Iteration procedures are identical to the IBM-704 version, but the number of points allowed has been extended to 20,000 and the number of regions to 511. In addition to the 120-degree periodic option allowed on the left and bottom of a rhombus in IBM-704 FLEER, the Philco-2000 version allows a doubly periodic option whereby the top and right sides may also be 120-degree periodic. As part of KARE, the new version may also be depleted whereas the IBM-704 version could not.

Without a good source guess, typical running times for individual KARE criticality problems are:

$$T = \frac{GN}{800} \text{ for one-dimensional problems}$$

$$T = \frac{GN}{600} \text{ for } r\text{–}z \text{ problems}$$

$$T = \frac{GN}{300} \text{ for } x\text{–}y \text{ problems}$$

$$T = \frac{GN}{250} \text{ for 90-degree periodic problems}$$

$$T = \frac{GN}{280} \text{ for FLEER geometry problems}$$

where T = machine time in minutes, G = number of groups, and N = number of flux points. Running times can be decreased by 25 to 50 percent through the use of a source and flux guess saved from a similar problem run at an earlier time. Descriptions of major segments of KARE are covered in other sections.

10. AMOK (Philco-2000)

E. D. Reilly, Jr.

AMOK, part of the KARE System, is a replacement for the IBM-704 program OBSCURE. Major improvements are:

1. The number of points has been extended from 2500 to 5400.
2. A 90-degree periodic option is allowed.
3. Diagonal lines are allowed.
4. Group constants for the fast groups, as well as for the coupled thermal groups, may be calculated by means

of FICS. Constants for OBSCURE had to be supplied manually as precalculated values.

5. Any number of source iterations may be performed; whereas OBSCURE was limited to one further source iteration beyond the point where the thermal group was split.
6. AMOK may be depleted according to the KARE depletion scheme. Running time for an average size problem of 2500 points is about 60 minutes.

D. Few-Group Three-Dimensional Diffusion Theory

1. TKO-1 (IBM-704)

W. R. Cadwell

The TKO-1[26] program solves the two-to-four group neutron-diffusion equations over a rectangular parallelepiped in x–y–z geometry. The parallelepiped is divided into as many as 511 regions of differing nuclear properties, with the interfaces between these regions composed of plane segments parallel to the boundary planes. The input diffusion coefficients and macroscopic cross sections are regionwise constant.

Either a zero flux or a zero current condition may be applied at each external boundary, and a logarithmic derivative condition may be applied at internal control rod boundaries. In addition, the plane $x = y$ is required to be a plane of symmetry so that the region of solution is an isosceles-right-triangular prism. A nonuniform grid of mesh planes is imposed on the region of solution, with each mesh plane parallel to a boundary plane of the parallelepiped and with the mesh intervals chosen so that all interfaces fall on mesh planes. The number of mesh points in the region of solution is limited to 2675 on a 16K computer and to 4725 on a 32K computer.

Seven-point difference equations are generated at each mesh point in the region of solution, and the resulting sets of group equations are solved using successive point overrelaxation. In general, the running time of a problem depends upon the number of groups G and the number of points N. For typical values of the convergence parameter, the running time in minutes is given approximately by

$$T = \frac{GN}{60}$$

where T = machine time in minutes, G = number of groups, and N = number of flux points. Thus, a maximum 4725-point problem with two groups will run in about 2.6 hours.

The input format of TKO-1 corresponds as closely as possible to that of PDQ-2. In addition to certain control information, the input required includes diffusion coefficients and macroscopic cross sections by group and region, the sequence of mesh intervals in each coordinate direction, and a description of the placement of regions in the mesh. The region description is accomplished by using a two-dimensional rectangular overlay process to specify the first plane and then overlaying changes on this plane to describe succeeding planes.

The output of the program includes a complete edit of the input, a picture of each different x–y plane with all regions and interfaces indicated, the region volumes, the region-integrated flux and source, and the pointwise flux and source values. A preliminary input edit, which includes the pictures of the mesh, may be run before beginning a problem.

The program requires a computer with 16K or 32K core storage, one 8K drum unit, an on-line card reader, an on-line printer, and at least seven tape units.

2. *UFO (IBM-704)*

E. D. Reilly, Jr.

UFO[56] is a three-space dimensional few-group neutron-diffusion program for the IBM-704. Its capabilities and limitations are:

1. Three-dimensional Cartesian coordinates are used.
2. Variable mesh spacing in all directions is permitted.
3. Material interfaces must coincide with mesh planes.
4. The whole mesh must be bounded by a rectangular parallelepiped.
5. Boundary conditions may be given (independently for each of the six faces) as zero flux, zero current, or specified ratio of current to flux.
6. Up to five energy groups are allowed.
7. Up to 512 different material compositions may be specified.
8. The number of mesh planes is limited as follows:

$$I > 3 \qquad J > 3 \qquad K > 3$$

$$I \cdot J \leq 4000 \qquad J \cdot K \leq 4000$$

where I–1, J–1, and K–1 are the number of mesh planes interior to the reactor region for the x, y, and z directions, respectively.

9. The number of mesh points is limited by $I \cdot J \cdot K \leq 15{,}000$.

UFO uses extrapolated Liebmann type flux iterations and Chebyshev type source acceleration (see Sect. 7.4.C.5). The program requires a 32K IBM-704 with eight tapes. Running time varies from 15 minutes for a 120-point problem to two hours for a 6000-point problem.

E. Few-Group One-, Two-, and Three-Dimensional Depletion

1. CANDLE (IBM-704)

W. R. Cadwell

CANDLE[57] is a one-dimensional few-group diffusion theory lifetime depletion program designed for the study of slab, cylindrical, and spherical reactors. The program is of use in estimating reactor lifetimes for given fuel loadings and in determining the time dependence of fuel distributions and flux shapes. Criticality is maintained during the lifetime of the reactor by means of the adjustment of a variable poison cross section or a variable transverse buckling. This buckling is presumably related to the effective height of the reactor for a given control rod bank position. To permit treatment of axial depletion in slabs and cylinders, provision is also made for controlling reactivity by moving the interface between a poisoned (rodded) and an unpoisoned region.

The program consists essentially of three interconnected sections. In the first section, group constants are calculated from effective microscopic cross sections. The fast-group cross sections are stored on a library tape, whereas the thermal-group cross sections must be supplied as input. Other input data required include the intial isotopic number densities, thermal self-shielding factors, and region-dependent resonance escape probabilities for U^{238}.

In the second section of the program the few-group spatial diffusion equations are solved using a version of WANDA to determine the eigenvalue, the fluxes at each point in the geometric configuration, and the value of the control parameter necessary to maintain criticality of the reactor. Two or four energy groups may be utilized with this few-group scheme. In the third section new isotopic number densities are calculated at each point for a given power-time interval. The program explicitly calculates buildup and depletion of isotopes in the U^{235} and U^{238} fission chains and the Sm^{149} and Xe^{135} poison chains and has provision for the inclusion of two burnable poisons.

The cycle of operations through the three sections of the program is automatically repeated an arbitrary number of times through the lifetime of the reactor. Running time for ten time steps is of the order of two hours or less. Output quantities available for each time step include the eigenvalue and control parameters for each iteration, region integrals of the power and of the number density of each fissionable element, and pointwise values of the flux, source, power, number densities, and macroscopic cross sections.

At the end of any time step a xenon override test may be employed. New isotopic number densities for all burnable elements are calculated for any specified time interval, with the fluxes reduced to some specified fraction of those obtained at the end of the time step. New group constants are calculated and an eigenvalue is computed under the condition of no external control. If the eigenvalue is less than one, it is not possible to override peak xenon and the calculations may be terminated. If greater than one, a criticality search may be performed and the series of time steps continued.

Computer requirements of the program include 8K core storage, five tape units, an on-line card reader, and an on-line printer.

2. *TURBO (IBM-704)*

W. R. Cadwell

The TURBO[58] program calculates the effects of fuel depletion and fission product accumulation in two dimensions, (x, y) or (r, z), by the use of few-group diffusion theory. The program is a direct generalization of the one-dimensional CANDLE program and includes provisions for control rod motion, temperature changes, and xenon transients.

Sums of products of microscopic cross sections and the appropriate number densities define the macroscopic cross sections at each point. The fast microscopic cross sections are contained in a program library, and the thermal cross sections and self-shielding factors are required as input. A correction for U^{238} resonance absorption is made in the epithermal group which requires an input resonance escape probability. The neutron flux and eigenvalue are determined from the few-group diffusion equations using the calculational sections of PDQ. The depletion calculation assumes that the neutron flux in each group remains constant over a time step. An average flux is calculated for each mesh rectangle, is normalized to a specified core power, and is then used in the depletion equations to recalculate the densities of fuel, poison, and fission-product isotopes.

The operation of the program differs from CANDLE in several respects because of the increased computer time requirements. The important differences are that no more than one time step is performed automatically and no criticality search is provided. The data deck is processed by the program for each time step to allow certain changes such as adjustment of the control parameter (smeared poison or transverse buckling) used to maintain a near-critical eigenvalue. A history tape is prepared containing the number densities, flux values, and power shape at each time step which are required as input to the next time step. In addition, an output tape is prepared for each time step containing the quantities that may subsequently be edited. The editing may be onto paper or punched cards, and the quantities available include pointwise and quadrant power, beginning-of-time-step and end-of-time-step number densities, pointwise values of the flux and the macroscopic data, power integrals, number density integrals, and flux-weighted average cross sections.

An auxiliary routine allows the study of the effects of replacing or interchanging subassemblies by changing the time-dependent densities at a particular time step. This may be done by supplying homogeneous densities in some region, by moving a region into another position of the same size and shape through a translation and/or rotation, or by specifying nonuniform number densities in a region point-by-point.

The computer time requirements depend on many factors, but primarily on the number of mesh points. In general, if the time required for a similar PDQ problem is known, adding one-third to this figure gives a good estimate of TURBO time exclusive of output. The computer hardware requirements include at least 8K of core storage, one 8K drum unit, 10 tape units, and an on-line printer, card reader, and card punch.

3. *DRACO (IBM-704)*

W. R. Cadwell

DRACO[59] is essentially a three-dimensional version of TURBO with various modifications and several additional features. It provides a means for studying the neutron flux, the power level, and the related buildup and depletion of materials at different stages in the lifetime of a reactor. Group constants are calculated at the beginning of each time step and the neutron-diffusion equations are solved using the calculational sections of TKO. It is this program which sets the mesh limitations in DRACO and determines the region of solution. The TKO fluxes are normalized to a specified

power, and new isotopic densities are calculated for the time-dependent elements U^{235}, U^{236}, U^{238}, Pu^{239}, Pu^{240}, Pu^{241}, Pm^{149}, I^{135}, Sm^{149}, Xe^{135}, B^{10}, lumped fission products, and one unnamed poison.

The program requires the following quantities as input for each time step: information describing the geometry of the problem, option control information, length of the time step, power level during the time step, initial eigenvalue guess, convergence criterion, percentage of homogeneous poison per group, integral of the fission spectrum for fast groups, the iodine yield for U^{235}, U^{238}, Pu^{239}, and Pu^{241}, thermal microscopic cross sections, flux guess, material buckling for two-group problems, resonance escape probability of U^{238}, homogeneous poison, isotopic densities, and thermal self-shielding factors. The only quantities that may not be changed between time steps are the geometry, the number of lethargy groups, the mesh spacing, and the time-dependent isotopic densities.

During a time-step calculation the most important information printed on-line pertains to the progress of the iteration. Information vital to the running of succeeding time steps and the maximum xenon case is accumulated on a history tape for each problem. A binary output tape is generated from which various quantities may be edited for off-line printing. On-line printing in addition to iteration information includes the region-integrated volume, the region-integrated flux for each group, the percentage of power for each fissionable element in each region, the percentage of total power contributed by each region, and the normalization factor used to obtain the power-normalized fluxes. The information available for editing on the binary output tape includes the region description which may be edited in picture form, the initial and final isotopic densities, the group constants, the source normalized fluxes and the source values, the pointwise element power, group power, and total power, and the power normalized fluxes.

DRACO running time is about one-third greater than the TKO running time for a similar problem. The program requires a computer equipped with 32K core storage, an 8K drum unit, 10 tape units, and an on-line printer, card reader, and card punch.

4. *CANDLE-TURBO-TNT (Philco-2000)*

W. R. Cadwell

The CANDLE, TURBO, and TNT programs[50,60] for the Philco-2000 computer are extensions of the corresponding CANDLE, TURBO, and DRACO IBM-704 programs. The

Philco-2000 programs are assembled for a computer with 32K core storage, 16 tape transports, 8 index registers, and auxiliary card-to-tape and tape-to-printer facilities. The three programs are consistent wherever possible in the type of input required and the availability of special options. In addition, there is consistency between these programs and the time-independent programs WANDA-5 and PDQ-4. (Under option, TNT may itself be used as a time-independent program.)

The calculations are based on few-group neutron-diffusion theory. Isotopic number densities are used to describe various material regions, each of which is initially homogeneous. Nonuniformity in the number density distribution results from the depletion or buildup of these isotopic densities in each mesh element as a function of the cross sections and neutron flux. The flux is assumed constant over each time interval of depletion and is recalculated for each succeeding step. Several options are available for describing homogeneous and lumped poisons, control rods, and other special regions. Provision is also made for the study of fuel replacement, stuck rods, maximum xenon, and other situations. The number of mesh points is limited to 500 in one-dimensional problems, 20,000 in two-dimensional problems, and 100,000 in three-dimensional problems. As many as 150 compositions may be used to describe different materials and/or subregions of interest. Either a zero flux or a zero flux derivative condition may be applied at each boundary, and a 180-degree rotational symmetry condition may be applied in two-dimensional problems.

The input required by these programs consists of a description of the geometry and values of number densities, self-shielding factors, resonance escape probabilities, transverse and material bucklings where appropriate, poison cross sections, macroscopic cross sections, and special-region polynomials. Corrections to the fast-fitted cross-section library are allowed and thermal cross sections must be provided. Certain other parameters used in the fitting procedure and in the depletion calculation may be specified.

Output available includes the eigenvalue and region integrals of the flux, power per fissionable isotope, and total power. Averaged end-of-time-step isotopic densities, flux-weighted beginning-of-time-step isotopic densities, and averaged flux-weighted macroscopic cross sections are also given for each region. Optionally, pointwise values of the flux, point-to-average power, number densities, and macroscopic cross sections may be printed from selected regions.

A number of branching options have been provided in these programs. Branch calculations are generally auxiliary studies

at some point in a problem, such as stuck rod and fuel replacement investigations. In particular, there are problems in which the nonuniform isotopic densities of the time-dependent elements for some time step of a problem are used as input to a second problem. These densities may be altered by expansion or contraction across axes of symmetry and/or by replacement in selected regions. The types of expansion and contraction permitted in a two-dimensional problem are reflection across the x-axis or y-axis, quarter-core to full-core expansion, contraction across the y-axis, 180-degree half-core to full-core expansion, and 180-degree half-core to quarter-core contraction.

Running times for CANDLE and TURBO time steps are about one-third greater than the times for corresponding WANDA-5 and PDQ-4 problems. Running times for TNT time steps range from 1 to 25 hours, depending upon the number of mesh points, the problem geometry, and the initial flux guess.

5. ZIP-2 (Philco-2000)

W. R. Cadwell

ZIP-2[50, 61] is a diffusion theory synthesis program for reactor design calculations. The synthesis technique is a method of forming a solution to the three-dimensional few-group neutron-diffusion equations by stacking a number of solutions to the two-dimensional $(x-y)$ equations. The stacking is performed by calculating flux-averaged diffusion coefficients, macroscopic cross sections, and bucklings from the $x-y$ solutions and using these as input to the ZIP-2 program which solves the one-dimensional (z) equations. These parameters are input to ZIP-2 in the form of (at most) fifth degree polynomials, with the fuel fraction as the independent variable. The polynomials are normally least-squares-fitted curves based on TURBO solutions at discrete fuel-fraction values.

The main sections of the program are: (1) a coefficient routine which prepares pointwise input for the WANDA section of the program by evaluating input polynomials which are functions of the fuel in the radial slices corresponding to the WANDA axial points; (2) that part of the WANDA-5 program which solves the one-dimensional few-group neutron-diffusion equations in slab geometry, with pointwise variable input; (3) a boundary search routine which provides the desired sequence of control rod insertions and withdrawals; and (4) a fission-product buildup and fuel-depletion routine which produces pointwise variable Xe^{135} and Sm^{149} poisoning and nonuniform fuel burnup.

In addition to the polynomial coefficients, the required input includes initial fuel number densities, initial fuel fraction, rod program descriptions, mesh spacing, time intervals, power fractions associated with these time intervals, full power level, and a number of control parameters. Output quantities available at each time step include the eigenvalue and the rod configuration number; flux-weighted group data averaged by region; region-averaged values of the power, fuel fraction, and number densities; pointwise values of the flux, power, fuel fraction, and number densities; and values of k_∞ or k_{eff} for each interval. The power, the fuel fraction, k_∞ or k_{eff}, xenon, samarium, and the flux may also be plotted versus the radius in centimeters.

Both 16K and 32K versions of the program are available. The 16K version allows 160 mesh intervals, 20 compositions, and 20 rod configuration programs, while the 32K version allows 400 mesh intervals, 50 compositions, and 50 rod configuration programs. Typical running time is 3 minutes per time step.

6. *BOX (IBM-704)*

P. V. Oby

BOX is a one-space dimensional few-energy group depletion program for the IBM-704 designed to be used in highly enriched, water-cooled and water-moderated reactor calculations. It is essentially a combination of separate routines:

1. A modification of the WOXX scheme, a cross-section scheme based on a method developed by Deutsch[68] wherein the various energy-group constants needed are derived from nuclear cross-section measurements averaged over appropriate neutron fluxes. For each energy and each material, the diffusion coefficient and slowing down, removal, and fission cross sections are developed as required for the iterative routine.
2. A modification of the WANDA program is used for iterative calculation of the neutron flux and power distributions and eigenvalue. Calculations are based on numerical approximations to the diffusion equations, utilizing the group constants obtained from the cross-section routine. Slab, cylindrical, or spherical configurations are permitted with allowable boundary conditions of zero flux or zero current.
3. The burnup routine BO1 is used for depletion. Depletion occurs after a criticality search with equilibrium xenon

has been made. The depletion calculation permits separate fuel and poison self-shielding, and the ratio of epithermal to thermal absorption is assumed to be the same for fuel and poison. Depleted fuel and poison masses are then used to compute a new set of group constants (by WOXX) for the next time step. Depletion is regionwise and is based on absorption in the thermal group only.

Fission product buildup is calculated, assuming a constant fuel volume, and is a function only of the fractional fuel depletion in a region; effects of epithermal fission and capture are ignored.

At each time step, the flux distribution and eigenvalue are determined for peak xenon override and cold shutdown conditions.

Control rods are represented by an area absorption method (window-shade technique) wherein rods are not considered as discrete boundaries and source neutrons are reduced proportionate to the rod absorption area. Criticality search may be performed.

Options include no xenon, steady-state xenon, or peak xenon. Also adjoint calculations may be performed.

Running time is about 10 to 15 minutes per time step.

7. CUREBO (IBM-704)

E. D. Reilly, Jr.

The depletion version of the program CURE, described under two-dimensional diffusion calculations, is CUREBO.[62] CUREBO is formed from CURE by adding a depletion calculation, BO2, which calculates the masses of fuel and poison remaining in each material as a result of steady-state operation of a critical reactor. If the reactor is not within a prespecified range about criticality, the calculation is not performed. Depletion is region-dependent and is based on thermal and epithermal fluxes and absorption cross sections. Time steps are determined by the total amount of fuel to be burned up. The calculations may be one of three types, depending upon the location of the burnable poison in the material:

1. Discrete poison: All burnable poison in the material is located in discrete substances separate from the fuel. This means that all of the burnable poison is subject to a self-shielding factor different from the fuel self-shielding factor.
2. Homogeneous poison: All burnable poison in the material is located in homogeneous substances with the fuel. This

means that all of the burnable poison is subject to the same self-shielding factor as the fuel.

3. Combination poison: Some of the burnable poison is in homogeneous substances, and the remaining burnable poison is in discrete substances. This means that some of the burnable poison is subject to the fuel self-shielding factor, and the remaining burnable poison is subject to a different self-shielding factor.

8. KARE Depletion (Philco-2000)

Depletion in the KARE System is essentially the same as that used in CUREBO (Sect. 7.4.E.7). Details of life studies in KARE are described in Sect. 7.4.C.9.

9. FLU (IBM-704)

E. D. Reilly, Jr.

Using flux integrals from CURE, FLU produces diffusion, slowing down, absorption, and fission group constants averaged over all regions of a given mesh plane. Together with a radial buckling, which FLU also calculates, these data are obtained for several x–y cuts and then fed into BOX to complete a one-channel flux synthesis calculation.

10. KLAG (Philco-2000)

E. D. Reilly, Jr.

KLAG [15, 63] is a multichannel flux synthesis program which operates as part of the KARE System on the Philco-2000. Using this technique, a reactor is divided into several axial zones and radial channels. It is assumed that there is no axial material variation within zones. A detailed two-dimensional KARE calculation is performed for each zone. Input to KLAG consists of fluxes and flux-weighted material properties averaged over the channels along with gross transfer coefficients which determine the leakage across channel interfaces. Each channel can be represented numerically by a line of mesh points in each energy group. All lines and groups are solved simultaneously by matrix methods. Detailed three-dimensional flux distributions can then be approximated by multiplying the two-dimensional flux distributions by the coarse mesh channel values obtained from KLAG. (For more detailed discussion of synthesis techniques, see Chap. 5.)

The program will allow for five energy groups, ten axial channels, and 300 axial mesh points with the restrictions that:

1. Number of groups times number of channels must be less than 20.
2. Number of groups times number of channels times number of points must be less than 900.
3. (Groups times channels)^2 times points must be less than 16,000.

Running time is approximately one to two minutes per problem for the KLAG part of a synthesis calculation.

F. Few-Group Constants Calculations

1. MUFT-4 (IBM-704), MUFT-5 (Philco-2000)

H. Bohl

Both programs, MUFT-4[64] and MUFT-5[65], solve the P_1 or B_1 multigroup equations for the first two Legendre coefficients of the flux and the isotropic and anisotropic components of the slowing-down densities due to a cosine source in space. Hydrogen may be treated exactly or in a Selengut-Goertzel approximation. For degradation by heavy elements, both age and Greuling-Goertzel approximations are available. The program also takes into account slowing down of neutrons by inelastic scattering and removal of neutrons resulting from capture and fission resonances. Only the nonthermal energy range is considered. MUFT-5, however, has a slowing-down treatment which is different from MUFT-4 in the following way. In MUFT-4, hydrogen slowing down is treated exactly, whereas the heavy element contribution to the slowing down is lumped together as one quantity. The coefficients of the heavy element Greuling-Goertzel slowing-down equation are sums and averages of the coefficients of what would be the individual isotopic equations. In MUFT-5, the heavy element slowing-down density is determined separately for each isotope of the composition.

A library of nuclear data must be available to run a problem on either program. The library contains the necessary cross-section data by isotope for a fixed group structure. In addition, for each isotope, there are parameters for computing the slowing-down densities. There may be parameters included in the library for computing the capture and fission resonance integrals and parameters which describe the inelastic scattering. Source spectra corresponding to different types of sources may also be in the library. For MUFT-4 the library is on the

same tape as the program and is limited to 45 isotopes and 100 lethargy groups. Data for the library are easily placed on tape by an auxiliary program, LTP1. New data may be added or information already on the tape may be corrected via LTP2. A printout of any library tape may be obtained using LTP3. For MUFT-5, a separate library tape (less than 80 groups) must be used when running any problem. This tape is prepared and altered by a set of auxiliary programs, MILC1, MILC2, and MILC3, which are analogous to LTP1, LTP2, and LTP3.

For either program, only isotope code numbers and their number densities along with resonance self-shielding factors, total buckling, and a few control parameters need be specified for any problem. In MUFT-4 input to each problem has to be completely specified. However, in MUFT-5, after the first problem has been specified, only the changes in the input of that problem needed to describe the next problem are specified. Both programs are limited to 15 isotopes per composition.

Few-group data are edited by both programs for three-, two-, and one-group schemes. For each scheme the program will print diffusion constants; absorption, removal, and fission macroscopic cross sections; source, flux, and current integrals; and nonabsorption probabilities and group ages. Also, an age-to-thermal quantity is printed for each scheme. Few-group absorption fission and nu-fission results may be requested for each isotope. In addition to this editing, an optional edit is available in MUFT-5 which will compute few-group blackness diffusion constants and absorption cross sections for an absorbing plate assumed adjacent to the MUFT composition region having the same flux spectrum as computed for the MUFT composition or a modified flux spectrum.

Average running time for a normal MUFT-4 problem is 11 seconds. If isotopic averaging is requested, an additional 15 seconds per isotope specified should be added to the normal average running time. Typical running time for individual MUFT-5 problems, excluding the reading of the library tape which is done only for the first problem of a set, is 5 seconds with the basic edit and 15 seconds with a 10-isotope isotopic edit. An additional 3 seconds is needed for the blackness edit.

2. SOFOCATE (IBM-704), KATE (Philco-2000)

H. Bohl

Both the SOFOCATE[66] and the KATE[67] programs compute thermal group nuclear constants. A neutron flux distribution is first calculated by using either a Maxwellian or Wigner-Wilkins spectrum and then the cross sections are averaged over the

distribution. In a Wigner-Wilkins calculation it is also possible to calculate a neutron distribution based on one mixture of isotopes and then to average over a second set of isotopes. In addition to the macroscopic averages of $D, \Sigma_a, \nu\Sigma_f$, it is also possible to obtain microscopic averages of any isotope in the library. In addition to this, KATE has the option of determining the neutron distribution with one composition of isotopes and to average this over a second composition of isotopes for a lumped absorber region. Macroscopic averages and blackness coefficients are calculated for the lumped absorber region. A further option in KATE will include particle self-shielding effects in the blackness calculation. A library tape of experimental microscopic cross-section data for each isotope is not used in KATE as was done in SOFOCATE. A compressed form of the library is maintained in core at all times.

Typical SOFOCATE problem running times are 15 to 30 seconds, whereas for KATE, typical problem running time is about 3 to 5 seconds.

3. WOXX (IBM-704), (Philco-2000)

W. H. Turner

WOXX[68] is a three-energy-group routine for calculating diffusion, slowing down, removal, absorption, and fission group constants for use with CURE. Neutron spectra in each group over which cross sections are averaged have the following characteristics:

1. Fast group, inverse energy dependence, fixed cutoff.
2. Epithermal group, inverse energy dependence, composition dependent cutoff.
3. Thermal group, hardened Maxwellian spectrum.

Various optional calculations are available, including steady state, peak, and transient xenon; thin-region calculations; two-group self-shielding of fuel and boron; fission product concentration calculation; and modification of removal cross sections to simulate the presence of control rods.

In the Philco-2000 version, the calculation of epithermal transmission probability in the thin-region modifications has been improved to account for zirconium resonance absorptions. Numerous options have been added including:

1. The calculation of water density under nonboiling conditions.
2. The automatic calculation of removal cross-section modification factors for use in the simulation of control rods.
3. The xenon cross section may be multiplied by the thermal self-shielding factor of the fuel if desired.

4. The gamma production cross sections and birth spectrum may be calculated for use in gamma heating studies.

WOXX calculations for a typical reactor require about 0.3 second per region on the Philco-2000.

4. FICS (Philco-2000)

G. L. Johns

FICS[69] is a group constant routine designed for use as an alternative to WOXX in the KARE System. It is based on the MUFT and KATE group constant programs and provides two-to-four group results. The FICS calculation for a typical reactor requires about 0.5 second per region.

In the fast energy range, 10 Mev to 0.625 ev, FICS calculates diffusion, slowing down, absorption, and fission group constants in one-, two-, or three-energy groups. In the one-group option, three-group constants are computed and then averaged over the entire fast energy range to obtain the desired quantities. The fast group constants are computed simply from predetermined microscopic cross sections which were obtained by curve fitting to MUFT parameters.

Below 0.625 ev, FICS generates one-group constants for diffusion, absorption, and fission which are functions of the temperature of the region. The thermal treatment is a variational procedure which computes an approximate Wigner-Wilkins flux spectrum as a linear combination of two lethargy and temperature dependent base spectra. The base spectra are obtained beforehand, using the KATE parameters. The coefficients for linearly combining the soft and hard base spectra may be computed by the program, borrowed from another region, or supplied as input. The thermal cross sections are determined by averaging lethargy dependent microscopic cross sections and diffusion constants over the composite spectrum.

Fuel and poison masses may be reduced by self-shielding factors which vary with depletion; modifications can be requested to improve the cross sections of thin, highly absorbing regions; and rod factors based on the area absorption technique may be computed and applied automatically. These region-dependent options are available in FICS in largely the same form as they appear in WOXX. Self-shielding and rod-factor calculations apply to the thermal group and slowest fast group (resonance group) only.

A xenon routine has been included which will compute the amount of Xe^{135} present in any fuel-bearing region for equilibrium, peak, or intermediate conditions. The thermal microscopic xenon absorption cross section is now obtained by

averaging over a thermal spectrum computed with no xenon present, and the thermal calculations are then repeated with xenon present to provide the final thermal constants for the region.

FICS contains an improved fission product routine over that used in WOXX. Contributions to the absorption cross sections of the thermal and resonant groups are computed as functions of the degree of fuel depletion. As an option, Sm^{149} may be excluded from the fission products. FICS is coupled to the two-group burnup scheme now used in KARE.

5. SWAK System (Philco-2000)

F. D. Federighi

All programs in the SWAK System are concerned with computing thermal spectra and cross-section averages. They are written in the FORTRAN language. They all either used or are compatible with MATAR, a matrix arithmetic subroutine. This subroutine is used extensively in these programs to simplify the coding problems arising in the manipulation of arrays. These programs are:

1. MIRAGE, reads in instructions signifying matrix operations and calls MATAR to perform them. It can be used for general array manipulation and also to generate tapes for the other programs.
2. ADL, a program of MIRAGE instructions which calculates asymptotic diffusion lengths and diffusion-hardened spectra.
3. SWAK, a program of MIRAGE instructions which calculates thermal spectra and spectrum-averaged cross sections based on a trapezoidal approximation to the integral equation. Any slowing-down kernel may be used.

6. ADL (Philco-2000)

G. P. Calame

ADL is a FORTRAN program which computes asymptotic diffusion lengths and diffusion-hardened spectra. The asymptotic diffusion length in a medium may be defined as the largest eigenvalue, L_1, of the equation[70]

$$\frac{D(E)}{L_j^2}\gamma_j(E) = \int_0^\infty \gamma_j(E')\,\Sigma_s(E' \to E)\,dE' - \Sigma_t(E)\,\gamma(E)$$

where $\Sigma_s(E' \to E)$ is the energy exchange kernel, $\Sigma_t(E)$ the total cross section, and $D(E)$ the diffusion constant in the medium. The corresponding eigenfunction, $\gamma_1(E)$, is the so-called diffusion-hardened spectrum.

ADL is one of the SWAK System programs and includes provisions for calculating the position-independent spectrum in an infinite medium.

G. Approximations to Transport Theory

1. *FLIP-1 (IBM-704)*

H. Bohl

FLIP-1[71] is an IBM-704 program designed to solve one-velocity transport problems in slab geometry. The following approximations are available as options: P_3, P_5, P_7, double-P_1, double-P_2, and double-P_3. In all approximations the flux components are computed over a maximum of 500 mesh intervals distributed through a slab containing no more than 50 homogeneous regions. The source function is assumed to be isotropic, but it may vary from mesh point to mesh point. Anisotropic scattering is permitted within limitations.

Application of the L^{th} order spherical harmonics approximation leads to $2L+1$ coupled first-order differential equations. These may be transformed into $(2L+1)/2$ second-order equations which are similar in form to the few-group diffusion equations. FLIP solves these equations by a Gauss-Seidel iteration technique. The double-P_L equations are treated in essentially the same way. In both types of approximation the iteration procedure starts from a zero flux guess in all groups. The first iterate of the scalar flux is then identical with the P_1 solution. With a convergence criterion of 0.00005, convergence requires about four to ten iterations in all P_L approximations. For the double-P_L approximations, four to 15 iterations may be required. The number of iterations usually increases slightly in the higher approximations. Extrapolation of the iterative process is available in FLIP but, because of the rapidity of convergence, its use has never been necessary; also, it might not prove very effective for this same reason.

The program requires, as input, values of the mesh spacing, sources, and cross sections for absorption and scattering.

FLIP-1 was designed to handle only conditions of zero directional flux or zero current at the boundaries. To handle gray boundary conditions, a second program, FLIP-2, was written. The gray boundary conditions are applicable at the left- and/or right-hand boundaries. If the boundaries are not

gray, then the boundary conditions of FLIP-1 are applicable. Only the double-P_1 approximation is now available in FLIP-2, which cannot handle more than 250 mesh intervals and 25 regions.

The running times for problems vary from less than 0.5 minute for small P_3 and double-P_1 problems to about 10 minutes for large P_7 and double-P_3 problems.

The method of solution described here has two main advantages. First, the iterative process is quickly convergent and the rate of convergence is not very sensitive to the problem parameters. In contrast, the convergence rate of the iterative process used in discrete ordinate programs goes to zero as leakage and absorption rates diminish.

Secondly, the FLIP equations are closely related to few-group equations which have already been programmed for various machines. Only minor changes are required to convert a two-group program into a program which solves the P_3 or double-P_1 equations. Thus, the FLIP method is available even to those reactor installations employing small programming staffs and small machines.

2. SLOP-1 (IBM-704)

H. Bohl

SLOP-1[72] is a one-dimensional thermal multigroup program with both up- and down-scattering designed to compute the flux level and energy spectrum, as a function of position, in a heterogeneous array of diffusing media. Slab problems may be treated in a double-P_1 approximation, whereas in cylindrical and spherical geometries only the P_1 approximation is available. The model is further restricted to isotropic slowing down into the thermal range, regionwise constant slowing down, no transverse buckling, and only one moderating material at a given temperature in any problem. Sets of transfer matrices for many temperatures may be contained in the library which is on the same tape as the program. The remainder of the library consists of cross-section data for various isotopes.

The library-program tape is created by a separate program, LTP7, and edited by the program LTP9. LTP7 requires, in addition to the cross-section data on cards, a tape which is in the format of the binary output tape of the program ECESS.[73]

Thermal double-P_1 multigroup problems require guesses for all four solution vectors because of the up- and down-scattering source terms. In typical SLOP-1 problems there will be available only a one-velocity spatial flux guess which

is combined with a Maxwellian spectrum to generate a flux guess in all groups, with the remaining three vectors set to zero. Experience with simpler double-P_1 programs has shown that, instead of attempting to solve immediately for the double-P_1 solution, a P_1 solution for the flux and current in all groups should be obtained. In addition to the preliminary computation of these guesses it was shown that a procedure by which one inner iteration is performed between the two double-P_1 second order equations with a group until good guesses for the third and fourth vectors are obtained in all groups will save many inner iterations in obtaining the double-P_1 solution vectors. In order to have flexibility in this solution procedure and to be able to solve both P_1 and double-P_1 problems, three modes of operation are available in the program: a P_1 approximation, a mock double-P_1 approximation, and a true double-P_1 approximation. The three modes of operation are completely under the control of the requestor as to the execution or skipping of any mode and the degree of accuracy of each approximation. Since the first two modes in a double-P_1 solution are used only for vector guesses, the convergence criteria should be less stringent for modes 1 and 2 than for mode 3. Group-dependent boundary conditions may be specified for both the P_1 and double-P_1 approximations.

In addition to the data in the SLOP-1 library the program requires as input the geometric description of the reactor or cell as to number of points (≤ 250 for P_1 and ≤ 140 for double-P_1), number of regions (≤ 25), and mesh size; the composition make-up of the regions as to temperature (the same in each region), presence or absence of a moderator, the level of the isotropic source feeding in from higher than thermal energies, and the number densities of the isotopes in the region; and the guess at the thermal flux which may come from a WANDA problem via binary cards, from decimal cards, or from a tape which has the results of a previous SLOP-1 problem of similar geometric description. The program is limited to 50 groups.

The edit produces the selected components of the solution vectors for certain groups along with pointwise fission rates and absorption rates. Few-group editing may be requested for as many as six few-groups and six different few-group schemes. The edit produces diffusion constants, cross sections, and transfer coefficients for each scheme.

The IBM-704 must have 32K or 16K core storage, nine tape transports, on-line printer, and on-line card reader. Typical running times for 36-group problems are 35 minutes for a 14-point double-P_1 problem and 90 minutes for a 100-point double-P_1 problem. Infinite medium two-point problems which

are run to obtain few-group constants take between 3 and 5 minutes.

3. *P1MG (IBM-704)*

H. Bohl

P1MG,[74] a one-dimensional P_1 multigroup program, was written for the IBM-704 to assess the accuracy of the few-group diffusion scheme under different conditions and to provide an alternate computational device when this scheme fails.

P1MG solves for the spatially dependent multigroup flux, taking into account (1) the slowing down of neutrons resulting from elastic and inelastic scattering, (2) the removal of neutrons from smooth and resonant absorption, and (3) the regeneration of fast neutrons resulting from fissioning which may occur in any of the fast multigroups or in the one thermal group.

The program incorporates the P_1 equations which result in solving the one-dimensional transport equation using Legendre polynomials. The slowing-down densities are computed by the method of Greuling and Goertzel.[75]

By replacing first- and second-order derivatives in these equations with conventional central difference approximations, a three-point equation relating the flux at adjacent points within a homogeneous medium is developed. With appropriate group-dependent boundary conditions and consistent interface conditions, each multigroup flux at any point in a multiregion reactor is computed, using a scheme similar to that which is used in the WANDA program. The reactor may be a slab, cylinder, or sphere.

For slab geometry, transverse bucklings are individually specified in the other two spatial directions for each region or by one total buckling in each region. Correspondingly, then, midpoint currents and anisotropic slowing-down densities are computed in all three directions.

The computation of resonance integrals is identical to the method in the MUFT-4 program, including the specification of self-shielding factors for each resonance. A separate value for the total buckling to be used in the resonance integrals is specified. It is possible to compute these integrals in both hydrogenous and nonhydrogenous regions. In addition, the program uses a prepared library of microscopic cross sections and additional isotope-dependent quantities as in MUFT-4.

The requestor supplies as input a physical description of the reactor, i.e., geometry, groups, points, regions, group-dependent boundary condition, bucklings, number densities,

mesh size, and thermal-group macroscopic cross sections in each region, and an initial pointwise source distribution which may come directly from a corresponding four-group WANDA problem.

The P1MG edit will print all of the multigroup fluxes, currents, and isotropic slowing-down densities along with pointwise and regionwise few-group macroscopic cross sections similar to the three few-group schemes in MUFT-4.

The program is capable of handling up to 80 lethargy groups, 200 mesh points, and 15 regions, each containing, at most, 10 different isotopes, if it is run with a 32,768-word core storage. The IBM-704 must be equipped with 16,384 or 32,768 words of magnetic core storage, 10 tape units, one drum unit, on-line card reader, printer, and punch units. In addition, an off-line printer should be available.

The average running time of a 55-group, 15-region, 200-point problem is about 45 minutes.

4. RANCH (IBM-704)

H. Bohl

The RANCH[76] program furnishes a numerical approximation to the one-dimensional, one-velocity neutron transport equation in slab geometry. Anisotropic scattering is permitted while the source is assumed to be isotropic but may vary from mesh point to mesh point. The method of discrete ordinates with the iteration process accelerated by overrelaxation is used to obtain the solution.

The following boundary conditions may be imposed on the solution: (1) two reflecting boundaries; (2) one reflecting boundary and one boundary whose incident vector fluxes are specified; (3) the incident vector fluxes are specified for both boundaries.

The number of angles at which the vector fluxes are calculated may either be 4, 6, 8, 10, or 12. The maximum number of mesh points allowed depends on the number of angles and is as follows:

Angles	4	6	8	10	12
Mesh Points	1,250	1,250	1,250	1,000	833

As input the RANCH program requires the macroscopic total and scattering cross sections, the source density, the scattering parameters a_1 and a_2, and the overrelaxation

parameter, ω. The cross sections, the scattering function, and the mesh intervals are assumed constant with respect to the space coordinate x within each of the allowable 50 regions. An option is also available for the requestor to specify the quadrature formula to be used to approximate the scattering integral. The output includes an edit of the input, the scalar fluxes, the vector fluxes, and certain region integrals. The angular moments at the boundaries are also available for certain problems.

The running time, roughly, is proportional to $(A)^2(N)(I)$, where A is the number of angles, N is the number of mesh points, and I is the number of iterations required for convergence. An 8-angle, 100-point problem requiring 40 iterations for convergence required 3.1 minutes.

5. P3MG1 (Philco-2000)

H. Bohl

P3MG1 solves the same problem that P1MG solves on the IBM-704 with the extension of the fast group representation to include the P_3 terms and the thermal group representation in a double-P_1 approximation, equivalent to a SLOP-1 one-velocity approximation. P_3 elastic scattering is treated exactly for hydrogen only, with the option of including the P_2 and P_3 components of the scattering cross section of a few selected heavy isotopes in the total and transport cross sections. The formulation of the equations permits the three geometries: rectangular, cylindrical, and spherical.

The transverse P_1 current is treated as in P1MG with the specification of transverse buckling components, B_x and B_y. In addition, the inelastic scattering source and the resonance absorption are computed in exactly the same manner as in MUFT-5. The heavy element slowing down is computed for the P_0 and P_1 components the same as in P1MG.

The P_2 and P_3 components of the slowing-down source due to hydrogen are determined from equations similar to those used for the P_0 and P_1 components in the Greuling-Goertzel approximation.

The multigroup parameters which are used to compute the macroscopic cross sections, inelastic scattering source, resonance absorption integrals, and P_0 and P_1 components of the slowing-down density are obtained from the same MILC library that is used with MUFT-5. The heavy element P_2 and P_3 scattering cross sections are supplied on cards for the few selected heavy elements in microscopic cross-section

form. The additional Greuling-Goertzel parameters required for the P_2 and P_3 hydrogen slowing-down equations are obtained simply from the corresponding parameters in the P_0 and P_1 slowing-down equations. The source into the thermal group is determined entirely by the slowing down out of the highest lethargy fast multigroup. The macroscopic thermal constants which are required are entered on cards.

The program is limited to 80 groups, the last one of which is the thermal group. The composition description and limits are the same as for MUFT-5. The limit on the number of compositions is such that the sum of the number of isotopes is less than 65. The number of regions in the problem is limited to 49 with as many as 250 mesh points distributed throughout. The boundary conditions may be specified by group.

Since the P_3 approximation results in a form of solution not unlike the SLOP-1 double P_1-approximation solution, the concept of three modes to indicate the three different solutions which the program will produce and the mode control strategy of SLOP-1 have been adopted. Mode 1 will compute the P_1-approximation solution to the problem; mode 2, a mock P_3-approximation solution to the problem analogous to the mock double P_1-approximation in mode 2 of SLOP-1; and mode 3, the true P_3-approximation solution to the problem. When the fast groups are operating in mode 1, 2, or 3, the thermal group produces corresponding P_1, mock-double P_1, or true double P_1 solutions. In addition, a spatial guess for the fission source may be computed from WANDA-5 which will pass the guess directly to P3MG. The use of any of the modes and the degree of accuracy desired for each of the solutions is in complete control of the requestor. Again, as in the case of SLOP-1 problems, experience with a more simple P_3 program indicates that if a very good spatial source guess (e.g., from a WANDA problem) is available for a P_3 problem, mode 1 should be skipped and only mode 2 (obtaining good P_2 and P_3 component guesses) and mode 3 need be used. If reasonable P_3 multigroup component guesses are available, even mode 2 can be skipped.

The output from the program will be a binary restart tape and edited results. The binary restart tape will contain the latest set of P_ℓ-components, and the fission source guess can be used as input to any future problem with a similar geometric description. The results that are edited will be the same as from P1MG plus an isotopic edit of the few-group results.

The program requires nine tape transports. The limits on the program as described above are stated for a 32K computer with eight index registers; however, the program will run on a 16K computer with eight index registers.

Typical running times for 55 group problems using only the P_1 approximation are 11 minutes for 44 points and 3 regions and 30 minutes for 200 points and 10 regions.

6. *TRANVAR (IBM-704, Philco-2000)*

F. D. Judge

TRANVAR[77] solves the one-dimensional, one-velocity transport equation for the average scalar neutron flux density in each region of a slab array. These fluxes are given in terms of the isotropic sources and scatterings in the slabs and the average first-collision probabilities between slabs.

Using the Boltzmann equation for the scalar flux, a variational expression for the average flux in the i^{th} slab can be written as $\bar{\psi}^i = J(\psi, \phi)$, where ϕ is the solution of an auxiliary Boltzmann equation, and the quantity J has the property that it is stationary in the vicinity of the exact solution. When approximate trial functions are used, the evaluation of J is, thus, insensitive to first order errors in the trial functions. In particular, if the trial functions are taken to be constant within each slab, then imposing the condition that J be closest to the exact value requires that the trial function $\bar{\psi}_T$ satisfy the equation

$$\bar{\psi}_T^j = \sum_k \left(\sigma_s^k \bar{\psi}_T^k + S^k\right) \frac{P_{jk}}{\sigma_T^k} \qquad \text{Eq. (7.103)}$$

where P_{jk} is the average probability that a neutron uniformly introduced into the j^{th} slab will have its next collision in the k^{th} slab. A similar type of equation must be satisfied by the auxiliary functions.

The use of these particular trial functions then gives exactly the result

$$J(\bar{\psi}_T^j, \phi_T^j) = \bar{\psi}_T^i$$

so that $\bar{\psi}^i = \bar{\psi}_T^i +$ (second order errors), where $\bar{\psi}_T^i$ can be obtained from Eq. (7.103) without having to solve the auxiliary equations. Therefore, the solutions of Eq. (7.103) represent good approximations to the solutions of the exact Boltzmann transport equation.

Approximating $\bar{\psi}^i$ by the use of Eq. (7.103) has a direct physical interpretation. That is, the average flux in one slab

is related by the first collision probabilities to the source plus scattered flux in all the slabs.

For a repeating binary lattice, results can be easily obtained analytically. In order to solve arbitrary slab lattice problems, TRANVAR was programmed for the IBM-704. Input quantities are the thickness, the scattering ratios, and the sources in each region. Output is the average scalar flux density in each region.

The Philco-2000 version of TRANVAR was produced directly from the IBM-704 FORTRAN version; it is identical in all respects to the earlier program.

7. TET (Philco-2000)

H. L. Teaford

TET[78] was originally programmed as an extension of the one-velocity transport program ETC-4. TET is used to solve the multigroup Boltzmann transport equation in one dimension for thermal neutrons. Up to 35 energy groups and 60 spatial regions may be considered. Any number of the groups may be epithermal. Up to 10 angles may be used in the vector flux.

The following assumptions are made in TET: (1) slab geometry; (2) a P_3 scattering law; (3) a linear spatial variation of the flux in each spatial subregion.

Problem running time varies considerably with materials, number of groups, etc. However, a problem of average complexity will take about one-half hour. The program is restricted to no more than 35 energy regions and no more than six distinct material compositions.

8. SWAKRAUM (IBM-704, Philco-2000)

F. D. Federighi

SWAKRAUM[79] computes the spatially dependent thermal spectrum in one-dimensional slab lattices, using the P_1, P_3, or double-P_1 approximation. The method of solution is based on a two- or four-mode representation of the energy dependence of the thermal group. Thus, it is assumed that the flux spectrum everywhere in the lattice can be well represented by a linear combination of two or four characteristic spectra. The resulting set of two or four coupled differential equations is solved simultaneously by a noniterative procedure.

Special features of the program include:

1. A routine permitting the use of blackness theory in P_1 calculations.

2. Printout of spectrum-averaged material constants and activations for any arbitrary detector.
3. Use of any arbitrary slowing-down kernel with a diagonal P_1 component. The P_2 and P_3 components are assumed to be zero.

A maximum of 18 regions and 251 mesh points can be treated while the energy spectrum can be calculated at up to 37 energies. Running times can be computed from the following approximate formula:

$$\text{Time (sec)} = 30 + 33 \times (\text{number of spectra}) + 8 \times (\text{number of materials}) + 1.7 \times (\text{number of mesh points})$$

Thus, most problems take from 4 to 8 minutes.

SWAKRAUM for the Philco-2000 is physically identical to SWAKRAUM for the IBM-704 except for the addition of edits for group constants and their regionwise integrals. The Philco-2000 version is five times as fast as SWAKRAUM on the IBM-704.

9. MO176 (Philco-2000)

R. M. Cantwell

MO176[80] is a FORTRAN program which solves the neutron transport equation in slab geometry in a few-group approximation. Fast groups are P_1 or P_3, with P_0, P_1, and P_2 transfer matrices, while thermal groups are P_1 or double-P_1 with P_0 and P_1 transfer. A variational thermal treatment, using either the Buslik scheme[81] or a transformed SWAKRAUM representation, is included as an option. Boundary conditions are general. Eigenvalue, slowing down, or purely thermal problems are done. Strategy of solution is quite variable.

A P_0 source, either a fission neutron source or a source to thermal, can be input pointwise or as regionwise constant and, for a purely thermal problem, a P_1 source to thermal can be input pointwise. Edits available include the P_0, P_1, P_2, and P_3 components of the flux at every mesh point in every group, the thermal P_0 flux, the converged fission source (if an eigenvalue calculation has been done), fast and thermal pointwise activations of two arbitrary sets of cross sections, and various region integrals. The maximum numbers of groups, points, regions, and compositions are 10, 250, 15, and 6, respectively.

Of the maximum of 10 groups no more than 6 can be fast or thermal.

This program requires a 32K memory, but no tapes are used (other than for input and output).

H. Monte Carlo Calculations

1. TUT-T5 (IBM-704)

H. G. Kuehn

TUT-T5,[82] a Monte Carlo program, provides a one-energy calculation of a regionwise distribution of absorption rates in a two-dimensional quarter-cell. The program is based on an analog Monte Carlo method in which neutron life histories are simulated using pseudorandom numbers, and capture probabilities are estimated by averages of random variables associated with the histories. A theoretical discussion of analog Monte Carlo methods is presented in Sect. 7.3. The random variable used in TUT-T5 sums the distances traveled in various regions and uses these sums to estimate the integral of the flux over the regions in question. Proof of the unbiased character of the TUT-T5 estimator has been presented in the literature.[83]

All neutron trajectories are confined to a single rectangular quarter-cell by reflecting each trajectory at the external boundaries. This basic quarter-cell is, thus, the fundamental unit of an infinite periodic lattice in the (x, y) plane. The basic quarter-cell may be divided into as many as 32 subrectangles, each being homogeneous and defining a separate region of the geometry. The program input requires for each region a detailed description of the region geometry, the source level for starting histories, a composition number (defined below), and macroscopic cross-section data.

In the course of a history, two general types of events are considered upon collision of a neutron with a nucleus, namely, elastic scattering and absorption. The relative probabilities of each event are specified by the macroscopic cross sections. In TUT-T5, all elements are assumed to be scattered isotropically in the laboratory system except for hydrogen, which is assumed to scatter linearly in the cosine of the scattering angle.

Approximately 1000 particle life histories are processed during an experiment. The time needed to complete an experiment is proportional to the number of collisions and boundary crossings made by particles until termination. Ex-

perience indicates that about 40 collisions are processed per second of computer time.

A composition in TUT-T5 consists of an arbitrary grouping of regions in the basic quarter-cell. For each composition, each experiment is regarded as yielding one sample from an approximately normal population whose mean is the capture probability for that composition. At the end of each experiment, the output of TUT-T5 consists of the sample means of the capture probabilities and their confidence intervals, obtained from a statistical analysis of these data using Student's t-distribution.

The total number of experiments to be processed is specified in the input of the problem. If desired, the program can be forced to stop at the end of an earlier experiment. Similarly, a problem restart will permit more experiments to be run for further statistical results.

In addition to the minimum standard equipment for an 8K computer, TUT-T5 requires two tape units for the program tape and the problem restart tape, respectively. The reader is referred to Chap. 3, Sect. 3.5, for a more detailed discussion of this program.

2. TRAC-1 (Philco-2000)

H. G. Kuehn

TRAC-1[84] is a Monte Carlo program on the Philco-2000 designed to estimate absorption rates. It solves the same geometric problem as does TUT-T5, either in a one-energy mode or, on an input option, in a mode which places a slowing-down region ahead of the one-energy thermal region. In the latter case epithermal capture probabilities, integrated over the epithermal energy spectrum, are provided for each composition, as well as the usual thermal capture probabilities. A more detailed discussion of the application and theory in TRAC-1 is presented in Chap. 3, Sect. 3.5.

The random variables in TRAC-1 are defined as linear combinations of the sum of the distances traveled by the particles in various regions and the number of particles absorbed in these regions. Statistics in large or heavily absorbing regions are improved by this method, which was suggested by M. Martino.[85] The coefficients for the linear combination are so chosen as to minimize theoretically the statistical error in each region for a fixed sample size. The problem output at the end of each experiment consists of the sample estimates of the capture probabilities per composition based on the distribution of captures and track lengths, as well as the linear

combination of these estimates. Confidence intervals for all three estimates are also included in the output. As in TUT-T5, additional experiment data may be obtained from a problem restart.

In the slowing-down mode the source is assumed uniform in energy between the limits E_L and $E_U (E_L < E_U)$ and spatially constant in each region, the levels being specified as in the one-energy mode. All absorption is assumed to be of the form c/v in the epithermal region, and the only moderation occurs through hydrogen scattering. As soon as the energy of the neutron falls to or below the input value E_T, the neutron is regarded as thermalized and the assumptions of the one-energy mode take over as in TUT-T5.

The rectangular quarter-cell in TRAC-1 may include up to 75 different regions and 99 compositions. The regions are arbitrarily grouped into compositions, and any one region may appear in as many (if any) compositions as desired. The geometry input for each region has been greatly simplified over TUT-T5. For the slowing-down mode, epithermal as well as thermal cross sections are required for the input.

An input option in one-energy mode problems allows for the normal region source function to be replaced by a specified point source. From a point source problem, a technique based on the reciprocity theorem[86] makes it possible to calculate the scalar flux at a single point of the quarter-cell. In the one-energy mode this same technique results in substantial reduction in the variance of the capture probability of a single region, particularly if the region is very small or a region of flux dip.

A library tape containing approximately two million floating point pseudorandom numbers and tables of random variables frequently used in history calculations has been prepared in advance. Thus, by decreasing the amount of computation for each history, the running time for each experiment has been reduced. Experience shows that, for similar problems, TRAC-1 runs approximately 3.5 times as fast as TUT-T5. Typical problems run from 5 to 20 minutes, depending upon the average number of collisions and boundary crossings per neutron. TRAC-1 requires a 32K computer with a minimum of six tape units.

3. *MARC-1 (Philco-2000)*

H. G. Kuehn

MARC-1,[87] a Monte Carlo program for the Philco-2000, is a multithermal group calculation of thermal activation rates in the same geometry as TUT-T5 and TRAC-1. The main

features of this program are its ability to calculate in either a normal or adjoint mode (based on normal or adjoint multigroup equations) and the ability to experiment with various hydrogen scattering kernels. The adjoint technique in MARC-1 is along the lines of that suggested by Maynard[86] for energy-dependent (nonself-adjoint) problems. While the normal mode is based on analog Monte Carlo, the adjoint mode makes use of infinite medium fluxes to reduce the variance and is motivated by the use of dual importance sampling (see Sect. 7.3).

The physical model implicit in MARC-1 may be described as follows: The basic rectangular quarter-cell (see geometry description for TUT-T5 and TRAC-1) may be subdivided into $R(\leq 45)$ rectangular subregions r, and the thermal energy range is divided into $G(\leq 36)$ energy groups i. Neutrons are introduced isotropically into this system with source spectrum $B^i(1 \leq i \leq G)$ and spatial density $S_r(1 \leq r \leq R)$. Scattering by hydrogen in group j may result either in transfer from groups j to group i (with probability proportional to $\alpha^{i,j}$) or in a new direction in group j. The angular distribution of such a scattering has a component which is isotropic and a component which is either forward or backward. Heavy element scattering may not change the energy group, and its angular distribution also has an isotropic and a delta-function component. Heavy element scattering is independent of the energy group while hydrogen scattering is not. Neutrons scatter from group to group and region to region and are ultimately absorbed in some group and region.

The input for MARC-1 consists of the basic geometry and composition description, the parameters required for special edit options described below, a specified file from a library tape prepared by the CRAM program,[87] and number densities and a definition of region mixtures of isotopes obtained from the CRAM file. For a given temperature, the requested file provides a source spectrum; microscopic cross sections for the various isotopes, including hydrogen; and transfer coefficients, i.e., probabilities of transferring from one energy group to another for hydrogen scattering.

As in TRAC-1, the neutron track lengths in each group and region are recorded as well as the final distribution of absorptions. These two estimates are combined to yield the linearly optimum minimum variance estimate of thermal activation rates.

For normal mode problems, the output consists of thermal absorption rates and thermal fluxes in each composition. Input options allow for any of the following additional edits: (1) thermal fission rates in each composition, (2) integrated fluxes in each composition and each energy group, (3) an arbitrary thermal reaction rate in each composition.

For adjoint mode problems, the regular output is the activation rate in a single composition or the thermal flux at a single point. Special edits may include an arbitrary thermal activation rate in a single composition or at a single point and integrated adjoint fluxes in each composition and in each energy group.

For all of the above edits, a statistical analysis provides confidence intervals for each of the estimates, as in TUT-T5 and TRAC-1. A problem restart will allow more experiments to be processed.

Experience indicates that MARC-1 is at least as fast as TRAC-1 (per collision) since the scattering routines, on the average, are simpler in MARC-1 than in TRAC-1. MARC-1 requires a 32K computer with a minimum of eight tape units.

4. *TRANVAR (IBM-704, Philco-2000)*

R. A. Pfeiffer

TRAM[85] is a two- or three-dimensional neutron transport program for the Monte Carlo determination of spatial and spectral variations of the neutron population below 100 ev in hydrogen-moderated assemblies. The computations are carried out by a nonbranching Monte Carlo method in which the principal random variables are obtained by a high-speed random address technique.

The input requirements of TRAM include a list of number densities for the elements of each material used in the problem. From this list, TRAM prepares tables of mean free paths and conditional probabilities for the collision processes for each of 32 energy groups.

Source particles are automatically generated with a uniform distribution inside each source region and with a region-dependent source rate specified as input. The source energy is stochastically determined by assuming that the particle has just been scattered by hydrogen with an incident energy of 100 ev.

All elements except hydrogen scatter isotropically in the laboratory system without energy exchange. Five types of hydrogen scattering are used in various proportions in the 32 groups to provide a model for proton thermal motion and chemical binding which gives infinite medium spectra and diffusion lengths in agreement with measured values.

Geometrically, a TRAM problem is composed of up to 50 zones which may contain up to 20 different types of materials. Zones are bounded by surfaces (up to 50 are allowed) which may be either linear or sections of elliptic cylinders with

axes parallel to the z-axis. Each surface may be designated as reflecting, transmitting, or trapping (incident particles are absorbed, counted in special trap registers, and removed from the game).

Each TRAM problem consists of 25 repetitions, with different random numbers, of the same basic experiment; each run consists of at least 100 particle histories and usually many more than this. A final statistical edit will print estimates with confidence limits of the path-length accumulations and capture rates in each spatial zone of the problem.

The TRAM program for the Philco-2000 contains a number of features in addition to those available in the IBM-704 version. While the IBM-704 program was core contained, TRAM is triply segmented. This expansion allows an increased capacity and, in addition, an extensive input checking routine has been included. A new random number generator, some new logic in the advancement of particles across surfaces within a problem, and the inclusion of a restart option complete the differences in the present program. The Philco-2000 TRAM characteristics are:

1. Capacity—(a) A maximum of 100 materials, 200 surfaces, and 200 zones are permissible. (b) The number of neighbor zones bounding a given surface of a given zone is essentially unlimited within the above restriction on total zones. (The IBM-704 limit was four.) (c) The number of pseudorandom numbers available is infinite for all practical purposes. The multiplicative congruence scheme is used. In the IBM-704 version, a table of one million random numbers was used, and on large problems this table was usually exhausted.
2. New logic—In the IBM-704 version, a neutron passing through an internal surface was considered to be born on that surface. Presently, the neutron's past history in preceding regions is properly accounted for.
3. New input format and input checking—Input errors were common in the IBM-704 version, even with the relatively small size problems that were permitted. TRAM now has a highly mnemonic input which should lead to fewer errors in the preparation of problems. In addition, there is now an extensive input checking routine built into the program which will catch punch errors on cards, errors in the format of the information submitted to the program even if the cards are correct, and inconsistencies between parts of the input. Experience has indicated that a vast majority of possible input mistakes are isolated by this routine.

4. Restart—A restart is now available. Problems may be taken off at the conclusion of any run and restarted at some later time.

A typical TRAM problem will take from one-half to three-quarters hour, with an overall range of one-quarter to two hours.

5. *NREP1-4 (IBM-704)*

H. G. Kuehn

The NREP1-4 programs constitute the Bettis-modified versions of the NYU Monte Carlo program REP, which estimates the resonance escape probability in a two-dimensional periodic reactor lattice. The lattice may consist of a staggered or rectangular array of concentric circular annuli, a set of infinite slabs, or a rectangle composed of subrectangles. Each region is regarded as a homogeneous mixture of nuclides: no more than 5 nuclides per mixture nor more than 10 different mixtures are permitted. The programs NREP3 and NREP4 are the same as NREP1 and NREP2, respectively, except that the former two programs allow more than one isotope of the resonance absorber. All of these programs are designed specifically to treat resonances of U^{238}.

The calculation follows the life of a typical neutron in an energy range (E_{min}, E_{max}) containing one or more resonances of U^{238}. The programs will treat up to 60 known resonances; higher resonances, if desired, are treated statistically making use of the Porter-Thomas distribution. The initial position and direction of the history of a neutron are chosen at random; the initial energy is chosen in the interval $(0, E_{max})$ based on the assumption that the neutron has slowed down from higher energies with no appreciable absorption. The motion of the neutron through the infinite array of cells in the lattice is simulated by confining the motion to a basic working cell which is assumed to have either reflecting or translating boundaries. Only elastic scattering is considered and is assumed to be isotropic in the center-of-mass system. A history is abandoned when its energy falls below E_{min}.

Each history has a weight, initially one, associated with it. Upon collision of the neutron with a nuclide this weight is multiplied by the survival probability associated with the collision. The average of all terminal weights constitutes the Monte Carlo estimate of the resonance escape probability, the fraction of neutrons which survives absorption above the energy E_{min}.

The target nuclide is assumed to be at rest for each collision. Doppler-broadening of the Breit-Wigner resonance scattering and absorption cross sections simulates the motion of the resonance nuclide. Upon collision of a neutron with the resonance nuclide at an energy between two adjacent resonances, the cross section taken is the sum of the background and contributions from these two resonances. The scattering cross section for the resonance material includes interference between resonance and potential scattering, but interference between resonances is neglected.

The basic output consists of the Monte Carlo estimate of the escape probability together with an estimate of the statistical uncertainty in this number. A spatial distribution of absorptions may also be obtained, and, in the event that an isotopic breakdown of the resonance absorber is given, region-wise absorptions by isotope are provided. A typical problem, consisting of 10,000 histories, requires about one hour of IBM-704 time. The NREP1-4 programs require a 32,768-word computer with a minimum of two tapes.

6. *EURIPUS-4, DAEDALUS-2 (IBM-704)*

H. G. Kuehn

EURIPUS-4 and DAEDALUS-2[88,89] are Monte Carlo programs written for the IBM-704 to provide information on the spatial density of neutrons slowing down past a given energy in an infinite homogeneous medium consisting of hydrogen and one other isotope. Whereas EURIPUS-4 calculates the one-dimensional spatial slowing-down density, together with low-order spatial moments of this function, DAEDALUS-2 determines the corresponding spatial distribution of angular integrals of the product of an arbitrary function with the vector flux density, together with low order moments of this product. The neutron source in either program may be monoenergetic with either isotropic or monodirectional angular distribution, it may be that source resulting from a deuteron-deuteron interaction, or it may be arbitrarily distributed in energy but isotropic in direction (e.g., a fission source). The volume displaced by a cylindrical tube from an accelerator to the source can be accounted for in the neutron first flight, but not thereafter.

The nonhydrogenous isotope may have arbitrary mass and energy-dependent differential-elastic and absorption cross sections. As many as 400 energy groups are permitted for

the description of these cross sections. Hydrogen scattering is assumed to be isotropic in the center-of-mass system while nonhydrogenous scattering is described for each energy group by supplying Legendre components of the scattering cross section. Although scattering angles are calculated by random choices, the spatial distributions and, in DAEDALUS, the energy distribution are obtained partly from analytic treatment which enables the output to be in the form of actual density functions at specified planes and energies rather than histograms covering finite intervals. At certain steps in the computation of both the spatial and energy distributions, part of the analytic treatment is replaced by sampling methods in order to maximize efficiency and/or to avoid roundoff error.

In addition to the methods described above, other special techniques were used to optimize the calculation. For example, in DAEDALUS neutron histories whose energies fall within a certain range are split in order to avoid an infinite contribution to the flux. In both programs a user-supplied integer is used to determine the number of digits to the right of the decimal point which will not be affected by roundoff error in the evaluation of spatially dependent output quantities.

Extensive test problems reveal that EURIPUS and DAEDALUS are capable of calculating slowing-down densities and fluxes with great accuracy, the running time for a typical problem being approximately 60 to 90 minutes. These problems are described in detail by H. J. Amster, et al.,[88] as well as the derivation of the formulas used by EURIPUS and DAEDALUS and a proof that the basic flux estimator used by DAEDALUS is unbiased.

Statistical analysis for both programs is based on an assumed normal distribution for all sample means. Probable errors (i.e., 50 percent confidence intervals) are supplied for each number estimated by the programs. EURIPUS and DAEDALUS require a 32,768-word computer with a minimum of five tapes.

I. Theoretical Cross-Section Calculations

1. SWAMI (IBM-704)

E. D. Reilly, Jr.

SWAMI is a nuclear optical model program (see Chap. 2, Sect. 2.2). According to the optical model, the elastic scattering of a neutron from a target nucleus can be described

through use of the Schrödinger equation with a complex potential well $V(r)$ where the imaginary part of $V(r)$ represents neutron absorption.

Neutron energy and well parameters, including spin-orbit terms, are input to SWAMI. SWAMI computes as output:

1. The angular distribution of neutrons scattered elastically from 0 degrees to 180 degrees in steps of 5 degrees.
2. The neutron polarization over the same angles.
3. The total cross section.
4. The average cosine of the scattering angle.
5. Penetrability data for use with inelastic cross-section calculations.

2. *ABACUS (Philco-2000)*

A. W. Thomas

ABACUS is a program for the theoretical prediction of high-energy nucleon-nucleus interactions (Chap. 2, Sect. 2.2). It provides for the numerical integration of the Schrödinger equation for the complex potential of the nuclear optical model under the following categories:

1. Continuum case: Calculates the nuclear penetrabilities, total cross section, shape elastic differential cross section, Rutherford scattering differential cross section (if the incident particle is charged), and the polarization.
2. Bound state: Calculates the discrete eigenfunctions and eigenvalues of the nuclear potential.
3. Wave-function integration: Evaluates an integral from $r = 0$ to ∞, where the integrand is a product of up to six wave functions and r to the power $n (-2 \leq n \leq 5)$.
4. Hauser-Feshbach: Calculates the compound elastic and inelastic differential cross sections based on the Hauser-Feshbach statistical model. It uses the penetrabilities supplied by the continuum case.
5. Spectrum: Automatically varies any one of several input parameters over a specified range and calculates any of the four previous categories for these values.
6. Automatic least squares fitting: Automatically varies up to six parameters to minimize the weighted, squared difference between any specified calculated cross sections and given experimental values for these cross sections.

Running times for ABACUS depend upon the categories used but will vary from 10 seconds for the continuum case to a maximum of 12 minutes for a multiparameter search.

J. Perturbation Calculations

1. PSP (IBM-704, Philco-2000)

E. D. Reilly, Jr.

PSP is a three-group perturbation calculation program designed for use with CURE on the IBM-704. It will compute contributions from specified regions to change in reactivity caused by given cross-section changes. When these changes are produced by a temperature perturbation, for example, the program will calculate an overall reactor temperature coefficient as well as the degree to which any given region of the reactor is contributing to that coefficient.

In addition to cross-section differences, PSP also requires the following information which is available as output from CURE or KARE:

1. Pointwise fluxes from each of three groups
2. Pointwise adjoints from each of three groups
3. The pointwise source
4. Details of mesh size and shape.

IBM-704 PSP is operable for CURE only and cannot be used with the REM and FLEER geometries. PSP for the Philco-2000 has been written as part of the KARE System. The physical equations for regionwise perturbations are identical to those of the IBM-704 version.

Principal improvements are:

1. In addition to the ordinary x–y and r–z capabilities of the IBM-704 version, the new program will also handle REM (x–y with diagonal lines) and FLEER (uniform triangular mesh) type geometries.
2. PSP problems can be run automatically; no manual intervention is required between the running of flux, adjoint, and PSP problems.

K. Modal Calculations

1. MULE (Philco-2000)

R. L. Ewen

The MULE program may be used to calculate fundamental and overtone modes for three different diffusion-theory eigenvalue problems. In order to calculate overtone modes, MULE uses the Wielandt iteration technique previously described in this chapter. It is limited to two neutron groups and to slab and cylindrical geometry; in the latter, both azimuthal and

radial overtones may be determined for cores which are uniform azimuthally.

The first eigenvalue problem included is the usual one in which the fission source is divided by a parameter λ. Use of the overtone λ modes in space-time kinetics analysis is described in Chap. 5. In the second problem the eigenvalue μ is the coefficient of a distributed thermal poison which must be removed for criticality. Overtone μ modes provide an approximate analysis of xenon spatial stability, as described in Chap. 5. The third eigenvalue problem considered is the familiar natural mode problem for a reactor with no feedback in which the eigenvalue ω arises from the $e^{\omega t}$ time dependence of the modes. These modes are useful in the analysis of pulsed neutron experiments.

MULE allows a series of modes to be calculated such that their adjoints are automatically obtained and the pertinent adjoint weighted integrals found for all combinations of modes Thus, all information required for both linear and nonlinear determination of modal expansion coefficients may be obtained.

The MULE program was written in FORTRAN and requires a 32K memory. It has been compiled and run on the Philco-2000 computer. Typical running times are 10 to 20 seconds per mode.

2. *XEP (Philco-2000)*

R. L. Ewen

The XEP program may be used to calculate the complex natural modes of slab reactors with xenon feedback. Within the usual discrete space representation, it provides an exact solution of the linearized xenon spatial stability problem with no temperature or control feedback, as discussed in Chap. 5. The natural xenon modes are defined by the eigenvalue problem, in which $\hat{x}$ and $\hat{\phi}_2$ refer to the unperturbed xenon and thermal

$$0 = \begin{bmatrix} -(\lambda_i + p) & 0 & \gamma_i \Sigma_{f_1} & \gamma_i \Sigma_{f_2} \\ \lambda_i & -(\lambda_x + \sigma_x \hat{\phi}_2 + p) & \gamma_x \Sigma_{f_1} & \gamma_x \Sigma_{f_2} - \sigma_x \hat{x} \\ 0 & 0 & D_1 \nabla^2 - \Sigma_1 + \nu\Sigma_{f_1} & \nu\Sigma_{f_2} \\ 0 & -\sigma_x \hat{\phi}_2 & \Sigma_r & D_2 \nabla^2 - \Sigma_2 - \sigma_x \hat{x} \end{bmatrix} \begin{pmatrix} i \\ x \\ \phi_1 \\ \phi_2 \end{pmatrix}$$

flux, respectively. The eigenvalue p arises from the e^{pt} time dependence of each mode.

In order to find the least stable overtone modes, which are a conjugate complex pair in reactors of interest, the Wielandt iteration technique is used with a complex eigenvalue estimate and complex vector iterates. A description of the Wielandt procedure has been given earlier in this chapter (Sect. 7.2).

The XEP program was written in FORTRAN and requires a 32K memory. It has been compiled and run on the Philco-2000 computer. Typical running times are 25 to 40 seconds per mode.

REFERENCES

1. R. B. Smith and C. H. Hunter, "The BKS System for the Philco-2000 Computer," WAPD-TM-233, April 1961.

2. G. Birkhoff and E. P. Wigner, Eds., "Nuclear Reactor Theory. Proceedings of Symposia in Applied Mathematics. Vol. XI," American Mathematical Society, Providence, 1961.

3. J. E. Wilkins, Jr., "Diffusion Approximation to the Transport Equation" in "Nuclear Reactor Theory. Proceedings of Symposia in Applied Mathematics. Vol. XI," G. Birkhoff and E. P. Wigner, Eds., pp. 105-115, American Mathematical Society, Providence, 1961.

4. G. J. Habetler and M. A. Martino, "Existence Theorems and Spectral Theory for the Multigroup Diffusion Model" in "Nuclear Reactor Theory. Proceedings of Symposia in Applied Mathematics. Vol. XI," G. Birkhoff and E. P. Wigner, Eds., pp. 127-139, American Mathematical Society, Providence, 1961.

5. R. S. Varga, "Numerical Solution of the Two-Group Diffusion Equations in x-y Geometry," IRE Trans. of the Professional Group on Nuclear Science NS-4, 52-62 (1957).

6. R. S. Varga, "Matrix Iterative Analysis," Prentice-Hall, Inc., Englewood Cliffs, New Jersey, 1962.

7. E. L. Wachspress, "CURE: A Generalized Two-Space-Dimension Multigroup Coding for the IBM-704," KAPL-1724, April 30, 1957.

8. R. S. Varga, "Numerical Methods for Solving Multi-Dimensional Multigroup Diffusion Equations" in "Nuclear Reactor Theory. Proceedings of Symposia in Applied Mathematics. Vol. XI," G. Birkhoff and E. P. Wigner, Eds., pp. 164-189, American Mathematical Society, Providence, 1961.

9. G. Birkhoff and R. S. Varga, "Reactor Criticality and Nonnegative Matrices," J. Soc. Ind. Appl. Math. 6, 354-377 (1958).

10. G. Bilodeau and L. Hageman, "A Survey of Numerical Methods in the Solution of Diffusion Problems," WAPD-TM-64, July 1957.

11. A. S. Householder, "The Approximate Solution of Matrix Problems," J. Assoc. Comput. Mach. 5, 205-243 (1958).

12. R. S. Varga, "On Estimating Rates of Convergence in Multigroup Diffusion Problems," WAPD-TM-41, April 1957.

13. D. A. Flanders and G. Shortley, "Numerical Determination of Fundamental Modes," J. Appl. Phys. 21, 1326-1332 (1950).

14. G. J. Habetler and E. P. Shelly, "Closure Properties of Oscillation Matrices with Applications," KAPL-M-GJH-4, August 3, 1960.

15. E. L. Wachspress, "A Numerical Technique for Solving Group Diffusion Equations," Nucl. Sci. Eng. 8, 164-170 (1960).

16. H. Wielandt, "Bestimmung höheren Eigenwerte durch gebrochene Iteration," Bericht der aerodynamischen Versuchsanstalt Göttingen, Report 44/J/37 (1944).

17. R. L. Ewen, "MULE — A Code for the Calculation of Two Types of Overtone Modes," Trans. Am. Nucl. Soc. 3 (2), 397-398 (1960).

18. A. M. Ostrowski, "On the Linear Iteration Procedures for Symmetric Matrices," Rend. Mat. e Appl. 14(5), 140-163 (1954).

19. D. Young, "Iterative Methods for Solving Partial Difference Equations of Elliptic Type," Trans. Amer. Math. Soc. 76, 92-111 (1954).

20. R. J. Arms, L. D. Gates, and B. Zondek, "A Method of Block Iteration," J. Soc. Ind. Appl. Math. 4, 220-229 (1956).

21. R. S. Varga, "Factorization and Normalized Iterative Methods" in "Boundary Problems in Differential Equations," R. E. Langer, Ed., pp. 121-142, The University of Wisconsin Press, Madison, Wisconsin, 1960.

22. S. V. Parter, "On 'Two-Line' Iterative Methods for the Laplace and Biharmonic Difference Equations," Numer. Math. 1, 240-252 (1959).

23. W. M. Kahan, "Gauss-Seidel Methods of Solving Large Systems of Linear Equations," Doctoral Thesis, University of Toronto, 1958.

24. G. J. Habetler and E. L. Wachspress, "Symmetric Successive Overrelaxation in Solving Diffusion Difference Equations," Math. Comput. 15, 356-362 (1961).

25. D. Young, "On the Solution of Linear Systems by Iteration" in "Numerical Analysis. Proceedings of Symposia in Applied Mathematics. Vol. VI," pp. 283-298, McGraw-Hill Book Company, Inc., New York, 1956.

26. W. R. Cadwell, "TKO — A Three-Dimensional Neutron-Diffusion Code for the IBM-704," WAPD-TM-143, October 1959.

27. B. A. Carre, "The Determination of the Optimum Accelerating Factor for Successive Over-relaxation," Comput. J. 4, 73-78 (1961).

28. E. H. Cuthill and R. S. Varga, "A Method of Normalized Block Iteration," J. Assoc. Comput. Mach. 6, 236-244 (1959).

29. G. H. Golub and R. S. Varga, "Chebyshev Semi-Iterative Methods, Successive Overrelaxation Iterative Methods, and Second Order Richardson Iterative Methods, Part I," Numer. Math. 3, 147-156 (1961).

30. G. H. Golub and R. S. Varga, "Chebyshev Semi-Iterative Methods, Successive Overrelaxation Iterative Methods, and Second Order Richardson Iterative Methods, Part II," Numer. Math. 3, 157-168 (1961).

31. L. A. Hageman, "Block Iterative Methods for Two-Cyclic Matrix Equations with Special Application to the Numerical Solution of the Second-Order Self-Adjoint Elliptic Partial Differential Equation in Two Dimensions," WAPD-TM-327, April 1962.

32. G. Birkhoff and R. S. Varga, "Implicit Alternating Direction Methods," Trans. Amer. Math. Soc. 92, 13-24 (1959).

33. J. Douglas, Jr., and H. H. Rachford, Jr., "On the Numerical Solution of Heat Conduction Problems in Two and Three Space Variables," Trans. Amer. Math. Soc. 82, 421-439 (1956).

34. J. Douglas, Jr., "A Note on the Alternating Direction Implicit Method for the Numerical Solution of Heat Flow Problems," Proc. Amer. Math. Soc. 8, 409-412 (1957).

35. J. Heller, "Simultaneous, Successive and Alternating Direction Iteration Schemes," J. Soc. Ind. Appl. Math. 8, 150-173 (1960).

36. D. W. Peaceman and H. H. Rachford, Jr., "The Numerical Solution of Parabolic and Elliptic Differential Equations," J. Soc. Ind. Appl. Math. 3, 28-41 (1955).

37. E. L. Wachspress, "Optimum Alternating-Direction-Implicit Iteration Parameters for a Model Problem," J. Soc. Ind. Appl. Math. 10, 339-350 (1962).

38. E. L. Wachspress and G. J. Habetler, "An Alternating-Direction-Implicit Iteration Technique," J. Soc. Ind. Appl. Math. 8, 403-424 (1960).

39. R. S. Varga and M. A. Martino, "The Theory for the Numerical Solution of Time-Dependent and Time-Independent Multigroup Diffusion Equations" in "Proceedings of the Second United Nations International Conference on the Peaceful Uses of Atomic Energy, Geneva, 1958," Vol. 16, pp. 570-577, United Nations, Geneva, 1958.

40. M. M. Loeve, "Probability Theory: Foundations, Random Sequences," D. Van Nostrand Company, Inc., New York, 1955.

41. G. E. Albert, "A General Theory of Stochastic Estimates of the Neumann Series for the Solutions of Certain Fredholm Integral Equations and Related Series; Mathematical Panel," ORNL-1508, August 28, 1953.

42. J. Spanier, "Monte Carlo Methods and their Application to Neutron Transport Problems," WAPD-195, July 1959.

43. C. T. Ionescu Tulcea, "Mesures dans les espaces produits," Atti Accad. Naz. Lincei, Rend. Classe Sci. Fis. Mat. Nat. (8) 7 (1949), 208-211 (1950).

44. G. Goertzel, "Quota Sampling and Importance Functions in Stochastic Solution of Particle Problems," AECD-2793, November 7, 1949.

45. H. Kahn, "Applications of Monte Carlo," AECU-3259, April 19, 1954.

46. H. Kahn, "Use of Different Monte Carlo Sampling Techniques" in "Symposium on Monte Carlo Methods, University of Florida, 1954," H. A. Meyer, Ed., pp. 146-190, John Wiley and Sons, Inc., New York, 1956.

47. O. J. Marlowe, C. P. Saalbach, L. M. Culpepper, and D. S. McCarty, "WANDA — A One-Dimensional Few-Group Diffusion Equation Code for the IBM-704," WAPD-TM-28, November 1956.

48. O. J. Marlowe, "WANDA — A One-Dimensional Few-Group Diffusion Equation Code for the IBM-704," WAPD-TM-28 (Addendum 2), July 1959.

49. O. J. Marlowe and M. C. Suggs, "WANDA-5 — A One-Dimensional Neutron-Diffusion Equation Program for the Philco-2000 Computer," WAPD-TM-241, November 1960.

50. W. R. Cadwell and H. P. Henderson, "Input Preparation for Diffusion-Depletion Programs on the Philco-2000 Computer," WAPD-TM-238, January 1961.

51. G. G. Bilodeau, W. R. Cadwell, J. P. Dorsey, J. G. Fairey, and R. S. Varga, "PDQ — An IBM-704 Code to Solve the Two-Dimensional Few-Group Neutron-Diffusion Equations," WAPD-TM-70, August 1957.

52. W. R. Cadwell, "PDQ-3 — A Program for the Solution of the Neutron-Diffusion Equations in Two Dimensions on the IBM-704," WAPD-TM-179, May 1960.

53. W. R. Cadwell, "PDQ-4 — A Program for the Solution of the Neutron-Diffusion Equations in Two Dimensions on the Philco-2000," WAPD-TM-230, June 1961.

54. J. L. Fletcher, J. P. Jewett, and E. D. Reilly, Jr., "FLEER. A Two-Dimensional Triangular Mesh Diffusion Program for the IBM-704," KAPL-2086, May 6, 1960.

55. E. L. Wachspress, R. D. Burgess, and S. Baron, "Multichannel Flux Synthesis," Nucl. Sci. Eng. 12, 381-389 (1962).

56. E. H. Auerbach, J. P. Jewett, and M. A. Ketchum, "UFO: A Three-Dimensional Neutron Diffusion Code for the IBM-704," KAPL-1999, March 24, 1959.

57. O. J. Marlowe and P. A. Ombrellaro, "CANDLE — A One-Dimensional Few-Group Depletion Code for the IBM-704," WAPD-TM-53, May 1957.

58. J. B. Callaghan, L. M. Culpepper, J. G. Fairey, E. M. Gelbard, C. M. King, T. J. Lawton, O. J. Marlowe, and D. S. McCarty, "TURBO — A Two-Dimensional Few-Group Depletion Code for the IBM-704," WAPD-TM-95, November 1957.

59. D. S. McCarty, C. M. King, J. T. Mandel, and H. P. Henderson, "DRACO — A Three-Dimensional Few-Group Depletion Code for the IBM-704," WAPD-TM-137, December 1958.

60. O. J. Marlowe, "Nuclear Reactor Depletion Programs for the Philco-2000 Computer," WAPD-TM-221, January 1961.

61. C. J. Pfeifer and F. R. Urbanus, "ZIP-2 — A One-Dimensional Few-Group Synthesis Nuclear Reactor Depletion Program for the Philco-2000 Computer," WAPD-TM-228, November 1961.

62. J. A. Archibald, Jr., "CUREBO: A Generalized Two-Space-Dimensional Coding with Cross-Section and Depletion Calculations for the IBM-704," KAPL-1885, April 30, 1959.

63. E. L. Wachspress, "Digital Computation of Space-Time Variation of Neutron Fluxes," KAPL-2090, October 1, 1960.

64. H. Bohl, Jr., E. M. Gelbard, and G. H. Ryan, "MUFT-4 — Fast Neutron Spectrum Code for the IBM-704," WAPD-TM-72, July 1957.

65. H. Bohl, Jr., and A. P. Hemphill, "MUFT-5 — A Fast Neutron Spectrum Program for the Philco-2000," WAPD-TM-218, February 1961.

66. H. J. Amster and R. Suarez, "The Calculation of Thermal Constants Averaged over a Wigner-Wilkins Flux Spectrum: Description of the SOFOCATE Code," WAPD-TM-39, January 1957.

67. H. J. Amster and J. B. Callaghan, "KATE-1 — A Program for Calculating Wigner-Wilkins and Maxwellian Averaged Thermal Constants on the Philco-2000," WAPD-TM-232, October 1960.

68. R. W. Deutsch, "Computing 3-Group Constants for Neutron Diffusion," Nucleonics 15 (1), 47-51 (1957).

69. G. P. Calame, F. D. Federighi, and P. A. Ombrellaro, "A Two-Mode Variational Procedure for Calculating Thermal Diffusion Theory Parameters," Nucl. Sci. Eng. 10, 31-39 (1961).

70. G. P. Calame, "Direct Calculation of Asymptotic Diffusion Lengths and Diffusion-Hardened Spectra" in "Reactor Technology Report No. 15 — Physics," KAPL-2000-12, December 1960, pp. II.12-II.16.

71. B. L. Anderson, J. A. Davis, E. M. Gelbard, and P. H. Jarvis, "FLIP — An IBM-704 Code to Solve the P_L and Double-P_L Equations in Slab Geometry," WAPD-TM-134, March 1959.

72. H. Bohl, E. Gelbard, P. Buerger, and G. Culpepper, "SLOP-1, A Thermal Multigroup Program for the IBM-704," WAPD-TM-188, October 1960.

73. W. W. Clendenin and G. R. Culpepper, "ECESS — An IBM-704 Program Computing Transport Equation Coefficients for a Monatomic Gas Moderator in the Thermal Energy Region," WAPD-TM-200, April 1960.

74. H. Bohl, Jr., E. M. Gelbard, G. R. Culpepper, and P. F. Buerger, "P1MG — A One-Dimensional Multigroup P_1 Code for the IBM-704," WAPD-TM-135, July 1959.

75. E. Greuling, F. Clark, and G. Goertzel, "A Multigroup Approximation to the Boltzmann Equation for Critical Reactors," NDA 10-96.

76. L. A. Hageman and J. T. Mandel, "RANCH — An IBM-704 Program Used to Solve the One-Dimensional, Single Energy Neutron Transport Equation with Anisotropic Scattering," WAPD-TM-268, February 1961.

77. F. D. Judge, "Variational Method in the Calculation of Reactor Neutron Flux Density," KAPL-2151, February 21, 1961.

78. C. W. Dawson, "Thermal Energy Transport Code, TET," David Taylor Model Basin Report 1613, April 1962.

79. G. P. Calame and F. D. Federighi, "A Variational Procedure for Determining Spatially Dependent Thermal Spectra," Nucl. Sci. Eng. 10, 190-201 (1961).

80. R. M. Cantwell, "MO176 — A FORTRAN Program to Solve Several P-Approximations to the Few Group Neutron Transport Equation in Slab Geometry," WAPD-TM-320, April 1962.

81. A. J. Buslik, "The Description of the Thermal Neutron Spatially Dependent Spectrum by Means of Variational Principles" in "Bettis Technical Review, Reactor Technology," WAPD-BT-25, May 1962, pp. 1-24.

82. J. Spanier, H. Kuehn, and W. Guilinger, "TUT-T5 — A Two Dimensional Monte Carlo Calculation of Capture Probabilities for the IBM-704," WAPD-TM-125, November 1959.

83. J. Spanier, "The Physics and Mathematical Analysis for the TUT-T5 Monte Carlo Code," WAPD-TM-186, January 1960.

84. H. J. Berwind and J. Spanier, "TRAC-1. A Monte Carlo Philco-2000 Program for the Calculation of Neutron Capture Probabilities," WAPD-TM-229, March 1961.

85. M. A. Martino and W. W. Stone, "TRAM, A Monte Carlo Thermal Neutron Code for the IBM-704," KAPL-2039, June 19, 1959.

86. C. W. Maynard, "An Application of the Reciprocity Theorem to the Acceleration of Monte Carlo Calculations," Nucl. Sci. Eng. 10, 97-101 (1961).

87. E. M. Gelbard, H. B. Ondis, and J. Spanier, "MARC — A Multigroup Monte Carlo Program for the Calculation of Capture Probabilities," WAPD-TM-273, May 1962.

88. H. J. Amster, H. G. Kuehn, and J. Spanier, "EURIPUS-3 and DAEDALUS — Monte Carlo Density Codes for the IBM-704," WAPD-TM-205, February 1960.

89. H. J. Amster and H. G. Kuehn, "EURIPUS-4 and DAEDALUS-2," WAPD-TM-205 (Addendum), August 1960.

Two additional general references which relate to the concepts discussed in the mathematics of Monte Carlo for reactor calculation are:

G. Goertzel and M. H. Kalos, "Monte Carlo Methods in Transport Problems" in "Physics and Mathematics," Vol. 2 of Progress in Nuclear Energy, Series I, D. J. Hughes, J. E. Sanders, and J. Horowitz, Eds., pp. 315-369, Pergamon Press, Inc., New York, 1958.

H. Kahn and T. E. Harris, "Estimation of Particle Transmission by Random Sampling" in "Monte Carlo Method," A. S. Householder, G. E. Forsythe, and H. H. Germond, Eds., pp. 27-30, National Bureau of Standards Applied Mathematics Series 12, U. S. Government Printing Office, Washington, D. C., 1951.

CONTRIBUTING AUTHORS

H.J. Amster, Bettis Atomic Power Laboratory
D.R. Bach, Knolls Atomic Power Laboratory
H. Bohl, Jr., Bettis Atomic Power Laboratory
L. Bohl, Knolls Atomic Power Laboratory
R.J. Breen, Bettis Atomic Power Laboratory
S.I. Bunch, Knolls Atomic Power Laboratory
W.R. Cadwell, Bettis Atomic Power Laboratory
G.P. Calame, Knolls Atomic Power Laboratory
R.M. Cantwell, Bettis Atomic Power Laboratory
R.J. Cerbone, Knolls Atomic Power Laboratory
K.J. Chock, Bettis Atomic Power Laboratory
D.R. Connors, Bettis Atomic Power Laboratory
N.J. Curlee, Bettis Atomic Power Laboratory
R.C. Dahlberg, Knolls Atomic Power Laboratory
W.B. Doub, Bettis Atomic Power Laboratory
R.L. Ewen, Bettis Atomic Power Laboratory
F.D. Federighi, Knolls Atomic Power Laboratory
F. Feiner, Knolls Atomic Power Laboratory
N.C. Francis, Knolls Atomic Power Laboratory
R.C. Gast, Bettis Atomic Power Laboratory
E.M. Gelbard, Bettis Atomic Power Laboratory
D.T. Goldman, Knolls Atomic Power Laboratory
M. Goldsmith, Bettis Atomic Power Laboratory
J.N. Grace, Bettis Atomic Power Laboratory
G.J. Habetler, Knolls Atomic Power Laboratory
L.A. Hageman, Bettis Atomic Power Laboratory
W.H. Hannum, Bettis Atomic Power Laboratory
E.C. Hansen, Knolls Atomic Power Laboratory
J. Hardy, Jr., Bettis Atomic Power Laboratory
D.R. Harris, Bettis Atomic Power Laboratory
R.L. Hellens, Bettis Atomic Power Laboratory
A.F. Henry, Bettis Atomic Power Laboratory
L.O. Herwig, Bettis Atomic Power Laboratory
H. Hurwitz, Jr., Knolls Atomic Power Laboratory
G.L. Johns, Knolls Atomic Power Laboratory
F.D. Judge, Knolls Atomic Power Laboratory
S. Kaplan, Bettis Atomic Power Laboratory
D. Klein, Bettis Atomic Power Laboratory

H.G. Kuehn, Bettis Atomic Power Laboratory
J.H. Leonard, Bettis Atomic Power Laboratory
C.R. Lubitz, Knolls Atomic Power Laboratory
D.B. MacMillan, Knolls Atomic Power Laboratory
S.G. Margolis, Bettis Atomic Power Laboratory
C.W. Maynard, Bettis Atomic Power Laboratory
J.E. Meyer, Bettis Atomic Power Laboratory
D.F. Molino, Knolls Atomic Power Laboratory
B.H. Mount, Bettis Atomic Power Laboratory
W.A. Northrop, Knolls Atomic Power Laboratory
P.V. Oby, Knolls Atomic Power Laboratory
P.A. Ombrellaro, Knolls Atomic Power Laboratory
R.A. Pfeiffer, Knolls Atomic Power Laboratory
K.S. Quisenberry, Knolls Atomic Power Laboratory
A. Radkowsky, Naval Reactors
C.H. Randall, Knolls Atomic Power Laboratory
J.V. Reihing, Jr., Bettis Atomic Power Laboratory
E.D. Reilly, Jr., Knolls Atomic Power Laboratory
J.R. Roesser, Knolls Atomic Power Laboratory
T.F. Ruane, Knolls Atomic Power Laboratory
D.S. Selengut, Knolls Atomic Power Laboratory
B.E. Simmons, Knolls Atomic Power Laboratory
W. Skolnik, Knolls Atomic Power Laboratory
R.E. Slovacek, Knolls Atomic Power Laboratory
G.G. Smith, Bettis Atomic Power Laboratory
J.H. Smith, Knolls Atomic Power Laboratory
J. Spanier, Bettis Atomic Power Laboratory
S. Stein, Bettis Atomic Power Laboratory
M.L. Storm, Knolls Atomic Power Laboratory
H.L. Teaford, Knolls Atomic Power Laboratory
A.W. Thomas, Knolls Atomic Power Laboratory
W.H. Turner, Knolls Atomic Power Laboratory
F.R. Urbanus, Bettis Atomic Power Laboratory
J.J. Volpe, Bettis Atomic Power Laboratory
E.L. Wachspress, Knolls Atomic Power Laboratory
S. Weinstein, Knolls Atomic Power Laboratory
R.S. Wick, Bettis Atomic Power Laboratory
W.B. Wright, Knolls Atomic Power Laboratory

INDEX

C

D

E

F

G

H

I

K

L

M

Q

R

T

X

Y

Z